EVIDENCE OF A YSZ CONDUCTIVE PHASE NEAR SOFC ANODES

Michael B. Pomfret[a], Oktay Demircan[a], A. Mary Sukeshini[a], Gregory S. Jackson[b], Robert A. Walker[a,c]

[a]Department of Chemistry and Biochemistry, University of Maryland, College Park, MD 20742
[b]Department of Mechanical Engineering, University of Maryland, College Park, MD 20742
[c]Chemical Physics Program, University of Maryland, College Park, MD 207

Introduction

To date, research into fuel oxidation in fuel cells has focused on engineering and electrochemical issues to improve the overall cell efficiency.[1-4] While progress in these areas is important, numerous questions remain about the actual chemical mechanisms by which fuel cells, particularly solid oxide fuel cells (SOFCs), oxidize fuel to produce electricity, CO_2 and water. Identifying these reaction pathways should help improve cell efficiency and help minimize the problem of anode poisoning.

Due to its ability to conduct oxide anions at high temperatures (800 °C), yttria stabilized zirzonia (YSZ) has become the standard electrolyte in a wide variety of SOFCs.[2,5,6] Although several studies have cited a potential chemical role for YSZ related to reaction spillover from the anode onto the electrolyte,[7,8] there has been no consideration for YSZ's role in side reactions that might occur during SOFC operation. Previous work suggests that YSZ reduces in an oxygen-poor atmosphere such as that found on the anode side of a SOFC.[9] Furthermore, even modest currents are known to reduce YSZ so that it becomes electrically conducting. [15-17] Reduced forms of zirconium (Zr^{3+} and Zr^{2+}) have been shown to be very efficient catalysts in organic and polymer synthesis.[10-13] Should reduced YSZ in SOFCs have similar catalytic properties, then many existing models of fuel cell oxidation mechanisms have to be re-examined to consider alternative reaction pathways that are accessible on the electrolyte surface. Published reports already suggest that YSZ-based SOFCs can operate without a metal anode.[14] This condition necessarily requires that YSZ be electrically conductive, a property not considered in traditional SOFC models, but supported by several recent reports.[15-17] Much of our understanding about processes occurring in SOFCs has resulted from studies using classical electrochemical methods such as cyclic voltammetry and impedance spectroscopy. However, most of these studies have neglected to consider oxidation pathways out of those processes occurring at the anode/electrolyte boundary.

This work employs impedance spectroscopy to investigate the electrical conductivity of YSZ in a working fuel cell. Further evidence of a reduced conducting phase of YSZ on the anode side of SOFCs comes from comparing impedance data in the presence and absence of electrochemical operation. These results demonstrate a larger potential role for YSZ – or any reduced species – as a participant in current collection and fuel oxidation. With a complete understanding of the chemical and electrochemical properties of each SOFC component can fuel oxidation mechanism(s) be exhaustively identified. By identifying the conductive and chemical properties of an electrolyte we can begin to evaluate another source of non-anodic SOFC fuel chemistry.

Experimental

Fuel Cell Construction. The SOFCs used in this study consisted of an electrolyte supported, three-layer architecture with a 1.5 mm thick, 8 mole % YSZ electrolyte (ITN Energy Systems, Inc.) sandwiched between a porous LSM ($La_{0.85}Sr_{0.15}MnO_3$) cathode and a Ni/YSZ cermet anode. Both the anode and cathode were prepared by a tape casting method. The 12 mm diameter cathodes were sintered in air by heating to 400 °C at a rate 0.3 °C/min. The temperature was held at 400 °C for one hour before the cathodes were heated to 1300 °C at 3 °C/min. After one hour at 1300 °C, the sample temperature was lowered to 25 °C at 3°C/min. Ni/YSZ cermet anodes were prepared by tape casting a commercially available, 50% post-reduction Ni content NiO/YSZ cermet (NexTech Materials Lot # 112-45) over a 12 mm x 2 mm area in the center of the YSZ electrolyte. These anodes were then sintered at 1300 °C – the careful temperature cycle used for cathode sintering is not necessary for anode preparation. Two gold electrodes were placed on either side of the NiO/YSZ at 2.3 mm and 3.9 mm, respectively. The NiO/YSZ was reduced by an atmosphere of 5% H_2 – 95% Ar to Ni/YSZ while heating the fully assembled fuel cell assembly to operational temperature (800 °C) at 3 °C/min.

The membrane electrode assemblies (MEAs) were attached cathode-side-out to an alumina tube (22.2 mm OD, 15.9 mm ID) with a high temperature, zirconia-based ceramic paste. An alumina fuel-feed tube (4.8 mm OD, 3.2 mm ID) was centered in the larger tube and the entire assembly was placed in a temperature-controlled furnace. A second feeder tube was centered near the cathode to deliver air. Electronic mass flow controllers (Brooks 5850E) regulated the flow rates of the fuel stream. Data from the mass flow controllers were collected by a National Instruments SCXI data acquisition system. The cathode flow was regulated by a rotameter.

Cell Operation and Evaluation. H_2 was used as fuel for this experiment at an operating temperature of 800 °C. A 70 sccm flow of H_2 on the anode side was balanced by a 35 sccm flow of air on the cathode side. All experiments used a fuel flow of 33% fuel, with a balance of Ar.

An Autolab PGSTAT30 (Eco Chemie) was used to monitor fuel cell performance. AC impedance spectra were taken using five electrode configurations as shown in **Figure 1**. The first configuration measured the total cell impedance using the Ni/YSZ anode as the working electrode and the cathode as the counter electrode. The second and third configurations measured the anodic overpotential using the same working and counter electrodes while introducing each gold electrode individually as reference electrodes. The fourth and fifth configurations used the same working electrode, but employed each gold electrode individually as two separate counter electrodes. These last two configurations intended to measure the impedance across the YSZ surface between Ni/YSZ anode and the respective gold electrodes. Impedance spectra were made under open circuit conditions over a frequency range from 100 kHz to 10 mHz. A 6.00 mA current was drawn from the cell when measurements are not being made.

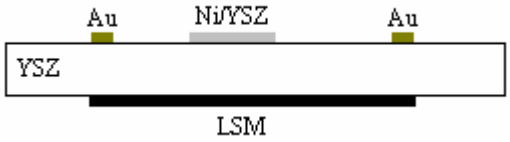

Figure 1. Scheme of the YSZ electrolyte supported fuel cell with a LSM cathode, Ni/YSZ cermet anode and two gold reference electrodes.

Results and Discussion

Once the SOFC is at 800 °C the performance is monitored with IV curves to ascertain system stability and reproducibility. Once cell performance has become stable, impedance measurements begin. **Figure 2** shows the impedance curves of the fuel cell. The data

corresponding to the cell operating without a reference electrode displays a polarization resistance (R_P) of 73.7 Ω that is largely electrolytic, but also contains cathode and anode related processes. When an inert Au reference is employed on the anode side, the data show the impedance associated primarily with the anode overpotential. Cathode impedance data are not represented in the curve, resulting in the smaller R_P. Ideally the two referenced impedance curves would be identical since the same anode is used in each measurement. The 12.1 Ω difference in the impedance curves when using two separate reference electrodes suggest an irregularity in reference electrode contact resistance, likely due to imperfections in the electrodes.

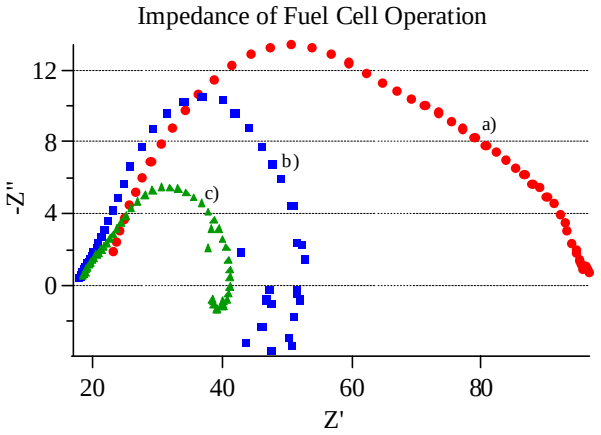

Figure 2. Impedance curves of the operational fuel cell with a) Ni/YSZ anode and LSM cathode, b) a gold reference 3.9 mm from the anode and c) a gold reference 2.3 mm from the anode.

To investigate the interaction between the two Au references and the Ni/YSZ anode, the impedance was measured between the anode and each of the references – now operating as counter electrodes – individually. **Figure 3** shows the impedance curves of the Ni/YSZ – Au systems. Also included is an impedance curve of an Au electrode 1.3 mm from the anode on an inoperable fuel cell without a cathode lead.

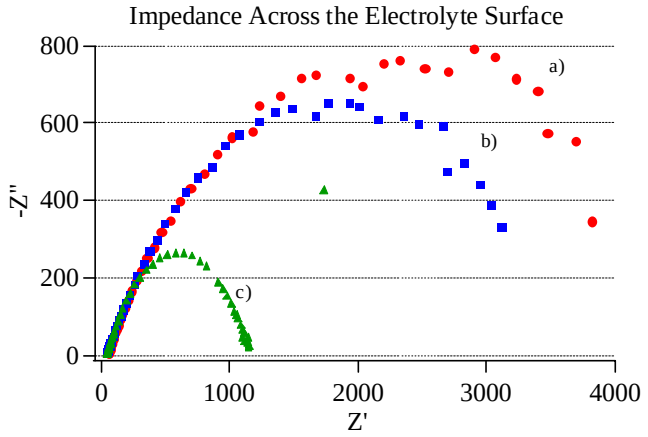

Figure 3. The impedance across the surface a) from a Ni/YSZ anode to a gold cathode 3.9 mm away, b) to a gold cathode 2.3 mm away, and c) to a gold cathode 1.3 mm away in a non-electrochemically active cell.

The oscillation of the 2.3 mm and 3.9 mm Au counter electrode curves at lower frequencies and the incomplete arcs indicate that the YSZ between the Ni/YSZ and Au electrodes never reaches full DC conductance. The arcs are fit as semi-circles and an impedance for the YSZ surface is extrapolated in each case. The resulting values were 3.41 kΩ for the 2.3 mm electrode separation case and 4.03 kΩ when the electrodes are 3.9 mm apart. These values are then normalized to 1mm, resulting in a mean value of 1.26 ± 0.23 kΩ/mm. Assuming uniform resistance across the YSZ surface, the first micrometer away from the anode has a resistance of ~1 Ω, implying that fuel oxidation and current collection can occur at considerable distances from the anode/electrolyte boundary.

The curve of the Ni/YSZ – Au electrode in the absence of electrochemistry gives a surface impedance value of 0.85 kΩ/mm, a drop of 31.4% from the operational fuel cell surface. The arc is also complete and does not oscillate suggesting a DC conductive YSZ surface. Given the extremely small current passed during impedance measurements, the conductivity in this case is thought to result primarily from chemically, not electrically, reduced YSZ as has been reported previously.[15-17] The difference in the conductivity of the cell without electrochemistry is likely due to the lack of O^{2-} flux. When electrochemistry is occurring the O^{2-} flux repopulates the reduced YSZ surface sites.

Conclusion

The present experiment clearly demonstrates the conductive behavior of the YSZ surface in a SOFC. The conductivity of the YSZ surface is enhanced when electrochemistry is halted. These results suggest a degree of YSZ reduction on the anode (fuel) side of SOFCs. This reduced electrolyte may participate in electrochemical fuel oxidation as well as non-electrochemical side reactions. Future experiments will aim to devise a chemical mechanism based on the knowledge of the presence of reduced YSZ on the anode side.

Acknowledgement. This work is supported by the Office of Naval Research through the MURI grant # 0110138816, in association with the Colorado School of Mines and CalTech.

References

(1) Minh, N. Q. *Solid State Ion.* **2004**, *174*, 271-277.
(2) Ormerod, R. M. *Chemical Society Reviews* **2003**, *32*, 17-28.
(3) Srikar, V. T.; Turner, K. T.; Ie, T. Y. A.; Spearing, S. M. *J. Power Sources* **2004**, *125*, 62-69.
(4) Weber, A.; Ivers-Tiffee, E. *J. Power Sources* **2004**, *127*, 273-283.
(5) Song, C. S. *Catal. Today* **2002**, *77*, 17-49.
(6) Zhu, W. Z.; Deevi, S. C. *Materials Science and Engineering* **2003**, *A362*, 228-239.
(7) Bieberle, A.; Swiss Federal Institute of Technology: Zurich, Switzerland, 2000.
(8) Basini, L.; Cavalca, C. A.; Haller, G. L. *J. Phys. Chem.* **1994**, *98*, 10853-10856.
(9) Pomfret, M. B.; Stoltz, C.; Varughese, B.; Walker, R. A. *Anal. Chem.* **2005**, *77*, 1791-1795.
(10) Miller, T. M.; Grassian, V. H. *Journal of the American Chemical Society* **1995**, *117*, 10969-10975.
(11) Miller, T. M.; Grassian, V. H. *Catalysis Letters* **1997**, *46*, 213-221.
(12) Marek, I., Ed. *Titanium and Zirconium in Organic Synthesis*; Wiley-VCH, Inc.: Weinheim, Germany, 2002.
(13) Busca, G. *Catal. Today* **1996**, *27*, 323-352.
(14) Hirabayashi, D.; Tomita, A.; Brito, M. E.; Hibino, T.; Harada, U.; Nagao, M.; Sano, M. *Solid State Ion.* **2004**, *168*, 23-29.
(15) Wright, D. A.; Thorp, J. S.; Aypar, A.; Buckley, H. P. *Journal of Materials Science* **1973**, *8*, 876-882.
(16) Nagle, D.; PaiVerneker, V. R.; Petelin, A. N.; Groff, G. *Mat. Res. Bull.* **1989**, *24*, 619-623.
(17) Levy, M.; Fouletier, J.; Kleitz, M. *J. Electrochem. Soc.* **1988**, *135*, 1584-1589.

PHYSICAL CHEMISTRY STUDIES OF PROTON CONDUCTION IN HETEROPOLY ACIDS

Fanqin Meng,[1] James Horan,[2] Jennifer L. Malers,[1,3] Steven F. Dec,[2] Andrew M. Herring,[1] John A. Turner[3]

Department of Chemical Engineering[1] and Chemistry and Geochemistry[2]
Colorado School of Mines
Golden, CO 80401-1887

Hydrogen and Electricity, Systems and Infrastructure Group[3]
National Renewable Energy Laboratory
Golden, CO 80401-3393

Introduction

The importance of fuel cells has been recognized as the world confronts more and more severe fossil fuel shortage. Among others, proton exchange membrane fuel cell system is seen to be best suitable for vehicle power applications. Although the PEMFC technology has advanced quickly in the past years, a number of issues remain to be resolved, such as to enhance the functionality of these devices under dry gas condition at 80 °C and above. However, the current state-of-art PEMs are based on perfluorinated sulfonic acid polymer such as Nafion®, which decomposes above 100 °C and requires rigorous hydration for continuous operation. HPAs are promising PEM materials because they have exhibited exceptional proton conductivity not only at ambient temperature, but also at elevated temperatures without external humidification.

The most thoroughly studied HPA, 12-tungstophosphoric acid, exhibited proton conductivity of 0.2 S/cm^2 at room temperature,[1] higher than that reported for Nafion®. Meanwhile, a variety of HPAs have shown high water retention and the protons remain mobile at elevated temperatures according to the literature and the work done in our laboratory. These properties are ideal for an electrolyte material in PEM fuel cells to be operated at elevated temperatures and low relative humidity. While this is a huge class of materials, only the few commercially available HPAs have been studied to any great extent. A large number of HPAs are readily available to synthetic chemists. Furthermore the simple salts of the HPA almost always contain residual protons. We therefore synthesized a library of HPA where charge, shape and hydration state were varied, and investigated their proton conduction structures in the solid state using TGA, IR and NMR techniques.

Experimental

HPA sample preparation. The syntheses of many heteropoly acids are well documented.[2] In general, HPAs are made by acidification of solutions containing the requisite simple anions or by introduction of the heteroelement after first acidifying the tungstate. Lacunary HPAs are obtained by removal of one or more tungsten with the terminal oxygen atoms at higher pH. The HPA anions are typically isolated as their potassium salts first, and then free acids are obtained by column exchange or an acid-ether extraction method.

Characterization Methods. TGA-DTA (thermal gravimetric analysis and differential thermal analysis) measurements were performed over a temperature range of 20 to 600 ºC using a Seiko SSC/5200 with a heating rate of 5 ºC min^{-1}. Powder X-ray diffraction patterns were recorded using a Scintag X-ray diffractometer using Cu K_α radiation. All MAS (magic-angle spinning) ^{1}H spectra were recorded on a two-channel Chemagnetics CMX Infinity 400 NMR spectrometer operating at 400.0 MHz, using a Chemagnetics 5mm double-resonance MAS probe equipped with a Pencil spinning module, sample spinning at 10 kHz. Proton diffusion measurements were performed with the use of a 5mm Doty Scientific, Inc. #20-40 z-gradient pulsed-field gradient NMR probe. The stimulated-echo pulse sequence[3] was used and the gradient coil was calibrated using water at 25 ^{o}C. The resulting NMR spectra were integrated and fit to a two-Gaussian decay using Spinsight® software available from Varian, Inc. DRIFTS (diffuse reflectance FTIR spectroscopy) samples were heated *in situ* (ambient temperature to 150 °C) under constant helium flow, the spectra were recorded on a Thermo Nicolet Nexus 670 FT-IR spectrometer using the Omnic®6.0 software package and with a specially designed Harrick Praying Mantis diffuse reflection attachment.

Results and Discussion

TGA results of the HPAs can generally be defined in terms of the following generalities. At ambient conditions a large amount of loosely bound disorganized water is associated with the HPA, many HPAs are hydroscopic so the amount of this low temperature water can be very variable depending on the ambient conditions. At ambient conditions the HPA secondary structure truly is a "pseudo-liquid" phase and explains the high conductivity of these materials at room temperature. Above 100 °C there is usually a significant but smaller amount of more tightly bound water which is held positionally but is free to rotate, it is this tightly bound secondary structure water and its movement that is important to understand so that HPA proton conductors for elevated temperatures can be designed. We have found that if one heats an HPA above 100 °C it will eventually, over a period of months, reach a limiting hydration state where the residual waters do not leave the lattice and are presumably necessary for structural stability. At temperatures above 200 °C a further mass loss is observed, which has been ascribed to a neutralization reaction in which the anhydrous proton associates itself with the HPA as an OH and two such protons leave with a structural oxygen atom as water leaving behind a neutralized HPA. This transition is irreversible and eventually a neutral oxide is formed. At much higher temperatures >400 °C an exotherm is observed which signifies the decomposition of this oxide.

DRIFTS spectra of the free acid HPAs not only show information on the bonding of water and protons but also show changes in the outer anion bands as these bonds become more or less involved in bonding to the secondary structure. The υ(OH) can be fit to a number of OH stretches involved with progressively stronger hydrogen bonding from a free OH at 3640 cm^{-1} to an OH involved in a strong O-H…O at 1100 cm^{-1}or lower. As the strength of the H-bonds increases, the peaks become progressively broader and appear at lower wavenumbers. Using the peak positions and areas under them it is possible to calculate an ΔH_{ave} for the hydrogen bonds in the system.[4] When a hydrogen bond is formed "the IR wavenumber of the OH stretching vibration shifts to a low wavenumber and generates heat ($\Delta H < 0$)."[5] The DRIFTS of 12-phosphotingstic acid from ambient temperature to 350 °C is shown in Figures 1-2.

We expect structures containing OH to be poor proton conductors, as the energy required to break the OH bond would be close to the energy required to neutralize the HPA. Only 21-HAs2W and 39-HB3W show no evidence of OH. For the vehicle mechanism to prevail structures with $H^+(H_2O)_x$ are expected to be favorable and 12-HSiW, 12-HSiV3Mo, 21-HAsW and 39-HB3W all show this phase above 100 °C. Of course we can't distinguish between $H^+(H_2O)_x$ and a mixture of $H_5O_2^+$ and H_3O^+. More favorable for low humidity applications would be proton conduction by a purely

Grotthus mechanism and a number of phases are present that do not contain $H^+(H_2O)_x$ which may exhibit this phenomenon.

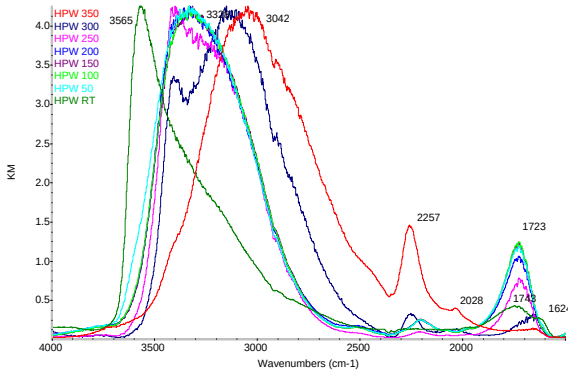

Figure 1. DRIFTS of the OH band region for $H_3PW_{12}O_{40}$ under He at different temperatures.

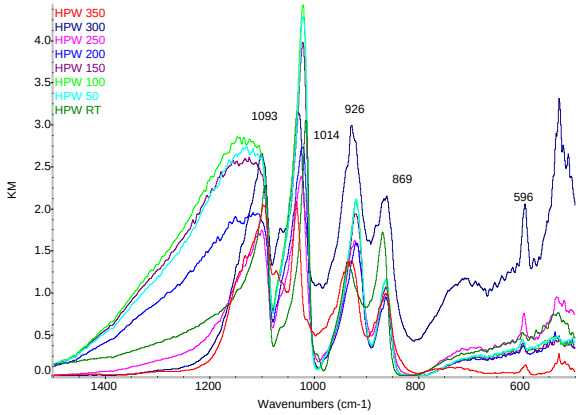

Figure 2. DRIFTS of the anion band region for $H_3PW_{12}O_{40}$ under He at different temperatures.

Table 1 summarizes some of the structural and diffusion data discussed above for the free HPA. Generally for the Keggin HPA, the maximum diffusion coefficients decrease and the activation energies increase as the central heteroatom becomes heavier. This is reflected in the increased observation of OH. The lacunary material, 11-HSiW, has a very low activation energy, but we suspect that not all the protons in the sample are mobile as the IR shows the presence of immobile OH. For this the calculated IR H-bond strength is instructive, where it matches the activation energy we can assume that all observed H_2O and H^+ are involved in H^+ transport, where it is much higher we can infer that some of the H_2O and H^+ are not available for H^+ transport. This is almost certainly the case for the sterically hindered 39-HB3W where presumably proton transport is facile between the sheets of the structure but restricted in other dimensions, note that the IR bond strength is higher than the observed activation energy. The activation energy matches the H-bond strength for 21-HAs2W and so presumably all the secondary structure is involved in proton transport and the same is almost true for 21-HP2W. The channels of the partial Rb salt of 21-diarsenotungstic acid, give a very high diffusion coefficient but this is not applicable at higher temperatures as the channels are easily dehydrated.

Table 1. Summary of Diffusion Coefficients for HPAs

HPA	Max Diffusion Coefficients $\times 10^{-6}$ $cm^2 \cdot s^{-1}$	Temperature of maximum D, °C	Ea before max T $kJ \cdot mol^{-1}$
12-HPW	25	117	13
12-HSiW	30	130	20
12-HZnW	2	108	27
12-HGeW	0.7	90	35
11-HSiW	3	108	6
39-HB3W	7	128	8
18-HP2W	1.2	> 150	20
21-HAs2W	3.7	> 150	20
21-H2Rb4As2W	30	25	-
21-HP2W	2.3	110	24

Conclusions

The HPA act as good model compounds for the study of proton conduction in the solid state, using TGA, NMR, IR, and X-Ray diffraction we were able to probe the proton conducting structures in these materials. This information was correlated with diffusion coefficients measured by pulse field gradient spin echo NMR in order to elucidate the proton conduction mechanisms observed.

Acknowledgment

This work was supported by the US DOE science initiative, DE-FC02-0CH11088.

References

1. Nakamura, O., Kodama, T., Ogino, I., Miyake, Y. *Chem. Lett.*, 17-8, **1979**
2. Early Transition Metal Polyoxoanions. *Inorganic Syntheses.* A. P. Ginsberg, John Wiley and Sons. 1990, **27:** 71.
3. Tanner, J. E. *The Journal of Chemical Physics* **1970**, *52*, 2523. 159
4. Miura, K., Mae, K., Li, W., Kusakawa, T., Morozumi, F. and Kumano, A., "Estimation of Hydrogen Bond Distribution in Coal through the Analysis of OH Stretching Bands in Diffuse Reflectance Infrared Spectrum Measured by in-Situ Technique", *Energy & Fuels*, **15**, 599 (2001).
5. K. Miura, K. M., W. Li, T. Kusakawa, F. Morozumi, A. Kumano, "Estimation of Hydrogen Bond Distribution in Coal through the Analysis of OH Stretching Bands in Diffuse Reflectance Infrared Spectrum measured by in-Situ Technique", *Energy & Fuels*, **15**, 599 (2001).

NOVEL PROTON CONDUCTIVE MEMBRANE BASED ON CLAY

Takuichi Arai, Gen Ikeda and Masatugu Nakanishi

Functional Material Dept.
Material Engineering Div. II
Vehicle Engineering Group.
Toyota Motor Corporation
1, Toyota-Cho, Toyota,
Aichi, 471-8572 JAPAN

Introduction

Perfluorinated proton conducting polymers such as Nafion® have been studied for using in proton exchange membrane fuel cell at low temperature. However, these polymers have several problems such as thermal stability and their costs. To improve above problems, applications of inorganic materials have been investigated as additives in an organic matrix[1] but are still far from essential solution.

In this study, a novel fully inorganic material, a kind of clay, is investigated as a proton conducting membrane. Montmorillonite (MON) which is the clay investigated in this study is layered compound, has high ion exchange capacity and can be expected to show proton conductivity by exchanging cations at interlayer of MON for protons.

Experimental

Membrane preparation MON membrane was prepared by phosphoric acid treatment method.[2] At first, 2.6 wt% of the MON dispersed solution was prepared by addition of sodium MON (Na^+-MON) in deionized water under constant stirring for more than 12 hours. Excess amount of conc. ortho phosphoric acid was added to the MON dispersed solution while stirring. After continuous stirring for 1 hour, the obtained mixture was a slightly turbid dispersion and was cast on polystyrene dishes. The opaque brown membrane was obtained after drying for 2 weeks at room temperature and following hardening process at 70 °C for 12 hours. The membranes were peeled from dishes and washed by deionized water to remove excess phosphoric acid and to obtain protonated MON (H^+-MON). Finally, the membranes were dried in air at 40 °C for 12 hours.

Characterization and measurement To confirm the result of cation exchange, elemental analysis of Na^+-MON and H^+-MON were done with X-ray fluorescence spectroscopy. Layered morphology and crystal structure were investigated by scanning electron microscope (SEM) and X-ray diffraction (XRD), respectively.

The proton conductivity was determined by ac impedance conductivity measurement using an impedance analyzer (NF corp., NF5090) in the frequency range between 1 Hz to 2 MHz. The temperature and humidity were controlled at 80 °C and 30-90 %RH, respectively, in a chamber.

Results and Discussion

Figure 1 shows a photograph and a cross sectional SEM image of the membrane. As shown in **Figure 1** (a) the membrane was self-supporting and showed flexibility in spite of entirely inorganic membrane.

MON is a layered clay containing cations in the interlayer and known to be bridged each other through phosphoric acid at the edge of layers. Layered structure observed in **Figure 1** (b) is thought to reflect the layered structure of bridged H^+-MON.

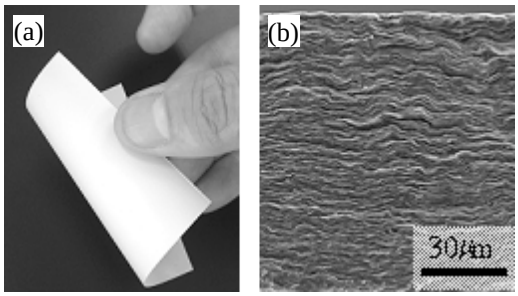

Figure 1. (a) a external view and (b) SEM image of cross section of the H^+-MON membrane.

The result of elemental analysis of H^+-MON showed elimination of sodium cations which is observed Na-MON, *i.e.*, sodium cations in the interlayer of the MON are completely exchanged for protons. The results of XRD measurement show 5 Å of increase in the interlayer distance of H^+-MON compared to Na-MON. The increment of interlayer distance should be a result of cation exchange because proton is expected to form hydronium ion which is larger than sodium ion. However, the difference in diameters of hydronium ion and sodium ion is smaller than 1 Å and it is difficult to explain the difference in interlayer distance by the difference of diameters of cations. Therefore, proton forms cluster larger than hydronium ion or excess amount of water is contained in the interlayer of H^+-MON.

The proton conductivity of H^+-MON membranes at 80 °C is shown in **Figure 2** as a function of relative humidity. The H^+-MON membrane exhibits high conductivity of $1x10^{-2}$ S/cm at 90 %RH. Observed conductivity strongly depending on relative humidity suggest proton conducting mechanism in H+-MON strongly depends on water content of the membrane, *i. e.*, dehydration of the interlayer cause rapid decrement in conductivity.

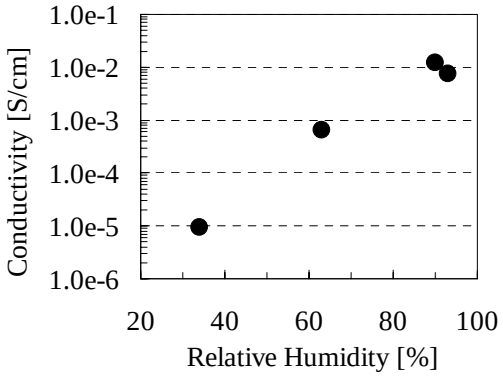

Figure 2. Proton conductivity of H^+-MON as a function of relative humidity at 80°C

Acknowledgment. The authors thank the valuable advices of Dr. Isayama of Fukuoka Industrial Technology Center and express appreciation to Kunimine Kogyo Ind. Ltd. for providing samples.

References

(1) Jones, D. J.; and Roziere, J. In *Handbook of Fuel Cells Fundamentals Technology and Applications*; Vielstich, W.; Gasteiger, H. A.; and Lamm, A. Ed.; John Wiley & Sons Ltd., 2003; (3), pp. 447-455

(2) Isayama, M.; Sakata, K.; and Kunitake, T. *Chem. Lett.*, pp. **1993**, 1283-1286

MESOPOROUS CERAMIC OXIDES AS PROTON EXCHANGE MEMBRANES

Warren H.J. Hogarth[1], João C. Diniz da Costa[1], John Drennan[2], G.Q.(Max) Lu[1]

[1]ARC Centre for Functional Nanomaterials
[2]Centre for Microscopy and Microanalysis
The University of Queensland, Brisbane 4072 AUSTRALIA

Introduction

While Nafion® is currently the benchmark proton exchange membrane (PEM) technology, it has many limitations. For example, many manufactures of PEM fuel cells for vehicle applications would like to operate the cells at high temperatures (>140^{o}C) because of CO poisoning, heat management and cost challenges.[1] At present, state of the art polymer membrane technology cannot operate in this temperature range because it degrades and looses water necessary to conduct protons. Current polymer technology is also limited in its operation lifetime and by mechanical properties.

Moving away from polymer technology has also presented similar problems. Solid acid membranes have been shown to operate well in limited temperature regimes. However they often suffer more significant mechanical shortcomings than their polymer counterparts.

Recently we proposed a new membrane design for high temperature operation based on surface functionalized mesoporous solid acid membranes[1] and demonstrated the first steps of an approach to systematically design the required membranes.[2] These membranes have the ability to be synthesized into robust thin membranes, are highly taylorable and do not suffer the same cost constraints as flourinated polymers.

Our recent work expands on these concepts demonstrating how it is possible to engineer membranes to predetermined requirements. We discuss the process of exploiting self assembly to engineer new PEMs based on current state of the art technology. The discussion is supported by a demonstration of how this process can be applied and demonstrates the flexibility that this easily tunable procedure affords.

Experimental

Samples were prepared using sol-gel synthesis techniques following a route similar to Tian et al.[3] and Soler-Illia et al.[4-6] Tri-block copolymers (Pluronic P123 or F127) were dissolved in a solution of ethanol before adding metal oxide and phosphor precursors. The molar ratio of copolymer:metal precursor:phosphor precursor:water was 70:1:2:20. Samples were either gelled to form xerogels or dip coated to form thin films under controlled temperature and relative humidities. Selected samples were calcined up to either 350^{o}C or 550^{o}C at 1^{o}C.min^{-1}.

Nitrogen Sorption. Surface area and pore size analysis was conducted using a Quantachrome Nova 1200 in a liquid nitrogen dewar. BET analysis was used to determine the surface area and BJH desorption isotherms were used for pore size distributions.

TEM. Transmission electron microscopy (TEM) was undertaken using a Tecnai T20 Field Emission Electron Gun Transmission microscope operating at 200 kV. Thin film samples prepared as described elsewhere[7] were scraped from their glass substrates and coated onto holey carbon film supported by a copper grid. The samples appeared to be stable under the beam.

a.c. impedance spectroscopy. Impedance spectroscopy was conducted using a Solatron 1260 in standalone mode for proton conductivity measurements. The frequency was cycled between 10 and 3.2e07 Hz. Samples were equilibrated at specific relative humidities over saturated salt solutions for a minimum of 7 days prior to testing.

Results and Discussion

Materials Design. The concept of the design of a new proton conductor needs to be considered from a fundamental basis. Detailed consideration must be given to the specific advantages and disadvantages of the current technology that should be retained and the failures of the competing technologies.

The unique properties of Nafion membranes are its stable perflourniated backbone for morphological stability and its highly interconnected, acidic, hydrophilic channel (or cluster) network that extend throughout the membrane. While extensive research on zirconium hydrogen phosphates was able to replicate the conductivity showed by Nafion,[8-11] it cannot be fabricated into a robust membrane. From a fundamental perspective, the key to the high proton conductivity of Nafion is its strong acidity, caused by anchored functional groups which are highly interconnected and able to arrange into the lowest energy configuration giving the highly interconnected pore network which provides the conduction pathways.

Materials Synthesis. Recent advances in mesoporous material synthesis provide an avenue to replicate the fundamental properties of Nafion while providing a robust supporting matrix and overcoming the shortfalls of zirconium hydrogen phosphates. Figures 1 and 2 demonstrate that self assembled, high surface area, ordered, interconnected, mesoporous zirconium phosphates can be synthesized forming the backbone of these new proton conductors. It has also been demonstrated that they can easily be synthesized into thin films, capable of being barrier to feed fuels.

Figure 1 shows a typical type IVb adsorption isotherm which is produced by these materials. The pronounced H2 type hysterisis loop indicates that the samples are mesoporous. The hysterisis is a consequence of the interconnectivity of the real porous network and is caused by pore blocking and network effects.[12] The pores have an average pore size between 2 and 4 nm.

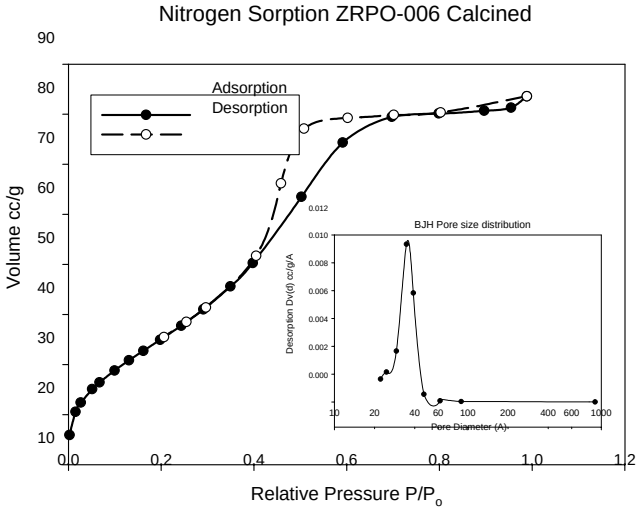

Figure 1. Typical nitrogen sorption isotherm for self assembled mesoporous zirconium phosphate.

Figure 2 shows the TEM image of the zirconium phosphate sample synthesized from trimethyl phosphate and zirconium tetrachloride precursors and Pluronic F127 as the structure directing agent. Long range hexagonal mesostructure is evident with pore diameters of approximately 4 nm confirming the nitrogen sorption results. This structure has also been synthesized using the appropriate alkoxide and phosphorous trichloride precursors. In

addition Figure 2 provides a good pictorial representation of the interconnected pore network and how these may form ion transport channels when functionalized.

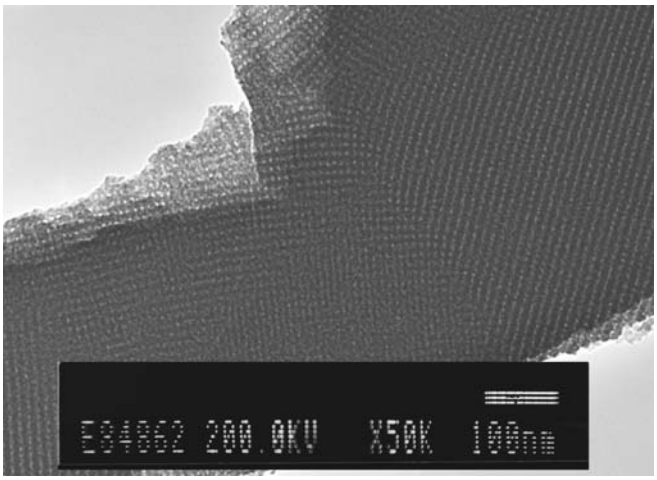

Figure 2. Two dimensional TEM pattern of mesoporous zirconium phosphate from a thin film sample heat treated to 130°C.

Functionalizing for Conductivity. After creating a highly controlled and taylorable functional matrix material, the next challenge is to engineer the conducting pathways. This can be achieved either during the synthesis steps or as a post-fictionalization process.

Figure 3 shows the inherent conductivity of the backbone and demonstrates the applicability of this class of materials as proton conductors. While the conductivity is low compared to Nafion, the conductivities are equal to that of other solid acids prior to functionalization. For example, the highest conductivity achieved was 1.5x10-6 S.cm^{-1} at 22°C and 85% RH. This is an improvement of approximately 2 fold on the results reported elsewhere for sol-gel zirconium phosphates[3, 13] and comparable to α-zirconium hydrogen phosphate.[14]

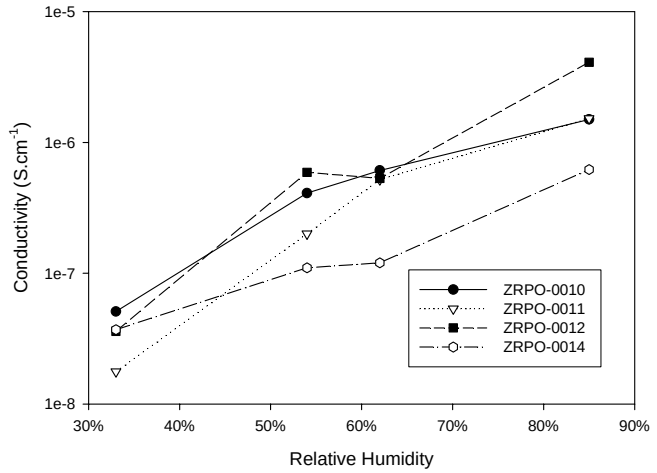

Figure 3. Proton conductivity of mesoporous zirconium phosphates, demonstrating the inherent conductivity of the backbone matrix.[2]

One of the greatest advantages afforded to materials design by the self assembly route is the taylorability of the process. Figure 4 displays the impact of tuning the synthesis of mesoporous zirconium phosphates on the proton conductivity. It demonstrates how significant improvement can be made by understanding the synthesis process.

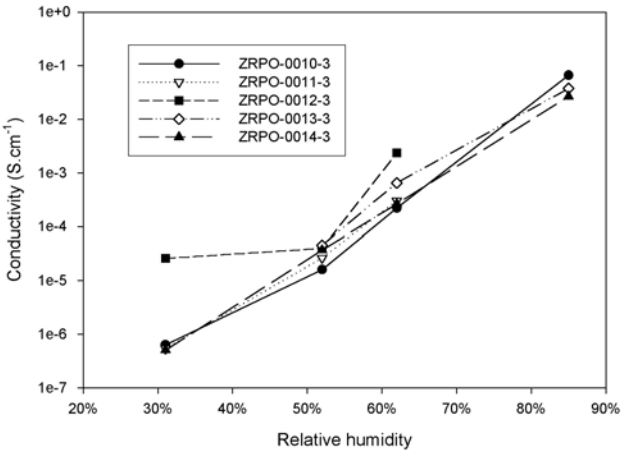

Figure 4. Proton conductivity of mesoporous zirconium phosphates after tuning the synthesis process.

Conclusions

We have demonstrated how the design of new fuel cell membranes can be achieved from a fundamental analysis. By taking the key properties of existing technologies and exploiting the advantages of ethanol-induced self assembly of mesoporous oxides we have been able to engineer designer materials to meet our required goals: a cheap, robust membrane which can be easily synthesized and which displays exceptional proton conduction.

Acknowledgement. The authors wish to thank the Australia Research Council Discovery Program (DP0344931) and the ARC Centre for Functional Nanomaterials for financial support. WH acknowledges the Australian-American Fulbright commission for financial support.

References

(1) Hogarth, W. H. J.; Diniz da Costa, J. C.; Lu, G. Q., *J. Power Sources* **2005,** *142* (1-2), 223.
(2) Hogarth, W. H. J.; Diniz da Costa, J. C.; Drennan, J.; Lu, G. Q. M., *J. Mater. Chem.* **2005,** *15* (7), 754.
(3) Tian, B.; Liu, X.; Tu, B.; Yu, C.; Fan, J.; Wang, L.; Xie, S.; Stucky, G. D.; Zhao, D., *Nat. Mater.* **2003,** *2*, 159.
(4) Soler-Illia, G.; Angelome, P. C.; Bozzano, P., *Chem. Commun.* **2004,** (24), 2854.
(5) Soler-Illia, G. J. D.; Sanchez, C.; Lebeau, B.; Patarin, J., *Chem. Rev.* **2002,** *102* (11), 4093.
(6) Soler-Illia, G.; Louis, A.; Sanchez, C., *Chem. Mater.* **2002,** *14* (2), 750.
(7) Soler-Illia, G.; Crepaldi, E. L.; Grosso, D.; Sanchez, C., *Curr. Opin. Colloid Interface Sci.* **2003,** *8* (1), 109.
(8) Alberti, G.; Boccali, L.; Casciola, M.; Massinelli, L.; Montoneri, E., *Solid State Ionics* **1996,** *84* (1-2), 97.
(9) Alberti, G.; Casciola, M., *Solid State Ionics* **1997,** *97* (1-4), 177.
(10) Clearfield, A., *Curr. Opin. Solid State Mat. Sci.* **1996,** *1*, 268.
(11) Clearfield, A.; Bortun, A. I.; Bortun, L. N.; Garcia, J. R., *Inorg. Chem. Commun.* **1998,** *1* (6), 206.
(12) Thommes, M.; Kohn, R.; Froba, M., *Studies in Surface Science and Catalysis*. 2002; (142), p 1695-1702.
(13) Rodriguez-Castellon, E.; Jimenez-Jimenez, J.; Jimenez-Lopez, A.; Maireles-Torres, P.; Ramos-Barrado, J. R.; Jones, D. J.; Roziere., J., *Solid State Ionics* **1999,** *125* (1-4), 407.
(14) Alberti, G.; Casciola, M. In *Layer Hydrates;* Colomban, P. Eds.; Cambridge University Press: New York, 1992; pp.238-251.

COMPOSITE PROTON EXCHANGE MEMBRANES

*Ping Liu and Gregory L Baker**

Department of Chemistry
Michigan State University
East Lansing, MI 48823

Introduction

The proton exchange membrane is one of the most important components of PEM fuel cells. Nafion® has long been the prototype membrane material, but its widespread application is limited by high cost and poor high temperature performance. One approach to low cost proton conducting membranes is the preparation of bicontinuous composite materials that combine a proton conducting phase with an insulating phase that provides mechanical stability.[1-2] Previous results from our lab (shown schematically below at left) show that mechanically stable Li^+ electrolytes are easily prepared by dispersing hydrophobic fumed silica particles in a hydrophilic polymer electrolyte matrix. The agglomerated silica forms a network structure within the polymer that dramatically improves the mechanical properties of the electrolyte.[3] Our hypothesis is that inverting the polarities and functions of the silica and surrounding polymer (shown at right) will lead to a similar network structure embedded in polymer, but in this case, the silica network will be the conductive phase. The silica networks in these materials might be thought of as a crude analog of the channel structure believed to be

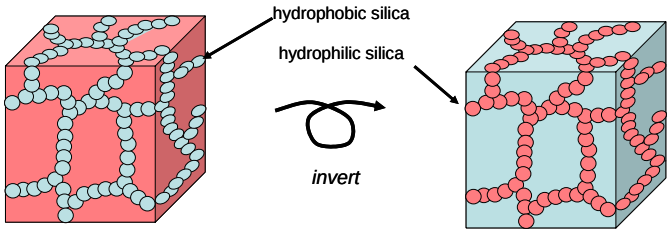

Scheme 1. Schematic diagram showing the structure of composite polymer electrolytes prepared by dispersing silica particles in a polymer matrix. At left, hydrophilic fumed silica is dispersed in a Li^+ conducting matrix to improve mechanical properties; at right, network formation polymer leads to a proton conducting network in a hydrophobic matrix.

important for ion conduction in Nafion®. Unlike Nafion®, however, the properties of these two-component composites can be easily tuned and membranes based on this approach should be available at lower cost.

The case described here is the preparation of silica particles decorated with sulfonic acids followed by their dispersal in a poly(vinylidine fluoride) (PVDF) matrix (Scheme 1). While a variety of organic and inorganic particles could be used, silica particles have good thermal and chemical stability, and are available in a broad range of sizes and surface areas. In addition, the chemistry needed to convert the silica surface to sulfonic acids is well-established and is practiced on a commercial scale. Since the number of sulfonic acid groups that can be placed on the surface is limited by the surface area of the particles (i.e. the number of silanols on the surface) we also can increase the effective concentration of acid groups by tethering polystyrene chains to the particle surface[2,5] followed by sulfonation of the polymer.[4] (Scheme 2).

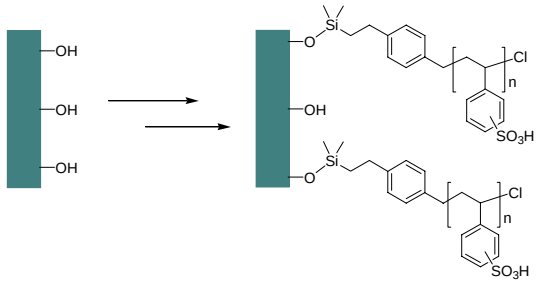

Scheme 2. Structure of the modified silica used in this work.

Experimental

Membranes were prepared by adding 0.01g of the modified silica (ground to a fine powder with a mortar and pestle) to 0.5 mL of DMF. After stirring until the solution was homogeneous, 0.5 mL of a solution of PVDF was added and the resulting solution was stirred until homogeneous (~4 hr). The solution was cast onto a glass slide heated to 50 °C on heating plat. After ~5 min, the glass slide was placed in a vacuum oven at 80 °C overnight. The dried membrane was cut into rectangular shape with a razor blaze, and the thickness of the membrane with measured with a micrometer. Membranes were conditioned by boiling the membrane in 8% HNO_3 for 30 min, rinsing with water, and then boiling the membrane in deionized water for 30 min. After blotting the membrane dry with filter paper, it was soaked in different concentrations of phosphoric acid and heated at 45 °C in a sealed vial for 3 days.

Results and Discussion

Scheme 1 shows the structure of the modified silica used in this work. Figure 1 shows influence of silica content on composite membrane on conductivity. Generally the conductivity rapidly increases with the silica (and sulfonic acid) content to ~30 wt%, followed by minor increases for >40 wt% silica. This behavior may represent a percolation threshold where the large increase in conductivity is related to increasing connectivity of the silica particle agglomerates in the PVDF matrix. The highest conductivity measured was 0.09 S/cm for a membrane with 50% silica, which is

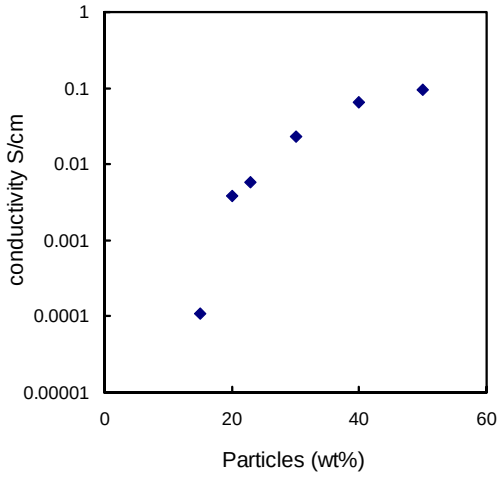

Figure 1. Room temperature proton conductivity of composite electrolytes as a function of silica content. Measurements were run at 100% humidity.

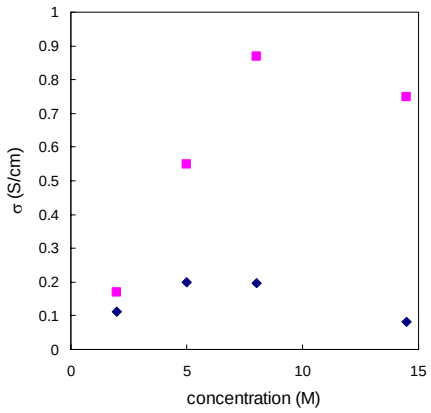

Figure 2. Conductivity of a membrane with 50 wt% silica after soaking in various concentrations of H_3PO_4 (squares). Data for H_3PO_4 solutions (diamonds) are shown for comparison

slightly higher then Nafion 117 measured under the same conditions (0.06 S/cm).

Addition of H_3PO_4 is a common strategy for increasing the protonic conductivity of polymer electrolytes. Figure 2 shows room temperature conductivity data for the membrane with 50% silica after soaking in different concentrations of H_3PO_4. Data for pure H_3PO_4 is shown for comparison. For these membranes, soaking in 8M H_3PO_4 resulted in the highest conductivity, which reflects a trade off between acid concentration and viscosity. Since PEM membranes that show useful conductivities >100 $^{\circ}$C are particularly desirable, we soaked membranes with various silica contents in 8M H_3PO_4 and measured their conductivity as a function of temperature at a water vapor pressure of 0.3 atmosphere. The data of Figure 3 show two effects. First, over the entire temperature range, the membrane conductivity increase almost linearly with the silica content, indicating the contribution of surface SO_3H groups to conductivity. Second, the temperature dependent conductivity of each membrane was similar, initially decreasing and then stabilizing at higher temperatures.

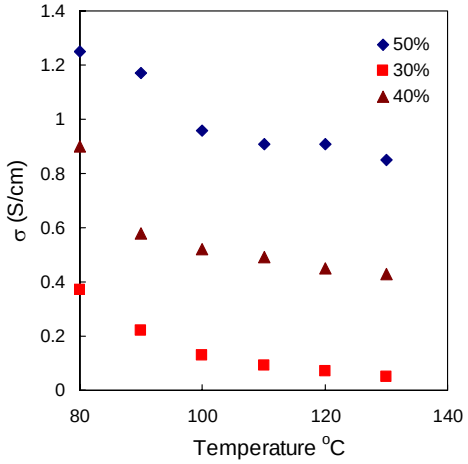

Figure 3. Temperature dependent conductivity for membranes prepared with different particle contents. Each membrane was soaked in 8 M H_3PO_4 prior to measurement.

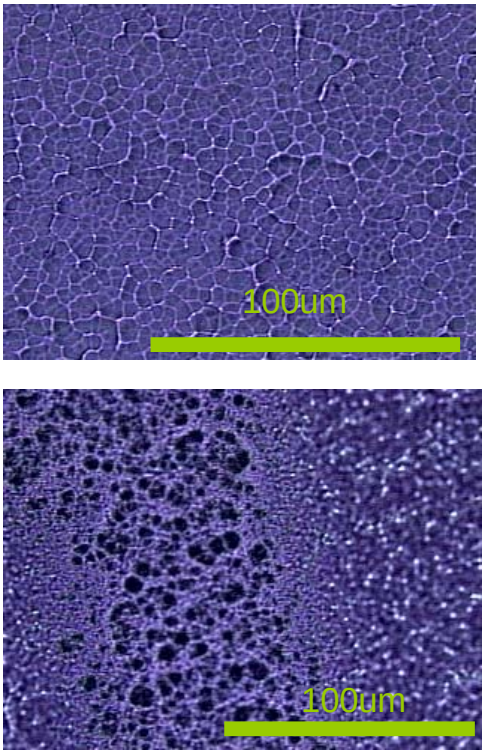

Figure 4. Transmission optical micrographs of PVDF (top) and a 50 wt% PVDF/silica composite (bottom) after soaking in H_3PO_4. The center of the lower micrographs shows the biphasic nature of the membranes.

Figure 4 shows the surface morphology of PVDF and a 50% PVDF/silica composite film. The biphasic structure is increasingly apparent as the silica content increases, in accord with the proposed model for network formation.

Conclusion

This paper provides proof of principle for the preparation of fuel cell membranes based on a "particle in polymer" approach. The composite membrane approach should permit some decoupling of the optimization of the conductivity and physical properties of the membranes. Current membranes have properties comparable to or better than Nafion®, and improvements in membrane properties are likely.

References

(1) G Alberti; M casciola, *Annu Rev Mater Res*, **2003**, *129-54*
(2) Kenji Miyatake; Masahiro Wantanabe, *Electrochem*, **2004**, *12-19*
(3) A S Khan; G L Baker; S Colson, *Chem Mater*, **1994**, *2359-63*
(4) T V Werne; T E Patten, *J Am Chem Soc*, **1997**, *7409-7410*
(5) Hunt, J. E.; Winans, R. E.; Ahrens, M.; and Xu, L. Prepr. Pap. - *Am. Chem. Soc., Div. Fuel Chem.*, **1999**, *44*, 610.

FORMATION OF CARBON DEPOSITS FROM HYDROCARBON FUELS IN SOLID OXIDE FUEL CELLS

Oktay Demircan, Mary Sukeshini, Bindhu Varughese, and Bryan W. Eichhorn

Department of Chemistry and Biochemistry,
University of Maryland,
College Park, MD 20742

Introduction

Fuel cells are currently drawing interest due to their high potential as stationary and portable power sources. Fuel cells are classified according to their electrolytes, which separate the anode compartment from the cathode compartment. High-temperature solid oxide fuel cells (SOFCs) employ solid oxide electrolytes making them distinct from other types of fuel cells. The solid electrolytes are electronic insulators and designed to conduct O^{2-} ions and operate at high temperatures (>500^{o}C).[1] The typical fuels used in fuel cells are either hydrogen or hydrocarbons. These high temperatures help the oxidation of hydrocarbons so that SOFCs can use fossil-derived natural resources such as natural gas, petroleum distillates, liquid propane and gasified coal, as well as renewable sources such as hydrogen, methanol, and ethanol. Logistic fuels (diesel fuel, gasoline, and jet fuel (JP-8)) are likely to be transition energy sources for fuel cells before hydrogen takes the place of fossil fuels.

Typical SOFC anodes are composed of a catalyst to oxidize the fuel, a conductive material to collect current, and an interface material between catalyst and electrolyte (8 mole % yttria stabilized zirconia, YSZ, in this study). Many research groups have focused on Ni based SOFC anodes due to its low cost compared to other metals. Ni is a well-studied catalyst for the oxidation of hydrogen. However, Ni also catalyzes coke formation[2] on the anode surface with hydrocarbon fuels which inhibits cell performance and causes anode degradation. Several research groups have considered different anode materials to avoid coke formation. Cu/CeO_2/YSZ anodes have been investigated for the electrochemical oxidation of longer chain hydrocarbons. Ceria (CeO_2) has been well established as a catalyst for methane oxidation and for hydrocarbon activation.[3] However, there is a distinction between Ni/YSZ and Cu/CeO_2/YSZ anodes. Gorte and co-workers[4] have observed that Cu/CeO_2/YSZ anode cell performance is enhanced by a factor of 2-3 after the formation of carbon deposits, which is in sharp contrast to Ni/YSZ behavior. They claimed that this improvement is caused by the increase in the anode conductivity due to the carbon deposit formation. The structure and composition of the carbon deposits and the formation mechanism have not been fully characterized.

In this study, the carbon deposits, produced on the SOFC anode surface with butane as a hydrocarbon fuel, were studied. The compositional and structural characterization of the carbon deposits were studied by using X-ray Diffraction (XRD), X-ray Photoelectron Spectroscopy (XPS), and Scanning Electron Microscopy (SEM). The effects of these carbon deposits on SOFC anode performance were investigated by using Linear Scan Voltammetry (LSV).

Experimental

Preparation of the membrane electrode assembly (MEA): The MEA for the single SOFC cell was prepared on a polycrystalline YSZ disk (8 mole % yttria stabilized zirconia disk) with a 25.4mm diameter and a 1.5mm thickness. The porous, LSM-YSZ (50% $La_{0.85}Sr_{0.15}MnO_3$-50% YSZ) cathode was prepared as a thin layer by tape casting methods. The porous YSZ layer (mixture of 60% YSZ powder-40% glycerin) for the anode was painted on the opposite side of the disk and then sintered at 1300^{o}C. 10% ceria and 5% copper, where needed, were deposited to the porous YSZ layer by using aqueous solutions of cerium and copper nitrates. The MEA was then sintered at 800^{o}C under reducing atmosphere. Pt and Au wires were placed on the cathode and anode sides, respectively, as current collectors. The MEA was then attached to an alumina tube by using zirconia-based ceramic paste.

To monitor the effects of carbon deposition on anode performance, a MEA with two different anodes (semicircle-design) was prepared. Both semicircle anodes were evaluated simultaneously by flowing first 5 hours H_2, and then followed by 100 hours butane, and lastly 5 hours H_2.

SOFC Operation Conditions: The complete SOFC was placed in a furnace and heated to 785^{o}C at a rate of 5^{o}C/min under Ar/H_2 flow. The diluent (Ar)/fuel (H_2 or butane) ratio is 2:1. The adjustment according number electrons per minute between H_2 and butane flows is accomplished by using the number of electrons produced by total oxidation of fuels so that the number of electrons per unit time is same for both fuel flows. Flow rates of fuel mixtures were controlled by using electronic mass flow controllers. A National Instruments SCIX data acquisition system was employed to accumulate all mass flow controller data.

Characterization Methods: For electrochemical measurements, an Autolab PGSTAT30 was used. XRD data were recorded by using a Bruker C2 Discover X-Ray Powder Diffractometer with a CuK_α radiation and a HiStar area detector. XPS data were acquired by using a Kratos Axis 165 spectrometer at a vacuum $4x10^{-10}$ Torr with a non-monochromatic MgK_α radiation. The X-ray power used for the measurements is 150W. SEM analyses were performed with an AMRAY 1820K Scanning Electron Microscope with an acceleration potential of 25kV.

Results and Discussion

The power density values, which are shown in **Figure 1**, were calculated by using simultaneous LSV measurements on both semicircular anodes,. As illustrated, the SOFC anode power densities with H_2 fuel after 100 hours of butane exposure increase by a factor of approximately 2 with respect to the initial H_2 fuel power density values. Similar enhancement values between 100 hours in our experiment and half an hour butane exposure in Gorte and co-workers[4] reveal that the longer butane exposure time has the same effect on the SOFC anode performance as the shorter time although the anode surface is completely covered with carbon deposits after a long butane exposure.

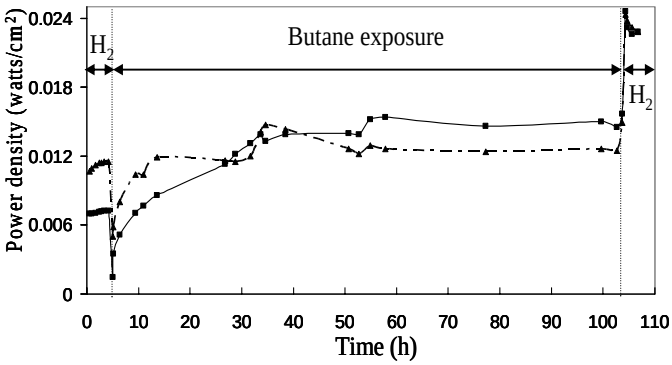

Figure 1. The SOFC power density vs. time plots for H_2-Butane-H_2 cycle representing 100 hours of butane exposure (━CeO_2/YSZ, and -- Cu/CeO_2/YSZ anodes)

SEM images of carbon deposits on anode surface and isolated from YSZ disk surface are shown in **Figure 2**. These carbon deposit spheres on the anode surface have diameters of approximately 5 μm and the thickness of carbon deposits isolated from YSZ disk surface is also 5 μm.

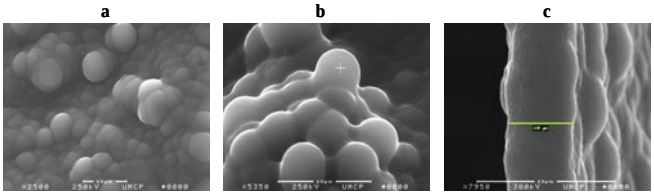

Figure 2. SEM pictures of a) Carbon deposits on anode surface b) enlargement of sample (a), c) the carbon film on YSZ disk. (White bars are 10 μm in all images, the green bar in (c) is 5 μm)

XRD patterns of 325-mesh graphite (average particle size of 44 μm), as well as the carbon deposits isolated from the electrolyte surface and both anode surfaces are illustrated in **Figure 3**. The two sharp peaks at 30^o, and 31.4^o are due to YSZ and the relatively sharp reflection at 28.5^o is due to CeO_2. The peak at 27^o is caused by SiO_2 in ceramic paste. The 325-mesh graphite XRD profile is shown as a standard to compare to the rest of the samples. The sharp graphite (002) reflection is observed at 26.5^o. All of the other samples have one broad peak shifted to 25.5^o, which is attributed to the graphite-like crystal structure discussed below.

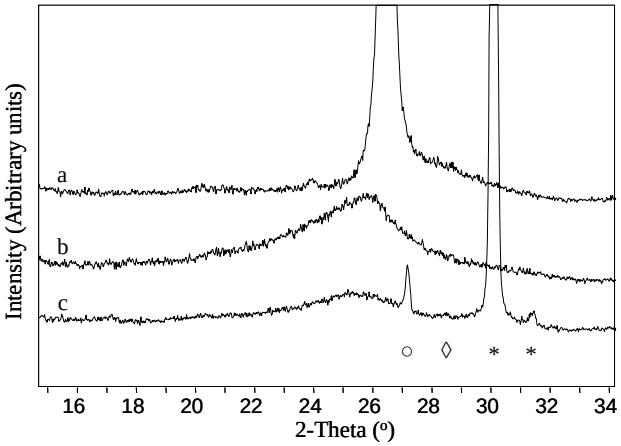

Figure 3. XRD Patterns a) 325-mesh graphite, b) carbon deposit isolated from anode surface, **c**) CeO_2/YSZ surface exposed to butane for 100 hours, (o: SiO_2 from ceramic paste, *: YSZ, ◊: CeO_2)

The shift to a lower angle and the broadness of the peak has been observed in many similar cases[5] and can be explained by the thickness (L_c) and the grain size (L_a) of the graphene layers of graphite-like structure. Due to a decrease in L_c, the d-spacing between graphene layers increases and fluctuates. As a result, this peak appears at a lower angle (2-Theta) with respect to the standard graphite (002) peak. The fluctuation in d-spacing causes the broadness. When the grain size, L_a, gets smaller (L_a<50 nm)[6], the possibility of diffraction diminishes, thus the intensity of the peak also decreases. These observations suggest that the carbon deposits on these anode surfaces have graphite-like crystal structures with small grain sizes, L_a, and small thicknesses, L_c.

The detailed C1s region XPS profiles of different semicircular anode surfaces (after linear inelastic scattering background subtraction) are demonstrated in **Figure 4** showing how the C1s regions can be fitted to a number of component peaks.

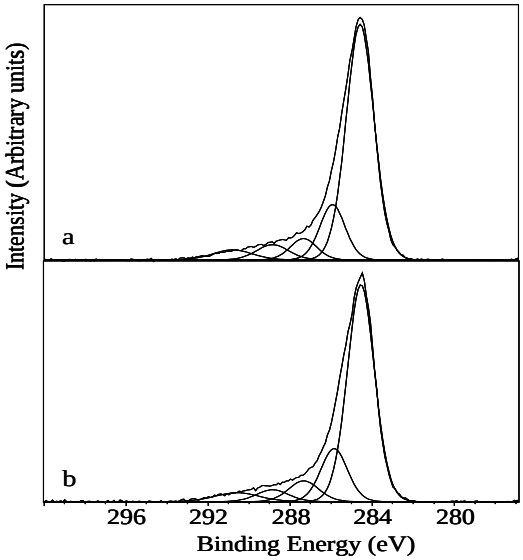

Figure 4. XPS C1s region of (a) CeO_2/YSZ anode surface, (b) Cu/CeO_2/YSZ anode surface.

The two spectra in **Figure 4** have a similar fitting features suggesting that the same type of carbon exists in both samples. The lowest binding energy peak at 284.3-284.6 eV is assigned to the sp^2 hybridized (graphitic) carbon atoms and is in agreement with binding energies reported for single crystal graphite.[7] The second lowest binding energy peak at 285.1-285.6 eV is attributed to sp^3 carbon atoms (C-H), which have also been reported elsewhere.[7] The higher binding energy peaks are consecutively assigned with respect to their chemical environments and oxidation levels. XPS results show that carbon deposits on the SOFC anode surfaces have graphitic carbon properties.

Acknowledgement

This work was supported by the Office of Naval Research thorough the Multiple University Research Initiative grant # 0110138816, in association with the Colorado School of Mines and the California Institute of Technology.

References

(1) Will, J.; Mitterdorfer, A.; Kleinlogel, C.; Perednis, D.; Gaukler, L. J. *Solid State Ionics* **2000**, *131*, 79.
(2) Gorte, R. J.; Kim, H.; Vohs, J. M. *J. Power. Sources* **2002**, *106*, 10.
(3) Minachev, K. M.; Kondratev, D. A.; Antoshin, G. V. *Kinet. Catal.* **1967**, *8*, 108.
(4) McIntosh, S.; Vohs, J. M.; Gorte, R. J. *J. Electrochem. Soc.* **2003**, *151*, A470.
(5) Tsai, .H. C.; Bogy, D. B. *J. Vac. Sci. & Tech. A-Vac. Sur. & Films* **1987**, *5*, 3287.
(6) Ergun, S. in *Chemistry and Physics of Carbon Vol.3.*, Walker, P. L., Ed. Marcel Dekker: New York, 1968, pp 289.
(7) Sherwood, P. M. A. *J. Electron Spectrosc. Relat. Phenom.*, **1996**, *81*, 319.

NEW ELECTROLYTIC SYNTHESIS OF BOROHYDRIDE ANIONS FROM BORON OXIDE IN A MOLTEN SALT MELT

Michael T. Kelly, Jeffrey V. Ortega, Todd J. Randall, and Ying Wu

Millennium Cell Inc.
1 Industrial Way West
Eatontown, NJ 07724

Introduction

Efficient storage of hydrogen remains a primary problem to be solved before the gas can be considered for any mass commercial applications. Traditional methods for storage are to compress or to liquefy the gas, or to employ a solid-state medium that absorbs hydrogen. The difficulties here are well understood and not easily addressed: Compressed methods are not volumetrically efficient, and solid-state methods are not gravimetrically efficient.

An area of growing interest in the field is the use of chemical hydrides. Chemical hydrides based on boron occupy an energy density middle ground, being more volumetrically appealing than compressed methods and more gravimetrically acceptable than solid-state storage. For this reason, boron based hydrogen storage has a greater likelihood of being adequate on both counts.

The main barrier to using chemical hydrides for hydrogen storage is an economic one. Synthesized by current methods they are too expensive to be considered a primary power source. There is a need, therefore, to identify new synthesis methods for boron hydrides. Herein we examine an electrolytic reduction leading to the formation of borohydride, starting from boron oxide and hydrogen gas.

Experimental

All chemicals were obtained from Aldrich Chemicals and used as received without further purification. The alkali bromide melt composition is 56.1 mol % lithium bromide, 18.9 mol-% potassium bromide and 25.0 mol % cesium bromide[1]. This eutectic melts at 226 ºC. Electrochemistry was carried out at 300 ºC in the melt, with hydrogen gas bubbling through the melt. A nitrogen gas jacket was maintained over the catholyte portion of the melt. The anolyte was open to atmosphere, with flowing N_2.

Electrochemistry was carried out with a Parr Instruments VMP model 4-channel potentiostat, in a two-electrode configuration. Typical cell potentials were 5 V. The cathode was a nickel frit (5 μm average pore size) obtained from Mott Corporation, with H_2 bubbling through it. The anode was a piece of Pt gauze. The electrolytic cell had two compartments separated by a glass frit of porosity "C" (25-50 μm).

The titrations for quantifying borohydride used the iodate method[2]. Briefly, a solution containing an unknown amount of borohydride is treated with an excess of potassium iodate (KIO_3). After adding potassium iodide (KI), the remaining iodate solution is acidified with sulfuric acid, and forms the triiodide anion (I_3^-). The triiodide is titrated with sodium thiosulfate ($Na_2S_2O_3$). This titration is self-indicating, as the deeply colored triiodide is converted to colorless iodide (I^-). The difference between the amount of iodate titrated and the measured amount added to the borohydride solution allows calculation of the amount of borohydride in the original solution. The titration appears to be unaffected by the presence of metaborate anions (BO_2^-), boric acid ($B(OH)_3$), or high concentrations of alkali bromides.

The presence of borohydride in solution was also verified by ^{11}B-NMR spectroscopy. Borohydride anions give a characteristic quintet, due to the boron signal being split four times by equivalent protons. The chemical shift for borohydride is 38.7 ppm, with a spin-spin splitting of 0.82 ppm[3]. The chemical shift for triborohydride is 28.4 ppm, with a spin-spin splitting of 0.32 ppm[3].

Results

The approach taken to making borohydride anions is based on a series of thermodynamically favorable reactions. Alkali metals are synthesized electrolytically, as in the cathodic equation (1).

$$M^+ + e^- \rightarrow M^0 \qquad (1)$$

Further, it is known that alkali metal will react with hydrogen gas to make the alkali metal hydride, according to equation (2).

$$2\ M + H_2 \rightarrow 2\ MH \qquad (2)$$

Next, alkali metal hydrides are known to react with boron oxide (B_2O_3) or trialkyl borate ($B(OR)_3$) to yield borohydrides[4], as shown in equations (3a) and (3b).

$$8\ MH + B_2O_3 \rightarrow 2\ MBH_4 + 3\ M_2O \qquad (3a)$$
$$4\ MH + B(OR)_3 \rightarrow MBH_4 + 3\ MOR \qquad (3b)$$

Given these three reactions, it follows that borohydride generation may occur through an electrochemical-chemical-chemical (ECC) mechanism.

Supplying voltage to an electrochemical cell containing molten lithium-potassium-cesium bromide eutectic will result in electrochemical synthesis of lithium metal and bromine gas. Potassium and cesium are also potential products but both of the heavier alkali metals are expected by thermodynamics to react with lithium bromide to yield lithium metal and the relevant bromide. For simplicity, lithium will be considered the sole product of electrolysis. If hydrogen is present in the cell the metal will react further to yield lithium hydride, which in turn generates borohydride from B_2O_3.

The initial experiment was designed to test whether molten salts were in fact adequate reaction media for equation (3a). Stoichiometric amounts of lithium hydride and B_2O_3 were added to an alkali bromide melt with stirring. After 15 minutes, the melt was allowed to cool to room temperature. The solid, in its entirety, was dissolved in aqueous 0.5 M NaOH solution. A portion of the solution was submitted to quantitative titration to determine the amount of borohydride present. Reaction yield was 66%, based on the amount of LiH added to the melt. The conclusion is that LiH reacts quickly with B_2O_3 in good yield, and the electrochemical experimentation should proceed.

The idea of the electrochemistry is to generate the LiH *in situ*, and allow the known borohydride generation reaction to proceed as demonstrated. The cathode for the electrochemical process was a nickel frit, with hydrogen gas passing through it. Passing the hydrogen through the cathode is done to promote the reaction between the lithium metal being generated at the cathode and the gas to make the hydride. The anode is platinum mesh. Conveniently, the anode product bromine is highly colored and the gas readily visible above the anode compartment. Bromine is not observed in or above the cathode compartment, suggesting that the cell separator is sufficient to prevent back reaction even though it is not selective.

Figure 1 shows a typical electrolysis at constant voltage, allowed to run overnight (16-24 hours). Cell potential is -5 V vs. the anode. A reasonably high current is achieved throughout the experiment, which was allowed to run overnight. After electrolysis voltage is stopped, the anode and cathode are removed from the cell. The entirety of the melt in the cathode compartment was dissolved in aqueous 0.5 M NaOH. A portion of the solution was submitted for

titration to quantify the presence of borohydride and an aliquot of solution was analyzed by ^{11}B-NMR to verify the presence of borohydride anions. A typical ^{11}B-NMR spectrum of the borohydride in aqueous solution generated by the methods described here is shown in figure 2. The presence of borohydride ions is unmistakable. Both the positioning of the quintet (the boron center split 4 times, once by each equivalent proton) and the splitting are in excellent agreement with both literature values and standards prepared in house.

The best electrolytic conversion measured is 8.3 %, determined by the maximum amount of borohydride that could be made considering the number of electrons that passed through the electrolytic cell, and how much borohydride was actually measured by titration. The latter amount was divided by the former to give yield. Typical experiments gave 4-5 % borohydride.

Close inspection of figure 2 shows that some amount of triborohydride $B_3H_8^-$ was also generated during the experiment. At present, it is postulated that $B_3H_8^-$ is generated when BH_4^- crosses through the separator. When molten lithium borohydride salts are electrolyzed, the oxidation product is diborane B_2H_6. B_2H_6 will react with BH_4^- to make $B_3H_8^-$. $B_3H_8^-$ has good aqueous stability and is not destroyed during the dissolution of the melt. The relative concentration of triborohydride to borohydride appeared higher in the ^{11}B-NMR spectrum when the separator cracked during the experiment or was otherwise flawed. The titration methods are not sufficient to determine the relative amounts of triborohydride vs. borohydride. Titration will underestimate the amount of borohydride generated if there is a substantial amount of triborohydride, so yield may be higher than reported.

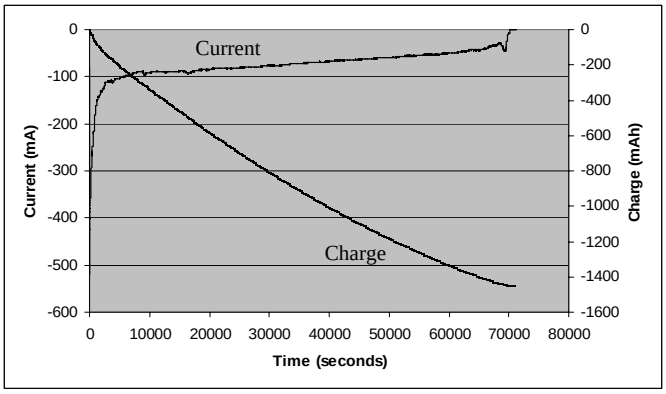

Figure 1. Constant potential electrolysis of alkali bromide an melt containing B_2O_3 to make BH_4^- anions. Cell potential was 5 V

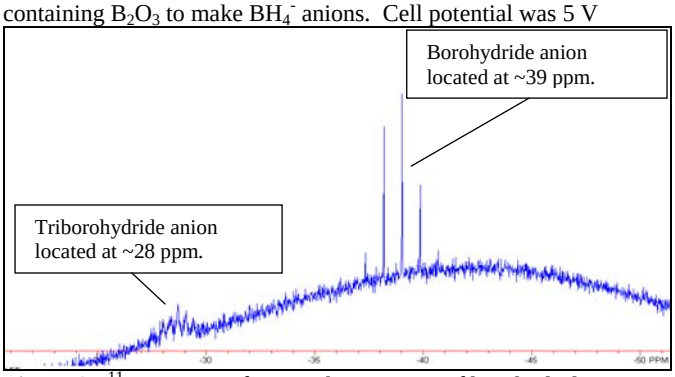

Figure 2. ^{11}B NMR confirming the presence of borohydride anions in solution. Also observed is the $B_3H_8^-$ anion.

Discussion

A practical synthesis must exhibit conversion better than the 8.3 % yield achieved to date. A number of observations indicate, however, that the difficulty is with the first chemical step. The reaction of lithium metal with hydrogen gas to make lithium hydride appears to proceed slowly. Experimentation with added lithium hydride showed that reaction with boron oxide is fast compared with the timescale of the experiment. The prior step, electrochemical generation of the metal takes place at a rate proportional to the current. When the melt is cooled to room temperature but before it is dissolved in aqueous solution, lithium metal appears in the melt and on the cathode. Solid, unreacted boron oxide can also be collected on filtering the aqueous solution. Since the products of the first step and the relevant reagents for the third step are readily found post electrolysis, it is reasonable to conclude that it is the middle step that is the kinetic bottleneck.

Solubility of hydrogen gas is also an issue for the second step. At the operating temperature of 300 °C, the amount of hydrogen dissolved in the melt is low, and therefore may not readily react with lithium. The lithium ends up in large pieces, which will not easily react to form the hydride.

A few other problems affect the reaction. The reaction takes place in a ternary eutectic. The melting point of such a melt is very sensitive to composition. Addition of B_2O_3 makes the melt viscous even 75 °C above the stated melting point. The electrolysis in effect withdraws lithium from the melt, further altering the composition and the melt of ten solidifies near the cathode. The formation of solid often blocks the pores in the cathode through which hydrogen enters the cell. Once blockage occurs, the formation of borohydride stops due to the loss of hydrogen to react with lithium, even if the electrolysis continues.

Fortunately, it appears that these problems are amenable to several solutions. It is unlikely that the methodology for making borohydride is limited to this specific melt. The melt requirements appear to be no more complicated than having anions and cations that are not reduced by strong hydrides. The number of solvent and ionic systems fitting this description is vast, and a change in composition and/or temperature is expected to solve a number of the problems discussed herein, and lead to substantially higher yield. Implementing efficient stirring and different hydrogen entry may also have notable impact.

Conclusion

A new method of making borohydride via electrolysis is described. The transformation employs hydrogen, boron oxide, and electrolytic potential as reagents and takes place in one pot, with no intermediate additions or separations required. The potential for evolving this electrolytic method into a lower cost route to borohydride is high.

Future work must focus on improving the electrolytic yield. Promising pathways involving the similar methods in different solvents or melt systems appear likely to succeed.

Acknowledgement. The gratefully acknowledge support from the Department of Energy, through Cooperative Agreement contract number DE-FC36-04GO14008.

References

(1) Kasajima, T.; Nishikiori, T.; Nohira, T.; Ito, Y. *Electrochem. and Solid State Lett.*, **2003**, *6* (5), E5.
(2) Lyttle, D. A.; Jensen, E. H.; and Struck, W. A. *Anal. Chem*, **1952**, *24* (11), 1843.
(3) Boron, Metallo-Boron Compounds and Boranes; Adams, R. M., Ed.; John Wiley & Sons: New York, 1964.
(4) Schlesinger, H. I.; Brown, H. C.; and Finholt, A. E. *J. Am. Chem. Soc.*, **1953**, *75*, 205.

STEAM HYDROLYSIS OF CHEMICAL HYDRIDES: MEETING THE CHALLENGE OF HYDROGEN STORAGE

Michael, A. Matthews, Thomas A. Davis, Josh Gray and Eyma Y. Marrero-Alfonso

University of South Carolina
Department of Chemical Engineering
301 Main, Swearingen Engineering center
Columbia, SC 29208

Introduction

This paper investigates the steam hydrolysis of chemical hydrides in order to evaluate this technology rigorously for its potential as a means of delivering hydrogen for fuel cells and internal combustion engines. Simple chemical hydrides (e.g. LiH, CaH_2), as well as complex hydrides ($NaBH_4$, $LiBH_4$, and others), react with liquid water to produce H_2. For example, $NaBH_4$ hydrolysis can be represented as:

$$NaBH_4 + (2+x)\ H_2O \rightarrow 4H2 + NaBO_2 \cdot xH_2O + \text{heat} \quad (1)$$

In equation 1, x is the "excess hydration factor", representing the fact that the solid byproduct can exist in varying degrees of hydration. In the liquid phase [2] an acid catalyst is required to liberate 100% of the hydrogen, because dissolved $NaBH_4$ is stabilized by the basic solution formed by the byproducts of the reaction (sodium borate and similar compounds). In reaction (1), the ideal case is where $x = 0$, in which case the mass yield is 10.7 kg H_2 per 100 kg of reactants. In practice, excess water is required so that the $NaBH_4$ and byproducts remain completely dissolved. Excess water rapidly reduces the mass efficiency of the system.

A recent discovery [1] shows that vaporizing water prior to contact with the hydride can produce hydrogen yields in excess of 90% without the need for a catalyst. Thermodynamic considerations show that, in principle, the heat liberated by the reaction is sufficient to vaporize the stoichiometric water required for the steam. Thus, it may be possible to develop a hydrogen reactor/delivery system that is autothermal at steady state, that produces pure hydrogen in 100% yield, that requires no catalyst, that does not involve strongly caustic solutions, and that uses a minimum amount of water. Furthermore, the solid reaction products should be nearly free of water, which in the long term will facilitate recycling and regeneration to the hydride.

The Department of Energy (DOE) designed the FreedomCAR Technical Targets for hydrogen storage in automobiles; selected targets are given in Table 1. [3] New technologies should meet these targets, such as the gravimetric efficiency (kg H_2/kg reactants) and specific energy (kWh/kg system).

Table 1. FreedomCAR Targets for Specific Energy [3]

Usable specific energy from Hydrogen			
Year	2005	2010	2015
Target (kWh/kg system)	1.5	2	3
Target (kg H2/kg system)	0.045	0.060	0.090

Technologies based on simple and complex chemical hydrides have the potential to meet the targets when ideal hydrolysis is assumed and system considerations are ignored. (Figure 1) One of the challenges is to obtain a gravimetricly efficient system with an acceptable rate of hydrogen delivery and controllable startup dynamics. Efficient water utilization and high rates of reaction are key factors to achieve these targets.

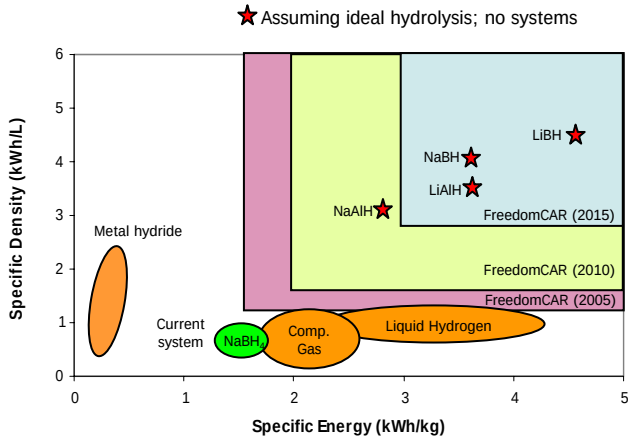

Figure 1. Potential of technologies to meet the FreedomCar targets

Experimental

The $NaBH_4$ steam hydrolysis reactor system consists of a cylindrical quartz reactor tube placed inside a Thermolyne Model 21100 tube furnace to maintain a constant temperature. One thermocouple placed in the center of the reactor vessel monitors the reaction temperature.

The reaction temperature is affected by the temperature of the incoming steam,which is controlled by a three-stage heater. The first stage of the heater system preheats the steam to approximately 100°C. This preheated liquid/vapor mixture then enters the second and third stages, which superheat the water vapor to the desired reaction temperature. A KD Scientific Model 200 Programmable Syringe Pump is used to pump the desired water flow to the evaporator. The experiments were performed with a water flow rate of 0.1 mL/min (0.0055 mol/min). The volumetric flow rate and cumulative volume of hydrogen are measured as the volume of water displaced from the Erlenmeyer flasks to the graduated cylinder. Condensed water is removed in a cold trap, leaving a stream of hydrogen with a trace amount of water.

The hydride is contained in the fixed bed reactor inside the furnace. All experiments are conducted with one gram of $NaBH_4$, which is mixed with glass beads or coated on glass beads and then loaded into the reactor between glass-wool plugs. After loading and prior to hydrolysis, the reactor is purged with nitrogen to remove oxygen and moisture and ensure that the reactants are continuously under a blanket of inert gas until the hydrolysis begins. The system is designed so hydrogen can also be co-fed with water at a controlled rate in order to control the partial pressure of steam.

Thermogravimetric analysis (TGA) and differential scanning calorimetry (DSC) are used for analysis of the solid reaction products. PerkinElmer TGA 7 Thermogravimetric Analyzer and DSC 7 Differential Scanning Calorimeter models are used. The temperature program is controlled via a Pyris software program. The temperature program from both the TGA and DSC scans from 25°C to 400°C at a rate of 10°C per minute.

Results and Discussion

Experimental results such as the maximum H_2 generation rate (mol H_2/kg$NaBH_4$*min) and the % of hydrogen yield are summarized in Table 2. Experiments were performed using $NaBH_4$ in two different physical forms, either powder or recrystallized as a thin film on glass beads. As shown in Table 2, additives were also used in a few experiments. Temperatures tested were 110°C and 140°C.

Stoichiometric rates for different excess of hydration values (x) are also presented for comparison.

The maximum apparent rate of the reaction, expressed as moles of H_2 produced per minute per kilogram of $NaBH_4$, was determined for each experiment by calculating the maximum slope of the collected hydrogen with respect to time (Table 2). The data show good reproducibility and is in agreement with previous work [1], which yielded a greater rate than the new experiments, but a similar H_2 yield. Hydrogen yields from 82% to 94% of the maximum were obtained without the need of an additive. The use of volatile additives, such as methanol and acetic acid, did not increase the reaction rate, and raising the temperature to 140°C decreased the reaction rate and yield. Experimental results from the past work [1] showed that for the different hydrides used, higher yields of hydrogen were obtained at the lowest temperature (110°C). An improvement in the rate of reaction is observed when the physical form of $NaBH_4$ is changed from powder to thin films coated on glass beads.

Calculations of the rate of reaction were also performed for idealized situations for x=0, 4 and 6. For example, if no excess water is added (x=0) when the water flow rate is 0.1 mL/min (0.0055 mol/min) and the reaction is instantaneous, the theoretical rate of hydrogen production is 11.1 mol/kg_{NaBH4}*min, as shown in Table 2.

Table 2. Rates and Yields from Steam Hydrolysis

Exp#	Description	T (°C)	Max Slope (mol/kg_{NaBH4}*min)	% of Theo. H_2 Yield
1	$NaBH_4$ Powder	110	0.812	88.2
2	$NaBH_4$ Powder	110	0.717	82.7
3	1% acetic acid	110	0.582	101.4
4	1% methanol	110	0.715	92.7
5	$NaBH_4$ Powder	110	0.717	94.0
6	$NaBH_4$ Powder	140	0.349	67.1
7	$NaBH_4$ Powder	140	0.269	40.8
8	6.5% methanol	110	0.545	68.5
9	15% methanol	110	0.589	82.0
Sharp data	$NaBH_4$	110	1.10	87.4
10	$NaBH_4$ Thin films	110	4.01	19.7
11	$NaBH_4$ Thin films	110	4.35	22.9
Theoretical Rates		(x=0)	11.1	100
		(x=4)	3.70	100
		(x=6)	2.78	100

All the experimental rates are lower than the theoretical rates partially because the excess water required to complete the reaction moves the slope to the right, decreasing the reaction rate. Both the initial rates and the yields were lower at 140ºC than at 110ºC. The lower rates and yields at higher temperatures are counterintuitive, but this is tentatively attributed to mass transfer limitations associated with the particle. Examination of the reactor contents after the experiments revealed that the solid particles were agglomerated. The agglomerated material was soft and wet after the 110ºC experiment and hard and dry after the 140ºC experiment. Presumably, the $NaBH_4$ on the surface of the particle reacts first and forms a layer of sodium borate ($NaBO_2$), which grows in thickness as the reaction proceeds. This layer retards steam diffusion through the $NaBH_4$ particle, decreasing the production of hydrogen. The lower reaction rates at higher temperatures would be explained if the dry form of $NaBO_2$ is less permeable to water vapor, which is yet to be proven.

Experiments conducted with thin films show that the reaction rate improved and is approximately the theoretical rate for an excess hydration factor of 3 (x=3). The hydrogen yield decreased with use of coated beads to approximately 20%. This smaller yield could be caused by channeling in the reactor. This theory is supported by the observation that when the reacted beads were contacted with 15 mol % acetic acid, they continue reacting, indicating that not all $NaBH_4$ was contacted with steam.

Separate aqueous solutions of 1 mol%, 6.5 mol% and 15 mol% of methanol and 1mol% of acetic acid were investigated. The initial rate of the reaction was about the same regardless of the type or concentration of the additive, but different yields were obtained. Yields of 68% to 93% of the maximum were obtained with methanol. The best yield with methanol is no higher than yields with pure steam (82% to 94%) as shown in Table 1. The use of acetic acid gave a yield of 100%.

During thermogravimetric analysis the solid byproducts lost approximately 17% mass (free water and water of hydration), but no mass loss occurred above approximately 275°C. Differential scanning calorimetry analysis produced two peaks around 100°C and 150°C, which tentatively are ascribed to structural transformations from changes in the degree of hydration of the borate. In this range of temperatures the TGA indicates that the sample is still losing water.

Conclusions

The data show that more than an 80% yield of H_2 can be obtained when $NaBH_4$ powder reacts with pure water vapor. Sodium borohydride powder gave high yields with slow rates and excessive use of water. Higher rates were obtained with thin films of $NaBH_4$ recrystallized on glass beads, while yields were low, potentially due to channeling in the reactor. The rates and yields are sensitive to operating temperature, the amount of water and physical form of $NaBH_4$.

The intrinsic reaction kinetics may be obscured because of impermeable byproducts. The TGA and DSC analysis showed the presence of free water in the solid byproduct, which affects the gravimetric efficiency of the system. Further understanding of the by-product properties and refinement in the reactor configuration will help to increase the rate and yield of the reaction and reduce the amount of excess water. These improvements may give insight to improve the mass efficiency of the system and will make this technology viable as a medium for hydrogen storage.

Acknowledgement. This work was carried out under Agreement No. DAAB07-03-3-K416 with the US Army Communications-Electronics Command (CECOM) for Hybrid Advanced Power Sources with guidance from the RDECOM / CERDEC Fuel Cell Technology Team at Fort Belvoir, VA and the Agreement No. DE-FC36-ϕ4GO14232 with the Depatment of Energy.

References

[1] Aiello R.; Sharp J.; Matthews M. *International Journal of Hydrogen Energy;* **1999**, 1123-1130.
[2] Amendola et al., J. Hydrogen Energy, 25, 969, 2000; U.S. Patent 6,534,033
[3] www.eere.energy.gov/hydrogenandfuelcells/pdfs/freedomcar_targets_explanations.pdf

SYSTEM PERFORMANCE OF A SODIUM BOROHYDRIDE HYDROGEN GENERATOR FOR PORTABLE APPLICATIONS

Richard M. Mohring, Kevin W. McNamara, Mark Boehler, Ying Wu

Millennium Cell Inc.
1 Industrial Way West, Eatontown, NJ 07724

Introduction

Successful implementation of PEM fuel cells for portable applications has been limited due to the lack of a suitable hydrogen source that is energy dense, safe and easy to use. For example, conventional hydrogen storage solutions such as compressed gas and solid-state metal hydrides are unable to deliver the run time in the size and weight specification of the application and require hydrogen recharging.

We report here recent advances in employing chemical hydride based fuel cartridges to provide hydrogen for portable fuel applications at the 20-50 W power output level. System designs and performance data will be discussed.

The power system (dubbed the "P1") consists of a sodium borohydride ($NaBH_4$) based hydrogen fuel cartridge module developed by Millennium Cell and a 30 W PEM fuel cell power module developed by Protonex Technology Corp., as shown schematically (simplified) in Figure 1. The left portion of the figure represents the hydrogen fuel cartridge, and the right portion represents the fuel cell power module. The fuel cartridge is an implementation of Millennium Cell's Hydrogen on Demand® technology which generates hydrogen based on catalyzed hydrolysis reaction of sodium borohydride[1,2]. It is envisioned that the fuel cartridge can be disposed of after use.

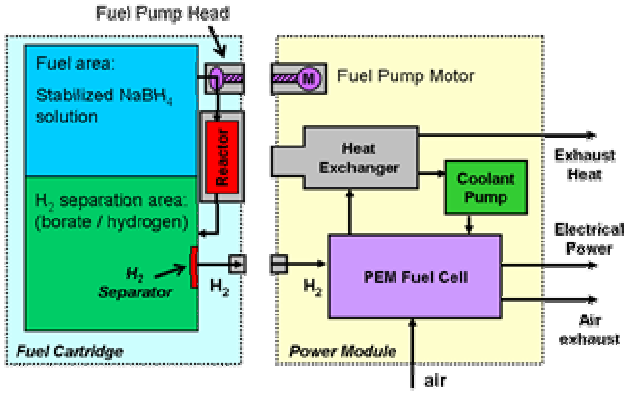

Figure 1. Schematic representation of the Protonex-Millennium Cell P1 power system.

In operation of the system, the fuel solution is moved from the fuel area via a peristaltic pump head mounted on the cartridge. The fuel passes through a thermally managed catalytic reactor and is converted into hydrogen, sodium metaborate, and water vapor. The products enter a separation area, and hydrogen is allowed to escape to an outlet tube through a hydrophobic membrane, where it is then passed to the fuel cell for consumption.

In order to operate the system, the two halves are mechanically coupled together. Two notable design features are the coupling of the fuel pump and heat exchanger. Although the peristaltic pump head is located on-board the fuel cartridge, the motor drive for the pump is actually located within the power module. This offers a number of advantages: there is no liquid-liquid interconnect, and as a result the potential for fuel leakage is minimized. Furthermore, it allows the motor to be reused for multiple cartridges, whereas the relatively inexpensive pump head can be disposed of with each cartridge as it is consumed.

Similarly, an inexpensive metal reactor is fitted with a thermally conductive fin which comes into intimate physical contact with a fixed heat exchanger (normally used for thermal management of the fuel cell) onboard the power module when the system halves are joined. In this way, the thermal conditions of the reaction can be accurately controlled.

Experimental

For purposes of detailed experimentation on the fuel cartridges, Millennium Cell developed a so-called "power module simulator" that in essence replaces the fuel cell system with instrumentation. As shown in Figure 2, the fuel cell itself is replaced by a thermal mass flow meter, so that the flow of hydrogen can be accurately measured and/or set at a particular level. The heat exchanger remains, but is controlled off a separate control loop based on the reactor temperature.

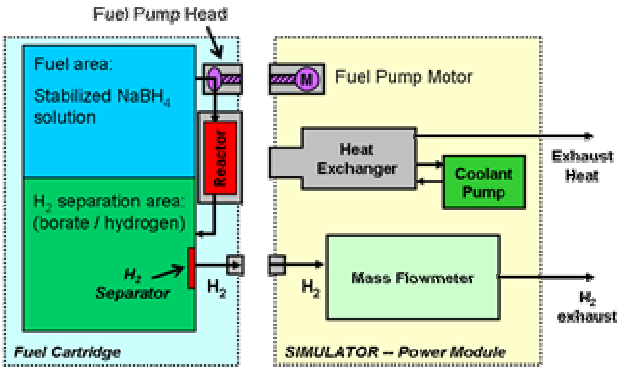

Figure 2. Schematic representation of the Millennium Cell fuel cartridge in relation to the power module simulator.

The performance of the fuel cartridge was evaluated under various conditions and results are reported below. The fuel used in performance evaluation was an aqueous solution of $NaBH_4$ in the 15-25 wt% concentration range, with 3 wt% NaOH as stabilizer. Most experimentation was done at room temperature, though limited tests were conducted at ~5 °C and ~35 °C.

The hydrogen stream was passed through a drying column before the flow rates were measured using a mass flow meter. A number of thermocouples were attached to selected locations on the fuel cartridge and simulator to record reactor temperature, hydrogen stream temperature, and skin temperature of the fuel module. In experiments where real-time conversion efficiencies were measured, the fuel reservoir was placed on a scale so that the fuel consumption was recorded by the weight loss of the fuel reservoir.

Results and Discussion

The conversion efficiency of sodium borohydride fuel was first evaluated. Although the system was designed to operate at an average of 425 sccm of hydrogen output (corresponding to approximately 30 W net electrical output), it was desirable that the conversion from sodium borohydride to hydrogen was as close to quantitative as possible over a much wider hydrogen flow output window. To this effect, the hydrogen yield was measured at a number of drastically different flow rates of the borohydride

solutions. As the data in Figure 3 show, highly efficient conversions were achieved over two orders of magnitude of hydrogen flow rate, from 10 sccm to 1000 sccm.

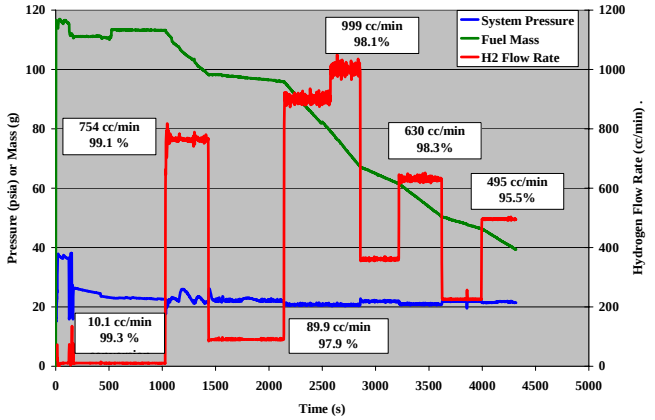

Figure 3. Hydrogen flow rates and corresponding borohydride conversion measured at various output levels.

In initial development, the fuel module was sized to achieve 12 hours of run time using 16 wt% borohydride solution. Figure 4 shows the test results of a typical full run evaluation at that concentration. The mass flow control was set to allow a constant hydrogen flow rate of 425 sccm, which corresponds to the final desired electrical power output. In these experiments, run time ranged between 11.0 and 12.2 hours, with borohydride conversion efficiency in the 93 – 100% range.

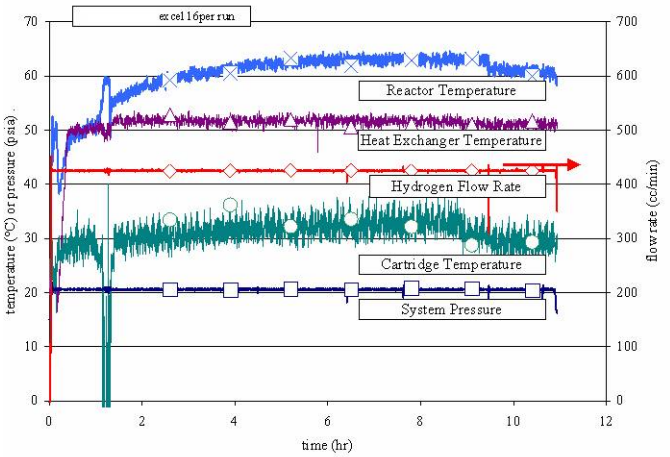

Figure 4. Cartridge data for full run on 16 wt% borohydride fuel. Hydrogen output was fixed at 425 sccm, and system pressure was controlled to maintain ~20 psia within the cartridge.

In further development, an integrated heat management technology was implemented to allow for use of higher concentration borohydride solutions. In the absence of thermal management, the conversion efficiency of the fuel drops as fuel concentration is increased[3]. Qualitatively, as the fuel concentration is increased, the reduction of availability of water as both a solvent and as a reagent negatively impacts the ability to complete the hydrolysis reaction. By keeping the temperature within a certain narrow window via thermal management, the vaporization of water can be kept to a minimum while not significantly decreasing the kinetics of the hydrolysis reaction.

Figure 5 shows the result of an experiment running on 20 wt% borohydride fuel. For this run, the cartridge was operated for 7 hours, stopped overnight, and operated for the remaining 9 hours of fuel stored within the cartridge on the second day. The experiment showed approximately 16 hours of operation, which greatly exceeded the design specification of 12 hour run time. With these improvements, the system was able to achieve a projected gravimetric energy density of 340-395 Wh/kg (depending on power output) based on total loaded system weight for a 72 hour mission, verified by independent testing[4].

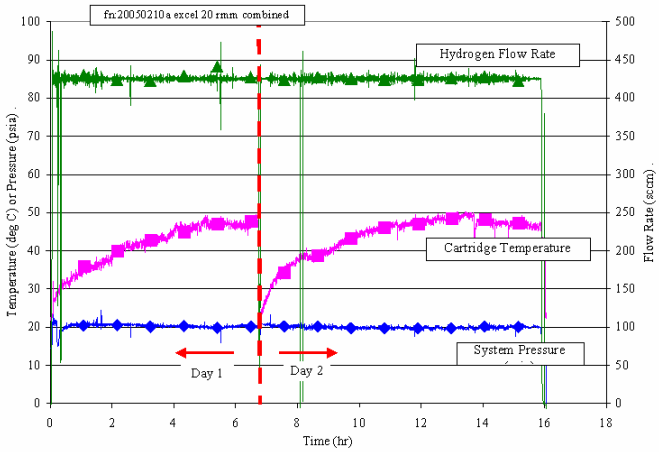

Figure 5. Data for full run on 20wt% $NaBH_4$ fuel, incorporating thermal management to maintain reactor temperature at an optimal set point (not shown). Hydrogen output was fixed at 425 sccm, and system pressure was controlled at ~20 psia within the cartridge.

Future work on this program ("P2") is directed at increasing the effective gravimetric energy density of the system above 425 Wh/kg for the 72 hour mission, while advancing the readiness level of the technology to be implemented into a field-testable device.

Conclusions

Millennium Cell has implemented its Hydrogen on Demand® technology for hydrogen generation from sodium borohydride into a working prototype 30 W power source. Concentrations of up to 20 wt% sodium borohydride have been consistently operated in the cartridge through a thermal management scheme. Future work will further optimize the thermal management to increase the sodium borohydride concentration that can be reliably processed in the reactor.

Acknowledgement

The authors wish to acknowledge Dr. Thom Reitz and the financial support of the Air Force Dual Use Science and Technology Program, under Technology Investment Agreement, FA8650-04-3-2411. We also want to thank Protonex Technology Corp. for a productive collaboration and many stimulating discussions.

References

(1) U.S. Patent 6,534,033. **2003**.

(2) Mohring, R. M., Wu, Y. *The First International Workshop on Hydrogen in Materials & Vacuum Systems*. Jefferson Lab, Newport News, Virginia, **2002**.

(3) Hovland, V.; Pesaran, A; Mohring, R. M.; Eason, I. A.; Smith, G. G.; Tran, D.; Schaller, R.; Smith, R. *Proceedings of Future Transportation Technology Conference*, **2003**.

(4) Burt, K. *Joint Services Power Expo*, **2005**.

HYDROGEN GENERATION VIA COMBUSTION OF METAL BOROHYDRIDE/ALUMINUM/WATER MIXTURES

Evgeny Shafirovich, Victor Diakov, and Arvind Varma

School of Chemical Engineering, Purdue University
480 Stadium Mall Drive, West Lafayette, IN 47907

Background and Approach

Alkali and alkaline earth metal borohydrides are known to be an excellent source of hydrogen, which can be generated by reactions of these compounds with water or oxidizing agents. Hydrolysis of sodium borohydride is a well-known process [1], extensively studied for hydrogen generation. Aqueous alkaline $NaBH_4$ solutions are stable and their contact with selected catalysts leads to the reaction

$$NaBH_4 + 2\ H_2O \rightarrow NaBO_2 + 4\ H_2 \qquad (1)$$

Water in this process is simultaneously a reactant and an additional source of hydrogen. As a result, borohydrides provide high hydrogen yield (>10 wt.% for stoichiometric mixtures), which makes them attractive for applications. However, moderate exothermicity of the metal borohydrides hydrolysis is an impediment for combustion-based hydrogen generation.

Recently, hydrogen-generating pyrotechnic compositions were proposed to feed fuel cells for portable electronics [2]. In such solid mixtures, hydrogen is generated by combustion reactions between alkali metal borohydride (or alkaline earth metal borohydride) and oxidizing salt (e.g., ammonium perchlorate, alkali metal perchlorate, alkaline earth metal perchlorate). The reactions are highly exothermic, easily initiated, and do not require any catalyst, which makes them cost effective and attractive for portable electronics applications. However, stoichiometric mixtures of the proposed reactants exhibit low hydrogen yield while the mixtures with high content of metal borohydride do not burn.

An alternative approach uses combustion of nanoscale aluminum with gelled water for hydrogen generation [3]. Here, water acts as an oxidizer for Al and simultaneously as the sole source of hydrogen. The adiabatic combustion temperature of Al/H_2O stoichiometric mixture is close to 3000 K (at pressure 1 atm), which indicates that the heat release is quite sufficient for self-sustained combustion. However, the use of nanoscale Al powder and gelling of water (for example, by adding polyacrylamide) are the necessary conditions for combustion of Al/H_2O mixture. The use of nanopowder decreases the ignition temperature of Al, while gelling leads to significant superheating of water during combustion. Hence, the mixture ignites easily and burns in inert atmosphere, producing hydrogen:

$$Al + 3/2\ H_2O \rightarrow 1/2\ Al_2O_3 + 3/2\ H_2 \qquad (2)$$

Unfortunately, low hydrogen yield of the Al/H_2O system (theoretical limit 5.6 wt.% for the stoichiometric mixture) is a drawback of this method.

To reach high hydrogen yield and combustion efficiency, we use metal borohydride/aluminum/water mixtures, in which water acts as an oxidizer for both aluminum and metal borohydride and simultaneously as a source of hydrogen, metal borohydride is an additional hydrogen source, and aluminum enhances reaction exothermicity. Nanoscale aluminum powders are used to ensure high combustion efficiency. Along with the three reactants, the mixtures include, in quantities about 1 wt.% each, a gelling agent (e.g., polyacrylamide) and a stabilizer (e.g., NaOH) to prevent hydrolysis of borohydride at room temperature.

Thermodynamic calculations were conducted for $NaBH_4/Al/H_2O$ system using THERMO software [4]. Figure 1 shows adiabatic combustion temperature and H_2 yield as a function of $Al/(NaBH_4+Al)$ mass ratio at pressure 1 atm. The H_2O fraction was taken to obtain stoichiometric ratios for reactions (1) and (2). Thus, the values of Al mass fraction 0 and 100% in Fig. 1 correspond to the reactions (1) and (2), respectively. With addition of Al, combustion temperature increases from the melting point of $NaBO_2$ (1239 K) to the melting point of Al_2O_3 (2327 K), and then to ~2900 K. The temperature curve slope increases significantly when Al fraction reaches ~50%, which corresponds to the boiling point of $NaBO_2$ (1707 K). This implies that Al-rich mixtures (50-70%) may exhibit high combustion efficiency and yet provide relatively high hydrogen yield (7-8%).

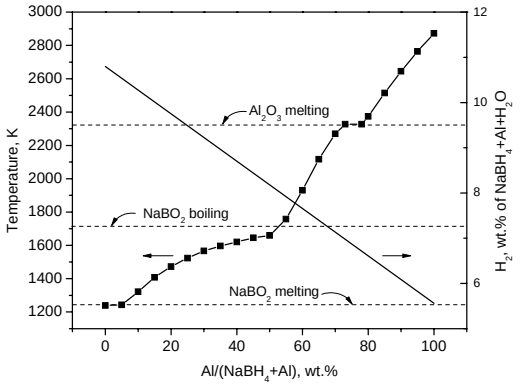

Figure 1. Adiabatic combustion temperature and hydrogen yield of $NaBH_4/Al/H_2O$ system, predicted by thermodynamic analysis (P = 1 atm).

Experimental

Experiments on combustion of $NaBH_4/Al/H_2O$ system were conducted in a 3 L stainless steel chamber equipped with hot-wire ignition system, pressure transducer and windows for reaction monitoring. Preparation of mixtures included addition of 2 wt.% NaOH and 3 wt.% polyacrylamide ($M_w = 5 \times 10^6$) in distilled water, and mixing the resulting gel with $NaBH_4$ and Al powders. Passivated Al nanopowder (average particle size 80 nm, free metallic aluminum 83%; Nanotechnologies) was used in the experiments. The obtained mixture was placed in a quartz cylinder (height 3 cm, diameter 1 cm) and ignited by Nichrome coil inside the chamber. The experiments were conducted in argon at initial pressure of 1 atm. A high-speed video camera (Phantom 5.1) was used for visualization of combustion and measurement of front velocity. The chamber pressure was monitored using a pressure transducer and the resulting gas composition was analyzed by gas chromatography.

Results

Experiments with various $Al/NaBH_4$ mixture ratios at stoichiometric water contents show that addition of Al significantly stimulates combustion. Reaction with no aluminum addition requires permanent heating by the igniter while Al-rich mixtures burn vigorously, similar to typical SHS processes (Fig. 2). Gas generation leads to increase in chamber pressure (Fig. 3), and analysis shows that the evolved gas is essentially hydrogen. Table 1 compares measured hydrogen yield in different mixtures with the theoretical values.

In summary, the used sodium borohydride/aluminum/water mixtures are combustible and exhibit higher hydrogen yield than

theoretically possible for reaction (2). Additional improvements are being investigated by using different borohydrides and by tuning the reaction conditions.

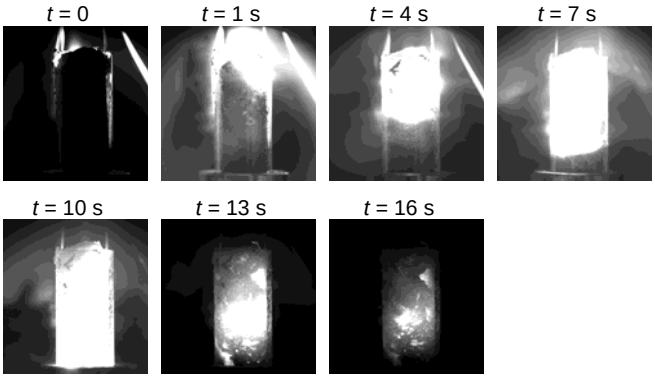

Figure 2. Images of combustion front propagation in mixture $NaBH_4$:Al:H_2O = 1:2:3 (mass ratio).

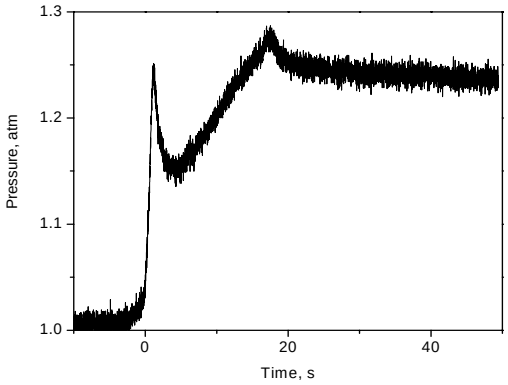

Figure 3. Chamber pressure variation during combustion of mixture $NaBH_4$:Al:H_2O = 1:2:3 (mass ratio).

Table 1. Theoretical and Experimental Hydrogen Yield for $NaBH_4$/Al/H_2O Combustion.

Al : $NaBH_4$ mass ratio	Al : (Al+$NaBH_4$) wt.%	H_2 yield wt.%		Efficiency %
		theoretical	measured	
0 : 1	0	10.8	8.3*	77*
1 : 3	25	9.5	6.5	68
1 : 2	33	9.1	6.0	66
1 :1.5	40	8.7	6.7	77
1 : 1	50	8.2	6.3	77
1.5 : 1	60	7.7	5.5	71
2 : 1	67	7.3	5.4	74
3 : 1	75	6.9	5.1	74
1 : 0	100	5.6	2.8	50**

*Obtained with continuous external heating.
**Compares well with literature data [3].

References

(1) Schlesinger, H.I.; Brown, H.C.; Finholt, A.E.; Gilbreath, J.R.; Hoekstra, H.R.; Hyde E.K. *J. Am. Chem. Soc.*, **1953**, *75*, 215.
(2) Desgardin, N.; Perut, C.; Renouard, J. *U.S. Patent Application* 20040065865, *European Patent* 1405824, **2004**.
(3) Ivanov, V.G.; Leonov, S.N.; Savinov, G.L.; Gavrilyuk, O.V.; Glazkov, O.V. *Combust. Explos. Shock Waves*, **1994**, *30*, 569.
(4) Shiryaev, A.A. *Internaional J. Self-Propagating High-Temperature Synthesis*, **1995**, *4*, 351.

ORGANOMETALLIC COMPLEXES FOR HYDROGEN STORAGE

Yufeng Zhao, A.C. Dillon, Y.-H. Kim, M.J. Heben, and S.B. Zhang

National Renewable Energy Laboratory, Golden, Colorado 80401

Introduction

Hydrogen is a renewable energy source that could replace petroleum to fuel cars, with a concomitant improvement in air quality.[1] However, without a suitable matrix, it's not safe to compress this highly flammable gas at the extremely high pressures required for feasible on-board vehicular storage. For decades, researchers have been struggling with metal-hydrides, chemical hydrides and carbon adsorbents. Although there has been some promising research,[2-5] practical hydrogen storage for vehicular applications is still far from being achieved. The simple principle for rechargeable hydrogen storage at near ambient temperature and pressure has not yet been demonstrated. Thus, the technological community realizes a breakthrough is necessary. Here we predict theoretically both a novel concept and realistic nanoscale materials that fulfill this purpose.

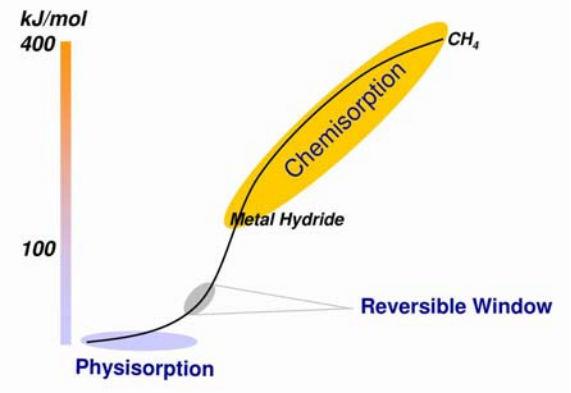

Figure 1. Schematic spectrum of hydrogen binding energies for different types of adsorbents.

There are two key parameters for hydrogen storage. The first is the binding energy relative to free H_2 molecules (not to free H atoms). The second is the capacity or weight percentage (wt%) of retrievable hydrogen gas from the material system (medium plus hydrogen). Ultimately, the weight of the container must also be included for the overall system calculation.

In nature, most hydrogen exists in chemical compounds like H_2O and CH_4. The binding energy of hydrogen in compounds ranges from ~100 kJ/mol in metal-hydrides to ~400 kJ/mol in CH_4, as shown in Fig. 1. Because the binding energy of hydrogen in metal-hydrides represents a minimum for in elements known to store hydrogen, light metals have been investigated as hydrogen storage media for nearly half a century. However, 100 kJ/mol is still too high for practical use as the extraction of hydrogen from metal hydrides requires elevated temperatures.[4] Although catalysts may improve the kinetics of the releasing process[6] by lowering the barrier, they can not reduce the binding energy.

Hydrogen storage on porous carbon materials[7] via physisorption has also been studied at great length. Recent activity in this area was inspired by the discovery of carbon nanotubes[8] and other nanoscale carbon materials, e.g., carbon nanohorns.[9,10] However, physisorption (5-10 kJ/mol) on carbon materials is too weak to stabilize a sufficient amount of hydrogen at room temperature and near ambient pressures.[11] Researchers have tried to enhance the van der Waals binding by increasing the surface area in contact with the H_2 molecules.[12] This, however, unavoidably decreases the hydrogen weight capacity. Induced dipole or charge transfer effects are other possibilities to enhance binding based on electrostatic interactions. [13] However, currently there is no evidence that a moderate binding energy can be achieved with a significant hydrogen capacity.

The ideal binding energy that allows for rechargeable hydrogen storage at room temperature and near ambient pressure is ~20-40 kJ/mol (Fig. 1). This binding energy is stronger than that expected for physisorption but weak compared to that of chemical or metal hydrides. Such an intermediate binding energy was demonstrated in the 1980s, by Kubas et al.[14] The so-called "Kubas complex" $W(CO)_3(P^iPr_3)_2(H_2)$ represents a fundamentally new concept of coordination between a transition metal (TM) and a H_2 ligand, which does not dissociate into hydrides. However, the H-H bond is noticeably elongated with respect to the free molecule. The stability of the molecular hydrogen ligand (dihydrogen) critically depends on the properties of the TM atoms. Empty TM *d*-orbitals, can accept a small fraction of the H-H bond charge, resulting in an intermediate binding energy. The importance of such a binding energy for reversible hydrogen adsorption was later realized.[15] Kubas complexes are generally formed with heavier transition metal atoms, e.g., W, Cr, and Mo, and the binding energy of H_2 is as large as 70~90 kJ/mol,[16] which will not satisfy the requirements for vehicular hydrogen storage. As we showed recently in a systematic investigation of all of the 3-*d* TM atoms,[17] the binding energy of the dihydrogen depends on the TM atoms to which it binds, and can range from 20 to 130 kJ/mol. Therefore, the ideal binding energy is easily achieved by choosing particular transition metals.

Still the right binding energy alone does not satisfy all of the on-board hydrogen storage requirements. Most transition metals are very heavy and adsorb small quantities of hydrogen at moderate temperatures. Recently, a few groups found that multiple dihydrogens may bind to free TM atoms.[18,19] So far this research has not drawn significant attention because free TM atoms will not allow for reversible hydrogen storage due to subsequent cluster formation upon H_2 discharge. The question then is, can the TM atoms be anchored to a light substrate that still allows the TM atoms to bind multiple dihydrogen ligands. This idea is similar to dispersing TM clusters in porous substrates for catalysis applications.[20] For hydrogen storage, however, a much higher standard is required for TM dispersion. The substrate materials have to be very light, and the TM should be separated atom by atom instead of existing in clusters. If one examines the periodic table of elements, carbon is probably the best substrate choice for anchoring TM atoms in organometallic complexes. This is because carbon is the sixth lightest of all elements, and carbon rings are known to complex with transition metals.

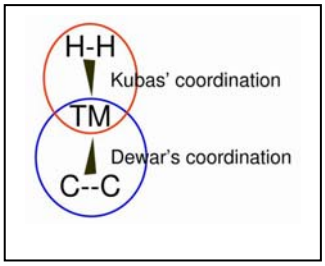

Figure 2. The concept of an organometallic complex with a carbon ligand that could be employed for hydrogen storage. In this sense carbon is used as the supporting material for TM atoms, and the hydrogen that is reversibly retrievable is represented by dihydrogen ligands.

Complexing a TM with a carbon ring may allow organometallic complexes to be the new frontier in vehicular hydrogen storage. As one of the most vigorous fields in modern chemistry, organometallic

chemistry has made vast contributions to a broad variety of technological fields including catalysis[21], light emitters, molecular devices, and liquid crystals.[22] By combining the concepts of Kubas coordination between H_2 and a TM with Dewar's coordination[23] between a carbon ring and a TM, a new class of materials has been predicted. Combining these two types of coordination in one complex (Fig. 2) provides the basis for this article. We will discuss the general principles for the design of organometallic complexes suitable for hydrogen storage and will also provide several examples.

General principle of organometellic design for hydrogen storage

In addition to the basic considerations discussed in the introduction, the organometallic complexs predicted to serve as hydrogen storage media must satisfy the following requirements:

i) Practically, the complexes must be able to survive multiple charging and discharging cycles. Thus, one of the most critical requirements is the complex stability. That means the interaction of the TM atoms with the supporting carbon material has to be much stronger than the interaction with hydrogen. This ensures that no TM atoms will segregate or coalesce into larger clusters.

ii) Geometrically, the TM atoms have to be well separated in the complex so that each TM atom has sufficient open space to take multiple dihydrogen ligands. Also considering the macroscopic scope, the materials must allow for efficient volumetric packing.

iii) In the condition where the TM atoms are well separated, all of the carbon atoms must be employed for supporting the TM atoms. This is required to maximize the hydrogen weight capacity.

iv) The maximum number of hydrogen atoms (including dihydrogen ligands and hydrides) in an organometallic complex can be estimated by the effective atomic number (EAN) rule:[24]

$$N_H = 18N_{TM} - 2b - n_{TM}N_{TM} - n_C N_C \qquad (1)$$

where N_{TM}(N_C), b, n_{TM}, and n_C are, respectively, the number of TM (carbon) atoms, the number of TM-TM bonds, the number of valence electrons per TM atom, and the number of electrons contributed per carbon atom to the TM orbitals. Notice, that when the TM atoms are completely separated from each other, i.e., b = 0, the EAN rule degenerates into the well-known 18-electron rule.

From the EAN rule, one can see that the formation of TM clusters will render the hydrogen storage irreversible. This explains why most bulk TM metals do not have significantly high hydrogen storage capacities at moderate temperatures. Also notice that the lighter TM atoms like Sc and Ti have fewer valence electrons, and hence can accept more hydrogen ligands.

v) Because the EAN rule does not distinguish the hydrides from hydrogen ligands, the chemical properties of the metal should be considered to determine which species will form. From the viewpoint of coordination chemistry, the formation of a hydride more closely resembles a classical covalent bond, whereas, a TM-dihydrogen is a nonclassical coordination. The hydride formation requires unpaired electrons in the TM atom, but the later case occurs when there are empty *d*-orbitals. Thus the number of hydrides that are formed is often correlated with the number of valence electrons in the TM atom. However, the valence electrons do not necessarily lead to hydride formation. In some cases they are used as a source for back donation, i.e., charge transfer from the TM to the anti-bonding orbital of the H_2 molecule.[15] The formation of a given species is determined by energy minimization that may be calculated.

Practically, TM-hydrides are difficult to extract. However, the existence of hydrides leads to stabilization of the storage medium, and results in only a small increase in weight. But according to Eq. (1), the formation of too many hydrides means that fewer dihydrogen ligands will coordinate with the TM, and the reversible hydrogen storage capacity will decrease.

Computational method

We use spin-polarized first-principle calculations as implanted in the Vienna Ab initio Simulation Package (VASP).[25] Ultra-soft pseudopotential with the PW91[26] generalized gradient approximation (GGA) yielding practically the same results to all-electron-like projector augmented-wave (PAW) potential with PBE exchange-correlation functional[27]. An energy cutoff of 400 eV was also employed. Two cubic unit-cell with dimensions between 16 - 25 Å were used as appropriate for the size of the organometellic molecule, to maintain a similar vacuum region.

Binding of dihydrogen ligands to different transition metal atoms

To predict the broad picture of multiply bound dihydrogens and hydrides to various TM atoms, we first studied a very simple complex based on TM interactions with cyclopentadienyl rings (Cp). Hydrogen then interacts with a single 3-*d* TM (from Sc to Ni) with a Cp ligand. When a TM atom binds to a Cp ring, an electron is transferred from the former to the latter to complete the last π bond of the Cp ring, giving rise to aromaticity. The charge transfer also enhances the binding through Coulomb interactions. The calculated binding energies for the CpTM systems are E_b = 3.76, 3.87, 3.47, 2.30, 2.69, 2.97, 3.27, and 3.02 eV, respectively for Sc, Ti, V, Cr, Mn, Fe, Co, and Ni. The number of dihydrogen ligands (N_{H2}) and total number of H (N, including those in dihydrogen and hydrides) bound to the CpTM is listed in Table I. Notice that n_v+ N +5 = 18, when the 5 electrons contributed by the Cp to the TM orbitals through Dewar's coordination are considered.

Taking CpSc as an example, Sc has only two remaining valence electrons after transferring one to the Cp ring. These valence electrons result in the preferential formation of a dihydride species rather than a dihydrogen ligand. Here, the dihydride is strongly bound (1.31 eV/2H). The resulting hydride complex, $Cp[ScH_2]$, has four empty *d* orbitals that can bind four additional dihydrogen ligands with a relatively constant and much lower binding energy of about 0.3 eV/H_2 as shown in Table II. For all the rest of the TM atoms, no more than three hydrides are formed. Note, there are up to 9 valence electrons (Ni) but the formation of hydrides does not initially occur. Instead the binding energy per dihydrogen ligand is much larger for Fe, Co, Ni complexes due to back donation.

Table I. Cp Ring Supported TM Atom Binding with Hydrides and Dihydrogen Ligands. The Number of Valence Electrons (n_v) in the Free TM Atoms and the Number of H Atoms (N) Reflect the 18-e Rule including 5 Electrons from the Cp Ring. The Number of Dihydrogen Ligands (N_{H2}) and Their Average Binding Energy (B) Are also Listed.

	Sc	Ti	V	Cr	Mn	Fe	Co	Ni
n_v	3	4	5	6	7	8	9	10
N	10	9	8	7	6	5	4	3
N_{H2}	4	3	3	2	2	2	2	1
B(kJ/mol)	30	48	61	52	54	99	112	131

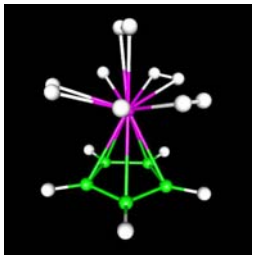

Figure 3. The optimized structure of $Cp[ScH_2(H_2)_4]$, where the Cp ring supported Sc atom binds two hydrides and four dihydrogen ligands. The consecutive binding energy of the four H_2 ligands is shown in Table II.

The fact that the Cp-supported TM atoms can bind multiple dihydrogen ligands shows great potential for the development of a vehicular hydrogen storage system. Sc and Ti bind most strongly with the carbon Cp ring. Also as shown in Table I, these two TM atoms have the highest capacity for dihydrogen ligands, and they bind these dihydrogens with an ideal energy for reversible hydrogen storage at near ambient temperature and pressure. Notice that 6.7 wt % of dihydrogen is stored in $Cp[ScH_2(H_2)_4]$. Unfortunately, according to our calculations, the naked $Cp[ScH_2]$ molecules would form a one-dimensional ionic crystal because the TM atoms are positively charged and the Cp rings are negatively charged. Therefore we have to seek a new architecture in order to achieve reversible hydrogen adsorption.

Hydrogen storage in organometellic buckyballs

The CpTM complexes can be considered as basic building blocks for larger organometallic molecules. For example, with the removal of the five H atoms from each Cp ring, we can envision twelve CpTM units symmetrically arranged in a fullerene structure to form a 12-TM coated $C_{60}TM_{12}$, resulting in an "organometallic buckyball" (OBB). The distance between adjacent TM atoms is 6 Å, allowing for accommodation of H atoms and multiple H_2 ligands.

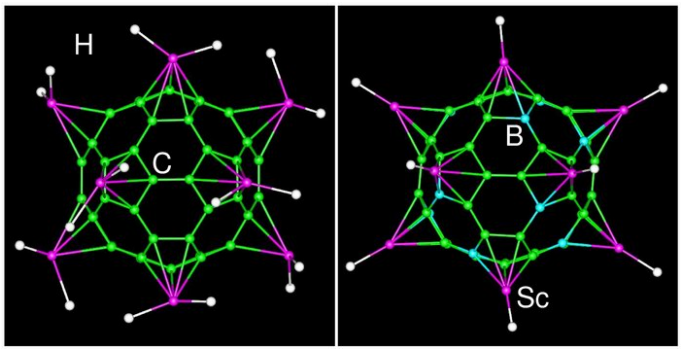

Figure 4. The optimized structure of $C_{60}[ScH_2]_{12}$ (a) and $C_{48}B_{12}[ScH]_{12}$ (b), in which multiple dihydrogen ligands are bound to each Sc atom.

The binding between the TM and pentagonal rings of the C_{60} is, however, weaker than in isolated CpTM molecules (e.g., 1.85 eV per Sc in $C_{60}Sc_{12}$ versus 3.76 eV per Sc in CpSc). This is because the quasiaromatic nature of the C_{60} molecule must be somewhat rearranged to achieve aromaticity that is centered on the TM-coordinated pentagonal rings. Similar to the Cp system each Sc on the C_{60} also binds with two H atoms to form an OBB hydride $C_{60}[ScH_2]_{12}$ (Fig. 4a). Also, similarly to the isolated $Cp[ScH_2]$, the $C_{60}[ScH_2]_{12}$ can bind four additional molecular H_2 ligands to form $C_{60}[ScH_2(H_2)_4]_{12}$. The four H_2 ligands charge and discharge reversibly at room temperature, with a storage density of 7.0 wt%. In sharp contrast to an isolated $Cp[ScH_2]$, however, the $Cp[ScH_2]$ units locked in the OBBs will not polymerize spontaneously. The local dipoles of the $Cp[ScH_2]$ units are spherically oriented, leaving a net positive charge on the exterior. Coulomb forces will cause the molecules to repel one another, prohibit polymerization, and insure reversible hydrogen storage. Thus, the OBBs offer a novel organization of the CpTM species in space that could greatly impact the field of hydrogen storage.

One can further enhance the stability of the complex by substitutionally doping with boron. Boron-doped buckyballs have been experimentally observed[28] and, according to Ref. 29, one can substitute up to 12 boron atoms in C_{60} to form $C_{48}B_{12}$. If OBBs are doped with boron, the B dopants pull more charge from the TM to the buckyball and enhance the TM binding energy. For Sc-coordinated $C_{48}B_{12}Sc_{12}$, the binding energy is increased to 2.7 eV/Sc. Furthermore, this charge transfer leaves each Sc in the hydrogen-bare $C_{48}B_{12}Sc_{12}$ with only one valence electron. Hence, each Sc in $C_{48}B_{12}Sc_{12}$ can bind only a single monohydride to form $C_{48}B_{12}[ScH]_{12}$ (Fig. 4b). The binding energy is then further increased to 3.6 eV/Sc. Then and perhaps most importantly, the B-doped variant permits the binding of five H_2 ligands per Sc, giving rise to the formation of $C_{48}B_{12}[ScH(H_2)_5]_{12}$. In this case, the amount of H_2 retrievable at room temperature is 8.77 wt%. The binding energies of the 5 H_2 ligands remain approximately the same, 30 kJ/mol (Table II).

To test the thermal stability of the OBB complex as shown in Fig. 4, we have performed high-temperature molecular-dynamics simulations. While the Sc-hydrides in $C_{60}[ScH_2]_{12}$ start to form clusters above 600 K, the $C_{48}B_{12}[ScH]_{12}$ remain unchanged at 1000 K for more than 10 picoseconds, indicating the high stability of the latter at room temperature. In this simulation, an H_2 ligand bound to the storage media would desorb within 0.1 picoseconds at 400 K.

Table II. Calculated consecutive binding energies of H_2 molecules (in kJ/mol). In the case of buckyballs, twelve H_2 were added per calculation. A similar trend with the Cp ring case is observed.

	1^{st} H_2	2^{nd} H_2	3^{rd} H_2	4^{th} H_2	5^{th} H_2
$Cp[ScH_2]$	28.0	27.0	44.4	22.3	
$C_{60}[ScH_2]_{12}$	28.9	33.8	40.5	25.1	
$C_{48}B_{12}[ScH]_{12}$	29.9	33.8	28.9	31.8	23.2

TM-coordintion of carbon molecules

We now discuss the energetics of different TM interactions with both buckyballs and carbon nanotubes. Changing the geometries of the various structures has variable effects on the hydrogen storage properties.

Basically, the energy of the TM-coated C_{60} becomes lower as the number of TMs interacting with the fullerene increases. That means the TM-coated OBBs are meta-stable structures. Also increasing the number of TM atoms dramatically will ultimately completely destroy the hydrogen storage capacity according to Eq. (1). The key point is whether the meta-stable structure is stable enough at the operational conditions, approximately room temperature and at near ambient pressures.

On C_{60}, a TM atom could possibly coordinate with three different sites: a) on top of a hexagon (η^6-bonding), b) on top of a pentagon (η^5-bonding), and c) on a double bond (η^2-bonding). For a single Sc atom, the binding energy on these three sites are, respectively, 1.75, 1.56, and 1.49 eV, with the η^6-bonding being most stable. When more Sc atoms are added, however, the situation changes. In the condition that Sc atoms are well separated (meaning no Sc-Sc bonds are formed), the binding energy of η^6-, η^2-bonding remains the same, but the binding energy of the η^5-bonding increases to 1.85 eV/Sc if all 12 pentagons simultaneously complex with Sc atoms. The stability of this configuration is attributed to an elegant rearrangement of the quasiaromatic nature of C_{60}. Now the aromatic nature appears to be shifted to each pentagon of the C_{60}. Specifically, after 1-e is transferred from each Sc to each of the pentagons in C_{60} aromatic five-membered rings are created. Such an effect was first observed in $C_{60}Li_{12}$,[30] and later was termed as a hexagon isolation rule.[31] Our OBB complex $C_{60}[ScH_2]_{12}$ is similar to $C_{60}Li_{12}$ in that the

Sc atom, like the Li atom, transfers one electron to the C_{60}. Unlike $C_{60}Li_{12}$, which is a ground state, the $C_{60}Sc_{12}$ is meta-stable. This is because the Li-Li bond is much weaker than the Sc-Sc bond; therefore, the Sc atoms prefer to form clusters or closely packed islands on C_{60} at elevated temperatures. Notice that Sc metal has the second smallest cohesive energy among the 3-*d* TM metals[32] but the second strongest binding with the Cp ring. Therefore, Sc may be the most promising candidate for complexation with C_{60}.

In $C_{48}B_{12}[ScH]_{12}$, two electrons are transferred to the doped buckyball. The enhanced binding of Sc atoms to the B-doped buckyball further stabilizes the OBB against clustering of Sc atoms as indicated by MD simulations described in the previous section. Again isolation of the Sc atoms on the hexagons makes the B-doped buckyball unique as metal cluster formation is unlikely. In contrast, carbon nanotubes (CNTs) do not have pentagons, and TM atoms would form clusters more easily on its highly conjugated surface.

To complete the study, it is necessary to consider an increase in the number of TMs coordinating with C_{60}. For example, if all of the 20 hexagons on C_{60} coordinate with Sc to form $C_{60}Sc_{20}$ (Fig. 5), the binding energy per Sc will be 2.25 eV due to the subsequent formation of 30 Sc-Sc bonds. The length of these Sc-Sc bonds are ~3.5-3.8 Å compared to 3.3 Å in the bulk metal. This is because the Sc atoms interact more strongly with C_{60} than with each other. According to Eq. (1), the maximum number of hydrogen atoms that a $C_{60}Sc_{20}$ could take is $18\times20 - 2\times30 - 60\times1 - 20\times3 = 180$. In our simulation, when hydrogen is added, the longer Sc-Sc bonds tend to break and the shorter ones become even shorter. This results in making more space for hydrogen interactions. However, due to steric repulsion, the total uptake is less than 180 hydrogen atoms but still as many as 150, with 50 of them are hydrides and a reversible hydrogen storage capacity of only 5.7 wt% is achieved.

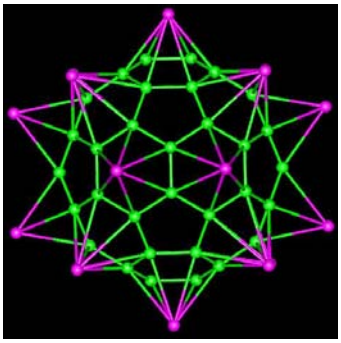

Figure 5. The optimized structure of $C_{60}Sc_{20}$. The twenty Sc atoms (pink) forms η^6-bonds on top of the hexagons of the C_{60} (green cage). For clarity, the stretched Sc-Sc bonds are not shown.

Additionally, we have found that, Ti atoms do not coordinate with C_{60} in the same manner as Sc, because the Ti-Ti interaction is stronger. Some Ti-C coordination is broken, and shorter Ti-Ti bonds are formed. This means $C_{60}Ti_{20}$ is even more prone to the formation of metal clusters.

Hydrogen storage in clusters of transition metal carbides

Well-controlled coordination of buckyballs with TM atoms may not be easy experimentally because the OBBs are meta-stable structures. Alternatively, we can examine already-existing transition metal carbides for hydrogen storage. These clusters have been well known since the metallocarbohedrene (MetCar), Ti_8C_{12} was discovered.[33] We have also examined here the nanocrystal, $Ti_{14}C_{13}$, as it is also a stabile structure. [34] In both cases, Ti atoms are dispersed in the carbon cages and coordination between the Ti atoms and H_2 ligands may occur (Fig. 6).

To estimate the hydrogen capacity in these molecules following Eq. (1), one has to pay attention to the different carbon atoms in the two clusters. In Ti_8C_{12}, the carbon atoms occur as dicarbon units, and the two electrons belonging to each C-C σ-bond do not coordinate with the Ti atom. Therefore, each dicarbon contributes six valence electrons to the Ti orbitals. Then considering of the 18 Ti-Ti bonds, the hydrogen capacity is $N_H = 18\times8 - 2\times18 - 4\times8 - 6\times6 = 40$ in Ti_8C_{12} corresponding to a hydrogen capacity of 7.1 wt%. In $Ti_{14}C_{13}$, each C atom contributes 4 valence electrons to the Ti orbitals and there are 36 Ti-Ti bonds. Now we have $N_H = 18\times14 - 2\times36 - 4\times14 - 4\times13 = 72$ corresponding to a hydrogen capacity of 8.0 wt%.

Actual simulations give capacities of 34 and 68 H atoms (6.1% and 7.6%), respectively, for Ti_8C_{12} and $Ti_{14}C_{13}$. The lower calculated capacity might be attributed to steric repulsion. The details of these results will be discussed elsewhere.

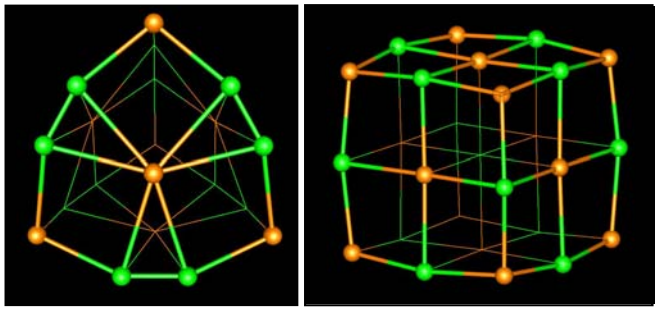

Figure 6. The optimized structure of Ti_8C_{12} (left) and $Ti_{14}C_{13}$ (right). The Ti and C atoms are shown, repectively, in orange and green. For clarity, the front sides are presented in ball-and-stick, the backsides are in wireframes, and no Ti-Ti bonds are shown.

Conclusion

We have theoretically demonstrated hydrogen storage with an optimal binding energy in novel organometallic systems. The most promising result is the high reversible hydrogen capacity at near ambient temperature and pressure. While we have shown a great potential of various nanoclusters including OBBs and MetCars, there is no reason to believe that other systems cannot be constructed based on these same principles. Efficient volumetric packing of these nanoscale structures could offer practical hydrogen storage for vehicular use in the near future. Our theoretical results are supported by our previous experiments, where defective carbon nanotubes with TM clusters adsorb dihydrogen.[2,35] Also, in other recent experiments it was found that when transition metals are milled in the presence of 10 wt% graphite, the hydrogenation properties are improved considerably.[36] This may be due to dihydorgen adsorption on TM atoms that are coordinated with carbon rings.

Acknowledgement. Support for this project comes from the Office of Science, Basic Energy Sciences, Division of Materials Science and the Office of Energy Efficiency and Renewable Energy Hydrogen, Fuel Cell, and Infrastructure Technologies Program of the Department of Energy under Grant No. DE-AC36-99GO10337. Y.Z. and S.B.Z. acknowledge DOE's NERSC for MPP supercomputing time.

References

(1) Crabtree, G.W.; Dresselhaus, M.S.; and Buchanan, M.V. *Physics Today* **2004**, 57, 39.
(2) Dillon, A. C., *et al.*, *Nature* (London) **1997**, 386, 377.
(3) Liu, C., *et al.*, *Science* 1999, 286, 1127.
(4) P. Chen, Z. Xiong, J. Luo, J. Lin, and K.L. Tan, *Nature* (London), **2002**, 420, 302.
(5) Lee, H. *et al.*, *Nature* **2005**, 434, 743.

(6) Haiduc, A. G.; Stil, H. A.; Schwarz, M. A.; Paulus, P.; Geerlings, J. J. C. *J. Alloys Compd*. 2005, **393** 252; Jensen, C. M. and Gross K. J. Appl. Phys. A **2001**, 72, 213.
(7) Carpetis, C; Peschka, W. *Int. J. Hydrogen Energy* **1980**, 5, 539; Rzepka, M.; Lamp, P.; de la Casa-Lillo, M. A. *J. Phys. Chem. B* **1998,** *102,* 10894.
(8) Iijima, S. *Nature* (London) **1991**, 354, 56.
(9) Ajima, K.; Yudasaka, M.; Suenaga, K.; Kasuya, D.; Azami, T.; and Iijima, S. A*dvanced Materials* **2004**, 16, 397.
(10) Bandow, S., et al. *Chem. Phys. Lett*. **2000**, 321, 514.
(11) Ye, Y., *et al*, *Appl. Phys. Lett*. **1999**, 74, 2307.
(12) Okamoto, Y.; Miyamoto, Y.; *J. Phys. Chem. B* **2001,** *105*, 3470.
(13) Jhi, S.-H. and Y.-Kyun Kwon, Phys. Rev. B **2005**, 71, 035408; Murata, K.; Hashimoto, A.; Yudasaka, M.; Kasuya, D.; Kaneko, K.; and Iijima, S. A*dvanced Materials* **2004**, 16, 1520.
(14) Kubas, G. L.; Ryan, R. R.; Swanson, B. I.; Vergamini, P. J.; Wasserman, H. J. *J. Am. Chem. Soc***. 1984,** 106,451.
(15) Kubas, G.J. *J. Organometallic Chem.* **2001**, 635**,** 37.
(16) Mediati, M.; Tachibana, G. N.; and Jensen, C. M. *Inorg. Chem.* **1992**, 31, 1827
(17) Y. Zhao, Y.-H. Kim, A.C. Dillon, M.J. Heben, and S.B. Zhang, *Phys. Rev. Lett.* **2005**, 94, 155504.
(18) Niu, J.; Rao, B.K.; and Jena, P. *Phys. Rev. Lett.* **1992**, 68, 2277.
(19) Gagliardi, L. and Pyykkö, P. *J. Am. Chem. Soc*. **2004**, 126, 15014.
(20) Gates, B.C. *Chem. Rev*. **1995**, 95, 511.
(21) Gladysz, J. A., *et al*. *J. Am. Chem. Soc*. **1986**, 108, 7863.
(22) Hudson, R. D. A. *J. Organometallic Chem*. **2001**, 637–639, 47.
(23) Michael, D. and Mingos, P. *J. Organometallic Chem*. **2001**, 635, 1.
(24) Crabtree, R.H. *The Organometallic Chemistry of the Transition Metals*; John Willey & Sons Inc., 1988.
(25) G. Kresse *et al*., http://cms.mpi.univie.ac.at/VASP
(26) Perdew J.P. *et al*, *Phys. Rev. B* **1992**, 4**6**, 6671.
(27) Perdew, J.P.; Burke, K.; Ernzerhof, M. *Phys. Rev. Lett*. **1996**, 77, 3865.
(28) T. Guo, C.M. Jin, and R.E. Smalley, J. Phys. Chem. **95**, 4948 (1991).
(29) R.-H. Xie *et al*., Phys. Rev. Lett. **90**, 206602 (2003).
(30) Kohanoff, J.; Andreoni, W.; Parrinelo, M. *Chem. Phys. Lett*. **1992**,198,472.
(31) Jemmis, E.D.; Manoharan, M.; and Sharma, P. K. *Organometellics* **2000**, 19, 1879.
(32) C. Kittel, *Introduction to solid state physics*, 7th ed. (Wiley, New York, 1960).
(33) Guo, B.C.; Kerns, K.P.; Castleman, A.W., Jr. *Science* **1992**, 255, 1411-1413.
(34) Pilgrim, J. S.; Duncan, M. A. *J. Am. Chem. Soc.* **1993**, *115*, 9724.
(35) A.C. Dillon *et al.*, Mat. Res. Soc. Proc. **801**, 167 (2003).
(36) Bouaricha, S.; Dodelet, J.-P.; Guay, D.; Schutz, R. *J. Alloys Compd*. **1999**, 285, 119.

EXFOLIATED GRAPHITE NANOFIBERS FOR HYDROGEN STORAGE

Angela D. Lueking, Ling Pan, Deepa Narayanan, Caroline E.B. Clifford

The Pennsylvania State University
University Park, PA 16802

Abstract

Exfoliation of graphite nanofibers (GNF) expands the interplanar spacing of the GNF which leads to increased hydrogen storage. The exfoliation technique plays a large role in the resulting GNF microstructure, surface area, and hydrogen storage properties. Variations in preparation conditions expand the GNF lattice from 3.4 Å to over 500 Å. The BET surface area of the exfoliated GNF increases as much as 10-fold to 555 m^2/g. Increased surface area correlates with low temperature physisorption of hydrogen at 77K with an observed uptake of 1.2% at 77K and 20 bar. Conversely, observed dislocations in the graphitic structure correlate with a fourteen-fold increased ambient temperature adsorption at 20 bar. These results suggest that selective exfoliation of a nanocarbon is a means by which to control the relative binding energy of the hydrogen interaction with the carbon structure and thus vary the operative adsorption temperature.

Introduction

Despite early hydrogen storage claims in carbon materials that were largely irreproducible, reports continue to emerge showing hydrogen uptake ranging from 3-17%. An explanation emerging from these reports is that post-synthesis treatments modify the carbon structure and enhance hydrogen adsorption. Nuclear diffraction has shown that hydrogen may become chemically bound to graphitic carbon during certain preparations [1], terminal carbons have been suggested to act as catalytic entities to dissociate hydrogen [2], and electron micrographs have suggested that simple exposure to hydrogen may expand the graphite lattice of certain carbon nanostructures [3].

In an effort to test the emerging hypothesis that defects, dislocations, and/or terminal carbons lead to increased hydrogen storage via hydrogen intercalation into the graphite lattice, we have worked to develop methods that expand the graphite lattice a priori in nano-carbonaceous materials. Unlike exfoliation of single-wall nanotubes, intended to separate bundles into individual tubes, our exfoliation method targets intra-particle spacings. Our method is derived from well-established techniques to exfoliate graphite, in which intercalation of graphite is followed by a thermal shock to expand the graphitic layers.

Herringbone GNF provide an interesting candidate for carbon exfoliation, with their slit-pore geometry, nano-scale dimensions, high aspect ratio, and graphitic layers that terminate along the fiber axis. Herringbone graphite nanofibers (GNF) provide an interesting candidate for carbon exfoliation, with their slit-pore geometry, nano-scale dimensions, high aspect ratio, and graphitic layers that terminate along the fiber axis. It was previously thought that the high aspect ratio and nanoscale dimensions of the GNF would preclude exfoliation. However, our preliminary data shows that we have successfully exfoliated herringbone GNF, with a resulting nanoscale structure that is previously unreported.

Experimental

Highly ordered, herring-bone graphite nanofibers were purchased from Catalytic Materials, Ltd; with a metal content of less than 1% as reported by the manufacturer; these GNF had a low baseline hydrogen uptake and were not activated prior to us. Based on preliminary studies with graphite exfoliation, the primary exfoliation method used in this study was a 50/50 mixture of nitric and sulfuric acids followed by thermal shocking at 700 °C (EGNF-700). A portion of this sample was subjected to an additional high temperature treatment by heating the sample under flowing Argon at 1000 ºC for 36 hours (EGNF-1000).

Characterization. Materials were characterized using standard BET methods with nitrogen at 77K (Quantachrome Autosorb I) and helium densitometry measurements (Hiden IGA-003). Scanning electron microscopy (SEM) (Philips XL20) and TEM (JEOL 2010 and JEOL 2010F) were used to characterize the microstructure of the material. Total ash content was determined by temperature programmed oxidation on a low-pressure Perkin Elmer Thermogravimetric analyzer 7 (TGA).

Hydrogen Uptake. A high-pressure thermo-gravimetric analyzer (Hiden Isochema IGA-003) was used to evaluate hydrogen uptake at pressures up to 20 bar. The IGA provided a highly sensitive (+1 μg) measurement with precise temperature and pressure control for automated measurements of adsorption and desorption isotherms. All samples were subjected to an in situ degas at 150 °C, unless otherwise stated. Hydrogen uptake measurements were normalized to sample mass after pretreatment, with buoyancy corrections determined from density measurements with helium. With a typical sample size of 50 mg, the error in the hydrogen due to instrumental limitations is +0.02 wt% absolute. Select samples were chosen for quality checks to ensure the reproducibility of the measurements.

Results and Discussion

The exfoliated GNF retains the overall nanosized dimensions of the original GNF, with the exfoliation temperature determining the degree of induced defects, lattice expansion, and resulting microstructure. Transmission electron microscopy (TEM) confirmed the herringbone structure of the lattice spacing and a 3.4 Å lattice spacing (Figure 1). The EGNF-700 fibers had dislocations in the graphitic structure and a 4% increase in graphitic lattice spacing to 3.5 Å (Figure 2). The EGNF-1000 fibers were significantly expanded along the fiber axis, with regular intervals of graphitic and amorphous regions ranging from 0.5 to >50 nm in width (Figure 3). The surface area of the starting material was increased from 47 m^2/g to 67 m^2/g for EGNF-700 and to 555 m^2/g for the ENGF-1000 (Table 1).

Table 1. Characterization of GNF before and after Exfoliation

	GNF	EGNF-700	ENGF-1000
Treatment	None	Acid intercalation; 700 °C 2 minutes	+ 1000 °C for 36 hours in Argon
BET Surface Area (m^2/g)	47	67	555
Helium Density (g/cm^3)	1.38	1.04	1.36
H_2 Uptake (77K, 20 bar)	0.34%	0.39%	0.39%
H_2 Uptake (300K, 20 bar)	0.02%	0.29%	0.03%
Ash Content (wt%)	1.5%	*	1.1%

*in progress

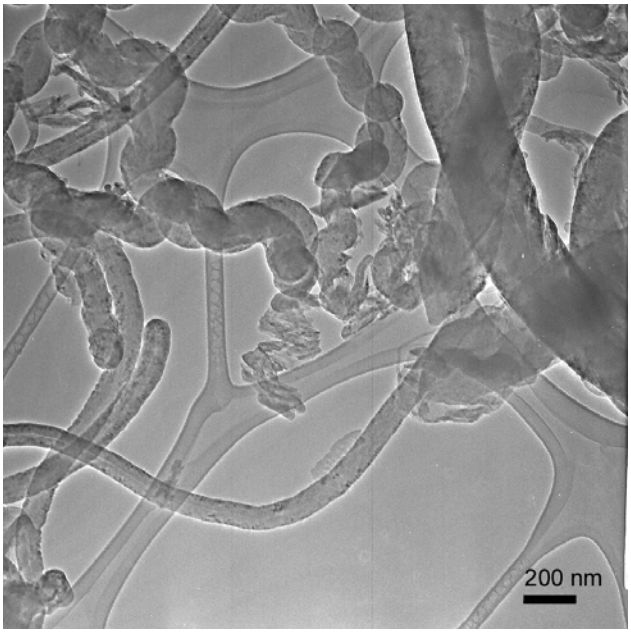

Figure 1. Transmission electron micrographs of untreated GNF.

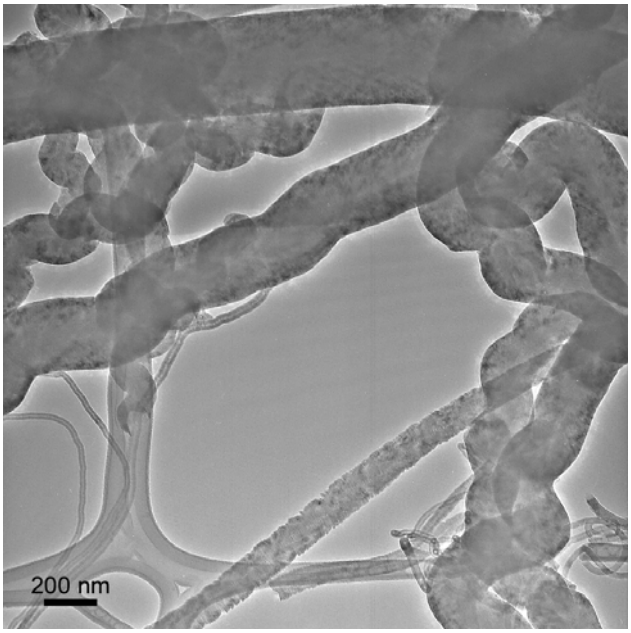

Figure 2. Transmission electron micrographs of exfoliated GNF after a 700 °C thermal treatment (EGNF-700)

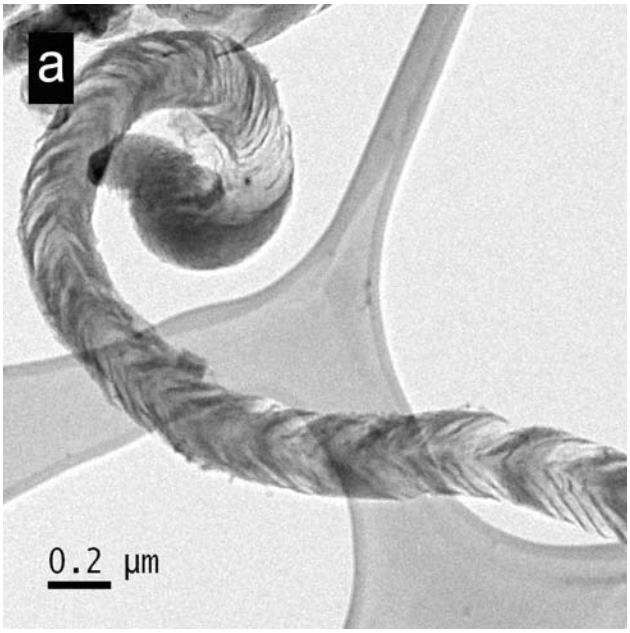

Figure 3. Transmission electron micrographs of exfoliated GNF after an extended 1000 ° thermal treatment.

Hydrogen uptake measurements at 20 bar indicate that the overall hydrogen uptake and operative adsorption temperature are sensitive to the structural variations and graphitic spacing. The increased surface area of the ENGF-1000 led to a 1.2% hydrogen uptake at 77K and 20 bar, a three-fold increase in hydrogen physisorption of the starting material (Figure 4). The uptake of the 700 °C treated material had a 0.29% uptake at 300K and 20 bar (figure 5); although low, this was a fourteen-fold uptake over the starting material and higher than other commonly used pretreatment methods. These results suggest that selective exfoliation of a nanofiber is a means by which to control the relative binding energy of the hydrogen interaction with the carbon structure and thus vary the operative adsorption temperature.

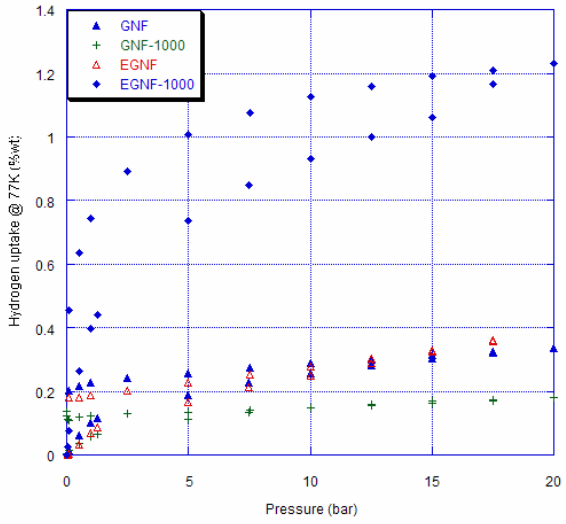

Figure 4. Hydrogen Isotherms for various fibers at 77K.

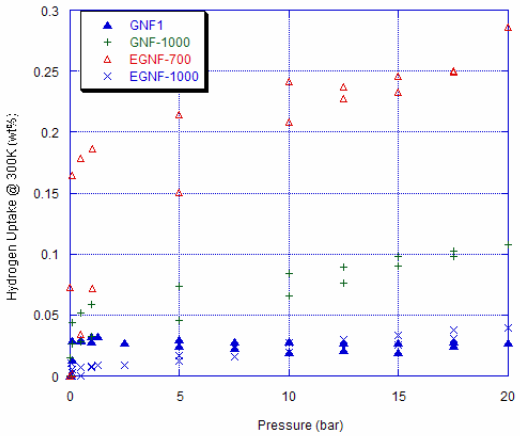

Figure 5. Hydrogen Isotherms for various fibers at 300K.

The overall hydrogen uptake for the EGNF-700 and EGNF-1000 is not close to the DOE hydrogen storage targets. We are, however, encouraged by the data that suggests that exfoliation is a means by which to control the carbon-hydrogen binding energy. At 77K, the hydrogen uptake for EGNF-1000 is comparable to recent reports of 2.7 wt% uptake in a spherical nanoporous carbon with surface areas between 946 and 1646 m^2/g at 77K and 50 bar[4] and 2 wt% for commercially available activated carbon fibers at 77K and 20 bar.[5]

Conclusions

A new exfoliated carbon fiber with nanodimensions was synthesized by graphite exfoliation followed by high temperature treatment. The exfoliated carbon nanofiber had a unique microstructure, with repeating units of high-density graphitic regions separated by low density regions that were amorphous in nature. An expansion along the fiber axis was accompanied by a ten-fold increase in BET surface area. At the other end of the preparation spectrum, GNF were prepared with mild dislocations within the graphitic structure and a 4% increased latticed spacing. Overall hydrogen uptake and operative adsorption temperature was drastically different for these two exfoliated materials, suggesting a means by which to control the carbon-hydrogen binding energy through variation of exfoliation conditions. Future work will include systematic variations on exfoliation conditions in an attempt to synthesize materials with an array of slit pore dimensions, and include subsequent chemical treatments to control the resulting surface chemistry on the exfoliated carbon structures.

Acknowledgement. The authors would like to thank E. Dickey for her feedback on the TEM presented in this work. This work was funded through start-up funds proved by PSU's Institute for the Environment, The Energy Institute, and the College of Earth & Mineral Sciences. Funding for exfoliation of carbon for hydrogen storage was provided, in part, by the H2E Center at Penn State University.

References

(1) Fukunaga, T., K. Itoh, S. Orimo, M. Aoki, and H. Fujii. *Journal of Alloys and Compounds*, **2001,** 327, 224.
(2) Browning, D.J., M.L. Gerrard, J.B. Lakeman, I.M. Mellor, R.J. Mortimer, and M.C. Turpin. *Nano Letters*, **2002**, 2, 201.
(3) Gupta, B.K. and O.N. Srivastava. *International Journal of Hydrogen Energy*, **2001**, 26, 857.
(4) Terres, E.; Panella, B.; Hayashi, T.; Kim, Y. A.; Endo, M.; Dominguez, J. M.; Hirscher, M.; Terrones, H.; Terrones, M. *Chem Phys Lett* **2005,** *403*, 363.
(5) Kadono, K.; Kajiura, H.; Shiraishi, M. *Appl Phys Lett* **2003**, *83*, 3392.

INELASTIC NEUTRON SCATTERING OF H_2 ADSORBED ON ACTIVATED CARBON

D.G. Narehood[a], H. Goto[b], P.E. Sokol[c], and P.C. Eklund[a]

[a] Department of Physics and Materials Research Institute Penn State University, University Park, PA 16802 USA

[b] Honda Fundamental Research Laboratories, Tokyo, Japan

[c] Indiana University Cyclotron Facility
Indiana University
Bloomington IN 47408, USA

Introduction

The properties of H_2 adsorbed in porous media and on surfaces are of interest for both applied and fundamental reasons. With the strong interest in moving from Petroleum to a Hydrogen economy, a determination of an adequate fuel storage device is essential. The microscopic properties of the adsorbed H_2 will undoubtedly play a role in this determination. On the fundamental side, adsorption of H_2 on surfaces is off interest due to the unique properties of the molecules. For instance, the overall symmetry requirements of H_2 restrict even rotational states to have a combined nuclear spin of 0 (para-H_2) while odd rotational states are restricted to have a combined nuclear spin of 1 (orho-H_2). In addition, due to the light mass of the molecule, its zero-point motion dominates the molecules momentum distribution.

Properties of the molecule such as the rotational behavior, ortho-to-para conversion, and momentum distribution are sensitive to the molecule's local environment. We have used inelastic neutron scattering (INS) to investigate these properties for H_2 adsorbed on an Activated Carbon (AC) for various fillings.

Experimental

AC Sample. In these studies, 2 g of a commercially available AC sample was utilized. The surface area of the sample was determined to be 1600 m^2/g from an N_2 adsorption isotherm taken at 77K**.** Prior to utilization of the sample in the INS measurements, the sample was baked at a temperature of 1000K under vacuum ($P \leq 10^{-6}$ torr) for ~24 hrs. This process was performed to remove strongly physisorbed impurities such as H_2O and CO_2 from the AC sample. After this treatment, the sample was stored in an inert helium atmosphere.

INS Measurements. The inelastic neutron scattering measurements were performed on the MARI time-of-flight (TOF) chopper spectrometer at the ISIS spallation source at the Rutherford Appleton Laboratory (Didcot, UK). Due to the low-resolution requirements and the desire to optimize intensity, the spectrometer was equipped with their "sloppy" chopper. This chopper was phased to select incident neutron energies of 50 meV, for the rotational and conversion studies, and 750 meV, for the deep inelastic neutron scattering measurements (DINS). TOF data were collected by neutron detectors covering a scattering angle of 3 to 135° as well as by the monitors, located in front of and behind the sample cell. Analysis of the monitor data allows a determination of the incident neutron energy and the time at which the neutrons are scattered from the sample.

For the INS measurements, the AC sample was placed in a sample cell with an annular geometry. This cell was then attached to the cold finger of closed cycle refrigerator and cooled to 20K where the sample was filled with n-H_2 (75% ortho-H_2, 25% para-H_2). A standard gas handling system allowed precise control of the amount of H_2 introduced to the sample. Both rotational and DINS spectra were collected for fillings ranging from ~0.38 filling to a full pore filling with the temperature held fixed at 20K. Temperatures were measured with a commercial Silicon diode thermometer placed at the top of the cell.

In addition to the INS spectra collected with the AC sample loaded with H_2, spectra were also collected with the just the sample cell and AC sample. These background spectra were subtracted from spectra collected with H_2, with an attenuation correction factor applied, to provide spectra consisting of scattering solely from H_2.

Results and Discussion

The INS spectra collected from neutrons with an incident energy of 50 meV have been utilized to probe the effect of the interaction of H_2 with the AC surface on the rotational states of the adsorbed molecules. The rotational energy levels for a free rotor are given by $E_{rot} = J(J+1)B$, where J is the rotational quantum number and B is the rotational constant, which for molecular hydrogen is 7.35 meV[1]. Each of these levels posses a degeneracy of $2J+1$. An energy level diagram with the rotational ground state and the first excited state is shown on the left in **Figure 1**. Indicated in the diagram are the neutron induced rotational transitions that can be observed in an INS spectrum. The transition between the J=0 and J=1 states requires both a change in rotational quantum number as well as a change in the combined nuclear spin of the molecule as a result of the overall symmetry requirements of the molecules wave-function. Introduction of an orientationally dependent potential in the Hamiltonian of H_2 can result in a splitting of the degenerate rotational states and a corresponding change in the energies of these states. Such behavior has been observed for H_2 absorbed on the pore walls in both xerogel[2] and zeolite[3].

A background subtracted INS spectrum with the rotational energy level transitions for H_2 on AC for the full pore filling is shown on the right in **Figure 1**. Clearly present in the spectrum collected after initial H_2 loading is an elastic peak, a peak at –14.7 meV, and a peak at 14.7 meV. The elastic peak is attributed to transitions between sublevels of the J=1 state, while the peaks at –14.7 meV and 14.7 meV are attributed to the J=1→0 and J=0→1 transitions, respectively, as indicated in the diagram. These transitions occur at their free-rotor values, allowing use to conclude that the rotational states are not altered and consequently, that the H_2-AC interaction does not posses and orientational dependence. At all fillings studied, the same rotational behavior is exhibited. This indicates, as expected, that the H_2-H_2 interactions does not produce an effect on the molecules rotational behavior.

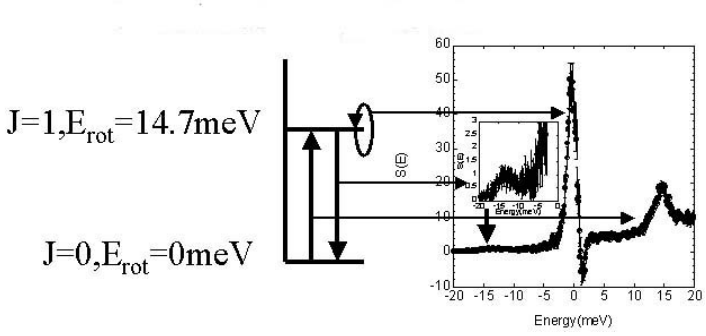

Figure 1. Rotational energy level diagram for H_2 (left) acting as a free rotor and a rotational spectrum collected from a full pore of H_2 adsorbed on AC shortly after H_2 loading (right).

After ~6 h after H_2 loading, only the peak at 14.7 meV remains in the spectra, which is a clear indication that all molecules in the

ortho-state have converted to the para-state. Because the intensity of the peak at 14.7 meV is directly proportional to the concentration of para-molecules in the system, the details of this ortho-to-para conversion process have been studied by following the time-dependence of the peak at 14.7 meV as shown in **Figure 3** for a full pore H_2 filling.

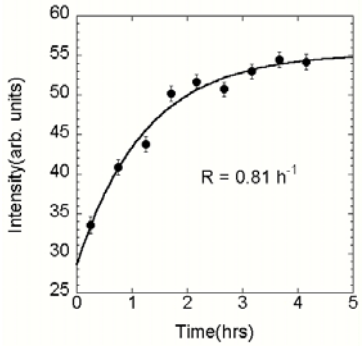

Figure 2. Time-dependent intensity of the peak at 14.7meV for the rotational spectra collected from a full pore filling of H_2 on AC.

We have found that the data in **Figure 2** is best fit with an exponential of the form

$$c_{para}(t) = 1\text{-}c_{ortho}(0)e^{-Rt}$$

where $c_{para}(t)$ is the time-dependent para concentration, $c_{ortho}(0)$ is the initial ortho-concentration, and R is the rate constant. For the conversion data shown in **Figure 2** R =0.81±.11h-1. The exponential form of the conversion, as well as the conversion rate, are independent of H_2 filling. The exponential conversion of the molecules as well as the independence of the conversion rate on H_2 filling indicate that the conversion is caused predominately by the interaction of the adsorbed molecules with the AC. This is in contrast to the bi-molecular conversion process observed for the bulk solid H_2[1]and H_2 adosrbed in the pores of zeolite[3]. The bi-molecular nature of the conversion process in these instances, indicates that it is the interaction of the H_2 molecules with each other that is responsible for the conversion.

The conversion we observe for H_2 adsorbed on AC is very much faster than observed in the previously mentioned systems. While it is difficult to make a direct comparison due to the different nature of the conversion processes, we can compare the times at which the original ortho-concentration is reduced by a factor of 2. The half-lives in the bulk solid H_2 (K = 1.8%/h, K = rate constant) and H_2 adsorbed on the pore wall of zeolite (K=8.5%/h) are ~70 h and ~19 h, respectively, in comparison to the half-life of ~1hr for H_2 adsorbed on AC. Conversion of the molecules adsorbed on the AC sample is greatly enhanced over the bulk and H_2 adsorbed in the pore wall of zeolite.

The DINS spectra collected from neutrons with incident energies of 750 meV have been used to study the momentum distribution of H_2 adsorbed on AC. Using the impulse approximation[5], mean kinetic energies (<KE>) have been extracted for the adsorbed molecules for each filling from the widths of scattering peaks appearing in DINS spectra such as the one shown in **Figure 3a**. The extracted <KE> for each filling are shown in **Figure 3b**. Included for comparison in the plot of <KE> vs. filling are values extracted for the <KE> of H_2 adsorbed on graphite in both the commensurate phase (solid line) and incommensurate phase (long dashes) as well as the estimate for contribution of the H_2-C interaction to the molecules <KE> (short dashes)[3]. Although we do not have <KE>'s for fillings lower than ~ 0.38 due to the correspondingly low scattering intensity, we expect the contribution of the H_2-C interaction to <KE> (~55-57K) to provide a lower limit for <KE> in our system as the filling approaches zero. It is probable that the <KE> in the low filling regime is greater than this estimate due to the curvature of the AC surface which will enhance the localization of the adsorbed molecules with respect to the case of H_2 on planar graphite.

Obvious in **Figure 3b** is the strong dependence of the <KE> on filling. The observed increase in <KE> to a filling of ~0.75 results from the strong contribution the molecules zero-point motion has on the mean kinetic energies. As the filling is increased, the localization of the molecules is in increased, which results in a corresponding increase in <KE>. The <KE> of the H_2 on AC at this filling is comparable to that of H_2 on planar graphite in the commensurate phase, indicating that the localization of the molecules in each case is comparable. At full pore filling, the <KE> does not approach the value extracted for the incommensurate phase of H_2 on planar graphite. Instead the <KE> is within error of the measured <KE> at the 0.75 filling. This lack of increase in <KE> is understood by the H_2 entering the micropores of the AC sample and not contributing to the compression of molecules adsorbed on the AC surface.

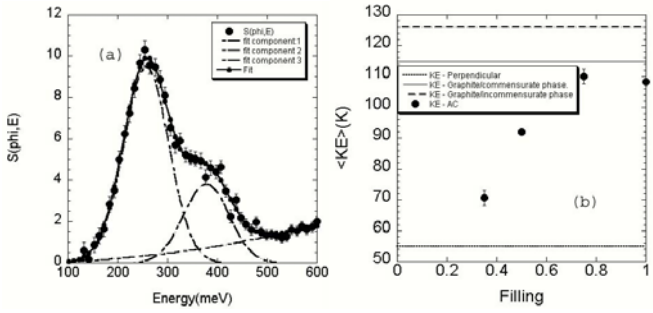

Figure 3. (a) A DINS spectrum collected from the full pore filling of H_2 on AC. (b) <KE> as a function of H_2 filling. Also shown for comparison are the <KE> for H_2 on graphite in the commensurate (solid line) and incommensurate phase (dashed line) as well as the contribution to the <KE> for H_2 on graphite from the H_2-C interaction.

Conclusions

We have studied the microscopic properties of H_2 adsorbed on AC as a function of H_2 filling. The adsorbed molecules exhibit free-rotor behavior at all fillings, indicating that a lack of orientational dependence in the H_2-AC interaction. The ortho-to-para conversion of the adsorbed molecules is also independent of filling and is well described by a exponential model. This conversion is much faster than exhibited in the bulk solid as well as for H_2 adsorbed in other porous media such as zeolite. The <KE> exhibits a strong dependence on filling, increasing as the filling in increased, except at the full pore filling. This lack of increase in <KE> results from H_2 entering the pores of the sample and not causing further localization of molecules adsorbed on the surface.

Acknowledgement. This work was supported by the Department of Energy under Grant DE-FC36-05GO15077 and by Honda Research and Development.

References

(1) Silvera, I.F.; *Rev. Mod. Phys.***1980**, 52, 393.
(2) Narehood, D.G.; Grube, N.; Dimeo, R.M.; Brown, D.W; Sokol, P.E.; *J.Low Temp. Phys.*,**2003**, 132, 223.
(3) Brown, D.W.; Sokol, P.E, Fitzgerald, S.A.; *Phys Rev. B.* **1999**, 59, 13258.
(4) Kellog, G.J.; Sokol, P.E.; Sinha, S.K.;Price, D.L.; *Phys Rev. B.* **1990**, 42, 7725.
(5) Hohenberg, P.C.; Platzman, P.M.; *Phys. Rev.* **1966**, 152, 198.

LOW TEMPERATURE CARBON DIOXIDE ACTIVATION OF MULTI-WALLED CARBON NANOTUBES FOR HYDROGEN STORAGE

John M. Andresen[1], James M. Blackman[1], Colin E. Snape[1], John W. Patrick[1] and Colin Jennis-McGroarty[2]

[1] School of Chemical, Environmental and Mining Engineering, University of Nottingham, University Park, NG7 2RD, UK
[2]The Energy Institute, The Pennsylvania State University, University Park, PA 16802, USA

Introduction

A major issue for the use of hydrogen as a transportation fuel is it's safe storage on-board vehicles. Carbon materials, such as carbon nanotubes, have been touted as a candidate for hydrogen storage at ambient temperatures and modest pressures, although some scattered results have been obtained (1-3). One promising candidate has been single-walled carbon nanotubes (SWNTs) where bundles of SWNT have been reported to adsorb 5-10 wt% of H_2 probably due to the interaction of hydrogen molecules with ropes of single-walled carbon nanotubes rather than storage of hydrogen within the tubes (4, 5). A less expensive alternative to SWNTs are multi-walled carbon nanotubes (MWNTs) and some studies have indicated that MWNT can be used for hydrogen storage (6, 7). One of the main issues is the accessibility of the hydrogen to the graphite like structures of the MWNTs due to the outer layer preventing the gas from entering the system. Making pathways available for the H_2 to pass through the structure, e.g. by activation of the MWNTs, could significantly enhance the hydrogen storage capacity of MWNTs and thus form a low cost alternative to SWNTs. This study focuses on low temperature carbon dioxide activation of multi-walled carbon nanotubes for hydrogen storage.

Experimental

The multi-walled nanotube sample was obtained from Nanostructured & Amorphous Materials, Inc. The activation was conducted at 550°C under a flow of carbon dioxide up to 32 hours. The hydrogen adsorption measurements were made on a custom built volumetric differential pressure apparatus (8)

Results and Discussion

Changes of surface area of multi-walled carbon nanotubes activated in carbon dioxide at 550°C has been reported earlier (9). Typically, the surface area will start increasing after a couple of hours of activation, peak after a certain time and then decrease. In this study a MWNT sample activated for 4 hours was tested for its hydrogen storage capacity at different pressures and the uptake curves are shown in Figure 1. The uptake increases from 0.3 wt% at 20 bar to over 1.6 wt% at 100 bar. All the uptake curves have an initial rapid uptake of about 0.1 wt% similar to the behavior of activated carbons and correlate well with the relative low surface area. The main hydrogen uptake takes place over the next 3-4 hours indicating a very slow diffusion of the hydrogen into the carbon structures. This process suggests that the activation process has made the interior structure of the MWNT accessible for the hydrogen. Scheme 1 shows a schematic of representation of low temperature carbon dioxide activation of MWNT. It is postulated that the CO_2 will start reacting with the MWNT walls and transfer the ordered carbon into gaseous species or amorphous carbon. As the activation time is increased the interior structure of the MWNT may become exposed and this could explain the increase in the hydrogen storage capacity of the activated sample.

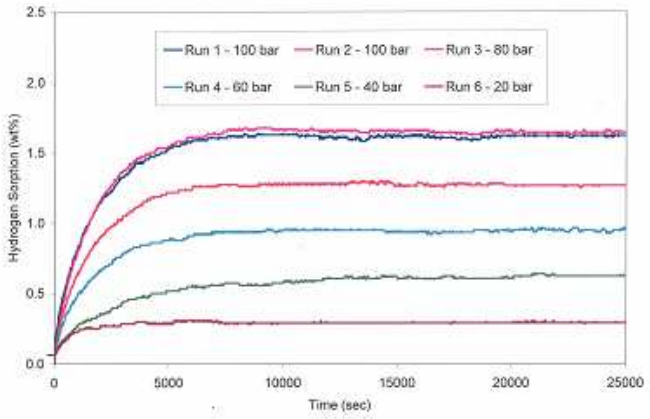

Figure 1. Hydrogen storage capacity at room temperature under different pressures for a MWNT activated at 550°C for 4 hours in carbon dioxide.

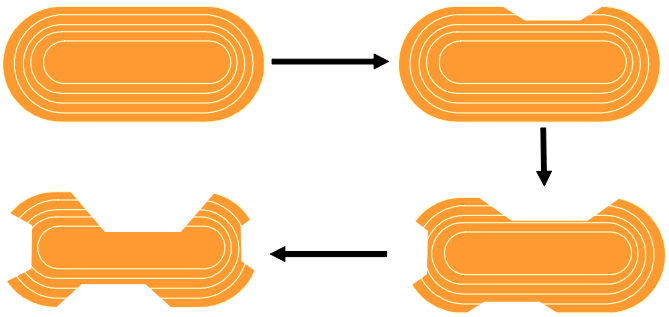

Scheme 1. Schematic of representation of low temperature carbon dioxide activation of MWNT.

Conclusions

It was found that the hydrogen storage capacity of the multi-walled nanotubes (MWNT) at room temperature was greatly enhanced by low temperature activation in carbon dioxide at 550°C. Hydrogen storage of the degassed samples showed an uptake of up to 1.6 wt% for the activated nanotube at 100 bar compared to 0.9 wt% for the non-activated sample.

References

(1) Dillon, A.C., Heben, M.J., Applied Physics A-Materials Science & Processing, 72 (2), 133-142, 2001
(2) Rodriguez-Reinoso, F., Linares-Solano, A., Chemistry and Physics of Carbon, Ed. Thrower, P.A., Marcel Dekker, Inc., New York, Vol. 22, 1, 1989.
(3) Hirscher, M., Becher, M., Haluska, M., Quintel, A., Skakalova, V., Choi, Y.M., Dettlaff-Weglikowska, U., Roth, S., Stepanek, I., Bernier, P., Leonhardt. A., Fink, J., J. Alloys and Compounds, 330, 654-658, 2002.
(4) Pradhan, B.K., Sumanasekera, G.U., Adu, K.W., Romero, H.E., Williams, K.A., Eklund, P.C., Physica B-Condensed Matter, 323 (1-4), 115-121, 2002
(5) Gennett, T., Dillon, A.C., Alleman, J.L., Jones, K.M., Hasoon, F.S., Heben, M.J., Chemistry of Materials, 12 (3), 599, 2000
(6) Chambers, A., Park, C., Baker, R.T.K., Rodriguez, N.M., J. Physical Chemistry B, 102 (22), 4253-4256, 1998
(7) Lueking, A., Yang, R.T., AICHE, 49 (6), 1556-1568, 2003
(8) Blackman J.M, Patrick, J.W, Snape, C.E., *Prepr. Pap.-Am. Chem. Soc., Div. Fuel Chem.* 2004, *49 (1),* 207-209
(9) Andresen, J.M., Chastain, E.K., *Prepr. Pap.-Am. Chem. Soc., Div. Fuel Chem.* 2004, *49(2),* 688-689

CATALYST CHALLENGES ON THE ROAD TO THE HDYROGEN ECONOMY

Thomas A Giroux

Engelhard Corporation
101 Wood Avenue, Iselin, NJ 08830

Overview

The ideal goal for hydrogen production would be derived from solar, wind or other renewable, natural sources of energy. The primary driving force is the decreased dependence on liquid petroleum with the positive consequence of elimination of primary pollutants and reduced green house gas emissions. It is not expected that these sources of energy will be available soon. Reforming of hydrocarbons and alcohols will be the primary source of hydrogen as a transitional solution.

The applications for hydrogen generation vary widely in scale, scope, and their demands on catalysis. Microreactors intended to power small portable devices such as a cell phone push the limits of coating technology. Manufacturers are looking to advances in catalyst activity to shrink hydrogen generators to the point where they could be mounted on the walls of a garage at home to refuel cars, feed fuel cells, and use captive energy for hot water for home heating. Developers of future distributed residential power suppliers want catalysts flexible enough to work with various fuels such as kerosene, natural gas, and LPG to make standalone hydrogen generators to power 1-5 kW fuel cells and cogeneration systems to redefine the electricity distribution infrastructure. Industrial users want reliable, durable, economic catalysts to help replace their bottle gas deliveries with process-critical moderate sized hydrogen generation skids to feed their metal processing, hydrogenation, and cooling needs. Even on the large scale, centralized hydrogen producers are looking at ways to debottleneck existing capital investments by taking advantage of new catalyst developments to boost productivity and throughput. Momentum continues to build as new processes and applications for distributed generation of hydrogen are being developed worldwide and present us with a spectrum of challenges and opportunities for catalyst product and technology developments.

We believe precious metals supported on ceramic monoliths, metal monoliths, and other high-geometry surfaces such as heat exchangers are the technologies for future generations of such hydrogen generation systems. These catalysts are durable against the daily start/stop cycles experienced in operations. The highly active catalyst washcoat deposited on the walls of monolithic structures can permit decreases of more than 10 times the size of the traditional base metal catalyst reformer. They offer greater structural stability, more rapid response to transient operation and lower pressure drop than pelletized catalysts. These properties contribute to a robust, reliable and durable reformer system capable of meeting the lifetime requirement for economical hydrogen generation systems especially when precious metal recycle is considered in the lifecycle cost of the system.

The talk will provide an overview of some of the critical catalytic issues that must be overcome in order to see the commercialization of distributed hydrogen generation. Included will be the limitations of traditional base metal catalysts for hydrogen generation and how precious monolithic catalysts circumvent many of these issues to provide a viable solution.

STRATIFIED CATALYSTS FOR METHANE PARTIAL OXIDATION

Gisele Tong, Julie Flynn, & Corey Leclerc

Department of Chemical Engineering
McGill University
3610 University St
Montréal, Québec H3A 2B2 CANADA

Introduction

Catalytic partial oxidation (CPO) is a viable process for the production of hydrogen for fuel cells. CPO is characterized by small residence times on the order of 1-10 ms and is exothermic, so once the catalyst lights off it remains catalytically active without heat input. The CPO catalyst has a small thermal mass, so it can be started in seconds[1,2]. The reactor is quite robust in that it can be used to convert methane[3], ethanol[4], gasoline[5], and diesel[6]. The short residence time and auto-thermal behavior make CPO ideal for small, hydrogen fuelled systems.

Catalysts design and selection for CPO has received much attention from the academic community. Many catalysts are active for CPO, but rhodium has been found to obtain the highest fuel conversions and highest hydrogen selectivities with the most stable operation[7]. Unfortunately, rhodium is expensive. In addition, rhodium pricing over the past two decades has not been stable with large spikes in pricing around 1990 and 2000.

The CPO process requires half a mole of oxygen per mole of methane.

$$CH_4 + \tfrac{1}{2} O_2 \rightarrow 2 H_2 + CO \qquad \Delta H = -36 \text{ kJ/mol}$$

Researchers have shown that, for methane, the CPO process takes place in two sequential steps[8,9]. The first step is a complete oxidation of one-quarter of the methane to use up all of the oxygen.

$$CH_4 + 2 O_2 \rightarrow 2 H_2O + CO_2 \qquad \Delta H = -802 \text{ kJ/mol}$$

The second step is reforming of the remaining methane by water and carbon dioxide.

$$CH_4 + H_2O \rightarrow 3 H_2 + CO \qquad \Delta H = 206 \text{ kJ/mol}$$
$$CH_4 + CO_2 \rightarrow 2 H_2 + 2 CO \qquad \Delta H = 247 \text{ kJ/mol}$$

The first, highly exothermic step supplies the heat to the endothermic reforming reactions.

In this work, catalysts were chosen based on the two step process. Instead of trying to optimize one metal to carry out both steps of the process, two metals were chosen, one to optimize the first step and the other to optimize the second step. The millisecond process is ideal for a stratified catalyst; the high space velocities lead to large amounts of heat convected from the exothermic step to the endothermic step, thus increasing the yield of hydrogen. In addition, rhodium is not used in the catalyst, so the price of the catalyst can be reduced by over 50% depending on the metal combination.

Experimental

The reactions are carried out in a quartz tube of 18 mm in diameter. Methane and air are fed to the reactor by mass flow controllers and are premixed up stream of the catalyst. The foam catalyst is wrapped in alumino-silicate paper to prevent gas bypass around the catalytic foam. Blank foams are placed immediately upstream and downstream from the catalytic foam to prevent the loss of heat due to radiation. A K-type thermocouple was placed through the downstream heat shield to make intimate contact with the back face of the catalyst. All temperature data shown come from the measurements of this thermocouple. In the case of stratified catalysts, two foams were placed in the reactor sequentially with the combustion catalyst upstream of the reforming catalyst. For comparison, experiments were carried out with pure rhodium and pure platinum catalysts as well. For these catalysts, a single foam was used that had the same axial dimensions as the two stratified catalysts combined. In addition, experiments were carried out with the reforming catalyst upstream of the combustion catalyst to assure that the order of the catalysts was important. **Figure 1** shows the reactor setup and a comparison of stratified versus single bed catalysts.

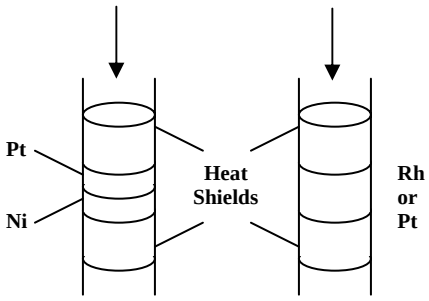

Figure 1. The stratified and single component reactor set-ups

Catalysts were made by first wash coating an 80 pores per inch, 17 mm diameter α-alumina foam monolith with a γ-alumina washcoat. After washcoating, a solution of metal salt was dripped onto the foam. The foam was then air dried and then calcined in air at varying temperatures and times depending on the metal. In this work, platinum, from hexachloroplatinic acid, nickel, from nickel (II) nitrate, and rhodium, from rhodium (II) nitrate, were used in this study. For all catalysts, metal loadings were typically between 4 and 5% by weight.

Gases leaving the reactor were separated and analyzed by gas chromatography. An HP-PLOT molesieve 5A column was used to separate methane, oxygen, nitrogen, and carbon monoxide, while a HP-PLOT Q capillary column separated carbon dioxide from the other gases. The gases were analyzed on a thermal conductivity detector. Carbon balances closed to within ±5%.

Results and Discussion

Stratified catalysts were compared to single component catalysts for varying feed stoichiometries. In these experiments, the methane oxygen ratio was varied between 1.7 and 2.1; 2.0 is the exact stoichiometry for the partial oxidation reaction. The stratified catalysts included a platinum (combustion) foam followed by a nickel (reforming) foam (Pt/Ni). This second catalyst was the reverse of the first one, with the nickel catalyst leading the combustion catalyst (Ni/Pt). The two single component catalysts were made up of rhodium or platinum.

Figure 2a shows the back face temperature of the catalyst for four different catalysts. All catalysts show a gradual decrease in back face temperature as the methane to oxygen ratio increases. Of particular importance is the temperature of the Ni/Pt catalyst. This catalyst experienced back face temperature significantly higher than the other three catalysts. Ideally, this process will be carried out at as low a temperature as possible, which does not favor the Ni/Pt catalyst.

Figure 2b shows the methane conversion with varying feed ratios. Again, all catalysts show a decrease in methane conversion as

the methane to oxygen ratio increases. The Pt/Ni catalyst performs as well or better than the rhodium catalyst. At higher ratios, the improvement of the Pt/Ni catalyst is significantly higher than the Rh catalyst. The Ni/Pt catalyst performs quite well, while the Pt catalyst does not perform as well especially at higher ratios.

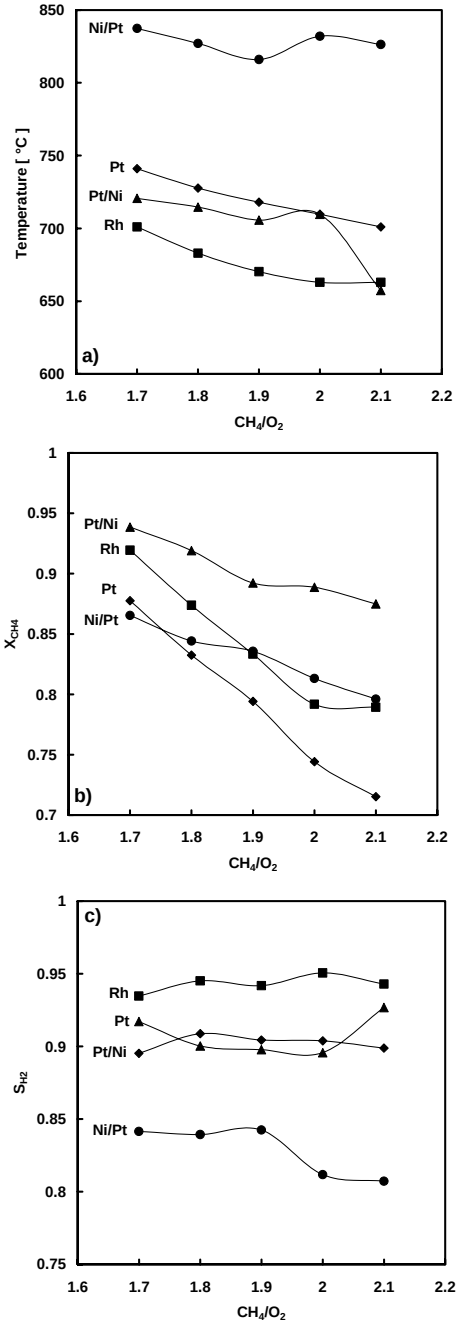

Figure 2. Results of experiments in which the feed ratio of methane to oxygen was varied for a) temperature, b) methane conversion, and c) hydrogen selectivity.

Figure 2c shows the hydrogen selectivity as a function of methane to oxygen ratio. Rhodium shows the highest selectivity to hydrogen. However, it is not much higher than the selectivities obtained from platinum or Pt/Ni. The Ni/Pt catalyst has the lowest selectivity of the four catalysts.

Figure 3 shows the temperature, conversion, and selectivities for a 10 hour long experiment. Since nickel is known to deactivate under these feed conditions, it was necessary to test the stability of the Pt/Ni catalyst. For all measurements, there was no reduction in performance for the Pt/Ni catalyst, indicating that it is stable over the 10 operating period.

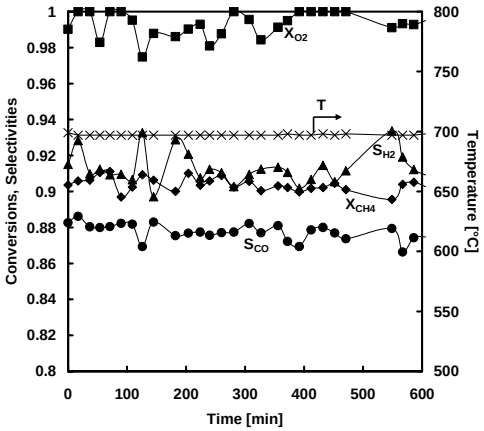

Figure 3. 10 hour experiment to determine Pt/Ni catalyst stability

Conclusions

A Pt/Ni stratified catalyst has obtained hydrogen yields that are comparable to rhodium, the best catalyst available for methane partial oxidation, over a wide range of operating conditions. It was shown that the order of the stratified catalysts is important. The catalyst was also shown to be stable over a 10 hour period despite the potential for deactivation.

Acknowledgements. Gisele Tong would like to thank the Natural Science and Engineering Research Council of Canada for financial support through the Undergraduate Student Research Awards. Julie Flynn would like to thank the Eugenie Ulmer Lamothe Scholarship Fund for financial Support. Corey Leclerc would like to thank Dr. Karthik Venkataraman for valuable discussions regarding the research.

References

(1) Leclerc, C. A.; Redenius, J. M.; and Schmidt, L. D. *Cat. Lett.***2002**, 79, 39.
(2) Williams, K. A.; Leclerc, C. A.; and Schmidt, L. D. *AIChE J.* **2005**, 51, 247.
(3) Hickman, D. A.; and Schmidt, L. D. *Sci.* **1993**, 259, 343.
(4) Deluga, G. A.; Salge, J. R. ; Schmidt, L. D. ; and Verykios, X. E. *Sci.*, **2004**, 303, 993.
(5) O'Connor, R. P.; Klein, E. J.; and Schmidt, L. D. *Cat. Lett.* **2000**, 70, 99.
(6) Krummenacher, J. J.; West, K. N.; and Schmidt, L. D. *J. Cat.* **2003**, 215, 332.
(7) Torniainen, P. M.; Chu, X.; and Schmidt, L. D. *J. Cat.* **1994**, 146, 1.
(8) Buyevskaya, O.V.; Wolf, D.; and Baerns, M. *Cat. Lett.* **1994**, 29, 249.
(9) Mallens, E. P. J.; Hoebink, J. H. B. J., and Marin, G. B. *J. Cat.* **1997**, 167, 43.

STEAM REFORMING CATALYSTS FOR MICROCHANNEL REACTOR

Junko M. Watson and Frank P. Daly

Velocys, Inc.
7950 Corporate Blvd.
Plain City, OH 43064

Introduction

Velocys Inc. has developed a microchannel processing system for hydrogen production by steam reforming of methane (SMR). The catalyst used for this system is Rh supported on alumina. Previously, Wang *et al* reported the use of Rh supported on spinel for SMR at short contact times [1, 2]. The effect of Mg, Ba, La, Pr and Y addition and pre-aging conditions on alumina stabilization under SMR conditions has been studied. Catalyst loading as well as coating methodology, key variables for microchannel devices, has also been studied. Catalyst performance was tested in a single microchannel device at 15 - 30 atm, 3:1 steam to carbon ratio, 3-6 milliseconds contact time, and temperature of 840 ^{o}C. Rh supported on hydrothermally pre-aged Mg/Al_2O_3 showed excellent durability over a period of 2,500 hours time on stream. Catalyst characterization including N_2 BET surface area, hydrogen chemisorption, XRD, TEM, and SEM was also performed.

Experimental

Catalyst Synthesis and Characterization. Catalysts were prepared via incipient wetness technique. The alumina precursor was alumina sol (Dispal 18N4-80, Sasol). The dopant precursors included lanthanum nitrate, barium nitrate, yttrium nitrate, praseodymium nitrate, and magnesium nitrate (Aldrich). Rhodium nitrate (Engelhard) was used as the Rh precursor. The alumina precursor was converted to aluminum oxide by calcining in air at 450^{o}C for 4 hours. The calcined alumina was then impregnated with magnesium nitrate and further calcined at 1000 ^{o}C for 4 hours. Thermal aging was performed at 1050 ^{o}C for 100 hours in air. Hydrothermal aging was carried out at 92 5^{o}C for 100 hours in 66% steam at steam partial pressures in the range of 0.6 – 17 atm.

Rh dispersion was measured by static volumetric H_2 chemisorption methods at 25 ^{o}C using ASAP 2010 (Micromeritics). BET surface area was also measured using ASAP 2010. TEM analysis was conducted on a JEOL 2010 high-resolution analytical electron microscope operating at 200 kV with a LaB_6 filament. TEM analysis was performed at the Pacific Northwest National Laboratory.

Testing Apparatus. Reaction experiments were conducted in a microchannel flow reactor made of alloy 617. The microchannel reactor (2" long rod with 0.5" DI) was EDM wire cut to create a slot sized at 0.16" x 2" x 0.01". A FeCrAlY fin was used as catalyst substrate after heat treatment at 900 ^{o}C for 8 hours in air. The catalyst is washcoated onto the substrate and inserted into the reactor slot. Reactor wall temperature was measured by a type K thermocouple which is inserted in a thermal well. The temperature was measured 0.03" away from the back side of the FeCrAlY insert. Catalyst is first reduced at 450 ^{o}C with 10 % H_2 in He for 2 hours. The SMR reaction conditions were 3:1 steam:carbon ratio, 3.0 – 6.0 millisecond contact time, 15 - 27 atm pressure, 800 – 900 ^{o}C reaction temperature.

Gases were controlled by Brooks 5850E mass flow controllers and water was fed using an Accuflow Series III HPLC pump. Gas composition was measured by micro GC 3000A (Agilent).

Results and Discussion

Figures 1 and 2 are lifetime test results at a 3:1 steam:carbon ratio, 4.5 ms contact time, 15 atm pressure and 850 ^{o}C reactor wall temperature for $Rh/La\text{-}Al_2O_3$ (thermally pre-aged) and $Rh/Mg\text{-}Al_2O_3$ (hydrothermally pre-aged), respectively. Test results were obtained using a single microchannel reactor containing a FeCrAlY fin coated with a catalyst having a rhodium oxide loading of 1.3 mg/in^2. The La/Al_2O_3 support was thermally pre-aged at 1050 ^{o}C for 100 hours in air at 1atm and the Mg/Al_2O_3 support was hydrothermal pre-aged at 925 ^{o}C for 100 hours in 66% steam at 25 atm. Measured surface areas of the supports are presented in Table 1. Under thermal pre-aging conditions, the La-stabilized alumina had a 6-fold higher surface area than the Mg-stabilized support (Figure 3); however, under hydrothermal pre-aging conditions, the Mg-stabilized support had a 3-fold higher surface area than the La-stabilized support.

For the thermally pre-aged $Rh/La\text{-}Al_2O_3$ catalyst, a continual decline in methane conversion was observed within 700 hours on stream (Figure 1). A thermally pre-aged $Rh/Mg\text{-}Al_2O_3$ catalyst displayed a similar trend in deactivation under the same conditions. However, when Rh was supported on hydrothermally pre-aged Mg/Al_2O_3, the SMR activity was steady for over 2500 hours (Figure 2). As displayed in Figure 2 the contact time was switched from 4.5 ms to 3.0 ms to move from equilibrium limited to kinetically limited conditions. For the next 1000 hours, no catalyst deactivation was observed.

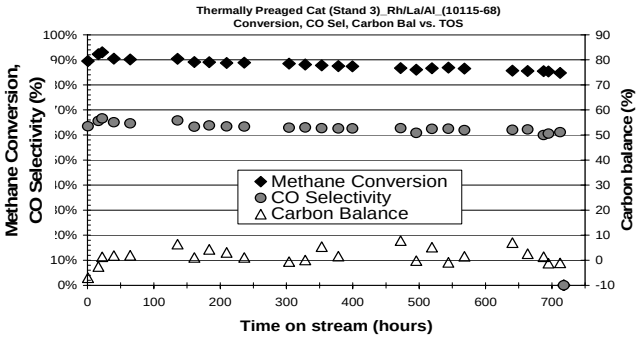

Figure 1. Thermally pre-aged $Rh/La\text{-}Al_2O_3$ catalyst performance (25 mg/in^2 total catalyst loading, 5 wt% Rh_2O_3)

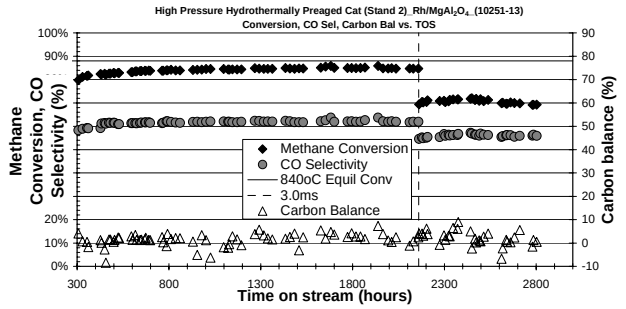

Figure 2. Hydrothermally pre-aged $Rh/Mg\text{-}Al_2O_3$ catalyst performance (13.6 mg/in^2 total catalyst loading, 9.3 wt% Rh_2O_3)

Table 1. BET Surface Area

	Fresh (m^2/g)	1 atm Thermal (1000°C, air, 100hrs) (m^2/g)	1atm Hydrothermal (66% steam, 925°C, 100hrs) (m^2/g)	25atm Hydrothermal (66% steam, 925°C, 100hrs) (m^2/g)
3%La/Al_2O_3	105.3	79.5	59.3	3.3
6%Mg/Al_2O_3	81.9	12.2	46.2	6.4

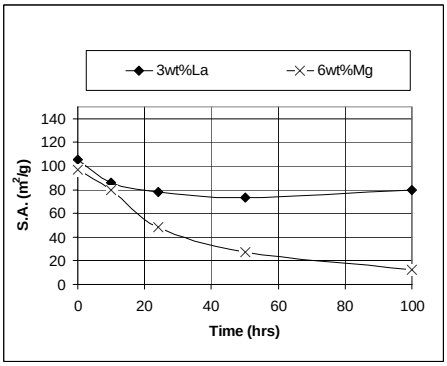

Figure 3. BET surface area with aging time on stream at 1000 °C in air.

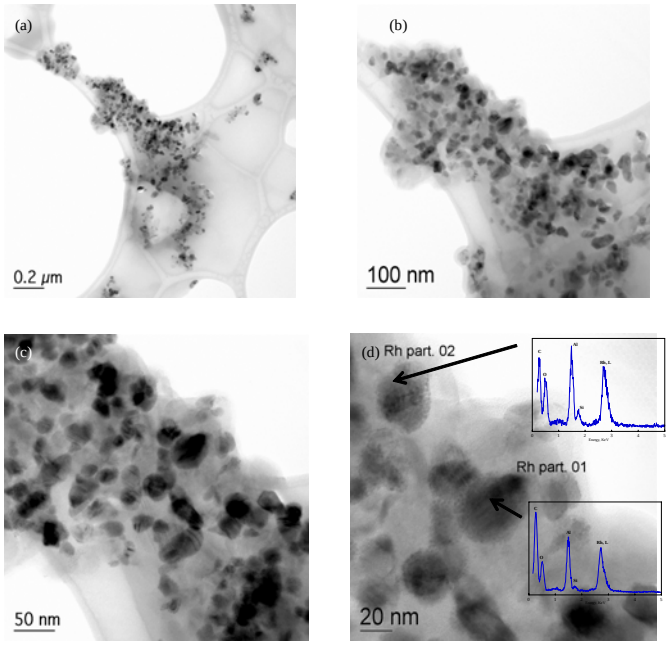

Figures 4 (a-d). TEM bright field micrographs of fresh Rh/La-Al_2O_3 (Specimen 10115-40)

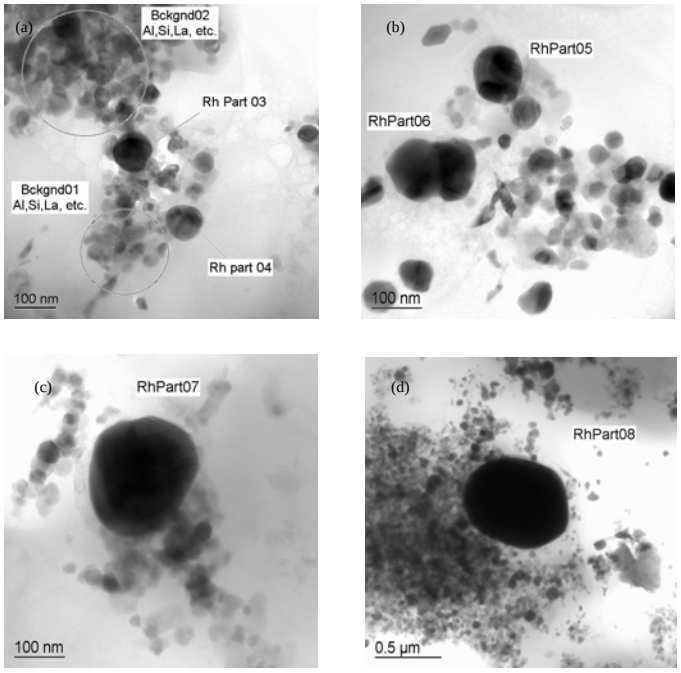

Figures 5 (a-d). TEM bright field micrographs of spent Rh/La-Al_2O_3 which was on stream for 1600 hours at 3 to 1 steam to carbon, 3.0 - 4.5 ms contact time, and highest wall temperature of 950 °C. (Specimen 10115-33)

Bright field micrographs of fresh Rh/La/Al_2O_3 catalyst (10115-40) are shown in **Figures 4** (a-d). 5.3 mg of the catalyst was coated on a FeCrAlY substrate. Rh loading was 24wt%. The dark particles were identified as Rh by EDS analysis and their sizes ranged from ~20 – 50 nm in diameter. **Figures 5** (a-d) are also bright field micrographs of spent Rh/La-Al_2O_3 which was on stream for 1600 hours under 3 to 1 steam to carbon ratio, 3.0 - 4.5 ms contact time, and the maximum wall temperature of 950 °C. Conversion and selectivity profiles of this sample also showed a continual decline similar to Figure 1. The range of Rh particle sizes on the spent sample, which consisted of 7.3 mg of catalyst with 21 wt% rhodium loading, was ~90 – 700 nm. The crystallite size has grown at least 3-fold and as much as 35-fold. This indicates that severe metal sintering was observed on the deactivated catalyst.

References

1. Wang, Y., Tonkovich, A.L.Y., VanderWiel, D.P. U.S. Patent No. 6,607,678, **2003**
2. Wang, Y., Chin, Y.H., Rozmiarek, R.T., Johnson, B.R., Gao, Y., Watson, J., Tonkovich, A.L.Y., VanderWiel, D.P. *Cat. Today* 2004, 98, 575-581.

HYDROGEN PRODUCTION BY CATALYTIC DECOMPOSITION OF METHANE OVER Ni AND Ni-Cu BASED CATALYSTS

I. Suelves[a], M.J. Lázaro[a], R. Moliner[a], Y. Echegoyen[a], J.M.Palacios[b]

[a] Instituto de Carboquímica CSIC, Miguel Luesma Castán, 4. 50015-Zaragoza
[b] Instituto de Catálisis y Petroleoquimica CSIC, Campus UAM, 28049-Madrid, Spain

Introduction

The social concern generated by presumable climate changes derived from the emission of greenhouse gases, in particular CO_2, will force in the near future the adoption of energetic policies promoting the progressive reduction of CO_2 emissions. Among them, utilisation of hydrogen as energy carrier, instead of usual liquid hydrocarbons, by the increasing use of fuel cells, instead of the traditional IC engines, is one of the most promising technologies proposed. [1]

It is generally accepted that in the near-to-medium terms, hydrogen production will continue relying on fossil fuels, primarily natural gas. [2]. Nowadays, among the different technologies used for large scale hydrogen production, steam reforming of natural gas, SMR, is one most widely used. However, this process involves the emission of CO_2, unless it is captured and stored what increase the cost of hydrogen production around 20-50% [2]. An alternative process to SMR is the thermocatalytic decomposition, TCD, of natural gas through the production of CO-free hydrogen and pure carbon as a reaction product of significant added value. TCD, however, still needs the knowledge of several scientific aspects, in particular, the different operating mechanism of reaction to select the most suitable catalysts and optimisation of the operating conditions.

In our previous work [3], TCD of methane using a commercial Ni catalyst it was proved the achievement of hydrogen yields close to the thermodynamic values. It was also shown that the time for catalyst deactivation depends on the operating conditions, so that, the higher the methane flow rate the shorter the catalyst life. The deposited carbon appears either as long filaments a few nanometres in diameter emerging from Ni particles or as uniform coatings on these particles. Operating conditions promoting high decomposition rates enhance the formation of uniform coating versus long filaments shortening the catalyst life. In this work, Ni and Ni-Cu catalyst were prepared in order to evaluate the influence of the amount of nickel in the samples and the presence of copper as a promoter on methane conversion, catalyst life and quality of the carbon produced.

Experimental

Catalysts. Catalysts with different Ni/Al and Ni/Cu/Al ratio were prepared by co-precipitation from an aqueous solution of the respective nitrates with sodium carbonates following the procedures described in literature [4]. The precipitates were then washed, dried and calcined at 450ºC.

A commercial catalyst composed of 65 wt% of Ni supported in a mixture of silica and alumina has been also used for comparison.

Activity tests. Prior to activity tests, all catalysts were subjected to a reduction treatment using a flow of pure hydrogen of 20 ml/min for 3h. Different reduction temperatures (550-650ºC) have been tested to evaluate the influence of the pre-reduction treatment on the catalyst behaviour and especially on the purity of the hydrogen produced.

Activity tests were run in a laboratory fixed bed quartz reactor 2 cm i.d., 60 cm height, using pure CH_4 as feeding gas at different reaction temperatures (700-800ºC). The outlet gas composition from the reactor was analyzed by gas chromatography using two packed columns and TCD detector. The evolution of CO and CO_2 has been followed by a gas chromatograph equipped with a flame ionization detector, modified with connection of two packed columns to a catalytic hydrogenation reactor. This way, levels of carbon oxides in the range of ppmv can also be measured.

Characterization techniques. The textural properties of the fresh and used samples were measured by N_2 adsorption at 77 K. The homogeneity, degree of Ni dispersion in the fresh catalysts and the study of the morphological appearance of the deposited carbon have been carried out in a scanning electron microscope (SEM). Powder X-ray diffraction (XRD) patterns for the study of the crystalline chemical species and transmission electron microscopy (TEM) studies have been also carried out.

Results and discussion

TCD of methane using Ni or Ni:Cu catalyst proceeds with hydrogen yields close to the thermodynamic values.
Figure 1 show some of the results obtained for the prepared catalysts and the comparison with the commercial catalyst used in our previous work [2]. The co-precipitation catalysts show a similar behaviour to the commercial one, even better when a small concentration of copper is introduced in its composition.

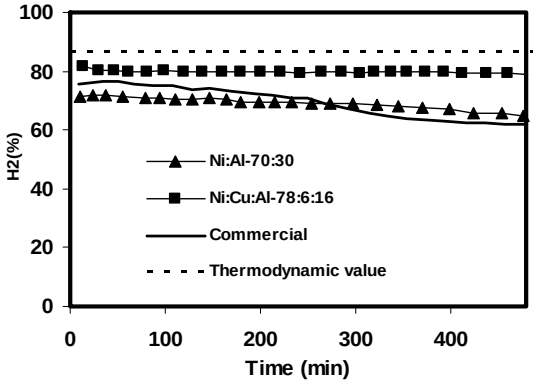

Figure 1. Hydrogen production (%vol) T: 700ºC- Methane flow:20 ml/min

Table 1 shows the initial, r_o, and the long term, rf, methane decomposition rates, and the carbon to catalyst weight ratio, Rw, for some selected samples.

No important differences in behaviour were found when the percentage of nickel on the samples was varied between 70-90%. Nickel percentages below 30% result in a low initial methane conversion. As shown in figure 1, the introduction of a small amount of copper increases both the initial and the long term decomposition rates of the catalyst but excessive copper concentrations (25%) results in lower methane conversions. It seems that copper is not, in fact, an active catalyst of the TCD of methane but a promoter acting through the isolation of Ni sites in the Ni lattice by partial cation replacement.

Table 1. Initial activity, final activity and accumulated carbon (T: 700ºC; Flow: 20ml/min; Time: 8h)

Ni:Cu:Al	r_0 (mmol/min.g)	r_f (mmol/min.g)	Rw
Comercial	1.9	1.6	9.1
70:-:30	1.7	1.5	8.5
90:-:10	1.8	1.5	9.2
25:-:75	0.7	0.1	3.0
75:2:23	1.8	1.6	10.2
78:6:16	2.0	1.8	10.7
50:25:25	1.5	1.5	8.9

At 700ºC the catalysts activity does not decay after 8 h on-stream (except for the catalyst with a percentage of nickel below 30%) and a weight ratio of carbon to nickel between eight and eleven was obtained without catalyst deactivation. When temperature was increased up to 800ºC a fast depletion of activity was observed for both Ni and Ni:Cu catalysts.

Regarding the purity of the hydrogen obtained, CO evolved decreases when pre-reduction temperature increases and when a small amount of Cu is introduced in the fresh catalysts. The presence of Cu also enhances the reduction of Ni species present as mixed oxides in samples after calcination, lowering its reduction temperature. The presence of NiO results in lower CH_4 conversions and also in a higher CO evolution whose presence is undesirable for further hydrogen use in low- temperature fuel cells.

Carbon characterization

The specific surface areas (not shown) of the still active catalyst are lower than that of the fresh catalyst, due to the presence of deposited carbon. However this deposited carbon must present some porosity since it is the dominant component in the samples at the end of the tests.

SEM examination of the deposited carbon shows that it appears as long filaments a few nanometres in diameter emerging from Ni particles coexisting with uniform coatings on the Ni particles. Although the relative concentration of these two carbon forms cannot be achieved, a simple examination of the respective SEM images evidences that long filaments are more abundant than uniform coatings for all catalysts tested at 700ºC. When the reaction temperature is increased up to 800ºC the morphology of the deposited carbon changes, appearing mainly as uniform coatings on Ni particles shortening the catalyst life.

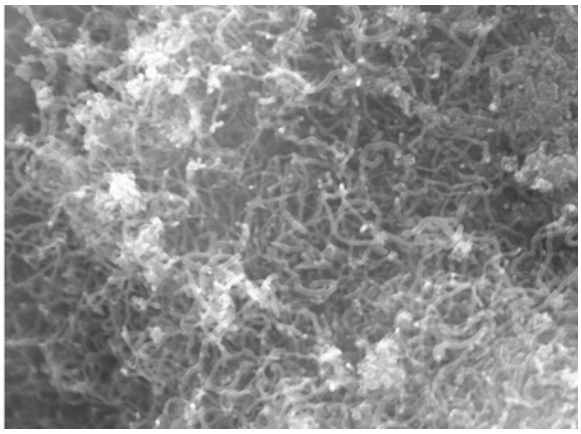

Figure 2. SEM micrograph of a still active sample (Co-precipitation catalyst Ni:Cu:Al-78:6:16.T:700ºC- Methane flow rate:20 ml/min)

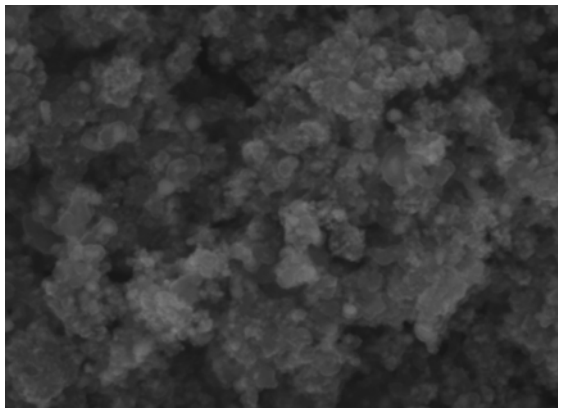

Figure 3. SEM micrograph of a deactivated sample (Co-precipitation catalyst Ni:Cu:Al-78:6:16. T:800ºC- Methane flow rate:20 ml/min)

Acknowledgement. This work has been supported with funds provided by the Spanish Ministery of Science and Technology. Research Project PPQ2002-03346 and by the Aragon Government by means of the recognition as Consolidated Research Group.

References

1. Green Book of Energy for Europe. European Commission. Brussels.November, 29. **2000**

2. Hart D., Freud P., and Smith A. Hydrogen Today and Tomorrow. IEA GHG Programme. April **1999.** ISBN 1 898373248

3. I.Suelves, M.J. Lázaro, R. Moliner, B.M. Corbella and J.M. Palacios. International Journal of Hydrogen Energy, in press

4. M.A. Ermakova, D. Yu. Ermakov, G.G. Kuvshinov. Applied Catalysis A: General 201, 61-70, **2000**

5. M.A. Ermakova, D. Yu. Ermakov, G.G. Kuvshinov and L.M. Plyasova. Jounal of Catalysis 187,) 77-84, **1999.**

ANALYSES OF HYDROGEN PRODUCTION FROM SUB-QUALITY NATURAL GAS (I): SQNG THERMAL DECOMPOSITION AND AUTOTHERMAL PROCESSES

Cunping Huang, and Ali T-Raissi
Florida Solar Energy Center
University of Central Florida
1679 Clearlake Road
Cocoa, FL 32922

Introduction

As the prices of fossil fuel increase, abundant sub quality natural gas (SQNG) resources become important alternatives to replace increasingly exhausted reserves of high quality natural gases. Since SQNGs contain highly concentrated hydrocarbons compared to other sources (such as landfill gas and biomass), SQNGs are good feedstock for the production of hydrogen. On the hand, hydrogen sulfide in SQNGs is a highly concentrated sulfur source that can be utilized through hydrogen sulfide methane reformation to produce hydrogen and carbon disulfide, a desirable raw chemical for the synthesis of sulfuric acid.

Using SQNGs as resources for the production of hydrogen, we must consider the removal of impurities, mainly hydrogen sulfide. Water and carbon dioxide can be reformed with methane to produce hydrogen, while nitrogen is an inert gas and can be removed through a pressure swing adsorption process. Hydrogen sulfide in natural gas not only causes severe corrosion to pipelines, but it also deactivates catalysts during steam methane reformation. Additionally, hydrogen sulfide is an extremely toxic air pollutant. During impurity removal processes the loss of methane is another important issue. It is acceptable if methane loss is less than 3%. With the offset of other advantages, losses between 3 and 10% can be acceptable, but a loss over 10% is unacceptable [1].

Note that utilization of SQNGs as energy sources is whether there is an alternative technology to economically and efficiently remove highly concentrated hydrogen sulfide from SQNG. As Lokhandwala et al [1] pointed out, the best treatment for natural gas right now is no treatment, which means that millions upon millions of tons of SQNGs must remain underground and require occasional monitoring for hydrogen sulfide release. However, with today's increasing demand for energy, thoughtful deliberation and evaluation must be given to these potentially valuable hydrogen resources. The objective of this paper was to analyze thermodynamically possibilities for efficiently producing hydrogen, sulfur and/or carbon disulfide from SQNG without the requirement of separating hydrogen sulfide. The catalyst deactivation issue and flowsheet development will be discussed elsewhere.

Review of technologies

Several technologies are currently studied for the treatment of SQNGs in term of removing hydrogen sulfide and/or utilizing it for the production of sulfur.

Amine absorption + Claus plant. This technology uses amine absorption to separate hydrogen sulfide from hydrocarbons. The separated hydrogen sulfide then undergoes a Claus process to produce sulfur. One of the technological merits of this approach is that both amine absorption and Claus plants are commercialized and suitable for large-scale SQNG treatment. However, it has some apparent disadvantages such as: high separation costs, the waste of the hydrogen component and environmental issues related to sulfur dioxide discharge.

Alkaline absorption + electrolysis (or photolysis). With the exception of amine absorption, hydrogen sulfide can be most readily absorbed and neutralized by an alkaline solution, while at the same time separating from hydrocarbons through the following reactions:

$$H_2S + 2NaOH = Na_2S + 2H_2O \quad (1)$$

$$CO_2 + 2NaOH = Na_2CO_3 + H_2O \quad (2)$$

Fe-Cl hybrid process ($FeCl_3$ + electrolysis). Mizuta et al [2,3] developed a hybrid process based on iron chloride for the production of hydrogen and sulfur from SQNGs. The process consists of a hydrogen sulfide absorption step and an electrolytic step according to the following reactions:

$$H_2S(g) + 2FeCl_3(aq) \longrightarrow 2FeCl_2(aq) + 2HCl(aq) + S(c) \quad (3)$$

$$2FeCl_2(aq) + 2HCl(aq) \longrightarrow H_2(g) + 2FeCl_3(aq) \quad (4)$$

$$\text{Overall reaction: } H_2S(g) \longrightarrow H_2(g) + S(c) \quad (5)$$

High temperature electrolysis. This process does not require a separation step. SQNGs can be fed into a high temperature cathode where hydrogen sulfide is directly converted into hydrogen and sulfur. Hydrogen produced goes with the process stream while sulfur is condensed and collected as a product [2,4-6]. The electrochemical reaction takes place as:

$$H_2S + 2e^- \longrightarrow S^{2-} + H_2 \quad (6)$$

$$S^{2-} \longrightarrow 0.5S_2 + 2e^- \quad (7)$$

Hydrogen sulfide methane reformation. Hydrogen sulfide in SQNGs can reform methane to produce hydrogen and, instead of producing elemental sulfur, sulfur disulfide. The latter is a high heat value chemical with multiple usages. This approach is a pure thermal process that is fundamentally different from the hybrid approaches reviewed above. The concept is similar to steam methane reformation:

$$2H_2S + CH_4 \longrightarrow 4H_2 + CS_2(l) \quad \Delta H_{298K} = 232.4 \text{ kJ/mol} \quad (8)$$

Analyses of thermal decomposition of SQNGs (O_2 flow rate = 0)

The stability of hydrogen sulfide in SQNG is a major concern for the decomposition of SQNG. In order to examine the thermodynamic performance of hydrogen sulfide during the pyrolysis of SQNG, we take an SQNG source found in Florida panhandle area as a case study. In this calculation we assume that the inlet component mole flow rates are equal to their mole fractions listed in Figure 1. For example, if the methane mole fraction in SQNG is 62.10% we use 62.10 mole/hr as an input to a Gibbs reactor operation in Aspen Simulation Platform for equilibrium flow rate calculations.

Equilibrium flow rates of methane, hydrogen and carbon. Figure 1 indicates that when the temperature is lower than 500 ºC, hydrocarbons (C_2 to C_6) are quickly decomposed to form methane and hydrogen. With increasing temperature the methane flow rate decreases and when the temperature exceeds 500 ºC, methane is decomposed into carbon and hydrogen. Until the temperature is greater than 850 ºC, equilibrium flow rates of methane and carbon depend only slightly on temperature increase, indicating the consumption of methane. As the hydrocarbons are decomposed, the produced hydrogen flow rate increases with the pyrolytic temperature and slowly reaches its limit with temperature exceeding 850 ^oC.

Equilibrium flow rates of hydrogen sulfide, carbon disulfide and sulfur dimer. During the thermal SQNG thermal decomposition process, if hydrogen sulfide is decomposed into hydrogen and elemental sulfur, the pyrolysis is considered practically little use since sulfur deposition will deactivate the catalysts for methane decomposition. The initial mole fraction of hydrogen sulfide is 10.0% corresponding to 10.0 kmol/hr input to a Gibbs reactor. Figure 2 depicts equilibrium flow rates of these species and shows that hydrogen sulfide is very stable below a temperature of 1050 ºC. Normally, the methane pyrolysis temperature is in the 700 to 900 ^oC

range within which no hydrogen sulfide decomposition is detected. The result suggests that hydrogen sulfide can be treated as an inert gas. Its presence does not affect the course of the methane pyrolysis. So, thermodynamically, no hydrogen sulfide separation is needed for SQNG decomposition. The problem remains though is the catalyst deactivation that will be discussed elsewhere. When temperature is greater than 1050 ºC methane reacts slightly with hydrogen sulfide resulting in low flow rates of carbon disulfide. Figure 3 also indicates that hydrogen sulfide decomposition in SQNG occurs at a higher temperature because the equilibrium flow rate of diatomic sulfur is less than that of carbon disulfide. In fact, during the SQNG pyrolysis, the diatomic sulfur flow rate maintains a very low level up to a temperature of 1600 °C. For example, the sulfur dimer flow rate is 0.00324 kmol/hr (lower than 0.3 ppm mole fraction in the outlet stream) at a temperature of 1000 ºC.

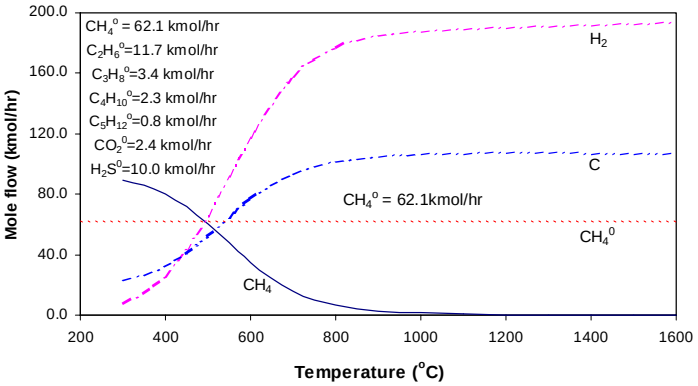

Figure 1. Temperature dependence of equilibrium CH_4, H_2 and C mole flow rates in SQNG pyrolytic process

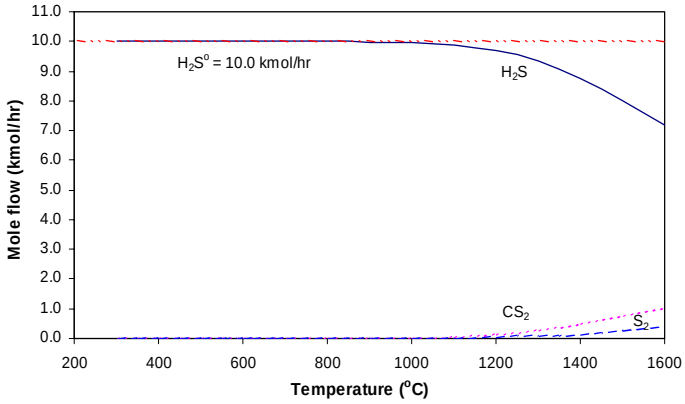

Figure 2. Temperature dependence of equilibrium H_2S, CS_2, and S_2 mole flow rates in SQNG pyrolytic process

Autothermal decomposition of SQNG (O_2 flow rate ≠ 0)

In this paper, air is considered as the oxygen source mixed with SQNG. Inlet airflow rates to the Gibbs reactor are 0, 10, 20, 30, 40 and 80 kmol/hr, respectively, corresponding to oxygen flow rates of 0, 2.1, 4.2, 6.3, 8.4 and 16.8 kmol/hr.

Equilibrium flow rates of methane, carbon and hydrogen. Figure 3 shows that all hydrocarbons are decomposed into hydrogen, methane and carbon within a temperature range of 300 to 500 ºC. The methane flow rate decreases with increases of either temperature or oxygen flow rate. Interestingly, equilibrium hydrogen output flow rates are independent of oxygen input within the range of 0 to 16.8 kmol/hr.

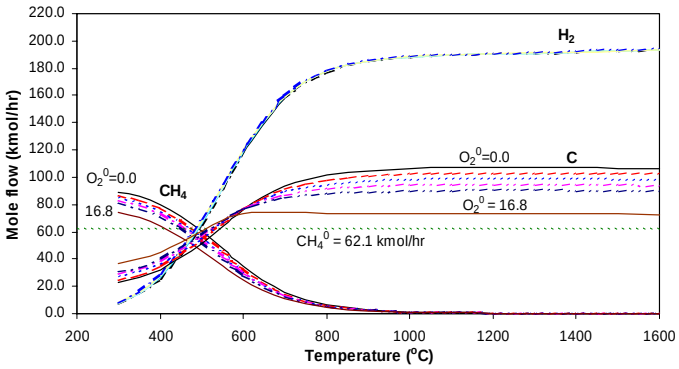

Figure 3. Temperature dependence of equilibrium mole flow rates of CH_4, H_2 and C in an SQNG autothermal process

Equilibrium mole flow rates of hydrogen sulfide, sulfur disulfide and diatomic sulfur. In autothermal decomposition of SQNG, oxygen inlet does not have significant effect on the stability of hydrogen sulfide (Figure 4). The hydrogen sulfide keeps stable within a temperature range of 700 to 900 ºC. In this range, even with oxygen input to the reactor hydrogen sulfide conversion still maintains at a very low level. For example, a maximum concentration of 1.45% at a temperature of 1000 ºC and 16.8 kmol/hr of oxygen flow rate. The result proves that hydrogen sulfide can be treated as an inert gas even with presence of oxygen.

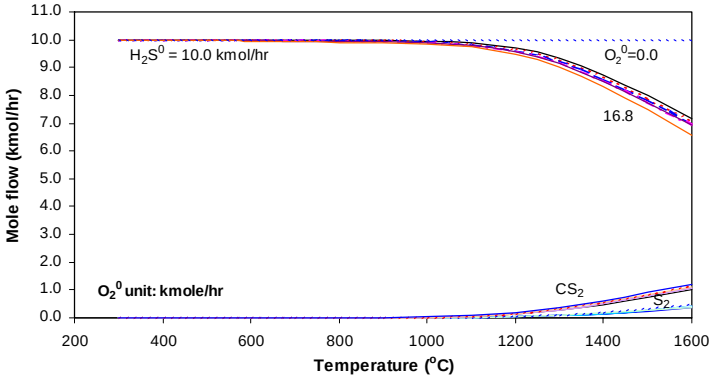

Figure 4. Temperature dependence of equilibrium mole flow rates of H_2S, CS_2 and S_2 in SQNG autothermal process

Acknowledgment. The authors are grateful for the financial support of the NASA-GRC Grant NAG3-2751 hydrogen project.

References

1. Lokhandwala, K. A., Baker, R. W., Toy, L. G. and Amo, K. D., U.S. Pat. No. 5,401,300, **1995**.
2. Zaman, J. and Chakma, A., *Fuel Processing Technology*, **1995**, 41, 159-198
3. Mizuta, S., Kondo, W., Fujii, K., Iida, H., Isahiki, S., Noguchi, A., Kikuchi, T., Sue, H. and Sakai, K., *Ind. Eng. Chem. Res.*, **1991,** 30: 1601
4. Lim, H.S. and Winnick, J., *J. Electrochem. Soc.*, **1984**, 131:562
5. Weaver, D. and Winnick, J., *J. Electrochem. Soc.*, **1987,** 134:2451
6. Winnick, J., *Sci. Techno.*, **1990,** 25:2057

DEACTIVATION KINETICS DURING THE STEAM REFORMING OF DIESEL- FUEL COMPONENTS

Sandeep K. Goud and Martin A. Abraham[*]

Dept of Chemical and Environmental Engineering
University of Toledo, Toledo OH 43606

William A. Whittenberger
Catacel Corp.
Garrettsville, OH

Introduction

The recent discussion regarding the coming hydrogen economy has provided unique opportunities to investigate available technologies for the delivery of hydrogen. Current fuel distribution systems are based on hydrocarbon fuels, such as diesel and natural gas, not hydrogen. Therefore, wide spread use of fuel cells will require development of a hydrogen distribution infrastructure or an efficient process to produce hydrogen from hydrocarbon fuels. Hydrogen generation from existing resources, such as natural gas, gasoline and diesel fuel, is a viable alternative for the near-term.

For the conversion of distillate fuels, such as diesel or jet fuel, the presence of sulfur-containing compounds leads to rapid deactivation of the catalyst. Development of a sulfur-tolerant catalyst would represent an important technical advance; for example, InnovaTek claims a sulfur-tolerant (up to 100 ppm S) reforming catalyst for conversion of diesel fuel that operates at a steam to carbon ratio of 3.6 for 220 hr with no deactivation [i]. Much of the recent desulfurization research has concentrated on ZnO-based sorbents for sulfur removal since the thermodynamics of ZnO-H_2S reaction is very favorable [ii, iii]. In addition, the sulfur capacity of ZnO (g S/g ZnO) is very high (~0.39 g S/ g ZnO).

This paper describes our efforts to understand the performance of a Pd based monolith catalyst in the steam reforming of n-hexadecane (as a surrogate for diesel fuel) for the production of hydrogen. The present study describes the effect of steam to carbon ratio (S/C), temperature (T) and sulfur content (S) on the deactivation of the catalyst. A statistical analysis of the experiments has been completed to determine the combined effect of these three parameters on the rate of catalyst deactivation. Novel catalysts in which base metal oxides have been incorporated into the washcoat have also been evaluated for deactivation, and shown to provide superior sulfur tolerance. A second statistically designed experiment has been used to evaluate the performance of the catalyst at various loadings of base metal oxide additive.

Experimental

At the University of Toledo, steam reforming of n-hexadecane, used as a simulant for diesel fuel, was performed in a continuous packed bed reactor, at temperatures between 750 and 850°C, at steam to carbon ratios (S/C) between 3 and 6, and in the presence and absence of sulfur (introduced as thiophene). Catalyst performance was evaluated in terms of hydrogen yield and reaction efficiency. Deactivation of the catalyst was evaluated and analyzed in terms of a deactivation rate constant calculated by assuming first-order deactivation.

Reactions were conducted in a continuous flow, packed bed reactor. Separate feeds for n-hexadecane and water were introduced into the pre-heater, which was maintained at 550°C. Following the pre-heater, the feed streams were mixed and introduced into the reactor, in which the catalyst sample had previously been inserted. Catalyst samples consisted of a 6 inch strip of stainless steel foil coated with the desired catalyst, and used as prepared by Catacel. Product gases were separated into permanent gases and condensables using a condenser operating with house cooling water. The gas stream was sent to a Shimadzu 2010 gas chromatograph equipped with a 1 m Shincarbon ST microbore packed column and a pulse-discharge ionization detector. Liquid samples were collected and analyzed off-line.

An experimental design was established to evaluate the performance of the palladium catalyst under a range of operating conditions. Three variables were to be tested (temperature, S/C, and sulfur loading), leading to an nine point experimental design.

Results and Discussion

Hydrogen yield was based on the stoichiometry of the reaction. Assuming complete conversion of hexadecane to CO2 and water provides:

$$C_{16}H_{34} + 32\,H_2O \rightarrow 16\,CO_2 + 49\,H_2$$

Then, the yield of hydrogen can be evaluated based on the molar flow rate of the feed hexadecane:

$$Yield = \frac{F_{H_2,out}}{49F_{C_{16},in}}$$

First order reaction rate constant and the rate constant for deactivation were calculated from the experimental data using a best-fit regression. Assuming first-order kinetics, and exponential decay, the conversion can be related to the residence time and on-stream time according to

$$-\ln(1-X) = k_0\tau\exp(-k_d t)$$

and thus a plot of ln(-ln(1-X)) vs. t provides a straight line, the slope of which is –kd and the intercept is ln(k_0).

The results from these experiments are provided in Table 1, in terms of maximum yield, deactivation rate constant and first order rate constant obtained for a particular experimental run. In general, first order rate constant was higher at higher temperatures and S/C ratios, but was lower in the presence of sulfur than in its absence. Similarly, deactivation was more rapid in the presence of sulfur, at low S/C ratios, and at lower temperatures. These results are consistent with what is previously known about the performance of steam reforming catalysts.

Since the catalyst was deactivated throughout the course of an experimental run, greater detail is provided in graphical format, in which the H_2 yield is compared as a function of on-stream time. Such results are provided in Figure 1, which illustrates the effect of S/C ratio at several different experimental conditions (T = 850°C, and S = 0, 50 ppm). In all cases, it can be seen that all of the samples deactivated during approximately 20 hr of on-stream time, and that the rate of deactivation was greater for the catalysts run at more difficult conditions (low S/C ratio, low temperature, and high sulfur loading). Samples tested at 850°C and S/C = 6 had the greatest hydrogen yield and the slowest rates of deactivation. Reactions run at the severe conditions (850°C ,50 ppm sulfur and S/C=3) produced very low levels of hydrogen even at short times on stream, demonstrating the rapid deactivation brought on by the presence of sulfur.

The reaction not only became less effective at longer times, but the composition of the gas product also changed. At longer times on stream and thus greater amounts of deactivation, thermal cracking products including ethane and ethane were detected in the gas product, at increasing concentrations. The amount of CO relative to CO_2 also decreased at longer run times.

[*] Corresponding Author. E-mail: martin.abraham@utoledo.edu

Table 1
Summary of Experimental Lab Reactor Results

Temp. (°C)	S/C	Sulfur (ppm)	H_2 Yield	k_0 (hr^{-1})	k_d (hr^{-1})
750	3	0	24.00	1090.9	5.16E-02
850	3	0	40.00	1746.6	5.28E-02
750	6	0	62.00	5878.6	6.00E-03
850	6	0	92.00	9683.1	2.64E-03
750	3	50	21.00	479.1	7.20E-02
850	3	50	28.00	1477.5	6.00E-02
750	6	50	48.00	3970.8	1.44E-02
850	6	50	85.00	9026.7	1.08E-02
800	4.5	25	80.00	4402.5	2.88E-02

A: 850°C, 0 ppm sulfur

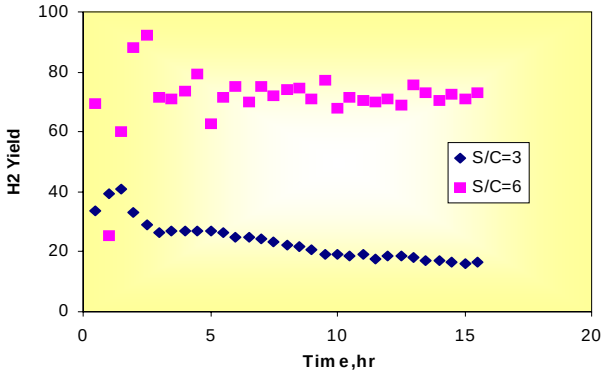

B: 850°C, 50 ppm sulfur

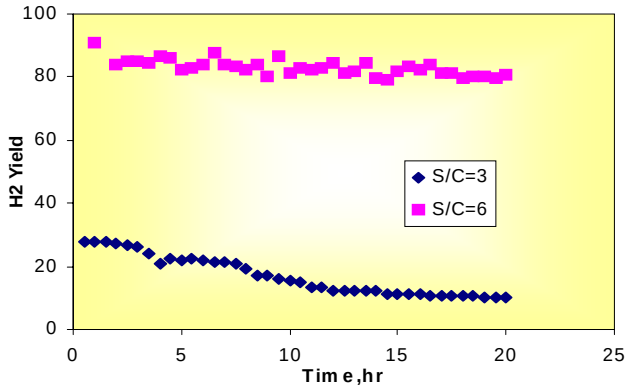

C: Deactivation Plot

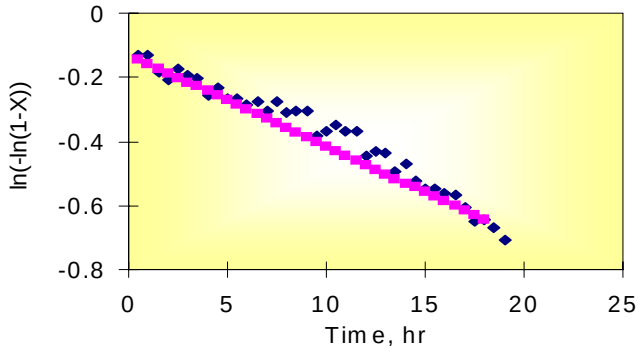

Figure 1. Summary of hydrogen yield at various experimental conditions, and the deactivation of catalysts during time on-stream.

In order to develop a more stable catalyst, the catalyst support matrix was enhanced with the presence of base metal oxides. Both CuO and ZnO were included in the catalyst matrix, at various loadings, and the performance of each of these samples was evaluated under standard reaction conditions of 800°C, S/C = 4.5, and 25 ppm sulfur. The catalyst without any base metals revealed the greatest activity of all samples, but also deactivated fairly rapidly. The samples with 5% CuO and ZnO (at either 2.5% or 5%) had the lowest rates of deactivation. The catalyst containing 5 wt % CuO and 2.5 wt % ZnO appeared to provide the best overall performance, based on a combination of catalytic activity and stability. As was observed with the unmodified catalysts, the composition of the gas product changed as a function of the time on stream, with the presence of cracking products observed at longer times and higher amounts of deactivation.

Analysis is currently ongoing to evaluate the catalyst surface area prior to reaction and compare them with those after the reaction. A more detailed kinetic analysis is also underway, to determine the reaction pathways that are more greatly impacted by the presence of sulfur and catalyst deactivation.

Significance

The conversion of distillate fuels to hydrogen is a critical technology path in the use of fuel cells as auxiliary power units for trucks and jet aircraft. Because of the presence of high sulfur levels in these fuels, the development of sulfur-tolerant reforming catalysts are essential. The current work provides further analysis of the influence of sulfur on the performance of steam reforming catalysts, and demonstrates a new generation of reforming catalysts that provides greater sulfur tolerance. The use of a monolith supported catalyst provides a unique operational advantage in that it permits a reforming device that is more lightweight and compact than existing units, thereby providing a unique opportunity for commercialization.

Acknowledgement.

Financial support for this project was provided by the National Science Foundation through an SBIR grant to Catacel Corp. and by the Ohio Department of Development through the Wright Fuel Cell Group.

References

[i]. Q. Ming, T. Healey, L. Allen, and P. Irving, *Catalysis Today*, **77** (2002) 51.

[ii]. G. Steinfeld *et al.*, AIChE Spring 2000 Meeting, March 5-9, 2000, Atlanta, GA.

[iii]. S. Allen, E. Ashey, D. Gore, J. Woerner and M.C. Cervi, *Naval Engineers Journal*, **110**(1998) 93.

CO_2 REFORMING OF METHANE OVER PLASMA PREPARED Pt/ZrO_2

*Xinli Zhu and Chang-jun Liu**

Key Laboratory for Green Chemical Technology, School of Chemical Engineering and Technology, Tianjin University, Tianjin 300072, China

Introduction

Methane and carbon dioxide are the two major man-made greenhouse gases. CO_2 reforming of methane can convert them into CO and H_2, further to synthesize valuable fuels and chemicals, e.g., ethylene and alcohols. Syngas produced by this reaction has a CO to H_2 ratio of near 1, which is particularly suitable for Fisher-Tropsch synthesis. CO_2 reforming of methane has attracted a worldwide attention. Various transition metals based catalysts have been tested for CO_2 reforming, including Ni, Rh, Pt and Co[1-7]. Although Ni based catalyst has been extensively studied, the problem of deactivation due to coke formation has not well resolved. Pt and Rh based catalysts also attracts much attentions according to their high activity and better performance of anti-carbon. Lercher and his coworker [2, 3, 7] developed a Pt/ZrO_2 catalyst showed better stability for CO_2 reforming. They also argued that Pt atoms on the support-metal perimeter determine the activity. In our previous work, we have successfully loaded Pd[8,9] and Pt[10] on ZSM-5 zeolite with a improved dispersion and quite smaller size of active particles using plasma treatment following calcinations thermally, compared to conventional wetness impregnation method. As a noble metal, it is necessary to reduce the Pt consumption in the catalyst.

In this work, we attempted to prepare more active Pt/ZrO_2 catalyst by the above-mentioned plasma technology. For the purpose of comparison, the catalyst prepared by conventional wetness impregnation was also tested.

Experimental

Catalyst preparations. Zirconium hydroxide was prepared from an aqueous solution of $ZrOCl_2 \cdot 8H_2O$ (Alfa Aesar, >99.9%) by hydrolysis with adding NH_4OH aqueous solution up to pH 9.8. After still placed for 12 h, the precipitate was filtered and washed with deionized water till no Cl^- was detected by 0.1 mol/L $AgNO_3$ solution. The gel obtained was dried at 383 K to form $Zr(OH)_4$. Pt was introduced onto the $Zr(OH)_4$ by impregnation with calculated H_2PtCl_6 aqueous solution for 12 h, followed by drying at 383 K for 12 h and calcinations at 923 K for 5 h to obtain conventional Pt/ZrO_2 (denoted as Pt/ZrO_2(C)). To prepare catalyst using plasmas, after dried at 383 K for 12 hrs, $Pt/Zr(OH)_4$ was first treated by argon glow discharge plasma. The obtained sample was then calcined at 923 K for another 5 hrs to obtain the plasma treated Pt/ZrO_2 (denoted as Pt/ZrO_2(P)). The details of plasma treatment have been described elsewhere previously[9,11]. The Pt loading for all the catalysts is 0.5 wt.%.

Catalytic performance. Catalytic performance was tested in a quartz tube with an inner diameter of 4 mm from 823 K to 1073 K increasing by a step of 50 K at ambient pressure. Typically, 50 mg catalyst was packed in the down-flow quartz tube. The catalyst was reduced by high purity hydrogen (>99.999 %) with a flow rate of 20 ml/min at 923 K for 2 hrs before reaction. Then CH_4 and CO_2 (>99.999 %) with a ratio of 1:1 were introduced into the micro reactor by mass flow controllers at given reaction temperature. At each reaction temperature spot, after stabilized for 20 min, the products sample were collected three times, then the reaction temperature was increased to the next spot. The gas hourly space velocity (GHSV) was 2.4×10^4 ml/(g-cat • h). Products after reaction passed through an ice strap to condense water, and then online analyzed by a gas chromatograph (Agilent 6890) equipped with a thermal conductivity detector (TCD) using a TDX-01 packed column and argon as carrier gas.

Results

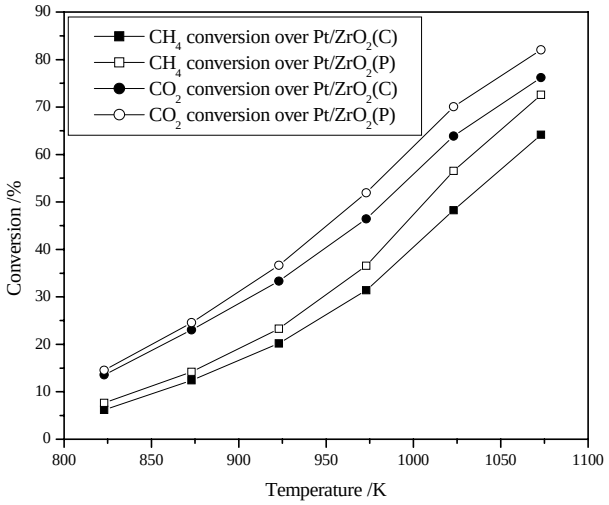

Figure 1. Effect of reaction temperature on conversion of CH_4 and CO_2. Reaction conditions: GHSV=2.4 × 10^4 ml/(g-cat • h), CH_4/CO_2=1:1.

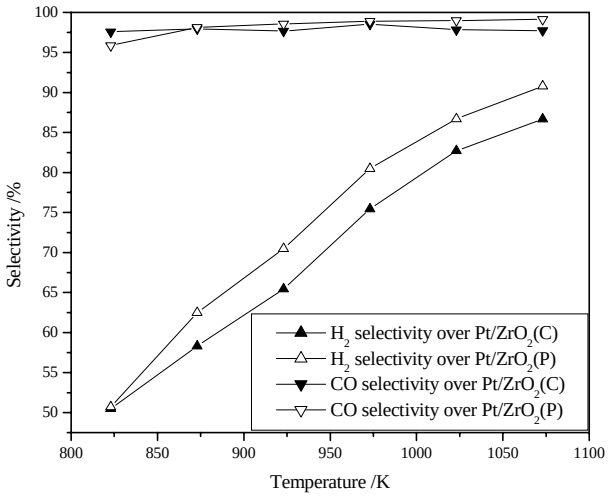

Figure 2. Effect of reaction temperature on selectivity of H_2 and CO. Reaction conditions: GHSV=2.4×10^4 ml/(g-cat • h), CH_4/CO_2=1:1.

The effect of reaction temperature on the conversion of CH_4 and CO_2 is presented in **Figure 1** At the reaction temperature of 823 K, the conversion of CH_4 over Pt/ZrO_2(P) is 1.5 % higher than that over

Pt/ZrO_2(C). With the reaction temperature increasing from 823 K to 1073 K, the difference of the conversion of CH_4 over the two catalysts becomes obvious. When temperature increased to 1023 K and 1073 K, conversion of methane over Pt/ZrO_2(P) increases to 8.3 % and 8.4 % higher than that over Pt/ZrO_2(C), respectively. The activity of CO_2 conversion shows the similar trend. The conversion of CO_2 over Pt/ZrO_2(P) is also increased from 1 % to 6 % higher than that over Pt/ZrO_2(C) with temperature increasing from 823 K to 1073 K.

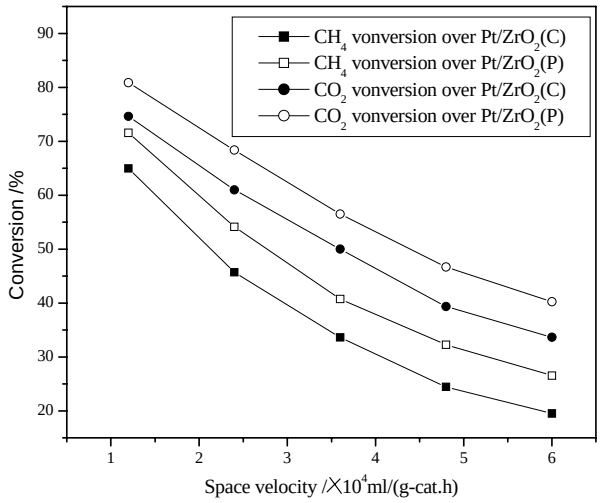

Figure 3. Effect of space velocity on the conversion CH_4 and CO_2. Reaction conditions: Reaction temperature=1023 K, CH_4/CO_2=1:1.

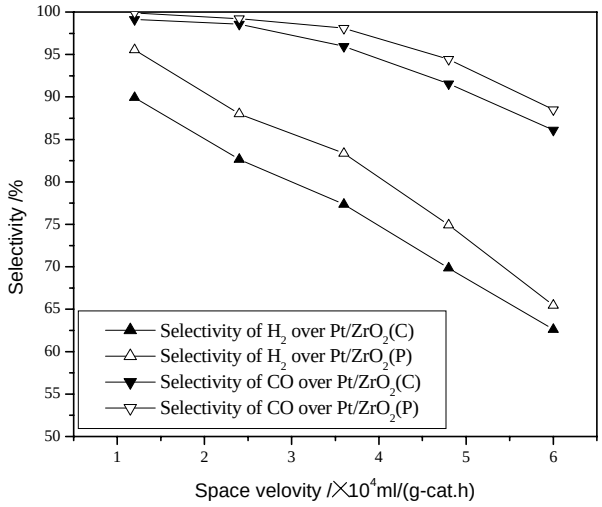

Figure 4. Effect of space velocity on the selectivity of H_2 and CO. Reaction conditions: Reaction temperature=1023 K, CH_4/CO_2=1:1.

Figure 2 shows the effect of reaction temperature on the selectivity of CO and H_2. Both catalysts exhibit high selectivity for CO (more than 95 %), and Pt/ZrO_2(P) possesses a slightly higher of selectivity of CO at most reaction temperatures. The selectivity of H_2 over Pt/ZrO_2(P) illustrates about 4.2 % higher than that over Pt/ZrO_2(C) except reaction temperature at 823 K.

Figure 3 and **Figure 4** demonstrate the effect of space velocity on conversion of CH_4 and CO_2, selectivity of CO and H_2, respectively, at reaction temperature of 1023 K. With the space velocity increasing from 1.2×10^4 ml/(g-cat • h) to 6.0×10^4 ml/(g-cat • h), the conversion of CH_4 and CO_2 decrease near lineally. The conversion of CH_4 and CO_2 over Pt/ZrO_2(P) are 6.0%-8.4% and 6.2%-7.4%, respectively, higher than those over Pt/ZrO_2(C). The selectivity of CO and H_2 are also decreased with space velocity increasing over both the two catalysts, but them over Pt/ZrO_2(P) are 0.8%-2.8% and 2.8%-5.5% higher than those over Pt/ZrO_2(C).

Conclusion

Pt/ZrO_2 catalyst was prepared using plasma treatment following by calcinations thermally. Its activity was compared to the catalyst prepared conventionally. Higher conversion and better selectivity present over the plasma prepared catalyst. Moreover, the activity and selectivity of plasma prepared Ni/Al_2O_3 catalyst even exhibit a more significant improvement, which will be reported later.

Acknowledgment. The support from National Natural Science Foundation of China is very appreciated (under the contract 20225618).

References

(1) Ashcroft, A. T.; Cheetham, A. L.; Green, M. L.; Vernon, P. D. F. *Nature*, 1991, *225*, 352.
(2) Bitter, J. H.; Seshan, K.; Lercher, J. A. *J. Catal.*, 1997, *171*, 279.
(3) Bitter, J. H.; Seshan, K.; Lercher, J. A. *J. Catal.*, 1998, *176*, 93.
(4) Bradford, M. C. J.; Vannice, M. A. *Appl. Catal. A*, 1996, *142*, 73.
(5) Ding, R. G.; Yan, Z. F. *Catal. Today*, 2001, *68*, 135.
(6) Wang, S. B.; Lu, G. Q. M. *Appl. Catal. B*, 1998, *16*, 269.
(7) Bitter, J. H.; Hally, W.; Seshan, K.; Ommen, J. G. V.; Lercher, J. A. *Catal. Today*, 1996, *29*, 349.
(8) Liu, C.-J.; Yu, K.-L.; Zhang, Y.-P.; Zhu, X.-L.; He, F.; Eliasson, B. *Catal. Commun.*, 2004, *4*, 303.
(9) Liu, C.-J.; Yu, K.-L.; Zhang, Y.-P.; Zhu, X.-L.; He, F.; Eliasson, B. *Appl. Catal. B*, 2004, *47*, 95.
(10) Zhang, Y.-P.; Ma, P.-S.; Zhu, X.-L.; Liu C.-J.; Shen, Y.-T.; *Catal. Commun.* 2004, *5*, 35.
(11) Liu, C.-J.; Vissokov, G.P.; Jang, B. W. L. *Catal. Today*, 2002, ***72***, 173.

EFFECT OF METHANOL FEED CONCENTRATION ON DIRECT METHANOL FUEL CELL PERFORMACNE

Jun Lin, Jeong K. Lee, Ryszard Wycisk and Peter N. Pintauro

Department of Chemical Engineering
Case Western Reserve University
10900 Euclid Avenue
Cleveland, OH 44106

Introduction

Fuel cell technology is a viable option for, at least partial, satisfaction of the future energy needs. It is predicted that hydrogen fuel cells will dominate the automotive applications while direct methanol fuel cells (DMFC) are to take over the demanding portable electronics market.

The advantage of DMFC comes from the fact that both, the volumetric energy density and gravimetric energy density of fuel and containment are greater for methanol than for hydrogen.

Commercialization of DMFC is impeded mainly by high methanol crossover of the current state of the art membranes (especially Nafion materials used in PEM systems). Un-oxidized methanol permeating through the membrane to the cathode causes several deleterious effects contributing to serious power loss. The effect can be, to a certain extent, minimized by using diluted aqueous methanol solution as the feed. It was found that for Nafion 117, MeOH concentration around 1-2 M is optimal. However, the requirement to use diluted feed translates into serious complications with accommodation of either large fuel tanks or specialized dilution subsystems.

Taking into account methanol oxidation stochiometry (i.e., one mole of H_2O is required for each mole of MeOH) the optimal feed concentration should be 64 wt. % (ca. 18 M MeOH). Use of feed of such a high concentration with a Nafion-based MEA leads to serious degradation of the DMFC power due to: (i) chemical oxidation of MeOH with O_2 at the cathode bringing about electrode depolarization, (ii) surface poisoning of the cathode by methanol oxidation intermediates, (iii) lowering of O_2 concentration for cathodic reduction, and (iv) excessive flooding. The energy conversion efficiency is further lowered by the irreversible loss of a significant fraction of the fuel.

Our group has been investigating blended polymeric membranes and composites for DMFC applications (1-3) with the aim of developing materials with reduced methanol crossover. Among the systems studied are: sulfonated polyphosphazene/polyacrylonitrile (SPOP/PAN), sulfonated polyphosphazene/poly(vinylidenefluoride-co-hexafluoropropylene) (SPOP/PVDF-HFP), sulfonated polyphosphazene/polybenzimidazole (SPOP/PBI) and various Nafion blends.

The general question that we ask is whether it may be possible to not only diminish the DMFC loss of performance, but ultimately, achieve an increase in power density at higher feed concentration when using membranes with reduced methanol crossover fabricated from Nafion or polyphosphazene blends.

In this paper, we will discuss the properties and fuel cell performance of membranes prepared from Nafion/FEP, Nafion/PVDF, SPEEK/PBI and SPOP/PBI blends. Fuel cell data collected at 60°C with 1-10 M methanol feed and ambient air shows that the blended membranes outperformed Nafion 117, especially at the higher methanol concentration where the power output was higher and methanol crossover lower than that of Nafion 117. Specific examples of DMFC operation with blended membranes will be given in this talk, along with our understanding of the relationship between membrane characteristics and DMFC performance.

Experimental

Materials. The sulfonated polyphosphazene blends were prepared according to references 1-3. Nafion-PVDF blends were prepared by spin-coating a clear solution of Nafion (dried from 5 wt% solution) and PVDF in dimethyl acetamide (DMAc) solution on silicon wafer. After evaporation of DMAc at 120°C and final annealing at 145°C for 1 hour, the membranes were boiled in 1.0M H_2SO_4 and rinsed with deionized water. Nafion-FEP blends was prepared in the following way: Nafion precursor (R1100, Ion-power) and FEP (FEP 100, DuPont) pellets were mixed and extruded using DACA microcompounder at 300°C. The blends were hot pressed at 300°C and 5000 psi into films, which were then immersed in 15% NaOH aqueous solution at 80°C for 24-72 hours to hydrolyze sulfonyl fluoride groups of the precursor. The membranes were then boilded in 1.0M H_2SO_4 and rinsed with deionized water.

Characterization. Conductivity measurements were performed by an AC impedance technique using an open-frame, two-electrode cell.[1-3] Methanol permeability was measured in a custom-built two-compartment diffusion cell.[3] The morphology of the membranes were determined using a scanning electron microscope (SEM, Hitachi S4500).

Preparation of Membrane Electrode Assembly (MEA). A two layer catalyst system was used for both the anode and cathode. The first anode layer was composed of platinum-ruthenium alloy (1:1, Alfa Aesar) with 7 wt % Nafion ionomer (5 wt % solution, Aldrich) that was deposited onto A-6 ELAT/SS/NC/V2 carbon cloth, where the catalyst loading was 3.0 mg/cm^2. The second layer, which was painted directly on the first, composed of platinum-ruthenium alloy and 30 wt % Nafion ionomer (5 wt % solution, Aldrich) with a loading of 1.0 mg/cm^2. Additionally, Nafion solution (5 wt % solution, Aldrich) was painted onto the surface of the second layer at a loading of 2 mg/cm^2. Similarly, the two layer cathode was made using platinum black catalyst ink and A-6 ELAT/SS/NC/V2 carbon cloth, where the first layer (3.0 mg/cm^2) composed of 7 wt % Nafion ionomer and the second layer (1.0 mg/cm^2) contained 40 wt % Nafion. As in the case of the anode, the second Pt-black layer was painted with Nafion solution (5 wt % solution, Aldrich). Both the anode and cathode were dried at 80 ^{o}C for 30 minutes, cured at 140 ^{o}C for 5 minutes and finally hot pressed onto the membrane. The prepared MEA was soaked in 1.0M H_2SO_4 for overnight, washed thoroughly with distilled water prior to fuel cell test.

Direct Methanol Fuel Cell Tests. Steady-state current density/voltage data were collected using a single cell test station (Scribner Series 890B) with mass flow and temperature control. The fuel cell (5.0 cm^2 geometric area) operated at 60^{o}C, with 1.0-10.0 M methanol (at a flow rate of 2 ml/min) and humidified air (70^{o}C and atmospheric pressure, at a flow rate of 500 sccm). The methanol crossover flux was determined by measuring the carbon dioxide concentration in the cathode air exhaust at open circuit, using a Vaisala GMM12B or GMM220A CO_2 detector. Prior to measurements, the sensor was calibrated with reference CO_2/N_2 gas mixtures containing 400-5000 ppm of CO_2.

Results and Discussion

Figure 1 shows the morphology of a Nafion/FEP blend containing 50 wt.% of FEP (50/50) and a Nafion/PVDF blend containing 50 wt% of PVDF (50/50). It can be clearly seen that Nafion/FEP membranes show strong orientation of the blended components, while Nafion/PVDF system doesn't show any orientation. This morphological difference could be related to the processing condition during the preparation of the two blends. For

Nafion/FEP blends, both melt extrusion and hot-pressing cause strong orientation of the dispersed phase. On the other hand, solution casting seems to result in a very homogeneous, fine morphology.

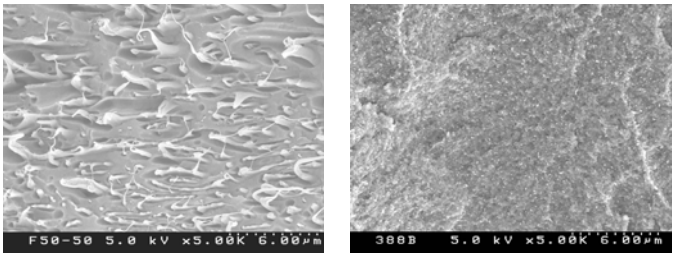

Figure 1. The SEM pictures of Nafion/FFP 50/50 (left) and Nafion/PVDF 50/50 (right).

The resulting membranes were characterized in terms of proton conductivity (in-plane and through-plane AC impedance) and methanol permeability. A comparison of fuel cell performance for a Nafion/FEP 50/50 blend is shown in the Figure 2. It can be seen that the blended membrane showed better performance than Nafion 117, especially at the higher methanol concentration of 5.0 M (where the power output was higher and methanol crossover lower than Nafion 117). Similarly, Nafion/PVDF blends and SPOP/PBI blends also showed better fuel cell performance than Nafion 117 at methanol concentration higher than 1.0 M.

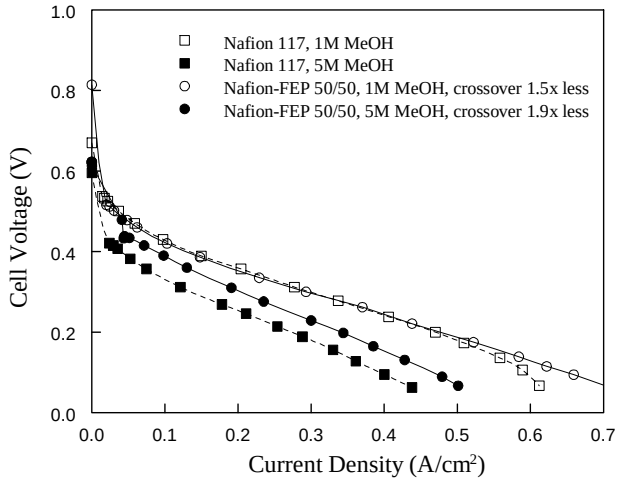

Figure 2. Direct methanol fuel cell performance with Nafion 117 and a Nafion-FEP blended membrane at 60°C, atmospheric pressure and 500 sccm.

In Figure 3, the maximum power densities of Nafion 117 and an SPOP/PBI membrane were plotted as a function of methanol concentration in the range of 1.0 to 10.0 M. The SPOP/PBI blend contained 3 wt% PBI and the IEC of SPOP was 1.2 mmol/g. It can be seen that maximum power density of Nafion 117 drastically decreased from 96 mW/cm^2 down to 9 mW/cm^2 as methanol concentration increased to 10 M. This Nafion 117 performance deterioration is attributed to the combined effects of the higher methanol crossover that resulted in a decrease of cathode potential and increased ohmic resistance of membrane with an increase of methanol concentration. Although at 1.0 M MeOH, the maximum power density of the SPOP/PBI-based MEA was lower than that of Nafion 117, the situation changed dramatically when methanol feed concentration greater than 2.0 M was used. Upon operation on 10.0 M methanol solution, the maximum power density of SPOP/PBI was 6.67 times higher than that of Nafion 117. Consequently, it could be stated that the decrease of fuel cell performance of SPOP/PBI was due to merely diminished cathode potential resulting from higher methanol crossover flux since the resistance of SPOP/PBI was almost constant in the whole range of methanol concentration.

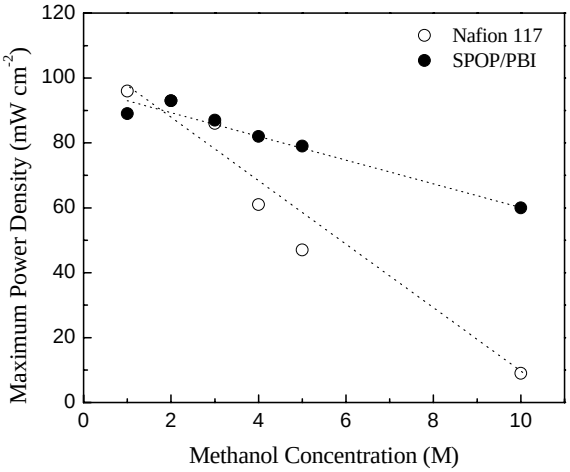

Figure 3. Maximum power density dependence on methanol concentration for SPOP/PBI blends compared with Nafion 117.

Acknowledgment

This work was funded by the Army Research Office, Grant No. DAAD19-00-1-0517. The authors would also like to thank DuPont, Atofina Chemicals and Unitel Technologies, Inc., for providing samples.

References

1. Carter, R., Wycisk, R., Yoo, H., Pintauro, P.N., "Blended Polyphosphazene/Polyacrylonitrile Membranes for Direct Methanol Fuel Cells", *Electrochem. and Solid-State Lett.*, **2002**, 5**,** A195.
2. Wycisk, R., Carter, R., Pintauro, P.N., Byrne, C., "Ion-Exchange Membranes from Blends of Sulfonated Polyphosphazene and Kynar Flex PVDF", in: *Advanced Materials for Membrane Separations*, I.Pinnau and B.D.Freeman (Eds.), ACS Symposium Series 876, ACS, Washington, DC, 2004, 335-351.
3. Wycisk, R., Lee J.K., Pintauro, P.N., "Sulfonated Polyphosphazene-Polybenzimidazole Membranes for Direct Methanol Fuel Cells", *J. Electrochem. Soc.*, **2005**, *in press.*

CATALYST LAYER NETWORK FORMATION AND ITS EFFECT ON FUEL CELL PERFORMANCE

Christine Hronec[1], Charles W. Walker[2] and Yossef A. Elabd[1]

[1]Department of Chemical Engineering
Drexel University
Philadelphia, PA 19104

[2]U. S. Army Research Laboratory
Sensors and Electron Devices Directorate
Adelphi, MD 20783

Introduction

Polymer electrolyte membrane (PEM) fuel cells are intensely being investigated as an alternative to current power sources because of their potential to achieve higher efficiencies with renewable fuels at a lower environmental cost.[1] Despite the numerous advantages of PEM fuel cells, there are several shortcomings with current PEMs, catalysts, and the catalyst layer (CL) structure that hinder fuel cell efficiencies. This study focuses on the morphology of the CL and its subsequent effect on fuel cell performance. Currently, membrane electrode assemblies (MEAs) or CL/PEM/CL composites are most often fabricated by hand painting the catalyst ink unto a decal followed by a decal/hot press ink transfer step.[2] Additional deposition techniques to form the CL in the MEA have been investigated, such as spraying, screen-printing, and rolling.[3] These studies reveal differences in fuel cell performance, which can be related to the morphology of the CL. A number of investigators have suggested that the structure of the CL, or more specifically the reactant gas/Pt/Nafion triple phase boundary (TPB), must be optimized to allow for the appropriate balance of hydrogen gas diffusion, catalytic activity, and proton conductivity.[4]

In this study, a new CL deposition technique was investigated: *in situ* sonication. The CL morphology and fuel cell performance of the new technique was compared to the standard hand painting ink transfer method. In addition, the microstructure of the CL was characterized before and after fuel cell testing to determine the effects that fuel cell tests may have on altering the CL morphology and subsequently fuel cell performance.

Experimental

Materials. Catalyst ink consisted of de-ionized water, 2-propanol (Aldrich, 99.5%), 5 wt% Nafion® in solution (Fluka), and Vulcan XC-72R (ElectroChem, 20wt% Pt/C). Teflon®-coated Fiberglass supports (5 cm^2, C.S. Hyde Co.) or decals were used for the decal/hot press MEA fabrication technique. In addition to the CL, MEAs consisted of a Nafion® 117 perfluorinated membrane (Aldrich) and carbon cloth diffusion layers (ETEK, Inc.).

CL Preparation. Catalyst ink was prepared by ultrasonically mixing Pt/C catalyst in a solution of 2-propanol/water (3:1 volume ratio) for 15 minutes. 10 wt% Nafion® binder was then added and the resulting suspension was ultrasonically mixed for an additional 15 minutes at 30°C.

In this study, four different CL/MEA preparation techniques were investigated (**Table 1**). Method A represents the most commonly used MEA fabrication technique, a decal/hot press transfer. For this method, the catalyst ink was hand painted unto a Teflon®/Fiberglass decal, allowed to dry, and subsequently applied in multiple painting/drying steps to obtain a desired Pt loading of approximately 0.5mg/cm^2 (multilayer hand painting). A dry Nafion® 117 membrane (> 5 cm^2) was sandwiched between two of these catalyst covered decals, with the catalyst side of each decal facing the membrane, and hot pressed at 150°C and 440 kg/cm^2 for 10 s (decal/hot press). The Teflon®/Fiberglass decals were then removed with the catalyst layers remaining on both sides of the membrane. Method B is similar to Method A, however, the decal/hot press step was replaced with a direct deposition of catalyst ink unto the Nafion® 117 membrane *via* multilayer hand painting. This method was explored to determine if direct deposition can replace the decal/hot press step to simplify the fabrication process.

In this study a new deposition technique, *in situ* sonication (ISS), was developed (Methods C and D in **Table 1**). For this technique, a Teflon® Petri dish was suspended in a sonicating bath with the CL substrate (Teflon®/Fiberglass decal or Nafion® 117) adhered to the bottom of the dish. The catalyst ink was applied directly onto the substrate and allowed to dry at 25˚C under sonication for 3 hrs.

Table 1. CL and MEA Preparation Techniques

Method	CL substrate	CL deposition technique	MEA Fabrication Technique
A	Teflon®/Fiberglass decal	Multilayer hand painting	Decal/hot press
B	Nafion® 117	Multilayer hand painting	Direct deposition
C	Teflon®/Fiberglass decal	*in situ* sonication	Decal/hot press
D	Nafion® 117	*in situ* sonication	Direct deposition

Instrumentation. A FEI/Phillips XL30 Field Emission Environmental Scanning Electron Microscope (SEM) was used for CL and MEA characterization. All samples were sputter coated with Pt for 20 seconds using a Denton Desk II sputter coater. Fuel cell testing was performed with a fuel cell test station (Fuel Cell Technologies, Inc.), where the MEA was sandwiched between carbon cloth diffusion layers (double sided at the anode and single sided at the cathode), flow-channel graphite blocks, and bolted between stainless steel heated endplates (fuel cell test fixture) with a testing cross sectional area of 5 cm^2. Fuel cell tests were performed at a hydrogen flow rate of 50 cm^3/min, an oxygen flow rate of 100 cm^3/min, a backpressure at the anode and cathode of 30 psi, and a cell temperature of 80˚C. Cells had an open circuit potential of approximately 0.9 V, and tests were conducted by sweeping potential from 0.9 to 0.2 V by increments of 0.02 V every 10 s and recording current.

Results and Discussion

The SEM images in **Figure 1** show clear structural differences in the CL prior to MEA fabrication when comparing two different deposition techniques, multilayer hand panting and ISS. Multilayer hand-painted samples reveal catalyst ink agglomeration and cracks on the order of 10 to 100 microns in size generating a non-uniform surface (**Figures 1 (a)** and **(b)**). CLs prepared by ISS forms a more uniform, well-packed layer as shown in **Figure 1 (c)**. Simultaneous sonication and solvent evaporation during CL preparation deters catalyst particle agglomeration. This suggest that prolonged sonication during deposition hinders the van der Waals attractive forces between catalyst particles that promote agglomeration.[5] For

Methods A and C, similar CL structures were evident after transferring from the decal to the Nafion® 117 membrane.

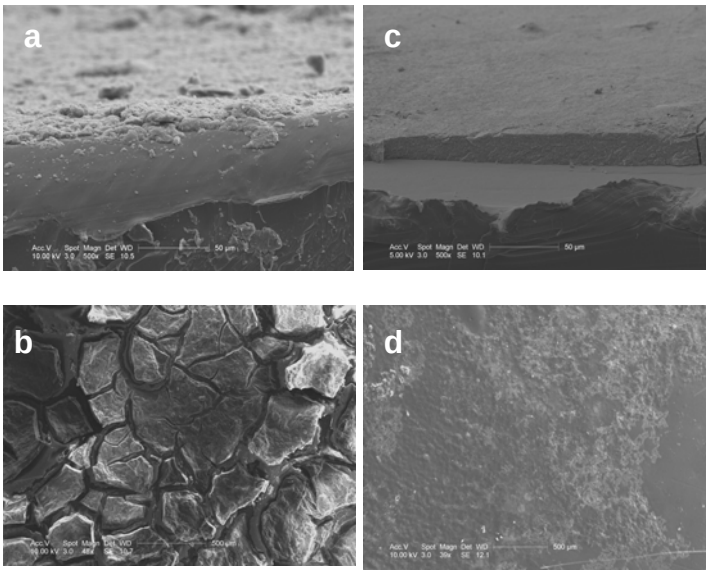

Figure 1. SEM images of the **(a)** cross section of hand painted CL **(b)** top view of hand painted CL **(c)** cross section of ISS CL and **(d)** top view of ISS CL. All samples shown here were deposited on a Teflon®/Fiberglass decal.

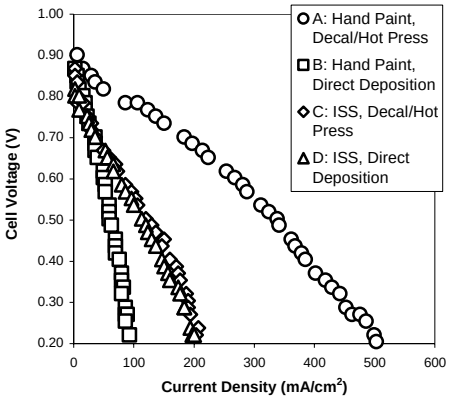

Figure 2. Fuel cell performance data for different CL preparation techniques.

Figure 2 shows the fuel cell performance of the four different CL fabrication techniques listed in **Table 1**. The MEA prepared by multilayer hand painting of the catalyst ink directly onto Nafion® 117 (Method B) displayed the lowest performance. CLs made by ISS, regardless of whether the decal/hot press transfer or direct deposition technique was used (Method C and D), had a similar fuel cell performance, while the standard multilayer hand painting and decal/hot press transfer method (Method A) demonstrated the highest performance. Based on the CL morphology shown in **Figure 1**, it appears that less catalyst surface area is available in Method A, where less pores are available for gas diffusion in Method C. However, based on **Figure 1**, it is unclear which CL possesses a more favorable TPB.

Figure 3 displays an MEA after a fuel cell test. The MEA prepared by Method A reveals catalyst particle agglomeration and cracks within the CL before and after fuel cell tests. These cracks allow for reactant gas flow to catalyst sites on the exterior of densely packed catalyst particle agglomerates. A noteworthy result is evident in a higher magnification image of the CL shown in **Figure 3 (b)**, where a network of Nafion® fibers and smaller catalyst particle agglomerates was formed. These networks were not present in the CL prior to fuel cell tests. These networks were present in post fuel cell MEAs prepared by the other techniques (Methods B-D); however more of these networks were evident in the MEAs prepared by Method A when compared to the other techniques. The morphology after or during fuel cell testing as opposed to before may contribute to the differences in fuel cell performance shown in **Figure 2**. A network of Nafion® fibers connecting catalyst particles dispersed throughout seems to provide a more favorable TPB, where high porosity allows for reactant gas diffusion, smaller catalyst agglomerates possess a higher available surface area for reaction, and the Nafion® fibers provide a pathway for proton diffusion to the PEM. This network was found within the CL microstructure in areas of high porosity. The mechanism for the formation of this network has not yet been determined; however it appears that CLs with higher initial porosity (e.g., Method A) allow for more network formation during fuel cell testing.

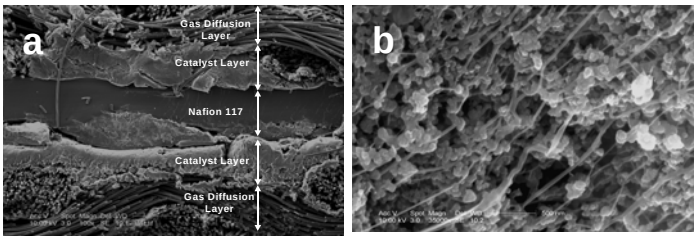

Figure 3 SEM image of **(a)** an MEA (Method A) after a fuel cell test and **(b)** the CL (magnified image) displaying a network of Nafion® fibers connecting catalyst particles.

Conclusions

In this study, a new deposition technique was explored, *in situ* sonication, which produced a more uniform and less porous CL. The fuel cell performance of this new technique was considerably lower than the standard fabrication technique. However, SEM images of the CL after fuel cell testing displayed different CL structures, a network of Nafion® fibers connecting catalyst particles. This network microstructure, and not the CL microstructure prior to fuel cell testing, may be responsible for the differences in fuel cell performance. Current investigations are focused on determining the causes leading to the formation of this favorable CL network.

Acknowledgement. Dee Breger (Drexel University, Department of Materials Science and Engineering) for SEM imaging assistance and NSF-BES-0216343 for SEM equipment.

References

(1) U.S. Department of Energy. Fuel Cell Handbook, 6th ed. B/T Books: Orinda, CA, 2002.
(2) Ahn, S.Y.; Lee Y.C.; Ha, H.Y.; Hong, S.A.; Oh, I.H. *Electrochimica Acta* **2004**, *50*, 673.
(3) Abaoud, H.A.; M. Ghouse, K.V.; Lovell, K.V.; Al-Motairy G.N. *International Journal of Hydrogren Energy* **2005**, *30*, 385.
(4) O'Hayre, R.; Prinz, F.B. *J. Electrochem. Soc.* **2004**, *151*, A756.
(5) Schueler, R.; Petermann, J.; Schulte, K.; Wentzel, H.P. *J. Appl. Polym. Sci.* **1997**, *63*, 1741.

THERMAL STABILITY IN AIR OF Pt/C CATALYSTS AND PEM FUEL CELL CATALYST LAYERS

Olga A. Baturina[1], *Steven R. Aubuchon*[2], *and Kenneth J. Wynne*[1]

[1] Department of Chemical and Life Science Engineering
Virginia Commonwealth University
Richmond, VA 23284-3028
[2] TA Instruments-Waters, LLC
109 Lukens Drive, New Castle, DE 19720

Introduction

Development of carbon-supported platinum catalysts was one of the major steps to commercialization of PEM fuel cells. The main advantages of these catalysts are high surface area, sufficient electronic conductivity of carbon and sluggish catalyst agglomeration under fuel cell operation conditions. Due to increased surface area of Pt/C catalysts, Pt loading in fuel cell cathodes can be reduced 20-40 times (compared to Pt black catalysts) to obtain a similar cell performance.

Unfortunately, using carbon support in Pt/C catalysts also has shortcomings. It is well known that carbon corrodes in a fuel cell environment[2]. As a result, a fuel cell might lose performance during long-life operation. Moreover, it has been found recently that Pt facilitates carbon oxidation in PEM fuel cell simulated conditions[3, 4]. In addition, Pt accelerates the thermal decomposition of Nafion®, (another component of PEM fuel cell catalyst layer) at high temperatures[5].

Due to increased interest to high temperatures PEM fuel cells (operating at temperatures 100-200^{0}C), it is important to explore the limits of thermal stability of carbon supported Pt catalysts and PEM fuel cell catalyst layers.

Experimental

20% and 40% Pt/Vulcan XC72 from E-TEK and 50% Pt/Vulcan XC72 (Tanaka KK, Japan) were used in these studies. Nafion 112 membrane was purchased from Ion Power, Inc. Catalyst layer was prepared by electrospraying Pt ink[1] consisting of ~40% of Nafion ionomer (equivalent weight of 1100, Aldrich) and ~60% of 50% Pt/Vulcan XC72 (dry base) on Nafion 112 membrane. Catalyst layer was sampled for TGA by scraping from the Nafion 112 substrate. Thermogravimetric analyses (TGA) were collected on a Q500 TGA (TA Instruments-Waters, LLC.). Heating rates of 2.5, 5, 10 and 20°/min were employed under an atmosphere of flowing air (100 mL/min).

Results and Discussion

Fig.1 contains the TGA (weight loss vs. temperature) curves for carbon supported Pt catalysts with different platinum loading in air. This data suggest that Pt accelerates decomposition of carbon in carbon supported catalysts; a shift between TGA plots for base carbon and Pt/C is ~200^{0}C. Decomposition of carbon supported catalysts occurs gradually in the beginning and ends with abrupt weight loss at ~ 400^{0}C. The residue above 400^{0}C is stoichiometrically consistent with elemental platinum as the decomposition product. In addition, further analyses of TGA curves for catalysts with different Pt loadings suggests that the amount of carbon loss during the TGA experiment increases with increasing Pt loading.

TGA and DTG (derivative weight loss) plots for catalyst layer, consisting of 50% Pt/C and Nafion® ionomer, Nafion 112 and 50% Pt/C and are presented in Fig.2 and 3, respectively. The TGA curve for the catalyst layer shows three distinct regions corresponding to three peaks on the DTG curve. The sample loses ~4% between 50°C

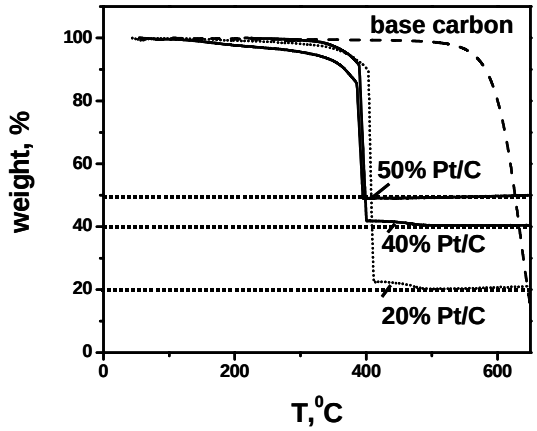

Figure 1. TGA (20^0/min) plots of 20%, 40% and 50% Pt/C in air.

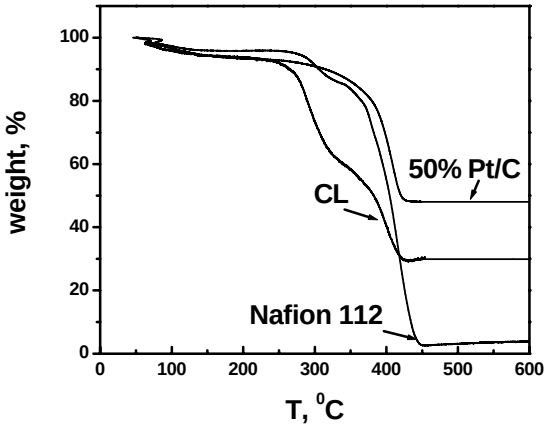

Figure 2. TGA (2.5^0/min) plots of 50% Pt/C, Nafion 112 and catalyst layer (CL) in air.

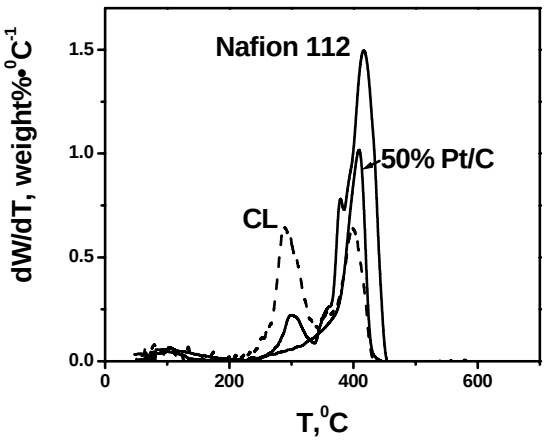

Figure 3. DTG (2.5^0/min) plots of 50% Pt/C, Nafion 112 and catalyst layer (CL) in air.

and 200°C, ~36% between 200°C and 350°C, and ~31% between 350°C and 425°C.

As the amounts of Nafion and carbon in the catalyst layer are 38% and 28% respectively, we assumed that the second region of the weight loss curve of the catalyst layer is related to Nafion decomposition and the third is due to carbon decomposition. This assumption was confirmed by the results of TGA-MS measurements.

Thus, presence of Pt in the carbon-supported catalyst layer lowers the temperature of Nafion decomposition by about 100^0C to 300^0C. Similar observation was made when thermal decomposition of Nafion in the presence of Pt catalysts was studied[5].

TGA-MS data will also be discussed as well as the potential application of TGA as an analytical tool to determine Pt concentration in catalyst coated membranes.

Conclusions

TGA was employed to characterize the thermal stability of Pt/C catalysts and PEM fuel cell catalyst layer in air. It was found that Pt/C catalysts decompose quantitatively in air to Pt at ~400°C. It was further determined that Pt/C catalyst decomposition is affected by Pt loading, as 50% Pt/C weight loss due to carbon oxidation becomes noticeable at 200 °C.

Pt facilitates decomposition of Nafion in PEM fuel cell catalyst layers; the thermal decomposition temperature of Nafion is lowered by about 100°C to 300°C in the presence of 50% Pt/C.

TGA may be useful as an analytical tool to determine Pt concentration in catalyst coated membranes.

Acknowledgement.. This work was supported by NASA's Space Science Office (Grant Numbers NAG5-12560 and NNC04GB13G) and the VCU School of Engineering Foundation.

References

(1) Baturina, O.A. and Wnek, G.E. *Electrochem. Solid-State Let.*, **2005**, *8 (6)*, 1.
(2) Kinoshita, K. and Bett, J.A.S. Carbon, **1973**, *11(4)*, 403.
(3) Roen, L.M.; Paik, C.H.; Jarvi, T.D. *Electrochem. Solid-State Let.*, **2004**, *7 (1)*, A19.
(4) Stevens, D.A.; Dahn, J.R. *Carbon*, **2005**, *43(1)*, 179
(5) Samms, S.R.; Wasmus, S.; Savinell R.F. *J. Electrochem.Soc.*, **1996**, *143(5)*, 1498.

PALLADIUM DEPOSITION ON PROTON EXCHANGE MEMBRANES FOR DIRECT METHANOL FUEL CELLS

H. Xu, H. R. Kunz*, J. M. Fenton***

*Department of Chemical Engineering
University of Connecticut
Storrs, CT 06269, USA

** Florida Solar Energy Center
University of Central Florida
Cocoa, FL 32922, USA

Introduction

Direct methanol fuel cells (DMFCs) have received attention for portable applications due to their high energy density and easy use of methanol. Unfortunately, the performance of DMFCs is still not satisfactory due to high methanol crossover despite considerable efforts to develop new membranes that are impermeable to methanol. The methanol that crosses over poisons the cathode catalyst and leads to a large loss in performance. One approach in developing new membranes is to introduce additives into Nafion® membranes to block the methanol. However, although these additives reduced the methanol crossover, they also decreased the conductivity of the membrane. Recently, Kim *et al* reported a palladized Nafion® membrane where palladium particles were deposited into the membrane via an ion-exchange and chemical reduction method[1]. The palladium significantly decreased the methanol crossover. Fortunately, since palladium is a pseudo-proton conductor[2], the conductivity of the membrane was not changed. This concept of making a barrier-layer membrane for DMFCs is very promising. However, the production of the membrane via ion-exchange and chemical reduction is quite complicated.

Experimental

Palladium (Alfa Aesar) was deposited onto Nafion® 117 and 112 membranes using a spraying technique. First, methanol and palladium were mixed; the mixture was then processed using an Omni® TH-115 homogenizer; the obtained palladium ink was then sprayed onto the membrane under nitrogen pressure. Composite membranes with different Pd thickness were prepared. The palladium-containing membranes were then characterized using Atomic Force Microscopy (AFM), X-ray Diffraction (XRD) and Scanning Electron Microscopy (SEM). Complete MEAs made by screen-printing ere tested for methanol crossover, membrane resistance and performance.

Results and Discussions

Figure 1 shows an AFM image of a Pd-deposited Nafion® 117 membrane. The thickness of the Pd films is 0.1μm at both the anode and the cathode. The image is of one side of the composite membrane from which numerous palladium particle protuberances stretch out of the Nafion® membrane plane. Palladium particles were successfully deposited onto the Nafion® membrane without any cracks.

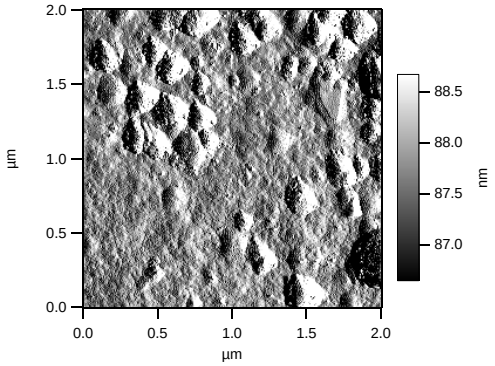

Figure 1. AFM Image of Pd-deposited Nafion® 117 Membrane

Figure 2 shows the methanol crossover current density for Nafion® 117 and Pd-deposited Nafion® 117 at two temperatures. The methanol concentration was 2M at the anode and nitrogen gas was supplied to the cathode. At 30°C, the methanol crossover was 70mA/cm^2 for the Nafion® 117 membrane; however, the crossover was reduced to 40mA/cm^2 for the Pd-deposited Nafion® 117 membrane at the same temperature. The effect of the Pd-deposited membrane on methanol crossover reduction is even more apparent at higher temperature. At 75°C, the crossover for the Pd-deposited membrane at 0.8V is 110mA/cm^2, which is much less than the 180 mA/cm^2 of Nafion® 117.

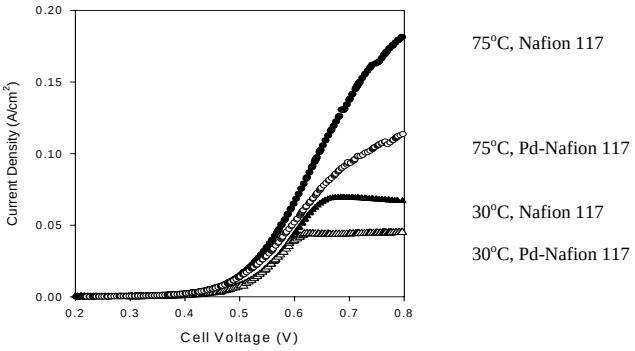

Figure 2. Methanol crossover for Nafion® 117 and Pd-deposited Nafion® 117 Membrane. Anode: 2 M meOH, flow rate: 5cc/min; cathode: N_2, 200cc/min, scan rate: 1mv/sec.

Figure 3 shows cell performance and resistance curves of two DMFCs, one based on the Nafion® 117 membrane, the other using Pd-deposited Nafion® 117. The resistances of the two cells are very close, around 0.25 Ohm-cm^2. This indicates that the deposition of Pd onto the Nafion® membrane does not change its resistance and therefore conductivity. However, the cell performance improved significantly by using the Pd-deposited Nafion® 117 membrane; the whole curve of Pd-deposited Nafion® 117 shifts up compared to the Nafion® 117 curve.

Obviously, the voltage gain with Pd-deposited Nafion® 117 membrane is due to reduced methanol crossover.

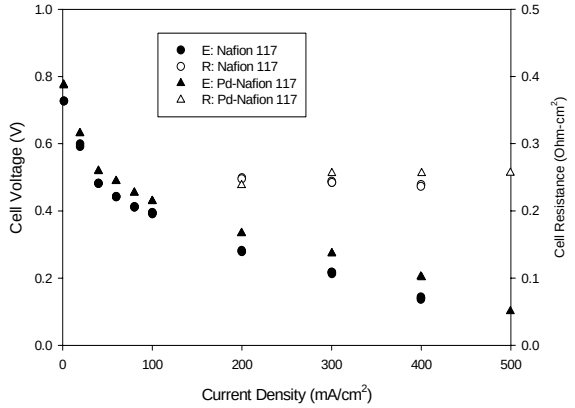

Figure 3. Cell performance and resistance for Nafion 117 and Pd-deposited Nafion 117 Membrane. Anode: 1 M meOH, flow rate: 5cc/min; cathode: air, 200cc/min.

Conclusions

Compared to un-coated membranes, palladium-coated Nafion® 117 membranes have reduced methanol crossover, but unchanged membrane conductivity, which results in an increase in cell performance. This work shows that there are promising applications of Pd-deposited proton exchange membranes for DMFCs. For further improvement of cell performance, the thickness of the palladium film needs to be optimized.

Acknowledgement. the financial support from the U. S. Army through the Connecticut Global Fuel Cell Center at the University of Connecticut is greatly appreciated.

References

1. Kim, Y. Jin, Choi, W. C., Woo, S. I, and Hong, W. H., *Electrochimica Acta*, **2004**, 49, 3227
2. E. S. Smotkin, WO02/11226 A2
3. Ye, X. R., Lin, Y. L., Wang, C., Engelhard, M. H., Wang, Y., and Wai, C. M., *J. of Mater. Chem*., **2004**, 14, 908

IN-SITU ELECTRON SPIN RESONANCE STUDY OF FUEL CELL POLYMER MEMBRANE DEGRADATION

Alexander Panchenko, Emil Roduner

University of Stuttgart, Germany

Introduction

The long term stability of the membrane is an important factor limiting the fuel cell lifetime. During extended use the membrane degrades, probably via reaction with hydroxyl and superoxide radicals which are regular intermediates of the oxygen reduction at the cathode. Only extremely stable membranes can withstand the aggressive chemical and physical environment in an operating fuel cell. Within a given set of operating conditions, intrinsic chemical and mechanical properties of the membrane as well as its water content impact its durability dramatically.

Here we present a novel method for monitoring radical formation and membrane degradation *in-situ* in a working fuel cell which is placed in the microwave resonator of an electron spin resonance (ESR) spectrometer. By introduction of a spin trap molecule at the cathode the formation of immobilized organic radicals on the membrane surface is observed, revealing the onset of oxidative degradation which is more pronounced for F-free membranes than for Nafion. At the anode, free radical intermediates of the fuel oxidation process are observed. No traces of degradation are detected at this side of the fuel cell.

Experimental

The *in-situ* fuel cell consists of two Teflon half-cylinders. Gas feeding channels inside each half-cylinder admit oxygen and hydrogen. The active part includes a Pt mesh as a spacer that allows gas distribution and at the same time provides electrical contact, and a Catalyst Coated Membrane (CCM, that is a membrane with Pt electrodes deposited on both sides) without any Nafion binder. The Pt loading corresponds to 0.77 mg*cm^{-2}. Nafion 115 and a F-free polyaryl-blend covalently cross-linked membrane were employed.

Results and Discussion

The concentration of *free* radicals produced in a fuel cell is extremely low and their lifetime is relatively short, so that it is not possible with conventional methods to observe them directly. We therefore employed the spin-trapping technique, using the spin trap molecules alpha-(4-pyridyl-1-oxide)-N-tert-butylnitrone (POBN) and 5,5-dimethyl-1-pyrroline 1-oxide (DMPO). It allows the trapping of short-lived radicals under formation of relatively stable nitroxide radicals (the spin adducts) which are detectable by ESR The spin trap solution is applied separately at the anode or the cathode side, permitting selective investigation of radical formation and of degradation reactions.

After five minutes of operation with 10 µL of 1 M aqueous solution of POBN at the anode side the POBN-•H adduct is detected (Fig. 1a). The spectrum is characterized by a g-factor that is typical for POBN radical adducts, and it consists of a triplet of triplets due to 1:1:1 and 1:2:1 splittings by one ^{14}N and by two equivalent ^{1}H nuclei, respectively. The result does not depend on the nature of the membrane.

The mechanism of formal H atom addition to the spin trap molecule is studied further in the following set of experiments: the fuel cell is fed with H_2 or D_2, and the POBN solution is applied. Both results in the spectrum shown in Fig. 1a. No influence of D_2 was observed. Then, the two experiments are repeated, but now using a heavy water solution of the spin trap. As a result the formal D adduct to POBN was observed, as revealed by the additional splitting (Fig. 1b). This is evidence of a mechanism involving reduction of POBN at the electrode surface followed by protonation by solvent molecules, H_2O or D_2O:

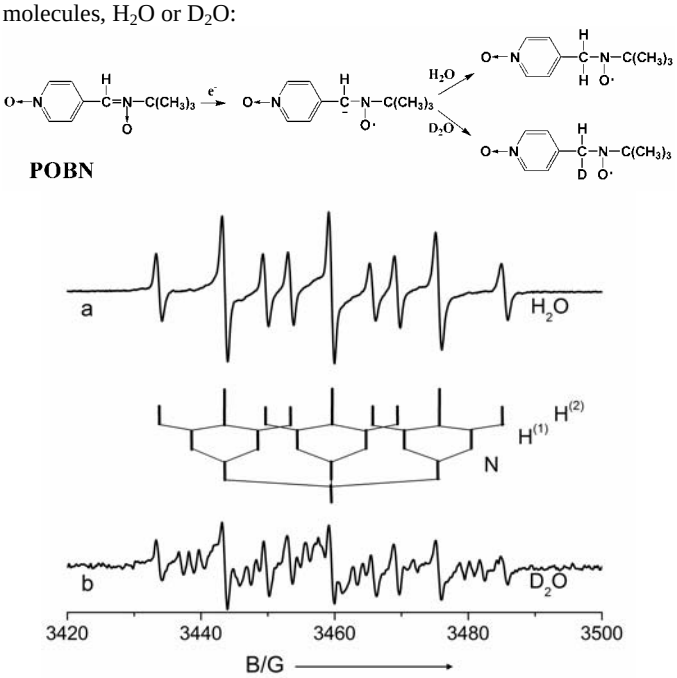

Figure 1. ESR spectrum obtained with an aqueous POBN solution at the anode side of the in-situ fuel cell. **a)** H_2O as solvent for the spin trap. **b)** D_2O as solvent for the spin trap. This spectrum represents a superposition of the D adduct and, from residual protons, the H adduct.

An analogous experiment was also performed with an aqueous DMPO solution at the cathode of the CCM based on a Nafion membrane. Fig. 2, recorded after five minutes of closed circuit operation, depicts the characteristic spectrum corresponding to the DMPO•OH adduct where the single proton coupling happens to be of the the same magnitude as the nitrogen coupling. Observation of this spectrum is quite remarkable, as it proves that •OH radicals are indeed formed at the cathode.

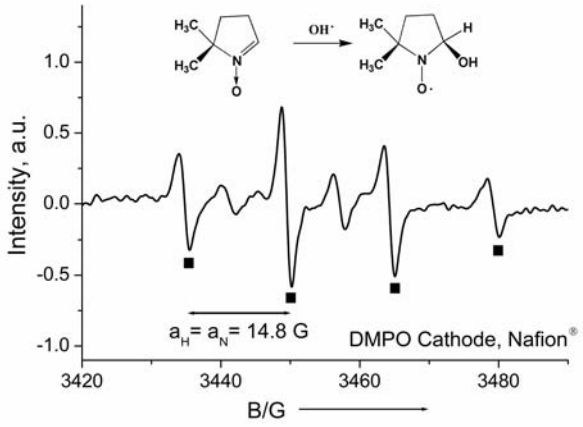

Figure 2. ESR spectrum obtained with DMPO water solution at the cathode side of the in-situ fuel cell. Lines marked with squares belong to the DMPO-•OH adduct. a_N and in particular a_H are quite different for adducts of organic radicals.

When the same experiment is performed with a F-free polyaryl-blend membrane $^{\bullet}$OH is not normally observed. Instead, a different signal with much broader lines builds up (not shown). The large line width is indicative of incomplete averaging of hyperfine anisotropy, and we conclude that the reduced mobility of the spin trap adduct must be due to the fact that the species is bound to the membrane. This means that we have trapped a radical defect on the membrane, originating from the reaction of $^{\bullet}$OH with the aromatic constituents, whereas Nafion because of its higher inertness leaves the spin trap sufficient time to trap $^{\bullet}$OH.

Conclusions

In summary, we have developed a method for the direct investigation of radical processes in a running fuel cell. We observed intermediates of the anode reaction when hydrogen was used as a fuel. Furthermore, evidence is provided for radical centers produced at the cathode side of the polymer membrane as a likely intermediate of oxidative degradation via free radical processes. The method opens numerous possibilities for more quantitative studies of membrane degradation, mechanisms of oxygen reduction, and fuel oxidation. Systematic studies as a function of current and voltage, temperature, gas pressure, and membrane humidity are expected to reveal what the critical operating parameters are which lead to membrane degradation in a fuel cell.

Acknowledgement. We thank J. Kerres and his group from the University of Stuttgart and T. Kaz from the German Aerospace Center for providing us with CCMs. Financial support by the Federal Ministry of Education and Research (BMBF), Germany, and the Graduate College “Advanced Magnetic Resonance Type Methods in Materials Science” is gratefully acknowledged.

References

(1) Panchenko, A.; Dilger, H.; Kerres, J.; Hein, M.; Ullrich, A.; Kaz, T.; and Roduner, E. *Phys. Chem. Chem. Phys.* **2004**, *6*, 2891.

MAGNETIC RESONANCE IMAGING (MRI): A NEW TOOL FOR FUEL CELL RESEARCH

Su Ha, Zachary Dunbar, and Rich Masel

School of Chemical Sciences
University of Illinois at Urbana-Champaign
600 S Mathews, Urbana Il, 61801

Introduction

The Direct Formic Acid Fuel Cell (DFAFC) is a promising candidate for portable power applications owing to its high energy efficiency and high power density.[1-3] During the DFAFC operation, formic acid is oxidized at the anode electrode producing electrons, protons, and carbon dioxide (CO_2). These protons are transported from the anode to the cathode through the polymer electrolyte membrane (PEM), and then combine with oxygen and the electrons to produce water at the cathode electrode. Additional water is moved from the anode to the cathode by both a molecular diffusion and an electro-osmotic drag processes. The excess water in the cathode is either evaporated or diffused back to the anode.

The proton conductivity of PEM and thus performance of the DFAFC decreases dramatically when the water content of the membrane decreases.[4-6] Therefore, to operate the cell with a high performance, a proper water management to maintain the membrane hydrated is so important. On the other hand, too much water in the cathode would cause the water flooding and limit the oxygen transport to the cathode electrode.[4-6]

Having a proper fuel (formic acid) distribution at the DFAFC's anode is another important aspect for achieving a good cell performance. CO_2 bubbles are generated as formic acid is oxidized at the anode electrode. This CO_2 evolution in the liquid feed anode of the DFAFC results in strongly two-phase flow, making the transport processes of fuel supply and product removal more complicated. If the CO_2 bubbles are not properly removed from the anode, they will block the catalyst sites from oxidizing formic acid and create a large pressure drop across the flow channels.[7,8]

Understanding both the water and fuel transport processes in DFAFC under the operating conditions is essential for developing its advanced fuel cell materials and designs. In this paper, we describe a novel method of using MRI technology for measuring both the water and fuel distributions at the cathode and anode of the operating DFAFC respectively. Additionally, we correlate the time dependant performance of the DFAFC with time-resolved MRI measurements of the water content in the cathode electrode.

Experimental

Construction of Test Fuel Cell. The MRI system generates strong magnetic fields. To prevent any distortions of these strong magnetic fields, we built a test fuel cell from nonmagnetic materials as it is shown in Figure 1. Both the anode and cathode current collectors were constructed out of titanium foil. In order to protect the titanium from being corroded by the formic acid solutions, they were electrochemically coated with 5 microns of gold. Both the anode and cathode flowfields have serpentine flow channels. The membrane electrode assembly (MEA) was fabricated in house using a 'direct paint' technique with the active area of 1 cm^2. The 'catalyst inks' were prepared by dispersing the catalyst powders into appropriate amounts of Millipore water and 5% recast Nafion® solution (1100EW, Solution Technology, Inc.). Then both the anode and cathode 'catalyst inks' were directly painted onto either side of the Nafion® 115 membrane. A commercially available platinum black (HiSPEC™ 1000 from Johnson Matthey) was used for the cathode catalyst layer at a loading of 8 mg/cm^2.

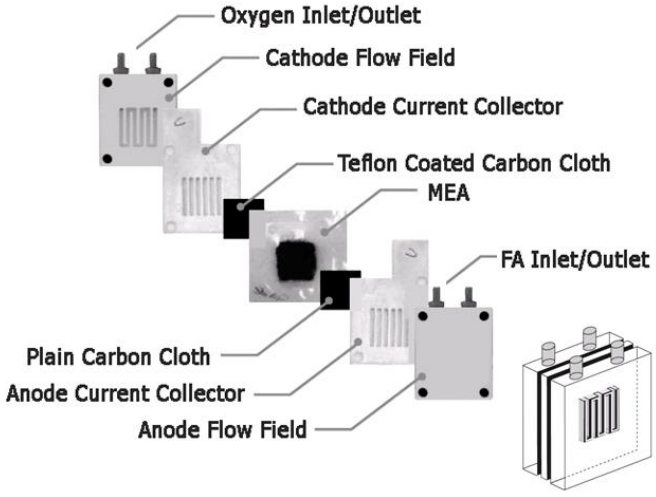

Figure 1. The Direct Formic Acid Fuel Cell Diagram

Palladium black from Sigma Aldrich was used for the anode catalyst layer at a loading of 6 mg/cm^2. The final catalyst layers contained 15% Nafion® by weight.

MRI Test System. To acquire MRI images of water and fuel contents in the operating DFAFC, we placed the cell in the cylindrical test section of our MRI system (14.7 T). The experimental setup is shown in Figure 2. Oxygen was supplied to the cathode of the DFAFC from a compressed gas tank. 5M Formic acid was supplied to the anode using a syringe pump. The experiments were performed using a Varian Unity/Inova NMR spectrometer with a 600MHz wide-bore (89mm) magnet (Oxford Instruments). The system is equipped with gradients with a maximum strength of 90 Gauss/cm. The nucleus observed in our MRI experiment was hydrogen atom (^1H). The experiments were performed at room temperature. The cell current was controlled by adjusting the external load resistance connected to the cell. The data was acquired and processed using VNMRJ 1.1C software.

A pulse sequence with a conventional spin-echo method was used to obtain images of water and fuel contents at the cathode and anode of the DFAFC respectively. For our experiments, a 128 x 128 point matrix was formed to image the field of view (FOV) of 1.4 cm x 1.2 cm. A slice thickness was 0.5 mm.

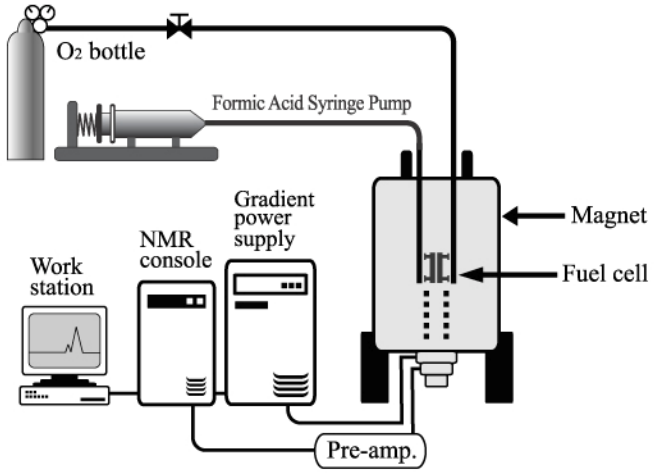

Figure 2. The MRI experimental Setup for Active Direct Formic Acid Fuel Cell Testing

Results and Discussion

In Figure 3, a constant voltage test of the DFAFC is reported at 0.70 V. According to Figure 3, the DFAFC initially generates the current density of 53 mA/cm^2 at 0.70 V. However, its current density gradually decreases as its operation time increases. After operating the cell for 135 minutes, its current density drops from 53 to 36 mA/cm^2.

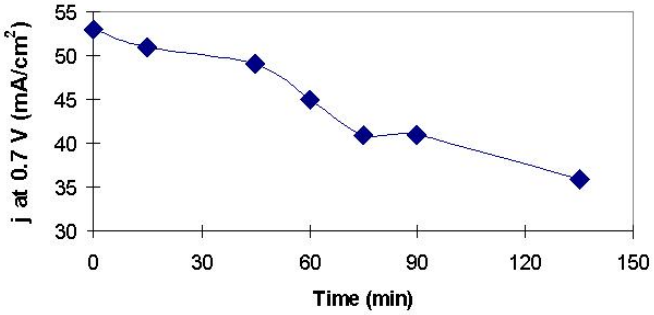

Figure 3. Plot of constant cell potential test at 0.70 V. The DFAFC was operated using 5M formic acid and oxygen with the applied magnetic field inside the MRI system.

Figure 4 shows the MRI image of the anode flowfield after operating the DFAFC with 5M formic acid for 135 minutes. In Figure 4, the bright image represents the 5M formic acid, which is flowing through the anode flow channels at a flow rate of 50 micro liter per minute. These anode flow channels are oriented vertically (up and down). According to Figure 4, the bottom part of the anode flow channels has more fuel (higher NMR signal which gives brighter image), while the upper part of the flowfield has less fuel (lower NMR signal which gives darker image). This would be explained in terms of CO_2 formation and orientation of the anode flow channels. As the formic acid is oxidized at the anode, CO_2 bubbles are formed which would rise up through the flow channels. Consequently, these CO_2 bubbles are accumulated in the upper part of the anode flow channels and occupy most of its volume. Since CO_2 has no hydrogen atom, there would be a weaker NMR signal to image from the flowfield area with partially filled CO_2.

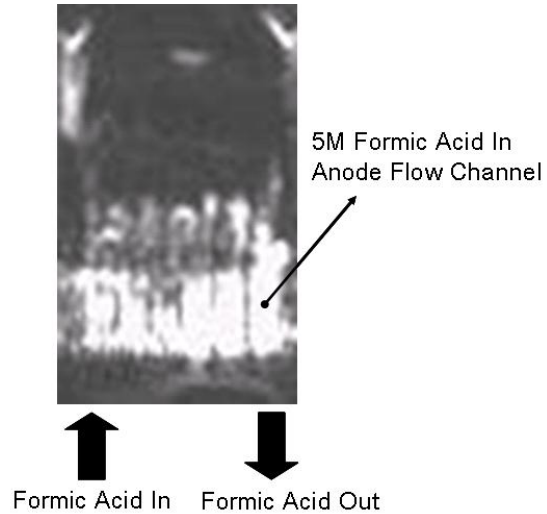

Figure 4. The MRI image of 5M formic acid flowing through the anode flow channels after operating the cell for 135 min.

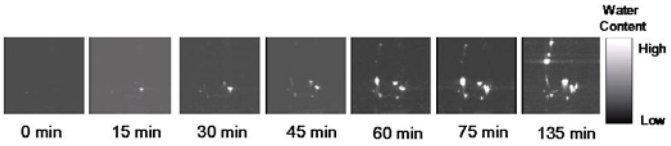

Figure 5. The MRI images of the water distribution in the cathode electrode after the DFAFC starts to operate at 0 min.

To investigate if there is any water flooding in the cathode of the operating DFAFC, we measured the MRI images of the water content in the cathode electrode of the operating cell in every 15 minutes (Figure 5). From Figure 5, at zero minute, no water is observed at the cathode electrode. According to Figure 5, as the cell operation time increases, the number of the water flooded spot also increases at the cathode electrode. Figure 5 shows that sizes of these water flooded spots also grow and shrink as the cell operation time increases. According to Figure 5, the cathode electrode of the DFAFC is severally flooded by water after operating it for 135 minutes. Comparing Figures 3, 4, and 5, we speculate that both CO_2 bubble accumulation at the anode and the water flooding at the cathode are two main causes of the current density drop of the DFAFC that we observe in Figure 4.

Acknowledgement

This material is based upon work supported by the Defense Advanced Research Projects Agency under U.S. Air Force grant F33615-01-C-2172.

References

(1) Ha, S.; Adams, B.; Masel, R. Journal of Power Sources, **2004**, 128 (2), 119.
(2) Zhu, Yimin; Ha, Su Y.; Masel, Richard I. Journal of Power Sources, **2004**, 130 (1-2), 8.
(3) Rice, C.; Ha, S.; Masel, R. I.; Wieckowski, A. Journal of Power Sources (2003), 115(2), 229-235.
(4) Berg, P.; Promislow, K.; St. Pierre, J.; Stumper, J.; Wetton, B. Journal of the Electrochemical Society, **2004**, 151 (3), A341.
(5) Larminie, J.; Dicks, A. Fuel Cell Systems Explained, John Wiley & Sons, Ltd., 2000.
(6) Rice, C.; Ha, S.; Masel, R. I.; Waszczuk, P.; Wieckowski, A.; Barnard, Tom, Journal of Power Sources, **2002**, 111 (1), 83.
(7) Barragan, V.M. Ruiz-Bauza, C.; Villauenga, J.P.G.; Seoane, B. Journal of Power Sources, **2004**, 130 (1-2), 22.
(8) Yang, H.; Zhao, T.S. Journal of Power Sources, **2005**, 139 (1-2), 79.

FUEL CELL DESIGN: THE IMPACT OF FUEL CELL DYNAMICS ON OPERATION

Warren H. J. Hogarth[1, 2] James P. Nehlsen[1], and Jay B. Benziger[1]

[1]Department of Chemical Engineering, Princeton University, Princeton, NJ 08544, USA
[2]ARC Centre for Functional Nanomaterials, The University of Queensland, Brisbane 4072, Australia

Introduction

Proton exchange membrane fuel cells are a very promising clean energy technology with the potential to help reduce harmful environmental and health pollution emissions. The main reasons that they show so much potential is that they have higher energy densities than batteries and can operate more efficiently than combustion engines which are limited by Carnot efficiency. It is therefore important, at least in the short term where energy will most likely still be derived from hydrocarbon sources, to ensure that the cells are capable of operating as close as possible to their highest efficiency to realize these benefits.

However, there are few reports in the literature which consider what is the optimal operating regime for a fuel cell.[1-3] While there is presently a significant focus on the design on new materials for fuel cells,[4,5] it is important to understand what is the optimal operation range in terms of power to be delivered, load being driven, current, voltage and efficiency, to best determine the benchmarks to be used.[6,7]

Experimental

Short term current-voltage data was obtained on both a fuel cell and a battery. The battery was a single cell, size AAA, nickel-metal hydride rechargeable battery (Radio Shack) rated at 1.2 V and 700 mAh. I-V data on the battery was obtained using an Arbin Instruments MSTAT4+ battery test station.

The fuel cell was a 5 cm^2 cell using Nafion 115 (Ion Power, Inc.) with two Pt catalyzed ELAT-style electrodes from E-tek (E-tek division of DeNora, Somerset, NJ). The fuel cell was operated with H_2 and O_2, 1 atm of pressure, at 80ºC, with both gas streams humidified to saturation at the cell temperature. The fuel cell I-V data was obtained on a Globetech fuel cell test station.

Results

Current-voltage data for both types of cells is shown in Figure 1. The data for the fuel cell is plotted versus total current rather than the more traditional current density in order to compare it to the battery data. The cell area is 5 cm^2. The internal resistance, R_{int}, of each cell is given by the slope of the voltage versus current line. R_{int} represents the overall cell resistance and is the value that would be used for the resistor when representing the fuel cell or battery as a battery and a resistor in series in a circuit diagram (Figure 2).[6,7] For the fuel cell, the linear "ohmic region" is used for this determination. The internal resistance of the battery is 0.096 Ω, and the fuel cell is 0.085 Ω.

When considering a battery and resistor in series as part of an electrical circuit, the internal resistance, R_{int}, of the fuel cell varies with the area of the cell. The value of $R_{int} \cdot A_{cell}$ is constant with area, but varies with the state of hydration of the membrane and the quality of the electrode-membrane interfaces. Reducing R_{int} by increasing the fuel cell area is equivalent to reducing the internal resistance of the battery by placing several batteries in parallel. The resistance values add for either fuel cells or batteries in series. Using the above values of R_{int} shows that 4.8 cm^2 of fuel cell area has the same internal resistance as the AAA sized battery used in this study.

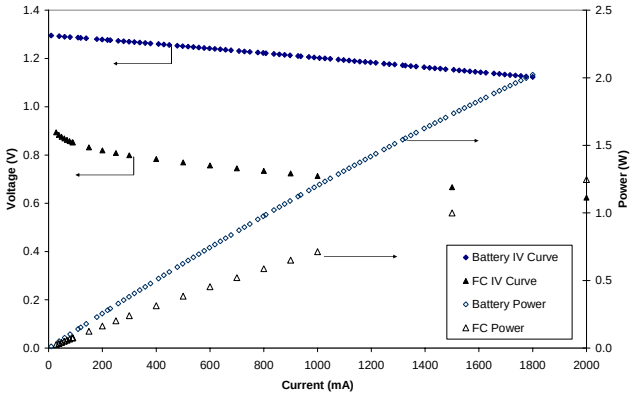

Figure 1. Current-Voltage data for both a standard H_2/O_2 PEMFC with humidified feeds, at 80ºC and 5 cm^2 area and a standard AAA nickel-metal hydride rechargeable battery.

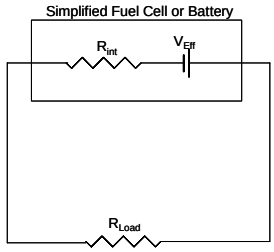

Figure 2. Equivalent circuit diagrams for a PEMFC or battery directly connected to an external load.

Figure 3 shows the same data plotted as a power performance curve (PPC), or power output as a function of load resistance. The load resistance, R_{load}, is equal to V_{load}/I. The efficiency shown on the secondary axis is the discharge efficiency, defined as V_{load}/V_{oc}, where V_{oc} is the open circuit potential of the cell. This efficiency value shows the power obtained from the cell divided by the power that could be obtained if there were no internal voltage losses. The efficiency of the fuel cell will always be less than a battery with identical internal resistance due to the initial voltage drop in the activation region.

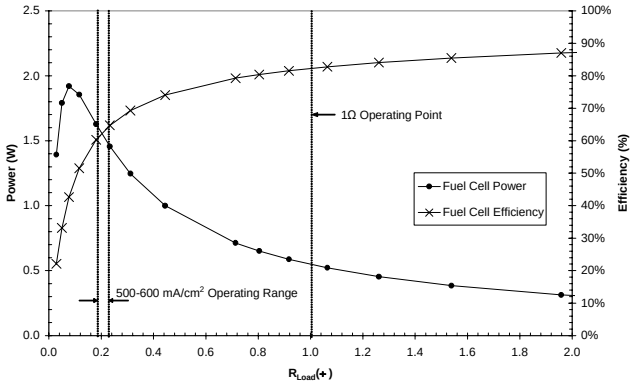

Figure 3. Detail of the PEMFC power performance curve (PPC) and efficiency curve. Highlighted are the 500 and 600 mA cm^{-2} and 1Ω operating points.

Discussion

A fuel cell is typically controlled by altering the load impedance. The load impedance can be manipulated in order to hold one of the dependent variables (current, voltage, or power) constant at a set point. In many laboratory situations, either current or voltage output from a fuel cell is controlled. Controlling one of these variables is not desirable in real applications however. By controlling either voltage or current, all of the degrees of freedom in the system are used, and the third variable, power, cannot then be controlled independently. Since the power output by the fuel cell and the power consumed by the load must balance exactly at all times (conservation of energy), the ability to regulate power output is vital. Therefore, both current and voltage must not be specified, leaving load resistance as the independent variable and power as the dependent variable. Controlling the load resistance and power in this way creates issues not normally observed under potentiostatic or galvanostatic control.

The main control problem is created because there is a peak in the PPC. If the peak is crossed while the cell is controlled, the necessary control action reverses. For a controller to be direct acting, it must operate to the left of the power peak in Figure 3. This will allow for more power to be provided as the load resistance increases (e.g. accelerating a motor). If the peak is crossed however, the controller will continue to increase the load resistance in response to the demand for more power but the cell is not capable of providing more power.

To operate at maximum efficiency, a fuel cell must be operated to the right of the power peak (Figure 3). In this case care must be taken not to cross back over the power peak when operating the cell near maximum power.

Fuel cell dynamics compound control problems. The peak in the power performance curve occurs when the load resistance equals the internal resistance of the cell. Unlike batteries, the internal resistance of fuel cells varies with the state of hydration of the membrane. As the load conditions change, more or less water is generated as the current increases or decreases. The state of hydration of the membrane can vary as the rate of water generation changes, and so the internal resistance of the fuel cell can vary during operation, particularly in less-than-saturated humidity conditions (Figure 4).

The minimum allowable load resistance therefore will change during operation. Using a current limiter to prevent the controller from crossing the peak would require the limit to be placed a safe distance from the peak to account for any drying of the membrane during operation, significantly reducing the maximum power output of the fuel cell.

Conventional fuel cell operating specifications do not seem to consider the need to control the power output from a fuel cell. Figures 3 and 4 show the relevant portions of the fuel cell data from Figures 1. A common design specification calls for operation at 500-600 $mA.cm^{-2}$, placing the operating point in the center of the linear ohmic region of the I-V curve. This operating point appears to be an obvious choice, providing the widest range of linear I-V behavior. However, conservation of energy requires that we instead consider the power output as the primary variable when designing a fuel cell to drive a load, and the power output is highly non-linear and non-monotonic in this region of the curve. The load resistance on this cell (or, equivalently, the internal resistance of the cell) needs only to change by 0.15 Ω to reach the peak.

Adding cells in series increases the necessary change in the load resistance to reach the peak, but increasing the area of the cells decreases it. Based on the single cell performance obtained here, a stack of 200 cells, with each cell of area 500 cm^2 and operating at 500 $mA.cm^{-2}$ could drive a load of 29 kW but would only require a load change of 0.31 Ω to cross the peak.

A better approach is to operate the stack at a much lower current density, away from the peak. Although this technique limits the power output from the stack, control is much simpler and efficiency is higher. The power output is also more linear at lower current densities (higher load resistances). This approach is often used for batteries, where the current drawn from each battery is kept relatively low compared to the location of the peak in the power performance curve for the battery. Perhaps a better option still is to use a hybrid system in which the fuel cell is used at a constant operating condition to charge a battery pack.

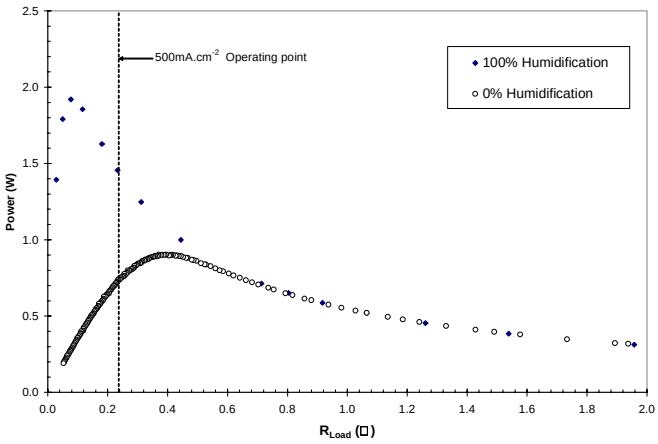

Figure 4. Basic power performance curve of PEMFCs operating under full humidification and no external humidification at 80°C.

Conclusions

Fuel cells are sensitive dynamic systems. Their dynamics and performance characteristics must be considered when designing cells, stacks, and control systems. Design specifications offered as guidelines do not reflect the operating regimes necessary to create stable, controllable fuel cell systems. Typical specifications select an operating point with linear current-voltage characteristics, but highly non-linear power output. When driving a load, power output must be regulated tightly. Current and voltage can be adjusted with transformers. Operating at lower current densities, perhaps closer to 100-200 $mA.cm^{-2}$, provides higher efficiency and more linear power output from fuel cells.

Acknowledgement. The authors would like to thank Jonathan Mann for conducting the fuel cell testing experiment. WH acknowledges funding from the Australian-American Fulbright Commission and the ARC Centre for Functional Nanomaterials. This work was supported in part by the Air Force Office of Scientific Research (Dynamics and Control).

References

(1) Arita, M., *Fuel Cells* **2002,** *2* (1), 10.
(2) Masten, D. A.; Bosco, A. D. In *Handbook of Fuel Cells;* Vielstich, W.; Lamb, A.; Gasteiger, H. Eds.; Wiley: Indianapolis, 2003; pp.714-724.
(3) Konrad, G.; Sommer, M.; Loschko, B.; Schell, A.; Docter, A. In *Handbook of Fuel Cells;* Vielstich, W.; Lamb, A.; Gasteiger, H. Eds.; Wiley: Indianapolis, 2003; pp.693-713.
(4) Hogarth, W. H. J.; Diniz da Costa, J. C.; Lu, G. Q., *Journal of Power Sources* **2005,** *142* (1-2), 223.
(5) Hogarth, W. H. J.; Diniz da Costa, J. C.; Drennan, J.; Lu, G. Q. M., *J. Mater. Chem.* **2005,** *15* (7), 754.
(6) Benziger, J. B.; Satterfield, M. B.; Hogarth, W. H. J.; Nehlsen, J. P.; Kevrekidis, I., *Submitted to Journal of Power Sources* **2005**.
(7) Hogarth, W. H. J.; Nehlsen, J. P.; Benziger, J. B., *Submitted to AIChE Journal* **2005**.

HIGH PERFORMANCE DRY FEED HYDROGEN PEMFCS: UNDERSTANDING THE WATER BALANCE AS A DESIGN TOOL FOR NOVEL POLYMER MEMBRANES

Warren H.J. Hogarth[1,2], Jay B. Benziger[1]

[1] Department of Chemical Engineering, Princeton University, Princeton, NJ 08544, USA
[2]ARC Centre for Functional Nanomaterials, University of Queensland, Brisbane 4072, AUSTRALIA

Introduction

Designing and operating an efficient fuel cell which has very tight control over the water inventory of the cell, is a very powerful tool for designing new fuel cell membranes and fuel cell modeling. In addition it is a simpler, commercially viable alternative to current fuel cell technology.

The water balance in PEMs is the most influential factor on proton conduction and hence on optimizing the operation of PEM fuel cells.[1] The proton conductivity of PEM membranes varies by orders of magnitudes as the water activity (relative humidity) varies at the cathode and anode (as the hydration level of the membrane varies). For this reason PEMFCs are almost always operated with close to 100% relative humidity feeds, restricting their operating regions and preventing a clear delineation of water migration within the cell.

Adding extra water to a fuel cell creates problems with flooding. Both commercial and laboratory operated fuel cells have significant performance limitations at high currents caused by an inability to remove all the water added and created within the fuel cell. This flooding phenomenon prevents oxygen and hydrogen reaching the catalyst and hence the fuel cell is starved of fuel. This excess water also prevents scientists from understanding how new membranes are affected by and affect the water balance in the fuel cell and provides great challenges for modeling fuel cells.

By stripping away the complexity of having multiple water sources in a fuel cell, it is possible to get a significantly more detailed understanding of how a PEMFC is working from a fundamental level. This can be done by operating a fuel cell with dry feeds and monitoring the exit concentrations or water (relative humidity) of the effluent streams. This creates what is termed an Autohumidified fuel cell. The design used in this analysis is a continuous stirred tank reactor (CSTR) design which ensures uniform concentration of the reactants at anode and cathode.[2-4] Based on this simple analysis, it is possible to observe the effects of flow rates, temperature and pressure on the membrane, electrode and gas diffusion coefficients and the general operation of the fuel cell. This not only provides valuable information for the design of a fuel cell, but also, important information which can be used for evaluating key properties of new fuel cell membranes.

While traditionally people have hesitated with the autohumidified approach because of issues associated with drying the membrane, we demonstrate the power of this technique by designing a new fuel cell which runs on completely dry feeds and is capable of operating as well as commercial fuel cell test cells with fully humidified streams at the same operating conditions. Concurrently we have significantly reduced the onset of flooding. Furthermore the new fuel cell is used for fundamental analysis and design of new fuel cell membranes.

Experimental

CSTR fuel cell experiments were conducted on a custom designed in-house cell to ensure that the gas composition was uniform within the cell and that the liquid water produced within the cell would drain from the cell preventing flooding (Figure 1). The cell temperature and pressure were tightly controlled and monitored. Relative humidity sensors with temperature probes were placed in the exit gas streams of both the anode and cathode. The cell area was 1.9cm^2. Control experiments were run on a commercial Globetech fuel cell test station with 5cm^2 area and serpentine flow channels.

Commercial Extruded Nafion® 1100 weight membranes and 5wt% Nafion solution were obtained from Ion Power, Inc. (Bear, DE). Composite membranes were cast with 3wt% composite TiO_2 with an average particle size of 20nm from Degussa-Hüls. All membranes were cleaned with a peroxide, water and sulfuric acid procedure prior to pressing into an MEA. A6 ELAT electrodes with 5wt% platinum on carbon were used for electrodes (E-tek division of DeNora, Somerset, NJ). MEAs were pressed at 140^{0}C for 90 seconds with 1 metric tonne over a constant area.

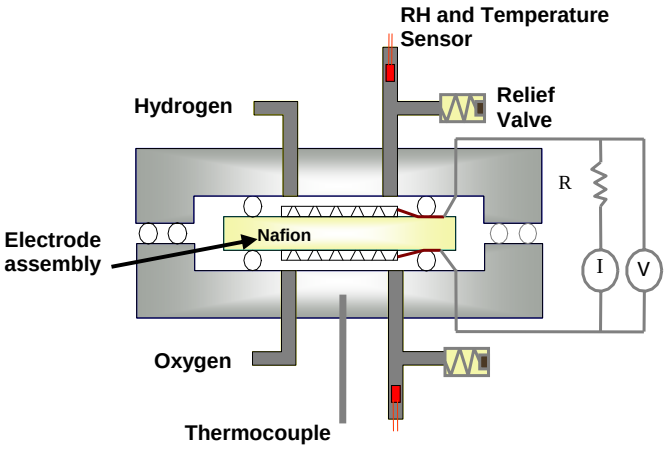

Figure 1. Schematic of custom autohumidified CSTR fuel cell setup which allows tight control of the water balance within the fuel cell and excellent performance with dry feed streams.[2]

Results and Discussion

Performance of Autohumidified CSTR Fuel Cell. If a fuel cell is limited by flooding then it would appear counter intuitive to be continually adding excess water in the feed streams. Figure 2 and 3 show that, through clever design, it is possible to operate a fuel cell equally as well as commercially available fully humidified cells under the same operating conditions by controlling the water balance in the fuel cell.

Figure 2 demonstrates that the polarization curves for the autohumidified CSTR fuel cell overlay those of the same membrane in a commercial Globetech fuel cell with serpentine flow channels. In addition, as can be seen by the CSTR 95^{0}C curve there are fewer limitations caused by mass transport at high current which is attributed to flooding of the fuel cell. Figure 3 displays the power performance curves for the same tests as Figure 2.[5, 6] This demonstrates that the internal resistances of the fuel cells are all equal as the internal resistance occurs at peak power which is essentially the same for all cells.

CSTR FC for fundamental fuel cell understanding. The autohumidified CSTR fuel cell is a powerful tool for design and assessment of new fuel cell membranes and for fuel cell modeling.[4, 7] By limiting the water generation in the fuel cell to the reaction and having uniform concentrations of both reactants and products in the cell it is possible to evaluate the performance of and hence design new membranes.

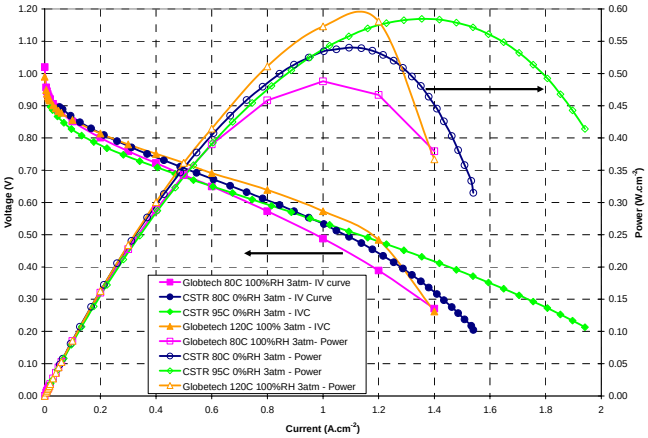

Figure 2. Polarization curves of the autohumidified CSTR and commercial Globetech fuel cells using standard operating conditions (shown) and Nafion 115.

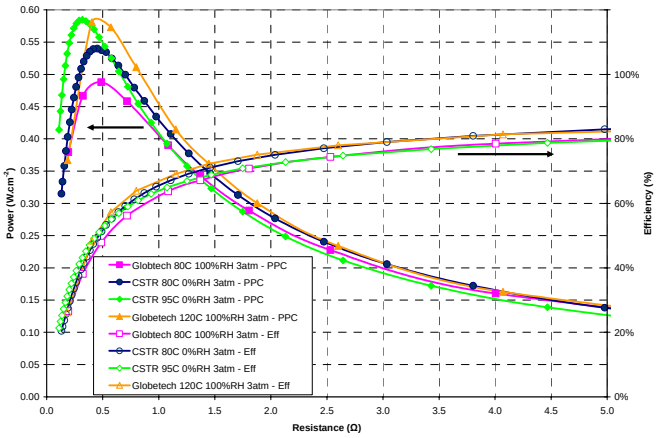

Figure 3. Power performance curves (PPC) of the autohumidified CSTR and commercial Globetech fuel cells using standard operating conditions (shown) and Nafion 115.

For example, by monitoring the relative humidities of the effluent streams it is possible to observe changes in the water content in the membrane and make inferences regarding the back diffusion of water. This can then be directly correlated to changes in the level of hydration within the membrane and hence conductivity. Careful monitoring of the relative humidity when the cell is subject to step changes in load and reactant flow rates also allows for comparison of the diffusion rates through the membrane. Additional data regarding the membrane hydration can be gather simultaneously be using a current interrupt method to monitor the internal resistance of the membrane.

As an example of how this approach can be used consider Figure 4. A recast composite 3 wt% TiO_2 Nafion 115 membrane was at 80^0C was subject to a series of step changes in the external load and the dynamic response of the system was measured as it returned to steady state. The recorded variables were: current, voltage, internal resistance of the membrane (as measured using a current interrupt technique), RH anode and RH cathode. Figure 4 shows that the response of the system and that the hydration of the membrane is not constant reinforcing the complex role that system dynamics play and membrane properties have on fuel cell performance.

This dynamic information can then be taken and used to compare different membranes, membrane materials and MEA setups to optimize material and fuel cell design. In addition it provides valuable information, necessary for the control and dynamic operation of fuel cells.

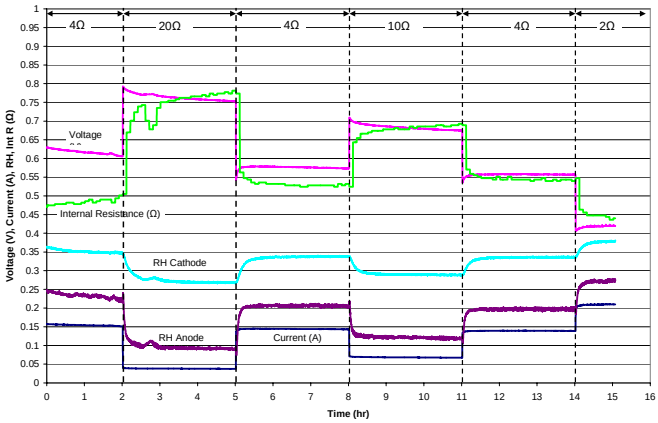

Figure 4. Steady state response of a composite polymer membrane in an autohumidified CSTR fuel cell to step changes in external load, displaying the response time of the fuel cell under dynamic operation.

Conclusions

The CSTR membrane fuel cell is capable of operating equally as well as commercially available fully humidified cells. Removing the complexity of adding water into a fuel cell and using simple fuel cell design significantly reduces issues associated with fuel cell flooding and allows for full accounting of the water balance within the cell. This allows important properties such as membrane diffusion coefficient to be derived which are not only important in the assessment of new membrane technology, but also are also important in developing robust fuel cell models.

Acknowledgement. The authors thank the National Science Foundation (CTS– 0354279 and DMR-0213707 through the Materials Research and Science Engineering Center at Princeton) and Tao Zhang for assistance with fuel cell testing. WH acknowledges funding from the Australian-American Fulbright Commission and the ARC Centre for Functional Nanomaterials.

References

(1) Yang, C.; Srinivasan, S.; Bocarsly, A. B.; Tulyani, S.; Benziger, J. B., *J. Membr. Sci.* **2004,** *237* (1-2), 145.
(2) Benziger, J.; Chia, E.; Karnas, E.; Moxley, J.; Teuscher, C.; Kevrekidis, I. G., *AIChE J.* **2004,** *50* (8), 1889.
(3) Benziger, J.; Chia, E.; Moxley, J. F.; Kevrekidis, I. G., *Chem. Eng. Sci.* **2005,** *60* (6), 1743.
(4) Moxley, J. F.; Tulyani, S.; Benziger, J. B., *Chem. Eng. Sci.* **2003,** *58* (20), 4705.
(5) Hogarth, W. H. J.; Nehlsen, J. P.; Benziger, J. B., *Submitted to AIChE Journal* **2005**.
(6) Benziger, J. B.; Satterfield, M. B.; Hogarth, W. H. J.; Nehlsen, J. P.; Kevrekidis, I., *Submitted to Journal of Power Sources* **2005**.
(7) Chia, E.; Benziger, J.; Kevrekidis, I. G., *AIChE J.* **2004,** *50* (9), 2320.

THE NATIONAL HYDROGEN STORAGE PROJECT

Sunita Satyapal[1], Carole Read[1], Grace Ordaz[1], John Petrovic[2]

(1) Office of Hydrogen, Fuel Cells and Infrastructure Technologies, U.S. Department of Energy, 1000 Independence Ave. SW, Washington, DC 20585
(2) Los Alamos National Laboratory (on assignment to DOE)

Introduction

U.S. petroleum dependence is driven by transportation, which accounts for two-thirds of the 20 million barrels of oil our nation uses each day. The U.S. imports 55% of its oil, and this is expected to grow to 68% by the year 2025 under a status quo scenario. Nearly all of our vehicles currently run on either gasoline or diesel fuel.

This situation requires that alternative energy carriers be developed to promote future national energy security. Hydrogen has the potential to be a very attractive alternative energy carrier. It can be clean, efficient, and derived from diverse domestic resources, such as fossil (oil, coal, natural gas), nuclear, and renewable (biomass, hydro, wind, solar, geothermal) energy resources. Hydrogen can then be employed in high-efficiency power generation systems, including internal combustion engines or fuel cells for both vehicular transportation and distributed electricity generation.

The potential energy security and diversity benefits of hydrogen are the basis of the Hydrogen Fuel Initiative launched by President Bush in January 2003. The Hydrogen Fuel Initiative commits government funding for accelerated research, development, and demonstration programs that will enable an industry decision on commercialization of hydrogen by the year 2015. Should industry decide to proceed, a full transition to a U.S. hydrogen economy would require decades. Although the implementation of a hydrogen economy would clearly take time, the key point is that research and development to address the viability of hydrogen needs to occur now.

At the present time, there are three primary technology barriers that must be overcome to enable an industry commercialization decision on hydrogen fuel cell vehicles. First, the cost of safe and efficient hydrogen production and delivery must be lowered to be competitive with gasoline without adverse environmental impacts. Second, fuel cell system costs must be lowered while meeting performance and durability requirements. Finally, on-board hydrogen storage systems must be developed that allow a vehicle range of greater than 300 miles while meeting packaging, cost, and performance requirements.

The barriers associated with hydrogen production, delivery and fuel cells are essentially cost-driven. However, with regard to the on-board hydrogen storage barrier, no approach currently exists that can meet the technical requirements of a greater than 300-mile range, irrespective of the present cost. Therefore, the focus of hydrogen storage research is on performance. New materials and approaches are needed. To accelerate and focus R&D in hydrogen storage, the DOE has initiated the implementation of a National Hydrogen Storage Project.

Storage Issues for Hydrogen-Powered Vehicles

Storing enough hydrogen on vehicles to achieve greater than 300-mile driving range is clearly a significant challenge. On a weight basis, hydrogen has nearly three times the energy content of gasoline (120 MJ/kg for hydrogen versus 44 MJ/kg for gasoline). However, on a volume basis the situation is reversed (8 MJ/liter for liquid hydrogen versus 32 MJ/liter for gasoline). On-board hydrogen storage in the range of 5-13 kg is required to encompass the full platform of light duty vehicles. The average fleet on-board storage requirement is approximately 8 kg.

System-Driven Storage Targets

On-board hydrogen storage system targets have been developed through the FreedomCAR Partnership between DOE and the US Council for Automotive Research (USCAR)[1]. These targets are *system*-driven, based on achieving similar performance and cost levels as current gasoline fuel storage systems. The storage system includes the tank, valves, regulators, piping, mounting brackets, insulation, added cooling capacity, and any other balance-of-plant components in addition to the first charge of hydrogen and any material such as solid sorbent or liquid used to store the hydrogen. Some of the key targets for the years 2010, and 2015 are shown in Table 1.

Table 1. Hydrogen Storage System Targets

Storage Parameter	Units	2007	2010	2015
Gravimetric energy capacity	kWh/kg (wt. %)	1.5 (4.5)	2.0 (6.0)	3.0 (9.0)
Volumetric energy capacity	kWh/liter (gm H_2/liter)	1.2 (36)	1.5 (45)	2.7 (81)
Storage system cost	$ /kWh ($/kg H_2 stored)	6 (200)	4 (133)	2 (66)
Cycle life (1/4 tank to full)	cycles	500	1000	1500
Minimum full-flow rate	(g/sec)/kW	0.02	0.02	0.02
Min/Max delivery temp from tank	C	-20/85	-30/85	-40/85
System fill time for 5-kg hydrogen system	min	10	3	2.5
Loss of usable H_2	(g/hr)/kg H_2 stored	1	0.1	0.05

Also shown is an example of near-term targets, such as those outlined for the year 2007. High pressure hydrogen tanks and liquid hydrogen meet some, though clearly not all, of the near term (2007) targets. These 2007 targets are therefore primarily for materials-based systems such as solid-state (e.g. metal hydride) or liquid (e.g. chemical hydride) systems. The focus of the DOE National Hydrogen Storage Project is on materials-based technologies to meet 2010 targets and with potential to eventually meet 2015 targets. Targets in interim years such as those shown in 2007 are meant to help guide research efforts, monitor and compare results, and provide feedback to DOE on technical progress to help refocus research and development as required. Currently, research priorities are on achieving the gravimetric and volumetric capacity targets in Table 1. It is important to note that to achieve *system-level* capacities of 2 kWh/kg (6 wt.% hydrogen) and 1.5 kWh/L (0.045 kg hydrogen/L) in 2010, the gravimetric and volumetric capacities of the material alone must clearly be higher than the system-level targets.

Vehicular Hydrogen Storage Approaches

Current on-board hydrogen storage approaches involve compressed hydrogen gas tanks, liquid hydrogen tanks, metal hydrides, carbon-based materials, high surface area sorbents, and chemical hydrogen storage[2,3]. Tanks, metal hydrides, high surface area sorbents, and carbon-based materials constitute "reversible" on-board hydrogen storage systems, since ' refilling' with hydrogen can take place on-board the vehicle. For chemical hydrogen storage approaches, replenishing the spent hydrogen is not easily

accomplished on-board the vehicle and thus these systems must be regenerated off-board.

The current status of vehicular hydrogen storage systems is shown in Table 2. These values are estimates provided by developers and are continuously updated as progress is made.

Table 2. Current Status of On-Board Hydrogen Storage Systems

Storage Approach	Gravimetric Energy Density (kWh/kg)	Volumetric Energy Density (kWh/liter)	Storage System Cost ($/kWh)
5000-psi gas tanks	1.9	0.5	$15
10,000-psi gas tanks	1.6	0.8	$18
Liquid H_2 tanks	1.7	1.2	$ 6
Metal hydrides*	0.8	0.6	$ 16
Chemical hydrides	1.4	1.0	$8
2010 System Target	**2.0**	**1.5**	**$4**
2015 System Target	**3.0**	**2.7**	**$2**

*Projection

As will be noted, none of the current systems meets the combined gravimetric, volumetric, and cost targets for either 2010 or 2015. Each of the current approaches will now be discussed in more detail.

The National Hydrogen Storage Project

The Department of Energy has conducted a number of workshops to identify R&D priorities and strategies for on-board hydrogen storage. These include a Hydrogen Storage Materials Workshop held in August 2002, a Compressed/Liquid Hydrogen Storage Workshop held in October 2002, a Hydrogen Storage "Think Tank" Meeting held in March 2003, and a Basic Energy Sciences Workshop held in May 2003. The proceedings of these workshops are available on DOE websites[4].

Based on inputs from the workshops, the DOE issued a "Grand Challenge" to the global scientific community for research in hydrogen storage in July 2003. This Grand Challenge called for the establishment of hydrogen storage Centers of Excellence on Metal Hydrides, Chemical Hydrogen Storage, and Carbon-Based Materials, with multiple university, industry, and federal laboratory partners. In addition, independent projects were solicited on new materials and concepts, off-board hydrogen storage systems, and analyses of life cycle cost, performance and environmental impact. Complementing the Grand Challenge, the DOE Office of Science issued a solicitation in 2004 for basic research to help overcome key hurdles in hydrogen production, storage, and conversion.

The new Centers of Excellence and independent projects, together with existing DOE hydrogen storage efforts, constitute the framework of the National Hydrogen Storage Project in the United States. The structure of the National Hydrogen Storage Project is shown in Figure 1. The Secretary of Energy announced the selections for the Hydrogen Storage Grand Challenge on 27 April 2004. These activities support the President's Hydrogen Fuel Initiative, announced in 2003, which pledged $ 1.2 billion over five years (FY 2004 to 2008) to accelerate hydrogen research. The DOE plans to provide funding at a level of $ 150 million over a five year period (subject to congressional appropriations) for the National Hydrogen Storage Project. The result of this R&D effort will be the development of hydrogen storage systems capable of meeting the long-term DOE targets.

The Metal Hydride Center includes Sandia National Laboratories in Livermore, California and multiple university and industrial partners. The Metal Hydride Center focuses on the development of advanced metal hydride materials including light-weight advanced complex hydrides, destabilized binary hydrides, intermetallic hydrides, modified lithium amides, and other on-board reversible hydrides. The Center involves 7 universities, 3 industrial partners, and 5 federal laboratories.

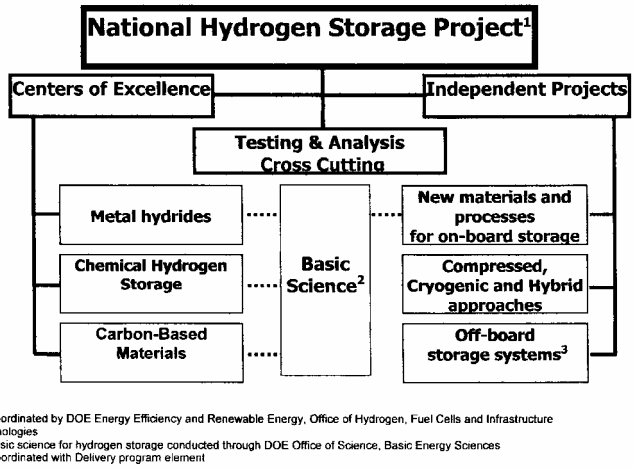

Figure 1. Structure of The National Hydrogen Storage Project.

The Chemical Hydrogen Storage Center includes the Los Alamos National Laboratory in Los Alamos, New Mexico and the Pacific Northwest National Laboratory in Richland, Washington. The Chemical Hydrogen Center focuses on three "tiers" of R&D for chemical hydrogen storage: borohydride-water, novel boron chemistry, and innovation beyond boron. The Center involves 6 universities, 3 industrial partners, and 2 federal laboratories.

The Carbon-Based Materials Center includes the National Renewable Energy Laboratory in Golden, Colorado. The Carbon-Based Materials Center focuses on breakthrough concepts for storing hydrogen in high surface area sorbents such as hybrid carbon nanotubes, aerogels, and nanofibers, as well as metal-organic frameworks and conducting polymers. The Center involves 7 universities, 1 industrial partner, and 4 federal laboratories.

The National Hydrogen Storage Project also involves independent projects on new hydrogen storage materials and concepts, materials and system testing, analyses, and off-board hydrogen storage needed for a hydrogen delivery infrastructure. Some of the new materials and concepts being studied are nanostructured materials, amine borane complexes, metal perhydrides, clathrates, lithium nitride, and irradiation activation of materials. As materials are developed, reliable test data is critical and therefore, to validate hydrogen storage capacities, an independent facility was established at Southwest Research Institute in San Antonio, Texas. This will help ensure unbiased, standardized testing of hydrogen storage materials and systems. Independent analyses is also critical, to help comparatively evaluate approaches and make down-selections. Current analyses activities, primarily by TIAX LLC and Argonne National Laboratory, include storage systems analyses to help optimize weight, volume and cost, as well as life-cycle cost, energy efficiency, and environmental impact analyses. Hydrogen storage analysis is integrated within a broader Systems Analyses and Integration effort within the Hydrogen Program. Thus hydrogen storage will be evaluated in terms of higher level systems

analyses of hydrogen pathways and transition scenarios to assess energy, environmental and economic impacts of hydrogen and fuel cell technologies. Subject to congressional appropriations, early results from the National Hydrogen Project will be reported within the next one to two years. All projects will be reviewed annually at DOE's public meeting (Hydrogen Program- Annual Program Review). Reports are available at http://www.hydrogen.energy.gov.

Recent Hydrogen Storage Developments

A new complex hydride system based on lithium amide has been recently discovered[5]. For this system, the following reversible displacive reaction takes place at 285°C and 1 atm: $Li_2NH + H_2 = LiNH_2 + LiH$. In this reaction, 6.5 wt.% hydrogen can be reversibly stored. However, the temperature is outside of the vehicular operating window. It has been demonstrated[6] that magnesium substitution can enhance the dehydriding reaction of $LiNH_2$ by lowering the dehydriding temperature to 220°C, as shown in Figure 2.

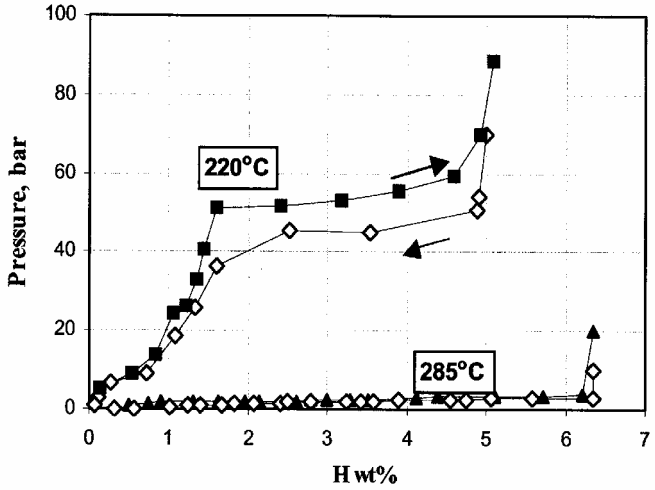

Figure 2. Hydrogen storage characteristics for lithium amide systems.

Single-walled carbon nanotubes (SWNTs), among several other carbon-based materials, are being studied for hydrogen storage.. A recent DOE-sponsored external peer review of hydrogen storage in single-walled carbon nanotubes has shown that experimental techniques used to measure hydrogen storage in carbon nanotubes were reproducible.[7] Based on experiments observed by the peer review, there was essentially no hydrogen stored in pure SWNTs at room temperature. However, as shown in Figure 3, approximately 2.5 wt.% was observed in metal-doped SWNTs at room temperature. DOE-sponsored work in this area will be expanded to include hydrogen storage in doped carbon nanostructured materials, other than SWNTs, both at room temperature and low temperatures (e.g. 77 K).

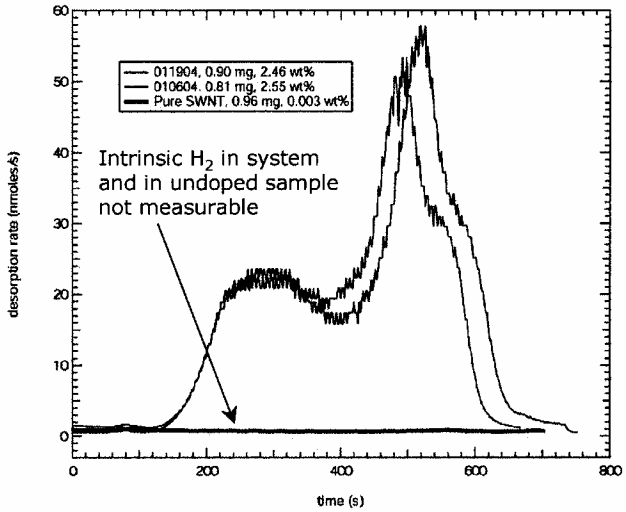

Figure 3. TPD desorption thermogram obtained for pure and metal-doped single-wall carbon nanotubes at room temperature.

Recently, a new type of liquid phase hydrogen storage material has been developed[8]. This liquid, based on N-ethylcarbazole, has been shown to possess a 5-7 wt.% gravimetric hydrogen storage capacity and a greater than 0.050 kg/L hydrogen volumetric capacity. Figure 4 shows the hydrogen evolution from N-ethylcarbazole with cycling at 197°C.

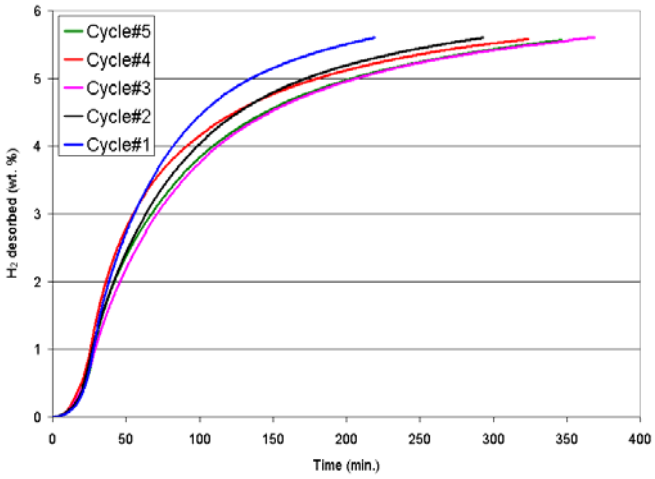

Figure 4. Cyclic desorption of hydrogen from N-ethylcarbazole at 197°C and 1 atm pressure.

Summary

The U.S. Department of Energy has established The National Hydrogen Storage Project to address the technologically-difficult issue of storing enough on-board hydrogen to allow a greater than 300-mile range for hydrogen-powered vehicles, which is a critical element required for the success of the Hydrogen Economy. The National Hydrogen Storage Project encompasses Centers of Excellence in Metal Hydrides, Chemical Hydrogen Storage, and Carbon-Based Materials, as well as Independent Projects and Basic Science projects. A large number of universities, industrial organizations, and federal laboratories are engaged in this research which is targeted at hydrogen storage in materials. Significant improvements in the capacities of on-board vehicular hydrogen

storage systems are expected to result from this DOE-sponsored Project. In addition to U.S. activities, the DOE is supporting the mission of the International Partnership for the Hydrogen Economy (IPHE), formed in November, 2003, to advance the transition to a global hydrogen economy. Along with Italy, Russia and the European Commission, the DOE is leading the first IPHE conference on hydrogen storage to effectively identify, evaluate and coordinate multinational research, development programs in the key area of hydrogen storage.[9] Results of these efforts will be available through www.iphe.net and www.hydrogen.gov.

References

1. Hydrogen, Fuel Cells & Infrastructure Technologies Program Multi-Year Research, Development and Demonstration Plan, www.eere.energy.gov/hydrogenandfuelcells/mypp.
2. FY2004 Annual Progress Report for Hydrogen, Fuel Cells and Infrastructure Technologies Program, DOE Office of Hydrogen, Fuel Cells and Infrastructure Technologies, October 2004.
3. Schlapbach, L.; Zuttel, A. *Nature*, **2001**, *414*, 353.
4. www.eere.energy.gov/hydrogenandfuelcells, www.sc.doe.gov/bes.bes.html.
5. Chen, P.; Xiong, Z.; Luo, J.; Lin, J.; Tan, K.L. *Nature*, **2002**, *420*, 302.
6. Luo, W. *Journal of Alloys and Compounds*, **2004**, *381*, 284.
7. M.A. Miller and R. Gorte, Carbon Nanotube Sorption Science: External Peer Review of NREL Activities, Southwest Research Institute Special Report prepared for the U.S. Department of Energy, Office of Hydrogen, Fuel Cells and Infrastructure Technologies, 1 March 2004; NREL Project Report, FY2004 Annual Progress Report for Hydrogen, Fuel Cells and Infrastructure Technologies Program, DOE Office of Hydrogen, Fuel Cells and Infrastructure Technologies, October 2004.
8. Air Products and Chemicals Project Report, FY2004 Annual Progress Report for Hydrogen, Fuel Cells and Infrastructure Technologies Program, DOE Office of Hydrogen, Fuel Cells and Infrastructure Technologies, October 2004.
9. www. iphe.net and references therein.

RELATIVE STABILITY OF $(NH_3BH_3)_2$, $[NH_3\text{-}BH_2\text{-}NH_3]^+$ BH_4^-, AND $[BH_3\text{-}NH_2\text{-}BH_3]^-$ NH_4^+

Maciej Gutowski, Rafal Bachorz, Tom Autrey, John Linehan

Chemical Sciences Division, Fundamental Science Directorate,
Pacific Northwest National Laboratory, Richland, WA 99352

Introduction

Hydrogen economy might provide a long-term solution for a secure and environmentally clean energy based on renewable resources.[1] On-board hydrogen storage was identified as a grand challenge for successful deployment of fuel cell technologies.[2] New materials that store both high gravimetric (≥90 gm H_2/ kg) and high volumetric (≥82 gm H_2/ liter) densities of hydrogen with operational temperatures between -20 and 85 ˚C are to be identified by the year 2015. In consequence of weak intermolecular interactions between H_2 molecules the volumetric requirements are difficult to meet for pressurized or liquefied hydrogen systems. Storage of H_2 through physisorption is also questionable in view of the anticipated temperature range of operation. Chemical binding of hydrogen in metals or non-metallic systems is being aggressively explored.[3]

The suitability of the solid NH_xBH_x (x=1-4) compounds for hydrogen storage has recently been evaluated using experimental[4,5,6] and theoretical methods.[7] The amine boranes have excellent weight percent storage for H_2 with BH_3NH_3 having 19% if 3 molecules of H_2 are produced and the salt $(NH_4)(BH_4)$ having 24% if 4 molecules of H_2 are produced. In both cases, the final product would be BN. Thus, the NH_xBH_x series of compounds (x = 1-4) are attractive targets for chemical H_2 storage materials. Since the BN unit is isoelectronic with the CC unit, these materials can be viewed as inorganic analogs of hydrocarbons. However, the NH_xBH_x compounds are solids rather than gases at ambient temperatures, due to the greater polarity and the stronger intermolecular interactions as compared to the C_2 organic analogs which are gases. The inherent polarity is dictated by the different electronegativities of the B and N atoms, 2.0 and 3.0, respectively.[8]

The computational results, obtained at the density functional level of theory, for the solids NH_4BH_4, NH_3BH_3, and BN and polymers NH_2BH_2 and NHBH, indicate that the NH_xBH_x compounds also display favorable thermodynamics: all four subsequent steps of hydrogen release from NH_xBH_x for x ranging from 4 to 1 are thermoneutral to within 10 kcal/mol.[7] The close thermoneutrality of hydrogen release from the NH_xBH_x compounds is in significant contrast to hydrolysis pathways of boron based hydrogen storage materials.[9]

The experimental studies have been focused primarily on ammonia borane (AB), NH_3BH_3, which is a molecular solid with melting temperature of 114 ºC.[4,5,6] The release of H_2 from AB can be accomplished at temperatures below 100 ºC with formation of a complex polyaminoborane $–(NH_2BH_2)_n–$. The next step of decomposition develops above 150 ºC and yields another H_2, a polyiminoborane material, $–(NHBH)_n–$, and a variable amount of borazine c-$(NHBH)_3$. The advantageous gravimetric and volumetric properties, as well as thermal decomposition characteristics, make AB a promising material for hydrogen storage.

An ideal material for hydrogen storage would have one additional important property: it would be on-board reversible, i.e., loading of the spent material with gaseous hydrogen should be possible at moderate pressures and with fast kinetics. Unfortunately, the first step of hydrogen release, i.e., AB → $–(NH_2BH_2)_n–$ + H_2, is exothermic by 5 kcal/mol for bulk AB[6] and the entropy term also favors hydrogen release on the account of a translational contribution from the gaseous molecular hydrogen: TΔS is typically 9 kcal/mol for hydrogen release at room temperature. As a result, an on-board rehydrogenation of spent material has not been demonstrated yet for AB.

There are, however, ways to improve the thermodynamics of hydrogen release from AB. First, one can control the chemical nature of products of the dehydrogenation step. For instance, we have demonstrated that the products of dehydrogenation are different for (i) AB confined in nanoporous templates and (ii) bulk AB.[6] In consequence, the first dehydrogenation step becomes practically thermoneutral for AB confined in a nanoporous template, which is a significant improvement in comparison with ΔH=-5 kcal/mol for bulk AB.

The second way to improve the thermodynamics of hydrogen release is to modify the reactant. Ammonia borane is not the only compound with the empirical formula NBH_6. It was demonstrated in a series of experiments that there is another compound, diammoniate of diborane (DADB), $[NH_3\text{-}BH_2\text{-}NH_3]^+$ BH_4^-; see an excellent summary by Parry on the synthesis and characterization of DADB.[10] AB and DADB may be viewed as the products of symmetrical and unsymmetrical cleavage, respectively, of B_2H_6. The synthesis of AB and DADB is currently well controlled, but very little is known about the physicochemical properties of DADB. The different properties of AB and DADB might be critical for hydrogen storage in the NBH materials. In particular, the thermodynamic stabilities of DADB and AB might be different. It is critical to characterize the structural and thermodynamic properties of DADB.

If $[NH_3\text{-}BH_2\text{-}NH_3]^+$ BH_4^- is a viable material, it might be instructive to characterize also its "umpolung" counterpart,[11] i.e., $[BH_3\text{-}NH_2\text{-}BH_3]^-$ NH_4^+. Per analogy with DADB and the umpolung relation, the latter will be named here "DBDA", see Fig. 1.

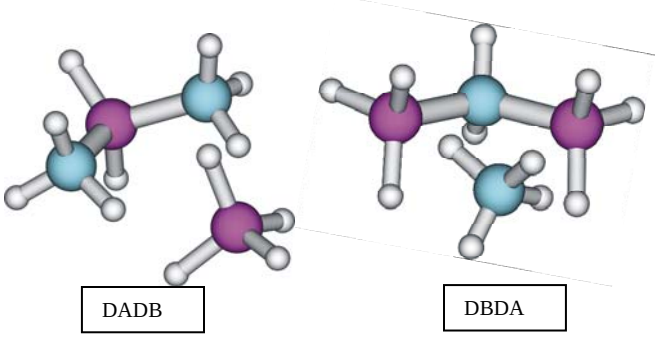

Figure 1. The boron atoms are colored in magenta, nitrogens in blue. Left, an ionic pair $[NH_3\text{-}BH_2\text{-}NH_3]^+$ BH_4^-, which is the simplest fragment of DADB. Right, an ionic pair $[BH_3\text{-}NH_2\text{-}BH_3]^-$ NH_4^+, which is the simplest fragment of DBDA.

The properties of molecular complexes $(AB)_2$, DADB, DBDA will be characterized in this report based on the results of electronic structure calculations.

Methods

Optimal geometries of NH_3BH_3, NH_4^+, BH_4^-, and complexes $(NH_3BH_3)_2$, $[NH_3\text{-}BH_2\text{-}NH_3]^+$ BH_4^-, and $[BH_3\text{-}NH_2\text{-}BH_3]^-$ NH_4^+ were determined at the second-order Moller-Plesset (MP2) level of theory using augmented, correlation consistent, triple-zeta basis sets.[12] The MP2 Hessians (matrices of second derivaties of electronic energy with respect to geometrical degrees of freedom) were determined at stationary points. Final single-point calculations were performed at the coupled-cluster level of theory with single, double, and non-iterative triple excitations[13] (CCSD(T)) at the optimal MP2

geometries. The relative electronic energies were first corrected for zero-point vibrations. Next, thermal corrections as well as the entropy terms were calculated for T=298 K and p=1 atm in the harmonic oscillator-rigid rotor approximation to derive the relative stability in terms of Gibbs free energy.

Let us illustrate our method of determination of intermolecular binding energy on the example of AB. The binding energy in a complex formed by the monomers A and B is split into the two-body interaction energy and a repulsive term that accounts for distortion of the monomers in the AB complex:

$$E_{bind}^{CP} = E_{\text{int}}^{CP} + \Delta E^{OB}.$$

The interaction energy between monomers is corrected for basis set superposition error using the function counterpoise method of Boys and Bernardi[14]

$$E_{\text{int}}^{CP} = E^{D}\left(G^{D}, B^{D}\right) - \left(E^{A}\left(G^{D}, B^{D}\right) + E^{B}\left(G^{D}, B^{D}\right)\right)$$

and the one-body term is given by

$$\Delta E^{OB} = \sum_{J}\left(E^{J}\left(G^{D}, B^{J}\right) - E^{J}\left(G^{J}, B^{J}\right)\right)$$

where:

E^{D} - energy of the dimer.

E^{A}, E^{B} - energies of the monomers.

G^{D}, G^{A}, G^{B} - geometry of the dimer, monomer A, monomer B, respectively.

B^{D}, B^{A}, B^{B} - basis set of the dimer, monomer A, monomer B, respectively.

Results and Discussion

$N_2B_2H_{12}$ can be viewed as either $(AB)_2$, or DADB, or DBDA, see Fig. 2.

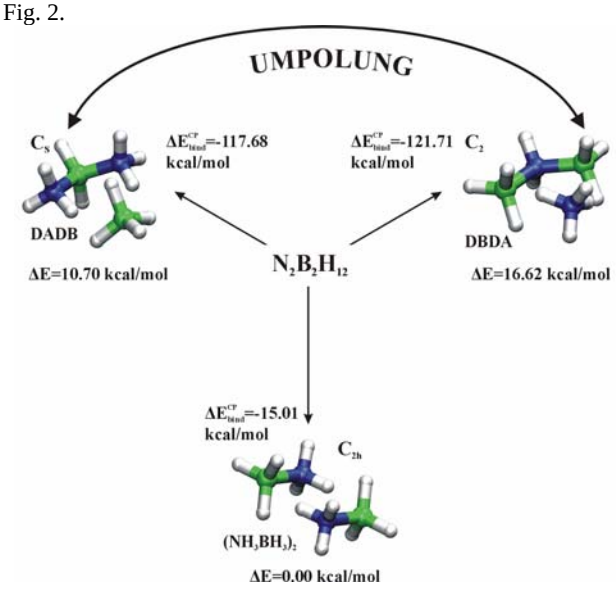

Figure 2. The relative stability of $(AB)_2$, DADB, and DBDA complexes and binding energies determined at the CCSD(T)/aug-cc-pVTZ level of theory. Boron atoms in green, nitrogens in blue.

We will start from the analysis of relative stability of noninteracting monomers, NH_3BH_3 + NH_3BH_3, $[NH_3\text{-}BH_2\text{-}NH_3]^+$ + BH_4^-, and $[BH_3\text{-}NH_2\text{-}BH_3]^-$ + NH_4^+, see Table 1.

Table 1. The relative stability of noninteracting momomers (in kcal/mol) in terms of electronic energy, ΔE_e, electronic energy corrected for zero-point vibrations, $\Delta(E_e+E_o^{vib})$, and Gibbs free energy, ΔG, determined in the harmonic oscillator-rigid rotor approximation for T=298 K and p=1.

Noninteracting Monomers	ΔE_e	$\Delta(E_e+E_o^{vib})$	ΔG
NH_3BH_3 + NH_3BH_3	0.0	0.0	0.0
$[NH_3\text{-}BH_2\text{-}NH_3]^+$ + BH_4^-	114.3	112.9	114.0
$[BH_3\text{-}NH_2\text{-}BH_3]^-$ + NH_4^+	124.0	122.6	123.8

Clearly, formation of ionic pairs $[NH_3\text{-}BH_2\text{-}NH_3]^+$ + BH_4^- or $[BH_3\text{-}NH_2\text{-}BH_3]^-$ + NH_4^+ from two NH_3BH_3 monomers is a strongly endothermic process, with the precursors to DADB being more stable than the precursors to DBDA.

The thermodynamically unfavorable step of formation of ionic pairs is compensated to a large extent by a more favorable intermolecular interaction term; see Table 2 and Fig. 2.

Table 2. The counterpoise-corrected values of E_{int}^{CP}, ΔE^{OB}, and E_{bind}^{CP} in kcal/mol.

Complex	E_{int}^{CP}	ΔE^{OB}	E_{bind}^{CP}
$(NH_3BH_3)_2$	-15.5	0.5	-15.0
$[NH_3\text{-}BH_2\text{-}NH_3]^+$ BH_4^-	-120.8	3.1	-117.7
$[BH_3\text{-}NH_2\text{-}BH_3]^-$ NH_4^+	-124.2	2.5	-121.7

The $(NH_3BH_3)_2$ complex has C_{2h} symmetry and therefore a zero dipole moment. The B-N distances are 3.25 A and the binding energy of -15.0 kcal/mol is a manifestation of polarity of the monomers. The $[NH_3\text{-}BH_2\text{-}NH_3]^+$ BH_4^- complex has C_s symmetry, the B-N distances is 3.07 A, and the B-B distance is 3.66 A. Its "umpolung" counterpart, $[BH_3\text{-}NH_2\text{-}BH_3]^-$ NH_4^+ has C_2 symmetry, the B-N distance is 2.96 A and the N-N distance is 3.40 A. Thus, the DADB and DBDA complexes differ not only in the distribution of the positive and negative electrostatic poles, but they also have different symmetries and geometries. Their dipole moments differ significantly: 6.8 and 5.6 D for DADB and DBDA, respectively, in consequence of the differences in interatomic distances. The large dipole moments reflect ionic character of DADB and DBDA. This ionicity also explains large values of binding energy.

Finally, the relative stability of complexes is displayed in Table 3

Table 3. The relative stability (in kcal/mol) of $(NH_3BH_3)_2$, $[NH_3\text{-}BH_2\text{-}NH_3]^+$ BH_4^-, and $[BH_3\text{-}NH_2\text{-}BH_3]^-$ NH_4^+.

Complex	E_e	$E_e+E_o^{vib}$	G
$(NH_3BH_3)_2$	0.0	0.0	0.0
$[NH_3\text{-}BH_2\text{-}NH_3]^+$ BH_4^-	11.4	10.7	10.9
$[BH_3\text{-}NH_2\text{-}BH_3]^-$ NH_4^+	17.2	16.6	17.7

The relative stability is dominated by the electronic energy contribution with zero-point vibrations and thermal corrections playing only secondary role. The AB dimer is more stable than molecular DADB and DBDA ionic pairs by more than 10 kcal/mol. The relative stability of AB, DADB, and DBDA in solid phases will be further affected by long-range interaction. We found in our earlier DFT calculations that the cohesive energy in AB is 16.6 kcal/mol per

formula unit.[7] The role of lattice energies in relative stabilities of AB, DADB, DBDA will be analyzed in our future study.

Acknowledgement. This work was supported by the PNNL's Laboratory Directed Research and Development program and the DOE Center of Excellence for Chemical Hydrogen Storage. Computing resources were available through a Computational Grand Challenge Application grant from the Molecular Sciences Computing Facility in the Environmental Molecular Sciences Laboratory. PNNL is operated by Battelle for the U.S. DOE under Contract DE-AC06-76RLO 1830.

References

(1) See http://www.eere.energy.gov/hydrogenandfuelcells/
(2) MRS Bulletin, vol. 27, issue 9, September 2002.
(3) Grochala, W.; Edwards, P. P. *Chem Rev*. **2004**, *104*, 1283.
(4) Baitalow, F.; Baumann, J.; Wolf, G.; Jaenicke-Röβbler, K.; Leitner, G. *Thermochim Acta* **2002**, *391*, 159.
(5) Autrey, T.; Gutowska, A.; Li, L.; Linehan, J.; Gutowski,, M. Prep. Pap. - *Am. Chem. Soc., Div. Fuel Chem.* **2004**, *49*, 150.
(6) Gutowska, A.; Li, L.; Shin, Y.; Wang, C.; Li, X-S.; Linehan, J.; Smith, R.S.; Kay, B.D.; Schmidt, B.; Shaw, M.; Gutowski, M.; Autrey, T., submitted for publication.
(7) Gutowski, M.; Autrey, T. Prepr. Pap. –*Am. Chem. Soc., Div. Fuel Chem*.,. **2004**, *49*, 275.
(8) Pauling, L., *General Chemistry*, Dover Publications, Inc., New York, 1988, p. 182.
(9) Amendola, S.C.; Sharp-Goldman, S. L; Janjua, M. S.; Spencer, N. C; Kelly, M. T; Petillo, P. J; Binder, Michael. *Int. J. Hydrogen Energy*, **2000**, *25*, 969.
(10) Parry, R.W. *J. Chem. Educ.* **1997**, *74*, 512.
(11) "umpolung" means a reversal of polarity.
(12) Kendall, R. A.; Dunning, T. H., Jr.; Harrison, R. J. *J. Chem. Phys.* **1992**, *96*, 6796.
(13) Watts, J. D.; Gauss, J.; Bartlett, R. J. *J. Chem. Phys.* **1993**, *98*, 8718.
(14) Boys, S.F.; Bernardi, F. *Mol. Phys.* **1970**, *19*, 553.

NEUTRON METROLOGIES FOR HYDROGEN STORAGE

D.A. Neumann, T.J. Udovic, C.M. Brown, T. Yildirim, M.R. Hartman, and J.J. Rush

NIST Center for Neutron Research
National Institute for Standards and Technology
Gaithersburg, MD 20899-8562

Introduction

The study of hydrogen in materials by neutron scattering, imaging, and trace-analysis techniques is a critical component of any broad-based research program into hydrogen storage systems. For the most part, this is due to the novel properties of the neutron and its interactions with matter, especially the different isotopes of hydrogen. The unusually large neutron scattering cross section for hydrogen can be routinely exploited by a range of experimental neutron methods in order to probe the amount, location, bonding states, and diffusion of hydrogen in any promising hydrogen-storage material. The thermal and cold-neutron beams at NIST and at other neutron scattering facilities combined with state-of-the-art instrumentation provide an array of neutron methods that give researchers access to a wide range of length scales, sensitivity, and dynamic range (Fig. 1).

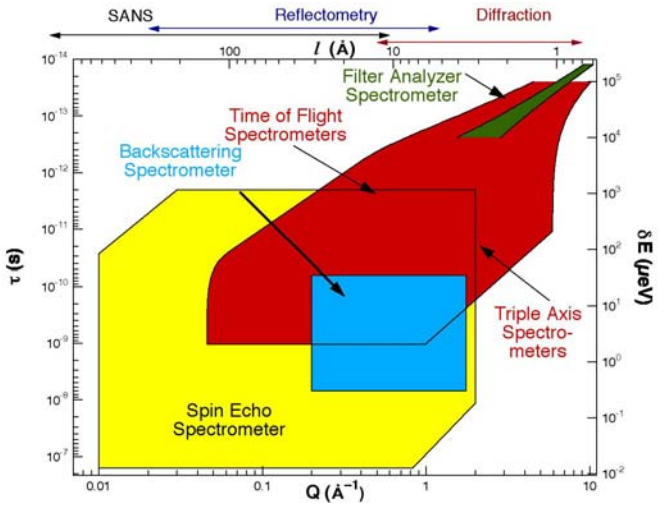

Figure 1. Neutron methods at NIST encompass an enormous range of time and length scales.

Quasielastic Neutron Scattering

Neutron spectroscopic techniques are invaluable for the study of hydrogen diffusion in these materials because of the unique ability of neutrons to simultaneously give information on both the time scale and the atomic scale geometry of the motion. Getting the hydrogen in and out of a hydrogen-storage bed is crucial to devising a functioning hydrogen-storage system. The information provided by quasielastic techniques allows one to develop the detailed understanding of this process required for the atomic scale optimization of these materials. (1)

Inelastic Neutron Scattering

Due to the large scattering cross section for hydrogen, neutron vibrational spectroscopy preferentially probes the motions of the hydrogen atoms. Thus, while this technique is roughly equivalent to Raman spectroscopy, the information one obtains is particularly relevant for hydrogen storage. Moreover, the simplicity of the interaction between thermal neutron and matter makes it possible to calculate the observed neutron spectrum from any model of the interactions including first principles methods. Such computational results are critical to interpret and to guide experimental studies. Figure 2 shows the measured neutron vibrational spectrum compared to *ab initio* calculations that include both one and two phonon processes. (2)

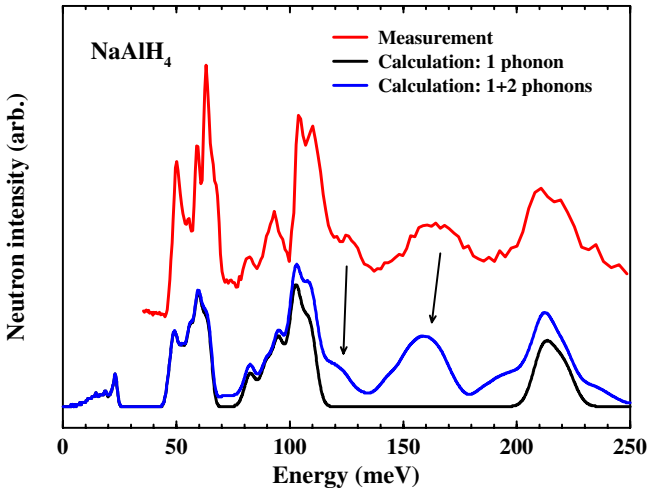

Figure 2. Neutron vibrational spectrum of $NaAlH_4$ compared with *ab initio* calculations that include one and two phonon processes.

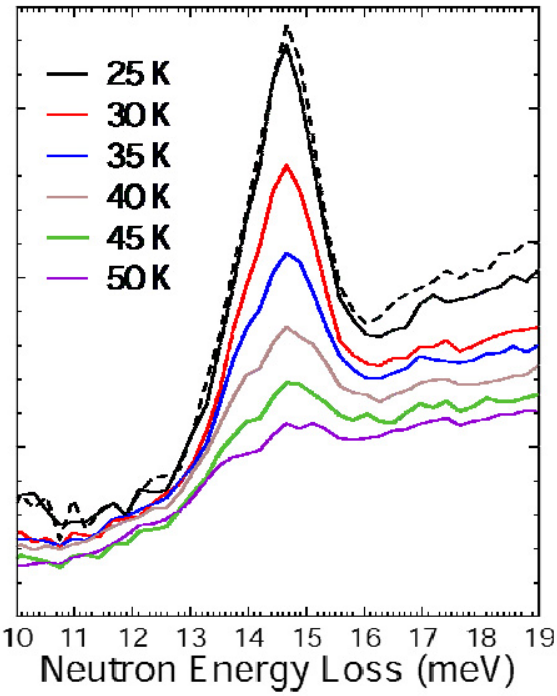

Figure 3. The temperature dependence of the rotational line of hydrogen molecules on single-wall carbon nanotubes. The decrease of intensity is due to hydrogen desorption.

Neutron spectroscopy can also be used to quantify the amount of hydrogen in a sample and can tell if the hydrogen is present as H_2 by measuring the characteristic rotational spectrum of the hydrogen molecule. This type of data also allows one to obtain information on the interactions responsible for binding the hydrogen in these materials. Figure 3 shows the temperature dependence of such a spectrum measured for hydrogen adsorbed on single-wall carbon nanotubes. (3)

Neutron Diffraction

Neutron diffraction is the preeminent technique for determining the crystallographic locations of hydrogen using standard methods including Rietveld refinement. Figure 4 shows a neutron diffraction pattern obtained at NIST for Ti-doped $NaAlD_4$. The refinement allows one to quantify several impurity phases. (4)

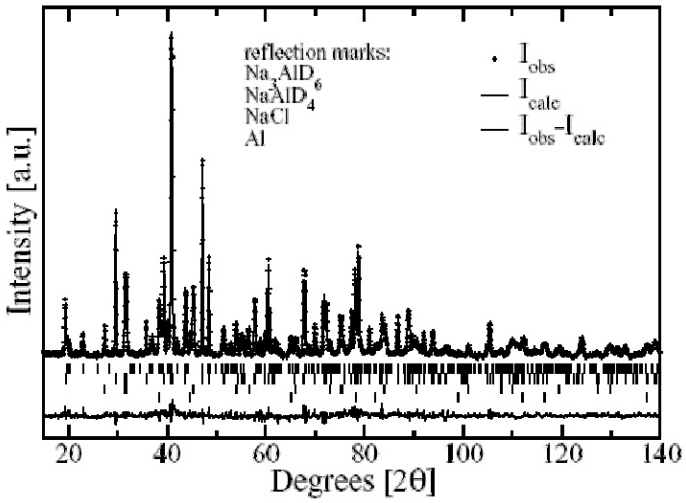

Figure 4. Neutron diffraction results for Ti-doped $NaAlD_4$

Prompt γ activation analysis

Neutrons can also be used to precisely quantify the amount of hydrogen actually present in a material. For example, neutron prompt γ activation analysis (PGAA) instruments provide *in situ* quantitative analyses of the amount of hydrogen in storage materials down to the microgram level. (Fig. 5) The *in-situ* capabilities currently being developed will allow one to precisely measure the amount of hydrogen adsorbed in materials as a function of temperature and pressure.

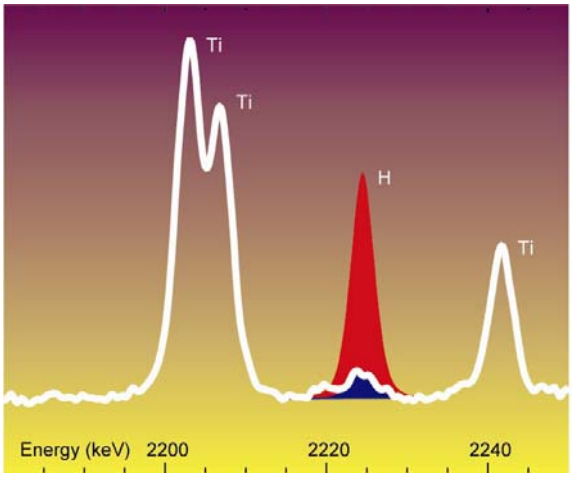

Figure 5. Prompt γ spectra of H in Ti turbine blades for two different processing methods. (5) The difference in the amount of H incorporated in the material is readily apparent. Similar measurements can be made for H in H-storage materials.

Neutron Imaging

One can employ the sensitivity of neutrons to image hydrogen in, *e.g.*, hydrogen-storage beds. Here, current capabilities for neutron imaging and tomography allow one to image hydrogen in real time with a resolution approaching 100 μm (Fig. 6).

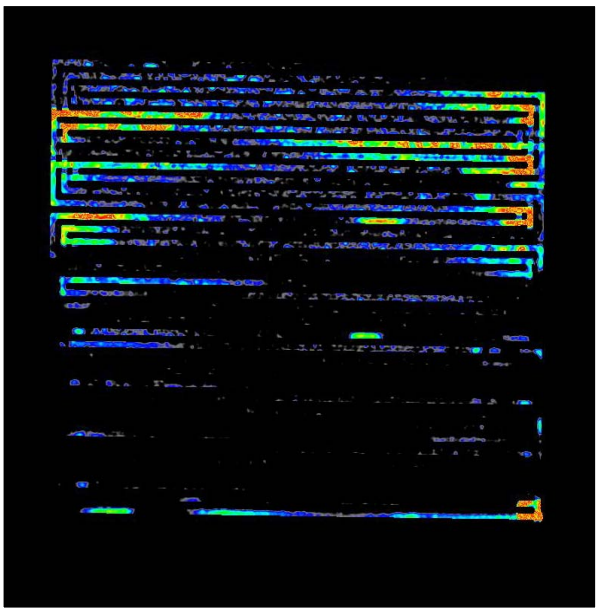

Figure 6. Neutron image of water in flow channels of a PEM fuel cell. See ref. 6.

Conclusion

Finally, it should be noted that all of these capabilities can be employed under conditions of pressure and temperature relevant to those of hydrogen-storage beds. Thus one can obtain information on how hydrogen storage materials will behave under real-world conditions.

Acknowledgements We acknowledge the valuable contributions of the many colleagues we have been fortunate to collaborate with over the years. We are particularly grateful to Muhammad Arif and David Jacobson for the neutron imaging figure and to Dick Lindstrom and Rick Paul for the prompt γ data.

References

(1) Hempelmann, R. *Quasielastic Neutron Scattering and Solid State Diffusion*, (Oxford University Press, **2001**).
(2) Íñiguez, J.; Yildirim, T.; Udovic, T.J.; Sulic, M.; and Jensen, C.M. *Phys. Rev. B* **2004**, *70*, 060101.
(3) Brown, C.M.; Yildirim, T.; Neumann, D.A.; Heben, M.J.; Gennett, T.; Dillon, A.C.; Alleman J.L.; and Fischer, J.E. *Chem. Phys. Lett*, **2000**, *329*, 311.
(4) Ozolins, V.; Majzoub, E.H.; and Udovic, T.J. *J. Alloys Compounds* **2004**, *375*, 1.
(5) Paul, R.L.; and Lindstrom, R.M. *J. Radioanal. Nucl. Chem*. **2000**, *243*, 181.
(6) Satija, R.; Jacobson, D.L.; Arif, M.; and Werner, S.A. *J. Power Sources* **2004**, *129*, 238.

CHEMICAL REACTION OF AMIDES AND HYDRIDES

*Zhitao XIONG, Jianjiang HU, Guotao WU and Ping CHEN**

Physics Department, National University of Singapore, 10 Kent Ridge Crescent, Singapore 119542

Introduction

There are strong pushes towards hydrogen economy worldwide. To overcome one of the technical barriers – onboard hydrogen storage, great efforts have been devoted to the development of solid-state materials, such as carbonaceous materials [1,2], alanates [3-5], B-N-H complex [6] and lithium nitride and imide[7] etc in the past several years. More recently, two ternary imides, i.e. Li-Mg-N-H and Li-Ca-N-H, were developed in our lab, in which drastic decrease in operation temperatures and uprising hydrogen desorption pressure were achieved.[8] Interesting results on Li-Mg-N-H system were also reported by Fujii et al,[9] Luo [10] and Orimo et al.[11] However, to make Metal-N-H system practically viable, systems, especially those ambient temperature systems, are highly needed.

Previous investigations reveal that the hydrogen-rich phases of Li-N-H and Li-Mg-N-H systems comprise of metal amides and hydrides [7-11]. It is probably the strong potential for the union of $H^{\delta+}$ in amide and $H^{\delta-}$ in hydride to H_2 that drives the two chemicals to react and give out hydrogen.[12] Assuming the hypothesis is valid and universal, a serial of new Metal-N-H systems can be developed by reacting various amides with hydrides. In the present work, 7 amide-hydride systems were prepared by mixing amides of Li and Mg with $LiAlH_4$, MgH_2, NaH and CaH_2, respectively (listed in Table 1). The interaction between amide and hydride was investigated by an in situ planetary ball mill, TPD, volumetric Release-Soak techniques and FTIR. To our expectation, five novel Metal-N-H systems were developed accordingly, among which three systems can release substantial amount of hydrogen (more than 4.2wt%) near ambient temperature.

Experimental

$LiNH_2$, LiH, NaH, MgH_2, CaH_2, $LiAlH_4$ are commercially available. $Mg(NH_2)_2$ was synthesized by reacting Mg nanoparticles with NH_3 at temperature around 300ºC. 7 amide-hydride systems, including $2LiNH_2+LiAlH_4$ (molar ratio of $LiNH_2$ to $LiALH_4$ is 2/1), $Mg(NH_2)_2+LiAlH_4$, $Mg(NH_2)_2+1.5NaH$ (1/1.5), $Mg(NH_2)_2+CaH_2$ (1/1) and $2LiNH_2+MgH_2$ were milled in a planetary ball mill at 200 rpm for two days, respectively. Pure $LiAlH_4$(2g) was also treated under the same conditions. The milling jar is equipped with two gas inlet ports, from which pressure changes in the jar can be monitored by a pressure gauge. The volume of the jar is 194.6ml. ~85g of stainless steel balls were used. After ball milling, the pressure within the jar was measured and the gaseous product was analyzed by Mass Spectrometer and ammonia-sensitive reagent. Only pure hydrogen is the detectable gaseous product. Details are summarized in Table 1. The as-prepared samples were then transferred to a micro-reactor for Temperature-Programmed-Desorption (TPD) testing. The details of TPD testing system and procedure have been described elsewhere.[7] Quantitative measurements of the hydrogen desorption from the post-milled samples were measured by a gas reaction controller provided by Advanced Materials Corporation. ~ 500 mg samples were tested each time. Results were also summarized in Table 1 and present in Figure 3. X-ray Diffractometer (Brucker D8-advance) and FTIR (PerkinElmer System 2000) have been applied to detect the structural and bonding changes before and after treatment. As most of the samples are sensitive to moisture, all the sample loadings and transferring were handled in a glovebox provided by MBRAUN.

Results and Discussion

$LiAlH_4$ only releases 5 psi of hydrogen after two days' ball milling (see Table 1), indicating the local heating due to the collision of balls is unpronounced. Striking high hydrogen pressure was accumulated in the milling jar filled of $2LiNH_2+LiAlH_4$ (151 psi), $Mg(NH_2)_2+LiAlH_4$ (168 psi) and $Mg(NH_2)_2+MgH_2$ (80 psi) samples, which account for 4.5wt%, 4.2 wt% and 2.4wt% of the starting compounds, respectively. The substantial amount of hydrogen released under the mild ball milling conditions reveals the thermodynamically favored interaction between the above amide and hydride systems. Other amide-hydride systems, i. e., $Mg(NH_2)_2+1.5NaH$ (1/1.5), $Mg(NH_2)_2+CaH_2$ (1/1), and $2LiNH_2+MgH_2$ (2/1), did not release much detectable hydrogen after ball milling (Table 1).

Table 1. Summary of the interaction between variety amides and hydrides

Amide-hydride molecules	Pres H_2 in BM jar (psi)	No. H released after BM	No. H released after TPD
$LiAlH_4$	5	--	--
$2LiNH_2+LiAlH_4$	151	3.8 (4.5wt%)	3.8 (4.6%)
$2LiNH_2+MgH_2$	0	0	3.8 (5.3wt%)
$Mg(NH_2)_2+LiAlH_4$	168	4.0 (4.2wt%)	1.3* (1.4wt%)
$2LiNH_2+MgH_2$	0	0	3.8 (5.3wt%)
$Mg(NH_2)_2+1.5NaH$	0	0	1.9* (2.0wt%)
$Mg(NH_2)_2+CaH_2$	9	0.1	2.0 (2.0wt%)
$Mg(NH_2)_2+MgH_2$	80	2.0 (2.4wt%)	1.6 (1.9wt%)

* Ammonia appears at temperature above 200ºC.

All the post-milled samples were subjected to TPD and volumetric Release testing. Results were presented in Fig. 1 and Table 1. It can be seen that upon heating hydrogen signal appears in the post-milled $LiNH_2+LiAlH_4$ and $Mg(NH_2)_2+LiAlH_4$ samples (Fig. 1). ~3.0wt% and 1.4wt% of hydrogen were desorbed at temperatures below 300ºC (Table 1), respectively. The general TPD features exhibit remarkable differences from the characteristic decomposition of pure $LiAlH_4$, $LiNH_2$ and $Mg(NH_2)_2$, further evidencing the occurrence of chemical reactions during the ball milling. Little amount of ammonia was detected at temperatures above 200ºC.

Heating the post-milled $Mg(NH_2)_2+MgH_2$ sample comes with hydrogen signals at temperatures above 70ºC , remarkably lower than those for the decomposition of individual MgH_2 and $Mg(NH_2)_2$ (Fig. 1). Additional 1.9wt% of hydrogen was desorbed at temperatures below 300ºC. The sharp peak at ~ 400ºC is the mixed signals of NH_3, H_2 and N_2, which is probably due to the decomposition of a Mg-N-H compound, such as MgNH.

Desorption of hydrogen from $2LiNH_2+MgH_2$ sample starts at temperatures near 100ºC and peaks at ~ 170ºC (Fig. 1). The temperature range is far below those for the decomposition of pure MgH_2 (above 280ºC) and $LiNH_2$ (above 300ºC). The amount of hydrogen desorbed is ~ 5.3 wt% of the solid sorbent (Table 1). Identical TPD features were also observed in $Mg(NH_2)_2+2LiH$ sample.

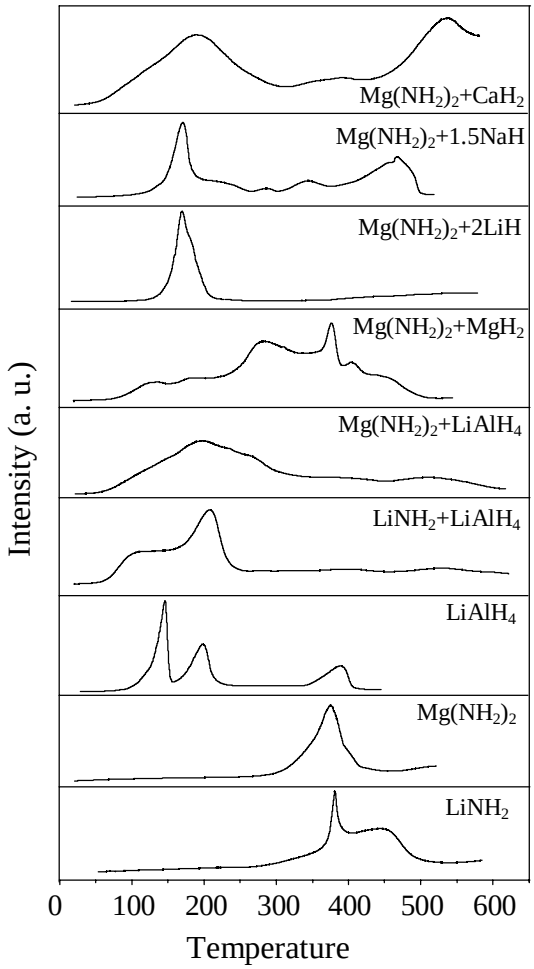

Figure 1. TPD profiles of post-milled samples except LiNH2 and Mg(NH2)2

Post-milled $Mg(NH_2)_2$+NaH (1/1.5) and $Mg(NH_2)_2$+CaH_2 (1/1) samples exhibit the majority of hydrogen desorption at temperatures above 50ºC with ~ 2.2wt% and 2.0wt% desorption capacity, respectively (Fig. 1 and Table 1). Structural decomposition occurs at temperatures above 350ºC.

FTIR was applied to detect changes in N-H bonding before and after hydrogen desorption in $Mg(NH_2)_2$-based systems. Pristine $Mg(NH_2)_2$ has the symmetric and asymmetric N-H stretching at 3274 cm-1 and 3328 cm-1, respectively (Fig. 2). After ball milling with $LiAlH_4$, those stretching vibrations disappear. However, features of imide N-H stretching do not manifest (Fig. 2), indicating the rearrangement of N and H atoms within the sample. The post-milled $Mg(NH_2)_2$+MgH_2 (1/1) sample also exhibits much depressed -NH_2 characteristics, a broad band in 3100 - 3250 cm-1 was developed instead, which has the characteristics of imide12. Strong imide-like features were developed in the post-desorbed $Mg(NH_2)_2$+2LiH sample. Clearly, part of H atoms previously bonded to N was released or transferred during its interaction with hydrides.

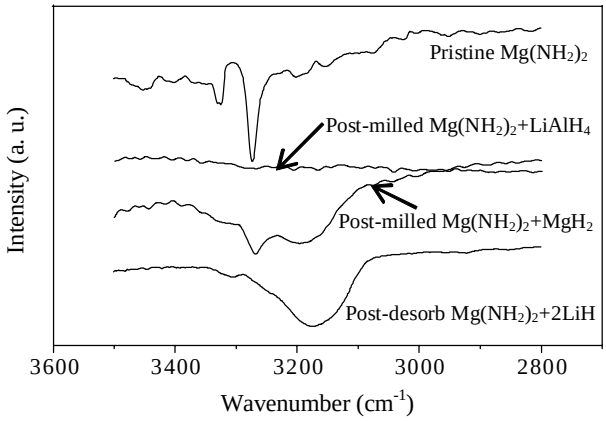

Figure 2. FTIR spectra of $Mg(NH_2)_2$-based samples

Conclusions

In summary, substantial amount of hydrogen can be released from various amide-hydride systems, demonstrating the universality of the interaction between amides and hydrides. Temperatures for hydrogen desorption are normally far below those for the decomposition of pure constituent compounds, revealing the thermodynamic favor for the interaction. Five new Metal-N-H systems were developed successfully (Table 1), which are worth of further development. As the H-deficient phase of Metal-N-H is somewhat with imide-like behavior, the following equation may account for the general features of the amide-hydride reaction:

M_1-NH_2 + M_2-H_n → (M1-M_2-NH) + H_2

M_1 and M_2 represent alkali and/or alkali earth metals. Structural changes before and after interaction appear to be rather important. However, the poor crystallinity of the ball milled samples brings difficulties for the X-ray characterization. The challenges posed to the Metal-N-H system for hydrogen storage purpose are the reversibility (especially for those ambient temperature systems), capacity, and the chemical stability, which are subject to further investigations and optimizations.

Acknowledgement. This work is partially financially supported by Agency of Science, Technology and Research (A*STAR, Singapore).

References

(1) Rosi, N. L.; Eckert, J.; Eddaoudi, M.; Vodak, D. T.; Kim, J.; O'Keeffe, M.; Yaghi, O. M.; Science, **2003**, *300*, 1127.
(2) Dillon, C.; Jones, K. M.; Bekkedahl, T. A.; Kiang, C. H.; Bethune, D. S.; Heben, M. J. Nature, **1997**, *386*, 377.
(3) Bogdanovic, R. A. Brand, A. Marjanovic, M. Schwickardi, J. Tolle, J. Alloy Comp. **2000**, *302*, 36.
(4) Sun, L.; Srinivasan, S. S.; Kiyobayashi, T.; Kuriyama, N.; Jensen,C. M. J. Phys. Chem. B **2003**, *107*, 10176.
(5) Gross, K. J.; Majzoub, E. H.; Spangler, S. W. J. Alloy Comp. **2003**, *356*, 423.
(6) Baitalow, F.; Baumann, J.; Wolf, G.; Jaenicke-Rossler, K.; Leitner, G. Thermo. Acta, **2002**, *391*, 159.
(7) Chen, P.; Xiong, Z. T.; Luo, J. Z.; Lin, J. Y.; Tan, K. L. Nature, **2002**, *420*, 302.
(8) Xiong, Z. T.; Wu, G. T.; Hu, J. J.; Chen, P. Adv. Mater., 2004,
(9) Leng, H. Y.; Ichikawa, T.; Hino, S.; Hanada, N.; Isobe, S.; Fujii, H. J. Phys. Chem.B **2004**, 108, 8763.
(10) W. F. Luo, J. Alloy. Compd **2004**, *381*, 284.
(11) Nakamori, Y.; Orimo, S. J. Alloy. Compd., **2004**, 370, 271.
(12) Chen, P.; Xiong, Z. T.; Luo, J. Z.; Lin, J. Y.; Tan, K. L. J. Phys. Chem. B, **2003**, 107,10967.

DOPED SODIUM ALUMINUM HYDRIDE: FUNDAMENTAL STUDIES OF A PROMISING NEW HYDROGEN STORAGE MATERIAL

Craig M. Jensen[1], Sesha S. Srinivasan[1], Rosario Cantelli[2], Oriele Palumbo[2], Annalisa Paolone[2,3], Carmen M. Andrei[4], Randi Holmstad[4], J.C. Walmsley[5], Bjørn C. Hauback[6], Hendrik W. Brinks[6], Meredith Kuba[1], Sandra Eaton[7], Dalin Sun[1], Keeley Murphy[1], and Ping Wang[1]

1) Department of Chemistry University of Hawaii, Honolulu, HI 96822.
2) Università di Roma "La Sapienza", Dipartimento di Fisica, Piazzale A. Moro 2, I-00185 Roma, Italy.
3) Instituto Nazionale per la Fisica della Materia, Corso Perrone 24, I-16152 Genova, Italy.
4) Department of Physics, Norwegian University of Science and Technology, 7491 Trondheim, Norway.
5) SNTEF Materials and Chemistry, 7465 Trondheim, Norway.
6) Institute for Energy Technology, P.O. Box 40 Kjeller, NO-2027 Norway.
7) Department of Chemistry and Biochemistry, University of Denver, Denver, CO 80208.

Point Defect Dynamics and Evolution of Chemical Reactions in Alanates by Anelastic Spectroscopy

We conducted the first measurements of elastic modulus and energy dissipation in Ti-doped and undoped sodium aluminium hydride. We have found that the dehydrogenation of the hydride can be monitored through its effects the elastic constants. After a well defined thermal treatment, a thermally activated relaxation process appears at 70 K in the kHz range. This denotes the existence of a new species, likely involving hydrogen, has a very high mobility. The species is estimated to "jump" at rate of 10^3/s at the peak temperature corresponding to a relaxation rate of about 10^{11} s^{-1} at room temperature. The activation energy of the process is 0.126 eV and the pre-exponential factor $7 \cdot 10^{-14}$ s, which is typical of point defect relaxation. The peak is very broad with respect to a single Debye process, indicating strong interaction or/and multiple jumping type of the mobile entity. The present data suggest that the indicated point-defect dynamics and stoichiometry defects should be included models of the reversible elimination of hydrogen from the doped hydride.

Electron-microscopy Studies of $NaAlH_4$ with TiF_3 Additive: Hydrogen Cycling Effects

The microstructure of $NaAlH_4$ doped with 2 mol % TiF_3 studied under different conditions using a combination of transmission electron microscopy and scanning electron microscopy, both with energy-dispersive spectroscopic X-ray analysis. The effect of the additive on particle and grain size was examined after the initial ball-milling process and after 15 cycles. The additive has an uneven distribution in the sample after ball milling. Selected-area diffraction and high-resolution imagining confirmed the presence of TiF_3. This phase accounts for most of the Ti in the material at this stage and showed limited mixing with the alanate. The grain size within particles for TiF_3 is larger than for the alanate particles. Diffraction form the latter was dominated by metallic aluminium. After cycling, the TiF_3 has decomposed and energy-dispersive spectroscopic X-ray analysis maps showed some combination of Ti with the alanate phase. There is no significant change in he measurable grain size of the Al-containing alanate particles between the ball-milled and the 15-cycled samples, but more cycles result in agglomeration of the material.

Electron Paramagnetic Resonance Studies of Fluctuating Titanium Species During Reversible Dehydrogenation of Ti-Doped Sodium Alanate

As part of our effort to characterise the active species in Ti-doped $NaAlH_4$ and elucidate its mechanism of action, we have carried out electron paramagnetic resonance (EPR) spectroscopic studies. We observe a major population of a spin isolated, Ti(III) species in $NaAlH_4$ immediately following the doping of the hydride with 2 mol % TiF_3. The 8,000-G wide EPR spectrum is dominated by a sharp Ti(III) signal with g = 1.976 and ΔBpp ~ 90 G. After one cycle of dehydrogenation-rehydrogenation, the signal is about 70% as intense as in sample before cycling a broader, multi-spin Ti(0) signal is also present with ΔBpp ~ 1500 G. After 3cycles, the broader signal is about 2.5 times as large as in the sample after 1 cycle. After 5 cycles there is no longer a signal with ΔBpp ~ 90 G or ΔBpp ~ 1500 G, but a dominant, multi-spin Ti(0) signal with ΔBpp ~ 650 G. There is also a signal near zero-field. After 10 cycles, the height of the signal with ΔBpp ~ 650 G is similar to that after 5 cycles, but the signal near zero-field has largely disappeared.

The uncycled spectrum of 2 mol % $TiCl_3$ doped $NaAlH_4$ also has a sharp Ti(III) signal with g ~ 1.97. Similar to the TiF_3 spectrum after 3 cycles, there is a broad signal with ΔBpp ~ 1500 G and a broad signal near zero-field. Analogous to the TiF_3 sample, one cycle of dehydrogenation-rehydrogenation of the $TiCl_3$ doped sample causes a substantial decrease in the signal with g ~ 1.97. After 3 cycles, the Ti(III) signal at g = 1.97 is essentially gone. The broader signal with ΔBpp ~ 1500 G continues to evolve in shape. By the time the sample has been cycled 5 times, the spectra are very similar to the TiF_3 spectra. There is now a signal with g = 2.01 and ΔBpp ~ 650 G. After 10 cycles the height of the signal with ΔBpp ~ 650 G is only a bit larger than after 5 cycles, as well as a slight increase in height of the signal near zero-field.

The 2 mol % Ti powder doped $NaAlH_4$ spectrum is remarkably similar to the spectra of TiF_3 and $TiCl_3$ doped samples after 5 and 10 cycles. There is appearance of the broad signal with ΔBpp ~ 500 G. However, the broad signal at zero-field is absent.

Despite the change in the oxidation state of the titanium, only a minor change occurs in the dehydrogenation and rehydrogenation kinetics of the hydride that is doped using TiF_3. Furthermore, although initially the relative amounts of Ti(III) and Ti(0) are radically different in Ti-doped $NaAlH_4$, depending on whether the hydride is doped using TiF_3 or $TiCl_3$ as dopant precursor, virtually identical kinetics are observed for the first 3 cycles of dehydrogenation-rehydrogenation regardless of which dopant precursor is employed. These findings suggest that the enhanced hydrogen cycling kinetics are due to a Ti species that is present in only a relatively minor amount. The slight kinetic improvement that is observed beyond the third cycle is similar to that observed when the hydride is ball milled without dopant. The finding that a significant amount of the Al-Ti alloy arises after the third cycle then suggests that the alloy is responsible for only this minor kinetic enhancement.

Synchrotron X-ray and Neutron Diffraction Studies of $NaAlH_4$ Containing Ti Additives

$NaAlH_4$, Na_3AlH_6 and NaH samples with Ti additives have been investigated by synchrotron X-ray diffraction and neutron diffraction. Directly after the ball milling there are no signs of any Ti-containing phases, and based on unit-cell dimensions of $NaAlH_4$, Na_3AlH_6 and Al there are no indication of any solid solutions. Combined

refinements of X-ray and neutron diffraction of $Na_{1-3x}Ti_xAlD_4$ and $NaAl_{1-x}Ti_xD_4$ do not give evidence of such solid solutions either. Hence it is concluded that Ti directly after ball milling is in an amorphous state. However, after cycling a shoulder on the high-angle side of the Al reflections appears that is interpreted as a fcc solid solution $Al_{1-x}Ti_x$ with $x \approx 0.07$. Furthermore, addition of TiF_3 by ball milling results in different phases compared to $TiCl_3$/$TiCl_4$. The latter gives NaCl, whereas no NaF is formed by the former additive. It has not yet been possible to determine by X-ray diffraction where the fluorine is in the sample.

Preparation of Ti-doped Sodium Aluminum Hydride from Mechanical Milling of NaH/Al with Off-the-Shelf Ti Powder

Ti-doped $NaAlH_4$ can be directly prepared by mechanical milling a 1:1 mixture of NaH and Al together with a few mole percent of off-the-shelf metallic Ti powder under argon or hydrogen atmosphere. The hydrogen storage materials that are produced through this process exhibit stable hydrogen capacities through 10 cycles of hydrogenation/dehydrogenation. We have conducted a systematic investigation of this new method for the preparation of Ti-doped $NaAlH_4$. Consideration of these results, together with those previously obtained for $NaAlH_4$ that was doped with Ti powder through milling under a hydrogen atmosphere, has provided insight into the nature of active Ti-species.

CHEMICAL CONTROL OF THE THERMAL DECOMPOSITION TEMPERATURE OF MULTINARY HYDRIDES AND COMPLEX HYDRIDES

P. P. Edwards[1], W. Grochala[2], S. R. Johnson[1] V. Kuznetsov[1] and M. O. Jones[1]

[1]Department of Chemistry, University of Oxford, South Parks Road, Oxford, OX1 3QR
[2]The Department of Chemistry, University of Warsaw, Pasteur 1, 02093, Warsaw, Poland

Hydrogen storage is regarded by many as ***the*** scientific and technological barrier inhibiting a transition to a hydrogen energy economy – certainly for the large scale utilisation of PEM fuel cells in cars[1].

The maximum hydrogen capacity of conventional (heavy) metal hydrides currently remains at around 2wt%, which is inadequate for onboard storage of hydrogen which requires a target gravimetric storage density of at least 6.5wt%. This requirement forces a natural focus on the light chemical elements of the periodic table. Simple atomic, mass-based calculations reveal that the main backbone of any efficient hydrogen storage material (HSM) must only be built from targeted chemical elements from an unforgiving and tantalizingly-short list, Li, Be, B, C, N, O, F, Na, Mg, Al, Si and P. Due to the toxicities and/or unfavourable chemical properties of hydrogen's compounds with Be, F, Si and P, the effective list of chemical cogwheels constituting a Hydrogen Storage Material might only consist of only eight elemental apostles (of course, heavier elements may enter the multi-component system but only as a low-abundant addition, for example, as a catalytic component). From these considerations any target material from our *Light Periodic Table* (Figure 1) is not an over-expansive playground for the chemist. Paradoxically, of course, this is the real intellectual and technical challenge; any revolutionary advance or breakthrough (and one is certainly needed) must derive from a deep understanding – and mastery – of the nature of the chemical and physical interactions of hydrogen with materials derived from our Light Periodic Table.
In this presentation, we give a brief overview of our developing programme centred upon an understanding of the thermal decomposition/sorption processes of multinary and complex hydride materials, with a particular emphasis on the rational control and chemical tuning of the strategically important thermal decomposition temperature, T_{dec}, of compounds and materials from the Light Periodic Table.

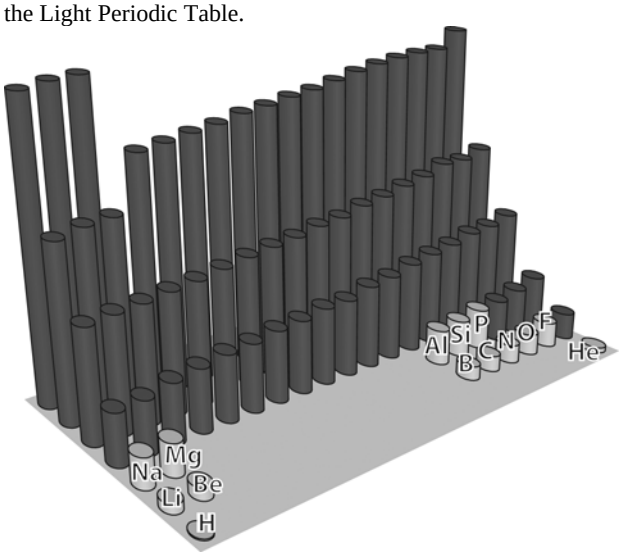

Figure 1. The Light Periodic Table.

From a chemical perspective, the reactions taking part in the decomposition, and thence the recharging of a hydrogen store, can be expressed in the following reduction / oxidation (redox) reactions;

$$M^{n+}H_n \longrightarrow M + \tfrac{1}{2}nH_2 \quad (1)$$

(*reductive elimination of H_2*)

$$M + \frac{n}{2}H_2 \longrightarrow M^{n+}H_n \quad (2)$$

(*oxidative addition of H_2*)

where M stands for an element, a lower hydride or potentially even a complex hydride (see below).

Making this direct link with the redox process, it has recently been shown[2] that T_{dec} is nicely correlated with the standard redox potential for the metal cation / reduced metal electrode potential E^0. This type of connection is illustrated in Figure 2 which is a representation of the experimental T_{dec} versus E^0 data for a wide variety of binary hydrides. This type of experimental correlation for a broad range of chemically disparate metal hydrides also establishes the beginning of a ' sorting-map' for the important chemical properties of hydrogen stores.

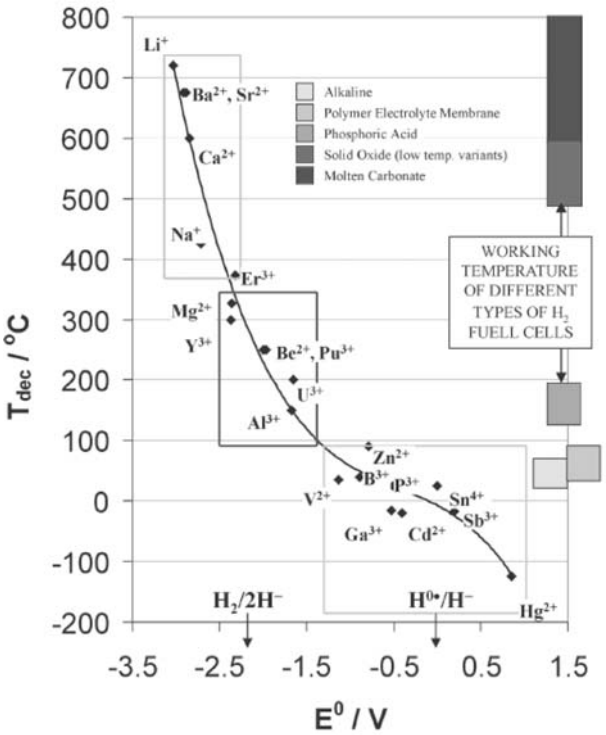

Figure 2. Correlation between temperature, T_{dec}, at which thermal decomposition of binary hydride MH_n to the constituent elements proceeds, and the corresponding redox potential of the redox pair M^{n+}/M^0 in acidic aqueous conditions. The ranges of the working temperatures for prototypical fuel cells are also shown (ref. 2).

Grochala and Edwards[2] (G and E) also established a rationalisation of this type of behaviour on the basis of thermodynamics and simple theoretical arguments whose origins lie in molecules.

In essence, along with an *increasing* electronegativity of the metal (and corresponding increase of the E^0 value) the energy of the valence orbital of M decreases and the orbitals become more contracted.

A substantial *decrease* of the ionicity of the M-H bonds and a decrease in the actual negative charge on the H centre result. This

type of ‘ screen play’ has H^- starting to resemble H^0 more and more as the metal’s electronegativity increases, where the attendant energy barrier for H_2 evolution decreases along with the characteristic T_{dec}. G and E have also attempted[3] to broaden the applicability of such an approach to ternary hydrides, and more recently to complex systems such as amido- (NH_2^-), imido- (NH^{2-}) and methyl anion (CH_3^-) model complexes of metal cations bound to the tetrahydroborate anion (BH_4^-). In Figure 3 we present the variation of the bridging BH bond lengths plotted against the respective E^0 value for the metal centre (*i.e.* the most typical redox pair associated with the designated oxidation state).

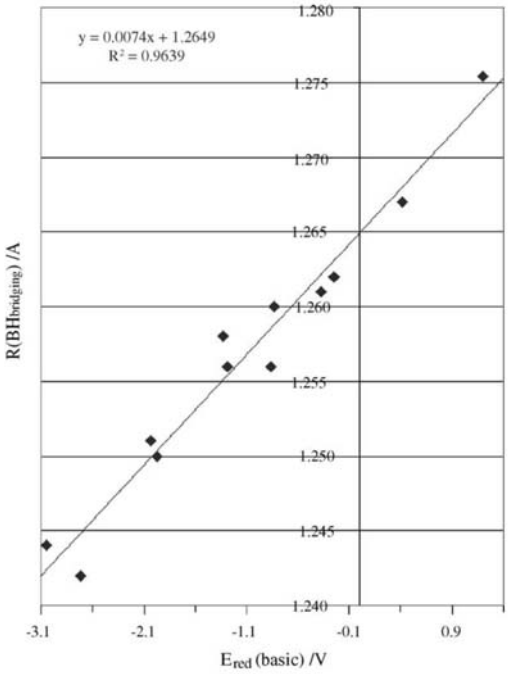

Figure 3. Correlation of bridging B-H bond distances with electrode potential (ref. 3)

In simple, terms, as the redox potential of the central metal centre increases, the bridging B-H bond length of attached BH_4^- anion becomes progressively longer. This important correlation supplements one’s chemical intuition of the third redox reaction associated with the liberation of elemental H_2 (see Eq. (1) and (2)), *viz.*

$$[M^{n+}L_n]HBH_3^- \longrightarrow [M^{(n-1)+}L_n] + \tfrac{1}{2}H_2 + \tfrac{1}{2}B_2H_6 \qquad (3)$$

since the value of the bridging BH bond length signifies the potential early stage of the BH bond rupture reaction yielding nascent H_2 and B_2H_6.

Here again, as the metal centre becomes a better electron acceptor (enhanced electronegativity), the charge density is transferred from the BH_4^- anion onto $[M^{n+}L_n]$, and the bridging BH bond which participates is the three centre M···H···B bonding becomes weaker and more ionic.

Interestingly, E^0 appears as a valuable predictor of the bond length of the bridging BH bond for a large family of systems, notwithstanding the wide variety of transition metal borohydride chemistries. We thus anticipate that the most potent oxidizing centres should release H_2 (and B_2H_6 via Eqn (3)) most easily… although (unfortunately) most probably irreversibly, in agreement with the earlier analysis of G and E.

In a parallel experimental study[4], we have highlighted the case of $LiBH_4$ as a highly effective chemical-activation agent, initially for MgH_2. The hydrogen desorption and absorption kinetics (Figures 4 and 5, respectively) show that the reaction of MgH_2 with quite modest amounts of $LiBH_4$ results in a spectacular increase in the kinetics of hydrogen desorption/absorption. Importantly, the rate of hydrogen desorption/absorption increased with each successive cycle for the first 4–5 cycles before stabilizing. Both the heat treatment and the initial cycling were necessary to activate the material: cycling a simple mixture of MgH_2 and $LiBH_4$ did not result in such ‘active’ material with fast kinetics

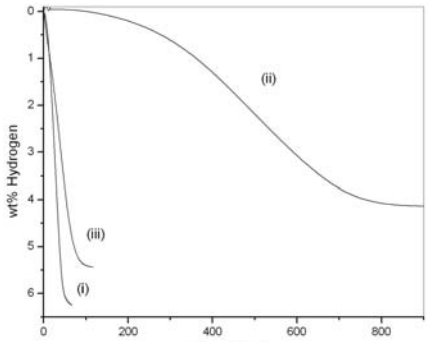

Figure 4. Hydrogen desorption kinetics at 300 °C under 10 mbar H_2 of i) $MgH_2/LiBH_4$, ii) as-received MgH_2 and iii) MgH_2 milled for 15 hrs; all samples measured on the sixth hydrogen desorption (ref. 4).

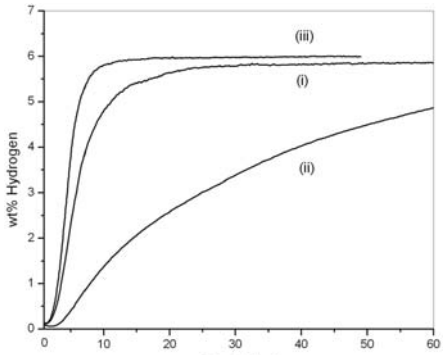

Figure 5. Hydrogen absorption kinetics at 300 °C under 10 bar H_2 of i) $MgH_2/LiBH_4$, ii) MgH_2 and iii) MgH_2 milled for 15 hrs; all samples measured on the sixth hydrogen absorption (ref. 4).

This type of ‘activation’ effectively supplements the approach outlined here. It also dovetails with the emerging route of ‘ destabilising’ hydrogen stores via innovative routes[5].

References

1. US Department of Energy, Office of Science (2004). Basic Research Needs for the Hydrogen Economy. *Report of the Basic Energy Sciences Workshop on Hydrogen Production*, [online]. Available from: http://www.sc.doe.gov/bes/hydrogen.pdf Accessed 14 April 2005.
2. W. Grochala and P. P. Edwards, *Chem. Rev.*, **104** (2004) 1283-1315.
3. P. P. Edwards and W. Grochala, accepted by *Journals of Alloys and Compounds*, (2005).
4. S. R. Johnson, P. A. Anderson, P. P. Edwards, I. Gameson, J. W. Prendergast, M. Al-Mamouri, D. Book, I. R. Harris, J. D. Speight and A. Walton, *Chem. Comm.*, **22** (2005) 2823.
5. J. J. Vajo, F. Mertens, C. C. Alm, R. C. Bowman, B. Fults, *J. Phys. Chem. B*, **108** (2004) 13977

Acknowledgements. We thanks thr EPSRC for their support of the UK-Sustainable Hydrogen Energy Consortium (UK-SHEC).

HYDROGEN PRODUCTION: AN OVERVIEW

David L. King

Energy Science and Technology Directorate
Pacific Northwest National Laboratory
P.O. Box 999, Richland, WA 99354
Fax: 509-375-2186, david.king@pnl.gov

Overview

Hydrogen is an attractive energy carrier because it can be produced from many sources, is a clean burning fuel that does not contribute to greenhouse gas emissions, and has the potential to significantly reduce the U.S. dependency on foreign oil. In the short term, it is anticipated that hydrogen will be produced from fossil fuels via reforming, an approach that still will co-produce CO_2. Thus, hydrogen production and consumption as a whole will still contribute to greenhouse gas production. This initial phase will also be necessary in order to establish the infrastructure for a hydrogen economy, define codes and standards, deal with safety issues, and gain public acceptance for the technology. In the longer term, the vision is to move hydrogen production to renewable sources based on biomass or solar energy, or through other sources that do not emit greenhouse gases, such as nuclear power. Coal may also be an important long term source of hydrogen, but carbon sequestration will be necessary to avoid greenhouse gas production. Thus, each approach to hydrogen production has its own benefits and challenges as well as the scale at which it is most efficient. This presentation will describe some of the technological approaches that are currently being examined for the production of hydrogen for both the short and long term, with an emphasis on the status of the technology, recent advances, and the challenges that remain.

PRESSURE SWING REFORMING OF LIQUID FUELS FOR HYDROGEN PRODUCTION

R. F. Socha, P. J. Berlowitz, F. Hershkowitz

ExxonMobil Research and Engineering Company
P.O. Box 998 Annandale, NJ 08801

Introduction

Steam reforming of hydrocarbons is a widely used process for manufacturing hydrogen on an industrial scale. Coupling this process, or other processes like partial oxidation and autothermal reforming, with a fuel cell presents significant challenges. Energy efficiency is a major design consideration, and at the scale of most fuel-cell applications, this along with rapid start-up and dynamic performance requirements dictate the characteristics of the system.

Pressure Swing Reforming (PSR) is a new process for the production of hydrogen from hydrocarbon fuels. It was first demonstrated in our laboratories using methane as the fuel. We have now extended the operation to a variety of gasoline-range fuels having sulfur contents up to 320 ppm. PSR uses a cyclic reverse-flow reactor to generate high-pressure (e.g., about 1000 kPa) undiluted synthesis gas ($CO+H_2$) at high temperature (up to about 1200°C) over a reforming catalyst, while the inlet and outlet gases remain at a relatively low temperature (less than 400°C). First, the reactor packing is heated by performing a regeneration step, burning waste fuel and air at low pressure as shown in the top of Figure 1. The process flow is then reversed with the primary fuel (e.g., gasoline) and steam as reactants and syngas as the product. This reaction can be run at higher pressure, especially if the fuel and water are initially present in the liquid phase and pressurized. The total cycle time (reforming plus regeneration) can be varied over a range of 5 seconds to 5 minutes in response to the overall flow rate.

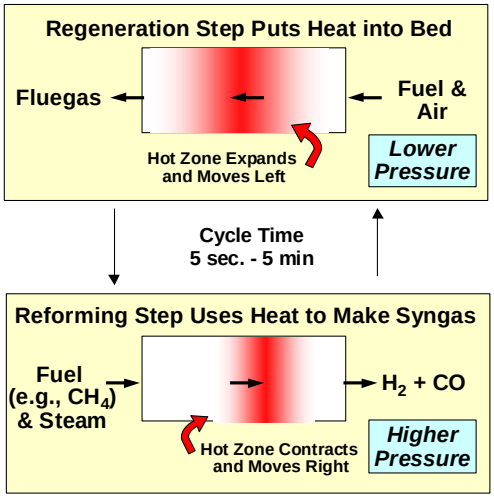

Figure 1. Cyclic reactor system moves heat in time - not across metal walls

The PSR minimizes the need for external heat exchange, making the process highly compact and efficient, and ideally suited to small systems incorporating a fuel cell.

To produce pure H_2, the synthesis gas is then fed to a separation step, which could be based on a membrane or pressure-swing adsorption. The purified hydrogen is then passed to a fuel cell, while the waste fuel returns to the PSR and is used to heat the catalyst. The O_2-depleted air from the fuel cell cathode is used as the oxidant. This configuration is shown schematically in Figure 2.

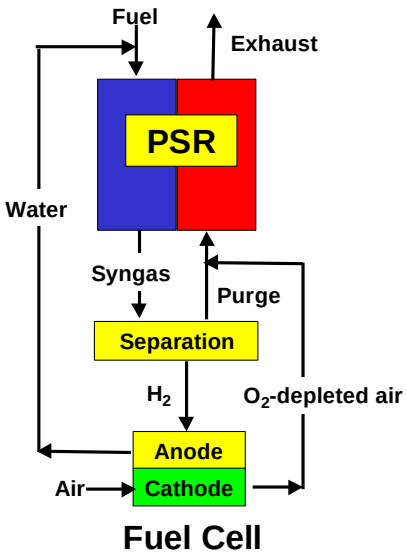

Figure 2. Simplified schematic of PSR integration with a fuel cell

Experimental

Reactions are carried out in the stainless steel double reactor shown in Figure 3. The gasoline fuel is injected into flowing steam in a specially designed mixer and fed to one or the other of the reactors though air-operated valves. While reforming is proceeding in one reactor, hydrogen (as a convenient surrogate for waste fuel) is combusted in the other reactor to provide the needed heat. The inlets and outlets to the two reactors are then switched so that reforming takes place in the second while the first reactor is reheated. The products are analyzed using an on-line mass spectrometer and samples are taken for quantitative analysis by gas chromatography.

The catalyst is a noble-metal washcoated on ceramic honeycomb monoliths. The total internal volume is about 1 liter. The entire operation is automated using LabVIEW software.

Figure 3. Dual-reactor for Pressure Swing Reforming (PSR)

Results and Discussion

We have been able to achieve gasoline conversions of greater than 95% at a gas hourly space velocity (GHSV) of 2500 (based on moles of carbon in the feed, equivalent to a space velocity of ~25,000 for typical catalytic partial oxidation or "autothermal" reformers) for many hours of operation. The conversion depends on a number of factors including the GHSV, the temperature and pressure in the reforming zone, the length of the operating cycle and the sulfur content of the gasoline feed.

Conclusions

ExxonMobil has demonstrated a novel process for the production of synthesis gas (and hydrogen) from liquid hydrocarbon fuels. This technology makes use of a cyclic reverse-flow scheme, which is more efficient than other current processors, especially on the scale used to power fuel-cell vehicles. We see numerous potential applications, including distributed hydrogen production, on-board Auxiliary Power Units (APUs), mobile, and automotive power.

Acknowledgement. We thank Bruce DeRites, Jeff Grenda, George Walchuk, John Brody, Greg DeMartin, John Siller, Elise Marucchi-Soos, Jeff Frederick, Rajeev Agnihoutri and Nick Rados for their contributions to this work.

STEAM REFORMING OF ALCOHOLS FOR HYDROGEN PRODUCTION

Yong Wang, Cathy Chin, Robert Dagle, Hyun-Seog Roh, David L. King, Jamie Holloday, and Daniel Palo

Pacific Northwest National Laboratories, 902 Battelle Blvd, Richland, WA 99352,

Introduction

Steam reforming of methanol and ethanol were studied. They both present different challenges. Methanol is clean, easy to activate, and is potentially an excellent fuel for hydrogen production for portable power applications. Conventional CuZnAl catalysts for methanol steam reforming have the disadvantages such as poor thermal stability and pyrophoric nature. We have developed a highly active and stable PdZn based catalysts for methanol steam reforming. Ethanol is renewable feedstock. Reforming of ethanol presents different challenges, particularly in improving hydrogen yield and minimizing catalyst deactivation due to coke formation. A highly active and selective Rh based catalyst has been developed for this particular applications

Results and Discussion

Steam reforming of methanol has been studied as a source of hydrogen production for the fuel cell due to its high hydrogen/carbon ratio, low sulfur content, and relatively low reforming temperature (250-350ºC) [i] Formation of CO as a by-product should be minimized to avoid deterioration of the fuel cell by CO adsorption. Most studies have been focused on Cu based catalysts which exhibit high selectivity to CO_2 and H_2[ii]. Copper based catalysts, however, have the disadvantages of poor thermal stability above 270°C and pyrophoric characteristic. Group VIII metals are markedly different from the copper catalysts. Over Group VIII metals catalysts methanol decomposes to CO and hydrogen. On the other hand, Iwasa *et al* were the first to report that Pd supported on ZnO and reduced at >300ºC has exceptionally high activity and selectivity to CO_2 and H_2 [iii]. The intriguing and promising performances of Pd/ZnO catalysts were attributed to PdZn alloy formation[iv]. The small amount of CO over PdZn catalysts in all literature reports was attributed to a small amount of metallic Pd species [v] which may be related to the catalyst preparation[vi]. We have confirmed this hypothesis using *in-situ* X-ray absorption experiments on the samples prepared using two different methods.

In the initial stages of our work on ethanol steam reforming, the role of the catalyst support was examined for ethanol steam reforming using Rh as the active metal. Rh was chosen since it is known to exhibit the highest activity of all the precious metals. It was also found that support identity rather than metal dispersion has significant effects on the activity with Rh/CeO_2-ZrO_2 exhibiting the best H_2 yield among the catalysts studied. In a subsequent series of experiments, the CeO_2-ZrO_2 support pre-calcination and catalyst calcination temperatures were systematically varied to evaluate the metal-support interaction and the related effects on H_2 yield. It was found the support pre-calcination temperature is not a significant factor between 500 and 800 ^oC despite the potential for sintering the CeO_2 phase. It has been established that acetaldehyde is a reaction intermediate and easily undergoes decarbonylation to form CH_4 and CO. Once CH_4 forms, high temperatures are required to reform it into CO and H_2. Therefore, in order to maximize H_2 formation, the CH_3 group (which is the precursor to CH_4) needs to be oxidized with steam before CH_4 is allowed to form. It is possible that Ce sites in CeO_2-ZrO_2 are partially oxidized under reforming conditions and these partially oxidized sites provide active oxygen species, which may suppress CH_4 formation. We speculate that the catalyst with appropriate pretreatment has better interaction between Rh and support as a result of the single calcination, resulting in more effective oxygen transfer. Further physicochemical characterization of this catalyst system will be presented.

References

[i] Peters, R.; Dusterwald, H.G.; Hohlein, B. *J.Power Sources*, 2000, 86, 507.
[ii] Trimm, D.; Onsan, Z.I. *Catal.Rev.*, 2001, 43 (1&2), 31.
[iii] Iwasa, N.; Kudo, S.; Takahashi, H.; Masuda, S.; and Takezawa, N. *Catal.Lett.*, 1993, 19, 211.
[iv] Chin, Y.; Dagle, R.A.; Hu, J.; Dohnalkova, A.C.; Wang,Y. *Catal.Today*, 2002, 77, 79.
[v] Suwa, Y.; Ito, S.; Kameoka, S.; Tomishige, K.; and Kunimori, K. *Appl.Catal.A:General*, 2004, 267, 9.
[vi] Chin, Y.; Wang, Y.; Dagle, R.A.; Li, X. *Fuel Processing Tech.*, 2003, 1681, 1

ANALYSES OF HYDROGEN PRODUCTION FROM SUB-QUALITY NATURAL GAS (II): SQNG STEM REFORMING AND AUTOTHERMAL STEM REFORMING

Cunping Huang, and Ali T-Raissi
Florida Solar Energy Center
University of Central Florida
1679 Clearlake Road
Cocoa, FL 32922

Introduction

Part (I) of this paper [1] has analyzed sub-quality natural gas (SQNG) pyrolysis and autothermal pyrolysis. Production of hydrogen via direct thermolysis of SQNGs produces two moles of hydrogen instead of four achieved by the steam reformation process. The main advantage of methane pyrolysis is the elimination of carbon dioxide production. However, coke formation that can cause catalyst deactivation occurs during the thermal decomposition of methane. Although some carbon-based catalysts may be able to resist deactivation, the lifetime of the catalysts still remains a big challenge.

The objective of Part (II) of this paper is to further explore the applicability of conventional technologies, namely steam reforming of methane (SRM) and autothermal steam reformation, in the treatment of SQNGs. Similarly to Part (I), a Gibbs reaction unit operation in the AspenPlus^{TM} chemical process simulator was applied as a thermodynamic analytic tool for equilibrium calculations for the SQNG + H_2O and SQNG + H_2O + O_2 systems. The main focus of the paper is to investigate the stability of hydrogen sulfide in these processes.

Steam reforming of SQNG (SRSQNG)

The compositions of SQNG applied in this paper are the same as in Part (I) with a 10% hydrogen sulfide concentration. The total carbon is calculated from the total hydrocarbons in SQNG, which is 110.10 mol/hr. The thermodynamic analyses are conducted in isothermal conditions, assuming that the inlet component mole flow rates are equal to their mole fractions. The inlet water flow rates are calculated based on the ratio of water to the total carbon moles (110.10 mol/hr), x = H_2O/C. The ratio of x is selected as: 0.25, 0.50, 0.75, 1.0, 1.5 and 2.0 corresponding the mole flow rates of 27.25, 55.05, 82.575, 110.10, 165.15 and 220.20 mol/hr, respectively.

Equilibrium flow rates of CH_4, H_2 and C. **Figure 1** demonstrates the flow rate of CH_4, H_2 and C with the reforming temperatures. CH_4 decomposition during SRSQNG is similar to that in SQNG pyrolysis. At temperatures above 850 ^oC since all the hydrocarbons are consumed, the hydrogen outlet rate remains constant. Compared to SQNG decomposition, which produces a maximum of 200kmol/hr hydrogen, the hydrogen production rate during the course of SRSQNG increases with water inlet flowrate and is greater than 200 kmol/hr. The greater hydrogen production results from the water splitting. However, when x is greater than 1.0, no significant increase in hydrogen production can be observed. When x = 2.0, the maximum hydrogen output is about 300 kmol/hr, indicating that only 100 kmol/hr of hydrogen is from the splitting of water, representing about 50% of the total water inlet. Water conversion increases with the decrease of water input, and reaches 100% when x is less than 1.0, suggesting that one mole of carbon can only split one mole of water in SRSQNG for the production of hydrogen.

In order to preclude carbon coke production during SRSQNG, the ratio x must be controlled. Carbon flow rates decrease with the increase of water inlet flow rate. At a lower x (< 1.0), carbon lay down occurs throughout the entire temperature range. Only when x > 1.0 does the carbon flow rate decrease to zero when the temperature is greater than 900 ^oC. This criterion is important to the reforming process in order to prevent catalyst deactivation.

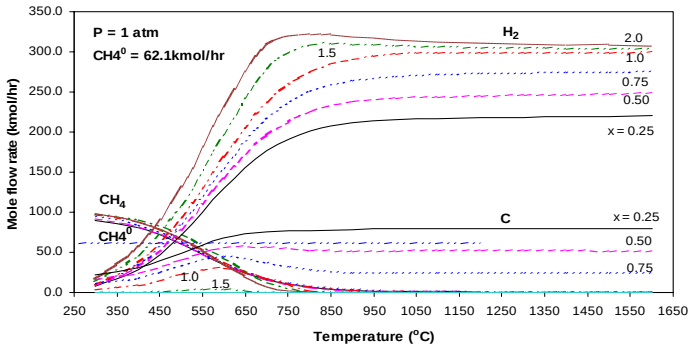

Figure 1. Equilibrium flow rates of CH_4, H_2 and C in SRSQNG (x = 0.25 to 2.0)

Equilibrium flow rates of H_2S, CS_2 and S_2. The equilibrium flow rates of H_2S at different x ratios are illustrated in **Figure 2**. The initial mole fraction of H_2S is 10.0%, corresponding to 10.0 kmol/hr inlet to a Gibbs reactor. H_2S decomposition during SRSQNG is similar to that in SQNG pyrolysis. H_2S does not significantly decompose at different water input levels when temperature is lower than 1200 ^oC, indicating that it is stable and can be considered as an inert gas in these conditions. Even when temperature is as high as 1600 ^oC, H_2S decomposition increase is still less than 30%. Interestingly, at temperatures greater than 1200 ^oC, water influence on the H_2S conversion can be separated into two significant ranges: when x < 1.0, H_2S conversion is higher than that when x > 1.0, suggesting that higher water input favors the stability of hydrogen sulfide.

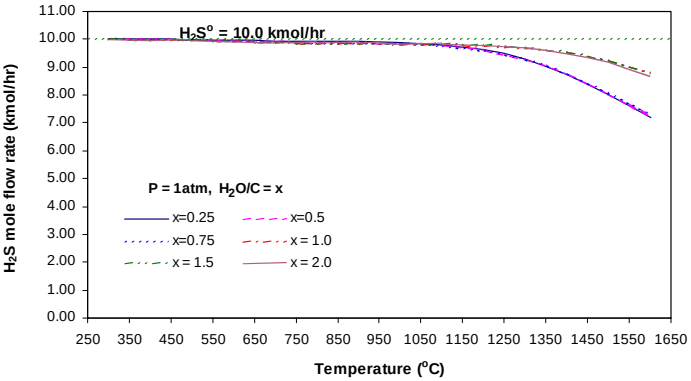

Figure 2. Equilibrium flow rates of H_2S in SQNGSR (x = 0.25 – 2.0)

Figure 3 illustrates the equilibrium flow rates of COS, CS_2 and S_2, which are dependent upon both temperature and input water flow rates. No SO_2 (or SO_3) is generated in the equilibrium mixture, showing that SRSQNG does not produce sulfuric acid gas, and therefore no environmental impact exists. Since SRSQNG occurs at temperatures between 700 to 900 ^oC, even though COS is a major byproduct its concentration is at a ppm range. The formation of COS is similar to the water gas shift process based on the reaction: CO + H_2S = 0.5H_2 + COS. Additionally, small amounts of CS_2 can be

observed when temperature exceeds 1200 °C. **Figure 4** indicates that the maximum CS_2 output flow rate occurs at a temperature of 1600 °C and is about 1.0 kmol/hr, accounting for less than 0.4% of total output gases. CS_2 is produced according to hydrogen sulfide methane reformation: $CH_4 + H_2S = 4H_2 + CS_2$.

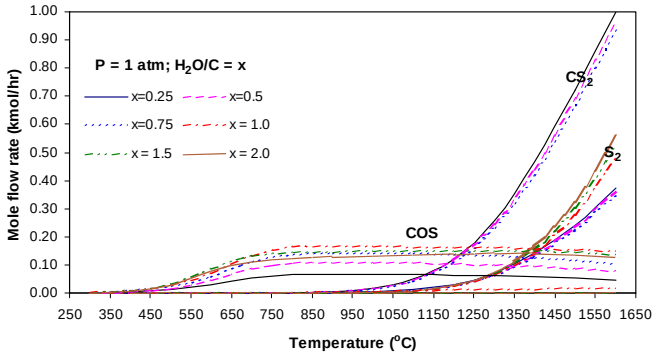

Figure 3. Equilibrium flow rates of COS, CS_2 and S_2 in SRSQNG (x = 0.25 – 2.0)

Autothermal steam reformation of SQNG (Auto SRSQNG)

SRSQNG is a highly endothermic process, requiring a large amount of energy input. To reduce the dependence of external energy sources, we can burn part of hydrocarbons in SQNG and the heat produced by internally burning can provide energy for SRSQNG. Two systems, SQNG + $0.0625H_2O$ + yO_2 and SQNG + $0.25H_2O$ + yO_2 are selected for investigating oxygen effects on SQNGSR. This preprint shows only results of x = 0.25.

Equilibrium flow rates of CH_4 and H_2. **Figure 4** depicts equilibrium flow rates of CH_4 and H_2 at various inlet oxygen levels, with x=0.25. Similar to the SQNG pyrolysis, all other hydrocarbons are decomposed into H_2, CH_4 and C within a temperature range of 300 ºC to 500 ºC. The CH_4 flow rates decreases with increases of either temperature or oxygen flow rate. On the other hand however, H_2 flow rates are independent of oxygen input ratio at y less than 0.375. When y increases to 0.50, hydrogen flow rate slightly decreases. The decrease is more significant for x=0.25 than for x=0.0625.

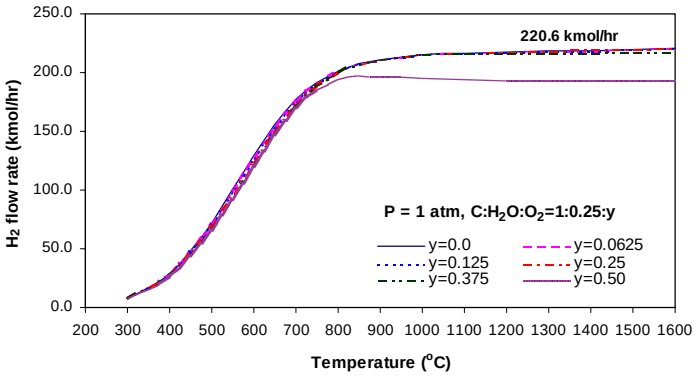

Figure 4. Equilibrium flow rates of CH_4 and H_2 at different oxygen inputs ($C:H_2O:O_2$=1:0.25:y)

Equilibrium mole flow rates of H_2S, COS, CS_2 and S_2. Equilibrium outputs of H_2S at x = 0.0625 and 0.25, with varying levels of oxygen input are similar to **Figure 2,** indicating the stability of H_2S during the course of autothermal SRSQNG. Unlike the effect of water on COS output rates, increasing the oxygen inlet rate results in the higher COS production rates shown in **Figure 5.** The effect is more significant at a low water input level. However, the effects of O_2 on output rates of CS_2 and S_2 are similar to the effects of H_2O.

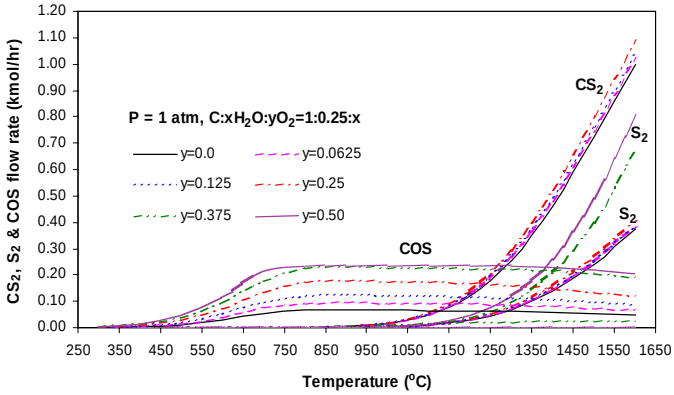

Figure 5. Equilibrium flow rates of COS, CS_2 and S_2 at different oxygen inputs ($C:H_2O:O_2$=1:0.25:y)

Heat of the autothermal SRSQNG. Heat requirements for the autothermal SQNGSR are depicted **Figure 6**. With increases in the oxygen inlet flow rate the total heat energy requirement decreases significantly, approaching energy neutral conditions. Comparing water inlet levels (y = 0.0625 and 0.25), it is found that at a higher water input to the system, higher oxygen inputs are required to reach a zero energy requirement condition.

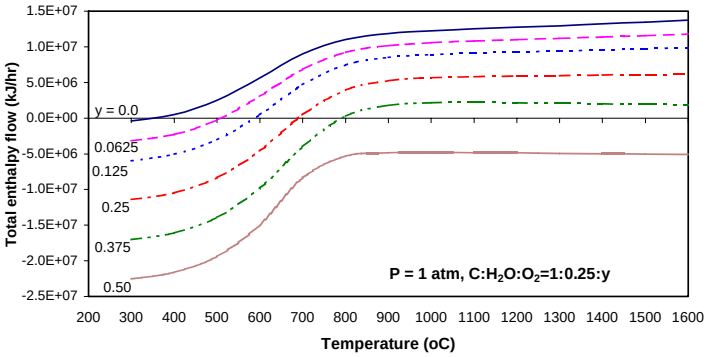

Figure 6. Total enthalpy change at different oxygen inputs ($C:H_2O:O_2$=1:0.25:y)

Acknowledgment

The authors are grateful for the financial support of the NASA-GRC Grant NAG3-2751 hydrogen project.

References

1. Huang, C., and Raissi, A., "Analyses of Hydrogen Production from Sub-quality Natural Gas (I): SQNG thermal decomposition and autothermal process" Preprint of the 230th ACS National Meeting, Washington, Aug 28-Sept 1, (2005)
2. Huang, C., and Raissi, A., "Liquid Hydrogen Production via Hydrogen Sulfide Methane Reformation" Preprint of the 228th ACS National Meeting, Philadelphia, August, 22-26 (2004)

A NEW PROCESS FOR THE PRODUCTION OF HYDROGEN FROM HYDROGEN SULFIDE

Prof.Israel E. Wachs, Andrew G. Gibson

Lehigh University Gibson Technologies
111 Research Drive 2293 LittlebrookeTrace
Bethlehem, PA 18015 Atlanta, GA 30338

Introduction

A new process for the production of hydrogen from hydrogen sulfide is described wherein carbon monoxide is reacted with hydrogen sulfide to produce hydrogen and carbonyl sulfide. The carbonyl sulfide is then reacted with oxygen to produce carbon monoxide and sulfur dioxide. The carbon monoxide is recycled back to the hydrogen sulfide reaction step.

Previous investigators have explored this basic chemistry but conversion and selectivities of desired products have been low. Recently, investigators under Prof. Israel Wachs at Lehigh University, have discovered a class of catalysts that dramatically improve conversion and selectivities to the point where the economics of this technology are a cost effective method of producing hydrogen.

Carbonyl sulfide (COS) is found in many industrial process streams such as those associated with natural gas production, petroleum refineries and coal gasification plants. COS is often catalytically converted by hydrogenation to methane (CH_4), hydrogen sulfide (H_2S), and water; by hydrolysis to carbon dioxide (CO_2) and H_2S, or by oxidation to CO_2 and SO_2. Hydrogenation is an expensive waste of increasingly valuable hydrogen (H_2) while hydrolysis and total oxidation produces CO_2, considered by many to be an environmental threat due to its alleged impact on global warming.

H_2S is encountered in refineries where hydrodesulfurization is widely used to remove sulfur from gasoline. Also natural gas geologic formations may contain as much as 10-30% . The H_2S is typically separated from the methane and the latter is distributed for consumer and industrial use. The H_2S is usually converted to elemental sulfur via the Claus process. In the Claus process, a first portion of the separated H_2S is oxidized by combustion to SO_2 and water. The remaining portion of the H_2S is reacted with water-laden sulfur dioxide in the presence of a suitable catalyst to produce additional water and elemental sulfur. Thus all of the potentially valuable hydrogen is lost to the atmosphere as water (The elemental sulfur is sold as a low priced commodity product).

The Wachs process (patented) would significantly improve the economies of sour gas recovery and would greatly benefit the operation of petroleum refinery operations.

Experimental

A series of experiments using selected metal oxides supported on oxides of different metals resulted in the choice of V_2O_5 on various metal oxides as a family of most effective catalysts for the oxidation of COS and CS_2 to CO and SO_2.

The CO thus generated could then be coupled with the known equilibrium reaction to reduce H_2S with CO , thus producing valuable H_2 and relatively "dry" SO_2.

1) $2COS + O_2 \rightarrow 2CO + SO_2$

2) $2CS_2 + 5\,O_2 \rightarrow 2\,CO + 4\,SO_2$

3) $CO + H_2S \Leftrightarrow H_2 + COS$

The oxidation reaction ,1), is very efficient over catalysts comprising a monolayer of vanadium(V_2O_5) on various metal oxide supports. For the supports examined, the Turnover Frequency trend (TOF) is: $CeO_2 > ZrO_2 > TiO_2 > NbO_2 > Al_2O_3 \sim SiO_2$.

COS and CS_2 are selectively oxidized to CO at yields between 90-100% (Table 1) .

The "dry" SO_2 thus produced (due to the H_2 being formed instead of H_2O) is advantageous to a Claus reactor because it favorably shifts the reaction towards the desired elemental sulfur product. Alternately, if used as a feed to a sulfuric acid plant, the moisture load and impurities to the SO_2 driers are greatly reduced, particularly in comparison to feedstocks obtained from smelters and other industrial sources.

Table 1. Oxidation of COS and CS_2 to CO Over V_2O_5 Supported Catalyst

Reactant	Temperature °C	TOF Yield $10^{-1} \times s^{-1}$	%
COS	330 max	0.3-2.0	90-100
CS_2	270 max	0.2-1.6	90

The CO thus produced is used to reduce the H_2S waste stream to hydrogen and co-product COS (equation (3 above). This COS is recycled to the process along with unreacted COS.

Results

The foregoing chemistry can be used to to design a process that yields valuable hydrogen from H_2S streams which now have only the value of their sulfur content. The hydrogen thus represents a value-added factor to H_2S streams.

In reference (1) a process outline describes the major steps as narrated below. See Figures 1 and 2.

CO may be obtained by oxidizing COS and/or CS_2 from industrial streams or by the steam reforming of methane. Figure 1 illustrates a COS/CS_2 oxidation reactor which may operate at temperatures ranging from 220º C to 350º C and a pressure from atmospheric to 500 psig. The reactants are fed in the vapor phase and contacted with a supported vanadium catalyst. The catalyst may be in the form of pellets or rings in a fixed bed or powder in a fluidized bed. Contact time in a fixed bed wherein the catalyst pellets or rings are packed into the tubes of a shell-and-tube reactor is in the order of 2-10 seconds. The effluent from this reactor contains the desired CO as well as unreacted COS/CS_2, O2, and byproduct SO_2. The components are separated in unit operations known to those skilled in the art. This oxidation reactor is shown again in Figure 2 where an additional fresh stream of COS and or CS_2 may also be introduced

In Figure 2, the hydrogen is generated by reacting H_2S and CO utilizing the known vapor phase equilibrium reaction described by Fukada, et. al., (2) (3). Temperatures in the range of 250ºC to 400ºC and pressures from atmospheric to 500 psig. are employed. A downstream series of separations is required to separate unreacted H_2S and CO for recycle. The H_2S can, for example, be absorbed in amine solutions and thermally desorbed for recycle. Other processing steps can be used to separate the hydrogen from COS.

The hydrogen product is collected and utilized for hydrogenation purposes or as a reactant in hydrodesulfurization

operations in a refinery. The COS is recycled to the oxidation reactor (Fig 1) to regenerate CO for the hydrogen reactor.

The SO_2 from these operations is a desirable feedstock for a sulfuric acid plant or a Claus plant (producing elemental sulfur) because of its low moisture content. The efficiency of both of these operations is enhanced by low moisture.

Conclusions

A catalytic process has been invented which permits the coupling of the known equilibrium reaction to produce hydrogen and a by-product COS with a new oxidation process for utilization of the COS. This is accomplished by oxidizing COS over supported vanadium catalyst(s) which results in high yields of CO. The COS becomes a useful recycle component, being alternately oxidized (by O_2)and reduced by the H_2S, thus yielding valuable hydrogen.

References

(1) Wachs, Israel E., US Patent 6,497,855, *Process for the Production of Hydrogen from Hydrogen Sulfide*, December 24, 2002

(2) Fukada, et. al., *Journal of Catalysis*, 49 3 79 (1977)

(3) Fukada, et. al., *Bulletin of Chemistry for Japan*, 51, 150 (1978)

CONVERSION OF HYDROGEN SULFIDE INTO HYDROGEN AND SULFUR

E. Krisanti, J.J. Robertson, G.B. Lucas, M.A. Plummer, and S.W. Cowley*

Department of Chemistry and Geochemistry
Colorado School of Mines
Golden, CO 90401

*MPr&d
Centennial, CO 80122-3708

Introduction

Hydrogen sulfide removal from natural gas or from gases produced by the petroleum industry typically involves air oxidation of hydrogen sulfide into elemental sulfur and water, as shown in equation (1). The Claus process, a gas phase oxidation reaction, and the Stretford™ process, a liquid phase oxidation reaction, are commonly used to remove hydrogen sulfide and produce sulfur in good quantity[1-2]. The Hysulf℠ process converts hydrogen sulfide directly into valuable hydrogen and sulfur, see equation (2).

$$8H_2S + 4O_2 \rightarrow 8H_2O + S_8 \quad \text{(Claus \& Stretford}^{TM}\text{)} \qquad (1)$$

$$8H_2S \rightarrow 8H_2 + S_8 \quad \text{(Hysulf}^{SM}\text{)} \qquad (2)$$

The Hysulf℠ process has two stages, see figure 1. In the first stage, at a reaction temperature of about 57 °C, hydrogen sulfide reacts with an anthraquinone to make the corresponding hydroanthraquinone and solid sulfur. In the second stage, at a temperature of about 200 °C, the hydroquinone is catalytically dehydrogenated to regenerate the anthraquinone and to make hydrogen gas, where R represents t-butyl in most of this work. Therefore, 2-t-butylanthraquinone is abbreviated as TBAQ and the corresponding hydro-2-t-butylanthraquinone as H_2TBAQ.

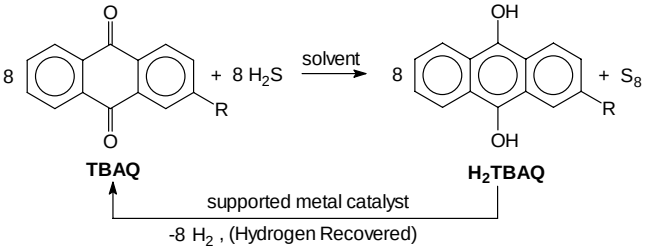

Figure 1. Two stage chemical process for converting H_2S into H_2 and S_8.

Although the Hysulf℠ process looks promising, a better understanding of the fundamental chemistry is required if the process is to be commercialized[3]. It is thought that the formation of a diradical anthraquinone intermediate is necessary for the reaction to proceed. The role of the solvent and substituents groups (R) in forming this diradial intermediate needs to be better defined. The goal of this study is to improve the rate of the anthraquione reduction and sulfur formation reaction in the first stage of the process by gaining a better understanding of the reaction mechanism, including the role of the solvent in promoting this reaction.

Experimental Methods

Reactor Tests. The reduction of TBAQ by H_2S was conducted in either a batch low pressure mini or batch high pressure micro glass stirred-tank reactor. The high pressure mini glass reactor is shown in figure 2. In a typical run, 30-60 mL of solvent containing 15 wt% of 2-t-butylanthraquinone (TBAQ) placed into the

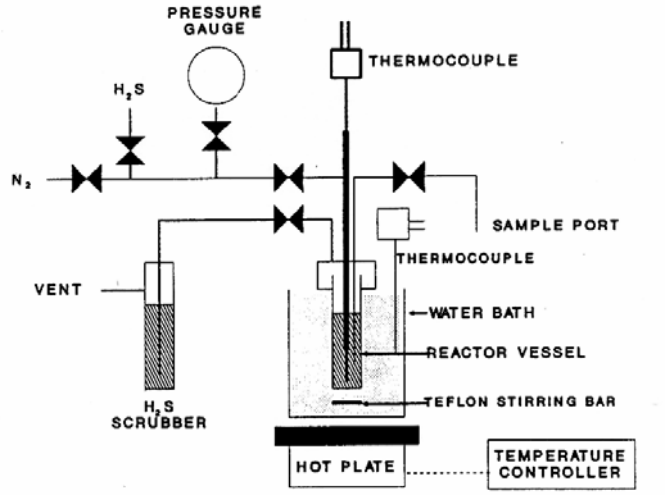

Figure 2. Schematic of batch mini reactor system.

reactor. The micro reactor was purged with N_2 gas for 15 minutes prior to continually flowing 60 cc/min of H_2S through the solution for the micro reactor at atmospheric pressure. Air removal is necessary to prevent oxidation of the H_2TBAQ product. The high pressure micro reactor was purged with N_2 gas prior to charging the reactor at a constant pressure of H_2S. The reaction was continually stirred using a magnetic stirring bar. A water bath was used to control the reaction temperature and an internal thermocouple was used to monitor the reaction temperature. A 1/16 inch o.d. stainless steel siphon tube was used to collect samples for NMR analysis. Unused H_2S was passed through a 1.0 M sodium hydroxide gas scrubber.

Analytical Methods. The effect of solvents and R groups on the formation of the diradical he products of the reaction were observed using a 60 MHz Varian EM360 or a 400 MHz ChemMagnetics NMR. The rate of TBAQ reduction by H_2S was monitored by measuring the increase in aromatic H_2TBAQ hydrogen signals centered at 7.5 and 8.6 ppm. The ratio of the H_2TBAQ peak areas to the total aromatic peak area was used to calculate the mole percent of TBAQ converted to H_2TBAQ.

Details of the TBAQ to H_2TBAQ reaction mechanism were studied using cyclic voltammetry (CV) and an electrochemical cell. A mercaptan or a bisulfide salt was added into the electrolytic cell to replace hydrogen sulfide as the protic agent. Lastly, sodium sulfide salt (NaSH) was added to the TBAQ solution to investigate the effect of the HS^- anion as an electron donor agent.

Results and Discussion

NMR was used to analyze the effect of H_2S pressure, temperature, and solvent polarity on the TBAQ reaction kinetics, and to identify the reaction intermediates produced in the stirred tank reactors. Figure 3 shows the change in the NMR spectrum TBAQ in N,N-dimethylacetamide (DMAC) solvent before and after reaction with H_2S. The reaction rate was found to be first order in H_2S and TBAQ and the rate law is given in equation (3).

$$\text{Rate} = k[H_2S][\text{TBAQ}] \qquad (3)$$

When the H_2S concentration was maintained constant through out the test, the rate is dependant only on the TBAQ concentration and a plot typical of a first order reaction was obtained, see figure 4. Significant TBAQ conversion was first observed after 15-20 minutes, indicating an induction period for the reaction. A

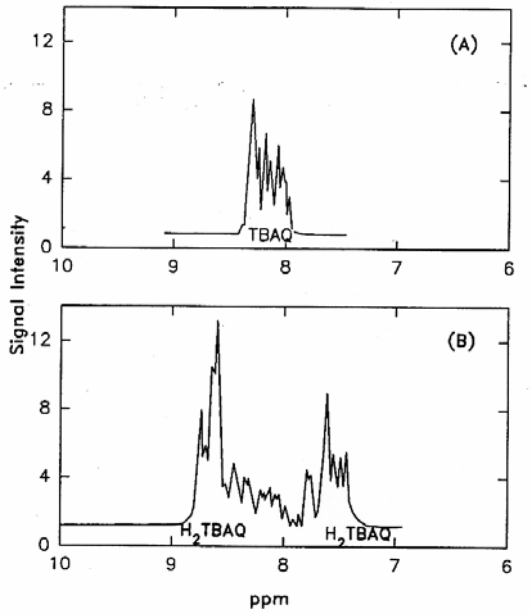

Figure 3. NMR of reactant TBAQ (A) and product H_2TBAQ.

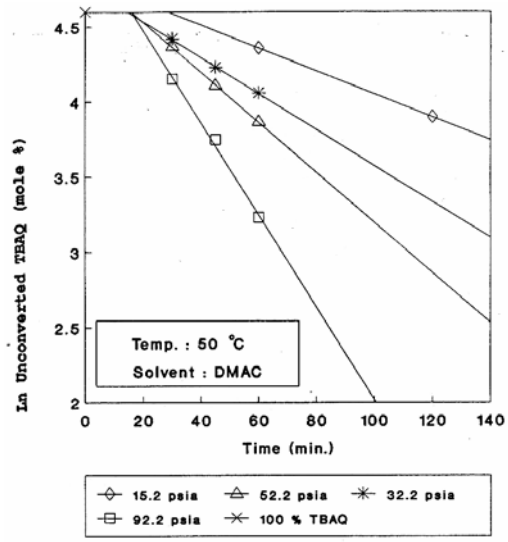

Figure 4. TBAQ conversion as a function of H_2S pressure.

temperature increase of 3 °C was observed when the solution containing TBAQ was initially charged with H_2S. After 2-3 minutes the excess heat dissipated and the reaction returned the desired temperature. The yellow colored feedstock briefly turned a bluish color, which is indicative of a rapid electron transfer reaction. The reaction proceeded to turn a green color and then a reddish brown color, which is indicative of H_2TBAQ formation. Eventually the reaction turned a very dark black color, which is typical of sulfur polymer formation, and finally a yellow solid (sulfur) was observed to precipitate out of solutions. The choice of solvent was also found to have a significant influence on the reaction kinetics. The reaction rate constant for DMAC is larger than that observed for N-methyl-2-pyrrolidinone (NMP). It is reported that H_2S solubility in both solvents is not much different[5-6]. Hence, there is a possibility that the molecular structure of the solvent plays an important role promoting the reaction.

After four hours of reaction time, NMP solvent gave ~53%, DMAC ~70%, N-methylacetamide ~35%, tetrahydrofuran 0%, and γ-butyrolactone 0% conversion of TBAQ to H_2TBAQ. The effect of solvent properties on TBAQ conversion was investigated further by NMR, see figure 5. There is a dramatic change in the NMR pattern

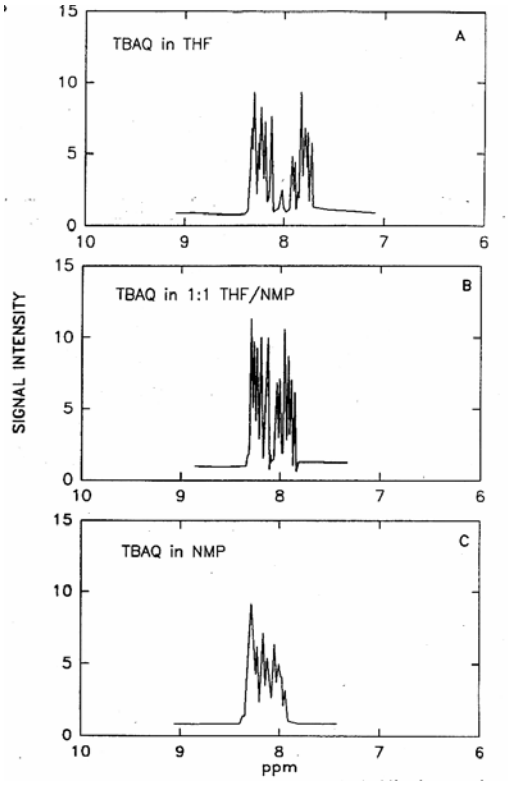

Figure 5. Effect of solvent on the NMR Proton Spectrum of the TBAQ aromatic region.

for the aromatic region of TBAQ as the relatively non-polar solvent THF (μ_D = 1.75 Debye) is replaced by the more polar solvent NMP (μ_D = 4.09 Debye). The NMR data suggest that anthraquinone is converted from the carbonyl to a diradical form as shown in figure 5. Computational analysis and reaction data suggests that the intitial step of the reaction requires the anthraquinone diradical and the formation of an HS^- species. The formation of these species is necessary to provide a good match between the TBAQ LUMO and HS^- HOMO energy levels. Cyclic voltammetry, computational analysis, and NMR analysis were used to obtain a more detailed picture of the reaction mechanism.

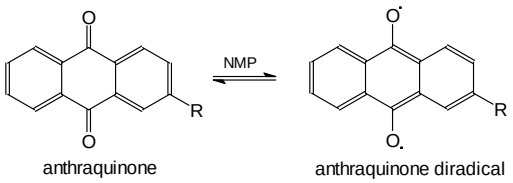

Figure 6. Conversion of anthraquione into anthraquione diradical in NMP solvent.

Conclusions

The experimental data show that solvent polarity is not the primary factor that affects the TBAQ conversion. The ability of the solvent to complex with the H_2S and/or the TBAQ to alter their respective HOMO and LUMO energy levels may be a requirement. Tertiary amides, such as NMP or DMAC, appear to be better solvents for TBAQ reduction than secondary amides, cyclic ethers, alcohols, or lactones.

Acknowledgement. This work was funded by Marathon Oil Company, MPr&d, and GRI.

References

(1) Kohl, A.L., and Riesenfeld, F.C., "Gas Purification, 4th Edition", **1985**, Gulf Publishing Company.
(2) Gary, J.H and Handwerk, G.E., "Petroleum Refining, **1984**, Marcel Dekker.
(3) Plummer, M.A, ""Gas Processing Developments: Sulfur and Hydrogen from H_2S", **1987**, Hydrocarbon Processing, April, 38, pp 38-40.
(4) Murieta-Buevara, F., and Rodrigquez, A.T., **1984**, "Solubility of Carbon Dioxide, Hydrogen Sulfide, and Methane in Pure and Mixed Solvents", J. Chem. Eng. Data, 29, 456.
(5) Hayduk, W. and Pahlevanzadeh, H., "The Solubility of Sulfur Dioxide and Hydrogen Sulfide in Associating Solvents", **1987**, Can. Chem. Eng., 65, 299.

HYDROGEN PRODUCTION AT THE PACIFIC NORTHWEST NATIONAL LABORATORY

Jamie Holladay, Daniel Palo, Robert Dagle, and Yong Wang

Pacific Northwest National Laboratory, 902 Battelle Blvd, MS k6-24, Richland, WA 99352, Fax: 509-376-3108, jamie.holladay@pnl.gov

Overview

Battelle, Pacific Northwest Division (Battelle) is actively developing compact portable or transportable fuel processors for hydrogen production to power hybrid fuel cell power systems. These systems are being developed under programs sponsored by the US Military, DOE, and Battelle. A broad range of fuels, such as methanol, ethanol, propane, natural gas, bench mark gasoline, and synthetic JP8, have been successfully reformed. For low power applications, methanol fuel processors were developed at outputs ranging from sub-watt to several hundred watts. For greater than 1 kW applications, fuel steam reforming systems operating on a variety of fuels, including synthetic JP8, have been developed. Each system employs Battelle's proprietary catalysts and patented microchannel architecture. These technologies enable compact hydrogen production systems for hydrogen storage or direct use in fuel cells. These fuel processors achieve over 70% thermal efficiency. Reactor design, catalyst properties and system considerations will be discussed.

CHEMICAL DURABILITY STUDIES OF PFSA POLYMERS AND MODEL COMPOUNDS UNDER MIMIC FUEL CELL CONDITION

David A. Schiraldi,[1*] *Chun Zhou*[1], *Thomas A. Zawodzinski Jr.*[2]

1. Case Western Reserve University, Department of Macromolecular Science and Engineering Cleveland, OH 44106, 2. Case Western Reserve University,Case Applied Power Institute & Department of Chemical Engineering,Cleveland, OH 44106

Introduction

Fuel cell technology has emerged as a promising platform from which to deliver future energy needs, directly converting the chemical oxidation of hydrogen or methanol to electricity. In the case of hydrogen fuel cells, Perfluorosulfonic acid (PFSA) polymers currently represent the leading candidates for use in proton exchange membranes, because of their high ionic conductivity and good mechanical, thermal and chemical stabilities. The chemical durability of these polymers is a critical issue for successful fuel cell applications and therefore has received a great deal of attention. Previous studies of membrane durability are both confusing and contradictory, suggesting radical attack at main chain carboxylate groups, tertiary C-F bonds in the main chain, and at side chain sulfonate groups. A systematic investigation of fuel cell membrane degradation mechanisms under operating conditions, using carefully selected model compounds as well as polymers, will be presented. This study shows that both carboxylic acid chain ends and ionomer side chains are kinetically-competent sites for peroxide radical attack. Degradation kinetics, reaction products, and radical trapping evidence will be presented in support of the conclusions.

Experimental

Key Materials. Nafion® film (structure shown in Figure 1) was purchased from Aldrich and used after transformation to its acid form. A developmental fluoropolymer ionomer was provided by 3M, and activated in a similar manner. Various model compounds (structures shown in Figure 2) were supplied from Synquest, 3M, and Lancaster.

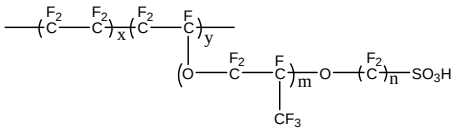

Figure 1. Chemical structure of Nafion ionomer

Methods

Durability Test Settings and Procedures. Aging experiments were carried out using Fenton's reagent[2]; the mechanism of the resulting radical generation using this treatment is shown in Figure 3. Two sets of Fe^{2+} and H_2O_2 reactant concentrations were employed – designated as "harsh" and "milder" – these are listed in Figure 3.

Nafion ionomer film samples were immersed in a flask containing Fenton's regaents as discussed above, and during the course of the aging experiment three additional follow-up additions of H_2O_2 were added in the flask to maintain the concentration of radical-generating species. Fluoride generation was measured (as will be discussed below) about every 24 hours. For Model Compound studies, the Model Compound was thoroughly mixed and stirred with the aqueous solution, and the H_2O_2 was added in the flask through an addition funnel. The reaction was allowed to sit for about 24 hours followed by fluoride concentration measurement, then the MC was separated and underwent subsequent aging and measurement. All the systems were continuously bubbled with nitrogen and maintained to be 70°C, which closely approximates polymer fuel cell operating temperatures. In an effort to separate the effects of model compound degradation from radical intermediates and any participation from the iron ions used in Fenton's reagent, selected model compounds were also subjected to hydrogen peroxide aging under UV irradiation (medium pressure mercury lamp). Samples were also UV aged in the absence of hydrogen peroxide to eliminate direct photolysis reactions as possible degradation pathways.

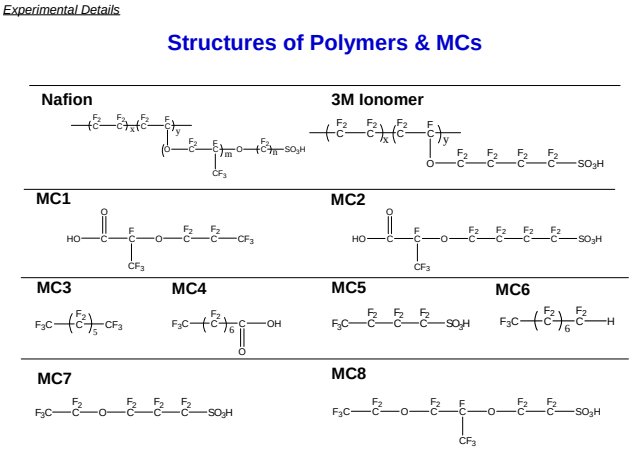

Figure 2. Chemical structures of Model Compounds

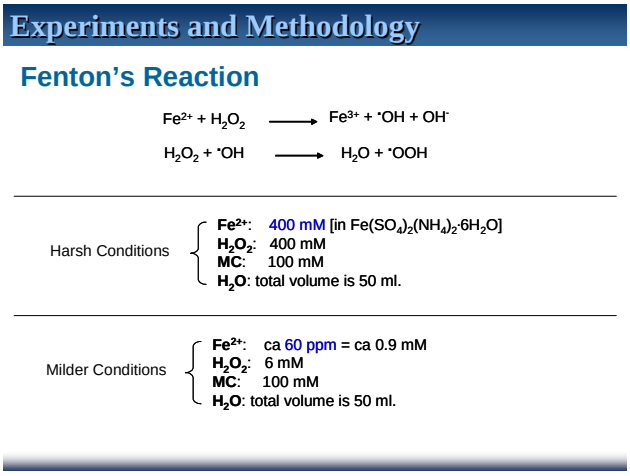

Figure 3. Fenton's reactions to create radicals (PH < 3)

Fluoride Concentration Measurement and Product Determination. The concentration of fluoride ions was measured by an ion selective electrode (ISE) (Mettler-Toledo), which was calibrated over the range 0.01 – 1000 ppm fluoride using NaF aqueous solutions. The interference from Fe^{2+} and Fe^{3+} as well as OH^- was eliminated by the dilution of tested sample (the sample was diluted for 100 folds), the validity of which was experimentally proven. Products of Fenton's reagent aging of model compounds were determined using ^{19}F nmr (Varian, 600 MHz).

Results and discussion

It is widely reported that fluoride ion is evolved in actual fuel cell effluent and during laboratory accelerated life studies[3-4]. The specific polymers sites from which fluoride is generated and mechanism of fluoride loss from the fluoropolymer membranes has not been unambiguously established, hence the motivation for this current work. We find that fluoropolymers, such as Nafion ionomer and the developmental alternative material from 3M, both generate fluoride ions at a linear rate when exposed to Fenton's Reagent. In our testing, the 3M material lost fluoride at approximately one third of the rate of the Nafion polymer. These polymers did not lose detectable levels of fluoride in the absence of hydrogen peroxide (i.e. neither hydrolysis, nor iron-catalyzed degradation are important in fluoride generation under our conditions).

Treatment of the model compounds with Fenton's Reagent also resulted in fluoride ion generation. The levels of fluoride ion generated from the most reactive model compounds closely matched those obtained with fluoropolymers. As can be seen in Figures 4 and 5, both the "harsh" and "milder" sets of Fenton's Reagent aging conditions resulted in largely linear fluoride release rates, and significant discrimination between specific model compounds. These results, when combined with 19F nmr analysis of the degraded model compounds, and with radical trapping of reaction intermediates, provide important insights into the mechanism of both model compound and PEM fluoropolymer membrane material degradation. Specific findings include: (1) confirmation that carboxylic end groups do indeed lead to rapid degradation of sulfonated fluorocarbon materials (supporting some literature reports); (2) the presence of alpha ether linkages enhance degradation rates; (3) the presence of tertiary C-F links significantly enhance radical degradation; (4) no evidence for degradation at the sulfonic acid moieties were observed, contradicting some literature reports; and (5) while carboxylic acid end groups are highly activated for degradation, side-chain fluoroether chain groups can also degrade at such a rate that they would be expected to contribute to the overall degradation of PEM membrane materials.

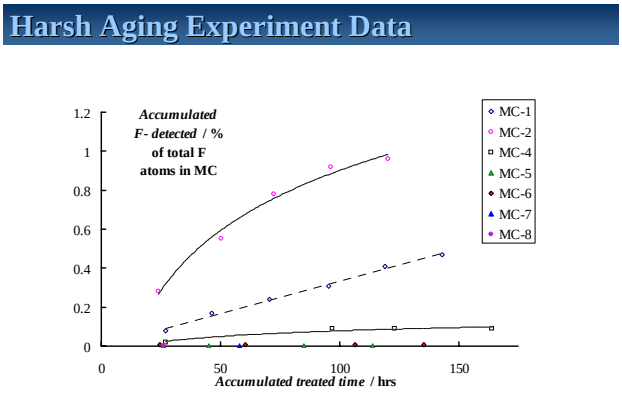

Figure 4. F^- concentration of Model Compound system as a function of aging time, Harsh Conditions

Table 1. Comparison initial rates of F^- generation

	F- Generated/Total Fluorine content, %
Nafion Ionomer	0.03 (0.26*)
MC-1	0.08
MC-2	0.28
MC-4	0.02
MC-5	0.008
MC-6	0.007
MC-7	< 0.001
MC-8	< 0.001

* Ratio % is Fluoride generated over the approximated total fluorine atoms on the side chains of Nafion.

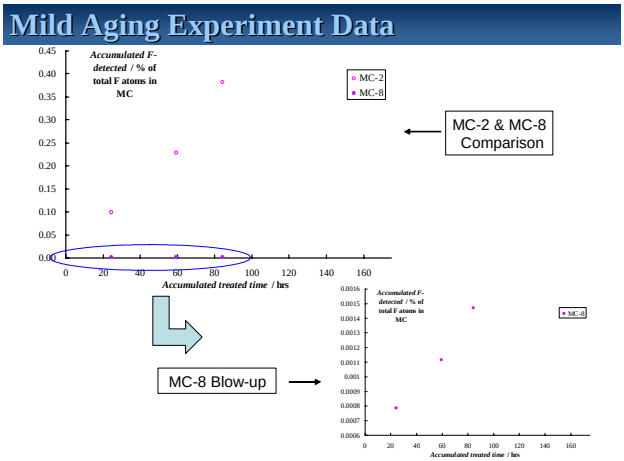

Figure 5. F^- Concentration of Model Compound system as a function of aging time, Milder Conditions

Conclusions

Operating under accelerated lifetime conditions, a systematic study of chemical decomposition products resulting from fluoropoplymer and model compound decomposition under Fenton's Reagent aging was performed. These data show that generation of fluoride is largely linear with treatment time, and is highly structure-dependent. Results to date strongly suggest that both carboxylic acid end group and side chain degradations can play kinetically-competent roles under simulated fuel cell operating conditions.

References

1. Gottesfeld, S.; Zawodzinski, T. *Advances in Electrochemical Science and Engineering*, Volume 5, Wiley, **1997**, edited by Alkire, R.C. et al..
2. Walling, C. *Acc. Chem. Res.* **1975**, *8*, 125.
3. Pozio, A.; Silva, R.F.; Francesco, M. De; Giorgi, L. *Electrochimica Acta* **2003**, *48*, 1543.
4. Baldwin, R.; Pham, M.; Leonida, A.; McElroy, J.; Nalette, T. *J. Power Sources* **1990**, *29*, 399.

Nafion® is a trademark of DuPont.

This research was supported in part by the Department of Energy, Cooperative Agreement No. DE-FC36-03GO13098. DOE support does not constitute an endorsement by DOE of the views expressed in this talk.

SHORT-SIDE-CHAIN PERFLUORINATED PROTON EXCHANGE MEMBRANES FOR PEMFC'S

Alessandro Ghielmi, Vincent Meunier, Luca Merlo, and Vincenzo Arcella

Solvay Solexis
viale Lombardia 20
20021 Bollate
(Milano) Italy

Introduction

Perfluorinated membranes known as ' short-side-chain' (SSC) are obtained by copolymerization of tetrafluoroethylene (TFE) and the sulfonyl vinyl ether monomer $CF_2CF\text{-}O\text{-}CF_2CF_2SO_2F$. Membranes with this chemistry were originally developed by Dow in the 80's, but relevant data in the literature are very scarce, due to the fact that these membranes were never widely available. The paper containing the most complete characterization is that by Tant et al.[1] The SSC perfluorinated membranes are presently becoming available again under the tradename Hyflon Ion. In the present paper more data are reported regarding the physical and electrochemical properties of the SSC membranes. From an applicative point of view, it is especially interesting to compare these properties with those of the long-side-chain (LSC) perfluorinated ionomer (Nafion), which is the current reference ionomer material for fuel cell (FC) membranes. While it is known that a higher glass transition temperature of Hyflon Ion (vs. Nafion) makes it more promising for high temperature PEMFC operation (T>100°C), favourable properties in terms of conductivity and FC performance are demonstrated also at lower temperatures, ranging from ambient temperature to temperatures in the order of 80°C currently used for the stationary application.

Experimental

Sample preparation. Membranes of different equivalent weight (EW) were obtained by melt extrusion of the polymer in the precursor (sulfonyl fluoride) form, and subsequent hydrolysis in a strong base at 80°C and acid exchange in a strong inorganic acid at ambient temperature. EW was determined by base titration of the sulfonic groups of a pre-weighed dry piece of membrane.

Tensile properties. Tensile properties were measured according to ASTM D1708. Measurements were carried out both on dry and wet membranes. Here, ' dry' stands for the membrane at laboratory conditions, i.e., 23°C and 50% relative humidity, while ' wet'refers to the membrane soaked in water at 100°C. In all cases the tensile test was carried out at laboratory conditions (23°C and 50% RH). In the case of wet membranes, these were extracted from the water and the measurement was carried out immediately.

Water uptake. Water uptake from liquid water at 100°C was measured by weighing the samples dry and after soaking in boiling pure water for 30 min. Weighing after water soaking was performed by blotting the samples dry on the surface and rapidly weighing.

Water uptake from water vapour at different relative humidities was measured by weighing the samples dry and after exposure to water vapour in a closed vessel containing water saturated with different salt systems, corresponding to different vapour activities.

Dry weight was determined on the samples kept for 1h at 105°C under vacuum.

Conductivity. Membrane conductivity as a function of relative humidity was measured by impedance spectroscopy analysis inside a thermostatted cell where relative humidity was controlled by injection of measured quantities of water vapor.

Fuel cell performance. Fuel cell performance was measured using a Fuel Cell Technologies test station with 25cm^2 active area single cells. Commercial Elat (E-Tek) gas diffusion electrodes with 0.5 mgPt/cm^2 catalyst loading (30% Pt/C) were used. Before taking the polarization curve measurement, the membrane-electrode-assembly was conditioned in the cell at the temperature, pressure and relative humidity conditions of the measurement and at a fixed voltage (0.4V) until the current was constant for at least three hours.

Results and Discussion

Tensile properties are shown in Figure 1 as a function of EW both for wet and dry membranes. It can be seen that stress at break is significantly growing with increasing EW's, which can be related to increasing crystallinities and molecular weights of the polymer.

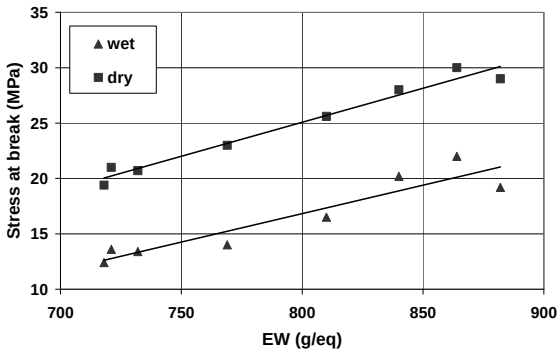

Figure 1. Tensile stress as a function of EW.

It was shown by Arcella et al.[2], that SSC membranes with EW around 850-900 g/eq have similar tensile properties compared to Nafion with EW=1100. This is true both in the dry and wet state, and can be likely related to similar levels of crystallinity.

Figure 2 shows the water uptake behavior from vapor at different relative humidities measured at 30°C on a membrane of EW=850. The curve measured on Nafion 1100 EW is also reported. A sigmoidal shape curve results, in agreement with previous data reported in the literature for Nafion. It can be seen that water uptake is similar for Hyflon Ion (850 EW) and Nafion (EW 1100) up to over 80% RH. At saturation, Hyflon Ion absorbs more water than Nafion, which is in agreement with higher water uptake values measured on Hyflon Ion in pure liquid water (about 45% water uptake for Hyflon 850 EW vs 35% water uptake for Nafion 1100 EW at 100°C).

Figure 3 shows the conducitivity of Hyflon Ion 850 EW vs. Nafion 1100 EW as a function of relative humidity at 35°C. It can be seen that the conductivity of Hyflon Ion is higher. Since this happens throughout the whole RH range, this can be related mainly to the lower EW of the Hyflon Ion (higher concentration of the ion-exchange groups), since the water uptake has been shown to be practically the same in a wide range of RH (Figure 2). This higher conductivity of an 850 EW Hyflon Ion clearly represents an advantage for fuel cell operation. It is noteworthy that higher conductivity levels are obtained with similar mechanical properties.

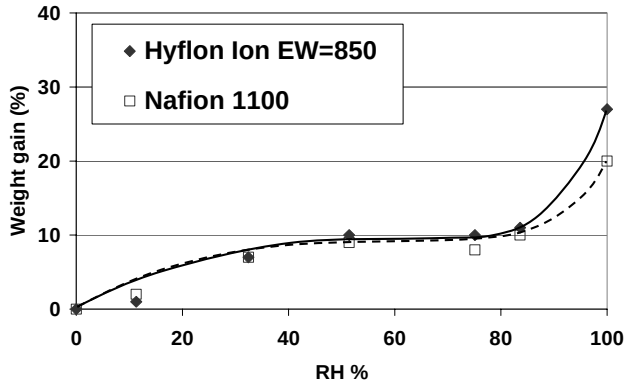

Figure 2. Water uptake from the vapor phase at different relative humidities.

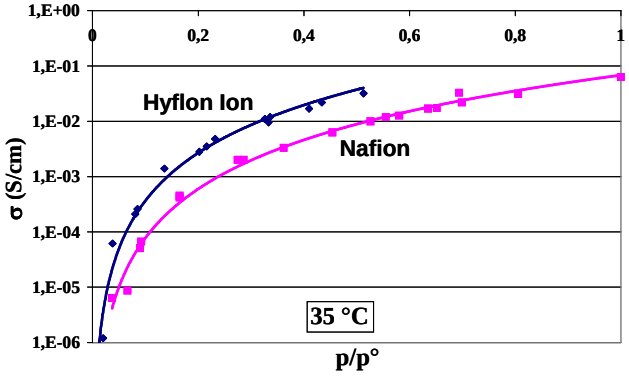

Figure 3. Conductivity data of ionomers at increasing RH (p/p^0)

Fuel cell performance of Hyflon Ion membranes 850 EW was measured at temperatures ranging from 30°C to 80°C and above. In all cases, it was found that the higher conductivity of the membrane delivers higher fuel cell performance in terms of polarization behavior. Figure 4 shows as an example the FC performances measured at 30°C in H_2 and air under complete reactant humidification. The gain given by the use of the lower EW SSC ionomer is apparent. Similar results are obtained at different temperatures, the gain in polarization behavior being more or less marked according to FC operating conditions. In no operating condition among those examined was the performance of Hyflon Ion found to be worse.

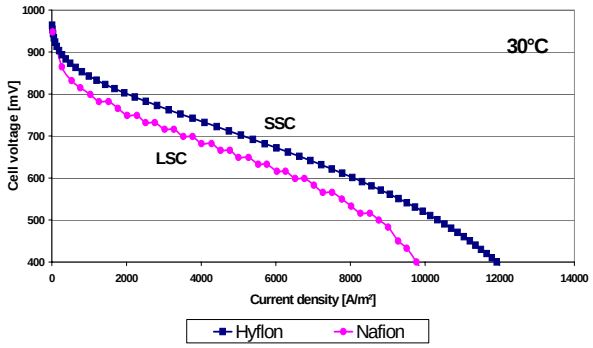

Figure 4. Fuel cell performance at 30°C.

Conclusions

Favorable mechanical, thermal and conductivity properties measured on short-side-chain (SSC) membranes make them ideal candidates to be employed in PEMFC's, both in high temperature systems (e.g. automotive, >100°C), in medium temperature systems (e.g. stationary, 70-80°C) and ambient temperature micro-FC's (portable application). SSC ionomer membranes are currently under development at Solvay Solexis with the tradename Hyflon Ion.

References

(1) Tant, M.R.; Darst, K.P. ; Lee, K.D. ; Martin, C.W.; Multiphase polymers: blends and ionomers, L.A. Utracki, R.A. Weiss (Eds.), ACS Symp. Ser. 395, ACS: Washington, 1989.

(2) Arcella, V.; Ghielmi, A.; Tommasi, G.; *Ann. N.Y. Acad. Sci.*, **2003**, *984*, 226.

IMPORTANCE OF SULPHONIC ACID DISTRIBUTION PATTERN FOR LOW EQUIVALENT WEIGHT POLYAROMATIC MEMBRANES

N. Walsby[1], M. Hogarth[1], D. Thompsett[1], H. M. Colquhoun[2], W, Mortimore[2], Z. Zhu[2]

[1]Johnson Matthey Technology Centre,
Blounts Court, Sonning Common, RG4 9NH, UK
[2]School of Chemistry, University of Reading,
Whiteknights, Reading RG6 6AD, UK

Introduction

There is a need for fuel cell membranes capable of operating at low relative humidities, either at 80°C or at higher temperatures. Polyaromatic membranes are the main rivals to commercial perfluorinated membranes. They are attractive because of their good thermo-mechanical characteristics and chemical stability, and because a vast range of different ionomers is possible.[1] Thus, we can systematically vary the ionomer structure and assess the significance of specific structural changes. Our general aim is to maximise the conductivity of polyaromatic membranes and to determine the ultimate performance limits of this class of membrane. The simplest way to increase proton conductivity is clearly to increase the concentration of sulphonic acid groups on the polymer chain. However, the maximum achievable concentration before the polyaromatic polymer becomes water-soluble has always been lower than in commercial perfluorinated membranes such as Nafion. We now report that controlling the sequence-distribution of sulphonic acid groups along the polymer chain can extend the concentration range possible with polyaromatics. Three aromatic polymers of very similar equivalent weight but different structure were prepared. The first (A) was a standard statistical polyethersulphone copolymer, the second (B) a statistical copolymer with more extended (3- and 4-ring) comonomers, and the third (C) a homopolymer with a highly extended (9-ring) repeat unit. The structures are shown in Figure 1.

Experimental

Polymer Synthesis[2] *Polymer A* was synthesized as described in US 5,693,740. The ratio of m:n was m=0.5n.

*Polymer B.*The dihalide monomers were made by conventional Friedel-Crafts reactions, and comonomers 4,4'-biphenol, 4,4'-dihydroxydiphenylsulphone, 4,4'-bis(4-chloro-benzenesulphonyl)biphenyl and 1,3-bis(4-fluorobenzoyl)benzene were polymerised in diphenylsulphone in the presence of K_2CO_3 at 290 °C.

Polymer C. Monomer synthesis: Isophthaloyl dichloride, 4-(4'-chlorobenzenesulphonyl)-biphenyl and aluminium chloride were heated with stirring in trichlorobenzene at 150 °C until HCl evolution virtually ceased. After cooling, the viscous solution was poured into a mixture of water and concentrated HCl. The aqueous phase was separated and the yellow viscous product was treated with hexane and then stirred in methanol. The white–yellow powder was dried under vacuum overnight and then recrystallized twice from DMF to give the monomer as a white powder. Polymerisation: the monomer underwent polycondensation with 4,4'-biphenol in diphenylsulphone in the presence of K_2CO_3 at 290 °C. The solid product was extracted with methanol and with water before drying under vacuum.

All polymers were sulphonated in concentrated sulphuric acid. Membranes were cast from ionomer solutions in NMP.

Fuel Cell Evaluation. Membranes were sandwiched between two electrodes in an electrochemical cell. The 3cm² active area electrodes were prepared using Toray TGP-H-60 carbon fibre current collecting substrate that was coated with a combination of carbon black, polytetrafluoroethylene polymer, platinum black electrocatalyst and Nafion® ionomer. The fabricated electrodes and membranes were pre-wetted in pure water prior to testing to ensure full hydration. The Membrane Electrode Assemblies (MEAs) were characterised using steady state electrochemical polarisation experiments. The fuel cell operated at 80°C with fully humidified hydrogen and oxygen, both at a pressure of 30 psig. Current-interrupt experiments were carried out to determine the ionic resistance of the membranes.

The long-term performance of membrane C was determined by fuel cell testing over an extended period until the MEA failed e.g. through the formation of pin-holes. Fully humidified hydrogen and air were supplied to the MEA, which contained 35µm thick membrane. Testing was carried out at 80 °C at a pressure of 30 psig at a constant current density of 500 mA/cm² with the same electrodes detailed previously, but with an active area of 49 cm^2.

Results and Discussion

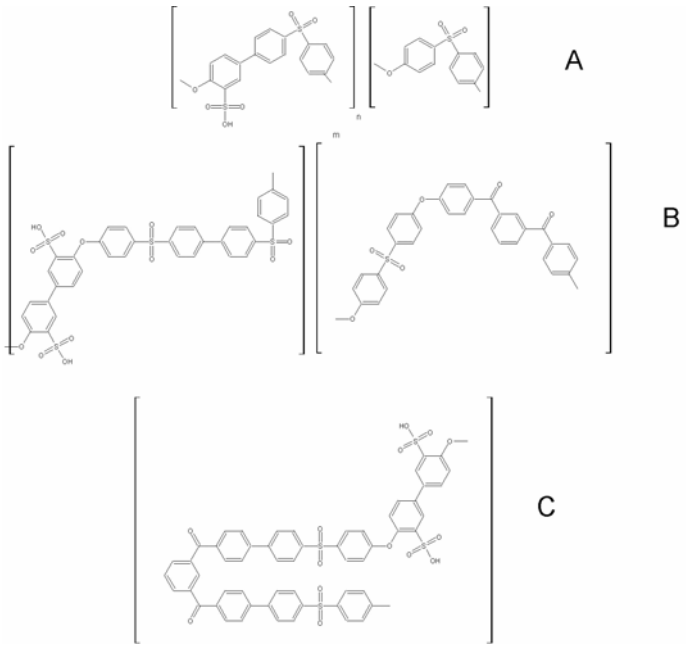

Figure 1. Structures of the polymers studied in this work.

Table 1 shows some of the characteristics of the polymers. Viscosity measurements on the unsulphonated polymers show A, B and C to be of high molecular weight (inherent viscosities > 1.0).

Table 1. Properties of polymers A, B and C.

	IV dL/g	Tg °C	IEC meq/g	$[SO_3H]$ mol/L
A	1.28	261	1.98	2.41
B	1.16	234	1.98	2.56
C	1.35	247	2	2.48

Acid-base titrations confirmed that the three polymers had very similar ion-exchange capacities. At around 2 meq/g, these ion-exchange capacities are very high (corresponding to an equivalent weight of ca. 500). The concentrations of sulphonic acid groups (calculated for dry membranes) are also similar and around 2.5

mol/dm³. In comparison, the measured ion-exchange capacity and concentration of sulphonic acid groups for the Nafion 1100 series membranes were 0.91 meq/g and 1.74 mol/dm^2 of dry membrane. For Flemion SH30 (Asahi Glass) the values were 1.02 meq/g and 1.86 mol/dm^2 of dry membrane.

The water uptake characteristics of membranes A, B and C as a function of temperature are shown in Figure 2. The water uptake values follow a general pattern common to ionomers: there is a gradual increase followed by a rapid swelling as the membrane becomes gel-like and finally dissolves. Kreuer[3] reported that, for sulphonated polyetheretherketoneketone of ion-exchange capacity 1.78 meq/g, the dramatic swelling that preceded dissolution began at ca 65 °C. For Nafion this temperature was reported to be 140 °C. Figure 2 shows that, despite similar concentrations of sulphonic acid groups, the water uptake behaviour is very different for membranes A, B and C. Membrane A has a higher water uptake at low temperatures and begins to swell dramatically at ca 60°C. For membrane B, excessive swelling is not encountered until 80 °C, while membrane C did not begin to swell excessively below 100 °C. It is clear that concentrating the sulphonic acid units in groups along the polymer chain and increasing the average separation between them, i.e. going from structure A to structure B, reduces the tendency of the membrane to swell in water. Taking this further and imposing a fully-defined "spacer" between sulphonic acid groups suppresses water uptake further. For fuel cell membranes this is highly advantageous as it allows the concentration of sulphonic acid groups to be increased beyond what was previously possible in polyaromatic membranes.

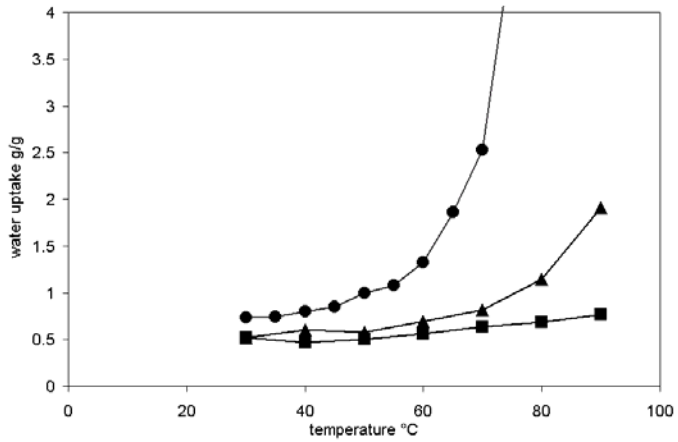

Figure 2. Water uptake as a function of temperature for membranes A (●), B(▲) and C (■)

The fuel cell data obtained with membranes A, B and C are shown in Figure 3, along with data for a commercial "state-of-the-art" membrane, Flemion SH30. All three aromatic membranes show excellent performance, comparable to that of Flemion SH30. The similarity in performance for membranes A, B and C indicates that, at these high concentrations of sulphonic acid groups and when compressed in a cell, differences in morphology resulting from the different structures give no clear advantage in terms of performance. A very clear difference, however, was seen in lifetime: membrane A barely survived long enough for the data to be collected. Membrane B was more robust but failed rapidly when tested in 50 cm^2 hardware. A lifetime test at a constant current density of 500 mA/cm^2 with membrane C is shown in Figure 4. The performance was stable for 500 hours. These differences reflect the difference in mechanical properties between the polymers in a fully humidified environment. The highly swollen polymer A, and to a lesser extent polymer B, are susceptible to partial dissolution and also liable to bursting under very small pressure differences.

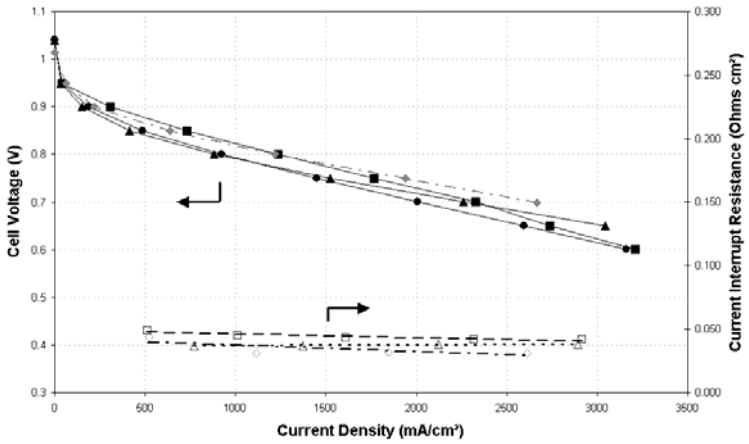

Figure 3. Oxygen polarisation data for membranes A (●), B(▲) and C (■) and Flemion SH30 (♦).80°C, 30 psig. Fully humidified H_2/O_2

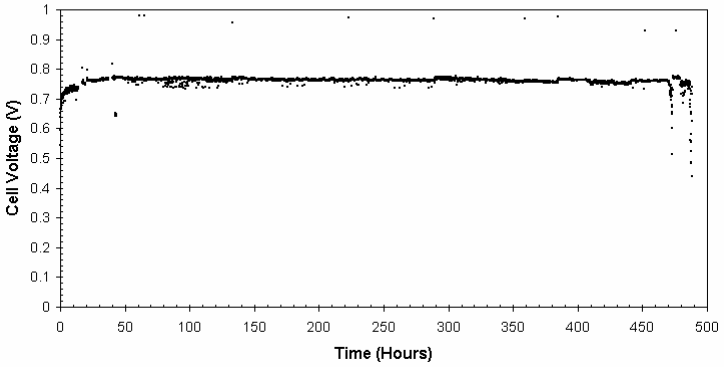

Figure 4. Lifetime test for membrane C in 49 cm^2 cell at a current density of 500mA/cm^2, 80°C, 30 psig. Fully humidified H_2/Air, stoichiometries of 1.5 and 2 respectively.

Conclusions

Imposing a fully-defined hydrophobic spacer between pairs of sulphonic acid groups along the polymer chain has a dramatic effect on the macroscopic swelling of polyaromatic membranes. The reduction in swelling enables membranes of lower equivalent weight to be used. This in turn improves conductivity and should enable the membrane to be used at lower relative humidities. Studies are underway to probe the differences in micro/nanostructure between the statistical copolymers and the homopolymer.

References

(1) Hickner, M. A.; Ghassemi, H.; Kim, Y. S.; Einsla, B. R.; and McGrath, J. E. Chem. Rev. **2004**, *104*, 4587
(2) Johnson Matthey, PCT/GB2005/000077
(3) Kreuer, K. D. *J. Memb. Sci.* **2001**, *185*, 29

THE USE OF HETEROPOLY ACIDS IN HIGH PERFORMANCE COMPONENTS FOR PROTON EXCHANGE MEMBRANE FUEL CELLS

Andrew M. Herring,[1] John A. Turner,[2] Steven F. Dec,[3] Fanqin Meng,[1] Jennifer L. Malers,[1,2] Ronald J. Stanis,[1,2] Niccolo Aieta,[1,2] and James Horan[3]

Department of Chemical Engineering[1] and Department of Chemistry and Geochemistry,[3] Colorado School of Mines,
Golden, CO 80401.
Hydrogen and Electricity, Systems and Infrastructure Group,[2]
National Renewable Energy Laboratory,
Golden, CO 80401.
Email:aherring@mines.edu

Introduction

There is increasing interest in using the heteropoly acids, HPA, as proton conducting components or additives in proton exchange membrane (PEM) fuel cells for elevated temperature operation, 120 – 200 °C, or to decrease the humidification requirements of PEMs.[1-6] Operation of a PEM fuel cell at these elevated temperatures will allow the integration of the stack into existing vehicular cooling systems, as well as stationary CHP, and use of hydrogen with an elevated CO content, simplifying the overall design of the reformer needed to generate hydrogen from hydrocarbons. The ultimate goal of a PEM requiring no external humidification will lead to further system simplification. The heteropoly acids (HPA) are a large and structurally diverse class of inorganic proton conducting materials[7] with extremely high room temperature proton conductivities, as high as 0.2 S cm^{-1} for 12-phopshotungstic acid.[8] importantly, for elevated temperature PEM fuel cell operation, the HPA are structurally stable to temperatures in excess of 600 °C and incorporate water molecules and protons to temperatures in excess of 300 °C depending on the system.

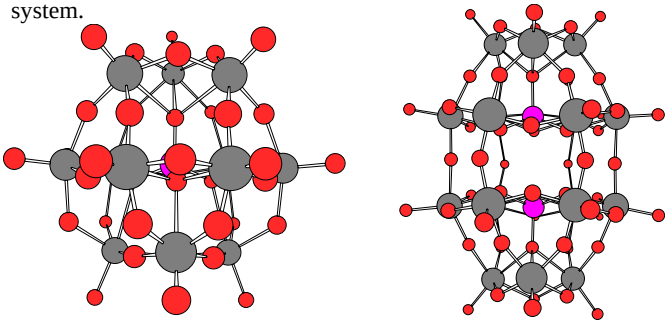

Figure 1. Structures of the Keggin anion, $H_3PW_{12}O_{40}$, 12-HPW , left and Dawson anion, $H_6P_2W_{18}O_{62}$, 18-HP2W, right.

Most studies to date have only considered the commercially available Keggin structures, consisting of a tetrahedral arrangement of three tungsten or molybdenum oxygen octahedral surrounding a central heteroatom, Figure 1. Many other structures are possible including the more thermally Dawson structure, Figure 1 and structures of increasing complexity. Importantly Lacunary structures may be derived from the parent Keggin or Dawson by the removal of 1,2 or 3 metal oxygen octahedral leaving a vacant site that may be used as a covalent attachment point for the synthesis of hybrid materials or a coordination site for another metal center.

Because of their structural diversity these materials are particularly suitable for incorporation into a wide variety of membrane materials. In addition, the HPA have interesting redox and catalytic properties that can be exploited for PEM fuel cell applications and must also be fully understood before a practical system incorporating HPA can be developed. We have continued to study HPA in perfluorinanted sulfonic acid, PFSA, polymers such as Nafion®. As the HPA are not immobilized in these systems they can migrate towards one or other of the electrodes leading to improvements in performance that may have more to do with the electrode/membrane interface than to intrinsic changes to the properties of the membranes alone.

Experimental

The HPA were either purchased from Aldrich (12-phosphotungstic acid (HPW) and 12-silicotungstic acid (HSiW)) or synthesized by literature methods (12-phosphodivanadomolybdic acid (HPV2Mo), 18-diphosphotungstic acid (18-HP2W), 21-diphosphotungstic acid (21-HP2W), and 21-diarsenotungstic acid (21-HAs2W)).

Nafion® 112 or 117 sheets were obtained from Ion Power, Inc. The Nafion® was cleaned by refluxing in 3% H_2O_2 for 1 h, deionized (DI) water for 1 h, 0.5 M H_2SO_4 for 1 h, and finally DI water for 1 h. It was then rinsed and stored in DI water in the dark. The Nafion® was doped with HPAs by refluxing in an aqueous solution of each HPA overnight. The Nafion® was placed in a mixed refluxed solution of 50 g of HPA and 250 ml of DI water for 24 h.

Infrared spectra were collected on a KRS-5 ATR attachment in a Thermo-Nicolet Nexsus 670 FT-Infrared spectrometer. Proton diffusion measurements were obtained on a Chemagnetics Infinity 400 NMR spectrometer operating at 400 MHz for ^1H using a 5mm Doty Scientific, Inc. #20-40 z-gradient pulsed-field gradient NMR probe. The stimulated-echo pulse sequence was used.[9] Spectra were recorded as a function of gradient pulse current using a 90° radio frequency excitation pulse of 6.5 μs, a gradient pulse width of 1.0 ms and a gradient pulse spacing of 3.2 ms. Spectra were recorded for 40 equally spaced values of gradient coil currents between 0.3 mA and 15 A in a random array by signal averaging 16 transients.

Membrane electrode assemblies (MEAs) were constructed using electrodes were purchased from E-Tek (ELAT) V2.2 hand fabricated, single sided coatings with 0.5 mg/cm^2 20% Pt on carbon. A 5% Nafion® 1100 solution was painted on each electrode until the loading was in the 0.4-0.5 mg/cm^2 range. The electrodes were then hot pressed at 150 °C and 80 psi for 5 min. Electrodes were then placed on the HPA doped Nafion® 112 and hot pressed at 145 °C for 90 sec.

Results and Discussion

The HPA interact strongly with polar molecules and so are expected to interact strongly with PFSA polymers.

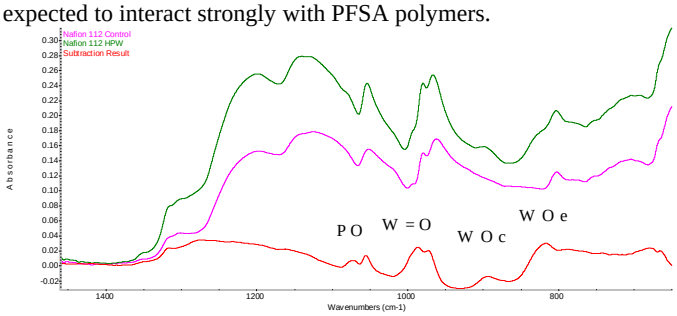

Figure 2. ATR IR of vacuum dried Nafion® 112 with and without 12-HPW and the subtracted spectrum.

The Infrared spectrum of vacuum dried Nafion® 12-HPW doped Nafion® is shown in Figure together with the result of subtracting the control spectrum from the doped spectrum. In the subtraction

result the four expected bands for the υ(PO), υ(W=O), υ(WO_c), and υ(WO_e) are clearly seen. Interestingly both the υ(PO), and υ(W=O) bands are split indicating bonding that bonding to the W=O of this Keggin anion is important. Obviously, these dry membranes in which the HPA bands are more obvious do not reflect the state of membranes hydrated in an actual fuel cell. On addition of water to the membrane further splitting of these IR bands is observed.

The effect on proton self-diffusion coefficients of doping Nafion® 112 with HPA are shown in Figure and Table 1. The maximum diffusion coefficient, $1.1x10^{-5}$ cm^2s^{-1}, for the Nafion® control is seen at 90°C. 12-HPW lowers this maximum temperature to 80°C, but increases the diffusion coefficient to $1.6x10^{-5}$ cm^2s^{-1}. With the exception of 21-HAs2W and 18-HP2W, all the other HPA increase the temperature of maximum diffusion, 21-HP2W to 100°C and HSiW to 130°C.

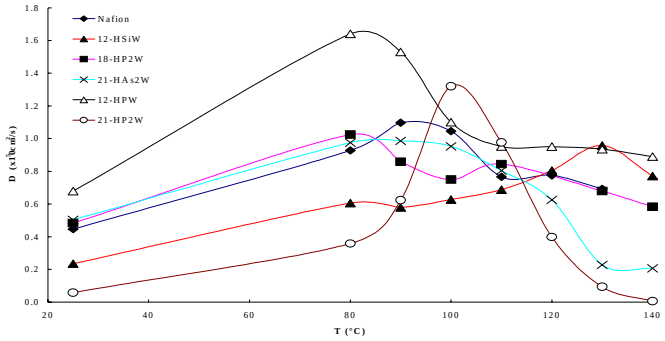

Figure 3. PFGSE data for the protons not associated with liquid water in HPA doped Nafion® 112 showing temperature vs. proton diffusion coefficient.

In Table 1 the activation energies for proton diffusion before the maximum temperature of diffusion are given. In general the E_a are all *ca.* 12 KJ mol^{-1} which is close to the literature value for diffusion in dry or nearly dry Nafion®.[10] Only 21-HP2W dramatically increases the Ea under these dry conditions, 21-HAsW21 decreases the E_a slightly.

Table 1. PFGSE data for the protons not associated with liquid water in HPA doped Nafion® 112 showing temperature vs. proton diffusion coefficient.

HPA	Max diffusion coefficent x 10^{-6} cm^2s^{-1}	Temperature of maximum D, °C	Ea before Max T, kJ mol^{-1}
Control	11	90	12
12-HPW	16	80	14
12-HSiW	10	130	13
18-HP2W	10	80	12
21-HAs2W	10	80	10
21-HP2W	13	100	31
11-HSiW	2.5	100	17

These changes to the Nafion® membranes are generally not reflected in the fuel cell testing of the corresponding MEAs. In general at 90°C or below the HPA doped membranes do as well as the undoped control or slightly worse. At 120°C slight improvements are seen for the commercial Keggin HPW and HSiW and the synthesized 21-HP2W doped Nafion®s. When the MEAs are constructed with no Nafion® in the electrodes dramatic improvements are seen in the performance of the doped Nafion® MEAs at 120°C.

From this data we deduced that we were actually seeing an improvement to the electrode/membrane interface in the doped MEAs. To test this hypothesis a Pt loaded ELAT anode was doped with the HV2MoP HPA. As can be seen, Figure , the improvement between the control MEA and the HPA anode doped MEA is dramatic. Examination of the data reveals that the biggest improvement in the polarization curve is in the ohmic region as the interfacial resistance has been dramatically reduced. It should be pointed out that additional contributions to this phenomenon on the fuel cell anode will also occur as the HPA when reduced by H_2 acts as a mixed protonic/electronic conductor.

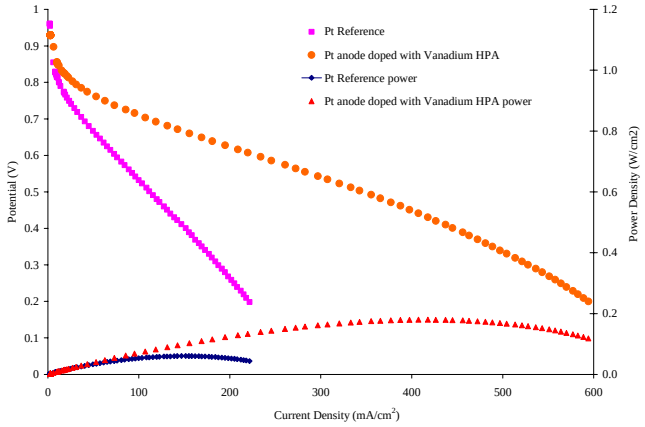

Figure 4. Polarization curves for a Nafion® 112 MEA with ELAT electrodes, both Pt control and Pt doped with $H_5[PMo_{10}V_2O_{40}]$ on the anode at 80**°C**.

Conclusions

HPA interact strongly with PFSA polymers and this interaction can be tailored to improve the proton conducting properties of these membranes. As unmodified HPA are water soluble and mobile their effect on an MEA actually occurs at the membrane/electrode interface, the interfacial resistance of which can be dramatically improved.

Acknowledgement. We would like to thank the DOE for financial support from award No. DE-FC02-0CH11088.

References

(1) Honma, I.; Nakajima, H.; Nishikawa, O.; Sugimoto, T.; Nomura, S. *J. Electrochem. Soc. 150*, (2003), A616.
(2) Honma, I.; Takeda, Y.; Bae, J. M. *Solid State Ionics 120*, (1999), 255.
(3) Vernon, D.; Meng, F.; Dec, S. F.; Williamson, D. L.; Turner, J. A.; Herring, A. M. *Journal of The Electrochemical Society submitted*, (2004).
(4) Kim, Y. S.; Wang, F.; Hickner, M.; Zawodzinski, T. A.; McGrath, J. E. *J. Membr. Sci. 212*, (2003), 263.
(5) Ramani, V.; Kunz, H. R.; Fenton, J. M. *J. Membr. Sci. 232*, (2004), 31.
(6) Staiti, P. *Journal of New Materials for Materials for Electrochemical Systems 4*, (2001), 181.
(7) Pope, M. T.; Müller, A., Eds. *Polyoxometalate Chemistry: From Topology Via Self-Assembly to Applications*; Kluwer Academic Publishers: Dordrecht, 2001.
(8) Nakamura, O.; Kodama, T.; Ogino, I.; Miyake, Y. *Chemistry Letters 1*, (1979), 17.
(9) Tanner, J. E. *The Journal of Chemical Physics 52*, (1970), 2523.
(10) Cappadonia, M.; Erning, J. W.; Stimming, U. *Journal of Electroanalytical Chemistry 376*, (1994), 18.

NANOCOMPOSITE NAFION® CONTAINING SULFONATED PARTICLES FOR PEMFC APPLICATION

Philippe Bébin, Magaly Caravanier, Hervé Galiano

Commissariat à l'Energie Atomique
Le Ripault Research Center, BP 16
37260 Monts, France

Introduction

Membranes commonly used in PEMFC are perfluorinated polymers containing sulfonic acid groups on side chains, like for example Nafion® manufactured by Dupont. However, for fuel cell application, this kind of membranes needs a high water content to reach satisfying proton conduction. Moreover, for temperature higher than 80°C, the proton conduction of Nafion® is unstable. To improve the fuel cell efficiency, the polymer electrolyte should have better water retention properties especially in hard conditions like, for example, temperatures around 100°C. The improvement of the membrane water retention should help keeping a significant proton conductivity under dehydrating conditions.

For last years, attention has been focused on organic-inorganic hybrid material to enhance the hydration properties of the membrane at high temperatures (near 100°C)[1-3]. Amongst the inorganic compounds suitable with a proton conductive organic matrix, the clay family is a promising candidate because of its advantageous hydrophilic properties and good thermal stability[4,5]. Laponite and Montmorillonite, due to their ionic sheets structure, allow the absorption of water with good retention capacity. These fillers used in Nafion® should then prevent the loss of the hydration water at high temperature but also under low relative humidity conditions.

In this work, the synthetic Laponites (Lp) are used because they can have a reproducible composition and a high level of purity[6]. The corresponding hybrid membranes are obtained by mixing the perfluoro-sulfonated polymer (Nafion®) with the synthetic inorganic particles. Nevertheless, the addition of clay, which is a poor proton conductor, inside Nafion®, which is highly proton conductive, can lead to a reduction of the global proton conductivity of the membrane. To enhance the proton conductivity of the hybrid material without loosing the benefits brought by the inorganic particles, some proton conductive groups are chemically bonded to the Laponite surface. The corresponding treatment and its efficiency are discussed, and the results, coming from chemical and electrochemical analysis for hybrid membranes prepared with both, unmodified (Lp) and grafted clay (Lp-g), are presented and compared to Nafion® ones. The influence of the hybrid membrane on the efficiency of PEMFC is also evaluated.

Experimental

Nanocomposite membrane preparation. Nafion® membranes, and Nafion® solutions (20wt.% of Nafion® in water/alcohols mixtures) are purchased from DuPont, and Laponite RD is purchased from Rockwood Industries. The surface of the clay, after being activated with an helium plasma, is chemically grafted with sulfonated styrene moieties using a DMF solution of p-styrene sulfonate (purchased from Aldrich). The corresponding dispersion is kept for 48 hours at reflux before washing the modified clay powder in DMF to remove all the monomers and oligomer moieties not attached to the Laponite particles. A pre-formed membrane of Nafion® is dissolved in a 15% (w/v) DMF clay suspension and the mixture is stirred at room temperature until complete dissolution. The mixture is then poured on a glass support using a Hand-Coater (Braive Instrument) in a clean laminar flow environment. The membrane is then heated in an oven at 120°C for 10 hours to enhance its mechanical properties. Finally, the membrane is soaked in a 3wt.% H_2O_2 solution at 80°C for 1 hour to oxidize the organic impurities. After 1 hour in pure water, the membrane is activated using a 0,5 M H_2SO_4 solution at 80°C for 1 hour before being rinsed again in de-ionized water for 1 hour. The sample is then stored in de-ionized water at room temperature until use.

Analysis. The proton conductivity measurements are performed using an impedance cell with two platinum disk electrodes of 0,5 cm in diameter. The cell containing the sample to analyze is placed in a Weiss WK 11180 climatic room that enables a controlled environment with relative humidity levels ranging from 0 to 98% and with temperatures ranging from RT to 95°C. The measurement conditions, i.e. the relative humidity and the temperature, are kept constant for at least three hours before performing the impedance analysis with an AC impedancemeter (Solartron SI 1260 Impedance/Gain Phase Analyser). The impedance spectra are recorded from 10 MHz to 1 Hz with a perturbation voltage amplitude of 10 mV.

Fuel cell tests are performed with an Electrochem fuel cell test station (RBL 488-50-150-800). The membrane electrode assemblies (MEAs) are prepared sandwiching the membrane between two E-Tek electrodes (0,35 mg Pt/cm^2) without hot pressing. The electrode area is 25 cm². The performance of the single cell is evaluated in the range of 80°C to 120°C with 3 and 4 bars of gas pressure. Hydrogen gas and oxygen or air are fully humidified passing through a bubble-type chamber.

Results and discussion

The good water retention properties of clays are expected to improve the proton conduction of Nafion® under low humidity levels. **Figure 1** shows the relationship between the proton conductivity and the relative humidity (from 50 to 98% RH) for Nafion®115 and for the nanocomposite membranes at 25°C.

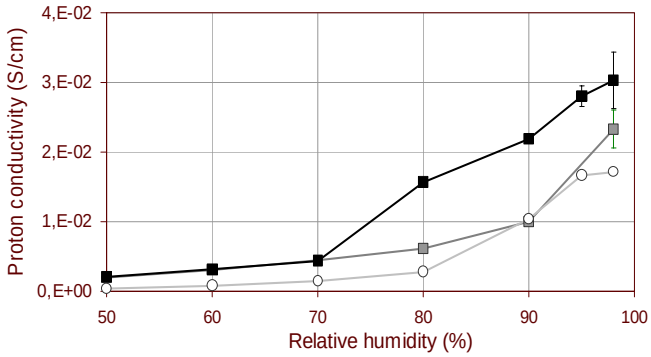

Figure 1. Variation of proton conduction at 25°C with relative humidity for Nafion®115 (○) and hybrid Nafion® containing 10wt.% of unmodified Laponite (Nafion®/Lp (■)) and containing 10wt.% of styrene-sulfonated Laponite (Nafion®/Lp-g (■))

As seen on Figure 1, the proton conductivity of the Nafion®/Lp-g membrane is higher than the one of the Nafion®115 whatever the relative humidity level. It is also higher than the proton conductivity of the Nafion®/Lp between 70 and 98% RH. The use of some proton conductive clay particles (Lp-g) as a filler for Nafion® induces a more significant effect on the proton conduction of the membrane than the use of non conductive clay particles. A 10^{-2} S/cm proton conduction level is then reached for a minimum of 75% RH with Lp-

g while it needs 90% RH when non conductive fillers are used. This level of humidity is, on the other hand, similar to the one needed when Nafion® is used without inorganic additives. An improvement of the working conditions is then expected for this kind of nanocomposite Nafion®, and, to evidence it, the levels of temperature and relative humidity needed to reach a 10^{-2} S.cm^{-1} conductivity are determined. The corresponding lines are presented in **Figure 2** as proton conductive maps for Nafion® and for the nanocomposite membrane (Nafion/Lp-g).

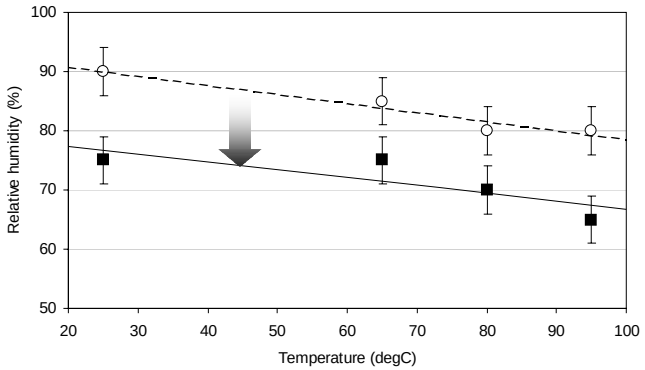

Figure 2. Temperature and relative humidity relationship for a 10^{-2} S.m^{-1} proton conductivity, for Nafion®115 (open circle and dotted line) and for Nafion®/Lp-g 10wt.% (black square and plain line) membranes

In Figure 2, a proton conductivity higher than 10^{-2} S/cm is obtained above the linear regression, while lower proton conductivity values are obtained below the corresponding lines. The relationships between temperature and humidity levels are linear and parallel for the two kinds of membranes with a decrease of the humidification level needed for the proton conduction when the temperature is increasing. The only difference between Nafion® and hybrid Nafion® is then the minimum level of humidity needed to have a satisfying proton conduction, which is about 10% lower for the nanocomposite Nafion® (Nafion®/Lp-g) compared to the pure Nafion®. The positive influence of the proton conductive filler is comparable on all the temperature range studied (25 to 95ºC).

The improvement of the hybrid membrane behavior can also be evidenced by fuel cell experiment. Nanocomposite Nafion® (Nafion®/Lp-g membranes) are tested in a fuel cell test station at different operation conditions, changing the cell temperatures (80-120°C), the reactant gases (H_2/O_2 and H_2/air), and the gas pressures (3-4 bars) in order to evidence the benefit brought by the particular formulation of the material. Good operation conditions, corresponding to fully hydrated fuel cell, are obtained at 80°C using H_2/O_2 gases under 4 bars. The hard operation conditions, corresponding to dehydrated fuel cell conditions, are obtained at 120°C using H_2/air gases under 3 bars. The polarization curves are presented on **Figure 3** for Nafion® and for nanocomposite Nafion® for the two working conditions.

In the good operation conditions, the use of Nafion® enables to reach about 600 mA.cm^{-2} of electronic current produced at 0.6 V, while the use of a Nafion®/Lp-g membrane leads to the production of about 720 mA.cm^{-2} at the same voltage. This difference corresponds to a 20% improvement in power density with the nanocomposite membrane (430 mW.cm^{-2} vs 360 mW.cm^{-2}). This gain decreases to 15% at 0,7 V. In the hard operation conditions, a Nafion® membrane can deliver 390 mA.cm^{-2} of current at 0,6 V while the nanocomposite one (Nafion®/Lp-g) can reach 500 mA.cm^{-2}. A 30% improvement in power density is then possible at 0,6 V, changing the commercial membrane for an hybrid one. This gain is about 25% at 0,7 V.

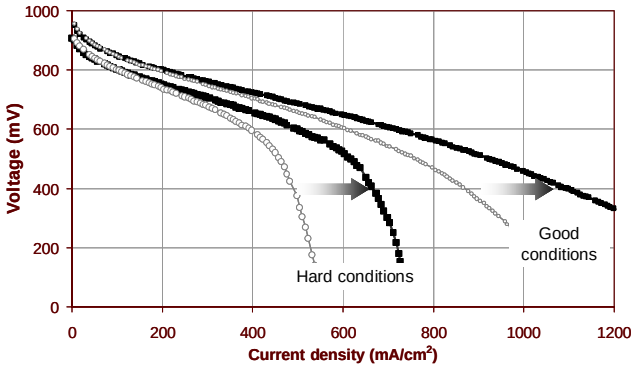

Firgure 3. Polarization curves of Nafion®115 and nanocomposite Nafion® (Nafion®/Lp-g (90/10 w/w)) under good operation conditions (80°C, H_2/O_2, 4 bars) and hard operation conditions (120°C, H_2/air, 3 bars).

Then, hybrid Nafion® presents a better behavior than the commercial Nafion®, whatever the operation conditions. Nevertheless, the gain in power density is always more significant under difficult humidification conditions than under fully humidification condititons. This improvement in fuel cell work has to be related to the good water retention of the inorganic filler while the sulfonic acid groups grafted to the particles surface enhance the global proton conductivity of the membrane.

Conclusions

The modification of clay particles by bonding styrene-sulfonic moieties at their surface has a significant positive effect on the behavior of a Nafion® membrane containing these particles. Indeed, the dispersion of this kind of fillers in Nafion® enhances both the water retention of the nanocomposite material and its proton conductivity.

Acknowledgements

The authors thank F. Bergaya from CNRS-Orléans and F. Poncin-Epaillard from CNRS-LeMans for their contribution in this project. S. Escribano from the Fuel Cell Laboratory of CEA is also acknowledged for her technical support on fuel cell experiments and analysis. The financial support of Région Centre was greatly appreciated for this project.

References

(1) Shao, Z.G.; Joghee, P.;Hsing,I.M., *J. Membrane Sci.*, **2004**, *229*, 242

(2) Chang, J.H.; Park, J.H.; Park, G.G.; Kim, C.S.;Park, O.O., *J. Power Sources*, **2003**, *124*, 18

(3) Kim, K.H.; Ahn, S.Y.; Oh, I.H.; Ha, H.Y.; Hong, S.A.; Kim, M.S.; Lee, Y.; Lee, Y.C., *Electrochimica Acta*, **2004**, *50*, 574

(4) Damay, F.; Klein, L.C.; *Solid State ionics*, **2003**, *162-163*, 261

(5) Greaves, C.R.; Bond, S.P.; McWhinne, W.R., *Polyhedron*, **1995**, 14 (23-24), 3635

(6) Qi, Y.; Al-Mulkhar, M.; Alcover, J.F.; Bergaya, F., *Applied Clay Sci.*, **1996**, *11*, 185

PREPARATION AND CHARACTERIZATION OF FLUORINE-CONTAINING POLY(ETHER KETONE)S WITH SULFONATED BIPHENYLENE UNIT

Yoshimitsu Sakaguchi[1], Shigenori Nagahara[1], Kota Kitamura[1], Masahiro Yamashita[1], Satoshi Takase[1], Kazushi Omote[2], Ai Nishichi[2], and Yoshinobu Asako[2]

[1]Toyobo Research Center, Toyobo Co., Ltd.
1-1 Katata 2-Chome, Ohtsu 520-0292, Japan
[2]Nippon Shokubai Co., Ltd.
5-8 Nishi Otabi-cho, Suita 564-0034, Japan

Introduction

As a new power source for transportation, stationary and mobile power applications from the viewpoint of environmental and new energy issues, solid polymer electrolyte membrane fuel cell is attracting much attention. Sulfonic acid-containing aromatic condensation polymers have been studied as possible candidates for the alternative of perfluorosulfonic acid polymer membranes, such as Nafion®, because their backbone structures are generally heat- and solvent-resistant with good mechanical properties. In many cases, however, perfluorosulfonic acid polymers are still used as a binder polymer for membrane electrode assembly, and it may cause problems in adhesion or delamination between the hydrocarbon membranes and the electrodes. A proton exchange membrane derived from partially fluorinated polymers may show good affinity with the perfluorosulfonic polymer binders and a binder made of partially fluorinated polymers also may show good affinity with nonfluorinated hydrocarbon polymer membranes with improved chemical stability.

Based on the above background, we have reported about preparation and properties of fluorine-containing sulfonated poly(ether ketone)s shown in **Figure 1**.[1] These polymers showed good proton conductivity by introducing adequate quantity of sulfonic groups, however, they showed pretty large swelling at the same time under higher humidified conditions. In this study, biphenylene structure is selected as a sulfonated segment instead of diphenyl fluorene unit in the figure to improve the dimensional stability of resulting membranes.

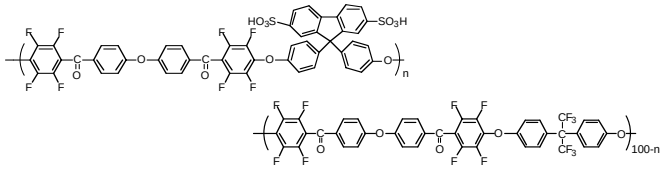

Figure 1. Sulfonic group-containing partially fluorinated poly(ether ketone) copolymers (S-HF-n).

Experimental

Preparation of sulfonated poly(ether ketone) copolymers (S-BP). Fluorine-containing poly(ether ketone) copolymers derived from 4,4'-bis(2,4,5,6-pentafluorobenzoyl)diphenylether (BPDE) and mixed diols of 4,4'-biphenol (BP) and 2,2-bis(4-hydroxyphenyl)-1,1,1,3,3,3-hexafluoropropane (6FBA) were prepared by aromatic nucleophilic substitution reaction with potassium carbonate in N-methl-2-pyrrolidone (NMP) according to a previous paper.[2] Sulfonation was carried out by dissolving the copolymers in concentrated sulfuric acid and stirred for designated time at room temperature. After the reaction, the reaction mixture was poured into water to precipitate the product. The sulfonated polymers thus obtained were washed with water until the washings were neutralized, and then dried under vacuum.

Preparation of films. Two grams of sulfonated polymers were dissolved in 10ml of NMP, and cast onto a glass plate on a hot plate to form films. The films obtained were placed in water overnight, then treated with 1M H_2SO_4 solution and pure water at 80°C for 1 hour, respectively, and then dried.

Characterization. Inherent viscosities were measured at a concentration of 0.5 g/dL in NMP at 30°C. Thermogravimetric analysis (TGA) was conducted at a heating rate of 10°C/min under flowing argon, using a Shimadzu TGA-50 thermogravimetric analyzer. Ionic conductivities of the films were measured at 80°C and 95%RH by using a Solartron 1250 Frequency Response Analyzer over the frequency range from 1Hz to 65KHz, and calculated based on the complex impedance plot. Ion exchange capacities of the films were measured by the back-titration with hydrochloric acid solution after the films were treated with sodium hydroxide aqueous solution. Methanol permeability was measured by monitoring the concentration of methanol with gas chromatograph using a H-shaped cell in which water and 5M-methanol aqueous solution are separated by a sample membrane.

Results and Discussion

Fluorine-containing poly(ether ketone)s were prepared by nucleophilic aromatic substitution reaction between BPDE and mixed diols of BP and 6FBA as shown in **Figure 2** (a copolymer containing n mol% of biphenol is abbreviated as BP-n). The previous paper[1] showed 6FBA unit in the copolymers was not sulfonated by concentrated sulfuric acid at room temperature, therefore, BP unit is expected as only one activated part for sulfonation in the copolymers. In general, sulfonated aromatic polycondensation polymers showed similar proton conductivity with Nafion® when their ion exchange capacity (IEC) is around 1.9 meq/g. Therefore, fluorine-containing poly(ether ketone) copolymer with BP:6FBA = 85:15 was prepared (BP-85).

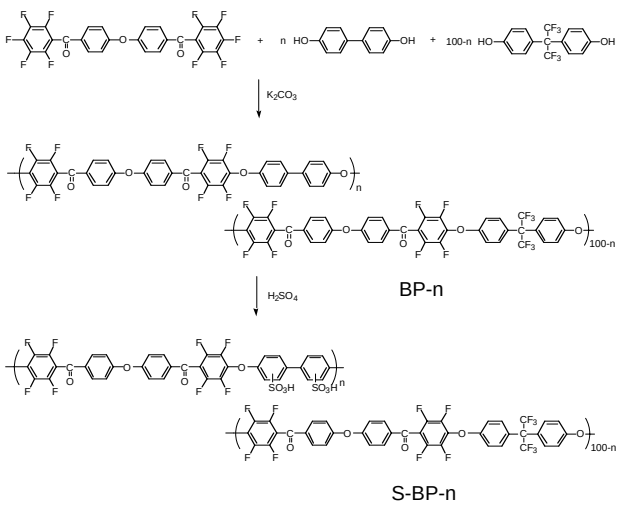

Figure 2. Synthesis of sulfonated poly(ether ketone) copolymers containing biphenylene unit (S-BP-n).

BP-85 was sulfonated in concentrated sulfuric acid at room temperature. Sulfonation for BP unit was slower than that for diphenyl fluorene unit (two hours is long enough for quantitative sulfonation for HF polymer), and complete sulfonation, two sulfonic

groups in one BP unit, was achieved for 62 hours reaction (measured IEC for the polymer was 1.98 and calculated IEC for complete sulfonation is 1.97). IR spectra before and after sulfonation are shown in **Figure 3**. Absorption peaks due to sulfonic groups are found in 1240 and 1100 cm^{-1}. ^{1}H NMR spectrum is shown in **Figure 4**. It is found that sulfonation was occurred on each benzene ring in biphenylene unit quantitatively. As sulfonation reaction was slow in this reaction system, a partially sulfonated polymer with 1.46 of IEC was also obtained by shorter reaction time of 17 hours.

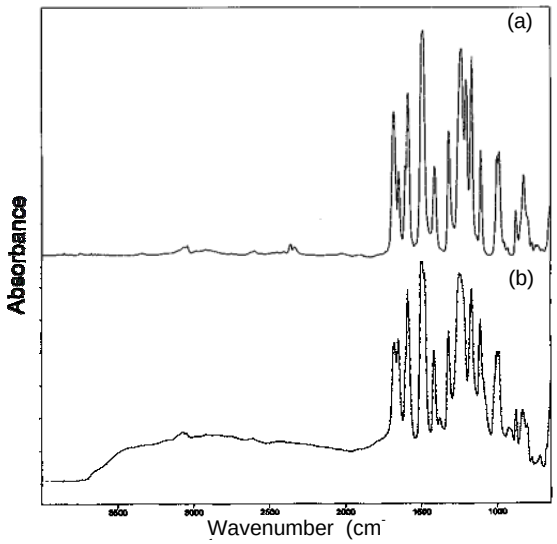

Figure 3. IR spectra of S-BP85 (a) before sulfonation and (b) after sulfonation for 62 hours.

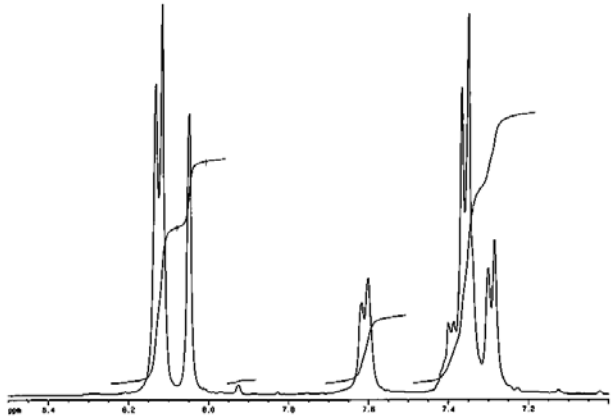

Figure 4. 1H NMR spectrum of S-BP85 sulfonated for 62 hours.

Table 1. Preparation of S-BP

Reaction time	IEC (meq/g)	η_{inh} (dl/g)		3% Weight loss temperature
		Before sulfonation	After sulfonation	
62hr	1.98	2.80	2.72	339°C
17hr	1.48	2.80	2.93	334°C

S-BP85(IEC=1.98) and S-BP85(IEC=1.48) showed lower swelling to water at higher temperature compared to S-HF100 and S-HF68, respectively. It is confirmed that replacement of diphenyl fluorine unit by biphenylene unit was effective to improve the dimensional stability of sulfonated poly(ether ketone) membranes. S-BP85 membranes also showed lower methanol permeability than corresponding S-HF membranes as shown in Table 2.

Table 2. Properties of S-BP85 and S-HF membranes

Polymer	IEC (meq/g)	S at 80°, 95%RH (S/cm)	MeOH permeability (μmol/m•s)
S-BP85(1.98)	1.98	0.29	0.25
S-BP85(1.48)	1.48	0.12	0.16
S-HF100	1.95	0.24	0.36
S-HF68	1.48	0.13	0.31

As it was possible to control the degree of sulfonation by changing the reaction time, sulfonation of BP100 was tried to improve dimensional stability further by eliminating flexible 6FBA unit. Sulfonated polymers having similar IEC to S-BP85 were obtained, however, their swelling properties and methanol permeabilities were almost the same as those of S-BP85 as shown in **Table3**.

Table 3. Properties of S-BP100 membranes.

Polymer	IEC (meq/g)	S at 80°, 95%RH (S/cm)	MeOH permeability (μmol/m•s)
S-BP100(1.91)	1.91	0.28	0.24
S-BP100(1.52)	1.52	0.17	0.17

Sulfonated poly(ether ketone) copolymers having partially fluorinated segments in this study showed improved performance as proton conductive membranes. As these polymers may show good adhesion with both aromatic hydrocarbon polymers and perfluorinated polymers, application of these polymers as a binder for MEA as well as a membrane is expected.

References

(1) Sakaguchi, Y., Kaji, A., Nagahara, S., Kitamura, K., Takase, S., Omote, K., Asako, Y., Kimura, K., ACS Polym. Prepr., **2003**, 45(1), 56.

(2) Kimura, K.; Tabuchi, Y.; Yamashita, Y.; Cassidy, P.E.; Fitch III, J.W.; Okumura, Y. Polym. Adv. Tech., **2000**, 11(8-12), 757.

MULTIBLOCK SULFONATED-FLUORINATED POLY(ARYLENE ETHER)S MEMBRANES FOR A PROTON EXCHANGE MEMBRANE FUEL CELL

Hossein Ghassemi, Tom A. Zawodzinski, Jr.

Case Advanced Power Institute and Department of Chemical Engineering, Case Western Reserve University, Cleveland, OH 44106

Introduction

Proton exchange membrane fuel cells (PEMFCs) offer potential advantages of clean and efficient energy conversion systems for automobiles, portable applications, and power generation. The primary demands on the hydrated proton exchange membrane (PEM) are high proton conductivity (above 0.01 S cm), low fuel and oxygen permeability, and high chemical, thermal and mechanical stability. Conventional PEMFCs typically operate with Nafion membranes, which offer quite good performance below 80 ◦C. However, to decrease the complexity and increase the efficiency and CO-tolerance of the PEMFC system, there is a strong need for PEMs capable of sustained operation above 100 ◦C and/or at decreased relative humidity of gases. Unfortunately, the proton conductivity of Nafion suffers greatly at temperatures above 80 ◦C due to loss of water. These factors, in addition to the high cost of Nafion, have triggered an extensive search for alternative PEM materials (1), some relying on other species than water to assist proton conduction.(2)

Sulfonated aromatic polymers have been recently studied (3-12) and in some cases showed satisfactory chemical and electrochemical stability for fuel cell applications. Among these polymers, sulfonated Poly(arylene ether sulfone)s have been extensively investigated for high temperature fuel cell applications. They are prepared by direct polymerization of the sulfonated activated halide with a bisphenol using otherwise nucleophilic substitution condensation polymerization conditions that are fairly similar to “polysulfone” preparation condiitons. These random copolymers display a hydrophilic/hydrophobic phase separated morphology that varies depending on the degree of sulfonation. The conductivity and water uptake of this series of copolymers also increase with degree of sulfonation. However, once the degree of sulfonation reaches 60 mole %, a semicontinuous hydrophilic phase is observed and the membranes swell dramatically, forming a hydrogel that is not useful as a proton exchange membrane.

Segmented multiblock (MB) copolymers are synthesized in order to create 'tailor-made materials' showing a combination of properties of the homopolymers. The combination of supramolecular phase separation in MB with self-ordering occurring on a molecular scale is assumed to provide interesting features changing the properties more than random copolymers. Multiblock copolymers composed of two or more long, contiguous sequences of chemically dissimilar repeat units, are able to spontaneously assemble into a wide variety of nanostructures, such as spherical or cylindrical micelles, bicontinuous channels, coalternating layers, and complex combinations.

In this article, we report new multiblock copolymers containing perfluorinated poly(arylene ether) as a hydrophobic segment and highly sulfonated poly(arylene ether sulfone) as a hydrophilic segment with the aim of providing polymeric materials with a highly phase-separated morphology. The phase formed by the hydrophobic block should enable good mechanical stability under fully hydrated state whereas the hydrophilic block should provide a high proton conductivity. The objective of this work is to produce thermally and hydrolytically stable, flexible membrane films with high proton conductivity even at lower water contents. We also report morphology of these MB copolymers using AFM. All polymers are characterized in terms of water-uptake and ion-exchange capacity.

Experimental

Materials. A series of multiblock copolymers **3** were synthesized from hydroxyl-terminated fully sulfonated poly(arylene ether) sulfones **1** and fluorine-terminated perfluorinated poly(arylene ether)s **2** according to a procedure reported elsewhere. (13)

Characterization. Conductivity measurements were performed on the acid form of the membranes using a Solatron SI 1280B Impedance analyzer. IR spectra are taken by a Perkin Elmer FT-IR Spectrum GX instrument using a ATR cell. Tapping mode atomic force microscopy (TM-AFM, Digital Instruments, Nanoscope IV) was performed in air.

Results and Discussion

As depicted in Figure 1, multiblock copolymers were prepared by the reaction of the dialkali metal salt of bisphenol-terminated disulfonated poly(arylene ether sulfone)s **1** with decafluorobiphenyl-terminated poly(arylene ether)s **2** in a polar aprotic solvent. The reaction was rapid and produced copolymers with light yellow color in high yield. The dialkali metal salts of bisphenol-terminated disulfonated poly(arylene ether sulfone) **1** were generated using 3,3’-disulfonated-4,4’-dichlorodiphenylsulfone and excess amount of biphenol in the presence of potassium carbonate at 180^{o}C. By controlling the amount of biphenol monomer samples with target molecular weight of 2.5K, 5K and 15K was prepared. The sulfonated copolymers were used in the next step without isolation. Similarly, decafluorobiphenyl-terminated poly(arylene ether)s **2** were synthesized using 6F-BPA and excess amount of decafluorobiphenyl in DMAc-benzene mixed solvent. It is known that perfluoroaromatic monomers are highly reactive toward the nucleophilic aromatic substitution reaction and high molecular weight polymers form at relatively low temperature and short period of time (9-11). Several fluorinated oligomers **2** were synthesized with molecular weights ranging from 2.8K to 60K. Low molecular weight samples formed white powder-like product after isolation, whereas the high molecular weight sample formed white fibrous material. The molecular structure of polymer **2** was confirmed by ^{19}F NMR in CDCl3, and compared with 6F-BPA and decafluorobiphenyl. Glass transition temperature for high molecular weight perfluorinated polymer **2** was traced by DSC and determined around 175◦C. Detection of Tg’s for the multiblock copolymers **3** has not been easy possibly due to the interfere of two separate phases.

Reaction of the preformed sulfonated **1** with the fluorinated oligomer **2** proceeded rapidly as evidenced by sharp increase in viscosity of reaction solution mixture in the first few hours. Dilution of the reaction mixture had little effect in lowering the viscosity of the solution. After isolation, products were treated in boiling water and boiling THF separately, in order to purify the product from unreacted starting oligomers. Multiblock copolymers **3** formed transparent films cast from solution. Films were flexible when fully hydrated and became brittle as their water content decreased.

The successful introduction of the sulfonate groups was confirmed by FT-IR spectra (Figure 2), where strong characteristic peaks at 1027 and 1097 cm-1 assigned to symmetric and asymmetric stretching of sulfonate groups were observed for all copolymers. The densities of these two peaks increase with higher ratio of sulfonated block to fluorinated block. The MB membranes were tested for ion exchange capacity by titrating with sodium hydroxide standard solution (Table 1). The multiblock copolymers had high water uptake both in salt and acid form. Conductivity of these materials in their

fully hydrated form in liquid water showed values between 0.08-0.32 S/cm (Table 1).

It was noticed that in spite of their relatively high water uptake (Table 1) the surface of the MB films is quite hydrophobic. This hydrophobicity further increased as the relative humidity decreased. It was observed that in several cases the proton conductivity of the membranes above water in various RH and temperature was surprisingly low. A highly fluorinated surface of these membranes might act as an insulator between the electrode and the proton conductive region of the membrane. More work is in progress to determine the contact angle of the MB membrane under different conditions and also to find a way to control their surface properties.

Figure 3 shows the representative morphology of Nafion 112, BPSH-40 and MB-150 derived from TM-AFM. BPSH-40 is a poly(arylene ether) sulfone random copolymer containing 40% sulfonated and 60% unsulfonated monomer (4, 12). All TM-AFM micrographs shown here were taken under partial hydration. Images from Nafion 112 and BPSH-40 suggest that the hydrophilic groups aggregate as isolated domains with some local connection of hydrophilic domains as evidenced by the proton exchange membrane's good conductivity. In the case of MB the hydrophilic blocks (dark area) clearly show the formation of the continuously connected nano-channels of about 10 nm average width. Furthermore, nano-structures of the hydrophobic domains (light regions) appear as lamellar/ cylindrical with average width of about 50 nm. This is direct evidence of well-ordered and continuous ionic channels formed by microphase separation between hydrophilic domains containing sulfonate groups and perfluorinated hydrophobic domains. Protons transfer through these nano-channels of MBs is most likely the reason for high proton conductivity of the multiblock copolymers.

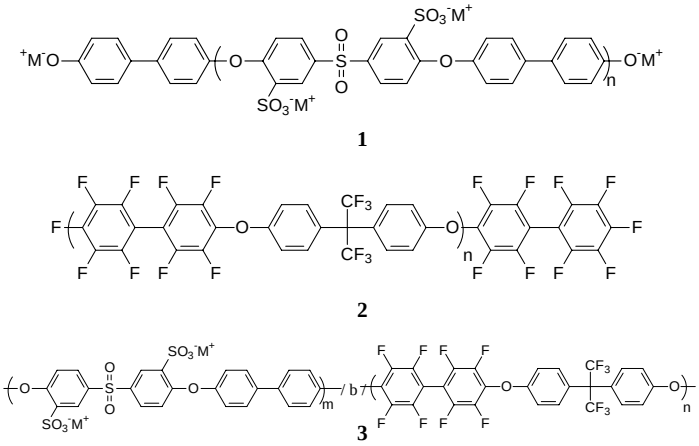

Figure 1. decafluorobiphenyl-terminated poly(arylene ether)s

Table I. Characterization of multiblock copolymers

Sample	Block size (Kg/mol)[1] S	F	IEC (meq/g)[2] Calc.	Exp.	Water Uptake (%)	Conductivity[3] (S.cm-1)
MB-229	5	2.8	2.05	2.29	470	0.32
MB-210	5	2.8	2.05	2.10	360	
MB-150	5	5	1.55	1.50	130	0.12
MB-117	5	5	1.55	1.17	115	
MB-095	3.2	5.3	1.17	0.95	41	0.08
Nf-1135	-	-	-	0.89	38	0.10

(1) Target value, (S) represents the sulfonated block and (F) represents the fluorinated block. (2) Samples were acidified in 0.5 M boiling sulfuric acid for 2 h and boiling deionized water for 2 h. (3) measured at room temperature in liquid water.

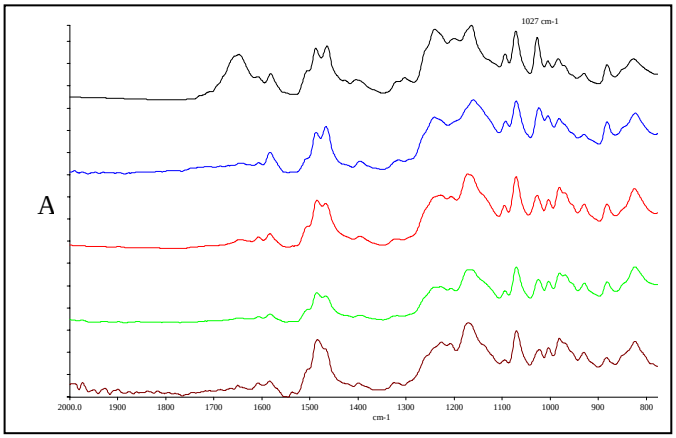

Figure 2. Influence of the relative size of sulfonated block on FT-IR of MB copolymers (sulfonated block size decrease from top to bottom)

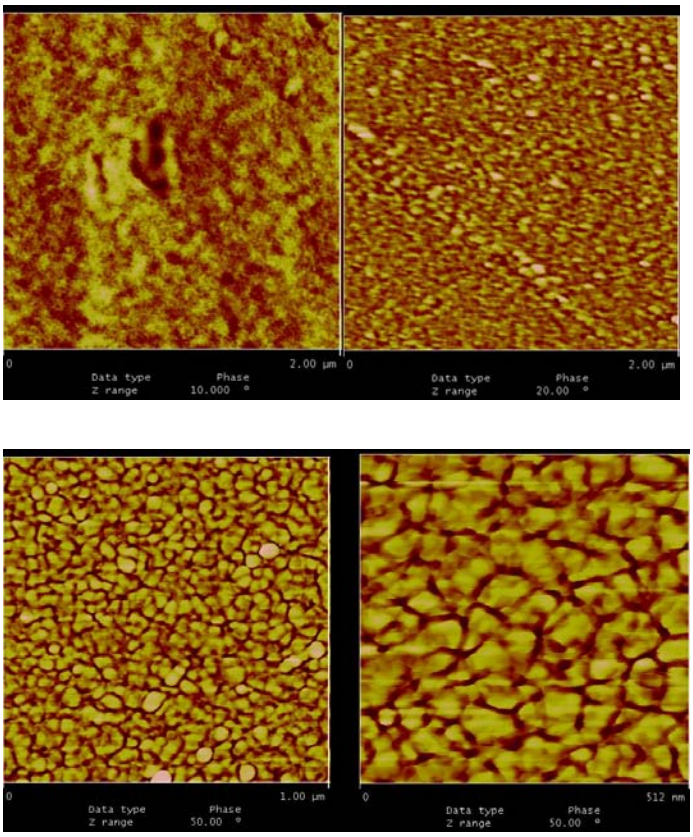

Figure 3. AFM tapping phase image for Nafion 112 (upper left), BPSH-40 (upper right) and multiblock MB-150 (bottom images)

Acknowledgement. The authors would like to thank the Department of Energy for support of this research effort.

References

(1) Michael A. Hickner, Hossein Ghassemi, James E. McGrath "Alternate Polymer Systems for Proton Exchange Membranes" Chemical Review**, 2004,** 104(10), 4587-4611

(2) Kreuer, K.D. "On the development of proton conducting membranes for hydrogen and methanol fuel cells". J Membr Sci 2001;185:29 – 39.

(3) Kobayashi, T.; Rikukawa, M.; Sanui, K.; Ogata, N. *Solid State Ionics* **1998**, 106, 219-225.

(4) Bae, J. M.; Honma, I.; Murata, M.; Yamamoto, T.; Rikukawa, M.; Ogata, N. *Solid State Ionics* **2002**.

(5) Kerres, J.; Ullrich, A.; Meier, F.; Haring, T. *Solid State Ionics* **1999**, 125, 243-249

(6) Wang, F.; Hickner, M.; Kim, Y. S.; Zawodzinski, T. A.; McGrath, J. E. *J. Membrane Science* **2002**, 197, 231-242.

(7) Cooper, J.E. *J. Polym. Sci. Part A; Polym. Chem*. **1971**, 9, 2361.

(8) (a) Hruszka, P.; Jurga, J.; Brycki, B. *Polymer* **1992**, 33, 248; (b) Miyatake, K.; Shouji, E.; Yamamoto, K.; Tsuchida, E. *Macromolecules* **1997**, 30, 2941.

(9) Iqbal, M.; Wightman, J. P.; Lloyd, D. R.; McGrath, J. E., *J Polym Sci Polym Chem Ed* **1984**, 22, 721.

(10) Ghassemi, H.; McGrath, J. E. *Polymer*, **2004,** 45(17), 5847-5854.

(11) Harrison, W. L.; Wang, F.; Mecham, J. B.; Bhanu, V. A.; Hill, M.; Kim, Y. S.; McGrath, J. E. *J. Polym. Sci. Part A; Polym. Chem*. **2003**, 41, 2264-2276.

(12) Ghassemi, H.; Grace, N.; McGrath, J. E. *Polymer*, **2004,** 45(17), 5855-5862.

(13) Ghassemi, H.; Harrison, W. L; Zawodzinski, T. A; McGrath, J.E.; Polym. Priprint, **2004**, 45(1).

HYDROCARBON AND PARTIALLY FLUORINATED SULFONATED COPOLYMER BLENDS AS FUNCTIONAL MEMBRANES FOR FUEL CELLS

*Natalie Y. Arnett, William L. Harrison, Limin Dong, and J.E. McGrath**

Virginia Polytechnic Institute and State University
Macromolecules and Interfaces Institute and the Department of Chemistry
*jmcgrath@vt.edu

Introduction

Polymer blends are recognized as a valuable technique to combine the properties of two different polymers[1], and has been the topic of several scientific reviews[2]. Polymer blending has been shown to improve many characteristics including impact strength, thermal behavior, and surface character[3]. One obvious advantage is that new polymers do not have to be synthesized to obtain novel materials. Several sulfonated copolymer blends have been investigated as candidates for application in proton exchange membrane fuel cells (PEMFCs). In general, these studies report that the unsulfonated copolymer reduces the aqueous swelling of the sulfonated polymer. However, it has been well documented that the majority of polymer pairs are thermodynamically immiscible[4]. Therefore, many polymer-blend pairs macrophase separate yielding poor adhesion at the interphase of the two polymers. Furthermore, due to the different possible microstructures within the blend, the surface composition can be significantly different from the bulk composition. However this possibility is not always undesirable as in the case of blends of fluorinated polymers that are interesting materials due to their hydrophobic surface properties.

The major objective of this research project is to develop membranes with interesting surface properties and characteristics through controlled polymer blending of fluorinated copolymers and non-fluorinated poly (arylene ether sulfone) copolymers (i.e., BPSH). The chemical structure and intrinsic viscosities of these copolymers are presented in **Figure 1** and **Table 1**, respectively. The partially fluorinated poly (arylene ether sulfone) copolymers (6FBPA-00, 6FS-35 or 6FS-60) have the potential to adhere favorably to Nafion electrode layers, while BPS-35 have mechanical and dimensional stability and good proton conductivity. This research was done in an effort to improve the adhesion and reduce interfacial resistance to commercially available Nafion® electrodes in alternative proton exchange based membrane fuel cells.

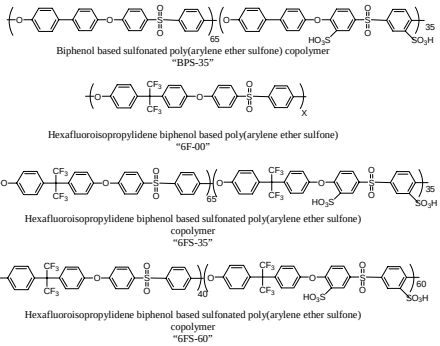

Figure 1. Chemical structures of the directly copolymerized poly(arylene ether sulfone) disulfonated random copolymers utilized.

Table 1. Intrinsic Viscosities of directly copolymerized poly(arylene ether sulfone) disulfonated random copolymers.

Copolymers	[η]
BPS-35	1.14*
6F-00	0.57**
6FS-35	0.52*
6FS-60	0.45**

*NMP with 0.5 M LiBr @ 25°C
**NMP @ 25°C

Experimental

Direct Copolymerization. A typical copolymerization for all sulfonated copolymers is shown in Figure 2 and will be described using the 6F-BPA, 4, 4'dichlorodiphenyl sulfone, and 60 mole percent 3, 3' disulfonated 4, 4'-dichlorodiphenyl sulfone (DCDPS). Firstly, 5.5 mmol 6F-BPA, 2.2 mmol DCDPS, and 3.3 mmol SDCDPS were added to a 3-neck flask equipped with an overhead mechanical stirrer, nitrogen inlet and a Dean Stark trap. Potassium carbonate (6.3 mmol), and sufficient DMAc (18 mL) were introduced to afford a 20% (w/v) solids concentration. Toluene (usually DMAc/Toluene = 2/1, v/v) was used as an azeotroping agent. The reaction mixture was refluxed at 150ºC for 4 hours to dehydrate the system. The temperature was raised slowly to 190ºC by controlled removal of the toluene. The reaction was allowed to proceed for 30 hours, during which the solution became very viscous. The solution was cooled to room temperature and diluted with enough DMAc to allow easier filtering. After filtering through filter paper to remove most of the salts, the copolymer was isolated by coagulation in stirred deionized water. The precipitated copolymer was also washed several times with deionized water to attempt to completely remove salts, and then extracted in deionized water at 60°C overnight. Finally, it was vacuum dried at 120ºC for 24 hours. The BPS-35, 6FS-35 and the 6F-00 were prepared using similar procedure with appropriate monomers and comonomer ratios.

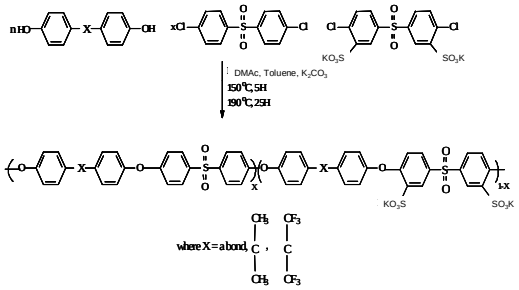

Figure 2. Synthesis of Disulfonated Poly (arylene ether sulfone) copolymers via direct copolymerization

Polymer Blending and Membrane Preparation

Polymer blends were prepared using several methods. Firstly, the potassium salt form by first redissolving approximately 1g of BPS-35 in 10 mL of DMAc (10% w/v). The desired amounts of 6F homopolymer or copolymers were added and the solutions were then stirred at room temperature for 24 hours. Solutions were filtered through a 0.45mm disk onto glass plates. The films were dried gradually via heating lamp with increasing intensity under nitrogen atmosphere. The films were released from the glass substrates by a razor blade. These films were not acidified.

The blending, casting, and drying procedures in the second method were the same as mentioned in the first blending technique. However, these blends were acidified.

In the third method, films of the copolymers were formed by casting transparent solutions (10% w/v) of the copolymers onto glass plates through a 0.45mm disk. The films were dried gradually via a

heating lamp with increasing intensity under nitrogen atmosphere. The films were released from the glass substrates by razor blade and were acidified before blending. The blending casting and drying procedures were the same as described above.

Acidification of Polymer Blend Membrane. The blended poly(arylene ether sulfone) copolymer films were acidified by first boiling in 0.5 M H_2SO_4 for 1hour and immediately followed by extraction in boiling deionized water for 1 hour as described earlier[5].

Characterization

Thermogravimetric Analysis (TGA). The thermal stability (weight loss) of the films in the acid form (5 to 10mg) was determined using a TA Instruments TGA Q 500. The films were first vacuum dried for at least 12 hours and then kept in TGA furnace at 150°C in nitrogen atmosphere for 30 minutes before TGA characterization. The samples were evaluated over the range of 30 to 700°C at a heating rate of 10°C/min in air.

Differential Scanning Calorimetry. The glass transition temperatures (Tg) of the films in the salt form were obtained on a TA Instrument DSC Q 1000. Scans were conducted under nitrogen at a heating rate of 10°C/min. Second heat Tg values are reported as the midpoint of the change in the slope of the baseline.

Contact Angle. The instantaneous (1-5 secs) contact angle measurements were obtained on a First Ten Angstroms (FTA 32) instrument that utilized the "sessile" method. Contact angle was a quantitative method used to determine the hydrophobicity or hydrophilicity of the film surface.

Specific Conductivity. A Hewlett-Packard 4129A LF impedance/gain phase analyzer was used to measure the resistance of each film in the acid form over a frequency range of 10Hz to 1MHz under fully hydrated conditions. The resistance of each film was measured at ~25°C using the conductivity cell.

Results and Discussion

Two partially fluorinated poly (arylene ether sulfone) copolymers were, respectively, blended at different weight fractions with a wholly aromatic, biphenol-based disulfonated poly (arylene ether sulfone) copolymers (BPS-35). Blended films were analyzed in both the salt and acidified form and clarity and miscibility observations were conducted visually. At low weight percentages (0-5 wt%) of the 6F homopolymers and copolymers in BPS-35 transparent films were observed. As the amount of 6F moiety increased, some white discoloration was seen predominately on the peripheral of the cast film. Moreover, at 30 wt% 6F-00 and the 6FS-60 films were opaque and showed large macrophase separation. However, at 30 wt% 6FS-35 a transparent, ductile film was obtained.

The surface characteristics of these solution cast copolymer blends were evaluated via contact angle. Surface enrichment of the fluorinated component revealed by a 26° change in the water-surface contact angle when 10wt% 6FBPA-00 (106°) was added to BPS 35 (80°).

The thermal properties (T_g) of the blends as a function of composition were investigated using DSC. It is well known that ion containing polymers display complex thermal transitions due to the presence of aggregates by the sulfonic acid (of varying sizes) and the influence to the ' normal' polymer transitions[6, 7]. Figure 3 shows selected DSC thermoscans (2nd heat). As shown, the 30wt% 6FS-60 blends displayed two weak, but detectable T_gs. The thermoscan suggested only partial miscibility because the T_gs of the blend was different from the 6FS-60 and BPS-35 copolymers.

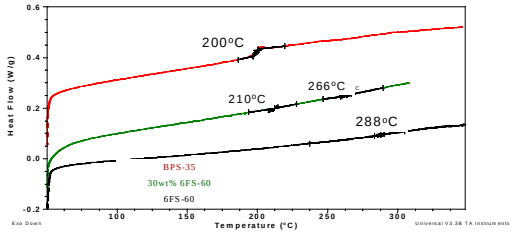

Figure 3. Influence of 6FS-60 blend composition on thermal transition (film in salt form)

Thermo-oxidative investigations of the 6F-00 in BPSH-35 displayed an increase with increasing 6F-00 incorporation. Conversely, the 6FSH-60 : BPSH-35 blends exhibited decreasing thermo-oxidative stability due to the increasing presence of the relatively unstable pendant sulfonic acid group.

Conclusions

A series of copolymer blends composed of varying weight percent BPS-35 with 6F-00, 6FS-35, and 6FS-60 have been made. The polymer blends were characterized via water uptake, conductivity, contact angle, DSC and TGA. The apparent miscibility is a function of blend's composition and copolymer chemical composition.

Current and Future Research

Titration of the polymer blends' actual ion exchange capacities (IEC), which may explain the consequence the blend fraction on the water uptake and conductivity data are ongoing. X-ray photoelectron spectroscopy (XPS) analyses on polymer blends are needed to acquire a better understanding on the surface properties and phenomena. Preparing blends using different copolymer compositions are being investigated as well as additional blending of the copolymers in the acid forms, which will introduce hydrogen bonding that, may improve miscibility. Membrane electrode assemblies (MEA) and voltage-current and durability tests are in progress.

References

1. D. R. Paul and C. B. Bucknall, Eds. Polymer Blends. John Wiley & Sons Ltd, New York, 2000, pp. 1217.
2. For example see: (a) JE Yoo and CK Kim *Polym Int.*, **2004**, **53**,1950; (b) Moon-Sung Kang, Jong Hak Kim, Jongok Won, Seung-Hyeon Moon and Yong Soo Kang, *J. Membr. Sci.*, **2004**.
3. Noshay, A.; McGrath, J. E. Block Copolymers: Overview and Critical Survey; Academic Press: New York, 1977.
4. Charoensirisomboon, P., Inoue, T., Solomko, S.I, Sigalov, G.M., Weber, M. *Polymer* **2000**, 41 7033-7042
5. Y.S. Kim, F. Wang, M. Hickner, S. McCartney, Y.T. Hong, T.A. Zawodzinski, and J.E. McGrath, *Journal of Polymer Science, Part B: Polymer Physics*, **2003,** 41(22).
6. Ehramann, M.; Muller, R.; Galin, J.C.; Bazuin, C.G., *Macromolecules.* **1993**, 26, 4910.
7. Eisenberg, A.; Kim, J., Introduction to Ionomers, Wiley-Interscience Pub., 1998; (b) Wilkes, G. L.; Tant, M. R.; Mauritz, K. A., Eds. Ionomers: Synthesis, Structure, Properties and Applications; Blackie Acadamic and Professional: New York, 1997.

COORDINATION OF B-N SPECIES TO TRANSITION METAL COMPLEXES

Vincent Pons; Melanie C. Denney; Karen I. Goldberg; D. Michael Heinekey

Department of Chemistry, University of Washington, Box 351700, Seattle, WA 98195-1700

Introduction

Hydrogen rich amineborane compounds have recently drawn significant attention since they represent a realistic solution to the problem of hydrogen storage.[1] Indeed, the high weigh percentages in hydrogen of ammonia borane (NH_3BH_3) and aminoborane polymer $(BH_2NH_2)_x$ both meet the 2015 Department of Energy target. However, in order to develop highly efficient catalysts for the hydrogenation/dehydrogenation of such B-N compounds, a fundamental understanding of the catalytic processes is needed. We present fundamental studies of the coordination of amineborane to unsaturated transition metal complexes as shown in Figure 1.

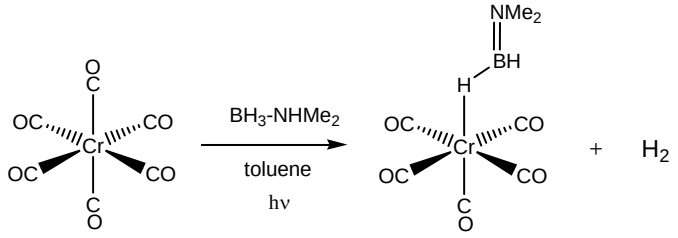

Figure 1. Photolysis of $Cr(CO)_6$ in toluene in presence of BH_3-$NHMe_2$.

Experimental

General Procedures. Unless stated otherwise, all manipulations were carried out under argon using Schlenk techniques. Dimethylamine borane and ammonia borane (Dr Tom Autrey, Pacific Northwest National Laboratory) were used as received. $Cr(CO)_6$ and $W(CO)_6$ were purchased and used as received from Sigma-Aldrich. NMR spectra were recorded on Bruker AV-300, AV-301, AV-500 and DRX-499 spectrometers. Proton NMR spectra were referenced to the solvent resonance with chemical shifts reported relative to TMS. The NMR studies were carried out in high-quality 5 mm NMR tubes, utilizing deuterated and protio solvents distilled from standard drying agents.

Photolysis of $Cr(CO)_6$ in toluene in presence of BH_3NHR_2 (R = H, CH_3). A J-Young NMR tube was charged with 3mg $Cr(CO)_6$ (0.013 mmol) and one equivalent of BH_3-NHR_2 (0.4 mg, R = H; 0.8 mg, R = Me). After addition via vacuum transfer of toluene (*ca* 1 mL), the resulting colorless solution was photolyzed (Hg lamp, 200 K) for 30 minutes to one hour to give a yellow solution. The coordination of borane species was monitored by ^1H and ^{11}B NMR (see discussion).

Results and Discussion

Photolysis of a toluene solution of chromium hexacarbonyl and one equivalent of Me_2NHBH_3 at 200 K leads to loss of H_2, formation of NMe_2=BH_2 and the cyclic dimer $(NMe_2$-$BH_2)_2$. At 180 K, three peaks are observed in the hydride region of the ^1H NMR spectra at -9.34, -13.87 and -18.1 ppm (Figure 2).

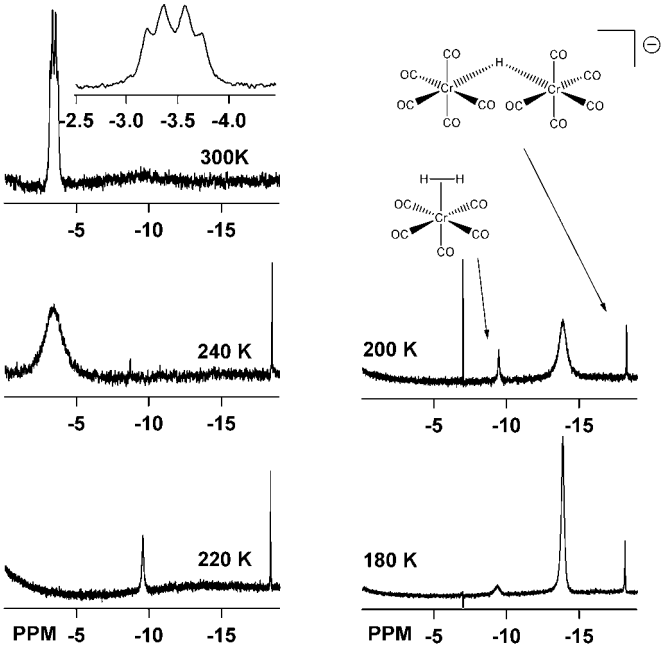

Figure 2. Variable temperature ^1H NMR spectra of $[Cr(CO)_5(\eta^1$-BH_2=$NMe_2)]$ (toluene-d_8, 499 MHz).

They are assigned to $[Cr(CO)_5(H_2)]$,[2] $[Cr(CO)_5(\eta^1$-BH_2=$NMe_2)]$ and the bridging hydride dimer $[(CO)_5Cr(\mu$-$H)Cr(CO)_5]^-$ respectively. Due to their thermal instability, as the temperature is raised the resonances corresponding to the dihydrogen complex and the bridging hydride disappear. However, the resonance at *ca* - 14 ppm broadens at 200 K to disappear at 220 K and reappear at *ca* -3.5 ppm at 240 K. This peak, assigned to $[Cr(CO)_5(\eta^1$-BH_2=$NMe_2)]$, sharpens at higher temperatures to give a quartet at 300 K ($J_{B\text{-}H}$ = 90 Hz). At low temperature, in the slow exchange regime, the resonance observed corresponds to the one of the Cr-H-B hydride. Above 240 K, an average of bridging and free B-Hs gives a peak at – 3.5 ppm. Similarly, Ogino and coworkers recently reported the synthesis and characterization of dynamic NMe_3-BH_3 complexes, $[M(CO)_5(\eta^1$-$BH_3.L]$ (M = Cr, Mo, W; L= NMe_3).[3]

At 290 K, the ^{11}B NMR spectrum shows three main species at 41.2 (t, J_{BH} = 130 Hz), 8.5 (t, J_{BH} = 112 Hz) and -9.5 ppm (q, J_{BH} = 95 Hz) (Figure 3). They correspond to bound NMe_2=BH_2, $(NMe_2$-$BH_2)_2$ and free NH_3BH_3 respectively. Within hours at - 26 °C, the sample decomposes and only the dimer $(NMe_2$-$BH_2)_2$ remains in solution. Addition of more $Cr(CO)_6$ and 30 minutes of irradiation do not lead to the formation of any new species as observed by ^1H and ^{11}B NMR. These results show that $(NMe_2$-$BH_2)_2$ does not bind to the unsaturated complex $[Cr(CO)_5]$.

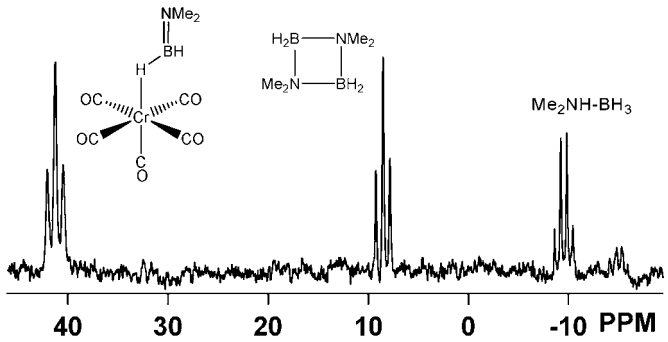

Figure 3. ^{11}B NMR spectra of $[Cr(CO)_5(\eta^1\text{-}BH_2{=}NMe_2)]$ (toluene-d_8, 499 MHz, 290 K).

Conclusions

We report the coordination of B-N species to group 6 pentacarbonyl transition metal complexes. Formation of the corresponding dihydrogen complex has also been observed after loss of hydrogen due to the dehydrogenation of the aminoborane adduct. Experimental data show that the cyclic dimer $(NMe_2BH_2)_2$ does not bind to $[Cr(CO)_5]$ while $NMe_2{=}BH_2$ does.

Acknowledgement. This research was supported by the Department of Energy. We thank Dr Tom Autrey of PNNL for a generous gift of NH_3BH_3 and Me_2NHBH_3.

References)

(1) Chen, Y.; Fulton, J.L.; Linehan, J.C.; Autrey, T. *J. Am. Chem. Soc* **2005**, *127*, 3254-3255 and references therein.
(2) Matthews, S.L.; Pons, V.; Heinekey, D.M. *J. Am. Chem. Soc* **2005**, *127*, 850-851.
(3) Shimoi, M.; Nagai, M.I.; Kawano, Y.; Katoh, K.; Uruichi, M.; Ogino, H. *J. Am. Chem. Soc* **1999**, *121*, 11704-11712.

ROOM TEMPERATURE HYDROGEN EVOLUTION FROM AMINE-BORANES

Frances H. Stephens and R. Tom Baker

Institute for Hydrogen and Fuel Cell Research
Chemistry Division, MS J514
Los Alamos National Laboratory
Los Alamos, NM 87545

Introduction

Chemical hydrides for hydrogen storage are being explored as alternatives to high pressure tanks (gas or liquid), adsorbed hydrogen, and metal hydride fuels. Chemical hydrides have the potential to be non-pyrophoric, non-hazardous, solid or slurried fuels for automotive applications where hydrogen is generated under controlled conditions on-board, on demand, and the spent fuel is regenerated off-board.

Ammonia-borane (H_3NBH_3) epitomizes an important characteristic required for a chemical hydride used in hydrogen storage: Low molecular weight vis-à-vis the number of hydrogen atoms present. The ideal molecular hydrogen storage capacity of H_3NBH_3 is 19.6 wt% (c.f. the DOE's goal of 6 wt% system storage by 2010). Because the molecule contains both hydridic and protic hydrogen atoms, it loses H_2 at temperatures above ca. 80 °C. Thermal decomposition in solution initially affords the cyclic oligomers borazane ($B_3N_3H_{12}$) and borazine ($B_3N_3H_6$).[1] Wideman and Sneddon demonstrated that large scale preparation of borazine from H_3NBH_3 could be achieved in high yield over 3 h by simply heating a tetraglyme solution of ammonia-borane.[2] Sneddon et al. also demonstrated that borazine could be thermally cross-linked at temperatures as low as 70 °C with concomitant H_2 evolution.[3] Ultimately H_3NBH_3 can be dehydrogenated completely, forming ceramic BN, but temperatures in excess of 500 °C are required.[4]

It is possible to obtain a large amount of hydrogen from H_3NBH_3, but low energy (i.e. minimal heat input) methods to utilize this fuel are only just being developed. Manners et al. have recently reported room temperature liberation of H_2 from H_3NBH_3 or dimethylamine-borane (HMe_2NBH_3) by addition of late metal catalysts. For example, select Rh(I) species catalyzed the dehydrocoupling of HMe_2NBH_3, forming H_2 and the cyclic dimer $[BH_2NMe_2]_2$ as well as linear aminoborane polymers.[5] The active catalytic species in this reaction was recently proposed to be a soluble Rh_6 cluster by a team at Pacific Northwest National Laboratory.[6] This research team also reported the use of mesoporous scaffolds to template the thermal H_3NBH_3 dehydrogenation. No borazine was observed during the reaction, and the authors suggested exclusive formation of linear polymers. This selectivity is important, since volatile products of dehydrogenation may negatively affect fuel cell catalysts used in series with a hydrogen storage material. Furthermore, preliminary thermodynamic calculations indicate that sequential dehydrogenations to form linear polymers $(NH_2BH_2)_x$ and $(NHBH)_x$ are thermoneutral to within 40 kJ mol^{-1}.[7]

In this communication we report the evolution of hydrogen from ammonia-borane catalyzed by a series of proprietary, non-metal catalysts.

Experimental

General Considerations. Chemicals were used as received. Dimethoxyethane was distilled from CaH_2 and stored over 4Å molecular sieves. Toluene was dried by the method of Grubbs.[8] Ammonia-borane was prepared via literature methods. All experiments were preformed in an inert atmosphere using standard glovebox or Schlenk line techniques.

Characterization Methods. ^{11}B NMR spectra were recorded on a Bruker 400 MHz spectrometer and were externally referenced to boron trifluoride etherate (0 ppm).

Dehydrogenation Reactions. In a typical reaction, 0.1 mmol amine-borane was dissolved in approximately 0.5 mL dimethoxyethane (H_3NBH_3) or toluene (HMe_2NBH_3). To this solution was added a solution of 0.1 equiv catalyst at 22 °C. The reaction mixture was placed in an NMR tube with a Teflon stopcock, and the headspace was evacuated to allow for H_2 (g) generation during the reaction. The reaction was then monitored by ^{11}B NMR spectroscopy.

Results and Discussion

For comparison purposes, a thermolysis study was performed in which a dimethoxyethane solution of H_3NBH_3 (ca. 0.4 M) was monitored at 80 °C over 24 h using ^{11}B NMR. After 2 h, in addition to the starting material (δ –22 (q) ppm), a small amount of borazane was observed (δ –10 (t) ppm), subsequently losing hydrogen slowly to form borazine (δ 32 (d) ppm) after 24 h. At this temperature, starting material remained after 24 h.

In contrast, the addition of 10 mol% of proprietary, non-metal catalysts to H_3NBH_3 resulted in complete consumption of the starting material after the same time period and heating regimen. The product mixture included small amounts of the soluble products borazine and borazane and a significant amount of insoluble colorless solid (characteristic of polymeric aminoboranes). In addition to borazine and borazane, a triplet at ca. δ –25 ppm was observed, consistent with internal $–BH_2–$ units in linear oligomers of aminoborane. (Experiments utilizing ^2H- and ^{15}N-labeled substrates are underway.) The observed production of small amounts of borazine and borazane is likely due to the addition of heat to a reaction mixture containing H_3NBH_3; the thermal decomposition of H_3NBH_3 and the catalyzed reactions are competitive at 80 °C.

The proprietary, non-metal catalysts also react with H_3NBH_3 under mild conditions to yield hydrogen. In this case, immediate and copious bubbling ensued when 0.1 equiv catalyst was added at 22 °C. While the ^{11}B NMR spectrum is complex in the region from –15 to 10 ppm, it is clear that a triplet at approximately δ –25 ppm grows in over 24 h *at room temperature*. This is consistent with internal $–BH_2–$ units in an aminoborane oligomer.

The reaction of the catalyst with the alkyl-substituted dimethyl amine-borane (HMe_2NBH_3) resulted in oligomerization. When 0.1 equiv of the catalyst was used, no peaks attributable to the cyclic dimer $[Me_2NBH_2]_2$ were observed in the ^{11}B NMR spectrum, in contrast to metal-catalyzed reactions.[5,6] A triplet of doublets around δ –20 ppm grows in over time, eventually becoming the major peak. Again, this upfield peak is due to the internal $–BH_2–$ units in an oligomeric product.

Conclusions

In contrast to transition metal catalysts, it can be concluded that these proprietary, non-metal catalysts increase the selectivity for linear oligomers. This discovery moves amine-boranes closer to commercialization as H_2 generating materials for portable power sources. Further experiments, including H_2 quantification, are underway to refine these experiments.

Acknowledgement. This work was performed in conjunction with the Chemical Hydrogen Storage Center of Excellence, supported by the Hydrogen, Fuel Cell, and Infrastructure Technologies Program of the Division of Energy Efficiency and Renewable Energy, U.S. Department of Energy, under contract DEPS-3603-G093013.

References

(1) Wang, J. S.; Geanangel, J. S. *Inorg. Chim. Acta* **1988**, *148*, 185.
(2) Wideman, T.; Sneddon, L. G. *Inorg. Chem.* **1995**, *34*, 1002.
(3) Fazen, P. J.; Beck, J. S.; Lynch, A. T.; Remsen, E. E.; Sneddon, L. G. *Chem. Mater.* **1990**, *2*, 96.
(4) Paine, R. T.; Narula, C. K. *Chem. Rev.* **1990**, *90*, 73.
(5) Jaska, C. A.; Temple, K.; Lough, A. J.; Manners, I. *J. Am. Chem. Soc.* **2003**, *125*, 9424.
(6) Chen, Y.; Fulton, J. L.; Linehan, J. C.; Autrey, T. *J. Am. Chem. Soc.* **2005**, *127*, 3254.
(7) Gutowska, A. et al. *Angew. Chem. Int. Ed.* **2005**, *44*, 2.
(8) Pangborn, A. B.; Giardello, M. A.; Grubbs, R. H.; Rosen, R. K.; Timmers, F. J. *Organometallics* **1996**, *15*, 1518.

CATALYSIS FOR HYDROGEN STORAGE

John C. Linehan[1], Tom Autrey[1], John L. Fulton[1], Yongsheng Chen[1] and Mahalingam Balasubramanian[2]

(1)Fundamental Science Division, Pacific Northwest National Laboratory, P. O. Box 999 MSIN K2-57, Richland, WA 99352, Fax: 509-375-6660, john.linehan@pnl.gov (2) Advanced Photon Source, Argonne National Laboratory

Introduction

The U.S. Department of Energy has recently issued a Grand Challenge in Hydrogen Storage.[1] The ambitious goals of this challenge demand the discovery of new hydrogen storage materials and new catalysts for H_2 release as well as regeneration. We have embarked upon a study of amine borane complexes to meet this challenge.[2] In previous work we examined the rhodium catalyzed dehydrocoupling of dimethylamine borane to release hydrogen at room temperature from this storage material. Below we describe a new aspect of our research on the hydrogen release from NH_3BH_3 using a homogeneous ruthenium catalyst. Other groups have investigated the ruthenium catalyzed dehydrocoupling of phorous boron bonds with concomit formation of hydrogen.[4]

Experimental

Methanol and tetrahydrofuran were purified and degassed before use. Borane ammonia complex was purchased from Aviabor and used as received. In situ ^{11}B NMR was performed on a Varian VXR-300 run unlocked in non-deuterated solvent referenced to BF_3-etherate as 0 ppm. The *in situ* Ru K-edge (22117 eV) XAFS spectra were collected on the bending magnet beamline (PNC-CAT, Sector 20) at the Advanced Photon Source, Argonne National Laboratory. Data were analyzed using AUTOBK and IFEFFIT routines.[3]

The reactions described here release large quantities of H_2 gas. The reactions can be exothermic and the gas release can be violent. Proper safety precautions including, but not limited to, pressure release devices, proper venting and personal safety equipment should be used.

Results and Discussion

The boron NMR results of the ruthenium ($Ru(DMSO)_4Cl_2$, DMSO is dimethylsulfoxide) catalyzed reaction of NH_3BH_3 in methanol at room temperature are shown in Figure 1. The boron cleanly and quickly converts from BH_3 attached to NH_3 to methylborate. The proton coupled boron NMR spectra of this reaction clearly shows that product peak contains no B-H bonds. Methyl borate forms very slowly at room temperature in methanol from NH_3BH_3 in the absence of a catalyst. At 80°C the non-catalyzed reaction occurs on a similar time-scale as the catalyzed reaction at room temperature.

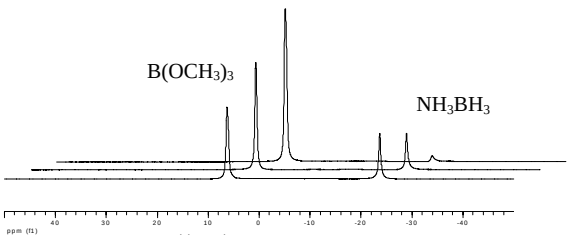

Figure 1. The $^{11}B\{^1H\}$ NMR of the reaction of NH_3BH_3 with methanol catalyzed with $Ru(DMSO)_4Cl_2$ at room temperature. The time evolution from front to back is 6 minutes, 11 minutes and 44 minutes after mixing.

The ruthenium edge EXAFS radial distribution functions of the ruthenium species relevant to this reaction are shown in Figure 2. These and the in situ EXAFS data (not shown) demonstrate that during the catalysis the $Ru(DMSO)_4Cl_2$ complex is completely converted to a new soluble catalytic species which does not contain any Ru-S or Ru-Cl bonds. The metal-containing catalytic species (or it's resting state) only has light element (O, B, or N) ligands directly bound to the ruthenium.

XANES data (not shown) demonstrate that the initial Ru(II) oxidation state stays as Ru(II) throughout the reaction. There is no obvious precipitate and no obvious oxidation change during the reaction.

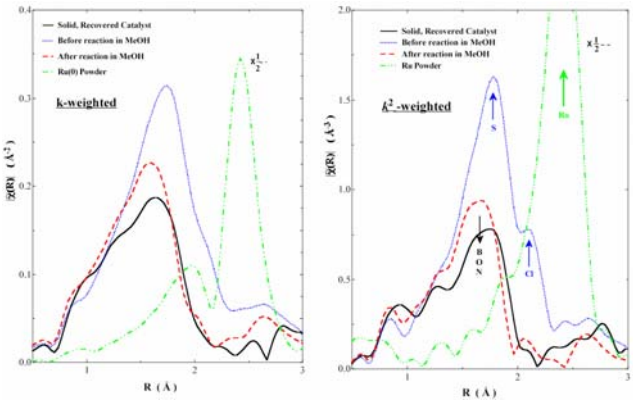

Figure 2. Radial distribution plots of ruthenium before and after reaction with NH_3BH_3 in methanol compared with ruthenium metal and the initial starting complex, $Ru(DMSO)_4Cl_2$.

Conclusions

In situ spectroscopies have been shown to be extremely useful in determining the reaction profiles of both the substrates and the catalysts during the reaction to release H_2 from hydrogen storage materials. While the structure of the ruthenium catalyst is unknown we know that the ligand field about the catalyst is completely changed during catalysis but the oxidation state remains +2. The boron-containing reaction products are dependent upon the solvent and the reaction conditions. Efficient release of H_2 from NH_3BH_3 has been demonstrated.

Acknowledgement. Work was supported by the Laboratory Directed Research and Development Program at the Pacific Northwest National Laboratory; the NS&T Initiative; and by the Department of Energy's Center of Excellence in Chemical Hydrogen Storage. Pacific Northwest is operated for the Department of Energy by Battelle. Use of the Advanced Photon Source was supported by the U.S. Department of Energy, Office of Science, Office of Basic Energy Sciences, under Contract No. W-31-109-ENG-38.

References

(1) Hydrogen, Fuel Cells & Infrastructure Technologies Program, 2003 Merit Review and Peer Evaluation Meeting, May 19-22, 2003, Berkely, CA.
(2) Chen, Y. S.; Fulton, J. L.; Linehan, J. C. and Autrey, S.T. *J. Am. Chem. Soc.*, **2005**, *127*, 3254.
(3) Newville, M. *J. Synchrotron Rad.* **2001**, *8*, 322.
(4) Dorn, H., Singh, R. A., Massey, J. A., Nelson, J. M., Jaska, C. A., Lough, A. J. Manners, I. *J. Am. Chem. Soc.* **2000**, *122*, 6669.

SPECTROSCOPIC STUDIES OF HYDROGEN FORMATION FROM AMINEBORANE COMPLEXES

Nancy Hess, Craig Brown, Luke Daemen, Eugene Mamontov, R. Scott Smith, Bruce D. Kay, Wendy Shaw, John Linehan, Benjamin Schmid, Ashley Stowe, Maciej Gutowski & Tom Autrey

Pacific Northwest National Laboratory
Los Alamos National Laboratory
National Institute of Standards
The University of Maryland
University of Oregon

Introduction

Currently there is great scientific and public interest in the challenges facing the conversion from a petroleum based energy economy to one based upon hydrogen as an energy carrier for fuel cell power applications.[1,2] The future of the Hydrogen Economy will depend upon significant scientific and engineering advances in hydrogen storage, hydrogen production and hydrogen utilization (fuel cells). [3-6]

We have been investigating the chemical and physical properties of chemical hydrogen storage materials containing boron and nitrogen as potential solid state hydrogen storage materials for on-board applications. Experimentally, we have focused on our efforts on determining the thermochemistry and kinetics of thermally activated release of hydrogen from ammonia borane (NH_3BH_3) confined within mesoporous silica and the catalytically activated release of hydrogen from dimethylamine borane (Me_2NHBH_3). We discovered that ammonia borane (AB) confined within the channels of mesoporous silica (SBA-15 or MCM-41) showed a significant rate enhancement for hydrogen release and a change in the enthalpy of reaction for the release of hydrogen.[7] These results are summarized in Figure 1, (A) shows the decomposition of bulk AB to yield polyaminoborane (PAB), the activation barrier, E_a 28 kcal mol, and enthalpy of reaction, ΔH_{rxn} -5 kcal/mol for loss of hydrogen in the solid state. (B) shows the decomposition of AB confined in SBA-15, E_a ca. 12 kcal/mol and ΔH_{rxn} -0.3 kcal/mol for loss of hydrogen. The observed change in thermochemistry and kinetics (ΔH_{rxn} and E_a) reflects a change in the chemical or physical properties of AB when it is confined within the nano-dimensional channels of SBA-15.

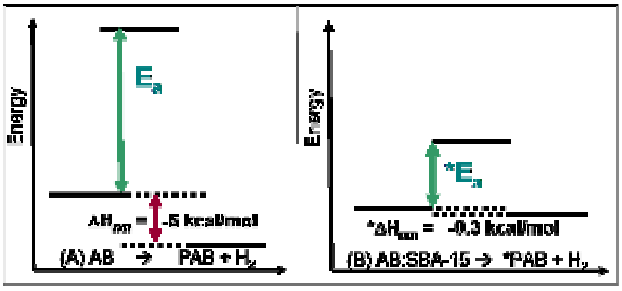

Figure 1. Energy level diagram comparison of E_a and enthalpy for H_2 formation from bulk AB and AB confined in SBA-15.

Recent mechanistic studies using deuterium labeling lead us to conclude that the formation of hydrogen from bulk AB occurs by a bimolecular pathway[8] contrary to what has been suggested in the literature.[9-11] This was also in contrast to our in-situ spectroscopic studies of the catalyzed dehydrogenation of dimethylamine borane where the hydrogen formation appeared to proceed by an intramolecular pathway.[12] Thus, while we have learned much about hydrogen formation from these solid state hydrogen storage materials one important question remains unanswered: What is the origin of the change in the activation barrier and enthalpy of reaction for hydrogen loss from AB in the mesoporous scaffold compared to the reaction in the bulk material? In this presentation we will highlight our recent spectroscopic studies aimed at elucidating the changes in the chemical and physical properties of AB in mesoporous silica.

Experimental

Ammonia borane from Aldrich (95%) was recrystallized from diethyl ether. Ammonia borane (99%) from Avibor and used as received. The synthesis and loading of the AB into the mesoporous silica has been described previously.

11-Boron and 1H NMR Spectroscopy. Amino borane samples were run on a Varian Unity Inova spectrometer operating at 800 MHz ^{1}H frequency, with a 4mm, 3-Ch Doty MAS probe. The Bloch decay experiment utilized a 200 kHz sweep width, a 8 μs ^{11}B 90° pulse, with and without ~30 kHz decoupling, 16-64 scans and a pulse delay of 5 seconds. ^{11}B spectra were referenced to BF_3CH_3OH (-0.9 ppm). The ^{1}H spectra utilized a 3 μs 90º pulse and were referenced to H_2O (4.8ppm), with 4 scans and a 10 second pulse delay. Samples were spun at 15 kHz, cooled to 10-20 °C and 128 scans were collected for each spectrum.

Raman Spectroscopy. Raman spectra were excited by 10mW of continuous wave, doubled diode YAG laser with output at 532 nm and collected on a Dilor XY 800 mm triple spectrometer with liquid nitrogen cooled charged couple device (CCD) detector with a spectral resolution of ca. 0.2 cm^{-1} at 500 nm. A confocal microscope with 50X objective with high numerical aperture was used to image the bulk and confined AB samples.

Quasi-elastic Neutron Spectroscopy. The Disk Chopper Spectrometer (DCS) and the High Flux Backscattering Spectrometer (HFBS) at the NIST Center for Neutron Research[13] was used to study the bulk and confined ammonia borane. Isotopically enriched ^{11}B samples were loaded into annular aluminum cells and cooled in a closed cycle refrigerator. On DCS, data were collected at a series of temperatures above the structural phase transition at 225 C to extract activation energies for proton motion. Use of an incident wavelength of 3.6 Å results in an instrumental resolution of ~0.3 meV at the elastic line. On HFBS, data were collected at several temperatures below 225 C to extract information on proton motions at higher resolution (1.2 μeV). By using both spectrometers, we can follow fast proton motions that occur on picosecond time scale on DCS to slower motions on the nanosecond time scale on HFBS.

Results and Discussion

In previous work we discovered the barrier for hydrogen release from ammonia borane embedded in mesoporous silica is significantly lower than the barrier for hydrogen release from bulk AB. The origin of this beneficial rate enhancement was surprising and not fully understood. Furthermore, solid state ^{11}B NMR results suggested the non-volatile products formed upon release of hydrogen were different than observed in the bulk material resulting in a change in the reaction enthalpy for hydrogen formation. There are two distinct possibilities that may lead to the observed changes, (1) changes in the physical properties such as an increase in defects sites that may be responsible for the nucleation or an increase in disorder of the extended hydrogen bonding network of the molecular crystal, ammonia borane, and (2) changes in the chemical properties such as interfacial interactions that catalyze the formation of hydrogen from the molecular crystal AB, e.g. the acidic nature of the interface catalyzing the nucleation event..

Raman spectroscopy can be used to monitor changes in the B-N, B-H and N-H stretching and bending frequencies and line shapes between bulk AB and AB confined within the mesoporous materials or deposited on metal oxide interfaces. Initial work has shown that AB associated with SBA-15 or MCM-41 results in an increase in the B-N symmetric stretch line width and the possible appearance of a lower frequency B-N stretch mode while the B-H and N-H stretching moieties show little change (Figure 2). These results suggest that there is a greater distribution of energetically distinct B-N entities when AB is associated with the interface and may reflect the importance of an –SiOSi bridge with B—N (e.g., O···B). The polymerization reaction of AB can also be followed using in situ Raman spectroscopy. IR may be able to provide insight into the interaction between B-H or N-H bonds with SiO-H and Si-O-Si groups of the mesoporous silica. Many different electrostatic interactions (SiO-H--HBH_2NH_3, N-H or B may also coordinate to O in Si-O-Si) can be envisioned and spectroscopic approaches will facilitate their interpretation. The same changes will be calculated at the DFT and SCC-DF TB levels to assist in interpretation of the experimental results.

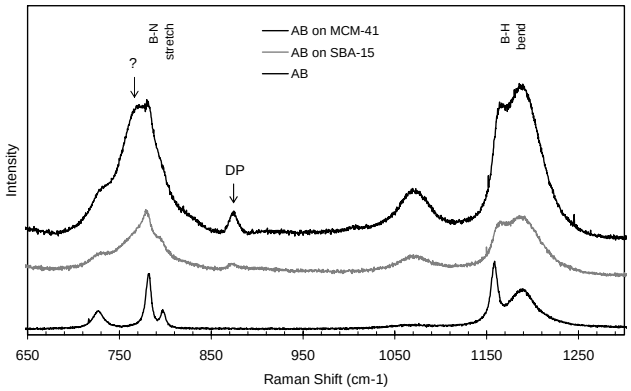

Figure 2. Raman vibrational spectra of bulk AB and AB confined in mesoporous MCM-41 and SBA-15. The B-N, B-H and N-H stretching and bending vibrations or AB occur in distinct energy regions of the vibrational spectrum. The B-N stretching mode at ca. 780 cm^{-1} and the B-H and the N-H rocking modes at ca. 1060 cm^{-1} appear most affected by the confinement in the mesoporous silica substrates. DP indicates the vibrational signature of possible decomposition products.

NMR Spectroscopy can be used to identify new species and/or changing environments. Qualitatively, the 1H NMR shown here suggests a change in the environment when AB is deposited on a scaffold, based on the significant narrowing of the resonances. This is consistent with several interpretations, including an increase in the mobility or an increase in the crystallinity of AB in the scaffold. Further NMR studies, as well as other spectroscopic characterization will be necessary to fully understand these initial observations.

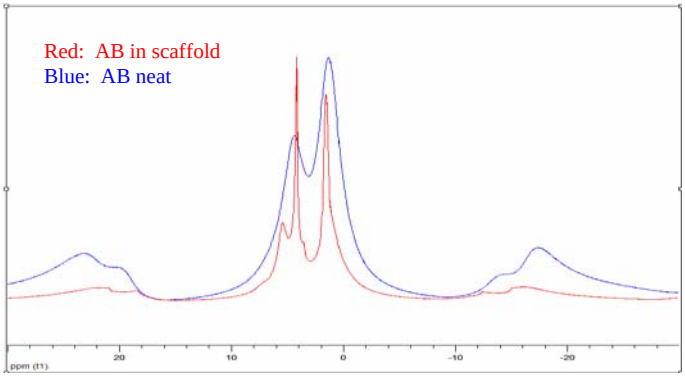

Figure 3. 800 MHz ^{1}H NMR of AB bulk (blue) and in the SBA scaffold (red). Confinement of AB results in significantly sharper lines, possibly due to an increased uniformity, or an increased mobility of the AB in the scaffold.

Quasi-elastic Neutron Spectroscopy can be used to probe the nano to picosecond timescales and sub-nanometer lengthscales of proton motion in materials. In general, the dependence of the ratio of the quasi-elastic scattering intensity to the total intensity on the momentum transfer provides information on the geometry and lengthscale of the individual proton motions. The timescale is extracted from the quasielastic peak widths. Results from both HFBS and DCS indicate that the deposition of AB on MCM-41 results in longer proton residence times and lower energy barriers for proton motion compared to bulk AB. The reduced activation energy for proton motions may partly explain the improved thermolysis and lowering the activation barrier for the loss of the first equivalent of H_2. In addition, the phonon density of states for neat AB compares well with other spectroscopic results, with the intense peak at 22 meV assigned to the librational NH_3 and BH_3 modes, whereas AB on MCM-41 displays a broad, featureless spectrum indicating a poorly crystalline material (Fig. 4). Clearly, deposition of AB on MCM-41 profoundly impacts the crystallinity and proton motions in AB.

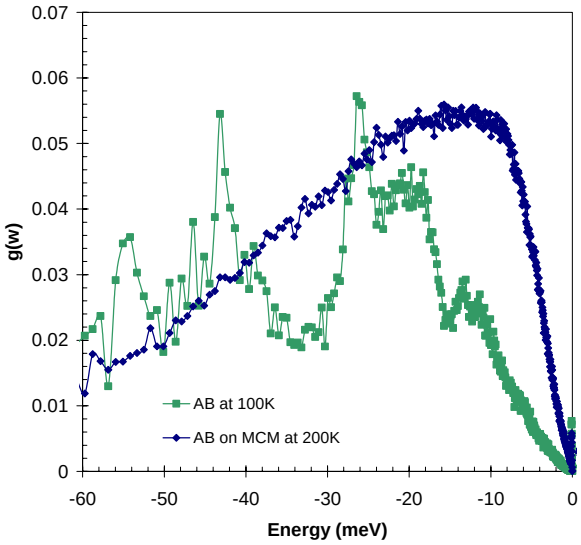

Figure 4. Phonon density of states for bulk AB and AB confined in MCM-41.

Conclusions

We have begun to combine multiple, complimentary spectroscopic tools to study the interfacial interactions between mesoporous silica scaffolds and ammonia borane. These experimental approaches combined with our theoretical efforts will provide information about the changes in the chemical and physical properties of AB at the interface.

Acknowledgement. The authors wish to acknowledge support from the Laboratory Directed Research and Development Program at the PNNL and the Nano Science and Technology Initiative. This research was performed in part using the Interfacial and Nano Science facility in the William R. Wiley Environmental Molecular Sciences Laboratory, a national scientific user facility sponsored by the U.S. Department of Energy's Office of Biological and Environmental Research and located at the Pacific Northwest National Laboratory. Pacific Northwest is operated for the Department of Energy by Battelle. We acknowledge the support of the National Institute of Standards and Technology, U.S. Department of Commerce, in providing the neutron research facilities used in this work. This work also utilized HFBS and DCS which are NIST facilities supported in part by the National Science Foundation under Agreement No. DMR-0086210. This work will continue in part

through the DOE Center of Excellence in Chemical Hydrogen Storage.

References

[1] Presidential State of the Union Address 2003. http://www.whitehouse.gov/news/releases/2003/02/20030206-2.html
[2] Scientific American, 2004, *Questions about a Hydrogen Economy*.
[3] National Academy of Engineering, 2004, *The Hydrogen Economy: Opportunities, Costs, Barriers, and R&D Needs.*
[4] Office of Science at the US Department of Energy. 2004, *Basic Research Needs for the Hydrogen Economy.*
[5] American Physical Society, 2004, *The Hydrogen Initiative.*
[6]http://www.eere.energy.gov/vehiclesandfuels/program_areas/freedomcar/index.shtml
[7] Anna Gutowska, Liyu Li, Yongsoon Shin, Chongmin M. Wang, Xiaohong S. Li, John C. Linehan, R. Scott Smith, Bruce D. Kay, Benjamin Schmid, Wendy Shaw, Maciej Gutowski, and Tom Autrey. *Nano-Scaffold Mediates Hydrogen Release and Reactivity of Ammonia Borane.* Angew. Chemie International Ed. **2005**, in press.
[8] R. Scott Smith, Bruce D. Kay, Liyu Li, Nancy Hess, Maciej Gutowski, Benjamin Schmid & Tom Autrey. *Mechanistic studies of hydrogen formation from amineborane complexes.* Prepr. Pap. –Am. Chem. Soc. Div. Fuel Chem. **2005**, *50*, 112.
[9] R. Komm, R. A. Geanangel, R. Liepins, *Inorg. Chem.* **1983**, *22*, 1684.
[10] V. Sit, R. A. Geanangel, W. W. Wendlandt, *Thermochim. Acta* **1987**, *113*, 379.
[11] D. -P. Kim, K. -T. Moon, J. -G. Kho, J. Economy, C. Gervais, F. Babonneau *Poly. Adv. Tech.* **1999**, *10*, 702.
[12] Yongsheng Chen, John L. Fulton, John C. Linehan and Tom Autrey, *In-situ XAFS and NMR Study of Rhodium Catalyzed Dehydrogenation of Dimethylamine Borane.* J. Am. Chem. Soc. **2005**. *127*, 3254.
[13] J.R.D. Copley and J.C. Cook, Chem. Phys. **2003**, 292, 477.

HYDROGEN EVOLUTION FROM ORGANIC "HYDRIDES"

Daniel E. Schwarz, Thomas M. Cameron, P. Jeffrey Hay, Brian. L. Scott, William Tumas, David L. Thorn

Chemistry Division
MS J514, Los Alamos National Laboratory
Los Alamos, New Mexico 87544

Introduction

New concepts of hydrogen storage are being explored for applications from portable power to transportation for the future "hydrogen economy".[1-3] The advantages of chemical hydrogen storage are the deliberate control of the thermochemistry, kinetics, and mass density for incorporating and releasing hydrogen. We are currently exploring an uncommon chemical process, the exergonic evolution of hydrogen gas at room temperature via catalysis from reduced organic compounds.

Experimental

2-(1,3-dimethylbenzimidazoline-2-yl)benzoic acid (**1**)[4], 1,3-dimethyl-2-phenylbenzimidazoline (**3**)[5], and 1,3-dimethylbenzimidazoline (**5**)[6] were all synthesized according to literature methods. The powder diffraction data were collected at room temperature on a Scintag XDS2000 diffractometer equipped with an air-tight environmental chamber to prevent sample degradation.

Catalytic dehydrogenation of **1**: The following is for a typical heterogeneous reaction for **1**, **3**, and **5** (**3** and **5** require the addition of a proton source such as acetic acid). To 0.5 mL of CD_3CN solution of compound 1 (19 mg, 0.07 mmol) in a 20 ml vial was added an acetonitrile solution of $Pd(O_2CCF_3)_2$ (1 mg, 0.003 mmol). Upon mixing a black precipitate formed and effervescence was observed. The reaction mixture was then transferred to an NMR tube for analysis. Conversion of **1** to **2** was confirmed by ^{1}H NMR spectroscopy. 2-(1,3-dimethylbenzimidazolium-2-yl)benzoate (**2**) was crystallized from a concentrated CH_3CN solution at -20° C. The black precipitate has a powder XRD pattern consistent with finely-divided palladium metal.

Catalytic dehydrogenation of **5**: For a homogenous system, using $RhCl(PPh_3)_3$ as the catalyst, a typical reaction is as follows: To 0.7 mL of CD_3CN in an NMR tube was added 15 mg (0.10mmol) of **5** and 60 mg (1.0 mmol) of acetic acid (97% grade). This solution was mixed then 0.3 mg (0.37 μmol) of $RhCl(PPh_3)_3$ was added. The NMR tube was heated at 70° C for 1 hour. A 43% conversion of **5** to **6** (+ H_2, ^{1}H NMR 4.5 ppm) was confirmed by ^{1}H NMR spectroscopy.

Results and Discussion

Hydrogen elimination from compound **1** comprises the catalyzed reaction between the "hydride" from the unique C-H of the imidazolidine and a "proton" from the carboxyl group (eq 1). This reactivity was confirmed by the reaction of 1,3-dimethyl-2-phenylbenzimidazoline (**3**) with acetic acid or benzoic acid under an inert atmosphere in the presence of finely divided palladium to afford hydrogen (eq 2) and the phenylbenzimidazolium cation (**4**). Compound **3** is stable toward these acids for days when no catalyst is present.

We sought to reduce the molecular weight of the organic hydride donor and thus prepared 1,3-dimethylbenzimidazoline (**5**). Compound **5** evolves hydrogen in the presence of acetic or benzoic acid and catalyst, similar to **3** (eq 3). The product 1,3-dimethylbenzimidazolium cation (**6**) can be re-converted to **5** with KBH_4.[6] Along with the heterogenous catalysts used for **1** and **2**, Wilkinson's catalyst, $RhCl(PPh_3)_3$, is a functional homogeneous catalyst (or catalyst precursor) for this system (eq 3). We have measured a mean TOF of 117/hour at 70° C.[7] Compound **5** is slightly unstable at elevated temperatures over the course of days in the presence of acid when no hydrogen-evolving catalyst is present, involving what we believe are intermolecular disproportionation reactions.[6]

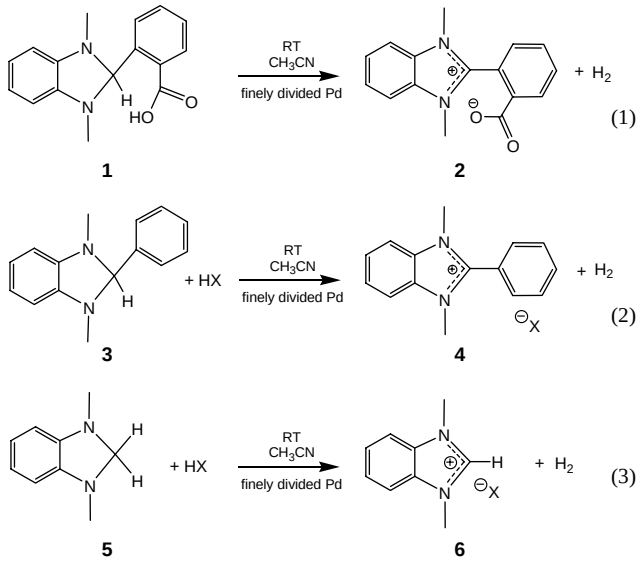

So far, we have not been able to reverse the hydrogen evolution in eq 1, 2, or 3 using Pd or $RhCl(PPh_3)_3$ catalyst nor have we been able to determine the equilibrium pressure of hydrogen. However, we have observed the following: the reaction in eq 1 progresses to completion even under 3.5 atmospheres H_2 pressure; preliminary *ab initio* calculations on the ambient-temperature transformation of **1** to **2** (eq 1) predict a strongly exergonic reaction; and the reaction of eq 3 generates heat which means that both entropy and enthalpy drive this reaction. These observations suggest that ambient-temperature hydrogen formation from benzimidazolidines and carboxylic acids is strongly favored ($\Delta G << 0$) and that using hydrogen pressure alone to drive the reaction backwards will be extremely difficult.[8] It stands to reason that acids much weaker than carboxylic acids could lead to hydrogen formation in eq 2 and 3, and preliminary results from our laboratory confirm that water is sufficiently acidic for Pd-catalyzed hydrogen evolution from compounds **3** and **5**. However, in the presence of water the reactions are far more complex than the reactions involving carboxylic acids due to further reactions of water and hydroxide with the benzimidazolium cations **4** and **6**. The organic products of the aqueous reactions are still under investigation.[9]

Conclusions

These "organic hydride" systems are sources of hydrolytically releasable hydrogen, reminiscent of inorganic hydrides such as $NaBH_4$ and LiH. However, by fine-tuning these organic systems for thermodynamically reversible hydrogen release we hope to enable more facile and efficient storage and regeneration than is possible for inorganic hydrides. We recognize that in addition to thermodynamic efficiency, the density of hydrogen storage is also a very important metric for hydrogen storage, and that organic frameworks with less substitution than compounds **1**, **3**, or even **5** are greatly preferred. A major emphasis of our ongoing research is realizing such higher-

density storage while maintaining favorable thermochemical and kinetic parameters for hydrogen evolution. Future work will also include detailed mechanistic studies and the development of more active heterogeneous and homogeneous catalysts for this process.

Acknowledgement. This work was supported as part of the DOE Center of Excellence for Chemical Hydrogen Storage through the Office of Energy Efficiency and Renewable Energy National Hydrogen Storage Project.

References

1. Fakioğlu, E.; Yürüm, Y.; Veziroğlu, T. N. *Int. J. Hydrogen Energy* **2004**, *29*, 1371-1376.
2. Seayad, A. M.; Antonelli, D. M. *Adv. Mater.* **2004**, *16*, 765-777.
3. Zuttel, A. *Naturwissenschaften* **2004**, *91*, 157-172.
4. Brunet, P.; Wuest, J. D. *Can. J. Chem.* **1996**, *74*, 689-696.
5. Reddy, A. P. R.; Veeranagaiah, V.; Ratnam, C. V. *Indian J. Chem., Sect. B: Org. Chem. Incl. Med. Chem.* **1985**, *24*, 367-371.
6. El'tsov, A. V. *Zh. Obshch. Khim.* **1967**, *3*, 199-204.
7. 0.2 M **5** in CD_3CN, 10x acetic acid, closed NMR tube.
8. **5** can be formed from **6** and water by disproportionation reactions not involving molecular H_2: Konstantinchenko, A. A.; Morkovnik, A. S.; Pozharskii, A. F.; Tertov, B. A. *Khim. Geterotsikl. Soedin.* **1985**, *12*, 1694-1695. Thus proof of the reverse of any of the reactions of eq 1-3 requires more than observing the appearance of benzimidazolidine.
9. Bourson, J. *Bull. Soc. Chim. Fr.* **1971**, 152-159.

X-RAY DIFFRACTION AND H-STORAGE IN ULTRA-SMALL PALLADIUM PARTICLES

D.G. Narehood[a], H.Goto[b], S. Kishore[c], J.H. Adair[d], J.A. Nelson[d], P.E. Sokol[e], and P.C. Eklund[a,d]

[a]Department of Physics
[d] Materials Research Institute and Department of Materials Science and Engineering
Penn State University
University Park, PA 16802 USA

[b] Honda Fundamental Research Laboratories
Tokyo, Japan

[c] Center for Magnetic Recording
UC San Diego
Lajiola, CA 92093 USA

[e] Indiana University Cyclotron Facility
Indiana University
Bloomington, IN 47408 USA

Introduction

Although Palladium has been widely investigated for its H uptake and kinetics, there exist a great deal of current interest in the system. This interest stems from the extensive amount of information available on the system, which makes it an excellent test case in which to study the changes in properties of the hydride that can occur as the metal particle size is reduced to the nanometer scale.

Reduction in the grain size of a metal has been recognized to lead to significant differences in its hydrogen uptake characteristics. Specifically of interest are the more favorable kinetics and/or enhanced H-storage that may possibly occur in very small diameter metal nanoparticles. In this paper we investigate the structural transformations and wt% uptake isotherms of very small, carbon-protected Pd nanoparticles (nano-Pd) with average particle diameter ~ 2-3 nm. The nano-Pd data are compared to that from micron-size grained bulk-Pd.

Experimental

Nano-Pd Samples. The two nano-Pd sample investigated in these studies exhibited mean particle sizes of 2.1 nm and 3.1 nm. These particle sizes were determined from the transmission electron microscope (TEM) images and extracted particle size distributions shown in **Figure 1**. Particle sizes of the nano-Pd samples were also determined from the XRD patterns, shown in **Figure 2**, collected with the nano-Pd samples under vacuum and held at a temperature of 50 ^{o}C. From the widths of the peaks in the diffraction patterns, the mean particle sizes for the two samples have been estimated to be ~2 and ~ 3nm, which are consistent with the results from the TEM analysis.

Both samples studied possessed a H-permeable carbon coating ~ 1nm thick. This coating has been applied to the nano-Pd to prevent agglomeration and grain growth at the temperatures used to degass and H-load the pristine metallic material. Prior to the x-ray diffraction (XRD) and isotherm measurements, the samples utilized were degassed in vacuum at T=200 ^{o}C for several hours. In both studies, ultra-high purity hydrogen gas (99.999%) was utilized.

XRD Measurements. XRD patterns were collected on a Rigaku RU200 rotating anode equipped with an Ag anode. This system was operated at voltages in the range of 40 to 50 kV and currents in the range of 100 to 150 mA. Samples were placed in a high pressure capillary tube cell mounted on a modified powder diffraction stage with a graphite analyzer between the sample and scintillation detector to eliminate background contributions in the collected patterns caused by fluorescence from the Pd samples. The orientation of the analyzer with respect to the scattered x-ray beam was adjusted such that the scattered Kα (λ = 0.56084 Å) component was selected through Bragg diffraction from the (002) plane of the graphite analyzer. Diffraction patterns were collected over 2θ ranges of 5 to 45 ^{o} and 10 to 20 ^{o} with a step size of 0.05 ^{o} and time per points of 10 to 20 seconds.

Thermogravimetric Upatake Measurements. Isotherms of the wt% hydrogen uptake versus hydrogen loading pressure, shown in **Figure 4**, were collected for the 3.1 nm sample, with the sample held at temperatures of 50 ^{o}C and 90 ^{o}C, and the bulk-Pd sample, with the sample held at a temperature of 90 ^{o}C. These isotherms were measured gravimetrically on 80 mg of the nano-Pd sample using a high-pressure thermogravimetric analyzer (TGA Model # 003 Hiden, Inc.) The apparent weight of the samples was measured as a function of He and H gas overpressure (P). Before being admitted into the sample chamber, the hydrogen gas was first passed through an oxygen/moisture trap (Megasorb Gas Purifier, Supleco Inc.). The data was corrected for buoyancy effects with the tabulated mass densities of H and He versus (P,T). Diffraction data were collected with the sample held at fixed temperatures of 50 ^{o}C, 90 ^{o}C, 125 ^{o}C, and 150 ^{o}C. For each temperature, diffraction patterns were collected for a range of pressures from 0 to 10 atm.

Results and Discussion.

The structure of the nano-Pd samples has been determined from the XRD patterns shown in **Figure 2**. Comparison of the patterns reveals that for every peak present in the diffraction pattern for the bulk-palladium sample, there is a corresponding peak in the pattern for the nano-Pd samples. This correlation between the peaks in nano-Pd patterns with those in the bulk-Pd pattern allows us to confidently conclude that both nano-Pd samples possess the same FCC structure as the bulk. We find no substantial difference in the lattice parameter between the bulk-Pd sample and the nano-Pd samples. Using the positions of the (111) and (220) peaks for the bulk-Pd sample, we find a value for the lattice constant of 3.89 Å, which is in good agreement with the accepted value of 3.8907 Å[1]. Again using the (111) and (220) peaks to determine the lattice spacing, we have determined that the 2 nm and 3 nm nano-Pd samples have a lattice constants of 3.90Å, which is essentially in agreement with the accepted bulk-Pd lattice constant.

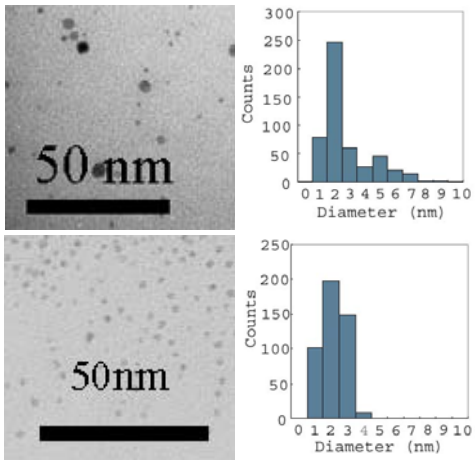

Figure 1. TEM images and extracted for the 3.1 mean diameter sample (upper) and the 2.1 mean diameter sample (lower).

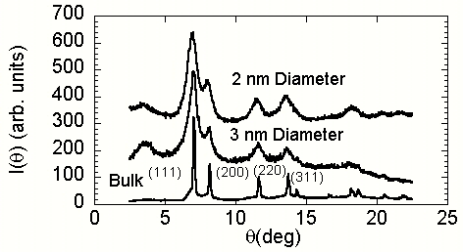

Figure 2. XRD scans collected from the 3 nm Pd sample, 2 nm Pd sample, and bulk Pd sample.

Shown in **Figure 3** are XRD patterns collected with the nano-Pd samples at a temperature of 50 ^{o}C in the limits of no hydrogen pressure and high hydrogen pressure. It is clear from a comparison of these patterns that the structure of the metal lattice is still the same, but that a shift in the position of the diffraction peaks to lower scattering angles occurs. Lower scattering angles correspond to larger lattice spacing and this shift is interpreted as the α to β phase transition. The lattice constant in the β phase has been determined to be 4.02Å, which is consistent with that observed for the bulk-Pd hydride in the β phase.

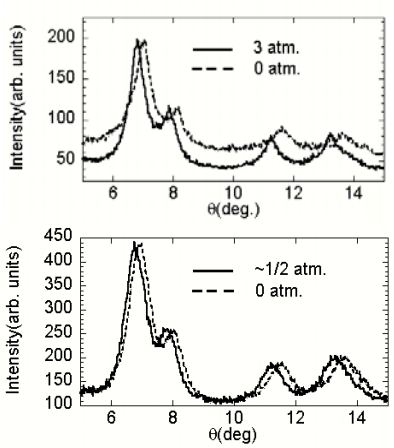

Figure 3. Comparison of the XRD patterns under low and high hydrogen loading pressure for the 3.1 mean diameter sample (upper) and the 2.1 mean diameter sample (lower).

Considerable differences are seen between the isotherm data of the bulk-Pd sample and the 3.1 nm nano-Pd sample, both of which are shown in **Figure 4**. As is easily seen in the isotherms, the bulk-Pd reference sample exhibits a flat plateau, characteristic of the co-existence of the α and β phases, and is in excellent agreement with the literature. This flat plateau is not present in the isotherm for the 3.1nm Pd sample. Instead, in the region in which phase co-existence should occur and the isotherm should be flat, it exhibits a noticeable positive slope. We have recently reported similar results for unprotected nano-Pd particulates with somewhat larger particle sizes[2].

Also notable in the isotherm data is the large disparity between the wt % uptake of the bulk reference and our nano-Pd sample. This results predominately from the high percentage of carbon in the nano-Pd sample, which is present as the coating protecting the Pd nano-particles from agglomeration. After corrections for the carbon coating, the wt % of H relative to just the Pd in the sample is ~.1 % for T = 50 ^{o}C at a pressure of ~ 1 atm. This wt% uptake is larger than observed in the bulk-Pd sample under the same conditions, which is in agreement with our earlier work[2]. This increase in hydrogen solubility in the α phase is attributed to the occupation of surface and subsurface sites, which occupy a greater percentage of volume in the nano-Pd samples.

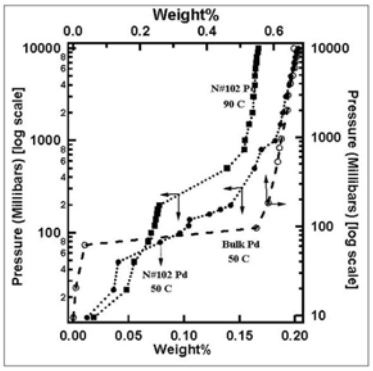

Figure 4. Hydrogen wt% uptake isotherms for both the nano-Pd sample (upper axis), at temperatures of 50 ^{o}C and 90 ^{o}C, and bulk-Pd (lower axis), for a temperature of 50 ^{o}C are shown.

The hydriding behavior of nano-Pd has been previously studied in both theoretical and experimental work. Suleiman et al.[3]have performed similar studies to those reported here on Pd clusters with diameters of 6.0 nm and 3.8 nm. In their studies, they find that the 6.0 nm particles posses an FCC structure and still undergo the α to β phase transition, while the 3.8 nm particles do not undergo this transition. In addition, they claim that the structure of the 3.8 nm sample is icosahedral. It is suggested that the lack of a phase transition is related to the icosahedral structure, which is claimed to be favorable for such small particles. Wolf and Lee[4] have examined the hydriding behavior of nano-Pd clusters that contain on the order of 500 Pd atoms through Monte Carlo simulations. They have also determined that the nano-Pd clusters do not undergo a phase transition. We find no support for either the experimental work or theoretical work. Both samples investigated posses smaller mean diameters and fewer atoms per particle than in previously mentioned work, yet both samples clearly maintain an FCC structure and under go the α to β phase transition.

Conclusion

We report striking similarities in the hydriding behavior of nano-Pd and bulk-Pd samples. This is despite the incredibly small number of Pd atoms composing the particles. The nano-Pd samples utilized in this work contain on the order of 100 – 300 particles, which not only means that a substantial volume (at least 30%) of the Pd atoms are within one lattice constant of the surface, but also that short-range forces should dominate the Pd-H interactions.

Acknowledgement. This work was supported by the Department of Energy under Grant DE-FC36-05GO15077 and by Honda Research and Development

References

(1) Rao, C.N., Rao, K.K., *Can. J. Phys.*, **1964**, 42, 1336.

(2) Kishore, S.; Nelson, J.A.; Adair, J.H.; Eklund, P.C.; J. L. *J. Alloys and Compounds* **2005**, 389, 234

(3) Suleiman, M.; Jisrawi, N.M, Dankert, O.: Reetz, M.T.; Bähtz, C, Kirchheim, R; Pundt, R. Winans, R. E. *J. Alloys and Compounds* **2003**, 356-357, 644

(4) Wolf, R.J.; Lee. M.W; *Phys. Rev. Lett.* **1994**, 73 (4), 557.

PREDICTING HYDROGEN DIFFUSION RATES BY ACTIVATED HOPPING AND QUANTUM TUNNELING IN COMPLEX METALLIC STRUCTURES

Bhawna Bhatia[*], Preeti Kamakoti[*], and David S. Sholl[*,#]

[*]Dept. of Chemical Engineering, Carnegie Mellon University, Pittsburgh, PA. 15213, USA
[#]National Energy Technology Laboratory, Pittsburgh, PA 15236, USA

Introduction

The use of metallic materials in hydrogen storage and purification demands not only a significant solubility of hydrogen in a these materials but ideally also rapid diffusion by hydrogen in the bulk. In order to develop suitable hydrogen storage materials a detailed knowledge of the microscopic mechanisms of hydrogen motion in these systems is required. Although the diffusion of hydrogen in metals has been studied for decades, methods that can predict the diffusion rates of hydrogen in the complex materials of practical interest are still limited. In the past several years, we have demonstrated how a modeling approach based on deriving lattice models for hydrogen diffusion in disordered metal alloys from Density Functional Theory (DFT) calculations can give accurate predictions of the properties of macroscopic hydrogen purification membranes[1-3].

Our previous modeling efforts have focused on descriptions in which hydrogen hopping between adjacent interstitial sites in a metal take place via an activated process that can be described using either classical or quantum corrected transition state theory. An important issue that cannot be addressed by this approach is the contribution to hydrogen transport from quantum mechanical tunneling between adjacent sites. Several approaches exist that allow tunneling in metals or on metal surfaces to be described accurately via DFT calculations[4-6]. Unfortunately, these methods require very extensive DFT calculations to characterize a single pair of adjacent sites. This greatly limits the application of these methods to complex alloys where H occupies interstitial sites with different types of neighboring atoms and thus large numbers of distinct hopping transition rates must be predicted in order to characterize long range diffusion.

Here, we describe a computational approach that allows tunneling contributions to hydrogen hopping between interstitial sites in complex metals to be readily described using DFT calculations. To examine the validity of this method, we have examined H diffusion in a number of C15 Laves phase intermetallics with composition AB_2. This is a useful test case for our methods because their structure contains a number of distinct interstitial sites which must all be examined before net diffusion can be predicted and because high quality experimental data exists over large temperature ranges for some examples[7-12]. The interstitial sites occupied by hydrogen in C15 AB_2 Laves phase intermetallics are tetrahedral sites formed by two A atoms and two B atoms (g sites), one A atom and three B atoms (e sites), and b sites formed by four B atoms. There are 17 tetrahedral interstitial sites per formula unit, 12 g sites, 4 e sites, and 1 b site for the C15 structure. Below, we show how we have used DFT-based methods to describe the contributions of activated hopping and quantum tunneling to hydrogen diffusion in ZrX_2 (X=V, Cr, Mn, Fe and Co) in the C15 Laves phase structure.

Computational Method

We have performed plane wave DFT calculations to examine H diffusion in ZrX_2, using the Vienna *ab initio* Simulation Package (VASP)[13] using the PW91-GGA exchange-correlation functional. Spin polarization was used for $ZrMn_2$, $ZrFe_2$, and $ZrCo_2$. A computational cell extended by periodic boundary conditions was used to describe a material of infinite extent. A cubic computational cell of A_8B_{16} in the C15 structure was used for all calculations. *k-space* was sampled using 3×3×3 *k*-points positioned using the Monkhorst-Pack scheme. Results using larger numbers of *k*-points gave only very minor total energy differences from calculations with 3×3×3 *k*-points. A cutoff energy of 270 eV was used throughout. Geometries were optimized until the forces on all unconstrained atoms were less than 0.03 eV/Å. Unless otherwise specified, all atoms were allowed to relax during geometry optimizations.

For interstitial H in ZrX_2 we first optimized the C15 lattice constant in the absence of H. This gave lattice constants of 7.32, 7.12, 7.00, 7.06, and 6.90 Å for ZrV_2, $ZrCr_2$, $ZrMn_2$, $ZrFe_2$, and $ZrCo_2$ respectively. These compare well with the experimentally established lattice constants of 7.45, 7.21, 7.14, 7.07, and 6.95 Å[14-17]. All calculations for interstitial H in these materials were performed by placing a single H atom in the computational supercell, corresponding to a net stoichiometry of $AB_2H_{0.125}$.

Transition states for hopping of H between adjacent interstitial sites were determined using the Nudged Elastic Band (NEB)[18] method. All atoms were allowed to relax during these calculations. Following convergence of the NEB calculations, the configuration most closely approximating a transition state was geometry optimized using a quasi-Newton algorithm that converges to critical points on the potential energy surface for starting points sufficiently close to a critical point. This procedure allowed the precise location of the transition states.

Vibrational frequencies for H in local minima and at transition states were calculated by assuming these frequencies are decoupled from metal atom vibrations. With this approximation, the metal atoms were constrained in the geometry associated with the minimum or transition state of interest and the Hessian matrix for local motion of the H atom was estimated using finite difference methods. This resulted in three real frequencies at each local minimum and two real frequencies at each transition state.

The local hopping rates between adjacent pairs of interstitial sites were predicted using the semiclassically corrected transition state formalism of Ferrman and Auerbach[19]. This formalism includes tunneling contributions and zero point effects but, crucially, only requires the energies and vibrational frequencies of H at the energy minima and transition state. Once the local hopping rates for each possible transition are known, an analytic expression exists to define the net diffusion coefficient of H in the C15 crystal structure[20].

Results and Discussions

The first step in describing the dynamics of interstitial H in Laves phase intermetallics is to calculate the binding energy of interstitial H in different environments in these materials. For all compounds, we examined H in all three interstitial sites described earlier. The adsorption and hence the site preference for H in C15 AB_2 intermetallics with A = Zr has been studied previously using DFT within the local density approximation (LDA) by Hong et al.[21] These calculations predicted that the g site is the most stable site for ZrV_2 and $ZrCr_2$ while the e site is the most stable site for $ZrMn_2$, $ZrFe_2$, and $ZrCo_2$. Our DFT-GGA calculations yield a slightly different result, namely that the g site is favored in all of these materials except $ZrCo_2$. This prediction is the same regardless of whether zero point corrections are included in the site binding energies. In all cases studied, the binding energies are very similar for both the e and the g sites. The b site formed by 4A atoms, however is found much less favored of all tetrahedral sites thus in our diffusion model we neglect diffusion from and into these sites. H

diffusion among e and g sites in C15 AB_2 materials involves two distinct types of hops between g sites, hops from g to e sites, and the reverse e to g hop. After determining the stable adsorption sites for H adsorption, we used DFT to characterize each of these hopping barriers for all the materials listed above.

We first consider H diffusion in C15 $ZrCr_2$, where we can compare our results with extensive experimental data. The predicted self diffusivity of H in $ZrCr_2$ both with and without tunneling contributions is shown in Fig. 1, along with experimental data for $ZrCr_2H_{0.2}$ from Renz et al.[7] As shown in Fig. 1 harmonic TST alone is clearly incompatible with the complete set of experimental data. Including tunneling corrections, however, accurately captures the change in apparent activation energy that is observed as T is varied. Fitting our predictions to the standard Arrhenius expression, $D = \nu \exp(-E/kT)$, in the same T ranges as the experimental analysis of Majer[9] yields E = 0.161 eV for T > 260 K and 0.049 eV for T < 170 K. The experimental values are E = 0.167 and 0.046 eV, respectively. An alternative analysis[7] is to fit the entire data set to $D = \nu_1 \exp(-E_1/kT) + \nu_2 \exp(-E_2/kT)$. Experimentally, this yields E_1 = 0.146-0.157 eV and E_2 = 0.021-0.039 eV for $ZrCr_2H_x$ with x = 0.2-0.5. Analyzing our data in the same way for the same range of T gives E_1=0.172 eV and E_2=0.049 eV. While the predicted activation energies are in good agreement with experiment, it is clear from Fig. 1 that the pre-exponential factor associated with diffusion is overestimated by our computational methods.

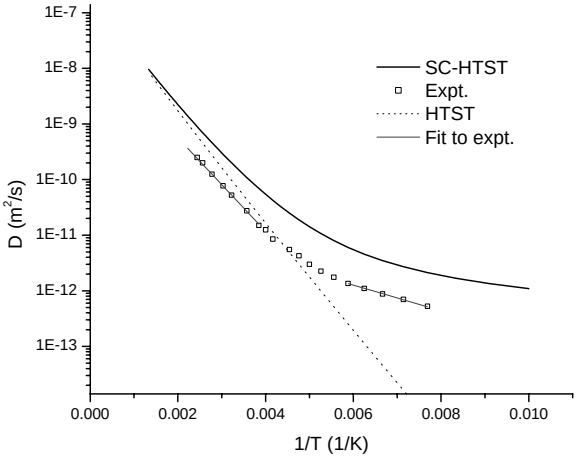

Figure 1. The net self diffusion rate for H in $ZrCr_2$ as predicted by harmonic transition state theory (HTST), semiclassically corrected harmonic transition state theory (SC-TST), and as measured experimentally by Renz et al.[7]. The fits to the experimental data in the low and high temperature regime reported by Majer[9] are also shown.

Similar to $ZrCr_2$, the temperature dependent diffusivities for H were predicted in $ZrFe_2$, $ZrMn_2$, $ZrCo_2$, and ZrV_2 including tunneling contributions. In each case, the rates of each possible hopping event were computed with the DFT-based semiclassical approach defined above and the net diffusion rate was found using the analytic expression that combines the individual rates. At room temperature and above, tunneling contributions are negligible in all materials. At temperatures lower than 200 K, however, tunneling contributions become increasingly dominant. As with the case of $ZrCr_2$ discussed above, our theoretical calculations predict the activation energy of H diffusion with a high degree of accuracy.

Conclusions

We have shown that a combination of plane wave DFT calculations and semiclassically corrected harmonic transition state theory provides a useful description of hydrogen diffusion rates in complex metal alloys. We have demonstrated this method by analyzing all possible hops within five different C15 AB_2 intermetallics. Crucially, this approach is well suited to describing complex alloys in which large numbers of distinct site to site hops must be characterized. We anticipate that this method will be very useful in describing the diffusion of hydrogen in complex metal alloys and intermetallics.

Acknowledgements. This work was partially supported by the Department of Energy Coal Research Program. DSS is an NETL Faculty Fellow.

References

(1) Kamakoti, P.; Sholl, D. S. *J. Membrane Sci.* **2003**, *225*, 145.
(2) Kamakoti, P.; Morreale, B. D.; Ciocco, M. V.; Howard, B. H.; Killmeyer, R. P.; Cugini, A. V.; Sholl, D. S. *Science* **2005**, *307*, 569.
(3) Kamakoti, P.; Sholl, D. S. *Phys. Rev. B* **2005**, *71*, 014301.
(4) Sundell, P. G.; Wahnstrom, G. *Phys. Rev. Lett.* **2004**, *92*, 155901.
(5) Sundell, P. G.; Wahnstrom, G. *Phys. Rev. B.* **2004**, *70*, 081403.
(6) Kallen, G.; Wahnstrom, G. *Phys. Rev. B* **2001**, *65*, 033406.
(7) Renz, W.; Majer, G.; Skripov, A. V.; Seeger, A. *J. Phys. Cond. Mat.* **1994**, *6*, 6367.
(8) Skripov, A. V.; Pionke, M.; Randl, O.; Hempelmann, R. *J. Phys. Cond. Mat.* **1999**, *11*, 1489.
(9) Majer, G. *Mat. Res. Soc. Symp. Proc.* **1998**, *513*, 109.
(10) Majer, G.; Kaess, U.; Stoll, M.; Barnes, R. G.; Shinar, J. *Defect and Diffusion Forum* **1997**, *143-147*.
(11) Eberle, U.; Majer, G.; Skripov, A. V.; Kozhanov, V. N. *J. Phys. Cond. Mat.* **2002**, *14*, 153.
(12) Skripov, A. V.; Combet, J.; Grimm, H.; Hempelmann, R.; Kozhanov, V. K. *J. Phys. Cond. Mat.* **2000**, *12*, 3313.
(13) Kresse, G.; Furthmuller, J. *J. Comp. Mat. Sci.* **1996**, *6*, 15.
(14) Pebler, A.; Gulbransen, E. A. *Trans. Met. Soc. AIME* **1967**, *239*, 1593.
(15) Pedziwiatr, A. T.; Craig, R. S.; Wallace, W. E.; Pourarian, F. *J. Solid State Chem.* **1983**, *46*, 336.
(16) Jacob, I.; Davidon, D.; Shaltiel, D. *J. Magn. Magn. Mater.* **1980**, *20*, 226.
(17) Miron, N. F.; Shcherbak, V. I.; Bykov, V. N.; Levdik, V. A. *Sov. Phys. - Crystallogr.* **1971**, *16*, 266.
(18) Henkelman, G.; Uberuaga, B. P.; Jónsson, H. *J. Chem. Phys.* **2000**, *113*, 9901.
(19) Fermann, J. T.; Auerbach, S. *J. Chem. Phys.* **2000**, *112*, 6787.
(20) Sholl, C. A. *J. Phys. Cond. Mat.* **2005**, *17*, 1329.
(21) Hong, S.; Fu, C. L. *Phys. Rev. B* **2002**, *66*, 094109.

SULFUR TOLERANT FUEL PROCESSING CATALYSTS

S.L. Swartz, G.B. Arkenberg, and E.M. Sabolsky

NexTech Materials, Ltd.
404 Enterprise Drive
Lewis Center, OH 43035

Introduction

A major requirement for near term implementation of fuel cell power generation systems is use of our existing hydrocarbon fuel infrastructure. Fuel cells operating on hydrocarbon fuels will have early opportunities for large market applications within a number of sectors, including residential and industrial heat and power systems, auxiliary power units for cars and long-haul trucks, and a wide array of military power systems. Infrastructure fuels (including natural gas, propane, gasoline, diesel and kerosene) are based on hydrocarbon compounds of differing complexity and contain sulfur impurities of varying amounts. In order for use with a fuel cell, the hydrocarbon fuel is first converted into a gas that is compatible with efficient fuel cell operation. This is the purpose of the fuel processing system. In general, the technical difficulty associated with fuel processing increases with carbon number and sulfur content of the hydrocarbon fuel. Today's technology requires bulky sulfur removal beds, which must be changed frequently and can allow slip into the catalyst beds, leading to catalyst deactivation. Therefore, catalysts that resist deactivation by sulfur would add design flexibility to fuel processor system developers.

Several types of fuel processors currently are being developed for fuel cells where hydrocarbon fuels are being targeted for use. These systems vary depending on the fuel cell type, the targeted fuel, and the design philosophy of the developers. The first step in fuel processing is a catalytic (reforming) stage to convert the hydrocarbon fuel to a syngas mixture of hydrogen and carbon monoxide. This is accomplished by reacting the fuel with water (steam reforming), with oxygen (catalytic partial oxidation), or a combination of steam and oxygen (autothermal reforming). After reforming, the fuel can be fed directly to a molten carbonate or solid oxide fuel cell. However, additional fuel clean-up processing steps are required before the fuel can be used within a PEM fuel cell, which require extremely clean hydrogen. These includes the water-gas shift (WGS) reaction to increase hydrogen content and reduce carbon monoxide content ($CO + H_2O \rightarrow CO_2 + H_2$), and selective oxidation ($CO + O_2 \rightarrow CO_2$) to further reduce the carbon monoxide content. An alterative approach is to collect the hydrogen using a hydrogen separation membrane (before, during or after the WGS step).

Regardless of the fuel cell type or the fuel processing system design, there is a critical need for new fuel processing catalysts and catalytic structures. Desired attributes include improved resistance to impurities in the fuel, stability under transient (start-up, shut-down) conditions, and ruggedness. For smaller scale systems, high catalytic activity is desired to minimize overall system size and weight. Of particular importance is tolerance of the catalysts to the presence of sulfur in the fuel – to minimize the extent of sulfur removal required and to provide flexibility to the fuel cell system designers on the location of sulfur removal components. NexTech Materials currently is developing a number of catalytic materials and components to enable fuel cells to operate on hydrocarbon fuels. These include water-gas-shift catalysts, hydrocarbon reforming catalysts, sulfur adsorbents, and sensors for carbon monoxide and hydrogen sulfide. NexTech's work on sulfur tolerant hydrocarbon reforming and water gas shift catalysts is discussed in this paper.

Sulfur "Tolerant" Water Gas Shift Catalysts

Over the past several years, NexTech Materials has pursued the development of WGS catalysts based on ceria-supported precious metals. Our work has demonstrated that these catalysts offer several advantages compared to existing copper-based WGS catalysts: (1) operation over a wider range of temperature (up to 400ºC); (2) no need for activation prior to use; (3) no degradation upon exposure to air (non-pyrophoric); (4) capability for regeneration of deactivated catalysts by simple air-atmosphere annealing; and (5) availability of conventional washcoating technologies for supporting ceria-based catalysts on monoliths to improve ruggedness. NexTech has shown that performance of these catalysts is sufficient for the fuel processing application, and that volumetrically efficient WGS reactors can be produced using monolith-supported forms.

NexTech is extending its WGS catalyst formulations to sulfur tolerant versions under a project supported by the U.S. Navy's Ship Service Fuel Cell Program. Logistic diesel fuels (e.g., NATO F-76) have extremely high levels of sulfur (up to 10,000 ppm), which makes them difficult to work with using conventional fuel processing methods. One approach being pursued by the Navy is to reform this fuel with a sulfur tolerant catalyst, to increase hydrogen content with a sulfur tolerant WGS catalyst, and to collect the hydrogen with a sulfur tolerant membrane. Depending on the sulfur tolerance levels achieved by the catalysts and membranes, the size of desulfurization components can be greatly reduced with this approach. NexTech is focusing its efforts on WGS catalysts that are tolerant to high levels of H_2S (10-100 ppm) in the syngas feeds (N_2, CO, CO_2 and H_2).

Several sulfur-tolerant catalyst formulations have been identified and are being subjected to long-term testing. This testing is being conducted at relatively high temperatures (400 to 450ºC), because this is the temperature range where the membrane is targeted for operation. Specifically, NexTech is pursuing two strategies for the design of sulfur tolerant catalysts. The first is to improve robustness of high activity WGS catalysts, i.e., to increase their sulfur tolerance hopefully without compromising activity. The second approach is to increase the WGS activity of catalysts that are inherently tolerant to sulfur. These two approaches are exemplified by micro-reactor data shown in Figure 1. These data were obtained at 450ºC in a dry syngas composition (10% CO, 15% CO_2, 50% H_2 and 25% He), $H_2O/CO = 4.8$, and space velocity of ~150,000 cc/g-hr. Under these conditions, the "Type 1" catalyst was very active at low H_2S levels and decreased rapidly upon introduction of 50 ppm H_2S. Conversely, the "Type 2" catalyst exhibited stable WGS performance with 50 ppm H_2S during 300 hours of testing. Under these high-sulfur conditions, the catalyst of "Type 2" is the best option. Data obtained in a second set of tests at 400ºC in a syngas composition (15% CO, 10% CO_2, 50% H_2 and 25% He), $H_2O/CO = 2.6$, and 10 ppm H_2S are shown in Figure 2. Under these conditions, the "Type 1" catalyst is a better option and both types are clearly superior to commercial high-temperature shift catalysts.

Sulfur "Tolerant" Reforming Catalysts

NexTech also is developing hydrocarbon reforming catalysts for use with sulfur-containing fuels. Catalyst formulations being pursued include perovskite structured oxides and ceria-supported precious metals. A rapid screening test is used for initial catalyst evaluations, with comprehensive testing conducted on promising formulations. The screening test involves micro-reactor testing of methane partial oxidation and/or steam reforming reactions in feeds having sub-stoichiometric oxidant (where carbon formation is expected). By measuring the increase of pressure drop through the catalyst bed, an initial screen of coking resistance is obtained. An example of this test is shown in Figure 3 for a series of perovskite structured catalysts tested in the partial oxidation mode.

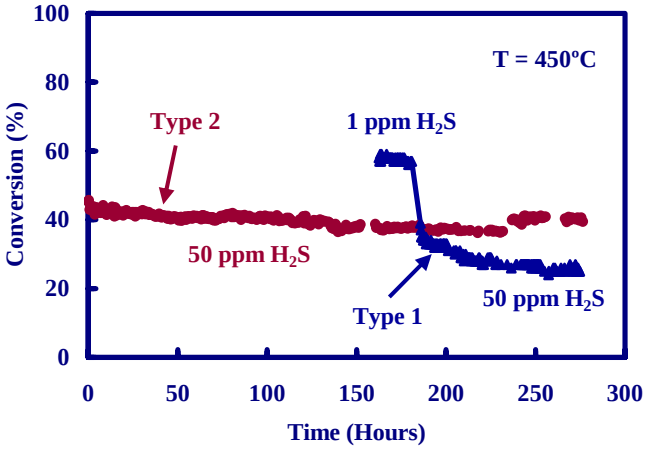

Figure 1. WGS performance of two types of sulfur-tolerant catalysts tested at 450ºC in syngas feeds of different H_2S contents.

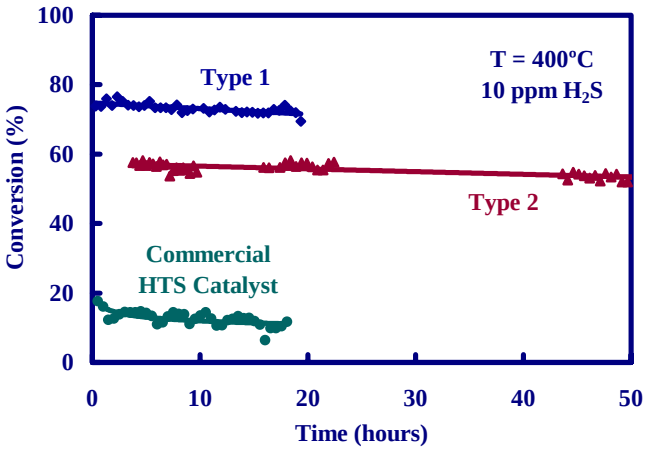

Figure 2. WGS performance of two types of sulfur-tolerant catalysts and a commercial catalyst tested at 400ºC (10 ppm H_2S).

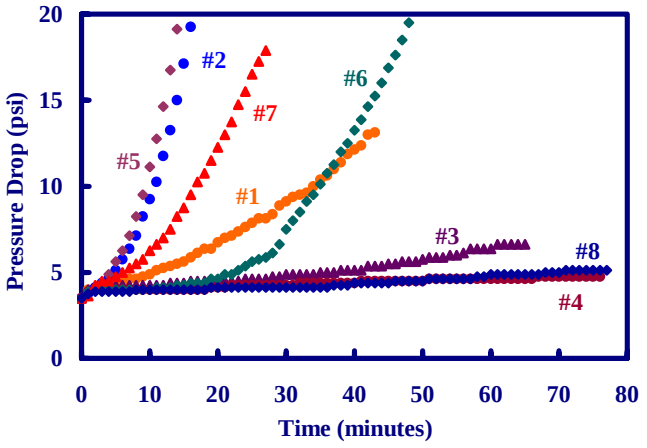

Figure 3. Pressure drop versus time for partial oxidation of methane at 700ºC with sub-stoichiometric oxidant (CH_4/O_2 = 3/1).

Based on the screening test results, several perovskite catalysts were selected for more comprehensive performance testing. These tests, typically 100-200 hours in duration, involved the measurement of methane conversions at temperatures of 650~800ºC under partial oxidation, steam reforming and autothermal conditions, with periodic exposures to H_2S (5-10 ppm levels). These perovskite catalysts were very effective for reforming of methane, especially when optimum synthesis methods were used (see Figure 4). Although none of the catalysts tested were completely immune to sulfur, three promising attributes were noted: (1) an onset period of a few hours after introduction of H_2S: and (2) relatively stable performance in the presence of H_2S after some activity loss; and (3) complete recovery of lost activity after H_2S was removed from the feed. An example of this behavior is shown in Figure 5.

Conclusions

The development of fuel processing catalysts that perform in the presence of sulfur in hydrocarbon fuels will greatly improve near term commercialization opportunities for fuel cell power generation systems. Two types of sulfur tolerant water gas shift catalysts have been demonstrated, with applicability depending on H_2S content and operating temperature. Several promising perovskite structured reforming catalyst formulations have been identified, and their sulfur resistance has been demonstrated for methane partial oxidation reactions. Future work at NexTech aims to extend the development of sulfur tolerant catalysts to different fuels and reforming reactions.

Acknowledgements. Funding for this work was provided by the Office of Naval Research (Contract No. N00014-04-C-0248) and by the National Science Foundation (Grant No. DMI-0419715).

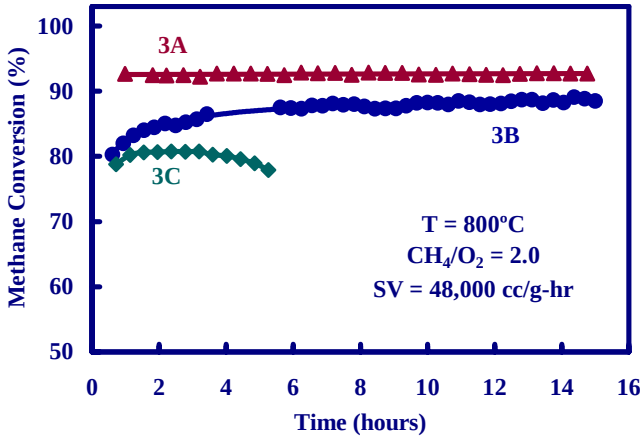

Figure 4. Effect of catalyst synthesis method on the stoichiometric methane partial oxidation for perovskite structured catalysts.

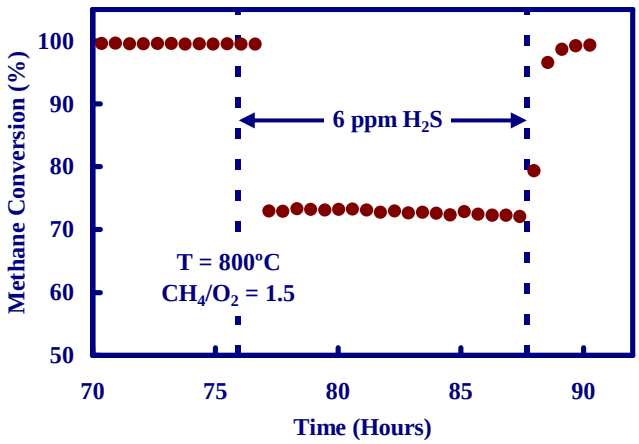

Figure 5. The effect of H_2S on methane conversion levels under partial oxidation conditions for a perovskite structured catalyst.

SURFACE STUDIES ON HIGHLY ACTIVE CeO_2 SUPPORTED CUPD BIMETALLIC CATALYSTS FOR THE OXYGEN-ASSISTED WATER-GAS-SHIFT REACTION

Elise B. Fox[*+], S. Velu, Karen Wilson[#] and Chunshan Song*

Clean Fuels and Catalysis Program
The Energy Institute
*Intercollege Graduate Program in Materials
Department of Energy and Geo-Environmental Engineering
Pennsylvania State University
209 Academic Projects Building
University Park, PA 16802, USA
[#]Department of Chemistry
University of York
Heslington, York, YO10 5DD, UK
[+]Presenting Author

Introduction

Reformed hydrocarbon fuels may become an important source of hydrogen for PEMFC's. In order to utilize these hydrogen sources, low levels of sulfur and carbon monoxide must be achieved. In a conventional fuel reformer for fell cell feed gases, the CO reduction steps of the high and low temperature water-gas-shift, and preferential oxidation can take up over 50% of the fuel cell systems volume and weight. In order to reduce this, the WGS and PrOx reactions are combined and performed in a single step, called oxygen-assisted water-gas-shift (OWGS) reaction. We recently developed a new series of highly active and less pyrophoric CuPd bimetallic catalysts supported on high surface area CeO_2 catalysts for the OWGS [1]. The catalyst containing about 30 wt % Cu and 1 wt % Pd has been found to be optimum in order to achieve high CO conversion close to 100 % around 230°C. The effect of temperature and space velocity on the catalytic performance has been evaluated. In the present study, we employed in-situ XPS and in-situ FT-IR studies over the $CuPd/CeO_2$ catalysts in order to understand the nature of active species involved in the OWGS reaction.

Experimental

Catalyst Preparation and characterization. The support CeO_2 was prepared by urea gelation method as described elsewhere and had a BET surface area of about 215 m^2/g.[5] Cu and Pd metals were deposited on the support surface using an incipient wetness impregnation (IWI) method, dried at 120°C overnight and calcined at 400°C for about 4 h using a heating rate of 2°C/min. TPR data were acquired on a Micromeritics AutoChem 2910 instrument. About 0.1 g of the catalyst was loaded in the reactor and heated in 5% H_2/Ar gas (25 cc/min) between room temperature and 500°C at a heating rate of 5°C/min. The H_2 consumption due to the reduction of constituent metal ions is monitored by a TCD detector equipped in the instrument.

XPS measurements were conducted at the University of York in a Kratos AXIS HSi instrument equipped with a charge neutraliser and a dual anode Mg K_α /Al K_α X-Ray source which was operated at 169 W. Spectra were acquired at normal emission with a pass energy of 20eV. Samples on the main stage can be heated up to 500°C under reactive gas exposure at pressures up to $1x10^{-7}$ torr. Higher pressure in-situ experiments were performed in the preparation chamber where pressures up to 0.1 bar and temperatures of 500°C were readily achievable.

Catalytic Studies. Oxygen-assisted water-gas shift reaction was performed at 180°C or 240°C in a fixed-bed down-flow reactor. A gas mixture containing 4% CO, 10% CO_2, 2% O_2 and balance (about 84%) H_2 was used as reactants. The CO/H_2O molar ratio was kept at 1/10. The effluent of the reactor was analyzed on-line using an Agilent 3000 A Micro GC equipped with thermal conductivity detectors with a CO detection limit of below 10 ppm. Prior to the reaction, the catalyst was reduced *in situ* at 225°C for 1h in H_2 flow.

Results and Discussion

XPS data of three samples, namely $Cu(30)Pd(0)/CeO_2$ containing only Cu without Pd, $Cu(0)Pd(1)/CeO_2$ containing only Pd without Cu and $Cu(30)Pd(1)/CeO_2$ containing both Cu and Pd in the unreduced as well as reduced form have been collected in order to understand the effect of Pd on the surface chemical properties of Cu/CeO_2 catalysts. The unreduced samples exhibited peaks corresponding to Cu^{2+}, Pd^{2+} and Ce^{4+}species in these samples. Upon reduction around 225°C, the Cu^{2+} and Pd^{2+} species are reduced mainly to their metallic states while Ce exists mainly in the Ce^{4+} state.

Figure 1 shows the XP spectra of reduced $CuPd/CeO_2$ catalysts in the Cu 2p and Pd 3d regions. The Cu 2p XP spectra exhibit sharp peaks around 932 eV for metallic Cu species. Significant differences in peak position and spectral intensity could be noticed in the Cu 2p spectra. Addition of Pd to the Cu/CeO_2 catalyst shifts the Cu $2p_{3/2}$ peak position towards lower BE by about 0.4 eV (932.4 eV for $Cu(30)Pd(0)/CeO_2$ and 932.0 eV for $Cu(30)Pd(1)/CeO_2$ catalysts) indicating that the reducibility of Cu is improved by the addition of Pd. This also leads to a decrease in intensity of the Cu 2p peak, suggesting that the surface dispersion of Cu is improved by the addition of Pd. The XP spectra collected in the valence band region, below 10 eV showed that Cu 3d bands are located close to the Fermi energy (E_F = 0) indicating that Cu is mainly involved in chemical interaction, converting CO into CO_2. The overall spectral intensity decreased upon addition of Pd, further supporting the core level observation that the Cu dispersion is improved by the addition of Pd. The XP spectra in the Pd 3d region indicate that the Pd is present mostly in Pd^0 state in the catalyst containing both Cu and Pd while significant amount of Pd^+ and/or Pd^{2+} is present in the catalyst without Cu. The presence of Cu helps retaining Pd in its metallic state. Thus, the existence of a synergistic interaction between Cu and Pd in the CuPd bimetallic catalysts supported on CeO_2 is clearly seen from the XPS data. The existence of Cu-Pd alloy on the surface of these Cu-Pd bimetallic catalysts could be responsible for the higher catalytic activity for CO oxidation [2].

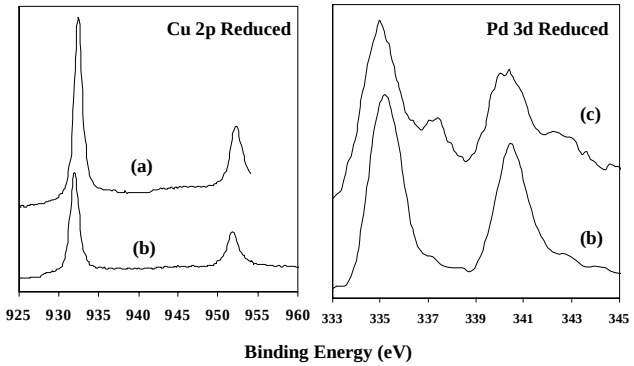

Figure 1. Cu 2p and Pd 3d XP Spectra of $CuPd/CeO_2$ catalysts; (a) $Cu(30)Pd(0)/CeO_2$, (b) $Cu(30)Pd(1)/CeO_2$, (c) $Cu(0)Pd(1)/CeO_2$

References

(1) Bickford, E. S.; Velu, S.; Song, C. S. Nano-structured CeO_2 supported Cu-Pd bimetallic catalysts for the oxygen-assisted water-gas-shift reaction *Catalysis Today* **2005**, *99*, 347-357.

(2) Hungria, A. B.; Iglesias-Juez, A.; Martinez-Arias, A.; Fernandez-Garcia, M.; Anderson, J. A.; Conesca, J. C.; Soria, J. Effects of copper on the catalytic properties of bimettallic Pd-Cu/(Ce,Zr)Ox/Al2O3 and Pd-Cu/(Ce,Zr)Ox catalysts for CO and NO elimination *Journal of Catalysis* **2002**, *206*, 281-294.

SYNTHESIS AND CHARACTERIZATION OF NON-NOBLE NANO-CATALYSTS FOR HYDROGEN PRODUCTION

Debasish Kuila*[1], Krithi Shetty[1], Wei Cao[2], Shihuai Zhao[3] Daniela Mainardi[4], and Naidu V. Seetala[5]

[1]Institute for Micromanufacturing/Chemistry, Louisiana Tech University, [2]Institute for Micromanufacturing, Louisiana Tech University, [3]Institute for Micromanufacturing, Louisiana Tech University, [4]Institute for Micromanufacturing/Chemical Engineering, Louisiana Tech University, [5]Department of Physics, Grambling State University

Introduction

Steam reforming is a process to produce hydrogen from organic sources with the aid of a catalyst. At present, there is no cost- and energy-efficient method for making hydrogen. Today, petrochemical plants generate millions of tons of hydrogen for different applications from methane for different applications. The expensive platinum catalysts require significant amounts of energy and produce 3 tons of carbon dioxide for each ton of hydrogen [1-5]. Coal gasification can produce considerable amounts of hydrogen and electricity due to availability of large size of coal deposits. However, energy necessary to sequester CO_2 is relatively expensive [6]. Of the many candidates being considered for hydrogen fuel sources, methanol and ethanol are readily available and currently being investigated [7-21]. Alcohols from biomass are easy to produce and safe to handle, store and transport.

A number of commercial and research-derived noble metals such as Pt, Rh, etc. with metal oxides, such as CeO_2, ZnO, MgO supports including more than one type of catalyst-support have been tested for hydrogen production from methanol and ethanol [7-10]. The performance is greatly influenced by the type of supports (CeO_2, Al_2O_3, SiO_2, ZrO_2, MgO or TiO_2) through interactions between catalyst and supports, with CeO_2 showing the highest selectivity to hydrogen. It has been speculated that a CeO_2 supported catalyst has a longer catalytic life time than that of Al_2O_3 [11]. Although a number of catalysts including Cu and Pd have shown promising results, problems with deactivation of the catalysts with an ensuing decrease in hydrogen and carbon dioxide and an increase in carbon monoxide production have been reported [9]. Currently, there is no proper understanding of these systems. In addition, the noble metal catalysts are expensive. Thus, fundamental research is necessary to find the optimized combination of catalyst and support for hydrogen production.

Microreactors have been used for production of hydrogen fuel for Proton Exchange Membrane (PEM)-based fuel cells by catalytic steam reforming of methanol [13]. However, they have not been used to explore the activity of catalysts for steam reforming. Advantages of micro-reactor systems include light weight and compactness, rapid heat and mass transport due to a large surface to volume ratio, and precise control of process conditions with higher product yields. The special emphasis of this project will center on non-noble metal catalysts for hydrogen production.

Experimental

Catalyst preparation. The silica supported Co or Ni catalysts were prepared by a sol-gel procedure developed in this laboratory.

Characterization. Scanning Electron Microscopy (SEM) associated with Energy Dispersive X-ray (EDX) from Amray 1830 instrument was used to investigate coating profiles and actual loadings of the nano catalysts. The specific surface area (SSA) of the silica encapsulated catalysts was characterized using Brunaur-Emmett-Teller (BET) method and Quantachrome NOVA 2000 analyzer. A Vibrating Sample Magnetometer (VSM) (880A Digital Measurement Systems) was used to study the magnetic properties of the catalysts at different stages.

Steam reforming of methanol. The catalytic reactions of steam reforming were conducted using a silicon based microreactor in the temperature range of 473-573 K under atmospheric pressure. Various flow rates in the range of 5-20 µL/min were controlled into the microreactors using a syringe pump. The parameters for reaction conditions were controlled using LabVIEW software. A cold trap separates out the gaseous products from aqueous methanol and water to calculate methanol conversion and thus also prevents the filament inside the mass spectrometer from high humidity. The gaseous products were diluted with helium and analyzed using a Mass Spectrometer (MS) (QMS 200 gas analyzer from Stanford Research Systems).

Results and Discussion

Characterization of silica sol-gel supported Co or Ni catalyst. The silica encapsulated Co or Ni was evenly coated in microchannels with nonuniform thickness. (Figure 1) This is due to the nature of the sol-gel process, generating pore structure of the catalyst support with high SSA, which is ~300 m^2/g from BETmeasurement. The EDX analysis shows that the Co catalyst loading is 7.85%, which is lower than intended loading of 12% due to catalyst preparation and deposition procedure.

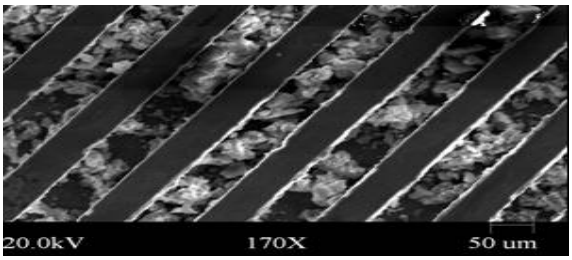

Figure 1. SEM image of Co/SiO_2 catalyst in a 50 µm channel-wide Si-microreactor

VSM studies of the as-deposited catalyst in microreactor show paramagnetic behavior mostly coming from the cobalt oxide (Figure 2). Hydrogenation of the catalyst reduces the oxide to pure metal, thus yielding ferromagnetic behavior. This ferromagnetic nature almost disappears in the post-catalyst due to the formation of Co carbide or carbonyl during the steam reforming reaction.

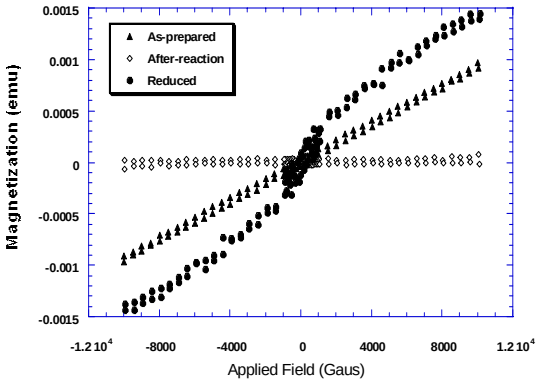

Figure 2. Magnetic studies using VSM of Co nano-catalyst: as prepared, reduced, and after steam reforming.

The saturation magnetization of the ferromagnetic component is used to estimate the catalyst activity in pre- and post-catalysts. It gives an estimate of the amount (~ 90%) of Co becoming inactive after the reaction.

Catalytic activity of steam reforming of methanol. The steam reforming of methanol was initiated at 473 K with the H_2O/CH_3OH ratio of 1, which has been reported in literature as the best conditions for steam reforming. The conversion of methanol declined as the flow rate was increased. But the flow rate had little influence on hydrogen production (Table 1).

Table 1. Steam reforming at 200°C with 1: 1 molar ratio of H_2O/CH_3OH.

Temperature (°C)	180	200	220	240	260	280	300
Methanol Conversion (%)	43.47	44.58	51.68	49.40	54.92	57.29	56.53
Hydrogen Percentage (%)	75.64	75.76	72.56	74.42	70.51	71.26	70.42
CO Percentage (%)	1.24	1.24	1.97	1.25	2.56	2.09	2.61

According to above results, higher methanol conversion is observed at lower flow rates. However, our mass spectrometer can not detect methanol when the flow rate is lower than 1 µl/min. Therefore, a fixed flow rate of 5 µL/min was chosen in our experiments to determine the influence of reaction temperature on both methanol conversion and selectivity to hydrogen (Table 2). The temperature for the experiments ranged from 180°C to 300°C and higher temperature yields a higher methanol conversion with a higher concentration of CO.

Table 2. Steam reforming at the flow rate of 5 µL/min with 1: 1 molar ratio of MeOH: H_2O.

Flow Rate (µl/min)	1.0	5	10	20	40
Methanol Conversion (%)	43.92	37.63	33.97	17.37	6.21
Hydrogen Percentage (%)	74.7	73.5	68.22	69.32	68.25

Preliminary results for Ni catalyst also show good trends and a conversion of 30% has been observed during the first few runs. Currently, we have developed a parallel array of microreactors to screen catalyst for Fischer-Tropsch (F-T) studies to make higher alkanes. This is also an ideal system for future hydrogen production studies due to significant decrease in catalyst development period with precise process control, flexible experiment operation and low operation/maintenance costs.

Computational studies

Computational studies are being conducted to gain a better understanding of the catalyst surface and mechanistic aspects of hydrogen production. The effect of nanoparticle size and temperature in the range of 300-1000 K at atmospheric pressure on SiO_2-supported Ni nanoparticles were investigated using molecular dynamics simulations. The annealing process of these nanocatalysts was simulated starting at a high temperature (1000 K), at which the system is fully equilibrated, and then successive simulations were run restarting always from the previous one until full equilibration was complete at 300 K. This procedure was further repeated for different nanoclusters sizes.

Preliminary results show clear differences in nanoparticles morphologies and structures depending upon the temperature of interest, and the characteristics of the liquid-solid transition in such nanoparticles. Nanoparticle surface characteristics, including exposed crystallographic phases, may play a key role in the catalytic activity and can be specially controlled and tailored by selecting a specific support. These simulations provide data needed to carry out more complete kinetic studies to simulate the complete steam reforming reactions taking place on the supported nanocatalysts.

Conclusion

The silica encapsulated Co or Ni catalysts were prepared using sol-gel method. Characterizations of the nano catalysts by SEM and EDX show even coatings of the silica supported catalysts in microchannels with lower loading than intended. The VSM studies showed transformation of Co magnetic properties at different stages. The highest conversion of methanol over Co catalyst is 57% at 280°C, at the flow rate of 5 µL/min, and 1: 1 molar ratio H_2O/CH_3OH, and much higher than that observed from the preliminary experiments over Ni catalyst (30%). Preliminary computational studies indicate that the crystallographic phases may be important for hydrogen production.

Acknowledgement. This work was supported by NSF-EPSCoR. Financial support in part from Pfizer Corporation is gratefully acknowledged.

*For Correspondence; Phone: 318-257-5121; Fax: 318-257-5104; dkuila@latech.edu

References

1. Mattos, L. V.; Rodino, E.; Resasco, D. E. *Fuel Processing Technology, 83* (**2003**) 147.
2. Matsumura, Y.; Nakamori, T. *Applied Catalysis A: General, 258* (**2004**) 107.
3. Takahashi, R.; Sato, S. Applied *Catalysis A: General, 273* (**2004**) 211.
4. Roh, H.; Jun, K. W.; Dong, W. S. *Journal of Molecular Catalysis A: Chemical, 181* (**2002**)137.
5. Yamazaki, O.; Tomishige, K.; Fujimoto, K. *Applied Catalysis A: General, 136* (**1996**) 49.
6. Energy Information Administration, unpublished file data of coal reserves data base (February 2004) available http://www.eia.doe.gov/pub/international/iea2002/table82.xls
7. Goula, M. A.; Kontou, S. K.; Tsiakaras, P. E. *Applied Catalysis B: Environmental, 49* (**2004**) 135.
8. Purnama, H.; Ressler, T.; Jentoft, R. E.; Soerijanto, H.; Schlogl, R.; Schomacker, R. *Applied Catalysis A: General, 259* (**2004**) 83.
9. Twigg, M. V.; Spencer, M. S. *Topics in Catalysis, 22*, 3-4, April (**2003**) 191.
10. Mizuno, T.; Matsumura, Y.; Nakajima, T.; Mishima, S. *Int. J. of Hydrogen Energy 28* (**2003**) 1393.
11. Zhang, X.; Shi, P. *Journal of Molecular Catalysis A: Chemical 194* (**2003**) 99.
12. Frusteri, F.; Freni, S.; Spadaro, L.; Chiodo, V.; Bonura, G. *Catalysis Communications 5* (**2004**) 611.
13. Pattekar, A. V.; Kothare, M. V. *Journal of Microelectromechanical Systems 13* (**2004**) 7.
14. Fatsikostas, A. N.; Verykios, X. E. *Journal of Catalysis, 225* (**2004**) 439.
15. Batista, M. S.; Rudye Santos, K. S.; Assaf, E. M. *Journal of Power Sources, 134* (**2004**) 27.
16. Srinivas, D.; Satyanarayana, C. V. V.; Potdar, H. S. Ratnasamy, P. *Applied Catalysis A: General, 246* (**2003**) 323.
17. Mariño, F. J.; Cerrella, E. G.; Duhalde, S. *International Journal of Hydrogen Energy, 23* (**1998**) 1095.
18. Men, Y.; Gnaser, H.; Zapf, R.; Hessel, V. *Catalysis Communications, 5* (**2004**) 671.
19. Bravo, J.; Karim, A.; Conant, T. *Chemical Engineering Journal, 101* (**2004**) 113.
20. Liu, Y.; Hayakawa, T.; Suzuki, K.; Hamakawa, S. *Applied Catalysis A: General, 223* (**2002**) 137.
21. Lwin, Y.; Daud, W. R. W. *International Journal of Hydrogen Energy, 25* (**2000**), 47.

REGENERABLE SORBENTS USED FOR THE REMOVAL OF SULFUR CONTAINING ODORANTS FROM WATER BEARING NATURAL GAS

Gőkhan O. Alptekin, Margarita Dubovik, Sarah J. DeVoss, and Robert Amalfitano

TDA Research Inc
12345 W. 52nd Ave
Wheat Ridge, CO 80033

Introduction

Fuel cells have the potential to revolutionize the way the power is produced and distributed, and distributed power generation is becoming a viable alternative to buying power from a central grid. However, there are still some hurdles to be overcome if fuel cells are to fully reach their commercial potential. One of the issues to be addressed is the need to provide an ample supply of high quality fuel to operate the fuel cells. Pipeline natural gas is the fuel of choice in distributed power generation systems because of its abundance and well-developed supply infrastructure. However, the natural gas contains sulfur impurities that can degrade the performance of the fuel cells. Although the majority of the sulfur in the natural gas is removed at the wellhead, some hydrogen sulfide (H_2S) and carbonyl sulfide (COS) exist as contaminants at low concentrations. In addition to the naturally occurring sulfur, pipeline gas also contains other organic sulfur species used as odorants. Because natural gas has no distinct odor, for safety reasons pipeline companies commonly odorize natural gas as it enters the transmission lines or local distribution facilities. These odorants allows detection of even minute leaks in the gas lines. Common odorants include mercaptans (such as ethyl, isopropyl, tertbutyl mercaptan), thiols (such as tetrahydrothiophene) and sulfides (such as dimethyl or diethyl sulfide). The concentration of sulfur in odorized natural gas can be as high as 10-15 ppm on volume basis.

Fuel cells, however, require clean feed streams with very low levels of sulfur and other impurities. Sulfur poisons the anode catalysts for both high and low temperature fuel cells. The problem is most severe in polymer electrolyte fuel cells (PEMFC), both because they operate at low temperature, and their platinum group catalysts are highly susceptible to sulfur poisoning. Sulfur also degrades the performance of the high temperature solid oxide fuel cells (SOFCs). A recent study by Siemens Westinghouse Power Corporation [1] shows that the performance of their fuel cell drops about 15% in the presence of 1 ppmv sulfur in the fuel. Although this poisoning effect is reversible, long-term stable electrochemical performance of the SOFCs requires sulfur concentrations to be reduced to sub ppmv levels.

In large central stations, sulfur removal is carried out upstream of the fuel cell with a two-step process consisting of hydrodesulfurization of organic sulfur species to H_2S and subsequent H_2S removal with a sorbent. However, this method is not practical for small-scale residential units. Most fuel cell manufacturers prefer a low temperature adsorbent that can directly remove organic sulfur from natural gas in a single step. A successful sorbent must meet a number of requirements. First of all, it must exhibit a high sulfur adsorption capacity to reduce the size of the sorbent bed and decrease the replacement frequency of the sorbent. It has to be low cost, so that it is affordable by households. It must reduce the total sulfur concentration of the fuel to ppb levels to ensure maximum protection for the fuel cell catalyst. It must operate in a passive manner and should not catalyze any undesirable side reactions or alter the composition of the gas by adsorbing hydrocarbons. It must tolerate other natural gas contaminants such as the heavy hydrocarbons, CO_2 and humidity. Finally, it should be easy to dispose of. The sorbent itself should be easy to handle and should not pose any toxicity, flammability or pyrophorocity problems.

TDA Research, Inc. is developing a passive adsorbent for the ambient temperature desulfurization of natural gas. This paper summarizes the test results showing the effects water vapor on sorbent performance and the regenerability of the sorbent.

Experimental

Testing System. The sorbent performance was measured in an automated bench-scale test unit. In this setup, the reactor cell consists of a quartz tube that contains a frit in the middle to support the pellets. We were able to test 0.5 to 2.0 g of sample (1/8" pellets were crushed into 1-5 mm size to be tested). The reactor was inserted in a tube furnace to provide heating as needed. All gas flows were controlled with electronic mass flow controllers. To introduce organic sulfur species we used calibrated gas cylinders that contain mixtures of odorant species with natural gas. A valve system was used to direct gases to a reactor by-pass line to make accurate measurements of the feed gas. All system components were made of either quartz, Teflon or Silcosteel (steel lines with a special glass coating) to minimize the adsorbtion of sulfur on the system components. All testing was done at near ambient pressure (3 psig). The apparatus is fully automated and can run without an operator for long periods of time, including overnight.

Sulfur Analysis. For the analysis of sulfur compounds we used a gas chromatograph equipped with a flame photoionization detector that is selective to sulfur species. The capillary column used to separate the odorants is a RTX-1, 30 meter, 0.53 mm ID, with 7.0 μm film thickness manufactured by Restek Corporation. Our detection limit was approximately 0.1 ppmv. The correlation between the amount of sulfur-bearing gases passed over the sorbent and the amount of sulfur accumulated in the bed allowed us to identify the effectiveness of the sorbent and provided an independent check on our analytical methodology.

Hydrocarbon Analysis. In these tests, we used simulated natural gas. This gas mostly consists of lower alkanes from methane to hexane, with some branched hydrocarbons such as the iso-butane or neo-pentane at representative concentrations. The gas also contained some nitrogen and CO_2. We used a GC equipped with a thermal conductivity detector to measure the concentration of the hydrocarbon species throughout the test.

Results and Discussion

Effect of Water Content of Natural Gas. In the screening tests, the samples were tested using certified gas mixtures of simulated dry pipeline gas. However, typical U.S. pipeline natural gas may contain up to 155 ppmv of water vapor (~7 lbs of water per million cubic foot of natural gas). It is anticipated that the competition by water vapor for adsorption sites will reduce the sulfur capacity of activated carbon, zeolite-based sorbents in real world applications due to their high affinity to water. Therefore, some of the samples were evaluated using a gas stream containing 45 ppmv water vapor with all other gas concentrations remaining identical (i.e., 12.3 ppmv DMS, 8.9 ppmv TBM and 8.9 ppmv THT at a GHSV of 60,000 h^{-1}). Figure 1 shows the effect of water vapor on the performance of Norit RGM3 Activated Carbon, unmodified zeolite-X (Grace) and TDA's SulfaTrap™ sorbent. The presence of water reduced the sulfur adsorption capacity of all sorbents. The capacity of the zeolite-X is reduced the most by approximately 83%, showing zeolite-X's high affinity for the water vapor. The water most likely adsorbs on the surface of the sites, competing with the sulfur. As shown in Figure 1, the capacity of the SulfaTrap™ sample is also reduced in the presence of 50 ppmv water vapor. However,

the competition with water vapor was less of a problem for the SulfaTrap™ sorbent.

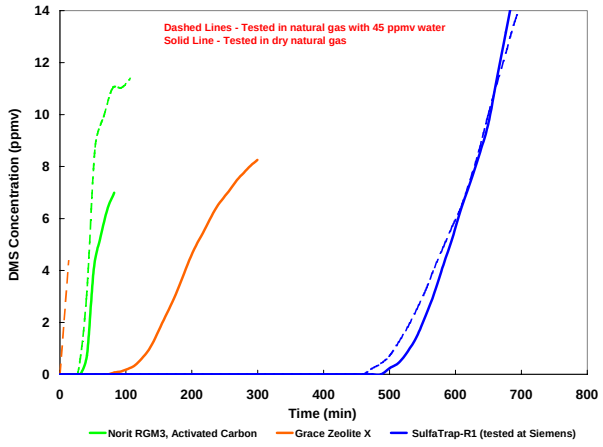

Figure 1. Effect of water on sulfur adsorption capacity of selected adsorbents. The samples were tested at 22°C and a pressure of 3 psig, gas hourly space velocity (GHSV) of 60,000 h^{-1}, with 12.3 ppmv dimethyl sulfide (DMS), 8 ppmv tert-butyl mercaptan (TBM) and 8 ppmv tetrahydrothiophene (THT).

Cyclic Tests. SulfaTrap™ sorbent can be regenerated with a mild temperature swing. The cyclic sulfur adsorption capacity of the sorbent was measured for ten consecutive adsorption/regeneration cycles. Each cycle started with a feed analysis, followed by sulfur adsorption. Once the test was completed, the sorbent bed was heated for the regeneration. These regenerations were carried out in either hydrogen or natural gas (both of which will be available on-site as fuel) containing no odorants. After the regeneration is complete (no further sulfur release was observed), the sorbent was cooled down to room temperature. The next cycle was then started. Figure 2 shows the DMS breakthrough curves for the ten cycle test. The sorbent maintained a stable total sulfur capacity and the DMS capacity of through this ten cycle test. As shown in Figure 3, the sorbent exhibited slightly higher sulfur adsorption capacity following the regenerations carried out in hydrogen show. The loss of capacity due to the natural gas regeneration can be even regained when hydrogen is used for regeneration.

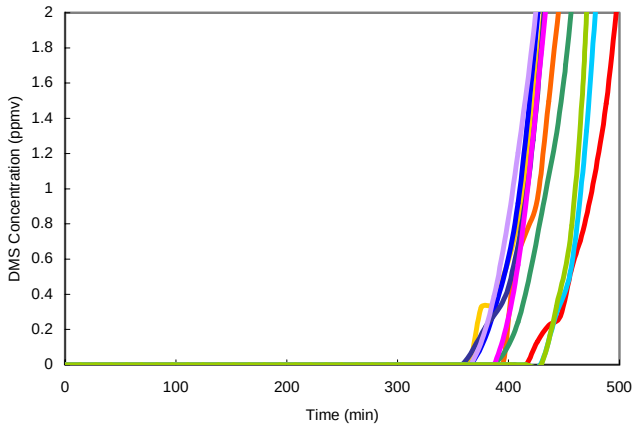

Figure 2. DMS breakthrough profiles during the 10-cycle test at 22°C, 3 psig, GHSV= 60,000 h^{-1}, with odorant inlets of 12.3 ppmv DMS, 8 ppmv TBM and 8 ppmv THT.

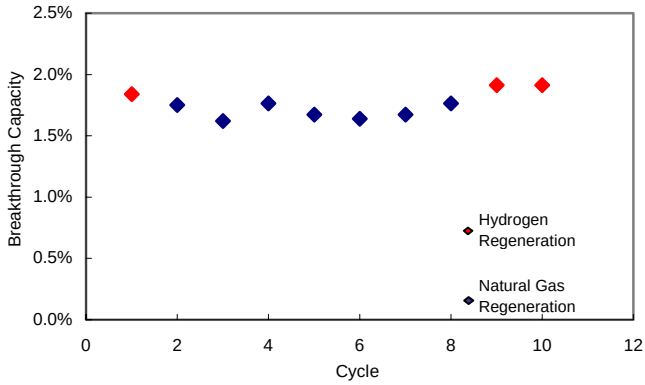

Figure 3. Sulfur capacity of the sorbent during the 10-cycle test at 22°C, 3 psig, GHSV= 60,000 h^{-1}, with odorant inlets of 12.3 ppmv DMS, 8 ppmv TBM and 8 ppmv THT. The capacity is defined as lbs of sulfur adsorbed per lb of sorbent.

Conclusions

A new sorbent was developed for removing sulfur-bearing odorants from natural gas at ambient temperature. SulfaTrap™ sorbent can achieve high sulfur capacity even in the presence of water. It was also shown that the sorbent can successfully be regenerated in either sulfur free natural gas or hydrogen.

Acknowledgements

We wish to thank Mr. Gordon Israelson, of Siemens Westinghouse Power Corporation for discussions. The funding for this research was provided by DOE Phase II SBIR Grant, Contract No. DE-FG02-03ER83795. The authors also thank Mr. Donald Collins of NETL, DOE and Mr. Norman Holcombe of NETL, DOE.

References

(1) Israelson, G.; *Journal of Materials Engineering and Performance*, Vol. 13(3), June **2004**

MASS TRANSFER STUDY OF HYDROGEN SULFIDE REMOVAL FROM REFORMATS WITH MICROFIBER ENTRAPPED ZnO / SiO_2 SORBENTS FOR FUEL CELL APPLICATION

H.-Y. Yang N. Sathitsuksanoh, Y. Lu, B. J. Tartarchuk

Department of Chemical Engineering
Auburn University
Auburn, AL 36849

Introduction

A significant challenge facing Fuel Cell applications is the development of on-site multi-step reformation technologies utilizing high energy density commercial-grade hydrocarbon fuels. So far, most designs have adopted packed bed reactors, which do not scale well with the small modular nature of fuel cells. Packed beds of catalyst/sorbent pellets of one to five millimeters in diameter suffer from high intraparticle mass/heat transfer. Mass transfer may be ameliorated by decreasing the particle size and increasing the face velocity, which in turn causes the high pressure drop and bypassing in packed bed. On the other hand, catalyst/sorbent pellets are not likely to withstand mechanical shaking in many applications (such as portable electric devices, propulsion devices, etc.); powdered catalysts may clump in a way that leads to fluid bypassing. Bare metals and catalysts washcoats have been used to avoid one or more of these problems [1-4], but surface areas per unit reactor volume have remained unacceptably low.

In this paper, we describe our research effort towards small, efficient, lightweight fuel processors based on microfibrous media technologies developed at Auburn University [5-12]. Microfibrous media carrier can be used, with large surface to volume ratios, to entrap micro-sized sorbent and/or catalyst particulates while withstanding considerable shaking and avoiding bypassing. This generic approach can also improve contacting efficiency, and promote regenerability while make more effective (cassette type) design of reactor possible [13-15].

Bulk H_2S removal is a key step of the fuel processor in ensuring the activity of various cleanup catalysts and high value membrane electrode assemblies. To accomplish this goal, the sintered glass fiber media entrap micro-sized ZnO/SiO_2 sorbent particulates was prepared. In this paper, the basic mass transfer study about this sorbents has been conducted

Experimental

Sorbents Preparation. Sintered glass fiber entrapped 150-250 mm (dia.) SiO_2 ($300m^2/g$, Grace Davison) support particulates were fabricated by regular wet layer paper-making/sintering procedure [5-12]. ZnO was then placed onto the supports by incipient wetness impregnation. 6g of glass fiber chops, and 0.7g of 30-60 mm (dia.) cellulose (100-1000 μm in length) were added into about 5L water and stirred at 50Hz to uniform suspension. The produced suspension and 12g SiO_2 were added into the headbox of the 6-inch (dia.) circular sheet former under stirring. A 6-inch circular preform was then formed by draining followed by pressing at ~ 400kNm-1 and drying in air at ~110°C. The As-prepared perform was directly sintered in air for 30 min at 925 °C, while burning off the celluloses. The sintered glass fiber entrapped SiO_2 particulates comprises 3.0 vol% of glass fibers, 45 vol% of 150-250 μm (dia.) SiO_2 particulates, and 52 vol% voidage. To place the ZnO onto the support, the as-prepared microfibrous entrapped SiO_2 paper was immersed into a ZnO sol-gel for 10min. The ZnO sol-gel was prepared by adding 70ml $NH_3 \cdot H_2O$, 42g $(NH_4)_2CO_3$, and 66g $Zn(Ac)_2 \cdot 6H_2O$ in series into 56ml water under vigorously stirring. The paper was subsequently removed from the ZnO sol-gel, drained under vacuum, and calcined at 80°C→ 100°C→ 120°C→ 140°C→160°C→ 180°C in air and hold for 20min at each temperature point. The final composite sorbent product had a ZnO loading around 20wt% (including the mass of the glass fibers).

For comparative study, ZnO/SiO_2 sorbent without microfiber was prepared by the impregnation as mentioned above; commercial ZnO sorbent (3/16" pellet, 25m2/g, 90wt%ZnO) from Sud Chemie was crushed and sieved into desired particle size for comparative study use.

Apparatus and Equipments. The H_2S removal tests were conducted in a fixed bed quartz reactor (9mm id.).The challenging model reformat gas contains 2% H_2S (balance H_2) (Airgas,USA). In regeneration cycle, the household air was applied to convert ZnS to ZnO at 600 °C. A Gas Chromatograph (GC S-500, Gow-Mac, USA) was used to analyze the H_2S concentration in outlet gas.

Results and Discussion

Particle Size Effect. It is believed that sorbent of small size can enhance the intraparticle mass transfer, thus improves the utilization. In this study, Sud Chemie ZnO sorbent pellets were crushed and sieved into desired particle sizes. The comparison between the performance of ZnO/SiO_2 and Sud Chemie sorbents is shown in **Figure 1**. In each experiment, 0.18 g effective ZnO was loaded. Reactor temperature kept at 400 °C and face velocity 1.28 cm/s. The only difference is the particle size. It is clearly illustrated that the breakthrough curves shift right and give sharper breakthrough curves and higher capacities with the decrease in sorbents size. This is because smaller particles offer larger surface, which in turn means more sorbents may be accessible to challenge gas, assuming challenging gas can diffuse through the same distance d in the spherical sorbents particles, where d is less than the size of particles in Sud Chemie cases. If the size of ZnO particles is less than d, then theoretically all ZnO could be consumed by H_2S, which will only demonstrate a step at the theoretical saturation time in the breakthrough curve. Although the particles of this size are impracticable due to the drastic increase in pressure drop, the particulates could be supported on other particles with reasonable size. This is an idea to get rid of the intraparticles mass transfer resistance that suffers almost all packed beds. Actually, through the impregnation process, nanosized ZnO was dispersed on the silica particles [16]. As expected, the silica particle impregnated with nanosized ZnO demonstrates the sharpest breakthrough curve and the breakthrough capacity is twice that of Sud 40-60mesh. For convenience, the breakthrough was defined at the point that the outlet concentration reached 1% inlet concentration (C_0).

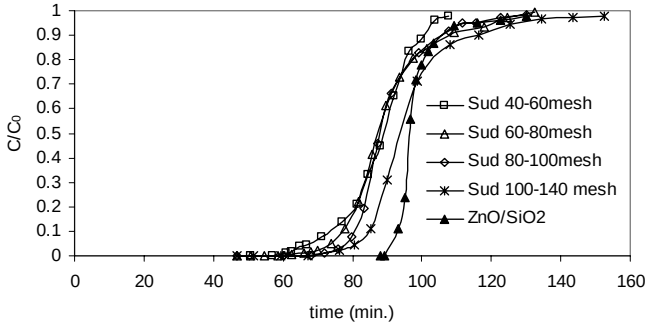

Figure 1. Breakthrough curves of Sud Chemie Sorbents with different size and ZnO/SiO_2 sorbents

External mass transfer study. In this study, the ZnO/SiO_2 sorbent is tested at 400 ^oC with challenge gas concentration (C_0) of 2%. In he first experiment, 0.1 g ZnO/SiO_2 (ZnO loading ratio 19%) sorbent was loaded and the face velocity is about 1.28 cm/s. In each of the following experiments, the weight of sorbent loaded and face velocity was twice of these in former experiment, thus the resident time was maintained unchanged, so did the theoretical saturation time. The breakthrough curves of $/SiO_2$ at different face velocities is shown in **Figure 2**. The breakthrough cure of glass fiber entrapped sorbent (GFE) with 0.019 g ZnO loaded at the face velocity of 1.28 cm/s is also shown for comparison.

All the breakthrough curves pass around the same point, which indicates the consistency of the theoretical capacity. It is a clear trend that the breakthrough curves become sharper with the increase in face velocity of challenge gas. For convenience, the breakthrough point was defined at 1% of inlet concentration. The capacity of sorbents in each experiment was calculated. As shown in **Figure 3**, the capacity at breakthrough increases significantly in low face velocity range. While, after the face velocity reaches 5 cm/s, the capacity is slowly approaching 0.37, about 90% of the theoretical capacity, which suggests that the unutilized ZnO is less than 10%. The breakthrough curve of glass fiber entrapped sorbents shows the capacity at breakthrough increases about 50% form the experiment m:V, though in both cases, the same type of sorbent (ZnO/SiO_2) with the same amount of ZnO had been loaded and . The only explanations for this improvement could be the enhancement of external mass transfer due to the glass fiber media.

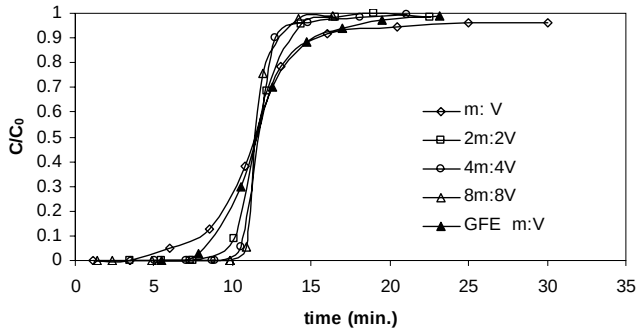

Figure 2. The breakthrough curves of ZnO/SiO_2 at different face velocities (C_0=2%, reactor temperature 400 ^oC).

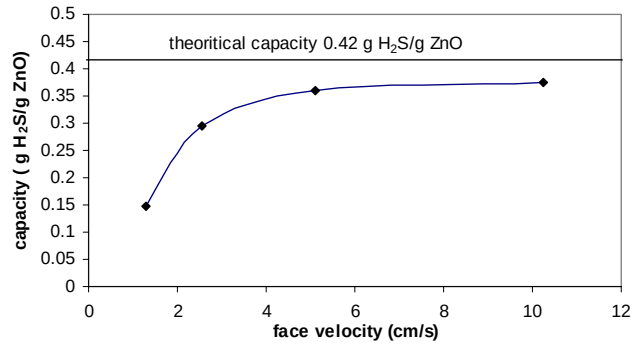

Figure 3. The breakthrough capacity of sorbent at different face velocities.

Due to the fast gas diffusion at high temperature, the improvement of microfiber media was not significant. It is known that the diffusivity decrease exponentially with the decrease of temperature. Thus, a series of experiments at room temperature was conducted. In these experiments, the challenge gas was fed at the same rate 23 ml/min, while the face velocity was about 0.51 cm/s. In each experiment, about 0.019 g ZnO was loaded. The comparison between the performance of ZnO/SiO_2 and ZnO/SiO_2 entrapped in glass fibers or glass mixtures of different fiber diameters was shown in **Figure 4**. Here there is a clear distinction in the performance of ZnO/SiO_2 particles and GFE. The hump in the breakthrough curve of former indicates that is a mass transfer dominated process, since the same sorbents entrapped in microfibers demonstrated much sharper breakthrough curves. Moreover, the fiber diameter also affected the mass transfer. The breakthrough curve of sorbents entrapped in the fiber with larger size, say 14μm, is not as sharp as that of smaller size, though this difference becomes not significant especially when the fiber diameter is less than 14μm.

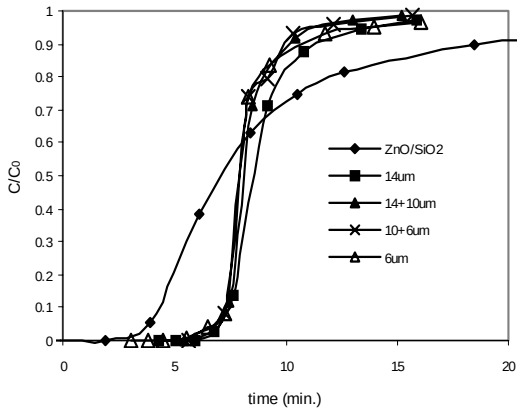

Figure 4. the performance of ZnO/SiO2 and ZnO/SiO2 entrapped in glass fibers of different diameters at room temperature.

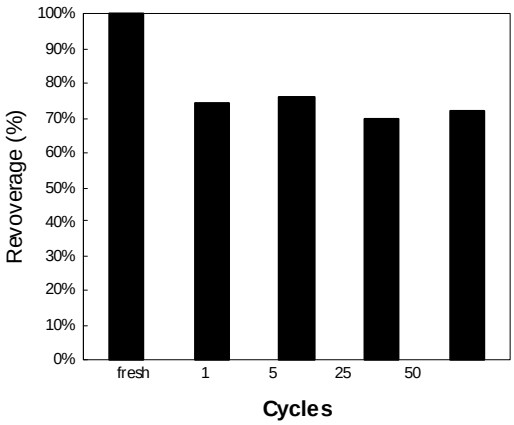

Figure 5. absorption/regeneration cycle test results over the GFE ZnO/SiO2 sorbents (absorption temperature 400 ^oC, regeneration at termperature 600 ^oC for 1 hour; define recoverage as the ratio of capacity of regenerated sorbent to that of fresh sorbent).

Regeneration. It is clear that the microfibers are able to enhance the external mass transfer thus improve the sorbents performance in the low concentration H_2S removal; ZnO nanosized particulates supported by SiO_2 can minimized the intraparticle mass transfer resistance. It is undoubted that it will also demonstrate outstanding performance in regeneration cycles, where oxygen, instead of H_2S in absorption case, diffuses in the sorbents. As shown in **Figure 5**, the regenerated sorbents have steady capacities which are around 75% of the capacity of fresh ones. From the mass transfer study of glass fiber

entrapped ZnO/SiO_2 sorbents, it is clear that the combination of these microfiber media nano-dispered ZnO on SiO_2 has offered a nice solution to the low concentration H_2S removal in onsite fuel processor.

Acknowledgment

Financial support from U.S. Army (DASG 60-00-C-0070) is gratefully acknowledged.

References

1. McCreedy, T. Trends Anal. Chem., 2000, 19, 396.
2. Srinivasan, S.; Hsing, I.M.; Berger, P.E.; Jensen, K.F.; Firebaugh, S.L.; Schmit, M.A.; Harrold, M.P.; Lerou, J.J.; Ryley, J.F. AIChE J., 1997, 43, 3059.
3. Watanabe, K.; Sakairi, M.; Takahashi, H.; Takahiro, K.; Nagata, S.; Hirai, S. J. Electrochem. Soc., 2001, 148, B473.
4. Wu, X.; Weng, D.; Xu, L.; Li, H. Surf. Coat. Technol., 2001, 145, 226.
5. Tatarchuk, B. J.; Rose, M. F.; Krishnagopalan, A.; Zabasajja, J.N.; Kohler, D. US Patent 5,304,330, 1994; US Patent 5,080,963, 1992.
6. Overbeek, R. A.; Khonsari, A. M.; Chang, Y.-F.; Murrell, L. L.; Tatarchuk, B. J.; Meffert, M. W. US Patent 6,231,792, 2001.
7. Tatarchuk, B. J. US Patent 5,096,663, 1992; US Patent 5,102,745, 1992.
8. Cahela D. R.; Tatarchuk B. J. Catal. Today, 2001, 69, 33-39.
9. Marrion, C. J.; Cahela, D. R.; Ahn, S.; Tatarchuk, B. J. J. Power Sources 1994, 47, 297-302.
10. Kohler, D. A.; Zabasajja, J. N.; Krishnagopalan, A.; Tatarchuk, B. J. J. Electrochem. Soc. 1990, 137(1), 136-141.
11. Ahn, S.; Tatarchuk, B. J. J. Appl. Electrochem. 1997, 27, 9-17.
12. Meffert; M. W. Ph.D. thesis, Auburn University, Auburn, AL, 1998.
13. Harris, D. K.; Cahela, D. R.; Tatarchuk, B. J. Composites, Part A: Applied Science and Manufacturing 2001, 32A(8), 1117-1126.
14. Lu, Yong; Tatarchuk, B. J. 226th ACS National Meeting, New York, NY, Sept. 7-11, 2003, CATL-042.
15. Lu, Yong; Tatarchuk, B. J. AIChE 2003 National meeting, San Francisco, CA, November 16-21, 2003, 331b.
16. Lu, Yong, Chang, B.-K., Yang, H.Y. Tatarchuk, Bruce J., ASM International, Columbus, OH, October 19, 2004 - 10:30 AM FUEL 4.5

INTEGRATED WATER GAS SHIFT (WGS) Pd MEMBRANE REACTORS FOR COMPACT HYDROGEN PRODUCTION SYSTEMS FROM REFORMING OF FOSSIL FUELS

Ying She, Zissis Dardas, Mallika Gummalla, Thomas Vanderspurt, Sean Emerson

United Technologies Research Center, 411 Silver Lane, East Hartford, CT 06108

Introduction

United Technologies Research Center (UTRC) is developing integrated Pd Membrane reactors for H2 production through reforming of fossil fuels. This is because, depending on the application, fuel & system design requirements, Pd membrane modules can be integrated in the reformer (catalytic steam reformer) or the Water Gas Shift (WGS) reactor, thus eliminating all the reactors, major part of the multiple heat exchangers and the air mixers in the traditional fuel processing system for H2 generation, down steam of the reactor that they are integrated with.

Metal supported tubular Pd membranes have high modularity and thus can be easily scaled up to any system capacity while they do not employ components with high reliability debits like rotating valves in high time frequency, as is the case for Pressure Swing Adsorption. This approach results in significant system cost savings and controls simplicity (thus higher system reliability) due to system simplification through component elimination.

Results and Discussion

Detailed system and reactor modeling, analysis, simulation, sensitivity analysis, parametric trade off & optimization studies were completed for an on board fuel processing system integrated with an ambient pressure 50 kWe PEM fuel cell stack and balance of plant. Parametric studies for the Pd membrane WGS reactor included reformate flow rate, composition, inlet temperature and pressure, sweep gas inlet temperature & flow rate, Pd membrane thickness, and tube support diameter, length and number of tubes. For example, Fig. 1 shows the influence of the inlet WGS reactor pressure on hydrogen recovery. As expected, hydrogen recovery increases with the increase in the pressure. Proprietary WGS catalyst kinetics integrated with mass & heat transfer processes were utilized to estimate require WGS catalyst volume. The optimum reactor & system design configuration and operating parameters were identified and the resulting system design had 6 points higher efficiency than the baseline design that does not employ a membrane reactor.

Significant accomplishments in Pd membrane permeance, selectivity & stability were demonstrated by the synthesis effort under development at UTRC. As shown in Fig. 2, hydrogen permeance & H_2/N_2 selectivity values with a proprietary synthesis approach based on electroless plating over modified porous stainless steel supports are ~50 m^3/m^3-hr-$atm^{0.5}$ and 150:1, respectively, with no evidence of performance deterioration for more than 300 hrs in hydrogen at temperatures in the 350-400 ^oC regime.

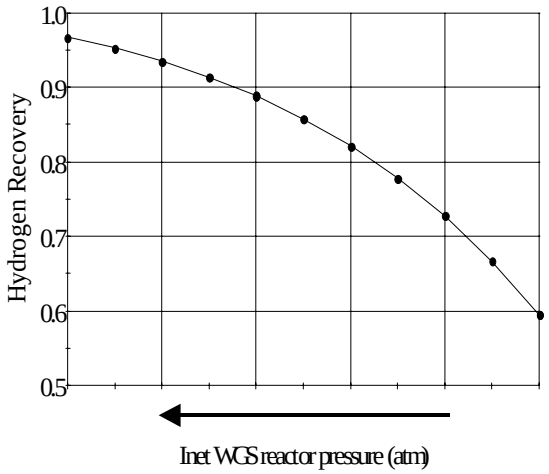

Figure 1. Effect of the inlet WGS reactor pressure on hydrogen recovery

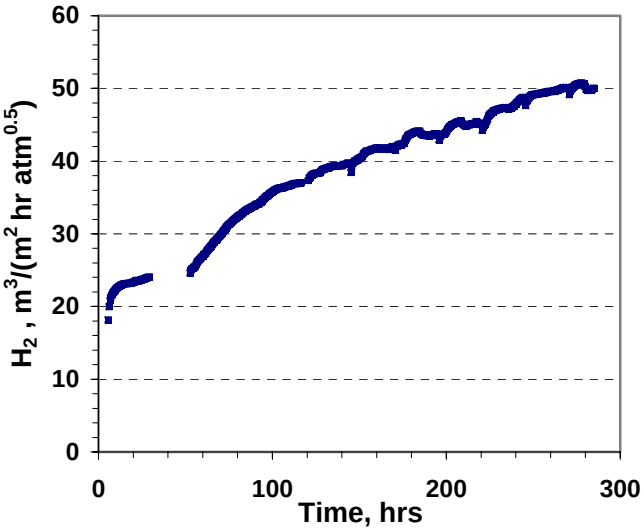

Figure 2. Hydrogen performance as a function of time

IN SITU FT-IR STUDY OF THIOPENE ADSORPTION AND REACTIONS ON SULFIDED Mo CATALYSTS

Dong Liu, Xue Kong, Zongxian Wang and Guohe Que

State Key Laboratory of heavy oil processing, University of Petroleum, Dongying, Shandong 257061, China

Introduction

Molybdenum based catalysts play an important role in the hydroprocessing of petroleum, and accordingly numerous studies have been made to clarify the surface structure and active sites by using infrared spectroscopy [1-5]. It is generally accepted that the sulfur vacancies is the active sites of HDS. The number of active sites on sulfide catalysts has typically been estimated by CO chemisorption [6,7], the HDS activity of sulfided molybdenum catalysts has been shown to correlate with both their CO and O_2 chemisorption capacities [8-10], the probe molecules selectivel adsorb on coordinately unsaturated Mo sites located on the edge planes of MoS_2 crystallites which are thought to be the active sites for hydrodesulfurization [11]. But the spectra of adsorbed CO on sulfided catalysts can only be found at low temperature, the results shows gap from real reactivity. NO can adsorb more easiely on sulfide catalyst at room temperature, little is known about the sites on which NO adsorb and what the relationship is between these adsorption sites and the active sites for hydrodesulfurization. The purpose of the current study is to investigate the relationship between the NO chemisorption sites and thiophene HDS activity using IR spectroscopy on sulfided Mo catalysts.

Experimental Section

Sample preparation: Two kinds of laboratory prepared catalyst (denoted by Cat.A and Cat.B) and Commercially available MoS_2 powders (denoted by Cat.C) were used in the present study. Cat.A was prepared by sulfurization of 15wt%MoO_3 / ɣ-Al_2O_3 in a stream of H_2S/H_2 gas mixture at 673K for 4h, MoO_3 / ɣ-Al_2O_3 was prepared by impregnation of ɣ-Al_2O_3 with aqueous solutions of ammonium heptamolybdate, following impregnation, the catalyst was calcined for 4h in air at 773K. Cat.B was prepared by the following method: aqueous solutions of ammonium heptamolybdate was scattered in gas oil well-proportioned, $(NH_4)_2S$ was introduced into the system, after sufidation keeping the temperature at 403K for 1h in a stream of N_2 to remove the water, the gas oil was displaced to high-pressure kettle and react in H_2 ambience at 693K for 1h, the toluene-insoluble distance was separated and then the sulfided water-solubility dispersed molybdenum catalyst attained.

Infrared Spectroscopy Measurements: Infrared spectroscopy measurements were carried out in a quartz cell. Catalyst samples were pressed into a self-supporting circular wafer with a diameter of approximately 13mm, and mounted on the sample holder, diagram of in situ infrared system shows in Fig1, and the quartz cell has been described in detail elsewhere [12]. A small well under the edge of the sample contained a thermocouple used to monitor the temperature of the system. The heating sector and the thermocouple are associated with temperature-programmed instrument to control the temperature of the system. IR spectra acquisition was accomplished using Nicolet Magna-750 Fourier transform-infrared spectrometer and consisted 60scans of the region of 4000-1200cm^{-1}, which took approximately 1min to acquire.

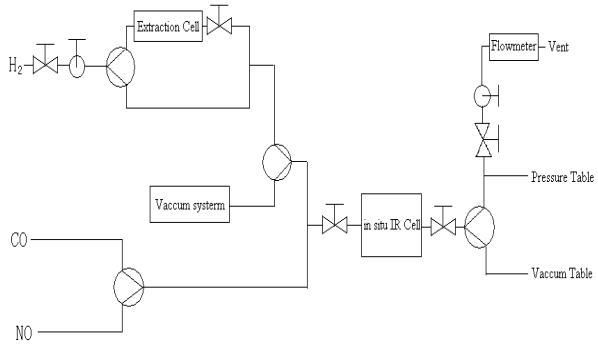

Fig1. Flow Diagram of In-situ FT-IR System

Depending upon the experiment, background spectroscopy was acquired for the wafer in UHV at corresponding temperature. After the catalyst exposed to pretreatment, NO was introduced into the cell and keeping the pressure of NO 0.08MPa for 1h at room temperature, outgassing about 5min and following acquisition of the IR spectrum of adsorbed NO on catalysts.

Thiophene Adsorption and HDS Activity Measurements: Thiophene Adsorption and HDS Activity Measurements were determined also in the stainless-steel cell as previous. H_2 carried the solid thiophene into the cell and the pressure of H_2/thiophene was 0.08MPa, HDS reactions were carried out at 673K for 1h in the cell. The infrared spectroscopy was recorded during the temperature increasing.

Results and Discussion

Infrared Spectroscopy of Adsorbed NO: The IR spectra of NO chemisorbed on Cat.A, Cat.B and Cat.C are displayed in Fig2.

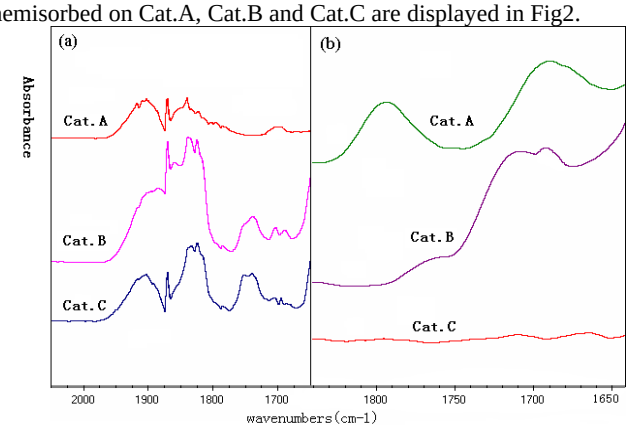

Fig2. IR spectra of NO adsorbed on Cat.A, Cat.B and CatC. (a) in 0.08MPaNO and
(b) after outgassing at room temperature.

The spectra of different catalysts differ in intensities and slightly in frequencies depending on the preparation method, Cat.A contain the characteristic doublet bands about 1800 and 1700cm^{-1}, which are ascribed to the symmetric and antisymmetric vibration modes of two NO molecules coupled in the adsorbed state as dinitrosyl $(NO)_2$ structures on the same unsaturated molybdenum site[13,14]. There were varieties from Cat.A When Cat.C was exposed to NO, the band at 1828cm^{-1} increased with the NO adsorption time prolonged, and also a band at 1743cm^{-1} appeared, while after outgassing these band disappeared swift. The absence of any band at about 1800 and 1700cm^{-1} corresponding to adsorbed NO on the Cat.C indicated that there exists few proportion of sulfur vacancies which could chemisorbed NO. In light of the results from XRD (Fig3.) analysis, the possibility that the low intensity of these bands may be attributed

to a low dispersion of the MoS_2 species.

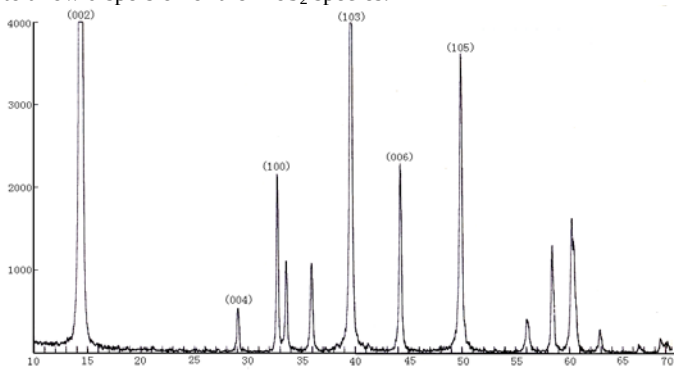

Fig3. XRD spectra of MoS_2 catalyst(Cat.C)

As expected, the spectra of NO adsorbed on Cat.B are more complex than those of Cat.A and Cat.C, when Cat.B exposed to NO, a band at 1743cm^{-1} also could be found and the band at 1828cm^{-1} raised, which is resemble to the band appeared on Cat.C. But after outgassing the spectra display bands at about 1778, 1707 and 1692cm^{-1}.The band at 1778cm^{-1} is ascribed to the symmetric vibration modes of two NO molecules coupled in the adsorbed state as dinitrosyl $(NO)_2$ structures on the same unsaturated molybdenum site, the lower frequency band at 1707 and 1692cm^{-1} correspond to antisymmetric vibration modes of dinitrosyl $(NO)_2$ species adsorbed on vacancies of sulfide molybdenum catalyst[13,14]. It is interesting to note that the band at 1778cm^{-1}, indicative of the symmetric vibrationg mode of dinitrosyl $(NO)_2$ becomes shifted about 22cm^{-1} to lower wavenumbers and the band corresponding to antisymmetric vibration modes of dinitrosyl $(NO)_2$ species appeared as two bands with respect to that of Cat.A(1800cm^{-1}). From XPS result (Fig4.), it is clear that MoS_2, MoO_2 and MoOS species exist at the surface of Cat.B, the density of electron of different species is different, so that two bands ascribed to adsorbed NO could be found located on 1707 and 1692cm^{-1}.

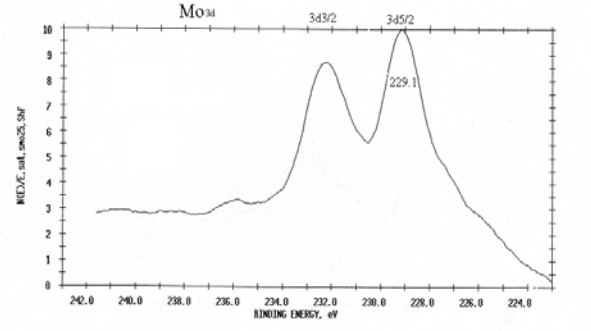

Fig4. Mo3d of XPS spectra of sulfide water-solubility Mo catalyst (Cat.B)

Form the results of our experiments, there are obvious differenced between the IR spectra of NO and thiophene adsorbed on the three catalysts above-mentioned, and the activity of thiophene hydrodesulfurization on the three catalysts show distinction to each other. Because only the unsaturated sites can adsorbed probe molecules, the surrounding of the active sites will make the spectra of adsorbed NO changed [20,21], so different absorbance peaks correlate to different active sites. On Cat.A, The doublet bands related to $(NO)_2$ structures on the same unsaturated molybdenum site [13,14] show that there exists one adsorption sites at least on the surface of sulfided Mo/Al_2O_3 catalyst. No evidence spectra of adsorbed NO on Cat.C indicated that there exists few proportion of sulfur vacancies to chemisorbed NO, a low dispersion of the MoS_2 species cannot produce adsorption sites. While NO adsorption on Cat.B shows more complex to Cat.A and Cat. C, for it was prepared at high dispersion, several unsaturated Mo sites at different chemical surrounding may exist. Comparing the intensity of the bands corresponding to adsorbed NO, it can be found that the intensity of the band on Cat.A is higher than that on Cat.B, as we all known, the intensity of adsorbed NO increased with adsorption sites on the surface of catalyst. The IR spectra of adsorbed NO suggest that the amount of the adsorption site densities decreased with the following order: sulfide $Mo/\gamma\text{-}Al_2O_3$ >sulfide water-solubility dispersed catalyst> MoS_2.

Exposure of Catalysts to Thiophene/H_2 at high temperature:

The IR spectra presented in Fig5. show that a sulfided 15wt%$Mo/\gamma\text{-}Al_2O_3$ catalyst becomes quite reactive toward thiophene when heated to 673K in the presence of thiophene/H_2, No reactivity is observed in the identical experiment for the sample of pure $\gamma\text{-}Al_2O_3$. From the result of Fig5a, the IR spectrum in the ν_{CH} region contains absorbance features at 3075, 3090 and 3109cm^{-1}, and which are ascribed to thiophene adsorbed on the surface of $\gamma\text{-}Al_2O_3$[15,16]. The IR spectrum in the ν_{CC} region shows peaks at 1400, 1408 and 1429cm^{-1}. Annealing of the catalyst at 573K for 1min leads to the production of new absorbance features in the ν_{CH} region at 2920 and 2860cm^{-1}, further annealing at 673K, the intensity of the bands at 2920 and 2860cm^{-1} increasing rapidly, these absorbance can be assigned to the ν_{CH} of CH_2 and CH_3 groups of adsorbed C_4 hydrocarbon species, the bands at 1610, 1380 and 1460cm^{-1} also could be found, the bands at 1380 and 1460cm^{-1} corresponding to δ_{CH}, while 1610 was the characteristic band of $\nu_{C=C}$[17], which confirmed that thiophene hydrogenated to C_4 hydrocarbon on Cat.A.

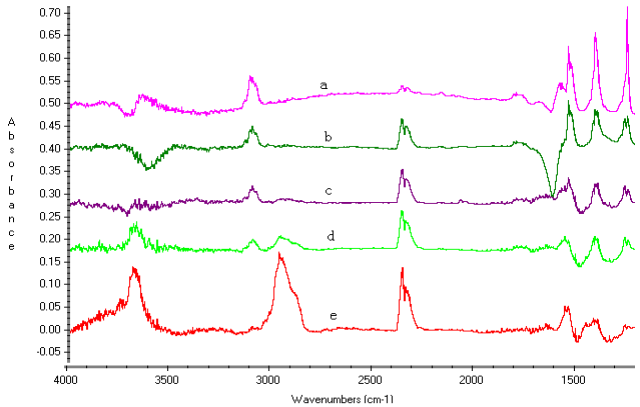

Fig5. IR spectra of adsorbed thiophene hydrogenation on Cat.A
(a) 323K; (b) 373K; (c) 473K; (d) 573K; (e) 673K

The IR spectra presented in Fig6a show that thiophene adsorbed on water-solubility dispersed molybdenum catalyst, there exist the band at 3075, 3090, 3109, 1400, 1408 and 1425cm^{-1}, which is identical to the band thiophene adsorbed on Cat.A. While new absorbance features are observed in the process of temperature increasing in the presence of thiophene/H_2, a weak and broad absorbance feature slowly develops at approximately 2640cm^{-1} which is likely due to S-H stretching vibration mode, Ratnasamy and Yerofeyev observed a similar absorbance feature in their studies of H_2 and thiophene adsorption on unsupported MoS_2 and also assigned it to an S-H stretching vibration [18,19]. Annealing at 673K, the bands at 2920, 2860, 1610 1380 and 1460cm^{-1} also could be found, which shows that thiophene can be hydrogenated to C_4 hydrocarbon on Cat.B, but the intensity of the bands corresponding to the products

produced from thiophene hydrodesulfurization lower than that on Cat.A.

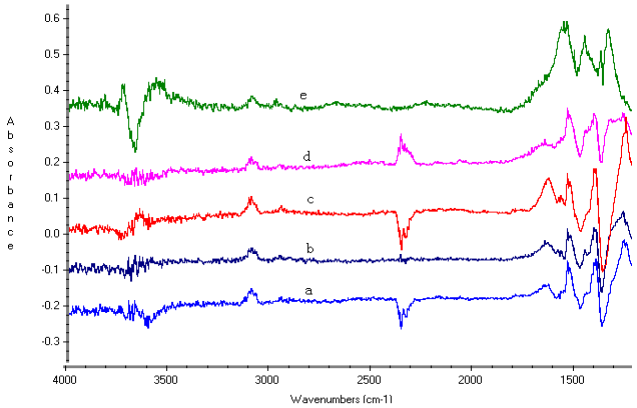

Fig6. IR spectra of adsorbed thiophene hydrogenation on Cat.B at different temperature

(a) 323K; (b) 373K; (c) 473K; (d) 573K; (e) 673K

Fig7 shows the IR spectra of thiophene adsorption and hydrodesulfurization in the presence of thiophene/H_2 on MoS_2. while thiophene adsorbed on MoS_2, there was no evidence absorbance peaks at ~1429cm^{-1}, which is ascribed to ν_{CC} of adsorbed thiophene on surface of the catalyst, after annealing at 673K in the presence of thiophene/H_2, the bands at 2920, 2860cm^{-1} could be found, but the bands corresponding to ν_{SH}, $\nu_{C=C}$ and δ_{CH} did not appeared. The results indicated that the activity of thiophene HDS on MoS_2 is lower than the above-mentioned catalyst. For MoS_2 exists as crystal, it cannot be reduced easily to produce sulfide vacancies which is the active sites for hydrodesulfurization.

As described in the results section, While H_2 and thiophene coadsorption on the three catalysts at room temperaure, a shoulder peak at 1429cm^{-1} on Cat.A and 1425cm^{-1} on Cat.B respectively appeared, which differ from the spectra of H_2 and thiophene coadsorbed on Al_2O_3, tt can be concluded that the IR spectra at ~1430cm^{-1} is caused by thiophene adsorbing on the metal center of the surface of the two catalyst. The fact that no absorbance feature is observed at ~1430cm^{-1} in the IR spectrum of Cat.C exposed to thiophene/H_2 may consistent with (a)H_2 adsorption on the sites more easily than thiophene or (b)adsoption sites cannot be produced on the surface of MoS_2 catalyst. Combined with the result of NO adsorption, it is proved that a low dispersion of the MoS_2 species cannot produce adsorption sites. The absorbance feature at ~1430cm^{-1} in the IR spectrum of thiophene adsorbed on sulfided Mo/Al_2O_3 and water-solubility dispersed molybdenum catalyst can be assigned to the symmetric ν_{CC} mode of thiophene adsorbed on MoS_2-like structures. Terbuck[22] as well as Patrick[16] also observed the same absorbance features at ~1430cm^{-1} on sulfided Mo/Al_2O_3 catalyst, and they all assign this adsorbance feature to thiophene η^1(S) bonded to cus $Mo^{\delta+}$ sites of MoS_2-like structures of the sulfided Mo catalyst. The peak position of this ν_{CC} mode is shifted to higher wavenumbers than is observed for liquid thiophene(1406cm^{-1}), it is well known that the vibrational frequencies of ring stretching modes of the heterocyclic aromatic molecules are sensitive to their bonding environment on a catalyst surface. The symmetric ν_{CC} mode of should be shifted to higher wavenumbers when thiophene is adsorbed on a metal center via its sulfur atom and should be shifted to lower wavenumbers when thiophene is π-bonded to a metal center, the fact that the peak position of the ν_{CC} mode shifts to higher wavenumbers when thiophene adsorbed on sulfided Mo/Al_2O_3 and water-solubility catalysts provides the evidence that thiophene is coordinated via its sulfur atom to cus Mo sites on the catalyst surface. Since the adsorbed species associated with the adsorbance features in the region of 2800-3000cm^{-1} region are believed to be thiophene hydrodesulfurized C_4 hydrocarbon fragments, Compared the spectra of different catalyst after annealing in the presence of thiophene and H_2 at 673K for the same time, it could be concluded that the trend in thiophene reactivity is observed to be the following: sulfide Mo/γ-Al_2O_3 >sulfide water-solubility dispersed catalyst> MoS_2. The observed trend of the reactivity of thiophene hydrodesulfurization reflects the catalyst activity strongly correlates to the dispersion status, high dispersion is propitious to improving the activity of the catalyst.

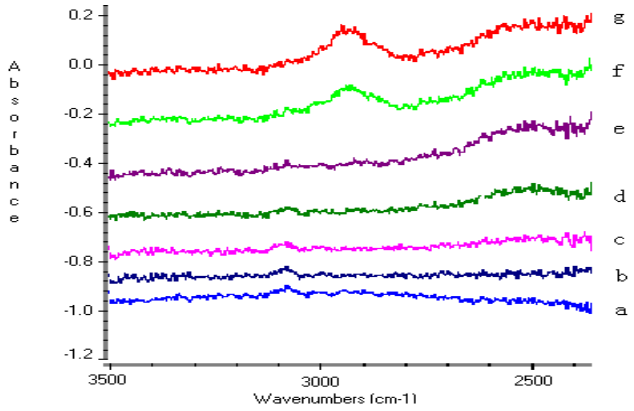

Fig7. IR spectra of adsorbed thiophene hydrogenation onCat.C at different temperature(a) 323K; (b) 373K; (c) 473K; (d) 573K; (e) 673K (f) after 30min under 0.04MPa H_2/thiophene at673K;(g) 1h under 0.04MPa H_2/thiophene at 673K;

Conclusion

The adsorption and reaction of thiophene on the surface of the sulfided molybdenum catalysts in the presence of hydrogen have been studied by FT-IR spectroscopy combined with NO adsorption. The IR spectra of adsorbed NO suggest that the amount of the adsorption site densities decreased with the following order: sulfide Mo/γ-Al_2O_3 >sulfide water-solubility dispersed catalyst> MoS_2. Thiophene is weakly chemisorbed to the sites located on MoS_2-like structures and on uncovered alumina regions of sulfide molybdenum catalyst. Based upon interpretation of IR spectra, the adsorption mode of thiophene on sulfide Mo portion of the catalyst surface has been determined to be η^1(s). Thiophene is observed to become reactive on sulfided Mo catalysts in the presence of gas-phase hydrogen and at high temperatures. Thiophene hydrodesulfurization(HDS) activities of several sulfided Mo catalysts decreasing in the following order: sulfide Mo/γ-Al_2O_3 >sulfide water-solubility dispersed catalyst> MoS_2, which are consistent to the adsorption site densities.

REFERRENCES

(1) Diemann, E., Weber, T., Muller, A. J. Catal. 1994,148:288
(2) Ratnasamy, P., Fripiat, J. J., J. Chem. Soc., Faraday Trans. 1970,66:2897
(3) Dong, L., Duckett, S. B., Ohman, K. F. et al. J. Am. Chem. Soc.1992, 114:151
(4) Luo, S., Rauchfuss, T. B., Gan, Z. J. Am. Chem. Soc, 1993, 115:4943
(5) Mitchell P C H, Green D A, Grimblot J et al. J. Bull. Soc. Chim. Belg. 1995,104:325
(6) Oyama, S. T., Catal. Today, 1992,15:179

(7) Lee, J. S., Lee, K. H. and Lee, J. Y., J Phys. Chem. 1992,96:362
(8) Tauster, S. J., Pecoraro, T. A., and Chianelli, R. R. J. Catal. 1980,63:515
(9) Bachelier, J., Tilliette, M. J., Duchet, J. C. et al. J. Catal. 1982, 76:300
(10) Bachelier, J., Duchet, J. C., Cornet, D. Bull. Soc. Chim. Belg. 1981,90:1301
(11) Muller, B., van Langeveld, A., D, Moulijn, J. A. et al. J. Phys. Chem. 1993, 97:9028
(12) Xue Kong, Dong Liu, Zongxian Wang et al. Prepr. Pap. ACS Div, Pet. Chem. 2003,48:265
(13) Yasuaki O, Yukihiro K, Yoshiyuki M. J. Catal. 1981,70:445
(14) Topsoe N Y, Topsoe H. J Catal, 1982,75:354
(15) Zili, W., Yongjun, C., Shuwu, Y., J. Catal. 2000,194:23
(16) Patrick M, Diana C P, Brian P W et al. J. Phys. Chem. B 2000, 104:3237
(17) Little L H. Infrared Spectra of Adsorbed Species[M]. London: Academic Press,1966
(18) Yerofeyev V I, Kaletchits I V. J Catal. 1984,86:55
(19) Ratnasamy, P., Fripiat, J. J. J. Chem. Soc. Faraday Trans. 1970, 66:2897
(20) Goldwasser, J., Fang, S. M., Houalla, M., et al. J. Catal.1989,115:34
(21) Redey, A., Goldwasser, J., Hall, W. K. J. Catal. 1988,113:82
(22) Tarbuck T L, Mccrea K M, Logan J W et al. J. Phys. Chem. 1998,102:7845

SYNTHESIS OF SULFONATED POLY(ARYL ETHER KETONE)S WITH PENDANT FLUORINATED GROUPS (SPAEK-6FP) FOR PROTON EXCHANGE MEMBRANES

Baijun Liu [a], *Gilles P. Robertson* [a], *Michael D. Guiver* [a,] *, *Serguei Mikhailenko* [b], *Serge Kaliaguine* [b]

[a] Institute for Chemical Process and Environmental Technology, National Research Council, Ottawa, Ontario K1A 0R6, Canada
[b] Chemical Engineering Department, Laval University, Ste-Foy, Quebec G1K 7P4, Canada

Introduction

Proton exchange membrane fuel cells (PEMFC)s are promising clean power sources for automotive and portable applications.[1] Nafion, with a perfluorosulfonic acid structure, has been successfully employed as a PEM because of its high proton conductivity and other outstanding properties. However, high cost, low operation temperature, and high methanol crossover of Nafion and other perfluorinated membranes have limited their further commercial application. Inexpensive fluorine-free and partially fluorinated polymers with improved performance are being investigated as alternative PEMs. Aromatic polymers such as sulfonated derivatives of poly(ether ether ketone) (SPEEK), poly(ether sulfone) (SPES), and polyimide (SPI) are regarded as promising materials for PEMs because of their stable structures and high performance.[2,3]

Recently, our group reported a series of SPAEEKs based on 4,4'-(hexafluoroisopropylidene)diphenol as an approach to increase the hydrophobicity and length of nonsulfonated segments and to improve the mechanical properties and hot water stability of the films, which showed some ideal properties as PEMs.[4] In the present work, sulfonated poly(aryl ether ketone)s (SPAEKs), specifically sulfonated poly(aryl ether ether ketone)s (SPAEEKs) and sulfonated poly(aryl ether ether ketone ketone)s (SPAEEKKs) with partially fluorinated pendant moieties were synthesized by direct copolymerization. The structures and selected properties such as thermal stability, water uptakes and proton conductivity, are discussed.

Experimental

Materials. (3,5-Ditrifluoromethyl)phenylhydroquinone was synthesized according to a reported synthetic procedure.[5] 1,4-Bis(4-fluorobenzoyl)benzene was received from Jilin University (China) and recrystallized from 1,2-dichlorobenzene before use. 4,4'-Difluorobenzophenone was obtained from Sigma-Aldrich Ltd. and purified by sublimation before use. 1,4-Bis(3-sodium sulfonate-4-fluorobenzoyl)benzene and sodium 5,5'-carbonylbis(2-fluorobenzenesulfonate) were synthesized according to a reported procedure.[6,7] Solvents were obtained commercially and used without purification.

Polymerization. The synthesis of SPAEEKK-6FP-50 is given as an example. To a 100-mL three-necked flask equipped with a magnetic stirrer, a nitrogen inlet and a Dean-Stark trap, were added 1,4-bis(3-sodium sulfonate-4-fluorobenzoyl)benzene (0.5264g, 1mmol), 1,4-bis(4-fluorobenzoyl)benzene (0.3223g, 1mmol), 6F-PH (0.6444g, 2mmol), anhydrous K_2CO_3 (0.3594g, 2.6mmol), DMAc (6ml) and toluene (12ml). The system was allowed to reflux for 3h while water was removed, and then the toluene was distilled off. The reaction mixture was heated to 160ºC. After 10h, another 4-5ml of DMAc was added into the viscous reaction mixture. The polymerization was complete after another 2h. The viscous solution was then poured into ethanol. The polymer was thoroughly washed with hot deionized water to remove the salts and solvents, and dried at 100ºC for 48h.

Characterization. FTIR spectra were measured on a Nicolet 520 Fourier transform spectrometer. ^{1}H NMR spectra were recorded on a Varian Unity Inova NMR spectrometer. Differential scanning calorimetry (DSC) measurements were performed on a TA Instrument 2920 DSC at a heating rate of 10^{o}C/min under nitrogen. Thermogravimetric analysis (TGA) was performed on a TA Hi-Res TGA 2950 thermal analyzer system at a heating rate of 10 ^{o}C/min under N_2. Viscosities of the copolymers in sodium form were measured in DMAc (0.5g/dL) at 30^{o}C using an Ubbelohde viscometer. The proton conductivities of the membranes were obtained on by AC impedance spectroscopy with a Solartron 1260 gain phase analyzer. The membranes were clamped between two electrodes and then placed in an open temperature-controlled chamber with water vapor at 100% relative humidity. Samples were hydrated in water at room temperature for at least one week before measurements. The water uptakes and swelling ratios of the polymers were measured by immersion of the polymer films (5mm × 50mm) in deionized water at 25^{o}C and 80^{o}C for 24h. The water uptakes and swelling ratios were calculated from the differences in weight and length.

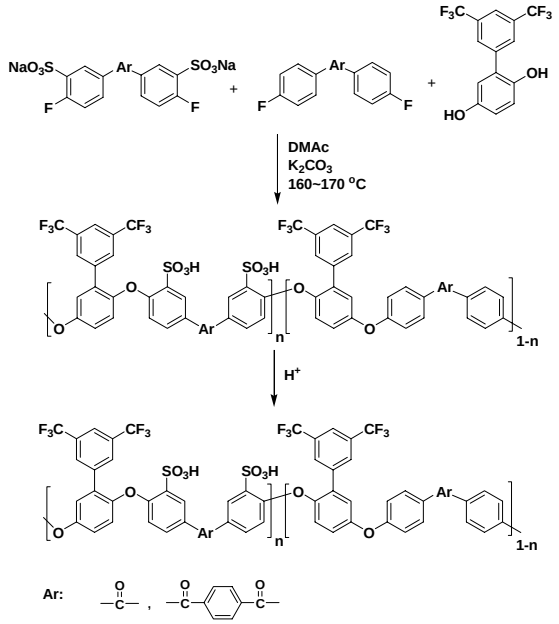

Figure 1. Synthesis of sulfonated poly(aryl ether ketone)s.

Membrane preparation. The films of the copolymers in sodium form were prepared by casting their DMAc solution (0.5g/12ml) onto glass plates and dried at 50^{o}C for 72h. The membranes in proton form were obtained by soaking the above films in 2N H_2SO_4 aqueous solution at room temperature for 24h. The films were thoroughly washed with water to remove excessive acid, and then dried at 120^{o}C for 12h. The thickness of the membranes was in the range of 30-60μm.

Results and Discussion

Copolymerization of 6F-PH with activated difluorinated aromatic ketones, 1,4-bis(3-sodium sulfonate-4-fluorobenzoyl)benzene/1,4-bis(4-fluorobenzoyl)benzene or sodium 5,5'-carbonylbis(2-fluorobenzenesulfonate)/4,4'-difluorobenzophenone was carried out in the presence of K_2CO_3 in DMAc as the solvent at 160-170^{o}C, as shown in **Figure 1**. The sulfonation content (SC) of the polymers

was controlled by the feed ratios of monomers. The inherent viscosities of the resulting polymers were above 0.96dL/g in DMAc at 30°C (**Table 1**).

^{1}H NMR spectra were used to confirm the structures and evaluate the sulfonation contents of the resulting polymers. All the results agreed with the expected structures. A typical ^{1}H NMR spectrum is illustrated in **Figure 2**. As expected, the SC values based on NMR experimental were in agreement with the values derived from monomer feed ratios.

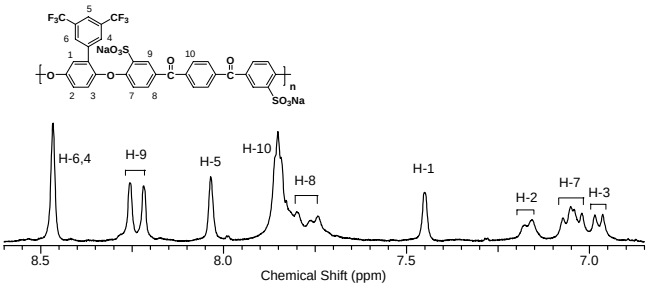

Figure 2. ^{1}H NMR spectrum of SPEEKK-6FP-100.

The thermal properties of the polymers in acid form (-H) and sodium form (-Na) were evaluated by DSC and TGA, as summarized in **Table 1**. The T_gs of the polymers in acid form were above 203°C. The polymers with high SC showed higher T_g values.

Table 1. Viscosities and thermal properties of the polymers

Polymer	T_g (°C) [a]	TD_5 (°C) [b]	T_d (°C) [c]	η_{inh} (dL/g) [d]
	-H	-Na/-H	-Na/-H	-Na
SPAEEK-6FP-40	203	473/330	470/267	1.01
SPAEEK-6FP-50	229	467/328	455/258	0.96
SPAEEK-6FP-60	231	468/319	465/252	0.98
SPAEEKK-6FP-40	212	487/341	487/270	2.40
SPAEEKK-6FP-50	219	478/358	473/279	2.09
SPAEEKK-6FP-60	235	479/358	481/279	2.79
SPAEEKK-6FP-70	239	477/324	470/261	1.70

[a] Glass transition temperature from the second heating cycle of DSC.
[b] 5% weight loss temperature measured by TGA.
[c] Onset temperature of decomposition.
[d] Measured at a polymer concentration of 0.5g/dL in DMAc at 30°C.

An obvious two-stage decomposition was observed from the TGA curves of SPAEEK-6FP-H and SPAEEKK-6FP-H. The initial decomposition was likely associated with the loss of the sulfonic acid groups in the range of 252-279°C, and the second loss was caused by the decomposition of the main chains of the polymers in the range of 479-489°C. Compared with the sulfonated PAEK-6FPs in acid form, the polymers in sodium form had high thermal stabilities against thermal decomposition. The temperatures at a 5% weight loss (TD_5) are above 467°C and the decomposition temperatures are above 455°C in N_2.

The water uptakes and dimensional swelling ratios of SPAEEK-6FP and SPAEEKK-6FP membranes were tested at 25°C and 80°C, and the results were listed in **Table 2**. After keeping the films in water at 25°C for 24h, all the polymers had swelling ratios below 30%, and water uptakes less than 30%. At 80°C, SPAEEK-6FP-40, SPAEEK-6FP-50, SPAEEKK-6FP-40, 50, 60 maintained their dimensional shape.

The proton conductivities of the membranes at 25 and 80°C are listed in **Table 2**. The conductivities of all the samples increased with increasing temperature. At the same temperature, high SC samples had higher conductivities. All of the samples exhibited proton conductivities > 1×10^{-2} S/cm at room temperature, which was regarded as the lowest value for PEM application in fuel cells. Some copolymers showed comparable proton conductivities to Nafion 117. At 80°C, proton conductivity values of SPAEEK-6FP-50, SPAEEKK-6FP-50 and SPAEEKK-6FP-60 were 1.1×10^{-1}, 1.0×10^{-1} and 1.6×10^{-1} S/cm, which are comparable to that of Nafion 117.

Table 2. Water uptakes, swelling ratios and proton conductivities of the SPAEK-6FPs at different temperatures

Polymer	Water Uptake (%) [a]	Swelling Ratio (%) [b]	σ (S/cm) [c]
	25/80 °C	25/80 °C	25/80 °C
SPAEEK-6FP-40	6/19	6 /18	2.0×10^{-2}/ 9.1×10^{-2}
SPAEEK-6FP-50	12/215	11/72	3.3×10^{-2}/ 1.1×10^{-1}
SPAEEK-6FP-60	29/--	29/--	8.4×10^{-2}/ --
SPAEEKK-6FP-40	5/7	5/12	1.3×10^{-2}/5.4×10^{-2}
SPAEEKK-6FP-50	10/15	6/15	3.2×10^{-2}/1.0×10^{-1}
SPAEEKK-6FP-60	12/54	10/35	4.6×10^{-2}/1.6×10^{-1}
SPAEEKK-6FP-70	21/2563	16/252	6.3×10^{-2}/ --
Nafion 117 [d]	19/30	13/20	7.5×10^{-2}/ 9.6×10^{-2}

[a] Calculated from the weight differences of the membranes before and after treatment in water for 24h.
[b] Calculated from the length differences of the membranes before and after treatment in water for 24h.
[c] Proton conductivities of the membranes at 100% R.H..
[d] Data from Ref. [4].

Conclusions

A class of poly(aryl ether ketone)s, SPAEEK-6FP and SPAEEKK-6FP series, were synthesized using a nucleophilic substitution polycondensation. Flexible films in sodium form were obtained via solution casting, and then transformed to their acid forms by immersing them in 2N H_2SO_4. The resulting polymers in acid form showed high T_g values above 203°C. The water uptakes and swelling ratios of the 6FP-40 and -50 films were reasonably low, and increased with increasing SC and measurement temperature. All of the polymers possessed proton conductivities higher than 1×10^{-2} S/cm at room temperature, some of the 6FP copolymers being comparable to conductivity values of Nafion 117.

Acknowledgement. The authors acknowledge the financial support from the NRC - National Science Council Taiwan Project on DMFC.

References

(1) Rikukawa, M.; Sanui, K., *Prog. Polym. Sci*., **2000**, *25*, 1463.
(2) Hickner, M.A.; Ghassemi, H.; Kim, Y.S.; Einsla, B.R.; McGrath, J.E., *Chem. Rev.*, **2004**, *104*, 4587.
(3) Gao, Y.; Robertson, G.P.; Guiver, M.D.; Mikhailenko, S.D.; Li, X.; Kaliaguine, S., *Macromolecules*, **2004**, *37*, 6748.
(4) Xing, P.; Robertson, G.P.; Guiver, M.D.; Mikhailenko, S.D.; Kaliaguine, S., *Macromolecules*, **2004**, *37*, 7960.
(5) Liu, B.J.; Hu, W.; Chen, C.H.; Jiang, Z.H.; Zhang, W.J.; Wu, Z.W.; Matsumoto, T., *Polymer*, **2004**, *45*, 3241.
(6) Wang, F.; Chen, T.L.; Xu, J.P., *Macromol. Chem. Phys.*, **1998**, *199*, 1421.
(7) Li, X.F.; Na, H.; Lu, H., *J. Appl. Polym. Sci*., **2004**, *94*, 1569.

PROTON EXCHANGE MEMBRANE FOR DMFC AND H_2/AIR FUEL CELLS: II. SYNTHESIS AND CHARACTERIZATION OF PARTIALLY FLUORINATED DISULFONATED POLY (ARYLENE ETHER BENZONITRILE) COPOLYMERS

*Mehmet Sankir, Yu Seung Kim[1], William L. Harrison[2], Anand S. Badami and James E. McGrath**

[1]Los Alamos National Lab (LANL), Los Alamos NM 87544,
[2]NanoSonic Inc, Blacksburg VA 24060
Macromolecules and Interfaces Institute,
Virginia Polytechnic Institute and State University,
Blacksburg, VA 24061, USA
jmcgrath@vt.edu

Abstract

Partially fluorinated disulfonated poly(arylene ether benzonitrile) copolymers were synthesized by direct nucleophilic substitution copolymerization reactions. The 2,6-dichlorobenzonitrile and 3,3'-disulfonated 4,4'-difluorodiphenyl sulfone (SDFDPS) and control amounts of 4,4'-biphenol and hexafluoroisopropylidene diphenol (hexafluorobisphenol A, 6F) were used to produce partially fluorinated disulfonated copolymers with various degrees of fluorination (0-100 mol% 6F). NMR analysis coupled with titration of sulfonated moieties confirmed both chemical structure and copolymer composition. The copolymers produced ductile films. Intrinsic viscosity analyses indicated high molecular weight copolymers were synthesized. Water uptake of membranes and cell resistance of MEAs were lowered by partial fluorination. The influence of this on direct methanol fuel cell performance was demonstrated. Characterizations including TGA, water uptake, proton conductivity and morphology will be presented.

Introduction

Proton exchange membrane fuel cell membranes require several qualities, such as good mechanical properties/stabilities, good proton conductivities, and have low permeabilities of the reactant fuels. Currently, perfluorinated sulfonic acid polymers are employed despite their reported limitations. Our research group and others have been investigating novel commercially viable proton conducting membranes for polymer electrolyte fuel cells. Alternative PEMs are primarily based on aromatic engineering polymers, such as poly ether sulfones and poly ether ketones that have been chemically modified to contain sulfonic acid groups along the main chain. In contrast, our approach has been to control the degree of sulfonation by copolymerizing sulfonated monomers. It has also been demonstrated that exact control (distribution) of sulfonation over the entire sequence is better via direct copolymerization versus post-sulfonation by titration and NMR studies [1-4]. The synthesis and characterization of high molecular weight, nitrile-functional copolymers using 3,3'-disulfonated 4,4'-difluorodiphenyl sulfone (SDFDPS), 2,6-dichlorobenzonitrile and 4,4'-hexafluoroisopropylidene diphenol (hexafluorobisphenol A, 6F) [5] and its nonfluorinated analogue [6] have been reported by our group. In this contribution, we report the synthesis and characterization of partially fluorinated disulfonated poly (arylene ether) copolymers and their direct methanol fuel cell (DMFC) performances.

Experimental

Reagents. 4,4'-biphenol was kindly provided by Eastman Chemical, 2,6-dichlorobenzonitrile was purchased from Aldrich and both were used without any purification. The 4,4'-hexafluoroisopropylidene diphenol (hexafluorobisphenol A), received from Ciba, was purified by sublimation and dried *in vacuo*. The disodium salt of 3,3'-disulfonated 4,4'-dichlorodiphenyl sulfone (SDCDPS) was synthesized through the reaction of 4,4'-difluorodiphenyl sulfone (Solvay Advanced Polymers) and fuming sulfuric acid, as described previously [7]. All other reagents were obtained from commercial sources and purified, as needed, via common procedures.

Synthesis of Partially Fluorinated Disulfonated Poly (arylene ether benzonitrile). Partially fluorinated disulfonated poly (arylene ether benzonitrile) copolymers were achieved at 35 mol percent disulfonation with various degrees of fluorination (0-100 mol% 6F) via direct copolymerization. A typical copolymerization is presented for 25 mol % 6F incorporated in 35 mol percent disulfonated poly(arylene ether benzonitrile). 2,6-dichlorobenzonitrile (1.3487 g, 7.8 mmol), 3,3'-disulfonated 4,4'-difluorodiphenyl sulfone (SDFDPS) (1.9350 g, 4.2 mmol), 4,4'-biphenol (1.6846 g, 9 mmol), 4,4'-hexafluoroisopropylidene diphenol (1.0139 g, 3mmol) and 1.9172 g potassium carbonate (15% mol excess) were transferred to 3-neck flask equipped with a mechanical stirrer, a nitrogen inlet and a Dean Stark trap. Dry NMP (15 mL) was used as the polymerization solvent while toluene (7.5 ml) was the azeotrope. The reaction mixture was refluxed for 4 h at 150 ºC to complete the dehydration process. The reaction temperature slowly increased to 180 ºC for 16 h just after the removing of the toluene gradually. The viscous reaction product was cooled and diluted with NMP and precipitated in deionized water as swollen fibers. After washing several times with deionized water, the precipitated copolymers were boiled in deionized water for 4 h to remove the salts. Copolymers were isolated by filtration then dried in a vacuum oven at 120 ºC for 24 h.

Film Casting and Membrane Acidification. Membranes in the potassium sulfonate form were prepared by first redissolving the copolymer in DMAc to afford 5-10% (w/v), filtered, then cast onto clean glass substrates. The transparent solutions were carefully dried with infrared heat at gradually increasing temperatures (up to ~ 60 ^{o}C) under a nitrogen flow, until the film was fairly dry. The sulfonated poly(arylene ether sulfone) copolymer films were converted to their acid form by boiling the cast membranes in 0.5 M sulfuric acid for 2 hours, followed by 2 hours extraction in boiling deionized water, which has been referred to as Method 2 [8].

Characterization

Intrinsic viscosities were determined in NMP containing 0.05 M LiBr at 30 ºC using an Ubbelohde viscometer. The thermo-oxidative behavior of both the salt-form (sulfonate) and the acid-form copolymers was performed on a TA Instruments TGA Q 500. Dried, thin films (5 to 10 mg in salt form) were evaluated over the range of 30 to 800 ^{o}C at a heating rate of 10 ^{o}C/min in air. Titration of the sulfonic acid groups was performed on acidified membrane samples of known mass by exchanging with sodium sulfate then back titrating with 0.01M NaOH. Thin film conductivity measurements were conducted on acidified membranes while submerged in deionized water using a Hewlett Packard 4129A Impedance/Gain-Phase Analyzer recorded from 10 MHz to 10 Hz. DMFC performances were evaluated at LANL.

Results and Discussion

Direct nucleophilic polycondensation was used to synthesize several series of high molecular weight partially fluorinated disulfonated poly(arylene ether sulfone) copolymers (Table 1). The chemical structure of disulfonated poly(arylene ether benzonitrile) copolymer can be seen in Figure 1a. Disulfonation was kept constant

at 35 mol percent for partially fluorinated copolymers. However, biphenol and 4,4'-hexafluoroisopropylidene diphenol were used together to obtain a series of partially fluorinated copolymers (Figure 1b)

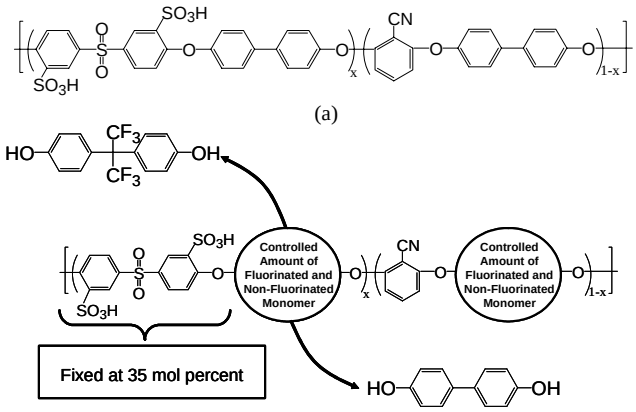

Figure 1. Chemical structure of (a) 35 mol percent disulfonated poly(arylene ether benzonitrile) and (b) 35 mol percent disulfonated partially fluorinated poly(arylene ether benzonitrile)

Copolymers showed very high thermooxidative stabilities. The five percent weight loss temperature for acid form of PAEB35, PAEB35+6F25 and PAEB35+6F50 was 350ºC. Thermooxidative stability was increased with increasing fluorination and the five percent weight loss temperature reached up to 400 ºC for PAEB35+6F75 and PAEB35+6F100 which is more than enough for 120 ºC fuel cell operation.

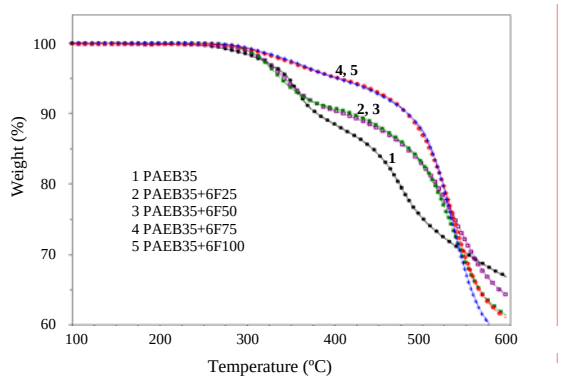

Figure 2. Influence of partial fluorination on thermooxidative stability of acid form of PAEB copolymers (10 ºC/min in air)

Table 1 shows membrane properties such as water uptake, proton conductivity, ion exchange capacity (IEC), methanol permeability as a function of degree of fluorination. Partial fluorination decreased water uptake which was important for long term performance. Although ion exchange capacities of the membranes decreased with increasing degree of fluorination, the decrease in proton conductivities was about 20 mS/cm. The minimum conductivity, 70 mS/cm, was sufficient for fuel cell applications. Hence, the water uptake was controlled without loosing much the proton conductivity.

Table 1. Influence of the Partial Fluorination on Several Features (XX denotes the mol percent 6F)

PAEB 35+XX	Intrinsic Viscosity dL/g	Water Uptake (wt. %)	IEC meq./g	Proton Cond. (mS/cm)	Membrane thickness (micrometer)	Methanol Limiting current (mA/cm2)	Methanol permeability x10^{-6} (cm^2/s)
0	1.00	40	1.87	90	55	65	1.2
25	0.87	35	1.70	80	55	63	1.2
50	0.70	31	1.56	80	55	71	1.3
75	0.65	27	1.44	70	50	89	1.4
100	0.65	24	1.33	70	51	77	1.4
Nafion 112	NA	19	0.92	110	50	190	3.3

The methanol permeabilities of partially fluorinated PAEB 35 copolymers (Table 1) were 2-3 times lower than Nafion 112. Nafion dispersions were used to make membrane electrode assemblies. Cell resistances were decreased and stabilized by increasing degree of fluorination due to better adhesion at catalyst layer-membrane interface (Figure 3). Higher initial cell performances were observed compared to Nafion due to the lower methanol permeabilities of copolymers (Figure 4). The initial performances were further improved with increasing degree of fluorination because of the interfacial effect.

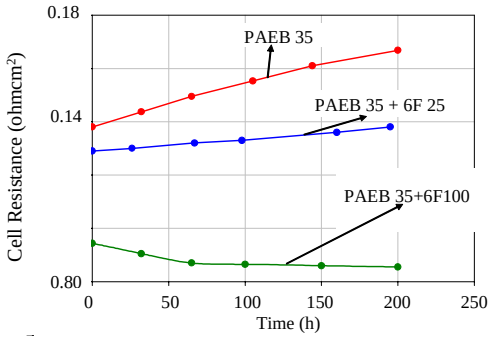

Figure 3. Cell resistance was lowered and stabilized with partial fluorination

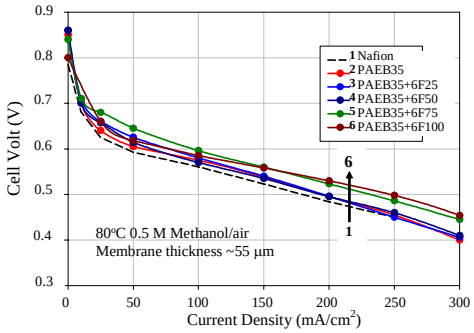

Figure 4. Initial cell performances were improved with partial fluorination

Partial fluorination also improved longer term performances (200 h). This effect was mainly attributed to the decrease in water uptake with increasing fluorination. It has been proposed that the

water uptake of a membrane was the critical factor for its long term performance [9]. Interfacial delamination between electrode layer and membrane occurred when their water uptake values were not close to each other. Hence, the water uptake depression with increasing fluorine content decreased the dimensional mismatch between the electrodes and the membrane (Figure 5).

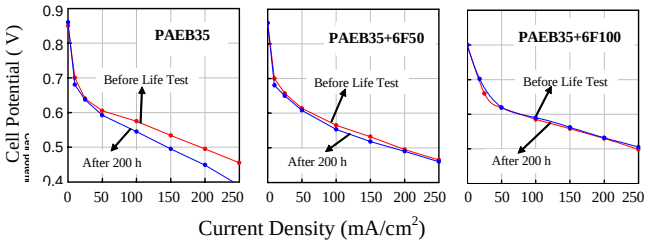

Figure 5. Long term performances were also improved with partial fluorination (Same studies have been conducted up to 2000 h)

Conclusions

The benzonitrile-containing, thermally stable, ductile, high molecular weight partially fluorinated disulfonated copolymers were successfully synthesized. These copolymers showed better initial and long term performances than Nafion 112 due to their lower methanol permeabilities. The partial fluorination has two important effects on a proton exchange membrane and/or membrane electrode assembly: It reduces the cell resistance and also lowers the water uptake of membrane. The former one is important for initial performance, while the latter is crucial for long term performance.

Acknowledgement. The university authors would like to thank the National Science Foundation "Partnership for Innovation" Program (HER-0090556) and the Department of Energy (DE-FC36-01G01086) for support of this research effort.

References

(1) Hickner, M.A.; Ghassemi, H.; Kim, Y.S.; Einsla, B.R.; McGrath, J.E. *Chemical Reviews*, 2004, 104, 4587
(2) Wang, F.; Hickner, M.; Kim, Y. S.; Zawodzinski, T. A.; McGrath, J. E. *J. Membr. Sci*. **2002**, 197, 231
(3) Wang, F.; Hickner, M.; Ji, Q.; Harrison, W.; Mecham, J.; Zawodzinski, T.; McGrath, J. E. *Macromol. Symp*. **2001**, 175(1), 387.
(4) Harrison, William L.; Wang, Feng; Mecham, Jeffery B.; Bhanu , Vinayak A.; Hill, Melinda; Kim, Seung Yu; McGrath, J.E. *J. Polym. Sci.: Part A: Polym. Chem.* **2003**, 42, 2264.
(5) Sumner, M.J.; Harrison, W.L.; Weyers, R.M.; Kim, Y.S.; McGrath, J.E.; Riffle, J.S.; Brink, A.; Brink, M.H. *J. Membrane Science* **2004**, 239, 199.
(6) Sankir, M.; Harrison, W. L.; Wiles, K. B.; Li, Y.; McGrath, J. E. Preprints of Symposia ACS **(2004)**, 49(2), 526-527
(7) Sankir M. et al , *Journal of Applied Polymer Science* (accepted)
(8) Kim, Y.S.; Wang, F.; Hickner, M; McCartney, S.; Hong, Y.T.; Harrison, W.; Zawodzinski, T. and McGrath, J.E. *J. Polym. Sci.; Part B: Poly. Phys.* **2003**, 41, 2816.
(9) Kim, Y.S., Advances in Materials for PEM Fuel Cell Systems, ACS Asilomar CA **2005**; Kim, Y.S.; Sumner, M.J.; Harrison, W.L.; Riffle, J.S.; McGrath, J.E.; Pivovar, B.S. *J. Electrochem. Soc.* **2004**, 151, A2150

DIRECT COPOLYMERIZATION OF WHOLLY AROMATIC AND PARTIALLY FLUORINATED DISULFONATED POLY(ARYLENE ETHER SULFONE)S

*Brian R. Einsla, Linda A. Harris, Melinda L. Hill and James E. McGrath**

Macromolecules and Interfaces Institute
Virginia Polytechnic Institute and Stated University
Blacksburg, VA 24061
*jmcgrath@vt.edu

Introduction

Proton exchange membrane (PEM) fuel cells are becoming increasingly important as alternative energy sources for stationary, automobile and portable power. The proton conducting PEM must possess several characteristics to be considered for fuel cell applications; including thermal, oxidative and hydrolytic stability, and mechanical durability. High temperature aromatic polymers are used in many areas such as microelectronics, automotive, structural adhesives and aerospace industries due to their excellent thermal and chemical resistance and superior mechanical integrity. These properties suggest that appropriate aromatic polymer systems should be good candidates for proton exchange membranes.[1]

The disulfonated poly(arylene ether sulfone) family of copolymers have great potential as PEMs.[2] These copolymers are prepared by direct copolymerization, which allows for increased control over the chemical composition and hence the ion exchange capacity (IEC). The result is higher acidity of the sulfonic acid sites, lower water uptake, and improved conductivity compared to post-sulfonated poly(arylene ether)s.[3] In particular, the wholly aromatic BPSH copolymers show similar DMFC performance to Nafion, while having lower methanol crossover.[4] A variation on the BPSH copolymers is the 6FSH series, which adds a hexafluoroisopropylidene linkage to every repeat unit of the backbone.[5] This partially fluorinated copolymer series may enhance the stability of membrane electrode assemblies (MEAs) prepared with Nafion electrodes.[4] It has been suggested that the compatibility of the MEA could be improved due to the similar fluorinated backbones and water uptakes. Although the water uptake values of these materials are lower than post-sulfonated polymers, the directly polymerized copolymers go through a percolation threshold at higher levels of disulfonation where the water uptake increases dramatically (above 100%) and mechanical strength is lost, as illustrated in Figure 7-1.

Experimental

Materials. 4,4'-Dichlorodiphenyl sulfone (DCDPS) was kindly provided by Solvay Advanced Polymers and dried under vacuum at 60 °C before use. 4,4'-Biphenol was obtained from Honshu Chemical Ind. Co. and dried under vacuum at 60 °C. 4,4'-(Hexafluoroisopropylidene)diphenol (6F) was obtained from DuPont and dried under vacuum at room temperature. Potassium carbonate was purchased from Aldrich and vacuum dried at 120 °C for 24 hours before use. N,N-Dimethylacetamide (DMAc, Fisher) was distilled under reduced pressure over calcium hydride prior to use. Fuming sulfuric acid (27% SO_3), sodium chloride, sodium hydroxide, and toluene were used as received from Aldrich.

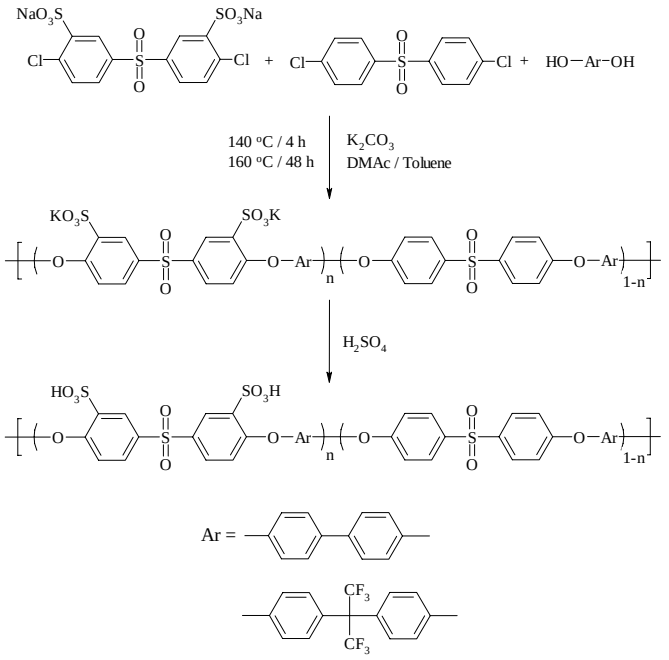

Figure 1. Direct synthesis of random disulfonated poly(arylene ether sulfone) copolymers.

Monomer Synthesis: Disodium-3,3'-disulfonate-4,4'-dichlorodiphenylsulfone (S-DCDPS). In a typical reaction, DCDPS (28.7 g, 99 mmol) was dissolved in 60 mL (390 mmol SO_3) of fuming sulfuric acid (27% SO_3) in a 100-mL, three neck flask equipped with a mechanical stirrer, condenser, and a nitrogen inlet/outlet. The solution was heated to 110 °C for 6 h to produce a homogeneous solution. The reaction was cooled to room temperature, dissolved into 400 mL of ice water, and 180 g of sodium chloride were added to produce a white precipitate of the product. The powder was filtered, redissolved in 400 mL of deionized water and neutralized to a pH of ~6-7 with aqueous 2 N sodium hydroxide. An excess of sodium chloride (~180 g) was added to salt out the sodium form of the disulfonated monomer. The crude S-DCDPS was filtered and dried at 120 °C for 48 h. The dry monomer was dissolved into 500 mL of hot methanol, filtered, and then allowed to cool to room temperature overnight. S-DCDPS was isolated by filtration and recrystallized in a mixture of isopropanol and water (6/1, v/v). The resulting pure product was dried at 120 °C under vacuum for at least 24 h.

Synthesis of Disulfonated Poly(arylene ether sulfone) Copolymers. A direct copolymerization of a 60 mol% partially fluorinated (6F-BisA) copolymer is discussed. First, SDCDPS (4.9120 g, 10 mmol), DCDPS (1.9145 g, 7 mmol) and 6F-BisA (5.6043 g, 17 mmol) were introduced into a 250-mL, three-necked flask equipped with a mechanical stirrer, a Dean-Stark trap, condenser and a nitrogen inlet/outlet. Potassium carbonate (2.77 g, 20 mmol) and 62 mL of DMAc were added to the reaction flask to afford a 20% (w/v) solid concentration. Toluene (31 mL) was added to the flask as an azeotroping agent. The Dean-Stark trap was filled with toluene and the reaction mixture was heated to 150 °C to dehydrate the system. After 4 h at 150 °C, the Dean-Stark trap was emptied and the oil bath temperature was heated to 175 °C for 48 h. The resulting viscous solution was cooled to room temperature, diluted with DMAc and precipitated into an excess of deionized water (3 L). The precipitated copolymer was collected by filtration and dried under vacuum at 80 °C for 24 h and 100 °C for 24 h. Yield: 98%.

Membrane Preparation. Membranes were prepared by solution casting the copolymers from DMAc. The solvent was evaporated under infrared heat at 40 °C. The membranes were removed from the glass substrates by submersion in deionized water and then vacuum-dried at 120 °C for 24 h. The copolymer membranes were converted to their acid form by immersion in boiling 0.5 M H_2SO_4 for 2 h followed by boiling deionized water for 2h. In all cases, tough, ductile, transparent membranes were obtained.

Characterization. ^{1}H NMR spectra were recorded on a Varian Unity 400 instrument operating at 399.952 MHz, in deuterated dimethylsulfoxide (DMSO-d_6). Intrinsic viscosity (IV) measurements were conducted in 0.05 M LiBr/NMP at 25 °C using a Cannon Ubbelohde viscometer. The water sorption values of the membranes were determined at 30 °C. The membranes were vacuum-dried at 120 °C for 24 h, weighed and immersed in deionized water at room temperature for 24 h. The wet membranes were wiped dry and quickly weighed again. The water uptake of the membranes was calculated in weight percent as follows: *water uptake = [(mass$_{wet}$ - mass$_{dry}$) / mass$_{dry}$] * 100*. Proton conductivity measurements were performed on membranes after being soaked in deionized water at 30 °C. An impedance spectrum was recorded from 10 MHz to 10 Hz using a Hewlett-Packard 4129A Impedance/Gain-Phase Analyzer.

Results and Discussion

The synthesis of disulfonated poly(arylene ether sulfone) copolymers has been reported. At high degrees of disulfonation (> 40%), it initially was difficult to synthesize high molecular weight copolymers using S-DCDPS in the partially fluorinated systems. Another procedure was introduced using the highly activated but more costly difluoro monomers (DFDPS and S-DFDPS) to produce high molecular weight copolymers. Herein, an alternative method to obtain high molecular weight copolymers from S-DCDPS at high ion exchange capacities (IECs) is presented. The conversion of DCDPS to S-DCDPS by the reported conditions was quantitative with no side-products.[6] The only impurity introduced was sodium chloride upon precipitation and isolation. A method was described to calculate the amount of salt present in S-DCDPS and use this monomer to produce high molecular weight copolymers.[6] Another procedure is described herein where the S-DCDPS was recrystallized in methanol to remove the salt impurity (Figure 2). The crude S-DCDPS was dissolved in hot methanol, filtered to remove sodium chloride, and allowed to cool to room temperature, which crystallized pure S-DCDPS. After filtration, excess methanol could also be removed by vacuum distillation or crystallization to obtain pure S-DCDPS. High molecular weight copolymers were generated using this purified monomer (Figure 1), as judged by the intrinsic viscosity (IV) values (Table 1). For example, the IV of the 6FSH-60 copolymer was measured in pure NMP and 0.05 M LiBr/NMP at 25 ºC. The IV of 6FSH-60 in NMP was 2.7 dL/g, which is close to the value previously reported for the copolymerization using the highly activated S-DFDPS (2.5 dL/g).[5] The dilute solution viscosity measurements were also conducted in 0.05 M LiBr/NMP to eliminate the polyelectrolyte effect in these sulfonated copolymers. The IV in LiBr/NMP was 0.91 dL/g.

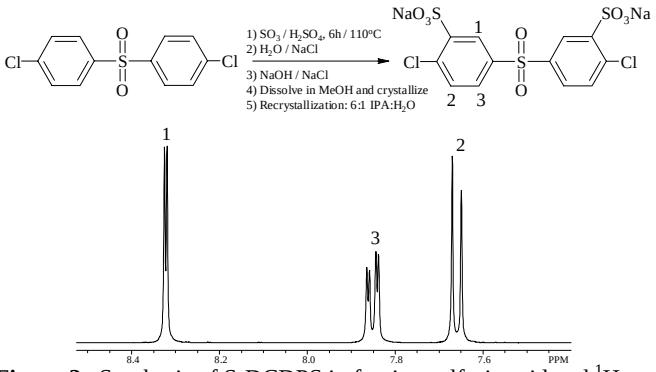

Figure 2. Synthesis of S-DCDPS in fuming sulfuric acid and ^{1}H NMR to confirm the structure (DMSO-d_6).

Table 1. Intrinsic Viscosity, Water Uptake and Proton Conductivity of Selected Copolymers

Copolymer	I.V. (dL/g)*	Water Uptake (%)	Proton Conductivity (S/cm)
BPSH-35	1.05	37	0.08
BPSH-40	0.98	58	0.10
6FSH-35	1.02	35	0.07
6FSH-60	0.91	200	-

*0.05 M LiBr in NMP at 25 oC

Conclusions

A revised procedure was developed to synthesize consistently high molecular weight copolymers derived from pure S-DCDPS. Recrystallization of S-DCDPS in methanol was utilized to remove the salt impurities. It was shown that very transparent, high molecular weight copolymers could be synthesized at lower temperatures in DMAc, as opposed to the previously reported high-temperature conditions in NMP.

Acknowledgement. The authors appreciate the support of this research by the NSF Partnership for Innovation (contract # EEC-0332648), UTC Fuel Cells (contract # PO 3651) and the Department of Energy (contract # DE-FC36-01G011086).

References

[1] Hickner, M.A.; Ghassemi, H.; Kim, Y.S.; Einsla, B.R.; McGrath, J.E. *Chem. Rev.* **2004**, *104*, 4587.
[2] Kim, Y.S.; Hickner, M.A.; Dong, L.; Pivovar, B.S.; McGrath, J.E. *J. Membr. Sci.* **2004**, *243*, 317-326.
[3] Kim, Y.S.; Wang, F.; Hickner, M.; McCartney, S.; Hong, Y.T.; Harrison, W.; Zawodzinski, T.A.; McGrath, J.E. *J. Polym. Sci., Part B: Polym. Phys.* **2003**, *41*, 2816-2828.
[4] Kim, Y.S.; Sumner, M.J.; Harrison, W.L.; Riffle, J.S.; McGrath, J.E.; Pivovar, B.S. *J. Electrochem. Soc.* **2004**, *151*, A2150-A2156.
[5] Harrison, W.L.; Wang, F.; Mecham, J.B.; Bhanu, V.A.; Hill, M.; Kim, Y.S.; McGrath, J.E. *J. Polym. Sci.: Part A: Polym. Chem.* **2003**, *41*, 2264-2276.
[6] Sankir, M. Bhanu, V.A.; Ghassemi, H.; Wiles, K.B.; Hill, M.L.; Harrison, W.; Sumner, M.; Glass, T.E.; Riffle, J.S.; McGrath, J.E. *ACS Div. Polym. Chem., Polym. Preprs.* **2003**, *44*, 1079-1080; *J. Appl. Polym. Sci.* **2005**, *accepted.*

PARTIALLY FLUORINATED DISULFONATED POLY（ARYLENE ETHER SULFONE）COPOLYMERS WITH CONTROLLED MOLECULAR WEIGHTS AND THEIR APPLICATIONS TO PROTON EXCHANGE MEMBRANE FUEL CELLS

Yanxiang Li[1], Juan Yang[1], Abhishek Roy[1], Brian Einsla[1], Feng Wang[2], and James E McGrath[1]*

[1]Macromolecular Science and Engineering & Macromolecules and Interfaces Institute
Virginia Polytechnic Institute and State University
Blacksburg, VA 24061
[2] PPG Industries Inc., 440 College Park Drive, Monroeville, PA 15146
*jmcgrath@vt.edu

Introduction

The electrochemical and mechanical properties of sulfonated copolymers such as Nafion™ , sulfonated polyethersulfones, etc. has become increasingly important as their potential application in proton exchange membrane fuel cells(PEMFC) becomes more evident[1,2]. Molecular weight is a fundamental parameter affecting all mechanical behavior of polymers as is well known. Most reports of new proton exchange membrane materials have included information on ion content (EW or IEC), protonic conductivity, and water uptake. Despite the large body of research on this topic, there is almost nothing in the PEM literature describing molecular weights of candidate materials, even including Nafion and other systems[3].

Sulfonated poly(arylene ether sulfone) copolymers are good candidates for PEMs due to their good acid and thermal oxidative stabilities, high glass transition temperatures and excellent mechanical strength[4]. Partially fluorinated 6F bisphenol monomer in the copolymer may improve certain properties of proton exchange membrane (PEM), such as providing a more hydrophobic membrane surface that will lower the water uptake. Furthermore the fluorine rich surface will be more compatible with electrodes that contain Nafion and may permit more durable electrode membrane assembly (MEAs), which display lower interfacial losses.

In this paper, the synthesis of partially fluorinated poly(arylene ether sulfone) disulfonated copolymers with controlled number average molecular weights (M_n) was described. M_n values of the copolymers were controlled by changing the amount of the monofunctional monomer, tert-butylphenol endcapper relative to the difunctional monomer[5] and were characterization by combination of proton NMR and intrinsic viscosity measurements. In our group, we have begun to utilize NMP with 0.05 M LiBr to measure intrinsic viscosity of ion-containing copolymers instead of simple dilute solution viscosity measurements in pure solvents. The small amount of salt effectively suppressed the polyelectrolyte effect allowing improved characterization of the ion containing materials[3]. Furthermore, we have also begun to examine the influence of molecular weight on several different critical parameters important for proton exchange membranes, such as water uptake, swelling ratio, protonic conductivity, and mechanical properties.

Experimental

Materials. Highly purified 4,4'-dichlorodiphenyl sulfone (DCDPS) was kindly provided by Solvay Advanced Polymers. The 6F bisphenol was provided by DuPont. Both were well dried in a vacuum oven before use but otherwise used as received. The 4-tert-butyphenol (BP) end capper was obtained from Aldrich and purified by sublimation before copolymerization. The 3,3'-disulfonated 4,4'-dichlorodiphenyl sulfone (SDCDPS) was synthesized as reported earlier[6-8]. The solvent N,N-dimethylacetamide (DMAc, Fisher) was vacuum-distilled from calcium hydride onto molecular sieves. Potassium carbonate was dried *in vacuo* before polymerization. Toluene and methanol were obtained from Aldrich and used as received.

Copolymerization. The step growth copolymerization employed a modified procedure from that reported previously[5]. A typical copolymerization for a controlled molecular weight of 40 kg/mol copolymer is described as follows: The 6F bisphenol (5.000g, 14.871mmol), 4,4'-dichlorodiphenyl sulfone (2.596 g, 5.287 mmol), 3,3'-disulfonated 4,4'-dichlorodiphenyl sulfone (2.820 g, 9.818 mmol), and 4-tert-butylphenol (0.071g, 0.469 mmol) were added to a three neck flask equipped with mechanical stirrer, nitrogen inlet and a Dean Stark trap. 1.15 equivalent of potassium carbonate and dry DMAc were introduced to afford 20% solid concentration. Toluene (DMAc/Toluene = 2/1) was used as an azeotropic agent. The reaction mixture was heated under reflux at 160 ^{o}C for 4 hours to dehydrate the system. Then, the bath temperature was raised slowly to 175 ^{o}C for 48 hours, which caused the DMAc to reflux. The solution became viscous and was cooled to room temperature, then diluted with DMAc to form about a 20% copolymer solution. The copolymer was isolated by precipitation in deionized water, filtered, and dried in a vacuum oven for 24 hours at 120 ^{o}C. The crude dry copolymer was then ground to a powder and washed with ethanol and deionized water extensively to remove any potential free endcapping agent and salt. The copolymer was finally vacuum dried at 120 ^{o}C for 24 hours. The resulting copolymers were designated as 6FS35-XX (salt form) or 6FSH35-XX (acid form), where the mole ratio of disulfonated monomer in the repeat unit was fixed at 35% for all copolymers and XX represents the target number average molecular weight (kg/mol). The molecular weight was controlled by varying the amount of monofunctional monomer 4-tert-butylphenol and the ratio of the difunctional monomers.

Characterization. ^{1}H NMR spectra were conducted with a Varian Unity 400 NMR spectrometer. Intrinsic viscosities (IV) were determined in NMP with 0.05 M LiBr at 25 ºC using an Ubbelohde viscometer.

Results and Discussion

Figure 1 shows the reaction scheme for the step growth polymerization of tert-butylphenol terminated poly(arylene ether sulfone)s containing 35% sulfonate groups. By changing the amount of endcapping regent, tert-butylphenol, according to the modified Carother's equation[9], and the stoichiometry of the feed comonomers, tert-butylphenyl terminated copolymers with different molecular weights (20 ~ 50 kg/mol) were successfully synthesized. Since 6F bisphenol monomer has low reactivity due to the strong electronegativity of -CF_3 groups, the reaction needed much longer reaction times, typically 48 hours or longer than biphenol system. The crude dry copolymers were ground to a powder and washed extensively with ethanol and deionized water to remove any possible free endcapping reagent and residual salt. This step may be important to obtain accurate NMR integration values to calculate molecular weight (M_n).

The molecular weight of the copolymer was calculated from the relative ^{1}H NMR integrals of the tert-butyl endgroups and the aromatic resonances. An example of a proton NMR spectrum of 6FS35-50 is shown in Figure 2. The calculation followed our literature method[5] : There are 18 methyl protons on the two end tert-butyl groups, the average aromatic protons per repeat unit is 15.3 and 15.3 aromatic protons are attached on the terminal phenyl rings. Thus, the following equation can be used to calculate the number of repeat unit:

$$(15.3n + 15.3)/18 = 136.94/2.00$$

Where n is the number of repeat unit and was calculated to be 79.55. Accordingly the average number molecular weight (M_n) of 6FS35-50 was calculated to be:

$$M_n = 79.55 \times 621.4 \text{ g/mol} + 585.4 \text{ g/mol} = 50{,}020 \text{ g/mol}$$

Where the average molecular weight per repeat unit is 621.4 g/mol and the molar mass of the endgroups is 585.4 g/mol. The molecular weights of 20 to 40 kg/mol copolymers were all calculated using the same method and listed in Table 1. It was reassuring that the experimental molecular weights was in close agreement with the target values.

The ^{1}H NMR spectrum in aromatic region and its assignment of 6FS35-50 copolymers was also shown in Figure 3. The chemical composition is exactly as expected. The degree of disulfonation was calculated based on the integration values of k, and a, b proton peaks[10]. The mol content of sulfonated unit in 6FS35-50 is 32.7%. The content of sulfonated unit in other copolymers were also calculated and listed in Table 1. The calculated values are in good agreement with the feed ratio, which suggests that the starting monomers were successfully incorporated into the copolymer chain.

Conclusions

Partially fluorinated poly(arylene ether sulfone) copolymers with different molecular weights were successfully prepared via direct step growth polymerization. The molecular weights were controlled by addition of the monofunctional monomer, tert-butylphenol, together with offsetting the stoicheometry of the feed comonomer ratios. The molecular weights were characterized by proton NMR and intrinsic viscosity measurement. The improved intrinsic viscosity measurement method in 0.05 M LiBr/NMP allows conventional extrapolates to zero concentration due to suppression of the polyelectrolyte effect. The experimental values were in close agreement with the theoretical values. The influence of the molecular weight on the properties of proton exchange membrane, such as water swelling and conductivity, will also be discussed at the meeting.

Acknowledgements. The authors appreciate the support of this research by the Department of Energy (contract # DE-FC36-01G011086) and UTC Fuel Cells (contract #PO 3651).

References

(1) Savadogo O. *J New Mater Electrochem Syst* 1998; 1: 47
(2) Y. S. Kim, L. Dong, M.A. Hickner, B.S. Pivovar, J.E. McGrath, *Polymer*, 2003, 44, 5729-5736
(3) M.A. Hickner, H. Ghassemi, Y.S. Kim, B.R. Einsla, and J.E. McGrath, Alternative polymer systems for proton exchange membranes (PEMs), *Chem. Rev*., 2004, 104, 4587
(4) J.J. Dumais, A.L. Cholli, L.W. Jelinski, J.L. Hedrick, and J.E. McGrath, *Macromolecules*, 1986, 19,1884
(5) F. Wang, T. Glass, X. Li, M. Hickner, Y.S. Kim, J.E. McGrath, *Polymer Preprint*, 2002, 43(1), 492-493
(6) F. Wang, Q. Ji, W. Harrison, J. B. Mecham, R. Formato, R. Kovar, P. Osenar, and J.E. McGrath, *Polymer preprints*, 2000, 41(1), 237
(7) F. Wang, M. Hickner, Q. Ji, W.L. Harrison, J. Mecham, T. Zawodzinski, and J.E. McGrath, *Macromolecular Symposia*, 2001,175, 387-395
(8) F. Wang, M. Hickner, Y.S. Kim, T. Zawodzinski, and J.E. McGrath, *J. of Membr. Sci*, 2002, 197,231-242
(9) F. Wang, J. Mecham, W. Harrison, and J.E. McGrath, *Polymeric Materials: Science & Engineering* **2001**, *84*, 913
(10) W.L. Harrison, F. Wang, J. Mecham, V.A. Bhanu, M. Hill, Y.S. Kim, and J.E. McGrath, *J. of Poly. Sci. Part A*, 2003, 41, 2264-2276

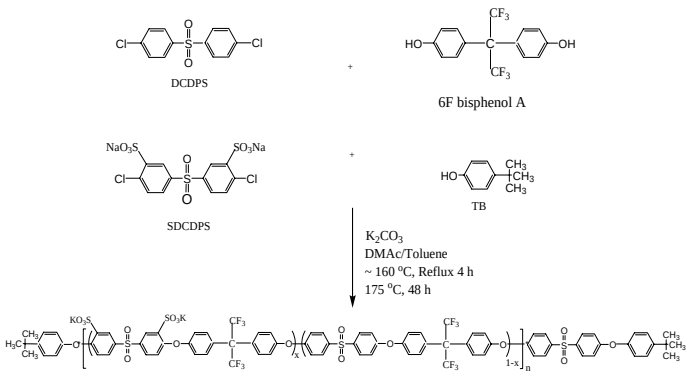

Figure 1. Synthesis of tert-butylphenol terminated partially fluorinated poly(arylene ether sulfone) containing sulfonate groups (x = 0.35)

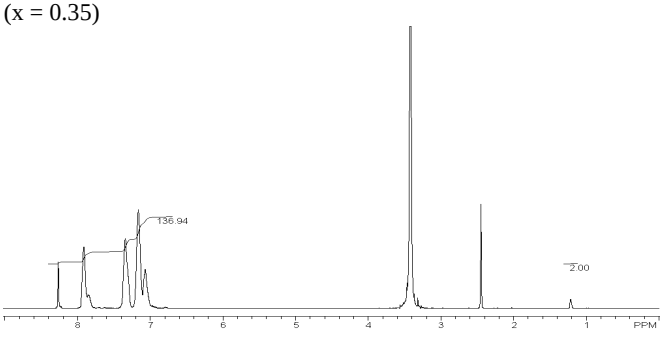

Figure 2. The molecular weight of the copolymer can be calculated from the relative ^{1}H NMR integrals of the tert-butyl endgroups and the aromatic resonances. (6FS35-50 copolymer in DMSO-d_6)

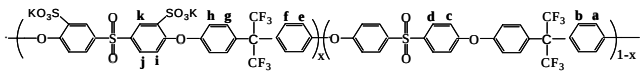

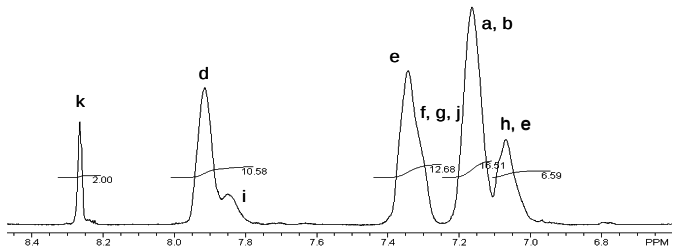

Figure 3. ^{1}H NMR spectrum of 6FS35-50 copolymer (aromatic region)

Table 1. **Characterization of 6FS35 series copolymers**

M_n (kg/mol)	M_n by NMR (kg/mol)	IV[a] (dL/mol)	Degree of sulfonation[b] (%)	
			Target	Calculation
20	19.9	0.25	35	32.5
30	28.5	0.39	35	33.7
40	41.1	0.52	35	34.1
50	50.0	0.58	35	32.7

a Intrinsic viscosities were determined in 0.05 M LiBr/NMP solution at 25 °C.
b Mole % of sulfonated monomer in repeat unit

NEW FUNCTIONALIZED LIQUIDS FOR PROTON EXCHANGE MEMBRANES IN FUEL CELLS

Jennifer Y. Kelly[1], Raymond N. Dominey[2], Paul R. Resnick[3], and Joseph M. DeSimone[1,4]

[1]Department of Chemistry
University of North Carolina at Chapel Hill
Chapel Hill, NC 27599-3290
[2]Department of Chemistry
University of Richmond
Richmond, VA 23173
[3]DuPont Fluoroproductsr
Fayetteville, NC 28306
[4]Department of Chemical Engineering
North Carolina State University
Raleigh, NC 27695

Introduction

There is a growing interest in materials for use as proton exchange membranes in fuel cells. Fuel cells are being targeted to power small electronic devices such as cell phones, laptops, military devices, and automobiles to name a few. DuPont's Nafion® (Figure 1) is the current benchmark material for proton exchange membranes due to its durability, high ionic conductivity and super selectivity. Nafion® is an amorphous copolymer of tetraflouroethylene (TFE) and perfluoro-2-(2-fluorosulfonylethoxy)propyl vinyl ether (PSEPVE) (Figure 1). There are opportunities however for improving the properties of Nafion®. At temperatures above 100 °C Nafion®'s mechanical stability is degraded and its conductivity compromises due to dehydration, thus Nafion® based PEM fuel cells are normally operated at 80 °C or below. Fuel cells running at these lower operating temperatures exhibit decreased catalytic activity both due to generally higher activation losses at lower temperatures but also, for typically envisioned hydrogen feedstocks, due to carbon monoxide poisoning of the platinum catalyst.. Another challenge for Nafion® membranes is methanol (MeOH) permeability. Severe MeOH crossover drastically decreases the open circuit potential and thus the power density of the fuel cell decreases. This results in unattainable optimum performance when Nafion® is used in direct methanol fuel cells.

Herein we report the low temperature synthesis of fluorinated oligomers in supercritical carbon dioxide ($scCO_2$). Our research efforts focus on synthesizing polymers containing TFE or vinylidene fluoride (VF_2), PSEPVE, and a cure site monomer. These liquid, fluorinated oligomers are subsequently crosslinked to form solid membranes. The membranes are hydrolyzed into the proton conducting form for use in hydrogen and methanol fuel cells.

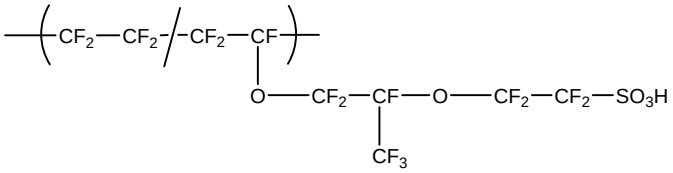

Figure 1. DuPont's Nafion.

Experimental

Materials. TFE was obtained by DuPont as a 50 weight-% mixture in CO_2 and used as received. PSEPVE was provided by DuPont and purified by passing through a neutral alumina column. 2-Bromotetrafluoroethyl trifluorovinyl ether (EVEBr) was obtained from Matrix Scientific and was used as received. α,α,α-Trifluorotoluene was obtained from Aldrich and used as received. Vinylidene fluoride was obtained from Synquest and used as received. SFC purity CO_2 was obtained from Air Products. Bis(perfluoro-2-N-propoxypropionyl) peroxide (dimer peroxide) was prepared in 1.1.2-triichloro-1,2,2-trifluoroethane according to a published procedure[1] and stored over dry ice. The concentration was determined by iodometry and was typically 20 weight-%.

Instrumentation. Infrared spectra were collected using a BIO-RAD FTS-7 spectrometer. Nuclear Magnetic Resonance spectra were collected using a Varian Unity Inova 600 NMR spectrometer.

Synthesis. The experimental set-up is shown in Figure 2. Polymerizations were carried out in a 25 mL high-pressure reaction vessel equipped with a stir bar, thermocouple, rupture disk and a sapphire window which permits visual observation of the reaction mixture with an endoscope. In a typical reaction the high pressure cell was purged with CO_2 to remove oxygen, then the cell was cooled to 15 °C and PSEPVE and EVEBr were charged via syringe while purging with argon. After sealing the cell TFE/CO_2 mixture (50 wt.-%) or vinylidene fluoride (VF_2) was introduced with a manual pump (HIP, Model 62-6-10) under stirring. To add the desired amount of TFE the pump was pressurized to 103 bar (psig). The volume of the TFE/CO_2 mixture was calculated from the density at 103 bar. By repeating opening of the valve between the pump and the reaction vessel and repressurizing to 103 bar the desired volume was introduced. To add the desired amount of VF_2 the pump was pressurized to 48 bar (700 psig). The volume of the VF_2 was calculated from the density at 48 bar. By repeating opening of the valve between the pump and the reaction vessel and repressurizing to 48 bar the desired volume was introduced. The reaction vessel was then heated to the desired reaction temperature which was typically 35 °C and the initiator solution was transferred via syringe to a small addition tube connected to the CO_2 line. The reaction view cell was then filled with CO_2 using an automatic syringe pump (ISCO, Model 260 D) while simultaneously introducing the initiator. After the reaction, the CO_2 was slowly vented.

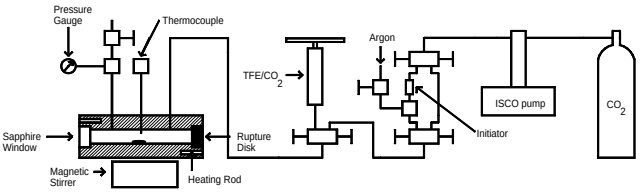

Figure 2. Experimental Set-Up for Synthesis of TFE or VF_2 Containing Terpolymers in $scCO_2$..

Results and Discussion.

Low molecular weight oligomers that are liquids at room temperature have tremendous utility. Such liquids can take on any shape and when containing a cure site monomer (CSM), can subsequently be crosslinked to form a chemically and mechanically robust, fluorinated, solid membrane. Carbon dioxide as a reaction medium for polymerization has enormous benefits. Using CO_2 instead of traditional organic solvents or aqueous based systems affords an environmentally friendly approach which avoids the use of fluorinated surfactants or fluorinated solvents. One can exploit the unique properties of CO_2 especially when used in the supercritical phase in that it has gas-like viscosities and liquid-like densities. Handling TFE as a 50 wt.% mixture in CO_2 enables safer management of this monomer. Furthermore low temperature polymerizations are possible in CO_2 which affords the ability to

minimize β scission and thus minimize acid chain ends that are thought to be involved in PEM ionomer degradation.

All monomers discussed are soluble in $scCO_2$. The reaction mixture is homogenous throughout the reaction. A viscous, slightly cloudy liquid is left after slow venting of CO_2. The products are soluble in α,α,α-trifluorotoluene and subsequently filtered to give a clear solution. The yields of terpolymers containing TFE, PSEPVE, and EVEBr ranged between 12 and 17 % depending on mole ratios charged, whereas when VF_2 was used instead of TFE, yields of at least three times more were obtained. The mole ratios of monomer to initiator of initiator charged ranged between 5 and 10 %. NMR and IR spectroscopy confirmed monomer incorporation into the oligomers.

Conclusions.

Low molecular oligomers containing TFE or VF_2, PSEPVE, and a CSM have successfully synthesized in $scCO_2$ at low temperatures. Product yield increased at least threefold when polymerizations were charged with VF_2 instead of TFE of the same mole %. The viscous liquds were diluted with trifluorotoluene.

Acknowledgement. Nafion® is a registered trademark of DuPont. We would like to thank DuPont for financial support of this project and we acknowledge partial support from the NSF Science and Technology Center for environmentally responsible solvents and processes (Grant No. 4-25151).

References.

[1] Zhao, C.; Zhou, R.; Pan, H.; Jin, X.; Qu, Y.; Wu, C.; Jiang, X. *J. Org. Chem.* **1980**, *47*, 2009-2013.

SYNTHESIS AND CHARACTERIZATION OF MULTIBLOCK COPOLYMERS FOR PROTON EXCHANGE MEMBRANES

*Xiang Yu, Abhishek Roy, James E. McGrath**

Institute for Polymeric Materials and Interfaces, Virginia Polytechnic Institute and State University, Blacksburg, Virginia 24061
jmcgrath@vt.edu

Introduction

Proton exchange membranes (PEM) as the key component for fuel cells have attracted considerable interest recently. Much effort has been made to develop PEMs that combine high proton conductivity, high chemical, thermal, and hydrolytic stability, and low cost[1,2]. Although Nafion, the currently state of the art PEM, shows good chemical and mechanical stability as well as high proton conductivity at relatively low ion exchange capacity (IEC), it suffers from some disadvantages including high cost, high methanol permeability, and limited operating temperature (80 ^{o}C).

Among the polymers developed as alternative PEMs are poly(arylene ether sulfone)s, synthesized by the direct random copolymerization of bisphenol monomers with disulfonated and unsulfonated 4,4'-dichlorodiphenylsulfone (DCDPS)[3-5]. While showing proton conductivity comparative to that of Nafion, the copolymers with high degrees of disulfonation were found to swell dramatically or even dissolve in water, and consequently lose their mechanical strength, making them unacceptable as PEMs[4-6]. This was noted when the percolation limit was exceeded, at which point the ionic domains aggregate and form a continuous phase[6]. Thus control of the copolymer morphology is important, namely, nanophase separation is desired to prevent the ionic phase aggregation.

On the other hand, although the poly(arylene ether) membranes with medium degrees of sulfonation showed satisfactory proton conductivity under fully hydrated conditions, it generally decreased rapidly with decreasing relative humidity or increasing temperature, and was much lower than that of Nafion. This is not surprising considering that, in this type of random copolymer, the ionic proton conducting sites are distributed randomly, with virtually no sequence length. Thus more "free water" needs to be present to maintain good proton conductivity[7]. Nafion, in comparison, reportedly has ionic channels dispersed in the hydrophobic matrix, a structure that greatly facilitates proton conductance at low relative humidity[8-10].

It is therefore desirable to design a PEM which contains proton conducting channels, but which should not swell too strongly in water. We will report in this article, and in the accompanying paper by Roy et al., that block copolymers may show the desired behavior. The synthesis and characterization of amphiphilic multiblock copolymers, containing disulfonated poly(arylene ether sulfone) as the hydrophilic block and perfluoro poly(arylene ether) as the hydrophilic block, will be discussed. Such copolymers are expected to produce nanophase separated morphology which should help reduce membrane swelling, as well as long sequences of sulfonic acid groups that form ionic channels[11].

Experimental

Materials. 4,4'-Isopropylidenediphenol (BPA), obtained from Dow Chemical, was recrystallized from toluene and dried in *vacuo* before use. Decafluorobiphenyl was purchased from Aldrich and dried overnight in *vacuo* at 60 ^{o}C before use. 4,4'-dichlorodiphenylsulfone (DCDPS) was obtained from Solvay Advanced Polymers and used as received. 3,3'-disulfonated-4,4'-dichlorodihenylsulfone (SDCDPS) was synthesized from DCDPS according to a process reported elsewhere[5]. 4,4'-biphenol was obtained from Eastman Chemical and used as received. N-methyl-2-pyrrolidone (NMP), purchased from Aldrich, was vacuum-distilled from calcium hydride and stored under nitrogen.

Synthesis of the perfluoro hydrophobic macromonomer. A typical polymerization procedure was as follows: BPA (1.174g, 5.142 mmol) was added to a three neck round bottom flask equipped with a mechanical stirrer, a condenser, a nitrogen inlet and a dean-stark trap. 10 mL of NMP was added to the flask and the mixture was stirred up to obtain a clear solution. Then K_2CO_3 (1.183g, 7.20mmol) was added, followed by 5 mL of toluene. The reaction bath was heated to 150 ^{o}C and kept at this temperature for 2 hours to dehydrate the system. The bath temperature was then raised to 160 ^{o}C to distill off most of the toluene. The reaction was cooled to 50 ^{o}C and decafluorobiphenyl (2.046g, 6.124mmol) was added, after which the bath temperature was raised to 110 ^{o}C and the reaction was allowed to proceed at this temperature for 5 hours. The mixture was precipitated into 200mL of water/methanol (50/50 volume fraction) and rinsed with water and methanol. The precipitated polymer was stirred overnight in methanol and then dried in *vacuo* at 100 ^{o}C.

Synthesis of the BPS hydrophilic macromonomer. A three neck round bottom flask, equipped with a mechanical stirrer, a condenser, a nitrogen inlet and a dean-stark trap, was charged with biphenol (0.412g, 2.213mmol), 3,3'-disulfonated-4,4'-dichlorodiphenylsulfone (SDCDPS) (0.912g, 1.856mmol), and 10 mL of NMP. The mixture was stirred until dissolved, then K_2CO_3 (0.430g, 3.12mmol) and 5 mL of toluene was added. The reaction bath was heated to 150 ^{o}C to dehydrate the system. The bath temperature was then slowly raised to 190 ^{o}C by the controlled removal of toluene. The polymerization was allowed to proceed at this temperature for 16 hours, and the resulting oligomer was used in the block copolymer synthesis without isolation.

Synthesis of the multiblock copolymer. The reaction bath for the hydrophilic macromonomer synthesis was cooled to 80 ^{o}C, and the highly fluorinated hydrophobic macromonomer (1.050g, 0.350mmol) was dissolved in 10 mL of NMP and added to the same reaction flask. The bath temperature was raised to 95 ^{o}C and kept at this temperature for 9 hours. The reaction mixture was precipitated into 300 mL of isopropanol to obtain a brownish fibrous polymer. The product was stirred in deionized water for 12 hours and in acetone for 12 hours, and dried in *vacuo* at 120 ^{o}C for 24 hours.

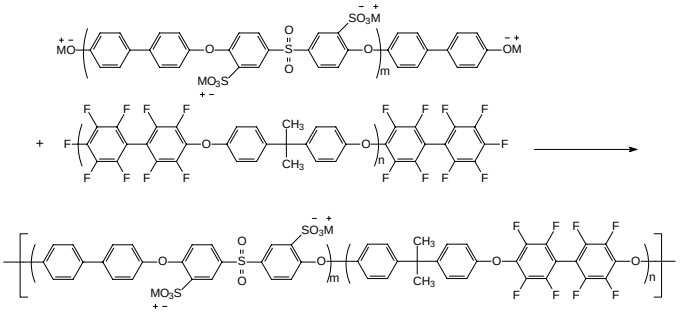

Scheme1. Synthesis of multiblock copolymers

Results and Discussion

Phenoxide terminated poly(arylene ether sulfone) (BPS) macromonomers with 100% degree of disulfonation were synthesized following a procedure similar to our group's earlier work.. Excess biphenol was reacted with SDCDPS to afford oligomers with a variety of target molecular weights. Similarly, fluoro-terminated telechelic macromonomers with different molecular weights were synthesized by reacting BPA with excess

decafluorobiphenyl, but under milder conditions, due to the much higher reactivity of the activated difluoride monomer.

As shown in Scheme 1, multiblock copolymers were obtained through the coupling reaction between the end groups of the two telechelics. At the end of the hydrophilic BPS oligomer synthesis, the amount of fluoro-terminated hydrophobic oligomer to be added was calculated from the target molecular weights of both telechelics and the amount of hydrophilic BPS oligomer that should have been obtained, such that a stoichiometry close to 1:1 was ensured, an important factor in high molecular weight polymer synthesis. The reaction time it took to obtain a viscous solution was longer for copolymers with higher block lengths, probably due to the lower concentrations of end groups available.

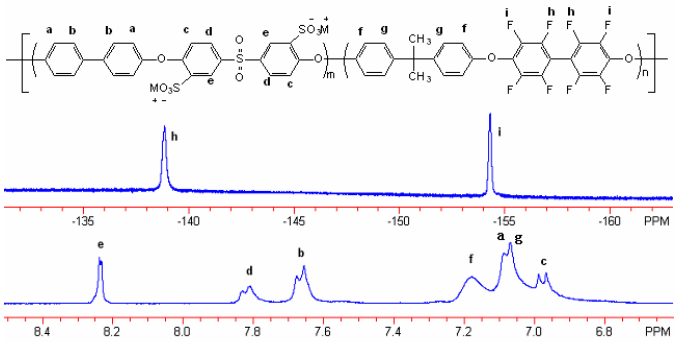

Figure 1. ^{19}F(upper) and ^{1}H(lower) NMR spectra of block copolymer XU1

Figure 1 shows the ^{1}H and ^{19}F NMR spectra of the multiblock copolymer XU3, as well as those of the hydrophobic and hydrophilic macromonomers used to produce it. The peaks due to protons in both oligomers (not shown) are present in the copolymer's spectra, whereas the protons at the hydrophilic oligomer chain ends diminish. These verify the copolymer's composition and support the success of the polymerization.

In Table 1 we can see that the proton conductivity of the block copolymers decreased from XU1 through XU3, reflecting the differences in the ion exchange capacity (IEC). This in turn is in agreement with the changes in block lengths, for although both hydrophobic and hydrophilic block lengths increase from XU1 to XU3, the hydrophilic/hydrophobic ratio actually decreases. Thus proton conductivity in liquid water should mainly be a function of IEC.

Table 1. Characterization of the multiblock copolymers

Polymer	Block lengths[a] (g/mol)	IV (dL/g)	Mn(GPC)[b] (g/mol)	IEC[c]	Water uptake	Proton Conductivity[d] (S/cm)
XU1	3k:3.5k	0.86	30k	1.61	71%	0.13
XU2	3.5k:4k	1.50	40k	1.58	42%	0.11
XU3	5k:5k	0.86	30k	1.38	58%	0.10

a: Block lengths are expressed in the form hydrophobic:hydrophilic
b: Polystyrene was used as the standard
c: Measured from ^{1}H NMR
d: Measured in liquid water at 30 °C

Figure 2 displays the proton conductivity of the block copolymers XU1 and XU3, as well as Nafion 117 as a function of relative humidity. The copolymers show conductivity slightly lower than that of Nafion, yet, in contrary to the results in liquid water, XU3 is the higher of the two, even though it has lower IEC. This indicates that the hydrophilic block length plays a more important role in the proton conductivity under partially hydrated conditions. This agrees with our expectations that, due to the shortage of "free" or "freezing" water in such cases, the proton conductance may rely more upon the ionic channels, which should be easier to form in polymers with longer hydrophilic block lengths.

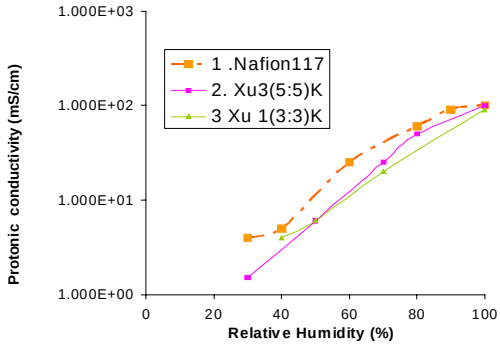

Figure 2. Proton conductivity vs. relative humidity for XU1, XU3 and Nafion 117

Conclusions

Multiblock copolymers with varying block lengths were synthesized by the coupling reaction between hydrophilic BPS and telechelic hydrophobic poly(arylene ether) oligomers. These polymer membranes possess high proton conductivity and relatively low water uptake, and show good potential as candidates for proton exchange membranes. Measurements under different conditions showed opposite trends in proton conductivity of the three polymers, suggesting that block lengths have a larger impact on conductivity in partially hydrated polymers, where the proton conductance should occur mainly through channels formed in between the hydrophilic domains. Since the BPA units in the hydrophobic blocks may not have long term stability, part of our future research will be focused on using alternative bisphenol monomers.

References

(1) Hickner, M. A.; Ghassemi, H.; Kim, Y. S.; Einsla, B. R.; McGrath, J. E. *Chem. Rev.* **2004**, *104*, 4587.
(2) Kerres, J. A.; *J. Membr. Sci.* **2001**, *185*, 3.
(3) Wang, F.; Hickner, M.; Ji, Q.; Harrison, W.; Mecham, J.; Zawodzinski, T.; McGrath, J. E. *Macromol. Symp.* **2001**, *175*, 387.
(4) Wang, F.; Hickner, M.; Kim, Y. S.; Zawodzinski, T. A.; McGrath, J. E. *J Membr Sci* **2002**, *197*, 231.
(5) Harrison, W. L.; Wang, F.; Mecham, J. B.; Bhanu, V. A.; Hill, M.; Kum, Y. S.; McGrath, J. E. *J. Polym. Sci. Polym. Chem. Ed.* **2003**, *41*, 2264
(6) Kim, Y. S.; Hickner, M. A.; Dong, L; Pivovar, B. S.; McGrath, J. E. *J. Membr. Sci.* **2004**, *243*, 317.
(7) Kim Y. S.; Dong, L.; Hickner, M. A.; Glass, T. E.; Webb, V.; McGrath, J. E. *Macromolecules* **2003**, *36*, 6281.
(8) Mauritz, K. A.; Moore, R. B. *Chem. Rev.* **2004**, *104*, 4535.
(9) Ioselevich, A. S.; Kornyshev, A. A.; Steinke, J. H. G. J. Phys. Chem. B 2004, 108, 11953.
(10) Moore, R. B.; Martin, C. R. *Macromolecules* **1989**, *22*, 3594.
(11) Ghassemi, H.; Harrison, W. L.; Zawodzinski, T. A.; McGrath, J. E. *Polym. Prepr (Am. Chem. Soc. Div. Polym. Sci.)* **2004**, *45(1)*, 68.

SYNTHESIS AND CHARACTERIZATION OF SEGMENTED SULFONATED POLY(ARYLENE ETHER)-B-POLYIMIDE COPOLYMERS AS PROTON EXCHANGE MEMBRANES

*Hae-Seung Lee, Brian Einsla, and James E. McGrath**

Department of Chemistry and
Macromolecules and Interfaces Institute,
Virginia Polytechnic Institute and State University
Blacksburg, VA 24061
*jmcgrath@vt.edu

Introduction

The proton conductive polymer membrane is one of the most critical components in polymer electrolyte fuel cells (PEFCs) and direct methanol fuel cells (DMFCs).[1] A high performance proton conductive polymer membrane has some essential requirements such as high proton conductivity, low water swelling, and good mechanical properties. The perfluorinated copolymers such as Dupont's Nafion™ have been most frequently used as fuel cell membranes because of their high performance, including high proton conductivity and good thermal and chemical stability. However, some problems limit further applications, such as high methanol permeability and a relatively low hydrated T_g. To address these weaknesses much attention has been given to polyimides for DMFC applications. Polyimides are well known for their high performance properties such as excellent thermal and oxidative stability, high mechanical strength, very low fuel permeability, and superior chemical resistance to solvents.

One aspect of our research has focused on disulfonated six-membered ring polyimide copolymers,[2] which show high proton conductivity and low methanol permeability (**Figure 1**). However, they hydrolytically degrade if they contain disulfonic acid groups at 80 °C due to the ease of hydrolysis of imido rings and limited suitability for fuel cell. Yet, their low methanol permeability is attractive and alternative methods to enhance their hydrolytic stability are the focus of our current research.

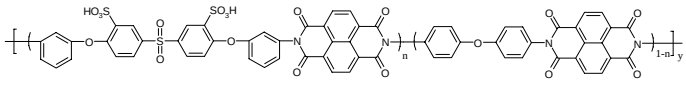

Figure 1. Structures of sulfonated polyimide copolymers.

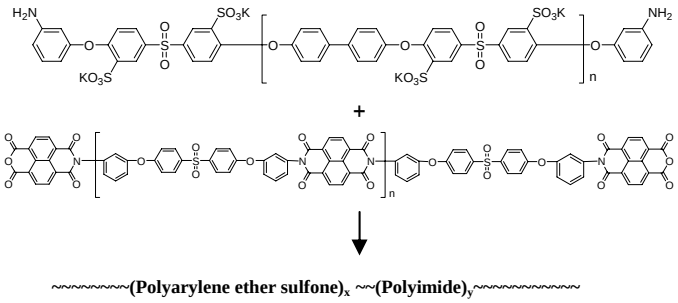

Scheme 1. Synthesis of segmented sulfonated poly(arylene ether)-B-polyimide.

As **Scheme 1** indicates, we are investigating multi phase segmented block copolymer systems which may afford higher hydrolytic stability under acidic conditions. The polyimide portion of the membrane allows for good mechanical properties and low fuel permeability and the sulfonated poly(arylene ether) permits the transport of protons by specific water transport mechanism. This paper describes the synthesis and properties of disulfonated six-membered ring polyimide copolymers. In addition to these, preliminary researches on segmented poly(arylene ether)-B-polyimide are addressed here as well.

Experimental

Materials. 4,4- dichlorodiphenylsulfone (DCDPS, BP-Amoco) and 4,4-biphenol (BP, Eastman Chemical) were all obtained in monomer-grade purity and were dried prior to use. Fuming sulfuric acid (SO_3 content~30%) was obtained from Alfa Aesar and used as received. *m*-Aminophenol (*m*-AP) was received from Aldrich and purified by sublimation. DMAc and toluene (both from Merk and Aldrich) were dried overnight over calcium hydride with a nitrogen purge and distilled at reduced pressure. Potassium carbonate (Aldrich) was dried in vacuum oven at 130 °C for twelve hours.

Sulfonated monomer synthesis. The reaction was conducted in oil bath at the stipulated temperature, using a 100 mL three necked flask fitted with an overhead stirrer and condenser. The temperature was monitored using a thermocouple. The reaction was carried at 110 °C for 6 hrs. The reaction mixture was cooled after the reaction, poured into a mixture of 200g ice and 200 mL de-ionized water, and the crude product was salted out by adding 60g sodium chloride. The product was stirred for 30 minutes and filtered. Finally recrystallization was carried in IPA/H_2O solution for purification.

Synthesis of poly(arylene ethers) of controlled molecular weights. For various molecular weights of poly(arylene ethers), different amounts of BP, DCDPS, and *m*-AP were used. A sample polymerization is as follows: 40.5mmol BP, 44.0mmol DCDPS, 7.1mmol m-AP and 51mmol potassium carbonate (15mol% excess) were dissolved in 70 ml of distilled DMAc and 35ml of toluene in a 3-necked flask equipped with condenser, Dean Stark trap, nitrogen outlet and mechanical stirrer. The reaction mixture was heated at 150ºC for 4 hours with refluxing toluene as the azeotropic agent. The reaction temperature was slowly increased to 180ºC by distillation and removal of toluene and allowed to react for 20 hours. The resulting viscous reaction mixture was diluted with DMAc and precipitated in vigorously stirring methanol and water mixture (1:1). The fibrous polymer was filtered and dried in a vacuum oven at temperatures up to 100ºC.

Characterization Methods. Proton NMR spectra were obtained with a Varian UNITY 400 MHz spectrometer using DMSO-d_6 as a solvent (5% w/v polymer solutions). Intrinsic viscosity (IV) measurements were obtained in NMP at 25ºC using a Cannon Ubbelohde viscometer.

Results and Discussion

Properties of sulfonated polyimide copolymers. Several properties of sulfonated polyimide copolymers were examined to determine their potential for fuel cell applications. It was found that the proton conductivity of the membranes increased at elevated temperature, high relative humidity and high IEC. Sulfonated polyimide copolymer membranes whose IEC were ~1.9 meq/g showed conductivities close to 0.1 S/cm in water at elevated temperatures and this result is equivalent to Nafion 1135 (**Figure 2**). The initial DMFC performance of several copolyimides was investigated, and it was found that these membranes had lower methanol permeability and performed comparably to Nafion 117 **(Figure 3)**. However, their hydrolytic stability at 80 °C was still much lower than Nafion or analogous poly(arylene ether)s.

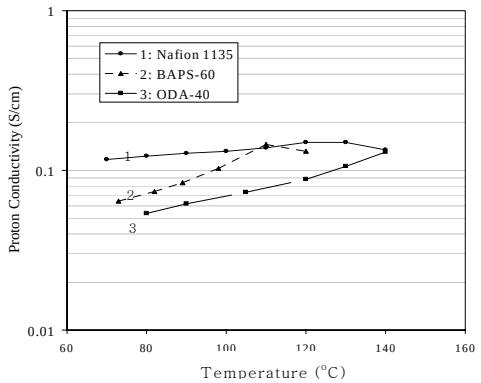

Figure 2. Proton conductivity of sulfonated polyimide copolymer and Nafion 1135 at elevated temperature and 100% RH.

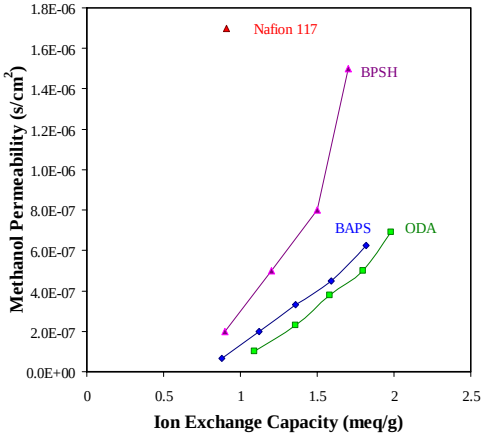

Figure 3. Methanol permeability of sulfonated polyimide copolymer(BAPS, ODA), sulfonated poly(arylene ether) (BPSH) and Nafion 1135.

Synthesis of poly(arylene ethers) with telechelic amine functionalization. A series of controlled molecular weight primary amine terminated poly(arylene ethers) were synthesized as controls (**Scheme2**).

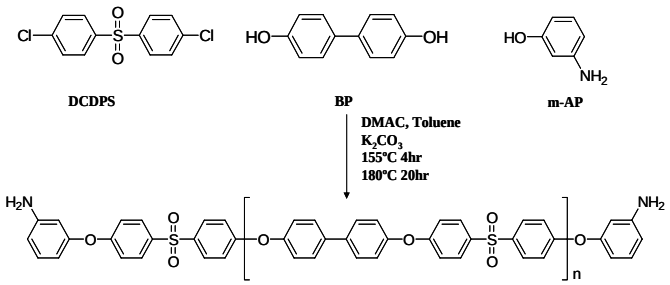

Scheme 2. Polymerization of primary amine terminated poly(arylene ether)

The telechelic primary amine functionality will allow the incorporation of these oligomers in segmented poly(arylene ether)-*b*-polyimide as shown in **Scheme 1**. Number average molecular weights($\overline{M}_n$) of 5,000, 10,000, 15,000, and 20,000 grams per mole were targeted and successfully synthesized. Characterization of molecular weight was estimated by intrinsic viscosity measurements. A more quantitative evaluation of $\overline{M}_n$ was achieved by integration of selected peaks of ^{1}H NMR spectra. As was observed, number average molecular weights matched well with the targeted molecular weights. A summary of the molecular weight characterization is shown in **Table 1**.

Table 1. **Molecular weight characterization of the polymers.**

Targeted Mn (g/mol)	Mn by NMR Analysis (g/mol)	Intrinsic Viscosity (dL/g)
5,000	5,880	0.22
10,000	12,370	0.37
15,000	18.120	0.42
20,000	19,960	0.47

Conclusions

Sulfonated polyimide copolymers showed high proton conductivity and low methanol permeability. Unfortunately, its performance was damaged under aqueous acidic condition because of poor hydrolytic stability. To address this drawback, synthesis of segmented sulfonated poly(arylene ether)-*b*-polyimide is underway. In the preliminary research for the synthesis of controlled molecular weight primary amine terminated telechelic poly(arylene ethers) were successfully synthesized. ^{1}H NMR and intrinsic viscosity measurements confirmed that control of molecular weight from 5K to 20K was successful.

Acknowledgment

The authors wish to acknowledge the support of the Army Research Laboratories under subcontract to General Technical Services LLC, PO# 05-1-084.

References

1. M.A. Hickner, H. Ghassemi, Y.S. Kim, B. Einsla and J.E. McGrath, *Chemical Reviews* **2004**, 104(10), 4587-4611

2. Einsla, B.R.; Hong, Y.T.; Kim, Y.S.; Wang, F.; Gunduz, N.; McGrath, J.E. *J. Polym. Sci.: Part A: Polym. Chem.* **2004**, 42, 862-874.

3. Watari, T.; Fang, J.; Tanaka, K.; Kita, H.; Okamoto, K. *ACS Polym. Mat.: Sci. & Eng. (PMSE)* **2001**, 85, 334.

4. A.L. Rusanov, *Adv. Polym. Sci.* **1994**, 111, 115-175.

5. Genies, C.; Mercier, R.; Sillion, B.; Petiaud, R.; Cornet, N.; Gebel, G.; Pineri, M. *Polymer* **2001**, 42, 5097-5105.

6. Savadago, O.. *J. New Mater. Electrochem. Systems* **1998**, 1, 47-66.

7. Genies, C.; Mercier, R.; Sillion, B.; Cornet, N.; Gebel, G.; Pineri, M. *Polymer* **2001**, 42, 359-373.

8. Brian R. Einsla, Yu Seung Kim, Michael A. Hickner, Young-Taik Hong, Melinda L. Hill, Bryan Pivovar, James E. McGrath. *Journal of Membrane Science* **2005**, (accepted)

SYNTHESIS OF (POLY(ARYLENE ETHER SULFONE)-SUBSTITUTED POLY(*P*-PHENYLENE)) MULTIBLOCK COPOLYMERS FOR PROTON EXCHANGE MEMBRANE

*Hang Wang, James E. McGrath**

Department of Chemistry
Virginia Polytechnic Institute and State University
Blacksburg, VA 24061
*jmcgrath@vt.edu

Introduction

The proton exchange membrane (PEM) is a key component in solid polymer electrolyte fuel cells. Currently the most used PEM is Nafion, which exhibits high conductivity and good chemical and thermal stability. However, it exhibits low conductivity at low water content. Other drawbacks include relatively low mechanical strength, moderate glass transition temperature and high cost[1]. Phase-separated hydrophilic-hydrophobic multiblock copolymers are promising materials that can be used as alternate PEMs. This is particularly due to their ability to form unique morphologies, such as: the spherical, cylinder, and lamellar shape. The morphology of these multiblock copolymers may play an important role in providing good conductivity even at low water content and determining the membranes' mechanical strength and water uptake.

Poly (*p*-phenylene) (PPP) soluble amorphous derivatives are a promising class of high-performance polymers because of their excellent thermal and mechanical properties[2]. We have previously reported synthesis of poly(2,5-benzophenone) derivatives via nickel-catalyzed coupling polymerization of 4'-substituted 2,5-dichlorobenzophenones[3]. These polymers were proven to be highly thermo-oxidative stable materials with good solubility and excellent mechanical properties. However, they do not form good films perhaps due to their extremely rigid rod-like chains.

A series of sulfonated poly (arylene ether sulfone) random copolymers (PAES) have been synthesized in our group in the past few years[4]. These high molecular weight sulfonated copolymers had excellent film forming behavior, high glass transition temperatures and high proton conductivities of greater than 0.1 S/cm, which was equivalent to Nafion control membranes.

This paper describes the synthesis and characterization of PAES-*b*-PPP multiblock copolymers, which are hoped, will combine the excellent thermal, mechanical properties, good proton conductivity and good film-forming ability.

Experimental

Materials. The synthesis of monomers via Friedel-Craft benzoylation of 1,4-dichlorobenzene has been previously reported. Triphenylphosphine (Aldrich) was recrystallized from Et_2O. Zn powder (Aldrich) was washed with acetic anhydride, filtered, washed with dry Et_2O, and dried under vacuum at 150°C. 2,2'-Bipyridine (BPY; Aldrich) and Dichlorobis(triphenylphosphine)nickel(II) (Aldrich) were used as received. Dimethylacetamide (DMAC) were dried over calcium hydride, distilled under vacuum and stored under nitrogen before use. 4,4'-dichlorodiphenylsulfone (DCDPS) and 4,4'-biphenol were obtained from BP Amoco and Eastman Chemical, respectively. The sulfonated comonomer, 3,3'-disulfonate-4,4'-dichlorodiphenylsulfone (SDCDPS) was synthesized in-house from DCDPS according to a modified literature method[5].

Synthesis of telechelic substituted poly(phenylene) and poly(arylene ether sulfone) oligomers. A 100mL Schlenk flask was first charged with $NiCl_2(Ph_3)_2$ (1.047g, 1.6mmol), PPh_3 (0.8387g, 3.2mmol) , Zn (3.2438g, 49.6mmol), 2,2'-Bipyridine (0.2504g, 1.6mmol) and a magnetic stir bar. The flask was sealed with a rubber septum, evacuated under flame for 10 minutes, and placed under an N_2 atmosphere by filling with N_2 followed by three evacuation-fill cycles. THF (10mL) was added via syringe through the rubber septum to initiate the reaction. The solution became deep red after 10 minutes. Then 2,5-dichloro-4'-phenylbenzophenone (3.7667g, 15mmol) and the end-capping agent 4-chloro-4'-flurobenzophenone (0.2346g, 1mmol) were charged under N_2 flow. The mixture was stirred and heated at 65°C for 24 h. After cooling to room temperature, the reaction mixture was poured into 40% HCl/methanol solution. The resulting precipitate was collected by filtration and washed with 10% sodium bicarbonate solution (3 times) and deionized water (3 times). After drying in a vacuum oven at 100°C overnight, the light yellow polymer was isolated and gave a yield of 95%.

The synthesis of hydroxyl terminated sulfonated poly (arylene ether sulfone) was reported earlier[6].

Copolymerization. The aromatic nucleophilic step was conducted in a 3-neck flask equipped with mechanical stirrer, nitrogen inlet and a Dean Stark trap. In a typical polymerization, biphenol (0.3742g, 2mmol), SDCDPS (0.7970g, 1.6224mmol) and potassium carbonate (0.4146g, 3mmol) were added to the flask. Dry DMAc and toluene were used as the solvents. The reaction mixture was heated under reflux at 150°C for 4 hours, which stripped off most of the toluene to dehydrate the system. The temperature was then raised slowly to 165°C for 36 hours. After that, poly (4'-phenyl-2,5-benzophenone) telechelic oligomer (1.051g, Mn=5800) was dissolved in 10 mL dry DMAc and added drop wise into the flask within one hour. The reaction was kept at 165°C for another 48 hours. The viscous polymer solution was cooled to room temperature, diluted with DMAc and filtrated to remove most of salts. The polymer was isolated by precipitation in isopropanol (IPA). It was washed extensively with deionized water several times to quantitatively remove the inorganic salts and finally vacuum dried at 120 °C for 24 hours.

Characterization. ^{1}H-NMR experiments were performed using a Varian 400MHz instrument in deuterated chloroform. The intrinsic viscosity (IV) of the polymers was measured in NMP with 0.05M LiBr at 25°C using a Cannon Ubbelohde viscometer. Number average molecular weights (Mn) and molecular weight distributions (MWD) of polymers were determined by gel permeation chromatography based on polystyrene standards. Glass transition temperatures were estimated by DSC using a Perkin Elmer Model DSC 7. Second-heat T_g values are reported.

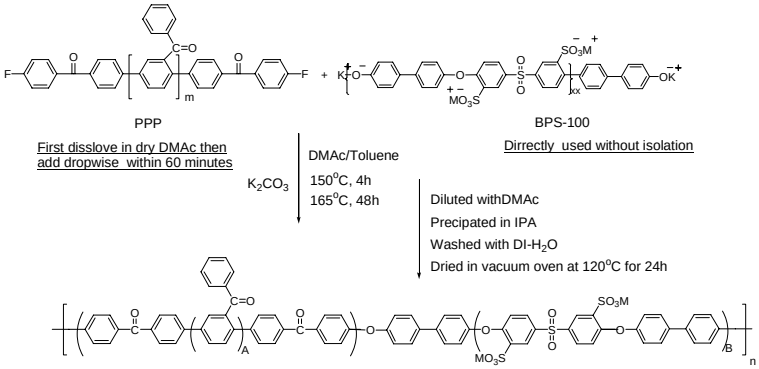

Scheme 1. Synthetic Scheme for Sulfonated Multiblock copolymers

Results and Discussion

A series of poly (4'-phenyl-2,5-benzophenone) telechelic oligomers with different molecular weights, shown in Table 1, were first synthesized by Ni (0) catalytic coupling of 2,5-dichloro-4'-phenylbenzophenone and the end-capping agent 4-chloro-4'-flurobenzophenone, following early procedure of Sheares, et al[2]. Molecular weight of telechelic oligomers were readily controlled by varying the stoichiometric ratio of end-capping agents and monomer. All telechelic oligomers were recovered by vacuum suction filtration in yields exceeding 95% after workup in a 40% hydrochloric acid/methanol solution to remove excess zinc. Carbon-13 NMR spectra were used to determine the degree of polymerization of telechelic oligomers, which were in good agreement with the target values. The peak assigned for the terminal carbonyl was compared with the peak corresponding to the carbonyl group on the benzophenone side groups for this calculation. In addition, both glass transition temperatures and intrinsic viscosities of these telechelic oligomers increase with increasing molecular weight as expect. Therefore, it is safe to say the poly (4'-phenyl-2, 5-benzophenone) telechelic oligomers with controlled molecular weight were successfully synthesized. More important, these telechelic oligomers have fluorine functional group at each end, which should be reactive in nucleophilic aromatic substitution reaction.

Table 1. Characterization of Poly (4'-phenyl-2,5-benzophenone) Telechelic Oligomers

No.	Stoichiometric Ratio between Monomer and End-capping Agent	M*n* (g/mol) (Target)	DP_n, (Target)	DP_n (C^{13} NMR)	IV (dl/g)	T_g (^oC)
1	5:1	2200	10	9.0	0.16	150
2	10:1	4000	20	16.5	0.21	161
3	15:1	5600	30	23.6	0.32	169
4	20:1	7600	40	36.9	0.46	182
5	25:1	9400	50	--	0.48	189

* The intrinsic viscosity (IV) of the polymers was measured in NMP with 0.05M LiBr at 25°C

** Glass transition temperatures were estimated by DSC using a Perkin Elmer Model DSC 7. Second-heat T_g values are reported.

To prepare the PAES-*b*-PPP multiblock copolymers, potassium phenoxide terminated oxide sulfonated poly (arylene ether sulfone) was first synthesized and, without isolation, previous made poly (4'-phenyl-2,5-benzophenone) telechelic oligomers were added in dry DMAc and the reaction was maintained at 165°C for 48h. This afforded a light- yellow copolymer in high yield (90%). A series of multiblock copolymers with various hydrophilic-hydrophobic length were made in this way. ^{1}H NMR showed characteristic peaks of both PAES and PPP oligomer. The multiblock copolymers gave intrinsic viscosity values as high as 0.94 dl/g in NMP with 0.05 LiBr at 25°C.

Atomic force microscope was used to study the morphology of these multiblock copolymers. From the phase image, channels and networks between the hydrophilic phases (darker) were observed, indicating some phase separation exists in these multiblock copolymers.

Conclusions

A series of poly (4'-phenyl-2,5-benzophenone) telechelic oligomers with different molecular weight were successfully synthesized by Ni (0) catalytic coupling reaction. These telechelic oligomers were then copolymerized with phenylate terminated sulfonated poly (arylene ether sulfone)s by nucleophilic aromatic substitution reaction in an attempt to form phase-separated hydrophilic-hydrophobic multiblock copolymers. High molecular weight multiblock copolymers with different block length were successfully synthesized and characterized.

Acknowledgements. The authors would like to thank the National Science Foundation "Partnership for Innovation" Program (HER-0090556) and the Department of Energy (DE-FC36-01G01086) for support of this research effort.

Reference:

(1) Hickner, M. A.; Ghassemi, H.;Kim, Y. S.; Einsla, B. R.; and McGrath, J. E. *Chem. Rev*. 2004, 104, 4587-4612

(2) (a) Schluter, A. D. *J Polym. Sci Part A: Polym Chem* 2001, 39, 1533-1556; (b) Phillips, R. W.; Sheares, V. V.; Samulski, E. T.; DeSimone, J. M. *Macromolecules* 1994, 27, 2354-2356; (c) Wang, Y.; Quirk, R. P. *Macromolecules* 1995, 28, 3495-3501; (d) Percec, V. Zhao, M.; Bae, J.; Hill, D. *Macromolecules* 1996, 29, 3727-3735; (e) Bloom, P. D.; Sheares, V. V. *J Polym. Sci Part A: Polym Chem* 2001, 39, 3505-3512

(3) (a) Ghassemi, H.; McGrath, J. E. *Polymer* 2004**,** 45, 5847-5854; (b)Ghassemi, H; Ndip, G; McGrath, J. E. Polymer, 2004, 45, 5855-5862

. (c) Ghassemi, H.; Harrison, W.; Zawodzinski, T. A., Jr.; McGrath, J. E. *Polymer Preprints* (American Chemical Society, Division of Polymer Chemistry) (2004), 45(1), 68-69; (d) Ghassemi, H.; Ndip, G.; McGrath, J. E. *Polymer Preprints* (American Chemical Society, Division of Polymer Chemistry) (2003), 44(1), 814-815.

(4) Wang, F.; Hickner, M.; Kim, Y. S.; Zawodzinski, T. A.; McGrath, J. E. *J. Membr. Sci*. 2002, 197, 231

(5) M. Ueda, H. Toyota, T. Ochi, J. Sugiyama, K. Yonetake, T. Masuko, T. Teramoto, J. Polym. Sci., Polym. Chem. Ed. 1993, 31, 85.

(6) Ghassemi, H.; Harrison, W.; Zawodzinski, T. A., Jr.; McGrath, J. E. *Polymer Preprints* (American Chemical Society, Division of Polymer Chemistry) (2004), 45(1), 68-69

SYNTHESIS AND CHARACTERIZATION OF SULFONATED POLYIMIDE COMPOSITE MEMBRANES FOR FUEL CELLS

Veena Choudhary and Pooja Chhabra

Centre For Polymer Science & Engg, Indian Institute of Technology, Delhi, India, I.I.T.Hauz Khas, New Delhi-110016, India

Abstract

The paper describes the synthesis and characterisation of sulfonated polyimides prepared by reacting 1,4,5,8-naphthalene tetracarboxylic dianhydride (NTDA),3,3,4,4-benzophenone tetracarboxylic dianhydride(BTDA) sulfonated diamine (4,4'-diaminodiphenylether-2,2'-disulfonic acid (ODADS)and common non-sulfonated diamines. A one step high temperature catalysed polycondensation in m-cresol was used for the synthesis of sulfonated copolyimides. Several samples were prepared by taking mixture of NTDA:BTDA (3:1 molar ratio) and by varying the molar ratio of sulfonated to nonsulfonated diamines in the initial feed. The structural characterisation of the copolymers was done using FTIR and elemental analysis.Ion exchange capacity and water uptake increased with increasing amount of sulfonated diamine. Thermal stability of the copolymers as determined using thermogrametric analyser in nitrogen atmosphere was found to be dependent upon the structure of diamines and the copolymer composition.

A MINIATURE MEMBRANE-LESS BIOFUEL CELL OPERATING AT +0.60 V UNDER PHYSIOLOGICAL CONDITIONS

Nicolas Mano and Adam Heller

Department of Chemical Engineering and Texas Material Institute-
The University of Texas at Austin-Austin-78712- USA

Introduction

Our work is aimed at engineering a power source enabling further miniaturization of autonomous implanted electronic devices, the size of which is now limited by their battery. As the size of microelectronic circuits and of sensors shrinks, the sizes of low-power sensor-transmitter packages (of potential relevance to physiological research and medicine) becomes increasingly dependent on the size of their power source. If stabilized for operation *in-vivo,* a miniature glucose/O_2 biofuel cell could power an implanted sensor-transmitter that would broadcast, for a few weeks, the local glucose concentration, relevant to diabetes management; or the local temperature, indicative of infection after surgery; or a pressure difference, indicating blockage of the flow of fluid in the central nervous system. [1]

Contrary to conventional cells which contain at least 9 components (anode, cathode, case, case seal, membrane, membrane seal, ion conducting electrolyte, plumbing to the anode compartment and plumbing to the cathode compartment), the miniature biofuel cell that we are developing contains only two, an anode and a cathode. [1-3] These consist of "wired" enzyme bioelectrocatalyst-coated 7 μm diameter carbon fibers.

By eliminating the membrane, the case and the seal, we were able to build a 0.88 mm^2 biofuel cell, the smallest ever, which we implanted and operated in a grape. The in-vivo power output of the cell, made of a pair of 0.44 mm^2 area smooth, non porous carbon fibers, was 2.4 μW at +0.52 V/AgAgCl, translating to a power density of ~ 5.5 μW.mm-2 and ~ 4.4 μW.mm-2 at +0.6V/AgAgCl.[2] Because this potential exceeded half the band gap of silicon, it could be converted, by a conventional silicon voltage converter circuit, to the standard 3V operating voltage of ICs

Here we show that the tailoring of a redox polymer, electrically connecting the reaction centers of glucose oxidase to the carbon fiber anode, led to an efficient biofuel cell, operating at a higher voltage and current density.

.

Experimental

Chemicals. Bilirubin oxidase (BOD) (EC 1.3.3.5, 1.3 $U.mg^{-1}$) from Trachyderma tsunodae was purchased from Amano (Lombard, IL) and purified as previously decribed.[4] Glucose oxidase (GOx) from Aspergillus niger from Fluka, Milwaukee, WI. Poly(ethylene glycol) (400) diglycidyl ether (PEGDGE) from Polysciences, Inc. (Warrington, PA); $NaIO_4$ and NaCl (Sigma, St. Louis, MO) were used as received. A fresh solution of BOD in pH 7.4, 20 mM phosphate buffer (PB) was prepared daily. All solutions were made with deionized water passed through a purification train (Sybron Chemicals Inc, Pittsburgh, PA). The synthesis of the BOD-wiring redox polymer **I** PAA-PVI-$[Os(4,4'\text{-dichloro-}2,2'\text{-bipyridine})_2Cl]^{+/2+}$ and GOx-wiring redox polymer **II** PVP-$[Os(N,N'\text{-alkylanated-}2,2'\text{ bi-imidazole})_3]^{2+/3+}$ were previously reported. [5-8]

Instrumentation and electrodes. The measurements were performed using a bipotentiostat (CH-Instruments, Austin, TX, Model #CHI832) and a dedicated computer. The 2-cm long, 7-μm diameter carbon fibers (Goodfellow, Cambridge, UK) were made by reported procedures.[5, 7-10] One end of the fibers was cemented to a copper wire using conductive carbon paint (SPI, West Chest, PA). The carbon paint was allowed to dry, then insulated with an epoxy cement. The active area of each fiber was 0.44 mm^2. Prior to their coating the 7μm diameter fibers (0.0044 cm^2) were made hydrophilic by exposure to a 1 torr O_2 plasma for 3 minutes.[11] The cathodic catalyst was made of 44.6 wt% of bilirubin oxidase, 48.5 wt % of polymer ***I*** and 6.9 wt% of the crosslinker PEDGE. [5, 7]. The anodic catalyst solution was made as follows : 100 μL of 40 mg/mL GOx in 0.1 M $NaHCO_3$ was oxidized by 50 μL of 7mg/mL of $NaIO_4$ in dark for 1 hour, and then 2 μL of the periodate-oxidized GOx was mixed with 8 μL of 10mg/mL of polymer ***II*** and a 0.5 μL droplet of 2.5 mg/mL of PEGDGE. 5 μL of the anodic catalytic solution was applied to the carbon fiber. The resulting anodic catalyst consisted of the cross-linked adduct of 39.6 wt % GOx, 59.5 wt % polymer ***II*** and 0.9 wt % PEDGE.

Results and Discussion

We described earlier a glucose electrooxidizing anode made by "wiring" glucose oxidase (GOx) with poly(4-vinylpyridine)-$[Os(N,N'\text{-dimethyl-}2,2'\text{-biimidazole})_3]^{2+/3+}$, comprising 10.7 wt % of osmium.[12] The unique features of this "wire" were its 13-atom long flexible tethers, binding the redox centers to the backbone, and the reducing redox potential of the dialkylated biimidazole complex of $Os^{2+/3+}$, -0.2 V vs. Ag/AgCl. The long tethers increased the frequency of effective electron transferring collisions between reduced and oxidized osmium centers and thereby the apparent electron diffusion coefficient, D_{app}, which reached in the crosslinked redox hydrogel 5.8 x 10^{-6} cm^2 s^{-1}, an order of magnitude higher than in earlier redox hydrogels.[13, 14] The effective collection of the electrons from the glucose-reduced GOx allowed poising of the anode at a potential as reducing as - 0.10 V vs. Ag/AgCl (only 0.26 V positive to the redox potential of the $FAD/FADH_2$ cofactor in GOx at pH 7.2) while glucose was electro-oxidized at a current density of 1.15 $mA.cm^{-2}$.

To build a faster glucose anode and to decrease the overpotential for glucose electrooxidation, we synthesized a new redox polymer with 12.8 wt % of osmium. The synthetic strategy for the polymer resembled that reported for the 10.7 wt % of osmium polymer.[12] The NH_2-spacer modified tris (N, N′-dialkylated 2,2′-biimidazole) $Os^{2+/3+}$ was condensed with 6-bromohexanoic acid-quaternized of poly(4-vinylpyridine) to form the amide. The (tethered complex/pyridine/carboxyl-pentylpyridinium) ratios for the 12.8 wt%-Os-polymer were 12.8/85/2.2.

Figure 1 represents the optimal composition (polymer/ enzyme/crosslinker) obtained for the bioelectrocatalysts made with the polymer containing 10.7 wt % osmium (solid circles) and the polymer containing 12.8 wt % osmium (open circles).

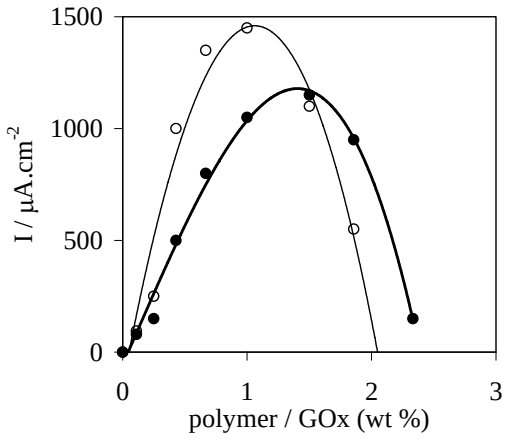

Figure 1. Dependence of the glucose electrooxidation current density on the polymer/GOx weight percentage ratio when the bioelectrocatlyst is made with a polymer containing 10.7 wt % of osmium (black circles), or 12.8 wt% of osmium (open circles). Electrode poised at + 0 V/AgAgCl in a 20 mM phopshate buffer, 37 °C, 1 mV.s^{-1} scan rate, 200 rpm, under 1 atm N_2, 15 mM glucose.

Increasing the osmium content to 12.8 wt. % allowed a lesser polymer/enzyme weight ratio, 1.0 vs. the earlier reported 1.5 for the polymer loaded with 10.7 wt.% Os, and increased the limiting current density by 20 % to 1.5 mA.cm^{-2}.

Using the novel anode, we built a miniature compartment-less biofuel cell, consisting of two 7 µm diameter, 2 cm long carbon fibers. The bioelectrocatalyst of the anode consists of glucose oxidase from *Aspergillus niger* (GOx) electrically "wired" by polymer II, having a redox potential of -0.19V vs. Ag/AgCl. The bioelectrocatalyst of the cathode, which was superior to platinum, was reported earlier. [4] It consisted of purified bilirubin oxidase from *Trachyderma tsunodae* (BOD) "wired" by PAA-PVI-$[Os(4,4'\text{-dichloro-}2,2'\text{-bipyridine})_2Cl]^{+/2+}$ and had a redox potential of + 0.36 V vs. Ag/AgCl.

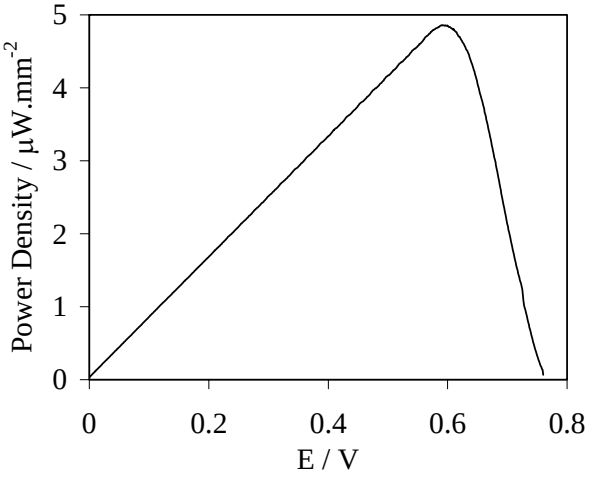

Figure 2. Dependence of the power density on the cell voltage for the cell made with a 7 µm diameter, 2 cm long carbon fiber anode coated with "wired" glucose oxidase and with the novel polymer containing 12.8 wt % of osmium . 15 mM glucose.

As illustrated in Figure 2, the power of the cell made of the two carbon fibers, peaked at ~ + 0.60 V/AgAgCl, where it reached 2.1 µW. The power density was 4.8 µW.mm^{-2}, above the 4.4 µW.mm^{-2} power density of the previously described +0.52 V cell.[2, 6] This value represents the highest operating voltage in a miniature membrane-less biofuel cell in a pH 7.2 physiological buffer solution. Because the redox potential of *A. niger* GOx at pH 7.2 is -0.35 vs. Ag/AgCl [15] and that of bilirubin oxidase from *Trachyderma tsunodae* is about +0.36 vs. Ag/AgCl.[16], the operating potential is just 0.11 V less than the difference between the redox potentials of the two enzymes. The cell lost ~ 8% of its power per day when operating at +0.6V/AgAgCl and at 37 °C in a physiological buffer solution.

Conclusions

Increasing the density of the polymer-bound redox sites, which electrically connect the reaction centers of GOx to the anode, increased the glucose flux limited current density by 20%, and decreased by 50 mV the overpotential for glucose electro-oxidation. A miniature, membrane-less glucose-O_2 biofuel cell built with the novel anode operated in a physiological buffer at 37.5ºC at the highest voltage to date, +0.60V, while producing 4.8µW.mm^{-2}.

Acknowledgement. The study was supported by the Office of Naval Research (N00014-02-1-0144) and by the Welch Foundation. N.M thanks The Oronzio de Nora Industrial Electrochemistry Fellowship of The Electrochemical Society

References

(1) Heller, A.,*Phys. Chem. Chem. Phys.* **2004,** 6, 209-216.
(2) Mano, N.; Mao, F.; Heller, A.,*J.Am. Chem. Soc.* **2003,** 125, 6588-6594.
(3) Soukharev, V. S.; Mano, N.; Heller, A.,*J. Am. Chem. Soc.* **2004,** 126, (27), 8368-8369.
(4) Mano, N.; Fernandez, J. L.; Kim, Y.; Shin, W.; Bard, A. J.; Heller, A.,*J. Am. Chem. Soc.* **2003,** 125, 15290-15291.
(5) Mano, N.; Kim, H.-H.; Zhang, Y.; Heller, A.,*J. Am. Chem. Soc.* **2002,** 124, 6480-6486.
(6) Mano, N.; Mao, F.; Heller, A.,*J. Am. Chem. Soc.* **2002,** 124, 12962-12963.
(7) Mano, N.; Kim, H.-H.; Heller, A.,*J. Phys. Chem. B* **2002,** 106, 8842-8848.
(8) Kim, H.-H.; Mano, N.; Zhang, Y.; Heller, A.,*J. Electrochem. Soc.* **2003,** 150, (2), A209-A213.
(9) Chen, T.; Barton, S. C.; Binyamin, G.; Gao, Z.; Zhang, Y.; Kim, H.-H.; Heller, A.,*J. Am. Chem. Soc.* **2001,** 123, 8630-8631.
(10) Mano, N.; Heller, A. In *A Miniature Membrane-less Biofuel Cell Operating Under Physiological Conditions*, ECS, Salt Lake City, 2002; 'Ed.'^'Eds.' Salt Lake City, 2002; p^pp.
(11) Sayka, A.; Eberhart, J. G.,*Solid State Technol* **1989,** 32, 69-70.
(12) Mao, F.; Mano, N.; Heller, A.,*J.Am. Chem. Soc.* **2002,** 125, (16), 4951-4957.
(13) Heller, A.,*J Phys. Chem.B* **1992,** 96, 3579-3587.
(14) Heller, A.,*Acc. Chem. Res.* **1990,** 23, 128-134.
(15) Stankovich, M. T.; Schopfer, L. M.; Massey, V.,*J. Biol. Chem* **1978,** 253, 4971-4979.
(16) Hirose, J.; Inoue, T.; Sakuragi, H.; Kikkawa, M.; Minakami, M.; Morikawa, T.; Iwamoto, H.; Hiromi, K.,*Inorganica. Chim. Acta* **1998,** 273, 204-212.

ELECTRON/ION MIXED CONDUCTIVE MATRIX FOR ELECTROCHEMICAL REGENERATION OF COFACTORS

Linda de la Garza, Yupo J. Lin, Michelle B. Arora , Marion C. Thurnauer, and Seth W. Snyder

Chemistry Division and Energy Systems Division
Argonne National Laboratory
9700 South Cass Ave.
Argonne, IL 60439

Introduction

Bioprocessing takes advantage of biocatalysts (enzymes or microorganisms) in a bioreactor. Biocatalysts have distinct advantages over chemical catalysts including higher selectivity and milder reaction conditions. Enzyme biocatalysts are preferred because they can be tailored or engineered to perform highly specific reactions. Microorganism biocatalysts are used in most cases because they do not require cofactor replacement, a critical barrier in most enzyme applications. Cofactor within the active site of the enzyme act as electron sinks donating/accepting electrons and protons to/from the substrate in order to convert it to the chemical product. For example, glucose fructose oxido-reductase converts glucose to gluconolactone by donating two electrons and two protons from glucose to the cofactor $NADP^+$ (nicotinamide adenine dinucleotide phosphate) converting it to NADPH and H^+. In a living cell, after the cofactor is consumed, it is replaced by fresh cofactor from the available cellular cofactor pool, allowing the enzyme to retain enzymatic activity. In a bioreactor, cofactors are depleted because the isolated enzyme has no fresh cofactor pool to draw from. Costly cofactors must be continuously added to the bioreactor for the conversion to continue. Most applications use inefficient methods to regenerate cofactor such as the addition of a second enzyme/substrate to catalyze a reaction that regenerates cofactor. The drawbacks are that additional substrate must be added for the second enzymatic reaction and the second reaction leads to unwanted byproducts that must be separated from the desired product. Therefore, a method to directly regenerate cofactor in a bioreactor without addition of a second enzyme/substrate reaction could address a significant barrier to enzymatic-based chemicals production.

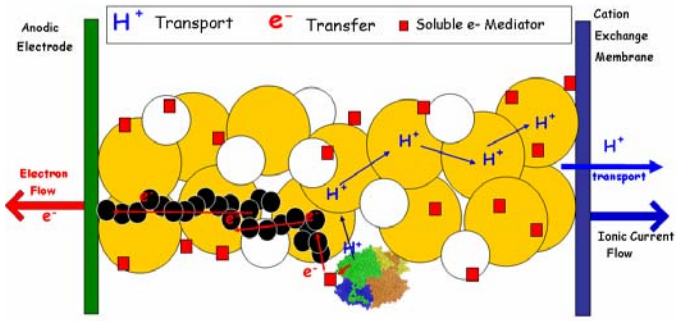

Figure 1. Scheme of the components of electron/ion mixed conductive matrix. A space fill model of GFOR enzyme is displayed. Yellow circles represent ionic resins, white circles represent enzyme capture resins, and the black circles represent carbon nanoparticles.

Direct cofactor regeneration can be achieved by controlling the transfer of electrons and protons to/from the cofactor or to an acceptor/donor provided by electrodes in an electrochemical cell.

To directly regenerate cofactor we constructed a novel porous composite conductive matrix to act as both an electron and proton bridge between the enzyme active site and electrode. As shown in **Figure 1**, three elements are required to form a conductive matrix that can effectively create an electron/proton bridge, (1) a network for proton transport, (2) a network for electron transfer, and (3) enzymes immobilized within the matrix.

Results and Discussion

Fabrication and conductivity tests of electron/ion mixed conductive matrix. Two methods, wet and dry processes, were developed to incorporate the carbon-black nanoparticles with ion-exchange and enzyme capture resin beads. In the wet process, a latex emulsion liquid with curing agent was used to form an elastomer polymer that binds the particles mixture. The porosity of the wafers made by the wet process is around 10-15%. To better control the wafer properties, a dry process to make the wafer was also developed. Thermoplatics were used to bind the particles mixture by hot-pressing all the particles in a mold under high pressure. The porosity of the wafer can be controlled by using removable additives such as sugar or passing air through the mold. Without the carbon particles in the matrix, the regular resin wafer is found to be electrically insulated.

In order to predict the optimal ratio of cation and anion resins in the matrix for effective transport of proton a porous-plug model of ion conductivities in the composite wafer was developed. Using the results of the experimental measurements of ionic conductivity of each tested composite wafer, this model can determine the pathways of ion transport inside the wafer structure. As shown in **Figure 2**, the ionic conductivity of the composite wafer is influenced by the pathways of ion transport. The better the ion-exchange resin network for ion transport (i.e., more ion transport via the pathway of resin network) the higher the ion conductivity of the composite wafer. The highest resin conductivity obtained from different samples is measured to be 0.03 S/cm which is better than the originally anticipated value of 0.01 S/cm for a composite wafer.

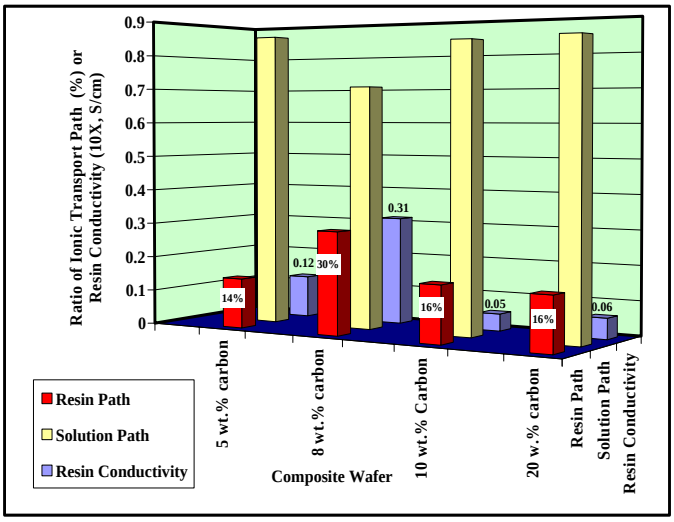

Figure 2. Results from semi-empirical model test for ion transport in the electron/ion conductive matrix in HCl solution.

A standard four-point electric impedance meter was used to measure the conductivity (electric or ionic) of the composite wafer.

The wafer porosity was determined using an organic dye. **Figure 3** shows the electric conductivities and porosities of the tested samples. A too high loading of carbon nanoparticles reduces the ionic conductivity of the wafer. Around 7-8 wt.% of carbon black is found to be the optimal condition. The electrical conductivities of the samples are in the range of 1.5 to 11 mS/cm. The hot-pressed composite wafer shows an increase of electrical conductivity by 5-fold (from 2 mS/cm to 11 mS/cm) and an increase in porosity by 3-fold (10-15% to 30-40%) compared with the wafer made by the wet method.

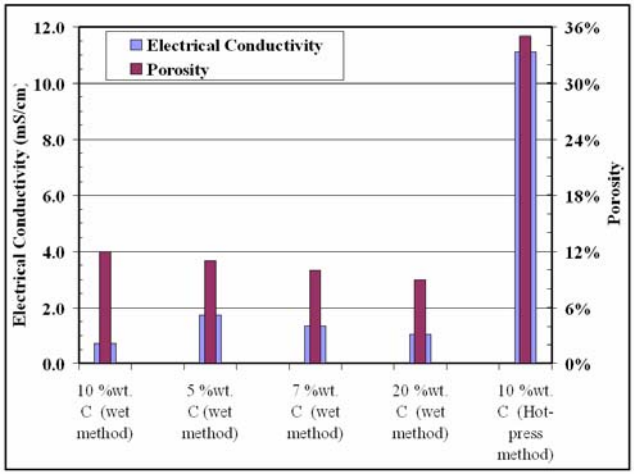

Figure 3. Electrical conductivity of different matrix compositions.

Electrochemical behavior of cofactor in the conductive matrix. Electrochemical behavior of a standard redox couple ferrocene methanol ($FcOH/FcOH^+$, water soluble standard) was undertaken to compare the composite matrix performance vs. a flat GC electrode. We found that the carbon black network in the composite matrix is effective enough to conduct the electron transfer reaction redox potentials for the $FcOH/FcOH^+$ couple. For the $NADH/NAD^+$ couple the composite matrix improved the oxidation potential more than 100 mV (i.e., more negative potential) than the GC electrode. This is very likely due to the simultaneous enhancement of both the electron and proton transfer in the cofactor oxidation/reduction. Several NADH oxidation mediators were evaluated as electron acceptors that potentially shift the oxidation potential to the negative direction. As shown in **Figure 4**, phenazine methosulfate gave larger catalytic currents due to NADH oxidation. The effects of phenazine methosulfate on NADH redox potential in the composite wafer are being carried out.

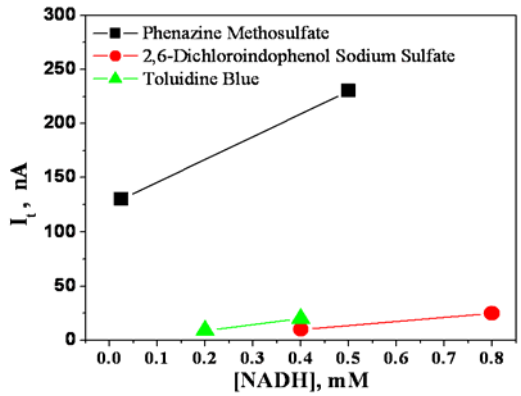

Figure 4. NADH electrocatalytic currents from several mediators.

Evaluation of the conductive matrix with immobilized enzyme. No significant change of ionic and electrical conductivities occurred with the inclusion of enzyme capture resin in the composite wafer matrix. Near 100% of GFOR enzyme was directly immobilized into the new prototype composite wafer with simple injection of the protein solution. The mechanism of capturing the electron from the reduced cofactor (NADPH) inside the GFOR enzyme dissolved in solution has been studied. The preliminary result shown in **Figure 5** indicates that the electron from the reduced cofactor of GFOR can be captured. This is evident by the lower concentration of the oxidized form of a blue indicating dye, 2,6-dichlorophenol indophenol, that turns colorless when it is reduced by an electron accepting mediator which captures the electron from the reduced cofactor (NADPH) inside GFOR. The re-oxidized (regenerated) cofactor ($NADP^+$) can continue to perform bioconversion of the substrate (e.g., glucose).

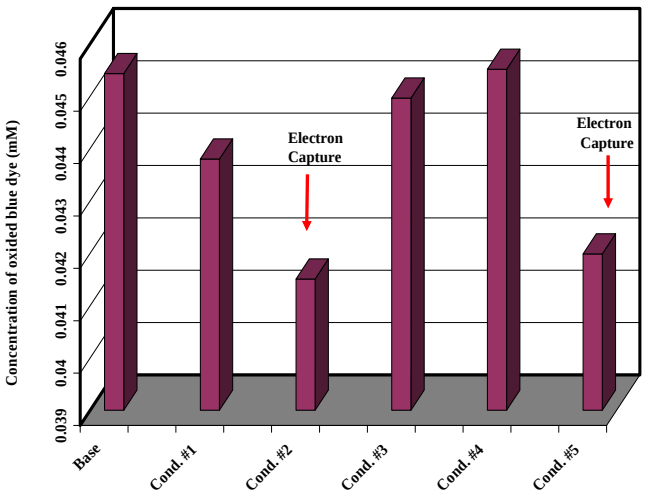

Figure 5. Electron capture from the cofactor in the GFOR enzyme.

Conclusions

We have successfully produced a composite matrix comprised of electronic/ionic mixed conductive wafer (carbon black particles with ion-exchange resin beads). The composite matrix reduces the oxidation potential of the $NADPH/NADP^+$ compared with a flat glassy carbon (GC) electrode. The matrix immobilized almost all of the introduced GFOR. A soluble mediator was used successfully as the electron acceptor to evaluate the capture mechanism of electron transfer from the cofactor inside GFOR.

Acknowledgments. The submitted manuscript has been created by the University of Chicago as Operator of Argonne National Laboratory ("Argonne") under Contract No. W-31-109-ENG-38 with the U.S. Department of Energy. The U.S. Government retains for itself, and others acting on its behalf, a paid-up, nonexclusive, irrevocable worldwide license in said article to reproduce, prepare derivative works, distribute copies to the public, and perform publicly and display publicly, by or on behalf of the Government.

ENZYME-CATALYZED OXYGEN REDUCTION: pH-DEPENDENT ELECTROSTATICS OF LACCASES

Alexander Kantarjiev, Boris Atanasov

Institute of Organic Chemistry, Bulgarian Academy of Sciences, Sofia-1113, Bulgaria

Plamen Atanassov

Department Chemical & Nuclear Engineering, University of New Mexico, Albuquerque, NM 87131

Introduction

Enzymatic bio-fuel cells employ enzymes to catalyze the corresponding anode fuel oxidation and cathode oxygen reduction reaction. Electron transfer between the enzyme and the electrode surface is usually facilitated by low-molecular weight mediators or via Direct Electron Transfer (DET) between the enzyme active site and electrode surface.[1] In the case of DET the structural and kinetic properties of the active site are of critical importance to the process effectiveness and impact cell design and performance.

Electrostatics of laccase (EC 1.10.3.2) is studied to reveal the pH-dependent mechanism of oxygen reduction by this enzyme. Laccases and other four-cooper oxidases (such as Bilirubin oxidase, for example) are being widely employed as cathode catalysts in bio-fuel cells demonstrating in many cases 4e$^-$ direct electron transfer mechanism at neutral or slightly acidic pH. It is universally accepted that copper sites play the key role in the catalytic process of coupled oxygen reduction and organic substrate oxidation. It is understood that this two-substrate, dual site enzymatic process follows formal "ping-pong" kinetics mechanism.

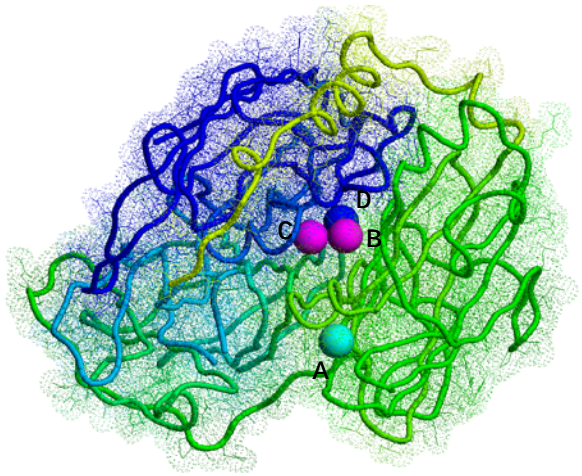

Figure 1. Structure of fungal laccases indicating the protein domains and its active site composed of four copper atoms grouped in two sub-sites: Cu (A) and the tri-copper site Cu (C-B-D)

Laccase is a member of four-cooper oxidases widely distributed in the living world. The presence of 4 Cu^{n+}, some of which change charges during redox action is coupled with transfer of four electrons (e$^-$) and four protons (H$^+$) to O_2. These enzymes demonstrate at quite limited pH-optimum of catalysis.[2] All of those features are indicators for quite substantial role of protein electrostatics for understanding principles of enzyme structure-function relationships and design of more effective electro-catalysis.

Main aim of this work is to analyze pH-dependent electrostatic free energy term, ΔG_{el}(pH) ("charge stability") of the protein (pdb1gw0.ent) at variable charges on 4Cu and 2O viewed in this study as reaction intermediates. To achieve this goal many other characteristics were calculated such as pH-dependent proton binding, pI and dipole moment(s) changes, influence of Cl$^-$ as inhibitor. All the calculations are being carried out in terms of given crystal structure of laccases available from the Protein Data Bank. For comparison analogous but limited calculation were made with laccases from other sources, ascorbate oxidase (AscO) and other members of the protein family.

Results and Discussion

More than 140 charge configurations at fixed protein structure were calculated simulating from completely Cu-depleted (APO) to all ligands targeted protein (HOLO). These configurations included all full combinatorial set of Cu-"valence hybrids" and possible O-intermediates. The pH-dependent "charge stability", ΔG_{el}(pH) is highly found to be sensitive to Cu^{n+} valence state and the position of Cu-ions. It was established that increasing the total charge in the copper centers ***n*** leads to an overall decrease in the protein stability. It was also shown that there is a very specific ranking of different copper sites in charge-dependent protein destabilization. The system is least sensitive for ***n*** changes is Cu type I (aCu-site), than followed by Cu type II (dCu-site) and most sensitive for charge accumulation in the Cu type III (b,cCu-site).

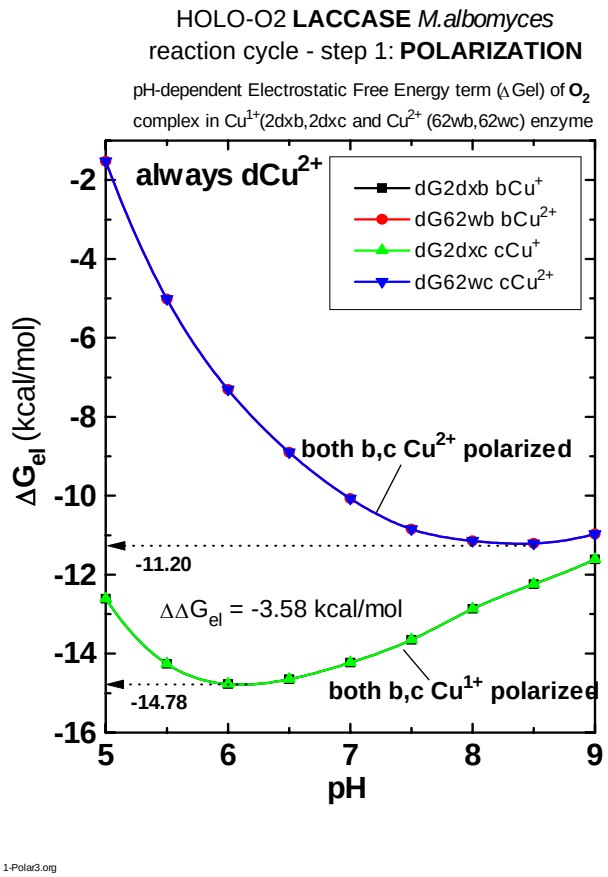

Figure 2. Electrostatic free energy calculation as a function of pH for laccase with fully oxidized copper B and C sites compared with the case of the same sites reduced.

New evidence was found that despite formal structural equivalence of bCu and cCu sub-sites (usually commonly described as undistinguishable type III copper centers) they behave energetically different. This difference is structurally expressed in the way that the bCu site is more close to the [2]O-atom from the residing oxygen undergoing reduction while the second [1]O-atom is more close to cCu and dCu ions. These configurations are found to be most sensitive to charge distribution variations. The proposed bCu..cCu sites non-equivalence for th is structure was at first shown in this study and explained as intrinsic property of O_2 activation and it is hypothesized that it plays significant role in the O-O splitting stage or the overall oxygen reduction reaction catalyzed by copper-containing oxidases.

Protein electrostatics allows us to unambiguously confirm the general assumption that the protein globule plays most significant role in "directing" the electron transfer process. It is of even more expressed in catalysis of such irreversible processes as oxygen reduction reaction. This effect is can be illustrated by charge-charge interactions visualized as a big "spring" the protein "shell", which favors reduced Cu+ making difference between sites (a<c<d<b) and thus correspond to directional electron transfer from aCu → bCu more than from aCu → cCu. Many indirect evidences shows fixed charge system on dCu^{2+}.

Inhibition of laccases by chloride ions has always been an impeding factor to their wider technological introduction in redox process catalysis. This inhibition mechanism was not well understood and thus there was no rational basis for decision-making in bio-fuel cell design solutions. This study attempted to address chloride inhibition, which is demonstrated quite unevenly among the copper-containing oxidase enzyme family. The fact that some copper-containing enzymes are inhibited by Cl^- and some are not was taken as an indication that the process is heavily influenced by the structure and accessibility of the oxygen-reduction active site (the tri-copper site). In this study, direct Cl^- binding to dCu was considered as inhibition of oxidase action. The calculation had shown, however, that the including Cl^- into the system do not change qualitatively its ET properties and it only slightly (c.a.0.3-0.4 kcal/mol) destabilizes the protein. In the case of ascorbate oxidase (AscO), an enzyme with quite similar 4Cu configuration in the active site, the azide ion (N_3^-) inhibitor is bond to corresponding bCu and not to dCu site. It is hypothesized in this study that in the case of laccase Cl^- obstrucs the water entrance "micro-channel" to the tri-copper oxygen reduction site. By this steric effect it prevents the conjugated proton transport to the reduced O-intermediates, thus preventing the completion of the oxygen reduction reaction. The paths of incoming molecular oxygen and expulsion of water molecules remain structurally unclear at this point. It should be noted, however that the overall redox process is highly "energy productive" and the protein is separated into 3 structural domains (even SS-linked). Given this structural features one can suggest that the protein globule dynamics during catalysis is very likely to ensure mass-transfer of reactant and the product in a concerted manner. Calculations of such transport, however, were outside of the scope of this work, which was limited to the electrostatics of the crystalline structure of laccases.

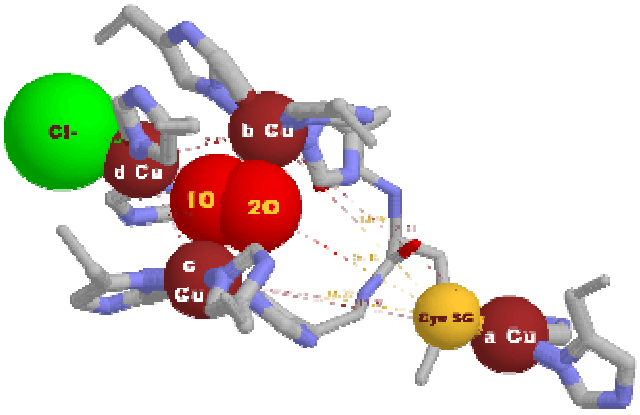

Figure 3. Structural representation of the active site of laccese inhibited by a chloride ion.

Conclusions

It has been established in this study that in 4Cu-enzymes oxidized Cu^{2+} destabilizes the overall protein and thus the structure energetically prefers the reduced Cu+ state. Such energetics supports electron transfer to the enzyme and thus facilitates the catalysis of the highly irreversible oxygen reduction reaction. The active site forms a true catalytic triad (b,c,dCu) resulting in highly asymmetric environment incorporating molecular oxygen. This environment is characterized by high electrostatic gradients between O-O and facilitates in consequence its hydrolytic breaking and "saturation" with H^+ completing by this an effective oxygen reduction as "concerted" process.

References

(1) Clabrese Barton, S; Gallaway, J.; and Atanassov, P.: Bio-Fuel Cells for Implantable and Micro-Scale Devices. *Chem. Rev.* **2004**, *104*, 4867-4886

(2) Solomon, E.I.; Sundaram, U.M.; and Machonkin, T.E:. Multicopper oxidase and Oxygenases. *Chem. Rev.* **1996**, *96*, 2563-2605.

ENZYME BASED HYDROGEN-OXYGEN FUEL CELL

Arkady Karyakin, Sergey Morozov, Mikhail Vagin, Elena Karyakina, Sergey Varfolomeyev

Faculty of Chemistry, M.V. Lomonosov Moscow State University, 119992, Moscow, Russia.

Introduction

Molecular hydrogen is considered nowadays as the most promising chemical fuel, in particular for fuel cells. Fuel electrodes use platinum (or platinum metals) as electrocatalysts. There are, however, crucial problems, which make impossible wide applications of fuel cells in future.

First, it is the problem with the *cost* and *availability*. Platinum-based fuel cells producing one kilowatt of energy will cost from $ 200 to $ 2000. Thus, the 100 kW engine will cost from $ 20 000 to $ 200 000, exceeding the cost of the whole car. Moreover, to equip 57.5 millions of cars available already in 2000 with the 100 kW fuel cells 11500 tons of Pt are required. It is much higher than the annual production (180 tons) and even comparative with the assured Pt resources (100000 tons).

Second, it is the *poisoning problem*. The cheapest hydrogen produced as reforming gas usually contains 1 ÷ 2.5 % of carbon monoxide (CO). However, even in the presence of 0.1 % CO the activity of platinum electrodes decreases irreversibly 100 times in 10 minutes. The only possibility to recover catalytic activity of platinum is to oxidize the absorbed CO at high electrode potential. However, in conventional fuel cell this requires the regime, which is closed to the short circuit. The latter obviously destroys the electrodes after a few cycles.

We propose biocatalysis as a valuable alternative to the catalysis by noble metals in respect to development of fuel electrodes. Certain enzymes being immobilized on electrode materials are able to deliver electrons between their active site and the electrode material, the phenomenon is called direct bioelectrocatalysis.

Bioelectrocatalysis of hydrogen oxidation and oxygen reduction. Hydrogen combustion reaction consists of the two redox half-reactions: hydrogen oxidation and oxygen reduction. The highest possible energy output of the fuel cell will be provided is oxygen is reduced into water without intermediate generation of hydrogen peroxide.

In nature there are enzymes *hydrogenases* responsible for activation and oxidation of molecular hydrogen feeding microorganisms with energy. Direct bioelectrocatalysis by hydrogenases has been reported more than 20 years ago by our group [1]. The most important feature of hydrogen enzyme electrode was a possibility to achieve hydrogen equilibrium potential pointing to possibility for 100% efficiency of energy conversion.

The most important feature of hydrogen enzyme electrodes is that they are practically insensitive to fuel impurities [2], and, thus, solve this crucial problem, which limits development of platinum-based fuel cells.

Considering oxygen reduction to water, there is a number of enzymes able to catalyze this reaction. First oxygen enzyme electrode was shown by Russian bioelectrochemical school more than quarter a century ago [3]. A certain disadvantage of enzyme electrocatalysis in this respect is that the enzymes do not catalyze oxidation of water into oxygen. An absence of the backward reaction does not allow achievement of O_2/H_2O equilibrium potential.

Enzyme based hydrogen-oxygen fuel cell. Both hydrogen and oxygen enzyme electrodes were combined in one system to elaborate the enzyme based hydrogen-oxygen fuel cell. We used as two kind of systems: fuel cell with liquid electrolyte, and fuel cell with solid electrolyte Nafion-type membrane separating anode and cathode [4].

Open circuit voltage of the membrane-containing fuel cell as a function of time is presented in figure 1. As seen, under flow of H_2 through compartment of hydrogen enzyme electrode an open circuit potential reaches the value of 1.15 V, which is at the record level for known hydrogen-oxygen fuel cells. In the absence of fuel cell voltage decreases, however, after restore of H_2 flow it again exceeds 1.1 V. A slow decrease of cell voltage with time is due to drying of this model system.

Conclusions

We have shown a possibility for construction of enzyme based hydrogen-oxygen fuel cell. Use of the enzymes instead of platinum metals solves the most crucial problem connected with the latter. In contrast to noble metals the enzymes are products of biotechnology and, thus, have a completely renewable source. Moreover, the cost of enzymes dramatically decreases upon their mass usage.

Enzymes as electrocatalysts of electrode reactions in fuel cells are highly specific to their reactions. This solves the third problem with platinum based fuel cells: decrease of energy conversion efficiency because of low selectivity. Indeed, as was shown, the enzyme based hydrogen-oxygen fuel cell displays the zero-current voltage at the record value.

Acknowledgement. Authors thank for financial support Program of RAS #26 on Hydrogen Energetics, INTAS Innovation grant 03-56-102, and Russian Science Support Foundation.

References

(1) Yaropolov, A.I.; Karyakin, A.A.; Varfolomeyev, S.D.; Berezin, I.V.; *Bioelectrochem. & Bioenergetics*, **1984** *12* 267-277.
(2) Karyakin, A.A.; Morozov, S.V.; Karyakina, E.E.; Zorin, N.A.; Perelygin, V.V.; Cosnier, S. *Biochemical Society Transactions*, **2005**, *33*, 73-75.
(3) Berezin, I. V.; Bogdanovskaya, V. A.; Varfolomeev, S.D.; Tarasevich, M.R.; Yaropolov, A.I. *Proc.Rus. Acad. Sci.*, **1978**, *240*, 615-618.
(4) Karyakin, A.A.; Morozov, S.V.; Karyakina, E.E.; Vagin, M.Yu.; Varfolomeyev S.D. *Patent of Russian Federation #* 2229515, **2004**.

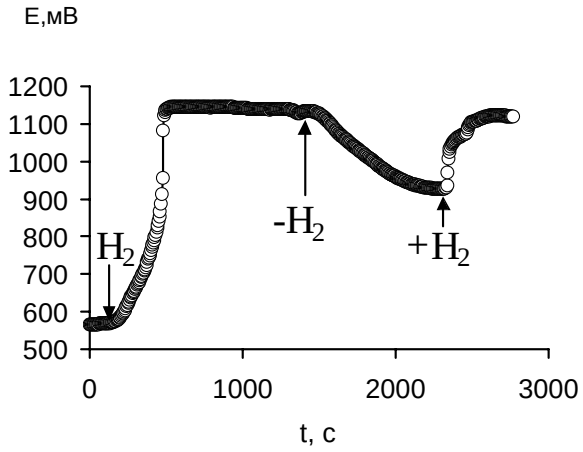

Figure 1. Zero current voltage of hydrogen-oxygen fuel cell with solid electrolyte membrane.

NANOBIOCATALYSTS FOR BIOFUEL CELLS

Ping Wang[1], Jungbae Kim[2], Hongfei Jia[1], and Xueyan Zhao[1].

(1) Department of Chemical Engineering, The University of Akron, Akron, OH 44325-3906, Fax: 330-972-5856, wangp@uakron.edu,
(2) Pacific Northwest National Laboratory

Abstract

Recent advances in nanobiocatalysis are promising for the development of high performance biofuel cells. Glucose oxidase electrodes were prepared via formation of composites with various nanostructured carbon materials such carbon fibers, carbon nanotubes, and nanoporous carbons. Significant enhancement on electrochemical reaction kinetics was observed on the composite-modified glassy carbon electrode. When these electrodes were applied in a model glucose/O2 biofuel cell, a power density of up to 960 μW/cm2 could be achieved. According to the quantitative analysis of the processes involved in the anode, the mass-transfer of mediator appeared to be the limiting factor to the power and current densities of biofuel cell. It is expected that the power density can be greatly improved by the improvement of electron transfer and optimization of the electrode structure.

ELECTRIC "CONTACTS" BETWEEN CONDUCTORS AND PROTEIN ACTIVE SITES – THE BASIS FOR BIOCHEMICAL FUEL CELLS. HYDROGEN-OXYGEN FUEL CELL.

S.D. Varfolomeyev, A.A. Karyakin[#], S.V. Morozov[#]

Institute of Biochemical Physics,
Russian Academy of Science, 119991, Moscow, Russia
[#]Moscow State University, 119992, Moscow, Russia

Introduction

The problems related to the mechanisms of electron transfer between electron-conducting structures (metals, semiconductors or organic conductors) and biopolymer molecules are central and most important in biofuel cells construction. Our interest in this area was to study the enzyme behavior at the interface "ionic conductor (electrolyte solution or solid electrolyte) - electron conductor (metal, carbon or semiconductor)". In the experiments with various enzymes, we have shown that the direct electron transport between a conductor and the active site of redox enzyme is feasible. The rates of electron transfer, which may well proceed by the tunneling mechanism, can exceed the rates of subsequent enzymatic steps. In this case, we can think of an electric "contact" between semiconductor and enzyme active site. The enzyme can act as electrocatalyst "pumping out" the electrons from conductor or donoring them into the conductor. This phenomenon was first revealed for blue copper-containing oxidase (laccase) reducing molecular oxygen to water; the source of electrons was the conductor matrix[1]. The phenomenon of bioelectrocatalysis is the basis for development of biological fuel cells. Different prototypes of hydrogen-oxygen fuel cells were constructed based on direct bioelectrocatalysis by hydrogenases and oxidases immobilized onto different carbon materials.

The phenomenon of direct electron transfer from protein active site to conductor (or reverse process) can be determined as DET-effect. Below are analyzed the DET-effect on an example of some enzymatic reactions.

Blue copper oxidase (laccase): The enzymatic electrochemical reduction of oxygen

Laccase is a copper-containing enzyme performing the four-electron reduction of oxygen, with different aromatic amines and phenols used as donors. The active site of the enzyme consists of four copper ions involved in a coordinated oxygen reduction. It was found that laccase in minor quantities (10^{-9} M) strongly shifts the stationary potential towards the zone of positive values and accelerates oxygen electroreduction[2]. The enzymatic nature of electrocatalysis in this case was proved by a specific inhibition of electrocatalytic effects by fluoride and azide ions, heat inactivation, and by comparing the pH dependence of the electrocatalytic effects and the catalytic activity in the oxidation of ferricyanide ion by oxygen. Experiments showed that the stationary potential of the electrode depends on oxygen partial pressure and the solution pH in accordance with the Nernst equation for the O_2/H_2O system. Rotating disc-electrode experiments did not detect intermediate hydrogen peroxide in the solution. The observed electrochemical process on the electrode with immobilized laccase is governed by the reaction of oxygen four- electron reduction to water:

$$O_2 + 4e^- + 4H^+ \rightarrow 2H_2O \qquad (1)$$

That was the first observation of DET-effect. This phenomenon was investigated experimentally in details[2].

Hydrogenase

As the carbon black electrode with immobilized hydrogenase from *Thiocapsa roseopersicina* was introduced into the buffer phosphate solution saturated with hydrogen, a potential equal to 0.000±0.001 V was set at the electrode (Fig.1).

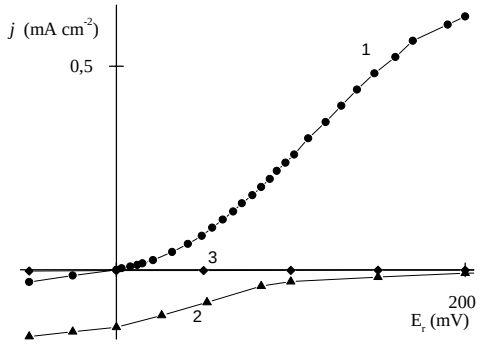

Figure 1. Carbon tissue electrode with directly adsorbed hydrogenase from *T. roseopersicina* in H_2 (1), Ar (2) and blank electrode (3). Phosphate buffer pH=7.0, 30°C. Potential vs. H_2/Pt electrode in same buffer.

Logarithm of current as a function of pH and logarithm of hydrogen partial pressure at different values of overvoltage was studied. The zero order of the electrocatalytic reaction rate with respect to substrate and product concentrations was observed. It was concluded that the hydrogen molecule addition and proton ejection out of the active enzyme center take place faster than the oxidation-reduction stages (electrochemical ones in the given case). To find the kinetics of electron exchange between the enzyme active center and the electrode, the dependence of current on overvoltage was considered. The absence of single slope of the polarization curve in semilogarithmic coordinates attests that, firstly, there is more than one stage (two by the number of transferred electrons) during the catalytic process, and, second, both these stages are dependent on potential and occur at relatively comparable rates. Thus, the formula for the description of the polarization curve should be complicated. The consideration of the process as a consequent two electrons transfer results in equation[3]:

$$j = \frac{\exp\left(2\frac{\alpha nFE}{RT}\right) - \exp\left(-2\frac{(1-\alpha)nFE}{RT}\right)}{K_1 \exp\left(\frac{\alpha nFE}{RT}\right) + K_2 \exp\left(-\frac{(1-\alpha)nFE}{RT}\right)} \qquad (2),$$

where K_1 and K_2 are the constants including the surface concentration of active enzyme and definite combinations of elementary constants. At $K_1 \neq K_2$ the branches of a polarization curve in positive and negative regions will be asymmetrical about the origin of the coordinates, as distinct from the case of single stage ionization reaction. Eq.2 describes the current-potential relationship well. The only kinetic scheme was found to obey the experimental data for hydrogenase catalysis, include the stages of electrochemical or one-electron redox steps. (Hydrogen - proton - electron -transfer, - electron - proton mechanism H_2peltelp mechanism). It was concluded that the kinetic properties of hydrogenase action obtained from electrochemical and homogeneous kinetics describe the same mechanism. The hydrogenase adsorbed on conductor possesses electrocatalytic activity in both the reaction of hydrogen oxidation and evolution. It is possible to describe quantitatively the observed electrocatalytic reactions. The data on the mechanism of hydrogenase action in electrocatalytic process coincide with those obtained in studying the homogeneous kinetics of this enzyme. In bioelectrocatalysis (according to the mechanism of direct electron exchange between the electrode and enzyme active site) it operated

in the same way as in the solution using the electrode as one of the substrates.

One of the most important problem of platinum-based hydrogen fuel electrodes is their poisoning by carbon monoxide. Despite CO is also an inhibitor of hydrogenase activity, the inhibition is completely reversible and characterized by a high inhibition constant. Thus, the use of biological catalysts is expected to avoid this crucial problem of modern fuel cells. Indeed, when the hydrogenase enzyme electrode was tested under different H_2 – CO mixtures, no recognizable inhibition was observed up to CO content of 0.1%. Only under 1% of CO the rate of hydrogen oxidation was decreased by approximately 10%[4]. Moreover, inhibition of hydrogen enzyme electrode by carbon monoxide is completely reversible. Even after exposing to pure carbon monoxide the hydrogenase electrode recovers 100% of its initial activity as soon as the atmosphere is changed back to hydrogen. We resume that using the enzymes as electrocatalysts one can solve the most important problem of the modern fuel cell technology: poisoning of the electrodes by fuel impurities.

The tunneling of electrons, a possible way for the explanation of DET-effects

Active sites of enzymes acting as catalysts of electrode processes are localized inside the protein globule. It is evident that under catalytic conditions electrons are transferred to sufficiently long distance by the DET mechanism. The main conclusion of the analysis given below is that the concept of the tunneling mechanism is adequate for the description of the DET effect. The simplest scheme contains a stage of electron transfer from the electrode to the active site of an enzyme and a reaction of a "catalytic" enzymatic transformation of an electron (or a vacancy) into the final product of the enzymatic reaction:

$$e \xrightarrow{k_1} e^{\#} \xrightarrow{k_{cat}} E + P \qquad (3),$$

where e and $e^{\#}$ are the oxidized and the reduced forms of the active site, k_1 is frequency or the rate constant of electron transfer between the electrode and the active site, k_{cat} is the catalytic rate constant of the enzymatic reaction characterizing the limiting stage of the catalytic process. In a stationary state with respect to $e^{\#}$, the intermediate form, with the material balance equation taken into account, the specific current from the electrode is expressed as:

$$j = -\frac{nFk_{cat}k_1}{k_1 + k_{cat}}[e]_0 \qquad (4),$$

where $[e]_o$ is the surface concentration of the enzyme. K_{cat} values for enzymatic reactions do not vary much and are distributed in a rather narrow zone around the average figure of 10^2 s^{-1}. The mechanism of electron tunneling in chemical and biochemical systems is a subject of a detailed analysis in the literature. The rate constant of electron tunneling depends on the height and the width of the barrier:

$$k_1(r) = v\exp(-r/A) \qquad (5),$$

where v is the frequency factor, r is the width of the barriers, A is a parameter whose value depends on the height of the kinetic barrier. Several quantum mechanical models of electron transfer allowing the values of the frequency factor and the parameter A to be calculated have been developed by now. The solution of the problem of tunneling across rectangular, triangular, and parabolic barriers with a continuous energy spectrum of electrons has been discussed in the literature. If to take into account the discrete character of the spectrum and motion of nuclei in molecules in electron tunneling between two molecules a theory of electron transfer in protein systems making it possible to calculate transfer rate constants on the basis of structure properties of the medium. It is to be emphasized that in all models of electron tunneling transition the dependence of transition rate constant on distance is expresses by Eq. 5. The physical sense and numerical values of the parameters v and A can vary depending on the model. According to the common model, the frequency factor v has a physical sense of the frequency of collisions of an electron with the barrier (the velocity of an electron in a molecule or a crystal) and equals ~ 10^{16} s^{-1}. The value of the parameter A having the dimension of distance is defined by the difference of electron energies and the height of the barrier. It is important to note that the magnitude of A only slightly depends on the shape of the barrier, the main factor determining its numerical value being the energetics of the process. It is of interest to evaluate the distances within which the rate of electron transfer to the active site of an enzyme is greatly exceeding the rate of catalysis. In this case the enzymatic reaction is the rate-determining stage. For carbon electrodes, it was found that for a parabolic barrier A = 0.594 Å. It was shown that for $k_{cat} = 10^2$ s^{-1}, $r_{cr} = 19.1$ Å. This means that if an electron-accepting particle in the active site of an enzyme is located at a distance from the electrode surface shorter than 19 Å, the rate of donation of electrons to the active site will surpass the rate of the catalytic stage and the catalytic enzymatic reaction will be the rate-determining stage. The model of electron transfer in bioelectrocatalysis can be verified by studying the dependence of the measured bioelectrocatalytic currents on the distance between the electrode and the electron-accepting point in the active site of an enzyme. A comparative study of DET-effects was conducted on electrodes obtained by enzyme adsorption directly on carbon and on carbon coated with a lipid monolayer. Electrodes without lipid monolayer and also with a monolayer of cholesterol in two orientations were prepared. Laccase was adsorbed on the surface of the lipid and electrocatalytic properties of the obtained systems were studied in the reaction of electrochemical reduction of molecular oxygen. Electrodes with a monolayer of adsorbed lecithin were also obtained and studied. The currents obtained in a system without cholesterol and with cholesterol in flat orientation are the same. With vertically oriented cholesterol the current is 5 times less. With the electrodes covered by lecithin the electron transfer efficiency is 270 times less. Thus, the concept of the tunneling of electrons accounts for the observed DET-effects. If the site accepting electrons from the electrode is located at a distance shorter than r_{cr} (r_{cr} 20-30 Å; the radii of protein molecules are 10-30 Å), the rate of its "occupation" with electrons will be much higher than the rate of the enzymatic reaction and the experiment will reveal the effects of a drastic acceleration of the electrochemical reaction by a protein catalyst.

Hydrogen-oxygen fuel cell

On the basis of immobilized hydrogenase and laccase was constructed the hydrogen-oxygen fuel cell with proton exchange membrane. The characteristics of the cell are presented in patent[5]. The great advantage of the enzymatic fuel cells is the renewable nature of the used catalysts. We believe that the future development of the enzymatic fuel cells technology will makes the advantage more and more attractive.

Acknowledgement. The financial support from INTAS grant 03-56-102 is greatly acknowledged.

References

(1) Berezin, I.V.; Varfolomeyev, S.D. *Enzym. Eng.* **1980**, *5*, 95.
(2) Bogdanovskaya, V.A.; Varfolomeyev, S.D.; Tarasevich, M.R.; Yaropolov, A.I. *Electrokhimiya*, **1980**, *16*, 763.
(3) Varfolomeyev, S.D.; Yaropolov, A.I.; Karyakin, A.A. *J. Biotechnology*, **1993**, *27*, 331.
(4) Karyakin, A.A.; Morozov, S.V.; Karyakina, E.E.; Varfolomeyev S.D., Zorin, N.A.; Cosnier, S. *Electrochem. Comm.*, **2002**, *4*, 417.
(5) Patent WO2004114494.

HIGH EFFICIENCY METHANOL CARBONYLATION PROCESS UTILIZING A GAS STRIPPED REACTOR AND IONIC LIQUID CATALYST SYSTEM

Gerald C. Tustin

Eastman Chemical Company
P.O. Box 1972
Kingsport, TN 37662

Introduction

Acetic acid (HOAc) is a commodity chemical with an annual worldwide demand in excess of 6.9 million metric tons.[1] Most of the acetic acid produced today is prepared by the carbonylation of methanol. Many technologies have been examined, and those examined up to 1993 are summarized in a review article.[2] The greatest advance in methanol carbonylation technology was the discovery of a homogeneous iodide-promoted rhodium catalyst system introduced by Monsanto. This technology was vastly superior to all previous technologies and was characterized by modest pressures (450-500 psig) and temperatures (175-190°C), high methanol conversions (99-100%), high acetyl selectivities from methanol (99-100%), and excellent rates (approximately 6 moles acetic acid/L-hr).

Although the original rhodium-catalyzed carbonylation process was a technical breakthrough, it was not perfect. The process requires approximately 14-15 wt. % water to maintain catalyst activity. Removal of this water is expensive. The catalyst also catalyzes the water gas shift reaction under methanol carbonylation conditions, and a loss of carbon monoxide efficiency results. Catalyst recycle is also a concern. The product is flashed at about 65 psig and 166°C after it leaves the reactor. The heel from the flash process contains the rhodium catalyst which is recycled to the reactor. If the depth of flash is too great, if there is not enough water present, or if the CO pressure is too low, the catalyst precipitates and fouls the evaporator. The flash process is a major bottleneck in the methanol carbonylation process.

Two technological advances have improved the methanol carbonylation process. One of these is the addition of lithium iodide to the Rh catalyst system.[3] The presence of the added salt resulted in a substantial increase in reaction rate. The Rh-Li system also allowed for the water level to be reduced to 4-5 wt. % which increased the CO efficiency from about 91 % to 97 % and lowered water separation costs. The depth of flash was also increased. Another major advance was the replacement of the rhodium catalyst with an iridium-ruthenium catalyst.[4] The process improvements resulting from the use of the Ir-Ru catalyst are comparable to those exhibited by the Rh-Li system.

Although significant improvements over the original Rh-catalyzed carbonylation process have occurred, several major opportunities for further improvement exist. These include elimination of the flash evaporator and further reduction in the water and methyl acetate (MeOAc) in the product exiting the reactor. Although several attempts have been made to operate the carbonylation process in the vapor phase with heterogeneous catalysts, none have been commercialized.[2]

The study presented herein describes another approach to catalyst immobilization: the use of a gas stripped reactor containing active catalysts dissolved in ionic liquids. Ionic liquids are appealing for this application because they have essentially no vapor pressure and hence stay in the reactor while products leave as vapor, they are thermally stable and reasonably inert under the reaction conditions, and they provide effective heat removal. Ionic liquids containing iodide ion solubilize the metal catalyst, stabilize the metal in its active state, and prevent the metal from volatilizing from the reaction mixture.

Experimental

Materials. Rhodium trichloride hydrate was provided by Johnson Matthey. Iridium trichloride hydrate was provided by Strem Chemicals. Palladium acetate was obtained from Aldrich. Butyltridodecylphosphonium iodide (BTDPI) was obtained from Cytec. 1-butyl-3-methylimidazolium iodide (BMIMI) was synthesized by the following procedure. 1-butylimidazole (400 g, 3.22 moles) was dissolved in tetrahydrofuran (400 mL) in a 3-liter flask equipped with a magnetic stir bar, reflux condenser and a pressure-equilibrated dropping funnel with a nitrogen inlet. Methyl iodide (570 g, 4.0 moles) was added from the addition funnel with stirring under nitrogen over seven hours at ambient temperature. The mixture was stirred for 2 hours at room temperature then refluxed overnight. The solvent and excess methyl iodide were then removed by distillation on a steam bath to provide BMIMI as a red-brown oil (870.7g). Methyltributylphosphonium iodide (MTBPI) was synthesized in an analogous fashion from tributylphosphine and methyl iodide. Methanol (MeOH) and methyl iodide (MeI) were reagent grade and were used without further purification.

Carbonylation reactions. The carbonylation procedure has been described in detail in the patent literature.[5] A brief but sufficient description will be provided here. The basic reaction system consisted of Brooks 5850 Series E mass flow controllers for gas delivery and an Alltech 301 HPLC pump for liquid feed delivery. The gas and liquid streams were fed to an electrically heated Hastelloy C vaporizer. The vaporized reactants were fed to an electrically heated Hastelloy C reactor containing the ionic liquid and catalyst, and the vapor product directed to a Hastelloy C condenser and product receiver. Pressure was maintained using a Tescom Model 44-2300 backpressure regulator. Heating and gas flow feeds were controlled by a Camile® 3300 Process Monitoring and Control System. Most of the reactions were performed in an unstirred reactor consisting of a 1.60 cm I.D. X 15.9 cm long Hastelloy C reaction tube fitted with a 5 micron Hastelloy C filter at the base which acted as a gas dispersion device and support for the ionic liquid catalyst system. Typical ionic liquid charge to the unstirred reactor was 10 mL which contained 0.32 mmole Rh. Some reactions were performed in a stirred 300 mL Hastelloy C autoclave with subsurface gas feed using the same feed and condensation systems used with the unstirred reactor. A typical ionic liquid charge to the stirred autoclave was 100 mL containing 3.2 mmoles Rh. Typical reaction pressures ranged between 200 and 250 psig, and typical reactor temperatures ranged between 190 and 250°C. Feed rates varied widely and are provided in the Results and Discussion section. Condensed methanol carbonylation products from the receiver were weighed and analyzed by gas chromatography using a 30 m X 0.25 mm DB-FFAP capillary column (0.25 micron thickness) programmed at 40°C for 5 minutes, 25°C/minute to 240°C and holding at 240°C for 1 minute using a thermal conductivity detector held at 250°C (injector temperature = 250°C).

Results and Discussion

Initial continuous methanol carbonylation experiments were performed in the unstirred reactor with a 10 mL charge of BMIMI containing 0.32 mmole Rh catalyst at 190°C and 200 psig with a 2.8 CO/1.0 MeOH/0.14 MeI molar ratio feed. The results are summarized in **Figure 1** which illustrates the acetic acid and methyl acetate space time yields and methanol conversions at three different space velocities (153, 302 and 455 hr^{-1}) over a period in excess of 200 hours. Essentially no decline in catalyst activity was observed over the duration of the experiment. At high space velocity, HOAc

space time yields exceeding 20 moles/L-hr were observed with about 90 % MeOH conversion. At the lowest space velocity the HOAc space time yield decreased, the HOAc/MeOAc ratio increased, and the methanol conversion approached 100 %. Acetaldehyde or propionic acid were not detected, and the condensed product contained only ppb levels of Rh. NMR analysis of the recovered ionic liquid revealed that about half of the butyl groups had been replaced by methyl groups but was otherwise unchanged.

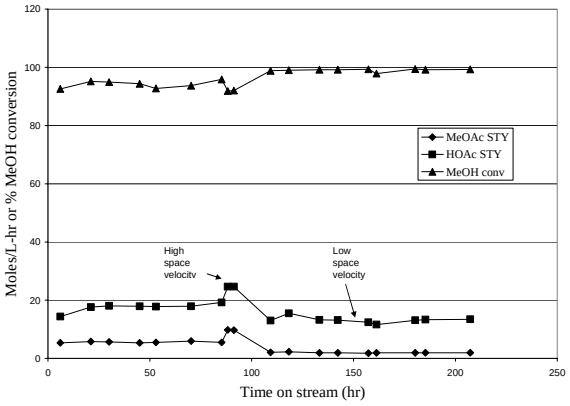

Figure 1. Space time yields and methanol conversions with the Rh/BMIMI catalyst system.

Although the initial results with the Rh/BMIMI catalyst system were very encouraging, the process used a large excess of CO. A CO conversion of approximately 70 % per pass is required for the process to be commercially attractive. Thus efforts focused on finding conditions that would allow for high CO conversion while retaining high methanol conversion and providing a product containing the lowest amounts of water and methyl acetate.

Two other metals were found to be active in the ionic liquid system: Pd and Ir. With the same temperature, pressure and reactant stream at a space velocity (SV) = 153 hr^{-1}, when Rh was replaced with Pd (0.325 mmole) in the 10 mL BMIMI ionic liquid, HOAc and MeOAc were produced at 2.4 and 3.6 moles/L-hr respectively at 59 % methanol conversion. This observation was interesting since Pd is normally a very poor methanol carbonylation catalyst, but the ability of high concentrations of iodide to promote methanol carbonylation with Pd has been reported in the literature.[6] Iridium is poisoned by excess iodide ion, and a soft Lewis base is needed to control the iodide level.[4] Therefore the Iridium system was prepared with Ir (0.30 mmole), Ru, Li in a 1/5/1 molor ratio respectively in 10 mL of a mixture prepared from a 2/1 molar ratio ZnI_2/BTDPI. At SV = 302 hr^{-1}, the iridium system produced HOAc and MeOAc at 4 and 5 moles/L-hr respectively at 92 % methanol conversion. Although Pd and Ir metals were active catalysts, Rh had the highest activity. Further development work was therefore directed towards optimizing the Rh system.

Although rhodium was examined in several different ionic liquids, three will be discussed here: BMIMI, BTDPI and MTBPI. For each salt, conditions were adjusted to optimize conversions. As conversions increase the vapor contains less CO, MeOH, MeOAc and water and more HOAc, and conditions need to be adjusted to keep the product in the vapor phase. This can be accomplished by lowering the pressure, by increasing the temperature or both. Since the phosphonium salts are more thermally stable than the imidazolium salt they were evaluated at higher temperatures and pressures whereas BMIMI was evaluated at lower temperatures and pressures. Definite differences were observed among the salts. For example, at 190°C BMIMI provided the highest carbonylation rates, but at 210°C BTDPI provided the highest CO conversion (77 %), and at 220°C MTBPI provided the highest HOAc/MeOAc ratio (38). To understand the differences among the three salts, a study of mass transfer effects was performed in the stirred autoclave using the 2.8 CO/1.0 MeOH/0.14 MeI feed at SV = 153 hr^{-1}. **Figure 2** summarizes the results.

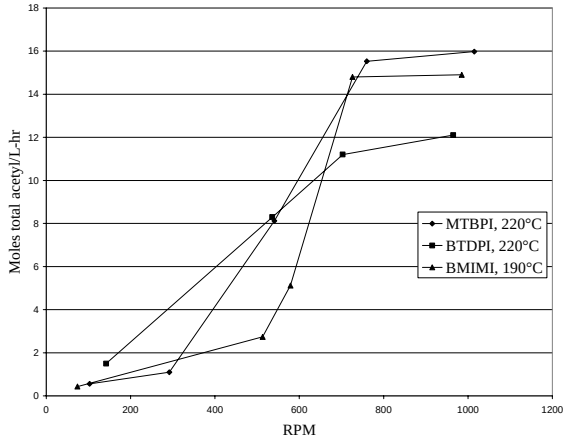

Fugure 2. Total acetyl production rate at various stirring rates.

At low stirring rate the catalyst is not in its active state, there are no water gas shift products in the vent gas and abundant methyl ether is produced. As the stirring rate increases the catalyst becomes active, the vent gas contains water gas shift products, and negligible methyl ether is produced. The ultimate rates achieved appear to correlate inversely with the ionic liquid melt viscosity at reaction temperature (25 cp for MTBPI, 37 cp for BMIMI and 51 cp for BTDPI).

Eventually conditions were optimized utilizing MTBPI as the preferred ionic liquid to provide commercially acceptable performance. When 1.28 CO/1.0 MeOH/0.1 MeI molar ratio were fed at SV = 110 hr^{-1} to a 0.057 molar Rh in MTBPI at 230°C and 225 psig, acetic acid was produced at a rate of 17 moles/L-hr at 76 % CO conversion and 100% MeOH conversion. The HOAc/MeOH ratio was 18 and the product contained only 1.1 wt. % water.

Conclusions

Iodide-containing ionic liquids provide an excellent medium for vapor phase methanol carbonylation and eliminate the need for a separate flash evaporator. The high rate of reaction coupled with the very high purity of the product result in reduced reactor costs, reduced liquid recycle and separation costs.

Acknowledgement. The author acknowledges Eastman Chemical Company for supporting this work and Regina Moncier for technical assistance.

References

(1) Anon., *Chemical Week* **2004**, June 30/July 7, 40.
(2) Howard, M.J., Jones, M.D., Roberts, M.S., Taylor, S.A., *Catalysis Today* **1993**, *18*, 325.
(3) Smith, B.L., Torrence, G.P., Murphy, M.A., Aguilo, A., *Journal of Molecular Catalysis* **1987**, *39*, 115.
(4) Sunley, G.J., Watson, D.J., *Catalysis Today* **2000**, *58*, 293.
(5) Tustin, G.C., Moncier, R.M., International Publication Number WO 03/093211, **2003**.
(6) Yang, J., Haynes, A., Maitlis, P.M., *Chem. Commun.* **1999**, 179.

EFFECT OF PROCESS PARAMETERS ON LIGHT OLEFINS PRODUCTION FROM METHANOL AND SYNGAS OVER SAPO CATALYSTS

Luckner Jean[a], Xiwen Huang[a] and James A. Guin[a]
Gregory C. Turpin[b] and Richard D. Ernst[b]

[a]Department of Chemical Engineering
Auburn University, Auburn, AL, 36849-5127
[b]Department of Chemistry
University of Utah, Salt Lake City, UT, 84112-0850

Introduction

The recent spike in energy prices has renewed attention on the production of chemicals from sources other than petroleum and focused attention on fossil fuels which are currently not recovered. In this light the use of SAPO catalysts in converting syngas either directly or indirectly to chemicals e. g. C_2-C_4 olefins, is of interest. The main feedstock of current interest is remote or flared natural gas, although any feedstock convertible to syngas is technically viable. This means that coal and biomass are potential resources for chemicals currently produced from petroleum. We are especially interested in C_2-C_4 olefins.

Flanigan, et al. have presented many of the most important properties of the SAPO catalysts in their foundational work[1]. A good review of the chemistry of methanol to hydrocarbons is presented by Stocker[2]. In his review it is noted that the pathway for methanol to olefins (MTO) is via a consecutive reaction with the dimethyl ether (DME) intermediate.

Many parameters such as acidity, pore size, composition, and method of preparation influence the activity of SAPO catalysts. Thus a particular SAPO, e. g., SAPO-34, may behave differently depending on its history and manner of preparation. A main obstacle in the MTO process is the rapid deactivation of the catalysts due to coke formation; however, regeneration is possible by oxidation as in a recirculating fluid bed. Here we have studied the effect of particle size on the activity, selectivity and lifetime of several small pore SAPO catalysts in the MTO reaction. Particle size variation was accomplished by grinding. It is possible that grinding could induce changes in the crystalline structure of the catalysts, however, this was not determined in our study, the main focus being on the particle size variations and the resulting reaction effects. A few other studies have examined the effects of particle size on this reaction[3,4]. We also report preliminary results on the effect of Ru incorporation on SAPO performance.

Experimental

The original SAPO catalysts used in our present work were samples prepared previously in our laboratory by Adekkanattu[5-8]. Studies were performed on SAPO-34, 44, 47, and 56. Original samples were ground in a Wig-L-Bug (Dentsply/Rinn) grinder with agate vial and ball for various times. Particle size was examined by SEM before and after grinding.

MTO reactions were performed at 1 atm in a quartz tube fixed bed, generally at 400 ^oC, using 0.3 g catalyst and 0.003 ml/min liquid methanol vaporized into nitrogen at 36 ml/min. (WHSV = 0.5 hr^{-1}). In addition to particle size, effects of temperature and incorporation of Ru were also studied[9]. Products were analyzed by GC with FID and Plot-Q capillary column. More details are provided in the thesis by Jean[10].

Results and Discussion

Figure 1 shows SEM micrographs of (a) the original SAPO-44 particles and (b) after grinding for 15 min. The reduction in particle size is fairly obvious from the scales on the figures, although some of the finer particles tend to form agglomerates. **Figures 2** (a) and (b) show the product distribution from MTO reactions over these SAPO-44 particles. We see that the ground particles have longer lifetimes, having increased from *ca.* 4 hrs to 10 hrs for the production of C_2-C_4 olefins. The selectivity of ethylene to propylene is not appreciably altered by the size reduction, however a notable change in selectivity to DME is apparent, as a result of the grinding. This latter finding is in keeping with the product distribution expected from particle size reduction in a diffusion controlled reaction with DME intermediate, i. e., an increase in selectivity of the intermediate due to lower intraparticle diffusional resistance[11]. As shown in **Figure 3**, similar results were obtained at 5 and 10 min grinding times, although particle sizes at lesser grinding times as viewed by SEM were not dramatically different from **Figure 1**(b). Similar changes in catalyst lifetime and DME selectivity, though not as large, were found in the performance of SAPO-34, 47, and 56. In a few cases, the grinding process caused a decrease in activity. An attempt to restore the activity of a spent SAPO-56 sample was unsuccessful, perhaps indicating the deactivation process, e. g., coke deposition, was uniformly spread throughout the particles, as opposed to being preferentially located around the external surface.

Figure 4 shows the performance of Ru-SAPO-44. Comparison with the unmodified catalyst in **Figure 2**(a) shows a small improvement, *ca*. 1 hr, in C_2-C_4 olefins based lifetime. Ru-SAPO-56 was also slightly improved, while, SAPO-34 was not improved by the Ru addition. These results are interesting, however, more work would be required, perhaps with other metals and conditions to fully determine the benefits of metals addition to the SAPOs.

Conclusions

Particle size reduction shows potential as an effective way to increase lifetime of SAPO catalysts based on C_2-C_4 olefins production, although for a completely deactivated catalyst grinding alone will not regenerate the catalyst. The selectivity of the intermediate DME is increased by particle size reduction in keeping with diffusional effects on selectivity of an intermediate in a series reaction pathway. Ru addition had only a small effect on the SAPO lifetimes in this limited study.

Acknowledgment. This research was supported by the U.S. Department of Energy Office of Fossil Energy, National Energy Technology Laboratory (NETL), under DOE Contract DE-FC26-02NT41594. The authors wish to acknowledge Dr. P. M. Adekkanattu for preparing the original SAPO catalysts.

References

1. Flanigan, E. M., Lok, B. M, Patton, R. L. and Wilson, S. T.: *Proc. 7th. Int. Zeolite Conf.*, Tokyo, 103, **1986**.
2. Stocker, M., *Microporous and Mesoporous Materials* 29, **1999**, 3 – 48.
3. Chen, D., Kjell, M. Fuglerud, T., Holmen, A., *ibid.*, 191.
4. Dahl, I. M. Wendelbo, R., Andersen, A., Akporiaye, D. Mostad, H. Fuglerud, T., *ibid.*, 159.
5. Annual Report for Period May 2001- May 2002, DOE Cooperative Agreement No. DE-FC26-99FT40540, Prepared by Consortium for Fossil

Fuel Science, University of Kentucky.
6. Annual Report for Period May 2002- May 2003, DOE Cooperative Agreement No. DE-FC26-02NT41594, Prepared by Consortium for Fossil Fuel Science, University of Kentucky.
7. Obrzut, D.L., Adekkanattu, P. M., Thundimadathil, J.,Liu, J., Dubois, D.R., Guin, J.A., *React. Kin. Catal. Lett.*, 80(1) **2003** 113.
8. Dubois, D.R., Obrzut, D.L., Liu, J. Thundimadathil, J., Adekkanattu, P. M., Guin, J. A. , Punnose, A. Seehra, M. S., *Fuel Proc. Technol.*, 83(1-3), **2003**, 203.
9. Wilson, D.R., Stahl, L., Ernst, R. D., *Organometallic Synthesis*, 3, **1986**, 136.
10. Jean, L., M. S. Thesis, Auburn University, **2005**.
11. Petersen, E. E., *Chemical Reaction Analysis*, Prentice Hall, **1965**, p. 97.

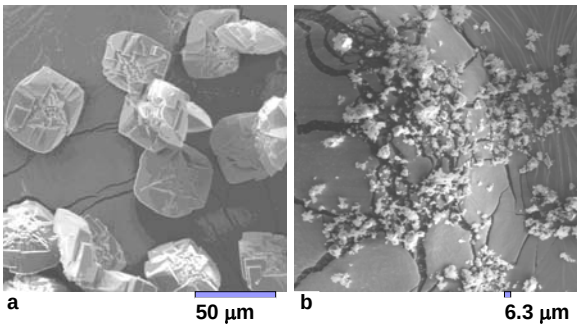

Figure 1. (a) SAPO-44 (Original Particles) (b) SAPO-44 (After 15 min Grinding)

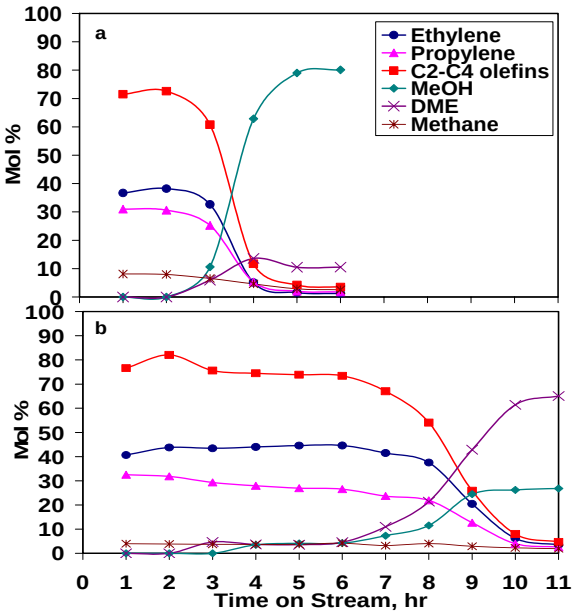

Figure 2. Product Distribution over: (a) Original Particles; (b) Ground Particles.

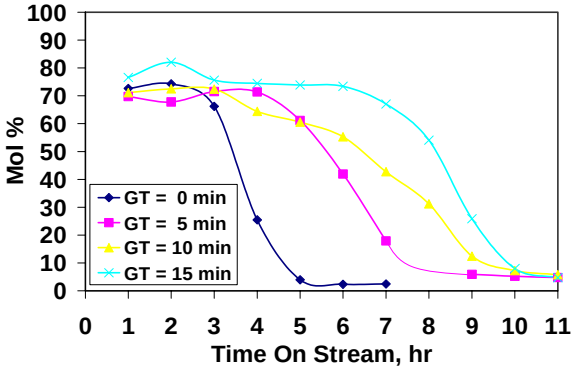

Figure 3. Effect of Grinding Time (GT) on C_2 - C_4 Olefins Production over SAPO-44.

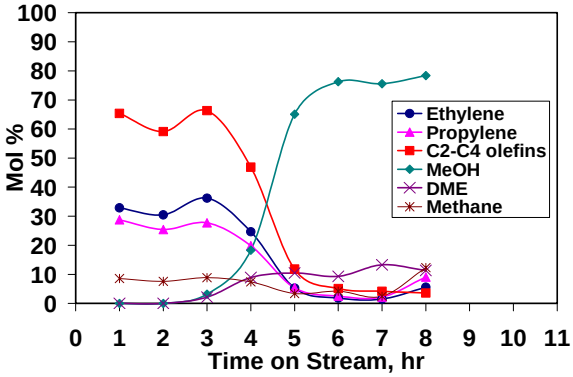

Figure 4. Product Distribution over Ru-SAPO-44.

STABILITY AND STRUCTURE OF COBALT CATALYTIC SYSTEMS IN FISCHER-TROPSCH SYNTHESIS: SUPERCRITICAL FLUID MEDIA VERSUS CONVENTIONAL GAS-PHASE MEDIA

N. O. Elbashir[a], P. Dutta[b], M. S. Seehra[b], C. B. Roberts[a]

[a]Department of Chemical Engineering, Auburn University, AL 36849,
[b]Physics Department, West Virginia University, Morgantown, WV 26506

1. Introduction

The limitations of the conventional media (gas-phase and liquid-phase) for Fischer-Tropsch synthesis (FTS) have driven research towards the application of supercritical fluid (SCF) solvents. The objective is to improve product control in the liquid fuels range and provide an opportunity for selective control of hydrocarbon distribution. The advantages of utilizing SCF solvents in the FTS reaction can be attributed to the fact that they offer high diffusivities (relative to a liquid phase FTS) and high solubilities and improved heat transfer (relative to a gas phase FTS). Utilization of cobalt-based catalysts in the FTS is known to provide the best compromise between performance and cost for the synthesis of hydrocarbons from syngas. Cobalt catalysts were also found to give the highest yields and longest lifetime producing mainly linear alkanes (paraffins)[1]. Since cobalt catalysts are not inhibited by the water-gas-shift (WGS), they give high productivity at high syngas conversion[2]. The efficiency of the synthesis process is critically dependent on the effectiveness and the stability of the cobalt catalyst. Most of the industrial cobalt-based systems used in the FTS reaction are either alumina supported or silica supported catalysts. Therefore, cobalt dispersion on the supported catalyst surface[3] and the interaction of the Co with the metal oxide support (which affects the electronic density as well as the structure of the metal crystallites[4]) are assumed to play significant roles in the catalyst performance measured by the hydrocarbon selectivity (C_{5+}) and the catalyst activity.

The stability of the cobalt catalyst structure represents a major challenge to commercial-scale plants. The catalyst cost in addition to its regeneration cost represents a considerable proportion of the overall process cost. In many cases the cost of regenerating the catalyst is more expensive than the fresh catalyst cost[5]. Deactivation of the catalyst was assumed to be due to carbonaceous formations (specifically crystalline carbides) in the catalyst surface[6], and also as a result of re-oxidation by the by-product water[7].

Several techniques (XRD, magnetization, and electron magnetic resonance) were used to characterize our catalysts to determine the surface structure of the catalyst and the electronic states (Co^0, CoO, Co_3O_4, Co^{2+}) before and after the reaction. Our objective is to study the sensitivity of the supported-cobalt catalyst structure (physico-chemical characteristics, oxidation states, and crystalline structure of the active phase) during the FTS reaction. In general, it has been shown that supercritical phase FTS results in better catalyst stability at long time-on-stream (TOS) compared to conventional gas-phase FTS.

2. Experimental

2.1 Catalysts. Three catalytic systems were tested under both conventional gas-phase and supercritical phase FTS (15% Co/SiO_2 HSA supported on high surface area silica, 15% Co/SiO_2 LSA supported on low surface area silica, and 15% Co/Al_2O_3). The two silica supported catalysts were prepared in our lab[8]. The alumina catalyst is a commercial catalyst purchased from United Catalyst Co. The silica supported catalysts were reduced in hydrogen environment, while the alumina supported catalyst was reduced in carbon monoxide environment.

2.2 Catalyst Characterizations. Room temperature X-ray diffraction (XRD) patterns of these catalysts were obtained with a Rigaku diffractometer using CuK_α radiation with λ = 0.15418 nm. Measurements of magnetization M versus temperature T and magnetic field H were done with a commercial SQUID (superconducting quantum interference device) magnetometer. Electron magnetic resonance (EMR) studies were carried out at the X-band frequency of 9.278 GHz with a variable temperature cryostat from Oxford Instruments. In this system, the microwave cavity remains at room temperature whereas the sample temperature can be varied from 4 K to 300 K. In the EMR resonance condition $h\nu = g\mu_B H_0$, the microwave frequency ν is accurately measured by a frequency counter and the resonance field H_0 by a NMR probe. The magnetic field is modulated at 100 kHz so that the experimental traces represent dP/dH versus H, with P being the power absorbed. The back ground for the magnetic theory and the interpretation of the magnetic data was discussed in some detail in our previous study [8].

2.3 Fischer-Tropsch Studies. The FTS reaction was carried out in a high-pressure FTS unit. A detailed description of this unit has been given elsewhere[9]. Hexanes (HPLC grade purchased from Fishers Co.) was used as the solvent for the supercritical phase FTS studies. The molar ratio between hexanes/syngas was kept at 3/1 whereby the syngas (H_2/CO =1) flows was at a rate of 50 $sccm/g_{cat}$. In this study we referred to the supercritical hexanes FTS experiments as SCH-FTS.

Analysis of reactants and products was carried out by two online GCs. The results from the two GCs were used for conversion and selectivity calculations. A Varian 3300 GC with capillary column (DB-5) and a FID detector was used for the analysis of C_2-C_{40} hydrocarbons and oxygenates. Analysis of permanent gases (H_2, CO, N_2, CH_4, CO_2, C_2H_4, and C_2H_6) was conducted by a Varian CP-3800 GC with a packed column (Hayesep-DB100/120) and TCD detector. The online injection of our samples to the two GCs was carried out by two automated six-way-valves. Quantitative analysis of the results from the Varian CP-3800 provided the necessary data for the calculations. Reactants conversion (CO conversion and H_2+CO (syngas) conversion), CH_4 selectivity, CO_2 selectivity, and C_2 (ethane and ethylene) selectivities were calculated using the response factor of N_2 from the TCD analysis as a reference. On the other hand, hydrocarbon product distributions (i.e. C_2 to C_{30} selectivity data) were determined from the FID and TCD analysis as described in detail elsewhere [9].)

3. Results and Discussion

Table 1 shows a summary of our catalyst XRD and EMR characterizations before (fresh calcined catalyst) and after the reaction (used catalyst after either conventional gas-phase FTS or SCH-FTS). Detailed discussions on the characteristics of fresh catalyst were given elsewhere[8]. Summarizing the results of Table1, we conclude that the LSA 15% Co/SiO_2 used sample (under gas-phase FTS condition) contains Co^0 only which is the product of the reduction of Co_3O_4 in the calcined unused sample. In the HSA 15% Co/SiO_2 used sample under (SCH-FTS conditions), we observed Co^0/CoO composite, the quantity of CoO being much less than that of Co^0. Thus either the reduction of Co_3O_4 to Co^0 is not complete since some CoO is observed or some oxidation of Co^0 to CoO has taken place subsequent to the FTS experiments because of the high surface area of the catalysts.

Table 1. Summary of the XRD and EMR characterization of the used cobalt-based catalytic systems under both gas-phase FTS and SCH-FTS.

	XRD & EMR Characterizations	
	Fresh	**Used**
Silica Catalysts		
HSA 15%Co/SiO_2 (Used 10 days in gas-phase)	SiO_2, Co_3O_4	SiO_2 (quartz, cristobalite, tridymite)
LSA 15%Co/SiO_2 (Used 13 days in SCH-FTS)	SiO_2, Co_3O_4, Co^{2+}	fcc-Co^0, CoO, Co_3O_4 (small) SiO_2 (cristobalite)
Alumina Catalysts		
15%Co/Al_2O_3 (Unused, reduced catalyst)	Co_3O_4;γ-Al_2O_3 ε-Al_2O_3 CoO, hcp Co^0	–
15%Co/Al_2O_3 (Used 13 days in SCH-FTS)	Co_3O_4, δ-Al_2O_3, Co^{2+}-	hcp-Co^0, CoO, Co_3O_4; γ-Al_2O_3, ε -Al_2O_3
15%Co/Al_2O_3 (Used 7 days in gas-phase-FTS)	Co_3O_4, δ-Al_2O_3, Co^{2+}-	hcp-Co^0, fcc-Co^0; γ-Al_2O_3

Three samples of the alumina supported catalysts were characterized; (1) unused 15% Co/Al_2O_3 which was reduced in CO environment.; (2) used sample of 15% Co/Al_2O_3 after SCH-FTS condition for 13 days; (3) used sample of 15% Co/Al_2O_3 after gas-phase FTS for 7 days for temperatures up to 260°C. Partial reduction of the alumina supported catalyst in CO environment (the unused sample) prior to in situ reduction with the syngas during FTS allows us an opportunity to evaluate the extent of in situ reduction. Our XRD characterization of the unused alumina catalyst showed two Al_2O_3 phases and Co_3O_4 with only a hint of the presence of the hexagonal-close-packed (hcp) phase of Co^0. For the used sample after supercritical phase operation the characterizations show presence of some CoO and hcp Co^0 and absence of Co_3O_4. Thus reduction of Co_3O_4 to CoO and hcp Co^0 has occurred. For the used sample from gas-phase FTS both fcc Co^0 and hcp Co^0 are present. Thus the reduction of Co_3O_4 to Co^0 is complete for that sample. The particle sizes of Co^0 determined from the width of the XRD peaks are 13 nm for fcc Co^0 and 14 nm for hcp Co^0.

Figs. 1 and 2 show an example of stability tests on the alumina-supported catalyst (15% Co/Al_2O_3) under different reaction conditions in the SCH-FTS and gas phase-FTS reactions at relatively long TOS. Syngas conversion is used to represent the activity of the catalyst. During the SCH-FTS testing, the catalyst showed good stability in syngas conversion (~ 80%) at 240 °C and 60 bar. The temperature was then decreased to 230 °C, while the pressure was kept constant at 60 bar. As a result, syngas conversion decreased to ~58%. A stable trend was observed under these conditions for more than 48 hrs TOS. The stability test was then followed by increasing the temperature to 250 °C and the pressure to 65 bar. At these conditions, syngas conversion reaches its highest level, 93%, at the initial 2 hrs TOS and then declined to ~87% for more than 100 hrs TOS. The aforementioned conditions were selected based on our previous investigations of the alumina-supported catalyst, whereby an optimum performance in both activity and selectivity was observed[9]. Upon returning to the initial conditions (240 °C and 60 bar), no significant changes in either syngas conversions was observed as shown in Fig.1.

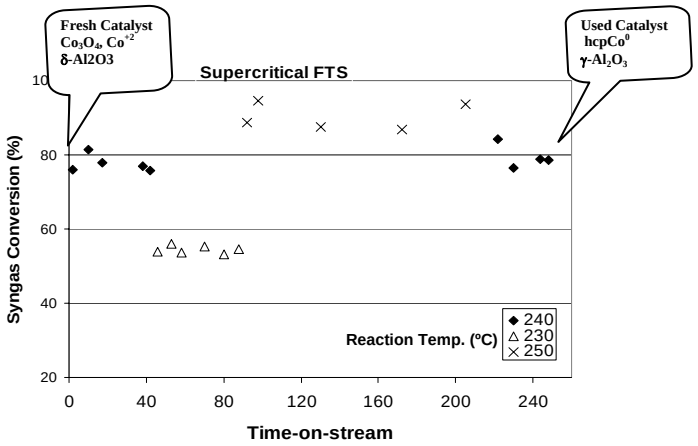

Figure 1. Stability of the 15% Co/Al_2O_3 catalyst activity (syngas conversion (%))with TOS in SCH-FTS at different reaction conditions (240 °C and 60 bar; 230 °C and 60 bar; 250 °C and 65 bar; and 240 °C and 60 bar). P_{syngas} = 20 bar, syngas flowrate 50 sccm/g_{cat}, and hexane/syngas molar ratio is 3.

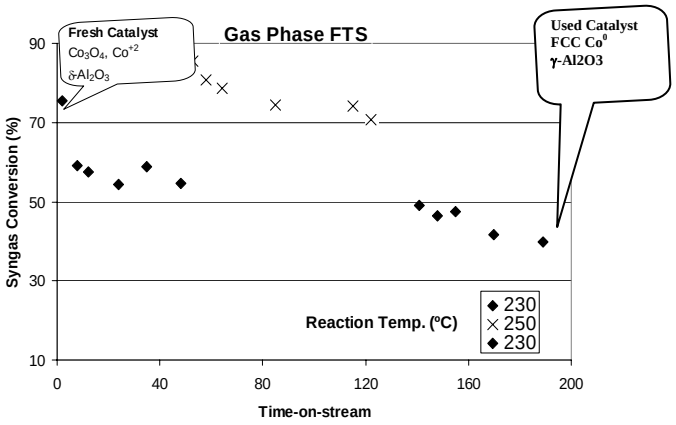

Figure 2. Stability of the 15% Co/Al_2O_3 catalyst activity (syngas conversion (%)) with TOS in gas phase-FTS at different reaction conditions (230 °C and 20 bar; 250 °C and 20 bar; and 230 °C and 20 bar). P_{syngas} = 20 bar, syngas flowrate 50 sccm/g_{cat}.

In the gas phase-FTS (Fig.2), the stability test was initialized at 230 °C and 20 bar for 50 hrs TOS. The catalyst reached a steady value of activity within 10 h of ~59% syngas conversion. Upon increasing the temperature to 250 °C, significant increase in syngas conversion (~88%) was obtained during the first 7 hrs. However, as the TOS was increased (up to 45 h) the syngas conversion decreased to reach 74%. The activity reached a steady value after 70 hrs TOS under the above conditions. Returning to the low temperature conditions (230 °C) resulted in a significant drop (c.a. 25%) in syngas conversion.

In order to understand the role of the reaction media on the catalyst structure and activity we conducted a correlation between the stability tests and the used catalyst characteristics. As discussed earlier our findings show that the dominant cobalt phase of the used sample from SCH-FTS is hcp Co^0, whereas, the dominant phase in the used sample from gas-phase FTS is fcc Co^0. It is noteworthy to mention here that the fcc Co^0 was not detected in the reduced catalyst before the reaction (reduced-unused 15% Co/Al_2O_3). This suggests that the in situ reduction during the SCH-FTS stabilizes the hcp Co^0 form, which has more surface defects (corners and edges) in the metallic phase than the cubic phase one (fcc Co^0). In a previous study, Rathousky, et al. stated that the metallic cobalt formed on the outer surface of the CoO crystal-lines enhances the adsorption centers of weakly bonded carbon monoxide molecules[14]. Another reason that may contribute to the stability in the catalyst activity in the SCH media is the good temperature distribution inside the fixed-bed-reactor compared to the poor one in the gas-phase media[16]. The control of temperature distribution in the reduction process is known to avoid the increase of cobalt-support interactions and agglomerations of cobalt nano-particles[10]. Our results shows that there is no significant difference between cobalt particle size of the unused catalyst and that of used catalyst from SCH-FTS (both have size >12 nm)[17]. Small particles could easily be reoxidized by water and other reaction conditions during the FTS reaction.

The used silica-supported catalysts showed different characteristics from that of the alumina supported ones. The XRD characterizations of the silica supported catalyst (Table 1) show the presence of quartz, cristobalite, and tridymite silicate forms; however, minimal amounts were detected in SCH-FTS used catalyst. It is also important to mention that no Co^0, CoO, Co_3O_4 XRD pattern was observed in the used catalyst from the gas-phase where only silicate forms were detected. This suggests that the in situ reduction of the catalyst during the gas-phase FTS is minimal. The presence of the silicate forms in the two used catalysts suggests that the in situ reduction during the FTS reaction is different from that in the alumina-supported catalyst.

4. Conclusions

Our XRD and magnetic characterizations of the used catalysts show that in situ reducibility of the cobalt oxide takes place during the FTS reaction in both gas-phase FTS and SCH-FTS conditions. In the latter, the in situ reduction of Co_3O_4 gave active crystal-lines of hcp and fcc Co^0 that were found to be very stable for a long TOS. As a result, the activity and selectivity of the catalyst in the SCH medium is more stable and recoverable than that under gas-phase FTS conditions. Our findings also show that the in situ reduction pathway of the silica supported catalyst is different than that of the alumina supported one; however, a stable form of fcc Co^0 has also been detected on the used catalyst from the SCH-FTS operation. Detailed discussions on the influence of the catalyst surface characteristics on both the activity and selectivity of the FTS reaction in both gas-phase and SCH phase were covered elsewhere[17].

Acknowledgments. The authors would like to acknowledge the financial support of the Consortium for Fossil Fuel Science (under the Department of Energy Grant DE-FC26-02NT41594) and by Nippon Oil Corporation, Japan (CBR and NOE).

References

(1) Chaumette, P.; Verdon, C.; Boucot, P. *Topics in Catalysis* **1995**, *2*, 301-311.
(2) Van Berge, P. J.; Everson, R. C. *Studies in Surface Science and Catalysis (Natural Gas Conversion IV)* **1997**, *107*, 207-212.
(3) Tauster, S. J.; Fung, S. C. *J. Catal.* **1978**, *55*, 29.
(4) Iglesia, E.; Soled, S. L.; Fiato, R. A. *J. Catal.* **1992**, *137*, 212-224.
(5) Zhan, X.; Arcuri, K.; Huang, R.; Agee K; Engman, J.; Robota, H. J. *Prep. Pap.-Am. Chem. Soc., Div. Pet. Chem.* **2004**, *49*, 179.
(6) Gruver, V.; Zhan, X.; Engman, J.; Robota, H. J. *Prep. Pap.-Am. Chem. Soc., Div. Pet. Chem.* **2004**, *49*, 192-194.
(7) Li, J.; Jacobs, G.; Das, T.; Zhang, Y.; Davis, B. *App. Catal .A: Gen.* **2002**, *236*, 67-76.
(8) Dutta, P.; Elbashir, N. O.; Manivannan, A.; Seehra, M. S.; Roberts, C. B. *Catal. Letters* **2004**, 98, 203-210.
(9) Elbashir, N. O.; Roberts, C. B. *Ind. Eng. Chem. Res.* **2005**, 44, 505-521.
(10) Khodakov, A. Y.; Griboval-Constant, A.; Bechara, R.; Zholobenko, V. L. *J. Catal.* **2002**, *206*, 230-241.
(11) Iglesia, E.; Reyes, S. C.; Madon, R. J.; Soled, S. L. *Adv. Catal.***1993**, *39*, 221-302.
(12) Reuel, R. C.; Bartholomew, C. H. *J. Catal.* **1984**, *85*, 78-88.
(13) Elbashir, N. O.; Roberts, C. B. *Prep. Pap.-Am. Chem. Soc., Div. Pet. Chem.***2004**, *49*, 157-160.
(14) Rathouský, J.; A., Z.; Lapidus, A.; Krylova, A. *App. Catal .A:Gen* **1991**, *79*, 167-180.
(15) Enache, D. I.; Rebours, B.; Roy-Auberger, M.; Revel, R. *J. Catal.* **2002**, *205*, 346-353.
(16) Yokota, K.; Hanakata, Y.; Fujimoto, K. *Chemical Engineering Science* **1990**, *45*, 2743-2749.
(17) Elbashir, N. O.; Dutta, P.; Manivannan, A.; Seehra, M. S.; Roberts, C. B. *App. Catal .A:Gen.***2005,** *285*, 169-180.

CHAIN INITIATION OF FISCHER-TROPSCH WITH ACETYLENE INCORPORATION

Yulong Zhang, Li Hou, John W. Tierney and Irving Wender

Department of Chemical and Petroleum Engineering, University of Pittsburgh, Pennsylvania, USA

Introduction

Fischer-Tropsch (F-T) synthesis converts syngas (CO and H_2), which can be produced from coal, natural gas, biomass and any carbonaceous materials, into long chain hydrocarbons which can be transformed to fuels and chemicals. It is very attractive to nations who have abundant coal or natural gas but lack indigenous oil. The mechanism of the FT reaction is still under debate although it has been investigated for about 80 years. Major obstacles are to distinguish many complex intermediates formed during F-T reactions. Schulz[1] pointed out that the F-T regime is established during the synthesis by restructuring catalyst surface and suppressing of undesired reactions. F-T active sites are difficult to characterize spectroscopically under high vacuum conditions. Use of probe molecules has been shown to be an effective way to study the F-T mechanism[2].

The F-T synthesis is a stepwise growth of hydrocarbon chains by addition of monomeric units. Unlike usual polymerization processes, the reaction proceeds by the addition of monomers formed in-situ from syngas. In previous studies, we found that long chain alkynes are incorporated more easily than corresponding alkenes[3]. It has been reported that ethylene is 10 to 40 times more easily incorporated into the F-T synthesis than are higher olefins. In this work acetylene is used as a probe molecule to study the mode of initiation of the F-T synthesis with consideration of possible differences in the pathways that occur with cobalt and iron catalysts.

Experimental

Supported cobalt catalysts were prepared by incipient-wetness impregnation of cobalt nitrate on alumina. A precipitated iron catalyst with a composition of 100Fe/4.4Si/1.25K was obtained from Dr. B. Davis of the University of Kentucky.

The F-T reaction was carried out in a computer controlled fixed bed reactor (stainless-steel with i.d. 3/8 inches). Acetylene was introduced from a tank of premixed gas containing (mol): 1% acetylene, 10% Ar, 44% CO, and 45% H_2 obtained from Praxair. H_2 was added when the H_2/CO ratio needs to be adjusted. Co catalysts were activated by H_2 at a rate of 50 ml/min, with a temperature program ramping from room temperature to 350°C at 1°C /min, holding at 350°C for 10 hours. Fe catalysts were activated similarly but kept at 350°C for 5 hours and 450°C for 2 hours. The F-T reaction was started by gradually increasing the CO and H_2 flow rate to avoid a temperature surge due to active sites present in the fresh catalysts. Products were analyzed by two online GCs (HP6890 and HP5890).

Results and Discussion

Addition of acetylene on cobalt catalysts increases the yield of C_2^+ products up to about C_{10}. It can be seen from Figure 1 that C_3 has a three fold increase upon addition of 1% acetylene. Compared to 1-hexyne, acetylene is 3 to 4 times easier to incorporate into the F-T products. A significant amount of acetylene is dimerized to C_4. Dimerization is not a part of the F-T reaction since it is not sensitive to sulfur. C_4 products are mainly internal olefins; however, they are also capable of chain initiation. As with cofeeding internal acetylenes we have reported earlier[3], isomers such as 2-methylbutane and 3-methylpentane are produced when acetylene is cofed.

One striking effect of cofeeding acetylene is initiation of the F-T chain growth at lower temperatures. At 120°C, appreciable amount of F-T products can still be obtained with cofeeding of 1% of acetylene, otherwise, the FT reaction has no activity at such a low temperature. Incorporation of acetylene on cobalt catalyst produces oxygenates; however, only C_3 oxygenates and a small amount of C_5 oxygenates are produced with cofeeding acetylene, apparently by hydroformylation of adsorbed unsaturated C_2 and C_4 species.

Acetylene can initiate FT on iron catalysts effectively; however, there are a number of differences between iron and cobalt catalysts. Only a small amount of dimerization was observed on iron catalysts. Instead of only one or two oxygenates as on cobalt catalysts, iron catalysts produces a spectrum of oxygenates which follows the Anderson-Schultz-Flory distribution as shown in Figure 2. Formation of oxygenates is an intrinsic property of iron catalysts.

Acetylenes initiate the chain but are not incorporated into the growing chain. The alpha value of the F-T reaction declines with cofed acetylene due to the increasing number of chain initiators. It is also evidenced by using phenylacetylenes as probes.

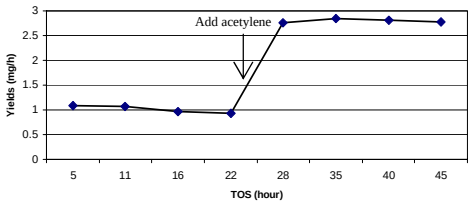

Figure 1. Yield of C_3 hydrocarbons with TOS on a cobalt catalyst ($10Co/90Al_2O_3$) at 100 psi., 180°C, H_2/CO=1, 1% acetylene.

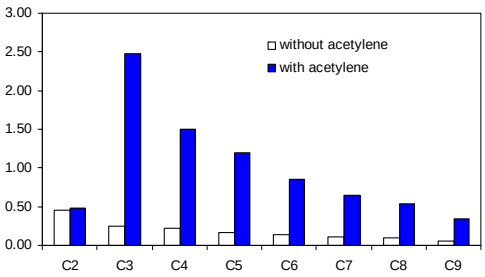

Figure 2. Oxygenated product distribution without/with acetylene incorporation on a iron catalyst ($10Co/90Al_2O_3$) at 300psi, 180°C, H_2/CO=1, 1% acetylene.

Conclusions

Acetylene is incorporated into the F-T reaction much more effectively than are higher acetylenes, a finding similar to results reported with olefin addition. Alpha values decreased upon addition of acetylene, indicating that acetylene, a two-carbon entity serves as a chain initiator. Oxygenates on cobalt catalysts is formed by hydroformylation while oxygenates are essential for chain growth on iron catalysts.

Acknowledgement. We thank the U.S. Department of Energy for financial support under grant No. DE FC26 99FT40540.

References

(1) Schulz, H.; Nie, Z. Q.; Ousmanov, F. *Catal. Today* **2002**, 71, 351-360.
(2) Turner, M. L.; Marsih, N.; Mann, B. E.; Quyoum, R.; Long, H. C.; Maitlis, P. M. *J. Am. Chem. Soc.* **2002**, 124, 10456-10472.
(3) Zhang ,Y.; Hou, L.; Tierney, J. W.; Wender, I. *Top. Catal.* **2005**, 33.

AEROGEL-SUPPORTED TRANSITION METAL CATALYSTS FOR FISCHER-TROPSCH AND RELATED REACTIONS

Gregory C. Turpin, Brian C. Dunn, Yifan Shi, Zhiru Ma, Ronald J. Pugmire, Edward M. Eyring, and Richard D. Ernst

Department of Chemistry, University of Utah Salt, Lake City, UT 84112

Introduction

The Fischer-Tropsch and Water Gas Shift reactions each offer the potential for providing solutions to important future energy concerns. In each case, catalysts employed for these processes tend to be late transition metals deposited on typical supports such as silica, alumina, or titania. While numerous studies have addressed the roles played by various catalyst and support combinations, far less attention has been devoted to studies involving aerogel supports, whose highly porous natures should promote more effective catalyst dispersal and enhanced mass transport of reactant and product molecules through the aerogel pores.[1] Additionally, catalytic studies utilizing aerogel supports may be carried out either under gas-phase or supercritical conditions, leading to further control over the nature of the reaction.[2]

The unique structures and properties of aerogels allow for the preparation of very new catalyst/support motifs. In one application, the highly porous aerogel backbone can serve as a framework onto which a more desirable support material may be deposited. This approach could be advantageous in cases in which the more desirable support either may be costly, or does not form a reasonable aerogel structure on its own. As will be described, this approach has been successfully applied to the preparation of a ceria-coated silica aerogel. A second opportunity for aerogels relates to the catalyst incorporation step. Since partial wetting of an aerogel structure can lead to drastic collapse of the pore structure, gas-phase incorporation processes could offer some advantages, including the potential of effecting single site metal incorporation and of delivering one metal selectively to another on the support surface.

Experimental

Catalyst Supports. Silica aerogels were prepared as previously described.[3] Solution phase loading of cerium(IV) alkoxides was accomplished by first replacing the solvents in a 10 mL solid monolithic alcogel sample through 4-5 equilibrations with 20-25 mL volumes of THF, after which the external solvent was replaced by a solution of the cerium alkoxide in THF. Subsequent equilibration led to an even distribution of cerium throughout the entire solution volume, within and outside of the alcogel. The alcogel monolith was then removed and subjected to two similar equilibrations with acetone, after which the monolith was placed in a CO_2 atmosphere, pressurized to supercritical conditions, and dried to form the aerogel.

Catalyst Preparations. The metal pentadienyl compounds were prepared according to literature methods.[4-6] For gas-phase incorporations of the transition metal complexes, the appropriate masses of organometallic compound and crushed aerogel were combined under nitrogen in a Schlenk tube which was then placed under static vacuum and rotated constantly until the separate organometallic phase was no longer visible. Oxygen gas was then passed over the doped aerogel, beginning at 25 ^{o}C, with the temperature thereafter slowly brought to 25-350 ^{o}C, depending on sample. Subsequently, the supported metal oxide was heated to 500 ^{o}C, and reduced in a hydrogen stream.

Catalytic Studies. Fischer-Tropsch reactions were carried out in a laboratory-scale packed bed reactor, as previously described,[3] except that C_1-C_{13} hydrocarbon products were analyzed by gas chromatography on a capillary column (DB-5, 0.53 mm I.D. and 30 m length) with an FID.

Results and Discussion

The high activities of copper-, gold-, and palladium-derived water gas shift catalysts supported on ceria[7,8] have led to an interest in examining their activities on aerogels. Unfortunately, ceria-based aerogels do not show the structural stability one finds for silica aerogels at higher temperatures.[9] To circumvent this problem, attempts to bind ceria on silica aerogels have been undertaken. The hydrolytically sensitive Ce(O-*i*-Pr)$_4$(*i*-PrOH)[10] does in fact readily incorporate into highly porous silica aerogel via standard solution methods, after which other metals of interest, such as palladium, can be incorporated by gas-phase or solution methods.

Gas-phase incorporation of metals such as iron and ruthenium occurs surprisingly well using their relatively air- and water-stable M(2,4-C_7H_{11})$_2$ or M(C_5H_5)(2,4-C_7H_{11}) compounds (C_5H_5 = cyclopentadienyl; C_7H_{11} = dimethylpentadienyl). Incorporation is immediate, occurring via protonation of a 2,4-C_7H_{11} ligand. Similarly, Co(*c*-C_8H_{13})(*c*-C_8H_{12})[11] undergoes facile incorporation (*c*-C_8H_{13} = cyclooctenyl; *c*-C_8H_{12} = cyclooctadiene). Cobaltocene, Co(C_5H_5)$_2$,[12] incorporates more slowly, yielding significant quantities of cyclopentene. Although spectroscopic data indicate that single-site incorporation is initially occurring for the metal under these conditions, agglomeration appears quite facile subsequent to oxidation. This, as well as the high reactivities of the aerogel surfaces with the metal pentadienyl complexes, appears to be a result of the aerogel surface providing a poorly coordinating environment.

Figures 1 and 2 present selectivity and activity results for a ruthenium catalyst prepared by gas-phase deposition onto a silica aerogel. The catalyst was examined for a total of 50 hours on stream and remained active until removed from the reactor. The time dependent activity of this sample is atypical and likely related to the calcination temperature.

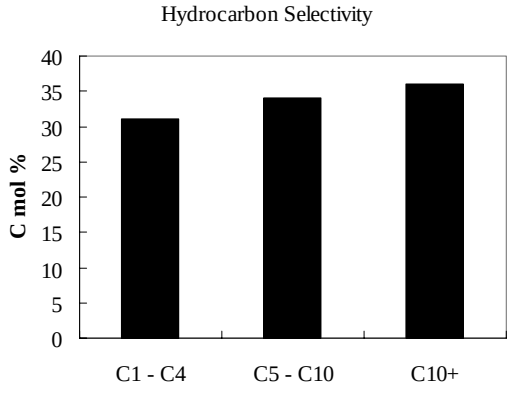

Figure 1. Hydrocarbon product distribution after 35 hours on stream from a 2% ruthenium catalyst supported on silica aerogel.

The gas-phase approach also allows for the selective delivery of one metal to another on a surface, via redox reactions. Thus, the 19 electron cobaltocene, which is a good reducing agent capable of reducing many metal oxides to the metals, should readily "target" a variety of presupported oxides. Of particular interest for Fischer-Tropsch applications would be ruthenium. Initial results indicate that not only does cobaltocene incorporate more readily into oxidized

ruthenium-doped aerogels, but the resulting catalysts are more active than ones derived from less selective cobalt incorporations.

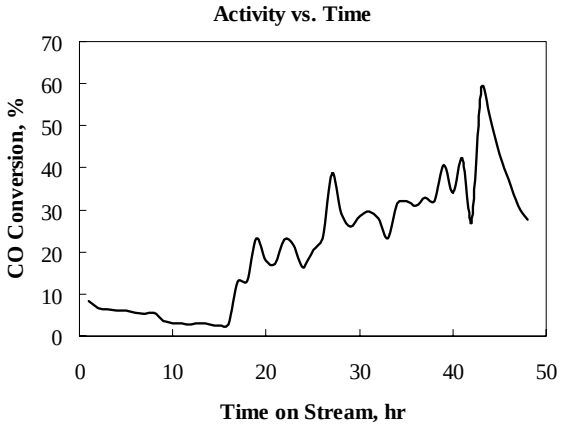

Figure 2. Carbon monoxide conversion as a function of time on stream for the 2% ruthenium catalyst.

Conclusions

Silica aerogels have been found to exhibit unusually high reactivities toward some relatively unreactive organometallic compounds, thereby allowing for the facile incorporation of a variety of metals, and even the selective delivery of one metal to another on the surface. The resulting catalysts have shown interesting reactivity trends for the Fischer-Tropsch process. The highly porous and reactive aerogels also readily incorporate cerium(IV) alkoxides, and thereby offer substantial promise as scaffolds to support other, less robust supports.

Acknowledgement. The U.S. Department of Energy provided financial support to the Consortium for Fossil Fuel Science for this study (contract # DE-FC26-02NT41954).

References

(1) Husing, N.; Schubert, U. *Angew. Chem. Int. Ed.* **1998**, *37*, 22-45.
(2) Elbashir, N.O.; Roberts, C.B. *Ind. Eng. Chem. Res*. **2005**, *44*, 505-521.
(3) Dunn, B. C.; Cole, P.; Turpin, G. C.; Ma, Z.; Pugmire, R. J.; Ernst, R. D.; Eyring, E. M.; Shah, N.; Huffman, G. P. Preprints of Symposia - American Chemical Society, Division of Fuel Chemistry **2004**, *449(1)*, 329-330.
(4) Wilson, D.R.; Stahl, L.; Ernst, R.D. *Organometallic Syntheses* **1986**, *3*, 136-141.
(5) Elschenbroich, C.; Bilger, E.; Ernst, R.D.; Wilson, D.R.; Kralik, M.S. *Organometallics* **1985**, *4*, 2068-2071.
(6) Gleiter, R.; Hyla-Kryspin, I.; Ziegler, M.L.; Sergeson, G.; Green, J.C.; Stahl, L.; Ernst, R.D. *Organometallics* **1989**, *8*, 298-306.
(7) Fu, Q.; Saltsburg, H.; Flytzani-Stephanopoulos, M. *Science* **2003**, *301*, 935-938.
(8) Qi, X.; Flytzani-Stephanopoulos, M. *Ind. Eng. Chem. Res*. **2004**, *43*, 3055-3062.
(9) Thundathil, M.A.; Lai, W.; Noailles, L.; Dunn, B.S.; Haile, S.M. *J. Am. Ceram. Soc.* **2004**, *87*, 1442-1445.
(10) Vaartstra, B.A.; Huffman, J.C.; Gradeff, P.S.; Hubert-Pfalzgraf, L.G.; Daran, J.-C.; Parraud, S.; Yunlu, K; Caulton, K.G. *Inorg. Chem*. **1990**, *29*, 3126-3131.
(11) Dumestre, F.; Chaudret, B.; Amiens, C.; Fromen, M.-C.; Casanove, M.-J.; Renaud, P.; Zurcher, P. *Angew. Chem. Int. Ed.* **2002**, *41*, 4286-4289.
(12) Eisch, J.J.; King, R.B. *Organometallic Syntheses* **1965**, *1*, 70-71.

HYDROGEN PRODUCTION FROM METHANOL IN SUPERCRITICAL WATER

Jayant B. Gadhe and Ram B. Gupta

Department of Chemical Engineering
Auburn University
Auburn, AL 36849-5127.

Introduction

The development of proton exchange membrane fuel cells for various transportation applications has resulted in a need of on-board and stationary reformers which can supply high purity hydrogen at low cost. Designing a process to produce H_2 at a very high pressure is an attractive approach for mobile and portable applications owing to its low storage volume. The reforming of hydrocarbons can be carried out in the presence of supercritical water instead of steam as used in the conventional processes, to produce H_2 at a very high pressure.

There are several advantages of carrying out the reforming reactions in supercritical water over the conventional processes. The density of supercritical water is higher than that of steam which results in a high space-time yield and the higher values of thermal conductivity and specific heat of supercritical water are beneficial for the endothermic reforming reaction. H_2 is available at a high pressure which can be stored directly, thus avoiding the problems associated with its compression. The process becomes economical as the compression work is reduced owing to the low compressibility of liquid feed as compared to that of gaseous H_2.[1] Hydrocarbons are completely soluble in supercritical water which minimizes the formation of char or slag which may otherwise cause catalyst deactivation. This is particularly important in the generation of H_2 from heavy oils such as diesel. The generation of H_2 by the steam reforming of biomass leads to the formation of significant amounts of tar and char which limits the yield of H_2 and the gaseous product contains higher hydrocarbons in addition to the desired light gases. Researchers have carried out the catalytic gasification of biomass or its model compounds in supercritical water to produce H_2-rich gas with effectively no tar or char formation.[2]

Methanol is chosen as feedstock for reforming because of its high hydrogen-to-carbon ratio and absence of carbon-carbon bonds. It is in the liquid state under normal conditions and hence can be stored and pumped easily. The major reactions involved in the methanol reforming are:

Methanol decomposition:	$CH_3OH \Leftrightarrow CO + 2H_2$	(1)
Water-gas shift reaction:	$CO + H_2O \Leftrightarrow CO_2 + H_2$	(2)
Methanation of CO:	$CO + 3H_2 \Leftrightarrow CH_4 + H_2O$	(3)
Methanation of CO_2:	$CO_2 + 4H_2 \Leftrightarrow CH_4 + 2H_2O$	(4)

To study the impact of pressure on the H_2 yield, equilibrium calculations were performed using Gibbs free energy minimization method and Peng-Robinson equation of state. **Figure 1** shows that as pressure increases, there is an increase in the CH_4 moles and decrease in the H_2, CO and CO_2 moles. It suggests that methanation of CO (reaction 3) and CO_2 (reaction 4) is favored at higher pressures. Methanation of CO results in a loss of 3 moles of H_2 while methanation of CO_2 results in a loss of 4 moles of H_2. To enjoy the benefits of the reforming of methanol in supercritical water which are mentioned before, it becomes important to prevent the loss of H_2 by minimizing the methanation reactions.

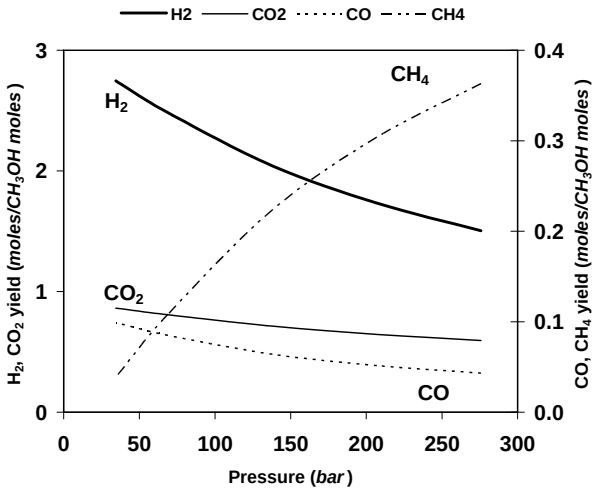

Figure 1. Dependence of gas yield on pressure using ASPEN+ equilibrium calculations. (10 wt.% methanol, 700 °C)

Experimental

Materials. Methanol (99.9%), KOH (88.7% assay) and $K_2CO_3 \cdot 1½H_2O$ (99.9% assay) were obtained from Fisher.

Apparatus. Figure 2 shows schematic of the apparatus used in the study. A tubular reactor made of Inconel 600 (Microgroup) having a composition of 73% Ni, 18% Cr, 9% Fe was used. The reactor wall provides the catalytic surface area for the reactions. Later the reactor was replaced with a Ni-Cu tubing (Supelco) having a composition of 67% Ni, 33% Cu.

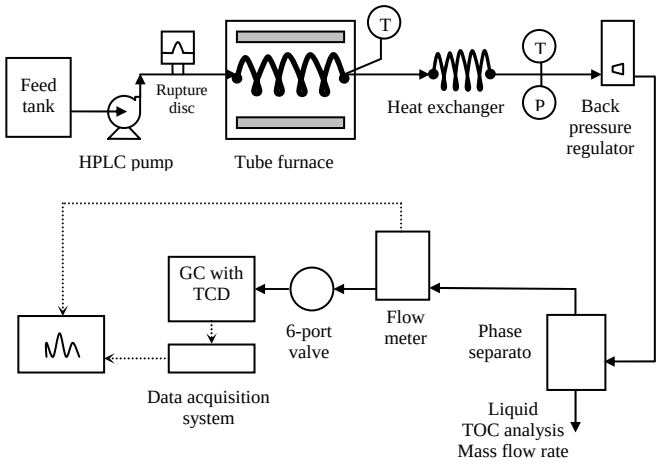

Figure 2. Schematic of the experimental setup used for methanol reforming in supercritical water.

Aqueous methanol from the feed tank was pumped to the reactor using an HPLC pump (Waters 590). The reactor was heated using a tube furnace equipped with a temperature controller (Thermolyne 21100). The gas mixture exiting the reactor was cooled using an air-cooled heat exchanger made of SS 316 tubing. Pressure was measured by a pressure gauge P. The pressure was let down to the ambient by means of a back pressure regulator (Straval). The gas-liquid mixture was separated in a glass phase separator having gas tight valves to prevent the escape of gases. The gas flow rate was measured using a gas flow meter (Omega FMA-1600). A six-port

injection valve (Valco) having a 100 μL sample loop was used for the online sample injection. The gas composition was measured using a gas chromatograph (Varian 3700) equipped with a TCD and 60/80 Carboxen-1000 carbon molecular sieve column. (Supelco) The mass flow rate of the liquid coming out of the phase separator was measured using a balance. The total organic carbon (TOC) content of the liquid was analyzed using a TOC analyzer (OI Analytical Model 700).

Results and Discussion

Figure 3 shows that as pressure is raised from 34 to 276 bar, the H_2, CO and CO_2 moles decrease while the CH_4 moles increase as anticipated, suggesting that the methanation reactions, of both CO and CO_2 are favored at the higher pressures. The H_2 yield (H_2 moles/ CH_3OH moles) has dropped from 2.75 at 34 bar to 1.50 at 276 bar. The increase in density at the higher pressures leads to an increase in the residence time which ranged from 7 seconds at 34 bar to 59 seconds at 276 bar which resulted in the near-equilibrium yields.

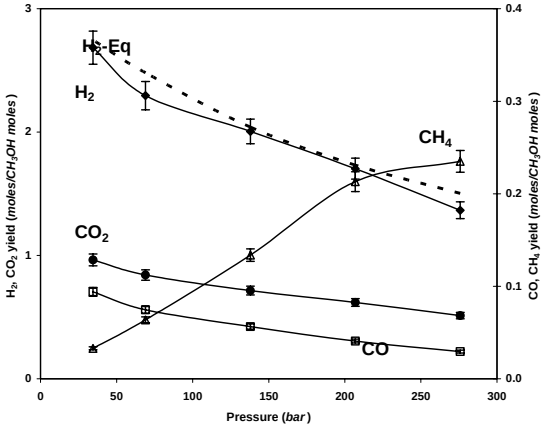

Figure 3. Effect of pressure on gas yield. (10 wt.% methanol, 0.5 mL/min, 700 °C, reactor length = 2 m)

The pressure variation was studied again in the Ni-Cu reactor at a lower residence time. **Figure 4** shows that the increase in pressure has a very little effect on the gas yields in this case. The H_2 yields which are higher than the equilibrium H_2 yields, remain fairly constant over the entire pressure range. The CH_4 yield is found to be almost negligible. This could be the combined effect of the low residence time, which ranged from 2 seconds to 17 seconds in this case and possibly the catalytic activity of the Ni-Cu reactor.

This behavior of the Ni-Cu reactor can be explained based on the mechanism of CO methanation. It proceeds via dissociative chemisorption of CO and H_2 to form intermediates which combine to form CH_4 as shown in reactions 5 to 7.

$CO \rightarrow C_s + O_s$ (5)

$H_2 \rightarrow 2H_s$ (6)

$C_s + H_s \rightarrow (CH)_s$ (7)

Alloying Ni with Cu results in the dilution of active Ni in an inactive matrix which diminishes the number and size of Ni clusters which are necessary for the dissociation of CO and deposition of C_s on the surface. The Ni-Cu tubing reduces the number of places where C_s can be formed and held and decreases the extent of methanation of CO and CO_2.[3]

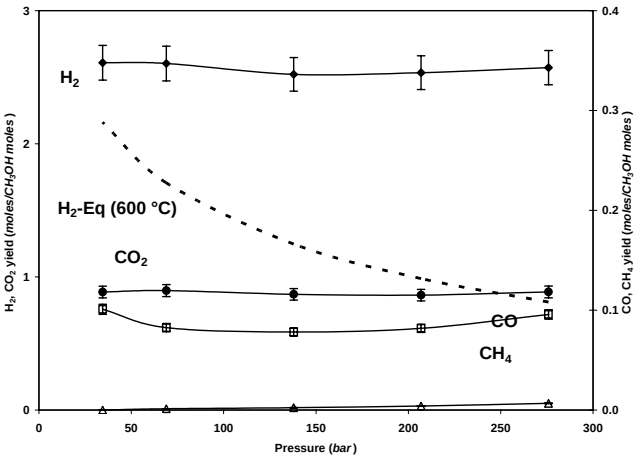

Figure 4. Effect of pressure on gas yield with Ni-Cu reactor. (10 wt.% methanol, 1 mL/min, 600 °C, reactor length = 1 m)

The performance of the Inconel 600 reactor can be improved by adding K_2CO_3 or KOH in aqueous methanol. **Figure 5** shows the increase in the H_2 yield and the decrease in the CH_4 yield.

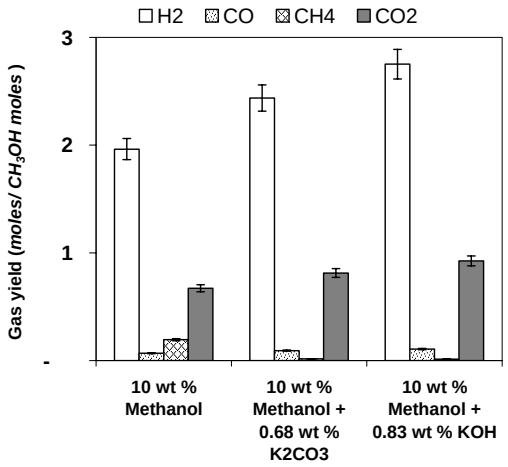

Figure 5. Effect of K_2CO_3 and KOH addition. (10 wt.% methanol, 1 mL/min, 700 °C, reactor length = 2 m)

Conclusions

CH_4 formation during reforming of methanol in supercritical water can be suppressed by (1) operating at a low residence time, (2) using Ni-Cu reactor or (3) adding K_2CO_3 or KOH in the feed.

References

[1] Boukis, N.; Diem, V.; Habicht, W.; Dinjus, E. *Industrial & Engineering Chemistry Research* **2003**, 42(4), 728-735.

[2] Antal, Michael Jerry, Jr.; Allen, Stephen Glen; Schulman, Deborah; Xu, Xiaodong; Divilio, Robert J. *Industrial & Engineering Chemistry Research* **2000**, 39(11), 4040-4053.

[3] Araki, M.; Ponec, V. *Journal of Catalysis* **1976**, 44(3), 439-48.

COPRODUCTION OF HYDROGEN AND CHEMICALS BY VAPOR PAHSE DECOMPOSITION OF METHANOL

F. Shi, Y. Zhang, J. W. Tierney and I. Wender

Department of Chemical Engineering
University of Pittsburgh, Pittsburgh, PA 15261, USA

Introduction

Methanol is produced in huge amounts from synthesis gas derived chiefly from natural gas. In 2003 world capacity for methanol synthesis was over 50 million tons per year. Very large plants are being built near resources of cheap natural gas. Methanol is a hydrogen-rich liquid, and provides a great deal of convenience in storage, transport and handling as a source of hydrogen.

Hydrogen can be generated from methanol in several ways:

Direct decomposition $CH_3OH = CO + 2H_2$
Steam reforming $CH_3OH + H_2O = CO_2 + 3H_2$
Partial dehydrogenation $2CH_3OH = HCOOCH_3 + 2H_2$

Partial dehydrogenation of methanol produces hydrogen as well as methyl formate (MF). MF has been proposed as a building block for a number of chemicals. It is a stable liquid and can be catalytically converted to a number of important chemicals including dimethyl formamide, formamide, ethylene glycol, acetic acid, dimethyl carbonate and formaldehyde.[1-4]

Since MF is an intermediate in a series of reactions, fast desorption and diffusion is essential for high selectivity to MF and hydrogen. In this study, works has started on the gas phase dehydrogenation of methanol to produce hydrogen and MF on a series of copper-based catalysts. The effects of supports and promoters are under investigation. The formation of hydrogen via steam reforming is also of interest.

Experimental

Catalyst preparation. A series of copper-based catalysts were prepared by incipient wetness impregnation of aqueous $Cu(NO_3)_2$ solution onto various supports: Zeolite (ZSM-5), Al_2O_3, and MgO. The impregnated samples were dried at 110˚C for at least 8 h prior to calcining at 350˚C in air for 3 hours. Before reaction, catalysts were reduced at 250˚C with 50 ml/min H_2/Ar gases for 3 hours.

Catalyst testing. Methanol dehydrogenation experiments, including direct decomposition and steam reforming, were tested in a quartz micro reactor with 0.6-0.8 g copper catalyst loading. Liquid methanol is fed using a syringe pump (100DX, ISCO) at a rate of 3 ml/hr and then is evaporated and mixed with 20 ml/min Ar in a 100 ml evaporator at 150˚C. All gas mixtures are heated with heating tapes before entering the micro-reactor and GC as well. Products were analyzed by two on-line Hewlett Packard GCs: one equipped with a TCD detector and with a Carbonsphere packed column (6 feet, 3/8 in) for analysis of H_2, CO, CH_4, CO_2; another equipped with a FID and HP-5 capillary column for analysis of methanol, methyl formate, dimethyl ether and other organic products. Liquid products are also collected with a cold trap at –80˚C and then are analyzed using GC-MS.

Results and Discussions

Thermodynamic calculations. Thermodynamic calculations for methanol dehydrogenation, including direct decomposition and steam reforming (methanol/water=1), have been conducted using ASPEN Plus 12, based on Gibbs free energy minimization method. Results for hydrogen and MF production are shown in Figure 1. At temperatures below 200˚C, methanol dehydrogenation to MF and hydrogen is favored; at temperatures above 300˚C, complete decomposition of methanol to H_2 and CO dominates. Although steam reforming can produce more hydrogen than methanol dehydrogenation, it decreases the formation of MF greatly.

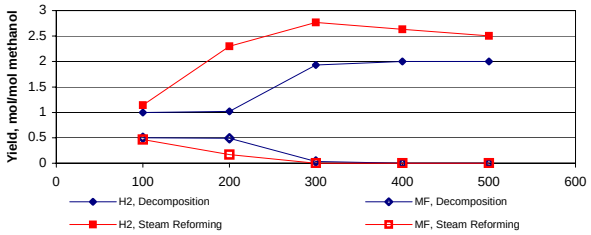

Figure 1. H_2 and MF productions by methanol dehydrogenation

Catalyst performance. Methanol dehydrogenation experiments have been carried out on copper based catalysts at different temperatures, from 150˚C to 250˚C with 10˚C intervals. Methanol conversion and hydrogen production at various temperatures are shown in Figures 2 and 3, respectively.

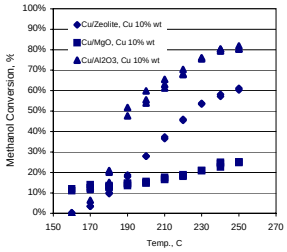

Figure 2. Methanol conversion at different temperatures

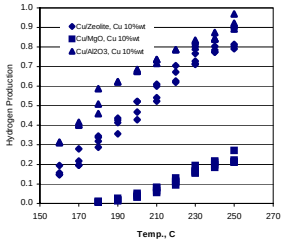

Figure 3. Hydrogen production at different temperatures

Figure 2 shows that the conversion of methanol increases with increase in temperature with three catalysts. Cu/Al_2O_3 is the most active catalyst and the conversion of methanol can reach 80% at 250˚C. Cu/MgO is the least active. Methanol conversion is below 25%. Hydrogen yields, shown in Figure 3, show the same trend with the conversion of methanol: Cu/Al_2O_3 >Cu/ZSM-5 >Cu/MgO. Dimethyl ether is also formed on Cu/ZSM-5 and Cu/Al_2O_3 catalysts due to acidity of the supports. In the above experiments, only limited amounts of MF are obtained. Modifications of catalysts are under investigation to improve MF selectivity. Effect of water concentration on H_2 and MF formation is also being studied.

Summary

Thermodynamically, lower temperature favors MF formation and the presence of steam decreases MF selectivity. Cu-based catalysts are active for decomposition of methanol in the order of Cu/Al_2O_3>Cu/ZSM-5>Cu/MgO. Promoters are needed to improve MF selectivity.

Acknowledgment. We thank the U.S. Department of Energy for financial support under grant No. DE FC26 99FT40540.

References

1. Iwasa, N.; Takezawa, N. *Top. Catal.* **2003**, 22, 215.
2. Hashimot, K.; Toukai, N. *J. Mol. Catal. A* **2002**, 186, 79.
3. Shreiber, E. H.; Roberts, G. W. *Appl. Catal. B* **2000**, 26, 119.
4. Lee, J. S.; Kim, J. C.; Kim, Y. T. *Appl. Catal.* **1990**, 57, 1.

GAS SEPARATION THROUGH ZEOLITE THIN FILM MEMBRANES

Margaret E. Welk, Tina M. Nenoff

Sandia National Laboratories, PO Box 5800, MS 0734, Albuquerque, NM 87185-0734
mewelk@sandia.gov

Introduction

The synthesis and testing of inorganic zeolite membranes has been intensely studied because of their potential applications in the domains of gas separation, pervaporation, reverse osmosis and in the development of chemical sensors and catalytic membranes.[1,2,3,4,5] Specifically, development of new technologies, such as zeolite membranes, for H_2 separation and purification has a high priority for the future of H_2 as a fuel source. H_2 is commonly produced by the reformation of hydrocarbons, creating CO_2, CO, CH_4 and H_2O as by-products. A successful membrane for the separation of H_2 from other reformate gases must have both high flux and high selectivity for H_2 in the presence of these other gas species. Inorganic membranes, which have good thermal stability and chemical inertness, are highly attractive. Distinctively, zeolite membranes combine pore size and shape tunability with the inherent mechanical, thermal, and chemical stability necessary for long term separations. The effective pore size distribution, and hence the separation performance, of a defect free zeolite membrane is intrinsically governed by the choice of the zeolitic phase.[6,7,8,9]

Numerous pure gas permeation studies have been performed on MFI-type zeolite membranes that allow ideal selectivities to be calculated.[10,11,12,13,14,15,16,17,18,19,20,21] Typical literature selectivity values of H_2 from CO_2, CH_4 and CO range from 2 to 8, below the values necessary for successful industry integration. It is well recognized that gas mixtures flowing through separation membranes will behave differently than pure gases owing to adsorption effects and other phenomena. Temperature effects on the permeation properties of such membranes also need to be understood. We report here the study of the permeance and selectivity as a function of temperature of both ZSM-5 and silicalite-1 zeolite membranes under the flow of three gas mixtures, two chosen as benchmarks (50/50 mol% H_2/CH_4 and 50/50 mol% H_2/CO_2) and one chosen to emulate an industrial methane reformate stream.

Experimental

Gases. Reagent grade pure gases were purchased from Matheson Trigas. H_2, CO_2, O_2, CH_4, N_2, CO were used to test the permeability of the membranes. SF_6 was used to asses membrane quality, He was used to clean and purge the unit, shown in Figure 1. Three reagent grade gas mixtures pre-mixed by Matheson Trigas were also tested: 50/50 mol% H_2/CH_4, 50/50 mol% H_2/CO_2 , and a four gas component mixture that approximates a methane steam reformate stream, excluding the water vapor (will be referred to as the reformate mixture) : 76.2% H_2, 13.6% CO_2, 6.8%CO, and 3.4% CH_4.

Membrane Synthesis. A thorough description of the silicalite membrane growth has been published elsewhere.[22] The support cleaning, seed synthesis,[12,22] and seeding methodology for the ZSM-5 membranes are identical to the steps for silicalite also can be found in the same reference. A description of the ZSM-5 gel and hydrothermal synthesis of the ZSM-5 membranes is presented here.

In the gel used for the hydrothermal synthesis, the silicon source for the membrane synthesis was colloidal silica Ludox SM-30; the source of aluminum was $Al_2(SO_4)_3{\cdot}18H_2O$, and NaOH is the alkalinity source. Ludox SM-30 was filtered prior to use to remove any SiO_2 flakes; all other reagents were used as received. 2.14 g of NaOH, and 0.832 g of $Al_2(SO_4)_3{\cdot}18H_2O$ were added to 68.4 g of H_2O, and stirred until dissolved. 20 g of Ludox SM-30 was added drop-wise to the mixture while stirring. Each gel was then aged for 24 hours while being stirred at room temperature. Gels that were not aged under agitation did not result in selective membranes. The aged gels in this work were homogeneous and no precipitate had formed prior to the reactions.

The alpha-alumina substrates supplied by Inocermic Gmbh have a 1.8 μm average pore size, a diameter of 13 mm and a thickness of 1 mm. Their high density ensures good mechanical properties and robustness. MFI zeolite seeds were rubbed onto both sides of the cleaned substrates; the seed synthesis and application has been described elsewhere.[23] The seeded substrates were held vertically in the Teflon lined Parr reactor using Teflon holders to prevent sedimentation on top of the membrane. The homogenous gel was then poured in the reactor until the membrane was fully immersed. The hydrothermal syntheses were carried out in Parr reactors with a 23 ml Teflon liner at 170°C for 12 hours under autogenous pressure.

After the hydrothermal synthesis, the two-sided membrane was removed from autoclave, washed with DI water and dried in air at 50°C for few hours. A permeation test on the as-synthesized, uncalcined membrane allows the rapid assessment of its quality before the time-consuming calcination step. At this stage, a good quality membrane should be impermeable for SF_6. The SF_6 kinetic diameter of 5.5 Å is similar to the pore dimensions of the calcined ZSM-5 zeolite (diameter range 5.1 – 5.6 Å). Substantial SF_6 diffusion through the uncalcined membrane indicates the presence of detrimental membrane defects larger than the zeolite pores which will be opened during calcination.[23] Any existing large defects (partial coverage of the substrate and micro-cracks) may be repaired by a second hydrothermal synthesis step, using a shorter reaction time and more diluted starting gel.

Once the quality of the membrane was established, the water was removed from the membrane pores by calcination in air. A calcination temperature of 600°C led to cracks in the membrane and drastic reduction in permeation performance unless a slow temperature ramp rate was used. The stress at the interface between the zeolitic layer and the alumina substrate due to thermal expansion mismatch has to be minimized by using slow heating rates,[24] below 1°C/min. A typical successful temperature profile for the calcination is a heating and cooling rate of 0.5°C/min with a maximum temperature of 600°C maintained for 6 hours. This ensures the removal of water from the pores without creating detrimental defects within the membranes.

Characterization Techniques. The zeolite membranes were characterized by X-ray diffraction (Siemens D500 diffractometer, Cu Kα radiation, Bragg-Brentano geometry) and by Scanning Electron Microscopy (JEOL–6300V equipped with a Link Gem Oxford 6699 EDAX attachment).

Permeation Measurements. The membrane permeations were measured at room temperature using pure gases and a constant trans-membrane pressure of 15 PSI controlled by a backpressure regulator. Each membrane was sealed to a custom stainless steel washer using a silicone elastomer (NuSil) high temperature epoxy. The membrane assembly was then placed in a standard VCR fitting (Swagelok) for testing. The gas flow through the membrane was measured using an acoustic displacement flowmeter (ADM 2000 from J&W) and a digital bubble flowmeter (HP-9301). Between permeation measurements with different pure (SF_6, H_2, CO_2, O_2, CH_4, N_2, CO) and mixed (50/50 H_2/CO_2, 50/50 H_2/CH_4, and the reformate mixture) gases, the whole system was purged, flushed with He and evacuated

several times. For the pure gases, the ideal gas selectivity was calculated as the ratio of the permeances in the steady regime.

Micro Gas Chromatograph. For the mixed gas studies, a Micro Gas Chromatograph (agilent) was attached to the permeate side of the membrane. Three columns were employed: a molecular sieve with Argon as a carrier gas to separate H_2, a molecular sieve with Helium as a carrier gas for CO and CH_4, and a Pora Plot column for CO_2. The permeate was autosampled once every 5 minutes. A constant trans-membrane pressure of 15 PSI was controlled by the back pressure regulator. Calibration curves were generated by flowing the gas mixtures through the permeation unit with a blank support in place of the membrane. Selectivities were calculated as the ratio of the gas species of interest.

Results and Discussion

Both ZSM-5 and Silicalite-1 are MFI type zeolites. Although they have identical structures, the pore chemistry differs owing to the presence of even a small amount of aluminum replacement of the silicon atoms in the ZSM-5 compound. The pore chemistry directly impacts adsorption and therefore, the permeation characteristics of the membranes, particularly the pure gas permeation results. Silicalite-1 membranes have a higher permeance for pure CO_2 than for pure H_2 because of the adsorption of CO_2 to the all-silica pore surfaces, At elevated temperatures, this adsorption effect disappears in the Silicalite membranes. The separation values obtained at between 200 and 300 °C approximate Knudsen separation values. See Figure 1. This is unsurprising given that the pore diameter of the Silicalite membrane is 5.6 Å, slightly larger than the kinetic diameter of H_2, CO_2, CO, and CH_4.

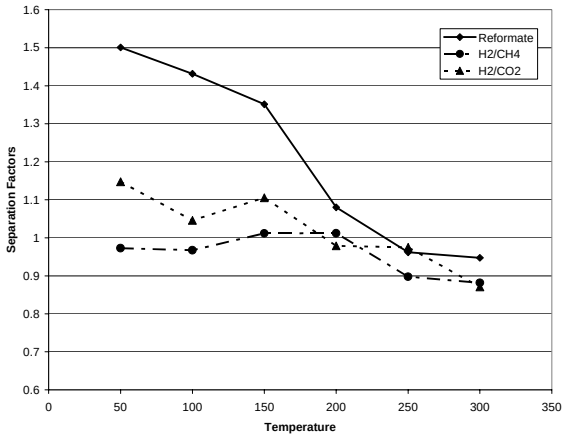

Figure 1. H_2 separation factors as a function of temperature of three gas mixtures: 50/50 mol% H_2/CH_4, 50/50 mol% H_2/CO_2, and a reformate stimulant 76.2% H_2, 13.6% CO_2, 6.8%CO, and 3.4% CH_4.

ZSM-5 has the same crystallographic structure and a similar framework pore diameter, however, exhibits different selectivity factors. Room temperature permeation results show that these ZSM-5 membranes are hydrogen selective beyond Knudsen values, with an H_2/CO_2 ideal selectivity of 15. Mixed gas studies at elevated temperatures are underway. The sodium form of this zeolite which we are studying charge balances the substitution of the Al^{3+} for Si^{4+} with Na^+ ions. These cations reside in the pore structure, thereby diminishing the pore diameter. In addition, the 0.25% substitution of aluminum for silicon adds acidity and therefore a combination of "hopping" sites for cations plus a "polarization" exhibited by the hydrophilic versus hydrophobic nature of the framework. This results in preferential adsorption of molecules onto and through these zeolites.

Conclusions

Further studies on these MFI-type zeolite membranes continue, and include elevated temperatures to 500°C, increased lifetime studies, pressure variations, and additional gas mixtures. The effects of different support materials on membrane performance are also under investigation.

Acknowledgement. Sandia is a multiprogram laboratory operated by Sandia Corporation, a Lockheed Martin Company, for the United Stated Department of Energy under contract DE-AC04-94-AL85000. We thank the DOE/Hydrogen, Fuel Cells, and Infrastructure Technologies Program for continued funding.

References

[1] Armor, J. N. *J. Membr. Sci.* **1998**, *147*, 217.
[2] Caro, J.; Noack, M.; Kolsch, P.; Schafer, R. *Microp. Mesop. Mat.* **2000**, *38*, 3.
[3] Chiang, A. S. T.; Chao, K-J. *J. Phys. Chem. Solids* **2001**, *62*, 1899.
[4] Noack, M.; Kolsch, P.; Schafer, R.; Toussaint, P.; Caro, *J. Chem. Eng. Technol.* **2002**, *25*. 221.
[5] Thoma, S. G.; Trudell, D. E.; Bonhomme, F.; Nenoff, T. M. *Microp. Mesop. Mat.* **2001**, *50*, 33.
[6] Vroon, Z. A. E. P.; Keizer, K.; Gilde, M. J.; Verweij, H. Burggraaf, A. J. *J. Membr. Sci.* **1996,** *113*, 293.
[7] Geus, E. R.; DenExter, M. J.; van Bekkum, H. *J. Chem. Soc. Faraday Trans.* **1992,** *88*, 3101.
[8] Bakker, W. J. W.; Kapteijn, F.; Poppe, J.; Moulijn, J. A. *J. Membr. Sci.* **1996**, *117*, 57.
[9] Bai, C.; Jia, M-D.; Falconer, J. L.; Noble, R. D. *J. Membr. Sci.* **1995,** *105*, 79.
[10] Lai, R. ; Gavalas, G. R. *Ind. Eng. Chem. Res.* **1998**, *37*, 4275.
[11] Hedlund, J.; Noack, M.; Kolsch, P.; Creaser, D.; Caro, J.; Sterte, J. *J. Membr. Sci.***1999,** *159*, 263.
[12] Tuan, V. A.; Falconer, J. L.; Noble, R. D. *Ind. Eng. Chem. Res.* **1999,** *38*, 3635.
[13] Lai, R.; Gavalas, R. *Microp. Mesop. Mat.* **2002,** *38*, 239.
[14] Xomeritakis, G.; Nair, S.; Tsapatsis, M. *Microp. Mesop. Mat.* **2000,** *38*, 61.
[15] Hedlund, J.; Sterte, J.; Anthonis. M.; Bons, A. J.; Carstensen, B.; Corcoran, N.; Cox, D.; Deckman, H.; De Gijnst, W.; de Moor, P-P.; Lai, F.;McHenry, J.; Mortier, W.; Reinoso, J.; Peters, J. *Microp. Mesop. Mat.* **2002,** *52*, 179.
[16] Noack, M.; Kolsch, P.; Schafer, R.; Toussaint, P.; Sieber, I.; Caro, J. *Microp. Mesop. Mat.* **2002,** *49*, 25.
[17] Lai, Z. P.; Bonilla, G.; Diaz, I.; Nery, J. G.; Sujaoti, K.; Amat, M. A.; Kokkoli, E.; Terasaki, O.; Thompson, R. W.; Tsapatsis, M.; Vlachos, D. G. ***Science***, **2003,** *300*, 456.
[18] Xomeritakis, G.; Lai, Z.P.; Tsapatsis, M. *Ind. Eng. Chem. Res.* **2001,** *40*, 544.
[19] Lovallo, M. C.; Tsapatsis, M *AICHE Journal* **1996,** *42*, 3020.
[20] Lovallo, M. C.; Gouzinis, A.; Tsapatsis, M. *AICHE Journal* **1998,** *44*, 1903.
[21] Poshusta, J. C.; Noble, R. D.; Falconer, J. L. *J. Membr. Sci.* **1999,** *160*, 115.
[22] Bonhomme, F; Welk, M. E.; Nenoff, T. M.; *Microp. Mesop. Mat.* **2003,** *66*, 181.
[23] Breck, D.W. Zeolite Molecular Sieves, (John Wiley and Sons, New York 1997).
[24] Dong, J.; Lin, Y. S.; Hu, M. Z. C.; Peascoe, R. A.; Payzant, E. A. *Microp. Mesop. Mat.* **2000,** *34*, 241.

HYDROGEN PERMEATION AND STABILITY OF A COMPOSITE PdCu MEMBRANE

Federico Guazzane, Erik Edwin Engwall, Ivan Peter Mardilovich, and Yi Hua Ma

Center for Inorganic Membrane Studies
Department of Chemical Engineering
Worcester Polytechnic Institute
100 Institute Road
Worcester, Massachusetts 01609 USA)

Introduction

The production of hydrogen from the steam reforming of hydrocarbons in a Pd or Pd-alloy membrane reactor has been proven to be a feasible and economically viable approach for hydrogen production[i,ii]. Composite Pd-Cu alloys have the advantage over Pd and Pd-Ag membranes of being mechanically stable and sulfur resistant[iii]. Morreale et al[iv] recently proved that the low hydrogen permeable Pd-Cu α phase was more resistant to sulfur poisoning than the highly permeable β phase. The $Pd_{60}Cu_{40}$ alloy, having the highest hydrogen permeability, looses its hydrogen transport properties at temperatures above 450ºC due to the β to α transformation. Moreover, the permeability of Pd-0 to 30 wt% Cu alloys decreases as the Cu content increases. Therefore, a low (10-20wt%) Cu content Pd-Cu alloy membrane would preferably be used at high temperatures (>500ºC) and sulfur contaminated atmospheres.

The main objective of this work was to assess the possibility of preparing a thin (<10μm) and stable low Cu content (~10wt%Cu) Pd-Cu membrane on a porous metallic support. Special attention was focused on hydrogen permeance and selectivity stability at 450ºC.

Experimental

The low Cu content Pd-Cu membrane was prepared by the coating and diffusion technique. That is, a 5μm thick palladium layer and a 2μm thick Cu layer were sequentially deposited by the electroless plating method on a porous metal support (0.1μm, Mott Co.). A detailed description on the support preparation and the plating procedures can be found in Ma et al[v] and Mardilovich et al[vi]. The Pd-Cu bimetallic structure was annealed in hydrogen atmosphere following a stage-wise temperature program i.e. the membrane was held for 12-24 hours at 250, 300, 350, 400, 450, 500 and 550ºC. Finally, the annealed Pd-Cu membrane was coated with an additional 3μm of palladium to achieve a leak free membrane. The total surface of the hydrogen permeable membrane was 120 cm^2 and its thickness was estimated to be 10 μm. The Cu content was targeted to be 10wt% although permeation results revealed that the Cu content was close to 5wt%.

The permeation apparatus consisted of a shell and tube stainless steel reactor where the membrane was housed using stainless steel and graphite ferrules. All parameters, pressure, temperature and gas fluxes were continuously logged using National Instruments data acquisition equipment. A detailed description of the permeation system used for membrane characterization was carried out by Mardilovich et al.

The He leak of the membrane was measured either in pure He atmosphere or in hydrogen atmosphere by feeding the shell side with a 99%H_2-1%He mixture gas and analyzing the tube flow with Gas Chromatography (GC). UHP Hydrogen was used as carrier gas and the TCD detector gain was set to high.

Results and Discussion

Hydrogen permeance. The hydrogen permeation rate of the Pd-5wt%Cu membrane was measured at 250, 300, 350, 400 and 450ºC. As seen in Figure 1, no decline in hydrogen permeance was observed at 450ºC over 500 hours indicating that no intermetallic diffusion, migration of support elements into the Pd-Cu layer, occurred for temperatures below or equal to 450ºC.

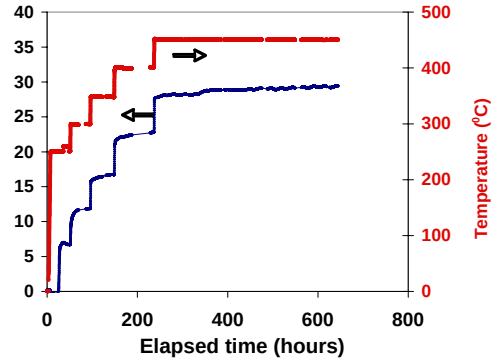

Figure 1. Hydrogen characterization carried out for the Pd-Cu membrane.

Figure 2 shows the hydrogen flux of the Pd-5wt%Cu as a function of $\Delta(P^{0.5})$ at 250, 300, 350, 400 and 450ºC. The hydrogen permeance value of 30 $m^3/(m^2\ h\ bar^{0.5})$ at 450ºC was slightly lower than the hydrogen permeance of a 10μm thick pure Pd membrane previously tested in our laboratory, which showed at 450ºC a hydrogen permeance of 34 $m^3/(m^2\ h\ bar^{0.5})$. The slightly lower hydrogen permeance of the Pd-Cu membrane is consistent with a low Cu content. As seen in Figure 2, the hydrogen flux seemed to be a linear function of $\Delta(P^{0.5})$ indicating that bulk diffusion was the rate limiting step. However, non-linear curve fitting procedure led to hydrogen exponent values of 0.6. The activation energy for hydrogen permeation, assuming Sievert's law, was determined to be 15.6 kJ/mol, which corresponded to a 5-8wt% Cu content. The Cu content was estimated by fitting Ea vs. Cu content experimental data from Howard et al.[vii] with a 3rd degree polynomial function.

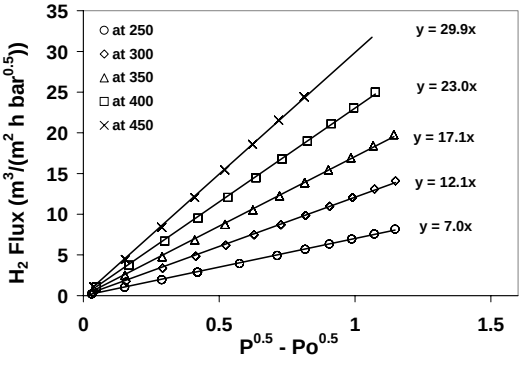

Figure 2. Hydrogen permeance at 250-450ºC for a 10μm thick Pd-5wt%Cu. Numbers beside experimental lines are the hydrogen permeance assuming Sievert's law was followed (n=0.5)

He leak stability. It was of great interest to determine the leak stability of the membrane at low temperatures (250-400ºC) and especially the leak behavior as a function of time at 450ºC in hydrogen atmosphere. The He leak in He atmosphere at 300ºC was equal to 0.0048 $m^3/(m^2$ h bar) (selectivity H_2/He = 1050) after exposure to hydrogen at 300ºC. After measuring hydrogen permeation rate at 350 and 400ºC the He leak was measured at 400ºC in He atmosphere and equaled 0.0054 $m^3/(m^2$ h bar) (selectivity H_2/He = 1760). Since the He leak was almost unchanged up to 400ºC it appeared that the membrane microstructure did not change as temperature was raised i.e. no changes in defects occurred at temperatures between 250 and 400ºC.

The initial He leak at 450ºC, determined with a GC analysis, equaled 0.0046 $m^3/(m^2$ h bar), which was equal to the He leak at 400ºC within the margin of error. That is, the He leak did not increase during the 50 minutes (1ºC/min) of the temperature change. Figure 3 shows separation factor and selectivity (H_2/He) as a function of time at 450ºC in hydrogen.

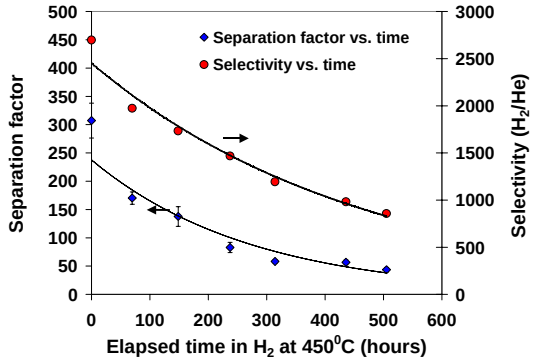

Figure 3. Separation factor and selectivity as a function of time exhibited by the Pd-5wt% Cu membrane at 450ºC in hydrogen atmosphere. The line through experimental points is a guide for the eyes

The separation factor and selectivity steadily decreased as a function of time at 450ºC in hydrogen. The decay seemed not to be linear occurring at a faster rate initially. The increase in leak might have been due related to the formation of pinholes and blisters. An average pinhole size after 500 hours at 450ºC in hydrogen was estimated by performing He and Ar permeation measurements and assuming slip-viscous mechanism (Knudsen and viscous component) for gas diffusion. Both gases led to an average pinhole size of 0.16μm at 450ºC.

Conclusions

The preparation of a low Cu content Pd-Cu alloy membrane was achieved on a porous metal support by the coating and diffusion method. The thin, 10μm, Pd-Cu membrane had a hydrogen permeance as high as 30 $m^3/(m^2$ h $bar^{0.5})$ at 450ºC and was stable for 500 hours. Leaks developed at a very slow rate at temperatures lower than 400ºC, however, the ideal selectivity of the membrane dropped from 2700 to 800 after 500 hours in hydrogen.

Acknowledgement. The authors gratefully acknowledge the financial support provided by Shell Hydrogen and Shell International Exploration and Production, Inc.

References

(i) Kikuchi E. "Membrane reactor application to hydrogen production." *Catalysis Today* **2000** 56(1-3): 97.
(ii) Lin Y. M. and Rei M. H. "Study on the hydrogen production from methanol steam reforming in supported palladium membrane reactor." *Catalysis Today* **2001** 67(1-3): 77.
(iii) McKinley D. L. U.S patent 3,350,845; **1967**
(iv) Morreale B. D., Ciocco M. V., Howard B. H., Killmeyer R. P., Cugini A. V. and Enick R. M. "Effect of hydrogen-sulfide on the hydrogen permeance of palladium-copper alloys at elevated temperatures." *Journal of Membrane Science* **2004** 241(2): 219.
(v) Ma Y. H., Mardilovich P. P., She Y. U.S patent n° 6,1502,987
(vi) Mardilovich P. P., She Y., Ma Y. H. and Rei M. H. "Defect free palladium membrane on porous stainless-steel support". *AIChe journal*, **1998** 44(2) 310-322
(vii) Howard B. H., Killmeyer R. P., Rothenberger K. S., Cugini A. V., Morreale B. D., Enick R. M and Bustamante F. "Hydrogen permeance of palladium-copper alloy membranes over a wide range of temperatures and pressures." *Journal of Membrane Science* **2004** 241(2): 207.

HIGHLY PERMEABLE AND SELECTIVE SILICA MEMBRANES FOR HYDROGEN SEPARATION AT HIGH TEMPERATURE

Yunfeng Gu, Pelin Phacarlioglu, and S. Ted Oyama

Department of Chemical Engineering
Virginia Polytechnic Institute and State University
Blacksburg, VA 24061

Introduction

Hydrogen separation membranes have been the subject of considerable research because of the importance of hydrogen in the refining and chemical industries and because of its potential as a clean, renewable fuel[1]. Many of the reactions that produce hydrogen such as steam reforming, dehydrogenation, and aromatization, are endothermic, equilibrium-limited reactions that could be enhanced by simultaneous reaction and separation. Hence there is particular need for membranes that are stable at the high temperatures (773-973 K) required for these reactions.

Silica-based membranes have been found to have good permeance for hydrogen and have received considerable attention. The first membranes were prepared on porous Vycor glass substrates by the chemical vapor deposition (CVD) of tetraethylorthosilicate (TEOS) at relatively low temperatures (473 K) using co-reagents such as H_2O[2], O_2[3], or O_3[4]. These conditions as well as methods such as the "opposing reactants"[5] or evacuation[6] techniques resulted in the deposition of the silica in the interior of the pores and gave rise to low permeance of the order of 10^{-8} mol $m^{-2}s^{-1}Pa^{-1}$. Improvements were obtained using a thermal decomposition method in which the TEOS was decomposed at high temperature (873-923 K) in an inert atmosphere using Vycor[7] or alumina[8] substrates. The resulting membrane had silica in the form of a thin outer layer of 20-30 nm thickness, and was denoted Nanosil to distinguish it from the previous materials. In this work we report the preparation and properties of a unique Nanosil-type membrane with an intermediate graded alumina substrate architecture which shows high permeability to hydrogen. The permeance at 873 K is high up to 5×10^{-7} mol $m^{-2}s^{-1}Pa^{-1}$, while its selectivity (> 5800 for CH_4) is excellent.

Experimental

Alumina Multilayer Substrate Preparation. The membrane was prepared using as a support a commercial macroporous alumina tube with nominal pore size of 100 nm. A 3-4 cm section of the support was connected to non-porous alumina tubes at both ends with ceramic glass joints. The support was dip-coated successively with a series of boehmite sols of decreasing particle sizes to form a graded multilayer γ-alumina substrate. The boehmite sols were prepared by carefully controlling the hydrolysis of aluminum alkoxides and the subsequent acid peptization of the boehmite precipitate. Three boehmite sols of median particle sizes of 40, 200 and 630 nm were obtained using the conditions listed in **Table 1** at a concentration of around 0.8M. They were denoted S40, S200, and S630. Before the membrane preparation, these original sols were diluted with distilled water and mixed with a polyvinyl alcohol (PVA) solution to form dilute dipping solutions with a 0.15 M concentration of the sol and a 0.35 wt% concentration of the PVA. The alumina support was dipped into the sol solution and was withdrawn after 10 seconds at a rate of 0.01 m s^{-1} using a motor-driven dipping apparatus. The dip-coated alumina was dried in ambient air for 24 h, and then was heated to 923 K in air at a rate of 1 K min^{-1} and calcined at 923 K for 2 h. The dipping-calcining process was repeated using successively smaller sols to form the three-layer γ-alumina substrate. Unsupported γ-alumina reference samples were prepared using the same procedure and parameters as the supported membranes.

Silica Layer Preparation. The final stage of the preparation of the composite membrane involved the deposition of a thin silica layer by the thermal decomposition of TEOS[9]. Briefly, the procedure was carried out in a concentric tubular apparatus with a quartz tube on the outside and the graded γ-alumina substrate on the inside. After heating the assembly to 873 K at a rate of 0.017 K s^{-1}, an argon gas flow (17 μmol s^{-1}) was introduced on the outer annular side and a dilute argon gas flow (17 μmol s^{-1}) with TEOS at a concentration of 0.019 mol m^{-3} was passed on the inner tube side. The TEOS deposition time was 3 h.

Characterization. A dynamic light scattering analyzer (Horiba Model LB-500) was used to measure the particle size of the boehmite sols. Single-gas permeation measurements were carried out at 873 K on H_2, CH_4, CO and CO_2 by admitting the pure gases at 200 kPa into the inner tube side, one end of which was closed, and measuring the quantity of gas flowing into the outer tube with a bubble flow meter at atmospheric pressure. The permeance of gas was obtained from the expression $F_i = (J_i / A)\, \Delta P$, where F_i is the permeance (mol m^{-2} s^{-1} Pa^{-1}), J_i the gas flux (mol s^{-1}), A the surface area (m^2) of the membrane section, and ΔP the gas pressure difference (Pa) between the shell and tube side. Permeation of He, H_2, and Ne was measured in a similar manner at 453-873 K. For low permeances a sweep gas at a known flow rate was used and the composition of the permeate stream was determined with a gas chromatograph (GC). The selectivity was calculated as the ratio of the permeances of H_2 to CH_4, CO or CO_2. A Field Emission Scanning Electron Microscope (FESEM, Leo 1550) was used to observe the cross-sectional microstructural of the membrane.

Results and Discussion

A key step in the synthesis was the formation of colloid boehmite sols of controlled particle size. The particle size of the sols is influenced by reaction conditions such as acid type, acid concentration and hydrolysis time, but past work in this area has yielded conflicting results. The results in **Table 1** show that long hydrolysis time and low acid concentration produce larger sol particles. These colloid sols have a relatively narrow particle size distribution due to the relatively long time of peptization. They were found to be stable for more than six months. The results of nitrogen physisorption on the unsupported γ-alumina references (obtained with a Micromeritics ASAP 2000) indicate that after gelling and subsequent calcination, the resulting γ-alumina membranes had different pore sizes and porosities. The larger the particle size of the sols, the larger the pore size and porosity of the resulting materials.

Table 1. Synthesis Parameters of Boehmite Sols with Different Particle Size

Boehmite Sol	Hydrolysis time / h	Molar ratio of H^+/Al	Median particle size / nm
S40	3	0.15	40
S200	24	0.07	200
S630	24	0.04	630

Cross-sectional images of the silica-on-alumina membrane reveal that three γ-alumina layers with different textures are observable, as shown in **Fig. 1**. There is no evidence of particle penetration into the support, indicating the success of the synthesis strategy of using large particles first. Significantly in this work, the use of dilute solutions (0.15 M) resulted in a relatively thin multilayer structure. The total thickness of the graded γ-alumina multilayer was around 1400 nm (1.4 μm). This is much thinner than

that of typical intermediate alumina layers of 6-10 μm in thickness even though they are not graded.

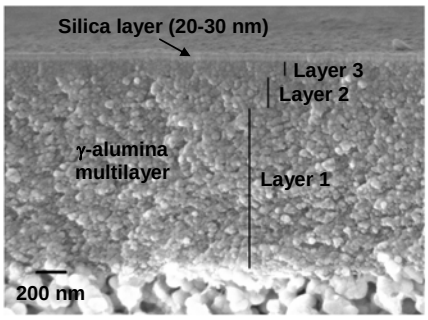

Figure 1. Scanning electron micrographs of fractured sections of the silica/γ-alumina multilayer with a graded three-layer structure.

The top γ-alumina layer has uniform pores and a smooth surface that leads to the formation of a stable silica layer on its surface. The layer is uniform and very thin (20-30 nm). The results here can be contrasted to our previous work with a single, non-graded intermediate layer. In that work again a silica layer of around 30 mm was obtained, however, the silica deposition time required at the same conditions was much longer (12 h vs. 3h) and resulted in a membrane with lower permeability (5-fold) and lower selectivity (2-fold). This implies that for a single intermediate layer a substantial amount of silica needed to be deposited inside the pores of the γ-alumina to repair imperfections before the top layer could be formed. The H_2 permeance was as high as 4.9×10^{-7} mol m^{-2} s^{-1} Pa^{-1} at 873 K, while the selectivities of H_2 over CH_4, CO and CO_2 through the composite membrane reached to 5900, 5100 and 1500, respectively. This indicates that a H_2 purity above 99.9% could be obtained using this composite membrane.

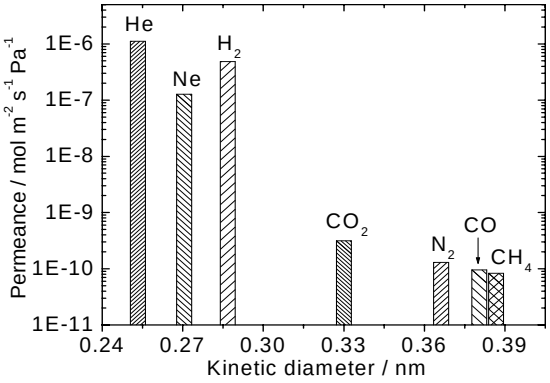

Figure 2. Single-gas permeances at 873 K of the silica-on-alumina membrane.

Fig. 2 shows permeances to single-component gases He, H_2, Ne, CO_2, N_2, CO and CH_4 through the composite membrane. It was found that the smaller the molecular size of the gas, the larger the permeance, demonstrating that a mechanism of molecular differentiation by size selectivity. The huge difference between the permeance of H_2 and CO_2 implies that a critical size in this material is around 0.3 nm. In fact, this size corresponds to the dimensions of the cavities in β-crystoballite, which has been suggested as a model for siliceous glasses similar to the amorphous silica of this membrane.

An unexpected result was the order of permeance of species with molecule size smaller than 0.3 nm, of He > H_2 > Ne, which was unusual since it did not follow the size (He = 0.26 nm, H_2 = 0.289 nm, Ne = 0.275 nm) nor the mass of the species (He = 4.0 au, H_2 = 2.01 au, Ne = 20.1 au). This unusual result can be quantitatively explained by a theory based on a mechanism involving jumps between solubility sites[10]. The governing equation is

$$Q = \frac{1}{6L}\left(\frac{d^2}{h}\right)\left(\frac{h^2}{2\pi m k T}\right)^{\frac{3}{2}}\left(\frac{\sigma h^2}{8\pi^2 I k T}\right)^{\alpha}\frac{(N_S/N_A)}{(e^{h\nu^*/2kT}-e^{-h\nu^*/2kT})^2}\,e^{-\Delta E_K/RT} \qquad (1)$$

In this equation Q is the permeance of a gas, L the thickness of the membrane, d the jump distance, m the mass of the species, h Planck's constant, k Boltzmann's constant, α is a constant that accounts for imcomplete rotation, σ is the symmetry factor of the species, I the moment of inertia, ν* the vibrational frequency of the species in the passageways between the sorption sites, T temperature, N_s the number of solubility sites available per m^3 of glass volume, N_A Avogadro's number, R the gas constant, and ΔE_K the activation energy for hopping between sorption sites. As shown in **Fig. 3**, the calculated curves, assuming a jump distance of 0.8 nm, fit the experimental points very well.

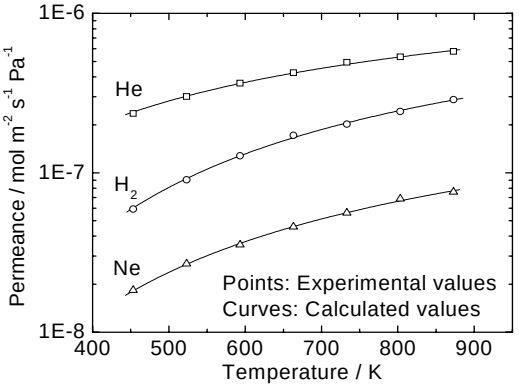

Figure 3. Experimental and calculated He, H_2 and Ne permeances for the silica-on-alumina membrane.

The thin γ-alumina intermediate layer formed by the sequential use of boehmite sols of increasingly small size displayed excellent performance in its role as an intermediate layer connecting the macroporous substrate with the hydrogen-selective Nanosil silica layer. The present Nanosil/Alumina composite membrane displayed much better permeation properties at 873 K in comparison to other silica membranes reported in the literature

References

(1) C. Song, *Catal. Today*, **2003**, 86**,** 211.
(2) M. Tsapatsis, G. R. Gavalas, *J. Membr. Sci.*, **1994**, 87, 281.
(3) W. G. Perkins, D. R. Begeal, *J. Chem. Phys.*, **1971**, 54, 1683.
(4) S-I. Nakao, T. Suzuki, T. Sugawara, T. Tsuru, S. Kimura, *Micropor. Mesopor. Mat.*, **2000**, 37, 145.
(5) G. R. Gavalas, C. E. Megiris, S. W. Nam, *Chem. Eng. Sci.*,**1989**, 44, 1829.
(6) B. K. Sea, K. Kusakabe, S. Morooka, *J. Membr. Sci*., **1997**, 130, 41.
(7) S. T. Oyama, D. Lee, S. Sugiyama, K. Fukui, Y. Iwasawa, *J. Mater. Sci*., **2001**, 36, 5213.
(8) D. Lee, L. Zhang, S.T. Oyama, S. Niu, R.F. Saraf, *J. Membr. Sci*., **2004**, 231, 117.
(9) S. T. Oyama, A. K. Prabhu, U.S. Patent 6,527,833 (**2003**) Assigned to Virginia Tech.
(10) S. T. Oyama , D. Lee, P. Hacarlioglu, R. F. Saraf, *J. Membr. Sci.*, **2004**, 244(1-2), 45.

GAS TRANSPORT AND MECHANICAL BEHAVIOR OF POLYMERIC DENSE FILMS AT ELEVATED TEMPERATURES

Vivek P. Khare, Alan R. Greenberg, Anandh Balakrishnan, Julie Diani and Sudhir Brahmandam*

Department of Mechanical Engineering, University of Colorado, Boulder, Colorado, 80309-0427, USA
*Laboratoire d'Ingénierie des Matériaux (CNRS) - ENSAM Paris, 75013, Paris, France.

Introduction

Polymeric membranes used in gas separation applications are often subjected to the simultaneous and competing effects of compaction and plasticization. Compaction refers to the decrease in membrane thickness due to mechanical deformation, i.e., creep, which occurs upon the application of a suitably high transmembrane pressure gradient. Compaction has been associated with a significant decline in membrane performance over time via a decrease in the free volume of the skin layer and an increase in the skin thickness due to the densification of the porous sublayer. In contrast, plasticization is associated with gases that have a sufficiently high solubility in the polymer to produce a large increase in the free volume and segmental mobility of the polymer matrix. Plasticization generally results in a depression in the glass transition temperature (T_g) [1], and usually leads to swelling and an increase in the permeability of glassy polymers. Literature studies report that prolonged exposure of polymeric membranes to a plasticizing gas leads to membrane "conditioning" that is reflected by a subsequent increase in the permeability of a non-plasticizing gas. Such conditioning results in decreased membrane selectivity and time-dependent performance degradation.

Previous studies of compaction and plasticization have generally employed either off-line mechanical testing or inferential characterization based on flux decline [2,3]; each of these approaches has major disadvantages. While off-line mechanical testing does not provide information about the effect of concomitant phenomena such as plasticization, inferential evaluation could lead to incorrect conclusions about cause-effect relationships, especially if the flux decline occurs due to other phenomena such as concentration polarization or stress-induced crystallization. Moreover, when membrane transport and mechanical responses are not measured simultaneously, it is difficult to establish a meaningful correlation between permselective performance and creep behavior because of the different time-scales involved. Since creep and plasticization are manifested as viscoelastic responses, they should become increasingly significant at elevated temperature, especially those close to the polymer T_g. Since elevated temperature separations offer significant thermodynamic and energetic advantages for many chemical processes, a growing number of applications require membranes that can operate in a high temperature and chemically challenging environment. Characterization of the simultaneous mechanical and transport responses at these high temperatures thus becomes an important input for strategies that optimize the long-term mechanical stability and permselectivity of polymeric membranes. Previous work has described the use of acoustic techniques for obtaining such simultaneous measurements, but the methodology is not easily adapted for high temperature measurements [4]. Consequently, the overall objective of this study is to develop an appropriate methodology for making simultaneous mechanical and transport measurements and to use the results to develop a better understanding of the fundamental factors governing the relationship between creep and gas permeability in polymer dense films at elevated temperatures.

Materials and Methods

Dense films were cast in our laboratory using cellulose acetate (CA) (Eastman Chemical Company; grade 398-10; T_g = 183°C) and poly(methyl methacrylate) (Polysciences; MW = 75000; T_g = 106°C); in addition, polybenzimiadazole (PBI) films supplied by Pall Corporation were used in the as-received condition (T_g ~ 450°C). We utilized a novel technique for conducting simultaneous transport and mechanical property (STAMP) measurements on the polymeric samples (Figure 1). The STAMP protocol was used to study the creep/transport behavior of 60-micron thick PMMA dense films from 25-115ºC, 45-micron thick CA dense films from 25-190ºC, and 50-micron thick PBI dense films from 25-425ºC. In a typical experiment, a dense film sample (50-mm diameter) was loaded into a STAMP permeation cell, and heated to the desired temperature in an inert nitrogen atmosphere and maintained at temperature overnight to establish steady-state conditions. Subsequently, the upstream pressure in the permeation cell was raised to either 4.1 MPa (600 psi) for the PMMA films or 3.1 MPa (450 psi) for the CA and PBI films, and the film thickness and flux were monitored as a function of time for 24 hours. Changes in the film thickness were measured using a linear variable differential transformer (LVDT), and the flux was measured using a pressure-rise technique. Systematic experiments were conducted in which the films were exposed to nitrogen (N_2) and carbon dioxide (CO_2) gases at constant pressure and temperatures. In order to maintain a constant transmembrane pressure gradient, a solenoid valve on the permeate side opened whenever the permeate pressure increased to a set low value. Transport properties are reported as GPU, where 1GPU = 10^{-6} cm^3(STP)/cm^2-s-cmHg.

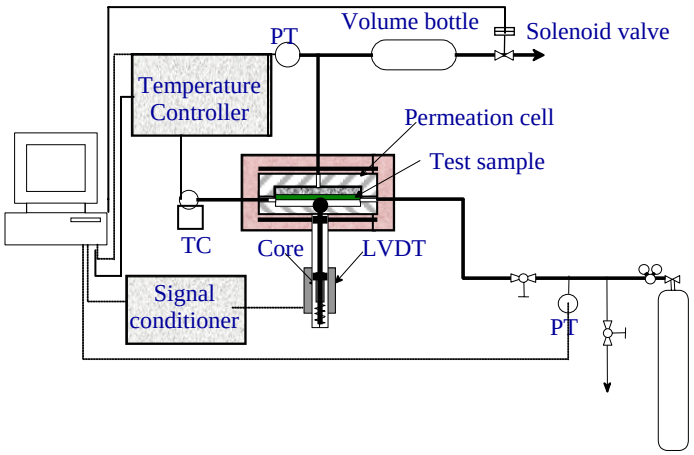

Figure 1. Schematic showing simultaneous transport and mechanical property (STAMP) measurement apparatus.

Results and Discussion

Two samples of the CA films were tested under N_2 pressure at each of the temperatures: 30, 110, 140, 160, 180, and 190 °C, respectively. As expected, an Arrhenius-type dependence of the initial film permeability with temperature was observed. Figure 2 shows the normalized permeance as a function of time at different temperatures. At temperatures <190°C, the permeance decreased by < 3% in 24 hr. In contrast, the permeance decrease was much more pronounced (~ 40%) at 190°C. This response is expected given the structural changes that occur when T > T_g. Likewise, one would expect creep to be more pronounced at 190°C. Figure 3 shows the

creep-time profiles of the films as a function of temperature. Here, creep is reported as percent compressive strain, which is calculated by dividing the measured change in the film thickness by the initial film thickness at the test temperature.

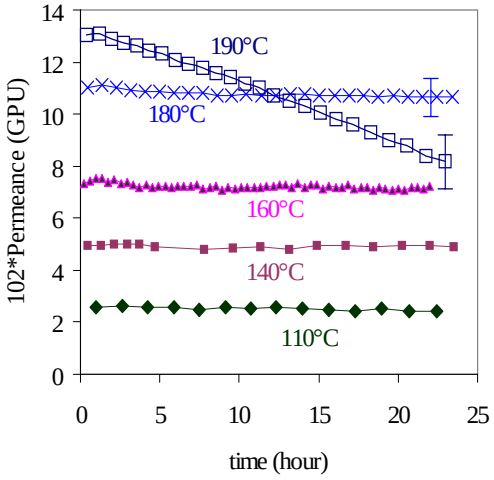

Figure 2. Nitrogen permeance versus time results for cellulose acetate dense films as a function of temperature. Upstream pressure is 3.1 MPa.

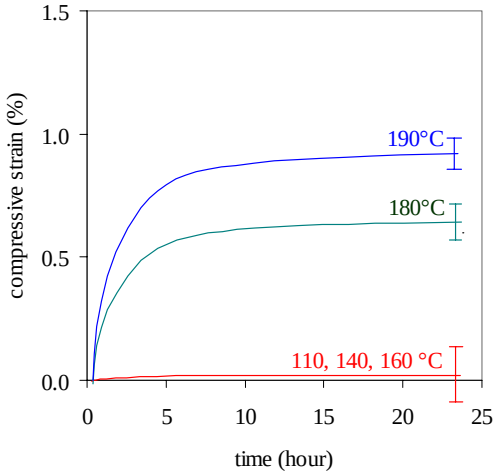

Figure 3. Creep response for cellulose acetate dense films as a function of temperature. Data obtained in nitrogen at an upstream pressure of 3.1 MPa.

As expected, creep is negligible at low temperatures and only the creep-time profiles at 180 and 190 °C evidence significant values of compressive strain, i.e. ~ 0.6 and 1.1 %, respectively. Although the strains are large enough to be measured accurately using the STAMP technique, they are nonetheless too small to explain the extent of the observed permeance decrease, especially at 190°C. If the flux decrease occurs due to a reduction in the polymer free volume, then a 40% flux decrease should imply a decrease of similar magnitude in the free volume, and hence the overall dimensions of the CA film. Clearly, it is difficult to reconcile the small decrease in the film thickness that is observed to the relatively large decrease in the permeance. In contrast to N_2 exposure, no Arrhenius-type relationship was observed under CO_2 pressure. In addition, the permeance increased with time at low temperatures with a maximum value at 25°C, consistent with the largest degree of swelling. For CO_2 exposure a net decrease in permeance with time was only observed at 190°C. The creep measurements corroborated the permeance data; a net increase in thickness was observed at temperatures below 190°C, with the maximum value at 25°. Under CO_2 exposure, film thickness decreased only at 190°C where the creep response (decreased thickness) dominated swelling (increased thickness) due to plasticization.

Similar creep and permeance results were obtained for the PBI and PMMA dense films although the respective magnitudes of the responses are somewhat different. These data support results obtained from preliminary molecular dynamic simulation studies using PMMA that suggest that pressurization leads to a shift in the free volume distribution towards smaller size free-volume elements without a significant change in the total free volume. Additional studies to confirm these results are currently underway.

Conclusions

Data obtained from coupled creep and gas flux experiments suggest that the time scales for mechanical and transport responses are rather different. In addition, the magnitude of observed isothermal permeance decreases at temperatures in the vicinity of T_g does not scale with the magnitude of the measured compressive strain. Results of initial molecular modeling work suggest that the changes in dense film permeance as a function of time may be related to changes in the free volume distribution. Overall, the preliminary studies described in this paper provide important initial insights regarding coupling effects between mechanical and transport behavior at elevated temperature.

Acknowledgement. The authors gratefully acknowledge financial support for this work from the Department of Energy Office of Fossil Energy, administered the National Energy and Technology Laboratory, Morgantown, WV (Project FE-01-0003).

References

(1) Sanders, E.S. *J. Membrane Sci*. **1988**, *37*, 63.
(2) Lawson, K.W.; Hall, M.S.; and Lloyd, D.R. *J. Membrane Sci*. **1995**, *101*, 99.
(3) Fleming, G.K.; and Koros W.J. *Macromolecules* **1986**, *19*, 2285.
(4) Reinsch, V.; Greenberg, A.R.; Kelley, S.; Peterson, R.; and Bond, L. *J. Membrane Sci*. **2000,** *171*, 217.

WATER/ETHANOL SELECTIVITY FOR AN AZEOTROPIC MIXTURE OF ETHANOL/WATER OF NOVEL ORGANIC-INORGANIC HYBRID MEMBRANES FROM POLY(VINYL ALCOHOL) AND OLIGOSILANE -WITH THE AIM OF ALCOHOL FUEL-

Tadashi Uragami, Shohei Yanagisawa, and Takashi Miyata

Faculty of Engineering, Kansai University, Suita, Osaka 564-8680, Japan

Introduction

Membrane separation techniques with easy operation and high energy savings are greatly appreciated in a variety of applications in the medical, food, industrial, energy and environment field. The chemical and physical structures of polymer membranes are engineered to improve membrane performance by several methods.

Alcohol is a clean energy source that can be produced by the fermentation of biomass. However, it needs to be highly concentrated. In general, aqueous alcohol solutions are concentrated by distillation, but an azeotrope (96.5 wt% ethanol) prevents further separated by distillation. Pervaporation, a membrane separation technique, can be used for separation of these azeotropes: pervaporation is a promising membrane technique for the separation of organic liquid mixtures such as azeotropic mixtures[1] or close-boiling point mixtures.[2]

Organic-inorganic hybrid materials are viewed as next generation materials in many applications because they have both the film-forming properties of a polymer and the stability of an inorganic compound. In this study, we prepared novel organic-inorganic hybrid membranes using the sol-gel reaction. It is well-known that poly(vinyl alcohol) (PVA) are highly water/ethanol selective during pervaporation of aqueous ethanol solutions. However, swelling of the PVA membrane in an aqueous ethanol solution results in an increase in both solubility and diffusivity of ethanol, which leads to lower water/ethanol selectivity. In this work, to control swelling of PVA membranes, mixtures of PVA and oligosilane were prepared by the sol-gel reaction and fabricated into PVA/Oligosilane hybrid membranes. The relationship between the structure of the PVA/Oligosilane hybrid membranes and their permeation and separation characteristics for an azeotropic mixture of ethanol/water by pervaporation is discussed in detail.

Experimental

Materials. Poly(vinyl alcohol) (PVA), which was supplied by Nippon Synthetic Chemical Industry Co. Ltd. at an average degree of polymerization of 1650 and a degree of saponification of 99.7 mol%, was employed as the organic component. Oligosilane (**I**), which is Compoceran 1000 supplied from Arakawa Chemical Industry Co. Ltd., was used as the inorganic component. Dimethyl sulfoxide (DMSO) dehydrated by a conventional method was employed as a casting solvent. All other solvents and reagents were purchased from Wako Pure Chemical Industries, Ltd., and were of analytical grade and were used without further purification.

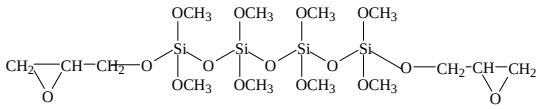

(**I**)

Preparation of PVA and PVA/Oligosilane Hybrid Membranes. PVA powder was dissolved in DMSO at 80°C to make a 2wt% casting solution. After removal of the insoluble impurities using a glass filter, it was stirred for 1 h at 25°C. The PVA membrane was prepared by pouring the casting solution onto Teflon plates, and then allowing the solvent to evaporate completely at 80°C for 24 h.

After the prescribed amount of oligosilane per a weight of PVA was mixed with the PVA dissolved in DMSO at 25°C to a concentration of 2wt%, 1M HCl was added to the PVA/Oligosilane mixture as an acid catalyst for the sol-gel reaction. The PVA/Oligosilane hybrid membranes were prepared by pouring the casting solutions onto Teflon plates, and then allowing the solvent to evaporate completely at 80°C for 30 h.

Permeation Measurements. The pervaporation was carried out using the apparatus described in previous studies under the following conditions: permeation temperature, 40°C; pressure of the permeate side, 5.0×10^2 Pa. The effective membrane area was 13.8 cm^2. An azeotropic mixture of ethanol/water was used as the feed solution. The permeate was collected in a U-tube at liquid nitrogen temperature. The permeation rates of aqueous alcohol solutions during pervaporation were determined from the weight of the permeate collected in the cold U-tube, the permeation time, and the effective membrane area. The compositions of the feed solution and permeate were determined by a gas chromatograph (Shimadzu GC-9A). The results from the permeation of aqueous alcohol solutions during pervaporation were reproducible, and the errors inherent in the permeation measurements were on the order of a few percent.

Contact Angle Measurements. The contact angles for methylene iodide on the surface of PVA and PVA/Oligosilane hybrid membranes were measured using a contact angle meter (Erma, Model G-1) at 25°C. The contact angles, θ, were determined by eq 1:

$$\theta = \cos^{-1}\{(\cos\theta_a + \cos\theta_r)/2\} \quad (1)$$

where θ_a and θ_r are the advancing contact angle and the receding contact angle, respectively.

Cross-link Density of PVA/Oligosilane Hybrid Membranes. The cross-link density, ρ, of the PVA/Oligosilane hybrid membranes was calculated from the network theory of rubber elasticity given in eq. 2:

$$\rho = E'/3d\phi RT \quad (2)$$

where the modulus, E', was determined from measurements with a dynamic mechanical analyzer (Rheogel-E4000 F3, 10 Hz; temperature, 40 °C; d is membrane density, ϕ is the front factor (where $\phi = 1$), R is the gas constant, and T is the absolute temperature.

Annealing of Membranes. The PVA and PVA/Oligosilane hybrid membranes were placed between filter papers and annealed under a nitrogen atmosphere at 100°C for 12h.

Results and Discussion

Effect of Oligosilane Content on the Permeation and Separation Characteristics of PVA/Oligosilane Hybrid Membranes. Figure 1 shows the effects of the oligosilane content on the normalized permeastion rate and the ethanol concentration in the permeate for an azeotrope of ethanol/water through the PVA/Oligosilane hybrid membranes during pervaporation. In all membranes, the ethanol concentration in the permeate was lower than that in the feed. These results suggest that the PVA and PVA/Oligosilane hybrid membranes are high water/ethanol selective. With increasing oligosilane content, the normalized permeation rate increased, but the water/ethanol selectivity decreased.

In **Figure 2**, the effects of the oligosilane content on the concentration in the PVA/Oligosilane hybrid membranes immersed in an azeotrope of ethanol/water and the apparent cross-link density of the PVA/Oligosilane hybrid membranes is shown. The ethanol concentration in the PVA/Oligosilane hybrid membrane increased, but the apparent cross-link density of those membranes decreased, with increasing oligisilane content. Although the crosslinked structure is formed between the hydroxyl groups in PVA molecule and the methoxy groups in oligosilane molecule by the sol-gel reaction, intermolecular hydrogen bonds of PVA molecules are cut because of introduction of oligosilane molecules between the PVA molecular chains. The

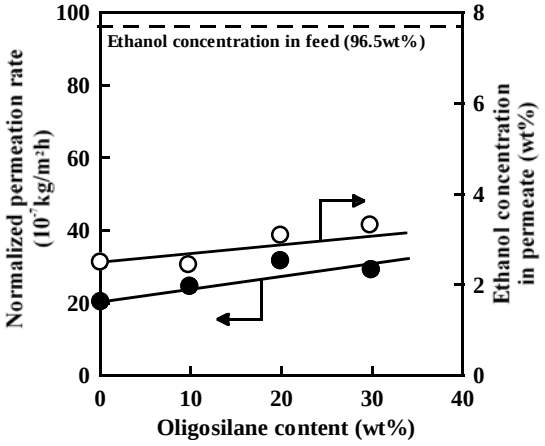

Figure 1. Normalized permeation rate (○) and ethanol concentration in the permeate (●) for an azeotropic mixture of ethanol/water through the PVA/Oligosilane hybrid membranes during pervaporation as a function of the oligosilane content.

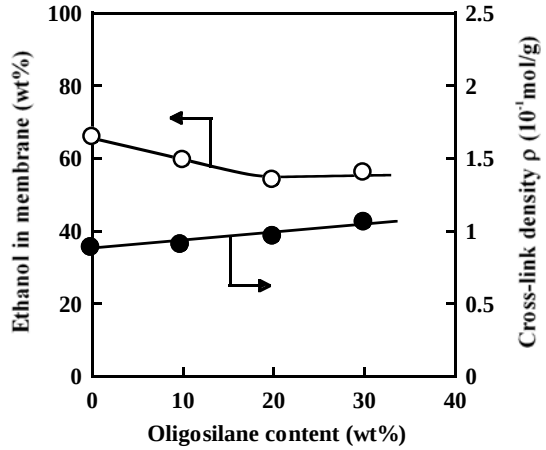

Figure 2. Ethanol concentration in the PVA/Oligosilane hybrid membranes for an azeotropic mixture of ethanol/water (●) and the apparent cross-link density of the PVA/Oligosilane hybrid membranes (○) as a function of the oligosilane content.

decrease in the apparent cross-link density in Figure 2 could be attributed to these facts. On the other hand, the increase in the ethanol concentration in the PVA/oligosilane hybrid membranes is due to the formation of an opened structure with the introduction of oligosilane molecule between the PVA molecules, i. e., the ethanol molecule with larger molecular size as well as the water molecule with smaller molecular size is easily incorporated in the PVA/Oligosilane hybrid membranes.In Figure 1, with increasing oligosilane content, the increase in the normalized permeation rate and the decrease in the water/ethanol selectivity can be attributed to the an opened structure of the PVA/Oligosilane hybrid membranes.

Effect of Annealing of PVA/Oligosilane Hybrid Membranes. Figure 3 shows the permeation and separation characteristics for an azeotrope of ethanol/water through the untreated and the annealed PVA/Oligosilane hybrid membranes as a function of the oligosilane content. The ethanol concentrations in the permeates in all annealed PVA/Oligosilana hybrid membranes were lower than those in the untreaterd PVA/Oligosilane hybrid membranes. These results suggest that the annealing treatment of the PVA/Oligosilane hybrid membranes significantly contributes to an improvement of water/ethanol selectivity for an azeotrope of ethanol/water. On the other hand, the

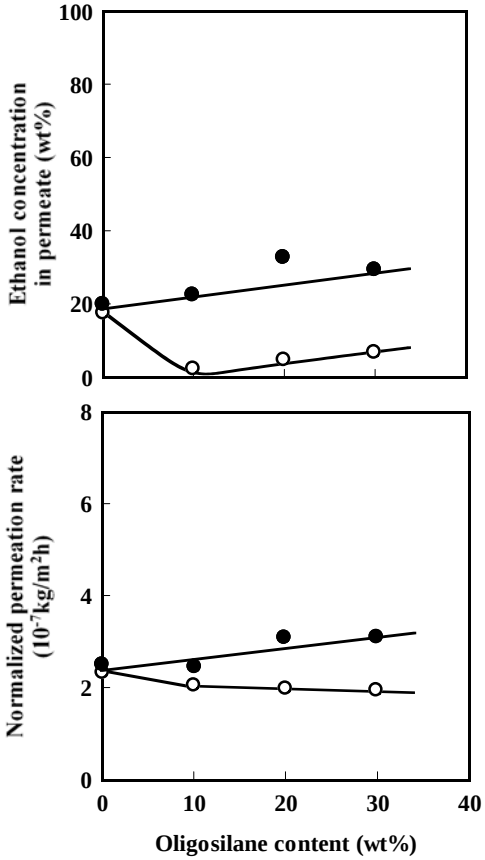

Figure 3. Effects of the oligosilane content on the normalized permeation rate and the ethanol concentration in the permeate for an azeotropic mixture of ethanol/ water through the untreated PVA/Oligosilane hybrid membranes (●) and the annealed PVA/Oligosilane hybrid membranes (○) during pervaporation.

normalized permeation rates of the annealed PVA/Oligosilane hybrid membranes were smaller than those of the untreated PVA/Oligosilane hybrid membranes. This result could be attributed to the fact that the condensation reactions between the PVA molecule and the oligosilane molecule was accelerated by annealing and consequently the structure of hybrid membrane became denser. The measurements of the ethanol concentrations in the untreated and annealedPVA/Oligosilane hybrid membranes for an azeotrope of ethanol/water supported that those in the latter were lower than those in the former.The apparent cross-link density of the latter was significantly higher than that of the former and the degree of swelling of the latter was lower than that of the former. When the PVA/Oligosilane hybrid membranes are annealed, the condensation reactions between the PVA molecules and the oligosilane molecules proceed, the cross-link density of the hybrid membrane increases, the membrane structure becomes denser, the degree of swelling of the hybrid membrane is depressed, and consequently the water/ethanol selectivity for an azeotrope of ethanol/water is improved.

References

1. Psaume, R.; Aurell, Y.; Mora, J. C.; Bersillon, J. L. *J. Membr. Sci.* **1988,** ,36, 373.
2. Blume, I.; Wijmans, J. G;Baker, R. W. *J. Membr. Sci.* **1990**, *49,* 253.

NOVEL MEMBRANE MATERIALS FOR CO_2 REMOVAL FROM MIXTURES WITH H_2

Haiqing Lin[1], Scott Matteucci[1] and Benny D. Freeman[1]
Sumod Kalakkunnath[2] and Douglass S. Kalika[2]

[1]Department of Chemical Engineering
University of Texas at Austin, Austin, TX, 78758
[2]Department of Chemical and Materials Engineering
University of Kentucky, Lexington, KY 40506

Introduction

Polymer membranes are used in many applications, including gas separations, due to their inherently low energy requirements for molecular scale separations. Hydrogen, a potential future energy source, is usually produced by steam reforming of hydrocarbons and requires removal of byproducts such as CO_2 and H_2S.[1] For membrane processes to be applicable to these separations, it is highly desirable to selectively remove CO_2, thereby maintaining H_2 at or near feed pressure to avoid expensive recompression of the desired H_2 product.

Gas permeability, *P*, is the product of gas solubility in the polymer, S, and gas diffusivity, D, as follows: $P=S\times D$.[2] The ability of a polymer membrane to separate two gases, such as CO_2 and H_2, is gauged by the ratio of their permeabilities, which reflects the tradeoff between favorable solubility selectivity (CO_2 is more condensable and, therefore, $S_{CO_2}/S_{H_2}>1$) and unfavorable diffusivity selectivity (CO_2 is larger than H_2, so $D_{CO_2}/D_{H_2}<1$). To achieve very high CO_2/H_2 selectivity, a membrane must exhibit favorable interactions with CO_2 to enhance solubility selectivity, and it must exhibit a very weak size-sieving ability to bring D_{CO_2}/D_{H_2} as close to 1 as possible. To date, the polar ether oxygens in ethylene oxide (EO) units are the best known groups to interact sufficiently strongly with CO_2 to have high solubility selectivity and remain flexible without significantly increasing the size sieving ability of the polymer.[3]

Previously, we have reported on crosslinked copolymers (PEGDA-*co*-PEGMEA) prepared by photopolymerizing mixtures of poly(ethylene glycol) diacrylate (PEGDA: $CH_2=CHCO(OCH_2CH_2)_nOCOCH=CH_2$, n = 14) and poly(ethylene glycol) methyl ether acrylate (PEGMEA: $CH_2=CHCO(OCH_2CH_2)_nOCH_3$, n = 8.5).[4] These materials exhibit very high CO_2 permeability and high CO_2/H_2 pure gas selectivity. In the current report, mixed gas CO_2/H_2 separation performance in these copolymers is evaluated. Decreasing temperature improves CO_2/H_2 mixed gas separation properties. The addition of MgO nanoparticles improves CO_2 permeability considerably with little reduction in selectivity.

Experimental

Film Preparation. Prepolymer solutions were prepared by adding 0.1 wt.% initiator (1-hydroxycyclohexyl phenyl ketone) to mixtures of PEGDA and PEGMEA. This solution was sandwiched between two quartz plates and then exposed to UV light. The detailed procedure has been reported elsewhere.[4] Nanocomposite samples were prepared by mixing MgO nanoparticles with the prepolymer solution and then polymerizing as previously reported.[4]

Permeation and Sorption Measurement. Pure gas permeability was measured using a constant volume/variable pressure apparatus.[5] Mixed gas permeability was measured using a constant pressure/variable volume apparatus.[6] Pure gas sorption isotherms were obtained using a dual-volume, dual-transducer apparatus.[5]

Results and Discussion

Three CO_2/H_2 mixtures (i.e., 10% CO_2/90% H_2, 50% CO_2/50% H_2, and 80% CO_2/20% H_2) have been tested at three temperatures (i.e., 35°C, 10°C and -20°C) in PEGDA-co-PEGMEA samples containing 30 wt% PEGDA and 70 wt% PEGMEA. As reported previously, higher PEGMEA content in the copolymers leads to larger fractional free volume, resulting in increased CO_2 permeability and CO_2/H_2 selectivity.[4] Therefore, this copolymer exhibits relatively high CO_2 permeability and high CO_2/H_2 pure gas selectivity. Furthermore, the PEGMEA content is low enough that this copolymer does not crystallize within the temperature range studied. In contrast, a copolymer containing 91 wt% PEGMEA and the balance PEGDA crystallizes at about 0°C, which has a deleterious effect on gas permeability.

Figure 1 presents CO_2 permeability as a function of CO_2 partial pressure at 35°C, 10°C and -20°C. In general, CO_2 permeability increases with increasing CO_2 partial pressure because of plasticization of the polymer chains by CO_2. The increase becomes more significant at lower temperatures because CO_2 sorption increases with decreasing temperature. Interestingly, at a CO_2 partial pressure of 17 atm, CO_2 permeability at -20°C is higher than that at 10°C and close to that at 35°C. Therefore, lower temperature might not necessarily lead to lower permeability. Additionally, the pure gas and mixture CO_2 permeability appears to fall on the same trend line, suggesting that the presence of H_2 has a negligible effect on CO_2 permeability.

Figure 2 presents H_2 permeability as a function of CO_2 partial pressure at various temperatures. H_2 permeability increases with increasing CO_2 partial pressure. Furthermore, H_2 permeability falls on the same trend line for each temperature, suggesting that the dependence of H_2 permeability on feed composition derives from the amount of CO_2 in the polymer (i.e., plasticization).

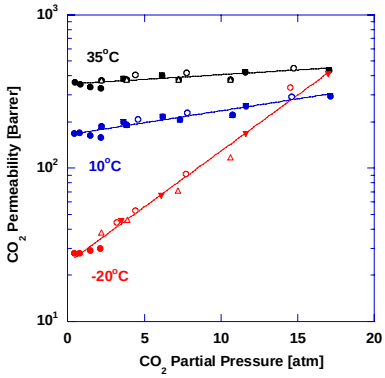

Figure 1. Effect of CO_2 partial pressure on CO_2 pure and mixed gas permeability. ○: pure gas; ●: 10% CO_2/90% H_2; Δ: 50% CO_2/50% H_2; ▼: 80% CO_2/20% H_2. The lines serve as guides to the eye.

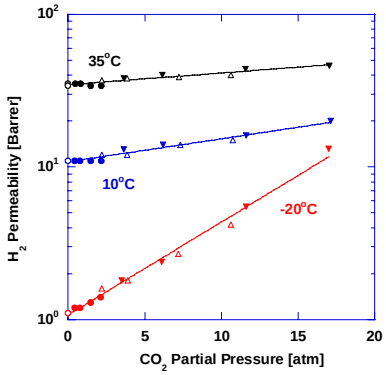

Figure 2. Effect of CO_2 partial pressure on H_2 pure and mixed gas permeability. ○: pure gas; ●: 10% CO_2/90% H_2; Δ: 50% CO_2/50% H_2; ▼: 80% CO_2/20% H_2.

Figure 3 presents CO_2/H_2 selectivity as a function of CO_2 partial pressure at 35°C, 10°C and -20°C. Mixed gas selectivity remains essentially independent of CO_2 partial pressure and mixture compositions at 35°C and 10°C. On the other hand, at -20°C, mixed gas selectivity increases with increasing CO_2 partial pressure and falls on the same trend line for different mixtures. As CO_2 partial pressure increases from 0.4 to 17 atm, CO_2/H_2 mixed gas selectivity increases by 35%, from 23 to 31. Typically, the sorption of a large amount of gas (such as CO_2 in this case) would significantly plasticize the polymer matrix, which is indicated by a decrease in glass transition temperature in the polymer/gas mixture.[7] Such plasticization would reduce the size sieving ability of the polymer, increasing CO_2/H_2 diffusivity selectivity, and, in turn, overall permeability selectivity as indicated in **Figure 3**.

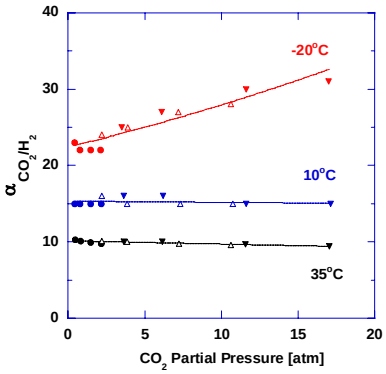

Figure 3. Effect of CO_2 partial pressure on CO_2/H_2 mixed gas selectivity. ●: 10% CO_2/90% H_2; Δ: 50% CO_2/50% H_2; ▼:80% CO_2/20% H_2.

Figure 4 presents a permeability/selectivity map for CO_2/H_2 separation.[8] The upper bound line drawn in the figure predicts the highest pure gas selectivity possible for a given permeability in polymer-based materials, which was calculated based on a model by Freeman.[9] The materials reported here exhibit superior separation performance. The effect of temperature on CO_2 separation properties is also illustrated in the graph. Lower temperature might improve both CO_2 permeability and CO_2/H_2 mixed gas selectivity. The CO_2/H_2 mixed gas selectivity of 31 and CO_2 permeability of 410 Barrers at -20°C and a CO_2 partial pressure of 17 atm is the best separation performance ever reported for CO_2/H_2 mixtures in solid non-facilitated transport polymeric membranes.

Figure 5 presents the effect of MgO nanoparticle content on pure gas CO_2 permeability at 35°C. The polymer matrix (XLPEGDA) is prepared from 100% PEGDA. At low MgO loadings, CO_2 permeability decreases, as predicted by conventional composite models.[10] However, at particle concentrations beyond approximately 32 wt.%, CO_2 permeability increases strongly, while CO_2/H_2 selectivity remains unchanged at about 8. As MgO loading is further increased to 44 wt.%, CO_2 permeability increases by one order of magnitude as compared to that of the particle-free polymer, while CO_2/H_2 selectivity decreases to 4.2. To understand the effect of nanoparticles on gas transport, sorption experiments have been performed for one composite (XLPEGDA with 44 wt.% MgO) at 35°C. Virgin nanocomposite samples sorb high amounts of CO_2. However, such sorption is largely irreversible. The reversible sorption is very similar to that in the pure polymer. Clearly, the strong increase in gas permeability upon adding nanoparticles must be derived in large measure from improvements in gas diffusivity.

Decreasing temperature improves CO_2/H_2 selectivity in the nanocomposite containing 44 wt.% MgO and the balance PEGDA. As temperature decreases from 35°C to -20°C, CO_2/H_2 selectivity increases from 4.2 to more than 10. As illustrated in **Figure 6**, mixed gas CO_2 permeability and CO_2/H_2 selectivity in the nanocomposite increase with increasing CO_2 partial pressure. Additionally, mixed gas CO_2 permeability in the nanocomposite is compared with pure gas CO_2 permeability in the pure polymer at -20°C. This comparison is reasonable because CO_2 permeability values for various compositions fall on the same trend line, as discussed above. Clearly, the addition of MgO nanoparticles improves CO_2 permeability.

References

(1) Kohl, A. L.; Nielson, R. *Gas Purification*, 5th ed.; Gulf Publishing: Houston, TX, 1997.

(2) Wijmans, J. G.; Baker, R. W. *J. Membr. Sci.* **1995**, *107*, 1-21.

(3) Lin, H.; Freeman, B. D. *J. Mol. Struct.* **2005**, *739*, 57-74.

(4) Lin, H.; Freeman, B. D.; Toy, L. G.; Bondar, V. I.; Gupta, R. P.; Pas, S. J.; Hill, A. J. *Polym. Prepr. (Am. Chem. Soc., Div. Polym. Chem.)* **2004**, *45*, 23-24.

(5) Lin, H.; Freeman, B. D. *J. Membr. Sci.* **2004**, *239*, 105-117.

(6) Merkel, T. C.; Gupta, R. P.; Turk, B. S.; Freeman, B. D. *J. Membr. Sci.* **2001**, *191*, 85-94.

(7) Chiou, J. S.; Barlow, J. W.; Paul, D. R. *J. Appl. Polym. Sci.* **1985**, *30*, 2633-2644.

(8) Robeson, L. M. *J. Membr. Sci.* **1991**, *62*, 165-185.

(9) Freeman, B. D. *Macromolecules* **1999**, *32*, 375-380.

(10) Petropoulos, J. H. In *Polymeric Gas Separation Membranes*; Paul, D. R., Yampolskii, Y. P., Eds.; CRC Press, Inc.: Boca Raton, Florida, 1994; pp 17-81.

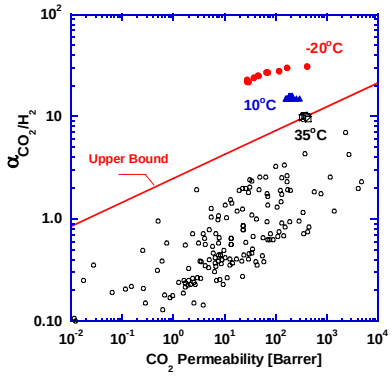

Figure 4. Permeability/selectivity map for CO_2/H_2 separation. Separation performance of PEGDA-co-PEGMEA is also presented at different temperatures.

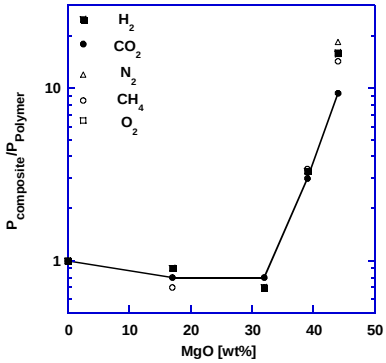

Figure 5. Effect of MgO nanoparticle content in XLPEGDA on pure gas permeability at 4.4 atm and 35°C.

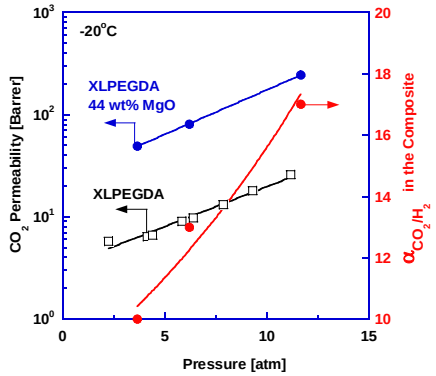

Figure 6. Effect of CO_2 partial pressure on CO_2 permeability and CO_2/H_2 mixed gas selectivity at -20°C in a nanocomposite containing 44 wt.% MgO and the balance PEGDA. The feed gas is 75/25 CO_2/H_2. Data for XLPEGDA are based on pure gas (CO_2) measurements.

HOLLOW FIBER MEMBRANE SIMULATION FOR CO_2 SEPARATION PROCESS

Jun Gyu Park, Hyung-Taek Kim

Dept. of Energy Studies, Ajou University
Wonchon-dong Yeongtong-gu
Suwon, Korea 443-749

Introduction

Separation of Carbon dioxide that is a kind of global warming gas is issued with the effectuation of UNFCCC (United Nations Framework Convention on Climate Change).

There are many methods about separation and recovery of CO_2 within exhaust gas by using fossil fuels. There are the adsorption, the absorption, the distillation, and the membrane separation. But these technologies have many defects up to date. Membrane is the most advanced technology and the most potential process for CO_2 separation from flue gas. Especially, membrane is a good for the facilities about the decrease of CO_2 discharge using the low energy consumption.

In this study, system models are simulated by FORTRAN and Aspen Custom Modeler™. First, we must remove water in front of membrane process. This simulation is changed temperature with pressure done by Aspen Plus™ .A simulation about one membrane module is made progress by using the FORTRAN, using those results, 4 bundles of membrane module is composed like a cascade. It is computed that required membrane area and number of module, permeated CO_2 concentration and the amount of permeated gas. And it is predicted consumption energy of pumps and compresses by Aspen Plus™.

In this study, when condition is fixed permeability and variety selectivity, we estimate required number of module, permeated CO_2 concentration and the amount of permeated gas.

Methods

First of all, we are simulation of dehydration process. Then using those results, 4 bundles of membrane module is composed like a cascade. Thereafter simulation using the FORTRAN is progressed. It is computed that required number of module, permeated CO_2 concentration and the amount of permeated gas by changing selectivity and fixed permeability. Last, it is simulated that the process with the recycle streams by using the FORTRAN. And we predict required energy in this process by Aspen Plus.

At $1 \sim 3$ *Stage*

$$L(I,J) = L(I,J-1) + V(I,J-1) + V(I+1,J-1)$$

AT 4 *Stage*

$$L(I,J) = L(I,J-1)$$

I : *i-th Module*

J : *iteration number*

At 1~3 stage have recycle steams but 4 stage don't have it. Therefore, equation of 1~3 stage add recycle steam. The recycle steam composition is the same value of feed steam.

We estimated required number of module, permeated CO_2 concentration and the amount of permeated gas by change selectivity. This method is fixing permeability for 20 and changing selectivity form 20 to 100.

Results and Discussion

Simulation for removal water

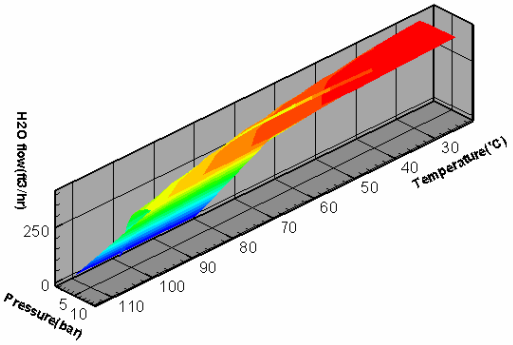

Figure 1. Result of removal water

Water is harmful effect to membrane modules. In front of process, we must remove water. In this case, composition of flue gas is 10% of CO_2, 17% of H_2O and 73% of N_2. Total volumetric flow is 2,410ft^3/hr from LNG power plant. Temperature is 130℃ and vapor fraction is 1. It is simulating by changing temperature and pressure of heat exchanger and flash dram. Temperature range is from 20℃ to 110℃ and pressure is from 1bar to 10bar.

Simulation of membrane process

Table 1. Input Parameters For 1 Membrane Module Process

Parameter	amount	parameter	amount
P_1	6 atm	Number of HF per module	5000
P_2	0.1 atm	Feed rate	1000 m^3/day
Selectivity	20	Length of HF	50 cm
Permeability	20	Pressure ratio	P_2/P_1

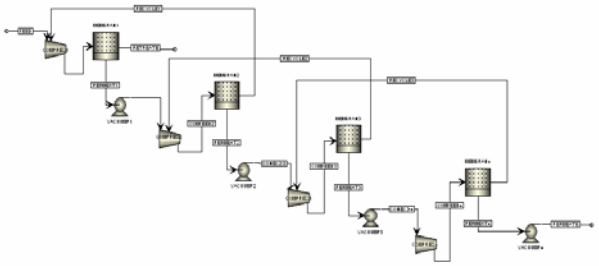

Figure 2. Membrane module process: There are 4 membrane modules and recycle

Fixing permeability for 20 and simulated during changing selectivity

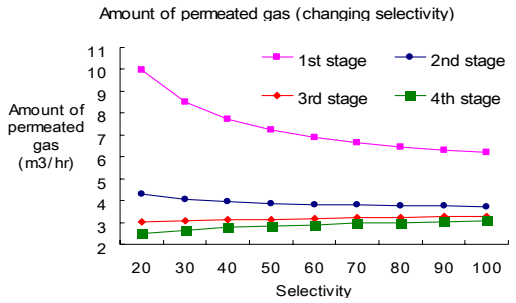

Figure 3. Amount of permeated gas during different selectivity

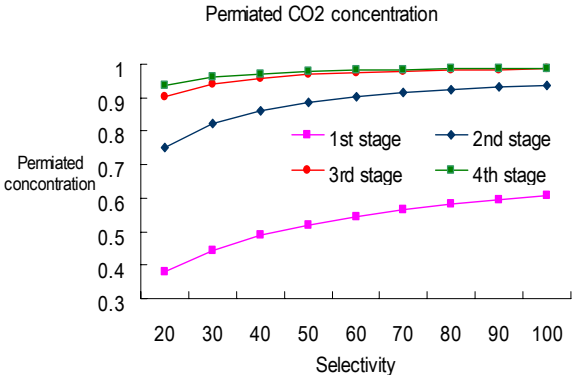

Figure 4. Permeated gas concentration during different selectivity

As selectivity increase, permeability of 1st stage is large decrease and permeability of 2nd stage is small decrease and permeability of 3rd & 4th is increased. Also figure 4, permeated concentration of each stage is increased. At selectivity is 100, CO_2 concentration at last stage is about 98%.

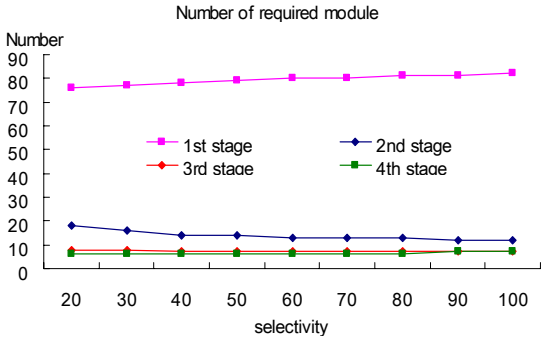

Figure 5. Number of required module during different selectivity

At Figure 5. we can know that number of required module is increased in order to 99% of CO_2 concentration. Because permeated flow is much small, it is more module needed in order to get high purity of CO_2, But when fixed permeability and changed selectivity , the value is not much different each other.

Table 2. Input parameters for energy cost estimation

Parameter	Amount
P1 (Feed pressure)	6 atm
P2(permeated pressure)	0.1 atm
Selectivity	20
Permeability	20
Number of HF per module	5000
Length of HF	50 cm
Number of HF per module	5000
Length of HF	50 cm

Table 3. Required energy consumption

Equipment	Net work requirement (kW)
1st compressor	3.7753
1st vacuum pump	2.9913
2nd compressor	9.0478
2nd vacuum pump	1.339
3rd compressor	3.8497
3rd vacuum pump	0.9876
4th compressor	2.7187
4th vacuum pump	0.8200
Total	25.5244

Total energy consumption is 25.5244kW. As you see Table 3, the required energy in 2nd stage is larger than 1st stage. While 1st stage is pressured form 1atm to 6atm, compressor of 2nd stage is less flow rate than 1st stage. So, energy consumption of 2nd stage is smaller than 1st.

Conclusions

In order to remove water in flue gas, we use cooling method. When temperature goes down about 40℃, almost all water is removed. Next we estimated number of module, permeated CO_2 concentration and the amount of permeated gas as changed selectivity. Membrane process required energy consumption about 25.5244kw for 4 compressors and vacuum pumps.

These results indicate that we can remove more CO_2 and get the high CO_2 concentration. If more bundles are attached, the separation units by using the hollow fiber membrane remove more CO_2 and get the high CO_2 concentration. Therefore, it is very useful that CO_2 separation process by using the hollow fiber membrane.

References

(1) James Marriott; Eva Sorensen; *Chemical Engineering Science 58*, **2003**, 4975-4990.
(2) R. Wang; S. L. Liu; T. T. Lin; T. S. Chung; *Chemical Engineering Science 57*, **2002**, 967-976.
(3) Li Xu; Lin Zhang; Huanlin Chen; *Desalination 148*, **2002**, 309-313.
(4) G. C. Kapantaidakis; G. H. Koops; *Journal of Membrane Science 204*, **2002**, 153-171.

MICROFLUIDIC ETHANOL BIOFUEL CELL

Anna Kinsella, R. Scott Martin, and Shelley D. Minteer

Department of Chemistry, Saint Louis University, St. Louis, MO

Introduction

Recent research has focused on microfluidic batteries and fuel cells (1-4), but the same microfluidic technology has not been thoroughly investigated for biofuel cells. This research focuses on the development of stackable, microchip- based biofuel cells. Microchip-based biofuel cells are compact and lightweight, making them viable portable power sources. In theory, they are also stackable, enabling multiple cells to be linked in series to increase power output. Microchip-based biofuel cells employ hydrodynamic flow of fuel through micron-sized channels containing microelectrodes. In this research, the enzyme pyrroloquinoline quinone (PQQ)-dependent alcohol dehydrogenase (ADH) is used as the catalyst in the biofuel cell to convert chemical energy to electrical energy. The cell is powered by the addition of ethanol through a micron-sized flow channel containing a bioanode, which is fabricated by micromolding carbon inks. This microelectrode is modified with a membrane containing the immobilized enzyme. We have successfully immobilized the enzyme on the electrode and electrochemical characterization has shown that the system is kinetically limited rather than transport limited.

Experimental

A 40 micron wide and 27.5 micron high micromolded carbon electrode is formed on a clean glass substrate using procedures described in Reference 5 and 6. A 100 micron PDMS channel is reversibly sealed over the micromolded carbon electrode. The carbon electrode is coated with a 2:1 ratio of PQQ-dependent alcohol dehydrogenase (ADH) to tetrabutylammonium bromide (TBAB)-modified Nafion membranes (prepared using the procedures described in Reference 7 and 8) by introducing the coating mixture to the 100 micron PDMS channel by hydrodynamic flow from a syringe at 1.0 microliters/min. The coating is allowed to dry overnight in the PDMS channel. Then, the PDMS channel is removed, leaving the immobilized enzyme coating on the carbon electrode. A 200 micron PDMS channel is reversibly sealed over a micromolded arbon electrode coated with immobilized enzyme. A 1.0mM ethanol fuel solution in pH 7.15 phosphate buffer is pumped over the coated electrode at flow rates ranging from 1.0 to 15.0 microliters/min. Cyclic voltammetry is performed to electrochemically characterize the coated carbon electrode. Fuel cell testing is performed by placing an external platinum cathode in the output reservoir of the 200 micron PDMS channel.

Results and Discussion

Figure 1 is schematic of the chemistry occurring at the bioanode. A micromolded carbon electrode is coated with a TBAB-modified Nafion membrane with PQQ-dependent ADH immobilized within. The ethanol fuel diffuses into the membrane and is oxidized by the PQQ-dependent ADH. The PQQ acts as the electron mediator to shuttle electrons from the enzyme to the electrode. Cyclic voltammograms of the bioanode in a fuel solution show sigmoidal voltammograms that are consistent with microelectrodes.

Power curves were generated with the bioanode in conjunction with an external platinum cathode at different flow rates. Figure 2 depicts the effect of flow rate on the maximum current density at the bioanode. The data depicts the average of three different fuel cells and the error bars correspond to one standard deviation. There is no statistical difference between current densities at flow rates ranging from 1mL/min to 15mL/min. This indicates that the system may have kinetic limitations as well as transport limitation.

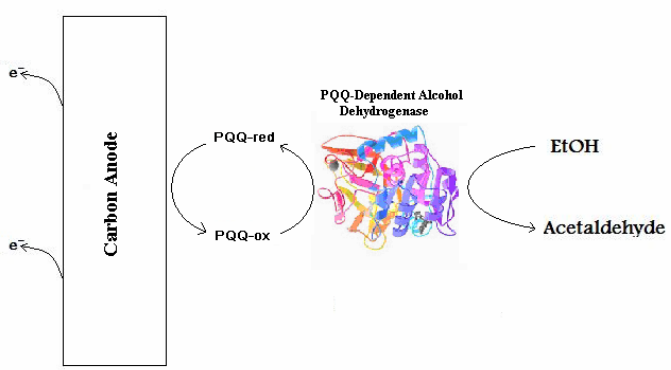

Figure 1. Schematic of the chemistry occurring at the PQQ-dependent bioanode.

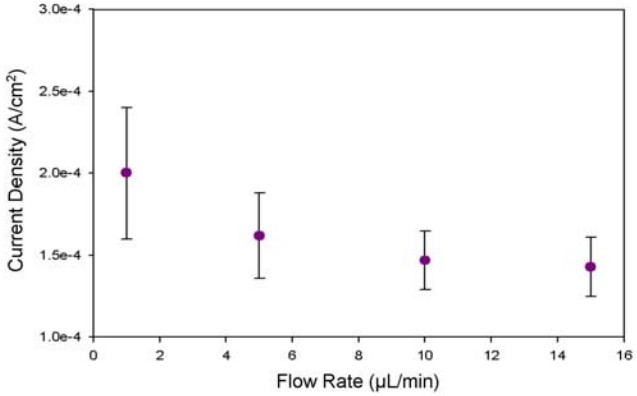

Figure 2. Plot of current density of an ethanol bioanode versus volumetric flow rate of 1.0 mM ethanol in pH 7.15 phosphate buffer (n=3).

Conclusions

Microfabrication and microchip-based systems can be used to form bioanodes. There is no statistical difference in the current densities for the various flow rates of fuel, which is evident that the system is kinetically limited. Future work will focus on integrating the cathode onto the microchip.

Acknowledgement. The authors acknowledge the Office of Naval Research for funding.

References

(1) Ferrigno, R.; Stroock, A.D.; Clark, T.D.; Mayer, M.; Whitesides, G.M. *JACS*, **2002**, *124*, 12930.
(2) Cohen, J.L.; Volpe, D.J.; Westly, D.A.; Pechenik, A.; Abruna, H.D. *Langmuir* **2005**, *21*, 3544.
(3) Choban, E.R.; Markoski, L.J.; Wieckowski, A.; Kenis, P.J. *J. Power Sources*, **2004**, 128, 54.
(4) Choban, E.R.; Markowski, L.J.; Stoltzfus, J.; Moore, J.S.; Kenis, P.J. *Proc. Power Sources Conference*, **2002**, 40, 317.
(5) Moore, C.M.; Minteer, S.D..; and Martin R.S. *Lab-on-a-chip.*, **2005**, *5*, 218.
(6) Kovarik, M.L.; Torrence, N.J.; Spence D.M.; and Martin, R.S. *Analyst* **2004**, *129*, 400.
(7) Schrenk, M.; Villigram, R.; Torrence, N.J.; Brancato, S.; and Minteer, S.D. *J. Mem. Sci.*, **2002**, 205, 3.
(8) Moore, C.M.; Johnson, V.; Hill, A.; Akers, N.L.; and Minteer S.D. *Biomacromolecules*, **2004**, 5, 1241.

ENZYME-BASED BIOFUEL CELLS WITH SWITCHABLE AND TUNABLE POWER OUTPUT

Eugenii Katz and Itamar Willner

Institute of Chemistry
The Hebrew University of Jerusalem
Givat Ram, Jerusalem 91904, Israel

Introduction

Electrical contacting of redox enzymes with electrode supports attracts substantial research efforts directed to the development of biosensors[1] and biofuel cell elements.[2] Recently, we reported on the effective electrical contacting of redox enzymes on electrodes by their structural alignment on electrodes through the surface reconstitution of flavoenzymes or pyrroloquinoline quinone (PQQ)-dependent enzymes on a relay-FAD monolayer assembly[3,4] or redox polymer-PQQ thin film,[5] respectively. This concept was further generalized by tailoring integrated, electrically contacted, cofactor-dependent enzyme electrodes by the cross-linking of affinity complexes between NAD^+-dependent enzymes and an electrocatalyst-NAD^+ monolayer[6] or thin film[7] associated with electrodes. Efficient electron transfer between redox enzymes and conductive electrode supports as a result of structural alignment and optimal positioning of the electron mediators allowed the development of noncompartmentalized biofuel cells.[8] Crossreactions of the anolyte fuel and catholyte oxidizer with the opposite electrodes were prevented due to the high specificity of the bioelectrocatalytic reactions at the electrodes, and thus the use of a membrane separating the catholyte and anolyte solutions could be eliminated. This kind of biofuel cell was suggested as an implantable device that uses physiological fluids, for example, blood, for the generation of electrical power that activates machinery units such as pacemakers or insulin pumps. Also, a noncompartmentalized biofuel cell can be used as a self-powered biosensor for glucose or lactate, because the output voltage and current signals are dependent on the substrate concentration.[9]

In the present paper, we wish to report on novel configurations of biofuel cells, in which the output power (voltage and current) can be reversibly switched between "ON" and "OFF" states and the magnitude of the voltage-current output can be precisely tuned by electrochemical or magnetic input signals.

Experimental

Electrical Switching and Tuning. The electrical switching and tuning of the biofuel cell output was accomplished by the integration of the biocatalysts active in the biofuel cell with a copper-poly(acrylic acid) matrix.[10] The electrodes were modified with a poly-(acrylic acid) thin film using the electropolymerization technique.[11] The polymer-modified electrodes were soaked in 0.1 M $CuSO_4$ solution for 1 h to saturate the polyacrylic film with Cu^{2+} ions and then biocatalytic anodic or cathodic enzyme-based systems were bound to the polymer-modified interfaces.[12] The system consists of two enzyme-functionalized electrodes (ca. 0.19 cm^2 active area) separated by a rubber O-ring (ca. 2 mm thickness). The first electrode functionalized with the reconstituted glucose oxidase (GOx) and the second electrode functionalized with cytochrome c/cytochrome oxidase (Cyt *c*/COx) assembly are acting as the anode and cathode, respectively. Two metallic needles (inlet and outlet) implanted into the rubber ring convert the unit into a flow cell. These needles were also used as external electrodes to apply electrical signals controlling conductivity of the polymer-modified electrodes. A peristaltic pump was applied to control the flow rate. Glucose solutions in 0.1 M TRIS-buffer, pH = 7.0, saturated with air were applied to power the biofuel cell.

Magnetic Control of Biofuel Cells. Biofuel cells composed of biocatalytic anode and cathode based on the enzyme-reconstituted systems[13] were inserted between the poles (diameter of 6 cm, separated by a distance of 1 cm) of an electromagnet (Model DPS-175, Scientific Equipment Roorkee, India) providing a constant magnetic field (±1% homogeneity) of variable strength that was measured with a Digital Gaussmeter (model DGM-102, manufactured by Sestechno, India). The enzyme-modified biocatalytic electrodes were positioned parallel to the direction of the magnetic field. Different magnetic fields applied on the electrochemical cell were generated by a sequential "ON" and "OFF" process. Glucose or lactate solutions saturated with air were applied to power the biofuel cells.

Results and Discussion

The assembly of the biocatalyst/copper-poly(acrylic acid) hybrid system with electrodes allows for the electrical control of the conductivity properties of the matrix, thus enabling the electroswitchable and tunable functions of the biofuel cell, **Figure 1**.

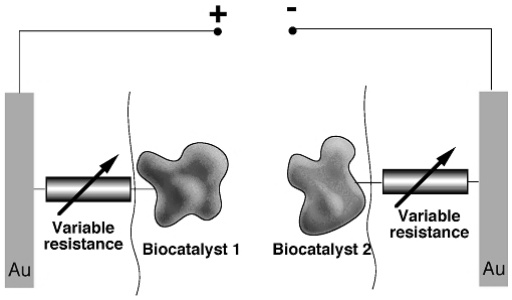

Figure 1. Electrically switchable and tunable enzyme-based biofuel cell with the variable resistances of the biocatalytic electrodes provided by the copper-poly(acrylic acid) thin film.

The anode consists of a Cu^{2+}-poly(acrylic acid) film on which the redox-relay pyrroloquinoline quinone (PQQ) and the flavin adenine dinucleotide (FAD) cofactor are covalently linked. Apo-glucose oxidase is reconstituted on the FAD sites to yield the glucose oxidase (GOx)-functionalized electrode. The cathode consists of a Cu^{2+}-poly(acrylic acid) film that provides the functional interface for the covalent linkage of cytochrome c(Cyt c) that is further linked to cytochrome oxidase (COx). Electrochemical reduction of the Cu^{2+}-poly(acrylic acid) films (applied potential -0.5 V vs SCE) associated with the anode and cathode yields the conductive Cu^0-poly(acrylic acid) matrixes that electrically contact the GOx-electrode and the COx/Cyt c-electrode, respectively. The short-circuit current and open-circuit voltage of the biofuel cell correspond to 105 μA (current density ca. 550 μA cm^{-2}) and 120 mV, respectively, and the maximum extracted power from the cell is 4.3 μW at an external loading resistance of 1 kΩ. The electrochemical oxidation of the polymer films associated with the electrodes (applied potential 0.5 V) yields the nonconductive Cu^{2+}-poly(acrylic acid) films that completely block the biofuel cell operation. By the cyclic electrochemical reduction and oxidation of the polymer films associated with the anode and cathode between the Cu^0-poly(acrylic acid) and Cu^{2+}-poly(acrylic acid) states, the biofuel cell performance is reversibly switched between "ON" and "OFF" states, respectively, **Figure 2**. The electrochemical reduction of the Cu^{2+}-polymer film to

the Cu^0-polymer film is a slow process (ca. 1000 s) because the formation and aggregation of the Cu^0-clusters requires the migration of Cu^{2+} ions in the polymer film and their reduction at conductive sites. The slow reduction of the Cu^{2+} -polymer films allows the controlling of the content of conductive domains in the films and the tuning of the output power of the biofuel cell. The electron-transfer resistances of the cathodic and anodic processes were characterized by impedance spectroscopy. Also, the overall resistances of the biofuel cell generated by the time-dependent electrochemical reduction process were followed by impedance spectroscopy and correlated with the internal resistances of the cell upon its operation.

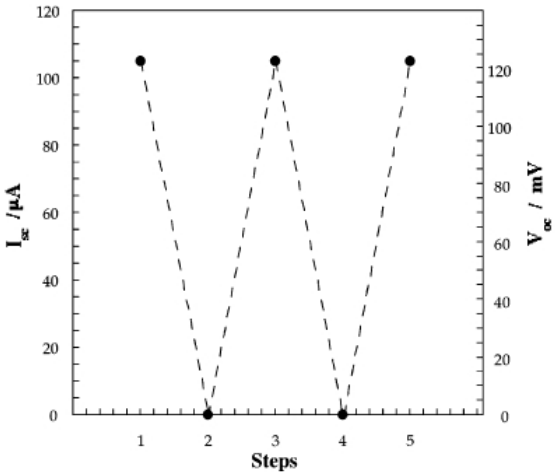

Figure 2. Reversible switching "ON" and "OFF" of the short-circuit current, I_{sc}, and the open-circuit voltage, V_{oc}, generated by the biofuel cell. The cell output is switched "ON" (steps 1, 3, and 5) by the application of the potential of -0.5 V to both biocatalytic electrodes for 1000 s and switched "OFF" (steps 2 and 4) by the application of a potential of 0.5 V to the biocatalytic electrodes for 5 s. The measurements were performed in the presence of 80 mM glucose solution saturated with air.

Magnetohydrodynamic effect recently demonstrated for bioelectrocatalytic systems[14] paves the way to control magnetically the performance of biofuel cells.[13] The effect of a constant magnetic field on bioelectrocatalytic transformations of three different enzyme assemblies linked to electrodes was examined and correlated with a theoretical magnetohydrodynamic mode.[15] The systems consist of surface-reconstituted glucose oxidase (GOx), an integrated lactate dehydrogenase/nicotinamide/pyrroloquinoline quinone assembly (LDH/NAD^+-PQQ), and a cytochrome c/cytochrome oxidase system (Cyt c/COx) linked to the electrodes. Pronounced effects of a constant magnetic field applied parallel to the electrode surface are observed for the bioelectrocatalyzed oxidation of glucose and lactate by the GOx-electrode and LDH/NAD^+-PQQ-electrode, respectively. The enhancement of the bioelectrocatalytic processes correlates nicely with the magnetohydrodynamic model, and the limiting current densities ($\mathbf{i}_L$) relate to $B^{1/3}$ (B = magnetic flux density) and to $C^{*4/3}$ (C* = bulk concentration of the substrate). A small magnetic field effect is observed for the Cyt c/COx-electrode, and its origin is still questionable. The effect of the constant magnetic field on the performance of biofuel cells with different configurations was examined, **Figure 3**. For the biofuel cell consisting of LDH/NAD^+-PQQ anode and Cyt c/COx cathode, a 3-fold increase in the power output was observed at an applied magnetic field of B = 0.92 T and external load of 1.2 kΩ. Besides the general biochemical implications of the results that might shed light on the magnetic field effects on biocatalytic electron-transfer reactions occurring at membrane interfaces, we demonstrated the utility of the magnetohydrodynamic effect for enhancing the power output of biofuel cells. Our results indicate that one has to search for the magnetic field effects on the electrode that controls the power output of the biofuel cells to improve the biofuel cell performance.

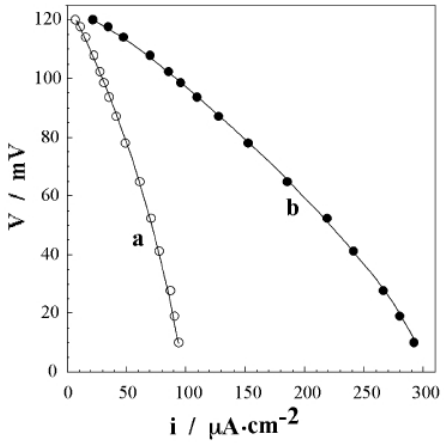

Figure 3. Enhancement of the performance of the biofuel cell composed of the LDH/NAD^+-PQQ-anode and COx/Cyt *c*-cathode: (a) in the absence of magnetic field; (b) in the presence of magnetic field, B = 0.92 T.

References

1. Willner, I.; Katz, E. *Angew. Chem., Int. Ed.,* **2000**, *39*, 1180-1218.
2. Katz, E.; Shipway, A. N.; Willner, I. In *Handbook of Fuel Cells - Fundamentals, Technology, Applications*; Vielstich, W., Gasteiger, H., Lamm, A., Eds.; Wiley: Chichester, 2003; Vol. 1, Part 4, pp 355-381.
3. Willner, I.; Heleg-Shabtai, V.; Blonder, R.; Katz, E.; Tao, G.; Bückmann, A. F.; Heller, A. *J. Am. Chem. Soc.,* **1996**, *118*, 10321-10322.
4. Zayats, M.; Katz, E.; Willner, I. *J. Am. Chem. Soc.,* **2002**, *124*, 2120-2121.
5. Raitman, O. A.; Patolsky, F.; Katz, E.; Willner, I. *Chem. Commun.,* **2002**, 1936-1937.
6. Bardea, A.; Katz, E.; Bückmann, A. F.; Willner, I. *J. Am. Chem. Soc.,* **1997**, *119*, 9114-9119.
7. Raitman, O. A.; Katz, E.; Bückmann, A. F.; Willner, I. *J. Am. Chem. Soc.,* **2002**, *124*, 6487-6496.
8. Katz, E.; Willner, I.; Kotlyar, A. B. *J. Electroanal. Chem.,* **1999**, *479*, 64-68.
9. Katz, E.; Bückmann, A. F.; Willner, I. *J. Am. Chem. Soc.,* **2001**, *123*, 10752-10753.
10. Chegel, V. I.; Raitman, O. A.; Lioubashevski, O.; Shirshov, Y.; Katz, E.; Willner, I. *Adv. Mater.,* **2002**, *14*, 1549-1553.
11. Katz, E.; De Lacey, A. L.; Fernandez, V. M. *J. Electroanal. Chem.,* **1993**, *358*, 261-272.
12. Katz, E.; Willner, I. *J. Am. Chem. Soc.,* **2003**, *125*, 6803-6813.
13. Katz, E.; .Lioubashevski, O.; Willner, I. *J. Am. Chem. Soc.,* **2005**, *127*, 3979-3988.
14. Katz, E.; Lioubashevski, O.; Willner, I. *J. Am. Chem. Soc.,* **2004**, *126*, 11088-11092.
15. Lioubashevski, O.; Katz, E.; Willner, I. *J. Phys. Chem. B,* **2004**, *108*, 5778-5784.

LAMINAR FLOW-BASED BIOFUEL CELLS: INDEPENDENT TAILORING OF THE pH AT THE CATHODE AND ANODE TO ENHANCE THE ACTIVITY AND STABILITY OF BOTH ENZYMES

Eric R. Choban, Lajos Gancs, Ranga S. Jayashree, Michael Mitchell, Jacob S. Spendelow, Seong Kee Yoon, and Paul J.A. Kenis

Chemical & Biomolecular Engineering
University of Illinois at Urbana-Champaign
600 South Mathews Avenue
Urbana, IL 61801

Introduction

Recently, research towards the development of biofuel cells has gained significant momentum. In enzymatic biofuel cells many of these efforts have focused on improving electrical between biocatalysts and electrodes communication by mediated or by direct electron transfer to enhance the performance.[1] Use of a mediator, be it free in solution or immobilized, typically increases the rate of electron transfer between the active site of enzyme biocatalysts and the electrode. For example, dissolved $NAD(P)^+$ and ABTS can function as a mediator for enzymatic anodes and cathodes, respectively. Electropolymerized methylene green for electro-oxidation of NADH is an example of an immobilized mediator. Bio-anodes can be formed from poly(methylene green) modified electrodes with dehydrogenase enzymes immobilized within a Nafion layer.[2] A recently reported bio-cathode is comprised of the enzyme laccase and a redox mediator (Os^{2+}) immobilized within a polymer hydrogel on carbon-fiber paper support.[3] An performance limiting issue in enzymatic biofuel cell systems for which no solution has been reported is that these cells are operated at a certain compromise pH that may be optimal for the activity and stability of one enzyme, but sub optimal for the other.[1] We intend to address this issue here.

Recently, we have developed membraneless microfluidic fuel cells that exploit a characteristic of fluid flow at the microscale, *laminar flow*, to keep two streams containing fuel and oxidant, respectively, separated while still in diffusional contact.[4] The fuel and oxidant containing streams merge in a Y-shaped microfluidic channel and continue to flow in parallel without turbulent mixing as schematically shown in **Figure 1**. Two physicochemical phenomena govern the chemical conversion and accompanied energy and mass transport phenomena in these laminar flow-based fuel cells: depletion of reactants at the electrode walls and diffusion across the mutual liquid-liquid interface. This membraneless fuel cell system eliminates several of the issues encountered in the more common polymer electrolyte membrane (PEM)–based fuel cells including the occurrence of fuel crossover and membrane dry out. Moreover, the membraneless fuel cell design is media flexible: the same fuel cell can be run in acidic or alkaline media. Of relevance to this work, one can even tailor the composition (e.g. pH) of the fuel and oxidant streams independently to optimize the reaction kinetics at the cathode and anode.[5]

This paper will report our preliminary results on tailoring the composition, in particular pH, of the individual cathode and anode streams in a laminar flow-based biofuel cell to maximize the activity and stability of the respective biocatalysts used at the cathode and the anode in a microscale biofuel cell. Being able to operate the individual electrodes at their respective optimum pH will not only increase the overall biofuel cell performance, it will also increase the stability of the enzymes used and thus it will increase the lifetime of the biofuel cell.

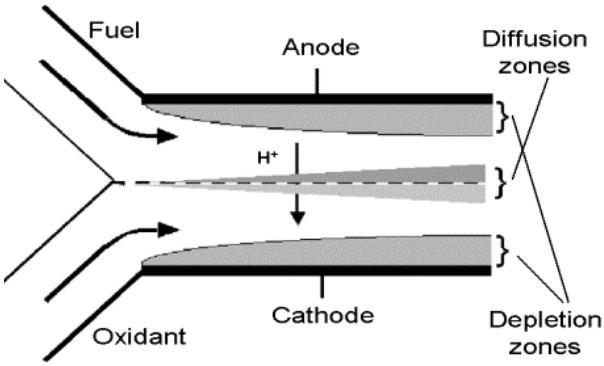

Figure 1. Schematic of a laminar flow-based, membraneless microfuel cell. The diffusion and reaction depletion zones are indicated (not too scale).

Experimental

Fuel Cell Assembly. Two graphite plates are placed side by side separated by 0.5 mm to 1.0 mm, and form the length of the channel where the fuel and oxidant streams flow next to each other. The 0.250 mm-wide inlets are milled out of the graphite plates with a drill bit. Before assembling the fuel cell, catalyst is applied to the sides of the graphite plates. The Y-shaped channel is capped with 1-mm thick polycarbonate slabs, while using polydimethylsiloxane (PDMS) as gasket material. The anode and cathode catalysts were unsupported Pt/Ru 50:50 atomic weight % alloy nanoparticles and unsupported Pt black nanoparticles, respectively, both deposited from a 10%wt Nafion solution to result in a loading of 2 mg/cm^2. An optical micrograph of an assembled cell is shown in **Figure 2**.

Fuel Cell Testing. Polyethylene tubing (I.D. 1.57 mm.) is used to guide the fuel and oxidant into the LF-FC and to guide the waste stream out of the cell. Fluid flow in all fuel cell experiments is pressure driven and regulated using a syringe pump. Operating conditions: flow rate per inlet channel = 0.3 ml/min; channel length = 2.9 cm; channel height = 1 mm and channel width = 0.75 mm. This flow rate and these cell dimensions correspond to a Reynolds number of around 0.1, well within the laminar flow range. To analyze the individual performance of each electrode, an external Ag/AgCl reference electrode in a 3.0 M NaCl solution was placed in a small compartment filled with 1N sulfuric acid and connected to the laminar flow based fuel cell using capillary tubing (ID 1.57 mm) ending in the waste stream collection beaker.[6] Polarization curves were obtained using an in-house fabricated fuel cell testing station equipped with a data acquisition device run with Labview.

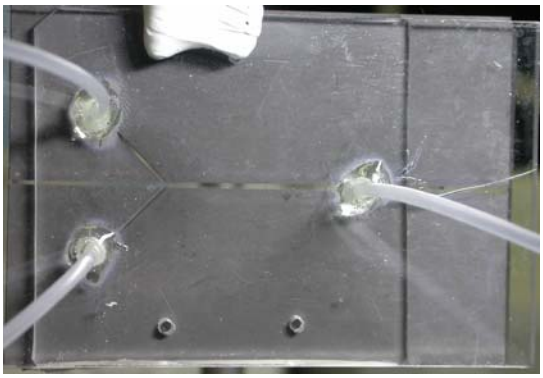

Figure 2. Optical micrograph of a membraneless fuel cell assembled from graphite plates. Main channel: 3 cm long, 1 mm wide and high.

Results and Discussion

In previous work we[5,6,7] and others[7] have reported on various membraneless fuel cells using different fuels (e.g. methanol, formic acid) and appropriate catalysts to obtain current densities as high as 10 mA/cm^2. The lack of a membrane lifts the constraint of only being able to operate in acidic media. Once mass transport issues at the cathode can be resolved, improved performance can be expected by running these fuel cells in alkaline media, as both fuel oxidation and oxygen reduction kinetics are known to be better in alkaline media. Moreover, the lack of a membrane and the ability to inject separate fuel and oxidant streams enables individual tailoring of the composition of these streams. **Figure 3** shows the individual anode and cathode performance of a membraneless fuel cell in which the anode is exposed to methanol in alkaline media (1N KOH) while the cathode is exposed to an oxygen saturated acidic stream (1N sulfuric acid). The difference in pH results in a very large open cell potential of 1.4V. The cathode curve drops fairly rapidly in region I due to the aforementioned mass transfer limitations (low solubility of oxygen in water). In the unusual region 2 the reduction of H^+ becomes the dominating cathode reaction, leading to the cathode curve to flatten. Until a short circuit current density of almost 50 mA/cm^2 is reached.[5]

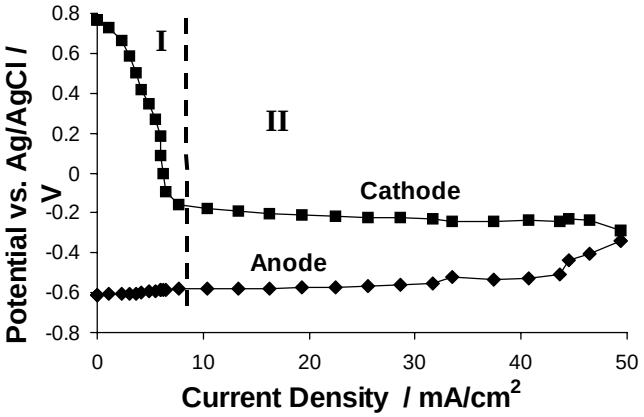

Figure 3. I-V performance curve of a membraneless fuel cell in which the anode and cathode are exposed to media of different pH. Fuel stream for this experiment: 1M formic acid in 1N KOH; Oxidant stream: oxygen saturated 1N sulfuric acid.

The ability to run the cathode and anode at different pH in a single fuel cell can be exploited in the further improvement of enzymatic biofuel cells. Different enzymes typically exhibit the best activity at different pH, yet in most biofuel cell designs a certain compromise pH is used, somewhere between the optimum pH of the respective enzymes used at the anode and cathode.[1] In preliminary experiments we have been able measure an open circuit potential of 0.4V and a maximum current density of ~75 μA/cm^2 in a membraneless fuel cell using methylene green as the mediator and NADH as the oxidizing agent dissolved in a phosphate buffer (pH 7) while using a stream of 1N sulfuric acid at the cathode. The performance of this cell is already similar to the performance of most recently reported biofuel cells.

In this paper we will report proof-of-principle experiments of membraneless fuel cells that enable enzymatic biofuel cells to be operated at conditions so both the anode and cathode enzyme chemistries can reach their full activity, thereby increasing the performance of the overall cell. In addition, operating both biocatalysts in their optimum pH is expected to improve their stability, and thus the longevity of biofuel cells.

Acknowledgment

This work was supported by the University of Illinois and the Beckman Institute.

References

1. Barton, S. C., Gallaway, J., Atanassov, P. *Chem. Rev.* **2004**, *104*, 4867-4886
2. Minteer, S. D., Akers, N. L., Moore, C. M. *Lab Chip* **2005**, *5*, 218-225
3. Hudak, N. S., Barton, S. C. *J. Electrochem. Soc.* **2005**, *152 (5)*, A876-A881
4. Choban, E.R., Markoski, L.J., Stoltzfus, J., Moore, J.S., Kenis, P.J.A., *40th Power Sources Conf., Cherry Hill, NJ, 10-13 June*, **2002**. Choban, E.R. Markoski, L.J. Wieckowski, A. Kenis, P.J.A. *J. Power Sources*, **2004,** *128*, 54-60. U.S. Pat. No. 6713206, **2004**.
5. Choban, E.R., Spendelow, J.S., Gancs, L., Wieckowski, A., Kenis, P.J.A., *Electrochimca Acta*, **2005**, *in press.*
6. Choban, E.R., Waszczuk, P., Kenis, P.J.A., *Electrochemical and Solid-State Letters*, **2005**, *in press.*
7. Cohen, J.L., Westly, D.A., Pechenik, A., Abruna, H.D., *J. Power Sources*, **2005**, in press.

DEVELOPMENT AND TESTING OF AN AIR BREATHING, MEMBRANE SEPARATED, ENZYME ANODE FUEL CELL FOR GLUCOSE FUELS

Christopher Apblett, David Ingersoll, Greg Roberts

Sandia National Laboratories
PO Box 5800
Albuquerque, NM, 87185-0603

Introduction and Background

The development of fuel cells as possible alternatives for portable power has been drawing considerable attention in recent years. Determining the power density of a fuel cell system requires the consideration of the volume of the fuel tank as well as the volume of the fuel cell converter. For long duration applications, such as sensors in remote sites, both batteries and traditional fuel cells (hydrogen and direct methanol) contain insufficient energy to operate for long periods of time while delivering technologically interesting (~mW) levels of continuous power. Environmentally harvestable fuels, such as glucose and sucrose (carbohydrates) from plant saps and animals have the potential to allow for continous fuel replenishment from the local environment. This would allow the volume of the fuel tank to be removed, significantly reducing the volume of the system and increasing the volumetric power density levels of the power system to well above the volumetric power densities of any available battery system or more traditional fuel cells.

In addition to harvesting fuel from the environment, oxygen must also be harvested from the environment, which requires special care in designing the cathode for the fuel cell to maximize the diffusive transport of oxygen to the electrodes in a passive system. This problem is further exacerbated in applications involving biological implantation. In this case, although there exist relatively constant and concentrated fuels in the biological systems, the unbound oxygen concentrations within these systems is quite low, and represents a mass transport limitation for the arrival of oxygen to the cathode of the fuel cell. Traditional cathodes, such as platinum black, are very active, but can quickly become poisoned by the other constituents within the vascular system. To prevent the cathode from being poisoned and inactivated by other contaminants in the vascular fuel stream, some form of membrane separator must be used that limits the cross diffusion of poisons to the cathode.

Catalysis of the fuel stream, as mentioned previously, can result in the poisoning of the anode catalyst by byproducts of the fuel oxidation when attempting to use carbohydrate based fuels. Several workers[1] [2] have investigated the oxidation of glucose on platinum and platinum alloy catalysts, and have demonstrated the poisoning of these catalysts. Enzymatic catalysis have much higher specificity to specific oxidation reactions, and are much less susceptible to contaminants in the fuel stream, i.e., less poisoning. Other researchers[3] [4] [5] [6] have developed and presented performance data on carbohydrate fuels (notably glucose). The current density of these fuel cells remains low and also have relatively short lifetimes, presumably due to the denaturing of the enzymes, or due to the loss of enzymes and/or mediators from the electrode into solution. This problem is exacerbated in a flow through system, as mediator or enzyme lost to solution is pumped away, severely restricting the amount of material that can redeposit onto the electrodes.

In light of these difficulties in realizing a carbohydrate fuel cell that can run on animal or plant carbohydrates, we have endeavored to fabricate a membrane separated, platinum cathode, enzyme anode fuel cell, and test it under both quiescent and flowthrough conditions.

Experimental

Miniature internally manifolded, closed cell graphite end plates were fabricated and used as the flow field and current collectors for the cells. The cathode electrode was a standard 50μm thick electrode comprised of Pt-Black with Nafion and Teflon binders, and the gas diffusion layer was a standard Toray backing. For the anode side, unteflonized toray paper was used, which had been treated by various methods for attaching glucose oxidase, the enzyme responsible for the first two electron oxidation from glucose. Various mediators were used along with this anode, and the Toray paper anode was placed directly in contact with the Nafion. The Nafion membrane was pH neutralized prior to assembly of the cell by soaking in a pH 7 phosphate buffer solution for 24 hours prior to assembly. The flow plates were attached over the electrodes by an acetate seal and lightly compressed to insure a leak free seal. The assembled cell was then placed into a test rig which allows for heating, flow control, and measurement of the power output of the cell. All experiments, unless otherwise noted, were performed at 25C, 20sccm flow of O_2 at atmospheric pressure, and 120μl/min flow rate of 50mM glucose fuel in a pH 5.4 phosphate buffer.

In the case of quiescent testing, the anode flow plate and test rig were replaced with a modified plate and rig, which was open on the backside of the anode to allow a static reservoir of liquid to rest directly against the anode toray paper. In this case, a fixed volume (0.8cc) of liquid was placed into the reservoir and allowed to equilibrate prior to the collection of the polarization curves.

Results and Discussion

The first experiments on the enzyme anode were half cell experiments with a Ag/AgCl reference electrode and platinum counterelectrode. These experiments used a well understood mediator of ferrocenyltrimethylundecylammonium bromide (FTMAB) along with the glucose oxidase in a co-immobilization onto the toray paper. The solution in this test was not stirred, so transport away from the electrode occurred only through diffusion. The data is shown in Figure 1 for a number of days after the preparation of the electrode. The electrochemical response is quickly lost, but is regained after spiking the electrode with more FTMAB mediator, indicating that the enzyme itself is stably bound to the electrode surface, but that the mediator is quickly being lost to the solution.

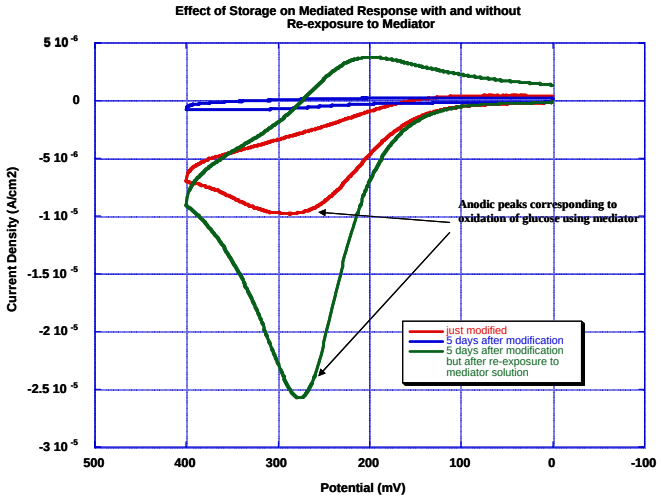

Figure 1. Half Cell CV of glucose oxidase/FTMAB electrode, 50mM glucose, room temperature. The performance is lost after a few days, but can be restored by the addition of more FTMAB.

FTMAB is a stable, reversible mediator molecule with a redox potential near +200mV vs. Ag/AgCl, making it unattractive for use with glucose oxidase. Glucose oxidase oxidizes glucose at roughly -300mV vs. Ag/AgCl, which means that almost 500mV are lost to the oxidation voltage. Against a Pt-O_2 cathode, this would result in, at best, an open cell potential of only 500mV. Better choices for mediators in terms of the potential are available, however, and these fall into several classes. The most promising for our work were phenazine derivatives, which operated in the -80mV to -180mV range vs. Ag/AgCl at neutral pH and room temperature. Using phenazine methosulphate with glucose oxidase in the half cell test previously described resulted in a much improved cyclic voltammetric response, with a redox potential for glucose at roughly -80mV, and having high current density for an enzymatic half cell. The addition of glucose fuel to the electrode only nominally affects the operating potential of this electrode. These results are shown in Figure 2.

These half-cell electrodes can be applied directly into the full fuel cell architecture, and tested against a neutralized seven mil Nafion membrane using a Pt-O_2 cathode. A typical polarization curve for these cells under flow through conditions is shown in Figure 3. As can be seen from the data, although the cell potentials are close to what would be expected from the half cell measurements, the current densities are well below those expected from the half cell. It is not expected that the Pt cathode would be limiting in this case in any form, as the activity of the Pt-O_2 reduction reaction is much

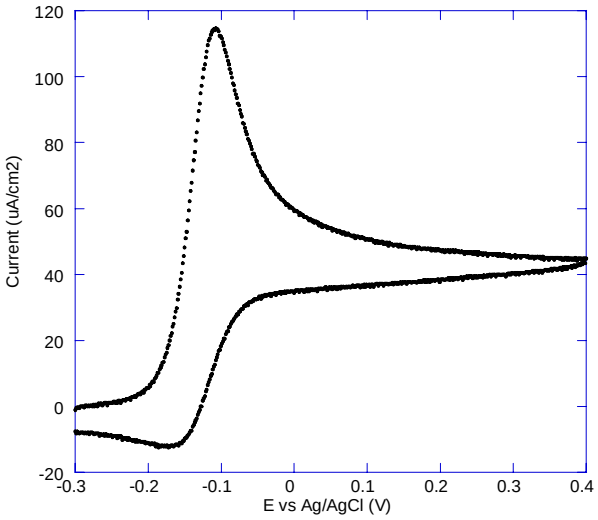

Figure 2. Half Cell performance of phenazine methosulfate and glucose oxidase immobilized on a glassy carbon electrode. The PMS is mediating at -80mV vs. Ag/AgCl, a significant improvement over FTMAB.

higher than the currents that are shown here. These cathodes have been tested against a H_2 cathode and shown to polarize by less than 30mV at a 1mA. Therefore, it can reasonably be expected that the low currents observed in this performance are being caused by poor performance at the anode.

This performance can be somewhat improved by moving from a flowthrough system to a quiescent system. By operating in this mode, current densities under the same conditions are increased above those found for the flow through system, indicating that the stability of the mediator may again be in question. The data for the quiescent case are also plotted in Figure 3. In this case, transport to the anode is through diffusion only, and the loss of the mediator to solution is also controlled by the diffusion of the mediator away from the anode. From this data, it can be seen that the supportable currents from the anode are much higher than in the case of the flow through configuration, and much closer to the values measured in the half cell case.

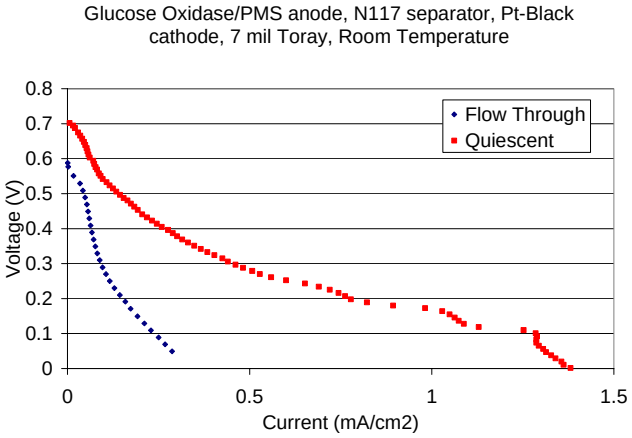

Figure 3. Flow through vs. Quiescent cell. 50mM glucose fuel at 120ml/min or static, 20sccm O2 flow cathode, room temperature, PMS mediated, phosphate buffered to pH 5.4. The loss in performance in flowthrough is due to loss of the mediator to solution.

Conclusions

From the initial experiments using oxygen cathodes and membrane separators in flowthrough fuel cells, it is apparent that mediator loss to the flowing solution is the largest contributor to power loss. Use of the phenazine derivative mediators was demonstrated to offer decent open circuit potentials for half cell and full cell performance, but suffer from quick loss to the solution which hampers long term operation. A means to stabilize the phenazine molecules to the electrode will need to be developed in order to extend the lifetime of the cell beyond its current level of a few hours. Work is underway currently to address this issue.

Acknowledgements

Sandia is a multiprogram laboratory operated by Sandia Corporation, a Lockheed Martin Company, for the United States Department of Energy's National Nuclear Security Administration under contract DE-AC04-94AL85000.

References

1 Beden, B., Largeaud, F., Kokoh, K. B, Lamy, C., *Electrochimicha Acta* **41** 5 (1996) 701-709.

2 Ernst, S., Heitbaum, J., Hamann, C., *Ber. Bunsenges., Phys. Chem.* **84** (1980) 50-55.

3 Willner, I., Katz, E., Patolsky, F., Buckmann, A., *J. Chem. Soc. Perkin Trans.* **2** (1998) 1817-1822.

4 Katz, E., Willner, I., Kotylar, A., *J. Electroanal. Ch*em. **479** (1999) 64-68.

5 Chen., T., Barton, S. C., Binyamin, G.,Gao, Z., Zhang, Y., Kim, H-H., Heller, A., *J. Am. Chem. Soc*. **123** (2001) 8630-8631.

6 Kim, H-H., Mano, N., Zhang, Y., Heller, A., *J. Electrochem. Soc.* **150** 2 (2003) A209-A213.

SYNTHESIS AND CHARACTERIZATION OF BIOELECTROCATALYTIC POLYMER COMPOSITES

G. Tayhas R. Palmore, and Jiangfeng Fei

Division of Engineering, Division of Biology and Medicine, Brown University, 182 Hope Street, Box D, Providence, RI 02912, Fax: 401-863-7677

Abstract

The molecule 2,2'-azinobis-(3-ethylbenzothiazoline-6-sulfonate) (ABTS) is an important redox-active compound with broad chemical, material, and biomedical applications. ABTS and its derivatives have been used as the electrochromic component in smart windows, as a chromogenic substrate in assays for enzymatic activity, and as a mediator for electron transfer in the cathode compartment of a biofuel cell. Interest in the use of ABTS in the bioelectrocatalytic reduction of oxygen to water has increased primarily because its redox potential is near that of oxygen under mildly acidic conditions. I will discuss the synthesis and characterization of polymer composites of ABTS and the performance of these composites in a hydrogen/oxygen biofuel cell operated at room temperature and atmospheric pressure.

DESIGN OF MACROPORE STRUCTURE FOR ENZYME FUEL CELLS OPERATION

Michael Cooney[✉], *Bor Yann Liaw*[✉], *Wayne Johnston, Vojtech Svoboda, Forest Quinlan, and Nathan Maynard*

Hawaii Natural Energy Institute, School of Ocean and Earth Science and Technology, University of Hawaii, Honolulu, HI 96822, USA

[✉]mcooney@hawaii.edu or bliaw@hawaii.edu

Introduction

There has been increasing attention concerning direct alcohol fuel cells (DAFCs) using platinum based catalysts [1]. Both methanol and ethanol have been proposed as reactants although ethanol is increasingly attractive because it exhibits less toxicity than methanol and is readily produced from renewable resources. Direct oxidation of ethanol on platinum, however, is plagued by fouling of the electrode surface by reactive intermediates such as those with CO groups. Despite improvements, however, fouling of the electrode remains problematic because the extra C-C bond in ethanol increases the number of chemical intermediates available to foul the electrode. Enzyme bioelectrocatalysts have been proposed as an alternative to transition metal catalysts for power generation; they oxidize alcohols at relatively low overpotential without producing CO-related intermediates that will foul the electrode, and they operate at lower temperatures [2]. Such reactant specificity has also led to the development of a membrane-less glucose biofuel cell in which glucose is oxidized at the anode by glucose oxidase whilst the reaction of the stripped proton with oxygen to form water at the cathode is catalyzed by the enzyme laccase [3].

Full realization of the membrane-less biofuel cell as a power source requires a 3-D solid-liquid boundary microstructure that balances the overall effective surface area against porosity, thus ensuring the maximum number of catalyst sites are available without suffering the liquid sealing effect, which occurs if the pore size is so small it blocks fuel transport. Without such a delicate engineering practice, the optimization of power density on those reactant specific electrodes cannot be realized. Control over porous microstructure has been addressed via sol gel techniques, and by entrapment in functionalized mesoporous silica, but these materials lack the required electronic conductivity. That said, electronic conducting conjugated polymers (ECP's), or their derivatives, have been proposed to immobilize redox enzymes in biosensors and biofuel cells [4]. While this approach has led to a widespread application in the biosensors, including those for measurement of ethanol [5], they have been only successful in addressing part of the issues important to enzyme fuel cells. The foremost critical one, namely the control over an effective 3-dimensional solid-liquid boundary microstructure for optimal power generation, remains untouched.

In this work we present data comprising *in situ* determination of the effective diffusion coefficient and in situ documentation of film growth using imaging ellipsometry to evaluate the effect of macropore structure on enzyme fuel cell performance. The results suggest that pyrrole films can pose significant mass transfer limitation as compared to direct absorption. Images of pyrrole deposition from imaging ellipsometry suggest that the growth of pyrrole films via electrochemical deposition is affected by monomer concentration, growth rate, and imposed potential. The deposition began with a one-dimensional filament growth on the metallic electrode support surface. As the density of the filaments increases with film thickness to a threshold the growth pattern changed from 1-D to 2-D as the film continues to grow. The density, porosity, and microstructure of the film are therefore varied as the film develops into a thick film. These results suggest new techniques are required to create a sufficient macropore structure and some ideas in this direction are suggested, including computer modeling to understand the effects of transport and reaction kinetics on the electrode behavior.

Experimental

Reagents. Alcohol dehydrogenase was purchased from Sigma, as was Crystalline NAD^+. Stock solutions of BSA (100 mg ml^{-1}) were dissolved in phosphate buffer (0.05 M, pH 8.0). Working solutions of lithium perchlorate were made on a daily basis by dilution with 0.05M phosphate buffer. Pyrrole solutions were made daily from a stock solution that was de-aerated and stored at –4ºC in the dark to avoid degradation over time. Ethanol (17.0 M, 200 proof) was diluted as needed (i.e. 300 mM) with ultra pure water.

Flow cell. The cell is built from a modular stacking design approach, which employs stackable polycarbonate plates that serve defined functionalities. The core stack comprises a 6 cm diameter hole of ¼" height with ports along the sidewalls of the reaction chamber for inlet and exit lines as well as the reference electrode. The working and counter electrodes are located on either side of the reaction chamber. The working electrode was constructed of either a carbon mesh material or 316 stainless steel wire mesh. The counter electrode was nickel sheet. All electrodes were pretreated by soaking in acetone for 5 minutes under mild agitation, rinsed with ultra pure water, and then soaked for an additional 5 minutes in 10% nitric acid. The electrodes were then copiously rinsed with ultra pure water and blot dried with absorbent paper. The electrodes were used immediately after drying. Media was delivered to the cell by peristaltic pumping from an external reservoir maintained at 37°C.

Immobilization. For direct absorption the pretreated carbon mesh was soaked *ex situ* in 20 µl of the ADH stock solution (50 mg ml^{-1}) for 15 minutes at 25°C. The cell was then fully assembled and filled to capacity with phosphate buffer solution, after which buffer solution (20 ml) was slowly pumped through the flow cell (~1.6 ml min^{-1}) to purge the cell of non-adsorbed enzyme (Fig 1). For pyrrole immobilization, the micro cell was assembled using the pretreated stainless steel mesh electrode and then filled to capacity with 0.3 ml of de-aerated immobilization solution (pyrrole monomer (0.1M), electrolyte salt (0.1M), and enzyme (50 mg ml^{-1}) dissolved in phosphate buffer. The working electrode was polarized in potentiostatic mode at +0.8 V vs. Ag/AgCl at 37 °C until a defined charge of 1.27 coulombs had passed. After polarization, immobilization solution was removed by syringe and 20 ml of phosphate buffer at 37°C was slowly pumped (~1.6 ml min^{-1}) to remove non-entrapped enzyme from the system.

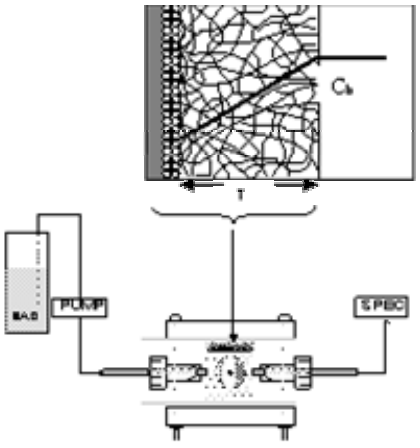

Figure 1. Micro flow cell system

Modeling. If the halo-enzyme complex scenario is used to describe the alcohol dehydrogenase catalyzed oxidation of ethanol in the presence of NAD^+, the following expression can be developed from a mass balance around the enzyme fuel cell.

$$F \bullet NADH_b = \frac{V_{max}^{NAD^+} \bullet (NAD_{res}^{+} - NADH_b - \frac{F \bullet NADH_b}{D'_{NAD^+,eff}})}{K_M^{NAD^+} + (NAD_{res}^{+} - NADH_b^{+} - \frac{F \bullet NADH_b}{D'_{NAD^+,eff}})} \quad (1)$$

The usefulness this equation is that the LHS can be measured experimentally and the RHS can be plotted in the form of a Lineweaver-Burke plot, assuming a value for the effective diffusion coefficient (D'_{eff}) is assumed. Further, if the assumption is made that the value for K_M will not change from that measured for the enzyme in free solution, then a value of effective diffusion coefficient can be derived assuming the Line-Weaver Burke intercept yields the value for K_M determined in free solution. The value of V_{max} can then be taken as the activity of the immobilized enzyme.

An interesting feature of equation 1 is that it permits the data to be plotted in Lineweaver-Burke form using the modeling concentration of enzyme at the enzyme surface. Why this is important can be seen in Figure 2, which uses the bulk concentration of NAD^+ along the x-axis, instead of plotting the concentration of NAD^+ at the enzyme surface. The varying intercepts illustrates that it is difficult to distinguish between mass transfer and kinetic limitation when using bulk concentrations. Thus the model illustrates the important point that the interpretation of real assay data to measured values of K_M and V_{max} from experimental data will not be accurate unless the effects of mass transfer on reaction kinetics are considered.

Figure 2: Lineweaver-Burke plot.

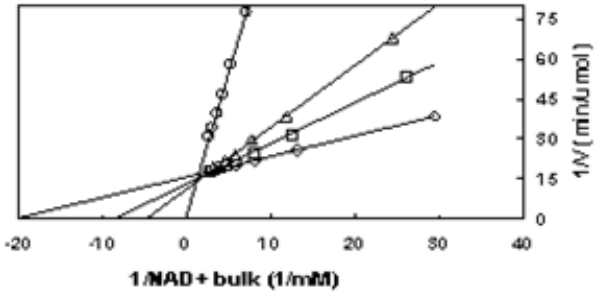

Results and Discussion

Study of Interplay of Reaction Kinetics and Transport via Modeling. Test of this procedure was conducted two types of immobilization techniques: 1) direct adsorption to carbon type electrode and 2) enzyme immobilized to stainless steel mesh by polypyrrole. For each case the solution to Equation 1 was used to estimate both the reaction velocity and the effective diffusion coefficient. The results are presented in Table 1.

Table 1. Summary of estimated model parameters

F (ml/min)	K_M (mM)	V_{max} (µmol/min)	D'_{eff} (cm^3/min)
		Carbon felt	
1.6	0.0501	0.0636	0.91
1.6	0.0500	0.0539	0.97
2.4	0.0490	0.0684	0.68
		Pyrrole immobilized enzyme	
0.27	0.057	0.0025	0.26

Direct adsorption to carbon felt provided 26 times the activity of the immobilized polypyrrole electrode (0.062 versus 00025 µmol min^{-1}). This may have been due to two factors. First the effective surface area of the carbon felt could have been much greater than the stainless mesh electrode. A second possibility is that the enzyme within the pyrrole film lacked the diffusive pathways for NAD^+, and hence did not contribute to the production of NADH. This would suggest that only enzymes immobilized at the surface of the immobilized film were available to catalyze the oxidation of NAD^+ to NADH in the presence of excess ethanol. As such, the fabrication of a polypyrrole film with increased diffusive pathways would increase activity. The modeling technique presented in this work provides a mechanism to test this hypothesis, provided a series of films of different thickness and porosity (as modified through the immobilized technique) are constructed and the effective diffusion coefficient calculated.

Characterization of Microstructure. For SEM images, electrodes with fabricated films were recovered from the micro-cell, dried in air, and transferred to the PBRC Biological Electron Microscopy Facility (PBRE-BEMF) for imaging taking. Figure 3 presents typical SEM images of pyrrole films that have been electropolymerized. One salient feature of the SEM images (A and B) is the cauliflower shape microstructure covering the electrode surface. The thicker the films the more pronounced cauliflower shape microstructure is developed. The cauliflower shape microstructure presents films that surpass a threshold thickness, usually less than 1 µm, and presumably possess a dense membrane structure that would inhibit mass transport. The ellipsometry image (C) revealed an initial open microstructure that might be preferred for fuel cell application, for thin films with a dense film forming at a threshold thickness.

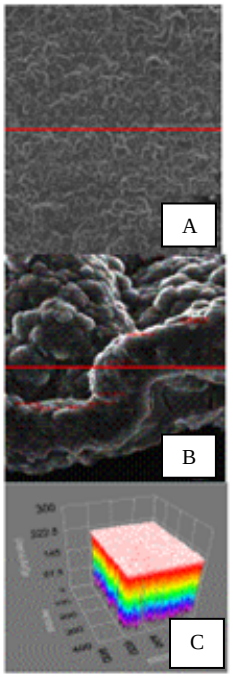

Figure 3. SEM and imaging ellipsometry images of PY films.

Acknowledgements

This work was funded by the Office of Naval Research (N0014-01-1-0928) through the Hawaii Environmental and Energy Technology (HEET) initiative (R. Rocheleau, PI), and by the Director of Central Intelligence Postdoctoral Fellow Research Program (HM1582-01-1-2013).

References

1. Lamy, C., S. Rousseau, E.M. Belgsir, C. Coutanceau and J.M. Leger, (2004). Electrochimica Acta, **49**: p. 3901 - 3908.
2. Palmore, G.T., H. Bertschy, S.H. Bergens and G.M. Whitesides, (1998). Journal of Electroanalytical Chemistry, **443**: p. 155 - 161.
3. Barton, S.C., M. Pickard, R. Vazquez-Duhalt and A. Heller, (2002). Biosensors and Bioelectronics, **17**: p. 1071 - 1074.
4. Bartlett, P.N. and P.R. Birkin, (1993). Synthetic Metals, **61**: p. 15 - 21.
5. Lobo Castanon, M.J., A.J. Miranda Ordieres and P. Tunon Blanco, (1997). Biosensors and Bioelectronics, **12**(6): p. 511 - 520.

SBA-15 SUPPORTED COBALT AND IRON CATALYSTS FOR FISCHER-TROPSCH SYNTHESIS

Dae Jung Kim [a], Brian C. Dunn [a], Min Kang [b], Jae Eui Yie [c], and Edward M. Eyring[a]*

[a] Department of Chemistry, University of Utah Salt, Lake City, UT 84112, USA
[b] Department of Molecular Science & Technology, Ajou University, Suwon 442-749, South Korea
[c] Department of Applied Chemistry, Ajou University, Suwon 442-749, South Korea

Introduction

Fischer-Tropsch (FT) synthesis is a promising pathway to very clean alternative fuels derived from coal syngas. It is important to develop active catalysts with high selectivity for production of long chain hydrocarbons. The activity of catalysts for FT synthesis depends primarily on the overall amount of exposed metal atoms. Thus, a highly active catalyst requires a high dispersion of cobalt metal. Mesoporous silica materials such as SBA-15 have been recently used as supports for cobalt.[1-4] The high surface area (500 - 1500 m^2/g) of the mesoporous materials gives higher metal dispersions at higher cobalt loadings compared with conventional amorphous silicas. Furthermore, the uniform pore diameters (2 - 30 nm) of the mesoporous silica materials permit better control of the cobalt particle size and the distribution of hydrocarbon products from the FT synthesis.[5] We have proposed that surface modification of SBA-15 via silylation increases the catalytic activity and hydrocarbon selectivity in FT synthesis.[6]

The objectives of this present study are to determine the relative merits of impregnation methods, advantages of iron over cobalt and the consequences of aluminum incorporation in SBA-15 on catalytic activity in Fischer-Tropsch synthesis. Six different catalysts were prepared. The physical and chemical properties of the catalysts were obtained from N_2 adsorption/desorption, XRD and TPR experiments. The catalytic performance in FT synthesis was evaluated with a fixed-bed reactor.fixed-bed reactor.

Experimental

Catalyst preparation. SBA-15 was obtained by a procedure described elsewhere.[6,7] Triblock polymer Pluronic P123 ($EO_{20}PO_{70}EO_{20}$, M_{av} = 5800, BASF) was used as the structure-directing agent of SBA-15. Anhydrous sodium metasilicate (Na_2SiO_3, Aldrich) was used as the silica source of SBA-15. Aluminum incorporation in SBA-15 was achieved using the following post-synthesis procedure. 1.0 g of calcined pure SBA-15 was added to a 50 mL ethanol solution containing $AlCl_3$ (Aldrich). The mixture was stirred at ambient temperature overnight, and filtered using a glass membrane filter. The filtered sample was dried in air at 100 ^oC overnight, and then calcined in air at 550 ^oC overnight. The amount of incorporated aluminum was analyzed by ICP-AES.

SBA-15 supported cobalt catalysts were prepared by three different cobalt impregnation methods: incipient wetness, post-synthesis and supercritical solvent. The cobalt post-synthesis impregnation was similar to that used to graft aluminum on SBA-15. The impregnation of the SBA-15 with cobalt using a supercritical solvent proceeded as follows: The SBA-15 was added to a 250 mL ethanol solution of $Co(NO_3)_2 \cdot 6H_2O$, and stirred at ambient temperature for 1 h. The suspension was transferred to an autoclave placed inside a furnace. The autoclave was purged ten times with 200 psi N_2 to remove any oxygen trapped in the system. The autoclave was heated to 350 ^oC at 5 ^oC/min, then held at 350 ^oC for 3h. The pressure inside the autoclave was maintained at 2000 psi by controlled venting through a high-pressure valve. The system was cooled to 200 ^oC ,and the gas inside the autoclave was vented for 1 h. The system was then cooled to ambient temperature. The cobalt impregnated sample was calcined in air at 550 ^oC overnight. In this study, iron impregnated SBA-15 samples were prepared by incipient wetness impregnation using $Fe(NO_3)_3 \cdot 9H_2O$ dissolved in ethanol solution. All calcined samples were reduced under hydrogen at 500 ^oC for 10 h to obtain active metallic cobalt or iron for the FT synthesis. Specifications of SBA-15 supported cobalt and iron catalysts used in this study are shown in Table 1.

Table 1. Specification of SBA-15 supported cobalt and iron catalysts.

Catalyst	Silica	Precursor	Co loading (Wt %)	Loading method
CAT1	SBA15	$Co(NO_3)_2$	6	IW
CAT2	SBA-15	$Co(ac)_2$[b]	6	PS
CAT3	SBA-15	$Co(NO_3)_2$	6	SS
CAT4	SBA-15	$Co(NO_3)_2$	20	IW
CAT5	SBA-15	$Fe(NO_3)_3$	20	IW
CAT6	AlSBA-15	$Fe(NO_3)_3$	20	IW

[a] IW: incipient wetness, PS: post synthesis, SS: supercritical solvent impregnation
[b] $Co(ac)_2$ is anhydrous cobalt acetate

Catalyst characterization. To evaluate the pore structure of the catalyst samples, nitrogen adsorption isotherms were measured using an Autosorb-1 instrument (Quantachrom). The isotherms were used to calculate the BET specific surface area (S), total pore volume (V_t), and average pore diameter (D_p). The pore structure of the samples was also evaluated using XRD patterns. The reduction of cobalt oxides in the sample was evaluated by temperature programmed reduction (TPR, Micromeritics). The H_2 consumption of the sample was calculated using the reduction of CuO as the standard.

FT synthesis and product analysis. The FT synthesis was carried out in a fixed-bed stainless steel reactor (5 mm I.D. and 168 mm length) at 100 psi and 265 ^oC. An H_2/CO molar ratio of 2 was used, and a ratio of sample weight to total gas flow rate (W/F) was 0.47 - 0.91. The gas flow rates for reactant gases (CO, H_2) and internal standard (Ar) were controlled by mass flow controllers (MKS). Iron carbonyl impurities in the CO reactant stream were removed by a PbO_2/Al_2O_3 trap. The test for the FT synthesis was carried out for 36 h on stream. Reactants and hydrocarbon products were analyzed by gas chromatography (Shimadzu). The GC oven was heated using a heating program as follows: 10 ^oC for 4 min, then heating from 10 to 350 ^oC with the heating rate of 20 ^oC/min and holding at 350 ^oC for 10 min. Reactants were separated on a capillary column (CarboPlot, 0.53 mm I.D. and 30 m length) with a TCD detector. Hydrocarbon products were separated on a capillary column (DB-5, 0.25 mm I.D. and 10 m length) with an FID detector.

Results and Discussion

The results of XRD patterns and nitrogen adsorption/desorption isotherms revealed that all cobalt catalysts having 6 wt% cobalt had the 2-D hexagonal structure of pure SBA-15. Pore structural parameters calculated from nitrogen adsorption/desorption isotherms for the cobalt SBA-15 catalysts are listed in Table 2. The BET surface area, pore volume and pore diameter of SBA-15 are decreased by cobalt impregnation. However, the three cobalt catalysts prepared by three different impregnation methods have similar pore structural values. This implies that the impregnation method does not have a significant impact on the pore structure of SBA-15.

Table 2. Physical and chemical properties of SBA-15 supported cobalt catalysts.

Catalyst	S[a] (m^2/g)	Vt[b] (cc/g)	D_p[c] (nm)	Co_3O_4[d] Diameter (nm)	Reduction[e] (%)
Pure SBA-15	724	1.243	8.09	-	-
1CAT	465	0.811	8.08	11.1	49
2CAT	472	0.858	8.08	-	18
3CAT	461	0.815	8.08	11.6	63

[a] BET Surface area, [b] Total pore volume, [c] average pore diameter, [d] Co_3O_4 crystallite diameter calculated from the widths of XRD peaks using the Scherrer equation (2 theta = 36.68°), [e] reduction degree of cobalt oxides during TPR at 30 – 500 °C.

The mean Co_3O_4 crystallite sizes deduced from the XRD data using the Scherrer equation and the reduction percentage of the cobalt oxides at temperatures less than 500 °C are presented in Table 2. The XRD peak at 36.68° for CAT2 was not detected. This suggests that most of cobalt oxides are present as cobalt silicates in the framework of the SBA-15, and the average crystallite size of Co_3O_4 on the surface of the SBA-15 is very small. The mean Co_3O_4 crystallite size on CAT3 is slightly larger than on CAT1. This result indicates that the crystallite size of Co_3O_4 is clearly dependent on the impregnation method. Figure 1 shows TPR profiles of three cobalt catalysts, CAT1, CAT2 and CAT3. CAT1 and CAT3 show similar TPR profiles with three typical peaks. However, the TPR profile of CAT2 with two peaks is significantly different.

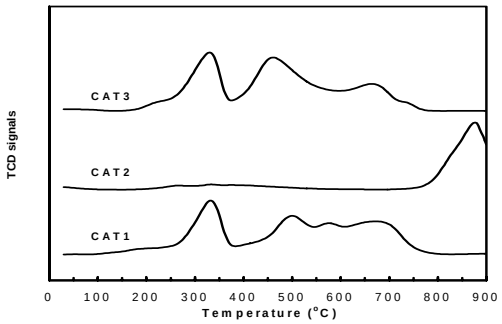

Figure 1. TPR profiles of three cobalt catalysts

For CAT1 and CAT3, the first peak at temperatures less than 380 °C can be assigned to the reduction of Co_3O_4, and the second peak in the 380 - 600 °C range corresponds to the reduction of cobalt oxides strongly interacting with the SBA-15. The third peak in the 600 - 760 °C range can be attributed to the reduction of cobalt oxides very strongly interacting with the SBA-15. The maximum temperatures of the three peaks for CAT3 are located at lower temperatures than for CAT1. In particular, the intensity of the third peak for CAT3 is very low. This suggests that highly irreducible cobalt oxides on CAT3 are less prevalent than on CAT1. CAT2 shows two peaks in its TPR profile. The first peak is at temperatures in the range of 200 – 500 °C, and the second peak is located at temperatures above 760 °C, corresponding to the reduction of cobalt oxides in the framework of SBA-15.

The reduction percentage of the cobalt oxides at temperatures less than 500 °C are presented in Table 2. CAT3 shows the highest reducibility of cobalt oxides among the three catalysts prepared by different impregnation methods. According to the TPR results, undesireable cobalt oxides (those not easily converted to active cobalt metal at lower temperature) were abundantly produced in CAT1. Catalytic activities of SBA-15 supported cobalt and iron catalysts in FT synthesis are summarized in Table 3.

Table 3. CO conversion, hydrocarbon selectivity and chain growth probability of SBA-15 supported cobalt and iron catalysts

Catalyst	W/F (g h/mol)	CO conversion (%)	Product selectivity (C mol%)				α[a]
			C_1	C_2-C_4	C_5-C_{10}	C_{10+}	
CAT1	0.73	15.7	8.6	38.6	39.0	13.8	0.86
CAT2	0.91	4.6	15.8	56.8	24.2	3.2	0.82
CAT3	0.67	21.1	7.3	32.4	45.3	15.0	0.88
CAT4	0.55	22.2	7.2	32.3	46.5	14.0	0.88
CAT5	0.47	23.8	6.2	6.5	32.8	54.5	0.95
CAT6	0.47	32.5	4.9	6.1	27.3	61.7	0.98

[a] chain growth probability obtained from Anderson-Schulz-Flory equation

CO conversion and higher hydrocarbon selectivity can be related to the reducibility of the cobalt oxides and pore structure of a cobalt catalyst. The three samples (CAT1, CAT2, CAT3) having the same loading of cobalt showed similar values in BET surface area, pore volume and average pore size. However, the three samples showed differences in the reducibility of cobalt oxides. CAT3 shows the highest CO conversion, C_{5+} selectivity and chain growth probability among the three catalysts obtained by three different cobalt impregnation methods. This result is quite consistent with the TPR result. In this study, to investigate the effect of active metal and aluminum incorporation of SBA-15 on catalytic activity, we prepared a cobalt catalyst (CAT4) and two iron catalysts (CAT5, CAT6). The three samples have the same metal loading. CAT5 shows higher CO conversion, C_{5+} selectivity and chain growth probability than CAT4. This indicates that iron in the SBA-15 is more effective than cobalt for FT synthesis. As the results of TPR and EXAFS tests, after aluminum incorporation of SBA-15, reducible iron oxides such as Fe_2O_3 on CAT6 were greatly increased compared to CAT5. This indicates that the increase of reducible iron oxides leads to an increase in catalytic activity of the iron catalyst.

In a summary, the cobalt impregnation method has a significant effect on catalytic activity and selectivity through differences in reducibility of cobalt oxides. Aluminum added iron-based catalyst is also advantageous.

Acknowledgment

The U.S. Department of Energy provided financial support to the Consortium for Fossil Fuel Science for this study (contract # DE-FC26-02NT41954).

References

1. Girardon, J. S.; Lermontov, A. S.; Gengembre, L.; Chernavskii, P. A.; Griboval-Constant, A.; Khodakov, A. Y. *J. Catal.* **2005**, *230*, 339-352.
2. Okabe, K.; Wei, M.; Arakawa, H. *Energy & Fuels* **2003**, *17*, 822-828.
3. Martinez, A.; Lopez, C.; Marquez, F.; Diaz, I. *J. Catal*. **2003**, *220*, 486-499.
4. Panpranot, J.; Goodwin, J. G.; Sayari, A. *Catal. Today* **2002**, *77*, 269-284
5. Wang,Y.; Noguchi, M.; Takahashi, Y.; Ohtsuka, Y. *Catal. Today* **2001**, *68*, 3-9.
6. Kim, D. J.; Dunn, B. C.; Cole, P.; Turpin, G.; Ernst, R. D.; Pugmire, R. J.; Kang,, M.; Kim, J. M.; Eyring, E. M. *Chem. Commun*. **2005**, 1462-1464.
7. Kim, J. M.; Stucky, G. D. *Chem. Commun*. **2000**, 1159-1160.

EFFECT OF PROCESS PARAMETERS ON LIGHT OLEFINS PRODUCTION FROM METHANOL AND SYNGAS OVER SAPO CATALYSTS

Luckner Jean[a], Xiwen Huang[a] and James A. Guin[a]
Gregory C. Turpin[b] and Richard D. Ernst[b]

[a]Department of Chemical Engineering
Auburn University, Auburn, AL, 36849-5127
[b]Department of Chemistry
University of Utah, Salt Lake City, UT, 84112-0850

Introduction

The recent spike in energy prices has renewed attention on the production of chemicals from sources other than petroleum and focused attention on fossil fuels which are currently not recovered. In this light the use of SAPO catalysts in converting syngas either directly or indirectly to chemicals e. g. C_2-C_4 olefins, is of interest. The main feedstock of current interest is remote or flared natural gas, although any feedstock convertible to syngas is technically viable. This means that coal and biomass are potential resources for chemicals currently produced from petroleum. We are especially interested in C_2-C_4 olefins.

Flanigan, et al. have presented many of the most important properties of the SAPO catalysts in their foundational work[1]. A good review of the chemistry of methanol to hydrocarbons is presented by Stocker[2]. In his review it is noted that the pathway for methanol to olefins (MTO) is via a consecutive reaction with the dimethyl ether (DME) intermediate.

Many parameters such as acidity, pore size, composition, and method of preparation influence the activity of SAPO catalysts. Thus a particular SAPO, e. g., SAPO-34, may behave differently depending on its history and manner of preparation. A main obstacle in the MTO process is the rapid deactivation of the catalysts due to coke formation; however, regeneration is possible by oxidation as in a recirculating fluid bed. Here we have studied the effect of particle size on the activity, selectivity and lifetime of several small pore SAPO catalysts in the MTO reaction. Particle size variation was accomplished by grinding. It is possible that grinding could induce changes in the crystalline structure of the catalysts, however, this was not determined in our study, the main focus being on the particle size variations and the resulting reaction effects. A few other studies have examined the effects of particle size on this reaction[3,4]. We also report preliminary results on the effect of Ru incorporation on SAPO performance.

Experimental

The original SAPO catalysts used in our present work were samples prepared previously in our laboratory by Adekkanattu[5-8]. Studies were performed on SAPO-34, 44, 47, and 56. Original samples were ground in a Wig-L-Bug (Dentsply/Rinn) grinder with agate vial and ball for various times. Particle size was examined by SEM before and after grinding.

MTO reactions were performed at 1 atm in a quartz tube fixed bed, generally at 400 ^oC, using 0.3 g catalyst and 0.003 ml/min liquid methanol vaporized into nitrogen at 36 ml/min. (WHSV = 0.5 hr^{-1}). In addition to particle size, effects of temperature and incorporation of Ru were also studied[9]. Products were analyzed by GC with FID and Plot-Q capillary column. More details are provided in the thesis by Jean[10].

Results and Discussion

Figure 1 shows SEM micrographs of (a) the original SAPO-44 particles and (b) after grinding for 15 min. The reduction in particle size is fairly obvious from the scales on the figures, although some of the finer particles tend to form agglomerates. **Figures 2** (a) and (b) show the product distribution from MTO reactions over these SAPO-44 particles. We see that the ground particles have longer lifetimes, having increased from *ca.* 4 hrs to 10 hrs for the production of C_2-C_4 olefins. The selectivity of ethylene to propylene is not appreciably altered by the size reduction, however a notable change in selectivity to DME is apparent, as a result of the grinding. This latter finding is in keeping with the product distribution expected from particle size reduction in a diffusion controlled reaction with DME intermediate, i. e., an increase in selectivity of the intermediate due to lower intraparticle diffusional resistance[11]. As shown in **Figure 3**, similar results were obtained at 5 and 10 min grinding times, although particle sizes at lesser grinding times as viewed by SEM were not dramatically different from **Figure 1**(b). Similar changes in catalyst lifetime and DME selectivity, though not as large, were found in the performance of SAPO-34, 47, and 56. In a few cases, the grinding process caused a decrease in activity. An attempt to restore the activity of a spent SAPO-56 sample was unsuccessful, perhaps indicating the deactivation process, e. g., coke deposition, was uniformly spread throughout the particles, as opposed to being preferentially located around the external surface.

Figure 4 shows the performance of Ru-SAPO-44. Comparison with the unmodified catalyst in **Figure 2**(a) shows a small improvement, *ca*. 1 hr, in C_2-C_4 olefins based lifetime. Ru-SAPO-56 was also slightly improved, while, SAPO-34 was not improved by the Ru addition. These results are interesting, however, more work would be required, perhaps with other metals and conditions to fully determine the benefits of metals addition to the SAPOs.

Conclusions

Particle size reduction shows potential as an effective way to increase lifetime of SAPO catalysts based on C_2-C_4 olefins production, although for a completely deactivated catalyst grinding alone will not regenerate the catalyst. The selectivity of the intermediate DME is increased by particle size reduction in keeping with diffusional effects on selectivity of an intermediate in a series reaction pathway. Ru addition had only a small effect on the SAPO lifetimes in this limited study.

Acknowledgment. This research was supported by the U.S. Department of Energy Office of Fossil Energy, National Energy Technology Laboratory (NETL), under DOE Contract DE-FC26-02NT41594. The authors wish to acknowledge Dr. P. M. Adekkanattu for preparing the original SAPO catalysts.

References

1. Flanigan, E. M., Lok, B. M, Patton, R. L. and Wilson, S. T.: *Proc. 7th. Int. Zeolite Conf.*, Tokyo, 103, **1986**.
2. Stocker, M., *Microporous and Mesoporous Materials* 29, **1999**, 3 – 48.
3. Chen, D., Kjell, M. Fuglerud, T., Holmen, A., *ibid.*, 191.
4. Dahl, I. M. Wendelbo, R., Andersen, A., Akporiaye, D. Mostad, H. Fuglerud, T., *ibid.*, 159.
5. Annual Report for Period May 2001- May 2002, DOE Cooperative Agreement No. DE-FC26-99FT40540, Prepared by Consortium for Fossil

Fuel Science, University of Kentucky.
6. Annual Report for Period May 2002- May 2003, DOE Cooperative Agreement No. DE-FC26-02NT41594, Prepared by Consortium for Fossil Fuel Science, University of Kentucky.
7. Obrzut, D.L., Adekkanattu, P. M., Thundimadathil, J.,Liu, J., Dubois, D.R., Guin, J.A., *React. Kin. Catal. Lett.*, 80(1) **2003** 113.
8. Dubois, D.R., Obrzut, D.L., Liu, J. Thundimadathil, J., Adekkanattu, P. M., Guin, J. A. , Punnose, A. Seehra, M. S., *Fuel Proc. Technol.*, 83(1-3), **2003**, 203.
9. Wilson, D.R., Stahl, L., Ernst, R. D., *Organometallic Synthesis*, 3, **1986**, 136.
10. Jean, L., M. S. Thesis, Auburn University, **2005**.
11. Petersen, E. E., *Chemical Reaction Analysis*, Prentice Hall, **1965**, p. 97.

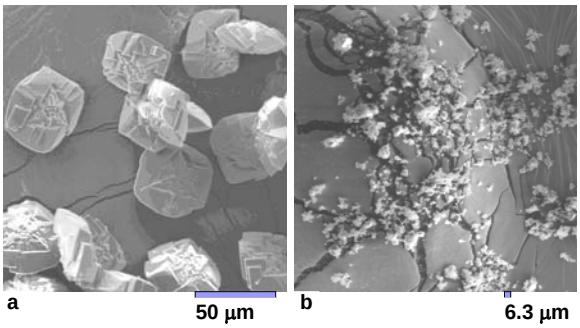

Figure 1. (a) SAPO-44 (Original Particles) (b) SAPO-44 (After 15 min Grinding)

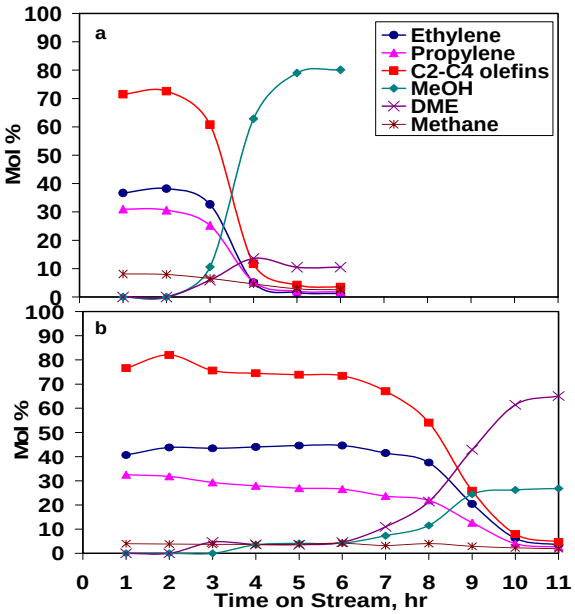

Figure 2. Product Distribution over: (a) Original Particles; (b) Ground Particles.

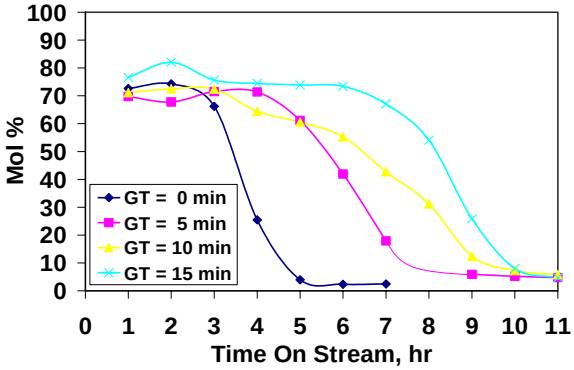

Figure 3. Effect of Grinding Time (GT) on C_2 - C_4 Olefins Production over SAPO-44.

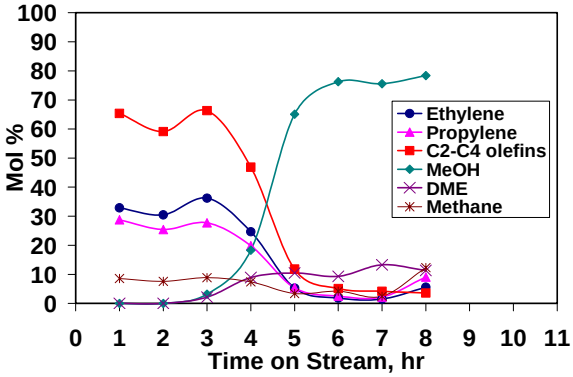

Figure 4. Product Distribution over Ru-SAPO-44.

CATALYTIC METHANE DECOMPOSITION USING A FLUIDIZED BED REACTOR FOR HYDROGEN PRODUCTION

Shankang Ma, Yuguo Wang, Naresh Shah, Gerald P. Huffman

University of Kentucky, 533 S. Limestone Street, Suite 107, Lexington, KY 40508-4005

Introduction

Previously, we have developed alumina supported binary catalysts, (M-Fe)/Al_2O_3 (M=Pd, Mo, or Ni), that are very active for catalytic dehydrogenation of lower alkanes to produce pure hydrogen and carbon nanotubes.[1,2,3] One major setback in such laboratory scale experiments is accumulation of carbon nanotubes (CNT), a potentially valuable byproduct, within the reactor. In a fixed bed mode of operation, this fouling due to CNT tangling and accumulation and quickly starts hindering the flow of the reactant and product gas streams, builds back pressure and reduces activity.

One possible way to dislodge nanotubes anchored to the catalyst particles on the surface of the alumina support is to mechanically breaking the nanotubes at these linkages by physical agitation. Fluidization of the bed should induce turbulent flow of the catalytic bed media and repeated inter-particle collisions that could shear nanotubes from the active metallic catalysts. Once freed, fine nanotubes should be carried away by the fluidizing gas stream to be externally collected and the catalyst should continue to further decompose methane, producing additional hydrogen and carbon nanotubes. In this paper, we report results from the preliminary tests carried out to validate the aforementioned hypothesis.

Most of the hydrogen production work using fluidized bed reported in the literature concern with the production of syngas.[4,5,6,7] When used for the production of carbon nanotubes, fluidized bed reactors are typically fed with higher carbon content gases and not methane.[8,9,10,11,12] Lee et al. [13] have used a fluidized bed reactor for hydrogen production from catalytic decomposition of methane using activated carbon catalysts with very low methane conversion. Weizhong et al.[14] have employed a two-stage fluidized bed reactor for production of hydrogen and carbon nanotubes from methane.

Experimental

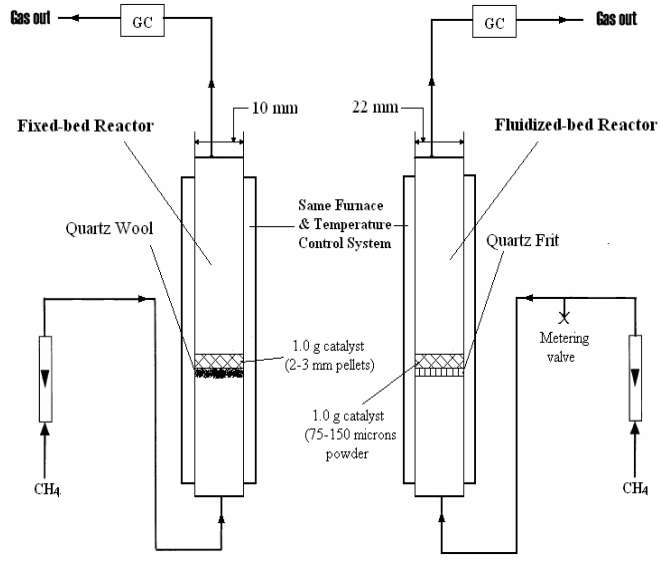

Figure 1. Schematics comparing fixed-bed (old) reactor and fluidized-bed (new) reactor

Figure 1 is a schematic diagram comparing salient features of our old fixed bed reactor with the new fluidized bed reactor. The two setups are identical except for larger reactor diameter (for high methane flow rate required for fluidization) and a quartz frit fused to the quartz wall of the reactor instead of a quartz wool plug (for catalyst support). Because there is no thermal methane decomposition at a reactor temperature of 700 °C, the pores in the quartz frit were never plugged with carbon. By increasing the methane flow rate from 10 ml/min to >~100 ml/min, the reactor mode can be varied from fixed bed to fluidized bed. At high methane flow rate (15 l/min) , the entire reactor can be emptied of the catalyst and attached CNT very quickly and new catalyst can be added to the reactor from the top (not shown in the schematic) at low or zero methane flow rate.

For all fluidized bed reactor experiments, 1 gram of as prepared 0.5%Mo-4.5%Fe/Al_2O_3 catalyst was used at the reactor temperature of 650-700 °C. To achieve good fluidization, the catalyst fluidized bed particle size was kept between 70 and 150 microns.

Results

Figure 2 shows volume percent hydrogen in the reactor exit stream as a function of time on stream for different methane feed flow rates. With increasing methane flow rate, hydrogen production efficiency decreases as methane-catalyst contact time decreases.

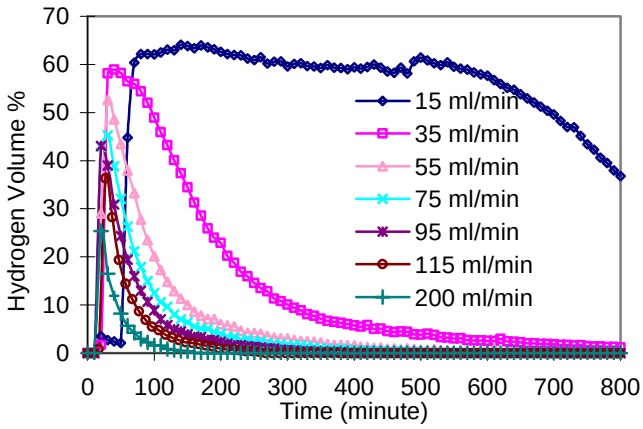

Figure 2. Time-on-stream hydrogen production at different methane flow rates.

Table 1. Hydrogen production efficiency at different methane flow rates and different reactor modes

	Methane Flow Rate (ml/min)	Linear Velocity (m/s)	Total Methane Input (ml) in 800 minutes	Total Hydrogen Produced (ml) in 800 minutes	Efficiency (H_2/CH_4)
Fixed Bed Mode	15	2.37	12000	9210	77%
	35	5.52	28000	4830	17%
	55	8.68	44000	3350	8%
	75	11.84	60000	3110	5%
Fluidized Bed Mode	95	14.99	76000	2830	4%
	115	18.15	92000	2000	2%
	200	31.57	160000	1790	1%

To compare efficiency of the hydrogen production, we have to compare areas under individual curves in figure 2. As shown in table 1, the reactor is most efficient in producing hydrogen at the lowest flow rate and highest reactant-catalyst contact time. As the flow rate increases, some of the methane just passes through the voids in the catalyst bed without coming in contact with any active metallic catalyst sites. At even higher flow rates, most of the methane acts simply as a fluidizing medium and not a reactant. As mentioned earlier, methane decomposition under these reaction conditions is purely a catalytic reaction and if a methane molecule does not come in direct contact with an active catalytic site, it will not undergo decomposition.

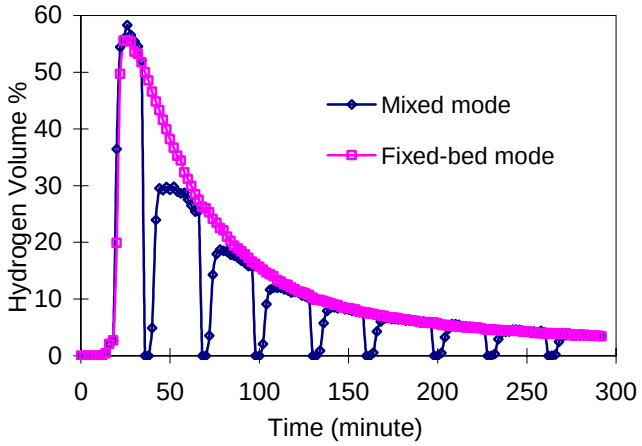

Figure 3. Comparison of fixed bed mode and mixed mode hydrogen production by catalytic methane dehydrogenation.

Based purely on these observations, there is no real advantage of operating the reactor in the fluidized mode. However, it is worth reflecting that the main reason for operating the reactor was not improving the activity. Rather, the tumbling and collisions of bed particles in a fluidized bed was hypothized to cause separation of nanotubes from the anchoring metal catalyst sites. To achieve both high hydrogen production efficiency and separation of nanotubes, a periodic mode switching experiment was performed. In such an operation, the reactor will be mostly operated in the high efficiency, low flow rate, fixed bed mode for generation of hydrogen. At regular intervals, the flow rate can be increased for short durations, at the penalty of low hydrogen production efficiency, to fluidize the bed to separate nanotubes from the bed material and remove them from the reactor. Figure 3 compares hydrogen production for a fixed bed mode operation and a periodically fluidized fixed bed (mixed mode) mode of operation. It is evident that after short fluidization, the active catalyst sites do not regain their catalytic activity because of separation and harvesting of the nanotubes.

During initial shakedown experiments of the new reactor set-up at different methane flow rates, we had noticed that at the very high methane flow rate (15 l/min), the catalyst bed can be fluidized very vigorously and expanded completely out of the length of the tube. As a result, all the catalyst bed material can be ejected out of the reactor almost instantaneously at the operating temperature just by increasing the flow rate. Figure 4 shows the hydrogen production for four such replenishing/complete blow out cycles.

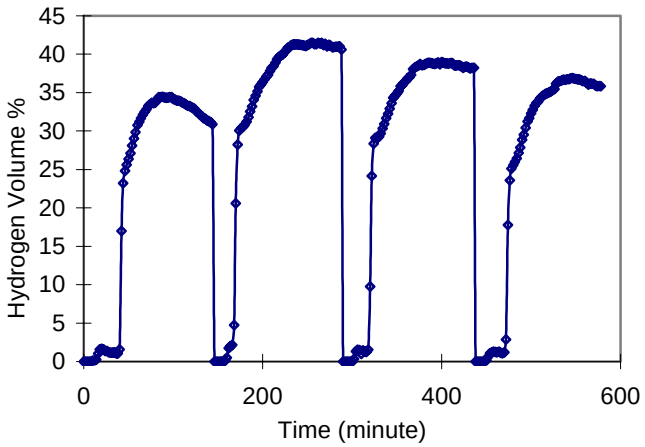

Figure 4. Semi-continuous hydrogen production by cyclic blowing out the catalyst bed with attached nanotubes and replenishing the reactor with completely new catalytic bed material at 650 °C.

Conclusions

To overcome the fouling of the fixed bed reactor by carbon nanotubes in methane dehydrogenation and to make hydrogen and nanotubes production continuous, fluidized bed mode and mixed mode catalytic dehydrogenation experiments were performed. These experiments showed that the hydrogen production is most efficient only in a fixed bed mode at the lowest methane flow rate. The results also negated the validity of the hypothesis that the tumbling and inter particle collisions of bed material would efficiently separate nanotubes anchored to the catalyst bed particles. A very high methane flow rate was successfully used to rapidly blow the entire bed material and attached nanotubes out of the reactor. The reactor was then replenished with fresh catalyst at the operating temperature to generate hydrogen in a semi-continuous way.

Acknowledgement. This research was supported by the U.S. Department of Energy, Office of Fossil Energy, under the management of the National Energy Technology Laboratory, U.S. DOE Contract No. DE-FC26-02NT41594.

References

1 Shah, N.; Panjala D.; Huffman, G.P. *Energy & Fuels*, **2001**, *15(6)*, 1528.
2 Shah, N.; Wang, Y.; Panjala D.; Huffman, G.P. *Energy & Fuels*, **2004**, *18(3)*, 727-735.
3 Wang, Y.; Shah, N.; Huffman, G.P. *Catalysis Today*, **2005**, *99*, 359-364.
4 Santos, A.; Menendez, M. Monzon, A.; Santamaria, J.; Miro, E.E.; Lombardo, E.A. *J. Catal*. **1996,** *156*, 83.
5 Bharadwaj, S.S.; Schmidt, L.D. *J. Catal.* **1994,** *146*, 11.
6 Opoku-Gyamfi, K.; Adesina, A.A. *Appl. Catal. A: Gen.* **1999**, *180*, 113.
7 Tomishige, K., *Catalysis Today* **2004**, *89*, 405–418.
8 Wang, Y.; Wei, F.; Luo, G.; Yu, H.; Gu, G., *Chemical Physics Letters* **2002**, *364*, 568–572.
9 Qian, W.; Wei, F.; Wang, Z. *AIChE Journal* **2003**, *49(3)*, 619-625.
10 Mauron, P.; Emmenegger, C.; Sudan, P.; Wenger, P.; Rentsch, S.; Zuttel, A. *Diamond and Related Materials*, **2003**, *12*, 780-785.
11 Corrias, M.; Caussat, B.; Ayral, A.; Durand, J.; Kihn, Y.; Kalck, P.; Serp, P. *Chem. Engr. Sc.*, **2003**, *58*, 4475-4482.
12 Venegoni, D.; Serp, P.; Feurer. R.; Kihn, Y.; Vahlas, C.; Kalck, P. *Carbon*, **2002**, *40*, 1799-1807.
13 Lee, K.K.; Han, G.H.; Yoon, K.J.; Lee, B.K. *Catalysis Today* **2004**, *93-95*, 81–86.
14 Weizhong, Q.; Tang, L.; Zhanwen, W.; Fei, W.; Zhifei, L.; Guohua, L.; Yongdan, L. *Appld. Catal. A: General*, **2004**, *260*, 223-228.

DETERMINATION OF DIFFERENT ELECTRONIC STATES OF COBALT IN FISCHER–TROPSCH CATALYSTS

M. S. Seehra, P. Dutta, and A. Manivannan

Physics Department
West Virginia University
Morgantown, WV 26506

Introduction

Recently, a number of studies of Fischer-Tropsch (FT) synthesis using cobalt catalyst supported on high surface area xerogel [1], aerogel [2,3], SiO_2 and Al_2O_3 [4,5] have been reported. The factors that effect the yields and product distribution of the FT products include operating temperature and pressure, surface area and pore size of the support, particle size and dispersion of cobalt and its electronic state (Co^0, Co^{2+}, Co^{3+}). To prepare the Co loaded catalyst, Co is usually impregnated as an oxide, followed by reduction and/or calcination to produce the desired Co^0 state which is the active catalyst. In order to compare the yield and product distribution with Co loading, it then becomes essential to determine the concentration of the various electronic states and phases of Co present in the catalyst. In this work, we summarize the results of our recent investigations for determining the different oxidation states of Co and their concentrations in Co/xerogel, Co/aerogel, Co/SiO_2 and Co/Al_2O_3 catalysts. Only summary of these results is presented below, with the details given in the quoted papers [1-5].

Experimental

The crystalline phases present in a catalyst were determined by room temperature x-ray diffraction (XRD) in a Rigaku diffractometer using CuK_α radiation ($\lambda = 0.15418$ nm). The XRD technique is able to detect phases with concentration ≥ 3 %. The magnetic phases such as Co^{2+}, Co^{3+},Co^0, CoO and Co_3O_4 were determined by magnetic measurements which were done using a commercial SQUID (superconducting quantum interference device) magnetometer. Additional information on states such as Co^{2+} was also determined by EMR (electron magnetic resonance) spectroscopy at the X-band frequency f = 9.28 GHz with a variable temperature (4 K to 300 K) cryostat. The important information on the electron state is contained in the g-value given by the EMR resonance condition $hf = g\mu_B H_0$, where h is the Planck's constant, μ_B is the Bohr magneton and H_0 is the resonance field of the EMR lines.

Results and Discussion

An example of the information obtained from the XRD studies is given in Fig. 1.Here we have shown the XRD patterns of Co/xerogel catalyst in which clear identification of Co^0, CoO and the support SiO_2 (xerogel) is made. (This figure is from the supporting materials of Ref. 1). In the Co/SiO_2 catalysts of Ref. 4, the XRD studies could only detect Co_3O_4, and Co^0 and CoO were absent [4]. Thus which phases of Cobalt (Co^0, CoO or Co_3O_4) are present in a catalyst depend on the experimental conditions the catalyst is exposed to and these different states can usually be detected by XRD.

Careful analysis of the temperature (T) and magnetic field (H) variation of the magnetization (M) provide additional details about the electronic states of cobalt and their concentrations. The presence of CoO and Co_3O_4 are detected from the peaks in susceptibility χ = M/H at temperatures T ≈ 300 K and T ≈ 40 K respectively [3-5] whereas if Co^0 is present, it dominates the measured magnetization from which its concentration can be determined [3]. In Fig. 2, we show our recent data from Ref. 3 on the χ vs. T variation in 10% Co/aerogel catalyst. The peak in χ near 20 K is due to Co^0 nanoneedles with diameter d ≈ 1 nm, whereas the peak in χ near 300 K (Fig. 3) is due to the presence of CoO. From the magnitude of the saturation magnetization of this sample at 5 K, the concentration of Co^0 was determined to be around 8%. If Co^0 is simultaneously present with either CoO or Co_3O_4, then from the behavior of the hysteresis loop of Co^0 in a field cooled sample, it can be determined whether Co^0/CoO or Co^0/Co_3O_4 are present as composite systems in core-shell structures or as individual phases. A shifted hysteresis loop under field-cooled conditions represents a core/shell structure [1]. An example of this is given in Fig. 4 for the 5% Co/xerogel sample. Here the hysteresis loop is shifted by 55 Oe when the sample is cooled in 10 kOe suggesting a core/shell structure for Co and CoO in this sample.

Another possibility for the cobalt state is that cobalt is incorporated substitutionally into the support (e.g as $Co_xSi_{1-x}O_2$) or chemisorbed on the surface of the support with bonding provided by surface absorbed H_2O and O_2. In such cases, the χ vs. T data follows the Curie-Weiss law: $\chi = \chi_0 + [C/(T-\theta)]$ where C gives the concentration of the Co^{+n} ions [4]. Furthermore, the variation of M vs. H at a low temperature (2 K) can be used to distinguish between Co^{2+} and Co^{3+} ions [4]. In the EMR studies of such materials, the presence of an EMR line at g = 4.3 is definite confirmation of the presence of Co^{2+} ions [6].

Next, the relationship between the different electronic states of cobalt and their concentrations with the F-T products and their distributions is discussed briefly.

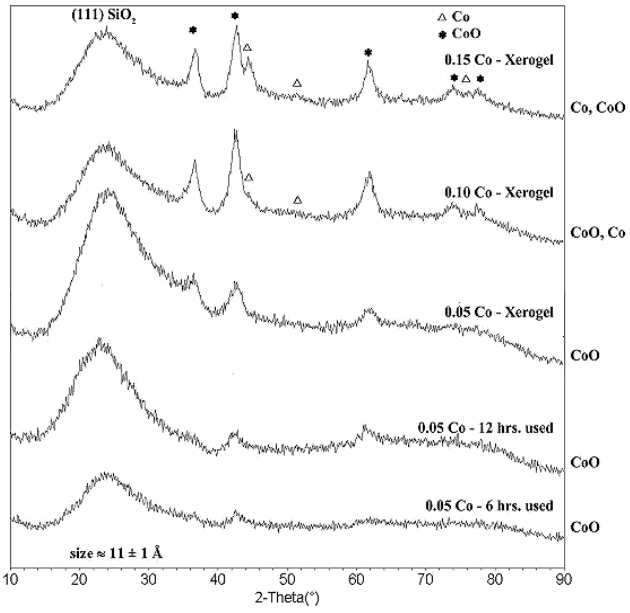

Figure 1. Room Temperature x-ray diffractograms of five samples of Co/xerogel with the peaks for Co^0, CoO and SiO_2 identified. The size ≈ 11 Å is for SiO_2 [Ref. 1].

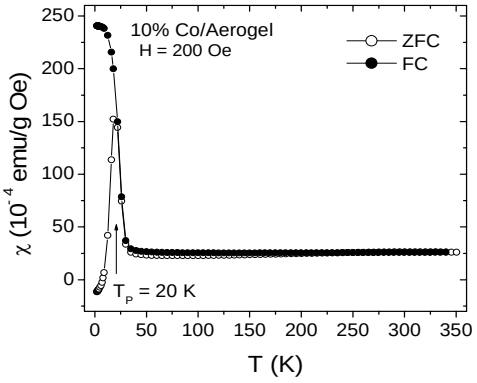

Figure 2. Temperature dependence of the magnetic susceptibility χ of 10% Co/aerogel catalyst for the ZFC (zero-field cooled) and FC (field-cooled) cases.

In the conventional gas-phase FT synthesis at 240^0C and 20 bar pressure, it was found that the presence of Co_3O_4 yields higher methane selectivity whereas the presence of Co^{2+} species yielded lower methane selectivity but higher olefin selectivity [4]. Similarly why the FT activity of 10 % Co/aerogel catalysts is not much better than that of 6 % Co/aerogel [2] has been explained in our recent work [3] in that the 10% Co/aerogel contains unreduced CoO and a complex cobalt silicate in addition to the desired Co^0.

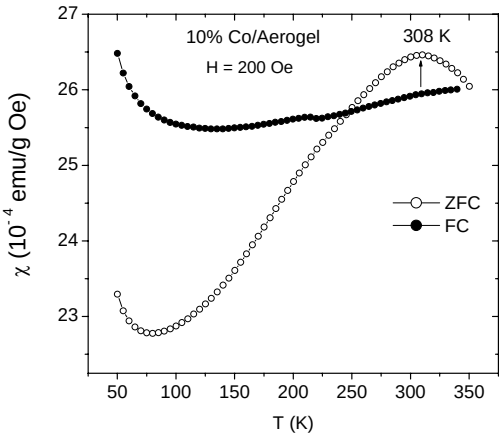

Figure 3. Expanded version of the χ data of Figure 2 for higher temperatures.

Conclusions

Here we have described how different electronic states and phases of cobalt in cobalt-based FT catalyst are determined using XRD, magnetometry and EMR spectroscopy. Such information is essential in understanding the nature of products and their distributions in FT synthesis.

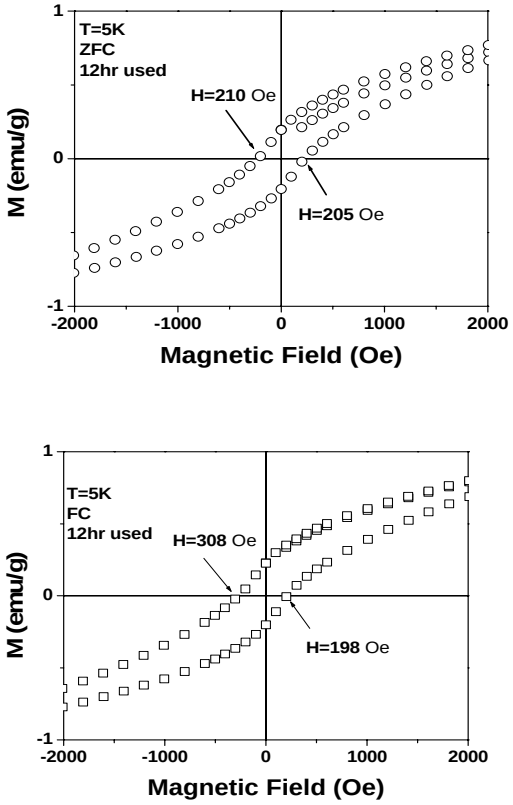

Figure 4. Hysteresis loops measured at 5 K for the 12-hr sample of 0.05 Co/aerogel under the ZFC and FC (H = 10 kOe) conditions. The loop shift for the FC case supports the core/shell model discussed in the text.

Acknowledgments

Support for this work was provided by the U. S. Department of Energy (Contract # DE-FC26-02NT41594). The authors thank Prof. Roberts (Auburn University) and Prof. Eyring (University of Utah), and their research groups for providing the samples used in this work.

References

1. Dunn, B. C.; Convington, D. J.; Cole, P.; Pugmire, R. J.; Meuzelaar, H. L. C.; Ernst, R. D.; Heider, E. C.; Eyring, E. M.; Shah, N.; Huffman, G. P.; Seehra, M. S.; Manivannan, A.; Dutta, P.; Energy Fuels, **2004,** 18, 1519-1521.
2. Dunn, B. C.; Cole, P.; Convington, D. J.; Webster, M. C.; Pugmire, R. J.; Ernst, R. D. Eyring, E. M.; Shah, N.; Huffman, G. P; Appl. Cata. A: General, **2005,** 278, 233-238.
3. Dutta, P.; Dunn, B. C.; Shah, N.; Eyring E. M.; Huffmam, G. P.; Manivannan, A.; and Seehra, M. S.; (to be submitted).
4. Dutta, P. Elbashir, N. O.; Manivannan, A.; Seehra, M. S.; and Roberts, C. B.; Catalysis Letters, **2004,** 98, 203-210.
5. Elbashir, N. O.; Dutta, P.; Manivannan, A.; Seehra, M. S.; and Roberts, C. B.; Appl. Catal A: General **2005,** (In Press).
6. Manivannan, A.; Glaspell, G.; Dutta, P.; Seehra, M. S.; J. Appl. Phys. **2005,** (In Press).

WHAT C-13 CHEMICAL SHIFT TENSORS CAN TELL US ABOUT METAL LIGAND INTERACTIONS IN CATALYSTS

Ronald J. Pugmire and Zhiru Ma

Department of Chemistry and Department of Chemical Engineering
University of Utah

Catalysts will play an increasingly important role in the development of C1 chemistry and the production of hydrogen. The NMR group at Utah is now focusing on understanding subtleties in catalyst structure and function. We have recently focused our research on catalyst systems with the goal to explore the feasibility of obtaining FIREMAT data on various metal-ligand complexes. The FIREMAT[1] experiment has proven to be a very useful tool for obtaining carbon-13 chemical shift tensor data.

Twenty years ago low temperature shift tensor principal values were obtained in the Utah laboratory on a series of metal diene complexes[2] and some of these data were later included in an extended data set by Oldfield, et. al.[3] The earlier Utah data was obtained by fitting the powder patterns of the complexes and the error in these STPV's can be as high as 5-10 ppm. We have now begun to revisit this topic employing the high resolution FIREMAT technique. The additional resolution obtainable by this experimental technique has led to the discovery of additional resonance lines in the spectra of several metal-ligand complexes that we have recently studied. An illustrative example is found in the spectrum of (bicyclo[2.2.1]hepta-2,5-diene)dichloropalladium (II) in which the diene-carbons are split into a doublet separated by 2 ppm. This spectral feature is due to a break in the crystal symmetry arising from slight differences (~0.02 angstrom) in the palladium-diene bond lengths. The PVST data of these carbons are readily obtained from the FIREMAT data and these values are given in Table 1. Similar NMR data have been obtained in (1,5 cyclooctadiene)dimethylplatinum (II). These data illustrate the high degree of sensitivity to local structural variations. The data we have obtained at this writing have laid the ground work of a wider range of complexes that will be studied. We will begin modeling these data by means of quantum mechanical techniques in the next few months. Exploration of the relativistic effects on the ligands will be included in our modeling efforts.

Table 1. Shift Tensor Principal Values in (bicyclo[2.2.1] heta-2,5-diene)dichoropalladium(II)

Carbon	δ_{iso}	δ_{11}	δ_{22}	δ_{33}
Diene (CH)	94.1	191.2	87.1	4.0
Diene (CH)	92.1	188.9	85.5	2.0
CH	66.1	100.1	68.7	29.6
CH2	52.4	66.1	56.0	35.0

References

1. A Sensitive High-Resolution Magic-Angle-Turning Experiment for Measuring Chemical-Shift-Tensor Principal Values. D.W. Alderman, G. McGeorge, J.Z. Hu, R.J. Pugmire and D.M. Grant, 1998**,** Mol. Phys., 95, 1113-1126.
2. Low Temperature Solution Studies of Copper(I) Complexes and Trans-Cycloalkenes and Solid State ^{13}C NMR Studies of Metal-Diene Complexes, Gregory Michael Wallraff, Ph.D. thesis, Department of Chemistry, University of Utah, 1985.
3. Solid-State NMR and Density Functional Investigation of Carbon-13 Shielding Tensors in Metal-Olefin Complexes, R. Havlin, M. McMahon, R. Scinivasan, H. Le, and E. Oldfield, J. Phys. Chem. A **1997**, 101, 8908-8913.

Acknowledgement. This work was supported by the Department of Energy, NETL, as part of the Consortium for Fossil Fuel Science.

OXYGENATE SYNTHESES USING METHANOL PLASMAS

*Yu Wang and Chang-jun Liu**

Key Laboratory of Green Chemical Technology, School of Chemical Engineering, Tianjin University, Tianjin, 300072 China

Introduction

Methanol can be produced from many feedstocks including renewable resource. It is an excellent alternative feedstock for syntheses of oxygenates, like acetic acid, ethylene glycol (EGL), aldehydes and others. Recently, we have theoretically investigated the feasibility of synthesis of EGL directly from the coupling of methanol [1]. An experimental study of methanol plasma using corona discharge has confirmed the possibility of this reaction [2]. In this work, we attempt to compare methanol conversions using corona discharge and dielectric-barrier discharge (DBD).

Experimental and Setup

Corona discharge reactor applied in this work has been previously reported [2]. The reactor is a quartz tube with an inner diameter of 6 mm. A cylindrical furnace is placed around the reactor for the reaction temperature control. This discharge reactor consists of two electrodes, a top metal wire electrode and a lower hollow electrode as the grounded one. The gap between the electrodes is fixed at 6 mm. The high voltage amplifier (Trek 20/20B), connected with a HP33120A signal generator, supplies a high voltage with DC or AC (at different waveforms) signal to the top wire electrode.

The DBD reactor used in this work was similar to that reported previously [3]. Discharge zone lies between a dielectric-barrier made of quartz and a stainless steel tube serving as grounded electrode with a length of 250 mm and a gap width of 1.1 mm. An aluminum foil is connected with a high voltage generator, which output a sinuous signal at a frequency of 25 kHz. Methane and carbon monoxide were introduced into the discharge gap (between the grounded electrode and quartz surface) both at 20 ml/min via two mass flow controllers.

The voltage and current were measured with a high voltage probe (Tektronix P6015 A) and a pulse current transformer (Pearson Electronics 411) via a digital oscilloscope (LeCroy Model LC 334A) (for AC). The discharge power was measured via a digital multimeter (Keithley 2000).

The feed gases and gaseous products were analyzed with an on-line gas chromatograph (HP 5890 with TCD and FID) and mass selective detector (HP 5971).

Results and Discussions

The previous DFT study has identified the reaction routes of methanol dissociation based on the grounded state. Methanol is dissociated by routes: methanol dissociation to $CH_3O\cdot$ + ·H, $\cdot CH_2OH$ + ·H and $\cdot CH_3$ + ·OH. The calculated energies for these three pathways using the B3P86 method are 100.56, 94.35 and 89.54 kcal/mol, respectively. The calculated results show that the dissociation of methanol to $\cdot CH_3$ and ·OH requires less energy and is the dominating dissociation route. Just a little more energy requested for the formation of $\cdot CH_2OH$, compared to the formation of methyl radical. The dissociation of methanol into $\cdot CH_3O$ and ·H is most difficult. Evidently, $\cdot CH_3$, $\cdot CH_2OH$ and $CH_3O\cdot$ can be obtained from methanol dissociation. Theoretically, the recombination of these radicals will generate several products including ethane, ethylene glycol, ethanol and dimethyl ether (DME).

The experimental investigation confirms that, using corona discharge, EGL can be produced directly from methanol, as shown in Table 1. In addition to EGL, CO, ethanol, propanol and trace ethane have also been produced. No DME was observed. With the present reactor design, the AC corona discharge leads to a more production of EGL. Compared to the negative corona discharge (DC-neg), the positive corona (DC-pos) is more favored for EGL synthesis. Also, the positive corona discharge generates more ethanol and propanol. At the present design of reactor system, however, the major product from methanol conversion using corona discharges (including AC and DC corona discharges) is syngas. The corona discharge is too energetic that the oxygenated hydrocarbon products will be destroyed quickly once they formed.

Table 1. Production Rate of Methanol Dissociation Using Corona Discharges

	Production rate (μmol/min)				
	CO	ethanol	propanol	EGL	ethane
DC-pos	169.1	0.007	0.06	0.8	trace
DC-neg	250.6	0.004	0.01	0.1	trace
AC-sin	328.0	1.9	3.6	8.7	trace

On the other hand, the experimental investigation using DBD plasmas exhibits a very different result (i.e., very different product distribution). Under the influence of DBD plasmas, the major product is still syngas. Some minor oxygenate products from this DBD plasma methanol conversion include aldehydes, acids (principally, HCOOH), and alcohols (with EGL). The oxygenate with highest selectivity (5.5%) is formic acid. The selectivity of EGL is 1.2%.

For either corona discharge or DBD, in order to increase the yields of oxygenates, it is important to keep the oxygenate molecules stable within the energetic discharges once they are formed. We have observed that the liquid drops within the discharges can help to remain the oxygenate molecules. It is potential to develop a liquid plasma technology for the oxygenate syntheses directly from methanol.

Summary

The present investigation has confirmed that different discharge plasmas will induce a different product distribution. The corona discharge can convert methanol directly into EGL and alcohols, while DBD can induce a synthesis of aldehydes and acids. The theoretical study has confirmed the feasibility of this kind of synthesis, which has major advantage with simple operation and small setup required. The drawback of the present synthesis is the low yield of objective oxygenates products. For future development, a liquid plasma conversion technology will be developed.

Acknowledgement. Part of equipment and setup were donated by ABB Switzerland Ltd. Support from Major Research Project of National Natural Science Foundation of China (No. 20490200) is very appreciated.

References

(1) Cheng, D.-G; Wang, J.-G; and Liu, C.-J. *DFT Study of Methanol Dissociation,* paper submitted.

(2) Li, H.-Q.; Zou, J.-J.; Zhang, Y.-P.; and Liu, C.-J. *Chem. Lett.* **2004**, *33*, 744-745.

(3) Wang, Y.; Liu, C.-J.; Zhang, Y.-P. Plasma methane conversion in the presence of dimethyl ether using dielectric-barrier discharge, **Energy Fuels** (accepted).

A THERMOSTABLE CU-MN BASED CATALYST FOR HIGH TEMPERATURE WATER-GAS-SHIFT REACTION

*Quangsheng Liu , Runxia He, Xieli Cu, Keduan Zhi, Wenping Ma**

Department of Chemical Engineering, Inner Mongolia University of Technology, Hohhot, P. R. China, 010062

Introduction

The water gas shift reaction (WGSR), $CO + H_2O \rightarrow CO_2 + H_2$, is an industrially important route to H_2 production and plays an important role in many current technologies such as methanol synthesis, methanol steam reforming, ammonia synthesis, coal gasification, as well as fuel cell technology[1].

Even though the chromium-promoted iron-based shift catalyst have shown excellent activity, high stability and certain resistance to the sulfur poisoning at 315-450℃, the existence of chromium in this catalyst make it environmental restrictions and press for discarding of chromium compounds. In addition, in order to avoid the Fe_3O_4 being reduced to metallic iron, which will catalyze the F-T synthesis reaction, large superfluous amount of steam must be used, which lead to the increasing of the operation costs. So radical solution to avoid the by-product formation is to replace the classical iron-base high temperature shift catalyst by an iron free catalyst capable of operation at these conditions[2]. Most of investigation about the iron free high temperature shift catalyst are the Cu-based high temperature shift catalyst[3-7]. All of these Cu-based high temperature shift catalyst can used in lower steam/gas ratio and show excellent resistance to the F-T side reaction less than 400 ℃. However, the reaction temperature high than 450℃ result in the activity of the catalyst decrease badly. Moreover, even the reaction temperature restore less than 400 ℃ the activity cannot restore. This means the mentioned Cu-based high temperature shift catalyst have bad resistance to high-temperature excursion higher than 400℃. This shortcoming restricts the popularization of the Cu-based high temperature shift catalyst. The present paper reports the results of a new Cu-Mn-Based catalyst for water gas shift catalyst that can be comparable to current used iron-based catalyst.

Experimental

Catalyst Synthesis. All reagent used were of an analytical grade. The Cu-Mn catalysts samples were prepared using the co-precipitation technique. Details of preparation procedures and characteristic were reported elsewhere[8]. In brief, the Cu-Mn based catalysts were precipitated with copper sulfite and manganese sulfite by alkali solutions in a beaker. The resulting slurry was subsequently aged followed by washing, drying and calcinations.

Fixed-Bed Reactor Test. The activity of Cu-Mn based (12-14 mesh, 0.5g) was examined in a bench-scale fixed-bed stainless steel reactor (ID = 6mm) under atmospheric pressure, 350 ^oC and 3000 h^{-1} (dry-gas basis). The composition of feed gas was 12% CO, 18% CO_2, 56% H_2 and 16% N_2 (internal standard). Prior to WGS reaction, the catalyst samples were reduced using the same reactant gas mixture under severe conditions: 530 ^oC, 3000 h^{-1} for 15 h. The gas compositions before and after the WGS reaction were analyzed online by a GC-8A gas chromatograph (GC).

Characterization Methods. The BET surface areas of the catalysts were measured by isothermal adsorption of N_2 at 77K using a surface area porosity analyzer ASAP2010. X-Ray powder diffraction (XRD) analysis of the samples were performed on D8 Advance X-ray diffraction-meter, Cu Kα radiation with a nickel filter was used with a power of 40 kV × 40 mA. The samples morphology(TEM) was studied on a JEM-2010 electron microscope. Thermal-Analysis were performed with DTG-50/50H.

Results and Discussion

Table 1 lists the bulk composition, BET surface areas before and after WGS reaction and CO conversion (X_{CO}, %) at 350 ^oC of the catalysts samples. The same experimental data of a commercial Fe-Cr WGS catalyst denoted as C12-4, which was supplied by United Catalyst Inc. (UCI), are also listed in Table 1 for comparison. The BET surface areas of both catalysts before reaction are are 52.4 and 70.2m^2/g, respectively. Both BET surface areas of Cu-Mn catalyst before and after reaction are lower than that of C12-4 catalyst correspondingly. After WGS reaction, the BET surface areas of Cu-Mn and C12-4 catalysts were decreased to 30.4 m^2/g and 40.4 m^2/g, respectively. But the decrease scope of Cu-Mn(42%) is almost same as that of C12-4. CO conversions at 350 ^oC during steady state for both catalysts are high and the activity of Cu-Mn is 11% higher than that of C12-4, which was not quantitatively correlated well with their surface areas. Due to the Cu-Mn and C12-4 catalysts experiencing very severe thermo-resistance test during reduction period (530 ^oC and 15 hours), the high CO conversions showed that both catalysts had excellent thermo-resistance property.

Table 1. Summary of BET and Reaction Results of Cu-Mn and C12-4 catalysts

Catalyst ID	CO Conversion %[a]	Special surfacearea m^2/g	
		Before reaction	After reaction
Cu-Mn	64.7	52.4	30.4
C12-4	53.8	70.2	40.4

a X_{CO}, % = (CO mole flow rate in - CO mole flow rate out)/ CO mole flow rate in × 100

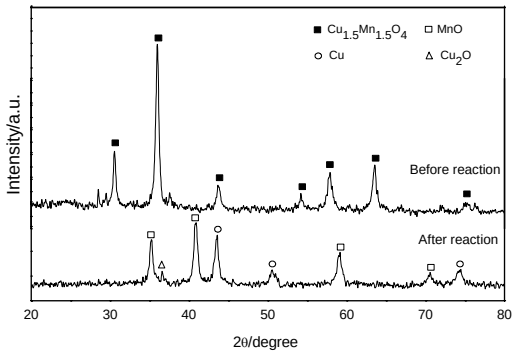

Fig.1 X-ray powder diffraction patterns of Cu-Mn catalyst before and after reaction

XRD spectra of the Cu-Mn catalysts before and after reaction are shown in Fig.1. The main crystal phase of this type Cu-Mn catalyst before reaction is single spinel structure-$Cu_{1.5}Mn_{1.5}O_4$ with small amount of unidentified phase (2θ=25-30^o). No obvious other

* Present address: Department of Chemical Engineering, West Virginia University, Morgantown, WV. 26505

crystallization is found. The crystal phase of this type Cu-Mn catalyst after reaction is mixture of three crystallization- MnO、Cu and Cu_2O, of which the Cu micro-crystallization is more than 90% of Copper component.

The thermo-analysis (TGA and DTA) is shown in Fig.2. A weight loss with an endothermic peak near 46℃ is attributed to dehydration of adsorbed water. It is followed by a gradual weight loss till 292℃ with an obvious exothermic peak, which can be assigned to forming of $Cu_{1.5}Mn_{1.5}O_4$ from its precursor. A metastable endothermic peak appears near 482℃, which can be attributed to the forming of an new undetermined crystallization phase corresponding to 2θ=25-30° in XRD spectra.

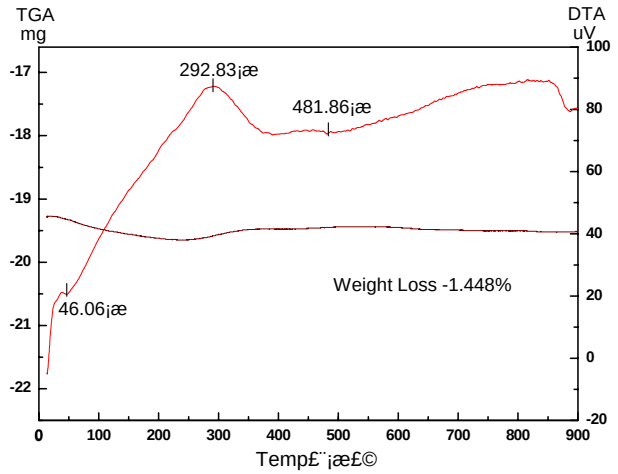

Fig.2 DTA/TGA trace of Cu-Mn catalyst after dryness

Transmission electron micrographs of Cu-Mn catalysts before and after reaction are shown in Fig. 3. The Cu-Mn catalysts before and after reaction are composed of clubbed, flake and polyhedron particle. The particle sizes before reaction distribute from10nm to 50nm. After reaction the particles sizes increase and distribute narrower than that before reaction. There appears micro-crystal on the flake particle after reaction, which is speculated to the Cu crystal resulted from reducing of $Cu_{1.5}Mn_{1.5}O_4$.

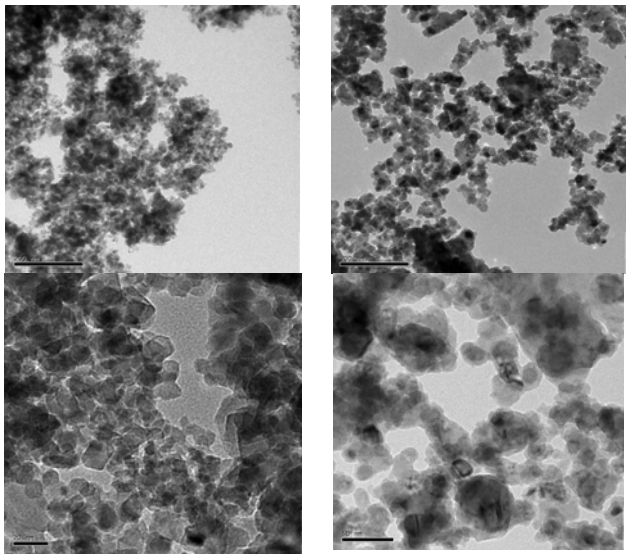

Figure 3. Transmission electron micrographs of Cu-Mn Catalyst
Left: Before reaction; Right: After reaction

Concluding Remarks

It can be concluded that the Cu-Mn based catalyst gives appreciably higher activity when compared to existed industrial high temperature shift catalysts based on iron/chromium oxides and additionally this catalyst system is a potentially superior catalysts in comparison to the current industrially operated iron/chromium oxides high temperature shift catalysts. It is a good alternative to the traditional high-temperature Fe-Cr WGS catalysts.

Acknowledgement. This study was supported by Natural Science Foundation of China (20066002) and Science Foundation of Inner Mongolia (20041001) in China.

References

(1) N. Schumacher, A. Boisen, S. Dahl, J. Catal., 2005, 229: 265-275
(2) Jack H. Carstensen，John B.Hansen，Peter S. Pederson，New Developments in High Temperature Shift Catalyst Technology Solve the Fishscher-Tropsch Problem, 1989 AICHE Ammonia Safety Symposium, San Francisco
(3) N. Yamamoto, B. Hashimoto, H. Shibano, Kokai Tokkyo Koho JP, 63/77546, 988.
(4) F. M. Gottschalk, G. J. Hutchings, Appl.Catal., 1989, 51: 127~139.
(5) Sh. B. Feng, R. Liang, X. D. Dong, Chinese J. Catal., 1996, 17: 391~393.
(6) Y. Tanaka, T. Utaka, R. Kikuchi, Appl. Catal., A: General, 2003, 242: 287~295.
(7) Y. Tanaka, T. Utaka, R. Kikuchi, J.Catal, 2003, 215: 271-278.
(8) Yunxia He, Preparation and Characteristics of Fe-Based, Cu-Based and RE-Based Water Shift Catalysts for Production of Hydrogen in Fuel Cell，Master Degree Dissertation, Inner Mongolia University of Technology, 2004.

HIGHLY FLUORINATED GRAFT COPOLYMERS AS PROTON EXCHANGE MEMBRANES (PEMs): IMPROVING PEM PROPERTIES THROUGH RATIONAL DESIGN

Tyler B. Norsten, Michael D. Guiver, Jianfu Ding

National Research Council of Canada
Institute for Chemical Process and Environmental Technology
1200 Montreal
Ottawa, ON K1A 0R6

Introduction

Microstructural analysis of Nafion and other newly emerging PEM materials has suggested that both chemical microstructure and nanoscale morphology of ionomer membranes can dictate material performance.[1-3] With this in mind, much current research is aimed at designing and developing alternative polymer materials based on non-fluorinated or partially fluorinated polymeric systems.[4] The majority of this work is based on non-fluorinated polyaromatic hydrocarbon-based condensation polymers that contain ionic functionality randomly located along the polymer backbone (Fig 1a). Generally these polymers can achieve suitable conductivity only at low EW (high degrees of sulfonation) resulting in high water-up take/swelling ratios that are unsuitable for practical PEM applications. It has been suggested that these sulfonated polymers struggle to form defined hydrophilic domains as the rigid polyaromatic backbone prevents co-continuous ionic clustering from occurring.[5]

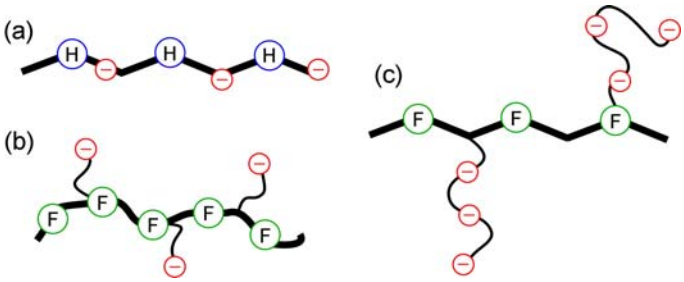

Figure 1. Graphical structure representations of: a) a typical polyaromatic-based PEM displaying a rigid and sulfonated hydrocarbon backbone, b) Nafion-based materials displaying a flexible perfluorinated backbone with short and flexible pendant side chains containing single sulfonic acid groups, and c) our hybrid material based on a highly fluorinated and rigid polyaromatic backbone with long pendant graft polymers containing multiple sulfonic acid groups.

Nafion, on the other hand, is a random copolymer comprised of a perfluorinated hydrophobic backbone that contains a number of short flexible pendant side chains with single hydrophilic/ionic groups (Fig 1b). It is this balance of hydrophobic-hydrophilic properties within the material coupled with the mobility of the sulfonic acid group, as a result of side chain flexibility that, in the hydrated form, leads to a co-continuous network of ionic channels through the material.

The phenomenon of microphase separation of block copolymers can be used to create well defined periodic microdomains of controlled morphology (e.g. cylinders, spheres, lamellae) on the nanoscale (10-100 nm). Recently research has shown that graft copolymers are also capable of creating similar nanoscale morphologies.[6] Herein we report the characterization of a series of highly fluorinated graft copolymers that can be used as proton exchange membranes.

The main chain is comprised of a highly fluorinated polyaromatic backbone, while the graft segments containing the ionic groups are comprised of flexible and monodisperse aromatic polymer side chains (Fig 1c). Like previous polyaromatic PEM structures, this design incorporates the use of a semi-rigid polymer backbone capable of creating mechanically durable high temperature membranes. Unlike most polyaromatic PEMs this design: incorporates a highly fluorinated backbone which provides a high degree of hydrophobicity and chemical stability to the material, ensures little or no sulfonation on the backbone resulting in minimal water-up take into the hydrophobic domains, and employs flexible side chains capable of microphase separating into a continuous ionic network. Furthermore, unlike Nafion, these side chains are reasonably long and contain multiple sulfonic acid groups which were designed to yield increased ionic domain interconnectivity and expected to provide better conductivity at low levels of hydration.

Experimental

Water Uptake and Swelling Ratios. Membrane films were dried at 65°C for 48h prior to the measurements. After measuring the lengths (0.5 cm x 5 cm) and weights of dry membranes, the sample films were soaked in deionized water for 24 h at predetermined temperatures. Before measuring the lengths and weights of hydrated membranes, the surface bound water was removed from the membrane by blotting the surface with a filter paper.

Ion Exchange Capacity. The IEC/EW of the membranes were determined by titration. A piece of membrane typically (4 cm x 4 cm) in the acidic form was immersed in 40 ml of 2.0 M NaCl solution for 24h. Solutions were titrated with 0.025 M NaOH solution to a phenolphthalein end point. After titration, the sample was rinsed with distilled water and dried under vacuum at 65°C until a constant weight (48h).

Conductivity. All conductivity measurements were performed in the longitudinal direction in Milli-Q water (18 MΩ resistivity). Membrane samples (20 mm x 10 mm) were acidified in 2M HCl, rinsed thoroughly and soaked in distilled water for a minimum of 24h before use. Variable temperature measurements were performed in a thermally controlled stainless steel vessel employing a two-electrode (platinum) ac impedance technique using and a Solatron 1260 frequency response analyzer. Spectra were recorded between 10^2 and 10^7 Hz with 10 points per decade at a maximum perturbation amplitude of 100 mV. All conductivities (σ) were calculated using the relation $\sigma = d/RS$, where d and S are the thickness and face area of the sample, respectively and R was derived from the low intersect of the high frequency semi-circle on the complex impedance plane with the Re(Z) axis. The impedance spectra were fitted on the basis of the Rs(C-Rp) equivalent circuit employing the corresponding instant fit function in the Zview 2.80 software by Scribner Associates Inc.

Transmission Electron Microscopy (TEM). Membranes in there sulfonic acid form were immersed in 0.5 M lead acetate solution for 48h and rinsed with water in order to stain the ionic domains. A 1 x 5 mm strip was then cut from the membrane. The thin sample was embedded in bimodal polystyrene by placing the strip in a glass vial containing several PS beads and heating at 120°C until the PS completely embedded the sample. The glass vial was then shattered and the embedded polymer sample collected. Thin films (40-50 nm) of the embedded polymer samples were prepared using an ultramicrotome (Ultracut-E, Reichert-Jung) fitted with a Diatome diamond knife. The slices were picked up with 400 mesh carbon coated copper grids for TEM analysis. The samples were analyzed using a Philips CM20 STEM equipped with a Gatan UltraScan 1000

CCD camera and INCA Energy TEM 200 EDX spectrometer operating at 120 kV.

Small Angle X-Ray Scattering (SAXS). Cu Kα X-rays (1.54 Å) were generated in an Osmic MaxFlux source with a confocal multilayer optic (OSMIC, Inc). Images were taken with a Molecular Metrology, Inc., camera consisting of a 3 pinhole system, 150 cm sample-to-detector distance (calibrated using silver behenate), and a 2 dimensional, multiwire proportional detector (Molecular Metrology, Inc.). The entire X-ray path length was evacuated from the optic to the detector in order to reduce the background from air scattering. This setup allowed neglecting the correction for background scattering as proved by experiment. Two-dimensional images were reduced to one-dimensional form using angular integration. Scattering vectors (q) were calculated from the scattering angles (θ) using $q = 4\pi \sin \theta/\lambda$, and domain periodicities (D) were calculated from Gaussian fits to the principal scattering maxima of the Lorentz-corrected intensities using $D = 2\pi/q$.

Results and Discussion

A series of highly fluorinated graft copolymers were prepared containing weight percents of 18, 25 and 37 graft chain. The graft chains were incorporated randomly into the polymer backbone and were prepared in such a fashion that they were all of uniform length and composition. The conditions for introducing the ionic groups were chosen such that sulfonation of the graft copolymers was selective to the graft chains. This synthetic methodology provided precise control over the amount of hydrophilic side chain that could be incorporated into the hydrophobic backbone.

The sulfonated materials were of high M_n (67000-105000 g/mol) and produced membranes with excellent mechanical properties when solvent cast onto optically flat surfaces. The polymers display good thermal properties with T_g's of 180°C and onset T_d's of 205°C in nitrogen. The IEC capacity of a material is the measure of its exchangeable protons. These protons in conjunction with water are the "vehicles" on which protons are transported through the membrane. Table 1 shows the IEC values for all the graft polymer membranes tested and relates them to N117 under identical test conditions.

Table 1. IEC/EW VALUES AND IONIC INTERDOMAIN DISTANCES FROM SAXS

Polymer	IEC (meq/g) / EW	Ionic Domain Periodicity (nm)
N117	0.96 / 1042	—
18%	0.87 / 1149	19.9
25%	1.41 / 714	15.8
37%	1.75 / 571	13.0

SAXS analysis (Fig 2b) of the lead stained membranes clearly shows that as the amount of ionic graft chain is increased from 18-37% the Bragg scattering vector (q) shifts to larger values indicative of smaller interdomain periodicities. Hence, larger ionic domains concomitantly produce smaller hydrophobic domains, which is a direct measure of the ionic domain periodicities shown in Table 1. This ultimately results in a higher connectivity of hydrophilic proton conducting networks with smaller separation distances.

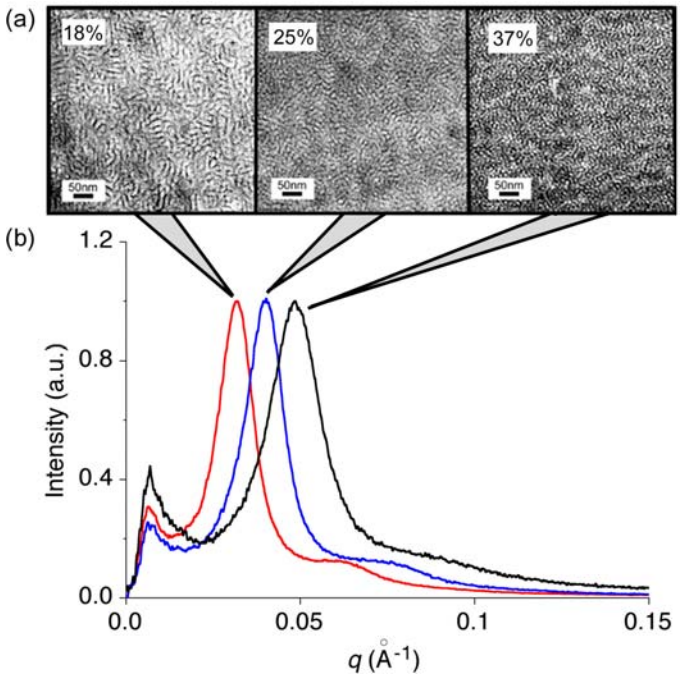

Figure 2. (a) TEM micrographs, the dark regions indicate the ionic domains, and (b) normalized SAXS data of lead stained ionomeric membranes containing 18-37% graft chain content.

The SAXS data is intimately correlated to the TEM micrographs (Fig 2a) which clearly show an increase of ionomeric content on going from 18-37% graft chain and the systematic shrinkage of the hydrophobic regimes. The TEM also indicates that a distinct lamellar morphology results from the 18% material which becomes less pronounced upon incorporation of addition side chain content. This is corroborated by the presence of the broad peak in the SAXS plot at ~2q for the 18% material which systematically flattens on going from the 25% to the 37% materials.

Water management within the membrane is a critical factor in the performance of PEM materials. Although these copolymer materials up-take more water than Nafion their swelling due to water up-take is less in most cases (Fig 3, bracketed numbers). This may be a result of the unique polymer microstructure allowing water only into the hydrophilic domains while the alternating hydrophobic domains serve to maintain dimensional stability. Figure 3 also shows that these materials display excellent proton conductivities over the temperature ranges studied.

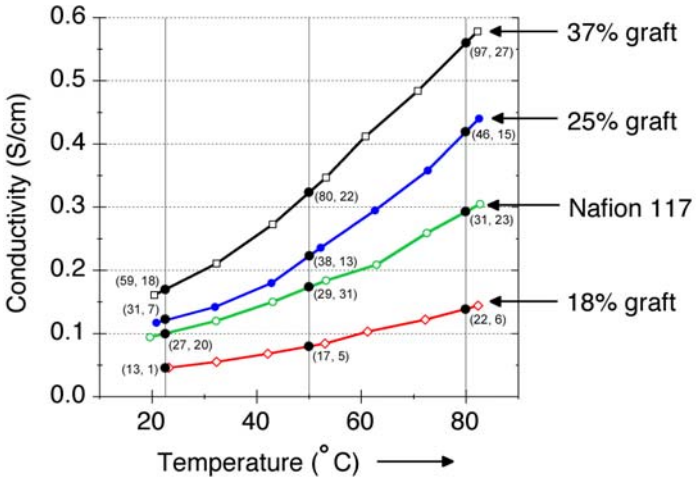

Figure 3. Proton conductivities as a function of temperature for the grafted ionomeric membranes and Nafion 117. The numbers in brackets represent (% water up-take, % swelling) respectively at the specified temperatures.

Conclusions

A series of highly fluorinated graft copolymers have been prepared that show excellent properties as PEM materials. Specifically, these materials display abilities to conduct protons and manage water that is comparable or superior to Nafion. It appears that the unique polymer structure resulting in microphase separation between opposing domains (e.g. hydrophobic and hydrophilic) is responsible for the excellent properties observed for these materials.

Acknowledgement. The authors are grateful to Ben Frankamp for performing SAXS analysis and Dashan Wang for TEM analysis.

References

(1) Mauritz, K. A. and Moore, R. B. *Chem. Rev.*, **2004**, *104*, 4535.
(2) Ding, J.; Chuy, C. and Holdcroft, S. *Chem. Mater.*, **2001**, *13*, 2231.
(3) Eladb, Y. A.; Walker, C. W. and Beyer, F. L. *J. Membrane Sci.*, **2004**, *231*, 181.
(4) Hickner, M. A.; Ghassemi, H.; Kim, Y. S.; Einsla, B. R. and McGrath, J. E. *Chem. Rev.*, **2004**, *104*, 4587.
(5) Kreuer, K. D. *J. Membrane Sci.*, **2001**, *185*, 29.
(6) Xenidou, M.; Beyer, F. L.; Hadjichristidis, N.; Gido, S. P.; Tan, N. B. *Macromolecules*, 1998, *31*, 7659.

NEW SUPER PROTON-CONDUCTIVE, HIGH ACID-CONTAINING FLUOROPOLYMER PEMS FROM CURED LIQUID PRECURSORS

Zhilian Zhou, Raymond N. Dominey and Joseph M. DeSimone

Department of Chemistry
University of North Carolina
Chapel Hill, NC27599

Introduction

Polymer electrolyte membrane (PEM) fuel cells are becoming increasingly popular as candidate solutions to power sources for portable electrical devices, transportation, and distributed power.[1-3] The next generation of fuel cell membranes must outperform today's most widely used material, Nafion®. Although this perfluoro-sulfonic acid based PEM material has many desirable features, several shortcomings limit its utility and performance. Key liabilities include high synthesis and processing costs,[4] diminished proton conductivity under conditions of low water availability,[5-7] high fuel crossover when used in direct methanol fuel cells (DMFC),[8] and limited mechanical strength at elevated temperatures.[9] Furthermore, the flat two-dimensional geometry of current PEM materials severely limits the power generation potential of fuel cells derived from these materials.

To address these deficiencies, we start from a fluoropolymer liquid precursor that is chemically cured into a network. This curing process is solvent-free. No further processing such as melt extrusion or solvent casting is necessary. By employing chemically crosslinked system, membranes with high ion loading can be achieved without dissolution in water. These high acid-containing fluoropolymer PEMs have very high proton conductivity and good mechanical integrity at the same time due to their chemical crosslinked natures. By this liquid precursor approach, flat and 3-dimensional membranes can be easily prepared by photo or thermal curing using soft lithography techniques. Patterned, 3-dimensional membranes can provide a much larger active surface area compared to traditional flat PEMs. Fuel cells comprised of a 3-dimensional membrane should have greater efficiency due to their increased power density.

Experimental

In order to incorporate a crosslinkable functionality, a styrene linkage was added to both chain ends of poly(tetrafluoroethylene oxide-*co*-difluoromethylene oxide) (PFPE) α-, ω- diol by reacting with 4-vinylbenzyl chloride in a phase transfer catalyzed reaction. The resulting product (S-PFPE) is a clear viscous liquid.

In order to make a styrene sulfonic acid precursor that is miscible with S-PFPE, a styrene sulfonate ester was synthesized by reacting 4-vinyl benzenesulfonyl chloride with a fluorinated alcohol.

To make a PEM material, S-PFPE with 1wt% photo-initiator and styrene sulfonate ester were mixed in the desired ratio and chemically crosslinked by irradiation with UV light. The resulting solid membrane is in the ester form, transparent and slightly yellow.

To convert the sulfonate ester group to sulfonic acid, the membrane was soaked in a mixture of NaOH aqueous solution and methanol for 12 h and then refluxed in the same mixture for an additional 10 h. After rinsing with distilled water, the membrane was stirred for a total of 24 h in fresh 20wt% HCl solution. The resulting membrane was in the acid form. Residual HCl was removed by washing with distilled water.

Characterization

Nuclear Magnetic Resonance (NMR) spectra were taken using a Bruker 400 MHz DRX spectrometer. Optical micrographs of the patterned membranes were taken using an Axioskop2 optical microscope equipped with an AxioCam HRm camera.

Ion exchange capacity (IEC) and equivalent weight (EW) of the membranes were determined by titration of the sulfonic acid group. In a titration measurement, a piece of membrane (typically 0.2~0.3g) in acid form was stirred with saturated NaCl solution overnight; the resulting solution was then titrated with standardized 0.01 mol/L NaOH solution using phenolphthalein as the indicator. The titrated membrane was dried in the salt form and the dry weight of membrane was accurately measured. The ion exchange capacity (IEC) and equivalent weight (EW) of the membranes are calculated as follows:

$$EW\ (H^+,\ g\ mol^{-1}) = [Dry\ weight\ /(V_{NaOH}*[NaOH])] - 22$$

$$IEC\ (meq\ g^{-1}) = 1000/EW$$

The thermal stability of the membranes was measured by a Perkin-Elmer Pyris 1 thermogravimetric analyzer (TGA). Dynamic mechanical and thermal analysis (DMTA) measurements were performed with a 210 Seiko dynamic mechanical spectroscopy (DMS) instrument, operating at fixed frequency and film tension mode.

After hydrolysis, the membranes were kept in water until no more weight change was observed. The water uptake of the membranes is calculated as follows:

$$Water\ uptake\ (wt\%) = (Wwet - Wdry)/\ Wdry\ *100$$

Proton conductivity was measured by AC Impedance over the frequency range of 1Hz – 1MHz. Impedance spectra were recorded using Solartron 1287 Impedance and Solartron 1255 HF frequency response analyzer.

Results and Discussion

IEC is the key factor that determines the properties of PEM materials. Membranes with IEC between 0.50 meq/g to 1.82 meq/g (EW= 1900~550) were prepared. It is common for linear PEM materials to dissolve in water if they contain a significant amount of acid groups. Due to the crosslinked nature, however, our PEMs with IEC as high as 1.82 meq/g remained intact after refluxing in methanol-water mixture for 10 h during hydrolysis.

Properties of these new PEMs, such as water uptake, dimensional change, proton conductivity, and fuel cell performance are under investigation and will be reported in the meeting.

Acknowledgement. We would like to thank DuPont for financial support of this project and we acknowledge partial support from the NSF Science and Technology Center for environmentally responsible solvents and processes (Grant No. 4-25151).

References

(1) Appleby, A. J.; Foulkes, R. L. *Fuel Cell Handbook*; Van Nostrand: New York, **1989**.
(2) Jacoby, M. *C&E News* **1999**, *77*, 31.
(3) Malhotra, S.; Datta, R. J. *J. Electrochem. Soc.* **1997**, *144*, L23.
(4) Gil, M.; Ji, X.; Li, X.; Na, H.; Hampsey, J. E.; Lu, Y. *J. Membr. Sci.* **2004**, *234*, 75.
(5) Savadogo, O. *J. New. Mater. Electrochem. Syst.* **1998**, *1*, 47.
(6) Gottesfeld, S.; Zawodzinski, T. A.; Alkire, R. C., Gerischer, H., Kolb, D. M., Tobias, C. W., Eds.; Wiley-VCH, 2002; Vol. 5.
(7) Si, Y.; Kunz, H. R.; Fenton, J. M. *J. Electrochem. Soc.* **2004**, *151*, A623.
(8) Cruickshank, J.; Scott, K. *J. Power Sources* **1998**, *70*, 40.
(9) Hickner, M. A.; Ghassemi, H.; Kim, Y. S.; Einsla, B. R.; McGrath, J. E. *Chem. Rev.* **2004**, *104*, 4587.

THE INTERACTION BETWEEN TIO_2 NANOPARTICLES AND NAFION® IN NAFION COMPOSITE MEMBRANES FOR PEM FUEL CELL APPLICATIONS

Paul W. Majsztrik, Hitoshi Ota, Andrew B. Bocarsly

Chemistry Department
Princeton University
Princeton, NJ 08544

Introduction

Nafion, which to date is the best membrane material for polymer electrolyte membrane fuel cells (PEMFCs), limits the operating temperature of the cell to under 90 °C. Operating a PEM fuel cell in this low temperature range: 1) requires that high-purity hydrogen fuel be used to prevent CO poisoning of the Pt catalyst, 2) produces low quality waste heat, 3) results in decreased catalyst efficiency, and 4) makes water management in the cell difficult. Operation of PEMFCs at elevated temperature (110-150 °C) improves each of these areas. One approach for developing an elevated temperature PEMFC is to create a composite Nafion membrane by the inclusion of metal oxide nanoparticles in Nafion[1,2,3]. Adding certain metal oxide particles (TiO_2, SiO_2, etc.) improves the performance of Nafion at elevated temperature and reduced relative humidity. It has been proposed that the addition of metal oxides increases hydration in the membrane because the metal oxides are hydrophilic[2]. Instead, we propose that metal oxides crosslink the polymer, allowing the polymer to maintain its structure at elevated temperatures and low humidity.

This work investigates the interaction between TiO_2 nanoparticles and Nafion in TiO_2 composite membranes. The purpose of this investigation is to discover how TiO_2 nanoparticles interact with Nafion and if the size or surface characteristics of the particles effects this interaction. Composite membranes prepared using four different size TiO_2 particles are analyzed in order to determine if particle size or surface properties affect the interaction. A mechanism for the thermal decomposition of plain and TiO_2 composite Nafion is suggested.

Experimental

Nafion composite TiO_2 membranes were prepared by recasting using a 5% by weight Nafion solution (Ion Power) mixed with a solvent (either isopropanol (IPA) or dimethyl sulfoxide (DMSO)) and TiO_2 particles. Four different types of TiO_2 particles were used as fillers: 21 nm particles (Degussa-Hüls), 10 nm and 5 nm anatase TiO_2 particles (Nanostructured and Amorphous Materials, Inc.), and 1-2 μm particles (Alfa Aesar). The particles were suspended in a mixture of DMSO or IPA and Nafion by sonication, cast on a flat glass surface, and the solvent was removed at ~80 °C in a vacuum oven (for DMSO) or at 75 °C without vacuum (for IPA). The membranes were then annealed, cleaned, and acid exchanged.

Analysis of the interaction of the TiO_2 particles with Nafion was performed using Thermogravimetric-Mass Spectrometry (TG-MS) analysis ((TG)(Seiko EXSTAR6000), (MS) (Agilent 6890N)) and Thermogravimetric Analysis (TGA) (Perkin Elmer TGA 7). For the TGA scans, a heating rate of 1 °C/min was used and samples were held at 100 °C for 60 minutes to allow for water removal. All TGA runs were performed under Argon. The TG-MS scans were performed on samples dried at 70 °C in a vacuum oven and a scan rate of 10°C/min was used.

The thermogravimetry-mass spectrometry (TG-MS) and temperature programmed desorption or decomposition (TPD-MS) analyses of Nafion/Inorganic composite membrane were performed with the TG-MS system by coupling TG-DTA (Seiko EXSTAR6000) with GC/MS (Agilent 6890N) and the TPD-MS system by coupling the pyrolyzer with GC/MS (Agilent 5973N). The pyrolysis temperature was programmed to increase from 25 to 500°C at a rate of 10°C/min under helium flowing at 60 ml/min. The gaseous decomposition products were introduced directly into the MS unit via a gas transfer tube with a deactivated fused silica capillary. The transfer lines were maintained at 200°C. The MS interface temperature was set at 250°C. The MS system was maintained at about 1×10^{-6} torr.

Results and Discussions

TG-MS data for the thermal decomposition of extruded Nafion and Nafion composite TiO_2 (21 nm particles) membranes are presented in f**igure 2**. From these data, we propose that plain Nafion decomposes in two steps while the Nafion TiO_2 composite decomposes in three steps, as illustrated in **figure 1**.

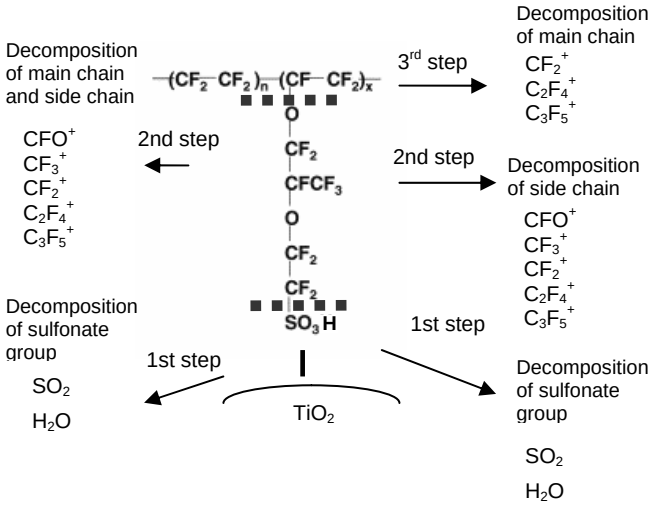

Figure 1. Proposed mechanisms for the thermal decomposition of (left) plain Nafion and (right) TiO_2 composites.

For both plain and TiO_2 membranes, free water is the first to be removed. The sulfonate group is removed next, concomitant with the removal of water bound to the sulfonate. The sharpening and shifting to lower temperature of the water and SO_2 peaks (MS plots) with the addition of TiO_2 indicates that there must be a chemical interaction between the acid groups in Nafion and the surface of the TiO_2 particles and that TiO_2 catalyses the reaction. We propose that there are coordinately unsaturated sites on the surface of the TiO_2 which bond to an O on the sulfonate. Along with the loss of H_2O and SO_2 is CFO from the ether linkages. This is visible as a small peak in the MS plot for the TiO_2 membrane but is not visible for the plain Nafion since the loss of the sulfonate group occurs over a broader temperature range and is thus, present in concentrations beyond the sensitivity of the instrument. Further support for this is seen in TG-MS scans showing the appearance of CF_2 and C_2F_4 along with H_2O and SO_2.

A comparison of the thermal decomposition of Nafion composites prepared with different size/types of TiO_2 (**figure 3**) suggests that the different TiO_2 particles interact differently with Nafion. The addition of 5, 10, and 21 nm TiO_2 particles all result in the bound water and SO_2 loss shifting to lower temperature and

occurring over a smaller temperature range. The 10 and 5 nm particles give the largest slope in the water and SO_2 loss region (~230 °C). This indicates that the 5 and 10 nm particles have the strongest interaction with the sulfonate group. Since the 5 and 10 nm particles have a pure anatase structure, while the 21 nm particles mixed rutile and anatase, this also should affect the interaction.

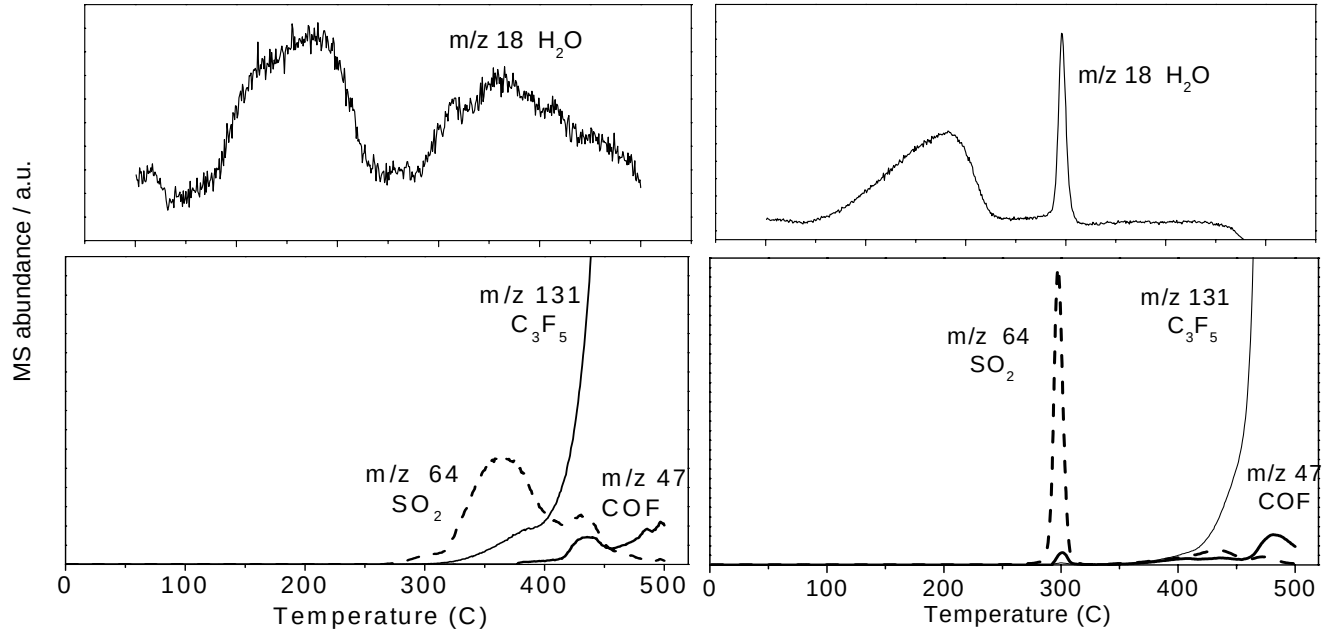

Figure 2. TG-MS scans for plain Nafion and Nafion TiO_2 composite

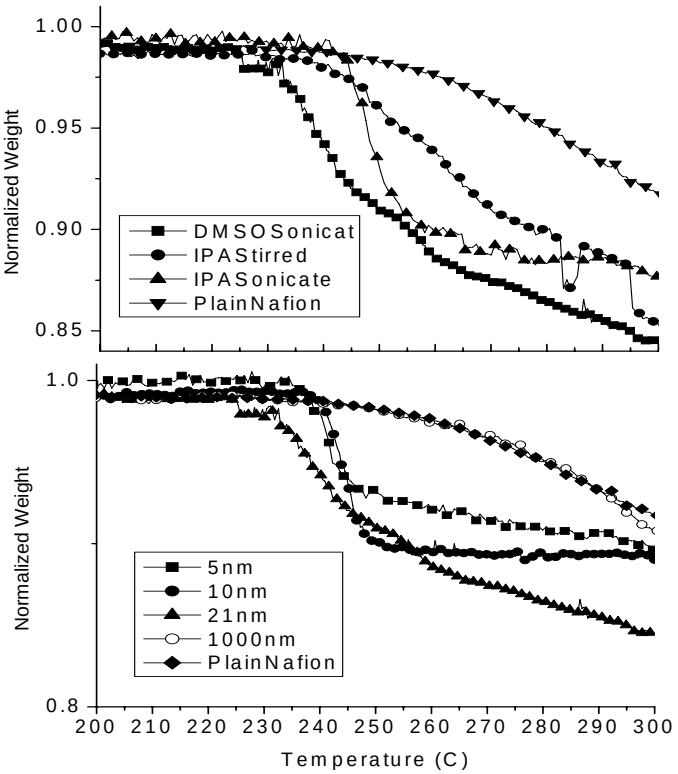

Figure 3. TGA scans (top) comparing Degussa-Hüls composite membranes prepared using different methods and (bottom) composite membranes prepared with different TiO_2 particles.

Perhaps the most interesting result shown here is the comparison of the thermal decomposition of plain Nafion to the Alfa Aesar TiO_2 composite. It was previously reported that membranes prepared with Alfa Aesar TiO_2 filler showed no improvement over plain Nafion when tested at elevated temperature[4]. The TGA curves for plain Nafion and the Alfa Aesar composite are identical (up to 300 °C), indicating that no chemical interaction is occurring between the particles and Nafion. This strongly suggests that it is the chemical interaction between metal oxide particles and Nafion which improves the performance of Nafion.

A comparison was also made between different membrane preparation techniques, namely sonication versus stirring to suspend particles and the use of isopropanol versus DMSO as the recasting solvent. TGA scans indicate that sonication results in better dispersion of particles (loss of sulfonate groups over a narrower temperature range) and that using isopropanol in place of DMSO produces membranes with less interaction between particles and polymer (shift to lower temperature of the sulfonate loss is greater in the case of membranes recast with DMSO).

Acknowledgements

The authors gratefully acknowledge Mitsubishi Chemical Group Science and Technology Research Center, Inc. for the use of instruments to obtain the TG-MS data and Tao Zang for the preparation of the IPA membranes.

References

1. K. T Adjemian, S. Srinivasan, J. Benziger, A. B. Bocarsly, *J. Power Sources*, 109 (2002) 356-364.
2. A.S Arico, V. Baglio, A. Di Blasi, E. Modica, P. L. Antonucci, V. Antonucci, *J. Power Sources*, 128 (2004) 113-118.
3. M. Watanabe, H. Uchida, M Emori, *J. Phys. Chem. B*, 102 (1998) 3129-3137.
4. K. Adjemian, Ph.D. Thesis, Princeton University (2002).

NANO-SCALE MODIFIED INORGANIC/ORGANIC HYBRID MATERIALS AS PROTON CONDUCTORS

Berryinne Chou, Hossein Ghassemi, and Tomas A. Zawodzinski

Chemical Engineering Department
Case Western Reserve University
10900 Euclid Avenue
Cleveland, OH, 44106

Introduction

Proton exchange membrane fuel cells (PEMFC) are considered to be the next generation energy source for transportation and many other applications. Proton exchange membranes are a key component in the fuel cell system. Various perflurosulfonic acid polymers have been used to achieve high proton conductivity, such as Nafion® and Dow membranes. For automotive industrial applications, high operation temperature can help fuel cell release the heat and reduce the size of the cooling system. High temperature also improves the catalytic activity on the electrodes and increases anode CO tolerance. Nafion, however, only gives good proton conductivity when it is fully hydrated and limits the operating temperature to no higher than 80°C. Therefore, developing new materials for high temperature fuel cells (exceeding 100°C) is challenging and very essential. In this work, the surface modified silica particles are bound with polymers to form proton-exchange membranes. Surface modification of silica particles was achieved by sultonation process[1] leading to the production of organic-inorganic hybrid particles with a high IEC value as 2.3 mmol/g. Modified silica particles were blended sulfonated polyether sulfone copolymers (BPSH)[2] with various degree of sulfonation. Membranes with different amounts of silica particles have been prepared by solution casting or melt press technique. These membranes were tested for their proton conductivity and other related properties, such as water up-take. The effect of membrane fabrication condition on their morphology and overall performance has been investigated. Proton conductivity of membranes was measured at different temperatures and humidity and the data was used to understand the proton transfer phenomena.

Experimental

Sultone treated silica particles. The solution which contained 1, 3 propane sultone and dry toluene (molar 1:10) was prepared and mixed with dry aerosil silica, 7 nm, (Degussa). The mixing procedure was performed in a dry box to avoid water absorption before sultone attaches to the silica surface. The chemical reaction was shown in the following scheme. The reaction was heated up at 80°C and stirred for 7 days.

Silica/Polymer composite membrane synthesis. Different polymers have been considered as the binders in this work. Dimethylacetamide (DMAc) was used as a solvent for all the polymers. The sultoned particles are kept in toluene solution before membrane casting. Membranes with different ratios of particles and polymers were cast on glass and dried at 50°C for 4 hours. The membranes were removed from the glass and dried to make sure all the excess sultone and solvents were removed. Before any further membrane characterization, the membranes were boiled at 0.5 M H_2SO_4 for 4 hours to remove all metallic impurities and converted to proton form.

Characterization Methods. Proton conductivity measurements were performed using a Solatron SI 1280B Impedance Analyzer. Voltage was applied with varying frequency from 0.1 to 20,000 Hz and the impedance response. The conductivity measurements were also done at different temperatures and different humidity generated by different LiCl concentration solutions. Water up-take measurements were done by suspending membranes over LiCl solution for 3 days (enough time to reach equilibrium) in a constant temperature chamber at 25°C. Samples to measure the uptake of water in liquid immersed membranes were placed at the bottom of vials filled with distilled water. The membranes were dried, weighed, replaced in vials, and weighed again. The time membranes were exposed to air was minimized to prevent water loss.

Results and Discussion

FT-IR spectra of the particles before and after sulton deposition has been tested and shown at **Fig 1**. In order to determine the surface modification, curve (a) has been subtracted from curve (b) and enlarged three times, as shown as curve (c). There are three peaks 1048, 1117, and 1170 cm^{-1} are the absorption from sulfonate groups. Titration was done to evaluate the ion exchange capacity (IEC) of these sultonated silica particles, 2.3 mmol per gram. Comparing to Nafion 1100 series membrane (0.92 mmol per gram) the sultonated silica particles have a much higher proton density.

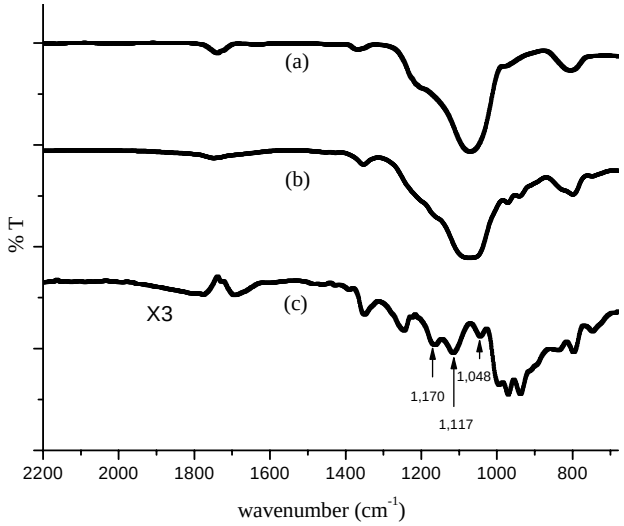

Figure 1. FT-IR of (a) Pure silica particles (b) Sultonated silica particles (c) Curve a Subtracted from curve b.

The conductivity directly tells us whether the protons can transfer through the membranes. The goal of this work is to achieve the conductivity of Nafion, 0.072 Ω^{-1} cm^{-1} in liquid water. Membranes with different BPSH copolymers and different amounts of surface modified silica particles were examined and **Figure 2** shows the conductivity. BPSH 0 is the polymer without any protons, therefore the conductivity must derive from the sulfonic groups from the modified silica surface. BPSH 0 membranes with higher ratios of particles have better conductivity, indicating the modified particles provide the proton and bring the conductivity. Membranes made with BPSH 20 containing different particle loadings also show very similar trends like BPSH 0. But the conductivities are generally higher than BPSH 0 type membranes due to the intrinsic protons from BPSH 20. Pure BPSH 35 and BPSH 60 had very good conductivity because of the high degrees of sulfonation. When the BPSH 35 and BPSH 60 are mixed with modified silica particles, the conductivity drops to a constant value.

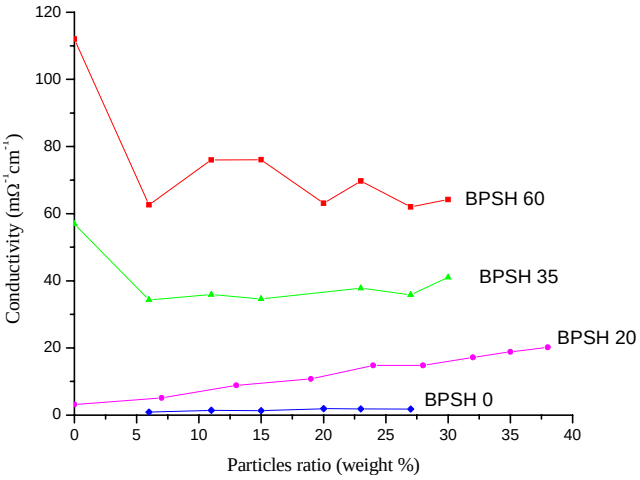

Figure 2. Conductivity with different BPSH with different amounts of surface modified particles. The measurements were done when the membranes were immersed in the liquid water at room temperature.

The water uptake (%) of the membranes were calculated by the weight gain of absorbed water with reference to the dry membrane and reported as weight percent. In order to understand the correlation between water up-take and proton density, IEC values were estimated from the IEC of BPSH with different amounts of modified silica particles. The surface modified silica particles have a very high IEC value, 2.3 mmol per gram. This is higher than BPSH 20, 35, and 60. In **Figure 3**, surface-modified particles help BPSH 20 absorb more water, agreeing the conductivity results shown in **Figure 2**. For the membranes that used BPSH 35 or BPSH 60 as binders, small amounts of surface modified particles lower the water up-take and conductivity. Silica particles prevent membrane from swelling, and the polymer matrix is not able to hold the water easily. As the particle loading increase, the water up-take increase again, possibly due to the high IEC values of the surface modified particles.

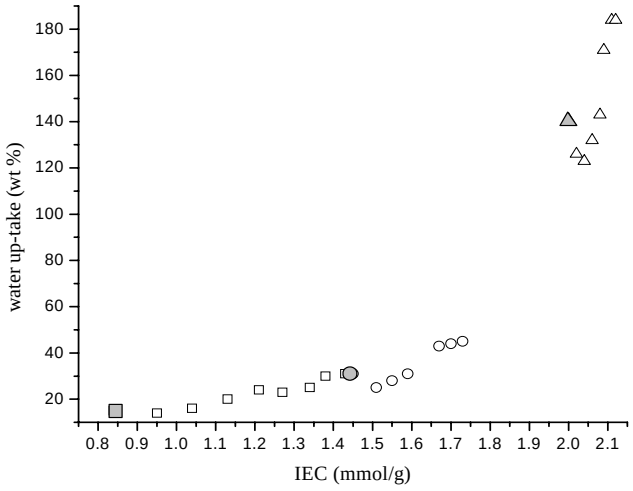

Figure 3. Water up-take of membranes with BPSH 20 (■) with different amounts of surface modified silica (□); BPSH 35 (●) with different amounts of surface modified silica (○); BPSH 60 (▲) with different amounts of surface modified silica (Δ).

Morphology is important to understand how well the particles are dispersed inside the membranes. **Figure 4** shows HRSEM pictures of the membranes with BPSH 20 and BPSH 60 mixed with particles. The original silica particles are 7 nm, and are expected to grow to 9~10 nm after sultonation. The particles' size is around 20~30 nm in **Figure 4** (a); 50~60 nm in **Figure 4** (b). Particle aggregation occurs during the membrane casting, especially in the BPSH 60 type of membranes. The ideal structure of the composite membrane has silica particles well separated and dispersed inside the polymer matrix, but close enough to form the network structure needed in order to provide a proton transfer path. Figure 4 indicates the membrane using BPSH 20 as a binder has better particle dispersion and less particle aggregation comparing to the membranes using BPSH 60 as a binder. The main factor which controls the compatibility between polymers and particles is still not well known in the work.

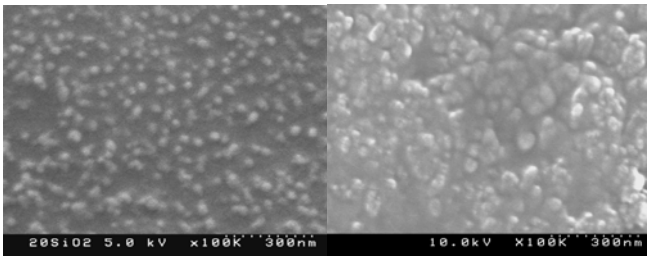

(a) (b)

Figure 4. High resolution scanning electron microscope pictures of (a) BPSH 20 with 38% surface modified silica. (b) BPSH 60 with 30% surface modified silica.

Acknowledgment

This work was supported by U.S. Department of Energy.

References

1. Alvaro, M.; Corma, A.; Das, D.; Fornes, V.; Garcia, H., *Chem. Commum* **2004,** *204*, (8), 956.
2. Wang, F.; Hickner, M.; Kim, Y. S.; Zawondzinski, T. A.; McGrath, J. E., *Journal of Membrance Science* **2002,** *197*, 231.

PARTIALLY FLUORINATED POLY(ARYLENE ETHER SULFONE) COPOLYMERS MODIFIED WITH ZIRCONIUM HYDROGEN PHOSPHATE FOR PROTON EXCHANGE MEMBRANES

Melinda L. Hill, Brian R. Einsla, and James E. McGrath

Macromolecules and Interfaces Institute
Virginia Polytechnic Institute and State University
Blacksburg, VA 24061
Email: jmcgrath@vt.edu

Introduction

Directly copolymerized disulfonated poly(arylene ether sulfone) copolymers have been shown to be advantageous for proton exchange membrane applications due to their excellent thermal and oxidative stability, high proton conductivity, and low methanol permeability.[1,2,3] However, these membranes can be further improved by the addition of an inorganic component. The addition of certain inorganic materials to proton exchange membranes may decrease the water uptake and methanol permeability, while increasing the mechanical strength of the membrane. The permeability to gases, especially oxygen, is an important property in hydrogen/air fuel cell systems, and it has been suggested that this is lowered by the addition of inorganic materials as well. Metal oxides, phosphates, and phosphonates are among the materials that have been investigated for proton exchange membrane additives.[4] The precipitation of zirconium hydrogen phosphate (ZrP) into Nafion membranes through an *in-situ* method has been shown to result in very small particles of ZrP dispersed within the pores of the membrane.[5-7] Nafion/ZrP hybrid membranes prepared by this technique can be used at higher temperatures than pure Nafion membranes.[6] The inorganic component may also prevent dehydration of the membranes at elevated temperatures.[7] The water uptake of the membranes may also be reduced upon addition of ZrP, and this has been shown to be an important factor in PEMFC performance.[8] Herein, we report the fabrication and initial characterization of organic/inorganic composite proton exchange membranes combining disulfonated partially fluorinated poly(arylene ether sulfone) copolymers and ZrP.

Experimental

Materials. 4,4'-Dichlorodiphenylsulfone (DCDPS) was obtained from Solvay Advanced Polymers and was dried at 60 ºC under vacuum for 24 hours before use. Hexafluoroisopropylidene biphenol was provided by DuPont and was dried at 60 ºC under vacuum for 24 hours prior to use. N,N-dimethylacetamide (DMAc, Aldrich) was distilled under reduced pressure over calcium hydride. Potassium carbonate (Aldrich) was dried at 120 ºC under vacuum for 24 hours prior to use. Toluene (Fisher Scientific) was dried over molecular sieves (5 Å, Aldrich). Fuming sulfuric acid (30% free SO_3), zirconyl chloride ($ZrOCl_2$, 30% in hydrochloric acid) and phosphoric acid (H_3PO_4) were purchased from Aldrich and used as received.

Synthesis and acidification of Partially Fluorinated Disulfonated Poly(arylene ether sulfone) Copolymers. Disulfonated poly(arylene ether sulfone) copolymers were synthesized according to a previously reported procedure.[2,9,10] A sample copolymerization reaction for a copolymer in which 35% of the repeat units were disulfonated proceeded as follows: Hexafluoroisopropylidene biphenol (3.3623 g, 10 mmol), DCDPS (1.8666 g, 6.5 mmol), S-DCDPS (1.7194 g, 3.5 mmol), and potassium carbonate (1.5894 g, 11.5 mmol) were charged to a three-neck round-bottom flask equipped with a nitrogen inlet, mechanical stirrer, Dean-Stark trap, and reflux condenser. DMAc (28 mL) and toluene (14 mL) were added, and the reaction mixture was heated in an oil bath at 155 ºC for four hours to reflux the toluene, thereby dehydrating the system. The oil temperature was then increased to 175 ºC for 24-48 h until an increase in viscosity was observed. The viscous solution was precipitated into an excess of deionized water. The resulting copolymer will be referred to as 6FS-XX, where XX represents the mole % of disulfonated repeat units, or the degree of disulfonation. The degree of disulfonation of the copolymers may be varied by changing the ratio of DCDPS to S-DCDPS.

The polymer fibers were dried in a vacuum oven at 100 °C for 24 hours, then dissolved in DMAc (10 wt%). The solutions were filtered through 0.45μm syringe filters and cast onto clean glass plates. The solvent was evaporated under an infrared lamp, and tough, ductile, transparent films were obtained. The films were acidified by boiling in 0.5M sulfuric acid for two hours, then washed in boiling water for two hours. They were dried in a vacuum oven at 100 °C for 48 h before further use. The acidified films are referred to as 6FSH-XX.

Formation of 6FSH-XX/Zirconium Hydrogen Phosphate Composite Membranes. After the dry, acidified films were weighed, they were hydrated in boiling deionized water for one hour. The films were then immersed in various concentrations of $ZrOCl_2$ for eight hours at 80 °C. After a brief rinse with deionized water, the films were then soaked in 0.5M H_3PO_4, resulting in the precipitation of ZrP in the hydrophilic domains of the membrane. The nanocomposite membranes were boiled in deionized water to remove any water-soluble $ZrOCl_2$ or H_3PO_4, and then dried in a vacuum oven at 100 °C for 48 h. After drying, the wt% of ZrP in the membranes was determined from the difference in dry weight before and after the addition of ZrP.

Results and Discussion

The copolymers were successfully synthesized and the structure was confirmed by ^{1}H NMR, and the intrinsic viscosity was measured at 30 °C in NMP with 0.05M LiBr to correct for the ionomer effect (0.6 dL/g). The amount of ZrP that could be incorporated into the membranes increased as the concentration of $ZrOCl_2$ was increased. The amount of ZrP incorporated into the 6FSH-35 membranes increased rapidly with concentration of $ZrOCl_2$ at concentrations below 10%, but subsequently leveled off at 25 wt% when the concentration was further increased, and no additional ZrP was incorporated for $ZrOCl_2$ concentrations as high as 30%.

As expected, the incorporation of ZrP into the disulfonated copolymer membranes resulted in a decrease in the water uptake (Table 1). A significant decrease in the water uptake of 6FSH-35 was observed, lowering it from 38% (with no ZrP) to 30% (for a sample with 25 wt% ZrP).

Table 1. Water Uptake and Thermogravimetric Analysis Data for 6FSH-35/ZrP Composite Membranes

Wt. % ZrP	Water Uptake, %	$T_{5\%}$, °C	Char Yield, %
0	38	385	2.4
15	34	384	8.7
25	30	385	21

The protonic conductivity of the composite membranes was measured as a function of temperature at 100% relative humidity (Table 2). The conductivity increased with temperature, reaching a value of 0.079 S/cm at 80 °C.

Table 2. Protonic Conductivity of 6FSH-35/ZrP Composite Membrane (25 wt% ZrP)

Temperature	Conductivity, S/cm
30 °C	0.019
50 °C	0.025
80 °C	0.079

Conclusions

Different amounts of ZrP were incorporated into partially fluorinated disulfonated poly(arylene ether sulfone) membranes. The amount of ZrP in each composite membrane was dependent on the concentration of the precursor solution, $ZrOCl_2$. An increase in the final amount of ZrP in the membrane was observed up to 10% $ZrOCl_2$, after which point the amount leveled off.

Thermogravimetric analysis showed that the char yield of the composite membranes increased as the amount of ZrP was increased. The proton conductivity of the composite membranes increased as a function of temperature, reaching a high value of 0.079 S/cm at 80 °C under 100% relative humidity.

Acknowledgement. The authors would like to thank the NSF Partnership for Innovation Program (EEC-0332648) and ARO/DARPA (Grant# DAAD19-02-1-0278) for their support of this research.

References

(1) Hickner, M.A.; Ghassemi, H.; Kim, Y.S.; |Einsla, B.; McGrath, J.E. *Chem. Rev.* **2004**, *104*, 4587-4611.
(2) Wang, F.; Hickner, M.; Kim, Y.S.; Zawodzinski, T.A.; McGrath, J.E. *J. Mem. Sci.* **2002**, *197*, 231-242.
(3) Kim, Y.S.; Dong, L.; Hickner, M.A.; Pivovar, B.S.; and McGrath, J.E. *Polymer* **2003**, *44*, 5729-5736.
(4) Alberti, G.; Casciola, M. *Annu. Rev. Mater. Res.* **2003**, *33*, 129.
(5) Grot, W.G.; Rajendran, G. *U.S. Patent 5,919,583*, **1999**.
(6) Costamagna, P.; Yang, C.; Bocarsly, A.B.; Srinivasan, S. *Electrochimica Acta* **2002**, *47*, 1023.
(7) Yang, C.; Srinivasan, S.; Arico, A.S.; Creti, P.; Baglio, V.; Antonucci, V. Electrochemical and Solid State Letters **2001**, *4*, A31.
(8) Pivovar, B.S.; Kim, Y.S. *Proceedings of the 206th Joint International Meeting of the Electrochemical Society*, October **2004**.
(9) Wang, F.; Hickner, M.; Ji, Q.; Harrison, W.; Mecham, J.; Zawodzinski, T.A.; McGrath, J.E. *Macromol. Symp.* **2001**, *175*, 387-395.
(10) Harrison, W.L.; Wang, F.; Mecham, J.B.; Bhanu, V.A.; Hill, M.; Kim, Y.S.; McGrath, J.E. *J. Polym. Sci.: Part A: Polym. Chem.* **2003**, *41*, 2264-2276.

IMPROVEMENT OF DMFC PERFORMANCE AND STABILITY USING MULTI-LAYER STRUCTURE MEMBRANES

Ruichun Jiang,[1] H. Russell Kunz,[1] James M. Fenton[1,2]

[1.] Department of Chemical Engineering,
University of Connecticut, Storrs, CT 06269
[2]. Florida Solar Energy Center,
University of Central Florida, Cocoa, FL 32922

Introduction

Direct methanol fuel cells (DMFCs) are desirable for transportation as well as portable applications such as cell phones, laptops since they use liquid fuel and are simple in system design. However, two major obstacles that currently prevent the widespread commercial applications of DMFCs are low activity of methanol electro-oxidation anode catalysts and crossover of methanol through the polymer electrolyte membrane.[1] Methanol crossover to the cathode not only lowers fuel utilization efficiency but also adversely affects the oxygen cathode, resulting in poorer cell performance.[2] Presently Nafion® is widely used as proton exchange membrane both in hydrogen PEM fuel cell and direct methanol fuel cells. Nafion® membranes have excellent proton conductivity under fully humidified conditions, good mechanical and chemical properties as well as long term stability. However, Nafion® has very high methanol crossover in direct methanol fuel cells. To reduce methanol crossover, thick Nafion® membranes, such as Nafion®117 (175 μm thickness), with higher cell resistance are often used in DMFCs, which also leads to higher cost since Nafion® is an expensive material.

A cheap material, sulfonated poly(ether ether ketone) (SPEEK), was synthesized via the sulfonation reaction of poly(ether ether ketone) (PEEK), and evaluated in DMFCs.[3] Membranes based on SPEEK with different degree of sulfonation (SD) were characterized and tested in DMFCs. SPEEK membranes showed good thermal stability, appropriate mechanical properties, reasonable conductivity, and low methanol permeability.

In this work, we innovated multi-layer structure DMFC membranes with methanol barrier layers based on low SD SPEEK. The thin barrier layer effectively reduced methanol crossover without much IR loss. The conductive layers provided proton-rich membrane/electrode interfaces that ensured less contact resistance with the electrode. DMFC performance and stability were greatly improved by applying this multi-layer structure membrane.

Experimental

SPEEK was obtained through a sulfonation reaction of PEEK (450PF, Victrex US Inc, Greenville, SC). The sulfonation of PEEK was performed by dissolving and modifying the polymer using concentrated sulfuric acid with the degree of sulfonation controlled by reaction time. The sulfonation degree was determined by elemental analysis measurements. SPEEK membranes with different sulfonation degrees were cast by heating and evaporating the solvent from the SPEEK/N-Dimethylacetamide (DMAC) solution in a flat glass dish. Membrane thickness was controlled by varying the solution amount in the casting step.

Two types of multi-layer membranes were prepared. The first type of membranes, with a Nafion®/SPEEK/Nafion® structure were fabricated by sandwiching a thin SPEEK membrane with SD=41% between two Nafion® membranes; while the second type of membranes were prepared by sandwiching a thin SPEEK membrane with SD=41% between two higher SD SPEEK membranes. Multi-layer membranes with the same total thickness (50 μm), but various middle layer thicknesses (5-15μm) were prepared and studied.

The electrodes were prepared by screen-printing the ink containing liquid Nafion® and catalyst onto single-sided ELAT diffusion substrates from E-TEK with an area of 5 cm^2. The MEA was prepared by sandwiching one piece of the membrane between two pieces of gas diffusion electrodes and then hot-pressing at 120°C for 10 minutes at a pressure of 3000 psi. MEAs were tested in a single cell with 5 cm^2 flow channel area (FC05-01SP, Electrochem. Inc., Woburn, MA).

Methanol crossover was determined by the limiting current method using linear sweep voltammetry, with a Solartron SI 1287 electrochemical interface (Solartron Instrument, Houston, TX). The measured limiting current provided the methanol crossover flux of the membrane studied.

Proton conductivity of membranes was calculated from the membrane resistance measured by electrochemical impedance spectroscopy (EIS). The EIS measurements were carried out using a Solartron (Houston, TX) 1250 frequency response analyzer together with the Solartron 1287 electrochemical interface.

MEA fuel cell performance was determined at 60°C and 80°C under ambient pressure with an in-house electrochemical test station that was equipped with a computer controlled Scribner 890B load box. Mean while, the membrane resistance was also measured by current interrupt in the MEA performance test and compared with the results of EIS measurement. DMFC performance with both single layer SPEEK membranes and multi-layer structure SPEEK membranes was investigated.

Results and Discussion

Proton conductivity of SPEEK membranes as a function of temperature with 100% relative humidity was evaluated. The data indicates that the proton conductivities of SPEEK membranes are improved by increasing the sulfonation degree. The SPEEK membrane with a 60% sulfonation degree has proton conductivity slightly lower than Nafion® at temperatures higher than 60°C.

DMFC performance and methanol crossover of single-layer SPEEK membranes were tested. Figure 1 shows the DMFC performance at 60°C and 80°C with 1 M methanol/air, under ambient pressure. Here SPEEK-41 represents SPEEK membranes with 41% sulfonation degree, similar for SPEEK-51 and SPEEK-60. The 41% sulfonation degree SPEEK MEA shows relatively poorer performance due to large IR losses. At 60°C, DMFC performance was improved with increasing sulfonation degree. The cell performance with 60% sulfonation degree SPEEK is much higher than the MEA with the same thickness Nafion® 112 membrane. DMFC performance was improved at 80°C for SPEEK-41, SPEEK-51 and Nafion® 112 due to better reaction kinetics and membrane conductivity. However, cell performance with the SPEEK-60 membrane decreased at 80°C than that at 60°C and showed much lower cell voltage at each current density than that with Nafion® 112 and SPEEK-51 membranes.

Figure 2 shows methanol crossover limiting current results at 60°C and 80°C for the membranes described above. The value of methanol crossover increases slightly at 80°C than 60°C for SPEEK-41. However, a very large increasing of methanol crossover was observed at 80°C for SPEEK-60. The large methanol crossover of SPEEK-60 at 80°C results in a significant cell performance decrease. The large increasing methanol crossover for the SPEEK-60 is due to severe membrane swelling in the methanol solution. Yang et al. measured liquid uptake of Nafion® 115 and SPEEK membranes in 1 M methanol at different temperatures.[4] According to their result, liquid uptake increased slightly for their SPEEK-44 membranes and Nafion® 115 when the temperature was increased from 65°C to 80°C.

However, a large increase was observed for their SPEEK-58 indicating serious membrane swelling at 80°C.

MEAs based on multi-layer membranes were also tested in DMFCs. Figure 3 shows a DMFC cell performance using a multi-layer SPEEK membrane at 60°C and 80°C. Compared with SPEEK-60 membrane alone, improvement of performance can be observed by applying this multi-layer SPEEK membrane. Especially at 80°C, much higher values of cell voltage and power density at each current density were obtained with this sandwiched membrane. The SPEEK-41 barrier layer in the middle swells less in the higher temperature methanol solution and effectively slows down methanol crossover. The outer layers provided proton rich electrode-membrane interfaces, thus reduced contact resistance and improved catalyst utilization as well.

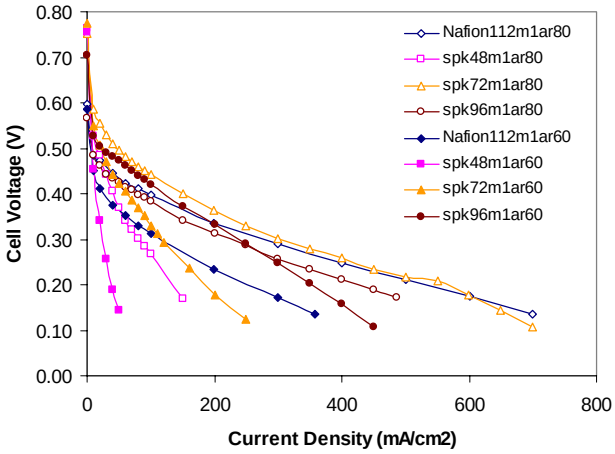

Figure 1. DMFC performance with Nafion® and SPEEK membranes at 60°C and 80°C in 1 M methanol/air at ambient pressure.

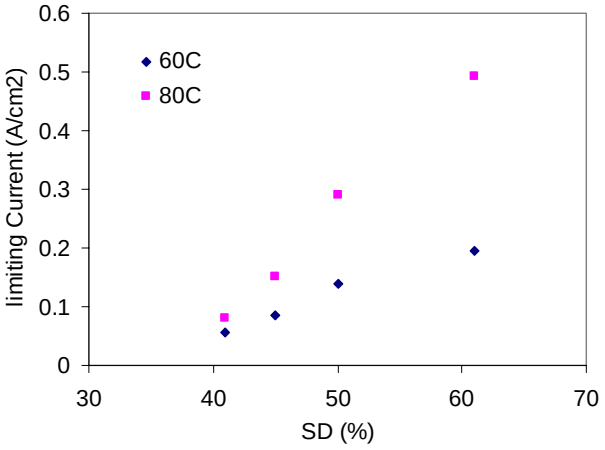

Figure 2. Methanol crossover of SPEEK membranes at 60°C and 80°C with 1 M methanol solution.

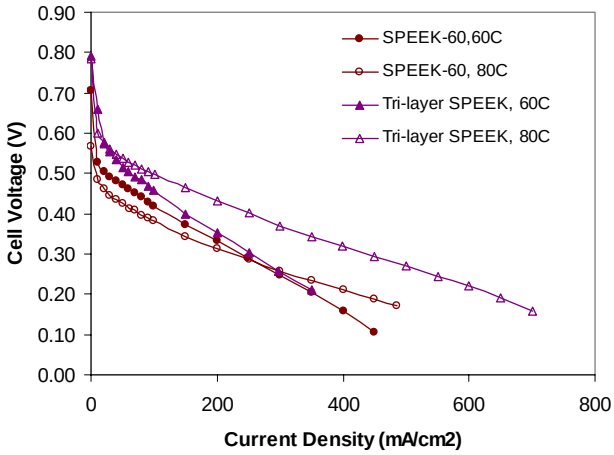

Figure 3. MEA performance with SPEEK multi-layer membrane [SPEEK-60(20μm)/SPEEK-41(10μm)/SPEEK-60(20μm)] with 1 M methanol/Air under ambient pressure.

Conclusions

SPEEK membranes with sulfonation degrees ranging from 40% to 60% show good potential for DMFCs applications. However, the DMFC performance with higher SD showed decreased performance at higher temperature (80°C) due to high methanol crossover. This largely increased methanol crossover was induced by severe membrane swelling of the higher SD SPEEK membrane in the higher temperature methanol solution. With the lower SD SPEEK membrane, DMFC performance becomes better at higher temperature (80°C) than that at 60°C. Due to the effect of less membrane swelling for the lower SD SPEEK membranes, their methanol crossover values increased in a much smaller scale with the increasing temperature than that with higher SD.

A series of multi-layer structure membranes with a thin and lower sulfonation degree (SD=41%) SPEEK barrier layer showed suppressed methanol crossover and acceptable cell resistance. The MEA with a 10 μm thickness SPEEK-41 middle layer showed much better performance than that with a same thickness single SPEEK-60 membrane. The SPEEK-41 barrier layer effectively blocked methanol crossover, especially at 80°C, less swelling of the barrier layer helped to significantly slow down methanol crossover. The MEA with the multi-layer membrane achieved improved methanol utilization and enhanced DMFC performance, and used less costly materials as the proton exchange electrolyte compared to Nafion®. Multi-layer structure membranes also show a promising strategy for DMFC improvement with other hydrocarbon based membrane materials.

References

(1) X. Ren, M. S. Wilson, S. Gottesfeld, J. Electrochem. Soc., **1996**, 143, L12.
(2) D. Chu and S. Gilman, *J. Elelctrochem. Soc*., **1994**, 141, 1770.
(3) R. Jiang, H. R. Kunz and J. M. Fenton, The 204th Meeting of Electrochemical Society, Orlando, Oct. **2003**, (Abstract No. 1024).
(4) B. Yang and A. Manthiram, *Electrochem. Solid-State Lett*., **2003**, 6 (11), A229.

MOLECULAR ARCHITECTURE FOR POLYPHOSPHAZENE ELECTROLYTES FOR SEAWATER BATTERIES

Mason K. Harrup, Frederick F. Stewart, Thomas A. Luther, Christopher J. Orme, and Eric S. Peterson*

Department of Chemical Sciences, Idaho National Laboratory, P. O. Box 1625, Idaho Falls, ID 83415-2208

Introduction

Batteries which use seawater not only as the electrolyte but also as the oxidant with inert cathodes have existed for a long time. Among the better examples of these cells are C. L. Optiz's magnesium/steel wool batteries from the late 1960's and M. A. Walsh's Rope Battery. These cells are attractive power sources for a variety of underwater applications as they have a potential for high energy density, moderate cost, and infinite storage properties when kept dry. The difficulty for these systems in seawater is that an adherent calcareous film forms upon them which reduce the current necessary to protect the structure, resulting in cathode performance deterioration. Lithium is particularly attractive as a battery anode material because of its light weight, high voltage, high electrochemical equivalence, and good conductivity. In such a lithium/seawater batteries, lithium serves as the anode and the cathode is the seawater. For lithium, the principal reactions are:

Anode	Li	-	e^-	$\rightarrow$	Li^+		
Cathode	H_2O	+	e^-	$\rightarrow$	OH^-	+	$\frac{1}{2}H_2$
Overall	Li	+	H_2O	$\rightarrow$	LiOH	+	$\frac{1}{2}H_2$

However, as apparent from the overall electrochemical reaction, lithium and water will also react directly with one another, essentially resulting in parasitic corrosion of the anode when exposed to water. The corrosion reaction is highly undesirable because it produces no useful electrical energy and consumes active lithium. Further, the reaction is highly exothermic and can have detrimental effects on the battery. Accordingly, the principal challenge with respect to reactive metal-water batteries is development of techniques that minimize this direct lithium-water reaction. Research in liquid electrolytes has typically focused on non-aqueous additives that enhance or result in formation of a calcareous film upon the outer surface of the lithium metal as a means of protecting the metal from direct contact with water. Unfortunately, the use of such non-aqueous liquid electrolytes results in the need for complex battery designs to retain the additives employed within the battery while still affording access to the water to allow the battery to function.

Given this, development of practical lithium/seawater batteries hinges upon developing novel solid polymer electrolytes with the appropriate physical and chemical properties. The membranes paradoxically must allow lithium atoms to pass from the metallic surface, oxidize to the ionic form, and then pass through the membrane to the water outside. At the same time, the membrane must exclude water, tramp ions, and gases such as oxygen and carbon dioxide. Also, the calcareous deposits noted above are avoided due to the presence of the membrane. Recent research at the INL has developed deliberately modified polymer electrolytes based upon the phosphazene family of polymers which have a high probability of addressing the above paradox. Initial studies were performed to determine the impact of molecular architecture within the polyphosphazene structure. The startling magnitude of the differences in electrolyte performance due to molecular architecture is discussed in this paper.

Experimental

Polymer Synthesis. The dichlorophosphazene polymer was made by ring-opening polymerization of phosphonitrilic chloride trimer (Strem) using previously described methods.[1-2] An average of 40-45% conversion to the linear polymer, $(PNCl_2)_n$ was achieved. The organophosphazenes (**1**-**4**) were made using standard literature procedures. A typical synthetic scheme is given here. A solution of was made with toluene. To this was added to a solution of *p*-methoxyphenoxide formed from the reaction of *p*-methoxyphenol and sodium hydride in dry THF. Once added the mixture was stirred for 3 hours. A solution of sodium 2-(2-methoxyethoxy)ethoxide was then prepared via reaction with sodium hydride in dry THF. This solution was then added to the polymer solution followed by heating at 108 °C for 18 hours. Once substitution was complete, the polymer was precipitated into water twice and hexane twice sequentially from THF to obtain a tan colored gum. The MEEP polymer (**1**) was synthesized according to the general procedure above but was isolated and purified in 66% yield via a novel route exploiting the lower critical solubility temperature (LCST) behavior of this material in aqueous solution.[3]

Water Permeation Measurements. The polymer membranes were cast directly on porous supports with an average thickness of 50 μm. These supported membranes were loaded into cells obtained from Millipore and modified for pervaporation experiments. Modification to the Millipore cells consisted of a pumping system to flow feed solution over the membrane at approximately 50 mL/min. A diaphragm vacuum pump capable of providing a transmembrane pressure differential of 550 mmHg was installed on the system with a cryo-trap between the pump and the cell. Permeates were collected for six to eight hours and quantified gravimetrically. Transmembrane fluxes are reported in terms of L/m^2h, where L = volume of permeate, m^2 = membrane area (0.0017 m^2), and h = experimental time.

Electrochemical Measurements. Each polymer was dissolved in dry THF and anhydrous $LiBF_4$ was added to the solution. A range of concentrations was employed, typically from 4 to 10 wt% salt vs polymer weight. Films of the salted polymers were cast directly on SS316 steel electrodes measuring 1.00 cm^2 and dried in a vacuum/Argon oven for several hours. A second steel electrode was placed on top of the films and impedance measurements were taken with a PARC model 273A potentiostat coupled to a Solartron SI 1260 impedance/gain-phase analyzer, with computer control provided by Z-plot for Windows (Scribner Assoc.). A frequency sweep technique was employed with a range of 10kHz to 1Hz. Conductivity reported is for the salt loading level that exhibited maximum conductivity for each individual polymer.

Results and Discussion

In formulating polymer electrolytes for seawater battery applications, the material must both conduct lithium ions as well as minimize water permeation. For polyphosphazenes, this requirement is met by incorporating some pendant groups that impart a hydrophobic nature along with some pendant groups that are highly polar to afford lithium ion conduction. How to best incorporate both of these opposing groups into one polymer was a question of molecular architecture that was the subject of our investigations. Since organophosphazenes can be considered to have three principal components – the backbone, the hydrophobic region and the conductive region. Three alternate molecular architectures result from this situation. The first of these architectures is to form a homopolymer from a single pendant group that incorporates both components. Groups of this type are readily commercially available as non-ionic surfactants. However, with this design, one has the

choice of connecting the surfactant moiety to the phosphazene backbone either through the hydrophobic portion, resulting in a core of hydrophobicity and a conductive region that is shifted away from the backbone; or through the conductive portion, resulting in a backbone centered ion channel surrounded by a hydrophobic sheath. Representatives of both molecular architectures were synthesized and are shown in Figures 1 and 2.

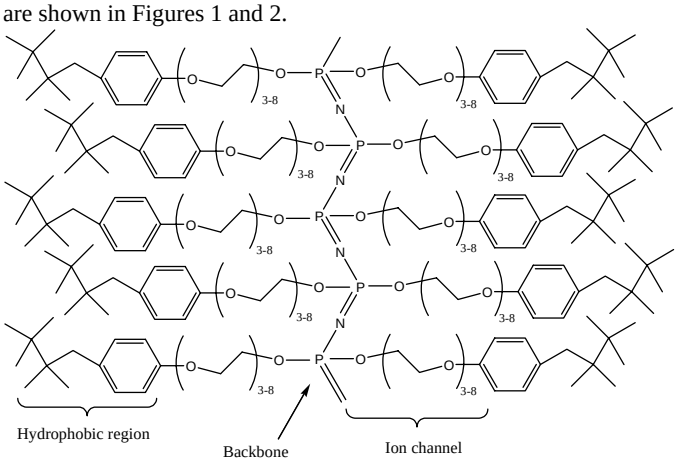

Figure 1. Structure of the triton polymer. This electrolyte possesses the correct molecular architecture to maximize ion conduction.

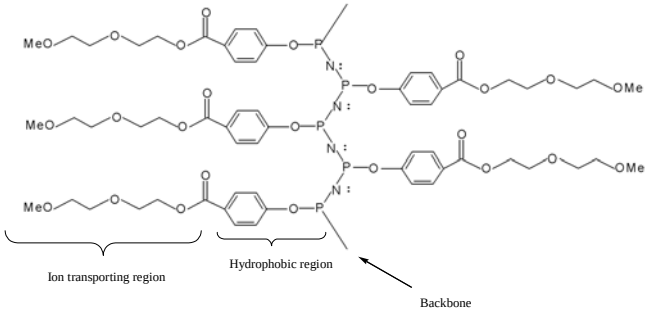

Figure 2. Structure of the DEG ester polymer. In this molecular architecture, the ion channel is "shifted" away from the backbone, resulting in the poorest conductivity.

The third choice for molecular architecture is to form a simple heteropolymer by mixing to different pendant groups – one polar and one hydrophobic. To complete our series for evaluation, a representative of this molecular architecture was prepared as well as shown in Figure 3.

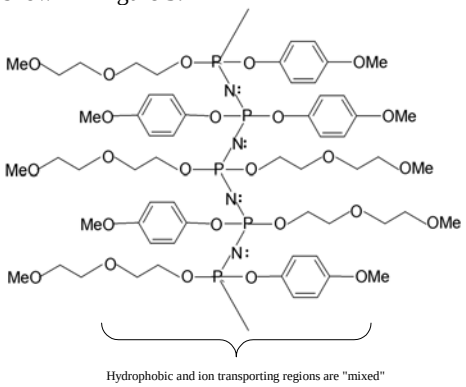

Figure 3. Structure of the 50/50 polymer. In this molecular architecture, the ion channel is "clogged" leading to reduced conductivity.

The water permeability and lithium ion conductivity were measured for these three representative polymers and the results are given in Tables 1 and 2. The well-studied MEEP polymer was also evaluated as a benchmark. As shown in Table 1, the water permeabilities for the three molecular architectures were very similar. This is attributed to the fact the ratio of hydrophobic portion to the conductive portion was very similar for all three polymers, and water transport can be understood to be reflective of this ratio. However, the ionic conductivity of the three polymers was very different – different by a factor of over 15,000. This is explained through the impact of molecular architecture. The mechanism of lithium ion conduction is dependant on a key role played by the nitrogen atoms in phosphazene backbone. This backbone assisted transport mechanism (BIM) affords much more facile ion transport than that via other possible transport mechanisms, such as a hand-to-hand mechanism. As a consequence, when the conductive region is centered on the backbone, the BIM becomes dominant and conductivity is markedly increased. When the conductive region is remote from the backbone, other transport mechanisms dominate and conductivity is lower. In the intermediate architecture, some of the conductive region is near the backbone, but there is no clear all-conductive region – resulting in an ion channel that is "clogged" by hydrophobic moieties. In this instance some BIM transport is possible, but other mechanisms must be responsible for moving through/around the hydrophobic portions. This mixed transport situation leads, logically, to an intermediate conductivity.

Table 1. Water Permeability of Polymer Electrolytes

Polymer Tested	Water Flux (L/M^2*h)
MEEP (**1**)	Dissolves readily
Triton (**2**)	0.013
50/50 DEG/MeOP (**3**)	0.011
DEG Ester (**4**)	0.040

Table 2. Conductivity of Polymer Electrolytes

Polymer Tested	Conductivity (nS/cm)
MEEP (**1**)	43,000
Triton (**2**)	850
50/50 DEG/MeOP (**3**)	41
DEG Ester (**4**)	0.054

Conclusions

Through this work, we have demonstrated that the molecular architecture within the polyphosphazene is critical to performance as an electrolyte membrane suitable for lithium seawater batteries.[4] From these studies, the backbone centered ion channel (BIM) mechanism of lithium transport was developed. Further studies have since confirmed this lithium transport mechanism[5], so all future polyphosphazenes for seawater battery applications will posses this correct molecular architecture.

Acknowledgement. This work was supported by the U.S. Department of Energy, under DOE-NE Idaho Operations Office Contract DE-AC07-05ID14517.

References

(1) Allcock, H. R., *Phosphorous-Nitrogen Compounds*, Academic Press, New York, **1972**.
(2) Singler, R. E.; Schneider, N. S.; Hagnauer, G. L.; Polym. Sci. Eng.**1975**, *15(5)*, 321.
(3) Harrup, M. K.; Stewart, F. F.; J. Appl. Poly. Sci., **2000**, *78(5)*, 1092.
(4) Harrup, M. K.; Stewart, F. F.; Peterson, E. S. *U. S. Patent # 6,146,787*, November 14, **2000**.
(5) Luther, T. A.; Stewart, F. F.; Budzien, J. L.; LaViolette, R. A.; Bauer, W. F.; Harrup, M. K.; Allen, C. W.; Elayan, A.; *Journal of Physical Chemistry B*, **2003**, *107*, 3168-3176.

PROTON CONDUCTING BEHAVIOR OF WATER FREE PEM: POLYPHOSPHORIC ACID IMBEDDED P(VDF-co-HFP) THIN FILM

Zijie Lu[1], Han Hong[2], and Daocheng Luan[2]*

1. PennState University, University Park, PA 16802 USA
2. Xihua University, Chengdu, Sichan, 610039 P.R. China

Introduction

The fuel cell based on 85~95 vol% phosphoric acid as proton electrolyte had shown certain success in temperature region of 180~200°C.[1] Recently using H_3PO_4 to dope various polymer electrolyte membranes for proton exchange membrane (PEM) fuel cell (PEMFC) and directly methanol fuel cell (DMFC) had received much attention for preparing high temperature-tolerance PEM.[2,3] It was found that polybenizimidazol (PBI) doped with H_3PO_4 at high doping level of 5.7 (mol ratio of H_3PO_4/repeat unit) the proton conductivity could reach 7.9×10^{-2} S/cm at 200°C.[4] The problem was that those PEMs could not be entirely anhydrous, as water played as a necessary plasticizer for improving conductivity and mechanical properties. In addition, only two H_3PO_4 has chance to bond to the polymer for each unit and the remaining "free acid" can be easily washed away. Meanwhile the methanol crossover could not be avoided for DMFC. To prevent the exudation of H_3PO_4, a porous film of PBI was made and the doping level could reach 14.6.[5] Again water is needed to have proton conductivity. However H_3PO_4 could be squeezed out of the film if it was applied in fuel cell stack. In sum, although H_3PO_4 doped polymer electrolytes are promising candidates for high temperature PEMs, the water issue would bring a series problem in fuel supply and heat recovery of fuel cell as well as the exudation of H_3PO_4, and thus reduce the power efficiency. Accordingly, preparing a good PEM based on H_3PO_4 still remained a big challenge.

Here we reported a water-free PEM based on a short chain polyphosphoric acid (PPA, the structure is shown as below) that was imbedded in the polymer matrix.

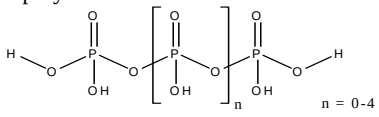

PPA was of 0%wt of free water and was highly soluble in organics. The mobility of PPA in polymer was so small that it could not move out of polymer matrix. Provided that the proton of OH groups along the backbone has certain capability to exchange, one would have chance to get the proton conductivity when the content of PPA and its distribution allow the formation of percolation.

Instead of PBI, the polymer matrix used here was poly(vinyledene difluoride-co-hexafluoropropene) [P(VDF-co-HFP)]. It is a good candidate for high temperature-tolerance PEM due to its excellent thermal stability and inertness to O_2 as well as strong acid.

Experimental

Materials. Polyphosphoric acid (115% equivalent), acetone, methyl ethyl ketone, dioxane and diethylene glycol dimethyl ether were purchased from Sigma-Aldrich company and used after being dried over 4A zeolite. P(VDF-co-HFP) was synthesized from free radical polymerization. In order to get good PPA distribution, low content –OH groups was introduced in to P(VDF-co-HFP) by coplymerization with trifluorovinyl comonomer bearing OH group.

Characterization. -OH functional structure was conformed by ^{1}H-NMR, ^{19}F-NMR in D_6-acetone (Bruker AVANE 300). Impedance of the PEM was measured with Solartron frequency response analyzer (1255B).

Preparation of PEM. According to the desired formulation, certain quantity PPA and functional P(VDF-co-HFP) were mixed in a mixture solvent (such as Acetone/MEK/dioxane/DMG). After casting on a glass substrate, a carefully drying process was carried out to prevent any bubbles. The film was easily peered off from glass surface when it was completely dried.

Results and Discussion

Film-forming behavior of P(VDF-co-HFP) with OH functional groups. It turned out to be every difficult to make a good film from normal P(VDF-co-HFP) with PPA at a content above 5%wt. But with OH functional P(VDF-co-HFP), a good film was made at PPA content 15.0%wt. as shown in figure 1. The OH functional structure was conformed by the small peak at δ = 3.84 ppm assigned to -C**H**$_2$-OH in ^{1}H-NMR as shown in figure 2.

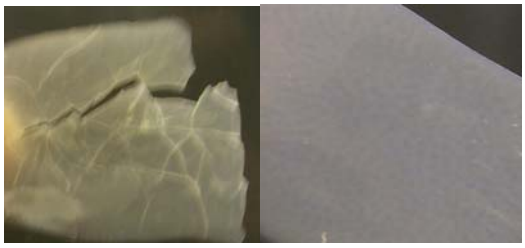

(a) **(b)**

Figure 1. The photos of the films from (a) commercial P(VDF-co-HFP) with 5.0%wt PPA and (b) OH functional P(VDF-co-HFP) with 15.0%wt PPA.

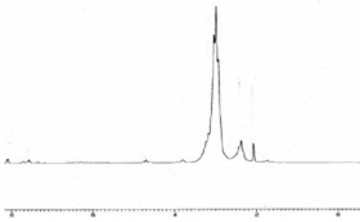

Figure 2. ^{1}H-NMR of OH functional P(VDF-co-HFP).

The SEM image showed that there was no obvious defect and no big hole in the film. This means the distribution of PPA was rather homogeneous.

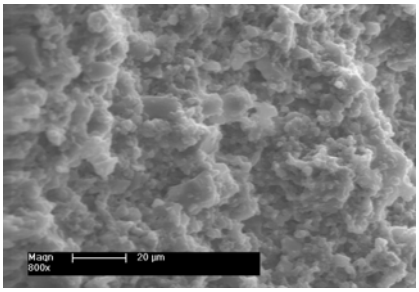

Figure 3. SEM image of the cross section of film from OH functional P(VDF-co-HFP) with 15.0%wt PPA.

Proton of OH groups in PPA. The key point of proton conductivity should lie on the exchanging ability of the proton on the PPA. Based on the studies of ATP, it was claimed that this kind proton exchanging did exist among the polyphosphoric acid segment as shown in figure 3. In this study, we also found that under completely dry conditions, the film did show charge movement within the film.

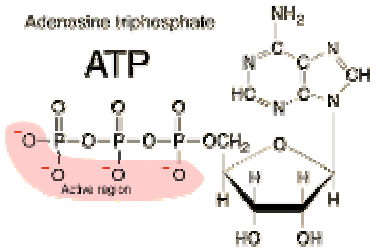

Figure 4. Proton exchanging possibility of the polyphosphoric acid segment.

Proton conducting behaviors. The proton conducting behavior of PPA/P(VDF-co-HFP) was investigated in comparison with Nafion 117 membrane at ambient temperature. In those samples, the effective dc resistance was determined by fitting the semicircular portion of the Nyquist plot (Figure 5) to an equivalent circuit model composed of a resistor, R, in parallel with a constant phase element (CPE). The data points of the low frequency region, where electrode effects are strong or dominant, were excluded from fitting. The un-imbedded P(VDF-co-HFP) polymer was an insulator, as expected. While PPA/P(VDF-co-HFP) showed certain ionic conductivity at room temperature (Table 1). Though the conductivity was two orders lower than wet Nafion, this composite polymer showed promise for further development because it was completely anhydrous. Since high temperature usually helped the increasing of mobility of protons, considering the thermal stability of both polymer matrix and PPA, it was likely for this kind of composite film to use as PEM at high temperature after optimizing the percolation issues of the PPA in polymer matrix to get high proton conductivity.

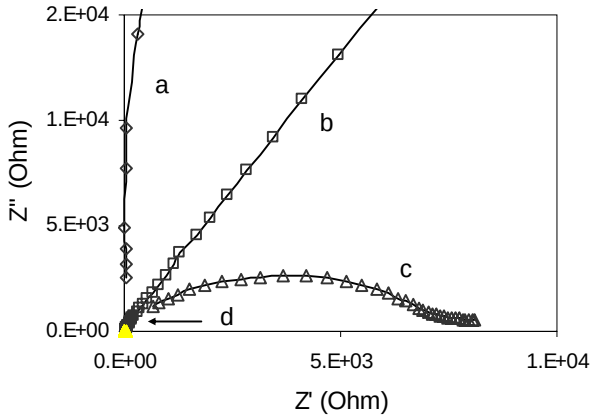

Figure 5. Nyquist plots of impedance measured using two-electrode method at room temperature. a: un-imbedded P(VDF-co-HFP) polymer; b: dry Nafion 117 with 2wt% H_2O; c: PPA/P(VDF-co-HFP); d: Nafion 117 soaked in water with 35wt% H_2O.

Table 1. The comparison of ionic conductivity of PPA imbedded P(VDF-co-HFP) with Nafion 117.

Materials	σ (S/cm) at 25°C
PPA/P(VDF-co-HFP)	1.3×10^{-4}
P(VDF-co-HFP)	2.4×10^{-8}
Wet Nafion (35wt% H_2O)	9.0×10^{-2}
Dry Nafion (2wt% H_2O)	2.3×10^{-5}

Conclusions

A composite film from P(VDF-co-HFP) imbedding inorganic oligomer polyphosphoric acid (15.0%wt) was made. The film showed very good morphology and mechanical properties. It also showed remarkable proton conductivity under completely dry conditions. Compared with the film from Nafion 117, whose proton conductivity was strongly depended on water content, the proton conductivity behavior of water-free film from PPA/P(VDF-co-HFP) was rather encouraging. Optimizing the percolation issues of the PPA in polymer matrix and investigating of temperature effect on the proton conductivity was undergoing.

References

1. Kinoshita, K. *Electrochemial Oxygen Technology*, New York: Willey, **1992**
2. Kawahara, M.; Morita, J.; Rikukawa, M.; Sanui, K.; Ogata, N. *Electrochem. Acta*n**2000,** *45*,1395
3. Tanaka, R.; Yamamoto, H.; Shono, A.; Kubo, K.; Sakurai, M. *Electrochem. Acta*n**2000,** *45*,1385
4. He, R.; Li, Q.; Xiao, G.; Bjerrum, N. J. *J. Membr. Sci.* **2003**, *226*, 169
5. Mecerreyes, D.; Grande, H.; Mihuel, O.; Ochoteco, E.; Marcilla, R.; Cantereo, I. *Chem. Mater.* **2004**, *16*, 604

BENDABLE, SPLICEABLE, TUBULAR BIOFUEL CELL CABLE

Shawn Applegarth & Stuart Wilkinson

Mechanical Engineering Department
University of South Florida
Tampa, FL 33620

Introduction

With recent advances in the bioelectrochemical aspects of biofuel cells (BFC), a demand for novel mechanical configurations has begun to emerge. Early biofuel cell research was carried out with bench top apparatus involving glassware. This was eventually superseded by stacked flat-plate designs, borrowed ostensively from H_2/O_2 fuel cells used in NASA's space program. Now the emphasis has shifted to microfluidic concepts for small-scale applications[1], and flow-through designs for macro-scale installations such as with wastewater flows[2].

This paper describes a new type of biofuel cell configuration dubbed "BFC cable". This prefabricated tubular biofuel cell can be produced in long lengths and shipped in a coiled state. The current design has an outside diameter of ¾ inch, and is totally flexible, with a minimum bend radius of 6 inches. In addition, the "BFC cable" can be easily spliced together or interfaced with plumbing fixtures (manifolds, valves, etc.) using just a pair of cutters and a screwdriver. To make a connection the "BFC cable" is simply cut to length and then pushed onto a standard hose fitting. A complex biofuel cell system can thereby be assembled quickly and easily.

Design Details

The anatomy of the "BFC cable" is shown in Figure 1. At the center is a fine stainless steel wire wrapped in a helical form (weak spring). This wire acts as the anode current collector, prevents tube collapse during bending and provides an unrestricted central passageway that permits fluid permeation into the next layer. The anode spring is also crucial in the splicing process, which will be

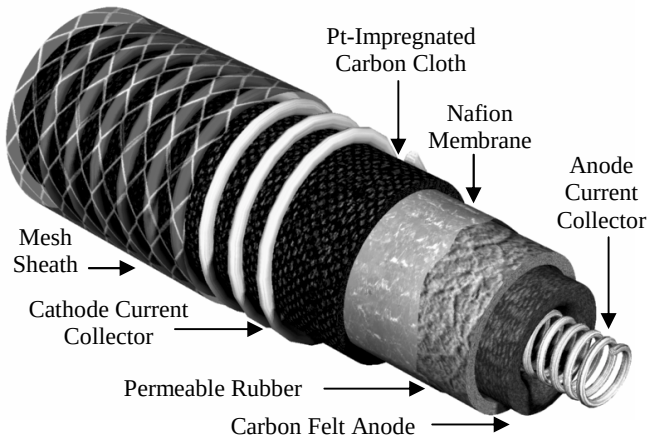

Figure 1. Anatomical configuration of the "BFC cable"

discussed later. Around the central spring is wrapped an annular anode layer made from electrically conductive carbon (graphite) felt. This felt provides a flexible, inert and non-toxic anodic scaffold structure with a high surface area capable of supporting a biofilm. The biofilm is formed *in-situ* once the system has been fully assembled, by circulating an inoculated liquid substrate through the central passageway. The inoculum must include direct-exchange microbes for successful operation since no mediation is provided. Over time the biofilm will naturally develop on the fibers of the carbon felt and act as a biocatalyst. The carbon felt anode is placed within the bore of a highly liquid-permeable rubber tube. The elastic nature of this tube allows it to expand around and tightly grip barbed-style hose connectors. The permeability creates a multitude of fluid passageways capable of transporting ions through the rubber. The outer surface of the rubber tube is surrounded by a Nafion ion-exchange membrane, which is itself bonded to one side of a platinum impregnated conductive woven carbon cloth. This latter integrated assembly (Nafion-Carbon Cloth-Pt) fulfills the role of an oxygen (air) cathode. The cathodic cloth assembly, which begins as a flat sheet, is wrapped around the rubber tube and sealed along a longitudinal overlap seam. The seal is accomplished using a rubber adhesive, which allows for expansion when a hose connector is inserted during splicing. This latter property is important since the woven carbon cloth can be readily flexed but not significantly stretched. The cathodic cloth is not itself bonded to the rubber tube, but held firmly in place by a wire wrapped around the outside. This wire also serves as the cathode current collector. The cathodic cloth becomes moist during normal operation and therefore requires pretreatment with water repellant. The "BFC cable" is completed by an external sheath of nylon mesh fabric, which provides some protection to the delicate cathodic cloth while allowing the air cathode to "breathe" and shed water.

Cable Connections

Splicing and interfacing are achieved using standard off-the-shelf metal barbed-style hose connectors. Plastic fittings are precluded, as they do not conduct electricity, while brass fittings must be avoided due to their biocidal properties. Stainless steel hose barbs are ideal, and widely available in a variety of configurations. As shown in Figure 2., the hose barb is simply pushed into the end of the "BFC cable". In so doing the anodic felt is readily squashed or crushed to accommodate the fitting, while the rubber expands and provides a positive grip. The anode current collector spring is

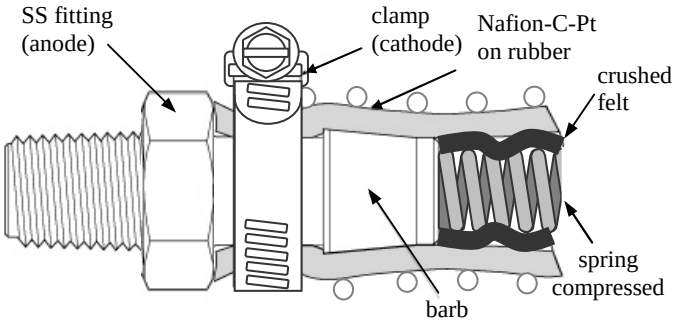

Figure 2. Typical "BFC cable" plumbing & electrical connections

compressed by the advancing hose barb and thereby creates a sprung-loaded electrical contact with the tip. The entire stainless steel connector therefore becomes the anode electrical terminal. A standard off-the-shelf stainless steel hose clamp (band and screw type) is used to ensure a liquid-tight joint, while the clamp screw serves as the cathode electrical terminal provided that some portion of the cathode current collector wire is clamped beneath the band.

References

(1) Palmore, G. T. R. in *Small Fuel Cells for Portable Applications*, Knowledge Press, Brookline, MA, **2002**, *5*, 79-98.

(2) Liu, H.; Ramnarayanan, R.; Logan, B. E. *Environ. Sci. Technol*. **2004**, *38*, 2281-2285.

AEROBIC POWER GENERATION BY A MINIATURIZED MICROBIAL FUEL CELL

Bradley R. Ringeisen,[*] Emily Henderson,[+] Jeremy Pietron,[*] Brenda Little,[§] Ricky Ray,[§] Joanne Jones-Meehan[*]

[*] Naval Research Laboratory/Code 6113, 4555 Overlook Ave. SW, Washington, D.C. 20375

[+] Wright State University/Mechanical and Materials Engineering Department, Dayton, OH 45435

[§] Naval Research Laboratory/Code 7303 and 7330, Stennis Space Center, MS 39529

Introduction

Within the next five to twenty years, networks with small, unattended sensors should be able to deliver a range of sensing capabilities (i.e., temperature, sentry, acoustic, magnetic, audio, etc.) for defense, intelligence, commercial and homeland security applications.[1] Current state-of-the-art networked sensors are relatively large (~200 cm^3 to >10^4 cm^3) and the size is often limited by the power source and the antenna. Recent advances and predicted improvements in low-power electronics, MEMs and RF communication technology will both shrink these devices and reduce power requirements to less than 100 μW, opening the possibility for non-traditional power sources to be utilized.[2-4]

For applications requiring long-time surveillance, sensing in corrosive environments (seawater, etc.) or function *in vivo*, power sources that can harvest energy from their environment are an attractive alternative to batteries and fuel cells that require replacement, recharging or fuel re-supply.[5] One example is a 1 m^2 footprint microbial fuel cell (MFC) that operates in an anaerobic environment on the seafloor by utilizing naturally occurring nutrients in the sediment.[6] Recently, we have shown that power can be continuously generated by a miniaturized microbial fuel cell functioning under aerobic conditions, opening the possibility for microbial-based power generation in more diverse environments. The miniaturized design creates shorter diffusion paths, the possibility for efficient series and parallel stacking, as well as, generating uniform nutrient flow over the electrodes. In this study, we used *Shewanella oneindensis* strain DSP10, a Gram-negative bacterium capable of respiring aerobically and anaerobically using a variety of compounds as terminal electron acceptors. DSP10 cells are used in the anode chamber, enabling power generation in both aerobic and anaerobic environments. The carbon and energy source fed to the bacteria is lactate, which can be found in marine, estuarine and freshwater environments. Therefore, a MFC operating aerobically could generate power throughout the ocean column instead of being confined to the seafloor.

Experimental

Miniaturized Microbial Fuel Cell. Figure 1 shows the miniaturized MFC used in this study. The MFC housed two 4X compressed 40 pore per cm reticulated vitreous carbon (RVC) electrodes. The anode and cathode were positioned to maximize proton diffusion across a 2.8 cm^2 Nafion™ membrane (125 μm thick) separating the two chambers, each with 1.5 cm^3 volumes. Attached 1/8" O.D. Teflon™ tubing enabled uniformly distributed flow of the anolyte and catholyte across the electrodes at rates of 1 to 50 mL/min.

Anode and Cathode Parameters. The anode and cathode used during in this study were 4X compressed 40 pore per cm RVC with equal 0.5 cm^3 volumes with macroscopic geometrical surface areas of 3.84 cm^2. The microscopic surface area of uncompressed 40 pore per cm RVC is reported by the manufacturer to be 65.6 cm^2/cm^3, but

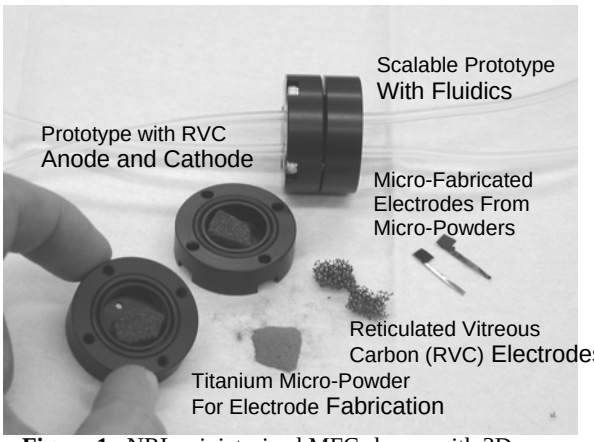

Figure 1. NRL miniaturized MFC shown with 3D reticulated vitreous carbon (RVC) electrodes. Also, other electrode materials are shown including carbon and titanium.

no surface areas are reported for the 4X-compressed material. We used environmental scanning electron microscopy to obtain images of the foam that indicate an increased density but fractured pore structure for the 4X compressed material (data not shown). From these micrographs we conclude that portions of the 4X compressed RVC will most likely not be available for electron transport due to broken pathways and reduced pore size. Based on cyclic voltammetry, the RVC appears to be an excellent electrode material with good electrochemical behavior.

The anolyte was an aerobic culture of *S. oneindensis* in 50 mL of Luria-Bertani (LB) broth with subsequent addition of lactate and anthraquinone 2,6-disulfonate (AQDS) after 48 h (final concentration was 30 mM lactate and 100 μM AQDS). Voltage data was taken in open circuit, short circuit and closed circuit (1200 Ω load) configurations when cell concentrations reached 10^8/mL. The catholyte was a 50 mM $K_3Fe(CN)_6$ prepared in 5X phosphate buffer saline (PBS).

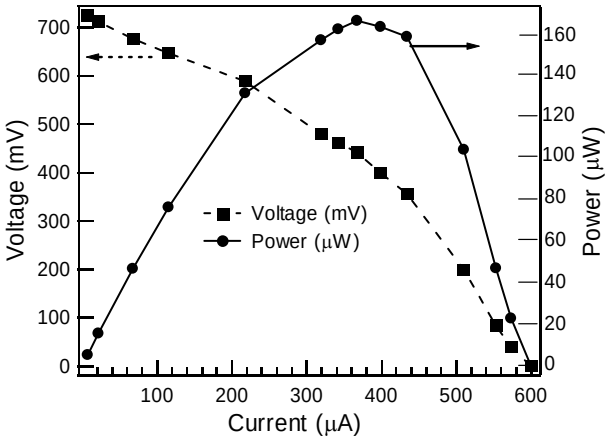

Figure 2. Voltage and power versus current for an aerobic miniaturized microbial fuel cell running on lactate fuel.

Results and Discussion

Voltage (V) was measured across variable resistance (R) to calculate current (I) generated from the miniaturized MFC (V = IR). Figure 2 shows the variance in voltage and power over the entire

range of current for the miniaturized MFC for the conditions described above. The peak power was 162 μW ($P = I^2R$) and was generated with 368 μA at 0.44 V. The open circuit voltage (V_{oc}) and short circuit current (I_{sc}) were measured at 0.725 V and 600 μA, respectively. These measurements were taken with 2 mL/min flow rates for both the anolyte and catholyte.

The current and power densities are maximized at 96 μA/cm^2 and 42 μW/cm^2 by using the geometric surface area of the electrodes in the calculation. In an attempt to make fair comparisons with other literature current densities, we will estimate of the actual microscopic surface area by using the following assumptions. Because the compressed carbon was roughly four times more dense than the uncompressed (65.6 cm^2/cm^3), one could assume that the microscopic surface area is 262 cm^2/cm^3. However, we observed only a moderate increase in current (20%) and power (15%) when using 4X compressed RVC rather than uncompressed RVC. Based on estimated surface area alone, one would expect up to a four-fold increase in output current. It is possible that portions of the compressed carbon were unavailable for electron transport (non-conductive due to fractures, compressed areas block mediators, etc.) and present only 20% more usable surface area per volume rather than four times. If this 20% increase in surface area is used (78.7 cm^2/cm^3), current and power per area are 9.3 μA/cm^2 and 4.1 μW/cm^2, respectively. By using the entire calculated microscopic surface area of 131 cm^2, current and power per area are 2.8 μA/cm^2 and 1.2 μW/cm^2.

This range in current and power density is in the same order of magnitude as those found in experiments using various *anaerobic* cultures with or without soluble electron mediators and higher than most studies when using anaerobic cultures without soluble electron mediators.[7-10] One would expect that by using *S. oneindensis* in an aerobic environment the current and power density of our MFC would be substantially lower than comparable literature cells utilizing various *Geobacter* spp. (i.e., *G. sulfurreducens*, *G. metallireducens*, etc.), which are capable of more complete oxidation of electron donors.[10] It is possible that the miniaturized scale of our MFC enhances efficiency and increases the current output above what would be expected for a macroscopic device in an aerobic environment.

One advantage of using a miniaturized MFC is the current and power output generated per volume. The anode and cathode chambers (1.5 cm^3) are at least an order of magnitude smaller than most microbial fuel cells and several orders of magnitude smaller than some MFCs. Using the maximum power data and the volume of the anode chamber, we calculated the current and power densities for our miniaturized MFC to be 245 μA/cm^3 and 108 μW/cm^3. These densities are nearly the same as the highest current per volume reported for any MFC in the literature where microbial H_2 evolution and direct microbe-to-electrode electron transport were both utilized for power generation (estimated at 400 μW/cm^3).[11] There is one example of a microfabricated MFC described by Chiao, *et. al*, but the calculated power per volume (0.5 μW/cm^3) is 200 times less than that calculated for our MFC.[12] In addition, our power per volume is 170 times larger than the best MFC using *S. oneindensis* (0.625 μW/cm^3).[13] By utilizing a high surface area electrode that resides over a third of the total chamber volume, our device most likely harnesses electrons from a greater percentage of the bacterial cells than most MFCs.

It needs to be pointed out that the power and current per volume for our device is obtained with continuous nutrient flow, a small working volume inside the fuel cell and a larger bath of anolyte and catholyte solution (50 mL) that resides external to the anode and cathode chambers. We have observed a moderate drop-off in current over time (50% over 24 h) when the flow was stopped and a slight increase in power with higher fluid flow rates (up to 10% for two times faster flow). Due to the small chamber size, a miniaturized MFC will need to be refreshed more often than larger devices, but we envision an environmental system that uses available nutrients and an oxygen cathode, either eliminating or minimizing the need for a fluidic pumping network.

Conclusions

This paper describes power generation by an aerobic, miniaturized microbial fuel cell. The current and power output of our device is similar to other MFCs described in the literature even though it is run in sub-optimal, aerobic conditions with microorganisms that are unable to oxidize electron donors as completely as other bacteria. This data suggests that there may be advantages to running MFCs in miniaturized reaction vessels rather than macroscopic chambers. If larger currents are required, then the smaller cells could be stacked in parallel rather than building a single device with a large electrode. On their own, we believe miniaturized devices may best serve as power sources for small, networked sensors or for *in vivo* applications.

Acknowledgement. This research was funded by the Office of Naval Research through Naval Research Laboratory Block Program (WU#61-6009).

References

(1) Warneke, B.; Last, M.; Liebowitz, B; Pister, K.S.J. *Computer* **2001**, *34*, 44.
(2) Roundy, S.; Leland, E.S.; Baker, J.; Carleton, E.; Reilly, E.; Lai, E.; Otis, B.; Rabaey, J.M.; Wright, P.; Sundararajan, V. *IEEE Pervasive Computing* **2005**, *4*, 28.
(3) Otis, B.P.; Rabaey, J.M. *IEEE J. Solid State Circuits* **2003** *38*, 1271.
(4) Scott, M.D.; Boser, B.E.; Pister, K.S.J. *IEEE J. Solid State Circuits* **2003**, *38*, 1123.
(5) Roundy, S.; Wright, P.K.; Rabaey, J. *Computer Comm.* **2003**, 26, 1131.
(6) Tender, L.M.; Reimers, C.E.; Stecher, H.A.; Holmes, D.E.; Bond, D.R.; Lowy, D.A.; Pilobello, K.; Fertig, S.J.; Lovley, D.R. *Nat. Biotechnol.* **2002**, *20*, 821.
(7) Skukla, A.K.; Suresh, P.; Berchmans, S.; Rajendran, A. *Current Science* **2004**, *87*, 455.
(8) Holmes, D.E.; Bond, D.R.; Lovley, D.R. *App. Envir. Microbio.* **2004**, *70*, 1234.
(9) Jang, J.K.; Pham, T.H.; Chang, I.S.; Kang, K.H.; Moon, H.; Cho, K.S.; Kim, B.H. *Process Biochem.* **2004**, *39*, 1007.
(10) Bond, D.R.; Lovley, D.R. *App. Envir. Microbio.* **2003**, *69*, 1548.
(11) Schroder, U.; Nieben, J.; Scholz, F. *Angew. Chem. Int. Ed.* **2003**, *42*, 2880.
(12) Chiao, M.; Lam, K.B.;Lin, L. *Proc. IEEE MEMS Conf.*, **2003**, Kyoto, Japan, 383.
(13) Park, D.H.; Zeikus, J.G. *Appl. Microbiol. Biotechnol.* **2002**, *59*, 58.

POLYANILINE-COATED HIGH−SURFACE-AREA CARBON FOAMS AS ANODE MATERIALS IN REAGENTLESS, AEROBIC, SMALL-SCALE MICROBIAL FUEL CELLS

Jeremy J. Pietron[†] *Joanne Jones-Meehan*[††], *Brenda Little*[†††], *Richard Ray*[†††], *Bradley R. Ringeisen*[††]

[†]Surface Chemistry Branch, Code 6170 and [††]Chemical Dynamics and Diagnostics Branch, Code 6110
Naval Research Laboratory
Washington, DC 20375
[†††]Ocean Science Branch, Code 7330
Naval Research Laboratory
John C. Stennis Space Center, MS 39529

Introduction

Small-scale microbial fuel cells (MFC) offer the possibility of low-cost, long-lived, low power-level (high-μW to low-mW) applications such as unattended sensor grids for ship and threat detection, self-sufficient water-borne chemical and biosensors, and temperature, vibration, acoustic, audio, magnetic and accelerometer surveillance via networked sensors. Appropriate bacteria can use biological fuels such as sugars and products of plant and animal decomposition likely to be found in biologically rich environments, particularly the littoral environment. Optimally, microbial fuel cells deployed in the littoral environment would be small, reagentless and operate in aerobic conditions.

We have recently developed MFCs using high-surface-area reticulated vitreous carbon (RVC) foams as both anode and cathode materials that feature surface area-to-volume ratios of roughly 65 cm^2/cm^3. This design parameter maximizes the current output per unit volume achievable with MFCs. *Shewanella oneindensis* was chosen to serve as the source of catabolic activity on the anode side as it works under both aerobic and anaerobic conditions, oxidatively breaking down lactate flowing through the cell and transferring electrons to freely diffusing anthraquinone 2,6-disulfonate (AQDS), which in turn transfers electrons to the 0.5 cm^3 (~3.8 cm^2 geometric area and 33 cm^2 microscopic surface area) current-collecting carbon foam. The catholyte consists of a ferricyanide solution as is common in laboratory microbial fuel cells. Configured as such, the microbial fuel cell generates 368 μA and 162 μW across a 1.2 kΩ resistor. Practical application will require both optimization of the cathode for utilization of ambient aqueous oxygen as the electron acceptor and *elimination of the diffusing electron-transfer mediator.* Park and Zeikus achieved current densities of 16 $\mu A/cm^2$ using *S. oneindensis*-based MFCs with carbon cloth anodes modified with Mn^{4+} ions or neutral red dyes.[1] Schröder and coworkers demonstrated MFC current densities of 90 $\mu A/cm^2$ using *E. coli* and conducting polymer (polyaniline)-modified platinum electrodes under anaerobic condtions.[2] In our study, we applied polyaniline to the RVC foam electrodes by direct electrochemical polymerization to act as a bound anodic electrochemical mediator between *S. oneindensis* and the graphite electrode, eliminating the need for a diffusing mediator

Experimental

Coating of Anodes with Polyaniline by Electropolymerization of Aniline. Polyaniline was deposited on 4X compressed 40-pore-per-cm RVC anodes by electrochemical polymerization of aniline using cyclic voltammetry, as described by Zotti *et al.*[3] Approximately 0.5 cm^3 of RVC foam was used as a working electrode in a three-electrode electrochemical cell with a gold foil counter electrode and a Ag/AgCl reference electrode. Sixty cycles between -0.05 V and 0.85 V versus Ag/AgCl at 50 mV/s in 0.1 M aniline/0.25 M H_2SO_4 (aq) were applied to the working electrode. Anodes were subsequently cycled in 0.25 M H_2SO_4 at 100 mV/s and showed oxidation and reduction waves characteristic of deposited polyaniline.[3]

Microbial fuel cell apparatus. The NRL miniaturized MFC comprises two 4X-compressed 40-pore-per-cm reticulated vitreous carbon (RVC) electrodes contained within in-house designed molded plastic housing. The anode and cathode are positioned to maximize proton diffusion across a 2.8 cm^2 Nafion™ membrane (125 μm-thick) separating the two chambers, each with 1.5 cm^3 volumes. The RVC was typically cut to ~0.5 cm^3. Attached 1/8"-O.D. Teflon™ tubing enables uniformly distributed flow of anolyte and catholyte across the electrodes at rates of 1 to 50 mL/min.

Anode and Cathode Parameters. The anode and cathode used for these experiments were 4X compressed 40 pore-per-cm RVC with equal 0.5−cm^3 volumes. The anolyte was an aerobic culture of *S. oneindensis* in 50 mL of luria burtani (LB) broth, with subsequent addition of lactate after 48 h to create a solution with 30 mM lactate. Voltage data were taken in open circuit, short circuit, and closed circuit (2200-Ω load) configurations when cell concentrations reached 10^8/mL. The catholyte was 50 mM $K_3Fe(CN)_6$ prepared in 5X phosphate buffer saline (PBS).

Results and Discussion

Figure 1 is a voltage−time plot for the polyaniline-modified MFC in closed-circuit configuration over several days, with lactate periodically added to the anode solution as fuel.

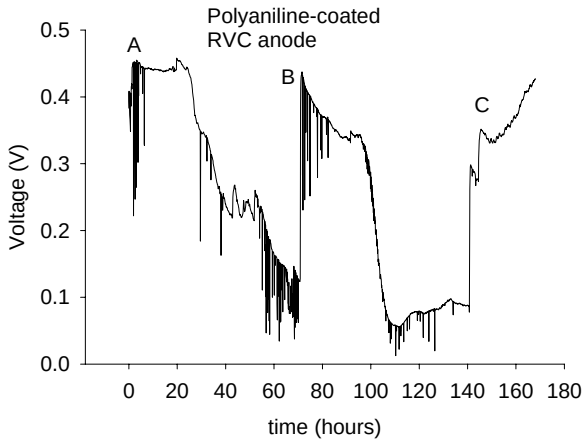

Figure 1. Voltage−time plot for the MFC with polyaniline-modified anode.

Initially data were gathered from the voltage plateau achieved after the first feeding with lactate, beginning at time "A". The MFC steadily produces 450 mV across the 2200 Ω resistor, yielding 205 μA and 92 μW for ~30 h, after which the voltage drops to about 140 mV over about 40 h. Fresh lactate was added at about 70 h (time "B") and the voltage rises to about 420 mV before decaying to a somewhat lower plateau of roughly 350 mV. The total time of useful power generation for this feeding is again roughly 30 h. Addition of fresh *S. oneindensis* to the anode reservoir with the next lactate feeding at "C" resulted in an initial rise to 350 mV and a steady rise nearly to the previous plateau of ~450 mV. Subsequent cycles of lactate depletion and re-feeding (not shown) again yielded declines in power output to ~350 mV. After this voltage decline, the anolyte was replaced, and the old solution was diluted and plated to LB agar to determine the extent of contamination. We found equal numbers of

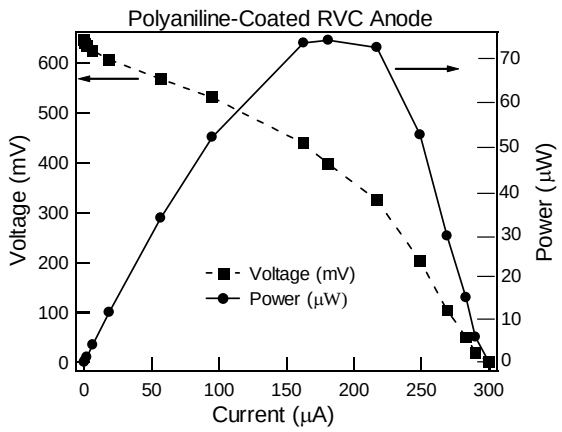

Figure 2. Voltage–Power–Current data for the MFC with polyaniline-coated anode.

S. oneindensis and *Bacillus* sp. (common environmental bacteria) in the contaminated anolyte (10^8/mL). Corresponding experiments with only environmental contaminants in the anolyte resulted in an output voltage of 0.2 mV with all other conditions the same. This result implies that environmental bacteria eventually start competing with *S. oneindensis*, resulting in a decrease in cell voltage. Future experiments will attempt to more thoroughly sterilize the electrodes and MFC housing.

Figure 2 shows both voltage and power versus current for a microbial fuel cell with a polyaniline-modified anode. Optimum power output occurs at ~400 mV with a 2.2 kΩ load, yielding ~70 μW. This power spectrum was measured shortly after time "B" shown in Figure 1, when the MFC was beginning to show signs of environmental contamination. However, the plot still shows the power and voltage spectrum characteristic of the mini-MFC operating with a polyaniline-coated RVC anode and no soluble electron mediator. The open circuit voltage (V_{oc}) is 650 mV and a short circuit-current (I_{sc}) is 300 μA.

The current and power densities estimated for our MFCs with polyaniline-modified anodes are in the 1.5–6.2 μA/cm^2 and 0.7–2.8 μW/cm^2 range, depending on the exact specific surface area of the compressed foams. Uncompressed foams feature surface areas of 65 cm^2/cm^3. The 4X-compressed foams, with which we were experimenting in our "unmodified" MFCs (no polyaniline, with AQDS) to try to improve our current per unit volume, have uncertain specific surface areas. In unmodified MFCs, the 4X-compressed foams improved currents, but only by about 20% (data not shown). The specific surface areas are certainly higher than with the uncompressed foams, but likely less than a full factor of four. Additionally, much of the diminished electrochemical utility of surface area, both in the polyaniline-modified anodes and in the unmodified anodes of compressed RVC, may be due to smaller pores that are less accessible to *S. oneindensis*. In the polymer-modified RVC, the problem of access to pores may be compounded by the thickness of the polymer film. *Alternately, if one calculates current and power density in terms of the geometric surface area of the approximately 0.5-cm^3 electrodes, each electrode is approximately a cube with 0.8 cm per edge and 0.64 cm^2 per side. Six sides yield a total geometric surface area of 3.84 cm^2, and thus current and power densities of 52 μA/cm^2 and 24 μW/cm^2.*

We find that in the absence of both a polyaniline-coated anode and a soluble electron mediator, our MFCs with bare RVC electrodes typically generate optimum power at 275 mV and 125 μA for a total power output of ~ 35 μW. This performance corresponds to current and power densities of 0.95–3.8 μA/cm^2 and 0.27–1.1 μW/cm^2 for the estimated specific surface areas, and 32.5 μA/cm^2 and 9.1 μW/cm^2 when using geometric surface areas. This in itself is an important result that demonstrates the potential advantages of using a miniaturized MFC versus a macroscopic device. The literature power density for *S. oneindensis* functioning in a mediatorless MFC is 0.03 μW/cm^2, a factor of 9 to 35 times lower than the value reported here using the much more conservative estimates from estimated specific surface areas.[1,4] The advantage of the MFC is even greater when using a polyaniline-coated anode, increasing the current density by 60% and the power density by over 150% from the bare RVC.

Future experiments will include electron microscopy of the polymer-modified electrodes to elucidate polymer film thickness, deposition of polymer films on uncompressed RVC, experimentation with polymer film thickness, polymer charge state (to optimize electron-transfer characteristics) as well as trying other electrochemically active polymers. Ideally, correct choice or modification of polymer film will allow growth *S. oneindensis* directly on the polymer, improving electron transfer characteristics and rendering the MFC completely self-contained.

Conclusions

A small, aerobic, mediatorless MFC using polyaniline-modified RVC has been described. Current and power densities are modest when considering microscopic specific surface areas, but quite promising when considering geometric surface areas. Much improvement is likely possible through optimization of electrode porosity, polymer thickness, polymer charge state and selection of polymer.

Acknowledgement. Research supported by the Office of Naval Research through Laboratory block WU#61-6009.

References

(1) Park, D. H.; Zeikus, J. G. *Appl. Microbio. Biotechnol.* **2002**, *59*, 58.
(2) Schröder, U.; Nießen, J.; Scholz, F. *Angew. Chem. Int. Ed.* **2003**, *42*, 2880.
(3) Zotti, G.; Cattarin, S.; Comisso, N. *J. Electroanal. Chem.* **1987**, *235*, 259.
(4) Kim, H.J.; Park, H.S.; Hyun, M.S.; Chang, I.S.; Kim, M.; Kim, B.H. *Enzyme Microbial Technol.* **2002**, *30*, 145.

ELECTRICITY AND HYDROGEN PRODUCTION USING DIFFERENT TYPES OF MICROBIAL FUEL CELL TECHNOLOGIES

Bruce Logan[1,2], Hong Liu[1], Jenna Heilmann[1], SangEun Oh[1], Shaoan Cheng[1], and Stephen Grot[3]

[1]Department of Civil and Environmental Engineering,
[2]The Penn State Hydrogen Energy (H_2E) Center, Penn State University, University Park, PA, 16802, U.S.A.
[3]Ion Power Inc., Bear, DE, U.S.A.

Introduction

Virtually any form of biodegradable organic matter can be used to produce electricity in a microbial fuel cell (MFC), including carbohydrates such as glucose, starch, fatty acids, amino acids and proteins (*1-4*). The process can also be used with animal and human wastewaters, resulting in both electricity generation and wastewater treatment method (*5*).

Further improvements in MFC performance are needed. Factors that affect MFC performance include: the rate of substrate degradation, the rate of electron transfer from bacteria to anode, circuit resistance, proton mass transfer in the liquid, oxygen diffusion from the cathode into the anode chamber, and the performance of the cathode. Most MFCs are operated at neutral pH in order to optimize bacterial growth conditions. However, the low concentration of protons at this pH makes the internal resistance of the cell relatively high compared to chemical fuel cells that use acid or alkaline electrolytes. There are two ways to decrease the internal resistance without changing the bulk solution pH. One is to increase the solution conductivity by increasing the ionic strength (IS); the other is to decrease the electrode spacing. Up to now, these two factors have not been systemically examined in MFCs for their effect on power generation. MFC performance can also be affected by temperature as a result of its effect on: bacterial kinetics, oxygen reaction rates catalyzed by Pt on the cathode, and the rate of mass transfer of protons through the liquid. MFC studies are normally conducted at elevated temperatures of 30-37^{o}C. However, operating the reactor at lower temperatures may reduce operational costs, especially if the reactor is used for wastewater treatment. Thus more information is needed on the performance of MFCs as a function of temperature.

The cathode electrode materials and methods of construction can also affect MFC performance. Oh *et al.* (*6*) have shown that the relative size of the anode and cathode electrodes affects power output. High Pt loading rates (0.5 mg cm^{-2}) are usually used in MFCs in order to ensure that a lack of sufficient catalyst does not limit power generation. However, Cheng et al. (*7*) found that Pt loadings on a carbon cloth electrode as low as 0.1 mg cm^{-2} did not affect performance. They also found that the cathodes prepared with Nafion® as the bonding agent achieved higher power densities than those using PTFE. Both carbon paper and cloth have been used in MFC systems, but the effect of these carbon materials on power generation in air-cathode MFCs has not been examined.

In this study, we examined the effect of solution ionic strength, electrode spacing, and temperature on electricity generation using a single chamber, membrane-free MFC. Two different cathode materials were evaluated in order to ascertain the effect of these materials on power generation.

Electricity is not the only possible product using MFC technologies. It is shown here by using a completely anaerobic system (no oxygen at the cathode), hydrogen can be produced from fermentation end products if the electrochemical potential achieved by bacteria is augmented using an external power source. This makes it possible to produce hydrogen directly from the oxidized organic matter. We call this MFC adapted process a bio-electrochemically assisted microbial reactor (BEAMR).

Methods

MFC construction. The single chamber MFC consisted of an anode and cathode placed in a plastic cylindrical chamber 4 cm long by 3 cm in diameter (empty volume 28 ml) as previously reported (*8*). The anode electrode was made of plain toray carbon paper (without wet proofing; E-Tek, USA), and was pierced in several places, forming holes ~1 mm in diameter) so that water motion in the chamber was not blocked when the anode was placed at the far end of the chamber or moved to within 2 cm of the cathode. The cathode was made of carbon paper containing 0.5 mg/cm^2 of Pt (10% of Pt/C catalyst, 30% wet-proofing; E-TEK, USA).

All MFCs were inoculated with domestic wastewater and a nutrient medium amended with sodium acetate (1 g/l). Maximum power density was determined by changing the circuit resistor and measuring power output over a complete batch cycle of operation. Each cycle was re-started by refilling the medium in the reactor when the voltage dropped below ~30 mV. The conductivity of the solution was increased by adding NaCl. Electrode spacings were 4 cm or 2 cm, and temperature was 32 or 20^{o}C as indicated.

BEAMR process. A two chamber, glass bottle reactor was composed of anode and cathode chambers separated by a proton exchange membrane (NAFION™ 117) constructed as previously described except the cathode was not aerated (*6*). The anode was plain carbon cloth and the cathode was made of carbon paper containing 0.5 mg-Pt/cm^2. The reactor was inoculated as described above, and fed a phosphate buffer (50 mM, pH=7.0) and nutrient medium containing acetate. The anode potential was set by the potential of the respiratory enzymes used to make energy for the cell from the oxidation of organic matter. A voltage in the range of 250-850 mV was applied to the circuit by connecting the positive pole of a programmable power supply.

Calculations and analysis. Voltage (V) produced by the MFC was measured using a multimeter with a data acquisition system with power ($P=IV$) normalized by the cross sectional area (projected) of the anode. Electrode potentials were measured by using a multimeter. The Coulombic efficiency was calculated as: $E=C_p/C_T \times 100\%$, where $C_{p,}$ is the total coulombs calculated by integrating the current over time. C_T is the theoretical amount of coulombs that can be produced from acetate. Gas composition was measured by gas chromatography (*22*).

Results and Discussion

MFC experiments. Increasing the solution ionic strength from 100 to 400 mM by adding NaCl increased power output from 720 mW/m^2 to 1330 mW/m^2. Power generation was also increased from 720 mW/m^2 to 1210 mW/m^2 by decreasing the distance between the anode and cathode from 4 cm to 2 cm (Figure 1). This increase in power density corresponded to a decrease of internal resistance from 161 Ω to 77 Ω when the electrode spacing was reduced from 4 cm to 2 cm. No further improvement in power generation was observed if the medium IS was increased to 400 mM because there was little change in internal resistance. The internal resistance was 71 Ω for an electrode spacing of 2 cm (Is=400 mM), which is only 10% lower than that obtained under the same conditions but with a 4 cm electrode spacing (79 Ω). Improvements on both the cathode and anode potentials were seen with a decrease in the electrode spacing with the low IS solution (IS=100 mM), while no improvement was observed when the solution IS was increased to 400 mM. Power output was also increased by 68% by replacing the cathode

(purchased from a manufacturer) with our own carbon cloth cathode containing the same Pt loading.

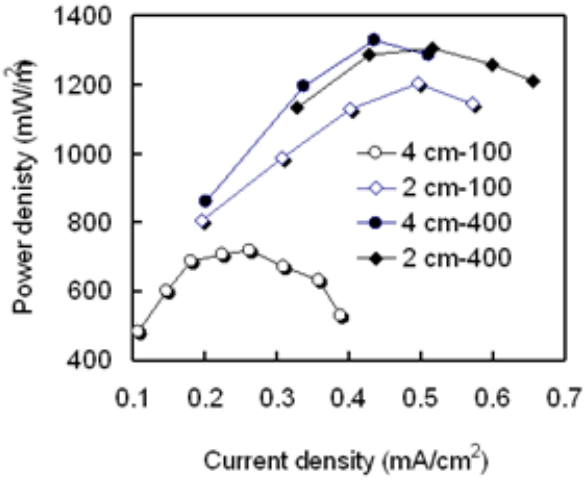

Figure 1. Effect of electrode spacing (2 and 4cm) on power generation at different current density using medium with different ionic strengths (100 and 400 mM) at 32°C.

Coulombic efficiency and energy recovery were both improved by decreasing the electrode spacing when the low IS solution was used (IS=100 mM). However, the Coulombic efficiency and energy recovery were not affected when using the higher IS solution (IS=400 mM).

The performance of conventional anaerobic treatment processes, such as anaerobic digestion, are adversely affected by temperatures below 30°C. However, decreasing the temperature from 32°C to 20°C reduced power output by only 9%, primarily as a result of the reduction of the cathode potential.

BEAMR experiments. Hydrogen production via bacterial fermentation can produce only a maximum of 4 moles of hydrogen per mole of glucose, but typically only 2 mol are produced. Acetate that is produced (2 mol/mol) cannot be further converted to hydrogen by bacteria. Using the BEAMR process, acetate was converted to hydrogen by augmenting the electrochemical potential achieved by bacteria to produce hydrogen directly from the oxidized organic matter. A small voltage (a minimum of 0.25 V) was applied to the circuit of a completely anaerobic microbial fuel cell resulting in the recovery of more than 90% of the protons and electrons produced by the bacteria from the oxidation of acetate (Coulombic efficiency range of 60-78%). This is equivalent to an overall yield of 2.9 mol-H_2/mol-acetate (assuming 78% Coulombic efficiency and 92% recovery of electrons as hydrogen).

This bio-electrochemically assisted process, if combined with hydrogen fermentation, has the potential to produce 8-9 mol-H_2/mol-glucose at an energy cost equivalent of 1.2 mol-H_2/mol-glucose. This assumes 2-3 mol-H_2/mol-glucose from bacterial fermentation, and ~3 mol-H_2/mol acetate (two moles of acetate produced per mole of glucose from the fermentation process). Production of hydrogen by this process is not limited to carbohydrates, as in a fermentation process, as any biodegradable dissolved organic matter can be used in this process to generate hydrogen from the complete oxidation of organic matter.

Acknowledgement. The Penn State researchers were supported by National Science Foundation Grants BES-0331824 and BES-0124674, a seed grant from The Huck Institutes of the Life Sciences at Penn State, and the Stan and Flora Kappe endowment.

References

(1) Park, H.S.; Kim, B.H.; Kim, H.S.; Kim H.J, Kim, G.T.; Kim, M.; Chang, I.S.; Park, Y.K.; Chang, H.I. *Anaerobe* **2001**, *7*, 297-306.
(2) Kim, H.J.; Park, H.S.; Hyun, M.S.; Chang, I.S.; Kim, M.; Kim, B.H. *Enzyme Microbiol. Technol.* **2002,** *30*, 145-152.
(3) Bond, D.R.; Lovely, D.R. *Appl. Environ. Microbiol*. **2003,** *69*, 1548-1555.
(4) Rabaey, K.; Boon, N.; Siciliano, S.D.; Verhaege, M.; Verstraete, W. *Appl. Environ. Microbial*. **2004**, *70*, 5373-5382.
(5) Liu, H.; Ramnarayanan, R.; Logan, B.E. *Environ. Sci. Technol.* **2004**, *38*, 2281-2285.
(6) Oh, S. E.; Min, B.; Logan, B. E. *Environ. Sci. Technol.* **2004**, 38, 4900-4904.
(7) Cheng, S.-A., H. Liu and B.E. Logan. 2004. Extended Abstract, Proc. 228th American Chemical Society Annual Meeting. CD ROM.
(8) Liu, H.; Logan, B.E. *Environ. Sci. Technol.* **2004**, *38*, 4040-4046.

MEDIATOR-LESS MICROBIAL FUEL CELL

Byung Hong Kim, In Seop Chang, Jae Kyung Jang and Jiyoung Lee

Korea Institute of Science & Technology,
39-1 Hawolgok-dong, Sungpook-ku, Seoul 136-791, Korea

Introduction

Cyclic voltammetry showed that some anaerobic bacteria are electrochemically active. They oxidize electron donor in the anode compartment of a fuel cell-type device without an electron acceptor, transferring electron to the electrode [1-7]. Electrochemically active bacterial consortia can be enriched in fuel cell-type electrochemical cell under various nutritional conditions. They were studied as a novel wastewater treatment process with energy recovery and as a novel biochemical oxygen demand sensor.

Electron transfer to the electrode

There are conflicting reports on the electron transfer from bacterial cells to the anode in a microbial fuel cell (MFC). Though an electron shuttle is involved in the electron transfer [7], the effluents from enriched MFCs were devoid of electrochemically active soluble compounds. A cell surface cytochromes mutant (*mtrA*) of *Shewanella oneidensis* was not electrochemically active whilst the wild strain showed the activity in cyclic voltammetry and generated electricity in an MFC (Figure 1). These results show that the electron transfer is a process through direct contact between bacterial cell and the electrode.

Microbial diversity in the enriched MFCs

Electrodes were retrieved from MFCs enriched with different nutritional conditions to analyze microbial diversity through the conventional culture method and 16S rDNA analysis. Less than 0.1% of the population could be cultured on solids media with various combinations of electron donors and acceptors. Small ribosomal RNA gene analyses showed that the fuel (electron donor) determines the dominating bacterial group in MFCs during the enrichment process. *Deltaproteobacteria* comprise around 70% in an acetate enriched MFC [8], whilst they were devoid in an MFC enriched with wastewater from a starch processing factory [9]. Fluorescent in-situ hybridization (FISH) confirmed these results.

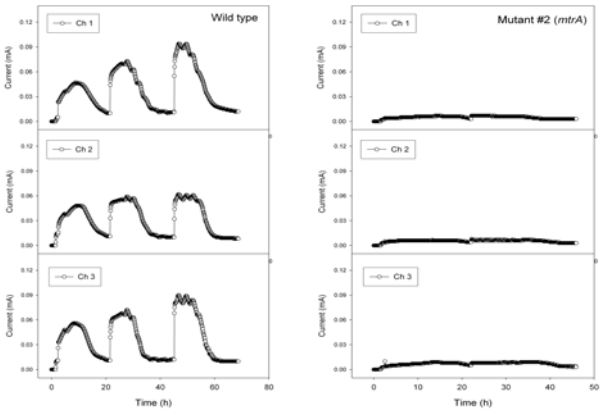

Figure 1. Current generation catalyzed by wild and *mtrA* mutant strains of *Shewanella oneidensis* with the addition of lactate as fuel. Each strain was tested using 3 separate fuel cells.

Optimization

Various rate-limiting factors were identified in electricity generation using an MFC [8]. They are (1) fuel oxidation, (2) electron transfer to the anode, (3) circuit resistance, (4) proton transfer from the anode compartment to the cathode compartment, (5) oxygen supply to the cathode, (6) oxygen diffusion into the anode compartment, (7) uneven fuel flow in the anode compartment, and others. Different factors limit the performance of MFCs under specific nutrient conditions. Oxygen diffusion into the anode compartment was most serious in an oligotrophic MFC reducing the coulomb yield, whist proton diffusion is the bottle-neck in a large scale MFC. Based on these findings, studies were made to test various MFC designs including a membrane-less MFC [11] and reduced membrane size for oligotrophic MFCs [12].

MFC as a biochemical oxygen demand (BOD) sensor

Since the current or the coulomb is directly proportional to the concentration of the fuel used in the MFC, it could be used as a BOD sensor. Since the fuel used in MFCs determines the bacterial population, enrichment was made using samples to be analyzed. When low BOD values such as river water was determined, oxygen diffused in the anode compartment was more than needed for the complete oxidation of degradable organic concentration in the samples. Nitrate is the electron acceptor preferentially used over the electrode. The terminal oxidase inhibitors such as azide and cyanide could be used to reduce the effects of the electron acceptors of higher redox potential inhibiting the aerobic respiration and denitrification (Figure 2) [13].

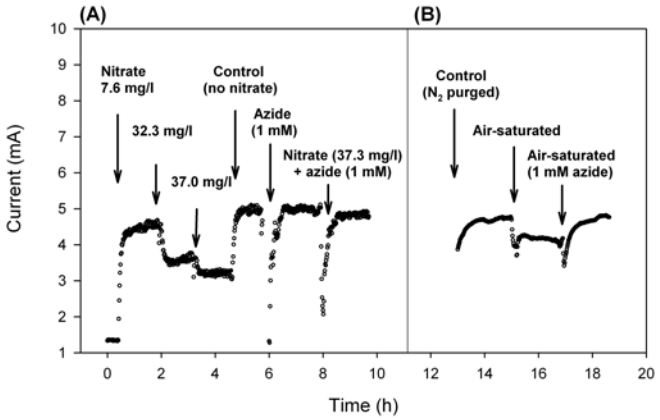

Figure 2. The current generation from MFCs fed with artificial wastewater (AW) containing nitrate and azide (A) and with aerated AW containing azide (B). AW with the BOD concentration of 113.5 mg/l was fed to MFCs at a feeding rate of 0.35 ml min^{-1}. Different nitrate concentrations and gas treatments (N_2 and air) are indicated in the figure.

Membrane-less MFC

The cation specific membrane used in a 2-compartment fuel cell is expensive, and can be suffered from fouling in the use with wastewater. A reactor was designed with the anode at the bottom and the cathode on the top without membrane. The fuel was fed through the bottom, and the cathode at the top was aerated. The performance of the membrane-less MFC was much lower than those with membrane in terms of power density. This was analyzed due to the slow proton diffusion with the increase distance between the anode and cathode. Another problem was the uneven fuel flow through the

electrode section. This could be improved using perforated electrode [14].

Stabilization of sediment

Sediment was collected from a local river to fill the bottom 1/3 of a 20 L reactor with anode buried in the sediment and cathode in the overlaying water. A set of 3 reactors was operated under the closed circuit conditions connecting the 2 electrodes, whilst the second set of 3 reactors under open circuit conditions. The closed circuit reactors generated a current of 7.6 mA/m^2 over a year. The anode redox potential was measured as 0.3 volt in the closed rectors and -0.5 volt in the open circuit reactors. More gas production was observed from the open circuit reactors than the closed ones, but more reduction in organic contents was achieved in the closed circuit reactors. The organic content reduction from the open circuit reactors seems due to methanogensis at the redox potential of –0.5 volt. Methane generation is not expected from the closed circuit reactors with the redox potential of 0.3 volt. These results show that this system can be used to accelerate sediment stabilization with reduced green-house effect gas, methane.

The current density of the closed circuit reactors is relatively low in comparison with small size MFCs. When the cathode was supplied with acid or increased aeration the current increased, showing that the reactor performance is limited by cathode reaction. This could be improved in an open system with bigger water body.

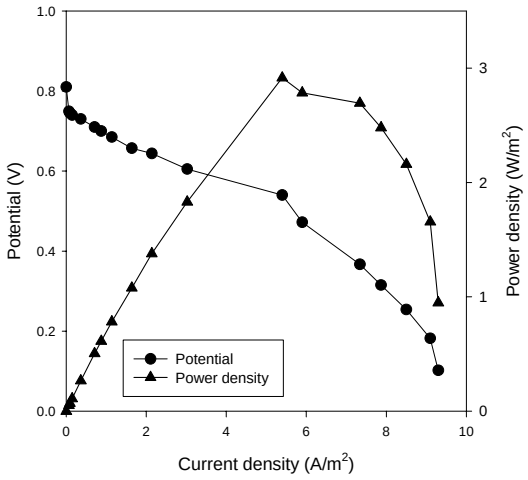

Figure 3. Polarization curve of a microbial fuel cell. The MFC was operated continuously with artificial wastewater of biochemical oxygen demand of 300 mg l^{-1} BOD, at the retention time of 8 hr.

Performance of MFSc

When an MFC is applied to treat wastewater, reduced generation of excess sludge is expected considering that a major proportion of energy carried by the organic contaminants is transformed into electricity. When an MFC with a capacity of 100 ml was operated in a continuous mode with artificial wastewater containing glucose and glutamate (300 mg l^{-1} BOD), a maximum power density of 2.9W/m^2 was achieved with a BOD removal rate of 41.7kg/m^3 day (Figure 3). The sludge generation ratio was 0.1g dry weight/g BOD removed.

The power density of a membrane-less MFC with the capacity of 2 L was one order of magnitude lower than the smaller MFCs with membrane. The performance was improved with decreasing the distance between the anode and cathode, and with acidification of the cathode area. These results clearly show that the proton mass transfer is the rate-limiting factor.

Conclusions

Electrochemically active microbial consortia can be easily enriched with wastewater as the electron donor (fuel). In most cases the effluent from MFCs fed with wastewater contained BOD less than 10 mg L^{-1} with the sludge production less than 1/4 of the conventional activated sludge process. MFC as a novel wastewater treatment process is promising not only because of the energy recovery in the form of electricity but also because of energy saving to treat sludge generated. But there are many bottle-necks to be solved before commercialization including proton mass transfer, cathode materials with better affinity for oxygen among others.

MFC can be used as a BOD sensor as well as stabilizing sediment to improve water quality in lakes.

Acknowledgement. This study was supported partly by the Ministry of Science & Technology through the National Laboratory Programme.

References

(1) Kim, B. H.; Kim, H. J.; Hyun, M. S.; and Park, D. H. *J. Microbiol. Biotechnol.* 1999, *9*, 127.
(2) Kim, B. H.; Kim, H. S.; Kim, H. J.; Kim, G. T.; Kim, M.; Chang, I. S.; Park, Y. K.; and Chang, H. I. *Anaerobe*. 2001, *7*, 297.
(3) Kim, H. J.; Park, H. S.; Hyun, M. S.; Chang, I. S.; Kim, M.; and Kim, B. H. *Enzyme Microb. Technol.* 2002, *30*, 145.
(4) Pham, C. A.; Jung, S. J.; Phung, N. T.; Lee, J.; Chang, I. S.; Kim, B. H.; Yi, H.; and Chun, J. *FEMS Microbiol. Lett.* 2003, *223*, 129.
(5) Bond, D. R.; and Lovley, D. R. *Appl. Environ. Microbiol.* 2003, *69*, 1548.
(6) Holmes, D. E., D. R. Bond, and D. R. Lovley. *Appl. Environ. Microbiol.* 2004, *70*, 1234.
(7) Bond, D. R.; and Lovley, D. R. *Appl. Environ. Microbiol.* 2005, *71*, 2186.
(8) Lee, J.; Phung, T. N.; Chang, I. S.; Kim, B. H.; and Sung, H. C. *FEMS Microbiol. Lett.* 2003, *223*, 185.
(9) Kim, B. H.; Park, H. S.; Kim, H. J.; Kim, G. T.; Chang, I. S. Lee, J.; and Phung, N. T. *Appl. Microbiol. Biotechnol.* 2004, *63*, 672.
(10) Gil, G. C.; Chang, I. SKim, .; B. H.; Kim, M.; Jang, J. K.; Park, H. S.; and Kim, H. J. *Biosen. Bioelectron.* 2003, *18*, 327.
(11) Jang, J. K.; Pham, T. H.; Chang, I. S.; Kang, K. H., Moon, H.; Cho, K. S.; and Kim, B.H. *Process Biochem.* 2004, *39*, 1011.
(12) Kang, K. H.; Jang, J. K.; Pham, T. H.; Moon, H.; Chang, I. S.; and Kim, B. H. *Biotechnol. Lett.* 2003, *23*, 1357.
(13) Chang, I. S.; Moon, H.; Jang, J. K.; and Kim, B. H. *Biosen. Bioelectron.* 2005, *20*, 1856.
(14) Moon, H.; Chang, I. S.; Jang, J. K.; Kim, B. H. *Biochem. Eng. J.* 2005, *in press*

MICROBIAL FUEL CELLS: A BIOTECHNOLOGICAL APPROACH TO POWER GENERATION

James J. Sumner and Scott R. Crittenden

US Army Research Laboratory
AMSRD-ARL-SE-EO
2800 Powder Mill Road
Adelphi, MD 20783

Introduction

In the mid-1980's a new class of anaerobic microbes was found in the Potomac River by D. Lovely then of the USGS. (Ref. 1) These organisms were found to directly oxidize organic material in the aquatic sediment and reduce solubilized iron chelates. This type of organism was found to be very prevalent in marine sediments and freshwater aquifers. They are typically anaerobic but some are facultative (grow in both aerobic and anaerobic environments). One of the unique characteristics exhibited by these microbes is the ability to directly oxidize organics and produce free electrons as part of their metabolic cycle. Specific mechanisms of this process are still being investigated. (Ref. 2)

In nature, these anaerobic microbes metabolize organic matter in the sediments of aquifers including organic acids, sugars and anhydrides. The electrons produced are normally donated to moieties such as Fe (III), Mn (IV), oxygen, nitrates, or sulfates. Engineers rapidly found the microbes were ideal candidates for bioremediation of aquatic environments, including removal of hydrocarbons, PCBs and fuel oils from marine and freshwater environments especially in the groundwater table. (Ref. 3) The ability to reduce metals and precipitate them has also been used to remove soluble uranium from aqueous solution in order to dramatically reduce the volume of radioactive wastes. Although much has been discovered about these organisms the actual electron donation mechanism is still being explored. (Ref. 2)

Recent reports describe power harvested from marine sediments containing these microbes. (Ref. 4) A fuel cell was constructed by implanting a carbon electrode into the anaerobic region of seabed sediments. A platinum electrode was placed in the saltwater above the seabed. The fuel cell produced power in the tens of milliWatt range. After weeks of operation the electrodes were removed and the carbon anode scraped of microbes that had cultured on it. The recovered bacteria were very similar to those found in the Potomac.

Power production from these organisms in the laboratory was first described in 2003 and 2004. D. Lovely and B. Logan authored these articles and are also active in bioremediation using these organisms. Power production of up to 0.5W/m^2 of electrode area has been achieved along with electron transfer efficiencies of 86%. Final power efficiency is as yet unreported and the only fuels utilized so far have been simple organics such as acetate and sugars as well as waste water. (Ref. 5)

Our goal is to increase the efficiency and power density of the microbial fuel cell by replacing the semi-permeable membrane used to separate the anodic and cathodic compartments of the cell. Current systems use Nafion 117 which is ideal for PEM fuel cells as it is capable of preventing hydrogen gas from passing but protons move relatively freely when properly hydrated. In this application Nafion 117 is "overkill". There is no need for this level of selection. The only need is to keep cells from moving from the anodic to the cathodic compartment and shorting out the system. The Nafion was replaced with a dialysis membrane which has a much lower resistance yet still easily stops the cells. This should increase both power output and efficiency.

Experimental

Microbes and Media. We used the facultative bacterium *Shewanella putrefaciens* (ATCC#49138, Raven Biologicals, Omaha, NE). The media for culture maintenance and fuel cell operation was trypticase soy broth (TSB) (BD, Franklin Lakes, NJ) *S. putrefaciens* was resuspended from a lyophilized pellet form and then incubated aerobically in TSB for 24 to 48 hours at 30 C. Many other fuels (e.g. sugars, acetate, hydrocarbons, etc.) could be used, especially if *S. putrefaciens* is replaced with one of the other metal reducing anaerobes, however, it is necessary to make sure that neither the growth media nor the electrolyte contains any electron acceptors except for the carbon electrode. Otherwise the microbes can donate their electrons to these acceptors and not the electrode, thus reducing or eliminating power production.

Fuel Cell and Electrodes. A microbial fuel cell has been constructed and power production has been demonstrated from organic fuels directly, without a reformation process. The fuel cell is a modified design from that described in reference 5B. Pictured in **Figure 1,** it consists of an H-shaped glass vessel assembled from process pipes (Ace Glass, Vineland, NJ) with the halves separated by a semi-permeable membrane. The membranes used in these experiments are either Nafion 117 (DuPont, Wilmington, DE) or dialysis membrane (Benoylated, Sigma, St. Louis, MO).

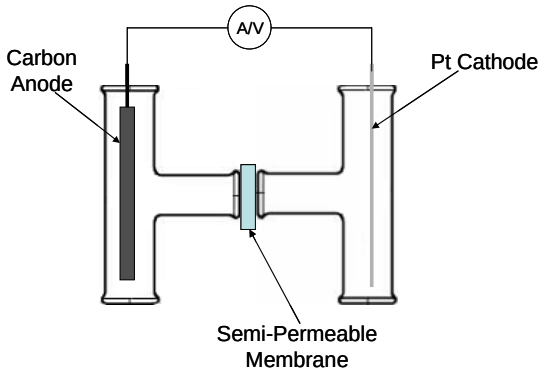

Figure 1. Microbial Fuel Cell.

The anode was constructed of a 0.25 in. by 4 in. graphite rod connected to a copper lead with silver epoxy. The joint was sealed with a non-conductive epoxy. Platinum wire (0.5mm by 25cm, Alfa Aesar, Ward Hill, MA) served as the cathode. The anodic compartment was first bubbled with nitrogen to displace all oxygen and subsequently continually flushed with nitrogen to prevent introduction of oxygen after inoculation.

The voltage was measured across an adjustable (1 Ohm to 10,000 Ohms) resistor. Data was collected using an electrochemical workstation (CHI, Austin, TX) set to monitor potential versus time.

Results and Discussion

Two identical fuel cells were constructed with the anodic chamber continuously purged with nitrogen and the cathodic compartment open to atmosphere. The anodic chamber was filled with TBS and the cathodic with Trizma at pH 7. The cells were allowed to equilibrate for several hours before the anode was inoculated with approximately 100 uL of *S. putrefaciens* culture stock. The data was collected as a voltage drop across a 10,000 Ohm resistor verses time for several days. The only difference between the two fuel cells was that one had a dialysis membrane separating the compartments and the other had Nafion 117. Typical results are shown in **Figure 2**.

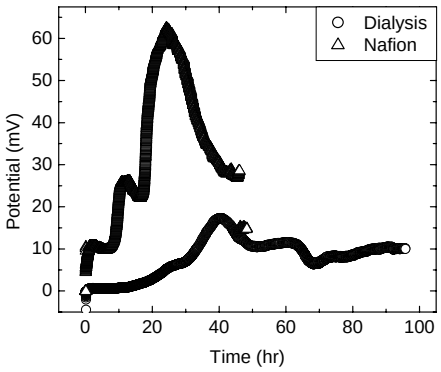

Figure 2. Voltage verses time for identical fuel cells with either Nafion (higher trace) or dialysis membrane (lower trace) separators. Note the power reduction and slowed kinetics of the dialysis membrane.

The results are opposite of the initial expectations. The fuel cell with the dialysis membrane was not only lower power but also slower to respond than the Nafion separated cell. This is probably due to the fact that oxygen can easily cross the dialysis membrane. *S. putrefaciens* is a facultative so it can survive the oxygen environment but the oxygen can act as an electron acceptor thus reducing the number of electrons donated to the electrode.

Conclusions

Leaving the cathodic compartment open to atmosphere could introduce small amounts of oxygen to the anodic compartment compromising the performance of the fuel cell utilizing the dialysis membrane. The convention for this type of device is to leave the cathode open to allow oxygen to react with generated protons to yield water. However with the platinum surface and electrons provided from the completed circuit the protons should be able to form hydrogen gas. This can be tested by purging both halves with nitrogen.

Much more than just the membrane affects the power output of a microbial fuel cell. The low power production in this system could be from the relatively low surface area anode or the growth media could have electron acceptors present. These issues will be addressed in the near future. Many other characteristics need to be met for a successful technology. The maximum power output and efficiency are only the beginning. Other characteristics include fuel tolerance, temperature range, storage conditions and resistance to chemical contaminants.

Recent work has shown that the whole organism may not be necessary as it has been reported that ruptured cell membranes can produce free electrons from nicotinamide adenine dinucleotide (NADH) which opens another realm of opportunities. (Ref. 6)

Acknowledgements. The authors would like to acknowledge Dr. Doran D. Smith and Dr. Deryn Chu of the US Army Research Laboratory for helpful discussions concerning this work.

References

(1) A) Lovely, D.R.; Phillips, E.J.P. *Applied and Environmental Microbiology*, **1986**, 51(4), 683-689. B) Lovely, D.R.; Phillips, E.J.P. *Applied and Environmental Microbiology*, **1986**, 52(4), 751-757.

(2) For Example: A) Lovely, D.R.; Phillips, E.J.P. *Applied and Environmental Microbiology*, **1988**, 54(6), 1472-1480. B) Leang, C.; Coppi, M.V.; Lovely, D.R. *Journal of Bacteriology*, **2003**, 185(7), 2096-2103. C) Holmes, D.E.; Bond, D.R.; Lovely, D.R. *Applied and Environmental Microbiology*, **2004**, 70(2), 1234-1237.

(3) For Example: A) Anderson R.T.: Vrionis H.A.; Ortiz-Bernad I.; Resch C.T.; Long P.E.; Dayvault R.; Karp K.; Marutzky S.; Metzler D.R.; Peacock A.; White D.C.; Lowe M.; Lovley D.R. *Applied and Environmental Microbiology*, **2003**, 69(10), 5884–5891. B) Lovley D.R. *Nature Reviews|Microbiology*, **2003**, 1, 36-44. C) Lovley D.R.; Anderson R.T. *Journal of Hydrology*, **2002**, 8, 77–88. D) Lovley D.R. *Science*, **2001**, 293, 1444-1446.

(4) A) Bond, D.R.; Holmes, D.E.; Tender, L.M.; Lovely, D.R. *Science*, **2002**, 295, 483-485. B) Tender, L.M.; Reimers, C.E.; Stecher, H.A.; Holmes, D.E.; Bond, D.R.; Lowry, D.A.; Pilobello, K.; Fertig, S.J.; Lovely, D.R. *Nature Biotechnology*, **2002**, 20, 821-825.

(5) A) Bond, D.R.; Lovely, D.R. *Applied and Environmental Microbiology*, **2003**, 69(3), 1548-1555. B) Finneran, K.T.; Johnsen, C.V.; Lovely, D.R. *International Journal of Systematic and Evolutionary Microbiology*, **2003**, 53, 669-673. C) Chaudhuri, S.K.; Lovely, D.R. *Nature Biotechnology*, **2003**, 21(10), 1229-1232. D) Liu, H.; Logan, B.E. *Environmental Science and Technology*, **2004**, 38(14), 4040-4046. E) Liu, H.; Ramnarayanan, R.; Logan, B.E. *Environmental Science and Technology*, **2004**, 38(7), 2281-2285.

(6) Magnuson, T.S.; Hodges-Myerson, A.L.; Lovely, D.R. FEMS Microbiology Letters, **2000**, 185, 205-211.

INTERCEPTED HYDROLYSIS STRATEGIES FOR BIOMASS REFINERIES

J. Michael Robinson, Jessica Burrow, Robert Caudle, Luis Galvan

Chemistry Department
The University of Texas of the Permian Basin
4901 East University Blvd.
Odessa, TX 79762

Introduction

Massive historical efforts to fractionate biomass into monomeric aldose sugars have not achieved high yields in a commercial manner. Lack of success has been attributed to the very complex nature of various biomass resources, severe conditions required, concomitant degradation reactions, lack of reagent selectivity between biomass components, and commercially impractical reactors. At the heart of the biomass hydrolysis problem is the inherent reactivity of the aldose sugar products required for fermentation into ethanol. Rather than aldoses, products more stable to the hydrolysis conditions had to be considered to solve this hydrolysis problem.

Indeed, recent intercepted hydrolysis strategies that instantaneously convert aldoses into different functional groups have been shown to solve this problem. As shown in Fig 1, conducting either simultaneous reduction, or oxidation, with the hydrolysis allows facile conversion of the incipient aldehyde into either alcohol or acid functional groups, respectively. While useful chemicals are formed directly from such intercepted hydrolyses, chemical reaction processes rather than fermentations are then utilized to produce fuels and other chemicals in a biomass refinery scheme.

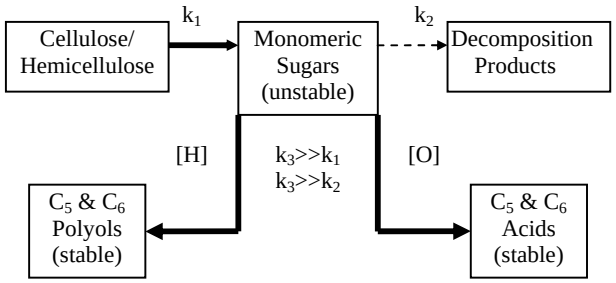

Figure 1. Oxidative and Reductive Intercepted Hydrolysis Strategies

Results and Discussion

Figure 2 illustrates a completely integrated biomass refinery Scheme that uses a reductive intercepted hydrolysis strategy and subsequent chemical reduction processing methods.

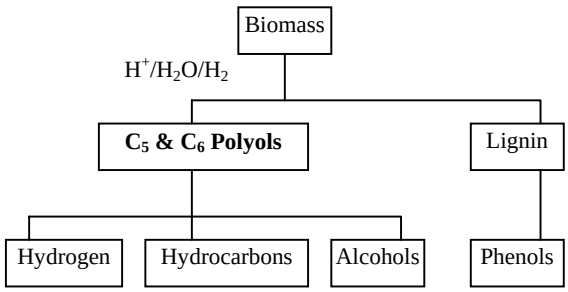

Figure 2. Reductive Intercepted Hydrolysis Scheme

Conducting a "intercepted dilute acid hydrolysis and hydrogenation" (**IDAHH**), provides a solution of polyols (xylitol, sorbitol), rather than aldoses (xylose, glucose), quantitatively fractionated from lignin solids.[1] Conversions approaching the theoretical amounts are obtained with wood sawdust in 3-6 hr at <190 °C with 0.8% H_3PO_4. The dual slopes of the rate of hydrogen consumption shown in Fig. 3 indicate correspond to the easily hydrolyzed hemicellulose versus the slowly reacted crystalline cellulose. With the ideal yield of polyols containing no detectible phenols, this is a remarkably clean fractionation from lignin. Lignin is subsequently converted into phenols.

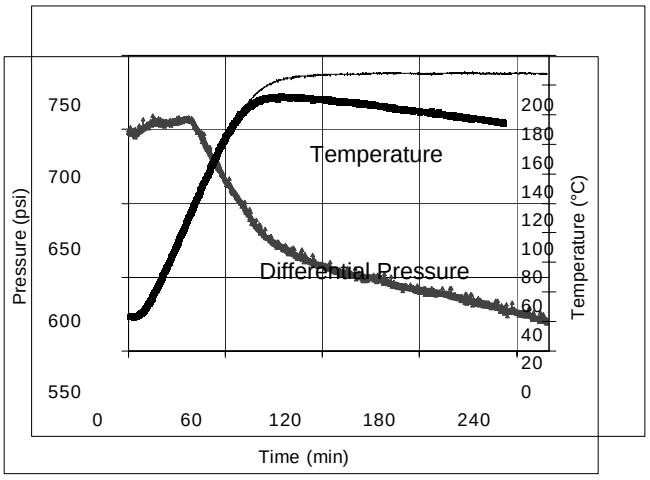

Figure 3. Hydrogen Consumption Curve for Pine Sawdust.

We have established a *chemical* process (Fig. 4) for the production of various hydrocarbon fuels and chemicals from biomass derived polyols.[2,3,4] Polyols are converted into mainly liquid hydrocarbons by reduction with boiling hydriodic acid. Hydrocarbons phase separate and the aqueous acid is recycled. A second step converts remaining halocarbons into alkenes. An electrochemical regeneration of the primary reducing solution provides an economically improved process and is the subject of a new patent application. C_{12} alkenes can be hydrogenated to increase octane rating from 78 to ~83 AKI and hexenes may be hydrogenated to solvent grade hexane for seed oil extraction.

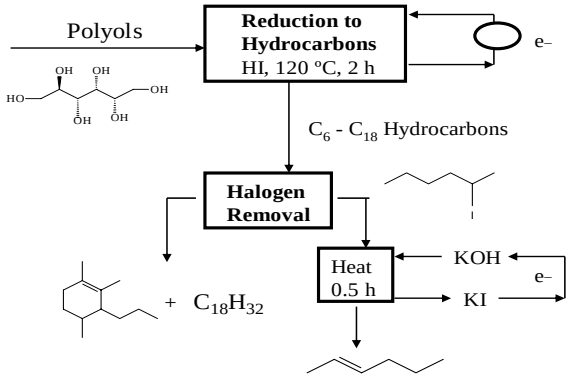

Figure 4. Polyols to Hydrocarbons Process

Polyols are also converted by other means into hydrogen, or small alcohols. Dumesic's process can produce hydrogen from monomeric sugars and the preferred substrate is indeed polyols.[5] Biomass derived hydrogen can perhaps best be used internally in our refinery to initially fractionate biomass and in subsequent reactions as well. Additionally, mixtures of methanol and ethanol can be obtained by catalytic hydrogenolysis using 5% H_2SO_4 and Ru/C at 200 ^oC.[6]

Similarly, a selective oxidation hydrolysis strategy achieves polyhydroxy acids in solution apart from lignin, Fig. 5. Aldonic acids are selectively reduced into high octane oxygenate fuel additives, lactones with 108 and 113 AKI.[7] Polymers and other products may also be produced.

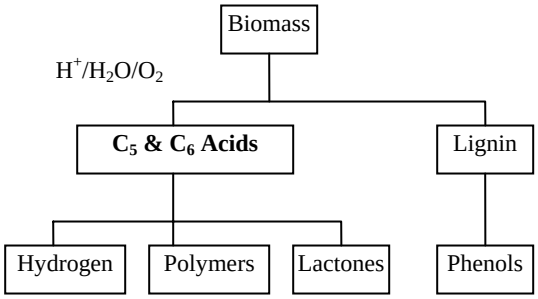

Figure 5. Oxidative Intercepted Hydrolysis Scheme

Polyols and aldonic acids provide alternative "sugar platforms" for biomass conversion to hydrocarbon fuels and solvents, alcohols, lactone fuel additives, hydrogen and other chemicals. Economic estimates from engineering models of these intercepted hydrolysis schemes and products will also be presented.

Acknowledgements

The Robert A. Welch Foundation Chemistry Department Grants, a National Renewable Energy Lab contract, a U.S. Department of Energy Basic Energy Sciences - Advanced Research Projects grant, and the Texas Higher Education Coordinating Board - Advanced Technology Program have supported this research.

References

1. Robinson, J. M.; Burgess, C.E.; Bently, M.A.; Brasher, C.D.; Horne, B.O.; Lillard, D.M.; Macias, J.M.; Mandal, H.M.; Mills, S.C.; O'Hara, K.D.; Pon, J.T.; Raigoza, A.F.; Sanchez, E.H.; Villarreal, J.S. *Biomass and Bioenergy*, **2004,** *26(5),* 473-483.
2. Robinson, J.M.; Burgess, C.E.; Mandal, H.D.; Brasher, C.D.; O'Hara, K.O.; Holland, P.L. *Amer. Chem. Soc. Fuel Chem. Div. Preprints* **1996**, *41(3),* 1090-1094.
3. Robinson, J.M. U.S. Patent 5,516,960, **1996**.
4. Robinson, J.M.; Banuelos, E.B.; Barber, W.C.; Burgess, C.E.; Chau, C.; Chesser, A.A.; Garrett, M.H.; Goodwin CH, Holland PL, Horne BO, Marrufo LD, Mechalke EJ, Rashidi JR, Reynolds BD, Rogers TE, Sanchez, E.H.; Villarreal, J.S. *Amer. Chem. Soc. Fuel Chem. Div. Preprints* **1999**, *44(2),* 224-228.
5. Cortright, R.D.;.Davda, R.R.; Dumesic, J.A. *Nature* **2002,** *418*, 964-967,
6. Abreu, C.A.M.; Lima, N.M.; Zoulalian, A. *Biomass and Bioenergy* **1995**, *9*, 487-492.
7. Robinson, J.M. U.S. Patent pending , **2004**.

MEASURING CELLULASE ACCESSIBILITY OF DILUTE-ACID PRETREATED CORN STOVER

Tina Jeoh, David K. Johnson, William S. Adney and Michael E. Himmel

National Bioenergy Center, National Renewable Energy Laboratory, 1617 Cole Blvd., Golden, CO 80401

Introduction

To enable a new biorefinery industry, lignocellulosic biomass must be cost effectively hydrolyzed to fermentable sugars. Biomass recalcitrance is defined as the natural resistance of this substrate to the action of cellulases and other polysaccharidases. In order to maximize the fermentable sugar stream from corn stover, a dilute-acid pretreatment step has been used traditionally to facilitate enzyme access to the cellulose fraction. A key factor for successful enzymatic digestion of lignocellulosic biomass is providing cellulase enzymes access to the β-(1→4) glycosidic bonds of microcrystalline cellulose. Any effective pretreatment of the biomass feedstock; therefore, must increase accessibility of cellulases to the cellulose fraction in the cell wall microfibrils. The specific physical properties of biomass that are thought to hinder cellulase accessibility include the hemicellulose-containing microfibril sheath[1] and the lignin rich[2] structures in the cell wall.

Trichoderma reesei Cel7A, a cellobiohydrolase that is extremely efficient on crystalline cellulose, is the "workhorse" of the *Trichoderma* cellulase system, constituting 60% of the cellulase protein secreted by the fungus. In this study, we report the effectiveness of dilute-acid pretreatment of corn stover on improving accessibility to cellulases using fluorescence-labeled, purified *T. reesei* Cel7A as a probe.

Experimental

Substrate preparation. The samples used in this study were produced from corn stover collected from Pioneer 34M95 maize harvested in Colorado in 2002. Corn stover aliquots were subjected to thermal chemical pretreatment in NREL PDU's pilot-scale vertical reactor using a fixed residence time of approximately 1 min at temperatures ranging from 180-200ºC; solid loadings between 20-35% (w/w); and acid loadings of 0.03-0.06 g acid/g dry biomass. The pretreated corn stover samples used in this study were provided by Dan Schell (NREL). Raw corn stover was Wiley-milled to 200 mesh and hydrated with 5 mM sodium acetate buffer, pH 5.8 under vacuum. Sodium azide (0.2%) was added after re-hydration. Pretreated corn stover (PCS) samples were washed repeatedly with several exchanges of distilled water and stored in 5 mM sodium acetate, pH 5.0 with 0.2% sodium azide. The concentrations of the PCS suspensions were established by determination of oven-dry weights on triplicate 1.0 mL samples.

Enzyme Preparation. *T. reesei* Cel7A was purified from Spezyme CP (Genencor International) by the following procedure. Spezyme CP was loaded onto a Resource Q anion exchange column (Amersham Biosciences) and eluted with a linear gradient of 0 to 1.0 M NaCl in 20 mM BisTris, pH 5.8. The fractions with activity on *p*-nitrophenyl-β-D-lactopyranoside (*p*NPL) were pooled, concentrated in an Amicon concentrator with a PM-10 membrane (Millipore), spiked to a final concentration of 1 mM gluconolactone, and loaded on a *p*-aminophenyl-β-D-cellobioside (*p*APC) affinity column[3]. Bound protein was eluted as a major peak (indicated by absorbance at 280 nm) with 10 mM cellobiose in 100 mM sodium acetate buffer with 1 mM gluconolactone (pH 5.0). When applied to SDS-PAGE, an aliquot from the chromatographic peak yielded two bands, one corresponding to Cel7A and the other to a higher mobility band corresponding to the molecular weight (MW) of the catalytic domain. The unbound fraction and the wash fractions were concentrated and examined by SDS-PAGE, which indicated the presence of a band corresponding to Cel7A. All fractions containing Cel7A were pooled, spiked with a final concentration of 1.0 M ammonium sulfate, and loaded on a HiLoad 16/10 phenyl-sepharose hydrophobic interaction column (Amersham Biosciences). The bound protein was eluted with a linear ammonium sulfate gradient decreasing from 1.0 M to 0 M in 20 mM BisTris buffer, pH 5.8. Fractions with activity on *p*NPL were pooled and concentrated. On SDS-PAGE gel, the concentrated protein solution showed a single band with MW corresponding to *T. reesei* Cel7A. Cel7A was labeled with Alexa Fluor 594 succinimidyl esters (Invitrogen) according to the manufacturer's recommended protocol.

Cellulase accessibility experiments. Cellulose accessibility of the raw and pretreated corn stover samples was determined with purified, Alexa Fluor 594 labeled *T. reesei* Cel7A. The experiments were conducted in triplicates, with each sample containing 1.0 μM *T. reesei* Cel7A and PCS concentration equivalent to 1.0 mg/mL final cellulose concentration. Final reaction volume was 250 μL in 5 mM sodium acetate (pH 5.0). The reactions were conducted at 38ºC, rotating end-over-end and assayed at 1, 4, 24, 48 and 120 hours. For select samples, 5-minute reactions were conducted in a 38ºC water bath and agitated manually for the duration of the reactions. Enzyme and substrate used in the 5-minute reactions were pre-incubated at 38ºC for a minimum of 30 minutes. Each reaction was initiated with the addition of the enzyme and terminated by filtration through 1.0 μm glass fiber filters in a 96-well vacuum filter manifold (Innovative Microplate). The reaction supernatant was assayed for reducing sugars using the BCA method[4] against a cellobiose standard curve. The bound enzyme fraction was assayed by fluorometry as described previously[5]. The solid fraction retained in the filter was re-suspended with 250 μL distilled water and transferred to a 96-well microtiter plate. A set of *T. reesei* Cel7A standards was included with each microtiter plate for the standard curve. PCS was added to the wells with Cel7A standards to match the reaction samples. The plates were read in a FLUOstar OPTIMA (BMG Labtechnologies) plate reader at excitation/emission wavelengths of 584/612 nm.

Results and Discussion

The range of pretreatment conditions applied to this set of corn stover samples resulted in the removal of 67 - 97 % xylan, with higher xylan removal resulting from higher pretreatment severities. Up to about 85 % xylan removal, there was a strong correlation between the cellulose conversion after 5 days of incubation with *T. reesei* Cel7A and the extent of xylan removal (Fig. 1).

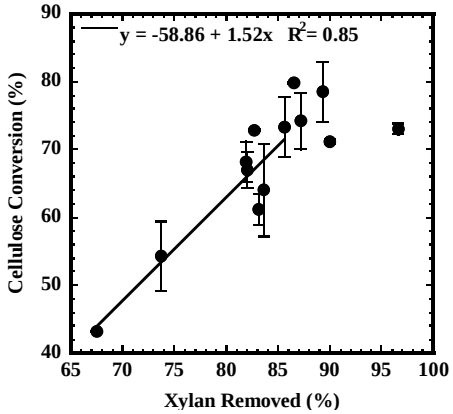

Figure 1. PCS cellulose conversion at 120-hours with respect to xylan removal.

The data in Fig. 1 suggests that removing up to 85 % of the xylan facilitates cellulase access to the cellulose fraction in corn stover. To study this further, bound enzyme concentrations were measured over the hydrolysis time course. At 1-hour, we observed higher bound Cel7A concentrations for PCS samples with higher extents of xylan removal (Fig. 2), indicating that removal of xylan from the biomass does indeed allow more cellulases to adsorb.

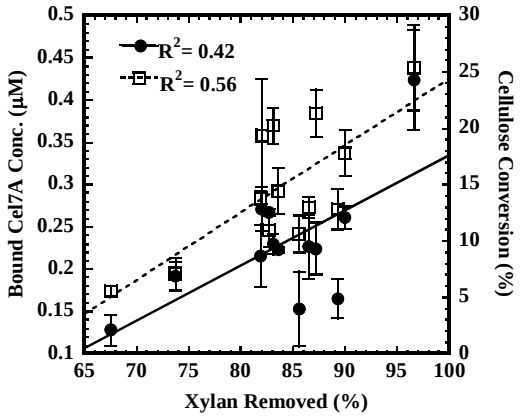

Figure 2. Concentration of Cel7A bound to PCS and cellulose conversion after 1-hour incubation at 38°C. (●) bound Cel7A concentrations, (□) cellulose conversion.

Furthermore, higher concentrations of adsorbed Cel7A facilitated higher cellulose conversions (Fig. 2).

The question of the effect of diffusion through the biomass matrix by Cel7A was studied by measuring the bound enzyme concentration after incubation for 5 minutes on select samples. Logistically, five minutes was the shortest reaction time possible to obtain reliable data. As shown in Fig. 3, the concentration of bound Cel7A did not change significantly from 5-minutes to 1-hour.

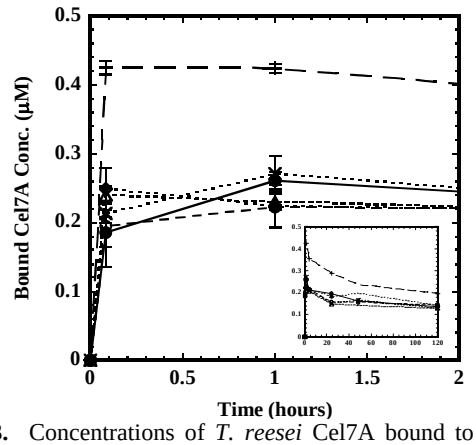

Figure 3. Concentrations of *T. reesei* Cel7A bound to PCS at 5-minutes and 1-hour. Inset shows data for 120-hour reaction period for the same sample set. Samples shown have 82 - 97 % xylan removed. Lines are drawn only to guide the eye.

The inset graph in Fig. 3 also shows that the bound concentrations decreased with reaction time over the full 5-day reaction period. The data therefore suggests that the maximum possible bound cellulase concentration is achieved rapidly and access to cellulose by the enzyme is not limited by diffusion.

The lignin component in biomass is often cited as decreasing the effective cellulase concentration in the system by acting as an adsorbent[6]. The raw corn stover samples contained 11.4% lignin on a dry weight basis. As the dilute-acid pretreatment did not remove any lignin, with the loss of the hemicellulose fraction, final lignin content of the PCS samples was in the range of 29-38%. After 120-hours incubation with Cel7A, 43-78% of the cellulose was hydrolyzed. Yet, in most of the samples, less than 15 % of the total cellulase remained bound by the end of the reaction (Fig. 4).

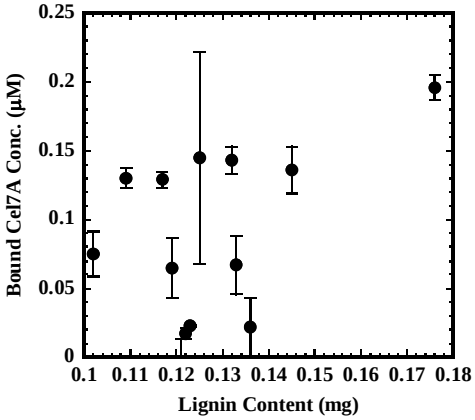

Figure 4. Concentration of Cel7A bound to PCS at 120-hours with respect to the amount of lignin in the reactions (Total Cel7A concentration in each reaction was 1.0 μM).

Furthermore, no correlation was observed between the amount of lignin present in the reactions and the concentration of bound Cel7A at 120-hours. This result supports a previous observation where the activity of *T. reesei* cellulases on pure cellulosic substrates was not inhibited by the addition of a lignin-rich biomass residue[7].

Conclusions

It is known that the extent of xylan removal from corn stover by dilute-acid pretreatment increases with higher severities, with minimal change in the amount of lignin. The effect of these changes on the accessibility of the cellulose fraction to cellulases was examined and our results indicated that cellulase-cellulose interactions were enhanced by this pretreatment. Higher extents of xylan removal resulted in greater cellulase adsorption and higher overall cellulose conversions. Adsorption of Cel7A was not diffusion-limited. Furthermore, *T. reesei* Cel7A appears to have a low affinity to lignin, thus biomass recalcitrance in this case is most likely not due to loss of this cellulase via adsorption to lignin.

Acknowledgement. The authors wish to thank the US DOE Office of the Biomass Program for funding this work.

References

(1) Irwin, D. C.; Cheng, M.; Xiang, B. S.; Rose, J. K. C.; Wilson, D. B., *European Journal of Biochemistry*, **2003,** *270*(14), 3083-91.
(2) Kim, T. H.; Kim, J. S.; Sunwoo, C.; Lee, Y. Y., *Bioresource Technology*, **2003,** *90*(1), 39-47.
(3) Sangseethong, K.; Penner, M. H., *Carbohydrate Research*, **1998,** *314*(3), 245-50.
(4) Kongruang, S.; Han, M. J.; Breton, C. I. G.; Penner, M. H., *Applied Biochemistry and Biotechnology*, **2004,** *113-16*, 213-31.
(5) Jeoh, T.; Wilson, D. B.; Walker, L. P., *Biotechnology Progress*, **2002,** *18*(4), 760-9.
(6) Converse, A. O.; Ooshima, H.; Burns, D. S., *Applied Biochemistry and Biotechnology*, **1990,** *24-5*, 67-73.
(7) Meunier-Goddik, L.; Penner, M. H., *Journal of Agricultural and Food Chemistry*, **1999,** *47*(1), 346-51.

MEASUREMENT OF POROSITY IN DILUTE ACID PRETREATED CORN STOVER

Claudia Ishizawa, Mark Davis and David K. Johnson

National Renewable Energy Laboratory
1617 Cole Blvd., Golden, CO 80401-3393

Introduction

Pretreatment has been established as an essential process to increase the susceptibility of lignocellulosic materials to the action of cellulolytic enzymes. The degree of chemical and/or physical modification of the substrate varies with the source and type of feedstock, as well as with the pretreatment conditions. Pretreatment can alter the structure, composition, surface and reactivity of biomass. Considerable interest exists in developing fast and reliable methods to measure these properties and to correlate them with the performance of the material during enzymatic hydrolysis.

Several workers have found good correlations between porosity and the enzymatic digestibility of cellulose in pretreated biomass[1,2]. However, the characterization tools commonly used on porous materials, i.e., electron microscopy, gas adsorption, and mercury porosimetry, are not useful on biomass because they require dry samples and drying frequently causes collapse of the pore structure. Attempts to prepare dry fibers with undamaged pores have not met with great success. From the literature, two methods for wet-fiber characterization were identified: the solute exclusion technique[3] and thermoporosity by NMR[4]. In this work, the applicability of these methods to the study of corn stover after dilute sulfuric acid pretreatment was evaluated.

Experimental

Pretreated Corn Stover. The samples used in this study were produced from corn stover collected from Pioneer 34M95 maize harvested in Colorado in 2002. The corn stover was subjected to dilute acid pretreatment in NREL PDU's pilot-scale vertical reactor using a fixed residence time of approximately 1 min at temperatures ranging from 180-200ºC; solid loadings between 20-35% (w/w); and acid loadings of 0.03-0.06 g acid/g dry biomass. The compositions, cellulose enzymatic digestibilities, and ethanol yields potentials for these samples was measured previously. Following pretreatment, samples were stored at 4ºC and pH~1. Prior to use, the samples were thoroughly washed with distilled water until the wash was colorless and neutral in pH. After the last washing the samples were filtered into a press cake of approximately 20% (w/w) solids. The pretreated corn stover samples were provided by Dan Schell (NREL).

Solute exclusion method. The accessible pore volumes of ToyoPearls (commercial chromatographic resins), unpretreated corn stover, and pretreated corn stover were determined by the solute exclusion technique of Stone and Scallan[3]. This technique measures the accessible pore volume in water-swollen materials using a series of molecules of known molecular size (molecular probes).

A series of dextrans (obtained from Serva Electrophoresis GmbH), polyethylene glycols (from Sigma-Aldrich and JT Baker), and analytical grade glucose were selected as probe molecules. About 1.0 g of ToyoPearl or 0.5 g of corn stover was weighed into a tared plastic snap cap centrifuge tube, and 1 g of 1.0% (w/v) probe solution was added. The tubes were periodically hand shaken for about 30 s during 2-3 h. After this time, the solution was filtered using a 0.45µm nylon filter, transferred, and then sealed into HPLC vials for analysis. The solids were washed and dried at 105ºC to determine dry solid weights. Three replicate samples were prepared for each solution. A distilled water blank was prepared for each pretreated corn stover.

The concentration of molecular probe in the filtered liquids was measured using an Agilent 1100 HPLC equipped with a refractive index detector. The HPLC was run without a column and with a simple union fitting between the injector and the detector. The eluent was nanopure water at a flow rate of 0.4 ml/min. The injection volume was 10 µl and analyses were repeated 4-5 times for each sample.

The inaccessible water expressed as milliliters of water per gram of dry substrate, can be calculated using the following equation[1]

$$d_i = \left(\frac{W+q}{p}\right) - \left(\frac{W}{p}\cdot\frac{C_i}{C_f}\right)$$

where d_i is the inaccessible water (ml/g) for solute of size i; W is the mass of solution; q is the mass of water in sample of solids; p is the dry mass of the sample; C_i is the initial solute concentration; and C_f is the final solute concentration.

The accessible pore volume (A_i) for a solute of size i is given by

$$A_i = d_{560} - d_i$$

where d_{560} represents the total water volume in the substrate.

Thermoporosity. This method uses the changes in the physical properties of a liquid when it is confined within small pores. In particular, the melting temperature of the liquid is depressed and related to the pore distribution through the Gibbs-Thompson equation[4]

$$\Delta T = \frac{K}{r}$$

where ΔT is the melting point depression of the liquid; K is a constant depending on the characteristics of the material; and r is the pore dimension.

Two techniques have been extensively used to observe the freezing-melting behavior of water in confined pores: differential scanning calorimetry (DSC) and nuclear magnetic resonance (NMR). DSC measures the heat transfer, whereas NMR records the fractions of frozen and unfrozen liquid as a function of temperature.

In this study, we report results obtained using NMR spectroscopy. The ^{1}H NMR experiments were conducted with a Varian Unity 300 MHz (7.0T) spectrometer. The spectra were collected using a $\pi/3$ pulse and a 5s recycle delay. For each experiment, approximately 0.8-1.2 g of undried corn stover was introduced into a 10mm NMR tube. The sample was cooled to 230K and then the NMR signal of the unfrozen water was recorded at intervals of 10K until 285K was reached. Samples were allowed to equilibrate for 5-8 minutes at each temperature. At 285K, the signal is directly proportional to the total amount of water in the sample, and at temperatures below 273K, the signal is proportional to the weight of unfrozen water. The pore volume per g of biomass was then calculated by dividing the signal at lower temperatures by the signal at 285, multiplying by the total weight of water in the sample, and dividing by the dry weight of the sample.

Results and Discussion

The solute exlusion method was validated before it was applied to the measurement of the porosity of pretreated biomass samples. Four different chromatographic resins of known porosity were selected as standards. The particle sizes and pore sizes of the ToyoPearl resins are summarized in Table 1.

Table 1. PROPERTIES OF TOYOPEARL RESINS*

ToyoPearl	Particle size (µm)	Pore size (Å)
HW-40S	20-40	50
HW-40C	50-100	50
HW-50F	30-60	125
HW-55S	20-40	500

*from the manufacturer

In Figure 1, the accessible pore volume and the pore size distribution curves for the ToyoPearl resins are shown. The error bars indicate the magnitude of one standard deviation of the volume accessible to individual probes, from 3 measurements in each case.

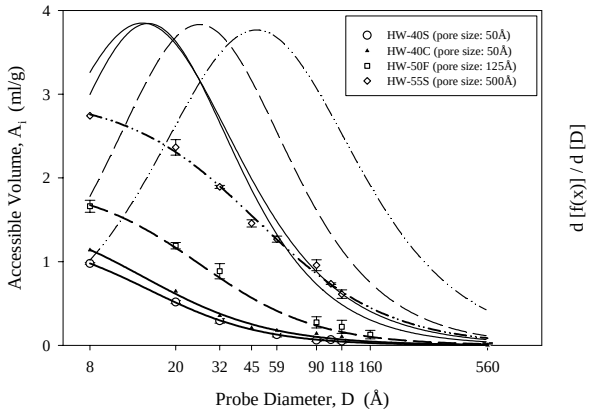

Figure 1. Accessible pore volume and pore size distribution curves for ToyoPearl resins.

From the results, it is easy to distinguish between the different pore size resins. Two resins had the same pore size distributions but different particle size, and we can observe that the measurements are not affected by the particle size.

After testing and verifying the solute exclusion method with the ToyoPearl resins, the same conditions were used to determine the porosity of pretreated corn stover. Figure 2 shows data from the measurement of accessible pore volume in pretreated corn stover compared to the accessible pore volume in unpretreated corn stover.

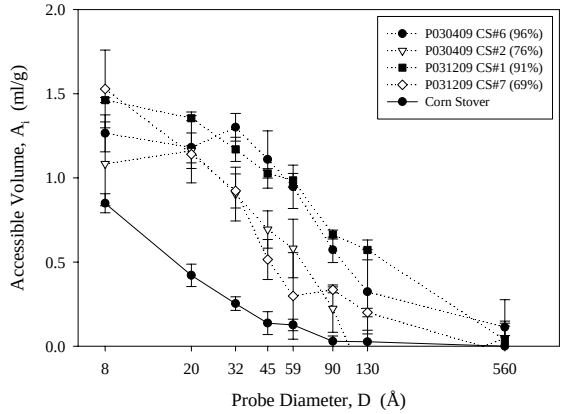

Figure 2. Accessible pore volume of unpretreated corn stover and pretreated corn stover. Ethanol yield are indicated in parenthesis.

The results show that there is significantly less accessible pore volume in the unpretreated corn stover compared to that in the acid pretreated samples, in particular in the range from 10 to 100 Å. However, it is clear that the differences in accessible pore volume in the selected pretreated samples cannot be detected because of the poor reproducibility of the measurements. The variability of the measurements is higher with the pretreated corn stover samples than with the Toyopearl resins; an explanation for this can be the higher level of heterogeneity in the pretreated corn stover.

Typically the effectiveness of a pretreatment is judged by the level of hemicellulose hydrolysis or more simply by the extent of xylan removal. High levels of xylan removal normally indicate effective pretreatment and that the cellulose will be relatively easily saccharified using cellulase enzymes. The solute exclusion method showed differences in the accessible pore volume between the unpretreated and the pretreated corn stover, but only very small differences were observed amongst the pretreated samples that gave from 70 to 96% ethanol yields. A poor correlation was found between the accessible volume and cellulose digestibility.

NMR thermoporometry represented an alternative method to measure the total pore volume in the range of 20 to 200Å. Using the Gibbs-Thompson equation a relationship between temperature and pore size can be established. It was found that a melting temperature for water of 240 K corresponds to a pore size of 20 Å, whereas 270 K corresponds to 200 Å. In Figure 3, the intensity vs. inverse of temperature (IT) curve for unpretreated and four pretreated corn stover samples, and water are shown.

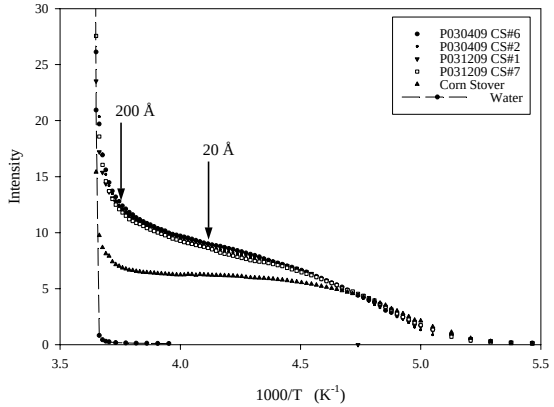

Figure 3. IT-curve for unpretreated and pretreated corn stover, and water.

The curves exhibit similar results to those obtained with the solute exclusion method. All pretreated samples showed a larger porous structure than the starting corn stover material. However, no significant difference was found between the pretreated corn stover samples that produced different ethanol yields.

Conclusions

The solute exclusion method was successfully validated with four standards of different pore size distribution. However, when the method was used on corn stover, only differences in the accessible pore volume between unpretreated and pretreated corn stover can be detected. Only small differences were observed amongst the pretreated samples that gave ethanol yields ranging from 70 to 96%, and a poor correlation was found between the accessible volume and cellulose digestibility. NMR thermoporosity measurements were also unable to detect significant differences in the porosity of unpretreated and pretreated corn stover in the range of 20-200Å, even though this technique was more reproducible than the solute exclusion method.

Acknowledgement. The authors wish to thank the US DOE, Office of Biomass Programs, for funding this work.

References

(1) Grethlein, H. E.; Allen, D. C.; Converse, A. O. *Biotecnol. Bioeng.* **1984**, *26*, 1498.
(2) Grethlein, H. E. *Biotechnology* **1985**, *3*, 155.
(3) Stone, J. E.; Scallan, A. A. *Cellul.Chem. Technol.* **1968**, *2*, 343.
(4) Hansen, E. W.; Schmidt, R.; Stöcker, M. *J. Phys. Chem.* **1996**, *100*, 11396.

HIGH TEMPERATURE CONCENTRATED ACID HYDROLYSIS KINETICS OF PRETREATED PINE SAWDUST USING A CO-ROTATING TWIN-SCREW EXTRUDER

W. Scott Miller and Roger D. Hester

School of Polymers and High Performance Materials
The University of Southern Mississippi
Hattiesburg, MS 39406

Introduction

Very limited kinetic data exist on high-temperature concentrated acid hydrolysis of lignocellulosic materials. Most kinetic data published have been for lignocellulosic hydrolysis using dilute acid. In 1945 Saeman showed that the dilute acid saccharification of wood involves essentially two consecutive first-order reactions, cellulose to glucose and glucose to decomposition products[1].

Saeman was able to successfully model dilute acid hydrolysis of a number of wood species following this approach; however, he did make the observation that the experimental data indicated that there were in fact two reactions involved in the formation of glucose. The first, which was significantly faster than the second, was attributed to the "easily" hydrolysable fraction of cellulose. The second reaction involved the slower reaction of "difficult" to hydrolyze crystalline cellulose. The exact origin of the easy cellulose was not identified but was estimated to be roughly 10 % of the total theoretical glucose. Recent research has indicated that the origin of the easily hydrolysable cellulose is attributed to the amorphous regions of the cellulose[2]. The degree of amorphous regions available for hydrolysis within the cellulose can be significantly increased with pretreatment of the lignocellulosic material.

In 1985 Harris and co-workers published a more complete dilute acid model for cellulose hydrolysis[3]. This model contained reaction kinetics for seven different reactants and products: cellulose, glucose, levoglucosan, disaccharides, glucosides, and decomposition products. Most importantly, the cellulose was broken into two fractions, an easily hydrolysable fraction and difficult to hydrolyze cellulose fraction.

The Harris model assumed a 10 % easily hydrolysable fraction and achieved an excellent fit to experimental data. However, due to the assumptions made and the large number of differential equations used, it is difficult to determine with confidence, the magnitude of each rate constant. The purpose of this paper is to highlight a recent high-temperature, acid-hydrolysis kinetic study of southern yellow pine sawdust that was pretreated with concentrated acid using a co-rotating twin-screw extruder reactor (TSR).

Experimental

Sample Generation. The lignocellulosic material used was southern yellow pine sawdust, obtained from a particleboard plant located in the southeastern United States. Sieve shaker studies determined that the average sawdust size distribution was 4.5 % 40/45 mesh, 18.0 % 45/50 mesh, 17.1 % 50/60 mesh, 44.3 % 60/100 mesh, and 15.3 % 100 plus mesh. Following NREL laboratory analytical procedures it was determined that the material had an average moisture of 10 wt. % and composition of 34.3 wt. % cellulose on a dry sawdust basis[4].

Before high temperature acid hydrolysis the sawdust was pretreated by vibrationally feeding 4 g/min. of "wet" material into the TSR over one minute time intervals. The sawdust was then thoroughly mixed within the TSR with one part "wet" sawdust to 0.8 parts sulfuric acid. The acid was injected into the TSR as a 70 wt. % aqueous solution. The barrel temperature of the TSR was set at 60 °C. Orifices, having a 1/8" inside diameters, were placed at the exit of the TSR to achieve an average TSR exit pressure of 780 psi. The above TSR conditions were chosen from previous design-of-experiments approach that defined the capacity and strength limitations of the current equipment employed[5]. The pretreated lignocellulosic paste leaving the TSR had a Bingham type material rheology with a yield stress of 31,000 dyn/cm^2 and an apparent viscosity of 3,700 poise.

The extruder screws and barrel were fabricated at our machine shop from an acid resistant stainless steel alloy, AL6XN (Carpenter Technology Corp., Reading, Pennsylvania). Each 24-inch long screw had a 0.865 inch outside diameter with flights that produced a pitch of 0.438 inches. The trapezoidal flights had a tip width of 0.190 inches and a channel depth of 0.120 inches. The distance between screw centers was 0.75 inches. This design provided for complete screw intermeshing with an open passage between screws of about 30 %. The void volume within the 24 inch-long extruder available for material transport was 103 cm^3. Under the operating conditions used to generate the pretreated lignocellulosic material, roughly 79 % of the usable TSR void volume was filled with packed extrudate, producing about 10 minutes of material residence time within the TSR.

This amount of residence time allowed the sawdust to undergo significant particle size reduction and solubilization as a result of the high shear, high temperature, and high acid concentration environment. Upon exiting the TSR, 38.2 % of the dry sawdust solids were liquefied and capable of passing through a 15 micron filtering crucible. Of the 0.343 grams per dry gram of sawdust available for glucan production, 12.1 % was solubilized in the form of glucose. Application of NREL laboratory procedures showed that of the 38.2 % of dry sawdust solids that were liquefied, a total of 0.152 grams, or 44.2 % of the available glucan, was present in the form of glucose and soluble low molecular weight polysaccharides or oligomers.

Kinetic Analysis. The generated extrudate paste was mixed with water to achieve the acid concentration desired. The mixture was then placed in a custom fabricated 9.5" long zirconium reactor with an outside diameter of 0.50" and an interior diameter of 0.25". The reactor was sealed with threaded zirconium caps utilizing FETFE® O-Rings (Ace Glass, Vineland, NJ). The reactor was then placed in a heated oil bath for a specified time. Following the high temperature hydrolysis reaction the reactor was immediately placed in an ice bath for cooling. The resulting product was then diluted and prepared following NREL laboratory procedures for high pressure liquid chromatography (HPLC) compositional analysis[4].

Five different acid concentrations were prepared which ranged from 5 to 30 wt. % acid. These solutions were subjected to high temperature acid hydrolysis at 110, 120, and 130 °C with six time intervals collected at each combination of temperature and acid concentration. The experimental design resulted in seven unique sets of data having six data points each. Each experimental condition was replicated once.

Results and Discussion

To provide a more reliable model for our system, we have been able to achieve an analytically derived equation of glucose concentration as a function of time, acid concentration and temperature by incorporating the easy and difficult cellulose fractions into Saeman's model. The reaction scheme used is as follows:

where k_E is the easily hydrolysable cellulose fraction rate constant, k_0 is the difficult cellulose fraction rate constant and kg is the decomposition products rate constant.

Previous laboratory analysis of our pretreated TSR paste material indicated that the fraction of "easily" hydrolysable cellulose was much greater than 10 % of the theoretical total. NREL laboratory analyses indicated that roughly 44 % of the cellulose material exiting the TSR was in the form of glucose and solubilized low molecular weight polysaccharides which were capable of passing through a 15 micron filter. The fact that the material is solubilized indicates that at least 44 % must be easily hydrolysable. To take into account any other easily hydrolysable material that was not necessarily solubilized, we conducted the following analysis.

Research by Saeman and Harris et. al. has demonstrated that k_0 and kg are similar in magnitude and that k_E is much greater than both k_0 and kg. Following this assumption it can be said that nearly all glucose formed from cellulose in the early stages of a hydrolysis reaction results from the easily hydrolysable fraction. Thus, at the start of high temperature acid hydrolysis the following expression can be used as an approximation:

$$G \cong G_0 + E_0(1-\exp(-k_E t)) \qquad \text{Equation 1}$$

where G is the glucose concentration, G_0 is the initial glucose concentration, E_0 is the initial concentration of easily hydrolysable cellulose, k_E is the easily hydrolysable cellulose rate constant, and t is the time. In all expressions the concentrations are in moles/liter and the time is in minutes.

Using data collected at 110 °C and 7.82 wt. % acid hydrolysis conditions, it was then possible to do a nonlinear regression analysis of the first four data points to determine the two unknowns, E_0 and k_E, in Equation 1. From the two data sets, the resulting analysis yielded an average k_E and easily hydrolysable cellulose fraction, E_0, of 50 %. As expected, the fraction of easily hydrolysable cellulose was slightly higher than the amount of solubilized material (44 %) that had passed through the 15 micron filter.

The set of three differential equations representing the reaction of easily hydrolysable cellulose, difficult to hydrolyze cellulose and decomposition products can be simultaneously solved to give the following:

$$G = (k_E*E_0)/(kg - k_E)(1/(\exp(k_E*t)) - 1/(\exp(kg*t)))$$
$$+ (k_0*H_0)/(kg - k_0)(1/(\exp(k_0*t)) - 1/(\exp(kg*t)))$$
$$+ G_0/(\exp(kg*t)) \qquad \text{Equation 2}$$

where G is glucose concentration, k_0 is the difficult to hydrolyze cellulose rate constant, E_0 is the concentration of easily hydrolysable cellulose, kg is the rate constant of decomposition products formation, H_0 is the concentration of difficult to hydrolyze cellulose, G_0 is the initial concentration of glucose and t is the reaction time.

At the same hydrolysis condition used to determine E_0, Equation 2 has only two unknowns, k_0 and kg, because k_E has been determined. Using all of the glucose concentrations versus time data at 7.82 wt. % acid and 110 °C, nonlinear regression was used to find both k_0 and kg. Subsequent division of k_E by k_0 at each replication of the experimental condition produces an average multiplication factor of 50, i.e., $k_E = 50\ k_0$. This is the same relationship that Harris used in his research. Assuming that this relationship holds true at each hydrolysis condition, it is then possible to conduct nonlinear regression of Equation 2 to find k_0 and kg values at each of the remaining six reaction conditions.

Research conducted by Saeman used the following relationship for the dependence of a rate constant on acid concentration and temperature:

$$k = A(C_{acid})^B \exp(-E/RT) \qquad \text{Equation 3}$$

where k is a rate constant, A and B are constants, C_{acid} is the acid molar concentration, E is the activation energy in calories, R is the gas constant and T is the absolute temperature.

After transforming Equation 3 into logarithmic space, multiple linear regression was used to estimate k_0 and kg. This approach, as functions of temperature and acid concentration, produced the following reaction rate expressions:

$$k_0 = 4.779*10^7(C_{acid})^{1.032}(\exp(-18{,}180/(RT))) \qquad \text{Equation 4}$$

$$kg = 1.877*10^8(C_{acid})^{1.728}(\exp(-18{,}830/(RT))) \qquad \text{Equation 5}$$

where C_{acid} is the acid molar concentration, R is the gas constant, T is the absolute temperature, k_0 is the rate constant in minutes for the difficult to hydrolyze cellulose and kg is the rate constant in minutes for decomposition products. The rate constant for k_E is simply $50*k_0$.

Conclusions

Southern yellow pine sawdust is one of the most difficult lignocellulosic materials from which to extract the potential glucose present. Utilizing the TSR pretreatment technique it has been possible to obtain a significant quantity of glucose and low molecular weight polysaccharides, roughly 50 %, before high temperature acid hydrolysis begins. Application of the kinetic rate constants obtained from the static batch reactor hydrolysis studies described above demonstrates that more than 55 % of the theoretical glucose available in the pine sawdust can be obtained in a short reaction time, less than 20 minutes.

Application of this technology for the production of sugars for fermentation to ethanol shows great promise. However, from these studies it has been demonstrated that high glucose yields using short reaction times is dependent upon forming as much easily hydrolysable cellulose as possible in the pretreatment step. Future studies will explore continuous high-temperature, acid-hydrolysis kinetics and further optimization of the easily hydrolysable cellulose fraction obtained in the TSR pretreatment process.

Acknowledgement.

The authors wish to thank the Department of Energy EPSCoR program for funding, Derek Jacobs for laboratory assistance, and Jim Bridges and Steve Selph for TSR fabrication.

References

1. Saeman, J. F. *Industrial and Engineering Chemistry* **1945**, *37*, 43-52.
2. Ladisch, M. R. In *Biomass Handbook*; Kitani, O.; Hall, C., Eds.; Gordon and Breach Science Publishers: New York, 1989; pp 434-451.
3. Conner, A. H.; Wood, B. F.; Hill, C. G.; Harris, J. F. *Journal of Wood Chemistry and Technology* **1985**, *5*, 461-489.
4. Sluiter, A.; National Renewable Energy Laboratory, 2004; Vol. 2004.
5. Miller, W. S.; Hester, R. D. *Chemical Engineering Communications,* Submitted **2005**.

OPPORTUNITES FOR BIORENEWABLES IN OIL REFINERIES

T.L. Marker, J. Petri, T. Kalnes, M. McCall, D. Mackowiak
UOP LLC
28 East Algonquin Road
Des Plaines ,IL 60017

Doug Elliott
Pacific Northwest National Lab
902 Battelle Boulevard
Richland,WA 99352

Stefan Czernik
National Renewable Energy Laboratory
1617 Cole Blvd
Golden CO 80401

Prof David Shonnard
Michigan Technological University
1400 Townsend Drive
Houghton, MI 49931

Introduction

Although bio-fuel production has been expanding worldwide, so far there has been little integration with petroleum refineries. The segregation of bio-fuels increases the cost of bio-fuels use, since existing infrastructure for fuels distribution and production is not utilized. Bio-fuels could play a stronger role in reducing U.S. dependence on foreign oil if economical blending or coprocessing options could be developed in traditional oil refineries. This study identified some economically attractive opportunities for biofuel coprocessing, blending, and integration into typical oil refineries and defined areas where additional research is needed. A variety of biofuel feed types were evaluated as refinery feedstocks, including vegetable oils and greases, pyrolysis bio-oils and crude Fischer Tropsch liquids.

Key parts of the project included modeling, scoping experiments, cost estimates and economics. Economics were based on $ 40/bbl crude in a typical 150,000 bbl/d refinery, and sensitivities to higher crude prices of $ 50/bbl and $ 60/bbl were included. Life cycle analyses of key processes were compared, as well as opportunities for use of biorenewables to reduce refinery CO2 production.

Table 1. Costs of Biorenewable Feedstocks

Potential Bio Feedstock	$ /bbl
Pyrolysis Oil	16
Crude Tall Oil	16
Brown Grease	21
Yellow Grease	40
Inedible Tallow	41
Jatropha Oil (India)	43
Palm Oil (Malaysia)	46
Soybean Oil	73
Rapeseed Oil	78

Experiments and Modeling

Properties of key feedstocks analyzed are shown in Table 2.

Table 2. Typical Properties of Biorenewables

	Crude	Resid	Soy oil	Yellow Grease	Pyrolysis Oil
%C	83-86	84.9	77.6	76.4	56.2
%H	11-14	10.6	11.7	11.6	6.6
%S	0-4	4.2	.0006	.04	-
%N	0-1	.3	.0011	.03	.3
%O	-	-	10.4	12.1	36.9
H/C	1.8-1.9	1.5	1.8	1.8	1.4
Density	.86avg	1.05	.92	.89	1.23
Tan #	<1	<1	2	30	78
ppm alkali metals	60	6	100	100	100
Heating Value BTU/lb	18,000	17,500	16,000	16,000	6560

The primary goal of the project was to look at economics of processing a variety of biorenewable feedstocks at petroleum refineries; only experiments that were needed to complete the economics were conducted. Proof of principle experiments were completed in:

1. cracking vegetable oils and grease in an FCC to make green gasoline and green olefins;
2. hydrotreating vegetable oil, grease and tall oil to make green diesel;
3. hydrocracking and FCC cracking of hydrotreated pyrolytic lignin to make gasoline;
4. blending pyrolysis oil and lignin with VGO and LCO.

Results and Discussion

When added to the FCC, vegetable oil readily cracks to make gasoline and olefins and makes less LCO and CSO when compared to a typical VGO feed. Green diesel, produced by hydrotreating vegetable oil and grease, can be made under typical diesel hydrotreating conditions from a variety of feedstocks, including high free fatty acid material. Green diesel requires no methanol feed and produces extremely high cetane material.

Pyrolytic lignin, which is the water insoluble fraction of pyrolysis oil, can be hydrotreated and cracked to make gasoline and diesel at conditions that minimize hydrogen requirements. The water soluble fraction of the pyrolysis oil can be reformed to make hydrogen; thereby, providing a biorenewable substitute for expensive natural gas typically used to make hydrogen in refineries.

The economics of various processing routes were compared for a variety of feedstocks. Vegetable oils and grease economics are shown in figures 1, 2, and 3. Subsidies are needed to allow rapeseed or soybean oil to become attractive, but low priced grease and tall oil can be economically processed without subsidies. As the price of crude increases, more options become economically attractive without subsidies.

LCA of green products were completed, which clearly show the environmental value of green diesel, green gasoline and biodiesel.

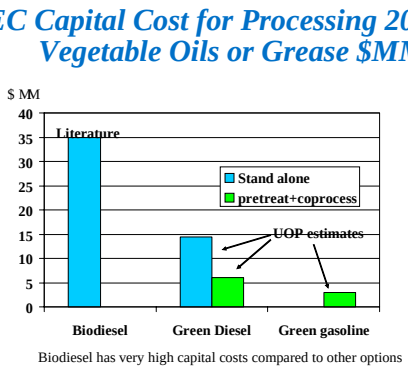

Figure 1. EEC Cost for Processing 2000 bpd of Vegetable Oil or Grease

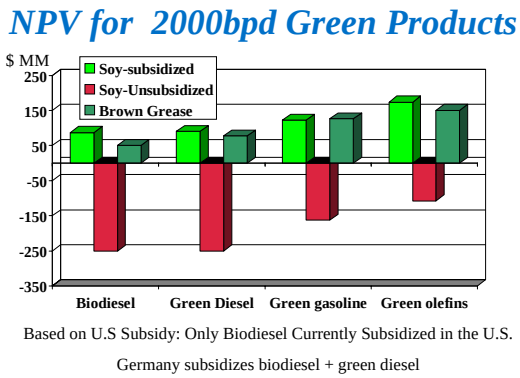

Figure 2. NPV for 2000 bpd of Green Products

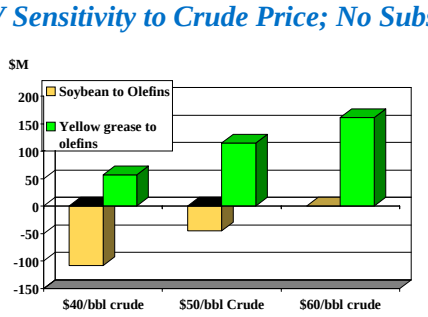

Figure 3. NPV Sensitivity to Crude price

Acknowledgment. This work was supported by the U.S. Department of Energy, the Office of the Biomass program.

PARALLEL PROCESSING BIOREFINERIES

Edwin S. Olson

Energy & Environmental Research Center
Box 9018
Grand Forks, ND 58202-9018

Issues in Agriculture-Based Feedstock Economies

Extensive development of an agriculture or biomass-based chemical industry is a long-term answer to both energy security and stimulation of rural communities in the United States. Two problems with production agriculture are the long-term excess productive capacity at acceptable prices and the widely fluctuating prices brought about by recent changes in federal farm program policy (1). The excess productive capacity problem could be alleviated by stimulating greater production of industrial products in biomass refineries. The biomass refinery, or "biorefinery," comprises biomass or agricultural processing facilities where raw products are converted via a chemical or biochemical process to high-value products and includes current plants, such as wet and dry mill ethanol plants, as well as more complex fiber and chemical industries, such as the new Blair, Nebraska, plant for production of dilactide and its conversion to polylactide and ethyl lactate. Currently, ethanol plants are being constructed, but it must be understood that government policy and fuel regulations are driving this operation. Many of the more complex plants will have the ability to utilize a variety of feedstocks and/or produce a greater variety of chemicals than the ethanol and lactide plants, which is very important in establishing a price-stable, market-driven industry, not one highly dependent on government subsidy and policy. As in a petroleum refinery, product flexibility allows profitability to be maximized by varying the product slate depending on current pricing, inventory, and demand. Thus the second problem of price fluctuation is solved by flexibility in the production at the refining level. And as in petroleum refining, ideally none of any feedstock will be wasted.

Parallel Processing Biorefinery (PPB) Concepts

Parallel processing of streams in a chemical plant can be an efficient way to produce a variety of materials. Parallel processing has always been an important feature of petroleum refining to achieve high efficiencies and allow flexibility in product selection. In contrast, biomass processing has been stuck on series processing. For example, grain or corn starch fermentation ends in ethanol with a low-value distillers grain by-product. Somewhat better is Blair lactate fermentation, which produces lactide polymer and an ethyl lactate by-product. In this case, the ethyl lactate is a way to utilize the racemic lactate by-product from the lactide separation tower. The process is parallel in the sense that two fermentations can be conducted on the same substrate to produce ethanol and lactate, and these two streams are then combined to produce ethyl lactate, but the fermentations may be conducted in different manners and using different equipment. This type of processing offers the potential for multiple parallel acid fermentations, producing a variety of acids that are combined with a variety of alcohols to produce many ester products. Ideally, the same equipment could be used in some or all of the parallel processes.

Opportunities in Biomass Feedstock Diversification or Flexibility

Today, about 99% of U.S. ethanol is made from the starch component of corn. Unlike the currently used starch feedstocks for the production of ethanol, such as corn, barley, and potatoes, or sucrose feedstocks, such as sugar cane, lignocellulosic feedstocks from fast-growing tree and grass crops and agricultural by-product or waste paper and other materials, are vast and cheap. For the parallel processing biorefinery, the diverse feedstocks should be converted to fermentable materials and/or a uniform chemical feedstock using the same equipment or process. This goal of flexibility in feedstocks is achievable with a thermal depolymerization process, such as the fast-pyrolysis technologies used in the Waterloo or Ensign processes, or acid pyrolysis in the levulinic acid processes. In fact, this flexibility may be the greatest advantage for fast pyrolysis over hydrolytic technologies.

The rationale for using pyrolysis to generate fermentable sugars from biomass is provided by recent technology performed by Ensyn Group, Inc., and earlier work performed by Weyerhauser Corporation, Crown Zellerbach, and the University of Waterloo in Ontario, Canada. The Weyerhauser work, which led to three U.S. patents, resulted in the development of a sawdust pyrolysis process for production of anhydroglucose at yields of about 25% of dry sawdust. Similar anhydroglucose yields were achieved by the University of Waterloo in pyrolysis of a variety of biomass feedstocks. Ensyn is currently operating two fast-pyrolysis units that have potential for producing an intermediate carbohydrate fraction for further processing.

The fast-pyrolysis process utilizes a low-pressure, high-flow-rate gas (steam, nitrogen, or a pyrolysis gas comprising carbon monoxide and carbon dioxide) to effect rapid removal of pyrolysis products from the heated zone, thereby preventing their destruction. The Ensyn process uses a hot sand bed to supply the energy for pyrolysis. Key products yielded from biomass pyrolysis include anhydrosugars, saccharinic acids, phenolics, furans, and smaller aliphatic aldehydes and carboxylic acids, which are derived from cellulose, hemicellulose, and lignin components of the biomass. Several anhydrosugars are present in the pyrolysis products, and most are not likely to be fermentable. However, the main anhydrosugar, levoglucosan, can be converted to glucose and fermented.

Given that greater product diversity will support the viability of biorefinery industries and consequently help sustain growth in rural economies, other pyrolysis products require further investigation to determine their potential for utilization in future fast-pyrolysis biorefinery concepts. There are several commercialized chemical transformations and uses of other pyrolysis products, and many more currently are under investigation. In addition to furans (2, 3) and other products described above, levoglucosenone has elicited considerable interest in the chemical community. Levoglucosenone (1,6-anhydro-3,4-dideoxy-α-D-*glycero*-hex-3-enopyranose-2-ulose) is formed during cellulose pyrolysis in phosphoric acid. This compound has potential importance as an intermediate for pharmaceutical syntheses (4 and references therein), owing to its chiral centers and functional groups (enone and acetal). Inexpensive sources of this intermediate are desired, as is further investigation of routes to chiral pharmaceuticals. Although several groups are exploring acid-catalyzed pyrolysis, it seems more practical to convert levoglucosan, available in large amounts from the fast-pyrolysis process, to levoglucosenone, since the levoglucosan is in fact an intermediate in the formation of levoglucosenone.

Opportunities in Parallel Fermentation Processes

The Energy & Environmental Research Center (EERC) recently proposed its concept of the dual-fermentation biorefinery (DFB) for efficient ester production (5–7). The DFB concept comprises the integration of ethanol production via yeast fermentation with the production of lactate via bacterial fermentation and the subsequent direct esterification of ethanol and ammonium lactate to produce high-value ethyl lactate. The key to the technical and economic

success of the DFB process is a highly efficient direct esterification that integrates the streams by facilitating the isolation and purification of the organic salt stream without extractions and membrane technologies. Using an ammonium salt concentrate avoids extractions and neutralizations needed in other processing schemes. Based on earlier U.S. Department of Agriculture patents for acid esterifications, EERC researchers developed (on the bench scale) an esterification process capable of extracting high yields of ethyl lactate from a 70% aqueous solution of ammonium lactate. Ammonia is recycled to the fermenter.

A PPB could also be configured with multiple fermentations to produce a variety of other ethanol-based carboxylate esters including ethyl acetate, propionate, butyrate, and succinate (6). These esters have high values as biodegradable low-toxicity solvents and chemical intermediates for the preparation of polymers and plasticizers, and several are potential high-octane gasoline additives with significant blending advantages versus ethanol. The PPB concept can potentially utilize a variety of biomass feedstocks, including starch hydrolysate, lignocellulose hydrolysate, hydrolyzed anhydrosugars from rapid pyrolysis, or pentoses from hemicellulose, and the separate fermentations may utilize different hydrolysates.

Another option for a PPB plant is to expand the variety of alcohols produced. This can be accomplished via the conversion of ethanol to n-propanol, isobutanol, n-butanol, and other higher alcohols (the Guerbet reaction). These have substantial markets as alcohols (solvents, fuel additives, chemical feedstocks) and can be used in esterification with the products from bacterial fermentation as previously discussed.

Commercialization of the PPB concept in any of the above configurations would provide ethanol plant product diversification options and enable revenue maximization through selective commodity production in response to changing market demands. In addition to providing diversified products for food, chemical, polymer, and fuel markets, the DFB concept is a unique opportunity for integrating recent and previous technical advances for processing carboxylic acids and their ester products.

References

1. Van Dyne, D.L.; Blase, M.G.; Clements, L.D. In *Perspectives on New Crops and New Uses* Janick, J., Ed.; ASHS Press: Alexandria, VA, 1999; p. 114.
2. Coutterez, C.; Gousse, C.; Gheneim, R.; Fang, S.W.; Gandin, A. In *Chemical and Materials from Renewable Resources;* Bozell, J.J., Ed.; Am. Chem. Soc.: 2001, p. 98.
3. Gravitis, J.; Vedernikov, N.; Zandersons, J.; Kokorevics, A. In *Chemical and Materials from Renewable Resources;* Bozell, J.J., Ed.; Am. Chem. Soc.: 2001, p. 110.
4. Witczak, Z.J. In *Chemical and Materials from Renewable Resources*; Bozell, J.J., Ed.; Am. Chem. Soc. 2001: p. 81.
5. Olson, E.S. U.S. Patent (provisional) Jan 2002.
6. Olson, E.S.; Aulich, T.R.; Sharma, R.K.; Timpe, R.C. Ester Fuels and Chemicals from Biomass. *Appl. Biochem Biotechnol*. **2003**, *105–108,* 843–851
7. Nagel, M.C. Biofuels, Technical Insights, Frost & Sullivan, Oct 2002.

REACTIVE DISTILLATION FOR THE BIOREFINERY: PRODUCTION OF ORGANIC ACID ESTERS

Navinchandra Asthana, Aspi Kolah, Dung Vu, Carl T. Lira & Dennis J. Miller

Department of Chemical Engineering & Material Science
Michigan State University
East Lansing, MI 48824

Introduction

The emerging development of the biorefinery concept for making fuels and chemicals from renewable biomass feedstocks has opened opportunities for novel reaction pathways and processes. Without doubt, the ultimate viability of the biorefinery lies in the successful development of these pathways and processes from economical and environmentally acceptable standpoint. While catalysis and new reaction pathways for biorenewables have received considerable attention over the past decade, separation processes for the biorefinery have lagged in their development.

Reactive distillation has been used extensively in the petrochemical industry to manufacture products such as methyl acetate and methyl tertbutyl ether. It is particularly effective when equilibrium reactions must be driven to completion; this is possible when one of the reaction products has volatility either greater than or less than the reactants.

In our laboratories, we have recently applied reactive distillation to the formation and recovery of several biorenewable chemicals. These applications include the recovery of propylene glycol and ethylene glycol from aqueous solution via reaction with acetaldehyde to form low-boiling acetals [1], transesterification of vegetable triglycerides and other organic esters for fuel and related applications, and formation of organic acid ethyl esters from their parent acids and ethanol. In this paper, we focus on organic acid ester formation using reactive distillation as a viable, low-cost route for production.

Reactive Distillation for Organic Acid Ester Production

The biorefinery concept is best visualized as an integrated facility involving both biological catalytic conversions (e.g. fermentation) and chemical catalytic conversions. Carbohydrate fermentations to ethanol and some organic acids are already mature, so that the platform species for organic acid ester formation are readily available and will continue to become lower in cost over time. Numerous applications for esters have been identified, including solvents, plasticizers, and fuels and fuel additives. In many cases, performance of the ester is superior to its petrochemical counterpart, but replacement has been limited by the higher cost of the ester. We present here a chemical catalytic approach using reactive distillation to form organic acid esters that will significantly lower the cost of their production and take full advantage of the existing biologically-based platform species.

We examine the formation of ethyl esters of lactic acid (a monobasic acid), succinic acid (dibasic) and citric acid (tribasic); these species have widely diverse physical and chemical properties but are already produced commercially via fermentation. The esters of these acids are desirable target species because of their attractive properties. Ethyl lactate and diethyl succinate are excellent solvents because they have low vapor pressures, very low toxicities, and excellent dissolving power. Tri-ethyl citrate has attractive plasticizer properties and low toxicity and is attracting attention in light of the toxicological hazards associated with using di-octyl phthalate as a plasticizer in children's toys. Beyond their desirable properties, these organic acid esters serve as prototypical compounds for the application of reactive distillation.

There have been a number of attempts to synthesize ethyl lactate in an efficient manner by utilizing lactic acid and ethanol [2-6]. While the chemistry involved in lactic acid esterification with ethanol is very simple, obtaining purified ethyl lactate in high yield is difficult because of the equilibrium limitation resulting from the presence of water. Further, ethyl lactate formation is further complicated by the tendency of lactic acid to polymerize in solution to linear dimer and higher esters, particularly as water is removed. Thus, good yields are difficult to achieve via conventional means, resulting in a relatively high selling price (>$ 3.00/kg) for the ester.

Reactive distillation circumvents these difficulties by driving the reaction to completion via water removal during reaction. Because of this, a high purity product stream is produced that contains only ethyl lactate and lactate oligomer esters. The oligomer esters are easily separated from ethyl lactate and can either be used as co-products (e.g. for plasticizers, etc.) or further reacted to increase the yield of ethyl lactate to near its theoretical limit.

Diethyl succinate is currently produced either from maleic anhydride via dimethyl maleate transesterification and hydrogenation, or by direct esterification of succinic acid with ethanol in multiple reaction-distillation steps. Triethyl citrate is synthesized using pure citric acid and ethanol. Since both acids are polybasic, the extent of reaction to final product is rate limited as well as equilibrium limited. They thus pose good opportunities for the application of reactive distillation.

Experimental Methods

Reagents. Aqueous lactic acid solution containing 88 wt% was obtained from J. T. Baker. Absolute ethanol (99% purity) and HPLC grade water were procured from J.T. Baker. Ethyl lactate was procured from Acros Organics. Succinic acid, citric acid, monoethyl succinate, diethyl succinate and triethyl citrate were procured from Sigma-Aldrich. All chemicals were used as received for reactive distillation experiments.

Reactive distillation. Lactic acid esterification reactions were performed in a pilot-scale reactive distillation column with a height of 5.5 m and an inside diameter of 0.05 m., packed with Sulzer Katapak structured packings containing Amberlyst 15 ion exchange resin [1]. The column is equipped with feed pumps, ports to remove samples and monitor column temperature, a reflux splitter, and a reboiler with overflow for level control. The entire column is wrapped in heating tape and insulated to minimize heat loss. In continuous operation for esterification, aqueous lactic acid solution is fed near the top of rectifying zone, 4.5 m above the reboiler, while ethanol is fed near the bottom of the stripping section, 0.09 m above from the reboiler.. Typically, the column takes about six hours to come to steady state. Samples are collected from the distillate and bottoms streams for product analysis at steady state. Material balances were conducted for each run to characterize column performance and quantify product distribution.

Batch esterification. Batch esterification reactions were performed in an 80 mL glass reactor equipped with a water condenser, sample port, thermocouple and an outer heating oil jacket for isothermal operation at elevated temperature. Samples were drawn periodically for analysis.

Analysis. Ethanol and water from all samples were analyzed by gas chromatography (Varian 3600; TCD with He as a carrier gas) using two different stainless steel column (3.25 mm X 4 m) packed with a liquid stationary phase of Porapak-Q. Lactic acid, its oligomers, succinic acid, citric acid, and their respective esters were quantitatively analyzed by HPLC using a reverse-phase C18 column with water and acetonitrile as mobile phase, and with UV detector set

at a wavelength of 210 nm. Compounds were identified by comparing their retention times with known standards.

Results and Discussion

Lactic acid esterification via reactive distillation. In optimized operation, water and ethanol constitute the distillate stream from the column and the bottoms stream contains only ethyl lactate and lactate oligomer esters. Fig. 1 delineates the effect of ethanol mole ratio on lactic acid conversion and desired product purity. Reducing the mole ratio of ethanol from 3.6 to 1.4 had little effect on acid conversion, but formation of L_2E and higher oligomer esters increased. The molar yield of L_1E decreased with decreasing mole ratio because of a lower concentration of ethanol in the reactive zone, but a lower ethanol feed rate also resulted in less ethanol and water in the bottoms stream and thus a higher purity ester product (open squares in Fig. 1).

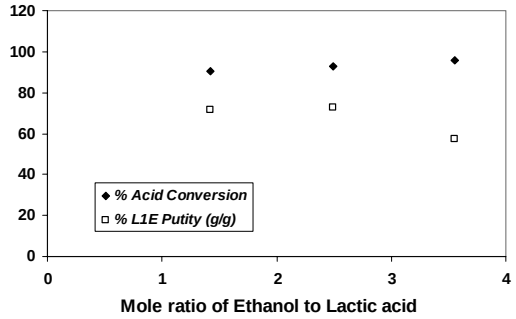

Figure 1. Effect of Mole Ratio of ethanol to lactic acid. Lactic acid and ethanol feed temp.: 25°C; Reflux ratio: 0

Fig.2 shows the effect of reflux ratio on acid conversion and bottoms product purity. Lactic acid conversion and bottoms product purity were both adversely affected by increasing reflux ratio – this is because reflux contains significant water which causes ester hydrolysis. The best mode of operation is therefore with no reflux, making the column operate as a reactive stripping column.

Increasing ethanol feed temperature from 25°C to 78°C (saturated liquid feed) and up to 85°C (vapour feed) has a deleterious effect on lactic acid conversion and L_1E yield, although water and ethanol are removed from the bottoms stream of the column and thus better product purity is observed (Fig 3).

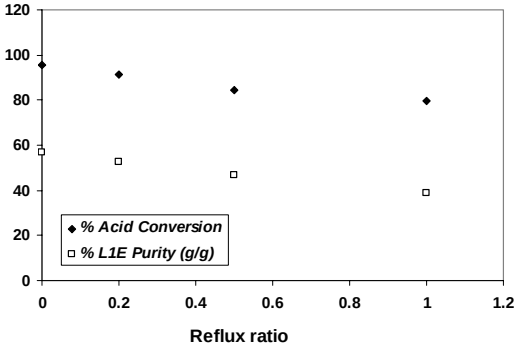

Figure 2. Effect of Reflux Ratio. Ethanol to lactic acid molar ratio 3.6 : 1; Lactic acid and ethanol feed temp.: 25°C

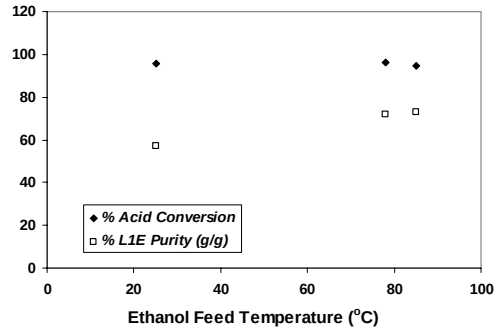

Figure 3. Effect of Ethanol feed temp. Ethanol to lactic acid molar ratio 3.6 : 1; Lactic acid feed temp.: 25°C; Reflux ratio : 0

Succinic acid and Citric acid esterification. Batch esterification reactions for succinic acid (SA in Table 1) and citric acid (CA) were conducted with molar ratio of ethanol to succinic acid and citric acid of 10 and 15, respectively. The reactions were catalyzed by Amberlyst 15 cationic exchange resin as catalyst (5 w/w solution).

Esterification takes place via sequential conversion of –COOH groups in acids. The rate of esterification of the first –COOH group is fast, but subsequent esterification rates are relatively slower and are highly dependent on temperature. Results in Table 1 are at 1 hr.

Table 1. Batch esterification of citric and succinic acids

T (°C)	SA Conv (%)	% Selectivity		CA conv (%)	% Selectivity		
		Mono ES	Di ES		Mono EC	Di EC	Tri EC
80	77.3	63.5	36.4	29.3	87.2	12.3	0.4
90	88.6	49.4	50.5	59	70.4	26.1	3.4
100	92.5	40.4	59.5	76.9	53.3	37.1	9.4
110	95.6	26.7	73.2	87.4	43.6	43.8	12.4

Conclusions

We have shown that ethyl lactate can be synthesised from aqueous lactic acid solution in high purity using reactive distillation. Ethyl esters of succinic and citric acids can be synthesized in high yield using various reactor configurations at high temperature.

Acknowledgement. Financial support from the National Corn Growers Association and U.S. Department of Energy are greatly appreciated.

References

[1] Dhale A. D., Myrant L. K., Chopade S. P., Jackson J. E., Miller D. J. *Chem. Eng. Sci.*, **2004**, *59*, 2881-2890.

[2] Cockrem M. C. M. "Processes for Production of Esters", *US 6664413*, 2003.

[3] Kaimal T. N. B., Vijayalaxmi P., Ramalinga B., Laxmi A. A., "Process for Preparation of Alkyl Esters From Commercial Lactic acid", *US 6342626*, 2002

[4] Datta R., Tsai S-Perng, "Esterificaiton of Fermentation-Derived Acids via Pervaporation" US 5723639, 1998.

[5] Jafar J. J., Budd P. M. & Hughes R., *Journal of Membrane Science*, **2002**, *199*, 117-123.

[6] Tanaka K., Yoshikawa R., Ying C., Kita H.& Okamoto K., *Chem. Engg. Sci*, **2002**, *57*, 1577-1584.

CONVERSION OF BIOMASS RESIDUES TO TRANSPORTATION FUELS WITH THE HTU® PROCESS

J. E. NABER and F. GOUDRIAAN, J.A. ZEEVALKINK

Biofuel B.V.; Rendorppark 30, 1963 AM Heemskerk, The Netherlands, TNO-MEP; Postbox 342, 7300 Apeldoorn, The Netherlands

Introduction

The uniquely innovative HTU® process for the thermochemical liquefaction of biomass offers excellent opportunities for conversion of biomass to a transportable form of energy. Suitable feedstocks include residues from agriculture and forestry, and also peat. Biomass is quantitatively and efficiently converted by treatment in liquid water at temperatures from 300 to 350°C and pressures from 100 to 180 bar. The product is ' Biocrude', a heavyorganic liquid with 10-15%w oxygen and a heating value of 30-35 MJ/kg. It readily separates from water. Due to the low oxygen content it can be further upgraded cost-effectively by hydrodeoxygenation to a clean diesel-type fuel with high cetane number, that offers excellent prospects for direct blending with existing (conventional) automotive diesel fuels.

The development of the HTU® Process has now reached a stage that a follow-up with commercial demonstration can be undertaken. Based on the results of the R&D, the conceptual designs have been concluded with a basic design package. Subsequently, a technical and economic feasibility study for a first commercial demonstration plant showed excellent perspectives. The results confirmed that the HTU® process is well placed technically and economically, with an excellent potential for upscaling and rapid rate of commercial development.

An international consortium has been formed and preparations are now being made for the design and construction of the first commercial demonstration of the HTU® process at a scale of 25,000 tons biomass (dry basis)/year. The HTU®-1 unit is planned for start-up in 2008 at a location next to the Waste Burning Facility of the Afval Energie Bedrijf AEB (Waste Processing Agency) of the City of Amsterdam.

Based on the products from HTU®-1, a parallel programme has been developed for the demonstration of HTU®-diesel. This programme includes

- Hydrodeoxygenation of some 30 tons of light biocrude
- Assessment of diesel quality and formulation of additives package
- Engine testing and monitoring of field test with 3-5 trucks/buses
- Commercial distribution and logistics

At least two follow-up commercial units of each 200,000 tons biomass throughput (dry basis)/year at the same location (start-up in 2011) and nearby, will allow the commercial introduction of HTU®-diesel.

Key points for the further commercial development are:

- HTU® is a cost-effective route from (wet) biomass rest products into automotive diesel.
- Final products are fully compatible with traditional transport fuels
- Fuels can be used in existing engines and no separate distribution system is required
- The HTU® route further opens perspective for production of ' green' chemicals in existing chemical installations

CARBONIZATION OF CELLULOSE UNDER MECHANICAL PRESSURE AS A MEANS FOR INCREASING CHAR YIELD

Kouichi Miura, Hiroyuki Nakagawa,Ryuichi Ashida, Yuji Sakuramoto, and Kyosuke Nakagawa[*]

Department of Chemical Engineering, Kyoto University, Kyoto-Daigaku Katsura, Nishikyo, Kyoto 615-8510, JAPAN

Introduction

We have recently presented a new method that produces high strength granular activated carbons from biomass wastes without any binders[1]. A sawdust, a bamboo, a recycling paper, and a newsprint paper were employed as the raw materials. The samples were pre-carbonized under the mechanical pressure of around 10 MPa at the temperature range of 25 °C to around 300 °C, called hot press carbonization in this work, to prepare densified semi-chars. The semi-chars were subsequently carbonized and activated to prepare high strength activated carbons. The hot press carbonization surprisingly increased the char yield by 1.9, 4, and 5 times for the sawdust, the recycling paper, and the newsprint paper, respectively. The strength of the activated carbons was dramatically increased by the hot press carbonization. The BET surface area of the activated carbons produced from the sawdust and the recycling paper reached as large as 1000 m^2/g. It was found that cellulose in the biomass wastes played a crucial role to increase the char yield and to develop pore structures.

In this paper the mechanism of pyrolysis of cellulose under mechanical pressure was examined in detail to clarify the mechanism by which the char yield increased.

Experimental

A cellulose microcrystalline (MERCK) was used as a cellulose (Elemental composition on daf basis; C: 44.1 %, H: 5.7 %, N: 0.3 %, O: 49.9 %).

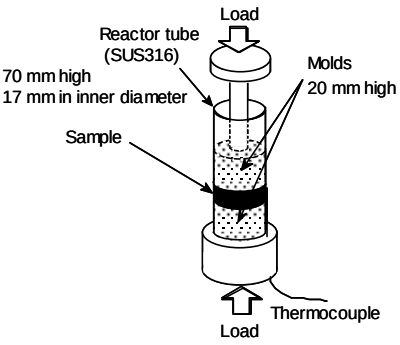

Figure. 1. Schematic of reactor used for hot press semi-carbonization.

Carbonization of the cellulose was performed in two steps: the first step is semi-carbonization below 300 °C to prepare semi-char and the second step is carbonization of the semi-char in a nitrogen atmosphere up to 900°C under atmospheric pressure to prepare char. The semi-carbonization under 10 MPa of mechanical pressure, which is called "hot press semi-carbonization", was performed using the reactor shown in Fig.1. About 2 g of sample were placed between the molds, heated radiationally by a so-called infrared-image furnace (Shinku-Riko, RHL-P610P) at the rate of 10 K/min to 300°C, where they were maintained for 15 min. Three other experimental conditions were employed for the semi-carbonization for comparison purpose. Their abbreviation and experimental detail are as follows:

Normal semi-carbonization: Heat treated like hot press semi-carbonization, but without the mechanical pressure and the upper mold.

Low temp. semi-carbonization: Heat treated at 260°C for 20 h without the mechanical pressure and the upper mold.

Gas pressure semi-carbonization: About 1 g of sample embedded in a tubing-bomb reactor under 1 MPa of nitrogen were heated at 10 K/min to 300°C at which they were maintained for 15 min. The pressure finally increased up to 6.5 MPa.

The second step carbonization was performed using a thermobalance in which about 2mg of semi-char were heated at 10 K/min to 900°C. Semi-chars and chars prepared were characterized by various analytical methods.

Results and Discussion

Semi-carbonization. Figure 2 shows the yields of semi-chars prepared under the four different conditions. The yields were significantly different, depending on the experimental conditions. The largest yield of 0.82 was obtained under normal semi-carbonization. Both gaseouos and mechanical pressures accelerated the semi-carbonization to decrease the semi-char yields down to

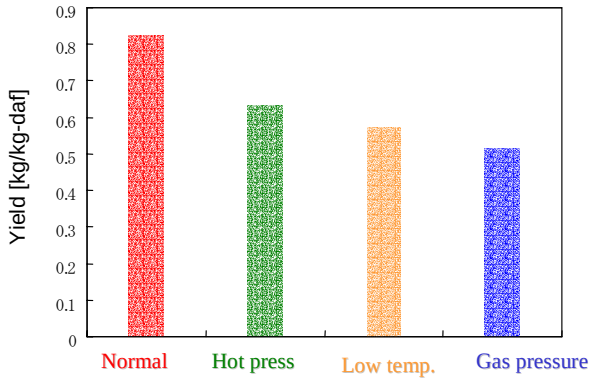

Figure 2. Yields of semi-chars obtained by different semi-carbonization conditions.

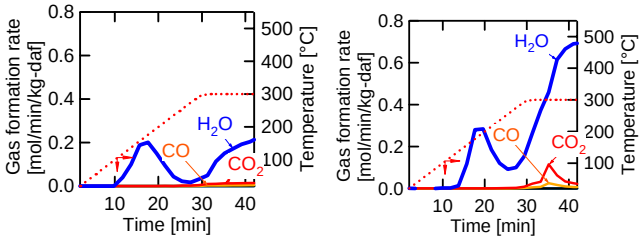

Figure 3. Gas formation rates during semi-carbonization. Left : normal semi-carbonization, right: hot press semi-carbonization.

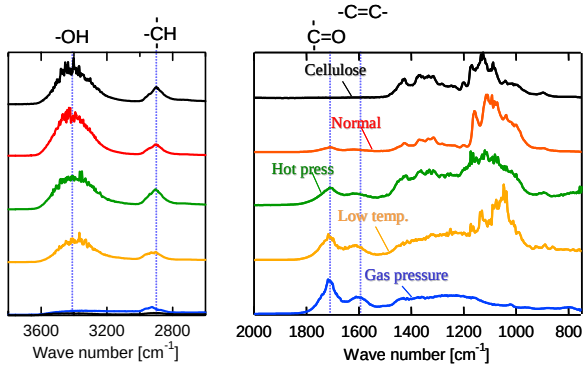

Figure 4. F.T.i.r. spectrum of the semi-chars obtained by four semi-carbonization conditions.

0.52 and 0.63, respectively. Low temp. semi-carbonization also decreased the semi-char yield down to 0.57.

Figure 3 compares gas formation rates during semi-carbonization between normal semi-carbonization and hot press semi-carbonization. The formation rates of the main gaseous product H_2O were significantly different between the two semi-carbonization methods, and the yields were 0.06 and 0.25 for normal semi-carbonization and hot press semi-carbonization, respectively. On the other hand, the tar yields were 0.12 and 0.03 for normal semi-carbonization and hot press semi-carbonization, respectively.

The overall stoichiometry of the semi-carbonization was formulated from mass balance as follows:

Normal semi-carbonization:

$$(C_6H_{10}O_5)_n \rightarrow 0.54nH_2O + 0.13(C_6H_{8.9}O_{4.3})_n + 0.87(C_6H_{8.9}O_{4.5})_n$$

Cellulose Tar Semi-char

Hot press semi-carbonization:

$$(C_6H_{10}O_5)_n \rightarrow 0.11nCO_2+2.33nH_2O+0.09(C_6)_n + 0.90(C_6H_{6.2}O_{2.7})_n$$

Cellulose Tar Semi-char

Figure 4 compares the F.T.i.r. spectra of the semi-chars prepared under four different conditions with the spectrum of the cellulose. It is clear that the semi-char prepared by normal semi-carbonization conditions retain the structure of the cellulose. On the other hand, the semi-chars prepared by other three conditions had distinct peaks attributed to >C=O, and the semi-char prepared by gas pressure semi-carbonization had lost the peaks attributed to –OH. These results show that the mechanical pressure accelerated the crosslinking reactions of –OH group, resulting in acceleration of gaseous components but suppression of the formation of tar. Similar effects appeared by both gas pressure semi-carbonization and low temp. semi-carbonization. The chemical compositions of tar and the semi-char produced by normal semi-carbonization were rather close to the composition of the cellulose, but they were significantly different from the composition of the cellulose for hot press semi-carbonization and were rich in carbon.

Carbonization. Figure 5 shows the weight changes during the carbonization for the semi-chars prepared under four different conditions. The ordinate of Fig. 4 represents the yield relative to the original cellulose. The yield at 900 °C was only 0.07 for the semi-char prepared under normal semi-carbonization, whereas the yields were, 0,27, 0.25, and 0.20 for the semi-chars prepared under hot press semi-carbonization, gas pressure semi-carbonization, and low temp. semi-carbonization, respectively.

Figure 6 compares the formation rates of gaseous products and tar between the semi-chars prepared by normal semi-carbonization and hot press semi-carbonization. Most significant difference between the two semi-chars is the tar formation behavior. For the semi-char prepared by normal semi-carbonization, a large tar formation peak appeared at around 350 °C, which accounted for more than 90 % of weight decrease (0.60 kg/kg-cellulose) during the carbonization. Furthermore, the chemical composition of the tar was rather close to that of the cellulose. On the other hand, the amount of tar formed was only 0.16 kg/kg-cellulose for the semi-char prepared by hot press semi-carbonization, and the chemical composition of the tar was rich in carbon and is significantly different from that of the cellulose. This difference in the tar formation behavior is reflected to the difference in the H_2 formation rates at higher temperature region. A large H_2 formation peak at around 760 °C for the semi-char prepared by hot press semi-carbonization is judged to come from aromatic ring condensation reactions of the char precursors retained due to the suppression of tar formation.

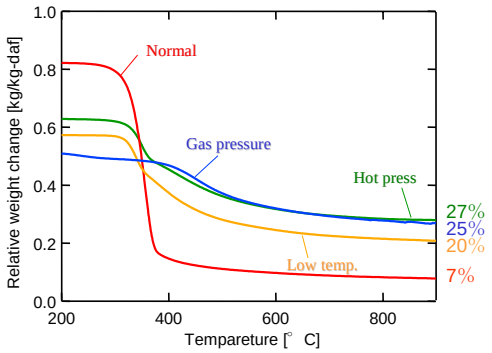

Figure 5. Weight changes during carbonization of the semi-chars prepared by four semi-carbonization conditions.

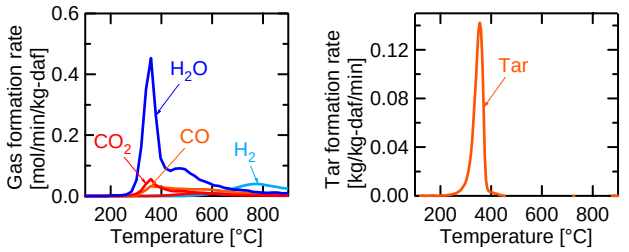

(a) Semi-char prepared by normal semi-carbonization.

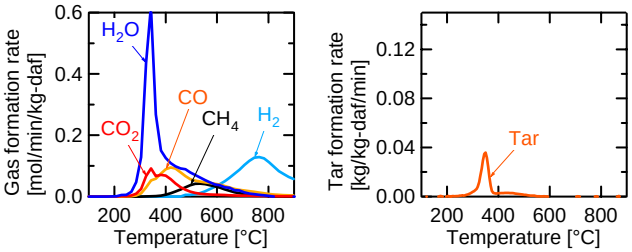

(b) Semi-char prepared by hot press semi-carbonization.

Figure 6. Gas and tar formation rates during carbonization of the semi-chars.

Conclusion

It was clarified that the final char yield of the cellulose is significantly affected by the dehydration reaction that proceeds rather slowly at around 250 to 300 °C under atmospheric pressure. The dehydration reaction can be accelerated by either hot press carbonization or gas pressure carbonization. Both mechanical pressure and gaseous pressure suppresses the evolution of tar components, which enhances the dehydration reactions among the tar components. Therefore, both mechanical pressure and gaseous pressure are judged to be effective to increase the char yield through the carbonization of biomass. However, only mechanical pressure can increase the strength of the char as well, which will be very advantageous when preparing high performance carbon materials from biomass.

References

(1) Miura, K; Nakagawa, H.; Ashida, R.; and Nakagawa, K. *Carbon 2003* (Oviedo, Spain), Abs. No. 177.

PRODUCTION OF BIO-CARBON ADSORBENTS FROM FOREST THINNING

Eun-Jae Shin[1], *Robert J. Evans*[1,2] *and Andrew M. Herring*[1]

[1]Department of Chemical Engineering, Colorado School of Mines, Golden, CO 80401, USA
[2]Electric & Hydrogen Technologies & System, National Renewable Energy Laboratory, Golden, CO 80401, USA
Tel: 303-384-2046, Fax: 303-274-3730
E-mail: eshin@mines.edu

Introduction

Large portions of the forested land contained in the US are at extreme risk of wild fire. It is, therefore, proposed to treat the forest to reduce the risk of catastrophic fires. The two most effective methods of forest treatment are mechanical thinning and prescribed burning or a combination of the two. There is, however, no economic incentive and there are still significant risks of sparking catastrophic wildfire and degrading air quality through the production of CO and particulate matter (PM) [1]. There is growing interest in converting forest slash to value-added fuels and chemicals. This has advantages that such value-added products reduce the nation's dependence on imported fossil fuels and, if a forest is harvested in a sustainable manner, a significant contribution is also made to the reduction of CO_2 emissions and so reduces climate changes [2].

Leadville, Colorado is surrounded by a large, fire-prone Lodgepole Pine forest, which means that a wood resource is available for the development of bio-carbons. Leadville also sits on a superfund site that was left behind by past mining activities. The impact on Colorado water resource is significant and protection of water by active and passive systems is important.

The objective of this work is to develop bio-carbon adsorbents from forest thinnings and apply them locally to the protection of natural waterways from acid mine drainage (AMD).

Experimental

Production of Char and Activation of Carbon. We made wood cubes out of fresh cut Lodgepole Pine with different sizes, i.e., 3mm, 6mm and 12mm. Sawdust and bark were also used to study the effect of sample sizes as well as sample materials. Variation in locations where the feedstock was from was also considered: (Location 1: ≅13 yrs), Location 2 (≅18 yrs) and Location 3 (≅ 25 yrs). We used the tree from Location 1 throughout the work if it is otherwise specified. We have used a quartz tubular reactor heated by an electric furnace to vacuum pyrolyze the biomass at moderate temperatures. The samples were charred at a pressure of 20 kPa over temperature range from 400ºC to 500ºC for 1hr. Chars obtained by vacuum pyrolysis have been found to be more reactive in the activation process, compared to those obtained by atmospheric carbonization [3]. Pretreatment of feedstock with phosphoric acid was also applied prior to charring. 5% of phosphoric acid solution was used to be penetrated through the sample overnight and the soaked samples were air dried at room temperature: weight percent of phosphoric acid to the sample was 1%. 20g of each sample were placed in the tubular reactor and heated to a desired temperature. 20 kPa pressure was obtained by using a water aspirator and the vacuum pyrolysis run time was 1 hr. Temperatures were varied from 400°C to 500°C.

Char was activated at 700°C with steam for 1hr in the same reactor under atmospheric pressure. Ar (>99% pure) was introduced to the reactor until it reached the temperature and it was switched to steam of 5 g/hr. After 1hr, Ar gas was again introduced to the reactor to cool it to room temperature.

Characterization of Char and Carbon. The chars and carbons were characterized primarily with BET surface area, Iodine (ID) number, DRIFTS, TGA and ESEM. BET surface area was measured with Micrometritics Flowsorb II 2300. All samples were subject to degassing for 2 hrs in He at 150°C before surface area measurements. Iodine (ID) numbers were also measured following a modification of test method ASTM D4607-86 [4].

For the DRIFTS experiments, the samples were ground in air and placed in Harrick Scientific, heatable variable atmosphere chamber in a Harrick Scientific Praying Mantis Diffuse Reflectance attachment. The DRIFTS was recorded at room temperature using Thermo-Nicolet Nexus 760 FT-IR spectrometer. TGA analysis was performed using a Seiko TGA balance, sample size about 2 mg at a heating rate of 10 °C/min from ambient to 700°C. Scanning Electron Microscope (SEM) images were taken by using FEI Quanta 600 with 100 magnification.

Results and Discussion

Characteristics of Chars. The yields of chars were about 25% of initial weight of wood that were pyrolysed at 400°C. At 500°C, the yield was lowered to 20%. For chemically pretreated samples, the char yield was about 35% and this high char yields could be explained with lower temperature crosslinking reactions that led to retention and incorporation of dehydration products and volatiles [5].

BET surface areas (SA) of chars obtained with non-pretreated samples are listed in the Table 1 where char yields and ID numbers are also included. ID numbers indicates the porosity of the chars and represents the surface area contributed by the pores larger than 10 Å [6]. To verify our approach to measure ID number, we tested it with a commercial activated carbon and the result is shown in Table 1. Based on the manufacturer's information (Fisher Scientific), our method was validated.

It is obvious that smaller sized samples resulted in higher surface areas. While 3mm cubes yielded highest surface area among the samples, that of sawdust was not as high as expected due to its small particle sizes. It can be attributed to less porous sites that sawdust might have, which coincides with lower ID number for sawdust, compared to that of 3mm cubes. Location also affected the results.

Table 1. Physical Characteristics of Chars generated at 400°C and 20 kPa pressure.

Wood Sample	Yield (%)	BET SA (m^2/g)	ID No. (mg/g)
Location 1			
3mm Char	21	270	161
6mm Char	24.8	170	-
12 mm Char	23.5	120	27
Sawdust	25.2	130	70
Bark	24.2	130	110
Location 2			
3mm Char	22	350	-
Location 3			
3mm Char	24.5	400	-
AC (Fisher)	-	1150*	992

*The manufacturer's information

For the char produced with 3mm cubes of Lodgepole Pine at 500°C, BET surface area was 120 m^2/g, which is lower than that of the char produced at 400°C. It can be rationalized with possible secondary reactions of the volatiles at higher temperatures, which

could lead to condensation on the surface.

The DRIFTS of the chars are shown in Fig. 1 where it can be observed that the band of aliphatic C-H bond at 2900 cm^{-1} is more abundant for bigger sample sized samples (6mm and 12mm) and bark. For all samples, there are lignin-like structures still remained.

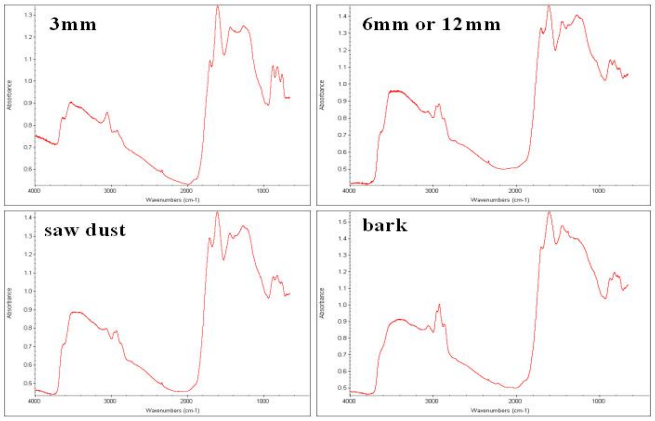

Figure 1. DRIFTS of the chars produced with Lodgepole Pine at 400°C and 20 kPa pressure.

TGA data for the chars is shown in Fig. 2. The weight loss of 3mm cubes was less than other samples, indicating that this char is by most stable.

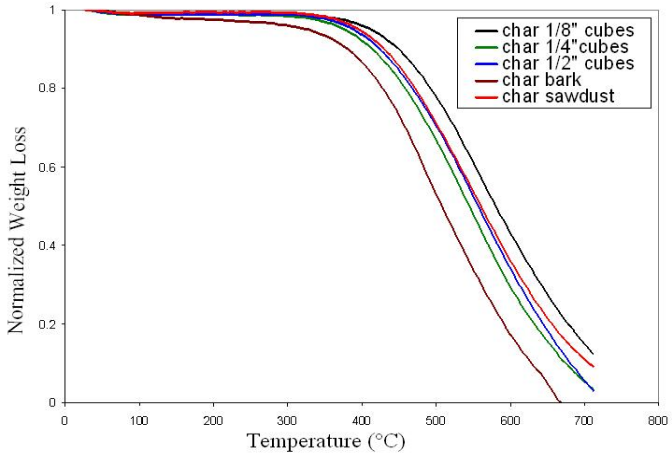

Figure 2. TGA for the chars produced with Lodgepole Pine at 400°C and 20 kPa pressure.

SEM images reveal morphology of a wood cube and its char as shown in Fig. 3 where it is obvious that porous sites were heavily developed by carbonization through removing volatiles.

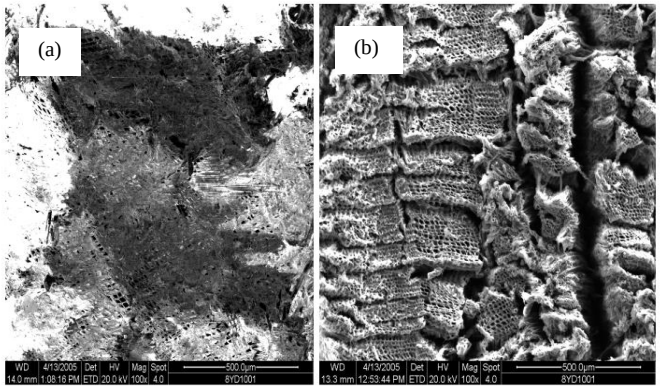

Figure 3. SEM images of (a) 3 mm Lodgepole Pine cube and (b) its char produced at 400°C and 20 kPa pressure.

Figure 4 shows porous sites of the chars produced without and with the pretreatment. More open pores are observed with the char obtained with the pretreated sample (Fig. 4 (b)).

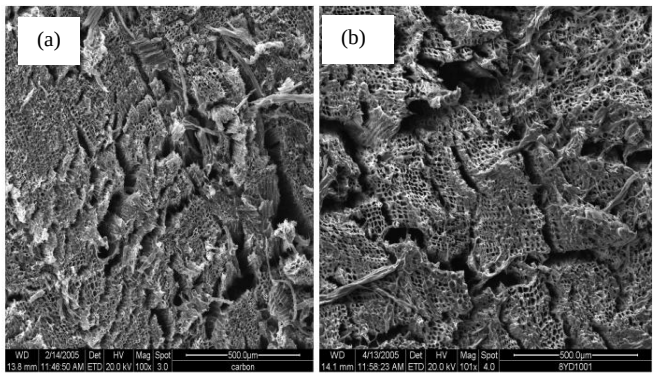

Figure 4. SEM images of the chars produced with Lodgepole Pine charred 12 mm cubes at 400°C and 20 kPa pressure: (a) non-pretreated and (b) 1% phosphoric acid pretreated sample.

BET surface area measured for the two chars in Fig. 4 (a) and (b) were 120 m^2/g and 400 m^2/g, respectively, which might be resulted from dehydration induced by the acid. Shafizadeh reported increased water yield from 11% to 21% during the pyrolysis of cellulose treated with 5% H_3PO_4 [7].

Characteristics of Activated Carbons. Carbon yields were about 50% and those of pretreated samples were about 70%. This can be again due to crosslinking induced by the acid [4].

The chars of non-pretreated sawdust and 3mm cubes, produced by vacuum pyrolysis were selectively activated and their BET surface areas were measured. The results were 750 m^2/g and 1000 m^2/g for sawdust and 3mm cubes, respectively.

The toxicological test for the carbons is under the way. In addition, the tests for the capability of the carbons as adsorbents for metal adsorption are in progress.

Conclusions

Our preliminary data have showed that by using vacuum pyrolysis at the moderate temperature followed by steam activation, it is possible to obtain high quality carbons that are comparable to commercial carbons, e.g. comparable BET surface areas. Moreover, when feedstock is pretreated with chemical reagents such as phosphoric acid, the quality of carbons can be even more improved.

With further study, we should be able to develop cost-effective activated carbons produced from local carbon sources, such as tree thinnings, for the protection of natural waterways from AMD.

Acknowledgment. The authors thank Alex Lauve, Jim Martineau and Sarah Stokes for their experimental assistance. This work was supported by the Division of Education and Research, Colorado Institute of Technology.

References

(1) MacNeil, .J.S. *Science*, **2000**, 289, 1448b.
(2) Kadam, K.L.; Wooley, R.J.; Aden, A.; Nguyen, Q.A.; Yancey, M.A.; Ferraro, F.M. *Biotechnol Prog.*, **2000**, *16*, 947.
(3) Cao, N.; Darmstadt, H.; Roy, C. *Energy & Fuel*, **2001**, *15*, 1263.
(4) Matsumura, Y.; Xu, X.; Antal, M.J. Jr. *Carbon*, **1997**, *35*, 819.
(5) Solum, M.S.; Pugmire, R.J.; Jogtoyen, M.; Derbyshire, F. *Carbon*, **1995**, 33, 1247.
(6) Srinvasakanna, C.; Bakar, M.Z.A. *Biomass and Bioenergy*, **2004**, *27*, 89.
(7) Shafizadeh, F.; Chin, P.S. ACS Symposium series, **1977**, *43*, 57.

NEW SOLID BASES FOR BIODIESEL SYNTHESIS

Karen Wilson[*]*, David G. Cantrell, Lisa J. Gillie*[2]*, Robert S. Watkins and Adam F.Lee*

University of York, Department of Chemistry, York, YO10 5DD, United Kingdom.

[2]University of Sheffield, Department of Engineering Materials, Sheffield, S1 3JD, United Kingdom.

Introduction

Fatty acid esters are widely used in the synthesis of lubricants, oleochemicals, surfactants, polymers and more recently biodiesel[1]. Biodiesel is a promising nontoxic and biodegradable renewable fuel comprised of mono-alkyl esters of long chain fatty acids, which are derived from vegetable oils or animal fats. Biodiesel is oxygenated and essentially free of sulfur making it a cleaner burning fuel than petroleum diesel with reduced emissions of SO_x, CO, unburnt hydrocarbons and particulate matter[2]. Biofuels are also carbon neutral as CO_2 emitted from the vehicle is consumed during photosynthesis by the crops as illustrated in **scheme 1**.

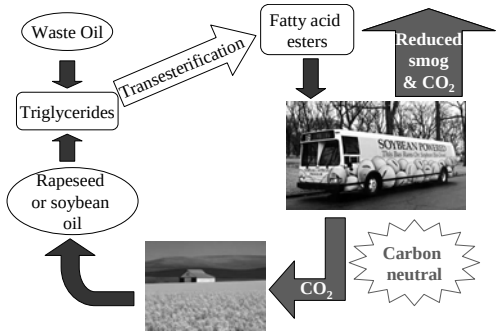

Scheme 1. Life cycle of fatty acid esters used for biodiesel.

Commercial biodiesel is produced from renewable resources including rapeseed, sunflower or soya bean oil which are composed of C_{14} – C_{20} fatty acid triglycerides. These are converted to the respective alkyl ester and glycerol by transesterification with short chain alcohols, typically methanol or ethanol. Transesterification can be performed using homogeneous basic catalysts, including Na or K hydroxides, carbonates or alkoxides. Base catalysis is preferred to acid catalysed routes using sulphuric or sulphonic acids, which are more corrosive with lower activities. However removal of the base after reaction is a major problem since aqueous quenching results in the formation of stable emulsions and saponification, making separation of the methyl ester difficult[3]. The use of a solid base catalyst offers several process advantages including the elimination of a quenching step (and associated basic water waste) to isolate the products, and the opportunity to operate in a continuous process[4,5] .

A variety of solid bases are known including alkali or alkali earth oxides, supported alkali metal ions, basic zeolites and clay minerals such as hydrotalcites.[6] Of the alkali earth oxides Ca-derived bases are the most promising as they are inexpensive, exhibit low methanol solubilities and are the least toxic. In addition promotion and control of basicity can be achieved via doping with alkali metals. Hydrotalcites ($[M^{2+}_{(1-x)}M^{3+}_x(OH)_2]^{x+}(A_{x/n})^{n-}.yH_2O$) are another interesting class of solid base whose acid/base properties can be easily controlled by varying their composition[7]. The structure of hydrotalcites is based upon layered double hydroxides with brucite like ($Mg(OH)_2$) hydroxide layers containing octahedrally coordinated M^{2+} and M^{3+} cations. A^{n-} is the counter anion which resides in the interlayer space to balance the residual positive charge of the hydroxide layers which results from isomorphous substitution of M^{2+} by M^{3+}. Variation of the Al content, (x) can modify the basic properties of the material, with stable pure hydrotalcite structures reported to form for compositions over the range $0.25 < x < 0.44$.

Here we report on the characterisation of a series of Li-doped CaO[8] and Mg-Al hydrotalcite[9] catalysts and correlate their physicochemical properties with their activity in biodiesel synthesis using glyceryl tributyrate as a model substrate for screening catalytic activity (**scheme 2**).

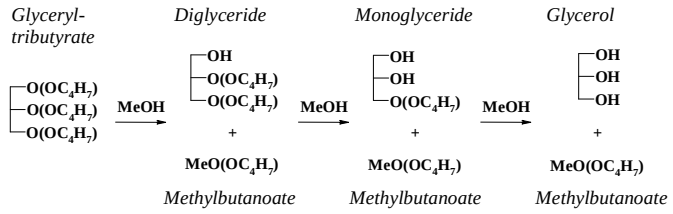

Scheme 2. Transesterification of glyceryl tributyrate with methanol to glycerol and methyl butanoate.

Experimental

Catalyst Preparation. A series of $LiNO_3$ impregnated CaO catalysts were prepared by wet impregnation with Li loadings in the range 0.26 - 4 wt %. In a typical preparation 10 g of CaO (Aldrich 99.9 %) was impregnated using 50 cm^3 of an aqueous $LiNO_3$ (Aldrich 99.9 %) solution of appropriate concentration. The slurry was stirred for 2 hours, then dried at 100 °C for 24 hours.

Mg:Al hydrotalcites were synthesised using an alkali free route to minimise risk of catalyst contamination according to the following method. 50 cm^3 of distilled water was heated to 338 K under vigorous stirring. To this, 100 cm^3 of an aqueous mixture of x mol $Mg(NO_3)_2.6H_2O$ and y mol $Al(NO_3)_3.9H_2O$ was added slowly over a period of 1 hour along with 100 cm^3 of an aqueous solution of 0.2 mol $(NH_4)_2CO_3$. The Mg:Al ratio was varied such that x+y = 0.15 mol and x:y = 1:1, 2:1, 3:1 and 4:1. The pH of the mixture was continuously held at pH 7.6 - 8 by the dropwise addition of NH_4OH (as 35% aqueous ammonia solution). The resulting mixture was held at 338 K while stirred vigorously for 3 hours and then filtered and washed with distilled water until the filtrate was as near pH 7 as possible. The precipitate was dried in an oven at 373 - 398 K for approximately 18 hours. All materials were calcined at 723 K for 3 hours and cooled under a flowing stream of wet nitrogen (100 $mlmin^{-1}$, relative humidity 95%) before catalyst testing. Reference Al_2O_3 and MgO materials were synthesised by the same method.

Catalyst Characterisation and Screening. Bulk and surface properties of the resulting catalysts were determined by a combination of elemental analysis, DRIFT, XRD, SEM, XPS and N_2 porosimetry. Transesterification reactions were performed at 60 °C using 0.01 mol of glyceryl tributyrate (Aldrich 98 %), 11.87 g of methanol (Fisher 98 %) and 0.1 g of dihexyl ether (Aldrich 97 %) added as internal standard with off-line GC analysis. Unless stated otherwise, 0.1g of Li/CaO or 0.05g of hydrotalcite were employed.

Results and Discussion

Li doped CaO catalysts. The evolution of surface species formed on CaO following $LiNO_3$ impregnation was followed by XPS. A strong loading dependent variation in the Li electronic state is indicated from a progressive shift in the Li 1s binding energy from ~56.3 eV to 55.7 eV for the highest loading 2.4 and 4 wt% Li samples is observed, matching that of the $LiNO_3$ reference. The

variation in Li 1s binding energy with loading is shown in **figure 1**, together with the corresponding integrated Li 1s and N 1s intensities.

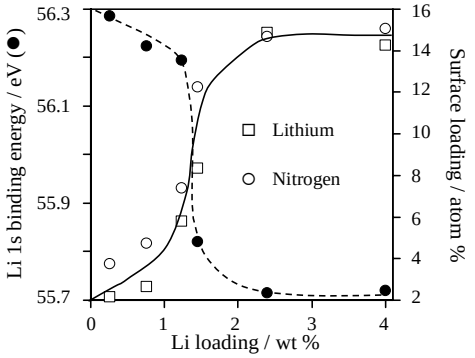

Figure 1. Correlation between Li 1s XPS binding energy and Li and N surface concentration as a function of $LiNO_3$ loading.

The transesterification of glyceryl tributyrate was subsequently investigated using this series of $LiNO_3$/CaO catalysts. A progressive conversion of the tri-glyceride to the methyl ester was observed, via first the di- and then mono-glycerides was observed as proposed in reaction scheme 2.

The initial rate of transesterification increased continuously with Li loading in the low surface coverage regime, passing through a maximum at 1.23 wt% Li. Higher loadings, associated with multilayer (bulk) $LiNO_3$, produced a dramatic decrease in activity. A strong correlation between the concentration of perturbed surface Li species identified in **figure 1** and the catalytic activity of Li-doped CaO is observed as shown in **figure 2** shows that both pass through a sharp maximum for 1.23 wt% Li and fall as bulk $LiNO_3$ overlayers are formed. Clearly the electronic state of Li in the submonolayer regime is critical to maintaining high activity in transesterification.

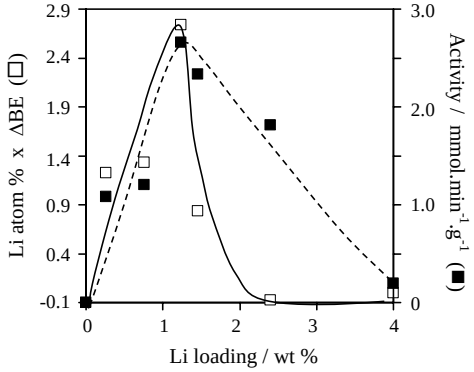

Figure 2. Correlation between activity and number of electronically perturbed Li sites in Li/CaO catalysts.

Mg/Al hydrotalcite catalysts. An alkali free precipitation route was successfully employed to prepare $[Mg_{(1-x)}Al_x(OH)_2]^{x+}(CO_3)_{x/n}^{2-}$ hydrotalcite materials with tunable basicity. The composition was varied over the range x = 0.25 – 0.55 with all resulting materials found to exhibit characteristic XRD patterns of the hydrotalcite phase. XPS revealed a decrease in both the Al and Mg photoelectron binding energies with Mg content which correlates precisely with the decrease in intralayer electron density resulting from exchange of Al^{3+} with Mg^{2+} in the brucite like layers. All hydrotalcite materials were effective catalysts for the transesterification of glyceryl tributyrate with methanol. The rate of tributyrate conversion and associated methyl butanoate and diglyceride formation were both first-order in triglyceride concentration. The initial rates for glyceryl tributyrate transesterification increased continuously with Mg content across the hydrotalcite series as shown in **figure 3**, while pure Al_2O_3 was completely inactive.

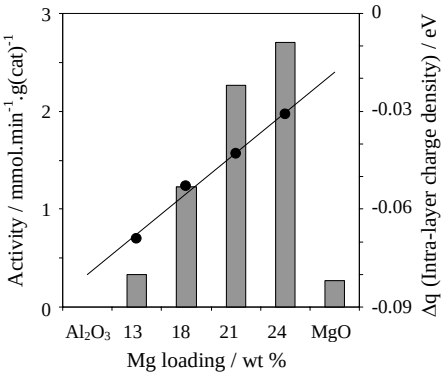

Figure 3. Initial rate of glyceryl tributyrate transesterification as a function of Mg content and change in intra-layer charge density for Mg:Al hydrotalcites.

The activities of the higher loaded 21 and 24 wt% Mg hydrotalcites are comparable to those reported for the best alternative Li-doped CaO solid base catalysts of 2.5 $mmol.min^{-1}.g(cat)^{-1}$. Pure MgO shows a lower activity and selectivity which may be attributed to a reduced number of accessible basic sites associated with its low porosity compared to the hydrotalcite materials. The catalytic activities of these hydrotalcites show a striking correlation with their corresponding intralayer charge densities towards tributyrate transesterification. This increased intralayer electron density of the Mg rich hydrotalcites would be expected to correlates with the Mg 2p binding energy which shifts from 49.9 to 49.5eV as interlayer electron density and corresponding basicity of these materials increases.

Conclusions

Both Li-doped CaO and Mg:Al hydrotalcite materials are effective solid base catalysts for the transesterification of triglycerides. Surface characterisation reveals that in both cases the electronic state of the surface species can be correlated with catalyst activity. In the case of Li-CaO the optimum activity is obtained upon deposition of a monolayer of Li, whereas with Mg:Al hydrotalcites, catalyst activity increases steadily with Mg content.

References

(1) Antolin, G; Tinaut, F.V; Briceño, Y; Castaño, V; Perez C; Ramirez, A.I. *Bioresource Tech*., **2002**, *83*, 111.
(2) Ma, F; Hanna, M. A., *Bioresource Tech*., **1999**, *70*, 1.
(3) Gryglewicz, S. *Bioresource Tech.*, **1999**, *70*, 249.
(4) Ono,Y; Baba, T. *Catalysis Today*, **1997**, *38*, 321.
(5) Clark J.H.; and Macquarrie, D.J. *Chem. Soc. Rev*., **1996**, *25*, 303.
(6) Tanabe, K; Misono, M; Ono Y; Hattori, H. *Stud. Surf. Sci. Catal*., **1989**, *51*.
(7) Cavani, F; Trifiro, F; Vaccari, A. *Catal. Today*, **1991**, *11*, 173.
(8) Watkins R.S; Lee. A.F; Wilson K. *Green Chemistry*, **2004**, *6*,335.
(9) Cantrell D.G; Gillie, L.J; Lee, A.F.; Wilson, K; *Applied Catalysis A*, **2005** *in press.*

MODELING CONDUCTIVITY IN POLYELECTROLYTES

Morton Litt

Macromolecular Science Dept.
Case Western Reserve University, Cleveland, OH 44106

Introduction

Polyelectrolyte membranes are very important in fuel cell development. Most of the work has been on Nafion®, both as-is and with many different materials included[1]. More recently, aromatic sulfonic acid containing polymers have been receiving much attention[2]. One of the main requirements is high conductivity, which is facilitated by water absorption in the materials. A major problem is that, while conductivity is satisfactory at 100% relative humidity, for most materials it drops rapidly as humidity is reduced and water content decreases[1,3]. A second problem in comparing materials is that they vary greatly in composition and equivalent weight. A third problem is that morphology affects conductivity greatly at equivalent water content. In addition, fluorocarbon sulfonic acids are much stronger acids than the aromatic sulfonic acids. The aromatic sulfonic acids can revert to the neutral form as water is removed.

Intrinsic conductivities of polyelectrolyte membranes can be compared if one considers only the aqueous phase in each polymer. This removes the complication of widely differing equivalent weights for different PEMs. It does not compensate for the differing morphologies and acidities, but by removing one complicating factor, it may be easier to understand the influence of the other factors on conductivity. This paper represents a first attempt at this analysis, for fully ionized systems.

Discussion

Basic modeling approach and application to HCl solutions. When one considers the question of proton conduction versus that of any other ion, it is obvious that it is much higher[4], e.g. the limiting ionic conductance at 18°C for H^+ is 315.8 S*cm.^{2}/equiv. while that of Li^+ is 33.4. This is usually explained by the Grothus effect, a proton jumping along a chain of H-bonded water molecules. Since the Li^+ ion solvates about the same number of water molecules as H^+ [5], this implies that the jump length is about 9 to 10 water molecules. The drop in ionic conductance with increasing electrolyte concentration is usually explained by assuming that the ion activity coefficient drops as concentration increases. However, there is another way of looking at the question that may be fruitful. A very primitive model is given below.

As ion concentration increases, jumps are obstructed because a jump requires reorganization of the solvent shell around nearby ions. This is especially true for the proton, since it can jump large distances if unobstructed. One can model this by postulating that the Grothus jump length becomes proportional to λ^{-1} (possibly to an exponent other than -1) as the ion concentration increases; this replaces the activity coefficient approximation. This is shown in Eq. 1 for fully ionized systems. (When the same approach is applied to fluorocarbon sulfonic acid polyelectrolytes, there are further complications that will be discussed later.)

$$C = C_0 * (1 - Pj_{G0}) / (1 - Pj_{G0} * (1 - \lambda^{-a})) \quad (1)$$

Figure 1. H^+ Equivalent Conductance, HCl solution, Exp. vs Calc. using Eq. 1

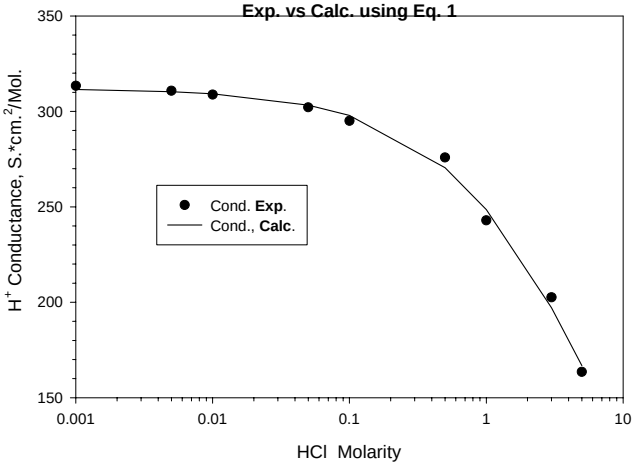

Here C is conductance at a given λ, C_0 is conductance at infinite dilution, Pj_{G0} is the probability of a proton transfer from one water to an adjoining H-bonded water molecule (part of a Grothus jump). λ is the ratio of water molecules to protons and a is a coefficient (near 1). This approach was applied to HCl solution conductance[6], subtracting the Cl^- contribution. The results are shown in Fig. 1 and Table 1.

Table 1. Best parameter values using Eq. 1

Parameter	Value	Standard Error	95% Dev. (S plane)
C_o, S*cm^2/Mol	312.0	2.6	~9.8
Pj_{G0}	.70	.03	~0.11
a	.72	.05	~0.19

The same approach can be applied to recent ^{1}H NMR determinations of the H^+ diffusion constant as a function of HCl concentration[7], Figure 2.

Figure 2. ^{1}H NMR Diffusion Constant for H^+, Exp. vs. Calc. using Eq. 1.

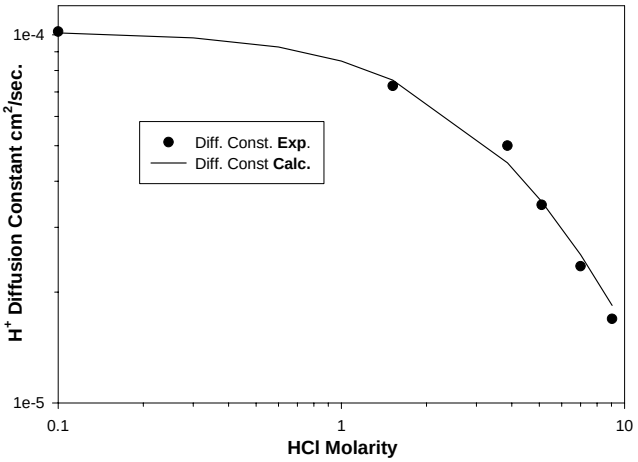

Table 2. B**est values for H^+ diffusion using Eq. 1**

Parameter	Value	Standard error	95% Dev. (S plane)
D_o *cm.*^{2}*/sec.*	1.02E-4	4.0E-6	~2E-5
Pj_{G0}	0.949	.017	~0.09
a	1.30	0.15	~0.8

The parameter values overlap at the 95% confidence level. However, parameter values are somewhat coupled and they can be varied over a relatively large range with little change in the fit. Also, slight changes in the procedure for calculating λ produce swings in the values. Almost as good fits can be obtained if *a* is fixed at 1. Pj_{G0} for Table 1 is then 0.90, and for Table 2 is 0.945, with a 1 σ overlap. The calculated values for a dilute solution Grothus jump length range from 3 to 20 water molecules. At a = 1, Table 1 fits well with the value of 9 to 10 obtained when the Li/H conductance values are compared[4].

Application to Nafion® and other fluorocarbon sulfonic acids. When this approach is applied to water insoluble polyelectrolytes, many other factors must be included. First, does the fraction of ionized acid change with water content? This is certainly true for aromatic sulfonic acids, and further complicates the problem. Fluorocarbon sufonic acids are superacids and are almost fully ionized even at λ's of 2 to 3[8]. Secondly, this is a two phase system, and Paddison has shown that the water dielectric constant decreases near the non-polar wall of the second phase[8]. Because of this, the average proton mobility will depend on the phase morphology. For a given λ the fraction of water as a function of distance from the wall differs if one considers "planar" micelles versus "cylindrical" pores. Using pore morphology, Paddison has calculated that the dielectric constant increases linearly from a low value at the wall to the bulk dielectric constant at about 0.5 nm away from the wall[8]. Proton mobility near the wall can be diminished for two reasons. First, a proton near the wall experiences less shielding from the discrete negative charges at the wall surface; the attraction is no longer homogeneous and there can be low energy wells that increase the activation energy for proton mobility. Second, the low dielectric constant implies lower entropy for the local water; the structure is more "rigid". This might decrease the Grothus jump length. One last point, the local phase orientation restricts the proton movement to specific directions which may not be parallel to the electric field direction.

The system can be modeled very crudely using the factors discussed in the previous paragraph. Litt[9] first proposed a lamellar model for Nafion®, while most investigators use some version of Gierke's model[5], approximately spherical domains interconnected by pores. Both lamellar and pore structures can be modeled using the same concepts, outlined below.

- Polyelectrolytes cannot be compared directly since only their aqueous phase participates in proton conduction. Measured conductivity is therefore proportional to the aqueous volume fraction of a particular system. This must be normalized by considering only the aqueous phase behavior in order to follow what happens as the water content is varied, and to compare different systems.
- Proton jump frequency is lowest at the water/electrolyte interface and rises with increasing dielectric constant to the bulk value, about 0.5 nm. from the interface. For want of better information, it is assumed that the mobility (jump length times frequency) is proportional to the dielectric constant. Mobility is constant when dielectric constant is constant, but depends on the ion concentration.
- Jump length in the whole system decreases as the proton concentration increases, as was postulated for bulk systems.
- The protons are approximately uniformly distributed in the aqueous phase.

Two regimes must be considered. At low λ, the dielectric constant is less than its bulk value throughout the whole system. At higher values of λ, the central aqueous region has the bulk properties. The volume of a single pore or lamella, per acid group, depends on λ. As λ increases, proton concentration decreases. The bulk conductivity reflects this. In the broader picture, the average area per acid group as well as the morphology will determine the aqueous layer thickness for a given λ.

Lamellar micelle model: The area per sulfonic acid was estimated to be about 0.6 nm^2, the cross-sectional area of two PTFE chains in the crystalline phase[9]. This does not change with changing λ, only the micelle spacing changes. If Padison's estimate of the distance from the wall to achieve the bulk dielectric constant holds here, this amounts to a λ of ~10 to 15. Let this be called λ_0. σ_0 represents the conductivity if there were no Grothus effect, the jump distance of a single water molecule. The equations for the different regimes are given below.

For $\lambda < \lambda_0$:

$$\sigma = (\sigma_0 / 2) / (1 - Pj_{G0} * (1 - \lambda^{-a})) \qquad (2)$$

For $\lambda > \lambda_0$:

$$\sigma = (\sigma_0 * \lambda_0^{\,2} / 2) / (\lambda^2 * (1 - Pj_{G0}(1 - \lambda^{-a}))) + \sigma_0 * \lambda_0 * (\lambda - \lambda_0) / (\lambda^2 * (1 - Pj_{G0}(1 - \lambda^{-a}))) \qquad (3)$$

The data used were taken from Gottesfeld and Zadowinski[1] for water in membranes first swollen in water or super-swelled in hot glycerol. Data for a Dow800 film are also included. They fall on the same curve once the aqueous volume fractions due to different equivalent weights are normalized. The data and calculated curve, for the normalized aqueous fractions, are shown in Table 3 and Figure 3.

Table 3. Parameter values for Nafion/Dow aqueous conductivity

Parameter	Value	St. Dev.	95% Dev.
σ_0, S/cm.	0.108	0.035	0.11
Pj_{G0}*	0.81	0.04	0.13
a	1.0	0.47	1.5
λ_0	16.3	4.3	14

Figure 3. Aqueous Phase Conductivity of Fluorosulfonic Acid Membranes, Experimental vs. Calculated Values, Eqs. 2 & 3

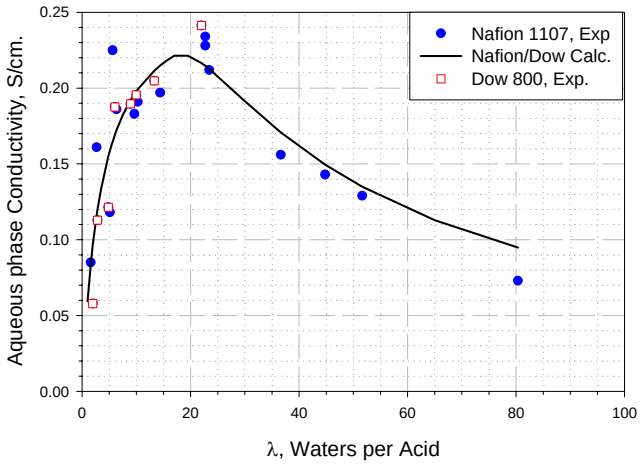

The limiting conductance for H^+ is calculated to be 160 $S*cm^2$/mole for a Grothus jump length of 5. For a Grothus jump length of 10, the limiting conductance is 320, essentially that of the literature value[4], 316.

Space is too limited to show the results of the calculations for a pore morphology. Whether one postulates that the surface charge density does not change or that the number of charges in the pore circumference does not change as λ changes, no fit can be found. The curves cannot reproduce the initial rise of conductivity as λ increases.

Conclusions

A very primitive model has been applied to aqueous proton conductivity, both in the bulk and in fluorocarbon sulfonic acid polyelectrolytes. The major feature is that the Grothus jump length decreases as λ decreases (acid concentration increases). For Nafion®, a very good fit was found using the lamellar micelle model; no fit was seen using a pore model. Using this model, the proton limiting conductance in Nafion® was calculated to be about that found for an aqueous proton. This shows that the model has some validity. The estimate for the limiting Grothus jump length is about 10, as is discussed by Kreuer[3].

References

1. Gottesfeld, S. and Zawodzinski, T. in *Advances in Electrochemical Science and Engineering, Volume 5*, Eds. Alkire, R. C., Gerischer, H., Kolb, D. M. and Tobias, C. W. Wiley, VCH, pp. 195-301
2. See for example, Kreuer K. D., Paddison S. J., Spohr E. and Schuster M., *Chem. Rev*. **2004**, *104*, 4637
3. Kreuer, K. D., Dippel, T. and Meier, J. in *Proton Conducting Membrane Fuel Cells I*, Eds. Gottesfeld, S. Halpert, G. and Landgrebe, A. *The Electrochemical Society, Pennington*, **1995**, 21
4. *Lange's Handbook of Chemistry (15th Edition)*, Ed. Dean, J. A., **1999**, McGraw-Hill p **8**.157
5. Gierke, T. D., Munn, G. E. and Wilson, F. C., J. *Polymer Sci. Part B-Polymer Physics* **1981**, *19(11)*, 1687-1704
6. *Lange's Handbook of Chemistry (15th Edition)*, Ed. Dean, J. A., **1999**, McGraw-Hill, pp **8**.164,165
7. Dippel, T. and Kreuer, K. D. *Solid State Ionics*, **1991**, *46*, 3
8. Paddison, S. *Annu. Rev. Mater. Res*. **2003**, *33*, 289
9. Litt, M. H., *ACS Polymer Preprints*, **38(1)**, April, 1997 p.80

MECHANISM OF ION TRANSPORT IN A SOL-GEL BASED ANHYDROUS PROTON CONDUCTING ELECTROLYTE

Jason E. Ritchie, Braja Ghosh, and Kyle Lott*

Department of Chemistry & Biochemistry, The University of Mississippi, University, MS 38677

Introduction

Proton conducting polymer electrolytes have important electrochemical applications in fuel cells and electrochromic displays. Nafion is the most widely used proton exchange membrane because of its mechanical and chemical stability, and its high H^+ conductivity when wet. However, Nafion requires hydration which limits its maximum operating temperature to around 100°C. Thus, a new electrolyte material is needed that can operate at high temperatures and low relative humidities.

We strive to gain a fundamental understanding of the mechanism of proton conductivity in our $MePEG_n$ polymer (scheme 1).[1-4] There are two general mechanisms for proton conductivity: the vehicle mechanism (which relies on the physical transport of a vehicle) and the Grotthus mechanism (which involves the proton being handed off from one hydrogen bonding site to another).[5] The Grotthus mechanism of H^+ conductivity is similar to Li^+ conductivity in PEG materials which rely on segmental motions and polymer reorganization.

Our group has shown an concentration dependence of ionic conductivity in a mixture of $MePEG_7SO_3H$ acid and our $MePEG_7$ polymer that seems to indicate a change in the mechanism of conductivity as a function of added acid concentration.[1] Our hypothesis is that the H^+ transport is accomplished primarily through a Grotthus mechanism and that H^+ transport is dependant on the volume fraction of polyethylene glycol (PEG) present with the Grotthus mechanism dominating at high PEG contents.

This work is important because, our system is a member of the relatively rare class of polymeric materials that display H^+ conductivity in the absence of water or plasticizing solvent.

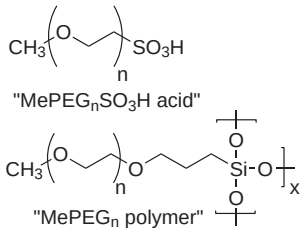

Scheme 1. Structures of $MePEG_n$ polymer and $MePEG_nSO_3H$ acid.

Experimental

The synthesis of the $MePEG_nSO_3H$ acids and $MePEG_n$ polymers have been described.[2] The densities were measured gravimetrically using tared micropipettes. Concentrations were calculated by dividing the density (g/mL) of the neat acid by its molecular weight (g/mol), yielding mol/mL.[2]

Electrochemical measurements were made with a PAR 283 potentiostat equipped with a PE 5210 Lock-in amplifier for AC-impedance.[1,2] GPC measurements were made with a Polymer Laboratories ELS-2100 detector and PL Mixed-D columns calibrated with PS MW standards (PL-EasiCal PS-2).

Results and Discussion

Synthesis. The MePEG polymer precursors synthesized for this study were prepared from a hydrosilation reaction between triethoxysilane and various length allyl-PEGs (Scheme 1).[2] This approach is similar to methods used by Hooper,[6] Zhang,[7] Allcock,[8] and Shriver[9] to prepare Li^+ conducting polymers.

The $MePEG_n$ polymer precursors were hydrolyzed and condensed to form the $MePEG_n$ polymer. This use of different PEG chain lengths allow for the control of volume fraction of PEG in the resulting polymer. In addition, we have prepared $MePEG_nSO_3H$ acids with 7, 12, and 16 repeat units which are miscible with the $MePEG_n$ polymers. These chain lengths are designed to allow us to control the mobility of the $MePEG_nSO_3^-$ ions by changing their physical size and to test the hypothesis that our proton conductivity is primarily through the Grotthus mechanism.

Ionic Conductivity. AC-impedance measurements were performed on anhydrous mixtures of polymers and acids. Figure 1 shows the activation of ionic conductivity (σ) for three different size $MePEG_nSO_3H$ acids (n=7,12,16) dissolved in the small $MePEG_3$ polymer at a low (0.26M) and high concentration (1.32M). As expected, the higher concentration of the acids produce larger ionic conductivities. However, the relationship between the conductivity and acid size reverses from high to low concentration. For example, the large $MePEG_{16}SO_3H$ acid has the largest ionic conductivity of the three MePEG acids at high concentration (1.32M), and the smallest ionic conductivity of the three MePEG acids at low concentration (0.26M). We attribute this conductivity dependence to the $MePEG_nSO_3H$ acid adding fluidity to the polymer & acid mixture.

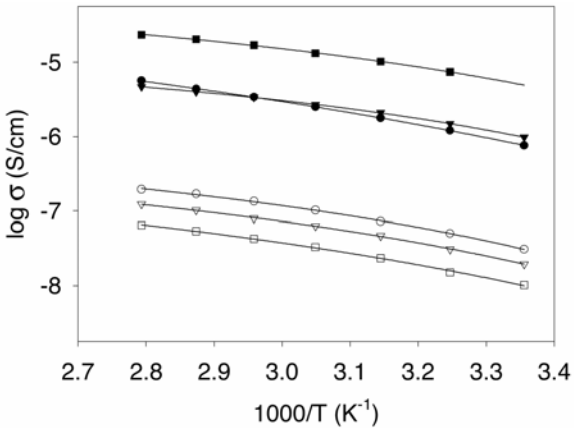

Figure 1. Activation of ionic conductivity (σ) of $MePEG_nSO_3H$ acids dissolved in the small $MePEG_3$ polymer at high (1.32M–$\lambda\tau\nu$) and low concentrations (0.26M–$\mu\nabla\rho$). $MePEG_7SO_3H$ ($\lambda\mu$), $MePEG_{12}SO_3H$ ($\tau\nabla$), $MePEG_{16}SO_3H$ ($\nu\rho$).

This increased fluidity in the mixture of $MePEG_{16}SO_3H$ acid and $MePEG_3$ polymer allows for both an increased rate of physical diffusion of the $MePEG_{16}SO_3H$ acid and an increased rate of motion of the segmental units of the polymer. This may result in a higher mobility of both the H^+ and $MePEG_{16}SO_3^-$ charge carriers, resulting in a larger overall ionic conductivity and a larger contribution from the vehicle mechanism of conductivity.

However, at the low concentration (0.26M), the $MePEG_nSO_3H$ acids are present at much lower weight fractions where it is expected that the fluidity of the mixture will be dominated by the high weight fraction $MePEG_3$ polymer. Figure 1 shows that the trend of ionic conductivity vs. $MePEG_nSO_3H$ acid size is reversed from high to low concentration yielding a trend where conductivity decreases with increased size of the acid. It is possible that this result indicates that

the mobility of the $MePEG_nSO_3^-$ anion is important to the overall ionic conductivity at this low concentration (i.e. the vehicle mechanism may be important). The higher ionic conductivity with the small $MePEG_7SO_3H$ acid may indicate that this acid has a larger D_{phys} than the larger acids.

Volume Fraction of PEG. Our hypothesis is that conductivity occurs through the Grotthus mechanism in the PEG region of the polymer and is dependant on the volume fraction of PEG. The calculation of volume fractions has been described.[2]

Figure 2 shows the dependence of equivalent conductivity (Λ) vs. the number of PEG units in the $MePEG_nSO_3H$ acids (n=7,12,16) dissolved in three $MePEG_n$ polymers (n=3,7,12). This plot shows that low concentration (0.26M) mixtures of the MePEG acids in the large $MePEG_{12}$ polymer have higher conductivities than mixtures of $MePEG_nSO_3H$ acids in the small $MePEG_3$ polymer. This dependence is likely due to the increase in the volume fraction of PEG units in a MePEG polymer with long PEG chains. In addition, the equivalent conductivity is larger in the high concentration point for each matching low (0.26M) and high (1.32M) concentration data point indicating that the mobility of one or both of the ions has increased in the high concentration samples. One possibility for this behavior is the increase in volume fraction of PEG in the high concentration samples leads to an increase in the mobility of the H^+ cation.

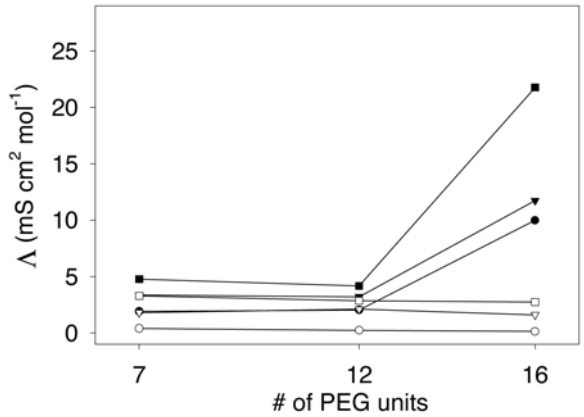

Figure 2. Dependence of equivalent conductivity (Λ) on the # of PEG units in the $MePEG_nSO_3H$ acid at high (1.32M–λτν) and low concentrations (0.26M–μ∇ρ). Samples are mixtures of $MePEG_nSO_3H$ in: the $MePEG_3$ polymer (λμ), $MePEG_7$ polymer (τ∇), and $MePEG_{12}$ polymer (νρ). All data points are at 55°C.

Low concentrations (0.26M) of the $MePEG_nSO_3H$ acids in the $MePEG_n$ polymers have no dependence on the size of the $MePEG_nSO_3H$ acid and a slope that is not significantly different than zero. This suggests that, at low $MePEG_nSO_3H$ acid concentrations, the mobility of the acid is not playing an important role in ionic conductivity. That is, the vehicle mechanism of H^+ conductivity is likely not important here.

Figure 3 shows the log of equivalent conductivity (Λ) vs. the inverse of volume fraction of PEG for a series of mixtures of $MePEG_nSO_3H$ acids and $MePEG_n$ polymers. Here, the results of experiments with four different concentrations of $MePEG_nSO_3H$ acids (0.26M, 0.43M, 1.05M, and 1.32M) are presented. According to free volume theory, diffusivity is exponentially related to the inverse of free volume,[10,11] and this type of plot has been used to determine the role of free volume in ion transport.

In Figure 3 the largest equivalent conductivities (i.e. ionic mobilities) are obtained for mixtures with the largest volume fraction of PEG (higher concentrations of the $MePEG_nSO_3H$ acid give mixtures with larger V_f of PEG). Linear regression gives a line with a slope of –5.37±0.55. While the correlation coefficient is somewhat small (r^2=0.751) and the scatter in the data appears large, an analysis of the residuals and a runs test indicate that the scatter is random, and that the regression line is not significantly non-linear. We conclude that the volume fraction of PEG in the mixtures is a good indicator of the overall ionic mobility in mixtures of our $MePEG_nSO_3H$ acid and $MePEG_n$ polymers.

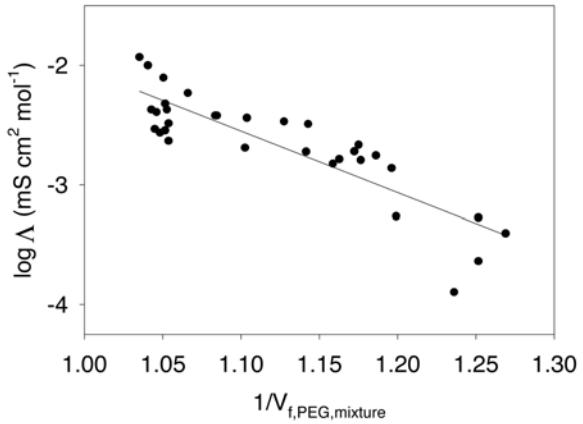

Figure 3. Dependence of equivalent conductivity (Λ) versus the inverse of volume fraction of PEG ($1/V_{f,PEG,mixture}$) in mixtures of the $MePEG_nSO_3H$ acids with the $MePEG_n$ polymers at 55°C.

Conclusions

Mechanism of H^+ Conductivity. Figure 2 clearly shows the lack of a dependence of the equivalent conductivity on the size of the $MePEG_nSO_3^-$ anion. This result strongly suggests that, at low $MePEG_nSO_3H$ acid concentrations, the mobility of the acid is not related to ionic conductivity, and that the low concentration trend in Figure 1 is due to some other factor. That is, the vehicle mechanism is not important at low concentrations.

More importantly, this system has shown an overall dependence on the free volume of the mixtures as measured by the V_f of PEG. In Figure 3, the V_f of PEG is correlated to the equivalent conductivity (i.e. ionic mobility). We conclude that the V_f of PEG in the mixtures is in control of ionic mobility. The V_f of PEG is important, because the Grotthus mechanism of H^+ conductivity in this system would be controlled by the rearrangement of ethylene oxide segments. Thus, the importance of V_f of PEG strongly suggests that the Grotthus mechanism is primarily responsible for conductivity in this system.

Acknowledgements. This research was supported in part by the NSF through the EPSCoR program (EPS-0132618).

References.

(1) Ritchie, J. E.; Crisp, J. A. *Anal. Chim. Acta* **2003**, *496*, 65-71.
(2) Ghosh, B. D.; Lott, K. F.; Ritchie, J. E. *Chem. Mater* **2005**, *17*, 661-669.
(3) Ghosh, B. D.; Lott, K. F.; Ritchie, J. E. *Macromolecules* **2005**, submitted.
(4) Lott, K. F.; Ghosh, B. D.; Ritchie, J. E. *Electrochem. Sol. St. Lett.* **2005**, submitted.
(5) Kreuer, K. D. *Chem. Mater.* **1996**, *8*, 610-641.
(6) Hooper, R.; Lyons, L. J.; Mapes, M. K.; Schumacher, D.; Moline, D. A.; West, R. *Macromolecules* **2001**, *34*, 931-936.
(7) Zhang, Z.; Sherlock, D.; West, R.; West, R.; Amine, K.; Lyons, L. J. *Macromolecules* **2003**, *36*, 9176-9180.
(8) Allcock, H. R.; O'Conner, S. J. M.; Olmeijer, D. L.; Napierala, M. E.; Cameron, C. G. *Macromolecules* **1996**, *29*, 7544-7552.
(9) Siska, D. P.; Shriver, D. F. *Chem. Mater.* **2001**, *13*, 4698-4700.
(10) Dickinson, E.; Masui, H.; Williams, M. E.; Murray, R. W. *J. Phys. Chem. B.* **1999**, *103*, 11028-11035.
(11) Cohen, M. H.; Turnbull, D. *J. Chem. Phys.* **1959**, *31*, 1164-1169.

INVESTIGATION OF PEM FUEL CELL BEHAVIOR: SWELLING AND VISCOELASTIC PROPERTIES

M.B. Satterfield, J.B. Benziger

Princeton University, Department of Chemical Engineering,
Princeton NJ 08544

Abstract

Recent work on PEM fuel cells has demonstrated the importance of membrane mechanical properties and swelling behavior on cell performance. Indeed, mechanical properties and swelling should be considered as integral factors when developing new membranes, improving cell design and creating models. The existence of two stable ignited states in autohumidified fuel cells and the cells' responses to dynamic conditions have revealed chemical-mechanical coupling in which the membrane's mechanical properties are changed by its water content which in turn changes cell performance and water production. This work presents several examples of fuel cell behavior for which mechanical properties and swelling are believed to be responsible and discusses the mechanical properties of membranes determined thus far and their relevance to cell performance.

Introduction

Previously we have presented results from auto-humidified PEM fuel cell operation, in which all feeds are dry and the water produced by the fuel cell is the only source of humidification. Under these conditions, complex phenomena caused by membrane chemical-mechanical coupling are observed. The cell's performance (water production) and the membrane hydration, conductivity, volume and stiffness continuously affect each other. This coupling shapes the cell's start-up behavior and response to dynamic operating conditions and enables the existence of two distinct stable ignited states. These behaviors have been previously reported and discussed,[1-3] and are examined here in light of membrane mechanical properties.

Figure 1 depicts the start-up behavior of a cell with different initial membrane water contents.

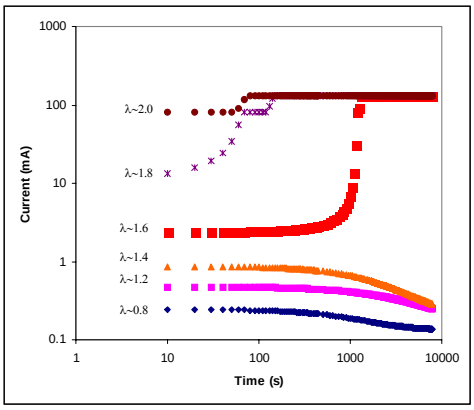

Figure 1. Autohumidified PEM fuel cell start-up behavior at 50°C with 10mL/min H_2 and O_2 flow rates and a 5 Ω load resistance. Initial water contents ($\lambda=H_2O/SO_3$) vary. The current through the external load was recorded every 10 s for 6 h. [3]

The figure shows the dependence of cell performance on membrane water content as well as the long time scale necessary for the cell to reach a true steady-state. In particular, the λ=1.6, 1.8 and 2.0 curves show a significant delay before igniting, as well as a partial ignition and delay in λ=1.8. These long time scales and response shapes are also observed when other parameters such as feed flow rates, load resistance and temperature are changed abruptly during operation, with no other perturbations to the system. The behavior is believed to be due to the viscoelastic relaxation of the polymeric membrane under the stress of both mechanical (clamping) and chemical (osmotic or swelling) pressure.

Figure 2 illustrates the existence of two ignited steady states, showing two steady-state polarization curves (each point equilibrated for 3-4 hours), one corresponding to a higher water content, the other to a lower. Between load resistances (RL) of 5Ω and 11Ω, there is a hysteresis where either state can exist, depending on the direction of approach.

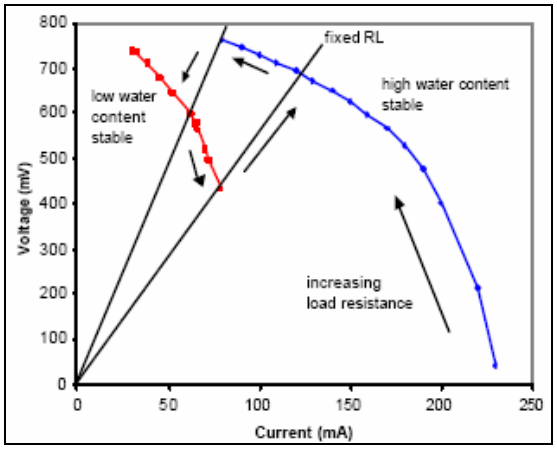

Figure 2. Steady state polarization curves for the autohumidified PEM fuel cell at 95ºC with H_2 and O_2 flows of 10 mL/min. The higher water content curve was taken after establishing steady state with a 2 Ω load resistance. The low curve was taken after establishing steady state with a 20 Ω load resistance.[1]

We believe that the existence of the lower ignited state is a result of the membrane water content being controlled by applied pressure. The force with which the cell is clamped together squeezes the membrane, reducing its potential water content.[4] The extent to which the membrane can swell against the applied pressure depends on its Young's Modulus and the swelling or osmotic pressure, which is related to the difference in chemical potential between water in the membrane and in the surrounding electrode space.

Experimental

Viscoelastic Properties. To address the cell's dynamic behavior, viscoelastic properties of the membrane are investigated. Constant-strain stress-relaxation and constant-stress creep experiments are performed at varying temperatures and humidities. Typical results appear in Figures 3 and 4 below.

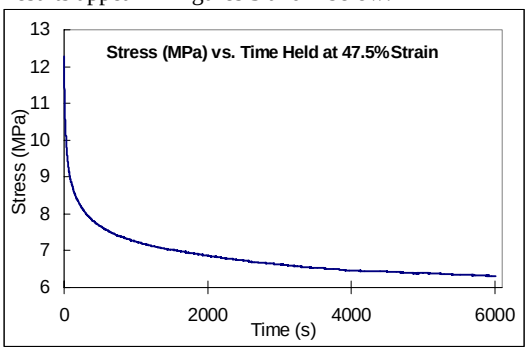

Figure 3. Stress Relaxation of Nafion 115 held at 47.5% strain for 6000 seconds under ambient temperature and humidity conditions.

For stress-relaxation experiments, the sample is quickly strained in the tensile direction by an Instron 1122 and held while the resultant stress is recorded over time. For creep experiments a free-hanging sample is loaded and strain is measured over time.

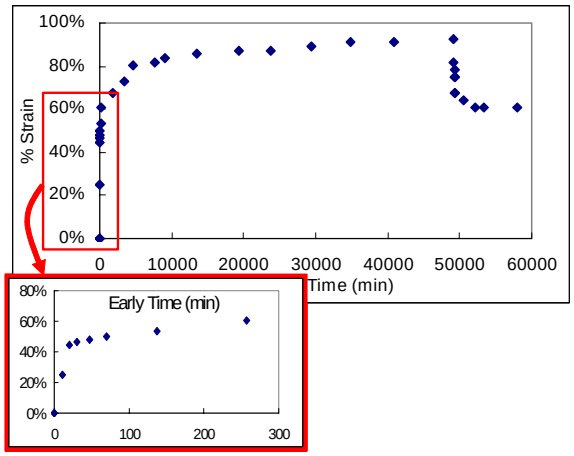

Figure 4. Creep behavior of Nafion 115 under 3.7 MPa of stress at 45C in 100% relative humidity. The bulk of the creep response occurs in the first 9000 seconds (150 min).

These data show considerable amounts of polymer creep and stress-relaxation, factors that should be considered in the design and operation of PEM fuel cells. More importantly, they exhibit time scales on the order of those witnessed in fuel cell dynamic responses, supporting the notion that polymer viscoelasticity is behind the cells' dynamic responses. Work is ongoing to quantify trends in behavior with temperature and relative humidity and to characterize membrane properties under fuel cell conditions. Both experiments are performed within an oven and a vapor barrier. As discussed below, humidity and temperature *significantly* affect membrane mechanical behavior.

Swelling Behavior. The membrane swelling behavior can be correlated to its stiffness or Young's Modulus. Tensile stress-strain tests were performed on Nafion 115 with an Instron 1122 at strain rates of 1-2 in/min and with varying temperatures and preconditioned water contents. Results for the Young's Modulus as it depends on water content (λ) and temperature appear in Figure 5.

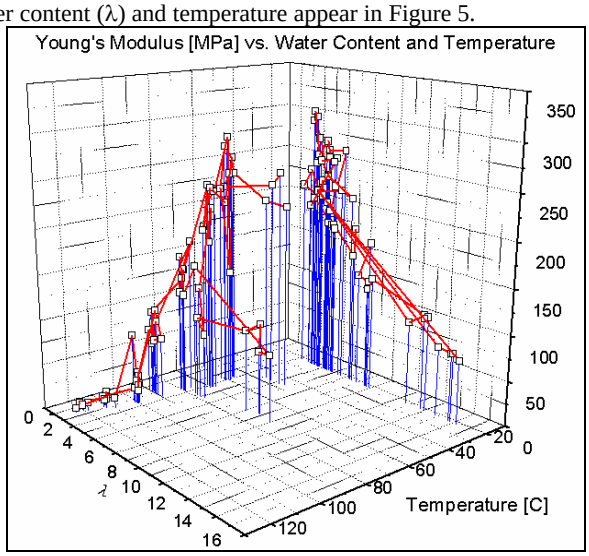

Figure 5. Dependence of Nafion 115 Young's Modulus (units in MPa) on test temperature and membrane water content ($\lambda=H_2O/SO_3$).

Clearly, increased temperature and water content dramatically reduce the membrane's Young's modulus, softening it from ~300 MPa to ~10 MPa over the range of conditions examined. This effect is important to note, as PEM fuel cell conditions necessarily involve elevated temperature and humidity, which together decrease the stiffness even further.

Of interest to swelling is the membrane's volume response to pressure, or compressibility β:

$$\beta = -\frac{1}{V}\left(\frac{\partial V}{\partial P}\right)_T$$

This compressibility can be found from the Young's modulus E by the simple relation

$$E = 3(1-2\nu)/\beta$$

were ν is Poisson's Ratio, typically 0.2-0.4 for polymers. The experimentally determined Young's modulus values yield compressibility values ranging from 0.002 to 0.2 MPa^{-1}. These values are compared to the osmotic pressure, p_{osm}:

$$p_{osm} = \frac{RT}{\bar{V}_{H_2O}} \ln\left(\frac{a_{H_2O}^{outside\ membrane}}{a_{H_2O}^{inside\ membrane}}\right)$$

The activity of water inside the membrane is calculated from the energy of mixing between the water and acid groups.

The membrane's compressibility is of the same order of magnitude as the calculated osmotic pressure, a result consistent with the finding that the membrane swells up to 20% when fully hydrated.[5] The result also indicates the potential for applied (clamping) pressure to control the membrane's swelling, thus causing the hysteresis in water content and ignited steady states, as witnessed in Figure 2.

Membrane swelling and water uptake under applied pressure is being further investigated with a controlled temperature and humidity compression device. This apparatus measures the membrane's water uptake and swelling pressure exerted over time under an applied pressure.

Acknowledgement. The National Science Foundation: CTS–0354279 and DMR-0213707 through the Materials Research and Science Engineering Center at Princeton.

References

(1) Benziger, J.; Chia, E.; Moxley, J. F.; Kevrekidis, I. G., *Chem. Eng. Sci.* **2005,** *60*, (6), 1743-1759.
(2) Benziger, J.; Chia, E.; Karnas, E.; Moxley, J.; Teuscher, C.; Kevrekidis, I. G., *Aiche J.* **2004,** *50*, (8), 1889-1900.
(3) Moxley, J. F.; Tulyani, S.; Benziger, J. B., *Chem. Eng. Sci.* **2003,** *58*, (20), 4705-4708.
(4) Escoubes, M.; Pineri, M.; Robens, E., *Thermochimica Acta* **1984,** *82*, 149-160.
(5) Morris, D. R.; Sun, X., *J. Appl. Polym. Sci.* **1993,** *50*, (8), 1445-1452.

STATES OF WATER- INVESTIGATING THE WATER-POLYMER INTERACTIONS AND TRANSPORT PHENOMENON IN PROTON EXCHANGE MEMBRANES

[1]Abhishek Roy , [2]Michael Hickner, [1]Tom Glass,[1]Yanxiang Li,
[1]Brian Einsla, [1]K.B. Wiles, [1]Xiang Yu
and [1]James E. McGrath (jmcgrath@vt.edu)

[1] Macromolecular Science and Engineering Program,
Macromolecules and Interfaces Institute
Virginia Polytechnic Institute and State University, Blacksburg, VA 24061
[2] Sandia National Laboratories, Albuquerque, NM 87123-0734

Introduction

Sulfonated copolymers studied in our laboratory phase separate to form a nano-scale hydrophilic and hydrophobic domain morphology[1]. The hydrophilic phase where in the sulfonic acid moieties reside absorbs water. Water confined in hydrophilic pores in concert with the sulfonic acid groups serve the critical function of proton (ion) conduction in these systems. It has been observed that the diffusion coefficients of both water and protons change with the water content of the pore. This change in proton and water transport mechanisms with hydration level has been attributed to the solvation of the acid groups and the amount of bound and bulk-like water within a pore. Water is known to reside in hydrophilic polymers in at least three different states as defined by the state's thermal properties[1]. *Non-freezing bound water* that is strongly associated with the polymer, shows no thermal transition by differential scanning calorimetry, but depresses the T_g of the copolymer. *Freezable bound water* which is weakly bound to the polymer (or weakly bound to the non-freezing water), displays a broad melting behavior around 0°C. *Free water* shows a sharp melting point at 0°C.

Synthesis of a controlled series of materials in both ion content and chemical composition, structure/property relationships between the functionality of the polymer backbone, the state of water, and the membrane transport has been achieved. It is anticipated that sulfone, ketone, phosphine oxide, and fluorine moieties incorporated within the polymer backbone will have a large influence on the state of water through the nano phase separation characteristics of the copolymers as well as direct interaction between the functional groups and water molecules.
The state of water in the copolymers is being quantified and characterized by differential scanning calorimetry and NMR T_2 & T_1 relaxation experiments. Self diffusion coefficients of water in a variety of copolymers were determined using pulse gradient NMR technique as a function of diffusive length.

Experimental Section.

a. Copolymer synthesis. Synthesis of hydroquinone based disulfonated poly (arylene ether sulfone)s copolymers (HQSH-xx ; xx: mole percent of disulfonated monomers) was carried out successfully via nucleophilic aromatic substitution[3]. To compare the effect of the functional group, 6F bisphenol based disulfonated poly(arylene ether ketone) copolymers with mono(Bxx) and diketone (PBxx) functional groups were synthesized .The structures of these three series of polymers are given below .

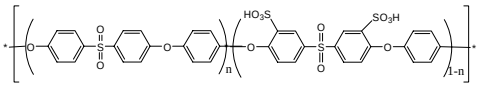

HQSH polymer in acid form

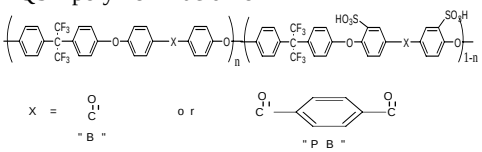

Ketone B & PB series in acid form.
The disulfonated copolymer membranes in their salt form were converted to the acid form by treating with 0.5 M sulfuric acid for 2 hours followed by immersion in deionized water for 2 hr .

b. Differential Scanning Calorimetry. The DSC experiments were performed in a TA DSC instruments using liquid nitrogen as cooling medium for sub ambient operation. The HQSHxx, Bxx and PBxx samples were equilibrated at various hydration level (from fully hydrated to 0% RH). The samples were placed in thermally sealed pans capable of withstanding pressure of 100 atm. Samples were cooled down to -70°C and then heated at a rate of 5°C per min under N_2 atmosphere.

c. T_2 relaxation measurements. The proton spin relaxation times, T_2, were measured in Varian Inova 400 MHz spectrometer using Carr-Purcell-Meiboom-Gill pulse sequence. The 90° pulse was of 13.8μs and the 180° pulse of 27.6μs. Total of 200 decay points were collected over 4 ms. Samples were equilibrated at room temperature in water. Just before the experiment they were removed from water and placed in the NMR probe

d. Determination of Self Diffusion Coefficient of water using pulse gradient stimulated echo NMR techniques[4]. Water self diffusion coefficients are measured in Varian Inova 400 MHz (for protons) nuclear magnetic resonance spectrometer with a 30 G/cm gradient diffusion probe. Total 16 points are normally collected and the signal to noise ratio is enhanced by co-adding 4 scans.

Results and Discussions

Fig 1 represents the thermograms of HQSH 35 at increasing water uptakes showing evolution of water melting endotherm and Tg depression. The transition from free water to loosely bound water is seen from the negative shift in the melting endotherm. The depression in melting point indicates interaction between the loosely bound water and the copolymer.

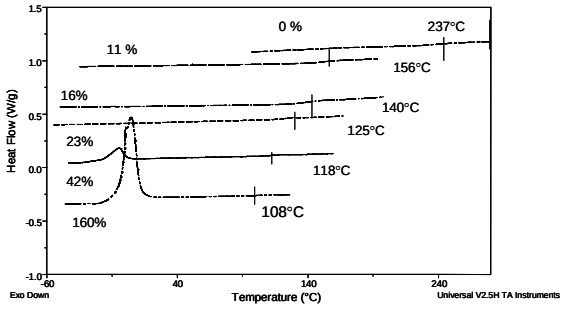

Figure 1. - Melting endotherm of HQSH 35

The tightly bound water can be correlated to the maximum amount of water for which there is no melting endotherms

The NMR T_2 relaxation measurements were also conducted on the fully hydrated samples. The experimental results were fitted

into a tri, bi or mono exponential decay function depending upon the type of water present[2] . Both DSC and NMR results were evaluated in proper quantification of three types water.

The integrated Δ H of fusion, the total amount of free plus loosely bound water and tightly bound water are reported in Table I.

Table I. H of fusion of water and quantification of states of water.

Sample HQSH	IEC (meq/g of SO_3H	Δ H (J/gm of water)	Total water λ (N H_2O/SO_3H)	Free +loosely bound water (λ)	Tightly bound water (λ)
20	1.2	50	14	5	9
30	1.6	130	29	20	9
35	1.8	180	48	39	9

It can be seen that the Δ H of fusion for water increases with increase in sulfonation level and free water content, which is likely due to better water-water interactions.

Self Diffusion coefficient of water. In a hydrated PEM, ^1H nuclei exchange rapidly between H_2O and H^+ environments. Accordingly the measured ^1H diffusion coefficient is a weighted average of the diffusion coefficient for separate environments. For a system having three states of water, the types of water differ from each other in their diffusive lengths. Thus the diffusion coefficient measured as a function of diffusion time will show a decay curve. Fig 3 represents the plot of diffusion coefficient as a function of effective diffusion time for the HQSH series. The effective diffusion time was varied by varying the Δ- term. It appears that the diffusion coefficient of HQSH 35 is higher than HQSH 30 and 25. This is in agreement with the amount of free water present in the sample.

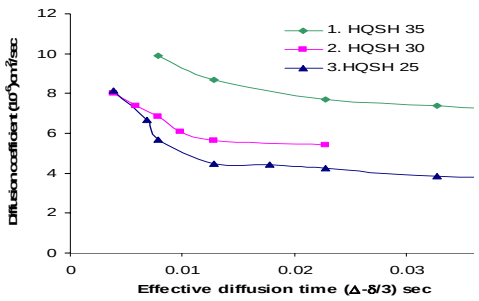

Figure 2. Diffusion coefficient of water as a function of effective diffusion time and copolymer composition.

Conclusions

The states of water were characterized for ion containing copolymers with DSC and NMR relaxation experiments. The of fusion for the free and loosely bound water was calculated and was found to increase with IEC and with free and loosely bound water content. Self diffusion coefficient was calculated using PGSE NMR experiments and was related to the different states of water. Further discussion of the results will be presented.

Acknowledgements. The authors would like to thank the National Science Foundation "Partnership for Innovation" Program (HER-0090556) and the Department of Energy (DE-FC36-01G01086) for support of this research effort.

References

1.Hickner,M.;Ghassemi,H.;Kim,Y.S.;McGrath,J.E., Chem. Rev. **2004**,*104(10)*,4587-4611
2. Kim, Y. S.; Dong, L.; Hickner, M. A.; Glass, T. E.; Webb, V.; McGrath, J. E.,Macromolecules **2003**, *36(17),* 6281.
3.Roy,A.; Einsla,B.;Harrison,W.L.;Hickner,M.;McGrath,J.E., Preprint of Symposia-American Chemical Society, Division of Fuel Chemistry **2004**,*49(2)*,614-615
4.Stejskal, E.O.; Tanner ,J.E., J. Chem. Phys **1965**, *42*, 288.

VISCOMETRIC BEHAVIOR AND MOLECULAR WEIGHT CHARACTERIZATION OF SULFONATED POLY(ARYLENE ETHER SULFONE) COPOLYMERS

*Juan Yang, Yanxiang Li, Hang Wang, Melinda Hill, Xiang Yu, Kenton B. Wiles, Hae-Seung Lee, James E. McGrath**

Department of Chemistry, Virginia Polytechnic Institute and State University, Blacksburg, VA 24061
*jmcgrath@vt.edu

Introduction

Proton exchange membrane (PEM), the key component of fuel cell, is responsible for the proton transport from the anode to the cathode, therefore directly determining the performance of the fuel cell. PEMs must have good mechanical, thermal and chemical stabilities and still have high proton conductivity. Many families of polymers with differing chemical structures and various strategies for incorporation of sulfonic acid groups have been explored as PEM materials. Sulfonated poly(arylene ether sulfone)s are promising candidates due to their good acid and thermal oxidative stabilities, high glass transition temperatures and excellent mechanical strengths. Our group has reported synthesis of poly(arylene ether sulfone) copolymers by directly copolymerizing sulfonated monomers.[1] This procedure is more preferable relative to post modification method since it is easy to control the degree of sulfonation and avoid the side reactions. However, this new synthetic route brought a whole new challenge in determining the molecular weight of the final polymer product. Molecular weight is a critical parameter defining PEM durability and this has not been properly characterized for any PEM membranes including Nafion, which is probably the most glaring omission in new ion conducting polymer research.[2] In the post modification method, sulfonic acid groups are formed by chemical modification of polymeric precursors and MW characterization of precursors is usually performed. The aim of this work was to study dilute solution behavior and develop techniques for the proper MW characterization of the ion-containing PEMs.

Experimental

Materials. *Tert*-butylphenyl terminated sulfonated poly(arylene ether sulfone) copolymers with different molecular weight (20 kg/mol ~ 50 kg/mol) were prepared by direct polymerization of the activated halides, biphenol and a t-butylphenyl endcapping reagent as shown in Scheme 1.[3] For all copolymers, the mole ratio of 4,4'-dichlorodiphenylsulfone(DCDPS) to 3,3'-disulfonated 4,4'-dichlorodiphenylsulfone (SDCDPS) was fixed to

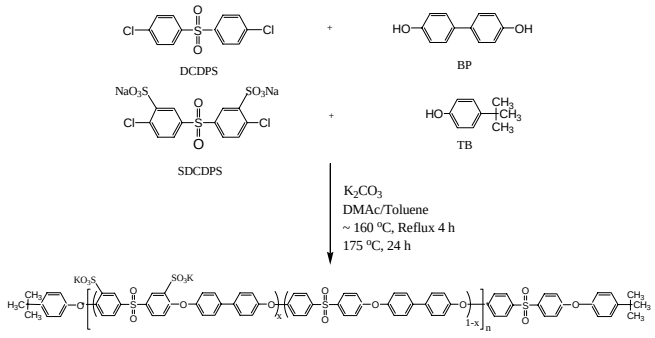

x=0.35 BPS35_20K, BPS35_40K, BPS35_50K

Scheme 1. Synthesis of tert-butylphenol terminated poly(arylene ether sulfone)s containing sulfonate groups 6.5/3.5. The molecular weight determined from ^{1}H NMR spectra was consistent with the theoretical values.

BPS35-control copolymer, with SDCDPS/DCDPS of 3.5/6.5 was also prepared from biphenol, DCDPS and SDCDPS under the similar polymerization condition without endcapping agent, in which the stoichiometry between dihalide monomers and biphenol was maintained at 1:1. GPC and intrinsic viscosity measurement show that it has higher molecular weight than all the other endcapped BPS35 as expected.

Intrinsic Viscosity Measurement. Viscosity measurements were carried out with a Cannon Ubbelholde viscometer with a flow time of about 98s for pure NMP at 25^{o}C. The temperature was regulated at 25 ± 0.1^{o}C. Each solution for viscometry was freshly prepared and was kept at 25.0 ± 0.1^{o}C for 10 min prior to the measurement. All the solutions were filtered in order to remove undissolved particles before introduction into the viscosimeter. The polymer concentration were suitably chosen to obtain relative viscosities in the appropriate range. After each determination, the viscometer was flushed at least 3 times with distilled water before rinsing with acetone prior to drying in the oven. This procedure was important because acetone is a precipitant for the copolymer. For the same reason, acetone vapor must be thoroughly removed before the introduction of the next solution.

GPC Measurement. GPC experiments were performed on a liquid chromatograph equipped with a Waters 1515 isocratic HPLC pump, Waters Autosampler, Waters 2414 refractive index detector and Viscotek 270 dual detector. LiBr/NMP was used as the mobile phase. The column temperature is maintained at 60^{o}C because of the viscous nature of NMP. Both the mobile phase solvent and sample solution were filtered before introduction to the GPC system.

Results and Discussion

Figure 1 presents the evolution of the reduced viscosity and inherent viscosity versus concentration of BPS35-control sample in salt-free NMP and in 0.05M LiBr/NMP respectively. The solution properties of BPS35 in the polar medium NMP with and without added salt are radically different. A polyelectrolyte effect is clearly observed. As one dilutes a charged macromolecule, they experience molecular coil expansion, exhibiting higher reduced viscosity as the concentration is reduced due to the charge repulsion along the polymer backbone.[4] The presence of small electrolyte LiBr, which determines the solution ionic strength, screens out charges and the repulsive interactions, affords a linear plot and enables us to obtain conventional extrapolations to dilute solution viscosity. Thus the key for the dilute solution viscosity measurements for ion-containing PEM is the introduction of a low molar mass salt, which is often quite appropriately able to screen the charges. However, based upon the consideration that the optimum salt concentration might depend upon the chemical structure, molar mass range, charged density etc., dilution viscosity measurements of different MW BPS35 samples in NMP containing various concentrations of LiBr from 0.01M to 0.1M were also performed. Linear plots were obtained for all the samples in all these salt concentrations. Intrinsic viscosity data obtained for different concentrations of salt were presented in table 1. One trend can be observed from the tabulated data. Increasing of the salt level decreases the intrinsic viscosity. It is clearly shown that the intrinsic viscosity drops significantly from the salt level of 0.01M to 0.05M for all the samples. Obviously 0.01M LiBr is not enough to screen the charges of BPS35. Furthermore, for the samples with the MW lower than 50K there shows only small decrease of intrinsic viscosity, probably within the experimental error, from the salt level of 0.05M to 0.1M. For the samples with MW equal or higher than

50K, there shows still further decrease of intrinsic viscosity from the salt level of 0.05 to 0.1M.

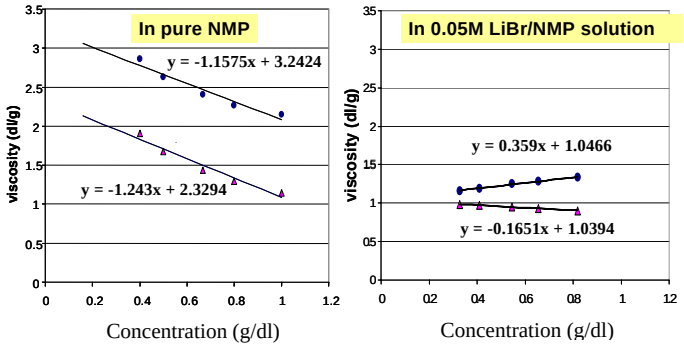

Figure 1. Evolution of the reduced viscosity and inherent viscosity versus concentration of BPS35-control sample in salt-free NMP and in 0.05M LiBr/NMP respectively.

Table 1. Summary of Intrinsic Viscosity Result of BPS35 at Different Salt Levels.

Sample	[η] [dl/g] 0.01M LiBr	[η] [dl/g] 0.05M LiBr	[η] [dl/g] 0.1M LiBr	$[\eta]_\infty$ [dl/g] (salt-free) Liberti-Stivala equation
BPS35_20K	0.51	0.43	0.41	0.43
BPS35_40K	0.70	0.56	0.52	0.54
BPS35_50K	0.95	0.74	0.68	0.59
BPS35_control	1.41	1.04	0.93	0.91

For salt-free polyelectrolyte solutions, an empirical analysis could also be performed to extract the intrinsic viscosity by extrapolation to infinite concentration using the Liberti-Stivala equation[5,6]

$$\eta_{red} = [\eta]_\infty + k\frac{[\eta]_\infty}{\sqrt{c}}$$

Where $[\eta]_\infty$ represents the intrinsic viscosity when the charges are shielded to the extent that the macromolecule behaves as a non-charged chain and is determined from the extrapolation to infinite concentration. Figure 2 shows the evolution of reduced viscosities for BPS35 with different molecular weights in salt-free NMP. The plot of η_{red} versus $c^{-1/2}$ is presented in Figure 3. The viscosity of BPS35 solutions is well represented by the Liberti-Stivala equation since a linear behavior is obtained. $[\eta]_\infty$ values of BPS35 samples with different molecular weights obtained by linear extrapolation were listed in Table 2.

The GPC measurement of BPS35 was also performed using NMP/LiBr as the mobile phase. The existence of charged groups in the copolymer coil may causes some specific problems in interpreting the results of GPC because, in addition to size exclusion, some additional mechanism might be involved.[7] Our result shows that GPC coupled with the light scattering detection seems to be a very promising way to characterize the MW of ion-containing PEMs. The detailed GPC data will be presented in the meeting.

Conclusions

Intrinsic viscosity measurements of BPS35 with different molecular weights were conducted in NMP with different concentration levels of LiBr. The salt (LiBr) was used to shield the polyions from intramolecular expansion and afforded linear plots. For salt-free BPS35 solutions, the viscometric behavior is shown to fit well with the Liberti-Stivala equation.

Acknowledgements

The authors would like to thank the Department of Energy for support of this research effort.

References

(1) Wang, F.; Hickner, M.; Kim, Y.S.; Zawodzinski, T.; McGrath, J.E.; *J. of Membr. Sci*, **2002**, 197,231-242

(2) Hickner, M. A.; Ghassemi, H.; Kim, Y. S.; Einsla, B. A.; McGrath, J.E.; Alternative polymer systems for proton exchange membranes (PEMs), *Chem. Rev.*, **2004**, 104, 4587

(3) Wang, F.; Glass, T., Li, X.; Hickner, M.; Kim Y.S.; J.E. McGrath, *Polymer Preprint*, **2002**, 43(1), 492-493

(4) Cohen, J.; Priel, Z.; Rabin, Y.; *J. Chem. Phys*. **1988**, 88, 7111

(5) Yan, L.; Dougherty, T. J.; Stivala, S. S.; *J. Polym. Sci. Part A2*, **1972**, 10, 171

(6) Aldebert, P.; Gebel, G.; Loppinet, B.; Nakamura, N.; *Polymer*, **1995**, 36, 431-434

(7) Blagodatskikh, I. V.; Sutkevich, M. V.; Sitnikova, N. L.; Khokhlov. A. R.; *J. Chromatography A*, **2002**, 976, 155-164

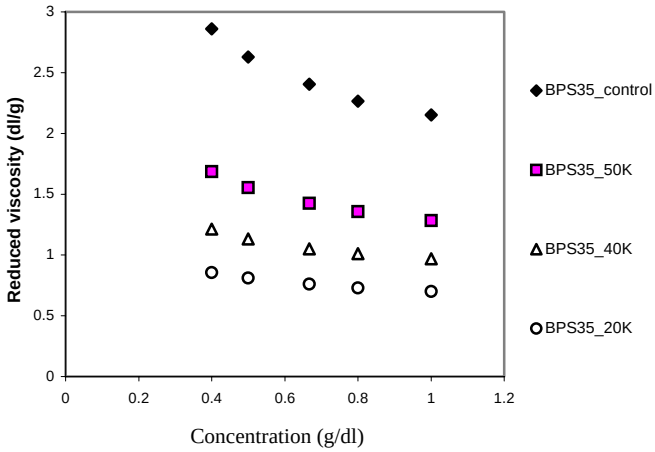

Figure 2. Concentration dependence of reduced viscosity of BPS35 in salt-free NMP

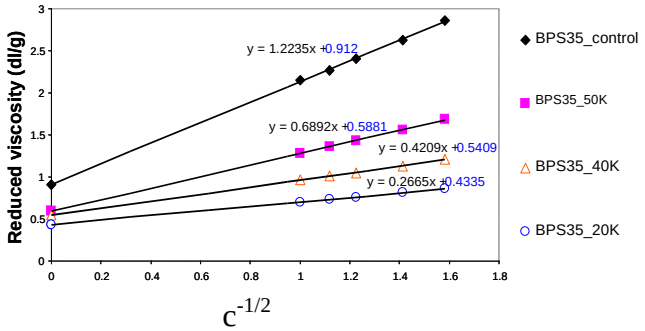

Figure 3. η_{red} versus $c^{-1/2}$ of BPS35 solutions in salt-free NMP

MORPHOLOGICAL ANALYSIS BY ATOMIC FORCE MICROSCOPY (AFM) OF PARTIALLY FLUORINATED DISULFONATED POLY(ARYLENE ETHER SULFONE) COPOLYMERS

*Anand S. Badami, Brian Einsla, Melinda Hill, Kenton B. Wiles and James E. McGrath**

Department of Chemistry
Macromolecules and Interfaces Institute
Virginia Polytechnic Institute and State University
Blacksburg, VA 24061, USA
*jmcgrath@vt.edu

Abstract

The realization of proton exchange membrane (PEM) fuel cells as commercially available energy conversion sources for a variety of applications depends largely upon the development of PEMs whose properties are enhanced over current perfluorinated sulfonic acid PEMs. An essential key to developing such materials lies in understanding how the morphology of a membrane affects its properties relevant to PEM usage such as proton conductivity and hydrolytic stability. The present study evaluates the relationship between the morphologies and select membrane properties of partially fluorinated poly(arylene ether sulfone) copolymers with disulfonation levels ranging from 10 to 60 mol%. Morphology was characterized by tapping mode atomic force microscopy. Molecular weight was estimated by intrinsic viscosity, and the water uptake and protonic conductivities of the polymers were also quantified. For disulfonation levels at or below 45 mol%, water uptake and conductivity were shown to scale proportionally with changes in morphological phase separation of the polymers. Analysis of two 35 mol% disulfonated membranes of different molecular weight suggested that molecular weight influences copolymer phase separation during membrane fabrication, but further study is required to elucidate the relationship between molecular weight, morphology, and membrane properties.

Introduction

The proton exchange membrane (PEM) fuel cell is fuel conversion technology for applications ranging from automobiles, homes, and portable electronic devices. PEMs must possess several characteristics to be viable, like high protonic conductivity, good mechanical properties, hydrolytic stability, low fuel permeability, and cost effectiveness [1]. While Nafion®, a perfluorinated sulfonic acid polymer, is currently the standard for use in PEMs, its limitations, which include cost and fuel permeability, have prompted research into alternative PEM materials. A promising alternative to Nafion® may be sulfonated poly(arylene ether sulfone) (BPSH) copolymers, which display good chemical/mechanical stability and proton conductivity, as well as reduced fuel permeability [2]. Sulfonated poly(arylene ether sulfone) copolymers synthesized with fluorinated comonomer (4,4'-hexafluoroisophenylidene diphenol or 6F-bisphenol) possess the positive membrane characteristics of BPSH copolymers and bond well to Nafion® electrodes. Understanding how the morphology of a membrane is related to its PEM properties is a necessary, but largely overlooked, step in developing new PEM materials. Consequently, the present study evaluates the relationship between morphology and membrane properties of partially fluorinated disulfonated poly(arylene ether sulfone) copolymers.

Experimental

Materials. Partially fluorinated poly(arylene ether sulfone) random copolymers with varying amounts of disulfonation (6FS-x; where x equals 10, 25, 35, 45, or 60 mol%) were synthesized as previously reported [3]. N,N-Dimethylacetamide (DMAc; EMD Chemicals, Gibbstown, NJ) was used as received.

Film Casting and Membrane Acidification. Copolymers in their potassium sulfonate salt form were dissolved in DMAc (7.5% (w/v) for microscopy, 10% (w/v) for all other characterizations). Solutions were syringe filtered through 0.45 μm Teflon® filters and cast onto clean glass substrates. The transparent solutions were dried under a 120V, 250W infrared lamp for 24 h and the resultant films were dried under vacuum at 60 °C for 12 h. Films were lifted from their substrates by immersion in deionized water. The 6FS-60 film was converted to its acid form (6FSH-60) by immersion in 1.5 M sulfuric acid for 24 h followed by rinsing and then immersion in deionized water for 24 h, which has been termed "Method 1" [2]. All other films were boiled in 0.5 M sulfuric acid for 2 h, rinsed, and then boiled in deionized water for 2 h, termed "Method 2" [2].

Characterization

Intrinsic viscosities of the potassium sulfonate salt form of the copolymers were obtained in NMP with 0.05 M LiBr at 30°C using an Ubbelohde viscometer. Conductivity measurements of acidified membranes were performed at 30 °C in water using a Hewlett-Packard 4192A impedance/gain-phase analyzer over a frequency range of 10 Hz-1 MHz. The cell geometry was chosen to ensure that the membrane resistance dominated the response of the system. The resistance of the film was taken at the frequency that produced the minimum imaginary response. To obtain water uptake values, membranes were dried for 24 h at 100 °C, weighed, and immersed in deionized water at room temperature for 24 h. The wet membranes were blotted dry and immediately weighed again. Water uptake was calculated as the ratio of the difference between wet and dry membrane weight divided by dry membrane weight and expressed as a weight percent. Atomic force microscopy (AFM) images were obtained using a Digital Instruments Dimension 3000 microscope in tapping mode, with micro-machined cantilevers with force constants of 40 N/m or 5 N/m. Samples were dried under vacuum at 60 °C for 12 h and then equilibrated at 50% relative humidity for at least 12 h before being imaged immediately at room temperature in a relative humidity of approximately 35%.

Results and Discussion

A series of partially fluorinated poly(arylene ether sulfone) copolymer (Figure 1) membranes with varying amounts of disulfonation (6FSH-x; where x equals 10, 25, 35, 45, or 60 mol%) were imaged using tapping mode AFM (Figure 2).

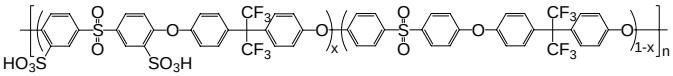

Figure 1. Chemical structure of partially fluorinated poly(arylene ether sulfone) copolymers.

The AFM images show that these 6FSH-x copolymers display a hydrophilic/hydrophobic phase separated morphology, with the hydrophilic sulfonated domains appearing darker than the hydrophobic domains. This is expected because BPSH copolymers have been shown to display similar phase separated morphology as a result of their direct copolymerization of biphenol units with hydrophobic diphenyl sulfones and hydrophilic disulfonated diphenyl sulfones [4]. 6FSH-x copolymers are synthesized similarly to BPSH, but with 6F-bisphenol instead of biphenol, which introduces fluorination into their structure.

Water uptake of the 6FSH-x copolymers was measured (Figure 3). There are two distinct parts of the water uptake vs. disulfonation plot. In the first part, regime I, water uptake gradually increases with an increase in disulfonation. The AFM images in

Figure 2 corroborate this observation because the connectivity of the hydrophilic (dark) domains appears to increase slightly with level of disulfonation, reaching a maximum between 35 and 45 mol% disulfonation.

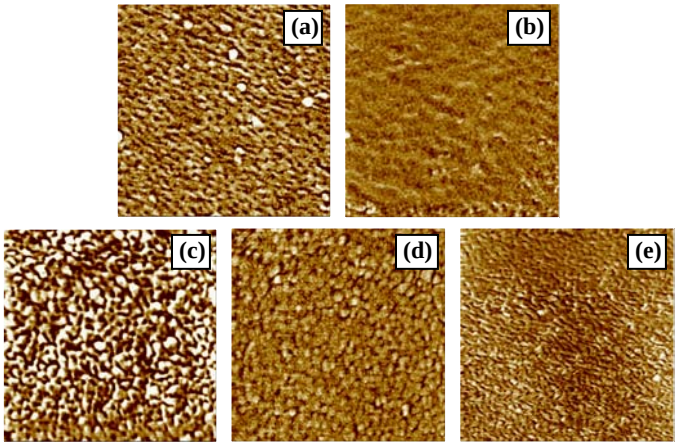

Figure 2. Tapping mode AFM phase images of 6FSH-x membranes with varying levels of disulfonation (mol%): (a) 10 (b) 25 (c) 35 (d) 45 and (e) 60. Scan sizes: 1µm, *Z* ranges: (a) 25° and (b-e) 8°.

In the second part of the graph, regime II, the water uptake increases dramatically as disulfonation increases to 60 mol%. This phenomenon has been observed before for BPSH membranes [4]. The swelling accompanying such a large water uptake would make BPSH-60 undesirable for use as a high-performance PEM.

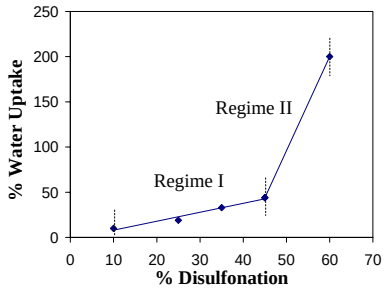

Figure 3. Effect of level of disulfonation on water uptake of 6FSH-x membranes.

Proton conductivity measurements were also made on the 6FSH-x copolymer series (Figure 4). Unlike water uptake, conductivity increases proportionally with level of disulfonation. Only the 6FSH-60 membrane displayed a proton conductivity above 0.08 S/cm, which is desired for high-performance fuel cell PEMs.

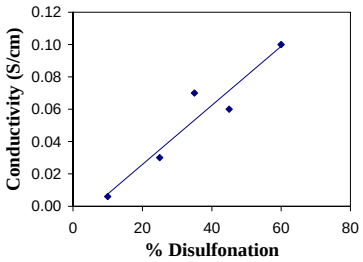

Figure 4. Effect of level of disulfonation on conductivity of 6FSH-x membranes.

A second 6FSH-35 membrane with a lower molecular weight than the one in Figure 1 was also imaged by tapping mode AFM. (Figure 5). The two 6FSH-35 copolymers have distinctly different molecular weights as indicated by their intrinsic viscosities (Table 1). Despite this difference, the water uptake and conductivity data for the two 6FSH-35 copolymers are essentially the same (Table 1). However, the difference in molecular weight is manifested in the multiphase morphology of the two membranes (Figure 5).

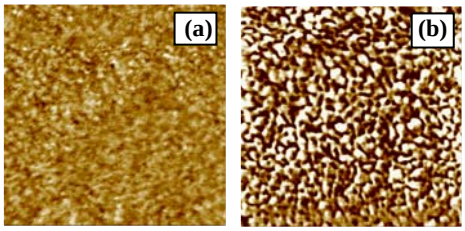

Figure 5. Tapping mode AFM phase images of 6FSH-35 membranes of (a) low and (b) high molecular weights (intrinsic viscosity data in Table 1). Scan sizes: 1µm, *Z* ranges: 6° and 8°.

Table 1. Properties of 6FSH-35 Membranes

6FSH-35 Membrane	Intrinsic Viscosity (dL/g)	Water Uptake (%)	Proton Conductivity (S cm^{-1})
low MW	0.50	33	0.07
high MW	1.01	30	0.07

The 6FSH-35 copolymer of lower molecular weight possesses smaller hydrophobic (bright) and hydrophilic (dark) domain structures than its higher molecular weight counterpart. This suggests that while molecular weight influences the phase separation of the ionomeric copolymers during membrane fabrication, it may or may not have as pronounced of an influence on membrane properties like water uptake and conductivity. Further study is required to assess whether molecular weight plays a greater role in affecting phase separation during membrane casting or acidification.

Conclusions

At low levels of disulfonation (≤45 mol%), both water uptake and proton conductivity of 6FSH-x membranes increase proportionally with disulfonation. These increases correspond to an increase in connectivity of the hydrophilic sulfonated domains in the morphologies of the membranes. While conductivity is favorable for PEM usage at 60 mol% disulfonation, water uptake is too high, preventing the membranes tested from being immediate candidates for high-performance PEMs. Morphological analysis of two 6FSH-35 membranes of two different molecular weights suggests that molecular weight influences copolymer phase separation during membrane fabrication, but it may or may not have as pronounced of an influence on all membrane properties. Further study is required to elucidate the relationship between molecular weight, morphology, and membrane properties.

Acknowledgement. The authors wish to thank the National Science Foundation "Partnership for Innovation" Program (HER-0090556) and IGERT Program (DGE-0114346), and the Department of Energy (DE-FC36-01G01086) for supporting this research.

References

(1) Hickner, M.A.; Ghassemi, H.; Kim, Y.S.; Einsla, B.R.; McGrath, J.E.. *Chem. Rev.* **2004**, *104*, 4587.
(2) Kim, Y.S.; Wang, F.; Hickner, M.; McCartney, S.; Hong, Y.T.; Harrison, W.; Zawodzinski, T.A.; McGrath, J.E. *J. Polym. Sci., Part B: Poly. Phys.* **2003**, *41*, 2816.
(3) Harrison, W.; Wang, F.; Mecham, J.B.; Bhanu, V.; Hill, M.; Kim, Y.S.; McGrath, J.E. *J. Polym. Sci., Part A: Polym. Chem.* **2003**, *41*, 2264.
(4) Wang, F.; Hickner, M.; Kim, Y.S.; Zawodzinski, T.A.; McGrath, J.E. *J. Membr. Sci.* **2002**, *197*, 231.

NANOSTRUCTURED MATERIALS BASED ELECTRODES FOR BIOFUEL CELLS

Xing-Hua Xia, Yan-Yan Song, Cui-Hong Wang and Jin-Hua Yuan*

Key lab of Analytical Chemistry for Life Science, Department of Chemistry, Nanjing University, Nanjing 210093, China

Introduction

Combination of biologically active components (enzymes, antibodies, nucleic acids and cells) with nanomaterials with unique properties has been promising for biosensing, genome analysis, bioelectric devices, biofuel cells. [1,2] To realize these applications, high stability and function density of the immobilized biologically active components are usually required. We recently focused on the preparation and characterization of biointerfaces based on assembly of nanostructured materials with rigid structure, good conductivity, good biocompatibility and larger active surface area. Glucose oxidation and direct electron transfer of hemoglobin were used as model to demonstrate importance of such materials for construction of functional electrodes for glucose biosensor and biofuel cells with high function density.

Experimental

Biocompounds (Sigma) were used without further purification. All the other chemicals were of analytical grade. Solutions were prepared with distilled water (>18 MΩ, Purelab Classic Co., USA).

All electrochemical experiments were carried out on a CHI650 Electrochemical Workstation (CH Instrument, U.S.A.). A traditional three-electrode system involving a Pt sheet as counter electrode, a saturated calomel electrode (SCE) as reference, and an ordered macroporous noble metal film (Pt or Au) as working electrode was used. The geometric area of the working electrode was controlled by a Viton O-ring and determined to be 0.19 cm^2. All potentials in this paper refer to the SCE.

Morphology of the 3D Au films was examined on a scanning electron microscope (Hitachi SEM-X650, Hitachi Ltd., Tokyo, Japan) at an acceleration voltage of 20 kV. High-resolution SEM micrographs (HRSEM) were also measured on a Semi-in-lens Field Emission SEM-4700 (Hitachi, Japan). Structural characterization was performed by means of X' Pert Pr X-ray diffraction (Philips). Attenuated total reflection (ATR) spectra were recorded on a Tensor 27 Fourier transform infrared spectrometer (Bruker, Germany) equipped with a multi-reflection ZnSe prism and a DTGS detector.

Preparation of ordered noble metal Macroporous Film electrodes. Monodispersed SiO_2 spheres were synthesized on the basis of Stöber method. [3] The vertical deposition technique [4] was used to self-assemble the silica spheres on gold/Cr/glass slides, forming (111) close - packed crystals. Before metal deposition, the silica colloidal crystals were sintered at 200 °C under nitrogen atmosphere for 2 h. Then, the silica template was immersed into a solution containing gold or platinum salt for 1h prior to electrolyzing in order to allow the solution to penetrate throughout the template. Using the silica template on gold slides as the working electrode, electrochemical deposition of gold in the spaces between silica beads was carried at 0.3 V (vs. SCE) until the required charge has been passed. This deposition potential was chosen to guarantee that the deposition be realized within the interspaces of the silica template without damaging its highly ordered structure. Thickness of the macroporous metal films was controlled by the charge used during the electrodeposition step. After the deposition, the silica template was etched for ca. 5 min using 5% aqueous HF to leave behind a highly ordered macroporous metal film. These films were characterized with AFM or SEM. Electrochemical cleaning of the electrode was performed using cyclic potential scan in a solution of 0.5 M H_2SO_4 at a scan rate of 100 mV/s. From the hydrogen region for Pt or the reduction peak for Au materials, the active surface areas were measured by assuming that a monolayer of AuO requires 0.386 mC or a monolayer of H_{ad} requires 0.21 mC per square centimer.[5,6]

Results and Discussion

The prepared platinum or gold macroporous film is of similar structure consisting of interconnected periodic hexagonal array of monodispersed pores. **Figure 1** shows the film structure of the 3D macroporous Pt film. X-ray diffraction result showed that the macroporous catalyst mainly consisted of (111) and (200) crystalline orientations. The average particle size of the Pt deposited in 200 nm hole size was calculated to be ca. 5.36 nm from a (111) X-ray diffraction peak of Pt fcc lattice in terms of the Scherrer equation. By controlling the deposition time, we obtained 3D macroporous Pt films with different surface roughness factor (R_f: ratio of the real active surface area which can be determined by the charge for hydrogen adsorption to the geometric area).

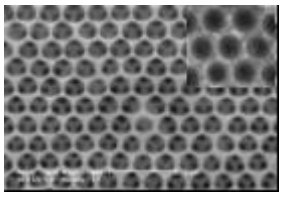

Figure 1. SEM photograph of a 3D macroporous Pt film prepared as described in the text.

The electrocatalytic activity of the Pt film electrode towards the oxidation of glucose in PBS was investigated. As shown in **Figure2**, there are two current peaks for the electrooxidation of glucose. The first current peak should be due to the electrosorption of glucose to form an adsorbed intermediate, releasing one proton per glucose molecule. The second current could be due to the direct oxidation of glucose on the Pt film electrode. In addition, it is clear that the electrocatalytic activity of the Pt film electrodes increases with the decrease in pore size. Understanding of this phenomenon is undertaking.

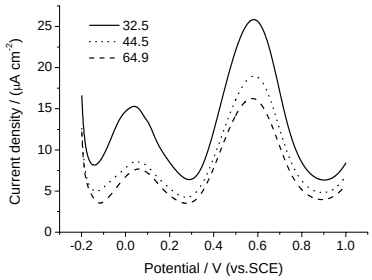

Figure 2. Current density-potential curves of the Pt film electrodes with pore size of 200 nm (solid curve), 320 nm (dotted curve) and 500 nm (dashed curve) in a solution of PBS+50 mM glucose at a scan rate of 2 mV/s.

Due to the high electrocatalytic activity of the Pt film electrode towards the oxidation of glucose, in principle, such electrodes can serve as suitable anode for implantable biofuel cells. In addition, it can be used as glucose sensor for evaluation of the glucose level in human body. Therefore, detection potential and solution PH for glucose sensing using a Pt film electrode with pore size of 200 nm was optimized. It was found that the optimal solution pH and the detection potential are 9.18 and 0.5 V vs SCE, respectively. Further

experiments were performed using 0.05 M phosphate buffer solution at pH 9.18.

Under the above optimal experimental conditions, amperometric response of the 3D Pt film electrode with a pore size of 200 nm is linear in glucose concentration in the range from 10^{-2} mol L^{-1} to 10^{-6} mol L^{-1} with a detection limit of 10^{-7} mol L^{-1} and a sensitivity of 31.3 mA cm^{-2} mM^{-1} estimated at a signal-to-noise ratio of 3, indicating that our sensing material can give higher sensitivity for glucose detection. The response of the normal interferents to glucose detection was evaluated. **Figure 3** shows the response of a 3D inverse opal Pt film electrode (pore size: 200 nm) and a directly deposited Pt electrode to glucose upon addition of 0.2 mM UA, 0.2 mM AP, and 0.1 mM AA. It was found that under the optimal detection conditions, negligible interference form these interferents was observed. The present results showed that increase in surface roughness factors can significantly increases the selectivity for glucose detection. This is due to the fact that the electrochemical reaction for glucose is kinetic controlled, while the reactions of interferents are diffusion controlled. The current for the latter is only determined by the geometric area. While in the former case, the current is significantly enhanced by increasing the real surface area. The results demonstrate that the present 3D inverse opal Pt film electrode is promising for fabrication of non-enzymatic glucose biosensors. In addition, the Pt film electrode can be easily cleaned with modulated potential cycling; they are promising for implantable biofuel cells and glucose biosensors.

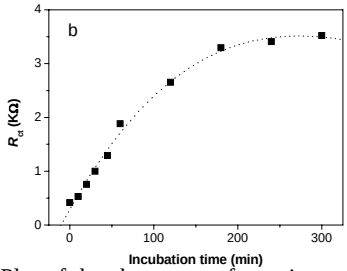

Figure 3. Plot of the charge transfer resistance R_{et} against incubation time. The data were obtained from electrochemical impedance measurements using ferricyanide as probe.

When look at the macroporous film electrode with high resolution SEM, we observed that the structures were consisted of Pt nanoparticles. Such nanoparticles are good biocompatible sites for immobilization of biocompounds, e.g., proteins, enzymes. For this proposes, we fabricated 3D gold film electrode and studied the immobilization and direct electron communication of hemoglobin on the film electrode via the gold nanoparticles as electron relays. Such electrodes have many advantages such as stable structure, high conductivity and high active surface area which is important for obtaining high function density. In addition, the structure provides suitable microenvironment for the immobilization of biocoumpounds whose bioactivity is fully retained. Attenuated Fourier infrared spectroscopic measurements showed that hemoglobin can be easily immobilized on such gold film structure. Appearance of the FTIR features for the secondary structure of the polypeptide chain demonstrates that the immobilized hemoglobin on gold film electrode retains its bioactivity.

We used the sensitive electrochemical impedance technique to probe the adsorption kinetics of hemoglobin (Hb) on gold film electrode using ferricyanide as probe. As shown in **Figure 3**, at the beginning, the Hb coverage increased with the adsorption time almost linearly (<180 min) and then its coverage reached a relative stable value with longer adsorption time (>180 min). This result demonstrated that a saturated monolayer of Hb with coverage of 87.4% was formed at the adsorption of 180 min. This monolayer of Hb on gold film electrode is stable within one month if stored at 4 ^{o}C.

Direct electron transfer between the adsorbed Hb and gold film electrode was characterized with cyclic voltammetry. **Figure 4** shows the cyclic voltammograms (CVs) of a 3D macroporous gold film electrode in PBS with pH 7.0 in the presence (curves b and c) and absence of Hb (curve a). Without Hb in the solution, there is no current peak in the scanned potential window. Addition of 0.2 mg ml^{-1} Hb into the PBS solution, a well-resolved pair of quasi-reversible redox peaks appeared (curve b) due to the direct electron communication of the adsorbed Hb and the gold film electrode. The anodic and cathodic peak potentials located at 0.27 V and 0.09 V (*vs* SCE), respectively. The observed direct electron transfer of the Hb can be due to the fact that the gold nanoparticles of the macroporous gold film electrode are effective adsorption sites that can penetrate easily to the active center of the Hb molecules. In addition, the gold nanoparticles of the macroporous structure would provide multiple adsorption sites for Hb molecules, retaining the bioactivity of the adsorbed Hb. Thus, it is possible to achieve fast direct electron transfer between the heme site of immobilized Hb and the electrode surface. The increased peak current with the increase of Hb concentration (compare curves b and c) demonstrated that more Hb molecules adsorbed on the electrode surface, indicating that concentrated Hb solution facilitated the adsorption of Hb on the electrode surface.

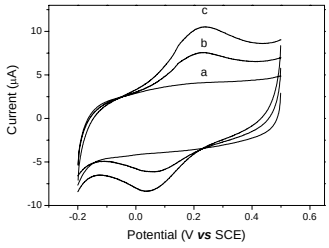

Figure 4. Plot of the charge transfer resistance R_{et} against incubation time. The data were obtained from electrochemical impedance measurements using ferricyanide as probe.

Conclusions

The as prepared 3D macroporous noble metal film electrodes are promising for construction of implantable glucose biofuel cells and glucose biosensor as well. In addition, such structured materials are stable and biocompatible and suitable for construction of bioelectronic devices with high function density via nanoparticles as electron relays for direct electron transfer.

Acknowledgement. This work was supported by grants from the National Natural Science Foundation of China (NSFC, No. 20125515; 20375016; 20299030) and the Doctoral Fund of Education Ministry of China (20020284021).

References

(1) Daniel, M.C.; Astruc, D. *Chem. Rev*. **2004**, *104*, 293.
(2) Shipway, A. N.; Katz, E.; Willner, I. *ChemPhysChem* **2000**, *1*,18.
(3) Stöber, W.; Fink, A.; Bohn, E. *J. Colloid Interface Sci.* **1968**, *26*, 62.
(4) Jiang, P.; Bertone, J. F.; Hwang, K. S.; Colvin, V. L. *Chem. Mater*. **1999**, *11*, 2132.
(5) Kozlowska, H. A.; Conway, B. E.; Hamelin, A.; Stoicoviciu, L. *J. Electroanal. Chem.* **1987**, *278*, 429.
(6) Xia, X. H.; Iwasita, T. *J. Electrochem. Soc.* **1993**, *140*, 2559.

DIRECT METHANOL FUEL CELLS WITH MEDIATED BIOCATALYTIC CATHODES

Nicholas S. Hudak and Scott Calabrese Barton

Department of Chemical Engineering, Columbia University, 500 W. 120th St., Suite 801, New York, NY 10027, Fax: 2128543054, nsh2001@columbia.edu

Abstract

The oxygen-reducing enzyme laccase can be used with a redox polymer mediator as the cathode catalyst in direct methanol fuel cells (DMFC). The biocatalyst has several advantages over precious-metal catalysts, including selectivity and low manufacturing cost. A biocathodic DMFC has demonstrated successful operation with 10 M methanol at the anode and air-saturated buffer solution at the cathode or with a mixed-reactant feed supplied to both electrodes. In order for the biocatalytic cathode to be used in a conventional DMFC, it must operate on gas-phase air. Sufficient catalytic activity, electron and ion transport, and hydration must be maintained in the presence of gaseous reactants. These properties will be studied along with the effect of any added solid electrolyte phase.

FABRICATION AND ELECTROCHEMICAL CHARACTERIZATION OF GLUCOSE OXIDASE-IMMOBILIZED CARBON ELECTRODE

Ying-Ying Horng[1], *Chia-Liang Sun*[2], *Li-Chyong Chen*[2], *Kuei-Hsien Chen*[2,3], *and Chia-Chun Chen*[1,3]

1. Department of Chemistry, National Taiwan Normal University, Taipei, Taiwan
2. Center for Condensed Matter Sciences, National Taiwan University, Taipei, Taiwan
3. Institute of Atomic and Molecular Sciences, Academia Sinica, Taipei, Taiwan

Abstract

We demonstrated the synthesis and related electrochemical properties of enzyme, glucose oxidase (GO_x), modified carbon cloth electrodes which are mediated by gold nanoparticles (Au NPs) in this report. The Au NPs with an average diameter of 4 nm are used as a significant electron relay or mediator for the alignment of the GO_x on the carbon support. Meanwhile, the GO_x is immobilized by flavin adenin dinucleotide cofactor on Au NPs. Therefore, the biological catalysts, GO_x, become much more stable on conductive carbon supports. Moreover, cyclic voltammetry are used to study the electrochemical behavior in a three-electrode system. The results show that immobilized GO_x is able to maintain its specific enzyme activity in the presence of glucose. Furthermore, the dependence of current density and the redox potential in the corresponding reaction is also investigated. As a consequence, under optimal condition, good electrochemical behavior and large current can be achieved, thereby indicating the potential application in biofuel cells.

ELECTRICITY GENERATION FROM FOOD AND ANIMAL WASTEWATERS USING MICROBIAL FUEL CELLS

SangEun Oh[1], Jungrae Kim[1], Booki Min[1], and, Bruce Logan[1,2]

[1]Department of Civil and Environmental Engineering,
[2]The Penn State Hydrogen Energy (H_2E) Center, Penn State University, University Park, PA, 16802, U.S.A.

Introduction

Wastewater containing high-strength organic contaminants is produced daily from industrial, animal, and agriculture procedures. For example, Approximately 20,000 food processing industries in the US annually produce 1.4 billion liters of wastewater (*1*). Agriculture manures are annually generated at 5.8×10^7 ton (*2*). Aerobic wastewater treatment costs can be very high for these wastewaters. However, recent approaches for dealing with these wastewaters not only consider treatment but also generate useful energy such as hydrogen or methane from the organic matter in the wastewater (*3,4*).

Recently, a new technology of using a microbial fuel cell (MFC) has been developed to generate electricity directly from marine sediments, anaerobically digested sludge, and domestic wastewater (*5-11*). Logan (2004; ref. *3*) compared the relative economic potential of hydrogen, methane, and electricity production through MFCs from a single large food processing plant and found that it was most economical when all the organic matter could be recovered directly as electricity in an MFC. A laboratory-scale MFC generated 10 to 16 mW/m^2 based on placing an anode electrode in a marine sediment (anaerobic) and a cathode electrode in the overlying seawater (aerobic) (*5,6,8*). Tender et al. (2002; ref.*7*) obtained over 25 mW/m^2 of power by in situ use of MFCs in marine sediments in the field (*7,8*). Domestic wastewater was also used as the source of a biocatalyst and substrate in MFC operations (*9-11*). A single chamber MFC continuously generated 26 mW/m^2 (maximum power density) while removing up to 80 % COD of wastewater (*9*). Liu et al. (2004; ref. *10*) generated more power (146 ± 8 mW/m^2) using an air-cathode MFC, that lacked a proton exchange membrane, in a batch mode operation. A flat plate MFC generated continuous power of 72 ±1 mW/m^2 at 1.1 h hydraulic retention time (HRT; 0.39 mL/min) with a COD removal rate of 2.4 mg/L-min (42 % removal) (*11*). It is also known that electricity can be generated in MFCs from typical fermentation end products such as acetate and butyrate (*10-13*), but actual waste streams or solutions containing a variety of these chemicals have not been directly tested.

In this study, we investigated the potential of producing electricity from food processing and animal wastewaters using a MFC.

Methods

MFC construction. Electricity generation from food processing and swine wastewaters was measured using two different MFC systems: a two chambered aqueous cathode system, and a one-chambered direct air cathode system. The two-chambered system was constructed by joining two media bottles (310 mL capacity, Corning Inc. NY) with a glass tube containing a proton exchange membrane (PEM; Nafion™117) clampe d between the flattened ends of the glass tubes fitted with two rubber gaskets (6.2 cm^2 cross section) as described previously (*13*). The surface area of proton exchange membrane was A_{PEM}=6.2 cm^2, and the anode and cathode had equal projected surface areas of $A_{An}=A_{Cat}$=22.5 cm^2. A one-chambered MFC (28 mL capacity) was constructed and operated as previously reported (*10*), and did not contain a PEM (117 Ω external resistance; $A_{PEM}=A_{Anode}=A_{Cathode}$=7.1 cm^2). For both systems, the anode electrode was made of Toray carbon paper (without wet proofing; E-Tek) and the cathode electrode was coated with a Pt catalyst (0.5 mg/cm^2, 10% Pt; De Nora North America, Inc.) on one side. The systems were inoculated with anaerobic dewatered sludge (1g; 85% water content) or swine wastewater. The pH of the wastewaters was adjusted to pH=7.0 using 2M NaOH or 2M HCl. Maximum power density was determined by changing the circuit resistor and measuring power output over a complete batch cycle of operation.

Samples. A wastewater sample was taken from a cereal processing unit at a food processing plant that is known to be high in COD (Cereal). The animal wastewater was collected from the Pennsylvania State University Swine Farm. The wastewater was used to inoculate the chamber without any modifications. Raw or wastewater diluted with ultrapure water (Milli-Q system; Millipore Corp., New Bedford, MA) was used as the medium.

Calculations and analysis. Voltage (*V*) produced by the MFC was measured using a multimeter with a data acquisition system with power (*P=IV)* normalized by the cross sectional area (projected) of the anode. Power (*P*) was calculated according to *P=IV (I=V/R)*, where *I* (A) is the current, *V* (V) the voltage, and *R*(Ω) resistance. The Coulombic efficiency, *E* (%), was calculated as $E=(C_{Ex}/C_{Th})\times100$, where $C_{Ex,}$ is the total coulombs calculated by integrating the current measured at each time interval (*i*) over time as $C_{Ex}=(\sum_{i=1}^{T}V_i t_i)/R$. C_{Th} , the theoretical amount of coulombs that is available from COD (*i*=c) or propionate (*i*=p) oxidation, was calculated as

$$C_{Th}=\frac{F\ b_i\ S_i v}{M_i} \qquad (2)$$

where *F* is Faraday's constant (96,485 C/mol-e$^-$), *b* the number of moles of electrons produced per mol of substrate (b_c=4, b_p=10), *S* the acetate concentration, *M* the molecular weight of the substrate (M_c=32, COD basis; M_p=74.08), and *v* the liquid volume (L). The concentrations of several solvent compounds (acetone, ethanol, propanol, and butanol) and organic acids (acetate, propionate, and butyrate) were determined by gas chromatography (Varian Star 3400) as described previously (*14*). Glucose was analyzed using the phenol-sulfuric acid method for reducing sugars (*15*). Alkalinity, chemical oxygen demand (COD), Total suspended solids (TSS), and ammonia were determined according to Standard Methods (*16*).

Results and Discussion

Food processing wastewater. The in-plant stream obtained from the cereal processing wastewater contained a COD of 8920 (Cereal) mg/L. The diluted wastewater (10×) was first tested for electricity generation using the two chambered MFC. Following inoculation and start up, the reactor was switched to the diluted Cereal wastewater (TCOD=892 mg/L; SCOD=595 mg/L). The voltage increased rapidly to 0.29 V within 5 hr, and voltage was gradually decreased over the next 400 h as the organic matter in the reactor was degraded (Fig. 1A). The maximum power density was 81±7 mW/m^2 of electricity (power normalized to the surface area of the anode carbon paper electrode) during the first 200 h. This power density is close to the maximum believed to be possible with this system. For example, with acetate as the substrate, the maximum power with this system was found to be 88 mW/m^2 (*13*). Coulombic efficiencies were 27.1% and 40.5% based on TCOD and SCOD, respectively. The open circuit potential (OCP) was 776 mV, and the individual electrode potentials (based on a Ag/AgCl reference electrode) were 298 mV and -478 mV for cathode and anode, respectively.

An analysis of the reactor contents during electricity generation demonstrated that sugars were rapidly reduced, resulting in the formation and release into solution of many volatile acids and alcohols typical of fermentation processes. Sugars were reduced within 50 h from 230 mg/L to <20 mg/L (Fig. 1B). The main volatile acid was acetic, which reached a concentration of 166 mg/L followed by propionate. After 50 h of reaction, the concentrations of these two volatile acids slowly decreased over the next 400 h to <20 mg/L.

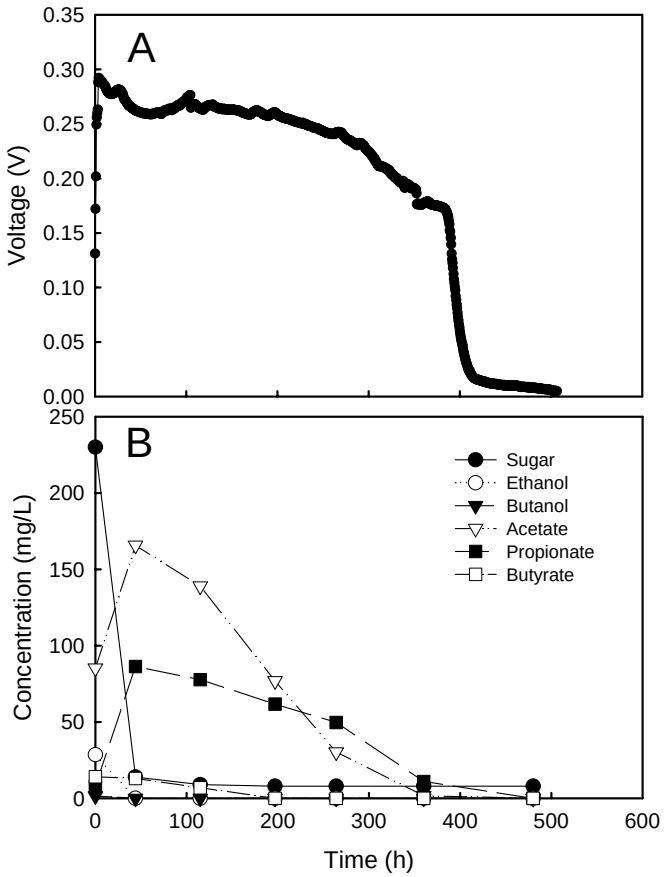

Figure 1. (A) Electricity generation by a two-chambered MFC using cereal wastewater, (B) Sugar, organic acid, and alcohol concentrations in the liquid in the anode bottle over time.(480 Ohm Resistor; liquid Volume: 250 mL; A_{PEM}: 6.2 cm^2 ;A_{Anode}=$A_{Cathode}$: 22.5 cm^2)

A power density curve taken following stable power generation indicated a maximum power density of 371± 10 mW/m^2 (150 Ω resistor). This maximum power density is less than that obtained using glucose (494±21 mW/m^2, ref.*10*) or acetate (506 mW/m^2, ref.*17*) in the same system, demonstrating that breakdown of the organic matter limited power densities generated by the system. However, this maximum power density was much larger than the power achieved using domestic wastewater in this system (28±3 mW/m^2, ref.*9*). It is therefore clear from the experiments with the biohydrogen reactor effluent that hydrogen generation can be successfully linked with electricity generation in a MFC.

Swine wastewater. The raw wastewater had a pH of about 7.1 ± 0.2 (n = 3) and an average chemical oxygen demand (COD) of 8300 ± 167 mg/L (n = 9). Voltage was slowly developed over two weeks after the MFC was loaded with the raw animal wastewater. After two sequential loadings of the wastewater into the chamber, power generation reached a maximum value of 213 mW/m^2 and then stabilized to average of 182 ±1 mW/m (voltage = 357 ±1 mV with 1000 Ω). The initial COD concentration of the animal wastewater of 8320 ±191 mg/L was reduced to 6090 ±60 mg/L (COD removal = 27%; CE = 8%) after 44 hr of operation. From the above results, we realized that bacteria in the animal wastewater were a suitable biocatalyst for generating power and degrading organic matter present in the wastewater. Power generation was measured as a function of different circuit resistances after achieving stable power generation with the 1000 Ω resistor. The circuit resistances loaded between two electrodes ranged from 2 Ω to 200 kΩ. The maximum power density was 261 mW/m^2 (Voltage = 191 mV with 200 Ω) with current density of 1.4 A/m^2.

To investigate if sufficient bacteria attached on the surface of the anode electrode, the anode chamber was filled with autoclaved animal wastewater (diluted by 1/10) for power generation. Power was produced from the sterilized wastewater in a similar manner to that obtained with raw wastewater based on maximum power (82 or 84 mW/m^2 with autoclaved wastewater; 77 or 79 mW/m^2 with raw wastewater). The Coulombic efficiency was about 20 % with raw wastewater, and 17 % with autoclaved wastewater. Thus, microorganisms attached on the electrode clearly were responsible for generating power, and the level of power generation was reproducible.

Acknowledgement. This research was supported by National Science Foundation Grants BES-0331824 and BES-0124674, United States Department of Agriculture grant 68-3A75-3-150, a seed grant from The Huck Institutes of the Life Sciences at Penn State, and the Stan and Flora Kappe endowment.

References

(1) Elitzak, H. Food Marketing, **2000**, 23(3):27-30. http://www.ers.usda.gov/publications/foodreview/septdec00/FRsept00e.pdf
(2) Dentel, S.K., Strogen, B., Sharma, A., and Chiu, P. *Proceedings*, IWA Conference on Resources from Sludge, Singapore March 2-3, **2004**.
(3) Logan, B.E. *Environ. Sci. Technol.* 2004, 38, 160A – 167A.
(4) Angenent, L.T., Karim, K., Al-Dahhan, M.H., Wrenn, B.A., and Domíguez-Espinosa, R. *TRENDS in Biotechnology*, **2004**, in press.
(5) Bond, D.R., Holmes, D.E., Tender, L.M., and Lovley, D.R. *Science* **2002**, 295, 483-485.
(6) Reimers, C.E., Tender, L.M., Ferig, S., and Wang, W. *Environ. Sci. Technol.* **2001**, 35, 192-195.
(7) Tender, L.M., Reimers, C.E., Stecher, III H.A., Holmes, D.E., Bond, D.R., Lowy, D.A., Pilobello, K., Fertig, S.J., and Lovley, D.R. Nat. Biotechnol. **2002**, 20(8), 821-825.
(8) Delong, E.F. and Chandler, P. Nat. Biotechnol. **2002**, 20, 788 - 789.
(9) Liu, H., Ramnarayanan, R., and Logan, B.E. Environ. Sci. Technol. **2004**, 38, 2281-2285.
(10) Liu, H. and Logan, B.E. Environ. Sci. Technol. **2004**, 38, 4040 – 4046.
(11) Min, B. and Logan, B.E. Environ. Sci. Technol. **2004**, 38(21), 5809-5814
(12) Bond, D.R.; Lovely, D.R. *Appl. Environ. Microbiol*. **2003,** *69*, 1548-1555.
(13) Oh, S. E.; Min, B.; Logan, B. E. *Environ. Sci. Technol.* **2004**, 38, 4900-4904.
(14) Logan, B.E., Oh, S.E., Van Ginkel, S.W. *Environ. Sci. Technol.* **2002**, **36** (11), 2530-2535.
(15) Dubois, M., Gilles, K.A., Hamilton, J.K., Rebers, P.A., and Smith F. Analytical Chemistry **1956**, 28(3),351-356.
(16) APHA; AWA; WPCF. American Public Health Association: Washington, DC, **1992**.
(17) Liu, H.; Cheng, S.-A.; Logan, B.E. *Environ. Sci. Technol.* **2005**, *39(2)*, 658-662.

BIOCONVERSION OF CELLULOSE INTO ELECTRICITY USING RUMEN MICROORGANISMS AS BIOCATALYSTS IN A MICROBIAL FUEL CELL

Hamid Rismani-Yazdi, Ann D. Christy, Burk A. Dehority, and Olli H. Tuovinen

Dept. of Food, Agricultural, and Biological Engineering
Ohio State University, 590 Woody Hayes Dr.
Columbus, OH 43210

Introduction

The diversity of biocatalyst microorganisms investigated in microbial fuel cells to date is limited and includes pure cultures such as *Shewanella putrefaciens*, *Escherichia coli*, *Geobacter sulfureducens*, and *Rhodoferax ferrireducens* as well as mixed consortia from municipal and industrial wastewater. Simple sugars, volatile fatty acids, and starch have been used as electron donors.[1] The scope of the study was to investigate the feasibility of using rumen microorganisms as biocatalysts and cellulose as the electron donor in a microbial fuel cell. Cellulose can not be easily dissolved or hydrolyzed under natural conditions due to its complex structure. Microorganisms in rumen of mammalian herbivores have great potential in the biodegradation of cellulosic materials due to their cellulolytic enzymes and their high cellulolytic activities.[2] For this study, rumen microbes and crystalline cellulose were evaluated for electricity production in a microbial fuel cell.

Materials and Methods

Microorganisms. Strained rumen fluid from a canulated cow was used as a biocatalyst. All cultures were incubated at 22±2ºC unless otherwise stated. Cellulose medium contained (per liter) 450 mg K_2HPO_4, 450 mg KH_2PO_4, 900 mg NaCl, 900 mg $(NH_4)_2SO_4$, 119.25 mg $CaCl_2{\cdot}2H_2O$, and 90 mg $MgSO_4$ plus 160 ml clarified rumen fluid (centrifuged for 5 min at 5000 *g*).[3] Crystalline cellulose (7.5 g/l) (Sigmacell-20, Sigma, St. Louis, MO) was ball milled for 24 h before it was used as the sole source of carbohydrate and electron donor. The medium was flushed with O_2-free CO_2. The pH was adjusted to 6.8 with NaOH, 4 g Na_2CO_3 was added, and CO_2 was flushed for an hour before autoclaving in a sealed round bottom flask. To determine the cellulolytic activity of the attached biofilm at the surface of the electrode in the anode compartment, biomass was scraped off and used to inoculate the cellulose media in culture tubes. Tubes were then incubated anaerobically at 39ºC and cellulose degradation was determined by visible decrease of cellulose in the media compare to uninoculated control. Where indicated, bacterial growth was inhibited with 2,000 IU of penicillin-G (Sigma) and 130 IU of streptomycin sulfate (USB Corporation, Cleveland, OH) per ml of media.

Microbial fuel cell and operation. A two-compartment biofuel cell was constructed as described by Bond and Lovley.[4] The working volume of the two chambers was 400 ml with 200 ml headspace. A proton-exchange membrane (Nafion 117; Electrosynthesis, Lancaster, NY) was used to separate anode and cathode compartments. Plain graphite 71 by 49 by 6 mm (83.98 cm^2) was used as the electrode. Chambers were autoclaved prior to the experiment. The anode compartment was gassed vigorously with O_2-free CO_2 passed through a hot copper column and filled with 360 ml cellulose medium and was inoculated with strained rumen fluid (10% vol/vol). The catholyte in the cathode compartment was 400 ml of 50 mM $K_3Fe(CN)_6$ solution in 100 mM K_2HPO_4 buffer flushed with air.[1] The power output of the fuel cell was monitored by measuring the voltage across a known resistance (1000 Ω) using a data acquisition unit. The power density, P (W/m^2) was calculated according to $P=V\times I/A$, where V is the voltage (V), I, ($I=V\times R$) is the current (A), and A is the surface area (m^2).

Results and Discussion

To study the role of rumen microorganisms as biocatalysts in a microbial fuel cell for electricity generation, strained rumen fluid was inoculated (10% vol/vol) anaerobically into the anode chamber. The final volume of anolyte was 400 ml. Cellulose was provided as the sole carbohydrate and electron donor. Electron flow commenced immediately after the inoculation and then declined gradually (**Fig. 1**). When the cell voltage reached below 0.2 V, after 97 h operation, the anolyte was removed and replaced anaerobically with 10 mM acetate and subsequently with fresh cellulose medium followed by reinoculation (10% vol/vol) with strained rumen fluid. Thereafter, the voltage rapidly increased and reached a consistent maximum of 0.58 ± 0.02 V, and a stable power production of 40 mW/m^2 was obtained over a period of about 82 h. At the end of these incubations, the anode was removed from the chamber and attached biofilm was scraped off. Inoculation of the cellulose medium in the culture tube with extracted biomass and its incubation at 39ºC revealed that electrode-attached microorganism were cellulolytic and hydrolyzed cellulose. Visual inspection clearly showed a loss of cellulose during the bioreactor run.

Penicillin and streptomycin were added to the cellulose medium in the anode chamber to inhibit bacterial growth. The effect of the antibiotics on electricity generation is shown in **Fig. 2**. The antibiotic amendment decreased the power output, demonstrating the involvement of bacteria in transferring electrons to the electrode while oxidizing cellulose and metabolites. Since the voltage did not reach the baseline, it was inferred that rumen fungi or bacteria were present that were resistant to the antibiotics. It is possible that anaerobic rumen fungi were involved in electron transfer to the electrode because eukaryotes are not affected by penicillin or streptomycin antibiotics. Microscopic observations of the anode contents from the antibiotic-treated chamber confirmed the presence of zoospores. Further experiments are needed to verify whether rumen fungi can transfer electron to the electrode directly or via secreting electron-transfer mediators. Stirring the anode contents at 300 rpm did affect the electricity production. The voltage obtained in the stirred fuel cell was higher than in the unstirred bioreactor.

Thus this work shows that it is possible to couple degradation of cellulose with generation of electricity, exploiting rumen microbial inoculum in a microbial fuel cell (MFC). By exploiting rumen microorganisms as biocatalysts in a mediator-less MFC, it was possible to generate as much as 40 mW/m^2 with cellulose as the substrate. Cellulose is a linear polymer of glucose connected through β-1,4-linkages and is usually arranged in microcrystalline structures which can be difficult to dissolve or hydrolyze under natural conditions. These results suggest that rumen microorganisms can generate electricity, evidence for the potential of rumen microorganisms as biocatalysts in microbial fuel cells while degrading cellulosic wastes.

Power generation was directed by both electrode-attached and suspended microorganisms. No external mediator was used in these experiments. These results add to the diversity of biocatalysts that can be used in microbial fuel cell applications. More research is needed to determine the optimal bioprocess conditions for these microorganisms to enhance their maximum power density outputs.

Acknowledgements

Partial support for this work was received from the Ohio Agricultural Research and Development Center, College of Food, Agricultural, and Environmental Sciences, at the Ohio State University.

References

1. Rabaey, K.; Boon, N.; Siciliano, S. T.; Verhaege, M.; Verstraete, W. *Appl. Environ. Microbiol.*, **2004,** *70*, 5373-5382.
2. Hu, Z.; Wang, G.; Yu, H. **Biochem. Eng. J.**, **2004**, *21*, 59-62.
3. Dehority, B.A., Rumen Microbiology, Nottingham University Press: Nottingham, U.K., **2003**.
4. Bond, D.R.; Lovley, D.R. *Appl. Environ. Microbiol.*, **2003**, *69*, 1548-1555.

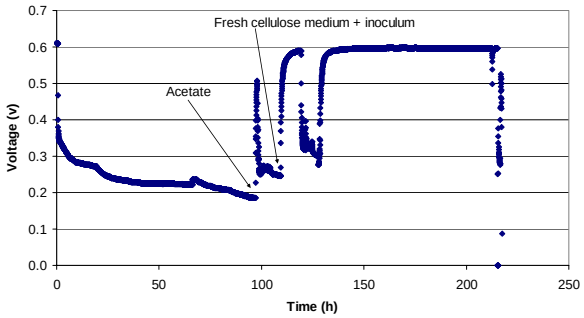

Figure 1. Electricity generation with rumen microorganisms. The bioreactor contained 7.5 g cellulose/l and 10% (vol/vol) strained rumen fluid as inoculum at pH 6.8 and at 22±2°C. At 97 h, 10 mM acetate was added. The anode solution was replaced with fresh cellulose media and inoculum at 110 h. The experiment was terminated at 215 h.

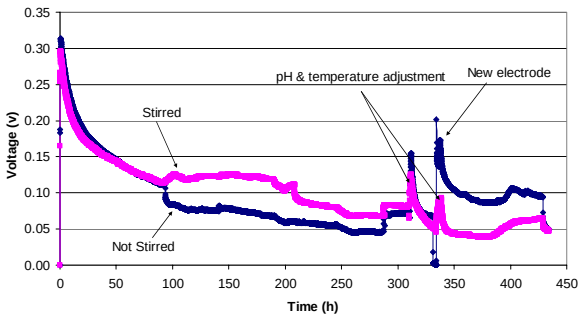

Figure 2. Electricity generation with rumen microorganisms. Initially, two bioreactors contained 7.5 g cellulose/l and 10% (vol/vol) strained rumen fluid as inoculum at pH 6.8 and at 22±2°C. The media contained penicillin-G 2,000 IU/ml and streptomycin 130 IU/ml. Stirring (300 rpm) was introduced to one bioreactor at 93 h. The pH was adjusted from 5.6 to 6.8 and the temperature was increased to 39°C at 310 h and 332 h. The anode was replaced with a new electrode at 332 h.

Biological Fuel Cells Exploiting the in situ Oxidation of Hydrogen Synthesized via Heterotrophic, Photo-heterotrophic and Photosynthetic Microbiological Activity

Uwe Schröder, Miriam Rosenbaum, Juliane Niessen, Falk Harnisch, Fritz Scholz*

Institut für Chemie und Biochemie, Universität Greifswald, Soldmannstr. 16, 17489 Greifswald, Germany

Introduction

To exploit the metabolic activity of microorganisms for electricity generation basically two major approaches can be followed, (i) the production of biohydrogen and biogas[1-3] combined with the subsequent conversion to electricity in conventional fuel cells or via combustion, and (ii) the direct electricity generation in microbial fuel cells.[4-6] Biofuel cells mostly exploit hetero-fermentative and metal-reducing microbes as biocatalysts. For biohydrogen production dark fermentative (e.g., *Clostridia*) as well as phototrophic hydrogen producing microorganisms (green algae, non-sulfur purple bacteria and cyanobacteria) are used. Our work aims to combine these approaches by means of microbial fuel cells that exploit heterotrophic (dark fermentation), photo-heterotrophic (photo-fermentation) or purely photosynthetic hydrogen synthesis for direct electricity generation via the in situ oxidation of the microbially produced hydrogen. Such integration shows a number of potential advantages. Thus, the combustion of biohydrogen in a conventional fuel cell requires the gas to be separated from the biomass, as well as its extensive purification. The separation of the hydrogen gas from microbial cultures is considered to be an important issue since large fractions of the gas remain dissolved in the microbial medium – promoting the possible growth of hydrogen consuming microorganisms and thus lowering the hydrogen yield. Additionally, high hydrogen partial pressures are known to limit the microbial hydrogen synthesis, which may act as a negative feedback inhibition of hydrogen production. A proposed method for the hydrogen removal is the purging with an inert gas, e.g., nitrogen. This procedure, however, is expensive and produces highly diluted hydrogen. With the concept of the direct electrochemical depletion of hydrogen from the bacterial solution by the implementation of electrocatalytic anodes into the microbial cultures these issues can be circumvented. It requires, however, the development of anodes that are resistant against biofouling and deactivation in the complex microbial environments. In 2003, we have presented a novel microbial fuel cell concept that is based on the anaerobic decomposition of glucose by *Escherichia coli*. Current densities much above all known systems have been reached.[7] The achievement is based on an anode composed of a layered composite consisting of platinum, allowing the electrocatalytic oxidation of hydrogen, overlaid by the conductive polymer polyaniline (PANI) that prevents poisoning and that also shows catalytic activity towards fuel oxidation. The further improvement of the anode concept and its adaptation to different microbial and substrate conditions has led to the development of a range of composite materials that allow higher stability and higher performance than the original Pt-PANI.[8] For the studies of the present communication, the following composites were used: Pt-Poly(tetrafluoroaniline) (**Pt-PTFA**), and Pt-Poly(3,4-ethylenedioxythiophene) (**Pt-PEDOT**)

One disadvantage using dark fermentation for hydrogen production and electricity generation is the incomplete substrate oxidation combined with the formation of organic acids (e.g., lactate, acetate, formate, succinate, propionate, butyrate) and alcohols. This limits the maximum substrate conversion efficiency to 4 mol hydrogen per mol glucose. Photo-heterotrophic non-sulfur purple bacteria may help solving this problem and increasing the substrate conversion efficiency, since they use the remaining organic acids as resource for photobiological hydrogen production in a second step utilizing dark-fermentation products (as illustrated in Scheme 1). With such a two-step MFC an increased hydrogen (and thus coulombic) yield is possible.[9]

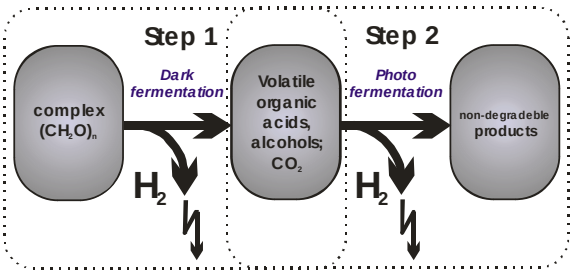

Scheme 1. Schematic illustration of the application of fermentation and photo-fermentation in a two-step microbial fuel cell system

Experimental

Metabolic analysis. Metabolic substrate diminution and non-gaseous fermentation product formation were followed using HPLC. The HPLC was equipped with a Rezex™ ROA-Organic Acid column in combination with the SecurityGuard™ cartridge AJO-4490. The chromatograms were recorded with 0.005 N sulfuric acid as the eluent; the detector was a differential refractometer. CO_2 and H_2 quantification was performed volumetrically, the separation of H_2 from CO_2 being achieved by absorption of CO_2 in NaOH solution.

Electrode preparation. For anode preparation, platinum mesh electrodes, platinum sheet electrodes, carbon cloth or paraffin impregnated graphite electrodes were electrochemically platinized in a stirred acidic solution containing 20 mM H_2PtCl_6 (Fluka) at a potential of –0.6 V for 500 s. The electrodes were subsequently coated with conductive polymers, e.g., polyaniline (Pt-PANI), poly(tetrafluoroaniline) (Pt-PTFA) or poly(3,4-ethylenedioxy-thiophene) (Pt-PEDOT) using oxidative electro-polymerization.

Electrochemical instrumentation. Two types of electrochemical experiments were used in this study for potentiostatically controlled and fuel cell experiments. For the potentiostatic experiments sealed (and for photobiological experiments illuminated) glass jars served as electrochemical cells hosting a working electrode, a reference and a counter electrode in a conventional three-electrode arrangement. The counter electrodes were graphite rods separated from the bacterial solution by a Nafion 117 perflourinated membrane. Silver | silver chloride electrodes, sat. KCl, 0.195 V vs. SHE, served as reference electrodes. The experiments were carried out using PGSTAT 20 and 30 potentiostats (Ecochemie, Netherlands). For the current measurement a permanent potential of 0.2 V was applied to the working electrode in order to oxidize microbial hydrogen under conditions similar to those present in a microbial fuel cell. Control experiments confirmed that varying the applied potential between 0.1 and 0.3 V did not noticeably affect the experimental results. Fuel cell experiments were carried out using a self-made simplified fuel cell models. The monitoring of redox potentials and currents under different external resistance loads was performed with a data acquisition system (Keithley Integra 2700 digital multimeter equipped with 7700 multiplexer, Keithley Instruments, Inc., Cleveland, USA) interfaced to a personal computer. The fuel cell setup was thermostatically controlled.

Results and Discussion

Dark fermentative processes that involve the microbial production of hydrogen from various substrates were used for electricity generation. As biocatalyst either single strains (e.g., *Escherichia coli* for glucose fermentation, *Clostridium butyricum* and

Clostridium beijerinckii for starch and molasses fermentation, or *Clostridium cellulolyticum* for cellulose fermentation), or microbiological consortia, isolated from heat-treated soils, were exploited. Whereas the use of single strains usually requires a careful selection of suitable microbe–substrate combinations, bacterial consortia allow flexible substrate utilization. Additionally, such consortia are generally more robust than cultures of single strains.

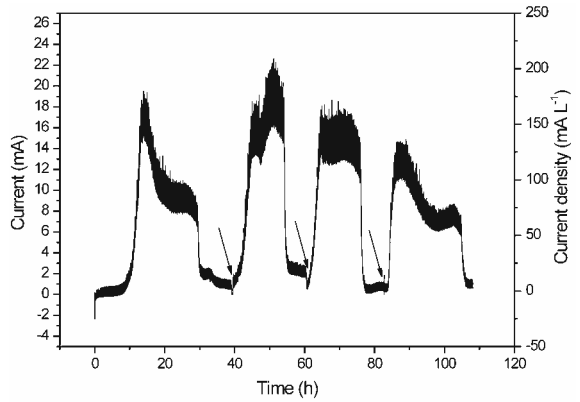

Figure 1. Current generation (semi batch) in a culture inoculated with heat-treated soil. Anode: Pt-PTFA composite (Mesh electrode, 100 cm^2). Substrate: glucose. E_{anode}= 0.2 V.

For the in situ hydrogen oxidation we currently use layered composite materials consisting of platinum covered by conductive polymer layers, which prevent deactivation of the electrocatalyst. Depending on the microbial environment, different polymers are used. Whereas fluorinated polyanilines (PTFA) are applied in MFCs using dark fermentation (*Clostridia*, *E. coli*, bacterial consortia (see **Figure 1**)) and photosynthesis (green algae *Chlamydomonas*, see **Figure 2**), poly(3,4-ethylenedioxythiophene), PEDOT, is used in MFCs exploiting the purple bacterium *Rhodobacter sphaeroides* for photo-fermentative substrate utilization.

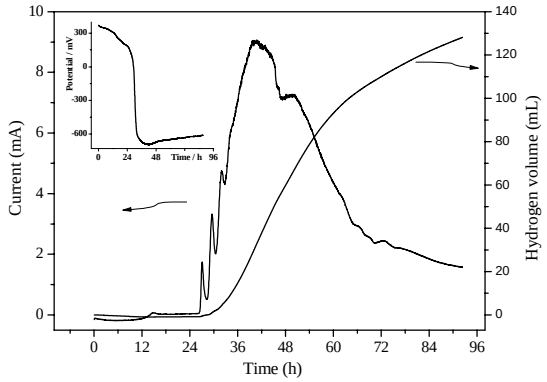

Figure 2. Left Y Axis: Current generation of a culture of the green alga *Chlamydomonas reinhardtii* CC125 in TAP-S, measured at a Pt-TFPA mesh electrode. E_{anode}= 0.2 V. The culture (550 ml) was sealed and constantly illuminated with fluorescence light. ϑ = 22°C. **Right Y Axis**: Total volume of the microbially produced and electro-chemically oxidized hydrogen, calculated following Equ. 1. **Inset Figure**: Redox potential of a culture of *Chlamydomonas reinhardtii* CC125, grown in a TAP medium and transferred (1:10 v/v) into TAP-S. [9]

In the case of the anaerobic growth of the green alga *Chlamydomonas reinhardtii* under sulphur deprivation, hydrogen is produced as the sole electron donor for electrochemical oxidation. Thus the charge, produced during a "green solar cell" experiment, can be directly translated into the volume of photosynthetic hydrogen (**Equation 1**). A comparison of the results of the in situ oxidation of photosynthetic hydrogen (**Figure 2 and Table 1**) with literature values indicates a promotion of the photosynthetic hydrogen by the electrochemical hydrogen depletion from the microbial culture.

$$V_{H_2} = \frac{\int I\,dt}{z \cdot F} \cdot V_{n/32°C} \qquad \textbf{Equation 1}$$

Table 1. Normalized data of the hydrogen production by *Chlamydomonas reinhardtii* under different conditions (25 °C, 1,013 bar, 1 L culture volume).

Reference	*Duration of experim. / h*	*Final H_2-yield/ ml L^{-1} culture*
Our work [9]	***90***	***235****
Melis et al. [11]	*130*	*114***
Kosourov et al. [12]	*140*	*162***

*calculated from the electrochemical data; **volumetric data

The exploitation of photoheterotrophic microorganisms like the purple bacterium *Rhodobacter sphaeroides* offers a means for increasing the yield of microbial fuel cells by establishing a two-step MFC (see **Scheme 1**) consisting of a primary, fermentative part and a secondary photo-fermentation. As we can show for the example of glucose, degraded by *Escherichia coli K12* to produce H_2, lactate, acetate, formate, succinate and ethanol in a first step, the remaining organic acids can be utilized via photo-fermentation – increasing the coulombic yield by nearly 50%.

Acknowledgement

This work was supported by the US Office of Naval Research, (ONR project N00014-03-1-0431), by the Deutsche Forschungsgemeinschaft (DFG) and by the support by the Fonds der Chemischen Industrie.

References

(1) Reith, J. H.; Wijffels, R. H.; Barten, H., Eds. Bio-methane and Biohydrogen; Dutch Biological Hydrogen Foundation (http://www.ecn.nl/_files/bio/Bio-methane_and_Bio-hydrogen.pdf): Petten, 2003.
(2) Levin, D. B.; Lawrence, P.; Love, M., *Int. J. Hyd. Energy*, **2004**, 29, 173-185.
(3) Akkerman, I.; Janssen, M.; Rocha, J.; Wijffels, R. H., *Int. J. Hyd. Energy*, **2002**, 27, 1195-1208.
(4) Katz, E.; Shipway, A. N.; Willner, I. In *Handbook of Fuel Cells – Fundamentals, Technology and Applications*; Vielstich, W., Gasteiger, H. A., Lamm, A., Eds.; Wiley, 2003; Volume 1: Fundamentals and Survey of Systems.
(5) Logan, B. E., *Environ. Sci. Technol.*, **2004**, *38*, 160A-167A.
(6) Shukla, A. K.; Suresh, P.; Berchmans, S.; Rajendran, A., *Current Science* 2004, *87*, 455-468.
(7) Schröder, U.; Nießen, J.; Scholz, F., *Angew. Chem. Int. Edn.*, **2003**, 42, 2880-2883.
(8) Nießen, J.; Schröder, U.; Rosenbaum, M.; Scholz, F., *Electrochem. Commun.*, **2004**, 6, 571-575.
(9) Rosenbaum, M.; Schröder, U.; Scholz, F., *Appl. Microbiol. Biotechnol.*, **2005**, *in press*, published online: 5 Februar 2005.
(10) Nießen, J.; Schröder, U.; Scholz, F., *Electrochem. Commun.*, **2004**, 6, 955-958.
(11) Melis, A.; Zhang, L.; Forestier, M.; Ghirardi, M.L.; Seibert, M., *Plant Physiol.*, **2000**, 122, 127-135.
(12) Kosourov, S.; Tsygankov, A.; Seibert, M.; Ghirardi, M.L., *Biotechnol. Bioeng.*, **2002**, 78, 731-740.

PHOTODEPENDENT HYDROGEN EVOLUTION BY PHOTOSYSTEM I ENTRAPPED IN HYBRID ORGANO-SILICATE GLASSES

Hugh O'Neill, Barbra R. Evans and Elias Greenbaum

Chemical Sciences Division
Oak Ridge National Laboratory
Oak Ridge, TN 37831-6194

Introduction

Photosystem I (PSI) is one of three major photosynthetic energy transducing protein complexes found in thylakoids of higher plants, cyanobacteria and algae. The primary function of this transmembrane multisubunit complex is to convert electromagnetic energy into the electrochemical energy required for metabolic cellular processes. At the core of PSI is a pair of chlorophyll a molecules known as P700. After absorption of a photon, the photochemistry of P700 induces a charge separation ($P700^+A_0^-$) in the reaction center by rapid electron transfer to peripheral iron sulfur complexes (F_A and F_B) via the intermediates A_0, $A_1$and F_x.[1] The photochemical reaction is completed within 100-150 ns and generates approximately a 1 volt potential difference over a distance of 6 nm.[2] In vivo, electrons are transferred to ferredoxin and eventually used to reduce $NADP^+$ to NADPH. The $P700^+$ is re-reduced by plastocyanin with electrons that originate from water via the Photosystem II complex. The quantum yield of this photochemical reaction is close to 100%.[3]

In an interesting variant to the natural metabolic pathway protons can be used as a terminal electron acceptor for PSI using platinum catalysts.[4, 5] The platinization reaction takes place at ambient temperature and physiological pH according to the following reaction:

$$PtCl_6^{2-} + 4e^- + h\nu \rightarrow Pt\downarrow + 6Cl^-$$

The platinization of PSI is achieved by photochemical deposition of metallic platinum from sodium hexachloroplatinate in solution (Fig. 1). The electrons are photogenerated by PSI with Na ascorbate as a sacrificial pool of reductant. The photochemistry of platinum deposition and catalyst formation precedes the onset of hydrogen evolution.

We report here on the employment of the sol-gel technique to entrap and stabilize PSI complexes and produce a stable photo-dependent hydrogen evolution catalyst. The spectrophotometric, photochemical and photocatalytic characteristics of the immobilized enzyme were examined to evaluate the properties of the reaction centers as the sol-gels were dehydrated. The effect of the solvent removal process on the properties of the entrapped reaction centers, particularly on their ability to carry out electron transfer reactions, was investigated.

Experimental

Isolation of Proteins. PSI and plastocyanin were isolated from market baby spinach leaves as previously described.[6]

Preparation of silica-gels. A mixture of tetramethylorthosilicate (TMOS; 6 g), H_2O (2.05 g) and 40 mM HCl (0.08g) was sonicated at 4°C until a homogeneous solution was obtained. The sample was then placed under vacuum (100 kPa) at 20°C for 30 min. The resulting viscous liquid was diluted with 1.4 g H_2O. This sol solution was stable for several hours at 4°C. In a typical immobilization reaction 0.1 ml PSI, 0.3 ml 10 mM sodium phosphate buffer pH 7.2, and 0.5 g glycerol were mixed with 1 ml of sol solution in a 4 ml plastic cuvette. Gelation occurred within a 5 min period. The samples were stored at room temperature in the dark and dessicated under silica-gel. For photo-dependent hydrogen production reactions, PSI and plastocyanin were co-immobilized in a covered cylindrical glass vessel [1.1 × 9.1cm (I.D.)] equipped with gas inlet and outlet ports. The contents covered the bottom of the vessel to a depth of approximately 1 mm. Aging and dehydration were carried out as described for the analytical samples.

Photochemical activity of PSI. The photochemical activity of PSI was determined from the light induced P700 absorption changes at 810 nm using the Dual Wavelength Emitter Detector Unit ED-P700DW-E connected to a PAM 101 Fluorimeter (Walz, Effeltrich, Germany).

Photocatalyzed Hydrogen Evolution. The experimental apparatus used for the continuous measurement of hydrogen was described previously.[5] The immobilized proteins were washed with several changes of 10 mM Na phosphate for 4 hours at room temperature in the dark to allow the diffusion of glycerol from the gels. This buffer was removed and replaced with a solution comprised of 5.0 mM Na-ascorbate, 0.5 mM sodium hexachloroplatinate in 10 mM Na-phosphate pH 7.1. The reaction vessel was assembled into the experimental apparatus and the contents were allowed to equilibrate with the humidified carrier gas. After a baseline had been achieved the 2 hour light on/1 hour light off cycle was commenced and the photocatalyzed production of H_2 was recorded as described previously. The same conditions were employed with the native enzymes except that the reaction was stirred.

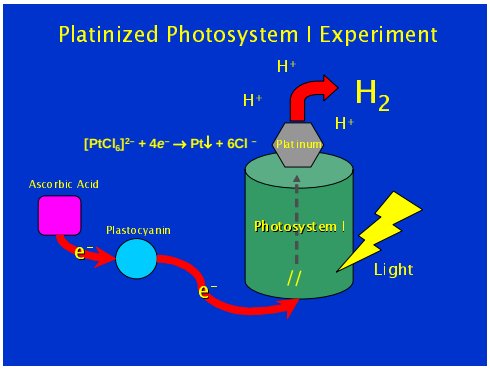

Figure 1. Photodependent platinization of Photosystem I

Results and Discussion

Sol-gel chemistry is an ambient temperature process for the synthesis of inorganic glasses. The utility of this technique for the immobilization of a range of biomolecules in silica glasses has been described.[7] As a prerequisite for this study it was essential to develop a strategy to stabilize PSI during the immobilization process and to preserve the optical properties of the silica glasses throughout the solvent removal process. Two modifications to a previously described method[8] were found to be necessary to achieve this goal. The methanol released during the hydrolysis of the alkoxide precursor was removed by evaporation and glycerol was used as a non-surfactant templating agent. Previous reports[9, 10] have employed these modifications separately. In this study the combination of both were required to attain a stable active PSI complex in an optically clear glass.

Photochemical activity. The photochemical activity of PSI was monitored by near infra-red absorption spectroscopy as described previously. The P700 photo-oxidation and $P700^+$ reduction curves of PSI in solution were compared to PSI entrapped in sol-gel at various time intervals after immobilization (Fig. 2). The P700 reaction centers were able to be photooxidized and recovered indicating that the samples were active directly after immobilization in the sol-gel and also after the solvent removal process was completed. The magnitude

of the photochemical response of the immobilized samples was slightly greater than the native sample after immobilization and when the majority of the water had been removed (91.4%) after 29 days. However the photochemical response decreased by approximately 50%, compared to the native sample, during storage for 8 months over desiccant in the dark. Although this indicates that the reaction centers lost some activity during long-term storage, a significant amount of activity did remain. These data demonstrate that the intra-molecular electron-transfer characteristics of PSI remain intact even after virtually all the solvent is removed.

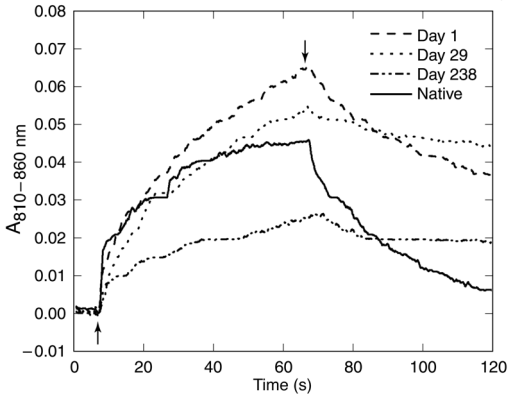

Figure 2. The P700 photooxidation and $P700^+$ reduction profiles of PSI at intervals after entrapment in sol-gels compared to the profile of the native preparation in solution. The up and down arrows indicate the start and finish of actinic light illumination (1400 µmol/m^2/sec, Schott KL 1500 light source)

Photocatalyzed Hydrogen Production. In this biomimetic reaction pathway the source of electrons was Na ascorbate with the electron relay protein plastocyanin serving as the mediator between Na ascorbate and the oxidizing side of PSI. Sol-gels that contained PSI co-immobilized with plastocyanin were prepared and aged as described in Materials and Methods. A characteristic light dependent evolution of hydrogen was observed (Figure 3A). The rates and yield of H_2 observed were similar for an experiment carried out with the native enzymes in solution (Figure 3B). This confirms that the PSI preparation was active after immobilization and able to facilitate intermolecular electron transfer from Na ascorbate via plastocyanin to platinum. This gives good confidence with respect to the structural and catalytic integrity of the PSI complexes.

Conclusions

PSI is a molecular photovoltaic structure that is capable of generating a 1 V potential over a 6 nm distance after absorption of a photon. It can carry out efficient e^- transfer directly from its active site to a metal surface in the absence of a mediator. Its protein architecture is such that two hydrophilic ends are separated by a hydrophobic middle region and therefore it has a natural disposition to orient itself. In this study we report on the entrapment and stabilization of PSI in an organo-hybrid sol-gel glass. The intra- and inter-molecular electron transfer properties of the protein complexes were preserved during immobilization and even after complete dehydration to a glass. The ability to manipulate PSI in a solid-state environment is essential for the exploitation of its unique optoelectronic properties for photo-fuel cells, photovoltaics and other bio-electronics applications. Although Na ascorbate was used as a sacrificial electron donor in this study to demonstrate photo-dependent hydrogen evolution we are currently exploring strategies to obtain reducing equivalents directly from photo-oxidation of water.

Acknowledgement. This work was supported by the Office of Basic Energy Sciences, U.S. Department of Energy, under contract number DE-AC05-00OR22725 with Oak Ridge National Laboratory, managed and operated by UT-Battelle, LLC.

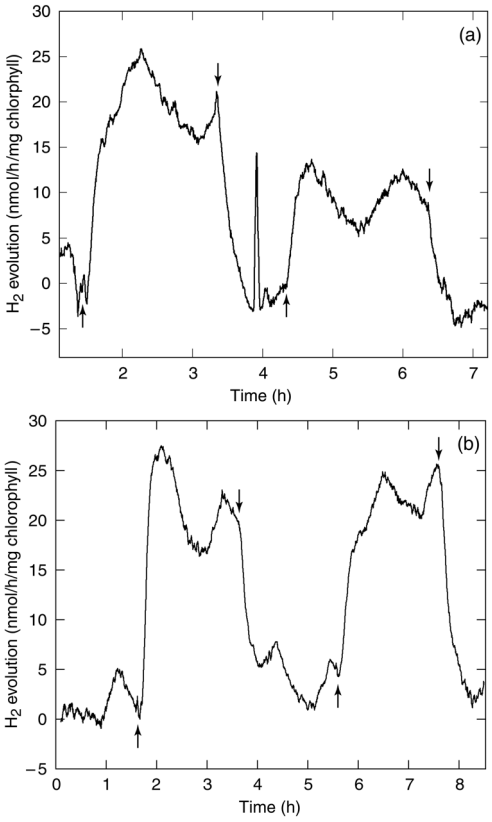

Figure 3. Light Dependent Evolution of Hydrogen by Platinized Photosystem I Reaction Centers. A: Photosystem I and plastocyanin co-immobilized in sol-gel. B: Native enzymes in solution. The reactions were carried out with 0.294 nmol Photosystem I (220 µmol chlorophyll), 20.2 nmol plastocyanin, 0.5 mM Na_2PtCl_6, and 5.0 mM Na ascorbate in 10 mM Na phosphate pH 7.11 at 20°C. Light cycles of 2 h on (↑) and 1 h off (↓) were used at a constant light intensity of 260 µmol/m^2/sec.

References

1. Owens, T.; Webb, S.; Mets, L.; Alberte, R.; Fleming, G. *Proc. Natl. Aca. Sci. USA* **1987,** 84, 1532-1536.
2. Brettel, K. *Biochim. et Bbiophys. Acta* **1997,** 1318, 322-373.
3. Zankel, K. L.; Reed, D. W.; Clayton, R. K. *Proc Natl Acad Sci U S A* **1968,** 61, 1243-1249.
4. Greenbaum, E. *J Phys. Chem.* **1988,** 92, 4571-4574.
5. Millsaps, J. F.; Bruce, B. D.; Lee, J. W.; Greenbaum, E. *Photochem Photobiol* **2001,** 73, 630-635.
6. Evans, B.; O'Neill, H.; Hutchens, S.; Bruce, B.; Greenbaum, E. *Nano Lett.* **2004,** 4, 1815-1819.
7. Livage, J.; Coradin, T.; Roux, C. *J. Phys- Condens Matt* **2001,** 13, R673-R691.
8. Ellerby, L.; Nishida, C.; Nishida, F.; Yamanka, S.; Dunn, B.; Valentine, J.; Zink, J. *Science* **1992,** 255, 1113-1115.
9. Gill, I.; Ballesteros, A. *J. Am. Chem. Soc.* **1998,** 120, 8587-8598.
10. Ferrer, M.; del Monte, F.; Levy, D. *Chem. Mat.* **2002,** 14, (9), 3619-3621.

PHOTOCATALYZED ELECTRON TRANSFER FROM SPINACH PSI TO METAL NANOPARTICLES

Barbara R. Evans[1], Hugh M. O'Neill[1], Jane Y. Howe[2] and Elias Greenbaum[1]

[1]Chemical Sciences Division, [2]Metals and Ceramics Division, Oak Ridge National Laboratory, Oak Ridge, TN 37831-6194

Introduction

Photosynthetic organisms such as plants and green algae convert solar energy to chemical energy by oxidizing water and reducing CO_2. A solar-powered biofuel cell that mimics photosynthesis is thus a very attractive concept for energy production. An essential step towards eventual assembly of such photocatalytic biofuel cells is the establishment of stable electron transfer between biocatalysts and metals.

The chloroplast photosystem I (PSI) protein complex transfers electrons across the chloroplast membrane following light activation of the two chlorophyll molecules in its P700 reaction center. PSI then accepts an electron from the small copper protein plastocyanin (PC). The biological electron acceptor is the iron-sulfur protein ferredoxin. PSI acts as a molecular diode with a potential of 1 V and a size of 6 nm, a property, together with its relative stability following isolation, that makes it a suitable photobiocatalyst for nanotechnology studies.[1,2] A mixture of spinach PC and PSI has been demonstrated to photocatalytically reduce hexachloroplatinate to metallic platinum at the reducing end of PSI to form a PSIPt catalyst that subsequently evolves H_2.[3] Covalent attachment of PC to PSI increased both the rate of both platinum deposition and H_2 production.[4] Decrease in H_2 evolution during successive light cycles was observed for both free and cross-linked PC and PSI, possibly due to growth of the platinum particle beyond the optimal size range of 50-500 atoms.[5]

The studies described here were carried out to investigate the stability of the cross-linked PCPSIPt catalyst and the effect of metal particle size on efficient electron transfer, the effect of limiting platinum particle size and the ability of PSI to transfer electrons to preformed metallic particles. Palladium-cellulose membranes containing catalytically active palladium nanoparticles deposited in hydrated bacterial cellulose pellicules[6] provided a convenient matrix for examination of interaction of PSI with dispersed metal particles. The porous microstructure of bacterial cellulose is composed of cellulose macrofibrils 40 to 60 nm wide that form a gel-like pellicule containing one-hundred times its weight in water. This hydrophilic form of cellulose has successfully been employed for immobilization of several types of cells and enzymes.[7,8]

Experimental

Isolation and cross-linking of proteins. PSI and PC were purified from spinach obtained from local markets and cross-linked by formation of peptide bonds with the reagent 1-ethyl-3(3-dimethylaminopropyl) carbodiimide hydrochloride (EDC) as described previously.[4] Recombinant spinach PC that was used in the platinization experiments was produced from a plasmid construct in a pET vector (Novagen, Inc.) with azurin signal peptide using a procedure adapted from a published method.[9]

Hydrogen evolution assays. The photoreactions were carried out at 23ºC with exclusion of incidental light in continuous flow systems using helium as the carrier gas. Hydrogen production was monitored by an in-line Figaro tin oxide hydrogen sensor as described.[3,4] The light source was a Fiber-Lite A3200 fiber optic illuminator (Dolan-Jenner Industries, Lawrence, MA 01843-1060) fitted with dual fiber optic cables and an OSRAM 150W quartz halogen lamp (OSRAM Corporation, Winchester, KY 40391) and a red filter transmitting light above 600 nm. Illumination was carried out with 2 h on/2 h off cycles with a light intensity of 531 µE m^{-2} s^{-1} at the reaction vessel.

Platinization of cross-linked PCPSI. Platinization was carried out by illumination of incubation mixtures containing 8 mM sodium ascorbate, 0.5 mM Na_2PtCl_6, cross-linked PCPSI (266 µg chl) in 50 mM sodium phosphate pH 7.1 at 23ºC for 2-h cycles in the continuous flow system with helium carrier gas. Excess hexachloroplatinate was removed by dialysis at 4ºC against 50 mM sodium phosphate pH 7.1. The dialyzed PCPSIPt (254 µg chl) solution was injected into the reaction vessel and sodium ascorbate added to a final concentration of 8 mM.

Preparation of palladium-cellulose. Bacterial cellulose membranes were prepared by cultivation of *Gluconacetobacter hansenii* (ATCC 10821) and cleaned before deposition of palladium from hexachloropalladate.[6] Palladium content was estimated by spectrophotometric determination of hexachloropalladate remaining in solution as 0.0483 mg cm^{-2}. Size and composition of the palladium particles was determined by transmission electron microscopy carried out at the Oak Ridge National Laboratory High Temperature Materials facility.

Loading of PC and PSI on palladium-cellulose. Plastocyanin and PS I were loaded into palladium cellulose membranes (diameter 3.8 cm, 5.13 µmol Pd) by filtration on disposable filter sterilization units. For experiments with proteins that were not cross-linked, plastocyanin (8 nmol) was preincubated with PS I (70 µg chl) in 50 mM sodium phosphate buffer, pH 7.1, for 20 min at 23ºC before loading onto a palladium cellulose circle of diameter 4.5 cm. The molar ratio was calculated from the P700 assay of the PS I prep to be 30 plastocyanin: 1 P700. A separate bacterial cellulose membrane containing 8 mM sodium ascorbate in 50 mM sodium phosphate buffer, pH 7.1 was placed under the palladium cellulose to provide a supply of ascorbate by diffusion into the palladium-cellulose layer.

Results and Discussion

Removal of excess hexachloroplatinate from the cross-linked PCPSIPt biocatalyst resulted in stabilization of the H_2 evolution rate at the level of the last platinization light cycle (Fig. 1), presumably by restriction of the platinum particle size. The dialyzed PCPSIPt catalyst evolved H_2 at a steady rate for 23 light cycles (Fig. 1).

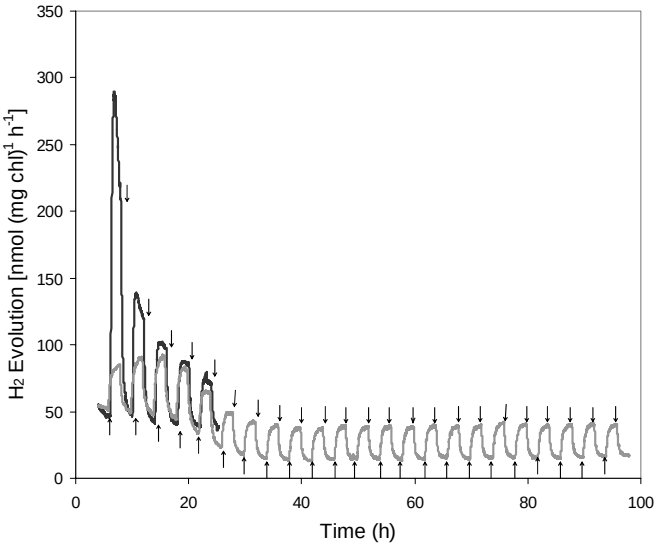

Figure 1. Photocatalyzed evolution of H_2 during platinization of cross-linked PCPSI (black), and following removal of excess hexachloroplatinate from the platinized PCPSI by dialysis (gray) were compared for light cycles of 2 h on (↑)/ 2 h off (↓).

To further investigate electron transfer to catalytic metal particles, PSI with free or covalently attached PC was loaded on hydrated bacterial cellulose membranes containing catalytically active palladium particles. The size of the particles was determined by TEM to range in size from 2 to 20 nm (Fig. 2). Preliminary studies demonstrated the suitability of bacterial cellulose for immobilization of PSI based on optical transmission in the visible range and stability of PSI photocatalytic activity in reduction of $NADP^+$ in the biological assay[4] with ferredoxin and ferredoxin:$NADP^+$ reductase (data not shown). Surface coverage of membrane surfaces based on the amount and size of PSI loaded was estimated to be nearly 100%. Illumination of these membranes resulted in stable photocatalyzed H_2 production during successive light cycles. In the palladium-cellulose membranes, cross-linked PCPSI evolved higher levels of H_2 that the free PC and PSI, similar to the previous results for the platinization reaction.[4]

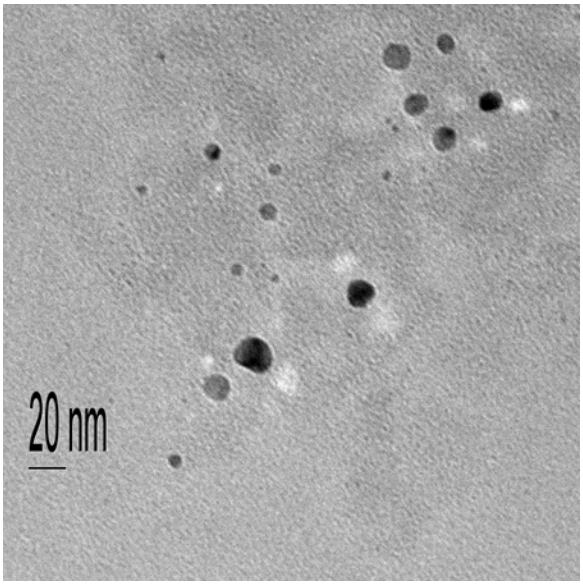

Figure 2. The size of the palladium particles deposited in the bacterial cellulose membranes was determined by imaging with TEM to range from 2 to 20 nm.

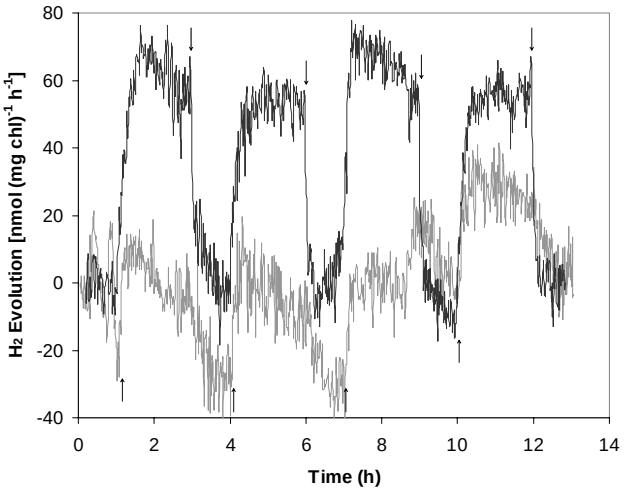

Figure 3. Following loading onto the surface of the palladium-cellulose membranes, cross-linked PCPSI (black) evolved H_2 at higher rate than free PC and PSI (gray).

Conclusions

The importance of particle size in the photocatalyzed electron transfer from PSI to metals was confirmed. Limiting particle size of platinum formed during photocatalytic platinization of cross-linked PCPSI resulted in formation of a stable metallized biocatalyst. Palladium-cellulose membranes contain palladium nanoparticles maintained in dispersion throughout the membrane matrix by the cellulose fibers. Free PSI and cross-linked PCPSI were able to transfer electrons to these palladium particles as evidenced by photocatalytic H_2 evolution. These results indicate that maintaining the correct metallic particle size range is essential for electron transfer from photosystems and other redox active biomolecules.

Acknowledgement. This research was supported by funding from the Office of Basic Energy Sciences, U. S. Department of Energy, and from the Bioflips/Symbiosys Program of the Defense Applied Research Program Agency, U. S. Department of Defense. Research at the Oak Ridge National Laboratory (ORNL) High Temperature Materials Laboratory (HTML) was sponsored by the Assistant Secretary for Energy-Efficiency and Renewable Energy, Office of FreedomCAR and Vehicle Technologies, U.S. Department of Energy under contract DE-AC05-00OR22725 with UT-Battelle, LLC. Oak Ridge National Laboratory is managed by UT-Battelle, LLC for the U.S. Department of Energy under contract DE-AC05-00OR22725. This work was sponsored by a contractor of the U.S. Government under contract DE-AC05-00OR22725. Accordingly, the U.S. Government retains a nonexclusive, royalty-free license to publish or reproduce this document, or to allow others to do so, for U.S. Government purposes.

References

(1) Brettel, K. *Biochim. et Bbiophys. Acta* **1997,** *1318*, 322-373.
(2) Lee, I.; Lee, J. W.; Stubna, A.; Greenbaum, E. *J. Phys. Chem. B* **2000**, *104*, 2439-2443.
(3) Millsaps, J. F., Bruce, B. D.; Lee J. W.; Greenbaum E. *Photochem. Photobiol.* **2001,** *73(6)*, 630-635.
(4) Evans, B. R.; O'Neill, H. M.; Hutchens, S. A., Bruce, B. D., Greenbaum, E. *NanoLett*. **2004**, *4(10)*, 1815-1819.
(5) Greenbaum, E. *J Phys. Chem.* **1988,** *92*, 4571-4574.
(6) Evans, B. R., O'Neill, H. M., Malyvanh, V. P., Lee, I. Woodward, J. *Biosens. Bioelectron*. **2003**, *18(7)*, 917-923.
(7) Iguchi, M.; Yamanaka, S.; Budhiono, A. *J. Materials Science* **2000,** *35(2)*, 261-270.
(8) Cannon, R. E.; Anderson, S. M. *Crit. Reviews in Microbiol.* **1991**, *17(6)*, 435-447.
(9) Chang, T. K.; Iverson, S. A.; Rodrigues, C. G.; Kiser, C. N.; Lew, A. Y. C.; Germanas, J. P.; Richards, J. H. *Proc. Natl. Acad. Sci. USA* **1990**, *88*, 1325-1329.

BIOFUEL CELL BASED ON THE BACTERIA *GLUCONOBACTER OXYDANS* AND THE MEDIATOR OF ELECTRON TRANSPORT 2,6-DICHLOROPHENOL INDOPHENOL

A.N.Reshetilov[1], S.V.Alferov[2], L.G.Tomashevskaya[1], O.N.Ponamoreva[3]

[1]G.K.Skriabin Institute of biochemistry and physiology of microorganisms, RAS, Prospekt Nauki 5, Pushchino, Moscow region, 142290, Russia
[2]Pushchino State University, Pushchino, Moscow region, Russia
[3]Tula State University, Tula, Russia

Introduction

Studies in the field of biofuel cells (BFC) are important for many reasons among which a search for the alternative and the possibility of creating ecologically safety sources of electrical energy are the most weighty.[1] One of the trends in this field of investigation is represented by the development of microbial BFC, which differ in constructions, type of microbial cultures, mediators and substrates [2-6]. The analysis of literature data shows that a search for efficient composition "the type of a microbial culture – the type of a mediator – the type of fuel" is one of the significant and unresolved tasks on construction of BFC. In this connection, studies, orientated to clarification of a relationship between BFC characteristics and the composition alluded above, are in great demand. The use of acetic-acid bacteria of the genus *Gluconobacter* as BFC biocatalyst appears to be promising. These bacteria have a number of unique characteristics, in particular, membrane localization of basic enzymes of cell metabolism. Due to this property substrates [7] and probably mediators may easily reach active centers of the enzyme. Microbial cultures of this genus are widely used for designing a range of mediator microbial biosensors [8-10]. At the same time literature provides no data on the use of bacteria of the genus *Gluconobacter* in BFC construction.

This work was focused on the study of the possibility of electromotive force (EMF) generation by biofuel cell when the strain *Gluconobacter oxydans* sbsp *industrius* B-1280 and the mediator of electron transport, 2,6-dichlorophenol indophenol, was used as a biocatalyst. Glucose was an oxidizable substrate.

Experimental

BFC model was represented as two-chamber cell analogous to that one described in [3]. Volumes of cathode and anode compartments were equal and added up to 1.0 ml. Compartments were separated with nonionselective acetate cellulose membrane (Vladipor MFA-MA № 5, pore diameter, 0,2μm, Russia). Membrane was used to keep the cells in the anode compartment and partially prevented the diffusion of the mediator and glucose to the cathode compartment. The obtained results show (data are not given) that glucose and mediator flowing through the membrane to the cathode compartment was not higher than 4% and 1%, respectively. Since steady-state value of voltage and current achieved for 20-30 min, changes in glucose and mediator concentrations were not taken into account. The measurements were taken at temperature 22^{o}C. Solutions in cathode and anode compartments were mixed by magnetic stirrer. Graphite electrodes, diameter, 6 mm, were used as anode and cathode. The working surface of each electrode was 2,0 cm^2. 2,6-dichlorophenol indophenol was used as the mediator (Sigma); glucose and chemicals for buffer solutions were pure for analysis grade. 30 mM sodium-phosphate buffer solution, pH 7.6, was basic electrolyte for both compartments. Bacterial culture *Gluconobacter oxydans* sbsp. *idustrius* B-1280 was taken from Russian microbial cultures collection, G.K.Skriabin IBPM, RAS. Fresh grown and once frozen and defrozen cells were used in the experiments. Voltage and current were measured with a galvanopotentiostat IPC-2 (Kronas, Russia), the input resistance of which was $10^{13}\Omega$ in the mode of potential measurement.

Results and Discussion

Addition of the composition "bacteria + the mediator + glucose" to the anode compartment was accompanied by generation of a potential difference equal to 55 mV (the mean value with the variation coefficient 6% for ten measurements).

The observed potential difference was interpreted as generation of EMF due to bacterial oxidation of glucose and electron transfer by reduced molecules of the mediator to the anode. The process of EMF generation proceeds in accordance with the mechanism given in [3, 4].

At switching-on of external ohmic load of 10 kΩ the steady-state difference of potentials was 5.6 mV at the current of 0.56 μA and the current density of 0.28 μA*cm^{-2}. The calculated value of the cell internal resistance was 88 kΩ. The power of BFC was $3*10^{-3}$ μW.

For comparison, in [3] one will find the description of BFC in which E.coli bacteria were used as a biocatalyst. As mediators, Neutral Red and potassium ferricyanide were employed in the anode and cathode compartments, respectively. Glucose was a substrate used for oxidation. At the external load of 120 Ω the generated potential was 460 mV at the current of 0.5 mA, which corresponds to the power of 0.23 mW. For that regime, the current density was $8.9*10^{-3}$ μA*cm^{-2}, as the surface of graphite felt electrodes was 0.5 m^2. Hence, the developed BFC exceeds by several times the one based on *E. coli* cells by current density, which characterizes the composition of *G. oxydans* with DCPIP as more effective than the one of *E. coli* with Neutral Red. It should also be noted that the used composition allows to carry out the measurements without additional deoxygenation of the anode compartment. The parameters of the developed BFC can be further improved by optimization of the biomass and mediator contents, use of electron transport mediators in the cathode compartment by analogy with described in [2,3], application of a cathode modified by some enzyme, for example, by laccase [11], use of a cation-selective membrane that separates the anode and cathode compartments).

Conclusions

The obtained data indicate the possibility of using a bacterial strain belonging to the genus *Gluconobacter* as a biocatalyst in the BFC. It seems advisable to continue investigations for possible optimization of the parameters of the proposed BFC model.

Acknowledgment. This work was supported by the Ministry of Industry and Science of the Moscow region and Russian foundation of fundamental research, project No. 04-04-97253.

References

1. Shukla A.K., Suresh P., Berchmans S., Rajendran A., Current Science, 2004, 87(4), 455.
2. Wilkinson S., Autonomous Robots, **2000**, 9, 99.
3. Park D. H. and Zeikus G., *Applied and environmental microbiology*, **2000**, 66, 1292.

4. Daniel R. Bond, Dawn E. Holmes, Leonard M. Tender, Derek R. Lovley., Science, **2002**, 295, 483.
5. Willner I., Arad G., Katz E., *Biochem. Bioenerg.*, **1998**, 44, 209.
6. Satoshi Sasaki and Isao Karube., *TIBTECH*, **1999**, 17, 50.
7. Lusta K.A. and Reshetilov A.N., *Appl. Biochem. Microbiol.*, **1998**, 34(4), 339, (Moscow, Interperiodica Publishing).
8. Ikeda T., Kurosaki T., Takayama K., Matsushita F., *Anal.Chem.***, 1996**, 68, 192.
9. Alferov V.A., *Ponamoreva O.N., Babkina E.E.,* Alferov S.V., Reshetilov A.N., (In Russian) *Izvestiya, Tula State University*, **2004**, 4, 126.
10. Gorton L., *Electroanalysis*, **1995**, 7, 23.
11. Tarasevich M.R., Bogdanovskaya V.A., Zagudaeva N.M., Kapustin A.V., *Electrical chemistry*, **2002**, 38(3), 378, (Moscow, Interperiodica Publishing).

BIOREFINERIES - THE DEPARTMENT OF ENERGY VIEWPOINT

Douglas Kaempf

U.S. Department of Energy, Office of the Biomass Program, EE-22
1000 Independence Ave., S.W., Washington, DC 20585
(202) 586-5264: douglas.kaempf@ee.doe.gov

Abstract

The biorefinery concept allows for maximum return on our limited biomass resources for production of fuels, chemicals and power to reduce our dependence on foreign petroleum imports. This presentation will present the research and development program of the Office of the Biomass Program for technologies needed to bring the biorefinery industry to reality.

CHEMICAL BUILDING BLOCKS FOR THE BIOREFINERY

Todd A. Werpy

Pacific Northwest National Laboratory
P.O. Box 999
Richland, WA 99352

The petrochemical industry has been established on the concept of producing both fuels and chemicals at a single integrated facility. This model allows the economy of scale from the production of fuels as well as the creation of higher value chemical constituents. This same model can be applied to a biorefinery in which fuels, chemicals and heat and power are produced in a single facility. One of the big challenges is deciding which chemicals will be integrated into that facility and what product options exist. This talk will focus on a specific example of using a 4 carbon building block (succinic acid) as a model for producing a variety of chemicals within a biorefinery.

FAST PYROLYSIS BASED BIO-REFINERIES

Tony Bridgwater

Aston University Bio-Energy Research Group, Birmingham B4 7ET, United Kingdom
T: +44 121 204 3381; F: +44 121 204 3680; E: a.v.bridgwater@aston.ac.uk

ABSTRACT

A biorefinery can be considered as the optimised performance of the use of biomass for materials, chemicals and energy applications. Performance relates to the following measures, but as these are not necessarily compatible or consistent in defining the best process system, optimisation usually requires their careful consideration:

- Carbon balance
- Cost
- Environment
- Impact
- Social aspects
- Yield

Bio-refineries have existed for many years, although the term biorefinery is relatively recent. Pulp and paper mills are one example, but there are many instances where fuels and chemicals have been co-produced such as RME plants where glycerine is co-produced with RME; bio-ethanol plants from ligno-cellulosics where lignin is used as a fuel and as a source of chemicals; food flavourings from pyrolysis of biomass where the resides are used as a fuel or a source of other chemicals.

In many examples, co-production of energy products or chemicals results from the requirement to dispose of wastes or byproducts in a satisfactory way. It is only relatively recently that the potential for optimised co-production of valuable products has been fully appreciated and strongly promoted, which has given rise to the concept of a biorefinery. Polygeneration is a European Commission term with the same connotations – the optimised production of fuels and chemicals.

This paper focuses on fast pyrolysis of biomass as the core of a system to optimise the use of biomass. This paper summarises the characteristics and advantages of pyrolysis forming the core of a biorefinery and outlines some scenarios in which the unique features of fast pyrolysis can be effectively exploited. Consideration is given to concepts based only on pyrolysis and pyrolysis products, concepts that broaden the scope to encompass other downstream processes and finally concepts in which pyrolysis can make a valuable contribution within the broader context of utilisation of biomass.

CARGILL'S VIEW OF BIOREFINERIES - THE REVOLUTION HAS BEGUN

Jim Stoppert

Cargill, 15407 McGinty Rond West, MS 69, Wayzata, MN 55391
(952) 742-5488: jim_stoppert@cargill.com

Abstract

Cost and technology have been the critical issues to be resolved in the path towards the bio revolution. Higher cost and unstable hydrocarbons have caused an acceleration down the path that will result in an earlier commercialization than many anticipated.

PROGRESS IN COMMERCIALIZATION OF POLYOL CHEMICALS FROM CORN

A. T. BRIX,
International Polyol Chemicals Inc, Blue River, OR 97413,
ATBrix@Earthlink.net,

TEITUR GUNNARSSON, IPCI Engineering
HONGBIN QI, Global Biochem

International Polyol Chemicals Inc. and its development partner Icelandic Green Polyols (hereinafter Polyol Partners) have developed a continuous catalytic process for the conversion of monomer sugars (glucose) to industrual glycols (ethylene glycol, propylene glycol and butanediols).

In concert with Global Biochem of China the Polyol Partners and GBT have built a 10,000 MT glycol facility in Changchun, China at the site of Global's main corn processing facility. Currently the partners are constructing a 200,000MT facility in Changchun. The paper outlines the process, general process economics and the future for green sugar based glycols.

BIOREFINERIES AND BIOFUELS: CURRENT ACTIVITIES AND FUTURE VISION OF PETROBRAS

Luiz Fernando Leite, João Norberto Noschang Neto, Juliana Vaz Bevilaqua

Petrobras R&D center, Av. Jequitibá n.950, Ilha do Fundão, Rio de Janeiro, Brazil, CEP 21949-900
lleite@petrobras.com.br

Introduction

PETROBRAS has been increasing its oil production and should reach 1.9 million bpd in Brazil, of which 75% will be produced from deep and ultra-deepwater reservoirs, accordingly the country will be very close to its oil self-sufficiency. The domestic crudes are heavier than normal imported ones, resulting in a higher yield of vacuum residue production. It is a sweet crude but contains more nitrogen compounds, which impair the yields of the refining catalytic process, due to the basic nitrogen species. Moreover the asphaltene content and naphthenic acidity levels are higher and the latter contaminant increases the corrosion problems in refining installations. Table 1 shows the main characteristics of domestic crudes compared to an imported one, the Arabian Light. There are also some heavy crude oils that come from onshore production areas, like Fazenda Alegre also shown in the table.

Table 1. Oil crude data

	Arabian Light	Cabiúnas	Marlim	Fazenda Alegre
º API	33.30	24.70	19.70	13.2
S (%w/w)	1.63	0.47	0.75	0.31
N (%w/w)	0.09	0.27	0.45	0.33
Asphaltenes (%w/w)	1.10	2.80	2.60	7.3
Metals (ppm)				
Ni	3.50	9	19	42
V	14	12	24	6
TAN (mg KOH/g)	< 0,05	0.51	1.23	0.8

The heavier crudes generate a greater volume of fuel oil, a lower added value product. For environmental issues, there is a trend of increasing the natural gas domestic consumption displacing the fuel oil market demand. This magnifies the need for a higher conversion to keep the balance of product demand / offer. PETROBRAS in particular has the additional challenge of matching the increasing supply of Brazilian oil with the need of producing diesel and gasoline with a more stringent specification concerning quality and environmental aspects. These required conversion units, as well as, the hydrotreating units needed in the future refining scheme to meet better fuel quality are very energy demanding processes, worsening the greenhouse gas emissions problems at refineries.

Biodesulfurization and biodenitrogenation

An option for upgrading the quality of the crude oil and the refining of its intermediary streams is to make bio-treatments, using microorganisms capable of removing sulfur, nitrogen and heavy metals. Compared with conventional technologies the bio-refining presents the following advantages: much less severity - requiring close to ambient operational temperature and pressures; lower energy consumption; no hydrogen demand – the hydrogen balance at refineries little by little is becoming more critical due to the high quality fuels requirement; and yet the product volume is preserved. On the other hand, there are some drawbacks in applying this kind of technology, such as: low concentration of microorganism aqueous solutions; low reaction rates; complementary technology; specific solution; and far removed from the refiner culture.

Furthermore there are some technological challenges still to be overcome, such as: high efficiency and stable bio-catalyst; high biomass production – high microorganism reproducibility; conceptual process – careful handling of microorganism solutions; bio-safety.

A bacterial strain F.5.25.8 (*Gordonia amicalis*) was cultivated, which presented good conversion from dibenzothiophene to 2-hydroxybiphenil, via the 4S pathway. This culture seems to be unique because it can simultaneously cleave carbon-sulfur and carbon-nitrogen bounds, removing both contaminants from typical petroleum streams. *Pseudomonas nitroreducens* strain can perform the quinoline degradation and was able to grow using this product as the only nitrogen source. Therefore some progress was obtained in the lab scale phase and a pilot facility is being built to up- scale this process phase.

Biofuels

Despite of the increasing in crude oil production and its oil reserves, PETROBRAS has changed its strategy and is positioning itself not only as a petroleum player but as an integrated energy company. In this sense it is broadening its activities to other energy source besides fossil fuels. One of the areas of increasingly grow is energy from renewable resources.

Alcohol. Brazil is the world's mayor ethanol producer from sugar cane, with a broad domination of the production chain considering the agriculture and industrial aspects. The production was 13 million m3 in 2004 and this is expected to expand to about 14 million m3 in 2006. The country has some competitive advantages, as the crop presents a high sucrose content and the seasonal conditions allows the production all year round, as the harvest in the Northwest region takes place from October to March and in the Center-South from April to December. This reduces the logistic and storage costs, therefore Brazil has the lowest alcohol cost production on a worldwide basis. It also is in a lead position in relation to bio-fuels application, as ethanol has been utilized for powering the domestic light vehicles fleet since 1975, when the National Alcohol Program was created. Today the Brazilian light vehicle fleet is powered by ethanol or gasohol, as a legal requirement a typical mixture is 24% ethanol plus 76% gasoline, so this rules out any chance of using an alcohol free fuel in the country.

PETROBRAS had a critical participation during the alcohol program implementation, offering its logistic assets for ethanol distribution all over the country and supported engine performance tests of gasoline plus ethanol fuel blending. The Company has a long experience in handling and commercializing this product. Moreover, in the eighties, PETROBRAS carried out the development of the Ethanol Production from Cassava technology, reaching a technical-economical production line, which was commercially applied but unfortunately wasn't a successful enterprise, due to the failure of the agricultural project.

Biodiesel. Biodiesel is a renewable fuel with clear social and environmental benefits, associated to man's fixation of rural areas, generation of work and income, and the minimization of gas

emissions that contribute to global climatic changes. Strategically biodiesel is also seen as a diversification from traditional energy patterns, mainly for those countries that import mineral diesel. This fuel composed of mono-alquil esters of long chain fat acid obtained from vegetable oils or animal fats, known as biodiesel, can bring some advantages such as higher lubricity and higher cetane numbers, bringing improvements in ignition quality. With the government regulatory standard already established, the search for good quality biodiesel production represents a technical, economical, social and environmental challenge.

The development of the technological process, with the best chosen oleaginous raw material and alcohol to be used for the esterification step, poses a difficult puzzle to solve. New production processes nurtured in the laboratory, must be up-scaled if they are to become commercially viable and the producers don't opt to import technology from the established markets. Furthermore another important technical aspect is the choice of alcohol, because worldwide biodiesel is produced with methanol and so Brazil's great challenge is the use ethanol and to make it achieve the same performance.

It is well known that around 85% of the biodiesel overall cost is directly related to the raw material cost: the seed or the vegetable oil. Given all the possibilities, Brazil has a vast number of options: castor bean, soy bean, turnip, domestic pine, babassu coconut, palm coconut, sunflower, peanut, cotton and a series of other oleaginous products. Not to mention bovine fat and used cooking oil among others. Brazil is a prominent country in the world scenario of bio-fuels, because of the previously cited huge alcohol production, as well as, climate conditions and favorable soil for growing biomass and the cultivation of different oleaginous products.

PETROBRAS is developing two parallel R&D projects: the first one, the trans-esterification process is starting directly with the oleaginous seed in the presence of a catalyst and ethanol. This process, patented by PETROBRAS, was validated in the laboratory, tested in a Pilot Plant and now is being up-scaled, via the implementation of a Prototype unit that should start its operation in the forthcoming November. The other project, a more conventional one, is the reaction of vegetable oils with ethanol in the presence of a catalyst for the corresponding ester production. PETROBRAS has recently applied for the process and equipment patents. The process was also developed in the laboratory, tested in a Pilot Plant scale and will be checked in a semi-industrial unit soon.

Biorefineries

The search for alternative sources of energy has become part of the priorities of the modern society, principally renewable. Therefore the biorefineries, i.e., a biomass based facility for producing products is in the spotlight. In the Brazilian scenario, it would be more economically sound to revamp and upgrade the existing Alcohol Distilleries, thus transform them into an integrated sustainable energy and fuels production unit. Nowadays only one third of the energy that could be obtained from sugar cane crop is actually used. From the alcohol production obtained from sugar cane, the residual bagasse can be used for electric power generation, as is done though inefficiently today, as well as, for a secondary production of alcohol, via its hydrolysis and fermentation. Furthermore through improved mechanical harvesting the sugar cane leaves can also be collected and chopped, instead of just being burned in-situ or just left to rot, from which other products can be obtained. The resultant straw can be used for energy generation, via burning, or be applied for more added-value products, such as: ethanol (through the conversion of lignocellulosic materials) and other hydrocarbons (by means of gasification and Fischer-Tropsch synthesis). PETROBRAS is developing technologies to produce ethanol from lignocellulosic materials either using acid and enzymatic hydrolysis. PETROBRAS is also developing alternative processes to conventional fermentation by means of Simultaneous Saccharification and fermentation (SSF).

As a matter to improve biodiesel co-products value, PETROBRAS has resume the know-how in producing ethanol from starch materials (cassava) and developed a process that intent to detoxify and produce ethanol from castor bean cake. The process employs acid hydrolysis and conventional fermentation and produces over 100 L of ethanol from each ton of castor bean cake. That way, it is possible to add value to the residual cake and reduce biodiesel production costs. The process is still in lab scale and soon will be scaled up.

These materials that are being tested for ethanol production have low market value and otherwise would be wasted. From the results achieved, it is possible to foresee integrated units where from oleaginous raw material it is possible to produce biodiesel with minor material inputs and waste outputs.

OPTIMIZATION OF ACID TREATMENT OF SERPENTINE MINERALS FOR CO_2 SEQUESTRATION

George W. Alexander[1], Hui Ou[1], Parvana Gafarova[1], and M. Mercedes Maroto-Valer[2]

[1] The Energy Institute and Department of Energy and Geo-Environmental Engineering, The Pennsylvania State University, 405 Academic Activities, University Park, PA 16802, USA
[2] School of Chemical, Environmental and Mining Engineering, University of Nottingham, Coates Building, University Park, NG7 2RD, United Kingdom

Introduction

Mineral carbonation that uses silicate minerals to sequester carbon dioxide into a permanent, solid and stable form is a promising concept for permanent CO_2 sequestration, due to the vast natural abundance of the raw minerals, the permanent storage of CO_2 in solid form as carbonates, and the overall reaction being exothermic [1, 2]. However, the primary drawback to mineral carbonation is the reaction kinetics [3, 4]. To accelerate the reaction, aqueous carbonation processes are preferred, where the minerals are firstly dissolved in solution. In aqueous carbonation, the key step is the dissolution rate of the mineral, where the mineral dissolution reaction is likely to be surface controlled. In order to accelerate the dissolution process, the serpentine can be ground to very fine particle size (<38μm), but this is a very energy intensive process [5]. Alternatively, magnesium could be chemically extracted in aqueous solution [4, 6].

The authors have previously shown that chemical surface activation helps to dissolve the magnesium from the serpentine minerals (particle size ~100μm), and furthermore, the carbonation reaction can be conducted under mild conditions (20°C and 650psig) compared to previous studies that required >185°C, >1850psig and <38μm particle size [4, 6]. The overall objective of this work is to optimize the active carbonation process previously developed in order to design an integrated CO_2 sequestration module. Several experimental factors have been outlined as having a potential influence on the mineral activation. In this work, computer experimental design tools have been used to screen and identify the variables that predominantly affect the carbonation reactions of acid treated serpentine minerals.

Experimental

Study samples. Serpentine samples from the Cedar Hills quarry in SE Pennsylvania are used in this work as the mineral carbonation feedstock. The samples were provided by the Department of Energy - Albany Research Center (ARC). The samples consist of a -5/32" (4mm) head sample and a -400 mesh (-38 μm) ground sample that has underwent magnetic separation from a separation pilot-plant study (O'Connor, 2004). The provided 4mm head sample was ground to the desired size fractions using a 4.75l batch ball mill with a ball charge of 30%. The mill was charged with 1500g samples of serpentine and ground for 9 minutes on a drive roll. The ground serpentine was sieved to the following size fractions: 300-150 μm, 150-75 μm, 75-38 μm, and -38 μm and with a hand magnet, wet separated to remove magnetite.

Statistical design. A Taguchi design of experiment (Minitab® software package) was used in this work to evaluate an optimum combination of control factors, including sulfuric acid concentration, particle size, reaction time, and temperature. In order to provide a balanced design, where no factor is weighted disproportionately, temperature variations were carried out upon optimization of concentration, particle size, and time. The orthogonal array of the above three factors with as many levels provides a balanced design, where no factor is weighted disproportionately.

Activation studies. Chemical activation was carried out on 50g samples of ground Cedar Hills serpentine. The size fractions were 300μm-150μm, 150μm-75μm, and 75μm-38μm. An additional experiment was performed with -38μm samples, to establish the value of further size reduction. The serpentine was reacted in 500mL of prescribed concentrations of sulfuric acid for predetermined times (Table 1), as determined by the Taguchi design. The samples were then filtered and dried overnight at 105°C.

Table 1. Orthogonal Design of Experiments.

Experiment	Molar Acid Concentration	Particle Size Fraction (D_{50}), μm	Reaction Time, hrs
1	1.5	300-150 (163)	1
2	1.5	150-75 (125)	3
3	1.5	75-38 (61)	6
4	3	300-150 (163)	3
5	3	150-75 (125)	6
6	3	75-38 (61)	1
6A	3	-38 (10)	1
7	5	300-150 (163)	6
8	5	150-75 (125)	1
9	5	75-38 (61)	3

Sample characterization. Particle size analysis for the individual size fractions was completed on a Malvern Mastersizer "S" utilizing laser scattering.

Analyses of chemical composition, solutions and solids, were carried out on a Leeman Labs PS3000UV Inductively Coupled Plasma Spectrometer (ICP). Solid samples, prior to analysis, were dissolved using a lithium metaborate fusion technique. Loss-on-ignition (LOI) values were determined by measuring the weight loss after heating at 900°C for 12 hours.

Results and Discussion

Particle size characterization. To better understand the effects associated with the individual particle size fractions, the parent serpentine was ground to different size fractions. Particle size analysis was carried out for each fraction to ensure that the desired size fractions have been prepared.

Figure 1 shows the particle size distribution of the fractions prepared. The analysis confirms the distribution of particles within each of the respective size fractions. In the following sections, the size fractions are referred to by the median particle size, or D_{50}, as determined from Figure 1.

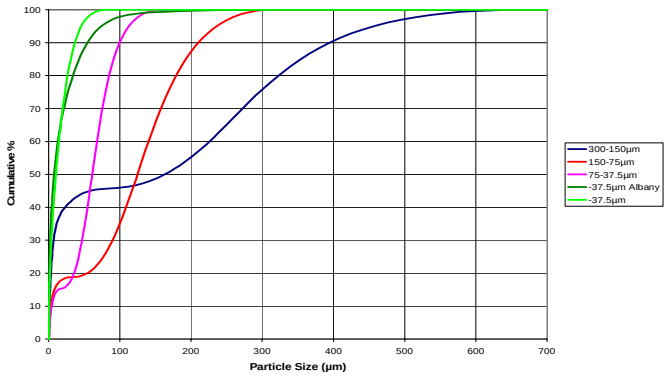

Figure 1. Particle size distribution of the fractions prepared.

Magnesium dissolution. Sulfuric acid has been determined to be an effective agent in the dissolution of magnesium from serpentine for its subsequent carbonation, while concurrently producing a high surface area silica byproduct [7]. ICP-AES analyses were conducted after the reactions to measure the concentrations of both the solutions and solids. As expected, lower % MgO in the solids generally corresponds to higher Mg^{2+} concentrations in solution, and vice versa. Accordingly, Figure 2 shows the effect of time, size, and acid concentration simply in terms of the percentage of magnesium removed from the serpentine samples.

The main effects plot shown in Figure 2 illustrates the influence of acid concentration and particle size on the extraction of magnesium. The dissolution of serpentine clearly increases with higher acid molar concentration. The particle size dependence shows that the benefits of grinding serpentine are realized at a median particle size of 125 microns and smaller. Additional ICP results also indicate some further benefits of comminution, as the lowest particle size factions have the lowest iron concentration. This is of interest during the carbonation, since it has been shown that as magnetite oxidizes, the carbonation of serpentine is inhibited due to the formation of a passive surface layer of hematite [9].

Characterization of serpentine with respect to time consistently shows that results are independent of reaction time, for times under 6 hours. Ongoing research into the effects of reaction time remains open, as additional studies have recently indicated the effects of time may be more on the order of days.

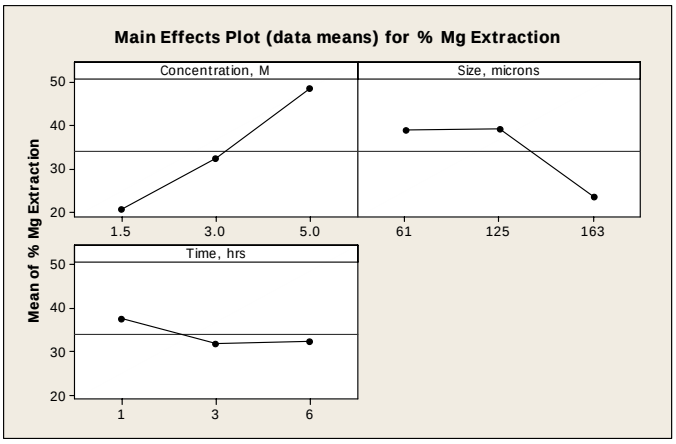

Figure 2. Effect of concentration, size, and time on yield.

Conclusions

In this work, computer experimental design tools have been used to screen and identify the variables that predominantly affect the acid treatment of serpentine minerals. This study has focused to date on the effects of varying the acid concentration, particle size, and the reaction time. The reaction yields and the characterization of the reaction products by ICP/AES were used to describe the influence of each of the experimental variables.

Contrary to expected, the reaction time, within this design of experiments, has been shown to be insignificant. These results are issues of further consideration to be addressed under the carbonation studies. The remaining results are as expected, including the dissolution of magnesium, which is to be utilized within the carbonation unit. Previous studies have shown that carbonation reactions could be carried out under a milder regime through the implementation of NaOH titration with the magnesium solution. The optimization of acid concentration, particle size, and reaction temperature will ultimately be determined according to the carbonation efficiencies.

Acknowledgement. The authors wish to thank the Department of Energy, University Coal Research Program (Award No. DE-FG26-03NT41809) for supporting this work. The authors are also grateful to Yee Soong and Dan Fauth from DOE/NETL and Bill O'Connor from Albany Research Center for providing samples and helpful discussions. This report was prepared with the support of the U.S. Department of Energy, under Award No. DE-FG26-03NT41809. However, any opinions, findings, conclusions, or recommendations expressed herein are those of the authors and do not necessarily reflect the views of DOE.

References

(1) Seifritz, W. *Nature*, **1990**, 345(7), 486.
(2) Lackner, K.S.; Butt, D.P.; Wendt, C.H. In *Proceedings of The 22nd International Technical Conference on Coal Utilization and Fuel Systems*, **1997**, Clearwater, Florida.
(3) Herzog, H.J. Carbon Sequestration via Mineral Carbonation: Overview and Assessment." **2002**, MIT Laboratory for Energy and the Environment, Cambridge, Massachusetts.
(4) Maroto-Valer, M. M.; Kuchta, M. E.; Zhang, Y.; Andresen, J.M.; Fauth, D. J. **2003** in *Proceedings of Third Annual Conference on Carbon Sequestration*, U.S. DOE National Energy Technology Laboratory, Alexandria, VA, May 3-6, 2004, Paper 0527.pdf (CD-ROM publication).
(5) Herzog, H.J. 1998, "CO_2 Capture, Reuse, and Sequestration Technologies for Mitigating Global Climate Change." DOE/PC/96354-98, MIT Laboratory for Energy and the Environment, Cambridge, Massachusetts.
(6) Maroto-Valer, M. M.; Kuchta, M. E.; Zhang; Y., Andrésen, J. M.; Fauth, D. J. **2005** *Fuel Processing Technology*, available on-line, in press.
(7) Maroto-Valer, M.M; Zhang, Y.; Kuchta, M. E.; Andrésen, J.M.; Fauth, D.J. **2004** "Utilization of Serpentine mineral for CO_2/SO_2 capture and sequestration", No: 2003-2790. Filled for full patent May 2004.
(8) Maroto-Valer, M.M; Fauth, D. J.; Kuchta, M. E.; Zhang, Y.; Soong, Y. **2003** in The Proceedings of *Second Annual Conference on Carbon Sequestration*, U.S. DOE National Energy Technology Laboratory, Alexandria, VA, May 5-8, 2003, Paper 2C2.pdf (CD-ROM publication).
(9) Fauth, D.J.; Goldberg, P.M.; Knoer, J.P.; Soong, Y. **2000**, *Prepr. Symp. Am. Chem Soc., Div. Fuel Chem.*, 45(4), 708.

AUTO-IGNITION BEHAVIOR OF METHYL DECANOATE

James P. Szybist and André L. Boehman

The Energy Institute
The Pennsylvania State University
405 Academic Activities Building
University Park, PA 16802

Introduction

An extensive body of literature reporting on emission and performance trends of emissions and performance with biodiesel and biodiesel blends exists. In general, particulate matter emissions are reduced an average of about 10% for B20 blends (20 vol% biodiesel, 80 vol% diesel), while NOx are increased 2-5%. Maximum engine output is derated slightly due to a lower calorific value, but there is no efficiency penalty on a BTU basis. For a review of biodiesel performance and emissions, see Graboski and McCormick[1].

Despite the well-established trends of the performance and emissions of biodiesel, there is very little understanding about how and why biodiesel behaves differently in diesel engines. Fisher et al.[2], who performed kinetic modeling of methyl butanoate, made a plea that more work on understanding biodiesel and other oxygenates is needed. Graboski and McCormick also stated that a more fundamental understanding of biodiesel needs to be developed.

This study attempts to identify premixed auto-ignition differences between a diesel-relevant compound, n-heptane, and a biodiesel relevant compound, methyl decanoate, using a motored engine experiment. Of particular interest for each compound is the magnitude of the cool-flame, and the intermediate products produced by it.

Experimental Procedure

An octane rating engine with modified intake air and fueling systems was used to study auto-ignition behavior of fuels in a motored engine. The carbureted intake manifold for the engine was removed and replaced with a system capable providing heated intake charges up to 260°C, and the fuel was delivered upstream of the intake with a gasoline fuel injector that was controlled independently of air flow. This allowed for premixed fuel and air charge to be delivered to the engine using non-volatile fuels. In this study, an equivalence ratio of Φ=0.25 was used for both fuels. The octane rating engine has a variable compression ratio, from 4 to 13.75, which allowed for a wide range of compressive temperatures and pressures.

The engine was operated without spark and with a premixed intake charge, thus any combustion that takes place can be attributed to auto-ignition of the fuel. The ignition process is identical to that in homogeneous charge compression ignition (HCCI) combustion, but in this experiment combustion was quenched instead of taken to completion in many cases. The tests were started a very low compression ratio, and then increased in a step-wise manner to increase the extent of reaction. Heat release data and an FTIR spectrum were collected at each compression ratio. A schematic of the experimental apparatus is shown in Figure 1.

In this study, the ignition behavior of n-heptane was compared to methyl decanoate. n-Heptane, obtained from Chevron Phillips Chemical Company, was used because it has studied extensively studied and its ignition process is well understood[3]. It was desirable to have the fuel fully vaporized and premixed with the air to minimize any mixing or vaporization effects on ignition and combustion. Biodiesel, which has an initial boiling point of around 300°C, could not be use because the maximum operating temperature of the intake system was 260°C. Thus, methyl decanoate (capric acid methyl ester), obtained from Proctor & Gamble Chemicals, which has a boiling point of 224°C was used as a biodiesel surrogate. Methyl decanoate is a fully saturated fatty acid methyl ester with a chain of 10 carbon atoms, whereas soy-based biodiesel has chains of 16 to 20 carbon atoms and can vary from 0 to 3 unsaturations.

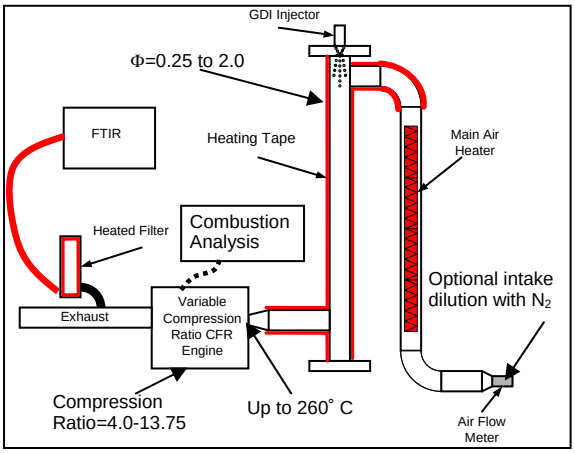

Figure 1. Schematic of the modified octane rating engine.

Results and Discussion

Both n-heptane and methyl decanoate exhibited strong cool-flame behavior. At low compression ratios, the cool-flame ignition occurred, but the maximum temperature in the cylinder did not get high enough for the main ignition to occur. As the compression ratio was increased further, the maximum temperature increased until the main combustion event occurred. Figure 2 shows the heat release and temperature profiles for n-heptane for a condition with only cool-flame heat release (a), and a condition for cool-flame heat release and main heat release (b). Figure 2 is also qualitatively representative of the auto-ignition of methyl decanoate.

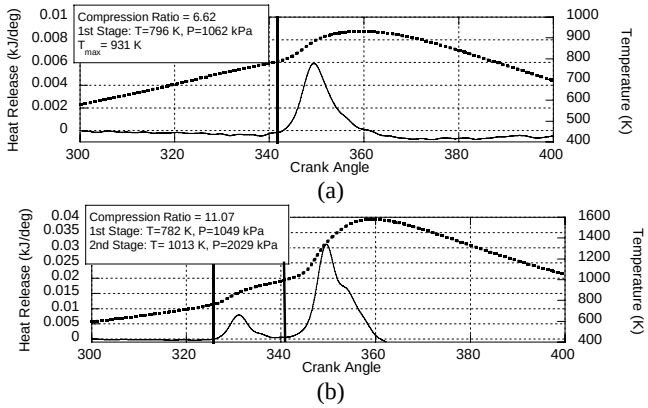

Figure 2. Heat release and temperature traces for n-heptane for (a) cool-flame only, and (b) cool-flame and main combustion.

The heat release during the cool-flame accounted for up to 16% of the total heat release for n-heptane, and up to 13% of the total for methyl decanoate. One significant difference between biodiesel and methyl decanoate, other than that carbon chain length, is that typically around 80% of its constituents are unsaturated. Minetti et al. studied the cool-flame of n-pentane and 1-pentene and found that the presence of the double bond greatly reduced the magnitude of the cool-flame[4]. Thus, it is expected that the magnitude of the cool-flame for biodiesel will be significantly lower than it is for methyl

decanoate, but given the long carbon chains present in biodiesel, it is expected that it will still be a major feature of the ignition process.

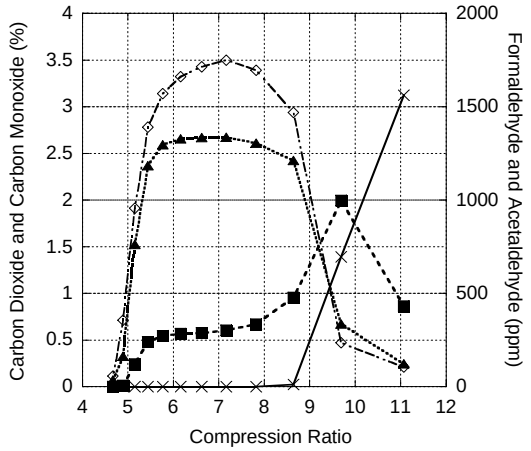

Figure 3. Exhaust composition for n-heptane as a function of compression ratio at Φ=0.25. (X) carbon dioxide, (■) carbon monoxide, (▲) formaldehyde, and (◊) acetaldehyde.

The concentrations of CO, CO_2, formaldehyde, and acetaldehyde, which were quantified using an FTIR, are shown in Figure 3 for n-heptane. The lowest compression ratio points for n-heptane were not sufficient for cool-flame ignition, and thus the concentrations of the exhaust species are zero. At a compression ratio of about 5, cool-flame ignition occurs and the concentrations of formaldehyde, acetaldehyde, and CO increase, while concentration of CO_2 remains zero. These concentrations remain relatively constant until a compression ratio of about 8.5 is reached and main ignition occurs. This results in a dramatic reduction in aldehyde concentration, which is due to their being consumed. Also, after an initial bump in CO concentration, the CO concentration also seen to decrease, and would have continued to do so if the compression ratio was increase further. The concentration of CO_2 increases from zero at the onset of the main combustion event, where it is seen to increase dramatically.

Similarly, Figure 4 shows the exhaust concentrations for methyl decanoate. Because of its higher boiling point, the intake system was operated at a higher temperature to ensure that the fuel was fully vaporized. This resulted in cool-flame ignition of methyl decanoate even at the lowest compression ratios. The trends in CO, formaldehyde, and acetaldehyde are similar to the trends observed for n-heptane, with relatively constant concentrations throughout the cool-flame regime, and dramatically reduced concentrations with the onset of the main ignition. However, there is a substantial difference with regard to CO_2, which is present in significant concentrations throughout the cool-flame ignition.

Mueller et al.[5] reported a similar trend of direct CO_2 production with dibutyl maleate. They concluded that dibutyl maleate, which is a diester, formed CO_2 through unimolecular decomposition. They also concluded that from a soot suppression standpoint, the formation of CO_2 directly from the ester group is an inefficient use of fuel-bound oxygen. This is because fuel-bound oxygen suppresses soot formation in diesel engines by bonding with carbon atoms, making them unavailable to participate in the reactions that lead to soot formation. A carbon atom is unavailable to participate in soot precursor reactions if it is bonded to a single oxygen atom, forming carbon monoxide. If two oxygen atoms are bonded to it, it is still unavailable to participate in soot precursor reactions. Mueller et al. concluded that other oxygenate compounds, such as ethers, were more effective at reducing soot because they did not form CO_2 from unimolecular decomposition.

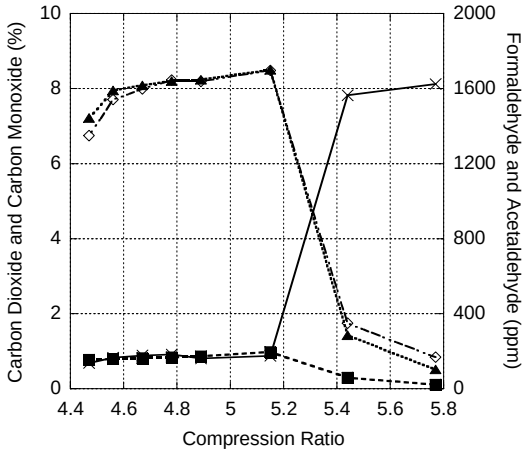

Figure 4. Exhaust composition for methyl decanoate as a function of compression ratio at Φ=0.25. (X) carbon dioxide, (■) carbon monoxide, (▲) formaldehyde, and (◊) acetaldehyde. f

Unlike the magnitude of the cool-flame, where there is expected to be a significant difference, the formation of CO_2 from unimolecular decay is expected to be the same for methyl decanoate and biodiesel.

Conclusions

Both n-heptane and methyl decanoate auto-ignited under similar conditions in a motored engine under HCCI-like conditions. Both fuels exhibited strong cool-flame behavior, accounting for 16% of the total heat release for n-heptane, and 13% for methyl decanoate. However, this is likely not representative of the cool-flame behavior of biodiesel because methyl decanoate is fully saturated while more than 80% of biodiesel's constituents have at least one unsaturation, and it is well-established that unsaturations reduce cool-flame magnitude. Nonetheless, it is expected that the cool-flame will remain as a feature of the auto-ignition process of biodiesel.

The cool-flame ignition of n-heptane produced high levels of CO, formaldehyde, and acetaldehyde, while CO_2 was only formed during the main ignition. Methyl decanoate, however, produced significant levels of CO_2 during the cool-flame. It is believed that this CO_2 is not from oxidation of the fuel, but from the unimolecular decomposition of the ester molecule. From a soot suppression standpoint, direct formation of CO_2 from an oxygenated fuel is an inefficient use of fuel-bound oxygen.

Acknowledgement. The authors wish to thank the Department of Energy for support under Grant DE-FC26-03NT41828.

References

(1) Graboski, M.S., and R.L. McCormick. *Progress in Energy and Combustion Science.* **1998**, *24(2)*, pp. 125-164.
(2) Fisher, E.M., W.J. Pitz, H.J. Curran, and C.K. Westbrook. *Proceedings of the Combustion Institute.* **2000**, *28*, pp. 1579-1586.
(3) Curran, H.J., P. Gaffuri, W.J. Pitz, and C.K. Westbrook. *Combustion and Flame.* **1998**, *114*, pp. 149-177.
(4) Minetti, R., A. Roubaud, E. Therssen, M. Ribaucour, L.R. Sochet. *Coubustion and Flame*. **1999**, *118(1-2)*, pp. 213-220.
(5) Mueller, C.J., W.J. Pitz, L.M. Pickett, G.C. Martin, D.L. Siebers, and C.K. Westbrook. *Society of Automotive Engineers.* **2003**, *Technical Paper 2003-01-1791*.

EVALUATION OF COAL-BASED DIESEL PRODUCTS AFFECT ON FUEL QUALITY

Stephen R. Kirby, André L. Boehman, and David J. Clifford

Energy Institute, Penn State University
University Park PA 16802

Introduction

Refinery integration of coal-derived jet fuel production via a combined RCO/LCO strategy, will require studying the physical and chemical nature of all products that are perturbed by introduction of coal components into the refinery. For successful utilization of coal-based jet fuels all non-jet-fuel components must fit existing and future product stream specifications.

Introducing coal-derived streams into the refinery will affect the quality, composition and performance of the resulting vehicular fuels. The >270°C cut of the hydrotreated stream would be low in sulfur due to the severe hydrotreatment. The effect on flash point will need to be determined if this stream is sent to the diesel pool. If this stream is combined with diesel fuel, it will add cycloparaffins, which will increase energy density [1] and boost value. However, the impact on cetane number and sooting tendency is unclear.

Key components within the coal-derived diesel cut must be identified, and their affect on the chemical and physical properties of any resulting blend determined. This study investigates the physical and chemical nature of diesel boiling range products that are produced as a result of the introduction of coal components into the refinery.

Experimental

Fuels used in this study were a petroleum-derived ultra low sulfur diesel from BP (BP15) and a coal-derived diesel cut (EI-175). EI-175 was produced from a 1:1 mix of LCO and RCO after severe hydrotreatment and hydrogenation.

Fuel chemical compositions were qualitatively analyzed by a Shimadzu GC-17A gas chromatograph coupled with a Shimadzu QP-5000 mass spectrometer. A Restek XTi-5 column (30 m x 0.25 mm x 0.25 um) was used in the gas chromatograph. The column temperature was programmed from 40°C (held for 4 min) to 320°C at a rate of 4°C/min with a final 15 min isothermal period. The split ratio was 20:1 and 1 uL was injected. Peak assignments were based on comparison with NIST spectra.

The derived cetane number (DCN) for each of the fuel blends was measured in accordance with ASTM D6890-03a. A correlation has been developed to convert the measured ignition delay into a DCN, which is correlated with the CN measured by ASTM D613 (CFR Cetane Rating engine). The ignition delay (defined as the elapsed time from injection to where the chamber pressure reaches $P_{initial}$ + 50 psi) under specified conditions is measured using the Ignition Quality Tester (IQT). The system is fully automated and an experiment consists of 15 pre-injections (to equilibrate system temperatures) followed by 32 injections. The reported DCNs are the average of these 32 injections of pre-filtered fuels.

Flash point was measured in accordance with ASTM D6450 using a MINIFLASH FLP fully automatic flash point tester. This tester utilizes the continuously closed cup (CCCFP) method. Values reported were based on the average of five measurements.

Kinematic Viscosity of the fuel blends was performed following ASTM method D-445-97 using a Cannon-Fenske Viscometer. Viscometer VE7 was loaded with 10 ml of sample fuel and immersed in the viscometer bath at 40°C. After allowing 20 minutes for the sample fuel temperature to equilibrate, the sample was forced into the test section of the viscometer using a pipette bulb. Time of flow was measured using a stopwatch with accuracy to 1/100 s. Five runs were performed per sample. Times (s) were converted to kinematic viscosities (cSt) using a calibration with viscosity standard S3 (lot# 99101) from Cannon Certified Viscosity Standards.

Results and Discussion

Figure 1 presents the qualitative chromatograms from a coal-derived diesel cut (EI-175) and a petroleum-derived ultra low sulfur diesel (BP15). Total Ion Chromatograms (TIC) are shown for both fuels accompanied by Selected Ion Chromatograms (SIC) for prominent ions within the respective TICs. Compositional differences between the two fuels are obvious. Lighter compounds found at earlier retention times in the chromatogram of BP15 are absent with EI-175. Such compounds were likely converted during hydrotreatment, or distilled out in the gasoline and jet-fuel cuts.

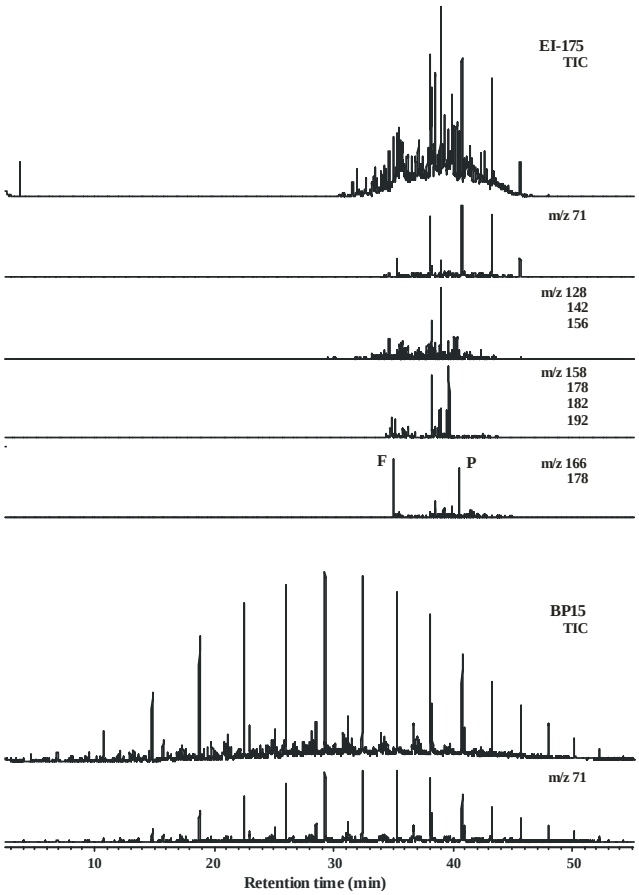

Figure 1. Chromatograms of a coal-derived diesel fraction (EI-175) and a petroleum-derived ultra low sulfur diesel. SICs were selected to describe aliphatics (*m/z* 71), two-ring aromatics (*m/z* 128,142,156), three-ring aromatics (*m/z* 158,178,182,192), and fluorene (F) and phenanthrene (P) (*m/z* 166, 178 respectively)

BP15 was almost exclusively aliphatic in nature with chains ranging from C7 to C24. EI-175 contained only a few aliphatic compounds ranging from C14 to C21. Two and three-ringed aromatics comprised the bulk of EI-175. Most abundant were phenanthrene, methyl phenanthrenes and their hydrogenated derivatives, as well as fluorene and dimethyl biphenyls.

Production of coal-derived diesel is presently limited such that large quantities for testing were not available. Based on the above observations fluorene and phenanthrene were chosen as readily

available representatives of coal-derived diesel compounds. BP15 was used as a carrier fuel with fluorene and phenanthrene as dopants from 0.5 wt% to 5 wt%. These blends were then tested for DCN, flash point and viscosity. Results for these tests are presented in Table 1.

Table 1. Fuel Properties of BP15 Doped with Fluorene and Phenanthrene

Fuel	BP15	BP15/Fluorene				BP15/Phenathrene			
Additive (wt%)	-	0.5	1	2	5	0.5	1	2	5
DCN	47.2	46.6	46.1	46.0	45.1	46.6	46.7	46.8	46.7
Flash Point (°C)	66.4	66.4	66.7	68.7	69.5	67.1	66.3	66.8	66.3
Viscosity (cSt)	2.5[1]	2.492	2.507	2.497	2.519	2.500	2.492	2.530	2.528

1 Value taken from BP15 specification

Addition of fluorene to BP15 decreased the DCN. As fluorene concentration in the petroleum-derived diesel was increased the DCN decreased. Phenanthrene addition to BP15 also decreased DCN. However, in contrast to fluorene, increasing the concentration of phenanthrene did not result in a continued decrease of DCN. Cetane number of a fuel indicates how easily it can be ignited under pressure and temperature in a combustion chamber. The higher the DCN the shorter the ignition delay which leads to less premixed combustion, lower peak cylinder pressure and lower NOx formation [2]. Therefore the presence of fluorene, or phenathrene, in a diesel fuel should increase the concentration of NOx in the emissions.

Fluorene addition to ultra low-sulphur diesel fuel generally increased the flash point, however, at 0.5 wt% fluorene no change in the solutions flash point was measured compared to the baseline fuel. Increasing the concentration of fluorene in BP15 resulted in increasing flash point temperatures. At 0.5 wt% phenanthrene a slightly higher flash point was measured than that of BP15 alone. Further increases in phenanthrene concentration had little or no affect on the flash point of BP15. The most abundant single compound in BP15 was tetradecane (b.p. 252°C). Addition of fluorene (b.p. 298°C) and phenathrene (b.p. 340°C) was sufficient to shift the affect of the lower molecular weight species in the diesel and increase the flash point. Increase in flash point would also lead to increases in ignition delay.

Addition of either fluorene, or phenanthrene, had little or no affect on the kinematic viscosity of BP15. Addition of these aromatic compounds should not affect the spray characteristics of the diesel fuel.

Conclusions

Coal-derived diesel fuel will be high in aromatics and hydroaromatics. Two representative compounds are fluorene and phenanthrene. The addition of these two compounds to an ultra low sulfur diesel fuel led to a decrease in DCN and an increase in flash point. No affect on viscosity was found.

Acknowledgement. The authors wish to thank the Department of Energy for support of project Grant DE-FC26-03NT41828

References

(1) Hazlett, R. N. *ASTM*, Philadelphia, **1991**.
(2) Lin, Y.; Lee, G; Rei, M. *Catalysis Today* **1998**, *44*, 343-349.

LNG-CHEMISTRY OF FUEL INTERCHANGEABILITY

Bruce Rising, Regulatory Affairs

Siemens Westinghouse, Orlando, Fl.
Bruce.rising@siemens.com

Abstract

The changing nature of the world's energy needs and power generation demands is creating pressure to bring new supplies of natural gas to the United States. While natural gas is often the fuel of choice for many power generation applications, the vast majority of the world's natural gas reserves are "stranded assets", located in remote regions of the world where there is minimal local demand for these fuels, and often minimal demand for large power stations. Traditional pipeline delivery methods are not viable for trans-oceanic movement of natural gas. LNG, liquefied natural gas, is one of several methods of monetizing these remote gas supplies. However, there may be some compatibility issues related to introducing off-shore natural gas supplies into the US market. One of the key concerns raised has been the interchangeability or substitution of one gas for another. For gas turbines equipped with diffusion combustion systems, few operability issues are expected. However there would be an expected increased NO_x with fuels that would include higher levels of hydrocarbons (such as propane and butane), and a commensurate reduction in the NO_x emissions for lean fuels that contain nitrogen or CO_2. For lean-premix gas turbines, the issues are more complex, since the design features and operating requirements are much more complex. Test results suggests that emissions (NO_x, CO, and VOC's) are affected by fuel quality. Minor changes to fuel composition are likely to be within pre-existing permit emission levels. However, some of the off-shore supplies have the potential of introducing more significant changes. Also, the rate-of-change of the gas properties (or gas quality) can affect system stability and reliability. Current specifications allow for +/- 4% variation in the Wobbe Index, although the specified range may require modifications to the combustor monitoring system, and new combustor diagnostic tools.

Introduction

The United States has experienced severe limitations in its ability to meet natural gas demand with domestic production. Currently the US consumes approximately 23 tcf per year of natural gas, with approximately 20% of this directed toward power generation. However, 15% of US supplies are currently imported to meet demand, and all of Mexico's imports of natural gas come from the US supply base.

Regulatory pressures currently limit access to large, untapped gas reserves on the North Slopes and the Alaskan National Wildlife Refuge (ANWR). Even without self-imposed restrictions on access, it may require up to a decade to bring these supplies to market, and to date there is little activity on this front. The only available substantial capacity to shore up domestic declines is to import gas supplies from the virtually unlimited off-shore sources. These activities are well underway now, and will continue for decades, with billions of investment dollars in Africa, Asia, and the Middle East.

US and World Energy Supply

US natural gas production not improved in recent years despite rapid increases in price of domestic natural gas to all users. In fact, despite increases in drilling, production has actually declined. A summary of recent US domestic production shows that there has been little improvement, despite significant increases in drilling. The net result has been increased pressure bring in offshore supplies, which are available at prices below 50 cents/million Btu. Supplies of natural gas are plentiful offshore. In fact, Nigeria currently flares more natural gas than the United States consumes.

Table 1. US Domestic natural gas production (bcf, as of July 2004)

Year to date July	Marketed	Extracted	Dry Gas
2002	11,674	561	11,113
2003	11,700 (E)	562 (E)	11,138
2004	11,589 (E)	557 (E)	11,032 (E)

The current US LNG receiving capacity is limited to four receiving terminals, although this is changing as a large number of new terminals proposed through the end of this decade. The Lake Charles facility, the largest in the US, is near full capacity and undergoing expansion. The Cove Point terminal in Maryland was recently reactivated; the terminal near Elba Island is also under expansion; and the Massachusetts terminal is still used, although there is reluctance to expands its use because of the proximity to large urban centers and national security concerns. In addition, there are approximately 200 LNG storage facilities scattered throughout the United States. Serving as peak-shaving facilities, these facilities take domestic pipeline natural gas, liquefy it, reintroducing the gas to the system as needed.

Fuel and Energy Issues Most of the worlds electricity production is thermally generated using the combustion process. In the US, approximately half of all electricity is produced by this method, with coal as the primary fuel source. But in the last fifteen years, there has been a significant expansion in the power sector, with most of the increase in generation based on natural gas fired systems. Coincidental with the expansion of natural gas as a primary fuel for power generation has been a significant push to reduce emissions. This led to the widespread implementation of premixed combustion, or DLN (for Dry Low NOx) as an important instrument to reduce the most significant pollutant associated with natural gas combustion—NO_x.

LNG Value Chain. To meet natural gas demand, four LNG receiving terminals were in operation in the US, although some were under-utilized until recently. LNG is part of a transport system and a filtering mechanism. Only gases that remain a liquid at –259F are extracted in the process, so in this sense it is somewhat like a filtering process. By concentrating the fuel as a liquid, the energy density of cryogenic fluid is significantly greater, although shipping the fuel is much more expensive because of containment requirements. LNG, as proposed from offshore sources, encompasses three primary

Figure 1. US Generation Supply Mix.

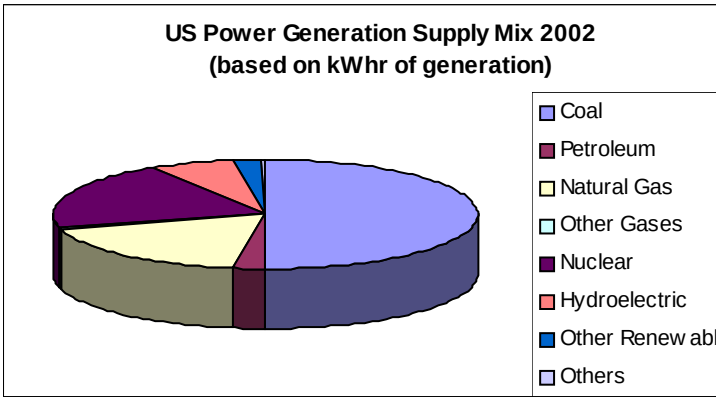

elements

- The collection and liquefaction of natural gas as a cryogenic liquid at the source
- Transportation of the cryogenic liquid.
- Offloading, and regasification of the LNG

Once the fuel is regassed, it can then be transferred to a pipeline or distributor. However, as described later, the fuel must meet the requirements of the tariff that governs several key fuel properties. The tariff in turn should be compatible with the equipment interconnected to the gas supply grid

Definition of Natural Gas. The term "natural gas" can have different meanings, depending upon whether one is a producer, supplier, shipper, or user. It has routinely been assumed to be primarily methane, with trace amounts of ethane, propane, and butane, and possibly some minor inert content. Usually, the condensed fractions of natural gas, components heavier than hexane, are extracted for other industrial-commercial uses, and not permitted into the gas pipeline. One of the difficult challenges that lies ahead is the bringing a common technical standard for the fuel.

The US EPA's definition for natural gas, is worth restating here. The definition of "natural gas" in § 72.2 of the May 26, 1999 revisions to 40 CFR Parts 72 and 75 states that in order for a gaseous fuel to qualify as natural gas, the fuel must either be > 70% methane by volume or must have a gross calorific value (GCV) between 950 and 1100 Btu/scf. The definitions of "natural gas" and "pipeline natural gas" in § 72.2 also limit thehydrogen sulfide (H_2S) content of these fuels to <1.0 gr/100 scf (for natural gas) and < 0.3 gr/100 scf (for pipeline natural gas). Further, the "natural gas" definition specifies that H_2S must constitute more than 50% (by weight) of the total sulfur in the fuel, and the "pipeline natural gas" definition specifies that H_2S must constitute at least 50% (by weight) of the total sulfur in the fuel.

Natural gas transporters operate with a gas tariff, a contractually established limit on specific properties of the natural gas. To maximize market flexibility, tariffs are usually quite broad, specifying only a maximum heating value, Wobbe index, and possibly a maximum inert content. Examples of tariff requirements include

1. Maximum nitrogen content of 3 or 4%
2. Maximum HHV of 1050 Btu/scf
3. Minimum hydrocarbon dewpoint of 10-20 ºF

Currently there is no general, broad-based regulatory requirement for a national standard for natural gas at this time. This may change if international supplies of natural gas introduce gas properties (heating value, Wobbe Index) and constituents (ethane, propane, and butane) that can deviate substantially from US domestic supplies.

On the other hand, the term "LNG" not only helps define the quality of the gas but also describes a system of storage and transportation. For LNG produced from domestic supplies, the gas composition and heating value of the LNG differ little from the original pipeline gas. Thus the term LNG does not offer sufficient insight into the interchangeability of the gas, only that the gas has passed through a refrigeration phase. Also, LNG is generic name that implies the cryogenic separation of the four basic hydrocarbons—methane, ethane, propane, and butanes.

Discussion-Fuel

Natural gas comprises a mixture of hydrocarbons, water, and inorganic components such as carbon dioxide and nitrogen. Processing of the gas is done to remove water and carbon dioxide, and other trace impurities. However, the mixture is not nearly as complex as is found in oil, but it must be understood to be properly used with the end-user needs in mind.

Fuel Requirements. Gas turbines are highly fuel flexible systems, although the fuel specifications set by the manufacturers are among the most detailed of any combustion device. Gas fuel specifications are dependent on several key factors. The maximum firing temperature of the gas turbine, and combustor design—DLN or non-DLN—substantially influence the requirements needed in any fuel specification. Independent of the gas turbine design, the fuel specification should, 1) minimize high temperature corrosion, 2) reduce combustion generated emissions, and 3) guarantee safe and reliable operation of the unit.

Gas Turbine Fuel Specification. The gas turbine fuel specification defines the requirements for the gas turbine and any relevant gas turbine auxiliary components. These include minimum and maximum values for the primary components, and in the case of liquid fuels the maximum allowable trace metal components. Gas turbine fuel specifications were developed through a combination of past experience with different fuels, laboratory testing, and full scale engine testing. Standard development, however, is not limited to the equipment manufacturer. For example, the ASTM has defined standards for gas turbine fuel oil, D-2880 by ASTM [1], as well as the ISO. But for each unique project, the fuel specification would be the governing document for fuel quality acceptance compatible with the project requirements, requirements that would include performance and emissions.

Interchangeability and Specifications. Interchangeability is the capacity to substitute one fuel for another, with little or no impact on the operability of the equipment. Historically, that definition has not included emissions, although the assumption has been that all

Table 2. Properties of Components in LNG

Hydrocarbon	BP °F	FP°F	Auto-ignition°F	Adiabatic Flame°F	Present in LNG
Methane	-258.9	-296.5	1166	3407	Yes
Ethane	-128	-297.8	959	3443	Yes
Propane	-43.8	-305.7	842	3573	Yes
iso-Butane	10.9	-255	698	3644	Yes
n-Butane	31.1	-216.9	698	3644	Yes
Pentane	96.9	-201	500		No
CO_2	-109	-69.8	NA	NA	No
N_2	77 K		NA	NA	Yes

natural gases are equally interchangeable. For domestic natural gases, that assumption was relatively straightforward, the gas composition did not vary much since the source gas was usually unchanging. However, off-shore sources of natural gas exhibit substantial compositional differences from domestic natural gas. The acceptance criteria were those established years ago by researchers in both government and industry. Much of the empirical work, concerned with mine safety, was carried out by the US Bureau of Mines, a function that was taken over by the Department of Energy. The industry experience was documented by American Gas Association.

The parameters for interchangeability have substantially focused on the specific properties of the natural gas. It would be easier to determine the composition, and quality, of the natural gas than the dimensions and design of the hardware installed by each user.

The key interchangeability parameters widely used in the gas turbine industry are

1. Wobbe Index, or Gas Index
2. Heating Value
3. Limits to hydrocarbon constituents (ethane, propane, and butane content)
4. Limits on the inert content (typically 3 or 4 % of nitrogen, by volume)
5. Dewpoint

Other gas parameters have been identified for application to other industries, including appliances and reciprocating engines. These include

6. Methane number
7. Weaver Index
8. Dutton Index

For the purposes of this paper, these additional parameters will not be reviewed, since no gas turbine manufacturers have identified any specific role for these parameters in regulating fuel quality to meet their equipment specifications.

Wobbe Index. The Wobbe Index is perhaps the most widely used parameter for interchangeability, although it does not encompass all of the critical parameters of concern. It effectively captures the heat release through an orifice, at a given pressure drop across that orifice. Two fuels of different composition, theoretically, could be interchanged, and the burner should function within its design parameters, if both fuels have the same Wobbe Index. This statement is accurate for fully diffusion flames, and gas jets where air in inducted with the fuel, such as the Bunsen-type burner. It has not been demonstrated completely that the Wobbe Index, for a fully premixed burner, can provide the same information. However, the widespread use of the Wobbe Index in nearly every burner application emphasizes the need to continue to use the Wobbe Index, or some relevant variation of the index, to qualify fuel interchangeability.

Heating Value. Another parameter often specified is the heating value of the fuel. The gas turbine fuel specification is typically stated in terms of lower hearing value (LHV), while the parameter most often specified by suppliers and in the Rate Tariff is the heating value on a higher heating value basis. The confusion between the two parameters has led to some misunderstanding regarding the acceptability of a specific gas. Typically the HHV is about 9% greater than the LHV.

But the Heating value parameter is not completely independent of the Wobbe Index, since the heating value parameter is already given as the numerator in the Wobbe Index calculation. However, both the heating value and Wobbe Index may be required as a minimum to determine suitable gas substitutions. For example, when comparing the applicability of a synthesis gas (which may have a heating value of only 300 Btu/scf) with a natural gas or a mixture of propane and air (which would be substantially higher and is often used to supplement the gas transmission grid during peak demand).

Hydrocarbon Content and Dewpoint. The higher hydrocarbon content is usually described as the C2+ (ethane and higher) or C3+ (propane and higher hydrocarbons). Siemens Westinghouse specifically defines the limits for the propane content, and defines the higher hydrocarbons for the C4+ components in the natural gas. But specifying these components is not totally independent of either the heating value or the Wobbe Index.

Liquids in a gas (or vapor) fuel system are highly undesirable. Liquids can be removed by filtration, which is quite common in most of today's gas turbine installations. Liquids can also form in some cases where there is a rapid decrease in pressure, as might occur through expansion across a valve. Alternatively, liquids can form if two gases of extremely different temperatures are mixed. For example, if a low-pressure pipeline that is nominally 50°F (or greater, do you want to cite the ASME code) is injected with cold gas from a high pressure pipeline, the resultant Joule-Thomson cooling effect could produce condensation within the mixture. This is most likely a rare occurrence, but with significant quantities of LNG expected to be shipped, and distributed within the US, the possibility must be considered.

To prevent condensation, a minimum superheat temperature is stated in the fuel specification. This temperature, usually about 50°F, is selected to prevent condensation from forming, even if there is a step-down in pressure as the natural gas is delivered to the fuel nozzles.

Tariff Specification The tariff establishes the gas supply limits between the wholesale and the shipper (or between the retail level, the LDC, and the shipper). Typically a tariff might have limits for heating value (1050 Btu/scf as an upper limit is common), Wobbe Index, and possibly the maximum amount of nitrogen or oxygen in the fuel. The tariff has traditionally not specified the gas temperature, although that appears to be changing with the introduction of LNG. Tariff's may specify a required delivery temperature to avoid the formation of condensation when LNG sourced gas is blended with domestic gas. However, the tariff is not the same as the specification, but it should at least meet the requirements stated in the fuel specification.

The final gate in the process is the delivery of the fuel. The Local Distribution Company, or LDC, is a key player in the value chain. Their responsibility is to deliver the fuel to the customers, and a fuel that meets the previously agreed tariff. However, for a large industrial user, with an existing fuel specification, both the tariff and the fuel specification need to be compatible.

Discussion-Environmental

As already described, gas turbines are fuel flexible systems, with natural gas and No. 2 fuel oil being the two dominant fuels used in industrial/commercial/utility applications. Because of the higher flame temperature associated with fuel oil, NO_x emissions are virtually always greater than those from methane-rich natural gas. The pressure to reduce NO_x, which can increase the formation of ground-level ozone, led to expanded use of fuels that produce less NO_x, and fuel system designs that minimize NO_x emissions. This resulted in a substantial development program by all manufacturers to introduce premixed combustor designs that would eliminate the need for water or steam to lower flame temperature (for NO_x control).

Emissions. The DLN combustor design used in many gas turbines is part of the overall strategy to reduce emissions from stationary sources and improve air quality. The pollutant of primary concern was NO_x, but the overall combustor design is optimized to

Figure 2. Emissions Change with Wobbe Index.

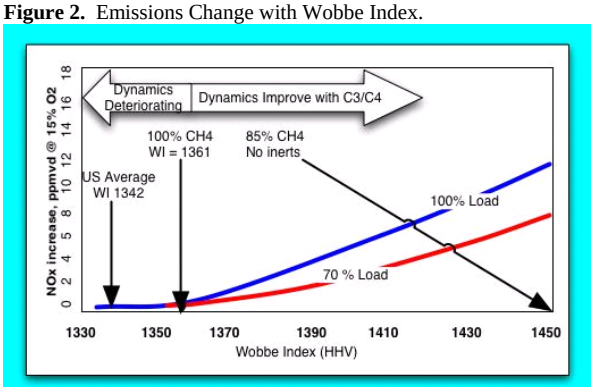

minimizing the other key emissions of CO, NO_x, and unburned hydrocarbons simultaneously. In this sense, some manufacturers describe the combustor as DLE, for Dry Low Emissions, although the term DLN is equally applicable to all premixed combustion designs.

NO_x emissions are generated by two principal pathways—thermal NO_x and Prompt NO_x. (The assumption here is made that natural gas is essentially free of fuel-bound nitrogen, and will not generate additional NO_x.) Kinetic models and flame temperature calculations show that as the C/H ratio increases, the adiabatic flame temperature increases, and the resulting NO_x is greater. This observation is readily evident in diffusion flame combustors. NO_x emissions from natural gas (C/H = 0.25, molar) are significantly lower than NO_x emissions from fuel oil (C/H= 0.52). Ethane, propane, butane, and higher hydrocarbons are intermediate between the two extremes (methane and distillate fuel oil). NO_x emissions from a diffusion combustor increase almost proportional to the C/H ratio.

Premixed, or DLN combustors operate at much lower combustion temperatures due to the premixing of air with the fuel. And much of the NO_x that produced is not thermal, but Prompt NO_x. However, similar trends still appear evident. Increasing the presence of higher hydrocarbons (which is tantamount to increasing the Wobbe Index) results in increased NO_x. Figure 2 shows the effect for one type of DLN combustor, operating pipeline natural gas, with higher hydrocarbons added to simulate the effect of operating on LNG.

Conclusions

Because of the potential influx for substantial quantities on non-domestic gas supplies, gas-fired equipment must be ready for a subtle, but important change to the fuel supply mixture. Simple diffusion combustor designs are very robust, and the only likely impact of introducing off-shore LNG is a change in emissions that should be relatively easy to predict from combustion computer models.

Advanced combustion technology devices that premix the fuel with the air prior to ignition may respond differently to the fuel supply changes. Predicting changes to premixed systems is more complicated and may require extensive testing and field evaluation of already installed system.

Current interchangeability parameters that are routinely used may not be sufficient to qualify whether fuel substitution can be accommodated by the end-user. Research into new fuel parameters, possibly based on molecular modeling, should be explored.

References

(1) ASTM International, 100 Barr Harbor Drive, PO Box C700, West Conshohocken, PA, 19428-2959 USA

INFLUENCE OF INORGANIC MATERIALS ON THE OXIDATIVE REACTIVITY OF TOBACCO CHARS

Xu Chen[1], W. Geoffrey Chan[2] and Mohammad R. Hajaligol[2]

[1]Philip Morris USA Postgraduate Research Program
4201 Commerce Road, Richmond, VA 23234
[2]Philip Morris USA Research Center
4201 Commerce Road, Richmond, VA 23234

Introduction

Knowledge of the intrinsic oxidation reactivity of tobacco char is important to understand and optimize the cigarette combustion process. The reactivity of carbonaceous materials in kinetic control conditions depends on the concentration of the active carbon sites, the catalytic active sites due to the inorganic materials, and the accessibility of these active sites [1]. Many alkali and alkaline earth elements have been demonstrated as catalysts in promoting the combustion reactivity of carbonaceous materials, including coal char [2], biomass char [3], cellulose char [4] and graphite [5]. After studying the oxidative reactivities of over 30 types of carbon materials, Lang et al [6] concluded that the catalytic effects of inorganic matter are significant in determining the oxidative reactivity, especially the nano-dispersed potassium (K), calcium (Ca) and magnesium (Mg). Removal of inorganic materials by acid wash and water wash considerably decreased the reactivities of lignite char [7] and straw char [3]. Like many other herbaceous materials, tobacco has relatively high inorganic matter. So it is important to understand the role of inorganic matter on the oxidative reactivity of tobacco chars.

Experimental

Two tobacco samples, a flue-cured lamina sample (labeled as sample A) and an air cured stem sample (labeled as sample B), were employed. The water washed and the acid washed samples were prepared in a flowing solvent reactor. A sample of 100 g of tobacco was put into a glass tube (25 inches in length and 2 inches in diameter) capped by two Teflon filters. Distilled water or 1M HCl flowed upward through the sample bed with a 70 ml/min flow rate for 5 hours. After acid washing, the samples were also washed with distilled water until most of the chloride was removed. The washed tobacco samples were dried in a vacuum oven overnight at 110 ^{o}C to remove the moisture. All of the tobacco samples were ground into powder (less than 0.5 mm size). Each of the samples was pyrolyzed in a benchtop tube furnace at 500 ^{o}C for 10 min holding time at the peak temperature in a stream of helium (1L/min).

The oxidation behavior of the tobacco chars was characterized by an isothermal thermogravimetric method in a Q-500 thermogravimetric analyzer (TA Instrument) with different oxygen concentrations balanced by helium in kinetic control conditions. Char samples were heated at 10 ^{o}C/min in a helium gas stream (90 mL/min) from ambient temperature to the desired temperature. After thermal equilibration for 30 min, the helium gas flow was replaced by the oxidative gas flowing at the same flow rate. The sample mass was limited to approximately 2 mg in order to minimize the impact of heat and mass transfer. After most of the combustible matter was consumed in the oxidation process, the temperature was increased to 550 ^{o}C to burn out the carbon content remaining in the char residue.

The N_2 BET surface areas of tobacco chars were determined using an Autosorb-1 volumetric gas adsorption apparatus (Quantachrome Corp), at -196 ^{o}C after degassing the sample at 150 ^{o}C for 3 hours.

Results and discussion

The ash and cation concentration analysis results of the untreated and the solvent washed tobacco samples are listed in Table 1. The dominant metallic elements were K, Ca and Mg. Sample B had higher K and Ca comparing to sample A. Water wash removed most of the potassium and some magnesium from tobaccos. The acid wash further removed most of the calcium and magnesium.

The surface areas of the tobacco chars are shown in Figure 1. The surface areas of the untreated tobacco chars were relatively low. High mineral content in tobacco samples may prevent pore formation and development in the pyrolysis process. After mineral removal by water or acid, the surface areas of tobacco chars increased significantly.

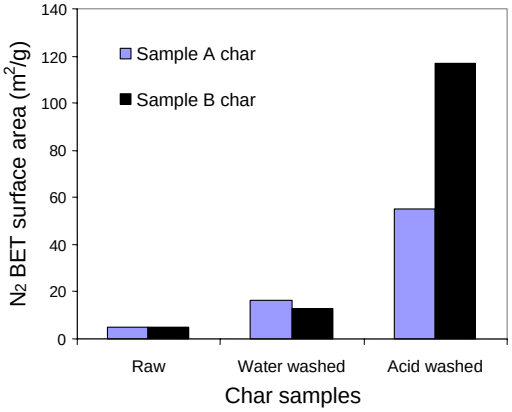

Figure 1. Surface area of raw and solvent washed tobacco chars.

The apparent combustion reactivity of char can be expressed by the following equation:

$$R = -\frac{1}{m}\frac{dm}{dt} = A\exp\left(-\frac{E_a}{RT}\right) \qquad (1)$$

where m is the mass of carbon remaining in the char at time t, A and E are the pre-exponential factor and the activation energy, respectively.

The reaction order of oxygen was determined by relating the intrinsic combustion rate R to the reactant gas partial pressure:

$$R = kP_{O_2}^{n} \qquad (2)$$

where P_{O_2} is the partial pressure of oxygen and k is a constant.

The intrinsic reactivities of sample A char measured at 623 K in 21% O_2 are shown in Figure 2. The reactivities of sample A char were nearly unchanged in the conversion from 0.05 up to 0.9. However, in the case of the solvent washed tobacco chars, the reactivities at the early stage of the reaction were very high, and then decreased sharply along with the conversion. In early conversion, the reactivities of water washed sample A char were higher than that of untreated sample char under the same condition. The global kinetic parameters of tobacco chars were calculated by using equation 1 at conversion from 0.1 to 0.8 and are summarized in Table 2. After water or acid wash, the activation energies of chars decreased significantly. However, the pre-exponential factors decreased as well. The intrinsic reactivities of sample A chars, shown in Figure 3, were calculated based on the

Table 1. Ash content and cation concentrations in tobacco samples measured by ICP-MS.

	Ash (wt%)	K (ppmw)	Ca (ppmw)	Mg (ppmw)	Na (ppmw)	Al (ppmw)	Fe (ppmw)
Sample A	12.57	28200	18500	6400	307	380	273
Sample B	17.83	73100	29900	8800	69	<33	58
Sample A water washed	4.84	150	20700	2500	37	160	305
Sample A acid washed	2.01	200	1000	150	<33	180	245
Sample B water washed	6.41	800	35900	5300	<33	<33	83
Sample B acid washed	0.53	200	1600	100	60	<33	75

kinetic parameters listed in Table 2. The effect of mineral removal on the intrinsic char reactivity became more apparent when the temperature was higher than 500 ^{o}C. The reactivities of the water washed and the acid washed sample A chars were quite similar from 400 ^{o}C up to 700 ^{o}C. It is noteworthy that although most of the potassium was removed by water wash, considerable amount of the calcium and some magnesium still remained in the tobacco residue. But these water insoluble cations did not appear to play an important role in the intrinsic reactivity. The reactivities of sample B char, which was not shown here, were higher than that of the sample A char due to the high mineral content, especially potassium. The reactivities of the washed sample B chars were similar as these of treated sample A chars. The correlation of char surface area and the reactivity is relatively poor. The acid washed chars had the highest surface area but also had the lowest reactivity. Again, it revealed that the reactivity contributed by part of the cations with intrinsically catalytic effect plays the most important role in the intrinsic reactivity of tobacco chars.

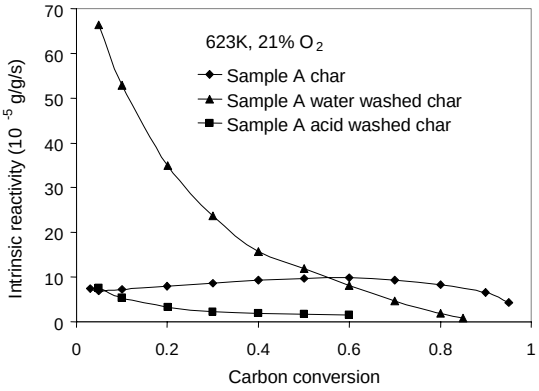

Figure 2. Intrinsic reactivities of raw and solvent washed sample A chars as a function of conversion at 623 K in 21% O_2.

Table 2. Kinetic parameters of tobacco chars in 21% O_2
*in 21% O_2 with 95% confidence interval

Sample	E_a (kJ/mol)	logA (s^{-1})
Sample A	199.1±2.5	12.64±0.22
Sample B	261.0±53.1	18.42±4.37
Sample A water washed	106.8±10.6	5.02±0.72
Sample A acid washed	149.4±19.5	7.77±1.40
Sample B water washed	134.2±18.0	7.13±1.14
Sample B acid washed	135.3±9.5	6.77±0.66

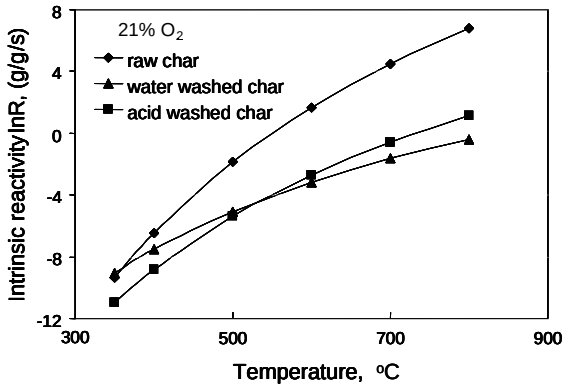

Figure 3. Intrinsic reactivities of sample A chars calculated using kinetic parameters listed in Table 2.

The reaction order of oxygen, shown in Figure 4, was characterized by monitoring the steady gasification rates of sample A char in a number of oxygen partial pressures and at carbon conversion from 0.1 to 0.8.

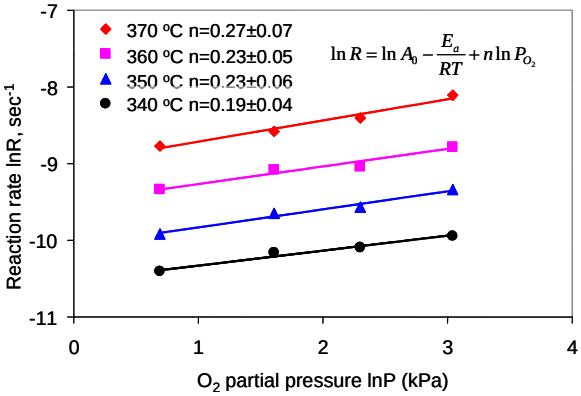

Figure 4. Oxygen reaction order in sample A char oxidation.

The reaction order lied in the range from 0.19 to 0.27. Most of the reaction orders reported in the literature for char oxidation below 900 K, as summarized by Hurt et al. [8], are in the range of 0.6 to 1. Similar low reaction order was reported by other researchers [9-10] in the study of the oxidation reactivity of graphite and brown coal char. Our preliminary experimental results showed that the oxygen reaction order of acid washed sample A char is close to 0.6. Again, the presence of inorganic materials may influence the reaction order. Additional work is required to explore a more quantitative explanation.

Conclusions

The influence of the inorganic materials to the intrinsic reactivity of tobacco chars was investigated. After removal mineral content from tobacco by water and acid wash, the reactivities of tobacco chars decreased considerably. The water soluble cations, especially potassium, were confirmed to play a key role in the intrinsic reactivity of tobacco char. The oxygen reaction order of the sample A char was from 0.19 to 0.27, which is below the reported value in the literature. The inorganic matter may also influence the reaction order.

Acknowledgement

The authors wish to thank Vicki Baliga, Bruce Waymack and Drs. Thomas McGrath, Stephen Haut and Jan Wooten (Philip Morris USA Research Center) for their technical assistance and discussions. We are also grateful to Drs. Adel Sarofim and Hong-Shig Shim (Reaction Engineering International), Professors Eric Suuberg and Robert Hurt (Brown University) for their helpful suggestions.

References

(1) Hippo, E. J., Jenkins, R. G. and Walker, P. L. Jr., Fuel, **1979**, 58, 338.
(2) Mccollor, D. P., Jones, M. L., Benson, S. A. and Young, B. C., Proc. Combust. Inst., **1979**, 22, 59.
(3) Zolin A., Jensen, A. Jensen, P. A., Frandsen, F. and Dam-Johansen, K. Energy Fuels, **2001**, 15, 1110.
(4) Ganga Devi, T. and Kannan, M. P., Fuel, **1998**, 77, 1825.
(5) Harker, H., Horsley J. B. and Robson D. J of Nucl. Mater. , **1970**, 37, 331.
(6) Lang, T. and Hurt, R. H. Proc. Combust. Inst., **2002**, 29, 423.
(7)Haykiri-Acma, H, Ersoy-Mericboyu, A. and Kucukbayrak, S. Thermo Acta, **2000**, 362, 131.
(8) Hurt, R. H. and Calo, J. M. Combust. Flame, **2001** 125, 1138.
(9) Tyler, R. J., Wouterlood, H. J. and Mulcahy, F.R. Carbon, **1976**, 14, 271.
(10) Smith, I. W. and Tyler, R. J. Combust. Flame, **1974**, 9, 87.

MOLECULAR MODELING OF THE EARLY STAGE OF CARBONIZATION OF PRIMARY HEAVY AROMATIC COMPOUNDS IN DECANT OIL AND ITS DERIVATIVES

G. Wang and S. Eser

Department of Energy and Geo Environmental Engineering
The Pennsylvania State University
University Park, PA 16802

Introduction

The carbonization of decant oil and its derivates, such as hydrotreated decant oil, coker charge, and a high-boiling fraction, produce significantly different needle coke textures [1]. The difference in the texture, in turn, reflects the difference in mesophase development- the formation of an intermediate liquid crystalline phase- controlled, to a large extent, by the reactions in the early stage of carbonization. Molecular compositional analysis of the decant oil and its derivatives has shown differences in the distribution of the alkylated PAHs in their constitution. Mesophase development results from thermally induced free radical polymerization and condensation reactions of alkylated PAHs. The formation and growth of mesogens into the carbonaceous mesophase are affected by the ease of free radical initiation and the subsequent free radical reactions that involve selective polymerization/ condensation at the reactive sites on the intermediate molecules.

Molecular modeling on carbonization of the three-ring aromatic isomers (phenanthrene and anthracene) have been studied earlier[2, 3]. These studies suggested that that the geometric configuration of oligomers (e.g., dimers and trimers) may explain the different degrees of mesophase development obtained from the carbonization of single aromatic compounds.

In this work, we selected phenanthrene, pyrene, chrysene benzopyrene and benzo[ghi]perylene as monomers to model the initial stage of free radical formation and polymerization using a semi-empirical software package to elucidate the important initial steps in liquid-phase carbonization of the industrial needle coke feedstocks.

Experimental

Experimental results from the compositional analysis and carbonization (mesophase development) of samples of a decant oil, hydrotreated decant oil, coker charge and vacuum bottom fraction were presented previously [4]. The modeling of the initial reactions of selected PAH was performed using a semi-empirical software program, CaChe MOPAC, Version 6.12. The minimum geometric configuration and frontier electron density of the starting PAH, related free radicals, and oligomers were calculated using the MNDOd method. MOPAC has been used by other researchers to calculate the electronic and thermodynamic properties PAH for predicting their pyrolysis behavior [5-7]. The practical advantage of MOPAC over the more rigorous *ab initio* MO calculations is the possibility of obtaining reasonably accurate results with much less computation time, particularly for the high- molecular-weight compounds found in decant oils and other coker feedtocks.

Results and Discussion

The calculated HOMO and LUMO energy of major PAHs in coker feedstocks are given in Table 1. Increasing the aromatic ring number (from 3 to 5) increases the HOMO energy, but decreases the LUMO energy. The difference between these two MOs, indicates, in general, the overall stability of the PAH molecules. Methyl group substitution on PAH makes these compounds less stable than their parent PAH. However, this effect appears to be less important than the difference in the aromatic ring configurations, as seen in the differences in the MO energies given in Table 1.

Table 1. HOMO and LUMO of PAH and their methyl substituted analogs

PAH	HOMO,eV	LUMO,eV	LUMO-HOMO,eV
Phenanthrene	-8.478	-0.481	7.997
Methyl-sub	-8.455 ~-8.483	-0.478~-0.528	7.931~8.005
Dimethyl-sub	-8.49~ -8.4636	-0.521~ -0.565	7.978~ 7.939
Trimethyl-sub	-8.419~ -8.443	-0.559~0.602	7.817~7.884
Tetramethyl-sub	-8.404~8.405	-0.632~ -0.639	7.765~7.772
Pyrene	-8.38	-0.902	7.478
Methyl-sub	-8.019~ -8.035	-0.896 ~ 0.944	7.075~ 7.148
Dimethyl-sub	-8.004 ~ 8.005	-0.967~-0.981	7.022 ~7.038
Trimethyl-sub	-7.987 ~-8.01	-0.965 ~-1.001	6.986 ~7.044
Chrysene	-8.26	0.719	8.979
Methyl-sub	-8.244 ~ 8.263	-0.729 ~-0.762	7.478 ~7.534
Dimethyl-sub	--8.218~ -8.24	-0.761~-0.790	7.434~ 7.479
Benzo[e]pyrene	-8.108	-0.889	7.219
Methyl-sub	-8.039 ~ -8.111	-0.883 ~-0.923	7.116~7.228
Dimethyl-sub	-8.076~ -8.083	-0.946 ~-0.954	7.119~7.137
Benz[ghi]perylene	-7.94	-1.071	6.869
Methyl-sub	-7.903 ~-7.940	-1.078 ~-1.106	6.797~6.862
Dimethyl-sub	-7.93 ~-7.940	-1.087~ -1.114	6.816~6.858
Trimethyl-sub	-7.919 ~-7.936	-1.122~ -1.247	6.672~ 6.814

Thermal homolysis of a weak C-C or C-H bond is the most common means of free radical initiation in the condensed phase carbonization. The kinetics of early reactions should relate closely to the ease of free radical formation, or the stability of the free radical formed. Bond dissociation energy (BDE) can serve as an indicator of such initiation. The MOPAC results for five PAHs and their methyl substituted analogs are listed in Table 2. The BDE was determined by the enthalpy change in a homolysis reaction. The enthalpy of H and CH_3 radicals were taken from the experimental data (i.e, 52.10, 34.82 kcal/mol, respectively). No experimental data was available for 4+ring aromatic radicals, and the MNDOd results would have errors, but the errors tend to be systematic as the other researchers reported[8]. In addition, since the BDE is calculated from the differences in the product and reactant properties, the error would be compensated. All the MOPAC data reported here are for standard state.

For unsubstited parent PAH, the initiation of free radical comes from various mechanisms such as molecular disproportionation, and hydrogen abstraction. But in the liquid phase carbonization of mostly alkylated PAH mixtures, the most probable means of initiation would be a side chain cleavage on the aromatic ring system. The energy of such a bond breaking on sub-PAH is about 10 to 15kcal/mol less than on unsubstituted PAHs. The effect of multi-methylation seems to be less important (as seen from the phenanthrene data in Table 2 and numbering notation is shown in Figure 1). However, the position of free radical formation depends on the configuration of PAH molecules. The 9-phenanthryl, 4-pyrenyl, 6-chrysenyl, 4-benzo(e)pyrenyl and 4-benzo[ghi]perylenyl are found to be the most stable or the easiest to form radicals in C1 to C3 methylated PAHs. Although the formation of 1- or 9-benzo(e)pyrenyl and 7-benzo[ghi]perylenyl shows significantly lower BDE from methyl substitutes, the formation of these free radicals would be less likely

to take place because of the steric hindrance of methyl groups in the bay area.

The local differences of the sites in PAH can be further examined using Frontier radical density results from MOPAC. An example of the six-member ring benzo[ghi]perylene is shown in Figure 4.

Table 2. MNDOd BDEs at various aromatic-ring sites

Radical position at Ar	-H from Ar	-CH_3 from MAr	-CH_3 from DMAr	-CH_3 from TMAr
1-aryl of Phen	108.2	93.4	93.4	93.3
2-aryl of Phen	109.8	99.5	99.5	98.8
3-aryl of Phen	109.3	98.7	98.7	98.8
9-aryl of Phen	106.8	94.1	94.1	93.4
1-aryl of Py	107.8	94.5	94.5	
2-aryl of Py	108.4	98.6	98.5	
4-aryl of Py	107.0	94.5	93.1	
1-aryl of Chr	107.5	93.6		
2-aryl of Chr	109.1	99.6		
3-aryl of Chr	108.4	98.7		
6-aryl of Chr	107.0	94.0		
1-aryl of BeP	104.4	76.7		
2-aryl of BeP	108.5	98.6		
3-aryl of BeP	108.0	94.2		
4-aryl of BeP	107.1	92.9		
9-aryl of BeP	104.1	76.1		
10-aryl of BeP	109.0	99.3		
1-aryl of BPer	107.5	93.6		
3-aryl of BPer	107.4	94.8		
4-aryl of BPer	107.1	93.1		
5-aryl of BPer	108.0	95.5		
6-aryl of BPer	108.4	98.6		
7-aryl of BPer	104.9	82.9		

A comparison of the radical frontier density with the BDE of benzo[ghi]perylene shows a good agreement. The most reactive sites are found in the 7, 5 and 4 positions. The discrepancy on 1,and 5 on the latter may be due to the fact that density map is obtained for the radical addition reaction only.

The PAH isomer distribution in a decant oil and a coker feed (which consists of thermally cracked product of decant oil) sample is shown in Table 3. A qualitative distribution of higher PAH in these two feedstocks is shown in Figure 2. The increased propoportion of thermally stable alkylated PAHs in the coker feed (CF) sample agreed with the PAH's stability results calculated from MOPAC.

Previous research on the PAH pyrolysis suggests that the kinetics of chemical reactions is controlled not only by the free radical initiation, but also by the steric configurations of the radicals and the stable molecules. The latter factor may be crucial for producing a well-developed mesophase.

Based on the calculation of reactive sites in PAH molecules, a condensation reaction for benzo[ghi]perylene is proposed in Figure 3. Initially, a bimolecular coupling of the two free radicals links the two PAH molecules the most reactive sites. Either a six- or a five-member ring will form by further linking of the reactive carbon sites on each molecule. The formation of a six-member ring should be more favorable.

Conclusions

A semi-empirical MOPAC software can be used provide information on the thermal stability of PAH that are found in decant oils and their derivatives. MOPAC can also be used to predict possible reactions for free radical initiation and subsequent reactions of the nascent free radicals to produce mesogens that lead to the mesophase formation. This information may help understanding the relationships between the kinetics of initial polymerization/ condensation reactions and the mesophase development in liquid phase carbonization. The high proportion of stable PAHs in the coker feed, for example, can explain the lower carbonization reactivity of this stream compared to that of the parent decant oil, and, thus, a higher degree of mesophase development obtained from the carbonization of the coker feed.

Acknowledgement

We thank for the financial support from the Energy Institute at The Pennsylvania State University, and for helpful discussions with Dr. X. Ma of the Energy Institute on molecular computations. We are grateful for many helpful discussions with Robert Miller and John Bassett form Chicago Carbon Company, Lemont, IL.

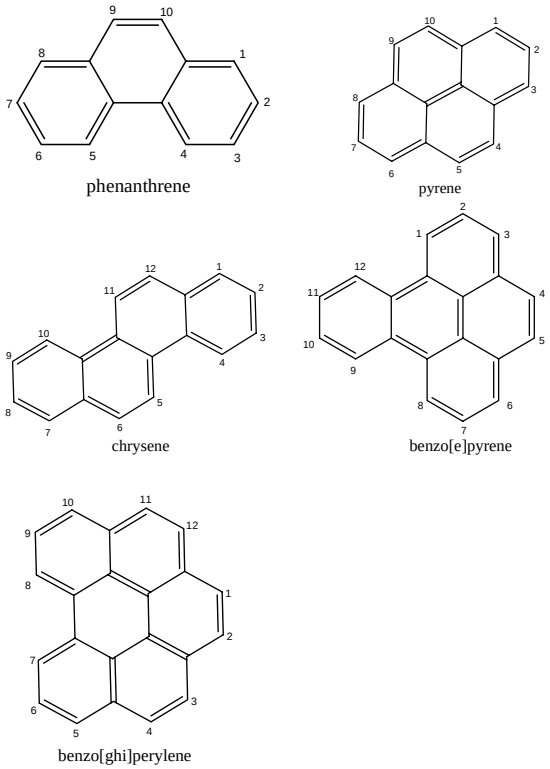

Figure 1. Structures of PAH present in decant oils and the numbering of the carbon atoms in these molecules.

Table 3. PAH isomer distribution in decant oil and coker feed

	DO	CF
3-MPHEN	31%	39%
2-MPHEN	35%	47%
9-MPHEN	19%	7%
1-MPHNE	15%	7%
2-MPY	40.2%	69.3%
4-MPY	29.5%	17.6%
1-MPY	30.3%	13.2%
3-MCHRY	44%	63%
2-MCHRY	22%	22%
6-MCHRY	10%	3%
5-MCHRY	11%	8%
4-MCHRY	10%	3%
1-MCHRY	3%	0%

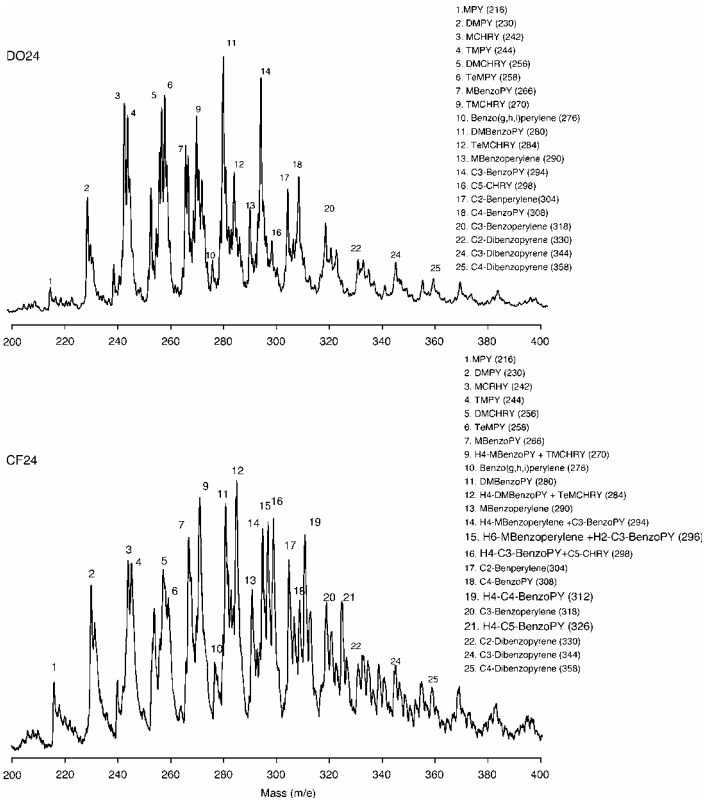

Figure 2. LD/MS chromatograph showing higher PAHs in decant oil (DO) and coker charge (CF).

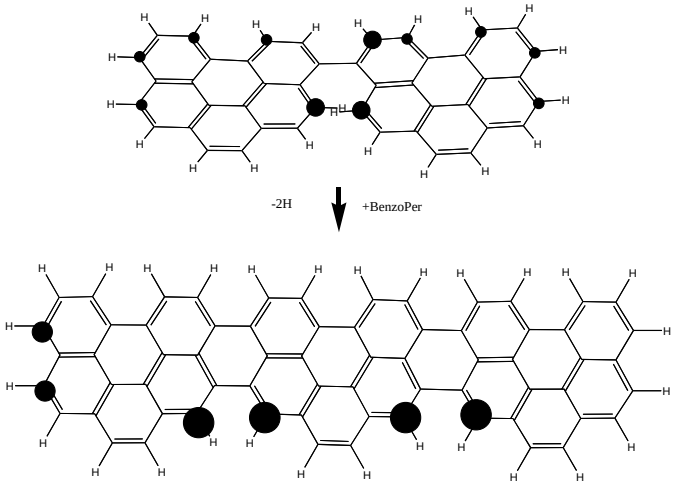

Figure 3. Polymerization and condensation of benzoperylene to produce mesogens and coke.

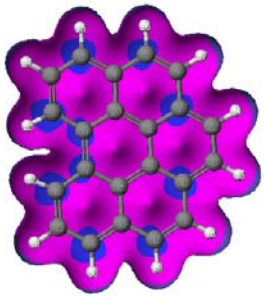

Figure 4. Fontier radical densities on benzo(ghi)perylene.

References

(1) Eser, S.; Wang, G.; Clemons, J., In *Heavy Hydrocarbon Resources*, *ACS Symposium Series 895*, Edited by Nomura, M.; Rahimi, P.; Koseoglu, O., **2004**; 95.

(2) Sasaki, T.; Jenkins, R. G.; Eser, S.; Schobert, H. H., *Energy & Fuels* **1993,** 7, 1039.

(3) Sasaki, T.; Jenkins, R. G.; Eser, S.; Schobert, H. H., *Energy & Fuels* **1993,** 7, 1047.

(4) Eser, S.; Wang, G. *Prepr. Pap.-Am. Chem. Soc., Div. Fuel Chem.* **2004**, *49 (1)*, 15.

(5) Chen, R.; Kafafi, S.; Stein, S. E., *Journal of the American Chemical Society* **1989,** 111, (4), 1418-1423.

(6) Poutsma, M. L., *Journal of Analytical and Applied Pyrolysis* **2000,** 54, (1-2), 5-35.

(7) Camaioni, D.; Autrey, S. T.; Salinas, T. B.; Franz, J., *Journal of the American Chemical Society* **1996,** 118, (8), 2013-2022.

(8) Ma, X.; Schobert, H. H., *Industrial & Engineering Chemistry Research* **2001,** 40, 743-750.

THE EFFECT OF REACTION TEMPERATURE AND FUEL TREATMENT ON DEPOSIT FORMATION OF JET FUELS

Ömer Gül, Leslie R. Rudnick. Harold H. Schobert*

The Energy Institute,
C205 Coal Utilization Laboratory
The Pennsylvania State University,
University Park, Pennsylvania 16802

Introduction

Future high-speed aircraft will be challenged to meet their onboard cooling requirements, because of weight limitations and higher heating loads. Therefore, the fuel will be required to serve as both propellant and coolant, and, thus, the fuel will need to be thermally stable. Thermal stability of aviation jet fuel refers to its resistance to decomposition at elevated temperatures to form deleterious solid deposits. The carbonaceous deposit formation appears to depend on a combination of different conditions, such as the temperature, the pressure, the concentration, the reactivity of starting fuel, and the nature of the substrate surface.

Temperature is one of the most important parameters that affect the rate and reaction mechanisms of fuel degradation. Three regimes for deposit formation have been defined (1,2) and are widely accepted. From their early work on n-dodecane stressing using a flow apparatus, Hazlett et al. (1,2) attributed fuel degradation and solid formation to different reactions in three temperature regimes: autoxidation at <260 °C, decomposition of oxygenated products at intermediate temperatures between 290 and 480 °C, and pyrolysis at ≥480 °C. It is widely considered that both autoxidation and pyrolysis of fuels are free-radical reactions, but the latter becomes important only at substantially higher temperatures as compared to the former. Pyrolysis regime is characterized principally by cracking reactions that form solid carbonaceous deposits. In addition, the metal surfaces can catalyze these types of reactions, which leads to faster deposit growth. Various metallic alloy candidates were examined to observe their catalytic activity in carbon deposit formation from jet fuel decomposition and found that Inconel X and Inconel 718 collected significantly less amount of deposit at 500 and 600°C during jet fuel stressing experiments (3,4). Naphthene-rich coal-based jet fuels have been shown to be more thermally stable than their petroleum derived counterparts (5).

The composition of jet fuels is very complex. Many studies have been carried out with light hydrocarbons (6-10) and with real coal-based jet fuel (11-13) candidates to understand the mechanism of carbon formation on metals or to understand the relationship between chemical composition and carbon deposit.

This study examines the thermal stability of saturated light cycle oil, saturated refined chemical oil, a 1:1 (vol %) blend of sat-RCO/LCO, and JP-8. Unfiltered and filtered fuel samples were stressed in a flow reactor, on Inconel 718 metal surface at three different temperatures to assess the amount of carbon deposit. Subsequent work will discuss the effect of factors such as the presence of trace impurity sulfur, nitrogen, and dissolved oxygen on deposit formation.

Experimental

Materials. The fuels tested were saturated light cycle oil (Sat-LCO)(EI-004), saturated refined chemical oil (Sat-RCO)(EI-006), 1:1 (vol %) Sat-LCO/RCO (EI-005), and JP-8. Jet fuels used were obtained from PARC. Fuels were evaluated either as received or first filtered on Al_2O_3 then thermally stressed. Aluminum oxide was obtained from Aldrich: activated, acidic, standard grade, 150 mesh, 155 m^2/g surface area. The alumina was activated for 1 hour at 100°C prior to use.

Inconel 718 was obtained from Goodfellow Metals Ltd (Cambridge, U.K.). The nominal composition of Inconel 718 alloy has been reported (11). Strips were cut and rinsed in acetone prior to use.

Thermal Stressing Experiments. Thermal stressing of fuels was carried out at three different fuel outlet temperatures; 470, 480, and 490 °C, and 250 psig (17 atm) in the presence of Inconel 718. The alloy foil was placed in the 26.5 cm and 0.635 cm OD glass lined stainless steel tube reactor. The flow system was initially purged with argon prior to fuel introduction to remove any air. However, it should be noted that O_2 was present as dissolved air in the fuel fed to the reactor. The fuel was pumped with a high-pressure liquid chromatography pump. The fuel was fed through the reactor over the Inconel for 5 hr at 4 ml/min. The unfiltered and filtered mixtures of 1:1 RCO/LCO were also pumped for 4 hour, then held in the reactor, at temperature for 1 hour. Fuels were preheated to 200°C before being fed to the reactor. Throughout the experiments, the reactor outlet temperature, wall temperature, fuel pressure, and liquid fuel flow rate were monitored. The stainless steel preheating section was 2 mm i.d. (0.3175 cm o.d.) and 61 cm in length. Fuel residence time in the preheating zone was 22 sec. at a liquid fuel flow rate of 4 mL/min. The fuel residence time in the reactor (4 mm. i.d., 0.635 cm. o.d. and 31.75 cm length) was 59 sec. at the same fuel flow rate. At the end of the reaction period (5 h.), the foils were cooled under an argon flow in the reactor. To verify the reproducibility of the experimental results, duplicate experiments were performed. The results of duplicate experiments showed that the TPO profiles were reproducible with respect to individual peak positions and relative peak intensities. The total amount of deposit measured for different jet fuel blends were reproducible to ±10% of the deposit mass. This flow reactor system has been reported (11**).**

Instrumental Analysis. Chemical composition of unfiltered and filtered jet fuels was determined using GC/MS. GC-MS analyses were temperature programmed from 35 (4min.) to 220 °C (10 min.) at a rate of 4 °C/min. The total amount of carbon deposit on Inconel strips was determined using a LECO RC-412 Multiphase Carbon Analyzer. Conventionally, the LECO RC-412 instrument has been used to measure the amount of deposition on metal surfaces (14,15). In the carbon analyzer, carbon in the deposit was oxidized to carbon dioxide by reaction with ultra high purity (UHP) O_2 in a furnace and over a CuO catalyst bed. The product CO_2 was quantitatively measured by a calibrated IR detector as a function of temperature in the furnace. The metal coupon was heated at a rate of 30°C/min in flowing O_2 (750 mL/min) to a maximum temperature of 900°C with a hold period of 6 min at the final temperature. In this study, only the deposits collected on the metal strips were measured.

An ANTEK total sulfur and nitrogen analyzer was used to determine the sulfur and nitrogen content of unfiltered and filtered fuels.

Results and Discussion

This study examines the thermal stability behavior and carbon deposit of thermally stressed jet fuel candidates as a function of fuel treatment and of reaction temperatures. These fuels are saturated-LCO (EI-004), saturated-RCO (EI-006), and a blend of saturated (1:1 vol) RCO/LCO. JP-8 was also used and studied as a conventional jet fuel.

The chemical composition, total sulfur, total nitrogen, the temperature and the filtration effect were correlated in terms of carbon deposit. Four different fuels were tested including the JP-8, and carbon deposit was determined for both filtered and unfiltered samples at three temperatures. Carbon deposits for the unfiltered and the filtered samples at each temperature is given in Table 1 in micrograms of carbon deposit per square centimeter of foil.

Table 1 shows that the range of carbon deposits for the unfiltered fuels were greater than for the filtered fuels. While the unfiltered-JP-8 gave the lowest carbon deposit regardless of the temperature, filtered Sat-RCO gave the lowest carbon deposit of the filtered samples.

Unfiltered saturated RCO and LCO each gave increasing carbon deposit with the increasing outlet temperature, but the blend produced more deposit at the intermediate temperature. Carbon deposits for JP-8 only increased slightly over the temperature range studied.

Filtration of fuels over Al_2O_3 showed a positive effect on reducing carbon deposit formation. All filtered fuels produced lower carbon deposit than unfiltered fuels. One can conclude that precursors or initiators of carbonaceous materials were removed by filtration, and, thus, lower carbon deposits were obtained.

Filtered sat-LCO and the blend each gave lower deposits when the outlet temperature was 490°C, whereas sat-RCO and JP-8 gave lower deposit when the outlet temperatures were 470 and 480°C.

In this work it was observed that filtered-jet fuels gave much more lower carbon deposits for all of the tested conditions. To further test the filtration effect on the carbon deposit formation, two different experiments were designed. Unfiltered and filtered blend (EI-005) was fed for 4 hour and then the HPLC pump was shut down, the fuel in the system was held for 1 more hour at the desired outlet temperature in two separate experiments. For these two runs, unfiltered EI-005 gave two times the carbon deposit as a 5 hour continuous feed experiment, but filtered EI-005 gave almost the same amount of carbon deposit as the 5 hour continuous feed of filtered EI-005. These findings confirm the results regarding 5 hour continuous feed that showed reduced deposit formation when fuels were filtered. These findings imply that some carbon deposit precursors have been removed from the fuels by filtering.

Detailed fuel chemical composition and heteroatom concentration are shown in Tables 2 and 3, respectively. Chemical classes were grouped for semi-quantitative GC/MS analyses as non-cyclic hydrocarbons (NCH), non-aromatic cyclohydrocarbons (NACH), alkylbenzenes, indanes, naphthalenes, tetralins, cis-/trans-decalins, and alkyldecalins. Non-cyclic hydrocarbons include paraffins and non-cyclic olefins. Non-aromatic cyclohydrocarbons include saturated cyclics, and compounds with unsaturated side chain or unsaturation in the ring. Tetralins and polycyclic aromatic hydrocarbons were not observed in these fuel samples. Totally saturated three-ring structures were observed in these fuels, which is consistent with the severity of hydrotreatment for these samples. Alkylated versions of these materials were not observed. Three ring cyclic structures including tetradecahydro anthracene, tetradecahydro phenanthrene, dodecahyro fluorene, perhydro acenaphthene, dodecahydro acenaphthylene were calculated and included in the non-aromatic cyclohydrocarbon category.

JP-8 consisted of mainly paraffins, and small amount of saturated cyclics, alkylbenzenes and naphthalenes (16**).** Saturated LCO, saturated RCO, and a blend thereof consisted mainly of paraffins, saturated cyclics, decalins, and a small amount of indanes. No alkyl benzenes, naphthalenes, or tetralins were observed for these fuels.

Comparison of GC/MS data of unfiltered and filtered fuels shows that mostly alkyl-substituted compounds were removed from the fuel. Song et.al. (5) showed that the stability of saturated cyclics with alkyl side chains decreases with increase in chain length. It was also highlighted that the stability of cycloalkanes decreases with increase in ring size, namely cyclohexane > decalin > octahydrophenanthrene or octahydroanthracene. In our samples, no cyclohexane was found; all of the saturated cyclics were alkylated cyclohexanes.

Filtration totally removed the nitrogen containing compounds from the fuels, whereas sulfur-containing compounds were only partially removed. Much previous work on thermal and oxidation stability has shown that trace amounts of sulfur compounds and contaminants such as metals significantly enhance fuel degradation (17-20). Whereas thiols are known to undergo thermolysis reactions even at low temperatures, benzothiophenes or dibenzothiophenes resist thermolysis as high as 400°C. Thermal stressing results in these studies confirm that sulfur-types in JP-8 are stable otherwise higher carbon deposits would be expected.

Table 3 shows that oxygen compounds were removed when the fuels were filtered. Peroxides are well known to initiate free-radical reactions (1), in this work, no peroxides were detected by GC/MS. This is probably due to decomposition in the injection port of the GC/MS. The injection port temperature was in the range of decomposition zone of oxygenated compounds. Hazlett et.al. (1) reported that oxygen containing compounds increase radical formation and carbon deposit. They also explained that above 343°C oxygenated compounds begin the propagation of radical reactions that lead to carbonaceous material. Song et. al. (5) used Activity Super-I neutral alumina gel to get rid of any polar compounds such as antioxidants and metal compounds. Thermally stressed fuels after treatment resulted in lower carbon deposit.

Acknowledgements. The authors would like to thank the AFOSR for funding this work, Geoff Wilson of PARC Technical Services for preparing the fuels used in this work.

References

(1) Hazlett, R.N.; Hall, J.M.; Maston, M. Ind. Eng. Chem. Prod. Res. Dev. **1977**, 16(2), 171-177.
(2) Hazlett, R. N. Free Radical Reactions Related to Fuel Research. In *Frontiers of Free Radical Chemistry;* Pryor, W. A., Ed.; Academic Press: New York, **1980,** pp 195-223.
(3) Altin, O.; Eser, S. Ind. Eng. Chem. Res., **2000**, 39, 642-645.
(4) Altin, O.; Eser, S. Ind. Eng. Chem. Res., **2001**, 40, 589-595.
(5) Song, C.; Eser, S.; Schobert, H.H.; Hatcher, P.G. Energy Fuels **1993**, 7, 234-243
(6) Yu, J. ; Eser, S. ; Ind. Eng. Chem. Res. **1997**, 36, 585-591
(7) Trimm D.L. :Albright, L.F., Crynes, B.L., Corcoran, W.H., Eds.; Academic Press: New York, **1983** pp. 203.
(8) Baker, R.T.K.; Harris, P.S. : Walker P.L., Jr., Thrower, P.A., Eds.; Marcel Dekker Inc.: New York, **1978** pp. 83.
(9) Albright, L.F.; Tsai, C.-H.T. : Albright, L.F., Crynes, B.L., Corcoran, W.H., Eds.; Academic Press: New York, **1983** pp. 233.
(10) Froment, G.F. Rev. Chem. Eng. **1990**, 16(4), 293-328.
(11) Rudnick, L. R., Gül, Ö., Schobert, H. H. *Prepr. Pap.-Am. Chem. Soc., Div. Fuel Chem.* **2004**, 49(2), 770-772.
(12) Gül, Ö., Rudnick, L. R., Schobert, H. H., *Prepr. Pap.-Am. Chem. Soc., Div. Fuel Chem.* **2004**, 49(2), 773-775.
(13) Altin, O.; Rudnick, L.R. *Prepr. Pap.-Am. Chem. Soc., Div. Fuel Chem.* **2004**, 49 (1), 30-33.
(14) Edwards, T.; Zabarnick,S. Ind. Eng. Chem. Res. **1993**, 32, 3117-3122.
(15) Heneghan, S.P.; Martel, C.R.; Williams, T.F.; Ballal, D.R.

Trans. ASME J. Eng. Gas Turb. Power, **1993**, 115, 480-485.
(16) Lai, W.-C.; Song, C. Fuel **1995**, *74*, 1436-1451.
(17) CRC Literature Survey on the Thermal Oxidation Stability of Jet Fuel; CRC Report No. 509; Coordinating Research Council, Inc.: Atlanta, GA, **1979**; pp. 138.
(18) (a) Bol'shakov, G. F. The Physico-Chemical Principles of the Formation of Deposits in Jet Fuels, English Translation, Air Force Base, Ohio, **1974**. (b) Bath, B. D.; Fathoni, A. Z. Energy Fuels **1991**, 5, 2-21. (c) Fodor, G. E.; Naegeli, D. W.; Kohl, K. B. Energy Fuels **1988**, 2, 729-734
(19) Hazlett, R. N. Thermal Oxidation Stability of Auiation Turbine 1986,108,648-653. Fuels; ASTM Monograph 1, ASTM Philadelphia, **1991**; pp. 163.
(20) Heneghan, S. P.; Harrison, W. E. 111. Prepr. Pap.-Am. Chem. Soc., Div. Pet. Chem. **1992**, 37 (2), 404-411

Table 1. Carbon Deposits For Filtered And Unfiltered Jet Fuels For Different Temperatures

Outlet Temp. (°C)	Treatment	EI-004	EI-005	EI-006	JP-8
470	Unfiltered	23.27	104.10	37.83	10.52
480	Unfiltered	70.60	158.62	117.15	10.95
490	Unfiltered	74.80	85.13	234.62	11.99
470	Filtered	11.66	12.03	6.72	5.46
480	Filtered	18.97	21.46	0.45	2.95
490	Filtered	2.24	1.39	4.17	8.44
470 4hr+1hr hold	Unfiltered		216.88		
470 4hr+1hr hold	Filtered		13.05		

Table 2. Compositions Of Unfiltered And Filtered Fuels

Fuel Type	Treatment	Non-cyclic hydrocarbons	Non-aromatic Cyclohydrocarbon	Alkyl Benzenes	Indanes	Naphthalenes	Cis-/trans-Decalins	Alkyl Decalins
JP-8	Unfiltered	86.89	6.85	6.07	0.00	0.20	0.00	0.00
EI-004	Unfiltered	38.75	27.93	0.00	0.00	0.00	2.25	31.07
EI-005	Unfiltered	22.94	25.87	0.00	0.96	0.00	35.50	14.73
EI-006	Unfiltered	2.23	27.72	0.00	3.32	0.00	51.33	15.39
JP-8	Filtered	89.49	6.48	3.80	0.00	0.23	0.00	0.00
EI-004	Filtered	59.98	22.92	0.00	0.00	0.00	1.77	15.34
EI-005	Filtered	22.35	25.68	0.00	2.07	0.00	39.50	10.39
EI-006	Filtered	2.82	26.30	0.00	3.18	0.00	54.98	12.72

Percent distributions belong to the ratio of GC-MS peak areas

Table 3. Sulfur And Nitrogen Contents Of Unfiltered And Filtered Fuels

Fuel Type	Treatment	Sulfur[a]	Nitrogen[a]	Total Oxygenates,%[b]
JP-8	Unfiltered	616.32	2.16	8.51
EI-004	Unfiltered	1.67	0.16	24.60
EI-005	Unfiltered	1.16	0.23	14.93
EI-006	Unfiltered	1.05	0.33	3.11
JP-8	Filtered	443.37	0.00	8.34
EI-004	Filtered	1.04	0.00	24.31
EI-005	Filtered	1.02	0.00	9.91
EI-006	Filtered	1.03	0.00	1.68

[a]: ANTEK total sulfur and nitrogen analyzer, values in ppm
[b]: Semi-quantitative GC/MS analyses results

EFFECTS OF STRUCTURES ON PHOTOELECTROCHEMICAL PROPERTIES OF NOVEL CYANINE DYES WITH DIFFERENT METHINE CHAINS AS SENSITIZERS FOR NANOCRYSTALLINE SOLAR CELL

Xiuying Chen , Xiaojun Peng

State key laboratory of fine chemicals,
Dalian University of Technology,
Dalian 116012, PR China

Introduction

Increasing attention [1,2] has been focused on nanocrystalline TiO_2 electrode sensitized by organic photosensitized dye since Grätzel [3] utilized cis-Ru[4,4´-(LL)]$_2$(NCS)$_2$ (L=2,2´-bipyridyl-4,4´-dicarboxylate) to sensitized TiO_2 nanocrystalline and photoelectric transfer efficiency can be up to 10%. Compared to the ruthenium bipyridyl complex, organic dyes are easier to be synthesized and cost less. Recently, organic dye sensitized TiO_2 solar cells have made great progress, and the highest overall yield of solar cells sensitized by organic dyes has exceeded 6% [4,5]. To obtain high efficient photosensitizer for solar cells material, the investigation on new dyes with improved molecular structure is necessary. Cyanine dyes have intense and broad absorption band in the visible and near-infrared regions, excellent sensitizing properties in photography. However, few works have been done on their application as sensitizers for solar cells. Sayama studied merocyanines with different chain length (-$(CH_2)_n$-COOH) anchoring on TiO_2 surface via ester group and found that IPCE value of the TiO_2 electrode sensitized by various dyes increased with the decrease of the distance from dye chromophore to TiO_2 surface, which is very worthwhile to design a new sensitizer [6]. Simultaneously, they found that the increase of methine chain (-$(CH=CH)_m$-) of the dyes enhances the difficulty of the electron transfer from the excited dye to the conduction band of TiO_2 [7]. As organic sensitizers for nanocrystalline solar cell material, the high photostabilities of the dyes play a significant role in photoelectrochemical applications. Chen had synthesized the N-benzylindotricarbocyanine dyes and found that introduing of large benzyl group on nitrogen atom improved the photostability greatly [8]. In this article, we report the synthesis and photoelectric properties of novel cyanine dye (Cyb3) and squarylium dye (Sqb) with common 3*H*-indole-*N*-carboxylbenzyl groups anchoring on nano-TiO_2, and two different kinds of methine chains.

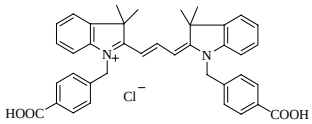

Cyb3

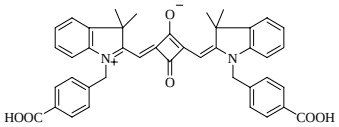

Sqb

Figure 1. Structures of Cyb3 and Sqb

Experiments

Materials and instruments. Oxide of indium and stannum were used as the photoanode electric fundus. (South Glass Science and Technology Holding Ltd., China). All other chemicals and solvents involved were analytical reagents of the highest available purity. Redistilled water was used for the solution. ^{1}H NMR spectra were recorded on a Varian INOVA 400M NMR spectrometer, and elemental analysis were performed on a PE 2400 Ⅱ elemental analyzer.

Synthesis. 2,3,3-Trimethyl-3*H*-indolenine (1) was synthesized according to the reference [9].

N-(4-Carboxyl)benzyl-2,3,3-trimethyl-3H-indolenine quaternary salt (2): 1.59g(10mmol) of 1 and 1.8g(10.1mmol) of p-chloromethyl benzoic acid were added into 25ml flask containing 10ml o-dichlorobenzene under N_2. After heating the mixture at 110°C for 12h, the precipitate was filtered and washed with acetone. 1.9g of rose pink powder was obtained with no further purification, and the crude yield was 58%.

Sqb: 0.658g (2mmol) indolenine quaternary salt (2) and 0.114g (1mmol) squaric acid were heated in butanol (9ml)/toluene (9ml) mixture solvents with 5ml pyridine as catalyst for 6h[10]. The resulting precipitate was filtered and recrystallized from acetic acid to give 0.271g of blue powder with 40% yield. Elemental analysis: calcd for $C_{42}H_{36}N_2O_6$ (%), C, 75.89; H, 5.46; N, 4.21; found, C, 75.81, H, 4.92, N, 3.95. ^{1}H NMR (400MHz, DMSO): δ=1.72(s, 12H, $C(CH_3)_2$),5.48(s, 4H, N-CH_2), 5.77(s, 2H,=CH), 7.18(t, 2H, Ar-H), 7.26(m, 4H, Ar-H), 7.31(d, 4H, Ar-H, J=8Hz), 7.55(d, 2H, Ar-H, J=7.6Hz), 7.93(d, 4H, Ar-H, J=8Hz).

Cyb3: 0.658g (2mmol) of 2 was added into 25ml flask containing 8ml pyridine under N_2. After refluxing for 10 min, 0.9ml (6mmol) trimethyl orthoformate was added by portions. The resulting precipitate was recrystallized from acetone to give 0.750g pink product with 60% yield. Elemental analysis: calcd for $C_{39}H_{37}ClN_2O_4$ (%), C, 73.98; H, 5.89; N, 4.42; found, C, 73.42, H, 5.23, N, 4.12. ^{1}H NMR (400MHz, DMSO): δ=1.73(s, 12H, $C(CH_3)_2$), 5.49(s, 4H, N-CH_2), 6.44(d, 2H, CH=CH, J=13Hz),7.29(m, 10H, Ar-H), 7.68(d, 2H, Ar-H, J=7.6Hz), 7.92(d, 4H, Ar-H, J=8Hz), 8.36(t, 1H, CH=CH, J=13Hz).

Preparation of nanoparticle colloid solution and nanocrystalline TiO_2 electrode. The preparation of TiO_2 nanoparticle colloid solution was prepared as described in reference [11]. A conductive glass of 2cm×2cm cleaned by redistilled water was coated by TiO_2 nanoparticle colloid uniformly, and then heated to 450°C for 30 min in the air, cooled down to room temperature (forming non-sensitized electrode) or to 80°C, immediately soaked in the methanol with concentration of 0.5mmolL^{-1} dye for 12h at room temperature, washed in ethanol, and finally dried in the air (forming sensitized electrode). The amount of adsorbed dye was determined by spectroscopic measurement of dye desorbed from the semiconductor surface in the dilute methanol solution of KOH. Film thickness was confirmed using a DEKTAK step apparatus.

Photoelectrochemical experiments. Photoelectrochemical measurements were made with a thin-layer solar cell comprising a nanocrystalline TiO_2 working electrode and a thin platinum layer sputtered on conducting glass as counter electrode. The redox electrolyte solution consisted of a mixture of LiI (0.3molL^{-1}), I_2 (0.03molL^{-1}) and PC (1,2-propanediol carbonate) as the solvent. The area of the semiconductor electrodes was 0.27×0.27cm^2. In photocurrent-photovoltage characteristics measurement, a 150W xenon lamp served as a light source. A high-intensity grating monochromator (DWA10, Optical instrument Factory, Beijing, China) was introduced into the path of the excitation beam to produce incident monochromatic light. Electrochemistry workstation (CHI650A, Chenhua instrument Company, Shanghai) was used to measure the working curve of the photoelectrode and white light as incident light. Light intensity meter (Model 550-1) was used and photocurrent reaction spectrum was corrected to normalization for light source spectrum. A three-electrode cell was composed of a platinum wire as working electrode, a platinum slice as counter electrode, and Ag/AgCl as reference electrode. The supporting electrolyte was $NaClO_4$ (0.1molL^{-1}).

Characterization of absorption spectra. JASCO V550 UV-Vis and PTI-700 spectrophotometer were used to measure the

absorption and emission spectra of the two dyes in methanol and sensitized electrode. References are methanol and indium stannum oxide conductive glass. All measurements were performed at room temperature.

Results and discussions

Synthesis and UV-Vis spectral properties of Sqb and Cyb3 in solution. Cyb3 and Sqb with different methine chains have been synthesized (**Scheme 1**). The dyes can anchor on nano-TiO_2 surface via N-carboxylbenzyl group.

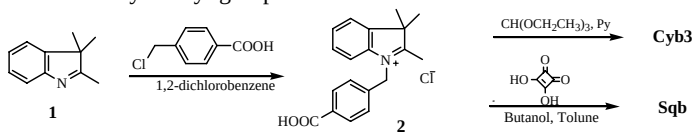

Scheme 1. Synthesis routes of Sqb and Cyb3

The absorption spectra of the two dyes in methanol are shown in **Figure 2**. The spectral properties are summarized in **Table 1**. The λ^{abs}_{max} are 554 and 632 nm in methanol respectively, with a little negative solvatochromism from methanol to chloroform as solvent. The λ^{em}_{max} of Cyb3 is 573 nm with Stockes shift ($\Delta\lambda$) 19nm in methanol. For Sqb, however, $\Delta\lambda$ is only 13 nm with λ^{em}_{max} 645nm in methanol. Compared to Cyb3, λ^{abs}_{max} of Sqb shifts to the longer wavelength by ca. 80nm with increasing length of the conjugated methine chain.

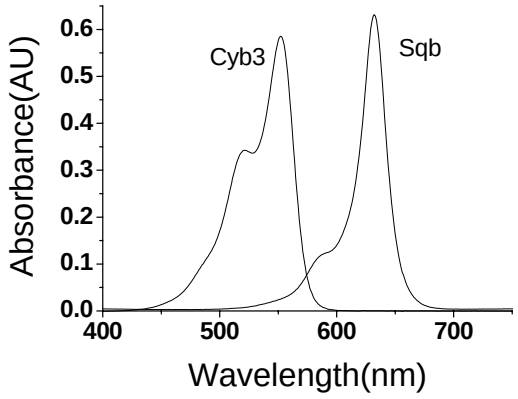

Figure 2. Absorption spectra of Cyb3 and Sqb in methanol

Table 1. Spectral properties of Cyb3 and Sqb in different solvents

Solvent	Cyb3			Sqb		
	λ^{abs}_{max} (nm)	λ^{em}_{max} (nm)	$\Delta\lambda$ (nm)	λ^{abs}_{max} (nm)	λ^{em}_{max} (nm)	$\Delta\lambda$ (nm)
Methanol	554	573	19	632	645	13
Ethanol	560	577	17	636	649	13
Acetonitrile	550	571	20	634	647	13
Chloroform	561	581	22	637	649	12

Energy level diagram. To judge the possibility of electron transfer from the excited dye molecules to the conductive band of TiO_2, cyclic voltammograms was performed to determine the redox potentials for the two dyes. Redox potentials of 0.37V (vs. SCE) or 0.61V(vs. NHE) or -5.45eV (vs. vacuum) and 0.32V(vs. SCE) or 0.58V(vs. NHE) or -5.42eV (vs. vacuum) averaging the related oxidation and reduction potentials are roughly regarded as the energy level of the ground state ($E^0(D^+/D)$) for Sqb and Cyb3 dye respectively. Considering the UV-Vis absorption spectra, the lowest energy of the excited state ($E^0(D^*/D^+)$) of the two dyes are about -3.62eV (vs. vacuum) and -3.26eV (vs. vacuum) (eq.1). Major absorption at 550-680nm and 450-570nm wavelengths corresponding to the energy difference between the ground state and the lowest excited state (Eg) of 1.83eV and 2.16eV for Sqb and Cyb3 respectively. **Fig.3** shows the energy level diagram of the two dyes in methanol. Obviously, the excited-state energy levels for the two dyes are more negative than the energy level of TiO_2 conductive band edge (-4.4eV, vs. vacuum) [1,12,13], suggesting that the electron injection should be possible thermodynamically. The driving force for charge displacement into the oxide is about 0.99eV and 1.35eV for Sqb and Cyb3 respectively. The redox potential of Sqb is less positive than the corresponding potential of Cyb3. The excited state of Sqb matches better the lower bound of the conduction band of the semiconductor than the LUMO of Cyb3, thus decreasing the energy loss during the electron transfer process.

$$E^0(D^*/D^+) = E^0(D^+/D) + Eg \qquad \text{(eq.1)}$$

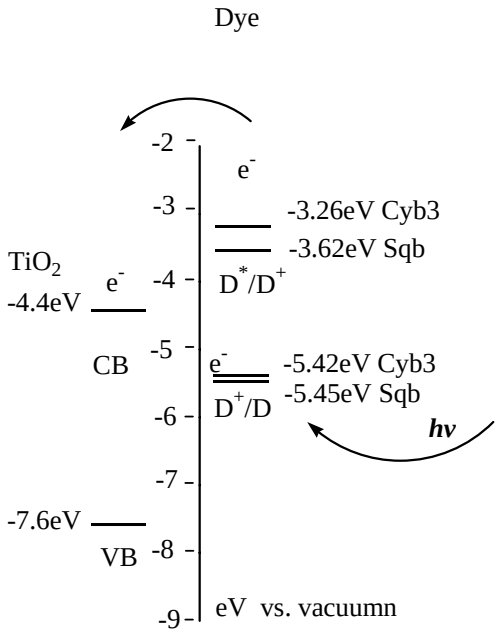

Figure 3. Energy level diagram for Cyb3 and Sqb

Absorption spectra of the two dyes on TiO_2 electrode. The absorption peaks of the two dyes on TiO_2 films are all extremely broadened (**Fig.4**), compared with their corresponding absorption peaks in methanol. It suggests that the dye molecules have formed H-aggregate or J-aggregate [14]. **Fig.5** is the proposed structure based on the geometry of the single crystal molecule (unpublished data). The dye moiety performs a plane due to the conjugated molecular structure and with the tilted large carboxylbenzyl group linked to the TiO_2 film surface via carboxylate form. To obtain the exact thickness of film and the optimal sensitized time, different sensitized conditions were investigated. 6.5μm thickness of film and sensitized time of 4h and 6h for Cyb3 and Sqb are obtained respectively.

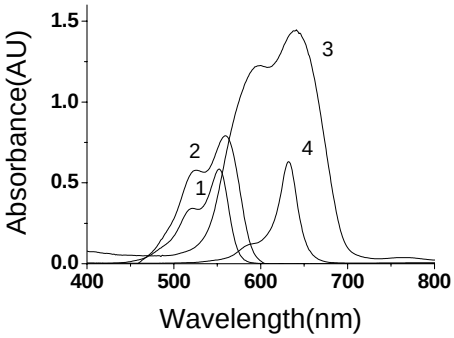

Figure 4. (1) absorption spectrum of Cyb3 in methanol, (2) absorption spectrum of TiO_2 electrode sensitized by Cyb3, (3) absorption spectrum of TiO_2 electrode sensitized by Sqb, and (4) absorption spectrum of Sqb in methanol. All electrodes were dried in air. Dyes were adsorbed in methanol solution (5×10^{-4}M). Total amount of the adsorbed dye was ca. 0.96×10^{-8}mol/cm^2 for Cyb3, 1.9×10^{-8}mol/cm^2 for Sqb respectively.

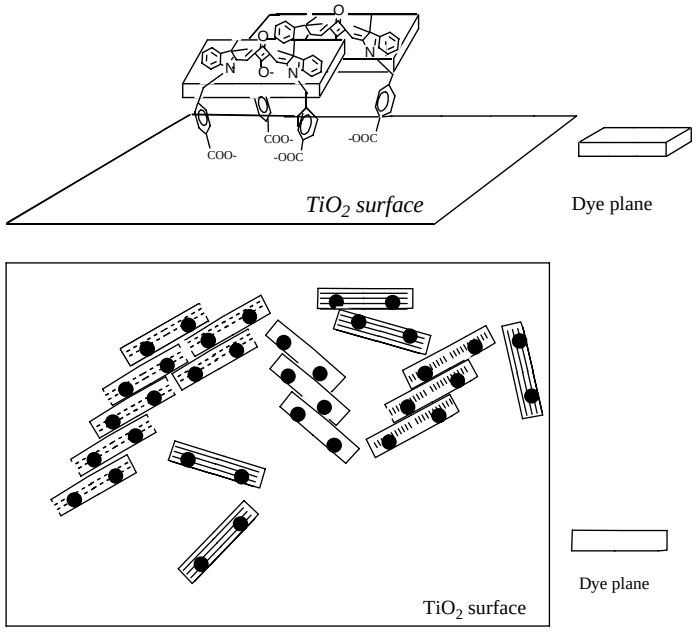

Figure 5. (a): Proposed structure of the aggregated dyes on TiO_2 surface (b): top view of the J-aggregated dyes on TiO_2 surface, closed circle is the carboxylbenzyl group anchoring on TiO_2 surface.

Photocurrent action spectra. Fig. 6 demonstrates the photocurrent action spectra of the dye-sensitized nanocrystalline TiO_2 electrodes normalized by incident light intensity for the two dyes. Sqb shows high light harvesting ability in the red visible region above 600nm, which indicates that Sqb can expand the photoresponse of large band gap semiconductor TiO_2 into the red visible region. Comparing the action spectra with the absorption spectra of TiO_2 electrode sensitized by the dyes (**Fig.4**), the two dyes have spectra selectivity for different regions of visible light. Cyb3 converts more efficiently the light in the shorter wavelength region, but Sqb does in the long wavelength region. The action spectra and the absorption spectra of the two dyes resemble well, which indicates that the photocurrent is generated by the injection of electrons from the excited molecules into the conduction band of the TiO_2 electrode. Cyb3 and Sqb convert visible light to photocurrent in the region from 400 to 600nm and 550 to 700nm. The maximum IPCE values for Cyb3 and Sqb are about 36% and 46% respectively. The latter is 1.3 times much higher than that of the former. Therefore, Sqb has higher electron injection efficiency than Cyb3 dye.

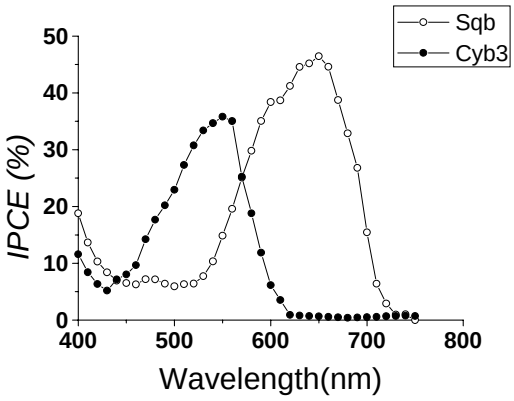

Figure 6 .Action spectra of the two dyes sensitized TiO_2 electrodes

IPCE is the monochromatic incident photon-to-current conversion efficiency, defined as the number of electrons injected by the excited dye in the external circuit decided by the number of incident photons, is observed from the short-circuit photocurrents recorded at various excited wavelengths by means of the following expression:

$$IPCE(\%)=I/P_{in}(1240/\lambda), \quad (2)$$

Where I is the short-circuit photocurrent ($\mu A/cm^2$), P_{in} is the incident light intensity ($\mu W/cm^2$) and λ is the excitation wavelength(nm).

Photocurrent-photovoltage characteristics curve and photoelectrochemical solar cells. The photocurrent and photovoltage curves are shown in **Fig.7**. The photoelectrochemical properties of dye sensitized TiO_2 electrode are given in **Table 2**.

Based on the characteristics curve, fill factor FF and the whole photo-electro transfer efficient η are obtained. FF is defined as

$$FF=P_{max}/(V_{oc}\cdot I_{sc}) \quad (3)$$

Where P_{max} is the largest output power of solar cells, I_{sc} is the short-circuit photocurrent, V_{oc} is the open-circuit photovoltage, η is defined as

$$\eta=(FF\cdot V_{oc}\cdot I_{sc})/P_{in} \quad (4)$$

Where P_{in} is the input power.

From **Table 2**, the I_{sc} (2.76mA/cm^2), IPCE (46%) and η (1.7%) of Sqb sensitized TiO_2 solar cell performs preferable IPCE values to Cyb3 sensitized one.

Several reasons were considered to lead to the different photoelectric properties of the two TiO_2 electrodes sensitized by Sqb and Cyb3. Firstly, as a sensitizer for solar cells material, it must possess the high photostability. In Sqb dye structure, Squarylium ring substituted the conjugated chain, which leads to the dye more stable under irradiation [15]. And spectrum range of Sqb shifts to the long wavelength region, which is favorable to absorb solar light. Moreover, the lowest excited energy level of Sqb dye matches well to that of TiO_2 nanoparticle conductive band gap (**Fig.3**). And the photoisomerization is one of the major decay pathways for methine dyes [16]. Sqb with methine chain substituted by squaric acid ring reduces cis-trans isomers. It is favorable to form ordered orientation on TiO_2 surface so as to increase the electron injection efficiency obviously.

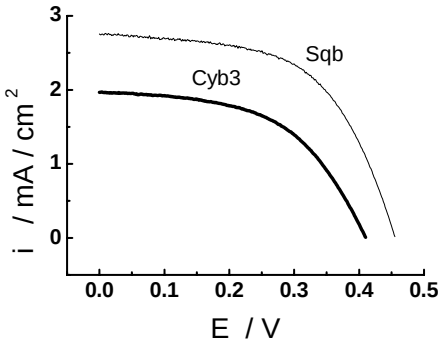

Figure 7. Photocurrent and photovoltage curves

Table 2. Parameters of the dye sensitized solar cells

	I_{SC}[a]/mA·cm^{-2}	V_{OC}[b] /mV	FF[c]	η /%	T[d]/ hour
Cyb3	1.97	410	0.527	1.01	4
Sqb	2.76	455	0.567	1.70	6

a) I_{SC} is the short-circuit photocurrent
b) V_{OC} is the open-circuit voltage
c) FF is the fill factor of cell
d) T is the sensitized time, and film thickness is 6.5μm, irradiated by 42mWcm^{-2} white light.

Conclusions

In this article, we synthesized two novel cyanine dyes to be used as the sensitizer for solar cells material. The photoelectrochemical properties of TiO_2 nanocrystalline solar cells sensitized by the two dyes were investigated. The I_{sc} (2.76mA/cm^2), IPCE (46%) and η (1.7%) of Sqb sensitized TiO_2 solar cell performs preferable IPCE values to that of Cyb3 sensitized one. The relationship of the molecule structure and the photoelectric properties were discussed, which is important to design an efficient molecule sensitizer.

Acknowledgement

This work was financially supported by "973" programme of the ministry of Science and Technology of China and National Natural Science Foundation of China (20128005, 20376010).

References

(1) Hagfeldt A., Grätzel M., *Chem. Rev*., **1995**, *95*, 49.
(2) Nazeeruddin M. K., Kay A., Rodicio K., Humphry-Baker T., Muller E., Liska P., Vlachopoulos N. and Grätzel M., *J. Am. Chem. Soc.*, **1993**,*115*, 6382.
(3) Regan O. B., Grätzel M., *Natur*, **1991**, *353*, 737.
(4) Hara K., Sayama K., Ohga Y., Shinpo A., Suga S. and Arakawa H., *Chem. Commun.*, **2001**, *6*, 569-570.
(5) Kitamura, T. Ikeda M., Shigaki K., Inoue T., Anderson N. A., Ai X., Lian T. Q., Yanagida S., *Chem. Mater.* **2004**,*16*,1806-1812.
(6) Sayama K., Tsukagoshi S., Hara K., Ohga Y., Shinpou A., Abe Y., Suga S., Arakawa H., *J. Phys. Chem. B.* **2002**, *106*, 1363-1371.
(7) Sayama K., Tsukagoshi S., Mori T., Hara K., Ohga Y., Shinpou A., Abe Y., Suga S., Arakawa H., *Sol. Energy Mater. Sol. Cells.* **2003**, *80*, 47-71.
(8) Chen X., Yao Z. G, *Chemical Journal of Chinese Universities.* **1996**, *17*,1613-1616.
(9) Mujumdar R. B., Ernst L.A., Mujumdar S. R., Lewis C.J., Waggoner A.S., *Bioconjugate Chem.* **1993**, *4*, 105.
(10) Sprenger H. E., Ziegenbeim W., *Angew. Chem. Internat. Edit.* **1967**, *6*, 553.
(11) Shen Y. C., Wang L., Lu Z. H., Wei Y., *Chinese J. Materials Research.* **1995**, *9*, 81
(12) Liska P., Ulachopoulos N., *J. Am. Chem. Soc.* **1988**,*110*, 3686.
(13) Vogel R., Hoyer P., Weller H., *J. Phys. Chem.* **1994**, *98*, 3183.
(14) Mishra A., Behera R. K., Behera P. K., Mishra B. K., Behera G. B., *Chem. Rev.* **2000**, *100*, 1973.
(15) Wang W., Yao Z. G., *Photographic Science and Photochemistry*. **1997**,*15*,321-326.
(16) Khazraji A. C., Hotchandani S., Das S., Kamat P. V., *J. Phys. Chem. B.* **1999**,*103*, 4693.

PROGRESS IN THE DEVELOPMENT OF COMPRESSION MOLDABLE COMPOSITE BIPOLAR PLATES

Donald G. Baird and Jianhua Huang

Department of Chemical Engineering
Virginia Polytechnic Institute and State University
Blacksburg, VA 24061-0211

Introduction

Graphite-based composite bipolar plates have been regarded as promising candidates for application in commercial PEM fuel cells [1]. The plates are made from a combination of graphite (or carbon) powder and a polymer resin with conventional processing methods such as compression molding or injection molding. The gas follow channels can be molded directly into the plate, eliminating the need for costly machining step. The composite plates offer the advantages of lower cost, higher flexibility and greater ease of manufacture than graphite plates. They are also light in weight compared to metallic and graphite plates.

The electrical conductivities of the composite bipolar plates are typically around 100 S/cm in the in-plane direction (perpendicular to the compaction direction of the molding) and 20-50 S/cm in the through-plane direction (see Figure 1). Various mechanical properties (flexural, tensile and impact strength, et al.) have been reported for the composite bipolar plates, but all of the plates fail to meet the industry's target values (PlugPower's target values: tensile strength > 41 MPa, flexural strength > 59 MPa, impact strength > 40.5 J/m or 0.75 ft-lb/in) [2]. It has been realized that it is difficult to increase the electrical conductivity and mechanical properties simultaneously for polymer composite plates [3].

Recently, we started with the PET based wet-lay sheet materials (mats consisting of graphite particles, thermoplastic fibers and carbon or glass fibers) using a slurry-making process and used them in compression molding to form bipolar plates with gas follow channels [4]. Although the polyester may not be an ideal matrix for the bipolar plate application because of water generated in the fuel cell environment, our preliminary results showed that the wet-lay composites could be very promising materials for producing bipolar plates. In this work we tried using more stable polymer fibers, PPS fibers, to make new wet-lay sheet materials for making the bipolar plates. PPS is a semi-crystalline polymer with superior chemical resistance and excellent mechanical properties, dimensional stability, and high temperature resistance. It was regarded as one of the ideal matrices for the composite bipolar plates.

Experimental

Wet-lay sheets (PPS-TC70) containing 70% (wt) graphite particles, 23% poly(phenylene sulphide) (PPS) fibers, 6% carbon fibers and 1% additives were generated with a slurry making process on a Herty papermaking machine donated by DuPont. The sheets were then cut and stacked in the mold. The assembly was then placed in a hydraulic press and pressed at 305~310°C about 10 minutes. The pressure used was typically 6.89 MPa (1000 psi).

The in-plane electrical conductivities were measured under ambient conditions according to ASTM Standard F76-86. The through-plane conductivities were measured based on the method proposed by L. Landis and J. L. Tucker [6] with some modifications. That is, after the sample was tested, the sample was removed and the resistance of the test cell (including GDL papers) was measured again under the same condition to obtain the "baseline" resistance. Subtracting the base resistance from the total one gave the sample resistance. The resistivity or conductivity of the sample could be determined from the resistance and sample size.

The tensile and flexural (three-point bending) tests were performed at room temperature (23°C) on an Instron 4204 tester in accordance with ASTM D638 and D790 standards, respectively. The specimen sizes were of L(Length)×W(Width) = 76.2×7.7 mm for the tensile test, and L×W=76.2×12.7 mm for the flexural test. The thickness of the samples was about 2 mm. The Izod impact test (unnotched) was performed on a Tinius Olsen 92T Impact Tester based on ASTM D-256. The sample has size of 64.0×12.7×3.3 mm.

To measure the half-cell resistance of the bipolar plates, a single-sided bipolar plate with size of 4.75" × 5.5" × 0.125" and active area of 15.5 in^2 (100 cm^2) was placed between two pieces of Toray carbon paper, each of which was in contact with a gold-plated copper plate (current collector) on the opposite side. The size of carbon papers is 10 cm × 10 cm on the channeled side and 4.75" × 5.5" on the flat side of the plate. While a constant current (typically 250 mA) passed through the cell, the potential drop between the collectors was measured. The half-cell resistance is then calculated based on the Ohm's law. The measurements were made with an applied load of one ton. The measurement of baseline resistance, that is, the resistance of the testing cell excluding the bipolar plate but including carbon papers and anything else, was performed following the half-cell testing.

Results and Discussion

In Figure 1 are presented the bulk conductivities (both in-plane and through-plane) of PPS based wet-lay composite materials. As PET based wet-lay composites, the PPS based composites have high in-plane conductivity (271 S/cm), well exceeding the DOE target value (100 S/cm) for the composite bipolar plates. The conductivity is also higher than that of the other polymer composite bipolar plates reported so far. Similar to other composite bipolar plates, the wet-lay composites have low through-plane conductivity. The difference between through-plane and in-plane conductivities is however large for the wet-lay composites.

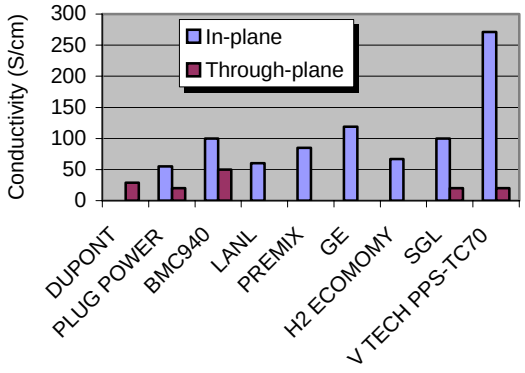

Figure 1. Electrical conductivity of composite materials used for making bipolar plates. (See Refs 2 and 6-11 for sources)

In addition to the electrical conductivity, the bipolar plates should also have adequate mechanical properties to be used in the fuel cell stacks. For example, PlugPower set their target values for flexural, tensile and impact strengths. As can be seen from Figure 2, the mechanical properties of composite bipolar plates available today are still significantly lower than these target values. The wet-lay composite bipolar plates, however, have different behavior. The tensile and flexural strengths of the PPS based plates reached 57.5

MPa and 95.8 MPa, respective, both of which exceed the PlugPower's target values.

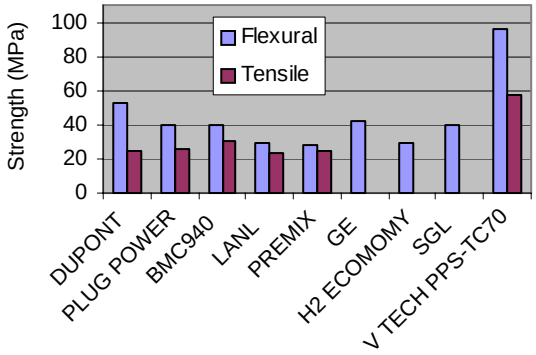

Figure 2. Tensile and flexural strength of composite materials used for making bipolar plates. Plug Power's targets are: flexural, 59 MPa; tensile, 41 MPa. (See Refs 2 and 6-11 for sources)

In Figure 3 is presented the Izod impact strength (unnotched) of PPS-TC70 composite plate. Also included in the figure are the impact data for other composite bipolar plates available from literature. Our plate's impact strength is five times higher than that of the Plug Power plates, over ten times higher than that of the DuPont's plates and two times higher than the PlugPower's target value (40.5 J/m or 0.75 ft-lb/in).

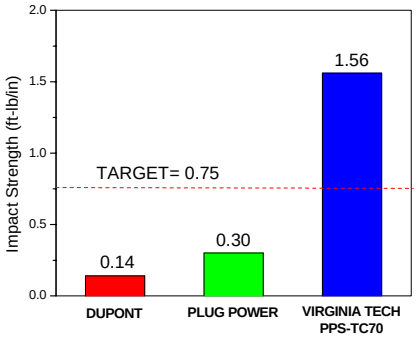

Figure 3. Impact strength (unnotched) of composite bipolar plates.

The outstanding mechanical properties of our composite plates are believed to be associated with the unique structure of the wet-lay sheet materials. Traditionally, for making the polymer composite bipolar plates, thermoplastics in powder form were used to allow uniform blending with the conductive fillers (mostly graphite particles) and then used in compression molding. Although these polymer particles might bind the whole composite together when heated and compression-molded, there are most likely many weld lines inside the composite. This is due to the use of excessive fillers and relatively low molding temperature to raise the electrical conductivity of the material. As a result, all of these polymer composite bipolar plates (including those reinforced with carbon fibers or other fibers) have inadequate mechanical properties. In contrast, the structure of the wet-lay composite materials is different. The starting materials for compression molding are preformed sheets consisting of fine thermoplastic fibers and reinforcing fibers. Compared to the blend of graphite and polymer powders, these sheets should form composites with much higher strength. In addition, long (1" or so) reinforcing fibers (carbon or glass fibers) could be used in the wet-lay process without any difficulties, leading to even greater strength of the composite.

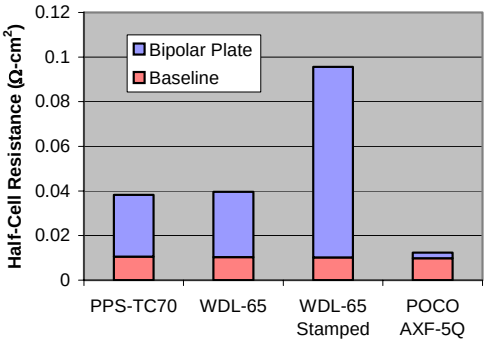

Figure 4. Half-cell resistance of bipolar plates at room temperature.

In Figure 4 are presented the half-cell resistances of the wet-lay composite bipolar plates as well as their baseline resistance. The data for the POCO AXF-5Q graphite plate (with the same design and geometric size) are also included for comparison. It can be seen that, while the baseline resistances in all cases are almost the same (about 0.01 Ω-cm^2), the bipolar plates made from different materials have much different half-cell resistances. The PPS based wet-lay composite plate (PPS-TC70) and PET based one (WDL-65) have similar half-cell resistances (~ 0.039 Ω-cm^2). The resistance of the plates is thus close to 0.029 Ω-cm^2). Comparatively, the POCO graphite plate has a much lower half-cell resistance (about 1/3 of the wet-lay composites). Considering the baseline resistance, the resistance of the graphite plate is more than 10 times smaller than that of the composite plates. This is reasonable considering the large difference in the through-plane conductivities of the materials (650 S/cm for graphite vs. 20 S/cm for wet-lay composites). Obviously, the through-plane conductivity of wet-lay composites needs to be increased to improve the performance of the bipolar plates.

Acknowledgements

This work was supported by the U.S. Department of Energy, Office of Basic Science (Project #DE-FC36-01G011086).

References

1. Busick D and Wilson M, in New Materials for Batteries and Fuel Cells, Materials Research Society Symposium Proceedings Vol. 575, D. H. Doughty et al. Ed, 2000. pp. 247-251.
2. Clulow J G et al., in "Fuel Cell Technology: Opportunities and Challenges", Topical Conference Proceedings, 2002 AIChE Spring National Meeting, March 10-14, 2002 New Orleans, LA. pp.417-425.
3. Vielstich W et al. Ed, Handbook of Fuel Cells – Fundamentals, Technology and Applications Vol. 3: Fuel Cell Technology and Applications, Wiley & Sons, 2003. pp.308 – 314.
4. Huang, J. and Baird, D.G. Proceedings of ANTEC 2003, Nashville, TN, May 4-8, pp. 2151-2155 (2003).
5. Landis, L and Tucker, J. L., R&D Magazine, October 2002, 36-38.
6. Lawrance R J, US 4,214,969 (1980).
7. Wilson M et al., US 6,248,467 (2001).
8. http://www.fuelcell-info.com.
9. http://www.dupont.com/fuelcells/pdf/plates.pdf.
10. http://www.sglcarbon.com/sgl_t/fuelcell/products/bma5.html.
11. http://www.h2economy.com/bp1.htm.

THE EFFECTS AND ANALYSIS ON PARTICLE ATTRITION IN FLUE GAS DESULFURIZATION BY CIRCULATING FLUIDIZED BED

Ma Shuang-chen, Zhao Yi

School of Environmental Science and Engineering
North China Electric Power University
204 Qingnian Road
Baoding, 071003, China

Abstract

The effects of particle attrition on flue gas desulfurization (FGD) by circulating fluidized bed (CFB) are analyzed incorporating the wearing phenomena of particles on actual operation, in which the increase of mass transfer coefficient after particle abrasion is thereby shown by enhanced coefficient. At the same time, the effects of voidage among particles and superficial gas velocity as well as particle size on enhanced coefficient are analyzed, which provide corresponding measures to further improve the fluidized bed reactor and increase desulfurization efficiency.

Key Words: FGD, CFB, Attrition, Enhanced coefficient

Introduction

Due to ternary mixtures of gas, liquid and solid in CFB, there exist simultaneously absorption process between flue gas and absorbents, adsorption process between bed materials and flue gas as well as evaporated droplets, absorption and adsorption process including recycled particles and also exist process of water evaporation. As a result, it occurs a special phenomenon in CFB, i.e. the turbulence and attrition each other between gas and solid lead to surface abrasion and size reduction of absorbents to different extent. To this phenomenon, Qian Feng et al presented an attrition matrix of quicklime particles in rapid CFB according to total material balance [1]. The effects of different parameters such as particle dimension, combustion temperature etc. on abrasion of fluidized particles were studied by Chiou-Liang Lin et al[2]. The results indicate that attrition rate of fluidized particles is increased when mean size is decreased and operating temperature is increased. It is all known that the mass diffusion through the product layer (produced by acidic components react with basic ones) would become difficult as SO_2 is removed by chemical reaction, if the layer formed and thick the mass transfer diffusion region, it would have a negative effect to mass transfer of SO2 and basic components. But the attrition exist in bed could make the layer fell off, and it is beneficial to improve SO_2 removal. In this paper, the effect of particles attrition on mass transfer coefficient is analyzed, and it is shown with enhanced coefficient. At the same time, various effects on mass transfer coefficient in CFB are analyzed through calculation.

1 Analysis of special phenomenon in CFB

The basic theory of FGD by CFB is that dry lime or lime droplets, which are used for absorbents, when flue gas enters into CFB from bottom of reactor and flows upward with corresponding velocity, the absorbents is atomized by nozzles, and then chemical reactions occur while touching with the fast flue gas flow, SO_2 is thereby removed from flue gas. As there present ternary mixture of gas, liquid and solid in CFB, the particulate matters in bed are probably worn down continuously by upward flue gas, which leads to continuously formation and separation of particles as a result of attrition on particle surface. There are various causes as to abrasion. Shamlou et al [3] presented that the main causes of particle attrition are chemical reaction, physical expansion, particle abrasion and static gravitation. By the attrition, the product layer covering on the surface of unreacted absorbents and difficult to remove, is fell off, consequently the fresh surface area is increased, the mass transfer and heat transfer are enhanced. At the time of particle size is decreased, the fresh particles, which still unreacted is exposed and continue to react with SO_2.

Moreover, partial particles are probably drifted toward the reactor wall after diffused by scour of airflow. When reach the wall, as the gas velocity is rather low, and the drag force of gas acting on particles is also quite low, which result in a portion of particles moving downward close to the reactor wall. When reach the bottom of reactor, the particles move upward again along with new entered flue gas. The particles keep a long time in reactor, thus they are worn down frequently. Surface attrition of particles is beneficial to absorption of SO_2, and particles with different size have different extent of reduction after abrasion. The attrition is most clearly at the beginning of absorbents fluidization and levels off to reach a minimum weight as the reaction goes along.

The obvious size reduction resulting from attrition may influence the operation parameters and fluidization properties of reactor to some extent, and also lead to significant loss of bed materials. To this, the theoretical studies on attrition of absorbents and variation of dimension in CFB are accomplished by Jeffrey L.Cook et al[4], who consider that the extent of abrasion are different when particles with various size and flue gas with same velocity contact with each other. Simultaneously, it is also dissimilar when contact occurs between particles with same size and flue gas with different velocity. Under various experimental conditions, the particle attrition in FGD process is considered beneficial to SO_2 removal.

There also exist agglomeration phenomena of fine particles in circulating fluidized bed reactor (CFBA) at the time of particle attrition. As the particles are recycled repeatedly in bed, the products and unreacted absorbents accumulate together, then the particulate adsorption each other and adhesion with water result in incompact floccules agglomerated by fine particles, which extend the evaporation time of droplets and consequently influence the rate of absorption. Through simulating analysis, Yan Yan et al[5] consider that the formation of particle agglomerates has a little influence on the absorption of SO_2, but it has inconspicuous enhanced effect on desulfurization in general. In addition, particle size is decreased as a result of cracking and surface abrasion. After a long residence time, particles are brought out of reactor when its moving velocity is greater than that of terminal. So it can be considered that CFB FGD goes with continuous attrition and agglomeration of particles. In this paper, the attrition of particles is analyzed predominantly.

2 Introduction of enhanced coefficient α

Before particle attrition is analyzed, the absorbents and mass transfer process can be assumed as follows:

(1) Suppose that absorbents are all regular spheroids, mean diameter is d_p, orbicular degree is 1, and it remains invariable in the course of water evaporation.

(2) Suppose that the product layer on the surface of absorbents is quite thin, and it come off with exposure of fresh particles simultaneously as soon as attrition begins.

(3) Suppose that fresh absorbents absorb SO_2 at once when product layer is worn down. The adsorbing and desorbing of gas-solid caused by attrition can be neglected, i.e., only influence of instant absorption on FGD is considered.

(4) Suppose that mass transfer process is only controlled by liquid membrane, i.e. the influence of gas membrane resistance on mass transfer can be neglected.

Absorption between gas and solid is shown in **Figure 1**:

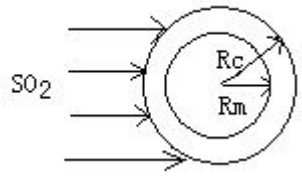

Figure 1. Schematic diagram of absorption process between solid (R_m is radius of unreacted particles; R_c is radius of particles including product layer)

The change of absorbent mass in CFB going with time is shown as follow[4]:

$$-\frac{dW}{dt}=\frac{Ka\cdot(W^2-W_{min}{}^2)}{(U-U_{mf})^2} \quad (1)$$

where W is the weight of particles in CFB,(kg); W_{min} is the minimum weight of particles after a long fluidization in CFB,（kg）; K_a is the attrition rate constant, (m^2/s^3); U and U_{mf} are the superficial gas velocity and the critical fluidization velocity respectively, (m/s).

Surface attrition of particles can be regard as abrasion of product layer. As the product layer is quite thin, i.e. the moles of particle reduction in unit time is equal to corresponding moles of fresh particles which is exposed, and it also means corresponding moles of SO_2 reacting with unreacted solids (in case of molar ratio is 1) The moles of fresh particles exposed in unit time is $\frac{K_a.(W^2-W_{min}{}^2)}{(U-U_{mf})^2\times 120}$, the unit is kmol/s.

If the particle diameter is d_p, in the case of taking no account of particle attrition, the mass transfer coefficient of liquid phase k_x has a relationship with Approach-to-Saturation Temperature (AST) and the molar ratio of calcium to sulfur (Ca/S). The value could be calculated by following formula[6]:

$$k_x=0.005\times Ca/S\times\exp(-0.0123\times AST) \quad (2)$$

Under the condition of considering abrasion, the increased value of fractional mass transfer coefficient of liquid phase can be expressed by introduction of enhanced coefficient ϕ. ϕ can be regarded as the enhanced multiple of mass transfer coefficient of liquid phase in the case of completely considering surface attrition of particles, then the mass transfer coefficient of liquid phase k_x' can be shown as follows:

$$k_x'=k_x.\alpha \quad (3)$$

$$\alpha=1+\phi \quad (4)$$

Where α is the enhanced coefficient of liquid phase when the effect of attrition is considered, ϕ is the enhanced factor produced by attrition of particles, ϕ is derived as:

$$\phi=\frac{K_a.(W^2-W_{min}{}^2)}{S.k_x(U-U_{mf})^2\times 120} \quad (5)$$

$$S=n.S_i=\frac{W_0}{\rho_s\cdot\frac{4}{3}\pi\left(\frac{d_p}{2}\right)^3}.\pi d_p{}^2=\frac{6W_0}{d_p\rho_s}=\frac{3\pi D^2.L(1-\delta)}{2d_p} \quad (6)$$

Where S is the overall superficial area of particles, (m^2), and S_i is the superficial area of single particle, (m^2).

The mass transfer process is controlled by liquid membrane, thus the overall mass transfer coefficient K'_x is approximately equal to k'_x. Then the equation of overall mass transfer rate of liquid phase, when considering particles abrasion, can be written as follows:

$$N_A=K_x'(x^*-x)=k_x.\alpha(x^*-x) \quad (7)$$

Where K'_x is the overall mass transfer coefficient of liquid phase in case of considering particles attrition, (kmol/m^2.s); x^* is the mole fraction of solute in liquid phase when balancing with ingredient concentration in gas phase, and x is the mole fraction of solute in liquid phase.

3 Establishment of parameters

3.1Calculation of critical fluidization velocity U_{mf}

U_{mf} is calculated as follows:

$$U_{mf}=\frac{(\varphi_s d_p)^2}{150}.\frac{\rho_s-\rho_f}{\mu}.\frac{\varepsilon_{mf}{}^2}{1-\varepsilon_{mf}}.g \quad (8)$$

Where φ_s is the spherical degree, according to assumption (1), φ_s =1; ρ_s, ρ_f are the density of solid and gas, respectively (kg/m^3); ε_{mf} is the critical voidage, the value is 0.4 in this calculation, and μ is the viscidity of fluidization medium,(Pa.s).

3.2The weight of bed materials W_0 in fixed bed

$$W_0=\rho_s.v_s(1-\varepsilon)=\frac{1}{4}(1-\varepsilon).\pi D^2L.\rho_S \quad (9)$$

Where ε is the voidage of particles; v_s is the effective volume of bed material, (m^3); L is the height of bed, (m), and D is the diameter of reactor, (m).

3.3The calculation of attrition rate constant Ka. In the paper, the product of gas constant and temperature in Arrhenius equation is replaced by the square of the excess velocity（$U-U_{mf}$）^{2},and it was found to suit the following equation:

$$K_a=K_o\cdot\exp\left[\frac{-Ea}{(U-U_{mf})^2}\right] \quad (10)$$

Where Ea is the activation energy for attrition, (kJ/kg), and K_0 is the frequency factor (s^{-1}). The equation is validated by Jeffrey L.Cook[4] and the calculated value of Ea and K_0 are 3.8925×10^{-3}kJ/kg and $2.89\times10^{-6}s^{-1}$ respectively.

4 Experimental results analysis

The desulfurization device of CFB FGD under experimental condition is developed, the operating and experimental results can be found in our former paper[7]. The operating parameters are listed as follows: operating temperature is between 50~90℃, humidity of flue gas is between 4%~7%, Ca/S is between 1.0~1.8, flue gas velocity is between 1.7~2.9m/s and flue gas flow rate is between 300~500m^3/h. In this paper, the effects of gas velocity, particles voidage and particles size on mass transfer enhanced coefficient are analyzed under the condition of Ca/S is 1.1,operating temperature is 50℃, ρ_s and ρ_f are 1.28×10^3kg/m^3 and 1.054kg/m^3 respectively.

In the case of U is 2m/s and d_p is 903μm, U_{mf} through calculation is 0.9545m/s ,and Ka is $2.88\times10^{-6}s^{-1}$, the enhanced coefficient can be achieved. It is obvious that mass transfer coefficient of liquid phase when considering attrition is increased inconspicuously, thus the mass transfer rate is increased inconspicuously. The change of enhanced factor under different voidage is shown in **Figure 2**.

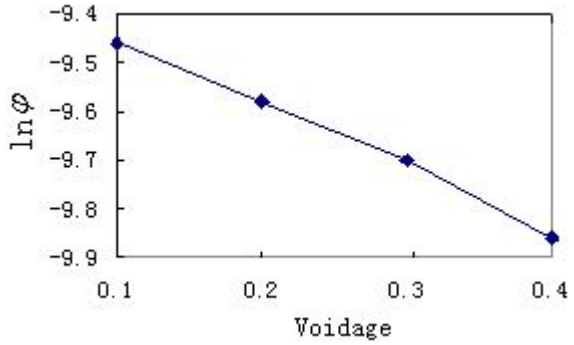

Figure 2. Change of enhanced factor under different voidage

It can be seen from **Figure 2** that the greater the particle voidage is, the enhanced factor of attrition on mass transfer coefficient is less apparently. It is probably because that the greater voidage is, the overall superficial area of particles is relatively smaller, which lead to the superficial area of fresh absorbents exposing in the same time is comparatively decreased and thereby the extent of increase for mass transfer is reduced.

When U is changed in the case of keeping other parameters invariable ($\mathcal{E}$ =0.1), the effect of attrition on enhanced factor is shown in **Figure3**.

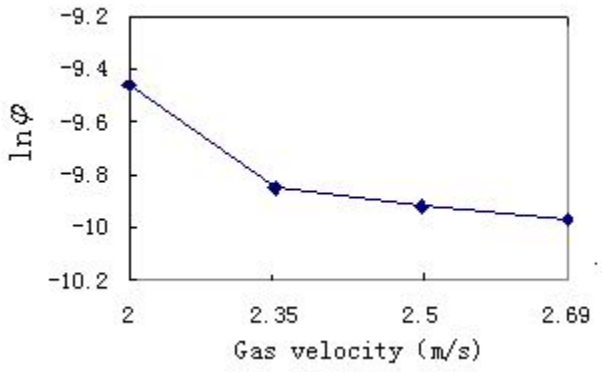

Figure 3. Effect of attrition on enhanced factor at different superficial gas velocity

It can be seen from **Figure 3** that the increase of U results in the inconspicuous increase of attrition rate constant, whereas lead to dissimilar reduction of enhanced factor, which can be interpreted that the increase of gas turbulence is beneficial to removal of superficial product layer. However, the contact time of fresh absorbents and flue gas is shortened because of greater gas velocity; the enhanced effect is thereby not very clearly.

When particle size is changed in the case of keeping other factors invariable, the effect of attrition on enhanced factor t is shown in Fig 4.

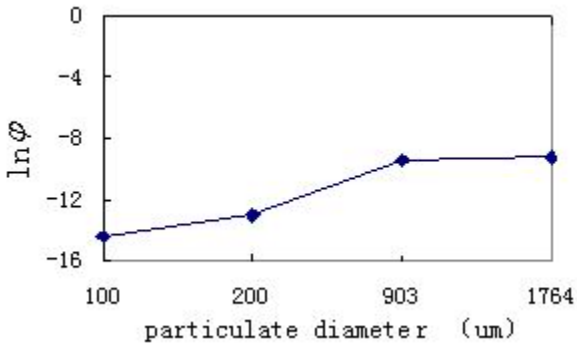

Figure 4. Effect of attrition on enhanced factor at different particles diameter

It can be seen from **Figure 4** that particle size has obvious influence on attrition. When the diameter is greater, the degree of abrasion is increased, which improves the mass transfer. When the diameter is extremely small, attrition is not clearly and is almost neglected, most fine particles is throw away along with flue gas, which can be interpreted that too big size lead to longer residence time and course of flue gas diffusing toward unreacted core, and also lead to poorer particles utilization as well as further attrition. On the contrary, too fine particles are beneficial to water evaporation and thus limit the reaction on the other hand, although it has greater surface area, which is available to improve absorption of SO_2.Thus it can be explicated that selecting greater particles can keep relatively high humidity and is apparently suitable to absorption of SO_2. Yan Yan et al [8] think that there exists an optimum initial diameter of droplet and initial absorbent concentration in CFB, in the case the absorbent can be utilized effectively when water is evaporated completely.

5 Conclusions

In this paper, the CFB FGD process is introduced and analyzed in detail, and the correlative analysis of particle attrition is carried out according to phenomena of particle attrition in CFB. The effect of abrasion on mass transfer coefficient of liquid phase is expressed by enhanced coefficient α .It is shown that particle attrition is beneficial to intensifying mass transfer coefficient of liquid phase. The effects of voidage, superficial gas velocity and particulate size on enhanced coefficient and mass transfer rate is analyzed through calculation and schematics. The results indicate that particle attrition in CFB plays a helpful part in improving absorbents utilization and further reaction, and it also has an inconspicuous intensify effect on mass transfer. The study works provide corresponding measures to further improve CFB device and increase desulfurization efficiency.

Acknowledgment. We would like to acknowledge the doctor fund and pre-research fund of North China Electric Power University for their supports.

References

1 QIAN Feng,YANG Wen-bo,Zhang zhen-fang. *Research of Environmental Science*, **2002**,15（4）,p.54-56
2 Chiou-Liang Lin. Ming-Yen Wey. *Korean J.Chem. Eng.*, **2003**,20(6), p.1123-1130
3 Shamlou,P.A,Liu,Z and Yates,J.G, Chem.Eng.Sci., 1990, (45),p.809
4 Jeffrey L.Cook, Soon-JaiKhang, Sang-Kwun.Lee,Tim.C.Keener. *Powder Technology*, **1996** ,(89),p.1-8
5 YAN Yan, PEGN Xiao-feng, WANG Bu-xuan. Proceedings of the CSEE, 2003,23（11）,p.173-177
6 Neathery James K. *AIChE Journal*, **1996**,42(1),259-268
7 Shuangchen Ma, Yi Zhao, Jianjun Huang, Xiaojun Sun. The Forth Asia-Pacific Conference on Combustion. Nanjing, 2003,p.220-224
8 Yan Yan**,** Xiaofeng Peng. *J.of Thermal Science*, **2000**,9(4),p.356-360

ULTRA-CLEAN TRANSPORTATION FUELS FROM COAL: AN OVERVIEW

John Shen and Edward Schmetz, U.S. Department of Energy, Germantown, MD 20874

Gary J Stiegel, John C Winslow and Robert M Kornosky, National Energy Technology Lab, U.S. Department of Energy, Pittsburgh, PA 15236

Suresh C Jain, National Energy Technology Lab, U.S. Department of Energy, Morgantown WV 26507

Introduction

A recent paper by EIA (Energy Information Administration) within the U.S. Department of Energy (DOE) indicates that coal-to-liquids (CTL) fuels, under the High B Case, could become a viable domestic source to supplement the petroleum liquids supply by 2010[(1)]. Ultra-clean fuels can be produced from coal via indirect coal liquefaction route. In this technology, coal is first gasified to form synthesis gas (carbon monoxide and hydrogen) which is cleaned to remove impurities and then converted to clean liquid fuels by use of a catalyst using a technology known as Fischer-Tropsch (F-T) synthesis. This paper will review the status of activities supported by the Office of Fossil Energy with DOE which are to help ushering in the early commercial production of CTL fuels.

CTL fuels production via indirect liquefaction is known to be capital sensitive, with syngas production accounting for two thirds of the cost. DOE has been supporting activities aimed to reduce the capital cost of this technology, including the developments of coal gasifier with higher efficiency, advanced syngas cleanup, and slurry-phase F-T synthesis. Significant advances have been made in all areas. A scoping economics study indicates CTL fuels based on these advanced technologies could be competitive with petroleum crude in the mid-$ 30 per barrel.

A hurdle for the commercial production of CTL fuels is the need to demonstrate the feasibility of the advanced CTL technologies operated in integrated system mode at commercial-scale units to include gasifier, gas cleanup, F-T synthesis, and power generation blocks. This feasibility demonstration has been the focus of two DOE initiatives: (a) Early Entrance Coproduction Plant (EECP), and (b) Clean Coal Power Initiative (CCPI). More specifically, these initiatives aim to produce CTL fuels along with power, chemicals, and steam in a mode called coproduction. Under this mode, a F-T synthesis step would be incorporated into an integrated gasification and combined cycle (IGCC) complex to help achieve higher plant efficiency and a more versatile product slate. This coproduction (poly-generation) mode is deemed to offer the earliest opportunity for the commercial production of CTL fuels in the U.S.

CTL Fuels Projects at the Waste Management Processors, Inc. (WMPI)

Two separate cost-sharing CTL projects were awarded to the WMPI by DOE, the first one under the EECP initiative and the second one under the CCPI initiative. The former is for the project definition and preliminary engineering design, and the latter for the detailed design, construction, and operation of the CTL demonstration plant. Work for both projects has been closely coordinated to ensure the smooth interactions between them. A brief project description is provided below.

Prime contractor: WMPI
Subcontractors: Shell Global Solutions, Uhde GmbH, Sasol Synfuels International, and Nexant, Inc.
Location: Gilberton, Pennsylvania
Feedstock: anthracite coal waste (culm) at 1.4 million tons per year
Products: 5,000 barrels per day of ultracleanfuels™, 131 Mw (92 Mw for internal use and 39 Mw for export) of electricity, sulfur, and steam.
Key process blocks: Shell gasification complex, Sasol and ChevronTexaco F-T synthesis and product workup units, and combined cycle plant.
Roles of other subcontractors: Uhde Gmbh will serve as a general engineering contractor for EPC (engineering, procurement, and construction). Nexant Inc. will serve as an engineering consultant.

In March 2005, WMPI received the air permit approval from the Commonwealth of Pennsylvania for the project. Efforts have been continuing to prepare the EIS (environmental impact statement) to comply with the NEPA (National Environmental Policy Act) and to seek product off take agreements. More detailed data on the project can be found elsewhere [(2)].

EECP CTL Project with the Texaco Energy Systems LLC

The EECP CTL project with the Texaco Energy Systems LLC was carried out in two phases. Phase I work (project definition and conceptual plant design) was completed in December 2000 and Phase II (research, development and testing) in June 2003. The plant design feedstock is petroleum coke rather than coal since the plant will be located at a site adjacent to a host refinery. This feedstock choice offers the advantages of (a) a lower feedstock cost, and (b) a lower capital cost by sharing the existing infrastructures at the host refinery site. A brief project description is provided below.

Prime contractor: Texaco Energy systems LLC
Subcontractors: General Electric (GE), Praxair, and Kellogg Brown and Root (KBR).
Location: Motiva refinery, Port Arthur, Texas
Feedstock: Petroleum coke at 1,235 short tons per day
Products: 457 barrels per day of wax, 125 barrels per day of F-T diesel, 35 barrels per day of F-T naphtha, 55 Mw power for export, sulfur, and steam.
Key process blocks: Texaco gasification complex, Rentech F-T synthesis unit, Bechtel Hy-Finishing℠ F-T product workup unit, and combined cycle plant.
Roles of other subcontractors: GE (gas turbine testing), Praxair (air separation technology), and KBR (facility engineering integration).

Highlights of the work included:

1. A conceptual F-T EECP plant design was completed which included a financial analysis of internal rate of return for various cases.
2. Confirmed the F-T reactor design basis which is to process a syngas from an advanced gasifier with hydrogen to carbon monixide ratio of 0.67.
3. Proposed a two-stage F-T wax/catalyst separation system which could yield a clean wax with 10 ppm solids content.
4. Identified integration of F-T synthesis with front-end gasification by feeding the F-T water and F-T spent catalysts into the gasifier

5. Confirmed the feasibility to combust low-Btu tail gas (75 Btu/standard cubic feet) from various sources in the plant in a commercial GE gas turbine.

Upon completion of the Phase II, Texaco decided not to proceed with Phase III work (preliminary engineering design) of the EECP project. This decision was partly due to the need to search for a new host refinery site for the project. The Motiva refinery site, which was chosen in the EECP project design study, became unavailable because of the merger between Chevron and Texaco. More detailed data for this project can be found elsewhere [3, 4].

CTL versus GTL Fuels

CTL plants would generally use iron catalyst in the F-T synthesis to take advantage of its intrinsic water-gas-shift activity and higher tolerance of trace impurities. Both attributes are considered beneficial for processing coal-based syngas from advanced gasifiers with low hydrogen to carbon monoxide ratio and containing trace impurities. This catalyst choice is different from the cobalt catalyst used in the gas-to-liquids (GTL) fuels production with a hydrogen-rich syngas. Despite the slight differences in chemical compositions because of the catalyst choice, CTL and GTL diesel have been shown to exhibit similar emission reduction benefits in engine combustion testing[5].

Conclusions

Prospects of higher crude price that began in 2004 are expected to rekindle interests in alternatives to conventional crude oil. The near commercial-readiness of IGCC plants to produce clean power from coal, coupled with the ability to coproduce clean CTL fuels in the same plant, offers the potential for improved energy security. The CTL demonstration projects at WMPI and Texaco, which are co-funded by DOE, are aimed to demonstrate the integrated system operations of advanced CTL technologies at commercial-scale units. In the ongoing WMPI projects, efforts have been underway to seek arrangements for product off take. CTL and GTL diesel fuels have similar attributes and have been shown to exhibit similar emission reduction benefits in engine combustion testing.

References

(1) Caruso, G.F., "Welcome and Opening Remarks", paper presented at the 13th Annual EIA Midterm Outlook and Modeling Conference, April 12, 2005, Washington, DC.

(2) Quarterly technical progress report (July to September 2004) submitted by WMPI PTY, LLC. under DOE Cooperative Agreement DE-FC26-00NT40693, November 2004

(3) Early Entrance Coproduction Plant, Phase I Preliminary Concept Report, submitted by Texaco Energy Systems Inc. under DOE Cooperative Agreement DE-FC26-99FT40658, May 2001

(4) Early Entrance Coproduction Plant, Phase II Final Report, submitted by Texaco Energy Systems LLC under DOE Cooperative Agreement DE-FC26-99FT40658, January 2004

EXSTOL: EXELUS SYNTHESIS GAS-TO-LIQUIDS TECHNOLOGY

Mitrajit Mukherjee, Sankaran Sundaresan

Exelus Inc., 99 Dorsa Avenue, Livingston, NJ 07039

Introduction

The Fischer-Tropsch (FT) Synthesis reaction converts synthesis gas (a mixture of CO and Hydrogen) into liquid hydrocarbons according to[1]:

$CO + 2\ H_2 \rightarrow$ "$–CH_2–$" $+ H_2O \qquad \Delta H = -170$ kJ/mol

where "$–CH_2-$" represents a product consisting mainly of paraffinic hydrocarbons of variable chain length. Because of the enormous exothermicity of the FT synthesis reaction, a very large heat transfer area is required. This is why a large number of 2nd generation FT technologies use slurry bubble columns as the reactor of choice. A principal advantage of slurry bubble column reactors (BCR) over fixed bed reactors is that the presence of a circulating/agitated slurry phase greatly increases the heat transfer rate to cooling surfaces built into the reactor[2]. Further, the small particle size minimizes the negative impact of diffusional resistances within the interior of the catalyst. However, conventional slurry bubble column reactors have several drawbacks[3]:

1. Liquid-phase back-mixing, which is a strong function of reactor diameter, results in a much lower kinetic driving force, requiring a larger reactor volume than a fixed-bed reactor operating at the same conversion.
2. Catalyst/liquid separation can be a significant technical hurdle, which limits minimum catalyst particle size and can be negatively impacted by catalyst particle attrition
3. Hydrodynamics of slurry bubble-column reactors is complex – scale-up issues can pose significant problems.

This paper summarizes the development of a break-through FT technology that has the ability to significantly improve the economics of the process using a multi-functional catalytic system. The cost reduction potential using this next-generation FT technology provides a very strong springboard for overall Gas-to-Liquids (GTL) process viability.

Exelus' Approach

Researchers at Exelus are developing a first-of-a-kind catalytic system for multi-phase reactions that blurs the line of distinction between the reactor and catalyst by incorporating many features one associates with a reactor within the catalyst body. The new catalyst system called the HyperCat, marries all the benefits of slurry operation (low pore-diffusion barriers, high heat and mass-transfer rates, low pressure drop) with the benefits of fixed-bed operation (no filtration issues, plug-flow behavior and easy scale-up) in one system. It is able to do so by achieving better control of the "micro-environment" at the catalyst surface through intensification of heat and mass-transport processes within the reactor. The high level of control allows ideal reaction conditions to prevail at the active sites, enhancing catalyst performance leading to significantly higher activity. As a result, reactor productivity is significantly enhanced – catalyst volume can now be reduced by 50% or more over a conventional slurry bubble column reactor. The higher levels of inter-phase heat and mass-transfer allow the use of steam-coils (low cost item) to be used for removing reaction heat instead of expensive shell-and-tube reactor designs. This will result in a significant reduction in the cost of the Fischer-Tropsch reactor leading to a corresponding decrease in the cost of a GTL complex.

Results & Discussion

Gas Hold-Up. Gas hold-up is a critical parameter in characterizing the hydrodynamic behavior and hence the performance of a bubble column reactor. It determines: a) the reaction rate by controlling the gas-phase residence time and b) the mass-transfer rate by governing the gas-liquid interfacial area. It is mainly a function of the gas velocity and the liquid physical properties. The gas hold-up of the HyperCat system was studied using an air-water system. The gas superficial velocities were varied from 0.1-1.0 m/s. The results are shown in **Figure 1**. The HyperCat gas hold-up is slightly lower than that in a conventional bubble column reactor (~ 30% reduction) and comparable to that in a slurry bubble column with 30-35% solids concentration.[4]

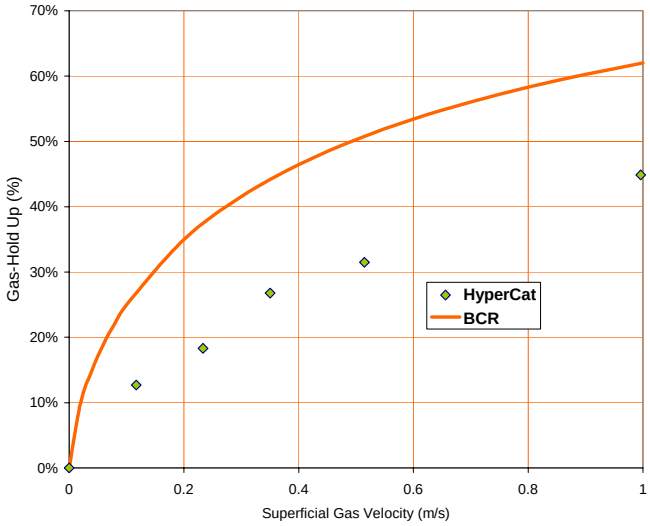

Figure 1. Gas hold-up – HyperCat versus empty bubble column

Liquid-Phase Axial Dispersion. The liquid phase axial dispersion in bubble column reactors is very high making them effectively back-mixed reactors for industrial scale systems. Liquid mixing in bubble columns is a result of global convective re-circulation of the liquid phase and turbulent diffusion due to eddies generated by the rising bubbles. Turbulent diffusion arises from motion on many scales and reflects both large-scale fluctuations caused by the large-scale eddies, and small-scale fluctuations arising from the entrainment of liquid in the wakes of the fast-rising bubbles[5]. By structuring the gas and the liquid flow, HyperCat reduces the axial dispersion for both phases leading to a large reduction in axial dispersion coefficients (D_{AX}). The real benefit of this reduced dispersion is that it is not a function of the reactor diameter as is the case with conventional bubble column reactors.

We measured the liquid phase D_{AX} for a range of gas velocities shown in **Figure 2**. The dispersion values measured for the HyperCat are roughly 2 orders of magnitude lower than those found in commercial scale reactors – which means that the HyperCat reactor will behave like a plug-flow reactor for both the liquid and gas-phases

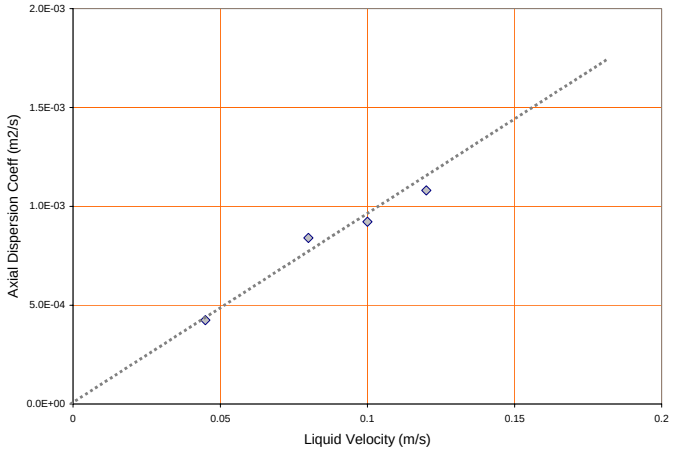

Figure 2. Liquid phase axial dispersion in HyperCat

Heat Transfer. The heat transfer coefficient of the HyperCat system was modeled using the gas-hold and liquid-phase dispersion data. The presence of gas bubbles in the heat-transfer zone allows continuous replacement of the liquid film in contact with the heat-exchanger surface leading to heat transfer rates which are similar to that obtained in a bubble column reactor under comparable gas velocities. However, since HyperCat system will operate at higher gas velocities than that possible in a slurry bubble column system, the heat transfer coefficient will be higher for the HyperCat system.

Catalyst Performance. A major stumbling block in converting structured carriers into structured catalysts is that for the same amount of active catalyst loading, structured catalysts give much lower activities than traditional powder catalysts[6].

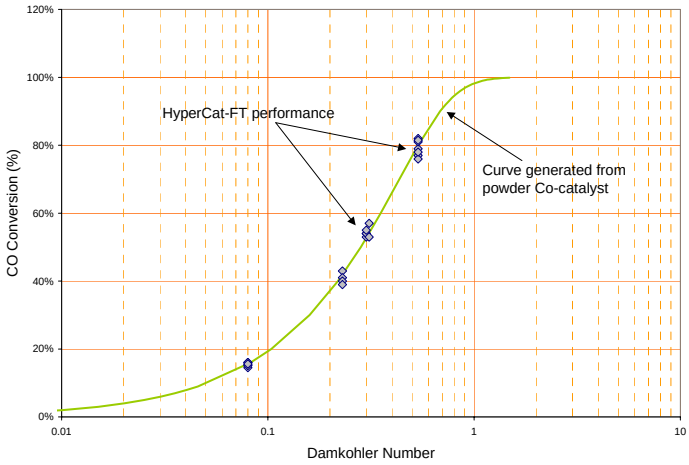

Figure 3. HyperCat-FT catalyst performance compared to powder FT catalyst

To ensure that we did not run into the same problem, we synthesized a powder catalyst (100μ diameter) and a HyperCat-FT catalyst using Cobalt as the active phase, Ruthenium as a promoter and γ-alumina as the support. We generated CO conversion versus Damkohler number (Da) curve using the following relationship[7]

$$Da = \tau k_{CO} = -(1/6)\ln(1 - x_{CO}) + (1/3)\, x_{CO}$$

where τ is the residence time, k_{CO} is the 1st order rate constant and x_{CO} is the CO conversion.

It is very clear from the data shown in **Figure 3** that there is virtually no difference in the performance of the HyperCat as compared to the powder catalyst. Thus, we have established that the HyperCat system can match the performance of powdered catalyst on equivalent Cobalt loading basis. This result is extremely important in light of other efforts being made to develop structured catalysts for Fischer-Tropsch reaction, which show that the activity of the structured catalyst is always lower than the powder catalyst[8].

Comparison with slurry bubble column reactor. Finally, we studied the effect of liquid dispersion on catalyst performance by comparing the performance of the powder catalyst in a bubble column reactor with the HyperCat-FT system. As shown in **Figure 4**, the CO conversion is much lower for a low Peclet number (bubble column reactor with a back-mixed liquid phase) as opposed to a higher Peclet number for the HyperCat system. The tests were conducted under the same process conditions and Damkohler number. The change in Peclet number did not change the liquid product distribution or the methane selectivity – which appear to be mainly a function of reaction temperature and pressure.

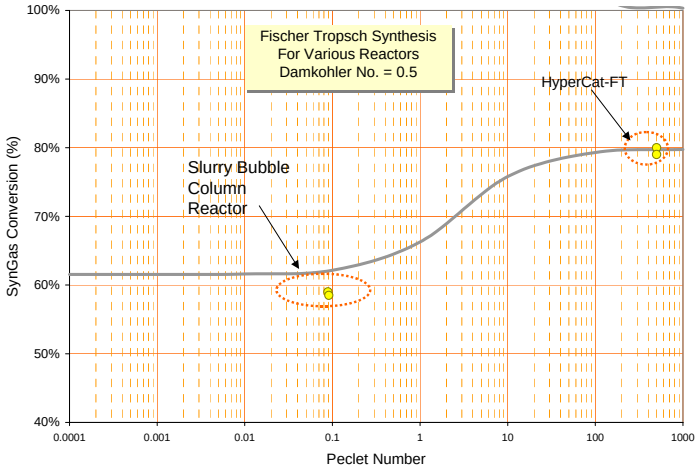

Figure 4. Effect of liquid phase axial dispersion on CO conversion

Conclusions

The Fischer-Tropsch reactor design challenge can be distilled down to the following critical issues:

(1) Achieve a high conversion per pass, in order to achieve high yields and reduce recycle and investment costs
(2) Eliminate the solids handling issue
(3) Provide high heat-transfer rates to remove the large reaction heat
(4) Minimize pore and film diffusion limitations

As seen from the above analysis issues 1 & 2 can be easily met in a fixed-bed reactor, while issues 3 and 4 are more suitable in a back-mixed bubble column reactor. However, one reactor alone is unable to satisfy all four requirements simultaneously. Exelus has developed a novel structured catalytic system that allows one to meet all four criteria in a single catalytic system. Hydrodynamic tests reveal that the HyperCat has similar gas-hold up as a slurry bubble column reactor but with a much lower liquid axial-dispersion coefficient. Modeling studies appear to indicate that the heat-transfer coefficient of this new system is similar to a bubble column reactor. Catalyst performance tests reveal that the performance of the HyperCat is similar to that of a powder catalyst when used in a plug-flow reactor.

Acknowledgement. This work was funded by grants from the U.S. Department of Energy

References

(1) Dry, M.E. "The Fischer–Tropsch process: 1950–2000", Catalysis Today, 71 (2002)
(2) De Swart, J.W.A.; Krishna, R.; Sie, S.T., Selection, design and scale up of the Fischer-Tropsch reactor, Stud. Surf. Sci. Catal. 1997, 107, 213–218.
(3) Burtron H. Davis, "Overview of reactors for liquid phase Fischer–Tropsch synthesis", Catalysis Today, 71 (2002)
(4) Krishna, R., Van Baten, J.M., Urseanu, M.I. and Ellengerber, J., A scale up strategy for bubble column slurry reactors, Catalysis Today, 66, 199 - 207 (2001).
(5) Alexander, B. F. and Shah, Y. T. Axial dispersion coefficients in bubble columns. Chem. Engng J. (1976) 11, 153-156
(6) Liu, W. "Mini-structured Catalyst Bed for Gas-Liquid-Solid Multiphase Catalytic Reaction", AIChEJ, p1519-1532, July 2002
(7) Post, M.F.M., "Diffusion Limitation in Fischer-Tropsch Catalysts", AIChE J, 35, 1007-1114, 1989
(8) Hilmen, A., E. Bergene, O.A. Lindvåg, D. Schanke, S. Erib, A. Holmenc, "Fischer–Tropsch synthesis on monolithic catalysts of different materials", Catalysis Today 69 (2001) 227–232

CLEAN FUEL PRODUCTION USING PLASMA ENERGY PYROLYSIS SYSTEM (PEPS®)

Ron Patun, National Defense Center for Environmental Excellence (NDCEE), Johnstown, Pennsylvania
Jay Ramamurthi, EnerSol Technologies, Inc., Lorton, Virginia
Arthur Hartstein, U. S. Department of Energy (DOE), Washington, DC

Overview

Statement of Problem. The U.S. imports about sixty (60) percent of its fuel requirements (Energy Information Administration 2005) This figure is expected to increase to about 70 percent by the year 2025 (Energy Information Administration 2005). This reliance on foreign sources of oil has created both national and economic security issues for the U.S. This paper will discuss the use of the Enersol PEPS® gasification process for the production of syngas from petroleum coke (petcoke), which can subsequently be converted to clean transportation liquid fuels. This process, compared to syngas produced from natural gas, has the advantage of using petcoke, an oil refinery by-product, rather the expensive natural gas that will have to be imported. This is a technology transfer opportunity for the Department of Energy (DOE) and the Department of Defense (DoD) to increase the domestic source of environmentally friendly transportation fuels

Proposed Solution, Use of PEPS®. The U.S. produces over 30 million tons per year of petcoke, most of which has low economic value, at a number of refineries. The petcoke is a by-product of thermal cracking of crude oil. PEPS®, a novel Gasification Technology, which utilizes plasma energy technology, can be used to thermally convert petcoke to produce syngas. EnerSol Technologies, Inc. developed the thermal treatment process, which is accomplished in the absence of excess air. After gas purification occurs, the clean syngas can be used to produce clean fuels by further processing using conventional Gas-to-Liquid (GTL) technologies such as Fischer-Tropsch (F-T) technology. This technology is able to produce clean fuels with no sulfur for DoD and Industry applications. In addition, the PEPS® can be used to produce only hydrogen gas instead of syngas for fuel cell or transportation applications.

Introduction

History of Plasma Energy Technology. Plasma energy technology has been studied since the 1960's. The technology was originally developed for the aerospace industry to simulate the reentry conditions of space vehicles. The technology was also used by the specialty metals industry to produce high purity metals. During the 1980's, the Government funded considerable research to apply this technology for treating the most difficult-to-treat wastes produced by our society. There is high interest in plasma energy technology because of its ability to achieve temperatures near 10,000 degrees Celsius. Such high temperatures are sufficient to melt inorganic compounds and metals while thoroughly destroying all organic constituents.

Review PEPS® Technology and Prior Work. During the performance of an earlier Army funded task, the PEPS® was used to demonstrate positive Demonstration/Validation test results on the treatment of three surrogate waste streams. Tests were performed to measure both performance and environmental benefits. The National Defense Center for Environmental Excellence (NDCEE) provided monitoring and coordination support. EnerSol Technologies Inc. housed operated the demonstration unit that was designed and built from an earlier Army project. The results of the high-temperature gasification process were independently validated by the NDCEE, Weston Solutions, and outside laboratories. Building on the success of the original PEPS® task, the Army tasked the NDCEE/EnerSol team to design a PEPS® that could demonstrate energy recovery opportunities**.**

Process Description

Process Flow Diagram. The Process Flow Diagram for the Clean Fuels PEPS® is shown in Figure 1. The major process operations include: petcoke preparation and feeder systems, reactor vessel, plasma torch, slag removal, solids removal, energy recovery, syngas purification, and pressurization of the syngas to be delivered to the F-T processing unit.

Design Capacity and Estimated Syngas Production. The design of the prototype unit has been established for a petcoke feed rate of 25 tons per day. Steam will be added to the reactor vessel to provide a source of hydrogen because petcoke has very low hydrogen content. In addition, oxygen gas is added to provide a source of oxygen for conversion to the carbon monoxide and dioxide. This system is designed to produce about 1,700 scfm of clean syngas.

System Description

Feedstock Handling. The feedstock handling equipment will provide crushing, screening, safe movement and feeding of the petcoke at the site. Safety and performance issues require: movement of the petcoke from the storage site to the feedstock handling without producing dust or particulate emissions, reduction of the size of the petcoke to meet the conversion required in the reactor, weighing the petcoke to establish actual throughput, and a means to physically introduce the waste into the reactor.

Plasma Reactor. The plasma reactor is designed to maximize petcoke conversion while minimizing fine particulate carryover with sufficient volume and gas phase residence time for petcoke conversion to syngas. Sufficient volume and residence time will be provided for the vitrification of inorganic components of the petcoke, which is tapped from the molten slag bath at the bottom of chamber. The selected inside lining material (refractory) will be designed to withstand a maximum processing chamber temperature of about 1650° Celsius and the corrosive nature of the gases produced. The reactor will have several penetrations/openings for torch mounting, solid feed, preheat burner, view ports, slag tap, exhaust gas discharge, and instrumentation. The steel and refractory will be designed to meet mechanical strength requirements.

Plasma Heating System (PHS). The plasma torch contained in the Plasma Heating System (PHS) provides the energy to produce the high temperature required for destruction of organic materials and the melting of inorganic materials. Design features of the PHS include: interface with the refractory-lined reactor, capability of remote operation, compatibility with both highly organic and inorganic components of petcoke, and ability to deliver heat energy to the reaction chamber in a safe manner. The PHS includes components such as a power supply, an arc starter, a plasma arc torch, a torch positioning system, a plasma gas supply, and a torch cooling system. The PHS torch is compatible with the processing chamber operating conditions and gas environment and is of appropriate size and power rating to process both the organic and inorganic components. In addition the PHS was designed to minimize operating costs and emissions, has high turn down capabilities, operates at lower loads, operates reliably with long life

and minimal maintenance, and has high thermal efficiency (low heat losses).

Solids Removal. According to process model calculations, approximately 20 lbs/hr of particulate matter exits the reactor in the syngas stream. This amount of particulate matter is excessive for the efficient operation of energy recovery equipment and will be reduced significantly from the gas stream before entering a heat exchanger.

Energy Recovery. Energy recovery operations will be utilized to recover a percentage of the heat energy available in the raw syngas stream. The energy could be used to produce electricity for the torch or for oxygen production. Water or steam is required as a process additive to the reactor to achieve optimum conversion of the petcoke to syngas. The simplest form of energy recovery is accomplished by producing superheated steam. This reduces the energy required by the plasma torch. The heat recovery system is designed to withstand 1,100°C syngas temperature, produce superheated steam, cool the syngas to approximately 370°C, function reliably with minimal downtime, accommodate the particulate loading in the syngas, and resist corrosion from contaminants in the syngas.

Syngas Purification. The syngas purification system is designed to purify or clean the syngas produced in the PEPS® reactor to meet the purity requirements of the F-T process. In addition, any by-products, such as wastewater, must meet applicable emissions limits, which are determined by the site, and both local and state requirements. The overall performance of the syngas purification system is driven by gas flow, gas composition, temperature and pressure. The expected conditions at the inlet to the syngas purification system are 1,700 scfm of syngas at a temperature of 1,370 degrees Celsius with a pressure requirement of either atmospheric or 50 pounds per square inch (psi). The Syngas Purification system will perform a variety of functions during systems operation including the removal of carbon, inorganic oxides, and heavy metal particulates. Some of these particulates are detrimental to the downstream catalyst bed. In addition, no particulate is desirable in the F-T process. The purification system is designed to remove sulfur compounds and nitrogen, both of which are detrimental to the life of the catalyst bed. Acid gases such as HCl may be present in small quantities and must also be removed.

Control Logic. The control system is being designed and configured to ensure safe and reliable operation of the equipment and subsystems using robust industrial computers. The hardware architecture and software configuration employ modular structures for ease of troubleshooting and maintenance. The control strategies, interlocks, and sequences are being developed with input from equipment suppliers and independent reviewers. A Hazard and Operability (HAZOP) review will be performed on this system, to ensure robust, reliable and fail-safe operations.

Syngas Pressurization. To meet the pressure requirement of the F-T process, the syngas must be compressed after exiting the syngas purification system. If the syngas is partially pressurized prior to the syngas compression equipment, the size of the reactor and other equipment will be reduced and compression (capital and operating costs) will be less expensive. The syngas compression equipment will be required to provide clean syngas to the F-T process that could operate at pressures of from 300-500 psia depending on the catalysts used in the F-T process. Compression of gases containing hydrogen is difficult due to the effects that hydrogen has on most metals. These effects are metal dusting and hydrogen embrittlement, which are detrimental to most metals and have a tendency to reduce the life of equipment. Therefore, the syngas compression equipment must be compatible with hydrogen gas.

Advantages of Using PEPS® Technology for Petcoke Gasification. The main drivers behind this technology are:

- PEPS® technology can convert low value by-products from oil refineries into clean syngas
- The clean syngas can be used to produce clean fuels
- Production of alternate clean fuels is essential to maintaining national security
- PEPS® technology has been proven to be effective for treatment of hazardous wastes and Risk Reduction Testing is planned to evaluate the amount and quality of syngas produced from petcoke samples or surrogates.
- All emissions are controlled. Off-gases meet Clean Air standards, wastewater is treated for safe discharge, and residual slag passes Toxicity Characteristic Leaching Procedure (TCLP) standards.

Acknowledgements. This project is being conducted by the NDCEE, which is managed by the Office of the Assistant Secretary of the Army (Installations and Environment) and operated by Concurrent Technologies Corporation. EnerSol Technologies, Inc. is providing system design. The Headquarters Department of Energy is providing Technical Monitoring.

Disclaimer. The views, opinions, and/or findings contained in this paper are those of the authors and should not be construed as an official Department of Army position, policy, or decision unless so designated by other official documentation.

Reference

Energy Information Administration, Annual Energy Outlook 2005, http://www.eia.doe.gov/oiaf/aeo/overview.html, 4/25/05

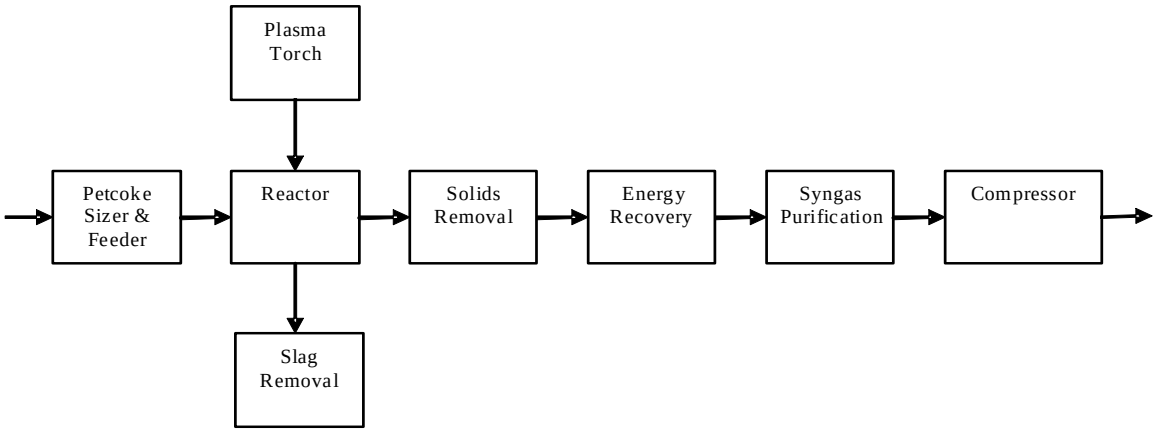

Figure 1. Process Flow Diagram

SCREENING OF POTENTIAL O-RING SWELLING ADDITIVES FOR ULTRA-CLEAN TRANSPORTATION FUELS

John P. Baltrus[1], Dirk D. Link[1], Paul H. Zandhuis[2], Robert J. Gormley[1]

[1] U.S. Department of Energy, National Energy Technology Laboratory, P.O. Box 10940, Pittsburgh, PA 15236-0940

[2] NETL Site Support Contractor, Parsons RDS, P.O. Box 618, South Park, PA 15129

Introduction

The primary components of Fischer-Tropsch (F-T) fuels are typically linear and branched alkanes.[1] As such, they will require additives in order to exhibit the properties of their petroleum-derived counterparts that are critical for use in transportation applications. Among the most important properties are lubricity and seal swelling capability.[2-4] A near-term solution to the seal swelling and lubricity deficiency of F-T fuels is blending the F-T fuel with conventional petroleum-derived feedstocks.[4] Unfortunately that solution negates many of the benefits derived by using a pure ultra-clean transportation fuel. For the same reason, addition of sulfur compounds, which would induce the desired lubricity properties, is not an option. Therefore other classes of compounds, specifically aromatics and oxygenates, are being investigated as additives to induce the desired properties. This study specifically deals with attempts to determine which classes of compounds are most efficient at promoting nitrile rubber o-ring swelling. Of particular interest is the determination of what specific compounds induce the greatest amount of swelling per unit weight or volume.

Experimental

Swelling studies. The swelling properties of the fuels were measured using ASTM Methods D-1414 and D-471. The o-rings used in the studies were buna-N (nitrile) N0602-70, obtained from Parker Seals, and having an o.d. and thickness of approximately 1.9 mm and 0.3 mm, respectively. Measurements were simultaneously conducted on three o-rings, as prescribed by the ASTM methods, in approximately 40 mL of fuel with an immersion time of 48 hours.

Extraction of Fuels. Extractions were performed using methanol in a procedure that has been previously described.[5] Briefly, the methanol-soluble components were extracted from the fuel and recovered in the methanol layer. This layer was isolated either for direct analysis or was further processing to isolate target analytes from co-extracted components using an HPLC separation method.[5]

Compositional Analysis. Analysis was performed with an Agilent GC-MS system (Agilent 6890 GC coupled to an Agilent 5973 Mass Selective Detector). Depending on the information desired, either a 100% non-polar column (Petrocol-DH 50.2, Supelco) or a polar column (Stabilwax-DA, Restek) was used. The polar column was used primarily for the analysis of extracts to help isolate polar components from the non-polar bulk matrix. Peak identification was performed using Agilent's ChemStation processing software against an NIST library of compounds, with additional confirmations obtained using the AMDIS software package.

Results and Discussion

Base measurements were conducted on petroleum-derived and F-T diesel and jet fuels. The results are reported in Table 1. As expected, the petroleum-derived fuels provided excellent seal swelling while the F-T fuels yielded poor swelling results.

Table 1. Swelling Results for Nitrile Rubber O-Rings in Various Fuels

Fuel	Volume Change (%)
Diesel – BP	16.2 ± 0.4
JP-5	14.0 ± 0.3
F-T Diesel	0.8 ± 0.1
F-T Jet (S-5)	0.6 ± 0.0
S-5 + 10% EI-037	8.5 ± 0.2
S-5 + 15% EI-037	13.6 ± 0.1
S-5 + 25% EI-037	25.4 ± 0.3
S-5 + 15% Aromatic 150	9.6 ± 0.5

A previous study attempted to determine the appropriate levels for spiking a synthetic jet fuel (S-5) with an aromatic-containing jet fuel (JP-5) or surrogate to induce acceptable levels of swelling of nitrile rubber o-rings.[6] It was determined that it required a greater volume of an aromatic solvent mixture, Aromatic-150 (ExxonMobile), to induce a given level of swelling than it did a petroleum-derived jet fuel to induce the same (or greater) degree of swelling. Specifically, a 30 % blend of Aromatic-150 in S-5 was required to induce the same degree of swelling that a 20 % blend of JP-5 in S-5 induced.[6] These results indicated that while aromatic species are able to induce swelling, some species (or combination of species) present in the petroleum-derived fuel were more proficient in swelling than the aromatic species in the Aromatic-150 solvent.

The S-5 jet fuel was blended with various concentrations of the Aromatic-150 solvent and a highly-aromatic coal-derived jet fuel precursor, EI-037 (Energy Research Institute, Pennsylvania State University), to determine what amount of blending agent would be required to achieve the swelling level imparted by a JP-5 fuel. The results are reported in Table 1. At least 15 volume percent of the blending agents was found to be required, with the coal-derived jet fuel having the greatest impact on swelling.

A comparison of Aromatic-150 and JP-5 was made using GC-MS with a 100% non-polar analytical column. The results showed that the region of overlap between Aromatic-150 and JP-5 ended at approximately the point where dodecane eluted. Therefore, it was inferred that whatever similar compounds in the two liquids may be responsible for swelling had to be present in the lower-boiling fraction of the petroleum-derived fuel.

The JP-5 fuel was then fractioned at specific cut-points to yield fractions with different classes of organic compounds in an effort to determine which classes of compounds induced the most swelling. For instance, the fraction of a JP-5 fuel with boiling point less than that of dodecane (212°C) induced considerably more swelling of nitrile rubber o-rings than the fraction with boiling point greater than 212°C (16.4 % vs. 9.2 %). The lower boiling fraction primarily contained single-ring aromatic compounds (alkylbenzenes), a small amount of naphthalene, and alkyl phenols, which are suspected swelling agents.

Another attempt to identify the species contained in JP-5 that may be responsible for swelling was made by conducting switch-loading tests. The nitrile o-rings were swelled in JP-5 fuel and then transferred to a synthetic S-5 fuel where the o-rings subsequently shrunk. It was assumed that the shrinking released a representative combination of the components of the JP-5 fuel that were previously absorbed by the o-rings. The components released into the S-5 fuel were then determined using methanol extraction followed by GC-MS analysis. The most prominent oxygenates were diethylene glycol

monomethyl ether (diEGME) and diethylene glycol monobutyl ether (diEGBE). Other species detected included naphthalene and two methylnaphthalene isomers. The GC-MS chromatogram for the extract is shown in Figure 1.

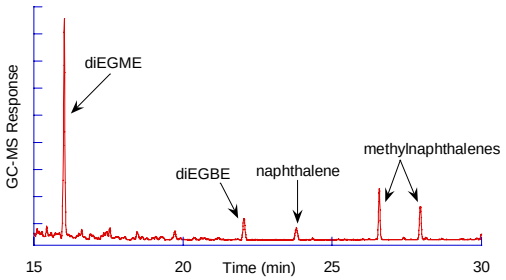

Figure 1. GC-MS analysis of a methanol extract of S-5 fuel after switch-load testing of o-rings immersed in JP-5 followed by immersion in S-5.

Both oxygenates were then tested separately for their ability to promote swelling of nitrile o-rings by spiking them at the 1% volume level in the S-5 fuel. The data in Table 2 indicated that both diEGME and diEGBE yielded poor swelling results. Others have tested the same compounds using optical ellipsometry to measure the degree of o-ring swelling and have reported a higher degree of sweling. The reason for the discrepancy is not understood, although the history of nitrile rubber may play a role in its susceptibility to swelling.

The coal-derived jet fuel precursor was characterized using an extraction method followed by GC-MS analysis to determine the most prominent aromatic compounds in the fuel. The results showed that naphthalene and naphthalene analogues were present in high concentrations. Naphthalene and some of its analogues were then tested as swelling agents at the 1% level in a synthetic S-5 jet fuel. The results are reported in Table 2. The compounds yielded very little swelling at that concentration, although additional tests of naphthalene at higher concentrations induced somewhat more swelling.

Based on the work of others[7], it was decided to further explore the use of Hansen Solubility Parameter (HSP) matching to predict which solvents would work best at inducing swelling in nitrile rubber. The solubility parameters are part of an approach for predicting polymer solubility based on the theory that the cohesive energy of a liquid is comprised of several individual forces. The main forces are D (dispersion), P (dipole interactions), and H (hydrogen bonding). Maximum solubility for the polymer is predicted when the D, P and H factor values are similar for the polymer and solvent. The HSP Handbook[8] was scanned for solvents whose parameters most closely matched those of nitrile rubber. Compounds containing sulfur and nitrogen functionalities were ignored because they would likely negate the environmental benefits of moving to ultra-clean fuels. Of the compounds that remained, the best HSP matches were found for oxygenates such as organic carbonates, lactones, plus select aldehydes, ketones and alcohols. Solubility issues were encountered with some of the compounds; specifically with those having a high hydrogen bonding factor. Results are reported in Table 2 for the compounds that were tested. It can be plainly seen that except for a couple of compounds, the enhancement in nitrile o-ring swelling was negligible.

Table 2. Swelling Results for Nitrile Rubber O-Rings in F-T Jet Fuel (S-5) Spiked With Various Organic Compounds

Fuel	Volume Change (%)
S-5 + 1% diEGME	1.7 ± 0.1
S-5 + 1% diEGBE	1.8 ± 0.1
S-5 + 1% (wt) Naphthalene	1.2 ± 0.2
S-5 + 6.4% (wt) Naphthalene	7.9 ± 0.3
S-5 + 1% Tetralin	0.9 ± 0.0
S-5 + 1% Decalin	0.8 ± 0.1
S-5 + 1% Propylene Carbonate	1.9 ± 0.2
S-5 + 1% Ethylene Carbonate	1.1 ± 0.2
S-5 + 1% Vinylene Carbonate	1.8 ± 0.2
S-5 + 1% γ-butyrolactone	2.4 ± 0.1
S-5 + 1% ε-caprolactone	4.6 ± 0.0
S-5 + 1% acetyl-acetone	2.6 ± 0.1
S-5 + 1% Allyl Alcohol	6.0 ± 0.1
S-5 + 1% Tiglic Aldehyde	2.3 ± 0.1
S-5 + 1% Methyl Vinyl Ketone	2.9 ± 0.1
S-5 + 1% Phenol	15.4 ± 0.4
S-5 + 1% 1,2,3,4-tetrahydro-1-naphthol	4.6± 0.0
S-5 + 1% 5,6,7,8-tetrahydro-1-naphthol	7.3 ± 0.2
S-5 + 1% 2-tert-butyl Phenol	8.9 ± 0.0
S-5 + 1% 2,4-dimethyl Phenol	12.8 ± 0.2
S-5 + 1% 2-ethyl Phenol	13.5 ± 0.2

The initial pretext for looking more closely at HSP matching to predict which compounds would be most active for o-ring swelling was the very good swelling that was observed for nitrile rubber when phenol was added to S-5.[8] It was observed that the HSP for phenol was fairly close to that for nitrile rubber and therefore it was suggested that the HSP might be a good predictor of nitrile solubility (swelling). Because phenol yielded such favorable swelling results, along with the fact that previous analyses of JP-5 fuel indicated that the most abundant oxygenates in the fuel were alkylphenols, it was decided to examine other phenol analogues. The results are reported in Table 2. All the phenol analogues yielded enhanced swelling. The relative degree of swelling was the least when two-ring structures were used and when a tert-butyl group was added to the phenol. A greater degree of substitution on the ring also yielded progressively poorer results compared with a non-substituted phenol, indicating that perhaps steric effects outweigh electronic effects in determining the ability of the phenol to induce swelling.

Conclusions

Through the use of switch-loading tests and an analytical method based on methanol extraction followed by GC-MS analysis, several possible compounds were identified for individual testing as possible swelling agents for synthetic fuels in contact with nitrile rubber. These compounds included naphthalenes and alkyl phenols. Another empirical method based on matching of Hansen Solubility Parameters also was used to identify additional candidate compounds to promote swelling of synthetic fuel. Of the compounds tested, phenol and its analogues provide the greatest degree of swelling per volume of the compound added to the fuel. Steric factors appear to limit the ability of the phenol analogues to promote swelling. Still to be examined is the possibility that synergistic effects may take place between certain classes of compounds.

Acknowledgement. The authors thank Richard Anderson for help with the GC-MS analysis and the U.S. Navy for providing the

JP-5 fuel. Reference to any specific commercial product, process or service is to facilitate understanding and does not imply its endorsement or favoring by the U.S. Department of Energy.

References

(1) Cookson, D. J; Smith, B. E. *Fuel* **1989**, *68*, 776.

(2) Anastopoulos, G.; Lois, E.; Zannikos, F.; Kalligeros, S.; Teas, C. *Fuel* **2002**, *81*, 1017-1024.

(3) Morgan, P.; Viljoen, C.; Roets, P.; Schaberg, P.; Myburgh, I.; Botha, J.; Dancuart, L. *SAE Technical Paper No. 982488* **1998**.

(4) Chang,, P. H.; Colbert, J. E.; Hardy, D. R.; Leonard, J. T. *Prepr. Pap.-Am. Chem. Soc., Div. Pet. Chem.* **2004**, *49* (4), 414-417.

(5) Link, D. D.; Baltrus, J. P.; Zandhuis, P. H.; Hreha, D. C. *Prepr. Pap.-Am. Chem. Soc., Div. Pet. Chem.* **2004**, *49* (4), 418-421.

(6) Harrison, W. III; Graham, J.; Minus, D.; Striebich, R. *results presented at the* Coordinating Research Council (CRC) Aviation Meeting, Alexandria, VA **2004**.

(7) Graham, J. L.; Striebich, R. C.; Minus, D. K.; Harrison, W. E. III *Prepr. Pap.-Am. Chem. Soc., Div. Pet. Chem.* **2004**, *49* (4), 435-439.

(8) Hansen, C. M. *Hansen Solubility Parameters, A User's Handbook*, CRC Press, Boca Raton, FL, 2000.

ITM CERAMIC MEMBRANE TECHNOLOGY TO PRODUCE SYNTHESIS GAS

Christopher F. Miller[1], Michael F. Carolan[1], Christopher M. Chen[1], Eric Minford[1], William E. Waldron[1], James J. Steppan[2]*

[1.] Air Products and Chemicals, Inc.
7201 Hamilton Blvd
Allentown, PA, 18195 USA

[2.] Ceramatec, Inc.
2425 South 900 West
Salt Lake City, UT, 84119 USA

Introduction

Air Products and Chemicals and its partners are developing Ion Transport Membrane (ITM) technology for the production of hydrogen and carbon monoxide (synthesis gas or "syngas"). The ITM Syngas process is a breakthrough technology that combines air separation and high-temperature synthesis gas generation processes into a single ceramic membrane reactor, with significant savings in the capital cost of synthesis gas production. Because synthesis gas is a feedstock for a range of different processes, ITM Syngas represents a technology platform that has numerous applications, such as hydrogen, clean fuels and chemicals.

Discussion and Results

ITM ceramic membranes are fabricated from non-porous, mixed-metal oxides and operate with exceptionally high oxygen flux and selectivity when exposed to an oxygen chemical potential gradient at high temperatures. A conceptualization of the ITM Syngas technology is shown in Figure 1. Oxygen from low-pressure air diffuses to the membrane surface where it adsorbs, dissociates and forms oxygen anions. The anions permeate through the dense ceramic membrane along the oxygen anion sublattice to the other side which contains high-pressure natural gas and steam. The oxygen anions are discharged into the reducing atmosphere and react with natural gas in a partial oxidation process to produce hydrogen and carbon monoxide. There is a balance flux of electrons through the membrane to complete the electrical circuit.

For the ITM Syngas process to be commercially viable, the membrane must have sufficient creep resistance, mechanical strength and thermodynamic stability in air, syngas and any contaminant environments. The family of materials which has been carefully designed to meet these requisite properties is perovskites with the formula $(La_{1-x}Ca_x)_yFeO_{3-\delta}$ where $0<x<0.5$, $y>1.0$ and δ makes the compound charge neutral. For example, Figure 2 shows the bending creep rate as a function of the A/B ratio, y, along with the grain size, for our ITM Syngas composition. The creep rate decreases by a factor of 2 as the A/B ratio increases from <1.0 to >1.0. This is notable since the test specimen for A/B>1.0 had smaller grain size, and the creep rate can increase significantly with decreasing grain size. Therefore, lower creep rates and longer membrane life can be obtained by using A/B>1.0 for the ITM Syngas materials.

Planar thin-film membranes with a microchannel design have also been fabricated from these materials that provide remarkable pressure handling capability and meet mechanical strength criteria, Figure 3. These membranes have achieved stable, high oxygen fluxes under process conditions due to their thin film structure and thermodynamic stability. Furthermore, as shown in Figure 4, commercial flux targets have been achieved with these membranes by meeting the aforementioned requisite properties, and also by advancing the reactor design to eliminate potential membrane contaminants.

This paper describes the development of the ITM Syngas ceramic membrane and the development of the reactor design, resulting in stable oxygen fluxes at our commercial target. Recent laboratory and pilot unit test results will be discussed, which will include oxygen flux data, an overview of reactor design modifications, and a comparison of membrane microstructure before and after flux testing.

Conclusion

Significant progress has been made in designing and manufacturing planar ceramic membranes, and in demonstrating targeted membrane oxygen fluxes, which are necessary steps toward commercializing the ITM Syngas technology. The potential economic benefits of the technology continue to be very promising.

Acknowledgements. The authors gratefully acknowledge the work of ITM Syngas team members at Air Products and Chemicals Inc., Ceramatec Inc., ChevronTexaco Energy Research and Technology Co., Norsk Hydro, Eltron Research Inc., SOFCo-EFS Holdings LLC, Penn State University, University of Pennsylvania, and Pacific Northwest National Lab. The co-funding by the U.S. DOE (DE-FC26-97FT96052) is also gratefully acknowledged.

Disclaimer

This paper was written with support of the U.S. Department of Energy (DOE) under Cooperative Agreement DE-FC26-97FT96052. The Government reserves for itself and others acting on its behalf a royalty-free, nonexclusive, irrevocable, worldwide license for Governmental purposes to publish, distribute, translate, duplicate, exhibit and perform this copyrighted paper.

Neither Air Products and Chemicals, Inc. nor any of its contractors or subcontractors nor the DOE, nor any person acting on behalf of either: 1. Makes any warranty or representation, express or implied, with respect to the accuracy, completeness, or usefulness of the information contained in this report, or that the use of any information, apparatus, method, or process disclosed in this report (Technology) may not infringe privately owned rights; or 2. Assumes any liabilities with respect to the use of, or for damages resulting from the use of such Technology.

Reference herein to any specific commercial products, process, or service by trade name, trademark, manufacturer, or otherwise, does not necessarily constitute or imply its endorsement, recommendation, or favoring by the DOE. The views and opinions of authors expressed herein do not necessarily state or reflect those of the DOE.

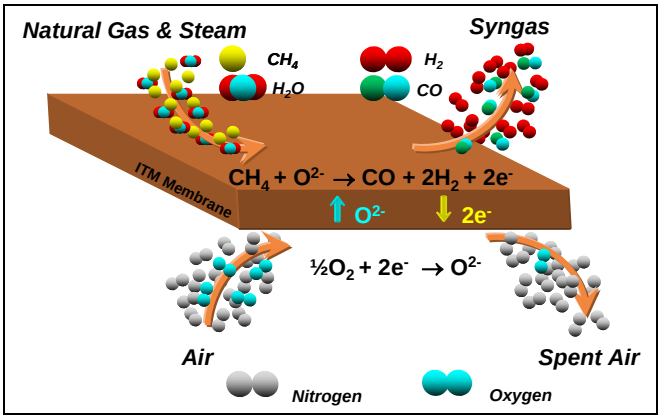

Figure 1. Conceptual ITM Syngas Technology.

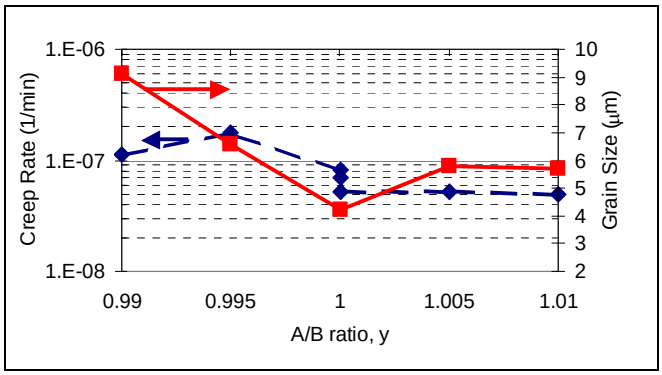

Figure 2. Creep rate as a function of A/B ratio, y.

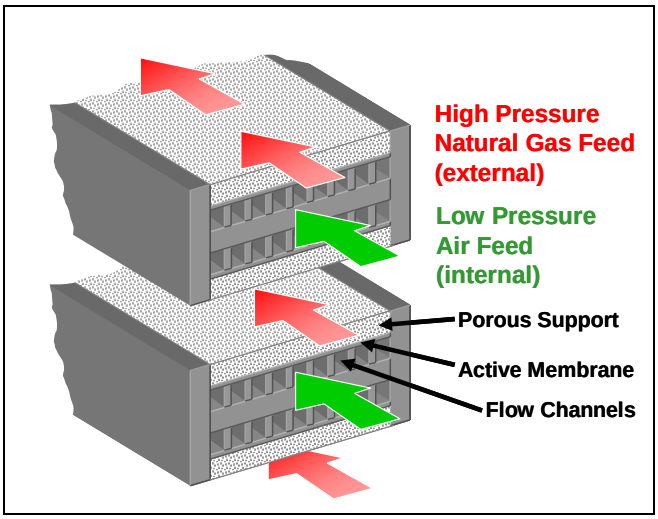

Figure 3. Planar ITM Syngas membrane.

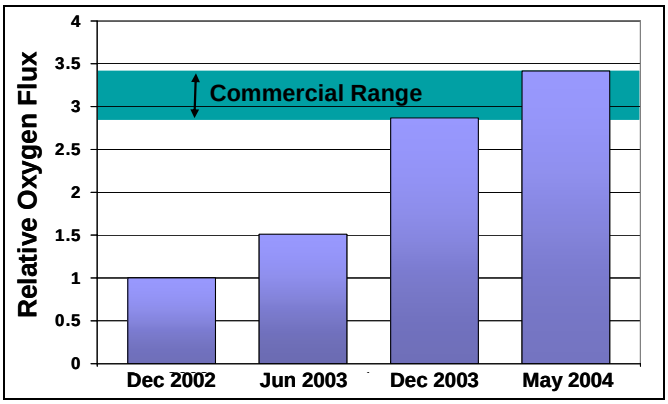

Figure 4. Advancement in oxygen flux performance.

THE EFFECT OF CO, H_2S AND H_2O ON THE HYDROGEN PERMEANCE OF PD-CU ALLOY MEMBRANES

Anthony Cugini, Bret Howard, Bryan Morreale, Osemwengie Iyoha, and Robert Enick

National Energy Technology Laboratory
U.S. Department of Energy
P.O. Box 10940
Pittsburgh, PA, 15236-0940

Introduction

Hydrogen is primarily produced through steam reforming of hydrocarbons or from coal gasification. Hydrogen production from coal gasification can provide a transition to the hydrogen economy as a result of the large volume of produced hydrogen in addition to the large volume of carbon monoxide, which can be further directed to a shift reactor to increase the hydrogen yield. Conventional methods of hydrogen production from hydrocarbons produce hydrogen with other gaseous components such as CO, CO_2, H_2O, H_2S and various other side reaction products from which hydrogen must be purified.

Robust, dense, metal membranes, such as Pd-Cu alloys, have the potential to separate and purify hydrogen from impure gas mixtures. An important application of membranes would be the implementation to in-situ and post-gasifier applications. Figure 1 illustrates one example of a membrane technology integrated into a gasifier application to enhance hydrogen production.

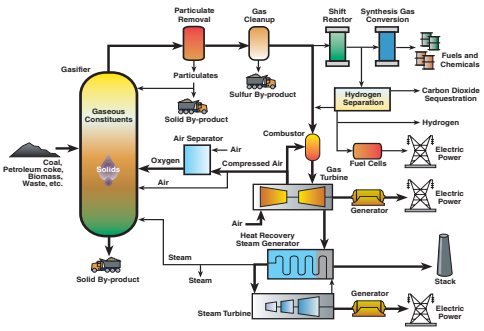

Figure 1. Integration of a hydrogen separation membrane into a gasifier application for the production of ultra-pure hydrogen from a coal-based gasification process.

Studies have shown that the integration of hydrogen membrane separation technologies into a gasification application improves the overall efficiency of the process as well as reduces the ultimate cost of the hydrogen product.[Parsons, 2003] However, the presence of various gaseous compounds may adversely affect the performance of metal membrane separations in these applications. For example, the presence of CO and H_2O in a H_2 feed stream was reported to reduce H_2 permeance through a Pd-Ag membrane by 40% and 70%, respectively [Hou, 2003]. Additionally, H_2S has been shown to diminish the permeance of Pd membranes [Edlund, 1993; ,McKinley, 1967; Edlund, 1994; Kajiwara, 1999]. Several research groups – including NETL – are exploring the viability of palladium alloy membranes (e.g. Pd-Cu) for gasifier and post-gasifier water-gas shift (WGS) membrane reactors and separators because of the relatively high hydrogen permeance of these alloys [Howard, 2004] and the H_2S-tolerance previously reported [Morreale, 2004; Edlund, 1993; McKinnley, 1967].

Results and Discussion

NETL has developed a Hydrogen Membrane Test (HMT) Unit for evaluating the performance of hydrogen separation membranes at elevated temperatures and pressures. This system is described in detail in previous publications [Howard, 2004; Morreale, 2004].

The viability of an 80wt%Pd-20wt%Cu alloy to purify hydrogen in the presence of impurities was assessed in the HMT by conducting diffusion experiments (of relatively thick membrane samples, generally between 100 and 1000 microns) in the presence of CO and H_2O at high-temperature and high-pressure conditions characteristic of a gasifier outlet stream, e.g. pressures up to 1.5 MPa and temperatures up to 1273 K [Iyoha, 2004]. The results for permeance of the membrane in the presence of equal volume mixtures of H_2-H_2O and H_2-CO are presented in Figure 2.

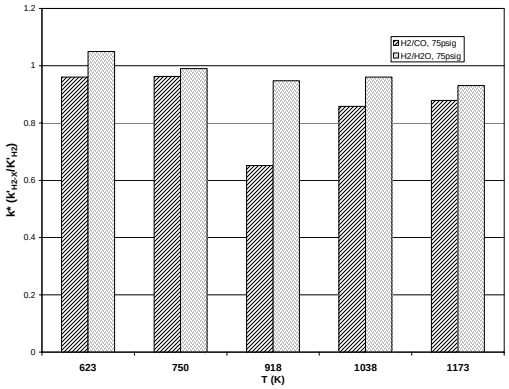

Figure 2. Impact of equal volume mixtures of H_2-CO and H_2-H_2O on the hydrogen permeance of the 80wt%Pd-20wt%Cu alloy at 75 psig. k*, a normalized performance value, is equal to permeance (mols/m^2/s/$pa^{0.5}$) in the presence of the mixed gas stream (H_2-CO or H_2-H_2O) divided by permeance in the presence of a neat H_2 feed.

Even though the membrane appears to be negligibly impacted by the presence of H_2O, SEM images revealed a significantly roughened membrane surface after H_2O exposure. Similarly, the membrane appears to tolerate the presence of CO in the feed gas, evident by the results illustrated in Figure 2.

Overall, the results indicate that H_2O has a negligible influence on membrane permeance, while the presence of CO is observed to slightly influence membrane permeance. This is most pronounced at 918 K where the Boudouard reaction ($2CO = C + CO_2$) is favored. The appreciable reduction in permeance (at 918 K) may be attributed to the significant deposition of carbon on the membrane surface at this temperature. However, it should be noted that the membranes operated stably for more than 720 hours in the presence of each of these contaminants. Additional testing is planned to investigate the effect of test conditions on the membrane surface. Furthermore, surface morphological changes of membrane candidates in the presence of harsh gasifier contaminants are currently being assessed. Analytical techniques, such as SEM/EDS, XPS and XRD analyses, are being used to evaluate the influence of contaminants on surface composition of alloy membranes candidates.

Previous published work had shown that Pd-Cu alloys of the right composition and right crystalline phase have the potential to operate in the presence of 1000ppm H_2S with negligible decreases in flux [Kamakoti, 2005]. In that paper, we reported that fcc-phase Pd-Cu alloys are resistant to sulfur in the gas phase (see Figure 3).

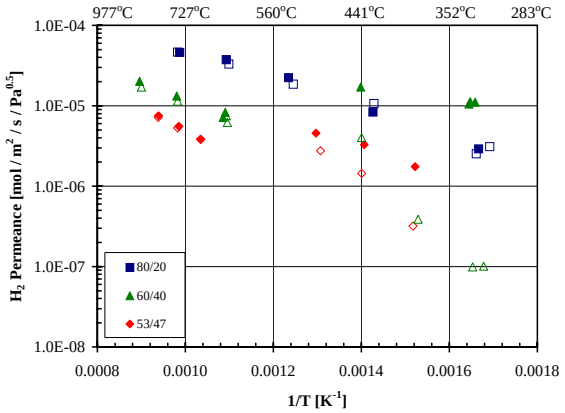

Figure 3. Permeance results of several palladium-copper alloys tested in the presence of 1000ppm H_2S as a function of temperature. Solid shapes represent results in the presence of neat hydrogen while open shapes represent the results in the presence of hydrogen-sulfide. Legend values are represented by: weight % palladium/weight % copper.

Currently, we are exposing coupons of Pd-Cu alloys (0, 53, 60, 80, and 100% Pd) to a flowing stream of H_2 with 1000 ppm H_2S to temperatures of 623 to 973K for different durations (1 h, 12 h, 25 h, and 7 days). These coupons are being analyzed by the aforementioned analytical techniques as well as gravimetric changes in an effort to characterize the effect of sulfur exposure on the alloy. The initial tests have already shown that each of the duration of sulfur exposure and the temperature can effect the surface composition, sulfur deposition, crystalline phase and morphology depending on the combination of time of exposure, temperature, and alloy composition. Additional tests are underway.

Conclusion

Pd alloy membranes have the potential of tolerating the impurities present in the production and separation of hydrogen from coal gasification processes. The impurities do appear to impact the surface for contaminant tolerant alloys but not in such a way as to significantly reduce the measured hydrogen flux.

Acknowledgement. This work was supported by the U.S. Department of Energy's Office of Fossil Energy

References

1. Edlund, Friesen, Johnson, Pledger, Gas Pur. and Sep. 8, 131 (1994).
2. Edlund, Pledger, J. Mem. Sci., 77 (1993) 255-264.
3. Hou, et al., Journal of Membrane Science 214, (2003) 43.
4. Howard, et al., Journal of Membrane Science 241, (2004) 207.
5. Iyoha et al., AIChE Spring Meeting, Atlanta, GA, 04, 05.
6. Kajiwara, Uemiya, Kojima, Int. J. of Hydrogen Energy, 24 (1999) 839-844.
7. McKinley, Nitro, US Patent, 3,350,845 (1967).
8. Morreale, et al., Journal of Membrane Science 241, (2004) 219.
9. Kamakoti et al., Science, 307, 569 (2005).
10. Parsons. "Hydrogen Production Facilities - Plant Performance and Cost Comparisons," Final Report to DOE, Contract No. DE-AM26-99FT40465 (2002).

Disclaimer

Reference in this paper to any specific commercial product, process, or service is to facilitate understanding and does not necessarily imply its endorsement or favoring by the United States Department of Energy.

DIRECT DECOMPOSITION OF METHANE TO HYDROGEN ON METAL LOADED ZEOLITE CATALYST

Lucia M. Petkovic, Daniel M. Ginosar, Kyle C. Burch, and Harry W. Rollins

Idaho National Laboratory
P.O. Box 1625
Idaho Falls, ID 83415-2208

Introduction

The manufacture of hydrogen from natural gas is essential for the production of ultra clean transportation fuels. Not only is hydrogen necessary to upgrade low quality crude oils to high-quality, low sulfur ultra clean transportation fuels, hydrogen could eventually replace gasoline and diesel as the ultra clean transportation fuel of the future. Currently, refinery hydrogen is produced through the steam reforming of natural gas. Although efficient, the process is responsible for a significant portion of refinery CO_2 emissions. This project is examining the direct catalytic decomposition of methane over a metal modified zeolite catalyst as an alternative to steam reforming. The energy required to produce one mole of hydrogen is slightly lower and the process does not require water-gas-shift or pressure-swing adsorption units. The decomposition process does not produce CO_2 emissions and the product is not contaminated with CO – a poison for PEM fuel cells.

Experimental

The acid form of a commercially available zeolite was co-impregnated with two metal precursors by the incipient wetness technique. The material was dried at 393 K for 2 hs. Five hundred milligrams of the dried material were loaded in a tubular quartz reactor, calcined under flowing air (Zero grade, US Welding) for 4h at 873 K, then for 0.5 h at 973 K, and reduced under flowing hydrogen for 0.5 h at 573 K. The temperature was increased to reaction temperature and a flow of 20 cm^3/min of pure methane (99.99%, Scott Spelcialty Gases, PA) was initiated. Product yields as a function of time on stream (TOS) were measured on a Hewlett Packard 5890 gas chromatograph equipped with both FID and TCD detectors and Carboxen 1010 Plot and Petrocol columns.

To regenerate the catalyst, a flow of air was passed for 1 h through the catalyst bed kept at 873 K. A second set of experiments was performed over the regenerated catalyst.

Catalyst characterization. B.E.T. surface areas and micropore volume were determined on a Quantachrome Autosorb 1-C apparatus at liquid nitrogen temperatures. The carbonaceous material deposited on the catalyst was characterized by temperature-programmed oxidation (TPO) on a Perkin Elmer Diamond TG/DTA microbalance under 100 ml/min flowing air. About 10 mg of sample were placed in the balance pan and heated from room temperature to 1073 K at 10 K/min. Transmission electron microscopy analyses were performed on a Philips EM 420 at 120kV.

Results and Discussion

Hydrogen yields as a function of TOS at different reaction temperatures are shown on Figure 1. Other reaction products (not shown) included benzene and higher aromatics. At 873 and 973 K the production of hydrogen was relatively stable but at 1073 K a marked decrease was apparent.

The catalyst samples were regenerated in flowing air at 873 K. This temperature was chosen to avoid volatilization of metal oxide species during regeneration. After regeneration, catalyst activity was recovered. However some loss was apparent particularly on the catalyst utilized at the highest reaction temperature. This loss of activity after regeneration may be ascribed to some carbonaceous deposits that may remain on the catalyst surface after regeneration.

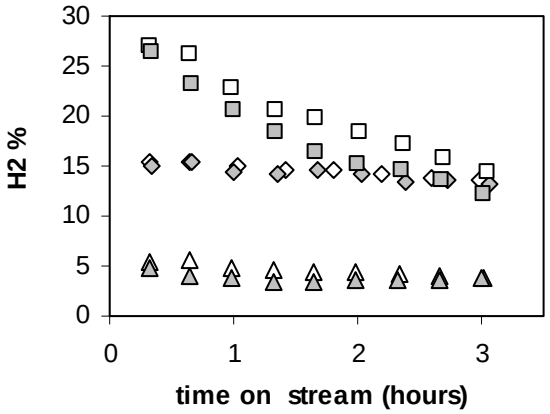

Figure 1. Hydrogen yields at 873 (triangles), 973 (diamonds), and 1073 K (squares) as a function of TOS. Hollow and filled symbols correspond to first and second set of reaction experiments, respectively.

Carbonaceous deposits were confirmed by the TPO studies as shown in Figure 2. The carbonaceous species deposited on the catalyst surface were more condensed as the reaction temperature increased, as expected. This is inferred from the higher temperatures necessary to oxidize and decompose the carbonaceous deposits during the TPO experiments. The carbonaceous deposits on the catalyst sample utilized at 873 K had desorbed completely at 873 K. However, temperatures as high as 973 K were necessary to desorb the carbonaceous material from the sample utilized at 1073 K.

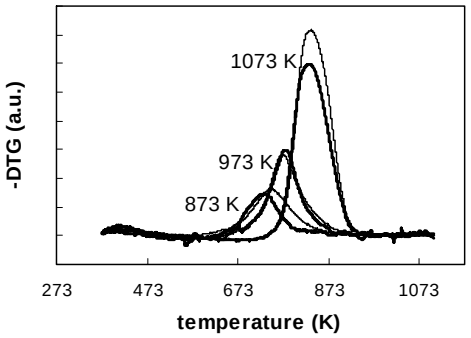

Figure 2. TPO profiles. Reaction temperatures are indicated. Thin and thick lines correspond to first and second set of reaction experiments, respectively.

For the TOS utilized in this study, the catalyst retained a high portion of its initial surface area and micropore volume as shown in Table 1. Transmission electron microscopy analyses showed a homogenous covering of the zeolite surface with carbonaceous deposits.

Table 1. Nitrogen Physisorption and TPO Results

Sample	BET SA (m^2/g)	MPV (cm^3/g)	% C
Fresh	403	0.12	–
873 K	407	0.13	3.1
973 K	310	0.10	4.5
1073 K	216	0.07	11.1

Li et al.[1] have reported that zeolite-supported nickel catalysts when utilized until complete deactivation produced 119 and 480 mol H_2/mol Ni, for ZSM5 and MCM22, respectively. The catalyst studied here deactivated slowly during long-term experiments and even at 30 h TOS the percentage of hydrogen was still above 6%. In this case, the integrated production was about 1200 mol H_2/mol metal, which indicates a more favorable hydrogen production.

Conclusions

A favorable production of hydrogen from direct decomposition of methane was found on the catalyst studied here, when compared with nickel-zeolite supported catalysts. Reaction temperature had a strong influence on catalyst regeneration. The catalyst utilized at 873 and 973 K could be regenerated without any significant loss of activity by calcination in air at 873 K. When the catalyst was utilized at 1073 K, a faster decrease in activity was found and the recovery of activity by regeneration was lower.

Acknowledgement. This work was supported by the U.S. Department of Energy Office of Fossil Energy under DOE Idaho Operations Office Contract DE AC07 05ID14517.

References

(1) Li, J.; Lu, G.; Li, K.; Wang, W. *J. Molec. Catal. A* **2004**, *221*, 105.

EFFECT OF ULTRASONIC IRRADIATION ON ENZYMATIC TRANSESTERIFICATION OF WASTE OIL TO BIODIESEL

Hong Wu, Min-hua Zong

Biotechnology Department, South China University of Technology, Guangzhou 510640, P. R. China

Introduction

Biodiesel(long-chain monoalkyl fatty acid esters), a renewable and green fuel, is made from vegetable or animal fats. At present, the high cost of biodiesel, of which the raw material amounts to 75%, prohibits its wide application. Compared with chemical method, enzymatic process[1,2] seems to be a promising alternative because of its mild reaction conditions, easy recovery of product, being free of chemical wastes and low demanding on raw materials, which makes it possible to use waste oil as substrate for enzymatic production of biodiesel.

Wastes edible oils, from restaurants and household disposals and being creating serious problems of environmental control and food safety, have been considered as good raw material for biodiesel production. Immobilized *Candida antarctica* lipase was found to be effective for the methanolysis of waste oil.[2,3] A three-step methanolysis protocol could be used to protect lipase from inactivation by methanol. Compared with one-step reaction, it needs a longer time to reach the reaction equilibrium. So, efforts should be made to increase enzymatic reaction rate. Reports on the enhancement of the activity of certain enzymes by applying ultrasonic irradiation on the enzymes[4,5] led us investigate its effects on the enzymatic transesterification of waste oil to biodiesel in a solvent free system.

Experimental

Materials. Waste oil was collected from the restaurant in South China University of Technology. The saponification value was 200.3 mg KOH/g, from which, the average molecular weight of the waste oil was known to be 840.2. Novozym 435 (lipase B from *Candida antarctica*, 164 U/g, 1unit corresponds to the amount of enzyme that produces 1 μmol methyl oleate from triolein per minute at 35 °C) was kindly donated by Novo Nordisk Co. (Denmark). Methyl palmitate, methyl stearate, methyl oleate, methyl linoleate, methyl linolenate and methyl heptadecanoate (as internal standard) were purchased from Sigma (USA). All other chemicals were also obtained commercially and of analytical grade. Ultrasonic irradiation experiments were carried out using a ultrasonic bath (Type NP-B-400-15; Newpower Co. Ltd., China).

Determination of power density. Power density at sample sites in the ultrasound bath was determined according to the method described by Barton.[6]

Reaction. The reaction was carried out in 50-ml flask capped with a septum, incubated at 40 °C and in the presence or absence of ultrasonic irradiation. The reaction mixture contained 66 U Novozym 435, 10 g waste oil and 0.38 g methanol (1 molar equivalent). Samples of 100 μl were periodically withdrawn and centrifuged (12000 rpm, 10 min) and the upper layer was mixed with methyl heptadecanoate for GC analysis. In the ultrasonic pretreatment experiment, Novozym 435 was immerged into 10 g waste oil and exposed to ultrasonic irradiation for a certain time.

Analysis. The methyl ester (ME) content in the reaction mixture was assayed with a GC2010 gas chromatography (Shimadzu Corp., Kyoto) using a flame ionization detector and a HP-5 capillary column (0.53 mm × 15 m, HP, USA). The column temperature was hold at 180 °C for 1 min, raised to 186 °C at 0.8 °C /min and kept for 1 min, then upgraded to 280 °C at the rate of 20 °C /min. Nitrogen was used as the carrier gas at 2 ml/min. Split ratio was 1:100 (v/v). The injector and the detector temperatures were set at 250 °C and 280 °C, respectively.

Results and Discussion

The use of an ultrasonic bath has the advantages of simplicity, low cost, and modest power outputs reducing the likelihood of localized heating effects with ultrasound probe and cuphorn systems. The most obvious limitations are that the operating frequency is normally fixed and power densities vary within the bath. Consequently standardization of sample locations is essential for comparative purposes. In our study, the water addition to the bath was as high as 230 mm from the bottom and the sample was fixed at the position of 180 mm from the bottom. The maximum power density with water as medium was obtained in the center and this location was used for all the following reactions. The power densities were 0.21W/ml, 0.28 W/ml, 0.36 W/ml and 0.48 W/ml, respectively, when the power outputs were 40 W, 60 W, 80 W and 100 W, respectively.

As can be seen in **Figure 1**, the reaction accelerated markedly with the increase in power output when it was below 80 W. Further increase in power output up to 100 W, however, resulted in little rise in conversion after reaction for 2 h and the ME content of the product was lower than 30% in spite of the higher initial reaction rate, suggesting partial inactivation of the enzyme. This has been proved by experiments showing that the enzyme retained only 81% of its original activity after being treated with ultrasonic irradiation at 100 W. However, the best result achieved was only comparative to the control which was carried out with shaking at 150 rpm. This is mainly due to the high viscosity of waste oil and little enhancement in mass transfer at low ultrasonic intensities and inactivation of enzyme at high ultrasonic intensities.

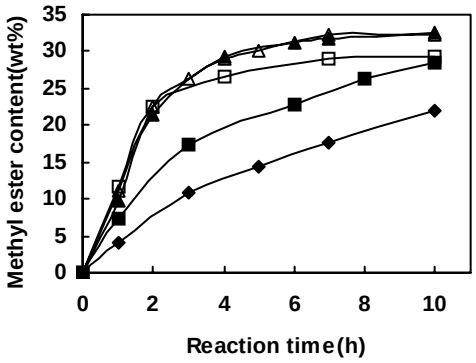

Figure 1. Effect of ultrasonic power on enzymatic transesterification of waste oil. The reactions were carried out at 40±2 °C in the presence of ultrasonic irradiation and the reaction mixture contained 10 g waste oil, 0.38 g methanol and 66 U Novozym 435. Control was carried out at 40 °C and 150 rpm. ◆,40 W; ■,60 W; ▲,80 W; □,100 W; △, control.

It has been reported that the reaction rate could be enhanced by pretreatment of enzyme with ultrasonic irradiation.[7] In our study, It was found that the reaction proceeded quite slowly during the first 1 hour of reaction as indicated by the low ME content of the reaction mixture (10.9%) and then accelerated. It seems that there exists a period for the enzyme to be activated. So, we speculated that

pretreatment of enzyme with ultrasonic irradiation might activate the enzyme and accelerate the enzymatic reaction. The results depicted in **Table 1** well supports the hypothesis.

Table 1. Effect of ultrasonic pretreatment on enzymatic transesterification of waste oil

Pretreatment means	Methyl ester content (wt%)
Ultrasonic irradiation	19.4
Shaking	12.1
Control*	10.9

Novozym 435 (66 U) was immerged into 10 g waste oil and then pretreated with ultrasonic irradiation (20 kHz, 80 W) at 40 °C for 30 min or with shaking at 40 °C and 150 rpm for 30 min. Methanol (0.38 g) was added to the reaction mixture and the reactions were carried out at 40 °C and 150 rpm for 1 h.
*Without pretreatment

Since the time enzyme was pretreated with ultrasonic irradiation could influence the reaction rate, effect of pretreatment time on the reaction was therefore investigated. As shown in **Table 2**, the reaction rate increased with increasing pretreatment time up to 30 min. Further increase in the pretreatment time, however, resulted in little change in reaction rate. So, the optimum pretreatment time was thought to be 30 min.

Table 2. Effect of ultrasonic pretreatment time on enzymatic transesterification of waste oil

Time（min）	Methyl ester content (wt%)
10	13.6
20	17.1
30	19.4
40	19.5
60	19.1

Novozym 435 (66U) was immerged into 10g waste oil and pretreated with ultrasonic irradiation (20 kHz, 80W) at 40°C for a certain period of time. Methanol (0.38g) was added to the reaction mixture and the reactions were carried out at 40°C and 150 rpm for 1 h.

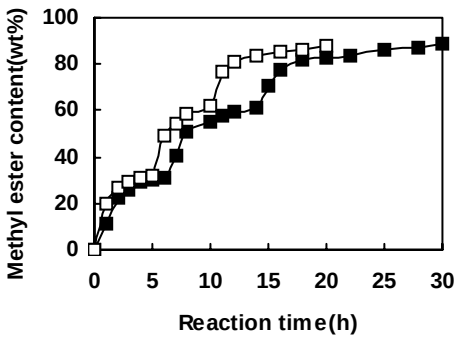

Figure 2. Time course of pretreated Novozym 435-catalyzed transesterification of waste oil. Reaction was performed at 40 °C, 150 rpm by adding 0.38 g methanol into the mixture containing 10 g waste oil and 66 U Novozym 435 pretreated or non- pretreated by ultrasonic irradiation (20 kHz, 80 W) at 40 °C for 30 min 0.38 g Methanol was added after 5 and 10 h or after 6 and 8 h and glycerol was rinsed with acetone after each step. □, pretreated; ■, non-pretreated.

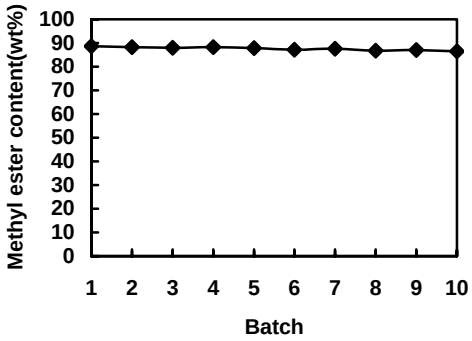

Figure 3. Operational stability of pretreated Novozym 435. Reaction conditions were the same as in Figure 2 and three steps served as one batch with a total reaction time of 20 h.

Figure 2 depicts the time course of pretreated Novozym 435-catalyzed transesterification of waste oil. During the three-step batch reaction, the reaction time of each step reduced to 5 h, 5 h and 10 h from original 6 h, 8 h and 16 h and one third of the total reaction time was saved. On the other hand, Novozym 435 pretreated by ultrasound showed good operational stability as indicated by a slight loss in activity after 10-batch operation (**Figure 3**).

Conclusion

Novozym 435-catalyzed transesterification of waste oil was markedly accelerated by pretreatment of the enzyme with ultrasonic irradiation at 20 kHz, 80 W for 30 min and Novozym 435 pretreated with ultrasonic irradiation showed good operational stability and so are potential for biodiesel production.

Acknowledgment

This work was financially supported by Science and Technology Project of Guangdong Province (Grant No. 2003C33102).

References

(1) Steinke, G.; Kirchhoff, R.; Muknerjee, K. D. *J. Am. Oil Chem. Soc.*, **2000**, *77* (4), 361-366
(2) Shimada, Y.; Watanabe, Y.; Sugihara, A.; Tominaga, Y. J. *Mol. Catal. B: Enzym.*, 2002, *17* (3-5), 133-142
(3) Wu, H.; Zong, M. H.; Lou, W. Y. *Chin. J. Catal*., **2004**, *25* (11), 903-908
(4) Vulfson, E. N.; Sarney, D. B.; Law, B. A. *Enzyme Microb. Technol*., **1991**, *13* (2), 123-126
(5) Sakakibara, M.; Wang, R.; Takahashi, R.; Takahashi, K.; Mori, S. *Enzyme Microb. Technol*., **1996**, *18*, 444-448
(6) Barton, S.; Bullock, C.; Weir, D. *Enzyme Microb. Technol*., **1996**, *18*, 190-194
(7) Zong, M. H.; Du, W.; Li, H. Q.; Liu, Y. *J South China Univ. Tech.*, **2000**, *28* (3), 101-104

THE FILM BOILING REACTOR: A NEW ENVIRONMENT FOR CHEMICAL PROCESSING

Thomas Avedesian,
Department of Mechanical Engineering
Cornell University,
Ithaca, NY 14850-7501

Wing Tsang
National Institute of Standards and Technology
Gaithersburg, MD 20899

Brian Urban
Department of Mechanical Engineering
Massachusetts Institute of Technology
Cambridge, MA 02139

Introduction

Film boiling is a well understood phenomenon. It is usually associated with nuclear meltdown. Less appreciated it that it can be used in chemical processing. In this paper we demonstrate the possibilities by considering the production of hydrogen through the decompositon of methanol. This paper is an extension of the earlier observation of Okuyama and Iida (1) who demonstrated that such a process can occur and was primarily interested in the heat transfer characteristics of the system. In this paper we report on detailed calculations on how process variables control yields and thus lay the basis for use of the phenomenon for chemical processing.

Concept

We describe a new type of chemical reactor for studying catalytic reactions involving organic liquids that is fundamentally different from existing reactor systems. It involves chemical reaction within the vapor film that surrounds a heated surface which is in the so-called 'film boiling' regime of heat transfer. The process has the capability for high temperature processing in a cold bulk liquid. It accomplishes this by a natural separation of the high temperature reacting (vapor) volume from the cooler bulk liquid containment that occurs in film boiling. By allowing high temperature, localized, reaction in a cold bulk liquid, problems of vapor containment are significantly mitigated. Additional advantages are the reactor's versatility, stability, simplicity (the reaction volume is self-assembled), the capability of easily controlling the temperature and pressure over a wide dynamic range. We illustrate these possibilities by studying the catalytic decomposition of methanol to form hydrogen and note that the simplicity of the system makes it particularly attractive for portable applications (2).

For the primary concept, a solid surface (for example a thin-walled horizontal tube) is immersed in a cold liquid (e.g., methanol, ethanol, aqueous mixtures, or other organic). The outside surface of the cylinder will be coated with a suitable catalyst. The tube is then heated electrically by passing a current through it to create a high surface temperature that transitions heat transport from single phase convection to nucleate boiling and eventually to the film boiling. In the film boiling regime a stable vapor layer blankets or physically surrounds the surface. Our reaction volume is this vapor film. Vapor will flow within the film and exit at the top with bubbles percolating into the pool liquid. As the vapor moves along the surface decomposition and/or pyrolytic reactions will occur to produce products at rates appropriate to the gas/solid interface temperature, the temperature gradient within the vapor film, the chemical species of the bulk liquid, and the catalyst. Because of the strong temperature gradient in the gas film, the reaction zone will be confined to the near-wall region of the film outside of which the reactions are frozen. With one boundary of the reaction volume being ' hot' (solid side) and the other ' old' (liquid/vapor interface side), the reactor surface and containment vessel will have very different temperatures which will greatly facilitate the problem of high temperature containment. We can thus realize high temperature reactions in a low temperature supply liquid. We term this reaction volume a ' filmboiling reactor' (FIBOR). The notion of 'self-assembled' refers to the vapor film being created automatically by surface heating, and the reaction volume disappears when power to the tube is turned off.

Properties of FIBOR. We present the results of our calculations in order to provide the technical justification for this concept. A particular strength of this approach is that the scientific and engineering basis for film boiling is well established (2) . Thus it is possible to make sound estimates on the relationship between product yields and process variables.

The chemical process that will be used for the present calculations is the conversion of methanol to hydrogen and carbon monoxide. This process was selected mainly because of its use by Okuyama and Iida to determine the effect the effect of film boiling on heat transfer. They were able to demonstrate the equivalence of results from film boiling and in a packed bed reactor and derived the following global rate expression

$$k(\text{methanol} = CO + 2H_2) = 17.54 \times 10^4 \exp(-6.82 \times 10^4 / RT_w)$$

where T_w = wall temperature, the pre-exponential factor is in units of mol / (m^2 sec Mpa) and the activation energy is in kJ/mol

With this relation and the physical properties pertinent to film boiling we were then able to derive from the solution of the conservation equations and a few simple assumptions process conditions for a horizontal cylinder coated with a platinum black catalytic surface. Some pertinent results are summarized in Figures 1-4. The first figure show the effect of cylinder temperature and angle about the cylinder on film thickness on the basis of a 5 mm diameter cylinder. The film thickness can be considered to be equivalent to a reactor volume. Figure 2 is a plot of the average residence time that takes a molecule to traverse about the perimeter of the cylinder. It can be seen that this "residence time" is small and is in fact close to that for the short contact reactors (4). Figure 3 gives the relation between the amount of methanol processed by the FIBOR as a function of the tube diameter and the wall temperature.

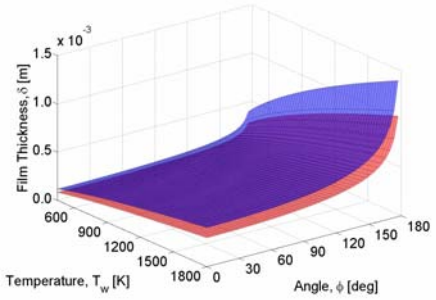

Figure 1. Film thickness as a function of wall temperature and the angle about the cylinder. The top surface is for the no slip condition and the bottom surface is the zero shear stress condition. Results are for a tube diameter of 5 mm.

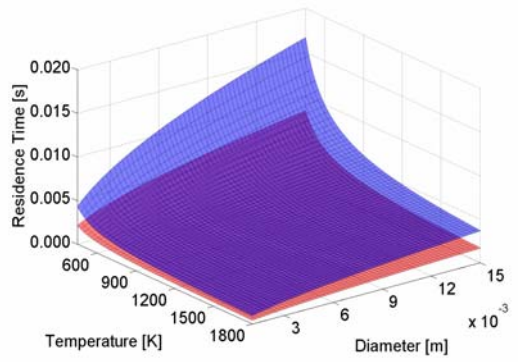

Figure 2. Residence time as a function of wall temperature and tube diameter**.** The top surface is for the no slip condition and the bottom surface is the zero shear stress condition

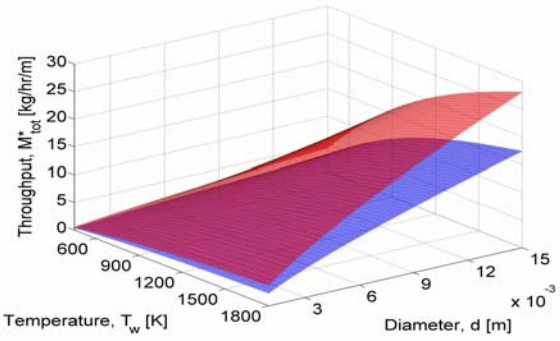

Figure 3. Thruput as a function of the temperature and diameter of cylinder. The bottom surface is for the no slip condition and the bottom surface is the zero shear stress condition

The key factor to be noted is the very large volumes of reactants that can be processed by a single cylinder. There is no reason why one cannot have an array of cylinders. When this is combined with the simplicity of the system portable applications become possible.

Finally we define the quantity termed the 'performance factor' as the ratio of molar throughput of hydrogen from methanol decomposition to the total energy required by the system (units of (mole/hr)/(W)). This is similar to an efficiency in that it is a measure of the amount of hydrogen that can be produced per unit total energy. When this is plotted against the process variables the results can be found in Figure 4. The sensitivity of the results to the surface temperature can be directly seen. There is however much less sensitivity to the tube diameter.

Extensions. There are many possible variations of this concept. The heated tube may be made porous to allow 'blowing' oxygen

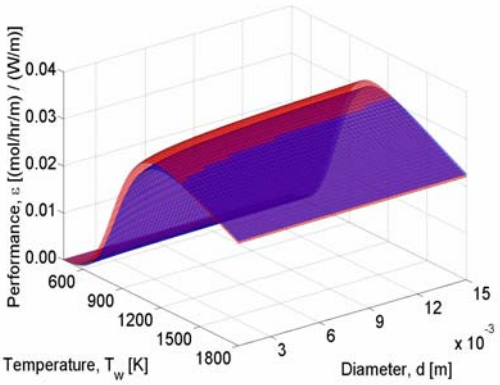

Figure 4. Performance factor as a function of temperature and tube diameter. Note that in this case the no slip and zero shear stress condition have minimal effects.

directly into the vapor film to scavenge carbon that would otherwise deposit on the surface, or direct off-line GC analysis through gas sampling of the vapors drawn through the porous walls. The pool liquid could be a miscible mixture, for example water and ethanol (leading to large cost-savings compared with using ethanol in gasoline as in gasohol). This would allow hydrogen production by steam reforming. FIBOR arrays could be configured in many different geometrical patterns to optimize the vapor thru-put in the film. There is obvious need for validation. We are beginning an experimental program toward these ends.

Summary and conclusions. A platform for catalytic conversion of organic liquids has been analyzed based on film boiling. It is shown that the physical conditions are very close to those found in short contact time reactors. The aspects of this new reactor platform are its simplicity, scalability and as a tool for developing a better understanding of the mechanism of catalytic conversions under real process conditions From the present analysis, the results show that catalytic conversion in the vapor produces appreciable amounts of hydrogen gas that suggest its use as a means of hydrogen production. A performance parameter is used to compare the hydrogen yield with the total energy input to the tube to maintain the vapor film and drive the reaction. This factor has a weak dependence on tube diameter but exhibits a maximum with wall. For methanol, optimal temperatures are predicted to be in the range of 1080K and 1225K for 1.5mm < d < 1.5cm.

References

1. Okuyama K, Iida Y. Film-boiling heat transfer with a catalytic decomposition reaction. JSME International Journal. 1994; Ser. B, 37: 123-131.

2. Trimm, D. L. and Onsan, Z. H. Onboard fuel conversion for hydrogen-fuel-cell-driven vehicles Catal. Rev. 2001: 43 (1-2); 31-84.2.

3. Lienhard JH. A heat transfer texbook (2nd edition), pp. 411-417, 437-439, Prentice-Hall, Inc., Englewood Cliffs, 1987.

4. Deluga, G.A., Salge, J.R. and Schmidt, L.D. Renewable hydrogen from ethanol by autothermal reforming. Science. 2004; 303: 993-997.

CATALYSIS OF ATOMIC HYDROGEN TO NOVEL HYDRIDES AS A NEW POWER SOURCE

R. Mills, J. He, Z. Chang, W. Good, Y. Lu, B. Dhandapani

BlackLight Power, Inc., 493 Old Trenton Road, Cranbury, NJ 08512

Introduction

A new chemically generated or assisted plasma source based on a resonant energy transfer mechanism (rt-plasma) between atomic hydrogen and certain catalysts has been developed that may be a new power source. The products are more stable hydride and molecular hydrogen species such as $H^-(1/4)$ and $H_2(1/4)$ as definitely shown in this paper. One such source operates by incandescently heating a hydrogen dissociator and a catalyst to provide atomic hydrogen and gaseous catalyst, respectively, such that the catalyst reacts with the atomic hydrogen to produce a plasma. It was extraordinary that intense extreme ultraviolet (EUV) emission was observed by Mills et al.[1–8] at low temperatures (e.g. $\approx 10^3$ K) and an extraordinary low field strength of about 1-2 V/cm from atomic hydrogen and certain atomized elements or certain gaseous ions which singly or multiply ionize at integer multiples of the potential energy of atomic hydrogen, 27.2 eV. A number of independent experimental observations confirm that the rt-plasma is due to a novel reaction of atomic hydrogen which produces as chemical intermediates, hydrogen in fractional quantum states that are at lower energies than the traditional "ground" (n = 1) state. Power is released,[1,7,9–11] and the final reaction products are novel hydride compounds[1,12–14] or lower-energy molecular hydrogen.[15] The supporting data include EUV spectroscopy,[1–8,11,15–20,23,25,26] characteristic emission from catalysts and the hydride ion products,[1,3,5,19,20,25,26] lower-energy hydrogen emission,[10,11,16–18] chemically formed plasmas,[1–8,19,20,25,26] extraordinary (>100 eV) Balmer α line broadening,[1–3,5,7,8,10,16,17,19,21–26] population inversion of H lines,[1,19,25–27] elevated electron temperature,[17,21–23] anomalous plasma afterglow duration,[1,6] power generation,[1,7,9–11] and analysis of novel chemical compounds[1,12–14]

The theory given previously[4,16–18,28] is based on applying Maxwell's equations to the Schrödinger equation. The familiar Rydberg equation (Eq. (1)) arises for the hydrogen excited states for $n > 1$ of Eq. (2).

$$E_n = -\frac{e^2}{n^2 8\pi\varepsilon_o a_H} = -\frac{13.598\,eV}{n^2} \tag{1}$$

$$n = 1,2,3,... \tag{2}$$

An additional result is that atomic hydrogen may undergo a catalytic reaction with certain atoms, excimers, and ions which provide a reaction with a net enthalpy of an integer multiple of the potential energy of atomic hydrogen, $m \cdot 27.2\,\text{eV}$ wherein m is an integer. The reaction involves a nonradiative energy transfer to form a hydrogen atom that is lower in energy than unreacted atomic hydrogen that corresponds to a fractional principal quantum number. That is

$$n = \frac{1}{2}, \frac{1}{3}, \frac{1}{4}, ..., \frac{1}{p}; \quad p \text{ is an integer} \tag{3}$$

replaces the well known parameter $n = \text{integer}$ in the Rydberg equation for hydrogen excited states. The $n = 1$ state of hydrogen and the $n = 1/\text{integer}$ states of hydrogen are nonradiative, but a transition between two nonradiative states, say $n = 1$ to $n = 1/2$, is possible via a nonradiative energy transfer. Thus, a catalyst provides a net positive enthalpy of reaction of $m \cdot 27.2\,\text{eV}$ (i.e. it resonantly accepts the nonradiative energy transfer from hydrogen atoms and releases the energy to the surroundings to affect electronic transitions to fractional quantum energy levels). As a consequence of the nonradiative energy transfer, the hydrogen atom becomes unstable and emits further energy until it achieves a lower-energy nonradiative state having a principal energy level given by Eqs. (1) and (3). Processes such as hydrogen molecular bond formation that occur without photons and that require collisions are common.[29] Also, some commercial phosphors are based on resonant nonradiative energy transfer involving multipole coupling.[30]

Two $H(1/p)$ may react to form $H_2(1/p)$. The hydrogen molecular ion and molecular charge and current density functions, bond distances, and energies were exactly solved previously with remarkable accuracy.[28,31] Using the Laplacian in ellipsoidal coordinates with the constraint of nonradiation, the total energy of the hydrogen molecule having a central field of $+pe$ at each focus of the prolate spheroid molecular orbital is

$$E_T = -p^2\left\{\frac{e^2}{8\pi\varepsilon_o a_0}\left[\left(2\sqrt{2}-\sqrt{2}+\frac{\sqrt{2}}{2}\right)\ln\frac{\sqrt{2}+1}{\sqrt{2}-1}-\sqrt{2}\right]\right\}\left\{\left[1+p\sqrt{\frac{2\hbar\sqrt{\frac{e^2}{4\pi\varepsilon_o a_0^3}}}{m_e c^2}}\right]-\frac{1}{2}\hbar\sqrt{\frac{k}{\mu}}\right\} \tag{4}$$

$$= -p^2\,31.351\,\text{eV} - p^3\,0.326469\,\text{eV}$$

where p is an integer, $\hbar$ is Planck's constant bar, m_e is the mass of the electron, c is the speed of light in vacuum, μ is the reduced nuclear mass, k is the harmonic force constant solved previously in a closed-form equation with fundamental constants only[28,31] and a_o is the Bohr radius. The vibrational and rotational energies of fractional-Rydberg-state molecular hydrogen $H_2(1/p)$ are p^2 those of H_2. Thus, the vibrational energies, E_{vib}, for the $\upsilon = 0$ to $\upsilon = 1$ transition of hydrogen-type molecules $H_2(1/p)$ are[28,31]

$$E_{vib} = p^2\,0.515902\,\text{eV} \tag{5}$$

where the experimental vibrational energy for the $\upsilon = 0$ to $\upsilon = 1$ transition of H_2, $E_{H_2(\upsilon=0\to\upsilon=1)}$, is given by Beutler[32] and Herzberg.[33] The rotational energies, E_{rot}, for the J to $J+1$ transition of hydrogen-type molecules $H_2(1/p)$ are[28,31]

$$E_{rot} = E_{J+1} - E_J = \frac{\hbar^2}{I}\left[J+1\right] = p^2\left(J+1\right)0.01509\,\text{eV} \tag{6}$$

where I is the moment of inertia, and the experimental rotational energy for the $J = 0$ to $J = 1$ transition of H_2 is given by Atkins.[34] The p^2 dependence of the rotational energies results from an inverse p dependence of the internuclear distance and the corresponding impact on I. The predicted internuclear distance $2c'$ for $H_2(1/p)$ is

$$2c' = \frac{a_o\sqrt{2}}{p} \tag{7}$$

The rotational energies provide a very precise measure of I and the internuclear distance using well established theory.[35]

Ar^+ may serve as a catalyst since its ionization energy is about 27.2 eV. The catalyst reaction of Ar^+ to Ar^{2+} forms H(1/2) which may further serve as both a catalyst and a reactant to form H(1/4).[17,18,28] Thus, the observation of H(1/4) is predicted to be flow

dependent since the formation of $H_2(1/4)$ requires the buildup of intermediates. The mechanism was tested by experiments with flowing plasma gases. Neutral molecular emission was anticipated for high pressure argon-hydrogen plasmas excited by a 12.5 keV electron beam. Rotational lines for $H_2(1/4)$ were anticipated and sought in the 150–250 nm region. The spectral lines were compared to those predicted by Eqs. (5-6) corresponding to the internuclear distance of 1/4 that of H_2 given by Eq. (7). For $p = 4$ in Eqs. (5-6), the predicted energies for the $\upsilon = 1 \rightarrow \upsilon = 0$ vibration-rotational series of $H_2(1/4)$ are

$$E_{vib-rot} = p^2 E_{vib\,H_2(\upsilon=0\rightarrow\upsilon=1)} \pm p^2(J+1)E_{rot\,H_2} \quad , J = 0,1,2,3... \quad (8)$$
$$= 8.254432\,\text{eV} \pm (J+1)0.24144\,\text{eV}$$

He^+ also fulfills the catalyst criterion—a chem ical or physical process with an enthalpy change equal to an integer multiple of $27.2\,\text{eV}$ since it ionizes at 54.417 eV which is $2 \cdot 27.2\,\text{eV}$. The product of the catalysis reaction of He^+, H(1/3), may further serve as a catalyst to form H(1/4) and H(1/2) [17,18,28] which can lead to transitions to other states $H(1/p)$. Novel emission lines with energies of $q \cdot 13.6\,\text{eV}$ where $q = 1,2,3,4,6,7,8,9, or\, 11$ were previously observed by extreme ultraviolet (EUV) spectroscopy recorded on microwave discharges of helium with 2% hydrogen.[16–18] These lines matched H(1/*p*), fractional Rydberg states of atomic hydrogen wherein $n = 1/2,1/3,1/4,...,1/p$; ($p \le 137$ is an integer) replaces the well known parameter $n = \text{integer}$ in the Rydberg equation for hydrogen excited states.

Rotational lines were observed in the 145–300 nm region from atmospheric pressure electron-beam excited argon-hydrogen plasmas. The unprecedented energy spacing of 4^2 times that of hydrogen established the internuclear distance as 1/4 that of H_2 and identified $H_2(1/4)$ (Eqs. (5-8)). $H_2(1/p)$ gas was isolated by liquefaction of helium–hydrogen plasma gas using an high-vacuum (10^{-6} Torr) capable, liquid nitrogen cryotrap and was characterized by mass spectroscopy (MS). The condensable gas had a higher ionization energy than H_2 by MS.[15] $H_2(1/4)$ gas from chemical decomposition of hydrides containing the corresponding hydride ion $H^-(1/4)$ as well from liquefaction of the catalysis-plasma gas was also identified by ^1H NMR as an upfield-shifted singlet peak at 2.18 ppm relative to H_2 at 4.63 that matched theoretical predictions.[11] $H_2(1/4)$ was further characterized in this paper by improved studies on the vibration-rotational emission from electron-beam maintained argon-hydrogen plasmas and from Fourier-transform infrared (FTIR) spectroscopy of solid samples containing $H^-(1/4)$ with interstitial $H_2(1/4)$.

Water bath calorimetry was used to determine that measurable power was developed in rt-plasmas due to the reaction to form states given by Eqs. (1) and (3). Specifically, He/H_2 (10%) (500 mTorr), Ar/H_2 (10%) (500 mTorr), and $H_2O(g)$ (500 and 200 mTorr) plasmas generated with an Evenson microwave cavity consistently yielded on the order of 50% more heat than non rt-plasma (controls) such as He, Kr, Kr/H_2(10%), under identical conditions of gas flow, pressure, and microwave operating conditions. The excess power density of rt-plasmas was of the order $10\,\text{W} \cdot \text{cm}^{-3}$. In addition to unique vacuum ultraviolet (VUV) lines, earlier studies with these same rt-plasmas demonstrated that other unusual features were present including dramatic broadening of the hydrogen Balmer series lines,[1–3,5,7,8,10,16,17,19,21–26] and in the case of water plasmas, population inversion of the hydrogen excited states.[1,19,25–27] Both the current results and the earlier results are completely consistent with the existence of a hitherto unknown predicted exothermic chemical reaction occurring in rt-plasmas.

Since the ionization energy of Sr^+ to Sr^{3+} has a net enthalpy of reaction of $2 \cdot 27.2\,\text{eV}$, Sr^+ may serve as catalyst alone or with Ar^+ catalyst. It was reported previously that an rt-plasma formed with a low field (1V/cm), at low temperatures (e.g. $\approx 10^3$ K), from atomic hydrogen generated at a tungsten filament and strontium which was vaporized by heating the metal.[2,3,5,7,8] Strong VUV emission was observed that increased with the addition of argon, but not when sodium, magnesium, or barium replaced strontium or with hydrogen, argon, or strontium alone. Characteristic emission was observed from a continuum state of Ar^{2+} at $45.6\,\text{nm}$ without the typical Rydberg series of Ar I and Ar II lines which confirmed the resonant nonradiative energy transfer of 27.2 eV from atomic hydrogen to Ar^+.[3,5,20] Predicted Sr^{3+} emission lines were also observed from strontium-hydrogen plasmas[3,5] that supported the rt-plasma mechanism. Time-dependent line broadening of the H Balmer α line was observed corresponding to extraordinarily fast H (25 eV). An excess power of 20 $\text{mW} \cdot \text{cm}^{-3}$ was measured calorimetrically on rt-plasmas formed when Ar^+ was added to Sr^+ as an additional catalyst.

Significant Balmer α line broadening corresponding to an average hydrogen atom temperature of 14, 24 eV, and 23-45 eV was observed for strontium and argon-strontium rt-plasmas and discharges of strontium-hydrogen, helium–hydrogen, argon–hydrogen, strontium–helium–hydrogen, and strontium-argon-hydrogen, respectively, compared to $\approx 3\,\text{eV}$ for pure hydrogen, krypton-hydrogen, xenon-hydrogen, and magnesium-hydrogen. To achieve that same optically measured light output power, hydrogen-sodium, hydrogen-magnesium, and hydrogen-barium mixtures required 4000, 7000, and 6500 times the power of the hydrogen-strontium mixture, respectively, and the addition of argon increased these ratios by a factor of about two. A glow discharge plasma formed for hydrogen-strontium mixtures at an extremely low voltage of about 2 V compared to 250 V for hydrogen alone and sodium-hydrogen mixtures, and 140–150 V for hydrogen-magnesium and hydrogen-barium mixtures.[2,3,5] These voltages are too low to be explicable by conventional mechanisms involving accelerated ions with a high applied field. A low-voltage EUV and visible light source is feasible.[8]

The catalyst product, H (1/*p*), may also react with an electron to form a novel hydride ion $H^-(1/p)$ with a binding energy E_B [1,12,14,19,28]:

$$E_B = \frac{\hbar^2 \sqrt{s(s+1)}}{8\mu_e a_0^2 \left[\frac{1+\sqrt{s(s+1)}}{p}\right]^2}$$
$$- \frac{\pi \mu_0 e^2 \hbar^2}{m_e^2} \left(\frac{1}{a_H^3} + \frac{2^2}{a_0^3 \left[\frac{1+\sqrt{s(s+1)}}{p}\right]^3} \right) \quad (9)$$

where *p* is an integer greater than one, s = 1/2, $\hbar$ is Planck's constant bar, μ_o is the permeability of vacuum, m_e is the mass of the electron, μ_e is the reduced electron mass given by $\mu_e = \sqrt{3/4}\, m_e m_p / (m_e + \sqrt{3/4}\, m_p)$ where m_p is the mass of the proton, a_H is the radius of the hydrogen atom, a_o is the Bohr radius, and e is the elementary charge. The ionic radius is

$r_1 = \frac{a_0}{p}\left(1+\sqrt{s(s+1)}\right), s = \frac{1}{2}$. From Eq. (9), the calculated ionization energy of the hydride ion is $0.75418\,\text{eV}$, and the experimental value given by Lykke[36] is $6082.99 \pm 0.15\,\text{cm}^{-1}$ (0.75418 eV).

Substantial evidence of an energetic catalytic reaction was previously reported[1] involving a resonant energy transfer between hydrogen atoms and K to form very stable novel hydride ions $H^-(1/p)$ called hydrino hydrides having a predicted fractional principal quantum number $p = 4$. Characteristic emission was observed from K^{3+} that confirmed the resonant nonradiative energy transfer of $3 \cdot 27.2$ eV from atomic hydrogen to K. From Eq. (9), the binding energy E_B of $H^-(1/4)$ is

$$E_B = 11.232\,\text{eV} \quad (\lambda_{vac} = 1103.8\ \text{Å}) \tag{10}$$

The product hydride ion $H^-(1/4)$ was observed spectroscopically at 110 nm corresponding to its predicted binding energy of 11.2 eV.[1,19]

Upfield-shifted NMR peaks are a direct evidence of the existence of lower-energy state hydrogen with a reduced radius relative to ordinary hydride ion and having an increase in diamagnetic shielding of the proton. The total theoretical shift $\frac{\Delta B_T}{B}$ for $H^-(1/p)$ is given by the sum of the shift of $H^-(1/1)$ plus the contribution due to the lower-electronic energy state:

$$\begin{aligned}\frac{\Delta B_T}{B} &= -\mu_0 \frac{e^2}{12 m_e a_0\left(1+\sqrt{s(s+1)}\right)}\left(1+\alpha 2\pi p\right) \\ &= -\left(29.9 + 1.37\,p\right) ppm\end{aligned} \tag{11}$$

where $p = \text{integer} > 1$. Corresponding alkali hydrides and alkali hydrino hydrides (containing $H^-(1/p)$) were characterized by ^1H MAS NMR and compared to the theoretical values. A match of the predicted and observed peaks with no alternative represents a definite test.

The ^1H MAS NMR spectrum of novel compound KH*Cl relative to external tetramethylsilane (TMS) showed a large distinct upfield resonance at -4.4 ppm corresponding to an absolute resonance shift of -35.9 ppm that matched the theoretical prediction of $p = 4$.[1,14–17] This result confirmed the previous observations from the rt-plasmas of intense hydrogen Lyman emission, a stationary inverted Lyman population, excessive afterglow duration, highly energetic hydrogen atoms, characteristic alkali-ion emission due to catalysis, predicted novel spectral lines, and the measurement of a power beyond any conventional chemistry[1] that matched predictions for a catalytic reaction of atomic hydrogen to form more stable hydride ions designated $H^-(1/p)$. Since the comparison of theory and experimental shifts of KH*Cl is direct evidence of lower-energy hydrogen with an implicit large exotherm during its formation, the NMR results were repeated with the further analysis by infrared (FTIR) spectroscopy to eliminate any known explanation.

Elemental analysis identified[12,14] these compounds as only containing the alkaline metal, halogen, and hydrogen, and no known hydride compound of this composition could be found in the literature which has an upfield-shifted hydride NMR peak. Ordinary alkali hydrides alone or mixed with alkali halides show down-field shifted peaks.[1,12–14] From the literature, the list of alternatives to $H^-(1/p)$ as a possible source of the upfield NMR peaks was limited to U centered H. The intense and characteristic infrared vibration band at $503\ \text{cm}^{-1}$ due to the substitution of H^- for Cl^- in KCl[37] enabled us to study the relationship between the upfield-shifted NMR peaks any U centered H that may somehow have caused the upfield-shifted peaks.

As further characterizations, the X-ray photoelectron spectrum (XPS) of the hydrino hydride KH*I was performed to determine if the predicted $H^-(1/4)$ binding energy given by Eq. (10) was observed, and FTIR analysis of these crystals with $H^-(1/4)$ was performed before and after storage in argon for 90 days to search for interstitial $H_2(1/4)$ having a predicted rotational energy given by Eq. (6). The identification of single rotational peaks at this energy with ortho-para splitting due to free rotation of a very small hydrogen molecule would represent definite proof of its existence since there is no other possible assignment.

Experimental

Electron-gun plasma spectroscopy. Vibration-rotational emission of $H_2(1/4)$ was investigated using a 12.5 keV electron gun with a beam current of $10\ \mu A$ as described previously[38,39] to initiate argon plasmas with 1% hydrogen in the pressure range of 450–1000 Torr. Krypton replaced argon in the controls, and argon, hydrogen, oxygen, nitrogen, water vapor, nitrogen-oxygen (50/50%), and argon or krypton with oxygen addition up to 100% oxygen served as further controls. The Ar^+ catalyst mechanism was tested by atmospheric-pressure-plasma-gas flow at 75 sccm and nonflow conditions. The electron gun was sealed with a thin (300 nm thickness) SiN_x foil that served as a 1 mm^2 electron window to the cell at high gas pressure (760 Torr), and the light emitted by beam excitation exited the cell through a MgF_2 window mounted at the entrance of a normal incidence McPherson 0.2 meter monochromator (Model 302) equipped with a 1200 lines/mm holographic grating with a platinum coating. The resolution was 0.5 nm (FWHM) at an entrance and exit slit width of $100\ \mu m$. The increment was 0.1 nm and the dwell time was 1s. The PMT (Model R8486, Hamamatsu) used has a spectral response in the range of 115-320 nm with a peak efficiency at about 225 nm. The emission was essentially flat for $200 < \lambda > 275\,\text{nm}$, but a notch in the response of about 20% existed in the short wavelength range with a minimum at 150 nm. Peak assignments were determined by an external calibration against standard line emissions.

Power balance measurements. The power balance of a rt-plasma comprising hydrogen and vaporized potassium catalyst from KNO_3 was measured calorimetrically using a Calvet calorimeter (International Thermal Instrument Co., Model CA-100-1) as described previously.[1] To maintain an isothermal reaction system and improve baseline stability, the calorimeter was insulated and placed inside a commercial forced convection oven (Precision Scientific 625 S) operated at $250\,°C$. The cell comprised a 20 cc stainless steel vessel. A filament (0.25 mm diameter by 10, 20, or 30 cm length Pt (Aldrich 99.99%) wound in a coil) served to dissociate hydrogen and to slowly vaporize the KNO_3 by heating a 0.7 ml volume, cylindrical flat base Alumina crucible (Alfa 15 mm high by 10 mm OD by 8 mm ID) which contained 250 mg of KNO_3 (Aldrich 99.999% pure). The filament also served as a precision resistor to calibrate the cell with KNO_3 alone. The filament was powered by a constant power supply (Pennsylvania State University 0–20 W ± 1%), and the power dissipated in the filament was recorded with a watt meter (Clarke-Hess Model 259 V-A-W Meter ± 0.03 W). The ultrahigh-pure-grade hydrogen (Praxair) was maintained at about 0.2 torr and a flow rate of about 0.1 sccm.

The cell was calibrated by measuring the steady-state Calvet response to constant power into the filament over the power range 1–16 W with hydrogen at 0.2 Torr pressure without KNO_3. At a constant oven temperature of $250\,°C$, the experiment was repeated by allowing the Calvet voltage to reach steady state with KNO_3 alone present and constant power applied to the filament. Hydrogen was

then maintained at 0.2 Torr with flow. The experiment was performed for a filament length of 10, 20, or 30 cm at a constant filament input power of 7.02, 9.82, and 15.01 W, respectively.

Synthesis of KH*Cl and KH*I. Potassium iodo hydride and potassium chloro hydride (KH*Cl and KH*I) were synthesized by reaction of atomic hydrogen with potassium metal (Aldrich Chemical Company 99%) as the catalyst with the corresponding alkali halide, KCl (Alfa Aesar ACS grade 99+%) or KI (Aldrich Chemical Company 99.9 %), as an additional reactant. The compounds were prepared in a stainless steel gas cell comprising a Ni screen hydrogen dissociator (Belleville Wire Cloth Co., Inc.), catalyst, and alkali halide as described previously.[12–14] The reactor was run at 650 °C in a kiln for 72 hours, then cooled under helium atmosphere. The sealed reactor was then opened in the environmental chamber. NMR samples were placed in glass ampules, sealed with a rubber septa, and transferred out of the chamber to be flame sealed in atmosphere. ^{1}H MAS NMR was performed on solid samples of KH*Cl and KH*I at Spectral Data Services, Inc., Champaign, Illinois as described previously.[1,12–14] Chemical shifts were referenced to external TMS. To eliminate the possibility that the alkali halide *MX* influenced the local environment of the ordinary alkali hydride *MH* to produce an NMR resonance that was shifted upfield relative to *MH* alone, controls comprising *MH* and an equimolar *MH/MX* mixture were run. The reference of each novel hydride comprised the corresponding ordinary hydride *MH* (Aldrich Chemical Company 99%) and equivalent molar mixtures of *MH* and *MX* prepared in a glove box under argon.

FTIR spectroscopy. FTIR analysis was performed on solid-sample KBr pellets using the transmittance mode at Department of Chemistry, Princeton University, New Jersey using a Nicolet 730 FTIR spectrometer with DTGS detector at resolution of 4 cm^{-1} as described previously.[9] The samples were handled under a inert atmosphere. KH*I samples were stored under argon for 90 days and analyzed before and after storage for trapped $H_2(1/4)$ molecules.

XPS Spectra. A series of XPS analyses were made on the crystalline samples using a Scienta 300 XPS Spectrometer. The fixed analyzer transmission mode and the sweep acquisition mode were used. The step energy in the survey scan was 0.5 eV, and the step energy in the high resolution scan was 0.15 eV. In the survey scan, the time per step was 0.4 seconds, and the number of sweeps was 4. In the high resolution scan, the time per step was 0.3 seconds, and the number of sweeps was 30. $C\,1s$ at 284.5 eV was used as the internal standard.

Results and Discussion

Vibration-Rotational Spectrum of $H_2(1/4)$. Molecular formation was anticipated under high-pressure conditions (~760 Torr). Thus, EUV spectroscopy of argon-hydrogen plasmas was performed to search for $H_2(1/4)$ from H(1/4) formed by Ar^+ as a catalyst. The normal incidence spectrometer was used at high pressure which required a window and a electron beam to maintain a plasma. Since the 15 keV beam rapidly transfers energy to the target gas and produces a large population of species with energies of a few 10's of eVs of kinetic energy, it was anticipated that the beam could directly or indirectly collisionally excite vibration-rotational states of $H_2(1/4)$. The corresponding emission provides a direct measure of the internuclear distance; thus, this method provides the possibility of direct confirmation of $H_2(1/4)$.

The 100–350 nm spectrum of a 783 Torr plasma of argon containing about 1% hydrogen is shown in **Figure 1**. Lyman α was observed at 121.6 nm with an adjoining H_2 band, the third continuum of Ar was observed at 210 nm,[39] and the $OH(A-X)$ bands were observed at 282.7 and 308.6 nm.[27,40,41] A series of sharp, evenly-spaced lines was observed in the region 145–185 nm. The series could not be assigned to any of the controls or known lines of the gases present or any possible contaminant gas. But, the series identically matched the P branch of $H_2(1/4)$ for the vibrational transition $\upsilon = 1 \rightarrow \upsilon = 0$. P(1), P(2), P(3), P(4), P(5), and P(6) were observed at 154.94 nm, 159.74 nm, 165.54 nm, 171.24 nm, 178.14 nm, and 183.14 nm, respectively. The sharp peak at 146.84 nm may be the first member of the R branch, R(0). The R-branch lines appeared to correspond to forbidden transitions.

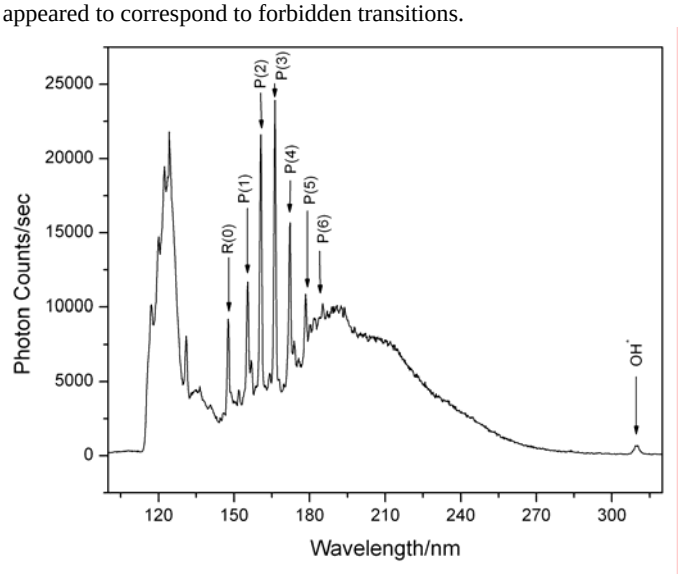

Figure 1. The 100–350 nm spectrum of a 783 Torr, 15 keV-electron-beam-maintained plasma of argon containing about 1% hydrogen.

The slope of the linear curve-fit of the energies of the peaks shown in **Figure 1** is 0.245 eV with an intercept of 8.224 eV which matches Eq. (8) very well for $p = 4$. The series matches the predicted $\upsilon = 1 \rightarrow \upsilon = 0$ vibrational energy of $H_2(1/4)$ of 8.25 eV (Eq. (5)) and its predicted rotational energy spacing of 0.241 eV (Eq. (6)) with $\Delta J = +1; J = 1,2,3,4,5,6$ and $\Delta J = -1; J = 0$ where J is the rotational quantum number of the final state. The spectrum was flow dependent as anticipated based on the reaction mechanism, and it was also in agreement with the selection rules for these transitions.[15] The series of lines was previously reported but unassigned.[38,39] The unprecedented energy spacing of 4^2 times that of hydrogen established the internuclear distance (Eqs. (5-8)) as 1/4 that of H_2 and identified $H_2(1/4)$.

Power Measurements. The least-squares fit of the Calvet voltage V as a function of the power applied to the filament heater at 0.2 Torr hydrogen pressure plotted for the input power range of 0.5 W to 16 W was

$$V = -0.061 + 0.233 \times P_T \tag{12}$$

where P_T is the total power loss from cell which must equal the power input P_{in} and any excess power P_{ex}:

$$P_T = P_{in} + P_{ex} \tag{13}$$

The Calvet voltage was allowed to reach steady state with KNO_3 alone at a constant filament input power of 9.82 W to a 20 cm long filament. The Calvet voltage significantly increased upon the addition of hydrogen as shown in **Figure 2**, and the output signal showed 0.81 W of excess power (Eqs. (12-13)) at the second steady state. The propagated error of the calibration and power measurements was ± 0.06.

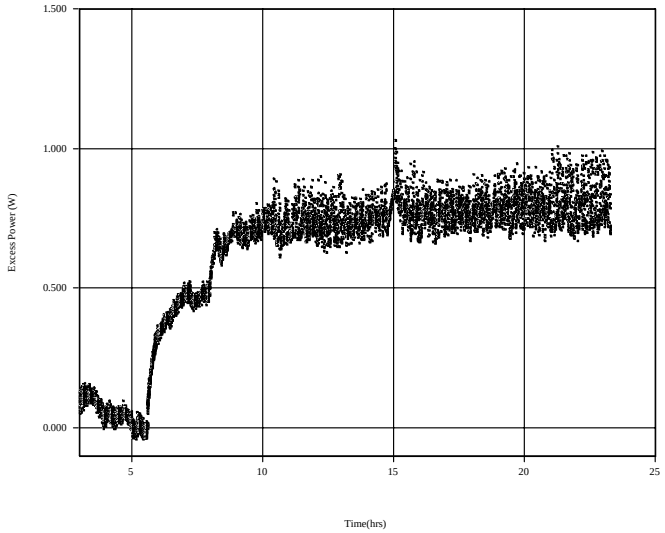

Figure 2. The excess power recorded as function of time following the addition of hydrogen.

Table 1. Input and excess power for a rt-plasma formed with potassium catalyst.

Filament Length (cm)	Input Power (W)	Total Power (W)[a]	Excess Power (±0.06 W)[b]
10	7.02	7.64	0.62
20	9.82	10.63	0.81
30	15.01	17.08	2.07

[a] Eq. (12)
[b] Eq. (13)

With constant power per unit length to the filament to maintain a constant filament temperature, the excess power was observed to be linear in filament length as shown in Table 1, and therefore filament area. This result is consistent with the dissociation of hydrogen as a rate limiting mechanism. Given a flow rate of 0.1 sccm and an excess power of 2.07 W observed with a 30 cm long filament, energy balances of over –28,000 kJ/mole H_2 (145 eV/H atom) were measured. The reduction of KNO_3 to water, potassium metal, and NH_3 calculated from the heats of formation only releases -14.2 kcal/mole H_2 (0.3 eV/H atom) which can not account for the observed heat. The most energetic reaction possible was the reaction of hydrogen with atmospheric oxygen to form water which releases -241.8 kJ/mole H_2 (1.48 eV/H atom) which is about 100 times less than that observed. But, the results are consistent with the formation of H^-(1/4) and H_2(1/4) having enthalpies of formation of over 100 times that of combustion.

NMR and FTIR Identification of H^-(1/4). The ^{1}H MAS NMR spectra relative to external tetramethylsilane (TMS) of KH*Cl samples from independent syntheses and controls were given previously.[1,12–14] The presence of KCl did not shift the resonance of ordinary hydride since the controls comprising an equal molar mixture of KH and KCl and KH as well as KH*Cl showed the same resonance at about 1.3 ppm which was assigned to ordinary hydride ion. KH*Cl samples showed a large distinct upfield resonance at -4.5 ppm which was not observed in either control.

The experimental absolute resonance shift of TMS is -31.5 ppm relative to the proton's gyromagnetic frequency.[42,43] The KH experimental shift of +1.3 ppm relative to TMS corresponding to absolute resonance shift of -30.2 ppm matches very well the predicted shift of H^-(1/1) of -30 ppm given by Eq. (11) wherein $p = 0$. The novel peak at -4.5 ppm relative to TMS corresponding to an absolute resonance shift of -36.0 ppm indicates that $p = 4$ in Eq. (11). H^-(1/4) is the hydride ion predicted by using K as the catalyst.[1,19] Furthermore, the extraordinarily narrow peak-width is indicative of a very small hydride ion that is a free rotator.

Samples with the -4.5 ppm peak were analyzed by FTIR spectroscopy to determine if there was any correlation between the -4.5 ppm ^{1}H NMR peak and possible IR vibration bands, in particular the substitutional H^- U-center band around 502 cm^{-1}. Two KH*Cl samples, 1 and 2, that exhibit equal intensity peaks at -4.5 ppm in the solid-state ^{1}H NMR spectra (**Figure 3**), show markedly different FTIR spectra (**Figure 4**), in which sample 2 has the U H^- vibration band at 502 cm^{-1}, while sample 1 does not.

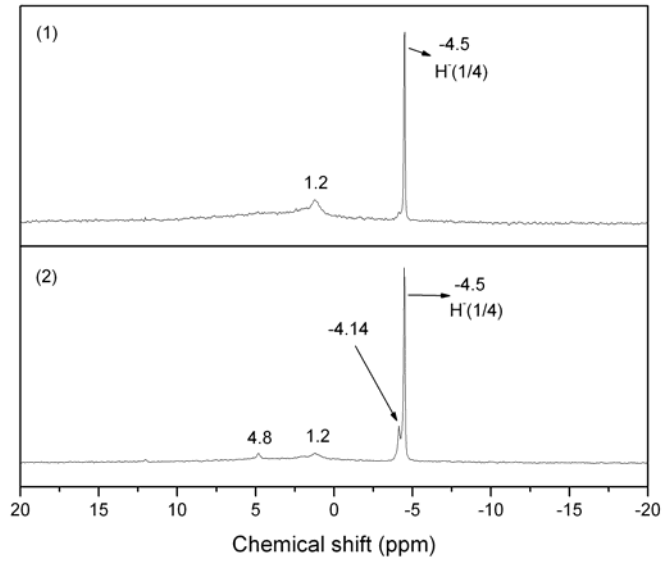

Figure 3. Solid state ^{1}H NMR spectra of samples 1 and 2.

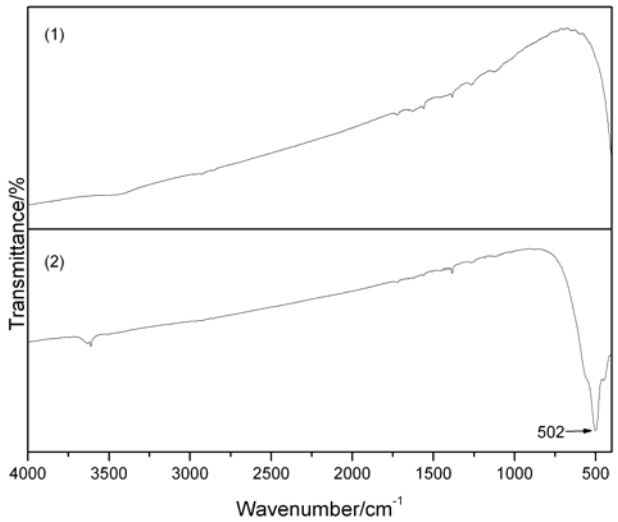

Figure 4. FTIR spectra of samples 1 and 2.

Thus, there is no relationship between the presence of U centers and the -4.5 ppm ^{1}H NMR peak. The IR band at 3613 cm^{-1} and 3641 cm^{-1} in sample 2 could arise from interstitial H_2O, which corresponds to the 4.8 ppm peak in its ^{1}H NMR spectrum. Since the NMR–FTIR comparison leads to the conclusion that the -4.5 ppm peak in ^{1}H NMR spectrum is not associated with the U H^- vibration

band at 502 cm^{-1}, the -4.5 ppm peak in ^1H NMR spectrum is assigned to the H^- (1/4) ion which matches theoretical predictions and is direct evidence of a lower-energy state hydride ion.

XPS Identification of H^- (1/4). A survey spectrum was obtained over the region E_b = 0eV to 1200 eV. The primary element peaks allowed for the determination of all of the elements present in the KH*I crystals and the control KI. No elements were present in the survey scan which could be assigned to peaks in the low binding energy region with the exception of the K $3p$ and K $3s$ peaks at 17 eV and 33 eV, respectively, the O $2s$ at 23 eV, and the I $5s$, I $4d_{5/2}$, and I $4d_{3/2}$ peaks at 12.7 eV, 51 eV, and 53 eV, respectively. Accordingly, any other peaks in this region must be due to novel species.

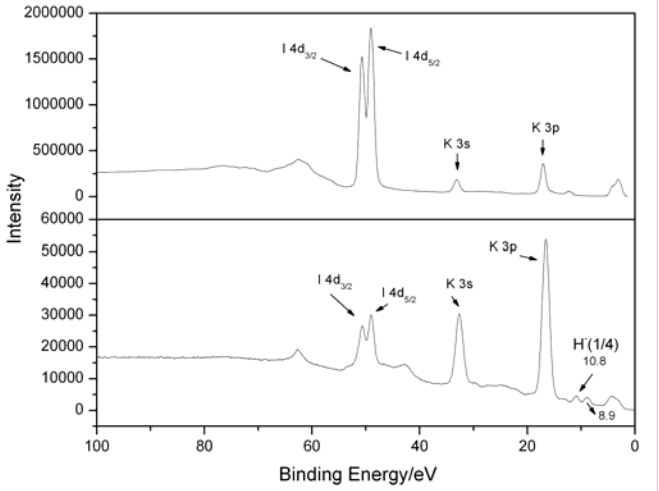

Figure 5. The 0–100 eV binding energy region of a high resolution XPS spectrum of the control KI (top) and KH*I (bottom).

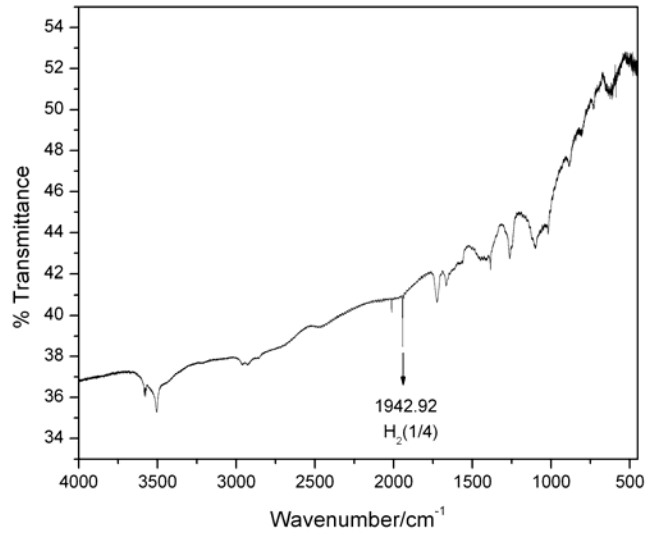

Figure 6. High resolution FTIR spectrum (490–4000 cm^{-1}) of KH*I having a peak assigned to H^- (n = 1/4) following storage in an inert atmosphere for 90 days.

As shown in **Figure 5**, the XPS spectrum of KH*I differs from that of KI by having additional features at 8.9 eV and 10.8 eV that do not correspond to any other primary element peaks but do match the H^- (n = 1/4) E_b = 11.2 eV hydride ion (Eq. (10)) in two different chemical environments.

FTIR Identification of H_2(1/4). Samples of KH*I having an upfield ^1H MAS NMR peak at -4.6 ppm that was assigned to the H^-(1/4) ion were stored under argon for 90 days, and the high resolution FTIR spectrum of the solid compound was recorded before and after storage. As shown in **Figure 6**, single rotational peaks were observed at 1943 cm^{-1} and 2012 cm^{-1} that were unchanged after storage. The peak at 1943 cm^{-1} (0.2409 eV) matched the theoretical prediction of 1947 cm^{-1} for H_2(1/4). From Eqs. (5-8), the unprecedented rotational energy of 4^2 times that of ordinary hydrogen establishes the internuclear distance of H_2(1/4) as 1/4 that of H_2.

As a pair, the 1943 cm^{-1} and 2012 cm^{-1} peaks further match the pattern expected for ortho and para- H_2(1/4) based on the results for H_2. Interstitial H_2 in silicon and GaAs is a nearly free rotator.[44–48] H_2 is FTIR active as well as Raman active due to the induced dipole from interactions with the crystalline site.[44] Furthermore, the Raman and FTIR vibration-rotational bands are split into two components with an intensity ratio of ~3:1 that are assigned to ortho-and para- H_2, respectively. The frequencies differ by 8 cm^{-1} because of the higher rotation-vibrational energy of para relative to ortho-H_2.[44]

The crystalline lattice may also influence the selection rules to permit an otherwise forbidden transition in H_2(1/4). The four-significant-figure match for the 1943 cm^{-1} peak indicates that H_2(1/4) can rotate freely inside of the crystal and confirms its small size corresponding to 1/4 the dimensions of ordinary hydrogen. Furthermore as shown in **Figure 7**, the intensity ratio of the 1943 cm^{-1} and 2012 cm^{-1} peaks is about 3:1 which matches the hydrogen ortho-para ratio at non-cryogenic temperatures. In this case, the proposed para- H_2(1/4) rotational frequency is 69 cm^{-1} higher than that of ortho- H_2(1/4. This frequency difference is about the same as the frequency difference between the J=0 and J=1 states of HD.[44]

The splitting can easily be calculated from the result of Lavrov and Weber[45] for free H_2 using the Morse-potential expansion with an inter nuclear distance of 1/4 that of H_2:

$$\frac{\Delta_{H_2(1/4)}}{\Delta_{H_2}} = \frac{\dfrac{12(256)B_e^2}{\hbar 16\omega_e}\left(\dfrac{4\hbar}{\mu 256\omega_e^2}\sqrt{\dfrac{2}{\mu 16B_e}}-1\right)}{\dfrac{12B_e^2}{\hbar\omega_e}\left(\dfrac{a\hbar}{\mu\omega_e^2}\sqrt{\dfrac{2}{\mu B_e}}-1\right)} \tag{14}$$

$$\text{In the case that } 1 << \frac{a\hbar}{\mu\omega_e^2}\sqrt{\frac{2}{\mu B_e}} \tag{15}$$

$$\Delta_{H_2(1/4)} = 16\Delta_{H_2} = 4^2\Delta_{H_2} = 70.4\,cm^{-1}$$

where the calculated H_2 result of 4.4 cm^{-1} (Ref. [45]) allowed for the cancellation of the curve-fit parameter a. The result agrees well with the observed ortho-para splitting of 69 cm^{-1}. Given the frequency match of the 1943 peak, the 3:1 intensity ratio, the match of the frequency difference between the peaks, and the absence of any known alternative, the 1943 cm^{-1} and 2012 cm^{-1} peaks are assigned to the J=0 to J=1 rotational transitions of ortho and para- H_2(1/4), respectively.

Conclusion

The possibility that a novel catalytic reaction of atomic hydrogen to form more stable hydride and molecular hydrogen species such as H^-(1/4) and H_2(1/4) may be a clean new energy source is supported by spectroscopic, chemical, and thermal data.

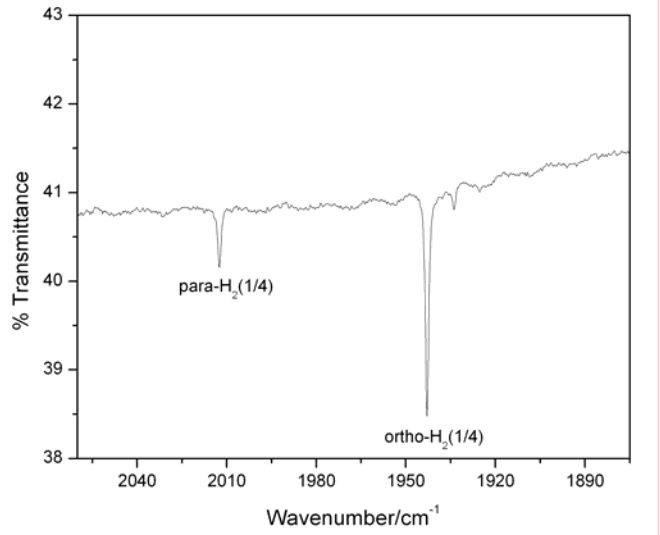

Figure 7. High resolution (0.5 cm^{-1}) FTIR spectrum (1875–2060 cm^{-1}) of KH*I showing the 1943/2012 cm^{-1}-peak-intensity ratio of 3:1.

References

(1) Mills, R. L.; Ray, P.; Dhandapani, B.; Good, W.; Jansson, P.; Nansteel, M.; He, J.; Voigt, A., *Eur. Phys. J. Appl. Phys.* **2004**, *28*, 83.
(2) Mills, R. L.; Nansteel, M.; Ray, P. *IEEE Trans. Plasma Sci.* **2002**, *30* (2), 639.
(3) Mills, R. L.; Nansteel, M.; Ray, P. *New J. Phys.* **2002**, *4*, 70.1.
(4) Mills, R. L.; Dong, J.; Lu, Y. *Int. J. Hydrogen Energy* **2000**, *25*, 919.
(5) Mills, R. L.; Nansteel, M.; Ray, P. J. Plasma Phys. **2003**, *69*, 131.
(6) Conrads, H.; Mills, R. L.; Wrubel, Th. *Plasma Sources Sci. Technol.* **2003**, *12*, 389.
(7) Mills, R. L.; He, J.; Nansteel, M.; Dhandapani, B. "Catalysis of Atomic Hydrogen to New Hydrides as a New Power Source," submitted.
(8) Mills, R. L.; Nansteel, M.; He, J.; Dhandapani, B. "Low-Voltage EUV and Visible Light Source Due to Catalysis of Atomic Hydrogen," submitted.
(9) Phillips,J.; Mills, R. L.; Chen, X. *J. Appl. Phys*. **2004**, *96*, 3095.
(10) Mills, R. L.; Chen, X.; Ray, P.; He, J.; Dhandapani, B. Thermochim. Acta, **2003**, *406* (1-2), 35.
(11) Mills, R. L.; Lu, Y.; Nansteel, M.; He, J.; Voigt, A.; Dhandapani, B. Prepr. Pap. *Am. Chem. Soc., Div. Fuel Chem*, **2004**, *49* (1).
(12) Mills, R. L.;, Dhandapani, B.; Nansteel, M.; He, J.; Shannon, T.; Echezuria, A. *Int. J. Hydrogen Energy*, **2001**, *26*, 339.
(13) Mills, R. L.; Dhandapani, B.; Nansteel, M.; He, J.; Voigt, A. *Int. J. Hydrogen Energy*, **2001**, *26*, 965.
(14) Mills, R. L.;, Dhandapani, B.; Greenig, N.; He, J. *Int. J. Hydrogen Energy*, **2000**, *25*, 1185.
(15) Mills, R. L.; Lu, Y.; He, J.; Nansteel, M.; Ray, P.; Chen, X; Voigt, A.; Dhandapani, B."Spectral Identification of New States of Hydrogen," submitted.
(16) Mills, R. L., Ray, P. *J. Phys. D Appl. Phys.* **2003**, *36*, 1535.
(17) Mills, R. L.; Ray, P.; Dhandapani, B.; Nansteel, M.; Chen, X.; He, J. *J Mol. Struct.*, **2002**, *643* (1-3), 43.
(18) Mills, R. L.; Ray, P. *Int. J. Hydrogen Energy*, **2002**, *27*, 301.
(19) Mills, R. L.; Ray, P. *Int. J. Hydrogen Energy*, **2003**, *28*, 825.
(20) Mills, R. L. *Int. J. Hydrogen Energy*, **2001**, *26*, 1041.
(21) Mills, R. L.; Ray, P.; Dhandapani, B.; Mayo, R. M.; He, J. *J. Appl. Phys.* **2002**, *92*, 7008.
(22) Mills, R. L.; Ray, P.; Dhandapani, B.; He, J. *IEEE Trans. Plasma Sci.* **2003,** *31*, 338.
(23) Mills, R. L.; Ray, P. New J. Phys. **2002**, *4*, 22.1.
(24) Phillips, J.; Chen, C. "Evidence of Energetic Reaction Between Helium and Hydrogen Species in RF Generated Plasmas," submitted.
(25) Mills, R. L.; Ray, P.; Mayo, R. M. *IEEE Trans. Plasma Sci.* **2003**, *31* (2), 236.
(26) Mills, R. L.; Ray, P. *J. Phys. D Appl. Phys.* **2003**, *36*, 1504.
(27) Mills, R. L.; Ray, P.; Mayo, R. M. *Appl. Phys. Letts.* **2003**, *82*, 1679.
(28) Mills, R. L., *The Grand Unified Theory of Classical Quantum Mechanics*, Jan. 2005, Ed. posted at www.blacklightpower.com.
(29) Sidgwick, N. V. *The Chemical Elements and Their Compounds*, Volume I, Oxford, Clarendon Press, 1950, p.17.
(30) Lamb, M. D. *Luminescence Spectroscopy*, Academic Press, London, 1978, p. 68.
(31) Mills, R. L. "The Nature of the Chemical Bond Revisited and an Alternative Maxwellian Approach," submitted; posted at http://www.blacklightpower.com/pdf/technical/H2PaperTableFiguresCaptions111303.pdf.
(32) Beutler, H. *Z. Physical Chem*. **1934**, *27B*, 287.
(33) Herzberg, G.; Howe, L. L. *Can. J. Phys.* **1959**, *37*, 636.
(34) Atkins, P. W. *Physical Chemistry*, Second Edition, W. H. Freeman, San Francisco, 1982, p. 589.
(35) Karplus, M.; Porter, R. N. *Atoms and Molecules an Introduction for Students of Physical Chemistry*, The Benjamin/Cummings Publishing Company, Menlo Park, CA, 1970, pp. 447-484.
(36) Lykke, K. R.; Murray, K. K.; Lineberger, W. C. *Phys. Rev. A* **1991**, *43*, 6104.
(37) Abeles, F. (Ed.), *Optical Properties of Solids*, 1972, p. 725.
(38) Wieser, J. ; Murnick, D. E.; Ulrich, A.; Higgins, H. A; Liddle, A.; Brown, W. L. *Rev. Sci. Instrum*. **1997**, *68*, 1360.
(39) Ulrich, A.; J. Wieser, J.; Murnick, D. E *Proceedings of SPIE*, **1998**, *3403*, 300-307.
(40) Shuaibov, A. K.; Dashchenko, A. I.; Shevera, I. V. *Quant. Electron*. **2001**, *31* (6), 547.
(41) Shuaibov, A. K.; Shimon, L. L.; Dashchenko, A. I.; Shevera, I. V. *Plasma Phys. Rep.* **2001**, *27* (10), 897.
(42) Baldridge, K. K.; Siegel, J. S. *J. Phys. Chem. A* **1999**, *103*, 4038.
(43) Mason, J. Editor, *Multinuclear NMR*, Plenum Press, New York, 1987, Chp. 3.
(44) Stavola, M.; Chen, E. E.; Fowler, W. B.; Shi, G. A. *Physica B*, **2003**, *340–342*, 58–66.
(45) Lavrov, E. V.; Weber, J. *Phys. Rev. Letts*. **2002**, *89* (21), 215501-1.
(46) Chen, E. E.; Stavola, M.; Fowler, W. B.; Zhou, J. A. *Phys. Rev. Letts*. **2004**, *88* (24), 245503-1.
(47) Chen, E. E.; Stavola, M.; Fowler, W. B.; Walters, P. Phys. Rev. Letts. **2002**, *88* (10), 105507-1.
(48) Leitch, A. W. R., Alex, V. Weber, J. *Phys. Rev. Letts.* **1998**, *81* (2), 421.

GEL PERMEATION CHROMATOGRAPHY COUPLED TO PHOTODIODE ARRAY-UV AND INDUCED FLUORESCENCE DETECTION FOR CHARACTERIZING SATURATED HYDROCARBONS, AROMATICS, AND FUELS

V.L. Cebolla[1], M. Matt[2], E.M. Galvez[1], L. Membrado[1], E. Mateos[1], J. Vela[1], M.H. Guermouche[3]

1: Instituto de Carboquímica, CSIC, Miguel Luesma, 4. 50015 Zaragoza, Spain
vcebolla@carbon.icb.csic.es

2 : Laboratoire de Chimie et Applications, Université de Metz, France

3: Institut de Chimie, USTHB, BP32, Bab Ez zouar, Alger, Algerie.

Introduction

Determination of hydrocarbon types and their further characterization are considered classical types of analysis in the petroleum industry. Traditionally, aromatic compounds in diesel fuels have been determined by High Performance Liquid Chromatography (HPLC) with detection by differential refractometry[1]. Apart from its technical limitations, determination of saturates is not carried out directly, but by difference after aromatics determination. Likewise, saturated hydrocarbons have been neither separated nor detected under liquid chromatographic conditions.

In previous works[2,3], we developed sensitive methods, based on Thin Layer Chromatography (TLC and HPTLC) with UV and fluorescence scanning densitometry, for separation and quantitative determination of hydrocarbon types in middle distillates, which included direct determination of saturates. The basis of this detection by fluorescence is the increase in emission intensity generated in a berberine-impregnated silica gel plate from an ion-induced dipole interaction between the corresponding alkane and berberine cation[4,5]. This technique takes place in absence of solvent, because it is removed before detection. Here we present an adaptation of this technique to liquid media, and its potential application to fuel characterization in combination with Gel Permeation Chromatography, and with an additional UV detection system.

Experimental

Materials and reagents. *n*-Alkanes and aromatics standards used were from Fluka (Basel, Switzerland); and Ultrascientific (North Kingstown, RI, USA). Berberine sulfate (95+%, from Across Chimica, Geel, Belgium) was used to induce fluorescence. Ten diesel fuels (straight-run gas oil) and ten kerosenes were used (Sonatrach, Algerie) to test the described techniques.

HPLC equipment. This consisted of: a pump (600E Waters, USA) for mobile-phase elution; a second pump (W6000A Waters) for a post-column introduction of a berberine sulfate solution through a coil placed between a photodiode array UV (PDA-UV, Waters) and 474 fluorescence detector (Waters, USA).

GPC separation conditions. *n*-Alkanes standards (50 mg L^{-1}), diesel fuels and kerosenes were separated using a set of three GPC columns which were connected in series; two PLGel 50 columns (5 µm, 50 Å, 7.5 mm x 30 cm, Touzart et Matignon, France) + 1 microstyragel 500 column (7.5 mm x 30 cm, Waters, USA). 20 µL of each sample was injected. Elution in both cases was done with THF as mobile-phase at 1 mL min^{-1}. Retention zones of aromatics families in gas oil were selected by using appropriate aromatics standards.

Detection conditions. Aromatics detection was carried out by absorbance using the PDA-UV detector. Fluorescence was induced for all samples by a 100 ppm berberine sulfate solution in a dichloromethane-methanol mixture (99.5:0.5, v:v). It was pumped at 0.2 mL min^{-1} flow by the second pump before fluorescence detection (λ_{exc}= 355 nm, λ_{em}= 520 nm).

Results and Discussion

Separation of *n*-alkanes by GPC and detection by induced fluorescence. *n*-Alkanes can be separated under GPC conditions and detected using the adaptation of berberine-induced fluorescence in liquid media (see Experimental). **Figure 1** shows a GPC-induced fluorescence chromatogram of a synthetic mixture of alkanes (*n*-C_{12}, C_{13}, C_{14}, C_{16}, C_{18}, C_{21}, and C_{25}).

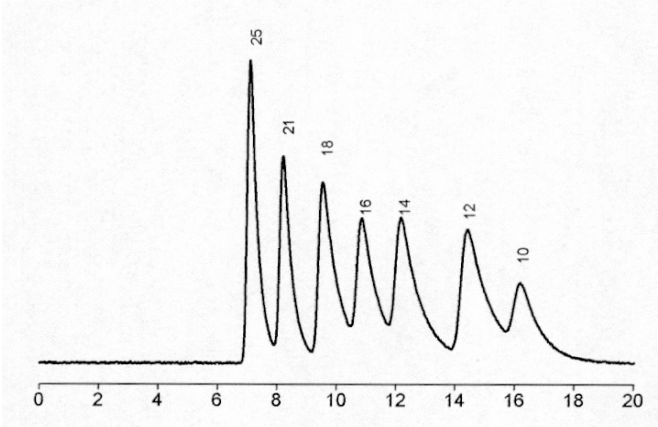

Figure 1.- GPC chromatogram of a mixture of *n*-alkanes. Detection by induced-fluorescence. Retention time in minutes. (see Experimental for conditions).

Fluorescent response shows adequate sensitivity (25 ng of *n*-heptane was detected using the above-mentioned conditions), and depends on the chromatographic conditions, as well as the mass and structure of the saturated hydrocarbon[4,5]. Under constant chromatographic conditions, response has a linear behavior with alkane mass, and therefore it is possible to carry out a quantitative determination of separated alkanes.

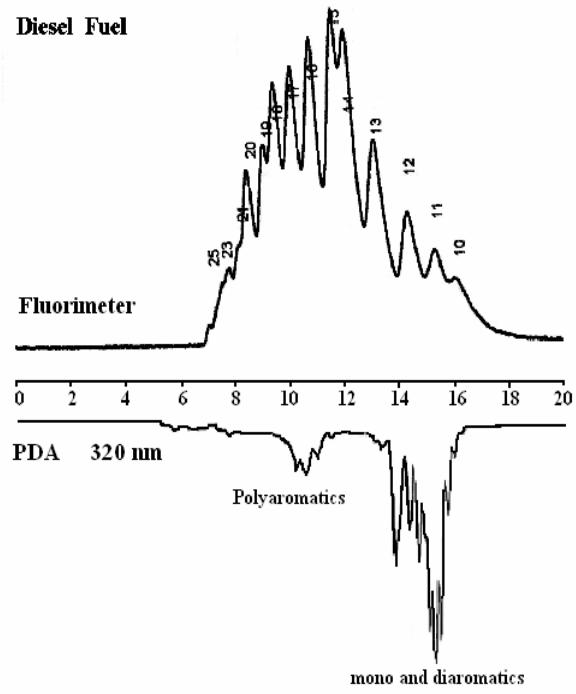

Figure 2.- GPC chromatogram of a diesel fuel. Retention time in minutes. Upper: detection by induced-fluorescence. Lower: detection by absorbance at 320 nm (see Experimental for conditions).

Characterization of diesel fuel and kerosene by GPC with PDA-UV combined to induced fluorescence. This technique has been applied for characterizing diesel fuels. **Figure 2** shows a representative chromatogram.

The use of three GPC columns allows the polyaromatics to be separated from mono- and diaromatics, as is shown by PDA-UV detection chromatogram. This detection system allows a selective detection of UV-absorbing compounds, mostly aromatics in this case, and not saturates.

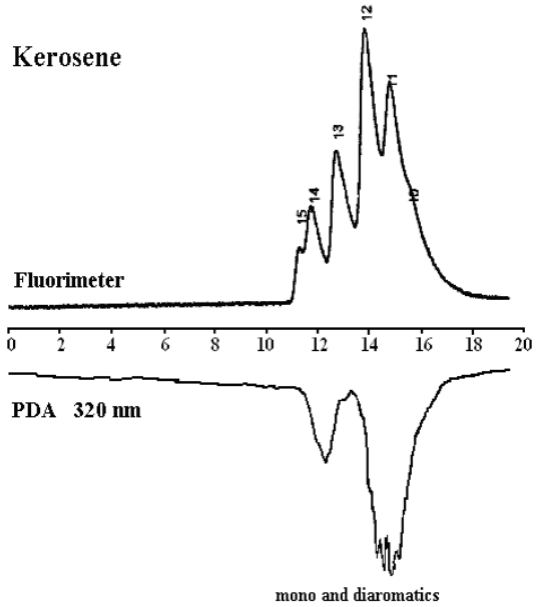

Figure 3.- GPC chromatogram of a kerosene. Retention time in minutes. Upper: detection by induced-fluorescence. Lower: detection by absorbance at 320 nm (see Experimental for conditions).

The induced-fluorescence chromatogram clearly shows responses of saturated hydrocarbons in the corresponding diesel fuel. Numbered peaks in **Figure 2** correspond to *n*-alkanes which range from C_{10} to C_{25}. However, aromatics give a certain response in berberine system. Aromatics response may be due to native emission (exciting at 355 nm), and / or a filter effect. Therefore, the combined use of induced-fluorescence and UV chromatograms gives an overall picture of the sample, providing interesting information about the diesel fuel compounds. In any case, the chromatogram corresponding to detection by induced-fluorescence shows that GPC conditions do not allow separation between saturates and aromatics to be carried out.

This technique has also been applied to kerosene characterization, as shown in **Figure 3**. The induced-fluorescence chromatogram shows that alkanes range from C_{10} to C_{15}.

In general terms, this technique provided repeatable results. The average coefficient of variation, calculated after injection of 5 samples of each ten studied diesel fuels and kerosenes, was 3 %. Therefore induced-fluorescence detection in HPLC conditions might be applied to gasoline analysis given that it is less limited by sample volatility than its HPTLC-based alternative.

It seems possible to couple this detection system to any type of standard fuel separation conditions, for example, to normal-phase HPLC columns to carry out a separation between saturates and aromatics.

Acknowledgement. Spanish authors also thanks Spanish Ministery for Science and Technology (MCYT) (project PPQ2001-2388) and Government of Aragon (DGA) for financial support.

References

(1) Standard Methods for Analysis and Testing of Petroleum and Related Products, **1992**, vol. 2, Institute of Petroleum, London

(2)Matt, M.; Gálvez, E.M.; Cebolla, V.L.; Membrado, L.; Bacaud, R.; Pessayre, S. *J. Sep. Sci.* **2003**, *26*, 1665.

(3)Cebolla, V.L.; Membrado, L.; Domingo, M.P.; Henrion, P.; Garriga, R.; González, P.; Cossío, F.P.; Arrieta, A.; Vela, J. *J. Chromatogr. Sci.* **1999**, *37*, 219.

(4)Cossío, F.P.; Arrieta, A.; Cebolla, V.L.; Membrado, L.; Domingo, M.P.; Henrion, P.; Vela, J. *Anal. Chem.* **2000**, *72*, 1759

(5)Cossío, F.P.; Arrieta, A.; Cebolla, V.L.; Membrado, L.; Garriga, R.; Vela, J.; Domingo, M.P. *Org. Lett.* **2000**, *2*, 2311

THE ADSORPTION OF ASPHALTENES COMPARED TO MODEL HEAVY MOLECULES OVER MACROPOROUS SOLIDS

Francisco López-Linares, Clementina Sosa, Manuel González, Pedro Pereira-Almao

Department of Chemical and Petroleum Engineering,
University of Calgary, Calgary, Alberta, T2N 1N4 Canada

Introduction

Asphaltenes precipitation is an important problem faced at different levels in the petroleum industry where it has an economic impact associated to the costs of oil production and processing.

It has been found that asphaltenes are strongly adsorbed on certain mineral components of rock reservoir [1,2] or in production wells as deposits of both organic and inorganic predominant nature [3]. Different studies relating asphaltenes adsorption on surface solids media, their characterization and precipitation capability are found in the literature [4, 5, 6].

Asphaltenes are defined as a fraction of a crude oil insoluble in n-heptane and soluble in toluene, so they are not a chemical family per se. They contain polynuclear aromatics and are the heaviest components of crude oils with highest heteroatom content [7]. Asphaltenes seem to contain a large heterogeneity of chemical functionalities whose activity depends upon the crude oil and/or their dilution extent.

Due the complexity of the asphaltene structures, the studies of their adsorption behaviour have limitations. To simplify that complexity the use of a set of structurally known heavy model molecules seems to be an alternative approach. These model molecules might contain properties and chemical functionalities similar to the ones present on some averaged well-characterized asphaltenic fractions such as molecular weight, aromaticity, naphtenicity levels, and number or nature of functional groups.

To explore this alternative, in this study we used three model molecules which contain some functional groups that have been identified in Athabasca asphaltenes [8]. The objective is to determine by comparison if those model molecules resemble the asphaltenes adsorption process on kaolin, a natural silica-alumina.

Experimental

Toluene (ACS or spctrophotometric grade), trioctylamine (95 %) concentrated in hydrochloric acid and anhydrous magnesium sulphate were obtained from Aldrich. The adsorbent used was synthesized in our laboratory to obtain macro porous extrudates with cylindrical shape. The starting material was a natural silica-alumina, kaolin. The final solid obtained had a 12-20 m^2/g surface area and an average meso pore diameter between 50 and 100 nm determined by Isotherm.

Asphaltenes from Athabasca bitumen (ATB-ASP) were obtained via n-heptanes precipitation method [9-10] then re-dissolved in toluene. Their average molecular weight was 4000 g/mol as estimate by VPO. The asphaltenes used were not washed and they might contain a small amount of resins. The model molecules selected were Violanthrone-78, Violanthrone-79 (both from Aldrich) and Xylenol Orange tretrasodium Salt (OmniPur – EDM) namely all the time in this work VO-78, VO-79 and XYO respectively with molecular weight in the range of 700-2500 g/mol. The XYO initially water soluble was transformed in organosoluble by adapting a procedure reported in the literature [11].

Adsorption method: several solutions at different concentrations were contacted with a specific amount of adsorbent in a static adsorption experiment. The adsorptions were carried out at constant solution / adsorbent ratio of 10:1 (cc/gr). The adsorption studies were performed using different concentrations of model molecules and asphaltenes solutions in toluene. The adsorption evolution was measured by means of the UV/VIS technique using a Cary 4E Spectrophotometer reading absorbance of λmax= 281 nm (for asphaltene) λmax= 577 nm (for VO-78) and λmax= 633 nm (for VO-79). A determination of the maximum wavelength was conducted following a reported procedure [12]. An equilibration period of 48 hours at room temperature (22 C) was fixed. Dilutions of some samples in the case of the asphaltenes redissolved in toluene were done in order to be able to measure the absorbance.

Results and Discussion

The adsorption studies were preformed over a natural silica-alumina (kaolin) at 22 C. Several solutions at different concentration from 1 to 30,000 mg/L for asphaltene and 1–10,000 mg/L for the model molecules were used. In Figure 1, the Up-take at equilibrium (mg/g) for the model molecules and asphaltenes versus the initial concentration (mg/l) at 22 C is displayed. The molecular weight is included in the leyend for each molecule.

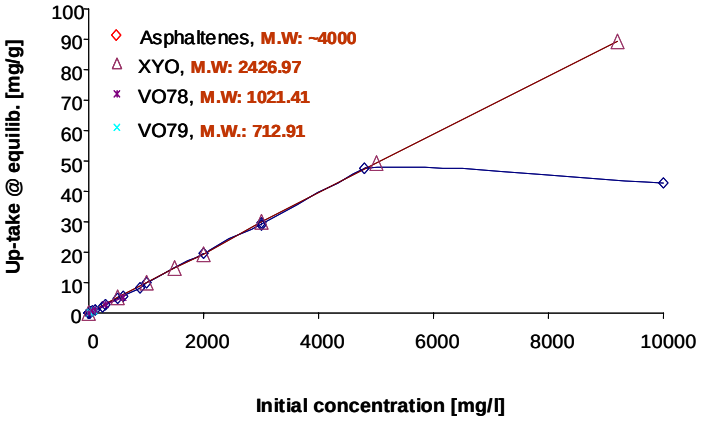

Figure 1. Adsorption behaviour of model molecules dissolved in toluene solution on natural silica-alumina (25 C)

As can be seen in the figure 1, for low initial concentration (5000 mg/l), all model molecules and asphaltenes have the same mass level of adsorption at equilibrium as the average asphaltene molecule. It suggests that at such concentration there is not limitation on the thermodynamic of the adsorption associated to the size of the molecule. However as soon as we increase the initial concentration above 5000 mg/l, it is observed that the bigger molecules, in this case asphaltenes, do not adsorb anymore, remaining in solution regardless their initial concentration. This behaviour could be related to difficulties of the asphaltenes to enter the pores of the adsorbent to reach (or not) the maximum level of up take associated to a monolayer. Moreover XYO, continues the Up-take until 10000 mg/l. The adsorption behaviour for this molecule is an indirect indication that it is smaller than the asphaltenes average molecule.

Figure 2 shows the adsorption isotherm for n-heptane asphaltenes (ATB-ASP), and Xylenol Orange (XYO) dissolved in toluene at ambient temperature. Here we can see the equilibrium Up-take (mg/g) of the molecules vs. the solution concentration at the equilibrium. Langmuir isotherm Type I behaviour was observed for

the two macromolecules evaluated suggesting a typical monolayer adsorption.

.

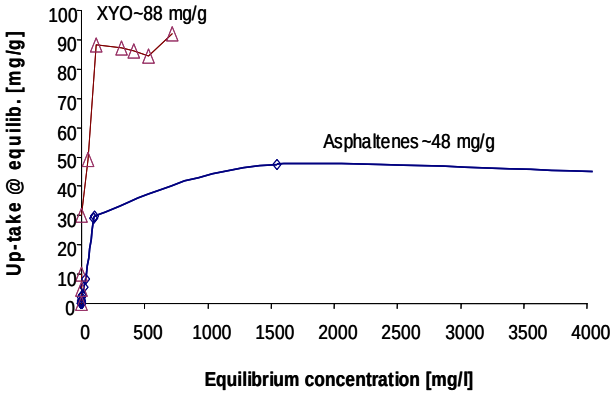

Figure 2. Adsorption isotherm of XYO and asphaltenes dissolved in toluene solution on natural silica-alumina (25 C)

At ambient temperature, the maximum adsorption was observed for XYO (~88 mg/g) while for asphaltenes, the adsorption reached approximately 48 mg/g. Perhaps relevant is the fact that the total mass uptake to eventually form the Langmuir monolayer follows about the molecular weight ratio of the two molecules being compared.

The adsorption kinetics was determined for each molecule at different initial concentrations. The results are displayed in Figure 3.

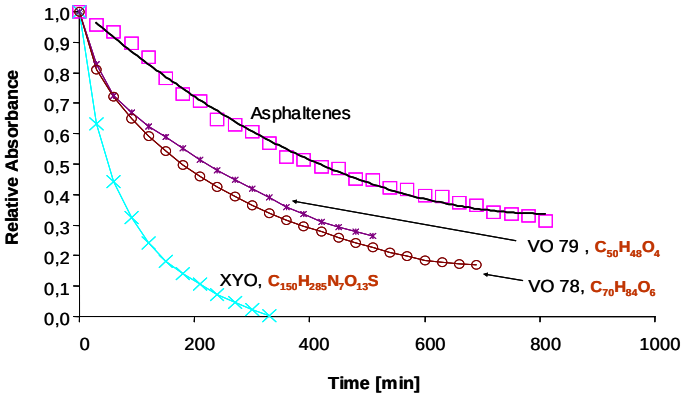

Figure 3. Kinetic of the adsorption of macro molecules/toluene solution on natural silica-alumina

.

This figure plots the relative absorbance (absorbance at time t / initial absorbance) vs. time (min). As it can be observed, all model molecules have faster initial adsorption rate comparing with the asphaltenes. Different from the thermodynamics of adsorption at low initial concentrations shown in previous figures, it is now evidenced that the rate of adsorption strongly depends on specificities of the molecules being adsorbed. XYO which contains the highest molecular weight of the model molecules employed showed the fastest initial rate of adsorption of all the molecules tested. These results indicate that a different process controls the kinetics of adsorption, which may be related to the type and content of heteroatoms present on those molecules. In Figure 3 the MW and the chemical formula of the different model molecules whose adsorption was kinetically evaluated are included. It can be noticed that the rate of adsorption increases with the oxygen content, when passing from asphaltenes to VO-78 and VO-79. Furthermore, the presence of both nitrogen and oxygen has a paramount effect on the adsorption rate, illustrated by XYO. It seems that the presence of nitrogen in the molecule contributes to increase the quickness of adsorption in comparison with the oxygen contained in the molecules.

Sulphur content in ATB–ASP is the highest of all molecules tested (~8 w %) vs. XYO (1.3 w %) nevertheless it doesn't seem to help at the rate of adsorption of asphaltenes when compared with the model molecules being tested.

Conclusions

The present study shows that the adsorption uptake at equilibrium of asphaltenes on a natural silica-alumina is independent, up to a certain initial concentration limit, of the structure and of the heteroatomic nature of the molecule. The total final uptake might depend more on the molecular size of them. Nevertheless the dynamic of the adsorption seems to be more determined by the nature and content of heteroatoms present on those molecules which allow them to interact stronger and faster with the solid surface. This work shows that it is possible to model the adsorption properties of asphaltenes via successive approximations both in molecular size and chemical functionalities starting with structurally known heavy molecules.

Acknowledgments. The authors acknowledge the substantial financial support provided by several institutions for the creation of a research group on topics related to the content of this paper at the University of Calgary, Alberta, Canada. In particular this work is being supported by the Alberta Ingenuity Fund through the Ingenuity Scholar support provided to Professor Pedro R. Pereira-Almao. It is also acknowledged the financial support in the form of discovery and strategic research grants respectively, provided by the National Science and Engineering Research Committee (NSERC) of Canada and the Alberta Energy Research institute (AERI) of the province of Alberta, Canada.

References

1. Pernyeszi, T., Patzko, A., Berkesi, O., Dekany, I., Colloids and Surfaces A-Physicochemical and Engineering Aspects, **1998**, 137, 373
2. Pernyeszi, T., Dekany, I., Colloids and Surfaces A-Physicochemical and Engineering Aspects, **2001**, 194, 25
3. Acevedo, S., Ranaudo, M. A., Escobar, G., Gutierrez, L., Ortega, P., Fuel, **1995**, 74, 595
4. Kokal, S., Tang, T., Schramm, L., Sayegh, S., Colloids and Surfaces A-Physicochemical and Engineering Aspects, **1995**, 94, 253
5. Marczewski A., Szymula M. Colloids and Surfaces **2002**, 208,259-266
6. Alboudwarej H. et al. The 5Th International Conferences on Petroleum Phase Behaviour and Fouling. Banff, Alberta Canada, June 13-17th, **2004**
7. Speight, J.G., ' Petroleum Chemistry and Refining", Taylor & Francis, Washington, **1998**.
8. Strausz, O. P., Mojelsky T. W and Lown E. M. Fuel, **1992**, 71,1355-1363
9. Alboudwarej H. et al. Energy & Fuel, **2002**, 16 (2), 462-469
10. Alboudwarej H. et al. AIChE Journal, **2003**, 49 (11), 2948-2956
11. Herrmann W. A., Kohlpaintner C. W. Angew. Chem. Int. Ed. Engl., **1993** (32): 1524-1544
12. Marczewski, A. Szymula, M., Colloids and Surfaces A-Physicochemical and Engineering Aspects, **2002**,208, 259-266

THE RELEVANCE TO CONSIDER CHEMICAL FUNCTIONALITIES IN SEPARATION SCHEMES PROPOSED FOR ASPHALTENE CHARACTERIZATION

Marco Antonio G. Teixeira

PETROBRAS R&D Center – Chemistry
Av. Um, Quadra 7, s/n, Cidade Universitária – sala 255
Rio de Janeiro, Brazil CEP:21949-900
marcoa@petrobras.com.br

Introduction

Asphaltenes are a class of macromolecular components found in crude oil and derivatives. They are expected to have the higher molecular weights and higher heteroatom contents among all of the oil fractions. However, though these concepts bring an idea of molecular definitions for asphaltenes, their separation from crude oils or fuel products has to be done by solubility criteria, with the use of precipitations using light alkanes, because a procedure able to isolate them based on chemical concepts has not been reached yet. This criterion is not only applied to laboratorial procedures, but it is also the basis for one of the refining options for vacuum resides, the well-known propane-deasphalting process.

The material yielded by the precipitation is actually a mixture of components. Some are included in the precipitate because of high molecular weight, some because of high polarity (and that must be understood as association capacity). The average molecular weight is commonly taken as an indication for both aspects, not only for the molecular size, because the apparent values measured by some techniques, specially vapor pressure osmometry (VPO), are well sensitive to the extension of the asphaltenic associations.

Actually, the ratio between the molecular weights measured in solvents of different polarities has been proposed as an indication of the association capacities of asphaltenes more than 2 decades ago (1), as it has also been proposed as the basis of recognition of the effectiveness of some molecular changes in the associative functional groups of asphaltene molecules more than a decade ago (2). Some efforts to characterize the importance of polar groups in this mechanism, like acidic and basic chemical functions, have been tried, but with non-conclusive results (3).

Though these and some other propositions can be found in literature, it has been more commonly accepted that further separation of alkane-insoluble material yielded by the precipitation from oils and fuels into fractions is an informative way to reach better knowledge about asphaltene properties. Probably as a result of the most accepted asphaltene isolation procedure, other solubility criteria have been the main basis of several propositions for this aim of fractionation too, normally with increasingly polar solvents being employed (4).

Other options for understanding the chemical and physico-chemical behavior of asphaltenes would be possibly developed if the reactivity of asphaltenes were understood in a more complete extension. More information about functional groups and reactivity is hardly achieved. Probably the reason for that is the difficulty to relate the possible results from these studies with the most popular concepts based on solubility and association.

The present paper describes some efforts developed to understand the role of acidic and basic functional groups in the association of asphaltenic species, with a comparison with the associability of asphaltenes evaluated by usually employed separation techniques.

Experimental

Initially precipitation of pentane asphaltenes and sequential dissolution was also done with the samples chosen for the study, which were a Light Arabian crude oil and also a Brazilian crude oil, 23°API. As said before, this is the most usual separation approach used to the study of asphaltene sub-fractions.

For that, 2 liters of n-pentane were refluxed with a 100-mL oil sample and the isolation of precipitated material was done by filtration with 0.45 micron membrane.

1g of the pentane asphaltenes was shaken for 18 hours with 20 mL of n-hexane at room temperature. Half of the precipitated material (iC6) yielded was separated for characterization and the other half was shaken for 18 hours at room temperature with heptane. Half of the solid material (iC7) yielded was separated for characterization and the other half was shaken for 18 hours at room temperature with n-octane, also yielding a iC8 fraction. All of the soluble fractions (iC5sC6, iC6sC7, iC7sC8, respectively) were recovered by slow evaporation of the solvents under a nitrogen flow (5 psi).

Dialysis is a very traditional separation technique and was also employed in this study. It was considered because the separation obtained is basically related to the hydrodynamic volume of the molecules in solution. It was done with the n-heptane asphaltenes precipitated by the IP-143 procedure (5), which are a more well studied reference material.

The dialysis experiments were carried out with solutions of 1.5 g of asphaltenes dissolved in 50 mL of toluene (concentration of 30 g/L). This solution was put into a semi-permeable membrane cartridge. The cartridge was immersed into 100 mL of toluene. The external toluene solution was sampled every hour, and an evaluation of the amount of asphaltene that had permeated the membrane was done (6). When the mass outside the cartridge reached the range of 0.2 to 0.3 g, the solution obtained was separated and another fresh 100mL portion of toluene was placed outside the cartridge. With that procedure, 9 fractions of permeates were obtained, and the non-permeate was also recovered.

Some reference reagents for the evaluation of acidic and basic properties were chosen: pyridine and formic acid, respectively. They were added to the samples in toluene. A mass of 50 mg was weighed, dissolved in 8 mL of toluene and then 2 mL of the reagent were added. An eighteen-hour contact time was given, and then the residue was dried under vacuum (below 0.5 mmHg) to constant weight at 50°C. A blank run was also done by redissolution of 50 mg of the heptane asphaltenes in 10 mL of toluene, and recovery of the dissolved material by evaporation of the solvent also after an 18-hour contact time.

Molecular weight measurements were done by vapor pressure osmometry using a Wescan 233 osmometer. Toluene was the solvent employed, and benzyl was used for calibration. The chamber temperature was kept at 80°C. The solutions were injected typically in the range of 0.4 to 8 g/L, depending on the response of the solutions.

Results and Discussion

The first relevant results to be discussed come from the characterization of the fractions yielded by sequential dissolution of the pentane asphaltenes precipitated from both oils, whose VPO molecular weights are in table 1. It can be understood that the first asphaltenes, that is, the departure material for the sequential dissolution, must be taken as the reference sample to evaluate associability. It is seen in table 1 that, though the molecular weights of the both pentane and heptane asphaltenes are very close (same order of magnitude) for both oils, the increase in the molecular weight of the fractions has completely different patterns from one

sample to the other. Actually, the iC7sC8 fraction of the Brazilian oil has a larger molecular weight value than the original pentane asphaltenes, and the opposite situation is seen for the corresponding fraction of the Light Arabian.

Table 1. Average molecular weights of asphaltenes and fractions from sequential dissolution

Original oil:	Brazilian	Light Arabian
Pentane asphaltenes	1520	1360
Heptane asphaltenes	3052	3130
iC5sC6	480	340
iC6sC7	1095	560
iC7sC8	2795	810
iC8	3710	2360

As it is not reasonable to believe in differences in the production of the fraction due to the molecular size of the solutes, because they were produced with the same solvent (what means same solvatation capacity), the result is believed to indicate that the associabilities of the components of the fraction in the toluene solutions used for VPO measurements in each case are completely different. Therefore, this result is an indication that the use of a sequence of solvents as a separation technique does not necessarily yield groups of similar components, as it could be expected.

Some relevant results were also achieved by the analysis of dialysis permeates of the IP-143 heptane asphaltenes of the Light Arabian crude oil. Figure 1 shows the data obtained and one of the possible curves that would show the trend described by the results.

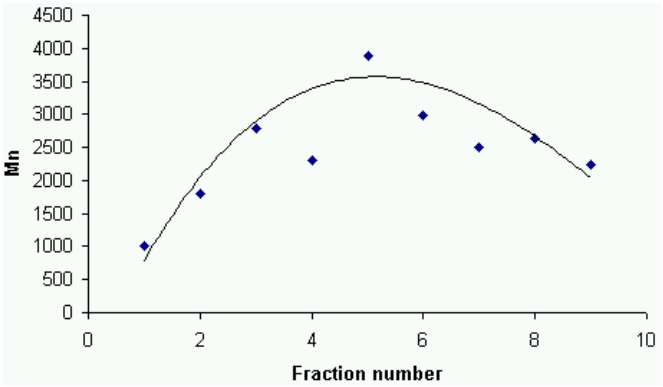

Figure 1. Average molecular weights of fractions of asphaltene dialysis a tendency curve.

Clearly there is a tendency for increasing values for the first permeate samples as the dialysis is developed, and that trend is reverted for the final dialysis samples. However, the fractionation by dialysis, as it was mentioned in the previous section, is based on the difficulty to permeate the membrane, which is a direct function of the hydrodynamic volume. So, it can be concluded that the samples that should be produced with higher hydrodynamic volume do not have the higher apparent molecular weight, as it would be expected.

This is probably due to the fact that the VPO measurements were done in more dilute solutions than the one employed for dialysis. Therefore, it can be accepted that there is some dissociation of the associated species because the solution is less concentrated when the molecular weight is being evaluated. Another point that could be considered would be the possibility of stronger interactions between the late permeate components and the ones in the retained material. This would indicate associative interaction of different natures in different permeates. Again, the conclusion is that a traditional separation technique cannot yield, by itself, conclusive results about asphaltenic fractions behavior, because there are physico-chemical aspects involved in the interactions of these complex systems that cannot be handled by a procedure based simply in fractionation.

Probably the aspects that should be inclusively considered would be the chemical ones. Among the aspects discussed in the literature (hydrogen bonding, charge transfer, and so on), one of the most important and less explored ones is the possibility of the existence of acid-base reaction products in the asphaltene components, yielding very stable associated species. That aspect was evaluated in this work with the contact of a sample with proper volatile reagents. The reagent was eliminated after the adequate contact time. Table 2 shows the molecular weights measured after that procedure applied to the Brazilian oil heptane asphaltenes.

Table 2. Molecular weights of heptane asphaltenes from the Brazilian oil studied with and without contact with toluene solutions of acidic/basic reagents

Sample	*Mn*
Original material	3052
Blank run	3020
Reacted with C_5H_5N	1423
Reacted with HCOOH	1499

Clearly the contact with toluene and subsequent evaporation of this solvent did not alter the measured molecular weight. The contact with the acidic or basic reagent decreased the average molecular weight, and in both cases in the same extension, showing that the same acid-base interactions were displaced in both cases.

Once this is a novel procedure, an evaluation of how repeatable it is was necessary. Therefore, the contact with the reagents was done for 3 times with 3 different heptane asphaltenes aliquots. Figure 2 shows the results obtained, which indicates the results can be considered reliable.

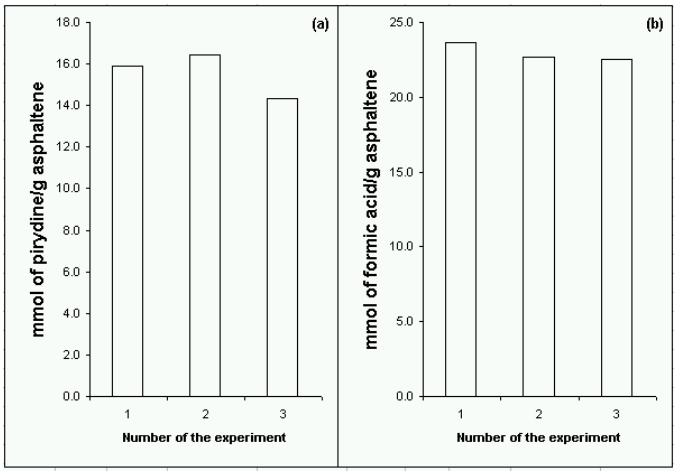

Figure 2. Evaluation of the repeatability of the procedure proposed to determine the equivalence of acidic or basic functional groups in asphaltenes.

From the data presented, it can be calculated that the average number of equivalent functional groups in an asphaltene macromolecule, considering the molecular weight of the departure heptane asphaltenes, was 5 in the case of the acid groups and 7.5 in

the case of basic groups. That indicates there is an excess of basic functional groups in the range of 2 to 3 per molecule. This can be the basis of a possible formulation of the mechanism of interaction of asphaltenes with resins. Additionally, if this kind of results is found to be general for asphaltenes, it can explain their deposition in acidification operations that has been known for about 4 decades (7). It can also explain the molecular weight reduction that is known for about 2 decades to happen in the distribution of species identified by gel permeation chromatography when this analysis is performed in the presence of formic acid (8).

Conclusions

It has been shown in the present paper that separation techniques applied to the study asphaltene interactions can yield data that do not cover all of the phenomena involved in their association behavior. To do so, they would probably have to consider chemical aspects. It has also been shown that a simple procedure of chemical reactions, with modifications of the samples before application of the separation techniques, can be solution to reach more complete results.

References

(1) Al-Jarrah, M.; Al-Dujaili, A. *Fuel Science and Technology Int'l*., **1989**, *7*(1), 69-88

(2) Acevedo, S. et al. *Fuel*, **1992**, *71*,. 1077-9

(3) Van den Ber,g F. G. A.. Prepr. Pap. - *Am. Chem. Soc., Div. Petr. Chem.*, **2001**, *46* (2), 121-4.

(4) Schabron, J.; Pauli, A.; Rovani Jr, J., *Fuel*, **2001**, *80*, 529-37. 596

(5) IP Standard Methods for Petroleum and its Products, The Institute of Petroleum, London **1965**, Part I, Section 2, Standard 143, p. 596

(6) Teixeira, M. A. G.; Gonçalves, M. L. A., *Petroleum Science and Technology* , **2000**. *18* (3-4), 273 -286

(7) Moore, E. W. *Jounal of Petroleum Technology* **1965**, 1023-8

(8) Nali, M. E Manclossi, A. *Fuel Science and Technology International*, **1995**, *13*(10), 1251-64

DETAILED ANALYSIS OF HEAVY NAPHTHAS USING MULTIDIMENSIONAL GAS CHROMATOGRAPHY

Colombe Vendeuvre[$], Fabrice Bertoncini[$], Didier Espinat[$], Didier Thiébaut[*], Marie-Claire Hennion[*]

$: Institut Français du Pétrole
IFP-Lyon - BP3 - 69390 Vernaison - France
* : Ecole supérieure de Physique et de Chimie industrielles de Paris
10, rue Vauquelin - 75231 Paris cedex 05 - France

Introduction

The detailed analysis of petroleum cuts is required for refinery processes monitoring and for product specifications. Two gas chromatographic (GC) techniques, providing different levels of detail, have been normalised to obtain the chemical composition of commercial gasoline (boiling up to 200°C)[1,2]. The first one is a high resolutive GC separation that provides individual components analysis with an identification based on retention indices[1]. The second one, widely used in refineries, is a multidimensional method (PIONA - Paraffin, Isoparaffin, Olefin, Naphthene, Aromatic - analyser) based on the separation of each different constituting chemical group in a dedicated column or trap[2]. However, these techniques are limited when analysing refinery cuts having a higher boiling range, such as heavy naphtha (C_8-C_{14}). Using high resolution GC, significant coelution may indeed occur above C_{10}, especially if blending cuts derived from fluid catalytic cracking (FCC) - olefinic naphtha - are analysed, because the high number of components is not compatible with the peak capacity of the GC column. The limitation of the PIONA analyser is related to the maximum number of carbon atoms (C_{10}) of molecules to be handled, principally owing to the high temperature required to elute hydrocarbons from the molecular sieves. Thus, both methods fail to provide the detailed or group-type analysis of heavy naphtha in the C_8-C_{14} range. One major advance in gas chromatography techniques was the introduction of comprehensive two-dimensional gas chromatography (GC×GC) giving a greater peak capacity than conventional GC[3]. The most interesting feature of GC×GC applied to petroleum samples is the combination of two independent separation mechanisms according to the volatility in one dimension, and to the polarity in the other dimension; hence, the boiling range and the chemical group distribution can be simultaneously obtained. However, the selectivity of the second dimension remains sometimes insufficient for a PIONA analysis with a carbon atom breakdown. In order to improve the detailed PIONA analysis of a heavy naphtha, a multidimensional approach is proposed : it is based on the fractionation by an olefin trap of the saturate and unsaturate fractions of a heavy naphtha followed by the GC×GC analysis of each fraction.

Experimental

Samples. All chemicals used in this study are hydrocarbons available at Sigma-Aldrich. A naphtha cut and a FCC cut were provided by IFP development units.

Instrumentation. In order to control the two separation steps independently, the olefin trap (**Figure 1**, #3) was installed in a first chromatograph (HP5890, Agilent Technologies, #1) and the set of capillary columns used for GC×GC (#10-11) was placed in a second chromatograph (HP6890, #2). Helium was provided to the injector (#5) of the first chromatograph by the auxiliary channel (Electronic Pressure Control, #6) of the second chromatograph to ensure a constant pressure during the analysis (150 kPa). Two 6-ways valves (Valco) were installed in a heated block (#4) in the first chromatograph to enable the backflush and/or isolation of the trap. An insulated transfer line went through the oven walls of the chromatographs to connect the olefin trap to the GC columns. The effluent from the first chromatograph was split at a tee connection located in the second chromatograph. From one side of the tee, a deactivated fused silica tubing (50cm×0.32mm i.d.) (Chrompack) (#12) was placed before the set of GC×GC columns consisting in a 10m-long PONA (Agilent Technologies) column (0.2mm i.d.; 0.5µm) (#10) connected to a 0.8m-long BPX50 (SGE) column (0.1mm i.d.; 0.1µm) (#11). From the other side of the tee, a retention gap of deactivated fused silica tubing (250cm×0.32mm i.d.) (#12) acted as a pressure drop to split the flow and to reduce the quantity of analytes injected in the capillary columns. Two FIDs set at a temperature of 300°C were used to monitor the signal from the GC(×GC) separation (FID A, #8) and from the olefin trap (FID B, #9). The separation in capillary columns could be performed either in a non-modulated mode (GC-GC) or in a modulated mode (GC×GC) using a home-made dual CO_2 jets modulator (#7). A specific data processing program developed in-house allows to display 2D chromatograms[4].

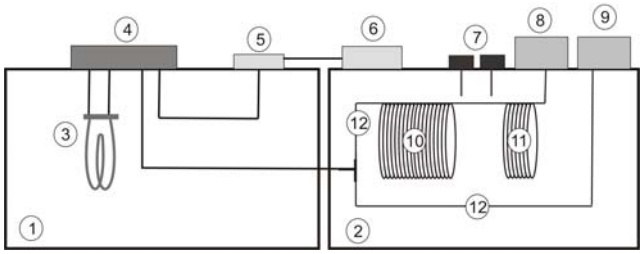

Figure 1. Olefin trap-GC×GC hyphenation. For item description, refer to text.

Results and Discussion

Selectivity. The olefin trap is constituted of silver silica giving specific interaction via silver complexation with double bonds of olefins. Its selectivity was studied by calculating the interaction enthalpy of paraffins and olefins in the C_8-C_{14} range from retention factors measurement. The retention of olefins heavier than undecene was too high in the operating temperature range and could not be studied. Results show that the interaction enthalpy of the heaviest paraffin (n-tetradecane, 80.4 kJ/mol) is lower than the lighter olefin (octene-1, 106.3 kJ/mol) indicating, from a thermodynamic point of view, the ability of the olefin trap to separate olefins from paraffins in the C_8-C_{14} range provided suitable desorption conditions of heavy olefins from the trap can be found.

Importance of backflushing the olefin trap. Chromatograms of figure 2 show the desorption (at 240°C) in the foreflush or in the backflush modes of octene-1, decene-1, dodecene-1 and tetradecene-1 after their trapping in the olefin trap (at 180°C, 15min). The trapping temperature is a compromise for fast elution of paraffins without breakthrough of olefins. As expected, peak tailing and retention of olefins observed in the foreflush mode were limited in the backflush mode.

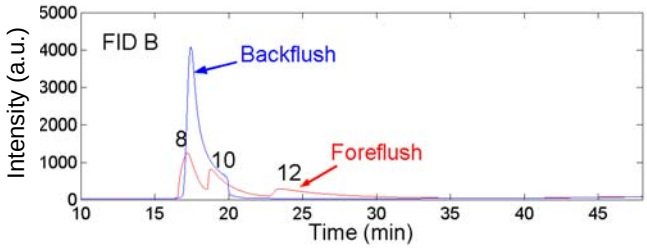

Figure 2. Backflush or foreflush desorption of olefins ($C_{8\text{-}10\text{-}12\text{-}14}$) from the olefin trap.

Capacity. The capacity of the trap was evaluated by injecting 0.4µl of solutions of octene-1 in pentane (concentration range: 0.062-36.5% (w/w). At low concentrations, the relationship between the area and the injected quantity of olefin is linear. Above 40 nmol, the trap has reached its maximum capacity : the area measured in the backflush step remains constant whereas breakthrough occurs in the foreflush step. The breakthrough of olefins corresponds to a very low injected quantity indicating that the number of sites available for complexation with silver is restricted.

Isomerisation in the trap. The high resolutive separation from GC columns allowed to highlight isomerisation of olefins in the trap as already shown elsewhere[5]. As systems implementing the olefin trap for the separation between olefins and saturates often use a hydrogenation step, isomerisation by a shift of the double bond cannot be evidenced. Isomerisation is obviously a drawback if one wants the individual identification of olefins.

Application to a synthetic hydrocarbon mix. A complete hydrocarbon mix, representative of all hydrocarbon families in the C_8-C_{14} range, was subjected to the olefin trap-GC×GC separation (Figure 3). Saturates were eluted in 15 minutes at 180°C from the trap while unsaturates were trapped. The trap was isolated to allow the GC×GC separation of saturates. After the elution of saturates is completed and the oven had cooled down to the initial temperature of the program, backflush desorption of unsaturates is performed by heating the trap to 240°C. GC×GC conditions were the same for saturate and unsaturate hydrocarbons.

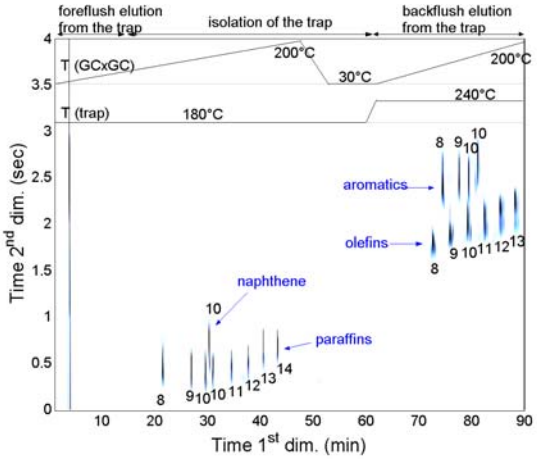

Figure 3. Olefin trap-GC×GC separation of a synthetic PIONA hydrocarbon mixture. The number of carbon atoms is indicated.

The multidimensional separation according to the unsaturation degree (olefin trap), volatility (1st apolar column) and polarity (2nd polar column) - allows to separate hydrocarbons in four groups : paraffins and naphthenes, olefins and aromatics. Within each group, a carbon atom breakdown is possible. The two GC×GC runs were not synchronised, meaning that the location in the second dimension of bands of saturates can not be directly compared to that of unsaturates.

Application to a naphtha + FCC blend. Figure 4 reports GC×GC chromatograms obtained after separation in the olefin trap (A) and without fractionation (B). Despite its high peak capacity, GC×GC fails in separating olefins from saturates (Figure 4B). Owing to the selective fractionation by the olefin trap, saturate and unsaturate hydrocarbons are independently analysed by GC×GC. Thus, it allows the deconvolution of the band of olefins from those of saturates, which is an immediate advantage compared to GC×GC. The repartition of unsaturate compounds according to the number of carbon atoms is given in Table 1.

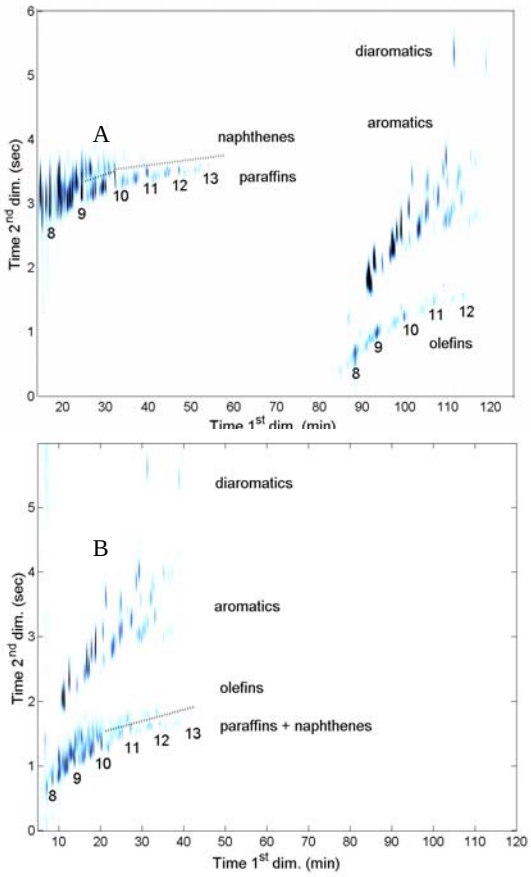

Figure 2. Olefin trap-GC×GC separation (A) and GC×GC separation (B) of a naphtha+FCC blend.

Table 1. Qantitative Analysis of Unsaturate Fraction

Number of carbon atoms	Olefins	Aromatics
8	1.92 ± 0.07	11.4 ± 0.36
9	2.04 ± 0.06	9.32 ± 0.31
10	1.42 ± 0.04	6.25 ± 0.17
11	0.94 ± 0.03	3.02 ± 0.09
12	0.65 ± 0.03	0.79 ± 0.03
13	0.22 ± 0.01	0.02 ± 0.01

Conclusions

The hyphenation of an olefin trap to GC×GC demonstrates an excellent resolution between all chemical groups in a complex naphtha C_8-C_{14} range and it can be regarded as an innovative solution to answer the delicate problem of the determination of olefins in such samples. Work is on progress to increase the separation within the saturate group.

References

(1) ASTM D 6733-01 : Standard test method for determination of individual components in spark ignition engine fuels by 50-meter capillary high resolution gas chromatography.

(2) ASTM D 6293-98 : Standard test method for oxygenates and paraffin, olefin, naphthene, aromatic (O-PONA) hydrocarbon types in low-olefin spark ignition engine fuels by gas chromatography.

(3) Z. Liu; J.B. Phillips., *J. Chromatogr. Sci.*, **1991**, 29, 227.

(4) C. Vendeuvre; F. Bertoncini; L. Duval; J.L. Duplan; D. Thiébaut; M.-C. Hennion, *J. Chromatogr. A*, **2004**, 1056, 155.

(5) J.S. Buchanan; M.E. Nicholas, *J. Chromatogr. Sci.*, **1994,** 32, 199

CORRELATION BETWEEN FATTY ACID COMPOSITION AND COLD FILTER PLUGGING POINT OF BIODIESELS

J. Hancsók, F. Kovács*, M. Krár*, S. Magyar*, K. Recseg**, T. Czuppon***

* University of Veszprém, Hungary, H-8201 Veszprém, P.O. Box 158.
** BUNGE Rt., Hungary, H-1095 Budapest, Kvassay Jenő út 1.

Introduction

According to recent projections, energy import of the EU member countries is likely to increase to 60 per cent of the total energy consumed. The World's total crude oil demand is estimated to raise to 5000 million metric tons, more than half of which is used in the transportation sector. There is a global need to search for new fuel sources and produce fuels in new ways in order to ease this enormous crude oil "hunger". The importance of alternative fuels, especially biofuels, is continuously growing in the recent years [1].

The European Union targeted the reduction of the CO_2, emitted from conventional fuels used in the transportation sector. With this climate goal the EU also wants to decrease its dependency on crude oil and to establish new jobs for the population working in the agricultural sector [2].

Directive 2003/30/EC of the European Parliament and the European Council specifies the Member States of European Union should ensure that a minimum proportion of biofuels and other renewable fuels is placed on their markets, and, to that effect, shall set national indicative targets [3]. A reference value for these targets shall be 2 %, calculated on the basis of energy content of all petrol and diesel oil for transport purposes placed on their markets by 31 December 2005. The reference value shall be increased to 5.75% by 31 December 2010 (0.75%/year increase) for the Member States. The EU member states were supposed to have produced 5 million tons oil equivalent (toe) for biofuels in 2003, but were only able to reach 1.49 million tons. By 2010, the biofuels goal is 18 million tons, but taking current development into consideration, the Biofuels Barometer 2004 report estimates biofuels production only reaching 11 million tons [4, 5].

A wide range of fuels can be produced from biomass (Fig. 1.) [1]. Transesterification carried out in the presence of alkali, acid or enzyme catalyst is a preferred method to upgrade vegetable oils for fuel purposes [6,7,8]. This particular paper will only deal with the production of vegetable oil methyl esters and correlations between the characteristics of the produced biodiesels and the fatty acid composition of vegetable oils.

Due to the increased demand on biofuels, the aim of our research was to evaluate a range of vegetable oils (from the standard rape oil to used frying oil) as a potential source of biodiesel production and to investigate the characteristics of their methyl ester derivatives.

Experimental

Apparatus. Alkali catalysed transesterification was carried out in a three-necked glass flask of 1 liter volume equipped with a variable speed magnetic agitator, condenser and thermometer. The experimental apparatus was capable of feeding sodium methylate solution in variable flow rates. A reflux condenser ensured that any methanol vapour was condensed and kept in liquid phase at higher reaction temperatures. The reaction mixture was heated with an oil bath.

Materials and their preparation. Sodium methylate solution (30 % m/m) and methanol of analytical grade was used for alkali transesterification. Vegetable oils (including used frying oils) with different origin and quality were used. The fatty acid composition of vegetable oils is summarized in Table 1.

Methods. Properties of the starting materials and products were determined by standard test methods given in standard EN 14214.

Experimental method. The starting vegetable oil was dried in vacuum at proper temperature, and then it was cooled down to room temperature. Excess methanol and appropriate quantity catalyst was added to the dry vegetable oil. The reaction mixture was refluxed for certain time after that it was poured into a separatory funnel and it was settled for sufficient time. The lower glycerol phase was removed afterwards the remaining upper methyl ester phase was washed with acidic solution and distilled water until neutrality. Finally the product was dried in vacuum at higher temperature.

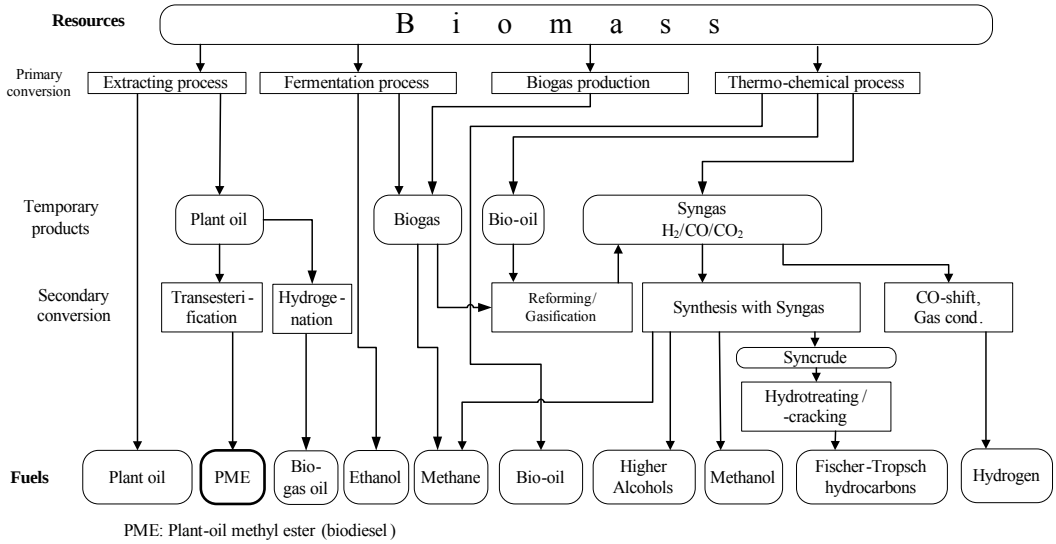

Figure 1. Conversion paths of various renewable fuels

Table 1. Fatty acid composition of biodiesel products

Fatty acids	A	B	C	D	E	F	G	H
C12:0	-	-	-	0.2	0.3	0.4	-	0.1
C14:0	-	-	-	1.1	1.3	0.3	0.7	0.4
C16:0	6,3	11.6	4.4	45.4	63.7	9.5	22.4	15.4
C16:1	0,1	0.1	0.2	0.3	0.1	0.3	0.5	0.3
C18:0	3,6	3.9	1.8	4.5	5.2	4.6	2.8	4.0
C18:1	28,5	23.5	61.9	37.8	23.5	71.6	15.7	41.9
C18:2	60,3	53.6	18.3	9.9	5.3	10.7	56.0	35.2
C18:3	0,1	6.3	9.9	0.2	0.1	0.7	0.5	0.8
C20:0	0,2	0.4	0.6	0.4	0.3	0.6	0.3	0.6
C20:1	0,2	0.2	1.7	0.1	0.1	1.0	0.1	0.4
C22:0	0,7	0.4	0.3	0.1	0.1	0.3	0.1	0.9
C22:1	-	-	0.9	-	-	-	0.9	-
SFA	10,8	16.3	7.1	51.7	70.9	15.7	26.3	21.4
MUFA	28,8	23.8	64.7	38.2	23.7	72.9	17.2	42.6
PUFA	60,4	59.9	28.2	10.1	5.4	11.4	56.5	36.0
MUFA/SFA	2,67	1.46	9.11	0.74	0.33	4.64	0.65	1.99
PUFA/SFA	5,59	3.67	3.97	0.20	0.08	0.73	2.15	1.68
TUFA/SFA	8,26	5.13	13.08	0.93	0.41	5.37	2.80	3.67
MUFA-SFA	18,0	7.5	57.6	-13.5	-47.2	57.2	-9.1	21.2
PUFA-SFA	49,6	43.6	21.1	-41.6	-65.5	-4.3	30.2	14.6
TUFA-SFA	78,4	67.4	85.8	-3.4	-41.8	68.6	47.4	57.2

SFA: Saturated fatty acids
MUFA: Mono-unsaturated fatty acids
PUFA: Poly-unsaturated fatty acids (more than 1 double bond)
TUFA: Total unsaturated fatty acids

Table 2. Main properties of biodiesel products

Properties	EN 14214 standard	A	B	C	D	E	F	G	H
Ester content %	>96.5	96.8	96.3	96.7	97.6	96.8	89.6	98.4	91.5
Density, 15°C, kg/m^3	860-900	885	885	883	875	902	885	884	884
Viscosity, 40°C, mm^2/s	3.50-5.00	4.22	4.16	4.49	4.50	4.51	5.63	4.23	4.71
Flash point, °C	>120	128	129	126	118	120	120	121	119
Oxidation stability, 110°C, h:m	>6:00	3:40	4:40	6:20	13:25	34:00	2:45	3:00	2:35
Acid value, mg KOH/g	<0.50	0.27	0.21	0.24	0.26	0.28	0.62	0.35	0.60
Iodine value, g Iodine/100g	<120	129	130	113	50	30	83	113	100
Cold filter plugging point CFPP, °C	seasonally depended	-1	-1	-10	13	18	1	7	7

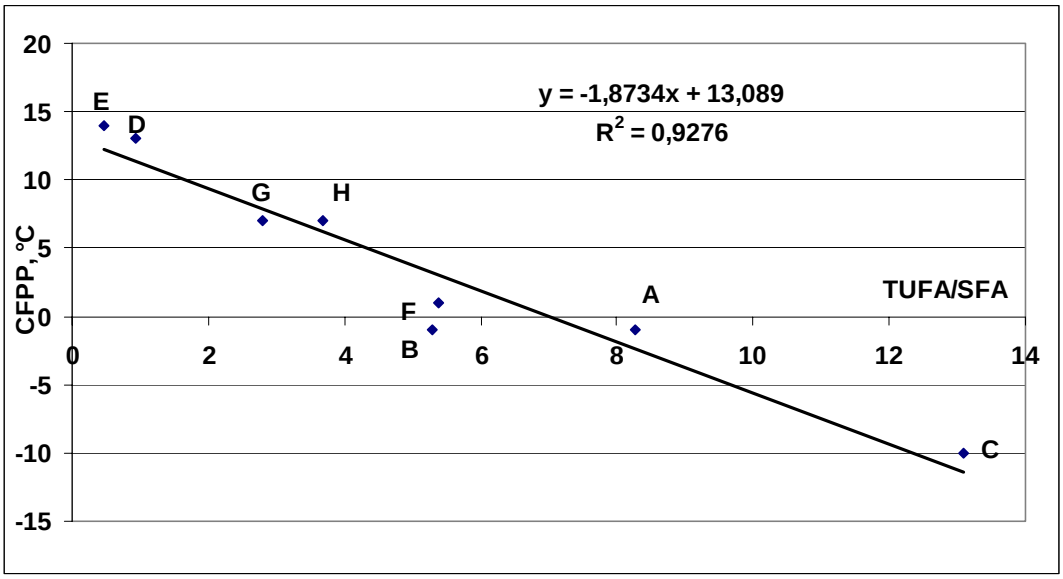

Figure 2. Correlation between TUFA/SFA and CFPP value

Results and Discussion

The properties of vegetable oil methyl esters are presented in Table 2. Out of the total 8 biodiesel samples, methyl ester content of 3 samples was less than 96.5 %, specified by EN 14214 standard. These were prepared from used frying oils with high polar, dimer and polymer content. Although these components are also transesterified, they will reduce the measured ester content during the GC analysis, because of their irregular retention time regarding to their altering much higher molecular weight.

Comparing the density values of the biodiesel products, we concluded that density of sample 'E' was higher than allowed by the standard. This alteration has some relation to its high SFA content and CFPP value. Kinematic viscosity of sample 'F' has not met the specification (5.63 mm^2/s) due to its relatively high MUFA content. Considering the viscosity and density values of other samples, it can be concluded that a relatively high variation in fatty acid composition of vegetable oils has some significant effect on density or on kinematic viscosity of biodiesels.

Oxidation stability of methyl esters, characterizing the storage stability of biodiesel, is influenced by the content of unsaturated molecules and number of double bonds that reflected in the Iodine Value (IV). Biodiesel sample 'E' showed the best oxidation stability (34 h with IV = 30 & SFA = 70,9 %) while sample 'A' showed the shortest value (3 h 40 min with IV = 129 & PUFA = 60,4 %).

As it is well known the relative oxidation rate of linolenic acid methyl ester (C18:3) is 2500 times higher than that of the saturated stearic acid methyl ester (C18:0) of same carbon number. A relatively high variation in the fatty acid composition has significant effect on the oxidation stability of biodiesels. Higher concentration of saturated fatty acids results in a better oxidation stability. Even a relatively small amount of poly-unsaturated fatty acids had very negative effect on the oxidation properties and thus the storage stability of biodiesels.

Most of the transesterified vegetable oils fulfill the required values of acid number (0.5 mg KOH/g sample). In some cases this value is out of the limit, but this difference is due to the mineral acid traces coming from the work-up process by acidic solution washing of crude biodiesel and not to the free fatty acid content.

Iodine Value characterizes the amount of double bonds present in vegetable oils or biodiesels, it does not, however, give any information about the ratio of poly-unsaturated/mono-unsaturated fatty acid content.

The lowest CFPP (cold filter plugging point) value was measured in case of sample "C" (-10°C). In this sample the concentration of saturated fatty acids was lowest (7.1%) and it contained the highest amount of unsaturated fatty acids (92.9%). The presence of saturated fatty acids had an undesirable effect on the CFPP values, even in a relatively low concentration. CFPP value of sample 'E', with a saturated fatty acid content of 70.9%, was 18°C, leading to pumping difficulties at ambient temperature.

Summarizing the previous, vegetable oils with relatively high mono-unsaturated fatty acid and very low saturated fatty acid content are suitable to produce biodiesel, which have both acceptable CFPP values and oxidation stability.

Based on the results it can be established that biodiesel 'C' has the best characteristics. (Sample 'C' was produced from neutralized rapeseed oil and the biodiesel standard – EN 14214 – was worked out on a basis of rapeseed oil methyl ester.)

One should aim at producing biodiesels containing highest possible amount of oleic acids and lowest possible amount of saturated fatty acids. Oleic acid has ideal characteristics, having preferable effect both on the CFPP values and oxidation stability.

Using our results we tried to look for a correlation between the CFPP values and the fatty acid composition. We have found that approximate linear correlation is obtained by plotting the CFPP values vs. the ratio of total unsaturated fatty acid (TUFA)/saturated fatty acid (SFA) (Fig.2). The deviation of the correlation is approximately 1.0 °C, which corresponds to the acceptable error of CFPP measurement.

Conclusions

Among our biodiesel samples, produced with the transesterification of various vegetable oils, sample 'C' fulfils the requirements of the valid European standard (EN 14214). As a result of the higher oleic and lower linoleic acid content it has better oxidation stability than the other products. In sample 'C' the

concentration of C18:0 is lower and that of C22:0 is only 0.3% resulting in a preferable CFPP value.

We have found a relatively good compromise between the oxidation stability, the CFPP value and the unsaturated fatty acid content.

We have found that approximate linear correlation is obtained by plotting the CFPP values vs. the ratio of total unsaturated fatty acid (TUFA)/saturated fatty acid (SFA). The deviation of the correlation is approximately 1.0 °C, which corresponds to the acceptable error of CFPP measurement.

Acknowledgement. The authors are grateful for the support of Cooperative Research Centre, University of Veszprém, Chemical Engineering Institute.

References

(1) Zuberbühler, U.; Specht, M.; West, D.; and Bandi, A. *4th International Colloquium on Fuels 2003,* 15-16. January 2003., 61-66.
(2) Altmann, B.-R., *Erdöl Erdgas Kohle*, **2005**, *121*(4), 156-159.
(3) Directive 2003/30/EC of the European Parliament and of the Council on the promotion of the use of biofuels or other renewable fuels for transport, 8 May 2003.
(4) Biofuels Barometer 2004, Observ'ER Eurec Agency, 2004.
(5) Gantz, R. *Hart's Global Refinig and Fuels Report,* 2005, *9*(3), 6.
(6) Vicente, G.; Martinez, M.; Aracil J. *Bioresource Technology*, **2004**, 92, 297-305.
(7) Canakci, M. and Gerpen, J.V. *Transaction of the ASAE***, 1999**, *42*(5), 1203-1210.
(8) Bélafi-Bakó, K.; Kovács, F.; Gubicza, L.; and Hancsók, J. *Biocatalysis and Biotransformation*, **2002,** *20*(6), 437-439.

EXSACT: NOVEL SOLID-ACID CATALYZED ISO-PARAFFIN ALKYLATION PROCESS

Mitrajit Mukherjee, Sankaran Sundaresan & Richard Porcelli

Exelus Inc., 99 Dorsa Avenue, Livingston, NJ 07039

Introduction

The recent ban on MTBE in several states (California, New York and Connecticut) has made it difficult for refiners to prepare gasoline blends that meet state and federal guidelines. EIA (Energy Information Administration) reports that the volume of total gasoline production can easily be restored to MTBE-free volume levels with alkylate. Alkylate is an ideal clean fuel component because it has a high octane rating, low vapor pressure and low toxicity. It is currently produced via iso-paraffin alkylation using as catalyst hydrofluoric acid (HF), which can be deadly if spilled, or sulfuric acid (H_2SO_4), which is also potentially harmful and increasingly costly to recycle. Exelus has developed an innovative iso-paraffin alkylation technology ExSact, as an economically viable alternative to HF/H_2SO_4 processes. The two main components of ExSact are:

1. A unique solid-acid catalyst that converts light hydrocarbons into alkylates &
2. A novel fixed-bed reactor that is designed to enhance the performance of this catalyst.

The synergistic integration of the "green" solid acid catalyst with the novel reactor is expected to provide refiners with a cleaner-by-design alternative to produce a high-octane gasoline component to meet both state and Federal requirements. This paper describes the successful development of this new "green" technology to produce alkylate.

Alkylation Background

Alkylation of isobutane with light (C_3–C_5) olefins in the presence of a strong acid catalyst involves a series of consecutive and parallel reactions occurring through carbocation intermediates[1]. The addition of proton to an olefin, followed by hydride abstraction from iso-butane, leads to a t-butyl cation. The t-butyl cation then combines with an olefin (say, C_4) to give the corresponding C_8 carbocation as shown in **Figure 1**. These C_8 carbocations may isomerize via hydride transfer and methyl shifts to form more stable cations. These C_8 cations undergo rapid hydride transfer as iso-butane regenerates the t-butyl cation to perpetuate the chain sequence.

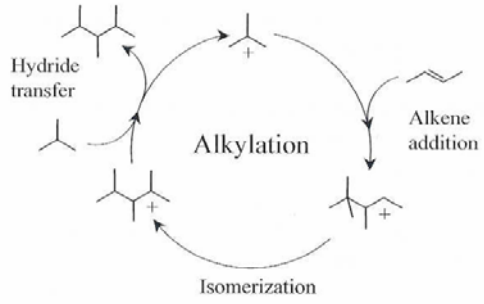

Figure 1. Simplified alkylation cycle[1]

Unfortunately, these are not the only reactions occurring during alkylation. There are a number of secondary reactions that, in general, tend to reduce the quality of alkylate. The C_8+ can continue to react with olefins and form larger cations. The successive addition of olefins to carbocations, or olefin polymerization, is the primary route to formation of large hydrocarbon residue or "coke", leading to catalyst deactivation.

Solid acid catalysts have been investigated as alternatives to liquid catalysts for isobutane alkylation for over 30 years[2]. These include $AlCl_3$; promoted zirconia; heteropolyacids, such as tungstates; liquid acids immobilized on silica, polymers, or other solid supports; and natural and synthetic zeolites. Solid catalysts can improve selectivity and reduce production costs, but their tendency to deactivate rapidly during alkylation has prevented virtually every known solid-acid alkylation catalyst from becoming commercially viable.

Exelus's Solid-Acid Catalyst Development

Using grants from the US Department of Energy and the National Science Foundation, Exelus started (in 2001) work on developing a viable solid-acid catalyst alternative to liquid acid catalyzed iso-paraffin alkylation technologies. Our goal was to develop a simple swing fixed-bed reactor process using a benign solid-acid catalyst. Our desire to use a fixed-bed reactor was influenced by two issues: a) to simplify process scale-up and b) to keep both capital costs and operating expenses as low as possible. This, however, is easier said than done for alkylation reactions. Iso-paraffin alkylation reactions are very fast and they suffer from severe pore diffusion limitations. As a result when catalyst particle sizes are increased from 100 μm (for slurry reactors) to 1.6 mm for fixed-bed reactors, the catalyst activity reduces by 10-fold as shown in **Figure 2**. To match the catalyst productivity of a slurry reactor, one would need to build a fixed-bed reactor with 10-times the volume – which is not practical for commercial scale system. In addition to using a fixed-bed reactor, we wanted to ensure that the solid-acid catalyst was both robust as well as benign i.e. environmentally friendly. We rejected right at the outset replacement of a liquid acid with a liquid-acid supported on solid particles or co-feeding toxic halogens or halogenated compounds to a solid-acid catalyst to maintain its activity.

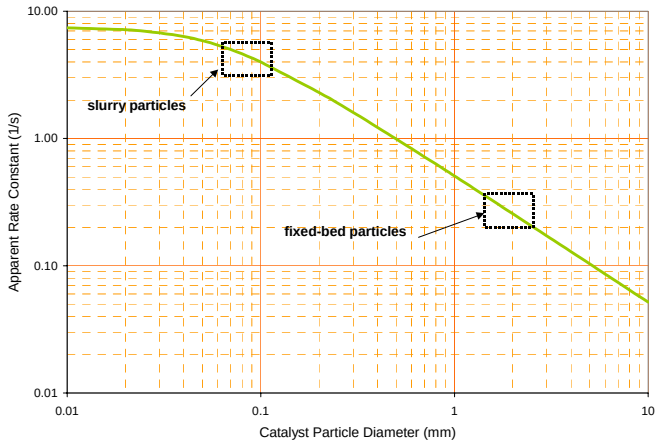

Figure 2. Reduction in catalyst activity with increasing particle size

Our development approach was to first understand the dynamics of the alkylation reaction by systematically studying the effect of both physical and chemical aspects of the solid-acid catalyst system design on product distribution and catalyst deactivation characteristics. Several different catalyst formulations encompassing a wide range of acid functions, number of acid sites and acid strengths were evaluated as part of this study. Many of our findings were in stark contrast to conventional (widely held) beliefs about solid-acid catalyzed alkylation reactions.

Through this systematic study, Exelus was able to identify an optimal "window" of design parameter values that were then used to develop the ExSact system. By judicious manipulation of the active material composition (number of sites and acid site strength), researchers at Exelus have developed a unique solid-acid catalytic system that has roughly 400% more active sites than a typical solid-acid catalyst. The catalyst activity of the solid acid was found to be higher than a typical liquid acid catalyst, which means that much lower amounts of catalyst are required to catalyze the iso-paraffin alkylation reaction, allowing one to design alkylation reactors with significantly lower volumes (hence cost).

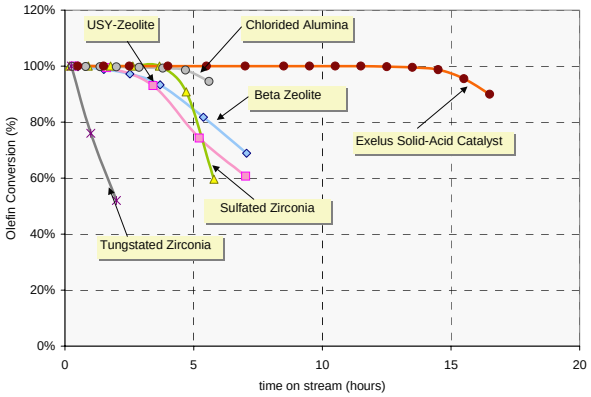

Figure 3. Exelus solid-acid catalyst performance compared to other commercially available systems

By integrating optimized acid-sites with superior mass transport characteristics and a pore architecture that reduces pore-mouth plugging, Exelus has developed a truly revolutionary solid acid catalyst. As shown in **Figure 3**, which compares the performance of Exelus solid-acid catalyst with other commercially available systems, the new catalyst system is easily able to achieve a quantum jump in performance over other solid-acid catalysts.

Novel Fixed-Bed Reactor Design

Through an extensive study of the solid-acid alkylation reactions, Exelus has developed a robust kinetic model that is able to predict product octane as well as catalyst lifetimes for a large range of reaction conditions. Kinetic analysis[3] revealed that the rate constant for the secondary (oligomerization) reaction is 2 orders of magnitude higher than the rate constant for the primary alkylation reaction. To achieve a substantial reduction in the rate of oligomerization, the olefin concentration (O) must therefore be kept 2 orders of magnitude lower than the iso-paraffin concentration (P). Kinetic analysis also revealed that the rate constant for the product degradation reaction is similar in magnitude to the rate constant for the primary alkylation reaction. By applying the kinetic model to novel reactor flow patterns, Exelus has been able to develop a unique fixed-bed alkylation reactor that enhances the primary reaction rate by optimizing both macro-mixing (residence time distribution) and micro-mixing (aggregate mixing) characteristics. The macro-mixing profile is optimized to reduce product degradation by minimizing the over-alkylation of iso-octane molecules to heavier (low octane) hydrocarbons. The desired micro-mixing characteristics (to achieve low olefin concentrations at the catalyst surface) are achieved by using proprietary turbulence enhancing devices called "Dispersion Accelerators."

The performance of the fixed-bed reactor was verified in Exelus laboratory over a period of 2 months through tests under commercially relevant process conditions. Product was sampled over the entire length of the reactor to quantify the rate of alkylate degradation. **Figure 4** shows the results of this test.

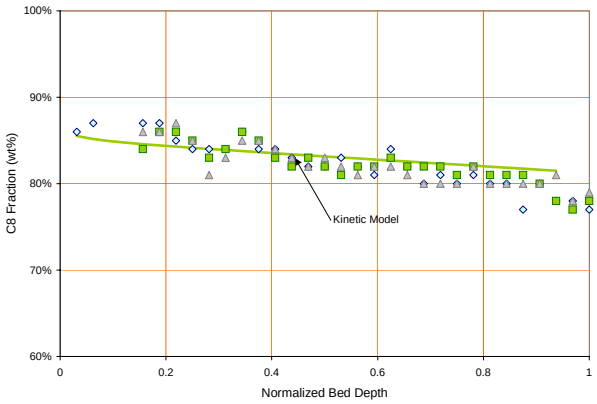

Figure 4. Performance of the Novel Fixed-Bed Alkylation Reactor

The kinetic model adequately describes the product composition for most of the reactor length. In effect, the yield of C8 alkylate is 20 wt% higher than that possible in a conventional recycle reactor, resulting in a net 1.5 octane number (RON) increase.

Comparison with Conventional Liquid Acid Processes

A comparison of the Exelus technology with competing liquid acid processes is presented below. We have used published data and pro-rated them (the sulfuric acid unit was pro-rated from a 7,500 bspd plant cost of $ 43.5 million while the HF plant was pro-rated from a 8,800 bpsd plant cost of $ 42.5 million) to reflect a plant capacity of 10,000 bspd.

Table 1. Comparison of the ExSact process with liquid-acid alkylation technologies

Parameter	ExSact Process	Hydrofluoric Acid Alkylation[4]	Sulfuric Acid Alkylation[5]
Plant Capacity (bspd)	10,000	10,000	10,000
Capital Expenses (million)	**$ 26**	**$ 46**	**$ 55**
Raw Material Consumption:			
Iso-butane Consumption	1.21 v/v olefin	1.2 v/v olefin	1.17 v/v olefin
Alkylate Yield	1.83 v/v olefin	1.8 v/v olefin	1.78 v/v olefin
Utility/Chemicals Consumption:			
Steam ($ 4/klb)	116,000 lb/hr	65,700 lb/hr	130,700 lb/hr
Power ($ 006/kWH)	600 kW	903 kW	4040 kW
Fuel ($ 4/MM Btu)	1.5 MM Btu/hr	47.7 MM Btu/hr	
Cooling Water ($ 005/gal)	12,740 gpm	15,750 gpm	15,600 gpm
Hydrogen ($ 0.55/lb)	70 lb/hr		
HF ($ 0.65/lb) or H_2SO_4 ($ 0.05/lb)	N/A	47 lb/hr	7920 lb/hr
Utility Costs ($/bbl)	**$ 1.40**	**$ 1.41**	**$ 2.90**

Investment costs are lower than liquid-acid technologies due to the following reasons:

1. Simpler reactor design using inexpensive materials of construction
2. Elimination of refrigeration equipment
3. No need for acid handling vessels

As a result, capital expenses to about $ 26 million for a 10,000 bbl/d plant – a reduction of 45-50% compared with hydrofluoric and sulfuric-acid alkylation processes.

Utility costs are about the same as an HF unit but significantly lower (about 50%) than a sulfuric acid plant for the following reasons:

1. Much lower power consumption
2. Inexpensive regeneration scheme using hydrogen

Finally, alkylate yields are higher due to elimination of acid-soluble oils that are formed during in liquid-acid catalyzed alkylation processes, resulting in lower feedstock consumption.

Conclusions

Exelus has developed a revolutionary refinery process (ExSact) that is designed to produce high-octane alkylate without the use of toxic liquid acids. The strength and distribution of its acid sites reduce olefin dimerization and paraffin cracking, while enhancing isobutane alkylation. Furthermore, the controlled pore structure of the catalyst reduces deactivation by coke formation and pore mouth plugging. The paraffin alkylation process using ExSact catalyst is fundamentally safer and cleaner than conventional liquid-acid catalyzed processes, eliminating the use and generation of toxic chemicals. Exelus has also developed a novel fixed-bed alkylation reactor to enhance the performance of the solid-acid catalyst. This new reactor uses innovative fluid dynamics and an unusual reactor residence time distribution designed to maximize alkylate production without sacrificing the product octane value. The innovations in the Exelus process are shown schematically in **Figure 5.**

The new solid-acid catalyst process promises significantly improved yields and selectivities, minimizing waste by-products and disposal problems associated with spent catalysts and regeneration of large quantities of liquid acids. Given the current push for eco-friendly processes to produce ultra-clean fuels, The ExSact technology is poised to fill a large void in the gasoline market for decades to come.

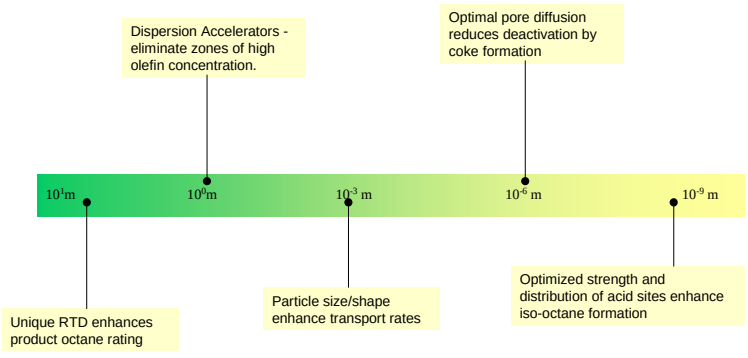

Figure 5. Innovations in the Exelus solid-acid catalyst alkylation technology

Acknowledgement

This work was funded by grants from the U.S. Department of Energy and the National Science Foundation

References

(1) Feller, A., Iker Zuazo, Alexander Guzman, Jan O. Barth and Johannes A. Lercher, *J. Catal. (216), 2003, 313-323*
(2) Corma, A.; Martinez, A. *Catal. Rev. Sci. Eng. 1993, 35, 483*
(3) Simpson M. F, Wei J, Sundaresan S, *Ind. Eng. Chem. Res. 1996; 35,3861-3873*
(4) UOP HF Alkylation Brochure, 2001
(5) Ackerman, Steve, Girish K. Chitnis and David S. McCaffrey, Jr., *Division of Petroleum Chemistry, 222nd ACS National Meeting, August 26-30, 2001*

REMOVAL OF NITROGEN FROM LIQUID FUEL BY SUPERCRITICAL FLUIDS

Olubunmi M. Ogunsola

TEMEC, P.O. Box 1072, Woodbridge, VA 22195, USA

Introduction

The U.S. import of oil is projected to double, to about 20 million barrels/day, by 2025. At the same time, the U.S. resources of oil shale and tar sands are estimated at about 2 trillion barrels about 76 billion barrels, respectively. These huge unconventional oil resources are currently undeveloped (Dyni, 2000; OTA 1980 White Paper). Unfortunately, development of these unconventional domestic energy resources is limited due to several constraints which include the presence of nitrogen and sulfur, which can lead to increased emission of nitrogen oxides and sulfur dioxide, respectively if these impurities (nitrogen and sulfur) are not removed.

In order to obtain high value transportation fuels that will meet the new more stringent environmental requirements the sulfur and nitrogen have to be considerably reduced. Current conventional method of nitrogen and sulfur removal by hydro-treating is very expensive due to huge demand of expensive hydrogen for their effective removal. Supercritical fluids have been successfully used to break the carbon-nitrogen and carbon-sulfur bonds in model compounds by a number of researchers, including Ogunsola and Berkowitz (1995) and Ogunsola (1991, 2000). Since the nitrogen and sulfur contained in oil shale and tar sands are similar to these model compounds, supercritical fluids are, therefore, good candidates for removing nitrogen from shale oil and sulfur from tar sands-derived crude.

This paper presents the preliminary results of a study aimed at removing of nitrogen from shale oil by supercritical water (SCW).

Experimental

The raw oil shale sample was prepared by crushing it to less than 1.16mm and subsequently sieved. A -1.16mm +0.833mm size sample was then used for the experiment. Extraction of the oil shale sample was conducted in a one-liter stainless steel autoclave reactor system. Detailed description of the system is given elsewhere (Ogunsola, 1991). About 30 grams of prepared sample were used for each run. The extraction was done by using supercritical water at 400^{o}C and 450^{o}C at varying hot pressure of 14MPa, 17.5MPa and 21MPa. Liquid extracts from the samples were analyzed for elemental analysis (carbon, hydrogen, nitrogen, sulfur, and oxygen) and aromaticity. Conversion efficiency, defined as the fraction of organic carbon in the oil shale recovered oil (toluene-soluble), the toluene-insoluble and THF-soluble fraction is considered to be the pre-asphaltene.

Results and Discussions

Table 1 below shows a summary of results obtained from this study.

Table 1. Summary of Results.

Temperature ^{o}C	400	450	400	450
Pressure, MPa	14	14	17.5	21
Conversion, %	35	22	30	32
Elemental Composition, %				
Carbon	76.8	77.0	79.2	80.4
Hydrogen	8.6	8.4	9.1	9.0
Nitrogen	1.1	1.3	1.3	1.5
Sulfur	9.97	12.4	8.3	6.4
Oxygen (by Difference)	3.5	0.9	2.2	2.7
H/C	1.34	1.31	1.38	1.35
^{1}H nmr, %				
H_{ar}	12.5	18.9	13.8	14.8
H_{ol}	0.0	0.0	0.0	0.0
H_{n}	7.6	6.6	5.1	7.8
Aromaticity, f_{a}	0.50	0.57	0.47	0.53

While it is obvious from the results on Table 1 that the carbon content of the liquid product increases with pressure at both temperatures, low temperature tends to favor hydrogenation of the oil. The aromaticity of the fuel could also be seen to be higher at higher temperature in this study. Extraction at low temperature appears to favor low nitrogen content of the fuel.

References

1. Congress of United States, Office of Technology Assessment: An Assessment of Oil Shale Technologies, June 1980 (OTA Report No. OTA-M-118)
2. Dyni, J. R. “Oil Shale” U. S. Geological Survey, February 2000.
3. Ogunsola, O.M. and Berkowitz, N. “Removal of Heterocyclic S and N from Oil Precursors by Supercritical Water” Fuel 74(10), p. 1485, 1995.
4. Ogunsola, O.M. “Decomposition of Isoquinoline and Quinoline by Supercritical Water” J. Hazardous Materials B74, p. 187, 2000.
5. Ogunsola, O.M. “Supercritical Water Extraction of Oil Shale” PhD Thesis, University of Alberta, Edmonton, Alberta, Canada, 1991.

STARTING DIESEL ENGINES AT LOW TEMPERATURES – IMPACT OF IGNITION QUALITY

Robert Freerks and Joshua D. Taylor†*

*Syntroleum Corp., 4322 South 49th West Ave., Tulsa, OK 74107
† National Renewable Energy Laboratory, Golden, CO 80401

Introduction

The US EPA is promoting technologies to reduce idling time of heavy duty vehicles[1]. Individual states have promulgated regulations restricting idling to as short as 3 minutes in some cases[2]. The California Air Resources Board has begun to enforce its idling vehicle rule effective February 1, 2005[3]. Idle time reduction will significantly reduce non-productive fuel use and emissions. However, starting diesel engines that have cooled from normal operating temperature can lead to increased emissions. In addition, starting engines at temperatures near 0ºC can be difficult and lead to significant white smoke emissions due to unburned fuel until the engine warms sufficiently to combust all fuel injected into the combustion chamber. Fuel quality can directly impact both the ease of starting a diesel engine and the emissions produced during the warm-up phase of vehicle operation.

White smoke emissions from diesel engines occur during cold starting due to unburned hydrocarbons in the combustion chamber forming aerosols in the exhaust. Hara[4] et al. studied the impact of alkyl nitrates on cetane number, auto-ignition temperature, cold starting and white smoke emission from diesel engines during cold starting. They concluded that low cetane fuels result in longer times from cranking to steady idle speed at 25ºC start temperature, and that a 30 cetane number fuel will fail to start below 15ºC. For 50 cetane number fuel, starting deteriorated rapidly below 0ºC. However, white smoke emissions were not effected by adding a cetane improver, 2-ethylhexyl nitrate.

It is generally accepted that the high cetane number of Gas-to-Liquids (GTL) diesel fuel will improve startability at low temperatures, but little data exists to support this view. It is not known if GTL fuel will reduce white smoke and hydrocarbon emissions during and just after starting a diesel engine in cold climates. This report documents comparison of GTL diesel fuel versus conventional ASTM D975 No. 2-D and No. 1-D fuels at cold-start conditions.

Test Program

Ignition delay of numerous pure compounds and several diesel fuels of varying quality and source have been measured as a function of temperature (Figure 1) using the Ignition Quality Tester (IQT™) and reported previously[5]. Reactivity of different fuel molecules is postulated to be related to the reactivity of various sites in a molecule and the number of those reactive sites available to radical attack. In particular, the slope of the ignition delay versus temperature curves is related to the strength of the C-H bonds in the fuel molecules since the bond strength is correlated with the rate of H-abstraction reactions. These results show that the ignition delay at reduced temperatures is not only a function of cetane number, but also a function of the fuel molecular structure, which modifies the slope of the curve. We propose that the temperature at which the ignition delay reaches a certain value can be correlated with the minimum ambient temperature at which an engine will start using this fuel. This cold-start ignition delay is a separate fuel property that can be measured using the IQT™. This paper is an initial attempt to relate the low-temperature ignition delay to the minimum ambient starting temperature for an engine using GTL fuels.

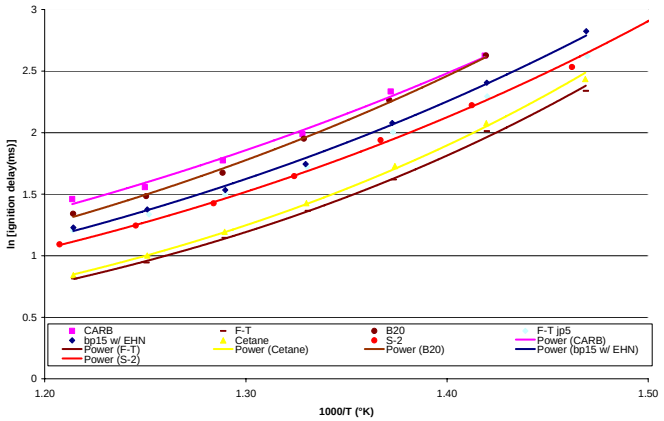

Figure 1. Arrhenius-type plot of fuel ignition delay data.

It is not well documented at this time how the compressed charge air temperature changes as ambient air temperature decreases,[§] or at what combustion chamber temperature cold start misfire and white smoke emissions occur. Therefore, there is a need for testing of starting ability of engines at low temperature in laboratory-controlled environments.

The impact of GTL fuel on diesel engine starting at low temperatures was investigated using a DDC Series 50 8.7 liter diesel engine. This program compared the performance of conventional No. 2 and No. 1 diesel fuels to Syntroleum S-2 Fischer-Tropsch GTL diesel fuel with respect to the ability of a diesel engine to start on a given fuel. No emissions measurements were made during these tests.

The fuel tested in this program was produced by Syntroleum at their Catoosa Demonstration Facility under a grant from the DOE. Syntroleum S-2 synthetic (GTL) diesel fuel is produced from natural gas using reforming technology to produce synthesis gas, which is fed to a Fischer-Tropsch reactor. S-2 is 100% paraffinic with both sulfur and aromatics below detectable limits. The fuel is composed primarily of normal and iso paraffins with an Iso/Normal ratio of 5:1. The fuel meets all ASTM D975 requirements and contains a complete additive package providing lubricity, corrosion, foam and oxidation performance. The cetane number of this fuel is above 74, which is the normal maximum calibration point for ASTM D613 Cetane Number measurements.

Tests were conducted as follows:

- Engine was flushed with test fuel and equilibrated at test temperature.
- Engine was cranked for 10 seconds or until starting occurred.
- If a start did not occur during a 10 second crank period, the engine was allowed to temperature equilibrate and cranking was again initiated two more times or until the engine started.

Starting performance of a fuel was deemed acceptable if it started during one of the three attempts at a temperature and at the next lower test temperature. If a start failure occurred at a temperature, the test temperature was dropped slightly and the test repeated to verify the start failure. For a limited temperature range, problematic starting was observed. Below some temperature, no amount of cranking resulted in a start condition. Figure 2 shows results for starting tests for the conventional No. 2-D fuel.

[§] A decrease in the intake charge air temperature of ~30-45°C results in a reduction of ~100-150°C in the compressed charge temperature assuming adiabatic compression.

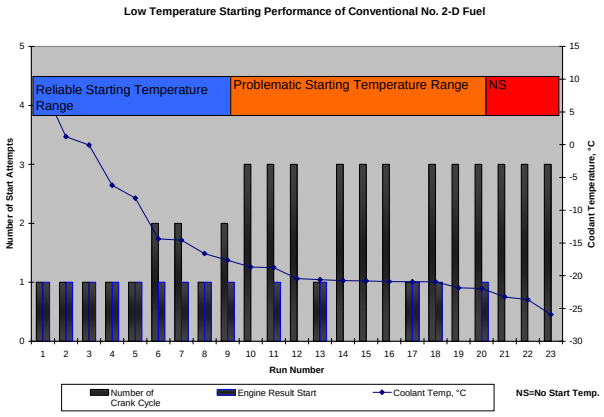

Figure 2. No. 2-D diesel fuel starting versus temperature.

Run number 9 in Figure 2 resulted in a start after two attempts at -18ºC. Run number 10 resulted in a no-start after three attempts at -19ºC. Below -22ºC, no starting was observed.

No. 1-D diesel fuel performance is shown in Figure 3. This fuel started reliably down to -16ºC and failed to start below -17ºC. Although No. 1-D fuel has lower viscosity and lower cloud point than No. 2-D fuel, the ignitability of this fuel was not as good and therefore the startability was not as good as No. 2-D fuel.

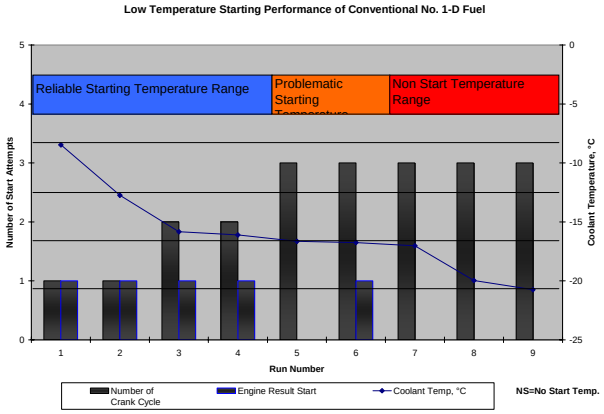

Figure 3. No. 1-D diesel fuel starting versus temperature.

Starting performance of S-2 is shown in Figure 4. Reliable starting was obtained down to -29ºC with problematic performance down to -32ºC. Below -32ºC, no starting was observed.

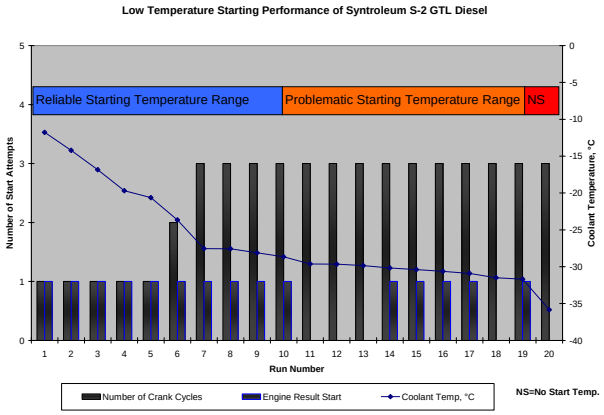

Figure 4. S-2 synthetic diesel fuel starting versus temperature.

Discussion and Conclusions

GTL diesel fuel with high cetane allows reliable starting of diesel engines at 11ºC lower ambient temperatures than conventional No. 2-D fuel. This 11°C difference in ambient air temperature would result in a difference of compressed charge temperature of ~33°C (assuming adiabatic compression). If we assume that the minimum ambient temperature at which the engine will start is correlated with the temperature at which the ignition delay is a certain value, we can relate the engine data (Figures 2-4) with the IQT™ data shown in Figure 1.

For example, if we assume a critical cold-start ignition delay of 6 ms, then the S-2 charge temperature would be 468°C (from Figure 1) and the 2-D charge temperature would be 502°C. This shows a 34°C difference, which agrees well with the difference in charge temperature we would expect from the adiabatic compression.

This data just begins to explain the real world performance of different fuels in engines under cold start conditions. Emissions measurements and additional performance data at cold temperatures is needed. The DOD RDECOM will be conducting a series of tests on synthetic F-T derived JP-8 fuel and blends utilizing engines of interest to the US Army later this year[6].

Acknowledgement. The authors would like to acknowledge the U.S. Department of Energy for their support of this research. The Office of Freedom Car and Vehicle Technologies supported work at NREL project under the Fuel Technologies Subprogram. Syntroleum was supported by DOE Project DE-FC26-01NT41099 FT Fuels Production and Demonstration.

References

(1) Levinson, T. National Idling Reduction Network News, **2005**. http://www.eere.energy.gov/vehiclesandfuels/pdfs/newsletters/feb05_network_news.pdf

(2) American Transportation Research Institute, Compendium of Idling Regulation, **2004**. http://www.atri-online.org/research/results/idling_chart.pdf

(3) California EPA ARB News Release 05-04, ARB Begins Enforcement of Idling Vehicle Rule, January 31, 2005. http://www.arb.ca.gov/newsrel/nr013105.htm

(4) Hara H., Itoh Y., Henein H. A. and Bryzik W. "Effect of Cetane Number with and without Additive on Cold Startability and White Smoke Emissions in a Diesel Engine", *SAE,* **1999**-0101476.

(5) Taylor, J. D.; McCormick, R. L. *Prepr. Pap.-Am. Chem. Soc., Div. Fuel Chem.*, **2005**, *50* (1), 325.

(6) Personal communications with Pat Muzzell, US Army RDECOM, April 2005

CRYPTOMELANE AS HIGH CAPACITY SULFUR DIOXIDE ABSORBENT FOR DIESEL EMISSION CONTROL

Liyu Li and David L King

Materials Division, Pacific Northwest National Laboratory
P.O. Box 999, Richland, WA 99354

Introduction

Cryptomelane, $K_xMn_8O_{16}$, has been identified as a high capacity sulfur oxide absorbent under oxidizing and inert conditions.[1] Cryptomelane can be synthesized either from a mixture of $KMnO_4$ and $MnSO_4$ or a mixture of $MnSO_4$ and KOH.[2] Under oxidizing conditions, cryptomelane synthesized from $KMnO_4$ and $MnSO_4$ is stable up to 600°C, and cryptomelane synthesized from $MnSO_4$ and KOH is stable up to 800°C. Over a temperature range from 250°C to 475°C, cryptomelane SO_2 capacity can be as high as 70 wt%, which is almost ten times as high as that of conventional metal oxide-based SO_2 absorbents. The dominant mechanism for SO_2 absorption by cryptomelane is through the oxidation of SO_2 to SO_3 by Mn^{4+} and Mn^{3+} followed by SO_3 reaction with Mn^{2+} to form $MnSO_4$.

In this presentation, we describe a study of the stability of cryptomelane under reducing conditions and lean-rich cycling conditions that simulate the proposed NO_x trap aftertreatment system.[3] It has been found that although the cryptomelane materials are not stable under most reducing conditions, the reduced form can be oxidized back to the original cryptomelane structure. Cryptomelane which has experienced lean-rich cycles up to 550°C still has very high SO_2 capacity.

Experimental Section

Cryptomelane was synthesized either from a mixture of $KMnO_4$ and $MnSO_4$ or a mixture of $MnSO_4$ and KOH.[2] The adsorbents were evaluated mostly as 40-80 mesh granules, formed by pressing a tablet at 20,000 psi for 5 minutes followed by crushing and screening.

A large portion of the stability study was carried out using a Netzsch STA 409 Thermogravimetric Analysis (TGA)-Differential Scanning Calorimetry (DSC)-Mass Spectroscopy (MS) system. Different gases, including air, 2% H_2 in Ar, 2% C_3H_6 (propylene) in Ar, and He were used for the TGA-DSC-MS analysis. To get a large amount of treated samples for other characterizations, cryptomelane was also treated in a tube furnace with flowing air, 2% C_3H_6 in Ar, simulated rich condition diesel engine exhaust, and simulated lean condition diesel engine exhaust. Lean-rich cycling treatments were carried out with an AMI-200R-HP unit (Altamira Instruments, Pittsburgh, PA), which can automatically switch the feed to a heated reactor between lean and rich exhaust gases at given time intervals. The composition of these simulated exhausts is given in **Table 1** below. Two samples were prepared for us by Caterpillar Inc. for subsequent testing and analysis. The exhaust compositions of those treatments are identified as "Lean Condition" and "Rich Condition" in **Table 1**. The two different feed compositions for lean-rich cycling experiments carried out in our laboratory are identified as "Lean-rich cycle A" and "Lean-rich cycle B".

Powder X-ray diffraction (XRD), BET surface area (SA), and scanning electron microscopy (SEM) images were collected on some of the tested materials. The SO_2-absorption tests were performed in a small fixed bed quartz tube reactor, which was heated by a small clam-shell furnace. Reactant gases were metered using mass flow controllers. The SO_2 analytical system comprised a HP6890 gas chromatograph equipped with a Sulfur Chemiluminescent Detector (SCD), which has been described in detail previously.[4] During the experimental run the analytical system operated continuously, sampling the effluent every three minutes. The minimum detection limit of the system to SO_2 is approximately 50 ppb. Typical measurements employed a 0.2 g 40-80 mesh particle sample. The standard absorption tests were performed at 325°C, using a feed gas of 250 ppm SO_2 in air, at a flow of 8,000 hr^{-1} gas hourly space velocity (GHSV).

Results and Discussion

Stability under oxidizing conditions. Two additional tests were performed to further check the stability in an oxidizing atmosphere. In the first test, cryptomelane prepared by the $MnSO_4$ oxidation method was treated at 600°C for 3 hr in air containing 10% H_2O, to test for steam/air stability. In the second test, cryptomelane prepared by the reflux method was treated at 500°C for 1 hr in simulated lean exhaust gas ("Lean Condition" in **Table 1**). Following these treatments, no structural changes were observed based on XRD analysis. The SO_2 capacities were measured following these two treatments. Even after these extreme conditions, cryptomelane still has more than 45 wt% SO_2 breakthrough capacity.

Stability under inert atmosphere. Cryptomelane shows high SO_2 capacity at 325°C under an inert atmosphere.[1] Its stability under ultra high purity helium was studied using TGA-DSC-MS. Under inert atmosphere, cryptomelane from the reflux method is stable up to 450°C, and cryptomelane from the $MnSO_4$ oxidation method is stable up to 580°C. At higher temperatures, cryptomelane decomposes. In general, cryptomelane is less stable under inert conditions than under air.

Stability under reducing conditions. As a high valence manganese oxide, cryptomelane is unstable under reducing conditions. **Figures 1(a)** shows the DSC analysis results of cryptomelane under 2% C_3H_6 in Ar. Cryptomelane is reduced at as low as 300°C. After reduction, Mn_3O_4 and MnO form. Mn_3O_4 is further reduced to MnO when the reduction temperature is higher than 550°C. A similar result was also obtained with 2% H_2 in Ar as reductant. Cryptomelane from the $MnSO_4$ oxidation synthesis method shows similar results.

Table 1. Composition of simulated diesel engine exhausts used in the study

Simulated Exhaust		Carbon Soot	CO	CO_2	C_3H_6	H_2	H_2O	SO_2	O_2	NO_2	NO	N_2
Lean Condition		$5x10^{-5}$ g/L	3250 ppm	7.1%	360 ppm	--	--	--	10.2%	--	230 ppm	Balance
Rich Condition		$2x10^{-5}$ g/L	2000 ppm	10%	1000 ppm	--	10%	--	0~1%	--	500 ppm	Balance
Lean-rich cycle A	Lean	--	--	10%	--	--	10%	--	12%	--	500 ppm	Balance
	Rich	--	4%	10%	4000 ppm	1.3%	10%	--	1.5%	--	500 ppm	Balance
Lean-rich cycle B	Lean	--	--	5%	--	--	--	5.15 ppm	12%	20 ppm	180 ppm	Balance
	Rich	--	2%	12.5%	333 ppm	2%	--	--	--	--	--	Balance

The MnO from reduced cryptomelane can be easily oxidized upon heating in an oxidizing atmosphere. **Figure 1 (b)** gives the DSC trace upon re-oxidation of the MnO product obtained by initial cryptomelane reduction in 2% C_3H_6 in He at 550°C. As can be seen, the MnO can be re-oxidized as low as 250°C. After oxidation at 500°C for 1hr, most of the reduced cryptomelane recovers the original cryptomelane crystal structure, as shown in **Figure 2**. The minority product of re-oxidation is Mn_3O_4.

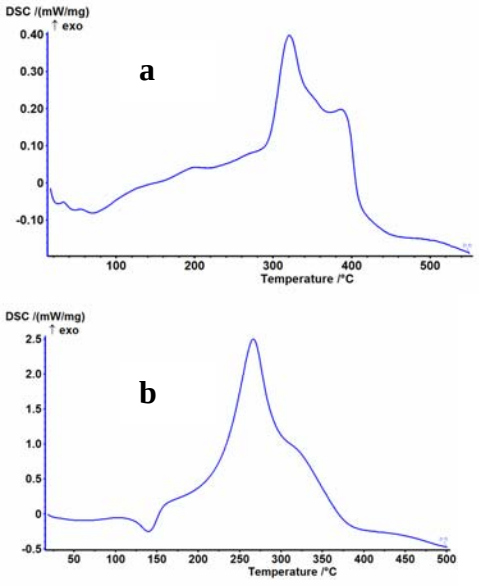

Figure 1. a: DSC trace of cryptomelane in 2% C_3H_6. Test condition: 10 °C /min heating rate, 2% C_3H_6 in Ar at 40 ml/min flow; b**:** DSC trace of 550°C, 2% C_3H_6 treated-cryptomelane heated in air. Test condition: 10°C/min, air at 40 ml/min.

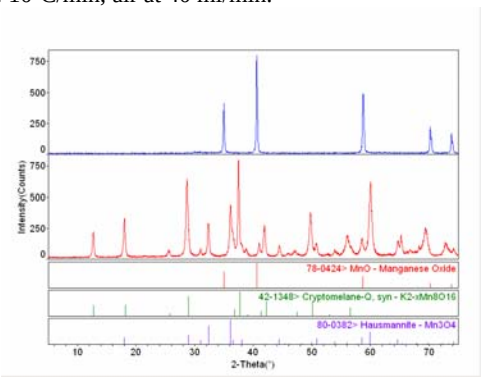

Figure 2. XRD patterns of reduced (top) and re-oxidized (bottom) cryptomelane. Reduction: in 2% C_3H_6 at 550°C for 1 hr; Re-oxidation: in air at 500°C for 1 hr

Stability under lean-rich cycling. To study the effect on cryptomelane of the lean-rich cycling protocols that have been proposed for NO_x traps, a cryptomelane sample was treated under simulated lean-rich cycles at 475°C for 6.5 hours (cycling at 6 minutes lean and 30 seconds rich). The exhaust composition was given in **Table 1** (lean-rich cycle A). Both lean and rich exhaust gas flowed at 26,000 hr^{-1} GHSV through cryptomelane.

Almost identical XRD patterns were obtained of the cryptomelane samples before and after the lean-rich treatment. Some morphology changes were observed under SEM, and the BET surface area decreased from 74 m^2/g to 20 m^2/g after treatment. **Figure 3** shows the SO_2 absorption performance of the lean-rich treated cryptomelane, which is close to that of the fresh absorbent. This indicates that the SO_2 absorption capacity of cryptomelane is not simply a function of its surface area.

NO_x traps may be required to operate over a temperature range 250°C to 550°C, therefore the SO_x trap should also operate stably over this same range. Subsequent experiments exposed cryptomelane to lean-rich cycling at 250°C, 400°C, and 550°C. Each treatment lasted 6 hours, with the cycling protocol 4 minutes lean (50,000 hr^{-1} GHSV) and 20 seconds rich (10,000 hr^{-1} GHSV). The lean and rich gases composition is given in **Table 1** (lean-rich cycle B). After 6 hours of lean-rich treatments all three samples give very high SO_2 capacities (> 45 wt%).

No structural changes were observed with cryptomelane from the reflux method after 250°C and 400°C lean-rich treatment. However, after 550°C treatment, cryptomelane from the reflux method was mostly reduced to Mn_2O_3, whereas cryptomelane from the $MnSO_4$ oxidation method only showed slight structure change after the same lean-rich treatment. The XRD analysis indicates that cryptomelane prepared by the $MnSO_4$ oxidation method is more stable toward lean-rich cycling than cryptomelane prepared by the reflux method.

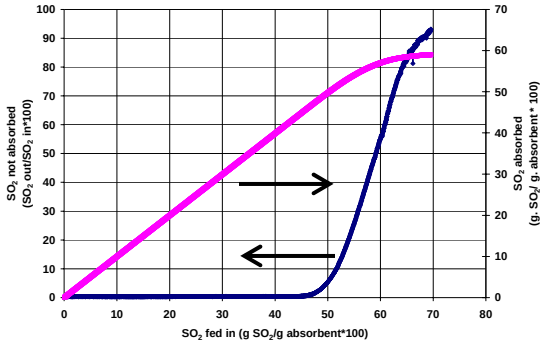

Figure 3. SO_2 absorption of lean-rich treated cryptomelane.

Treatment condition: 475°C for 6.5 hr, cycling at 6 min lean and 30s rich, lean and rich gas flows at 26,000 hr^{-1} GHSV. Lean and rich gas composition (A) is given **Table 1**. Test conditions: 325°C, 250 ppm SO_2 in air at 8,000 hr^{-1} GHSV

Stability of SO_2 -loaded absorbent. After SO_2 absorption on cryptomelane, $MnSO_4$ and K_2Mn_2 $(SO_4)_3$ form. These phases are stable up to 700°C under an oxidizing atmosphere. The stability of SO_2-saturated cryptomelane under reducing conditions was studied using TGA-MS. In terms of sulfur retention, spent cryptomelane is stable up to 600°C in 2% H_2 in He. Above 600°C, SO_2 and H_2S are released.

References

1. Li, L., King, D.L., *Ind. Eng. Chem. Res.* **2005**, *44*, 168.
2. DeGuzman, R.N., Shen, Y.F., Neth, E,J., Suib, S.L., O'Young, C.K., Levine,S., Newsam, J.M., *Chem. Mater.* ***1994,*** *6, 815.*
3. Takahashi, N., Shinjoh, H., Iijima, T., Suzuki, T., Yamazaki, K., Yokota, K., Suzuki, H., Miyoshi, N., Matsumoto, S.I., Tanizawa, T., Tanaka, T., Tateishi, S.S., Kasahara, K., *Catal. Today* **1996**, *27*, 63.
4. Li, L., King, D.L., *Ind. Eng. Chem. Res.* **2004**, *43*, 4452.

ADSORPTION PROPERTIES CHANGE OF Ni/Y ON SULFUR COMPOUNDS DEPENDING ON THE DIESEL COMPOSITION

Chang Hyun Ko, Vinay M. Bhandari, Jung Geun Park, Jong-Nam Kim, Sang Sup Han, Soon Haeng Cho

Separation Process Research Center, Korea Institute of Energy Research, 71-2, Jang-dong, Yu-sung-gu, Daejeon, Korea, 305-343

Introduction

The demand on clean transportation fuel has increased due to the strict regulation to protect environment or fuel cell application. Especially, fuel cell needs extremely low level sulfur concentration fuel because even small amount of sulfur can cause deactivation of catalyst in reformer. However, decrease of sulfur concentration in transportation fuel from 300 ppmw to less than 1 ppm by hydrodesulfurization (HDS) process, already applied in refinery plant, was extremely difficult due to the low reactivity of HDS catalysts for refractory sulfur compounds, which have steric hindrance such as benzothiophene (BT), dibenzothiophene (DBT) and 4,6-dimethyldibenzothiophene (4,6-DMDBT) [1].

Recently, Yang and co-workers introduced a new class of sulfur removal method in transportation fuel: removal of sulfur compounds in diesel at ambient temperature using sulfur selective adsorbents[2]. They reported that various kinds of metal-ion exchanged Y zeolites, such as Ni/Y, Cu/Y and so on, showed remarkably high capacity and selectivity for refractory sulfur compounds in commercial diesel[3-5]. They proposed that π-complexation bonding between sulfur compounds and metal cation exchanged inside the pores of Y zeolite impose such selectivity and capacity on zeolite based adsorbents[2,6]. However, no systematic study on sulfur compound adsorption has been reported yet.

For more understanding on this selective adsorption phenomenon, we investigated the adsorption properties of Ni/Y on BT, DBT and 4,6-DMDBT in model diesel. The model diesel contained 50 ppm BT, 50 ppm DBT and 50 ppm 4,6-DMDBT in n-octane. The capacity of Ni/Y was very high: 40 mg S/g. However, the capacity decreased drastically as soon as the presence of aromatics and moisture. We also compared the adsorption behavior of Ni/Y in model diesel with that in commercial diesel.

Experimental

Adsorbent preparation. Na-Y zeolite was obtained from Aldrich (Si/Al = 2.37). Ni/Y was prepared using liquid phase ion exchange method at room temperature. 1.0 g of Na-Y was stirred in 1 M nickel nitrate solution for 8-10 hours and then washed with deionized water to remove the excess nickel salt solution. The ion exchange process was repeated 3 times and each process time was more than 3 hours to ensure complete exchange of nickel ion instead of sodium ion. The ion exchange was carried out at room temperature and at pH ~5. After ion exchange and washing, the adsorbent was dried in vacuum at 298 K to remove the moisture. The dried sample was stored in air-tight bottles, kept in desiccators. Appropriate particle size (125 ~ 600 um) was obtained by sieving for breakthrough test to reduce pressure drop and maximize effluent contact time on adsorbent.

Reagents and standards. The refractory sulfur compounds vis. BT (95%), DBT (98%) and 4,6-DMDBT (97%) were used as-received from Aldrich without further purification. We chose n-octane (99%) as a solvent in model diesel and obtained from Junsei. A sample of commercial diesel was obtained from a gas-station in Daejeon, South Korea.

Breakthrough Test: Fixed bed adsorption. Breakthrough tests were carried out in quartz tubes, having inside diameter of 4 mm and outside diameter of 6 nm, with tube length of 300 mm. The experimental set-up consisted of a constant flow liquid flow pump, vertical glass column and feed solution bottles. Upflow conditions were used in all the experiments. The activation of Ni/Y was carried out using the procedures recommended by Yang and co-workers. The Ni/Y was heated from ambient temperature to 623 K for 3 hours and then maintained 623 K for 18 hours in helium gas atmosphere. The helium gas was initially passed through a column of 3A molecular sieves to remove moisture, if any, before passing through the adsorbent to remove moisture contamination after activation process. Ni/Y was green after ion exchange, but became pinkish color after proper activation treatment.

Sulfur Concentration Analysis. All the samples were analyzed using HP 6890 series gas chromatograph, equipped with SUPELCO 24158 SPB-1 SULFUR capillary column and a flame photometric detector (FPD). Identification of BT, DBT and 4,6-DMDBT was carried out using the standard solutions. We obtained relationship between peak area and sulfur concentration of each sulfur compound. We measured peak area of unknown sample by GC-FPD, then calculated the sulfur concentration based on this relationship.

Results and Discussion

Figure 1 showed the breakthrough curves of Ni/Y for model diesel, consisted of 50 ppm BT, 50 ppm DBT, 50 ppm 4,6-DMDBT in n-octane. A flow rate of 0.4 ml/min was used in this experiment. Ni/Y can purifie about 300 ml of 150 ppmw model diesel. The volume of purified model diesel means that sulfur adsorption capacity of Ni/Y calculated was about 40 mg S/g ads. The breakthrough point can be estimated by observing the development of color front in adsorbent. The pinkish color changed to brown color after breakthrough.

Figure 1 also indicated an interesting selectivity patterns. Firstly, BT was found to elute. Secondly, 4,6-DMDBT eluted. Finally, DBT came out from the Ni/Y adsorbent. This suggests that the selectivity of Ni/Y on refractory sulfur compound was DBT > 4,6-DMDBT > DBT.

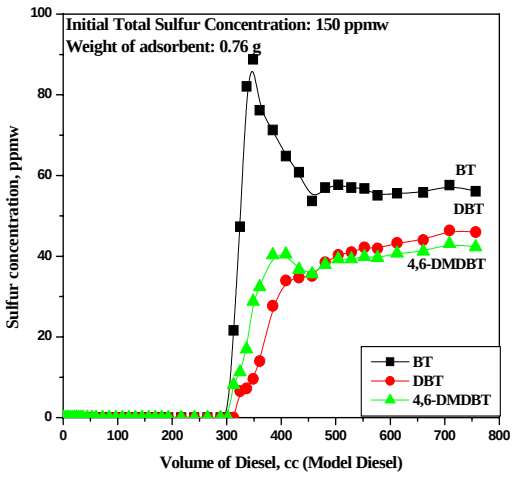

Figure 1. The breakthrough curves of refractory sulfur compounds for Ni/Y in model diesel.

Based on model diesel breakthrough test using sulfur compounds and n-octane solvent, Ni/Y had expected to be a

promising adsorbent for adsorptive sulfur removal in transportation fuel. To confirm this possibility, Ni/Y was applied for the purification of commercial diesel by breakthrough test. The flow rate was 0.2 ml/min and activation time to maintain 623 K was 10 hours. However, Figure 2 showed the drastic decrease in purification volume of commercial diesel compared to that of model diesel. As we used the same types of adsorbent, Ni/Y, the only difference in this experiment was the composition of the effluents: model diesel and commercial diesel. The decrease of adsorption capacity of Ni/Y for commercial diesel might be affected by the diesel composition.

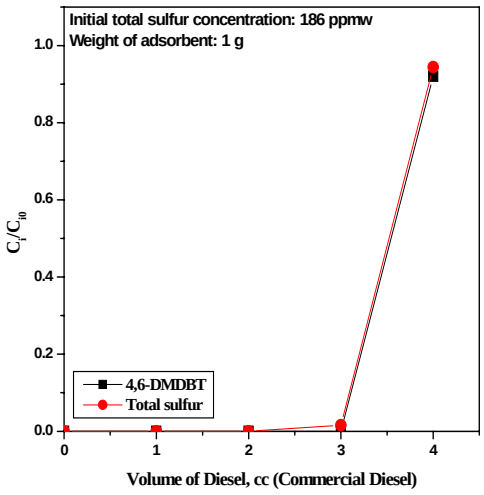

Figure 2. The breakthrough of refractory sulfur compound on Ni/Y using commercial diesel

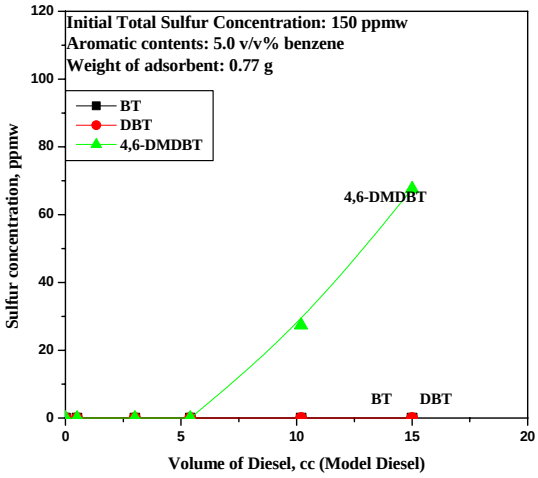

Figure 3. The breakthrough curve for sulfur compound on Ni/Y using model diesel after addition of 5 wt% benzene

Figure 3 showed the lowering of sulfur adsorption capacity after addition of benzene on model diesel. Ni/Y was able to treated 300 ml of pure model diesel, but Ni/Y was only able to purify less than 6 ml of 5 v/v % benzene added model diesel. As the only difference in both effluents was benzene composition, we were able to attribute adsorption capacity decrease to the presence of benzene in model diesel. In view of the fact that commercial diesel has a wide range for the aromatic content (15 ~ 47%), higher aromatics in commercial diesel could be one possible reason for the lower capacity.

We also examined the effect of moisture on Ni/Y for sulfur compound adsorption because moisture was one of the most frequently appeared species among various contaminating ones.

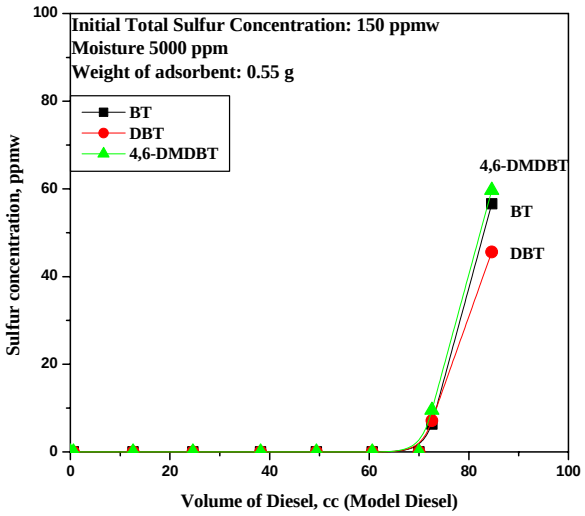

Figure 4. The moisture effect on the Ni/Y adsorption on sulfur compound

As shown in Figure 4, 0.5 wt% moisture reduced more than 60% of adsorption capacity. Thus, pre-treatment of moisture prior to adsorptive sulfur removal in commercial diesel might be an essential process to ensure the reliability and reproducibility of adsorptive desulfurization process.

Conclusion

We investigated the adsorption properties of Ni/Y on refractory sulfur compounds in model diesel by breakthrough test. Apart from high adsorption capacity on sulfur compounds in model diesel, adsorption capacity of Ni/Y decreased drastically due to the presence of aromatics and moisture.

References

(1) Yang, R. T. In *Adsorbents: Fundamentals and Applications* and references there in; Wiley: New York, 2003; chap. 10

(2) Yang, R. T.; Hernandez-Maldonado, A. J.; Yang, F. H. *Science* **2003**, *301*, 79.

(3) Hernandez-Maldonado, A. J.; Yang, R. T. *Ind. Eng. Chem. Res.* **2003**, *42*, 3103.

(4) Hernandez-Maldonado, A. J.; Yang, R. T. *Ind. Eng. Chem. Res.* **2004**, *43*, 1081.

(5) Hernandez-Maldonado, A. J.; Yang, R. T. *AIChE J.* **2004**, *50*, 791.

(6) Hernandez-Maldonado, A. J.; Yang, R. T. *J. Am. Chem. Soc.* **2004**, *126*, 992.

EFFECT OF HIGH SURFACE AREA SILICEOUS SUPPORTS ON THE STRUCTURE AND CATALYTIC PERFORMANCE OF Ni_2P CATALYSTS

Yong-Kul Lee and S. Ted Oyama

Environmental Catalysis and Nanomaterials Laboratory, Department of Chemical Engineering, Virginia Tech, Blacksburg, VA 24061

Introduction

Environmental regulations for reducing motor vehicle emissions has put considerable pressure on the refining industry worldwide to produce cleaner fuels, and has motivated much research for the development of new hydrotreating catalysts. Among alternatives to the widely used sulfides are transition-metal carbides, nitrides, and phosphides (1,2,3,4). Metal phosphides are a novel catalyst group for deep hydrotreating and have received much attention due to their high activity for hydrodesulfurization (HDS) and hydrodenitrogenation (HDN) of petroleum feedstocks (4,5,6,8). Previous studies of silica-supported Ni_2P employed a low surface area (90 $m^2 g^{-1}$) support (6,7). It is the objective of this work to investigate a mesoporous siliceous material (790 $m^2 g^{-1}$) as support. Particular attention is placed on understanding the effect of nitrogen, sulfur and aromatic compounds on the catalytic behavior, as these compounds are reported to inhibit HDS. The present study also includes the use of X-ray absorption fine structure (XAFS) spectroscopy to study the structure of the finely dispersed phosphide phases before and after reaction. As will be shown the samples after use show evidence for the formation of a surface phospho-sulfide phase of very high activity.

Experimental

Commercial SiO_2 supports (Cabot, Cab-O-Sil) of low surface area (L-90, 90 $m^2 g^{-1}$) was used as received. A mesoporous MCM-41 silica support was synthesized following a literature procedure (9). The supported Ni_2P catalysts were prepared with excess phosphorus (Ni/P=1/2) and a loading of 1.16 mmol Ni/g support (12.2 wt.% Ni_2P/SiO_2). Previous studies (6,7) had shown that this composition and loading level gave high activity and stability in hydroprocessing reactions. Samples prepared with low surface area silica (L90) were denoted as Ni_2P/SiO_2-L. The synthesis of the catalyst involved two steps (4,6,7). In the first step, a supported nickel phosphate precursor was prepared by incipient wetness impregnation of a solution of nickel nitrate and ammonium phosphate, followed by calcination at 673 K. In the second step, the supported metal phosphate was reduced to a phosphide by temperature-programmed reduction (TPR). In catalyst preparation, larger batches using up to 5.50 g of supported nickel phosphate were prepared in a similar manner by reduction to 873 K and 893 K for Ni_2P/SiO_2-L and Ni_2P/MCM-41, respectively. Sulfided Ni-Mo/Al_2O_3 (CR 424) was used as reference.

The prepared catalysts were characterized by XRD, N_2 adsorption and CO chemisorption. Also, X-ray absorption (XAS) spectra at the Ni K edge (8.333 keV) of reference and catalyst samples were recorded in the energy range 8.233 to 9.283 keV using synchrotron radiation at the National Synchrotron Light Source (NSLS) at Brookhaven National Laboratory (BNL), beamline X18B.

Hydrotreating was carried out at 3.1 MPa (450 psig) at two different temperatures, 573 K (300 ^oC) and 613 K (340 ^oC) in a three-phase upflow fixed-bed reactor. The feed liquid was prepared by combining different quantities of tetralin (Aldrich, 99%), n-tridecane (Alfa Aesar, 99%), quinoline (Aldrich, 99%), 4,6-dimethyldibenzo-thiophene (4,6-DMDBT, Fisher, 95%), dimethyldisulfide (DMDS, Aldrich, 99%), and n-octane (Aldrich, 99%).

Results and Discussion

Figure 1 shows the hexagonal structure of Ni_2P. The Ni_2P unit cell has two types of Ni and P sites (denoted as Ni(I), Ni(II) and P(I), P(II)), which form two different trigonal prisms in Ni_2P consisting of various Ni-P and Ni-Ni subshells.

Figure 1. Local structure of Ni_2P with two types of trigonal prisms.

Figure 2 shows the Fourier transforms of the Ni K-edge EXAFS spectra for the freshly prepared samples before reaction and a bulk reference Ni_2P sample. For the bulk Ni_2P the Fourier transform gives two main peaks, a smaller peak at 0.171 nm, and a larger peak at 0.228 nm. For the supported Ni_2P samples there are also two main peaks located at almost the same positions as those of the bulk Ni_2P reference, but with the larger peak weakened and broadened as the surface area of the support increases.

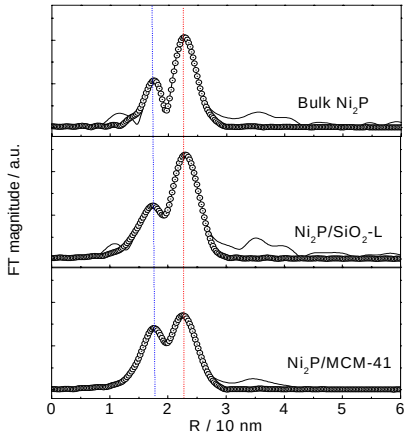

Figure 2. EXAFS analysis results for the fresh samples. The solid lines are the experimental curves and the circles are calculated points.

EXAFS analysis is particularly useful for characterizing the highly dispersed phase on the supports with large surface area. The Feff simulation allowed the assignment of those peaks that appeared in the Fourier transform. The first small peak centered at 0.180 nm was due to P neighbors at 0.2209 and 0. 2266 nm and the second larger peak centered at 0.230 nm was due to a mixed feature of P neighbors at 0.2369 and 0.2457 nm and of Ni neighbors at 0.26783 nm. For the curve fittings the three dominant shells of two Ni-P shells at 0.2266 and 0.2456 nm and one Ni-Ni shell at 0.2678 nm were selected from the simulation results and used as references for phase shift and amplitude calculations. These give reasonable parameters for all samples (Table 1). For example, fitting for the bulk Ni_2P gives 2 P neighbors at 0.2253 nm and 1.75 P neighbors at 0.2401 nm and 3.99 Ni neighbors at 0.2644 nm. In contrast to bulk Ni_2P, for the supported Ni_2P samples the coordination number of the second shell, Ni-P at 0.2456 nm, increases as dispersion increases, even though the Ni-P bond length decreases. Interestingly, the bond length for the Ni-Ni shell increases with the coordination number as the dispersion increases. It is thus likely that the more dispersed

Ni_2P catalyst contains more P atoms, and that the interstitial P atoms lengthen the distance between Ni atoms and weaken the Ni-Ni bond. Ni_2P/MCM-41 containing highly dispersed Ni_2P particles underwent less loss in P, even after the high temperature reduction. This suggests that the smaller particles have a stronger interaction between the Ni and P atoms.

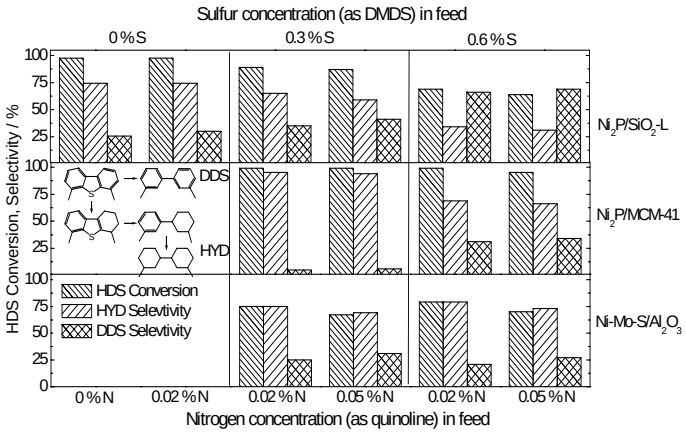

Figure 3. Comparison of hydrogenation/dehydrogenation activity for 4,6-DMDBT over Ni_2P/ SiO_2-L, Ni_2P/ MCM-41 and Ni-MoS/Al_2O_3.

Figure 3 compares the conversion and the product selectivities toward direct desulfurization (DDS) and hydrogenation (HYD) of 4,6-DMDBT as a function of nitrogen (as quinoline) and sulfur (as DMDS) content in the feed for the catalysts at 613 K and 3.1 MPa. The catalytic activity for the catalyst samples in HDS of 4,6-DMDBT followed the order, Ni-MoS/Al_2O_3 < Ni_2P/SiO_2-L < Ni_2P/MCM-41 under 0.35 % S, 0.02 % N, and 1% tetralin. The Ni_2P/MCM-41 showed much better resistance to the inhibition of S and N-compounds with maintenance of higher HDS conversion compared to Ni_2P/SiO_2-L. The EXAFS analysis confirms that the Ni-Ni bond length is widened with dispersion and this feature comes with an increase in Ni-P coordination and a decrease in Ni-P bond length. Thus the higher resistance to the sulfidation can be explained by the stronger interaction between Ni and P species for the highly dispersed Ni_2P catalysts. These results thus suggest that the HDS activity and the resistance to S and N-compound highly depend on the dispersion of the Ni_2P phase.

Conclusions

Nickel phosphide (Ni_2P) catalysts supported on silica and MCM-41 showed high HDS activity for 4,6-DMDBT compared to a commercial Ni-Mo-S/Al_2O_3 catalyst at 573 K (300 ^oC) and 613 K (340 ^oC) and 3.1 MPa based on equal sites (70 μmol) loaded in the reactor. The desulfurization was dominated by the hydrogenation pathway over the Ni_2P catalysts and showed less inhibition by S and N-compounds compared to the sulfide catalysts. Selectivity and performance was higher on the more dispersed catalysts in the order Ni_2P/MCM-41 > Ni_2P/SiO_2-L and this is attributed to the increase in the number of and quality of active sites. Smaller Ni_2P particles have better resistance to S and N compounds due to the stronger interaction between Ni and P in the dispersed Ni_2P phase. EXAFS line shape analysis indicates the formation of a phospho sulfide phase which is favored for the catalysts with shorter Ni-Ni bond length particularly under high S in feed and at relatively high temperature. The phase is responsible for the high activity of the nickel phosphide catalysts.

Acknowledgement. Support for this work came from the U.S.Department of Energy, Office of Basic Energy Sciences, through Grant DE-FG02-963414669 and Brookhaven National Laboratory under grant 3972.

References

(1) Schlatter, J. C.; Oyama, S. T;. Metcalfe, J. E. ; and Lambert, J. M. *Ind. Eng. Chem. Res*., **1988**, *27*, 1648.
(2) Oyama, S. T. (Ed.), The Chemistry of Transition Metal Carbides and Nitrides; Blackie Academic and Professional: London, 1996.
(3) Robinson, W. R. A. M.; van Gastel, J. N. M.; Korányi, T. I.; Eijsbouts, S. ; van Veen, J. A. R. ; and de Beer, V. H. J., *J. Catal.* **1996**, *161*, 539.
(4) Li, W.; Dhandapani, B.; and Oyama, S. T., *Chem. Lett*. **1998**, 207.
(5) Stinner, C.; Prins, R.; and Weber, Th., *J. Catal.* **2000**, *191*, 438.
(6) Oyama, S. T.; Wang, X.; Lee, Y.-K.; and Requejo, F. G., *J. Catal*. **2002**, *210*, 207.
(7) Oyama, S. T.; Wang, X.; Lee, Y.-K.; and Chun, W.-J., *J. Catal*. **2004**, *221*, 263.
(8) Oyama, S. T., *J. Catal*. **2003**, *216*, 343.
(9) Cheng, C.-F.; Park, D. H.; and Klinowski, J., *J.Chem. Soc., Faraday Trans.*, **1997**, *93(1)*, 193.

Table 1. Line-Shape Analysis of EXAFS Spectra and Physical Properties of the Supported Ni_2P Catalysts

Samples	Ni-P						Ni-Ni (I, II)			R (%)	CO uptake / μmol g^{-1}	BET surface area / m^2 g^{-1}
	Ni-P (I)			Ni-P (II)								
	CN	R	σ^2	CN	R	σ^2	CN	R	σ^2			
Ni_2P Feff reference	2	0.2266		1	0.2369		4	0.2678				
Ni_2P (bulk)	2.0	0.2253	3.00	1.7	0.2401	0.499	3.99	0.2644	6.00	0.48	-	-
Ni_2P / SiO_2-L	1.99	0.2234	4.900	2.6	0.2399	6.352	3.43	0.2612	8.001	0.96	25	88
Ni_2P / MCM-41	1.99	0.2210	2.884	3.5	0.2375	4.361	2.88	0.2631	8.477	1.24	41	487

ΔR filtered = 0.1427 - 0.27598 nm, S_o^2 = 0.9, CN: coordination number, R: bond distance (/nm), σ^2: Debye-Waller factor (/10^{-5} nm^2)

IMPROVING ENZYMATIC TRANSFORMATION OF WASTE EDIBLE OIL TO BIODIESEL BY ADDING ORGANIC BASE

Zhi-feng Chen, Ming-hua Zong, Hong Wu*

Biotechnology Department, South China University of Technology, Guangzhou 510640, P.R.China
*Author for correspondence (Fax: 86-20-22236669; E-mail: btmhzong@scut.edu.cn)

Introduction

Wastes edible oil, originated from restaurants and household disposals, is creating serious problems of environmental control and food safety. Production of biodiesel with waste edible oil as feedstock not only could reduce disposal problems, but, more importantly, would decrease the cost of biodiesel.

Presently industrial production of biodiesel from waste edible oil is performed by chemical alkaline catalysts, but it has been found that high content of free fatty acid (FFA) in waste edible oil (FFA>2%) would decrease the yield sharply due to soaps formed in the process[1]. Several studies showed that enzymatic methanolysis with waste edible oil was a promising alternative owing to its mild reaction condition and free of chemical waste.[2, 3] However, this conventional protocol was associated with many drawbacks such as deactivation of lipase caused by methanol and absorption of glycerol to lipase surface, thus resulting in serious negative effect on the reaction.[4, 5]

Du *et al.* have recently reported that methyl acetate was an effective acyl acceptor for biodiesel production.[6] To the best of our knowledge, the biodiesel production from waste edible oil with methyl acetate as the acyl acceptor has not yet been reported. Therefore, the transesterification of different kinds of waste edible oil to biodiesel with methyl acetate in a solvent free system was explored in this paper and the major influential factor on the reaction was further investigated.

Experimental

Materials. One waste edible oil (WDO-1) was collected from fast food restaurant, the other (WDO-2) was obtained from local restaurant waste oil pool and pretreated with activated clay. The refined corn oil (RCO) was purchased from local supermarket. Novozym 435 (lipase B from *Candida antarctica*, 164 U/g, 1unit corresponds to the amount of enzyme that produces 1 μmol methyl oleate from triolein per minute at 35 °C) was kindly donated by Novo Nordisk Co. (Denmark). Methyl palmitate, methyl stearate, methyl oleate, methyl linoleate, methyl linolenate and methyl heptadecanoate (as internal standard) were purchased from Sigma (USA). All other chemicals were also obtained commercially and of analytical grade.

Reaction. The reaction was carried out at 40 °C and 150 rpm. The reaction mixture contained 5 g waste edible oil, 6.93 g methyl acetate with the molar ratio of methyl acetate to total fatty acid being 16:3 and 246 U Novozym 435. The reaction conditions of the three-step methanolysis were the same as our previous study.[7] Samples of 5 μl were periodically withdrawn and mixed with methyl heptadecanoate for GC analysis.

Analysis. The methyl ester (ME) yield in the reaction mixture was assayed with a GC2010 gas chromatography (Shimadzu Corp., Kyoto) equipped with a HP-5 capillary column (0.53 mm × 15 m, HP, USA). The column temperature was hold at 180 °C for 1 min, raised to 186 °C at 0.8 °C /min and kept for 1 min, then upgraded to 280 °C at the rate of 20 °C /min. Nitrogen was used as the carrier gas at 2 ml/min. Split ratio was 1:100 (v/v). The injector and the detector temperatures were set at 250 °C and 280 °C, respectively. The water content of the waste edible oil and refined corn oil were measured by Karl Fischer titration using 787 KF Titrino (Metrohm Ltd. Switerland)

Results and Discussion

The transesterification of different oil with methyl acetate was first explored (**Figure 1)**. The ME yield of WDO-1 was close to that of RCO after reaction for 24 h. However, the ME yield of WDO-2 was only 77.5%, which was lower than that of WDO-1 and RCO.

To determine the reason for the differences in ME yield, some important parameters of three kinds of oil were measured and depicted in. **Table 1**. The major difference was found to be in the content of FFA. So, the effect of the FFA on the reaction was subsequently investigated by adding different amounts of oleic acid into the refined corn oil.

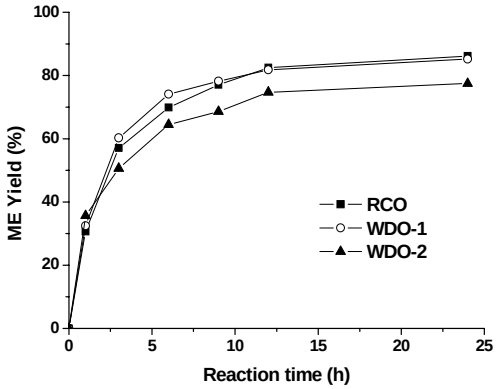

Figure 1. Time course of the reaction. The reactions were carried out at 40 °C and 150 rpm and the reaction mixture contained 5 g waste edible oil, 6.93 g methyl acetate and 246 U Novozym 435.

Table 1. Main parameters of waste edible oil and refined oil

	WDO-1	WDO-2	RCO
Water content (ppm)	320	300	250
FFA content (%)	4.6	27.8	0.1
Saponification value (mg KOH/g of sample)	193	191	187

As depicted in the **Figure 2**, the higher the FFA content, the lower the ME yield, which was similar to the result achieved in **Figure 1**, suggesting that the FFA content was the key influential factor on the reaction. However, the initial reaction rate was not significantly different, indicating that FFA showed no negative effect to the enzyme activity. Thus, acetic acid, the by-product of the process, formed in the transesterification of FFA with methyl acetate might be responsible for the decrease of the ME yield. Different amounts of acetic acid were then added directly into the RCO and the results obtained well supports the hypothesis (data not shown). This can be explained by the change of pH in the micro-environment of enzyme and thus resulted in the inhibition of enzyme activity.

To decrease the negative effect of acetic acid, some efforts have been tried by addition of different organic bases, such as tri-hydroxymethyl aminomethane (TB), triethylamine (TEA) and pyridine (PD) into the reaction mixture of WDO-2 at the beginning of the transesterification As shown in **Figure 3**, the reaction rate was markedly enhanced during the process, on the other hand, the improvement of the ME yield was also observed. Among the organic bases studied, TB was found to be the best for the reaction.

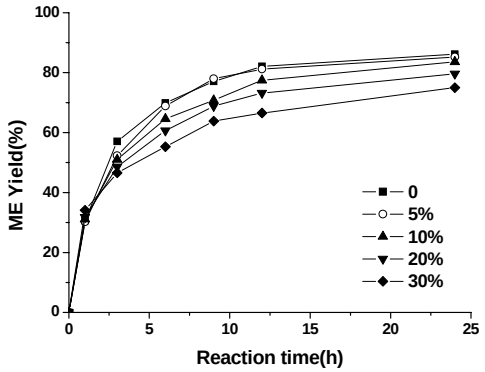

Figure 2. Effect of free fatty acid on the reaction. The reactions were carried out at 40 °C and 150 rpm and the reaction mixture contained 5 g mixture of RCO and oleic acid, 6.93 g methyl acetate and 246 U Novozym 435.

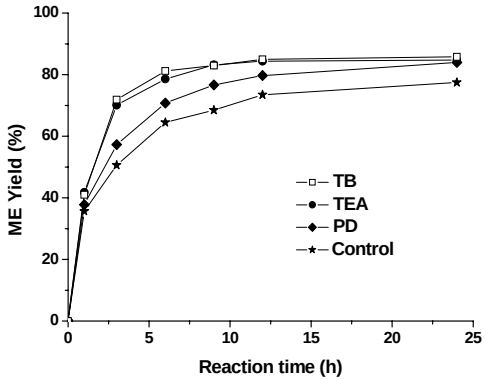

Figure 3. Effect of organic base on the reaction. The reactions were carried out at 40 °C and 150 rpm and the reaction mixture contained 5 g WDO-2, 6.93 g methyl acetate, 246 U Novozym 435 and 0.25 g different organic base.

A comparative study of biodiesel production with WDO-2 using three-step methanolysis and one-step transesterification with methyl acetate was also conducted here. The ME yield of the three-step after reaction for 72 h was 69.1%, which was much lower than those of the one-step with or without addition of organic base depicted in **Figure 3**, suggesting that the enzymatic transesterification with methyl acetate was more effective than the enzymatic methanolysis for biodiesel production.

Conclusion

The enzymatic transesterification with methyl acetate was an efficient alternative for the conversion of waste edible oil to corresponding methyl esters. The reaction rate and the ME yield were both effectively improved by addition of organic base to the reaction system.

Acknowledgment. This work was financially supported by Science and Technology Project of Guangdong Province (Grant No. 2003C33102).

References

(1) Ramadhas, A. S.; Jayaraj, S.; Muraleedharan, C. *Fuel*, **2005**, *84* (4), 335-340

(2) Wu, H.; Zong, M. H; Luo, Q.; Wu, H. C. *Prepr. Pap. - Am. Chem. Soc., Div. Fuel Chem.*, **2003**, *48* (2), 533-534

(3) Watanabe, Y.; Shimada, Y.; Sugihara, A.; Tominaga, Y. *J. Am. Oil Chem. Soc.*, **2001**, *78* (7), 703-707

(4) Shimada, Y.; Watanabe, Y.; Samukawa, T.; Sugihara, A.; Noda, H.; Fukuda, H.; Tominaga, Y. *J. Am. Oil Chem. Soc.*, **1999**, *76* (7), 789-792

(5) Dossat, V.; Combes, D.; Marty, A. *Enzyme Microb. Technol.* **1999**, *25* (3-4), 194–200

(6) Xu, Y. Y.; Du, W.; Liu, D. H.; Zeng, J. *Biotechnol. Lett.* **2003**, *25* (15), 1239-1241

(7) Wu, H.; Zong, M. H.; Lou, W. Y. *Chin. J. Catal*., **2004**, *25* (11), 903-908